Wolfgang Domcke
David R Yarkony
Horst Köppel
Editors

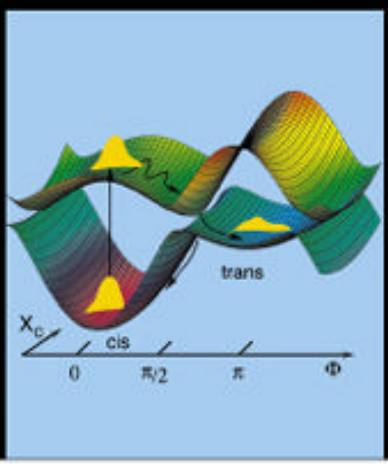

CONICAL INTERSECTIONS

Electronic Structure, Dynamics & Spectroscopy

Advanced Series in Physical Chemistry Vol. 15

Advanced Series in Physical Chemistry 15

CONICAL INTERSECTIONS

Electronic Structure, Dynamics & Spectroscopy

This page intentionally left blank

Advanced Series in Physical Chemistry 15

CONICAL INTERSECTIONS

Electronic Structure, Dynamics & Spectroscopy

Editors

Wolfgang Domcke
Technical University of Munich, Germany

David R Yarkony
Johns Hopkins University, USA

Horst Köppel
University of Heidelberg, Germany

World Scientific

NEW JERSEY • LONDON • SINGAPORE • BEIJING • SHANGHAI • HONG KONG • TAIPEI • CHENNAI

Published by

World Scientific Publishing Co. Pte. Ltd.

5 Toh Tuck Link, Singapore 596224

USA office: 27 Warren Street, Suite 401-402, Hackensack, NJ 07601

UK office: 57 Shelton Street, Covent Garden, London WC2H 9HE

British Library Cataloguing-in-Publication Data
A catalogue record for this book is available from the British Library.

CONICAL INTERSECTIONS: ELECTRONIC STRUCTURE, DYNAMICS & SPECTROSCOPY

ISBN 981-238-672-6

Typeset by Stallion Press
Email: enquiries@stallionpress.com

INTRODUCTION

Many of us who are involved in teaching a special-topic graduate course may have the experience that it is difficult to find suitable references, especially reference materials put together in a suitable text format. Presently, several excellent book series exist and they have served the scientific community well in reviewing new developments in physical chemistry and chemical physics. However, these existing series publish mostly monographs consisting of review chapters of unrelated subjects. The modern development of theoretical and experimental research has become highly specialized. Even in a small subfield, experimental or theoretical, few reviewers are capable of giving an in-depth review with good balance in various new developments. A thorough and more useful review should consist of chapters written by specialists covering all aspects of the field. This book series is established with these needs in mind. That is, the goal of this series is to publish selected graduate texts and stand-alone review monographs with specific themes, focusing on modern topics and new developments in experimental and theoretical physical chemistry. In review chapters, the authors are encouraged to provide a section on future developments and needs. We hope that the texts and review monographs of this series will be more useful to new researchers about to enter the field. In order to serve a wider graduate student body, the publisher is committed to making available the monographs of the series in a paperbound version as well as the normal hardcover copy.

Cheuk-Yiu Ng

This page intentionally left blank

PREFACE

The Born–Oppenheimer adiabatic approximation represents one of the cornerstones of molecular physics and chemistry. The concept of adiabatic potential-energy surfaces, defined by the Born–Oppenheimer approximation, is fundamental to our thinking about molecular spectroscopy and chemical reaction dynamics. Many chemical processes can be rationalized in terms of the dynamics of the atomic nuclei on a single Born–Oppenheimer potential-energy surface. Nonadiabatic processes, that is, chemical processes which involve nuclear dynamics on at least two coupled potential-energy surfaces and thus cannot be rationalized within the Born–Oppenheimer approximation, are nevertheless ubiquitous in chemistry, most notably in photochemistry and photobiology. Typical phenomena associated with a violation of the Born–Oppenheimer approximation are the radiationless relaxation of excited electronic states, photoinduced unimolecular decay and isomerization processes of polyatomic molecules.

During the last few decades, we have witnessed a change of paradigms in nonadiabatic chemistry. First, the remarkable advances achieved in femtosecond laser technology and time-resolved spectroscopy have revealed that the radiationless decay of excited electronic states may take place much faster than previously thought. The traditional theory of radiationless decay processes, developed in the sixties and seventies of the last century, cannot explain electronic decay occurring on a time scale of few tens of femtoseconds. Second, the development and widespread application of multi-reference electronic structure methods for the calculation of excited-state potential-energy surfaces have shown that so-called CONICAL INTERSECTIONS of these multidimensional surfaces, predicted by von Neumann and Wigner in 1929, are the rule rather than

the exception in polyatomic molecules. As a result, the concept of conical intersections has become widely known in recent years. That conical intersections may be responsible for ultrafast radiationless processes has been surmised as early as 1937 by Teller. Nowadays, it is increasingly recognized that conical intersections play a key mechanistic role in molecular spectroscopy and chemical reaction dynamics.

There are a number of intricate issues associated with conical intersections, concerning both the electronic structure, the nuclear dynamics, and the interaction of the molecule with the radiation field. Few of us are familiar with all these aspects of the problem, which have been analyzed in research papers scattered throughout the chemical physics literature. It is the intention of the present book to make this knowledge available to interested graduate students and researchers in the thriving field of femtochemistry.

The chapters of this book are all theoretical in character. This reflects the fact that the conical intersection is a theoretical concept, and as such is not directly accessible to experimental observation. Nevertheless, the concepts, techniques and results discussed in this book are crucial for the interpretation of the observations in time-resolved spectroscopy and chemical kinetics on femtosecond time scales. It is hoped, therefore, that this book is of value not only for the theoretician, but also for the practitioneer in molecular spectroscopy, photochemistry, and collision-induced reaction dynamics.

Wolfgang Domcke, Munich
David R. Yarkony, Baltimore
Horst Köppel, Heidelberg

HISTORICAL INTRODUCTION

Josef Michl
Department of Chemistry and Biochemistry,
University of Colorado,
Boulder, CO 80309-0215

In the last half century, our understanding of the qualitative features of organic photochemistry has undergone a spectacular transformation. In the mid-1900s, the community of chemists investigating light-induced reactions of polyatomic organic molecules was not even sure that the theoretical concepts already well established in the ground electronic state, such as a single potential energy surface dictating nuclear motions, would be applicable to electronically excited molecules. How useful would the Born–Oppenheimer approximation be, given the energetic proximity of other electronic states? Would there be time for vibrational equilibration and could transition state theory be applied? Kasha's and Vavilov's early formulation of their important empirical rule provided a ray of hope that at least the lowest excited state of each multiplicity could be thought of in such familiar terms. Of course, although the existence of metastable excited states was known, their recognition as triplet states and the appreciation of their importance in organic photochemistry were yet to come.

It was clear that in large organic molecules internal conversion from upper to lower excited states occurs on a subpicosecond scale. In the many organic molecules that exhibit no emission, such ultrafast conversion evidently occurred all the way to the ground electronic state, in some cases accompanied by a chemical transformation, in others not. When a chemical transformation did occur, it seemed to be almost always accompanied

by electronic relaxation all the way to the ground state. Only in very few exceptional cases, mostly simple proton transfer reactions, was the chemical product produced in an electronically excited state.

The initial versions of the theory of internal conversion seemed to work fine for the weak coupling cases in which this process was relatively slow and competed with fluorescence or with intersystem crossing to a triplet state. However, this theory did not cast light on the nature of the ultrafast process. Although theoreticians such as Teller[1] in the thirties, Kauzman[2] in the fifties, and Förster[3] in the early seventies seemed to have no doubt that ultrafast internal conversion proceeded by passage through conical intersections, in which potential energy surfaces touch,[4] they did not attempt to provide any guidance as to the nature of molecular geometries at which these points of rapid return occurred. This was first provided by Zimmerman[5] in his reformulation of the Woodward–Hoffman rules. He pointed out that in the Hückel approximation, the ground and excited potential energy surfaces touch at a point located on a symmetry-forbidden path of a pericyclic reaction, providing a natural explanation of the opposite nature of the rules for thermal and photochemical reactions of this type. A general analysis was also provided by Dougherty.[6] Oosterhoff[7] introduced electron repulsion into the theoretical treatment, which caused the exact degeneracy to be avoided along the symmetric path, and his emphasis on the exclusive importance of the resulting minimum in the "doubly excited state" for the interpretation of Woodward–Hoffman rules led to a lively controversy with the rules' authors, who preferred to emphasize the presence or absence of correlation-diagram-imposed barriers in the singly excited state at the start of the reaction path.[8] Michl's experiments led him to conclude that both are important: with a barrier along the way, the pericyclic minimum will not be reached even if it is present, and the "allowed" product will not form unless extra energy is provided (e.g. by a second photon) to pass above the barrier.[9] His 1974 review[10] summarized the state of understanding of the physical nature of processes involved in organic photochemistry at the time and of the qualitative MO arguments that can be used for the rationalization of specific reaction paths. The review referred to conical intersections as "funnels" and emphasized their tendency to occur at biradicaloid geometries, making these the likely starting points for vibrational relaxation after return to the ground state surface, thus permitting the prediction of likely products. It stated that true surface

touching "is a relatively uncommon occurrence and along most paths such crossings, even if 'intended', are more or less strongly avoided". At the time, general searching for geometries of true touching was not computationally feasible, and did not seem to be particularly important: given the higher dimensionality of the regions of near touching, it seemed that most of the internal conversion to the ground state would go through them. The qualitative MO arguments only provided a very approximate notion of what the funnel geometries were likely to be. However, some of the intriguing characteristics of conical intersections, such as dynamic effects, when a fate of a molecule emerging on a ground state surface after passing through a funnel may depend on the direction from which it entered the funnel on the upper surface, were clearly recognized.

In the next phase of development, numerical computations started to play a significant role. Several groups of authors explored conical intersections that are imposed by symmetry and therefore are easy to find. Quite a few were known in very small systems, and Evleth and coauthors apparently were the first to locate them in a large molecule.[11] Salem's extended work on photoreactions of carbonyl compounds[12] advanced Zimmerman's earlier more qualitative notions,[13] and the results of Michl and collaborators for H_4, taken as a model pericyclic entity, rationalized the nature of bonding[14] and cross-bonding[15] that occurs in pericyclic reactions, and the role of excimers in them. Bonačić-Koutecký and Michl later explored several other symmetry-imposed conical intersections related to *cis-trans* isomerization processes[16] and jointly with Koutecký came up with a generalized version[17] of the "3-state model" of biradical structure[18,19] that provided the first qualitative guide for searching for the geometry of a conical intersection starting from a symmetrical geometry, with an application to the primary process in vision.[20]

The modern era in work with conical intersections is characterized by the removal of the condition that a symmetry element be present. It was ushered in by the groups of Yarkony[21] and Ruedenberg,[22] working with small molecules, and the international team of Robb, Bernardi and Olivucci,[23] working with larger organic molecules. Armed with new algorithms and increased computer power, these groups showed that conical intersections are far from "relatively uncommon", as once thought, but instead are very common, and it now appears likely that it will be hard to find an avoided touching of surfaces that does not have a true touching in its vicinity. Of

course, it continues to be true that the dimensionality of the space of near touching is higher than that of true touching.

Robb, Bernardi, and Olivucci have been particularly prolific in identifying conical intersections along the paths of a vast number of organic reactions and refining the detailed understanding of organic reaction paths.[24] They developed a 2-state VB model for the visualization of the origin of the intersections[25] which complements nicely the 3-state MO model[17] mentioned earlier. Additional groups are publishing conical intersection geometries,[26] and although quantitative improvements are needed and can be expected in the future, the computational problem seems to be under control. Discussions of conical intersections have become standard in photochemistry textbooks.[27]

The opening sentence of this introduction stated that our understanding of the qualitative features of organic photochemistry has undergone a spectacular transformation in the last half century, and the above text documents it clearly. How about the quantitative features? We are nowhere near the end of the path. Unlike thermal reactions, whose absolute rates are now fairly predictable from a combination of potential surface calculations and transition state theory and/or modular dynamics, quantitative aspects of organic photochemical reactions, such as quantum yields, still cannot be predicted any better now than half a century ago. Although work on improving our ability to obtain reliable potential energy surfaces clearly has to continue, we need much more before this goal is achieved. We require procedures for the calculation of molecular dynamics on excited state surfaces of polyatomic organic molecules and the requisite nonadiabatic coupling matrix elements, particularly, in the regions of conical intersections. Without such information, we cannot even tell whether all the computational effort that has gone into identifying the lowest energy points in the conical intersection subspace in meaningful — one might guess that the internal conversion is likely to occur as soon as subspace is entered, or even slightly before, at a geometry at which the crossing is still weakly avoided, and that the geometries of the energy minima within the subspace are hardly ever reached.

In a fully quantum mechanical treatment of the issue, the geometry of the point of return to the ground electronic state is not even sharply defined. In short, we may not be doing so vastly better than we did at the time of the 1974 review as we would like to think, and perspectives for the future employment of imaginative theoretical photochemists are bright. At

least, we know much more about what to ask next, and how to go about getting the answers. These activities represent the subject of this book.

References

1. E. Teller, *J. Phys. Chem.* **41**, 109 (1937).
2. W. Kauzmann, *Quantum Chemistry* (Academic Press: New York, 1957) p. 696.
3. Th. Förster, *Pure Appl. Chem.* **24**, 443 (1970).
4. G. Herzberg and H. C. Longuet-Higgins, *Disc. Faraday Soc.* **35**, 77 (1963).
5. H. E. Zimmerman, *J. Am. Chem. Soc.* **88**, 1566 (1966).
6. R. C. Dougherty, *J. Am. Chem. Soc.* **93**, 7187 (1971).
7. W. Th. A. M. van der Lugt and L. J. Oosterhoff, *J. Am. Chem. Soc.* **91**, 6042 (1969).
8. R. B. Woodward and R. Hoffmann, *Angew. Chem. Int. Ed. Engl.* **8**, 781 (1969).
9. J. Michl, *J. Am. Chem. Soc.* **93**, 523 (1971).
10. J. Michl, *Top. Curr. Chem.* **46**, 1 (1974).
11. R. J. Cox, P. Bushnell and E. M. Evleth, *Tetrahedron Lett.* 207 (1990).
12. L. Salem, *J. Am. Chem. Soc.* **96**, 3486 (1974).
13. H. E. Zimmerman, *Adv. Photochem.* **1**, 183 (1963).
14. W. Gerhartz, R. D. Poshusta and J. Michl, *J. Am. Chem. Soc.* **98**, 6427 (1976).
15. W. Gerhartz, R. D. Poshusta and J. Michl, *J. Am. Chem. Soc.* **99**, 4263 (1977).
16. V. Bonačić-Koutecký and J. Michl, *J. Theor. Chim. Acta* **68**, 45 (1985).
17. V. Bonačić-Koutecký, J. Koutecký and J. Michl, *J. Angew. Chem. Int. Ed. Engl.* **26**, 170 (1987).
18. L. Salem and C. Rowland, *Angew. Chem. Int. Ed. Engl.* **11**, 92 (1972).
19. J. Michl, *Mol. Photochem.* **4**, 257 (1972).
20. V. Bonačić-Koutecký, K. Schöffel and J. Michl, *J. Theor. Chim. Acta* **72**, 459 (1987).
21. D. R. Yarkony, *J. Chem. Phys.* **92**, 2457 (1990).
22. G. J. Atchity, S. S. Xantheas and K. Ruedenberg, *J. Chem. Phys.* **95**, 1862 (1991) and reference therein.
23. F. Bernardi, S. De, M. Olivucci and M. A. Robb, *J. Am. Chem. Soc.* **112**, 1737 (1990).
24. For a list of references, see F. Bernardi, M. Olivucci, J. Michl and M. A. Robb, *The Spectrum* **9**, 1 (1996).
25. F. Bernardi, M. Olivucci and M. A. Robb, *Accounts Chem. Res.* **23**, 405 (1990).
26. J. Bentzien and M. Klessinger, *J. Org. Chem.* **59**, 4887 (1994).
27. M. Klessinger and J. Michl, *Excited States and Photochemistry of Organic Molecules* (VCH Publishers: New York, 1995).

This page intentionally left blank

CONTENTS

This page intentionally left blank

PART I

Fundamental Concepts and Electronic Structure Theory

This page intentionally left blank

CHAPTER 1

BORN–OPPENHEIMER APPROXIMATION AND BEYOND

L.S. Cederbaum

Theoretische Chemie, Universität Heidelberg, Im Neuenheimer Feld 229, D-69120 Heidelberg, Germany

Contents

1. Introduction

The purpose of this review article is to present a comprehensive account of what is generally known as the Born–Oppenheimer approximation, its meaning, its implications, its properties, and very importantly also its limitations and how to cure them. This approximation and the underlying idea have been a milestone in the theory of molecules and actually also of electronic matter in general. Still today this approximation is basic to all molecular quantum mechanics and even in those cases where it fails, it remains the reference to which we compare and in terms of which we discuss this failure.

The large mass of a nucleus compared to that of an electron permits an approximate separation of the electronic and nuclear motion. Molecules are complicated quantum objects and this separation greatly simplifies their quantum mechanical treatment. It also allows us to visualize the dynamics of molecules and provides the essential link between quantum mechanics and traditional chemistry. We should be aware that even the notion of molecular electronic states is a consequence of the approximate separability of the electronic and nuclear motion. Without this separability the introduction of molecular electronic states would be relatively useless and just a mathematical construction.

Most of our knowledge on the quality of the Born–Oppenheimer approximation stems from studies of the nuclear motion in the ground electronic state of diatomic and polyatomic molecules and in excited electronic states of diatomics. In diatomics, there is only a single vibrational degree of freedom and the Born–Oppenheimer approximation is accurate in most cases. In polyatomics, the electronic ground state is typically well separated energetically from other electronic states, and this supports the *a priori* validity of the Born–Oppenheimer approximation in these cases. Historically, the picture has thus emerged that this approximation is generally accurate with the exception of some more or less exotic cases. In the last two decades or so, there have been considerable advances in the development of experimental and theoretical techniques and a growing number of polyatomics in their excited electronic states have been investigated. These studies reveal a fast growing number of cases where the Born–Oppenheimer approximation fails. A particularly impressive failure is encountered in situations where so-called conical intersections of the electronic energies exist. For such an

intersection to appear, at least two nuclear coordinates are necessary. For polyatomics with their dense electronic states and many nuclear degrees of freedom, conical intersections of the electronic energies are generic features and their absence is rather unusual. We, therefore, expect to see a growing relevance of conical intersections in the future and shall concentrate in this article on cases where the standard Born–Oppenheimer approximation may fail and discuss its systematic improvement.

2. The Born–Oppenheimer Expansion

The objective of the present section is to provide a general ansatz to solve the Schrödinger equation for problems with several degrees of freedom. The ansatz is particularly efficient if there are slow and fast degrees of freedom. To be specific, we consider molecules where the nuclei and electrons are the slow and fast degrees of freedom, respectively, but shall keep the generality of the approach in mind.

The common molecular Hamiltonian is

$$H = T_n + T_e + U(\mathbf{r}, \mathbf{R}) \tag{1}$$

where T_n and T_e are the kinetic energy operators of the nuclei and electrons, respectively, and $U(\mathbf{r}, \mathbf{R})$ is the total potential energy of the nuclei and the electrons. The vector $\mathbf{r}$ denotes the set of electronic coordinates and $\mathbf{R}$ the set of nuclear coordinates. At the moment, we do not have to be specific about the choice of these coordinates and we will address the matter at several places of this review.

By setting the kinetic energy of the nuclei equal to zero, one defines the familiar electronic Hamiltonian:

$$H_e = T_e + U(\mathbf{r}, \mathbf{R}). \tag{2}$$

Obviously, H_e is an operator in the electronic space that depends parametrically on $\mathbf{R}$. Its eigenvalues $V_i(\mathbf{R})$ and eigenfunctions $\Phi_i(\mathbf{r}, \mathbf{R})$ fulfill

$$H_e \Phi_i(\mathbf{r}, \mathbf{R}) = V_i(\mathbf{R}) \Phi_i(\mathbf{r}, \mathbf{R}). \tag{3}$$

The set of eigenfunctions $\{\Phi_i(\mathbf{r}, \mathbf{R})\}$ form a complete basis in the electronic space at every value of $\mathbf{R}$

$$\sum_i \Phi_i^*(\mathbf{r}', \mathbf{R}) \Phi_i(\mathbf{r}, \mathbf{R}) = \delta(\mathbf{r} - \mathbf{r}') \tag{4a}$$

and we write the orthonormality condition in the form

$$\int \Phi_i^*(\mathbf{r},\mathbf{R})\Phi_j(\mathbf{r},\mathbf{R})d\mathbf{r} \equiv \langle i(\mathbf{R})|j(\mathbf{R})\rangle = \delta_{ij}. \tag{4b}$$

In the bra and ket notation, only the indices i and j are retained, and the dependence of the electronic wavefunctions on the nuclear coordinates is indicated.

Of course, we are interested in solving the Schrödinger equation for the total Hamiltonian in Eq. (1) describing the electronic plus nuclear motion in our system. To this end, we expand the total wavefunction Ψ in the electronic eigenfunctions of H_e:

$$\Psi(\mathbf{r},\mathbf{R}) = \sum_i \Phi_i(\mathbf{r},\mathbf{R})\chi_i(\mathbf{R}). \tag{5}$$

This expansion is known as the Born–Oppenheimer expansion.[1] Formally, Eq. (5) is exact, since the set $\{\Phi_i(\mathbf{r},\mathbf{R})\}$ is complete. It is only when the expansion is truncated that approximations are introduced. The Born–Oppenheimer expansion certainly provides a perfectly valid ansatz if $\Psi(\mathbf{r},\mathbf{R})$ describes a bound state solution of the full Schrödinger equation

$$H\Psi(\mathbf{r},\mathbf{R}) = E\Psi(\mathbf{r},\mathbf{R}). \tag{6}$$

It has been argued, see, for instance,[2] that the ansatz (5) may not be justified for describing continuum states. There are sufficiently many arguments which allow one to take the pragmatic stand point that the Born–Oppenheimer expansion is valid also for continuum states, see, for instance, Ref. 3.

From the Schrödinger Eq. (6) one can easily determine the coupled equations for the expansion coefficients $\chi_i(\mathbf{R})$ in the ansatz (5). Inserting Eq. (5) into (6), multiplying from the left by $\Phi_j^*(\mathbf{r},\mathbf{R})$ and integrating over the electronic coordinates leads to

$$[T_n + V_j(\mathbf{R})]\chi_i(\mathbf{R}) - \sum_i \Lambda_{ji}\chi_i(\mathbf{R}) = E\chi_j(\mathbf{R}) \tag{7a}$$

where the so-called *nonadiabatic couplings* Λ_{ji} describe the dynamical interaction between the electronic and nuclear motion. They are given by

$$\Lambda_{ji} = \delta_{ji}T_n - \langle j(\mathbf{R})|T_n|i(\mathbf{R})\rangle \tag{7b}$$

and are obviously operators in $\mathbf{R}$-space.

To proceed, we need a specific form of the nuclear kinetic energy operator. Using atomic units and conveniently scaled rectangular nuclear coordinates, we may express T_n as follows

$$T_n = -\frac{1}{2M}\boldsymbol{\nabla}\cdot\boldsymbol{\nabla} = -\frac{1}{2M}\boldsymbol{\nabla}^2 \tag{8}$$

where the gradient $\boldsymbol{\nabla}$ is a vector in nuclear space and the dot denotes the usual scalar product. M is an averaged nuclear mass, see Sec. 5.2, where an explicit choice of nuclear coordinates is discussed. Of course, in certain cases one may wish to choose more general nuclear coordinates and express the Laplacian in these coordinates. When better adapted to the geometric structure at hand, these coordinates will be curvilinear and the Laplacian (see, e.g. Ref. 4) and the nonadiabatic couplings (see Ref. 5) will have a more involved appearance.

With the definition (8), we readily obtain the following explicit form for the nonadiabatic couplings:

$$\Lambda_{ji} = \frac{1}{2M}[2\mathbf{F}_{ji}\cdot\boldsymbol{\nabla} + G_{ji}]. \tag{9a}$$

These elements split into a derivative operator and a c-number. The nonadiabatic *derivative couplings* are given by

$$\mathbf{F}_{ji}(\mathbf{R}) = \langle j(\mathbf{R})|\boldsymbol{\nabla} i(\mathbf{R})\rangle \tag{9b}$$

and are obviously vectors in the nuclear coordinate space. The nonadiabatic *scalar couplings* G_{ji} take on the following appearance

$$G_{ji}(\mathbf{R}) = \langle j(\mathbf{R})|\boldsymbol{\nabla}^2 i(\mathbf{R})\rangle. \tag{9c}$$

Note that some authors define the scalar couplings with a different sign than done here.

It is illuminating to express the coupled equations of nuclear motion in matrix notation. To this end, we define a diagonal matrix $\mathbf{V}$ of adiabatic potential energy with diagonal elements $V_j(\mathbf{R})$, which are the electronic energies in Eq. (3), a matrix $\mathbf{G}$ with matrix elements G_{ji}, and a matrix $\mathbf{F}$ with matrix element $\mathbf{F}_{ji}$. We recall that the latter quantities are vectors in nuclear space. We may thus view $\mathbf{F}$ as a matrix in electronic space, where each element is a vector in nuclear space, or, equivalently, as a vector in nuclear space with components which are matrices in electronic space. $\mathbf{F}$ may be called a *vector matrix*. Furthermore, $\boldsymbol{\chi}$ denotes a column vector with components $\boldsymbol{\chi}_j$, and ∇ in our matrix notation is also a vector matrix,

though a trivial one. It is the usual gradient in nuclear space, multiplied by the unit matrix in electronic space. Using the above straightforward notation, it is possible to rewrite the equations of nuclear notion (7) in the following appealing form:[5]

$$\left[-\frac{1}{2M}(\boldsymbol{\nabla}+\mathbf{F})^2+\mathbf{V}-E\right]\boldsymbol{\chi}=0. \tag{10}$$

This equation provides a natural theoretical formulation of the nuclear motion. Showing some analogy to gauge theories,[6,7] it is a helpful starting point for further investigations (see also Sec. 4).

The formulation (10) demonstrates that the coupled motion of electrons and nuclei can be reduced to the study of nuclear motion in the matrix potential $\mathbf{V}$. The impact of the coupling on the electronic motion has been transferred to the "dressed" kinetic energy operator, which now reads $-(1/2M)(\boldsymbol{\nabla}+\mathbf{F})^2$, instead of $-(1/2M)\boldsymbol{\nabla}^2$ for the "bare" nuclei.

For completeness, we would like to list below the relevant relations of the nonadiabatic couplings. These follow immediately from the definitions (9) and the orthonormalization (4b) of the electronic states:

$$\mathbf{F}^\dagger=-\mathbf{F} \tag{11a}$$

$$\mathbf{G}=(\boldsymbol{\nabla}\cdot\mathbf{F})+\mathbf{F}\cdot\mathbf{F} \tag{11b}$$

$$(\boldsymbol{\nabla}\cdot\mathbf{F})^\dagger=-(\boldsymbol{\nabla}\cdot\mathbf{F}) \tag{11c}$$

$$\boldsymbol{\nabla}\cdot\mathbf{F}=(\boldsymbol{\nabla}\cdot\mathbf{F})+\mathbf{F}\cdot\boldsymbol{\nabla} \tag{11d}$$

$$(2\mathbf{F}\cdot\boldsymbol{\nabla}+\mathbf{G})^\dagger=2\mathbf{F}\cdot\boldsymbol{\nabla}+\mathbf{G} \tag{11e}$$

$$\frac{\partial}{\partial R_\alpha}\mathbf{F}_\beta-\frac{\partial}{\partial R_\beta}\mathbf{F}_\alpha+[\mathbf{F}_\alpha,\mathbf{F}_\beta]=0. \tag{11f}$$

Here, a few comments are in order. The matrix of derivative couplings $\mathbf{F}$ is *antihermitian*. The matrix of scalar couplings $\mathbf{G}$ is composed of an hermitian as well as an antihermitian part. Of course, the dressed kinetic energy operator $-(1/2M)(\boldsymbol{\nabla}+\mathbf{F})^2$ in our basic Eq. (10) is hermitian, as is also the case for the nonadiabatic couplings Λ in Eq. (9a). The latter follows immediately from the relation (11e). The notation $(\boldsymbol{\nabla}\cdot\mathbf{F})$ is self evident from Eq. (11d). Since $\mathbf{F}$ is a vector matrix, it can be written as $\mathbf{F}=(\mathbf{F}_1,\mathbf{F}_2,\ldots,\mathbf{F}_{N_n})$, where the matrices $\mathbf{F}_\alpha$ are simply defined by their

matrix elements

$$(\mathbf{F}_\alpha)_{ji} = \left\langle j(\mathbf{R}) \middle| \frac{\partial}{\partial R_\alpha} i(\mathbf{R}) \right\rangle \tag{12}$$

and $\mathbf{R} = (R_1, R_2, \ldots, R_{N_n})$ are the N_n nuclear coordinates of the system under consideration. The relation (11f) plays an important role in the construction of diabatic states,[5,8] see also Sec. 4.

The equation of motion of the nuclei (10) and the relations (11) are valid for both real and complex choices of the electronic wavefunctions $\Phi_i(\mathbf{r}, \mathbf{R})$ and expansion quantities $\boldsymbol{\chi}_i(\mathbf{R})$. If these quantities are chosen to be real, the derivative coupling matrix $\mathbf{F}$ vanishes along its diagonal because of the antisymmetric nature of this matrix. In contrast, the scalar coupling matrix $\mathbf{G}$ contributes to the diagonal part of the dressed kinetic energy operator via its symmetric component $\mathbf{F} \cdot \mathbf{F}$, see Eq. (11b). If, on the other hand, the electronic wavefunctions are chosen to be complex functions, the derivative couplings do contribute to the diagonal of the dressed kinetic energy operator. In some cases, for instance, in the presence of an external magnetic field, the electronic wavefunctions are in general necessarily complex functions,[9,10] see also Sec. 6.1. In other cases we may choose them to be complex for convenience.

To this end, let us introduce a phase factor for each electronic state

$$\tilde{\Phi}_j(\mathbf{r}, \mathbf{R}) = e^{i\varphi_j(\mathbf{R})} \Phi_i(\mathbf{r}, \mathbf{R}) \tag{13}$$

thus defining new wavefunctions $\tilde{\Phi}_j$. These new wavefunctions are also eigenfunctions of the electronic Hamiltonian H_e and fulfill all the equations above. In particular, the equation of nuclear motion (10) and the relations (11) are valid when the new functions are used instead of the original ones. It is interesting to express the equation of nuclear motion in terms of the original derivative couplings $\mathbf{F}$ and the phases $\varphi_j(\mathbf{R})$. The result reads

$$\left[-\frac{1}{2M} [\boldsymbol{\nabla} + \mathbf{F} + 2i(\boldsymbol{\nabla}\varphi)]^2 + \mathbf{V} - E \right] \boldsymbol{\chi} = 0 \tag{14}$$

where $(\boldsymbol{\nabla}\varphi)$ is a diagonal vector matrix with elements $(\boldsymbol{\nabla}\varphi_i) \cdot \delta_{ij}$. Since the phases $\varphi_j(\mathbf{R})$ are at our disposal, we may choose them to simplify or improve the calculations, for instance, to make the $\tilde{\Phi}_j$ single valued in cases where the Φ_j are not.[18]

3. The Born–Oppenheimer Approximation

3.1. *Separation of Electronic and Nuclear Motion*

If the Hamiltonian were truly separable in the degrees of freedom defined by $\mathbf{r}$ and $\mathbf{R}$, the solution of the Schrödinger equation would, of course, be a product of a function of $\mathbf{r}$ and a function of $\mathbf{R}$. The separability one has in mind when discussing electronic systems is of a different origin, however. It relies on the different masses of the underlying particles and hence on their different velocities. The fast electrons can instantly adjust to the slow nuclei and, consequently, their wavefunction depends parametrically on the coordinates of the nuclei. The total wavefunction thus reads:

$$\Psi(\mathbf{r}, \mathbf{R}) = \Phi(\mathbf{r}, \mathbf{R})\boldsymbol{\chi}(\mathbf{R}). \tag{15}$$

Inserting this *adiabatic ansatz* into the Schrödinger Eq. (6), followed by multiplication from the left with Φ^* and integration over the electronic coordinates, immediately leads to the following equation for the nuclear motion

$$[T_n - \Lambda + V(\mathbf{R})]\boldsymbol{\chi}(\mathbf{R}) = E\boldsymbol{\chi}(\mathbf{R}) \tag{16}$$

in the electronic state under consideration. For simplicity, we have dropped the index of the electronic state. Clearly, this equation also follows from the general Eq. (7a), when all nondiagonal elements of the nonadiabatic couplings Λ_{ji}, $j \neq i$, in (7b) are put to zero. If the electronic wavefunction Φ is taken to be real, the derivative coupling $\mathbf{F}$ vanishes, and $\Lambda = G/2M$, as is seen from Eqs. (9). The resulting equation is called *Born–Oppenheimer approximation*.[11] If, on the other hand, the electronic wavefunction is complex, either by its nature or by choice (see preceding subsection), the element Λ in Eq. (16) contains derivative couplings. When the electronic wavefunction is deliberately chosen complex, it is appropriate to call Eq. (16) the *complex Born–Oppenheimer approximation*, to distinguish it from the common, i.e. real equation.

In which cases is the adiabatic ansatz (15) expected to be accurate? As shall become clear in the next subsection and from the discussion in Sec. 5, the adiabatic ansatz is accurate for an electronic state which is well separated energetically from all other electronic states. Under the same electronic conditions, the ansatz improves with increasing nuclear mass. On the other hand, we can expect that the larger the energetical distance of

the other electronic states is from the state under investigation, the weaker the dependence of $\Phi(\mathbf{r}, \mathbf{R})$ on the nuclear coordinates. This immediately implies that the nonadiabatic term Λ is the smaller, the better the ansatz (15) is. Neglecting Λ in Eq. (16) leads to

$$[T_n + V(\mathbf{R})]\boldsymbol{\chi}(\mathbf{R}) = E\boldsymbol{\chi}(\mathbf{R}) \tag{17}$$

which is commonly called the *Born–Oppenheimer adiabatic approximation*[11] or briefly the *adiabatic approximation*. The above discussion also implies that as long as Λ is small, its inclusion does provide an improvement to the adiabatic approximation. However, once Λ is sizeable, the adiabatic ansatz (15) itself and hence also (16) become doubtful. A sizeable Λ indicates in turn sizeable derivative couplings [see Eq. (11b)] and, consequently, other electronic states may be intruding (see next subsection).

3.2. *Group-Born–Oppenheimer Approximation*

The nonadiabatic couplings enter the nuclear equation of motion scaled by $1/M$ — see Eqs. (7) and (9) — and one is tempted to assume their impact to be small. A more precise analysis on their scaling with the nuclear mass will be given in Sec. 5. Indeed, if we assume the $\mathbf{F}_{ji}$ to be of the order of unity, the impact on the nuclear motion would be small and the adiabatic approximation discussed in the preceding subsection would be highly accurate. This is, unfortunately, not the case. By applying the gradient $\boldsymbol{\nabla}$ to the electronic Schrödinger equation (3), one readily obtains from the definition (9b) the following useful expression for the derivative couplings ($i \neq j$):

$$\mathbf{F}_{ji}(\mathbf{R}) = \frac{\langle j(\mathbf{R})|(\boldsymbol{\nabla} H_e)|i(\mathbf{R})\rangle}{V_i(\mathbf{R}) - V_j(\mathbf{R})}. \tag{18}$$

Apart from special cases, e.g. where the numerator vanishes due to spatial symmetries of the involved electronic states and nuclear coordinates, there is no reason to assume that it takes on particularly small or large values in general. However, the denominator does inform us on the situations in which the derivative couplings become large. In the vicinity of a degeneracy, the derivative couplings can be substantial and the adiabatic approximation for the involved electronic states can be expected to break down. In particular, in the presence of conical intersections of the potential surfaces $V_i(\mathbf{R})$ and $V_j(\mathbf{R})$, the nonadiabatic derivative couplings diverge and the adiabatic approximation becomes meaningless[12] (see also Chapter 2).

From the above we may expect the adiabatic approximation to be appropriate for electronic states well separated energetically from other electronic states to which they may couple. Equations (10) and (18) also provide us with straightforward extensions of this approximation. Let us assume that a group of electronic states are well separated energetically from all other states to which they may couple. We denote the subspace of the full electronic space spanned by this group by g. Clearly, the energy gap between g and its complement has only to be large in the relevant range of nuclear coordinates. In analogy to the Born–Oppenheimer approximation, where the matrix nuclear Schrödinger equation (10) has been limited to a single electronic state, we obtain a truncated version of this equation for the group g of states under consideration:[5]

$$\left[-\frac{1}{2M}\{(\boldsymbol{\nabla}+\mathbf{F})^2\}^{(g)}+\mathbf{V}^{(g)}-E\right]\boldsymbol{\chi}^{(g)}=0. \tag{19}$$

The superscript g denotes the truncated quantities; both matrices and vectors now refer only to the group g of electronic states. Due to the above considerations, we call this useful result the *group-Born–Oppenheimer approximation*. It should be clear that truncating Eq. (10) is equivalent to truncating Eq. (7a).

It is worthwhile to have a closer look at Eq. (19). Because of the quadratic structure of the dressed kinetic energy operator, $-(1/2M)(\boldsymbol{\nabla}+\mathbf{F})^2$, its block in the space spanned by the states belonging to g cannot be written as a single quadratic term, but rather as a sum of two quadratic terms

$$\{(\boldsymbol{\nabla}+\mathbf{F})^2\}^{(g)}=(\boldsymbol{\nabla}+\mathbf{F}^{(g)})^2-\mathbf{F}^{(c)}\cdot\mathbf{F}^{(c)\dagger}. \tag{20}$$

$\mathbf{F}^{(g)}$ is that part of the full vector matrix $\mathbf{F}=\{\langle j(\mathbf{R})|\boldsymbol{\nabla}i(\mathbf{R})\rangle\}$ where $|i\rangle$ and $\langle j|$ belong to our group g. The coupling between the group g and the rest of the electronic Hilbert space is given by $\mathbf{F}^{(c)}=\{\langle j(\mathbf{R})|\boldsymbol{\nabla}k(\mathbf{R})\rangle\}$, where $\langle j|$ belongs to g and $|k\rangle$ to the complement of g. We may now make use of Eq. (20) to rewrite Eq. (19) and obtain

$$\left[-\frac{1}{2M}(\boldsymbol{\nabla}+\mathbf{F}^{(g)})^2+\mathbf{W}^{(g)}-E\right]\boldsymbol{\chi}^{(g)}=0 \tag{21a}$$

where the matrix Hamiltonian is now in g space only, i.e. its elements i, j refer to states in our set g, and we have dropped the superscript for brevity

from $\boldsymbol{\nabla}$ and E. The quantities

$$W_{ji}^{(g)}(\mathbf{R}) = V_i^{(g)}(\mathbf{R})\delta_{ij} + \frac{1}{2M}\sum_{k\notin g}\langle\boldsymbol{\nabla} j(\mathbf{R})|k(\mathbf{R})\rangle\langle k(\mathbf{R})|\boldsymbol{\nabla} i(\mathbf{R})\rangle \tag{21b}$$

are the elements of the *dressed potential matrix* $\mathbf{W}^{(g)}$. In deriving (21b), we have used the antihermitian property (11a) of derivative couplings.

To compute the dressed potential surface, it is convenient to introduce the projector $\hat{P}^{(g)}$ which projects on the subset of electronic states g. Introducing

$$\hat{P}^{(g)} = \sum_{i\in g}|i(\mathbf{R})\rangle\langle i(\mathbf{R})| \tag{22a}$$

leads to

$$W_{ji}^{(g)}(\mathbf{R}) = V_i^{(g)}(\mathbf{R})\delta_{ij} + \frac{1}{2M}\langle\boldsymbol{\nabla} j(\mathbf{R})|(1-\hat{P}^{(g)})|\boldsymbol{\nabla} i(\mathbf{R})\rangle \tag{22b}$$

which can be evaluated within the group g of states without summing over the formally infinite set of states $|k\rangle$ which do not belong to g. Equation (22b) is often even simpler than it looks. For instance, if our group of coupled states contains two members — and this is a widespread situation — then the *non*diagonal term reduces to $W_{ji}^{(g)} = 1/2M\langle\boldsymbol{\nabla} j|\boldsymbol{\nabla} i\rangle$ because of the orthogonality relation (4b) (real electronic wavefunctions are assumed).

Let us return to the group-Born–Oppenheimer approximation (21a) and pay further attention to the corrections in (21b) due to the rest of the electronic states. From the definition of the derivative coupling (9b) and the expression (18), we may conclude that these corrections have only a weak impact on the nuclear dynamics in the g-manifold of states. The derivative couplings in (21b) connect states within this manifold with states outside the manifold, separated by a substantial energy gap. Furthermore, these couplings are weighted by $1/2M$ in Eq. (21b). The situation is actually equivalent to that discussed in the preceding subsection. By including a single state in our group g of states, Eq. (21a) boils down to Eq. (16), which — in particular for real electronic wavefunctions — is the well-known Born–Oppenheimer approximation. This can be easily seen by using the relations (9a) and (11b).

In analogy to Sec. 3.1, we may neglect in many cases to a good approximation the difference between the naked and the dressed potential matrices

$\mathbf{V}^{(g)}(\mathbf{R})$ and $\mathbf{W}^{(g)}(\mathbf{R})$. This leads to the following simplified equation of motion for the nuclei in the manifold g of coupled electronic states

$$\left[-\frac{1}{2M}(\boldsymbol{\nabla}+\mathbf{F}^{(g)})^2+\mathbf{V}^{(g)}-E\right]\boldsymbol{\chi}^{(g)}=0. \tag{23}$$

Note that the potential matrix $\mathbf{V}^{(g)}(\mathbf{R})$ is a diagonal matrix by definition, in contrast to $\mathbf{W}^{(g)}(\mathbf{R})$. Again, in analogy to the common treatment in Sec. 3.1, we call (23) the *group-Born–Oppenheimer adiabatic approximation* or briefly the *group-adiabatic approximation*. This approximation assumes that the states within the manifold g are much stronger coupled to each other — e.g. via the presence of a conical intersection of the potential surfaces — than to the rest of the electronic space.

Additional properties of the nonadiabatic couplings are discussed in Sec. 4.

4. Gauge Potentials and Quasidiabatic States

4.1. *Gauge Invariance of Group-Born–Oppenheimer Approximation*

The full Eq. (10) and its group-Born–Oppenheimer approximation (21a) are natural gauge theoretical formulations of the nuclear motion.[5] Gauge theories are widely used in other fields, e.g. elementary particle physics,[7,13] the simplest one in electrodynamics, where the vector potential appears.[4] We mention that there are also some other attempts in molecular physics and quantum chemistry[6,14–16] and that an intimate relation exists between gauge theory and the geometric phase in adiabatic transport in quantum systems.[17–19] In the presence of a conical intersection, this geometric phase leads to the well-known sign change of the adiabatic electronic wavefunction,[20] which has stimulated the first investigation of gauge potentials in the context of the Born–Oppenheimer approximation.[21]

It is beyond the scope of this work to enter the subject of gauge theory deeply. We shall only illustrate some results relevant to the group-Born–Oppenheimer approximation. For more details we refer to Ref. 5 and references therein.

There is always a freedom of choice in using basis sets. In the preceding sections we have used as basis set the eigenfunctions Φ_i of the electronic Hamiltonian H_e, see Eq. (3). If we transform these basis functions to a new

basis set $\tilde{\Phi}_i$ by a unitary transformation $\mathbf{U}^{(g)}$, $\mathbf{U}^{(g)}\mathbf{U}^{(g)\dagger} = 1$, this implies that we have transformed the nuclear wavefunction according to

$$\tilde{\boldsymbol{\chi}}^{(g)} = \mathbf{U}^{(g)\dagger}\boldsymbol{\chi}^{(g)} \tag{24}$$

because of the invariance of the total wavefunction $\Psi(\mathbf{r}, \mathbf{R})$ in Eq. (5). The question immediately arises whether such a transformation leaves invariant the form of the matrix Schrödinger equation (21a) in our subspace g of interacting electronic states. If the answer is positive, one says that this equation or equivalently the group-Born–Oppenheimer approximation is *gauge invariant* under the gauge transformation $\mathbf{U}^{(g)}$. Of particular interest is, of course, the case where this transformation depends parametrically on the nuclear coordinates $\mathbf{R}$:

$$\mathbf{U}^{(g)}(\mathbf{R})\mathbf{U}^{(g)\dagger}(\mathbf{R}) = 1. \tag{25}$$

It has been shown in Ref. 5 that the electronic basis set transformation leads to the following matrix Schrödinger equation:

$$\left[-\frac{1}{2M}(\nabla + \tilde{\mathbf{F}}^{(g)})^2 + \tilde{\mathbf{W}}^{(g)} - E\right]\tilde{\boldsymbol{\chi}}^{(g)} = 0. \tag{26}$$

In other words, the group-Born–Oppenheimer is a gauge invariant approximation. In the above equation, the dressed potential transforms as

$$\tilde{\mathbf{W}}^{(g)} = \mathbf{U}^{(g)\dagger}\mathbf{W}^{(g)}\mathbf{U}^{(g)}; \tag{27a}$$

in addition, the relevant relation

$$\tilde{\mathbf{F}}^{(g)} = \mathbf{U}^{(g)\dagger}\mathbf{F}^{(g)}\mathbf{U}^{(g)} + \mathbf{U}^{(g)\dagger}(\nabla\mathbf{U}^{(g)}) \tag{27b}$$

holds for the nonadiabatic derivative couplings in the new electronic basis. Since we did not specify the set g of interacting states, the above also holds for the full matrix Schrödinger equation (10); we just have to drop the superscript g. Equation (10) is thus also gauge invariant. It is important that the full equation and the truncated one share the basic property of gauge invariance.

To facilitate the above, let us consider explicitly the common case in which g contains two electronic states Φ_1 and Φ_2 which are taken to be

real. The matrix of derivative couplings then reads

$$\mathbf{F}^{(g)} = \begin{pmatrix} \mathbf{0} & \boldsymbol{\tau} \\ -\boldsymbol{\tau} & \mathbf{0} \end{pmatrix} \tag{28}$$

where $\boldsymbol{\tau}(\mathbf{R}) = \langle \Phi_i | \boldsymbol{\nabla} \Phi_2 \rangle$. The most general gauge transformation is

$$\mathbf{U}^{(g)}(\mathbf{R}) = \begin{pmatrix} \cos\lambda(\mathbf{R}) & \sin\lambda(\mathbf{R}) \\ -\sin\lambda(\mathbf{R}) & \cos\lambda(\mathbf{R}) \end{pmatrix}. \tag{29}$$

It is easy to show that

$$\tilde{\boldsymbol{\tau}} = \boldsymbol{\nabla}\lambda + \boldsymbol{\tau}. \tag{30a}$$

Here, $\tilde{\boldsymbol{\tau}} = \langle \tilde{\Phi}_1 | \boldsymbol{\nabla} \tilde{\Phi}_2 \rangle$ is just the derivative coupling in the transformed electronic basis. Hence, Eq. (27b) now takes on the explicit appearance

$$\tilde{\mathbf{F}}^{(g)} = \begin{pmatrix} 0 & \tilde{\boldsymbol{\tau}} \\ -\tilde{\boldsymbol{\tau}} & 0 \end{pmatrix} = \begin{pmatrix} 0 & \boldsymbol{\tau} \\ -\boldsymbol{\tau} & 0 \end{pmatrix} + \begin{pmatrix} 0 & 1 \\ -1 & 0 \end{pmatrix} \cdot \boldsymbol{\nabla}\lambda. \tag{30b}$$

A general remark on the transformed dressed potential in Eq. (27a) is also in order. According to Eq. (22b), the potential matrix $\mathbf{W}^{(g)}$ consists of the diagonal matrix $\mathbf{V}^{(g)}$ of the electronic energies and a, in general non-diagonal, correction matrix. By transforming to a new electronic basis, the matrix $\mathbf{V}^{(g)}$, of course, becomes a nondiagonal matrix of potential energies which we denote by $\tilde{\mathbf{V}}^{(g)}$. What happens to the correction matrix? Because of the projection operator in Eq. (22b), this matrix retains its form by the gauge transformation. We obtain the general relation:

$$\tilde{W}_{ji}^{(g)} = \tilde{V}_{ji}^{(g)} + \frac{1}{2M} \langle \boldsymbol{\nabla} \tilde{j}(\mathbf{R}) | (1 - \hat{\tilde{P}}^{(g)} | \boldsymbol{\nabla} \tilde{i}(\mathbf{R}) \rangle \tag{31}$$

which obviously also holds in our above explicit example of two states.

4.2. *Strictly Diabatic and Quasidiabatic Electronic States*

It is often cumbersome to solve the group-Born–Oppenheimer equation (21a) because of the terms $\mathbf{F}^{(g)} \cdot \boldsymbol{\nabla}$. Furthermore, these terms describe the coupling between electronic states in our g manifold via the momenta of the nuclei, and we commonly have more experience in understanding the impact of couplings via potentials than via momenta. It has, therefore, been popular and desirable, starting already many decades ago, to formulate the nuclear equations of motion in a so called diabatic electronic basis instead of the adiabatic one, which we have used above in Secs. 2

and 3.[22–26] Thereby these diabatic electronic states have been *a priori* assumed to depend so weakly on the nuclear coordinates that the derivative couplings can be considered small or even put exactly to zero. The basic question arises whether we can indeed eliminate the derivative couplings by choosing an appropriate basis of electronic states. Following previous work, we call a basis *strictly diabatic* if in that basis the derivative couplings vanish[8,27,28] and *quasidiabatic*, if in that basis these couplings are small, but not zero.[5]

The gauge invariance of the group-Born–Oppenheimer approximation provides a good starting point to discuss diabatic states. In contrast to Eq. (21a), where this approximation is formulated in the adiabatic electronic basis, Eq. (26) is expressed in an arbitrary basis. Elimination of the derivative couplings appearing in the latter equation amounts to setting to zero the left hand side of Eq. (27b):

$$\mathbf{F}^{(g)}\mathbf{U}^{(g)} + (\boldsymbol{\nabla}\mathbf{U}^{(g)}) = 0. \tag{32}$$

Note that $\mathbf{F}^{(g)}$ is the vector matrix of derivative couplings in the adiabatic electronic basis and the gauge transformation $\mathbf{U}^{(g)}(\mathbf{R})$ is the unitary transformation matrix connecting the adiabatic and diabatic basis sets. In the above example of two real electronic states, Eq. (32) is identical to Eq. (30a) where $\tilde{\boldsymbol{\tau}}$ is set to zero:

$$\boldsymbol{\nabla}\lambda + \boldsymbol{\tau} = 0. \tag{33}$$

Does Eq. (32) have a solution or, equivalently, do strictly diabatic states exist? There are two limiting cases where the answer to this question is obviously positive. If our set g of interacting electronic states contains all electronic states, then we can transform the adiabatic electronic states $\Phi_i(\mathbf{r}, \mathbf{R})$ to a set $\tilde{\Phi}_i(\mathbf{r})$ which does not depend parametrically on the nuclear coordinates. In this complete basis set of so called *crude adiabatic* functions,[29] the derivative couplings definitely vanish. The other limiting case is obtained by restricting ourselves to a single nuclear coordinate, say R_α, keeping all other coordinates frozen at arbitrary values. Along this path R_α we can just integrate Eq. (33) over R_α, determine $\lambda = \lambda(R_\alpha)$ and obtain via Eq. (29), a strictly diabatic basis along the path. Diatomics provide natural examples for this limiting case.

In general, no strictly diabatic basis exists in a finite set g of interacting electronic states.[8,27,30] To see this, let us return to Eqs. (27b) and (32) and

introduce the quantities

$$\mathbf{A}^{(g)}_{\alpha\beta} = \frac{\partial \mathbf{F}^{(g)}_{\beta}}{\partial R_\alpha} - \frac{\partial \mathbf{F}^{(g)}_{\alpha}}{\partial R_\beta} + [\mathbf{F}^{(g)}_{\alpha}, \mathbf{F}^{(g)}_{\beta}] \tag{34}$$

which are the α, β components of the so called *gauge field tensor*.[4,7,13] A necessary and sufficient condition for the existence of a solution of Eq. (32), and hence of a strictly diabatic basis, is the equality $\partial^2 \mathbf{U}^{(g)}/\partial R_\alpha \partial R_\beta = \partial^2 \mathbf{U}^{(g)}/\partial R_\beta R_\alpha$. Using Eq. (32), this immediately implies that all the components of the gauge field tensor have to vanish: $\mathbf{A}^{(g)}_{\alpha\beta} = 0$. This condition is, in general, only fulfilled in the complete electronic space and not in a subspace g; see the relation (11f) for derivative couplings. From the latter relation, it is easy to show that

$$\mathbf{A}^{(g)}_{\alpha\beta} = \mathbf{F}^{(c)}_{\alpha}\mathbf{F}^{(c)\dagger}_{\beta} - \mathbf{F}^{(c)}_{\beta}\mathbf{F}^{(c)\dagger}_{\alpha} \tag{35}$$

where $\mathbf{F}^{(c)}$ comprises the derivative couplings between g and the complementary space and has been introduced in Eq. (20).

We briefly reformulate the above necessary and sufficient condition for the existence of a strictly diabatic basis in the context of gauge theory. In contrast to the gauge potential $\mathbf{F}^{(g)}$, which transforms in a relatively complicated manner via Eq. (27b), the gauge field tensor $\mathbf{A}^{(g)}$ simply transforms as

$$\tilde{\mathbf{A}}^{(g)} = \mathbf{U}^{(g)}\mathbf{A}^{(g)}\mathbf{U}^{(g)}. \tag{36}$$

This can be shown using Eqs. (34) and (27b), i.e. the gauge field tensor is gauge invariant. Single valuedness of the electronic basis requires that $\mathbf{A}^{(g)} = 0$[5,13,16] and because of Eq. (36), the gauge field tensor vanishes for all unitary transformations. It can generally be shown that the gauge potential can be eliminated by a gauge transformation, once the gauge field tensor is zero.[13]

Owing to Eq. (35), there is no reason to expect that a strictly diabatic basis exists. Nevertheless, one can construct quasidiabatic states which are extremely useful in solving and understanding many relevant problems abundantly discussed in the literature. With their help it is possible to remove a substantial part of the derivative couplings and make the group-Born–Oppenheimer Eq. (26) more transparent and better amenable to explicit numerical calculations. That part of the derivative couplings which can be removed by an unitary transformation $\mathbf{U}^{(g)}(\mathbf{R})$ is called

the *removable* part, and the remaining part the *nonremovable* part. In the important two-state case, these parts of the derivative couplings have been analyzed in some detail.[5,8] In general, we may not expect to have eliminated even the removable part exactly, and it is convenient to denote the sum of all the remaining parts the *residual couplings*. Of course, as long as we insert the residual couplings $\tilde{\mathbf{F}}^{(g)}$ into Eq. (26), our solution is equivalent to that of the original Eq. (21a). It is only if we neglect the residual couplings that we have to check whether they are large or small.

In this context, let us briefly return to the two-state case. As discussed above, strictly diabatic states exist in one dimension, e.g. for a diatomic molecule with interatomic distance R. In a typical situation, the adiabatic potentials exhibit an avoided crossing and the diabatic potentials cross each other once a function of R. Assuming that the derivative couplings vanish at infinite internuclear distance, and using Eq. (30) then gives

$$\int \tau(R) dR = -\int \frac{d\lambda}{dR} dR = -\pi \tag{37}$$

and no residual coupling is found. In different situations, similarly simple results are obtained. With the aid of the same equation and $d\lambda = \sum_\alpha \partial\lambda/\partial R_\alpha \cdot dR_\alpha$, we obtain

$$\sum_\alpha \int \mathbf{F}_\alpha^{(g)} dR_\alpha = \pi \begin{pmatrix} 0 & -1 \\ 1 & 0 \end{pmatrix} + \sum_\alpha \int \tilde{\mathbf{F}}_\alpha^{(g)} dR_\alpha \tag{38}$$

which provides an idea about the overall size of the residual couplings if *ab initio* data on the couplings $\mathbf{F}^{(g)}$ are available. For such data see, for instance, Ref. 31.

To arrive at a quantitative criterion for quasidiabaticity, it has been proposed[5] to minimize the integral of $\|\tilde{\mathbf{F}}^{(g)}\|^2$, which is the Euclidean norm for matrices, over the nuclear coordinates. This natural requirement leads to the simple equation[5]

$$\boldsymbol{\nabla} \cdot \tilde{\mathbf{F}}^{(g)} = 0 \tag{39}$$

for the diabatic states, which in the language of gauge theory can be called *Lorentz gauge*. In the two-state case, it has been shown that this gauge is the best possible gauge, i.e. transforming to the Lorentz gauge eliminates from the derivative couplings what can be eliminated. The removable part is removed, and one is left only with the nonremovable part. We call the states which result from the above criterion *optimal quasidiabatic* states.

The expression (18) has been useful in assessing the relevance of the derivative couplings in the adiabatic electronic basis. What to expect for the residual couplings? By differentiating both sides of the identity $\tilde{V}_{ji}^{(g)} = \langle \tilde{j}|H_e|\tilde{i}\rangle$ with respect to the nuclear coordinates, we obtain the following expression ($i \neq j$):

$$\tilde{\mathbf{F}}_{ji}^{(g)}(\mathbf{R}) = \frac{\langle \tilde{j}|(\boldsymbol{\nabla} H_e)|\tilde{i}\rangle - \boldsymbol{\nabla}\tilde{V}_{ji}^{(g)}}{\tilde{V}_{jj}^{(g)} - \tilde{V}_{ii}^{(g)}}. \tag{40}$$

Here, the $\tilde{V}_{ji}^{(g)}(\mathbf{R})$ are the elements of the potential energy matrix in the quasidiabatic basis [see also Eq. (31)]. In contrast to Eq. (18) where the numerator cannot be expected to be small or even to vanish in general, the numerator in Eq. (40) can be made small by appropriately choosing the electronic basis. This happens when this basis depends only weakly on the nuclear coordinates. In the extreme case in which the basis is independent on the nuclear coordinates, the numerator in Eq. (40) vanishes by definition. We have seen above that in the two-state case a strictly diabatic basis can be determined along a single coordinate (e.g. for a diatomic molecule). Having only a single coordinate at our disposal, there is no reason to expect the denominator in Eq. (40) to vanish (avoided crossing situation), but the numerator can be made zero.

What happens in conical intersection situations? In the adiabatic electronic basis the derivative couplings become singular as one approaches the conical intersection[12] (see also Chapter 2). Starting from the Hamiltonian in a quasidiabatic basis with no singularities in the residual derivative couplings, we readily obtain singular couplings in conical intersection situations when transforming the Hamiltonian to the adiabatic electronic basis. Obviously, in these cases the part that becomes singular as one approaches the conical intersection is removable. We may transform back from the adiabatic basis to the initial quasidiabatic basis where no singularities are present.

Can the nonremovable part also exhibit singularities as one approaches a conical intersection? The nonremovable part of the derivative couplings originates from the fact that the gauge field tensor $\mathbf{A}^{(g)}$ does not vanish [see Eqs. (34) and (35) and text]. Since by construction this tensor assumes only finite values, there is no reason to expect the nonremovable part to exhibit singularities at conical intersections, see also the discussion in Ref. 32 and explicit examples in Ref. 5. Let us briefly consult Eq. (40) in a conical

intersection situation and consider for simplicity two states $\tilde{\Phi}_i$ and $\tilde{\Phi}_j$ of different spatial symmetry, and two coordinates, a totally symmetric one R_α and a nontotally symmetric one R_β, which can couple the two electronic states. Expanding all quantities in Eq. (40) around the geometry of the conical intersection $R_\alpha = R_\beta = 0$, we obtain by symmetry arguments:[12]

$$\begin{aligned} \tilde{V}_{jj} - \tilde{V}_{ii} &= a_\alpha R_\alpha + \ldots , \\ \tilde{V}_{ji} &= c_\beta R_\beta + c_{\beta\alpha} R_\beta R_\alpha + \ldots \\ \langle \tilde{j} | (\boldsymbol{\nabla} H_e) | \tilde{i} \rangle &= (b_{\beta\alpha} R_\beta + \ldots , b_\beta + b_{\beta\alpha} R_\alpha + \ldots). \end{aligned} \tag{41a}$$

a, b and c are real numbers and, in particular, a_α, c_β and b_β are nonzero. Insertion into Eq. (40) gives in the vicinity of the conical intersection

$$\tilde{\mathbf{F}}^{(g)}_{ji} = \frac{[(b_{\beta\alpha} - c_{\beta\alpha}) R_\beta , (b_\beta - c_\beta) + (b_{\beta\alpha} - c_{\beta\alpha}) R_\alpha]}{a_\alpha R_\alpha} \tag{41b}$$

The singularity at the conical intersection can be made to vanish if only two conditions are fulfilled by the quasidiabatic basis: $b_\beta = c_\beta$ and $b_{\beta\alpha} = c_{\beta\alpha}$. Since we have two independent coordinates R_α and R_β, these conditions can be met. In general, the quasidiabatic basis can perform more efficiently than just removing the singularity as one approaches the conical intersection.

To conclude this section, we briefly comment on the practical approaches to compute quasidiabatic states. A general account of the subject has been reviewed in Ref. 5 and additional recent developments are discussed in Ref. 41 and in this book.[33] Basically, we can divide the various methods proposed into two classes, depending on whether the derivative couplings in the adiabatic electronic basis (or some other well defined basis) are used or not. The method proposed by Baer[34,35] is the most prominent prototype scheme belonging to the first class. Baer gives a general method, in which use is made in a propagative manner of Eq. (32) to find a transformation $\mathbf{U}^{(g)}$ from the adiabatic to a diabatic basis. In those cases in which strictly diabatic states do exist, the method provides them by eliminating the derivative couplings. In most cases, however, a strictly diabatic basis does not exist as discussed above, and it has been argued that the methods leads to nearly diabatic states.[36] The analysis made in Ref. 5 demonstrates that Baer's method does lead to states which do fulfill the Lorentz gauge locally, i.e. in a small neighborhood of the reference nuclear coordinates at

which the propagative computation has started. In this neighborhood, the states obtained are thus optimal quasidiabatic states.

The second class of methods to construct diabatic states does not make use of the availability of derivative couplings. Such approaches, if successful, have the advantage that derivative couplings need not be computed. Although these couplings can now be computed by *ab initio* methods (see, for instance, Ref. 31), their determination is still a formidable task, in particular for several potential energy surfaces and not too small molecules with several nuclear degrees of freedom. The method of *block diagonalization* of the electronic Hamiltonian,[37] discussed and analyzed in detail in Ref. 5, provides a promising proposal of broad applicability. The electronic Hamiltonian H_e is usually represented as a matrix $\mathbf{H}_e$ in some initial electronic basis. Instead of diagonalizing this matrix to obtain the adiabatic potential surfaces as eigenvalues, we may block diagonalize it, i.e. bring $\mathbf{H}_e$ into a block diagonal form. One block — denoted g-block — comprises those electronic states which belong to the group g of states chosen to participate in the group-Born–Oppenheimer equation (26). The other block contains the remaining states and is not of our concern. Obviously, the eigenvalues of the g-block coincide with eigenvalues of the full Hamiltonian matrix $\mathbf{H}_e$, i.e. they are those adiabatic potential surfaces of the states participating in the group-Born–Oppenheimer equation for the nuclear dynamics.

There are infinitely many transformations which bring a Hermitian matrix into block diagonal form. It is intriguing and satisfactory that a single elementary condition is sufficient to determine uniquely (up to phase factors) the block diagonalizing transformation.[38] It is the simple and appealing requirement that this transformation does not do anything but block diagonalize, i.e. it is as close as possible to the unit matrix. The resulting transformation can be given explicitly and requires only the knowledge of those eigenvectors of $\mathbf{H}_e$ which belong to the g-block. Starting at some nuclear configuration, one can show that this block diagonalization leads locally to the Lorentz gauge, i.e. to optimal quasidiabatic states in the neighborhood of this configuration.[5] By using these quasidiabatic states obtained at a given nuclear configuration as the initial basis for block diagonalization at a nearby nuclear configuration, one defines a propagative block diagonalization procedure. This procedure has been shown[5] to yield identical results of those of Baer's method.[34,35] As discussed above, the latter method requires the derivative couplings, while the

block diagonalization approach does not. We remind that if the nuclear coordinate space is one dimensional, both methods give strictly diabatic states. Variants of the block diagonalization approach have been formulated and successfully used to generate quasidiabatic states in *ab initio* computations.[5,39,40]

5. Analysis in Powers of $(1/M)^{1/4}$

5.1. *General*

The large mass of a nucleus compared to that of an electron permits an approximate separation of electronic and nuclear motion, which is the basis for the treatments discussed in the preceding sections. Historically, there were several attempts to expand the solutions of the Schrödinger equation, i.e. the energies and the wavefunctions, in powers of a small quantity related to the ratio of electronic and nuclear masses. The breakthrough has been achieved by Born and Oppenheimer in their classic paper in which they have chosen $\kappa = (1/M)^{1/4}$ as the small quantity.[42] As done in the preceding sections, M is some average nuclear mass and we work in atomic units where the electronic mass is 1.

When studying the expansion in powers of κ, traditionally one first separates off the center of mass motion and expresses the remaining Hamiltonian for relative motion of nuclei and electrons in suitable nuclear coordinates describing molecular rotations and vibrations. The resulting expressions are rather complex and depend on the particular choice of coordinates made, see, for instance, Refs. 43–45. On the other hand, one also arrives at the correct analysis in powers of κ without first separating off the center of mass motion. This has been demonstrated by many authors, see, for instance, Refs. 3, 29 and 46–48.

The physics behind the expansion in powers of κ is most straightforwardly understood by resorting to the nuclear kinetic energy operator T_n in its simplest form, given in Eq. (8). There is no need to specify the underlying mass-scaled nuclear coordinates. It suffices to divide these coordinates into various classes according to their physical nature. For transparency, we divide the nuclear coordinates in this work into two extreme classes only; all other classes lead to results in between the results we shall obtain for these two classes below. Our first class comprises all quasi-rigid vibrations of the system. All other nuclear coordinates, describing soft or even free,

e.g. translational, nuclear motion, are collected in the second class. The respective nuclear modes of motion will be briefly denoted as rigid and soft. To be particularly simple, we initially assume that the electronic energy $V_j(\mathbf{R})$ under consideration depends only on the rigid coordinates.

Obviously, the energy V_j, which is the potential energy surface for the nuclear motion, has a minimum value V_{ej} at some equilibrium configuration $R_{e\alpha}$, where the set α comprises the rigid coordinates. In the vicinity of the minimum, the potential V_j is essentially quadratic, giving rise to a multidimensional harmonic oscillator. According to the standard theory, the frequencies of the harmonic oscillator scale as κ^2 and the root-mean-square displacements from the $R_{e\alpha}$ scale as κ. Born and Oppenheimer have exploited the latter property by introducing new coordinates Q_α for the displacement from equilibrium

$$R_\alpha = R_{e\alpha} + \kappa Q_\alpha. \tag{42}$$

For the harmonic oscillator, the root-mean square values of Q_α scale as κ^0 and can also be expected to be of order unity for all quasi-rigid motions beyond the harmonic approximation.

Expressed in the new coordinates Q_α, we may now rewrite the nuclear kinetic energy T_n in Eq. (8) and obtain the convenient result

$$T_n = -\frac{\kappa^2}{2}\boldsymbol{\nabla}_Q^2 - \frac{\kappa^4}{2}\boldsymbol{\nabla}_S^2 \tag{43}$$

where $\boldsymbol{\nabla}_Q$ is the gradient with respect to the coordinates $\mathbf{Q}$ and $\boldsymbol{\nabla}_S$ is the gradient with respect to the remaining coordinates, i.e. the soft coordinates. The kinetic energies for the quasi-rigid and soft motions scale differently with the nuclear mass. To proceed, we expand the potential energy in a power series in Q_α about the minimum and readily obtain

$$V_j(\mathbf{Q}) = \kappa^0 V_{ej} + \frac{1}{2}\kappa^2 \sum_{\alpha,\beta} V_{j\alpha\beta} Q_\alpha Q_\beta + \frac{1}{6}\kappa^3 \sum_{\alpha,\beta,\gamma} V_{j\alpha\beta\gamma} Q_\alpha Q_\beta Q_\gamma + \cdots . \tag{44}$$

where the linear term in κ vanishes.

To complete the expansion of the general matrix Schrödinger equation (7) in powers of κ, we need to analyze the nonadiabatic coupling Λ_{ji} as well. Inspection of Eq. (9) shows that these couplings split into a term Λ_{ji}^Q, arising from the quasi-rigid motion, and a term Λ_{ji}^S, corresponding to

the soft motion

$$\Lambda_{ji} = \Lambda^Q_{ji} + \Lambda^S_{ji} \tag{45a}$$

which scale differently with κ. Remembering that $\boldsymbol{\nabla} = \boldsymbol{\nabla}_{\kappa Q} + \boldsymbol{\nabla}_S$, where by definition $\boldsymbol{\nabla}_{\kappa Q} = \kappa^{-1}\boldsymbol{\nabla}_Q$, we can easily see from Eq. (9a) that

$$\Lambda^Q_{ji} = \kappa^3 \mathbf{F}^Q_{ji} \cdot \boldsymbol{\nabla}_Q + \frac{1}{2}\kappa^4 G^Q_{ji} \tag{45b}$$

and

$$\Lambda^S_{ji} = \kappa^4 \left(\mathbf{F}^S_{ji} \cdot \boldsymbol{\nabla}_S + \frac{1}{2} G^S_{ji} \right). \tag{45c}$$

The derivative couplings $\mathbf{F}^Q_{ji}$ and $\mathbf{F}^S_{ji}$ and the scalar couplings G^Q_{ji} and G^S_{ji} are defined as usual, just replace $\boldsymbol{\nabla}$ in the definitions (9) by $\boldsymbol{\nabla}_{\kappa Q}$ and $\boldsymbol{\nabla}_S$, respectively. These couplings are, in general, functions of the nuclear coordinates and should be expanded in powers of κ as well. Fortunately, the leading terms of these quantities do *not* depend on κ, i.e. they scale as κ^0.

Having completed the analysis of all the operators appearing in the matrix Schrödinger equation

$$[T_n + V_j - E]\boldsymbol{\chi}_j = \sum_i \Lambda_{ji}\boldsymbol{\chi}_i \tag{46}$$

we may now turn to analyze the equation itself. To lowest order in κ, one immediately obtains $E = V_{ej}$, which is the electronic energy at the equilibrium configuration. The nuclei are frozen in space, κ does not appear, and only the electrons move. In the next order, κ^2, we have:

$$\frac{\kappa^2}{2}\left[-\boldsymbol{\nabla}^2_Q + \sum_{\alpha,\beta} V_{j\alpha\beta} Q_\alpha Q_\beta \right] \boldsymbol{\chi}_j(\mathbf{Q}) = (E - V_{ej})\boldsymbol{\chi}_j(\mathbf{Q}). \tag{47}$$

Now the nuclear motion is harmonic, but the nuclei move only along the rigid coordinates. The soft motion, e.g. translation, is frozen. What happens in the order κ^3? At first sight, one may be tempted to assume that the cubic anharmonicity of $V_j(\mathbf{Q})$ in Eq. (44) contributes to this order. From a perturbational point of view, this is not the case, however. The harmonic wavefunctions are even functions of the coordinates, and the expectation values of all odd anharmonic terms vanish. These terms will contribute to the energy in second order perturbation theory, i.e. earliest in κ^4 (note

that when adding cubic anharmonicity to Eq. (47), it appears within the brackets as a linear term in κ).

Interestingly, the impact of the nonadiabatic couplings begins at the same order of κ as that of the anharmonicity. As can be seen from Eqs. (45b,c), the scalar nonadiabatic couplings enter the Schrödinger equation (46) already at κ^4. When real electronic states are used, the diagonal element $\mathbf{F}_{jj}$ of the derivative couplings vanish. In the presence of a magnetic field,[10] or when phase factors are attached to the electronic states, as discussed at the end of Sec. 2, the $\mathbf{F}_{jj}$ do not vanish in general. Consequently, the derivative couplings lead to effects already in the order κ^3 [see Eq. (45b)]. Does this result imply that nonadiabatic couplings are more relevant than anharmonicities? The answer depends on the values of the nonadiabatic couplings in the actual system under investigation.

At what order of κ do other electronic states mix into the description of the dynamics? As can be seen from Eq. (46), this mixing depends on the nonadiabatic couplings Λ_{ji} between our electronic state Φ_j and the other states Φ_i, $i \neq j$. For the rigid coordinates, these couplings scale as κ^3, but their contribution to the energy starts at second order perturbation theory and hence as κ^6. This mixing implies that the total wavefunction ceases to be merely a product of an electronic and a nuclear wavefunction. The adiabatic ansatz (15) looses its validity and one has to resort to the expansion (5) of the total wavefunction.

Summarizing, if perturbation theory is applicable throughout and real electronic wavefunctions are used, the lowest order contributions to the energy are all proportional to even powers of the small parameter κ. In growing powers of κ, these contributions are:

κ^0: Electronic energy.
κ^2: Harmonic energy of quasi-rigid motion.
κ^4: Contribution of soft motion, anharmonic contribution of quasi-rigid motion; contribution of scalar nonadiabtic coupling.
κ^6: Contribution of coupling between electronic states (derivative couplings via quasi-rigid motion); contribution of coupling between soft and quasi-rigid motion.

If perturbation theory is applicable, the smallness of κ not only justifies the separation of electronic and nuclear motion, but also the separation of quasi-rigid and soft motion. We know, however, that perturbation theory

breaks down in many cases. A prototype case is encountered in the presence of a conical intersection between potential energy surfaces. The derivative couplings diverge at such intersections, and the participating electronic states must be included on the same footing in the calculations. This leads to the group-Born–Oppenheimer approximation discussed in Sec. 3.2. In analogy to the above analysis, it is evident that the energetic contribution of the derivative couplings between the electronic states within our group g and the remaining states begins at κ^6. Since the values of these derivative couplings are of the order of unity, the smallness of κ justifies the group-Born–Oppenheimer approximation. There is a price to pay, however. The diverging derivative couplings between the electronic states of our group g must be correctly included in the calculations of the nuclear motion, and although they appear in the equations with a prefactor $\sim\kappa^3$, see Eq. (45b), one cannot resort to the smallness of κ.

5.2. *Traditional Approach for Quasi-Rigid Molecules*

In the traditional approach, the center of mass motion of the molecule is explicitly separated off, and nuclear coordinates are introduced which suitably describe molecular vibrations and rotations. The procedure is not unique and the resulting kinetic energy operators depend on the choice of coordinates made. We follow here the transparent analysis of Mead[45] which is briefly sketched below. The center of mass coordinate is defined as usual, and the nuclear relative coordinates are introduced one at a time. Starting with an arbitrary chosen nucleus, the new coordinate for each nucleus is defined relative to the center of mass of the nuclei already introduced. This definition of relative nuclear coordinates, which we denote by $\bar{\mathbf{R}}_\alpha$, leads to a particularly simple form of the kinetic energy operators (Jacobi coordinates; for a discussion of suitable nuclear coordinates, see Ref. 51). The relative electronic coordinates $\mathbf{r}_i$ are defined, as usual, relative to the center of mass of the nuclei.

Now, an average nuclear mass M is introduced and coefficients $b_\alpha = \mu_\alpha/M$ are defined, relating the reduced masses of the above coordinates $\bar{\mathbf{R}}_\alpha$ to the average mass. Defining mass-scaled coordinates, $\mathbf{R}_\alpha = b_\alpha^{1/2}\bar{\mathbf{R}}_\alpha$, leads to the following kinetic energy operator

$$T = T_e - \frac{1}{2M}\boldsymbol{\nabla}^2 + T_{mp} \tag{48a}$$

where the term T_{mp} is called *mass polarization*. With the above choice of relative nuclear coordinates, the mass polarization takes on a particularly simple appearance

$$T_{mp} = \frac{\kappa^4}{2b} \left(\sum_i \mathbf{p}_i \right)^2 . \tag{48b}$$

Here, b is a quantity defined by $M_n = bM$, where M_n is the total mass of the nuclei, and the $\mathbf{p}_i$ are the canonical *electronic momenta*. Other choices of nuclear coordinates typically lead to more intricate expressions for T_{mp} in which also the nuclear momenta appear. The electronic operator T_e is not affected by the choice of nuclear coordinates.

To separate rotational degrees of freedom from the vibrational ones, a molecule-fixed coordinate system is introduced with three angles giving the orientation of this frame relative to the laboratory. Variables conjugate to these angles are provided by the vector $\mathbf{J}$ of angular momentum, which is conveniently defined relative to the molecular-fixed frame. The effect of a component of $\mathbf{J}$ is to rotate the nuclei about the respective axis, while holding the electrons fixed, see e.g. Ref. 52. The remaining internal nuclear degrees of freedom describe the vibrations of our quasi-rigid molecule. There are various conventional methods to introduce them, depending on the purpose at hand, for instance, analyzing vibrational spectra. For our present purpose, i.e. analysis in powers of the small parameter κ, the particular choice of these vibrational coordinates is irrelevant. For simplicity, we shall not introduce a new notation for these coordinates and denote them by R_α, as done in the preceding subsection. The nuclear kinetic energy now takes on the following appearance in matrix notation:

$$T_n = \frac{1}{2M} [\mathbf{J}\mathbf{A}(R)\mathbf{J} - \boldsymbol{\nabla}_R \mathbf{B}(R) \boldsymbol{\nabla}_R] \tag{49}$$

where the matrix $\mathbf{A}(R)$ is the inverse of the nuclear inertia tensor and the matrix $\mathbf{B}(R)$ depends on the particular choice of vibrational coordinates made.

We are now in the position to make direct contact with the general analysis in Sec. 5.1 by identifying these vibrational coordinates with the rigid coordinates in Eq. (42). These, in turn, have lead to the introduction of new coordinates Q_α for the displacement from equilibrium. In analogy to Eqs. (42) and (43), the nuclear kinetic energy in Eq. (49) is easily rewritten

to give

$$T_n = -\frac{\kappa^2}{2}\boldsymbol{\nabla}_Q \mathbf{B} \boldsymbol{\nabla}_Q + \frac{\kappa^4}{2}\mathbf{J}\mathbf{A}\mathbf{J}. \tag{50}$$

As in Eq. (43), the kinetic energy for the quasi-rigid motion scales with κ^2, while that for the soft motion scales with κ^4. Since the translational motion has been separated off exactly and a quasi-rigid molecule is considered here, we are left only with the rotational motion as soft motion.

The difference to the analysis made in the preceding subsection is that matrices $\mathbf{A}$ and $\mathbf{B}$ appear in Eq. (50) which depend on the vibrational nuclear coordinates. These can be expanded in a power series in the Q_α in the vicinity of the equilibrium geometry $R_{e\alpha}$, giving

$$\mathbf{A} = \mathbf{A}_e + \kappa \sum_\alpha \mathbf{A}_\alpha Q_\alpha + \frac{\kappa^2}{2} \sum_{\alpha,\beta} \mathbf{A}_{\alpha\beta} Q_\alpha Q_\beta + \cdots . \tag{51}$$

and an analogous expression for $\mathbf{B}$. The interpretation and analysis of the nonadiabatic couplings presented in the preceding subsection is also valid here. Just for completeness, we mention that the precise expressions for these couplings follow from Eq. (45): replace there $\boldsymbol{\nabla}_Q$ and $\boldsymbol{\nabla}_S$ by $\mathbf{B}\boldsymbol{\nabla}_Q$ and $\mathbf{A}\mathbf{J}$, respectively, The derivative couplings with respect to the vibrational coordinates are defined, as usual, as the electronic matrix elements of $\boldsymbol{\nabla}_R$, and those with respect to rotation as matrix elements of $\mathbf{J}$. The scalar couplings, which are, according to Eq. (9), electronic matrix elements of the nuclear kinetic energy operator multiplied by $2M$, follow immediately from the terms of this operator in Eq. (49).

All the analysis and discussion of the preceding subsection can now be carried over to the present situation. If perturbation theory is valid and real electronic wavefunctions are used, the lowest order contributions to the energy in growing powers of κ listed in Sec. 5.1 apply also here. One, of course, has to identify the quasi-rigid motion and the soft motion in Sec. 5.1 with vibrational and rotational motion, respectively. Then, the discussion in Sec. 5.1 for cases in which perturbation theory breaks down, in particular in the presence of conical intersections, also remains valid. Where are the differences between the general analysis in Sec. 5.1 and the present one for quasi-rigid molecules? First, mass polarization, see Eq. (48), contributes here in the order of κ^4. This contribution is obviously missing in Sec. 5.1, where the translational motion has not been separated off *a priori*. However, as discussed there, the translational motion starts to contribute

also at κ^4. Second, the leading contribution due to the coupling of vibrations and rotations scales as κ^6. In the present case it arises from the second order contribution of the terms linear in κ in the expansion (51) of the matrix $\mathbf{A}$. Third, and most important, the main differences between Sec. 5.1 and the present traditional analysis are due to the matrices $\mathbf{A}$ and $\mathbf{B}$. Their expansions (51) give rise to additional contributions in higher orders of κ and to a more general definition of anharmonicity.

6. Miscellaneous

The aim of the present section is to supplement the discussions of the Born–Oppenheimer approximation and of conical intersections presented in this book. In particular, we would like to briefly discuss three subjects: the presence of external fields, nonstationary electronic states, and the role of molecular rotations in conical intersection situations. Each of these subjects presents by itself a large area of research and would deserve a detailed account. Here, we shall only touch upon these subjects without going into any details.

The basic idea underlying the Born–Oppenheimer approximation is the separation of the electronic and nuclear motions in terms of the small quality $\kappa = (1/M)^{1/4}$ as elaborated in Sec. 5. The discussion in Sec. 3.2 has made clear that the existence of the small parameter κ is, however, insufficient to solve the problem. The coefficients in the expansion of the Schrödinger equation in powers of κ also play a relevant role. Indeed, some of these coefficients can be very large — and in conical intersection situations even diverge — and hinder the separation of electronic and nuclear motion, inspite of the smallness of κ. This has led to the introduction of the group-Born–Oppenheimer approximation. We would like to stress that the failure or even breakdown of the Born–Oppenheimer approximation is a consequence of the forces prevailing in the system. For instance, if all the forces among the light and heavy particles in the system were harmonic forces, no conical intersections or similar diabolic features would appear, and the Born–Oppenheimer approximation would turn out to be an excellent approximation for all states throughout.[53,54]

6.1. *Born–Oppenheimer Approximation in Magnetic Fields*

Following the above line of thought, we may ask the question whether the quality of the Born–Oppenheimer approximation is influenced by the

presence of an external field.[10] We shall discuss here very briefly the impact of an external magnetic field. Details can be found in Ref. 49. Inspite of the difficulties encountered in separating the center of mass motion in the presence of a magnetic field,[9] it is possible to formulate a Born–Oppenheimer expansion as done in Sec. 2 and to arrive at an equation analogous to the basic Eq. (7a).[49] The kinetic energy operator of the nuclei, T_n, however, must be replaced in the magnetic field by an effective operator. For a homonuclear neutral diatomic molecule this operator takes on the following interesting appearance:[49]

$$T_n(\mathbf{B}) = -\frac{1}{M}\left[\boldsymbol{\nabla} + i\frac{Z}{4}\cdot[\mathbf{B}\times\mathbf{R}]\right]^2 . \tag{52}$$

Z and M are the charge and mass of one of the nuclei, respectively. $\mathbf{B}$ is the magnetic field and $\mathbf{R}$ denotes the relative position vector of the two nuclei.

The expression for the nonadiabatic couplings in Eq. (7b) is still valid in the presence of the magnetic field $\mathbf{B}$. One has just to use the operator $T_n(\mathbf{B})$ in Eq. (52) instead of $T_n = T_n(\mathbf{B} = \mathbf{O})$ in the field-free case. One peculiarity is that the diagonal element of the derivative couplings cannot be made to vanish in the magnetic field case. Another peculiarity is the appearance of $[\mathbf{B}\times\mathbf{R}]\cdot\boldsymbol{\nabla}$ and $([\mathbf{B}\times\mathbf{R}])^2$ in the expression for the nuclear kinetic energy. These quantities, of course, diverge as the molecule dissociates, i.e. $|\mathbf{R}| \to \infty$, for any field strength. The consequences are far reaching. In particular, the Born–Oppenheimer adiabatic approximation (17) does not provide a meaningful description of the nuclear dynamics. This can be best seen in the dissociative limit, where one expects two separate atoms moving in a magnetic field. Instead, this approximation treats the nuclei with respect to their relative motion as naked charges in a magnetic field.

What is missing in the widely used Born–Oppenheimer adiabatic approximation when a magnetic field is present? It does not contain the effect of the screening of the nuclear charges through the electrons against the magnetic field. As shown in Refs. 10 and 49, the screening is provided by the nonadiabatic couplings. These couplings can diverge at large interatomic distances to compensate for the above mentioned misbehavior encountered in the Born–Oppenheimer adiabatic approximation. How to remedy the situation? By recognizing that in a magnetic field, the operator $\dot{\mathbf{R}} = -i[\mathbf{R}, H]$ and not the canonical momentum $-i\boldsymbol{\nabla}$ controls adiabaticity, it has been possible to rearrange the Born–Oppenheimer expansion.

In particular, this has led to the derivation of the well-behaved *partially-screened Born–Oppenheimer approximation*,[49] where the screening is correctly described. It should be noticed that in the absence of a magnetic field, $-i\boldsymbol{\nabla}$ and $\dot{\mathbf{R}}$ are identical. The physical origin of the screening is discussed in Ref. 50.

From the above it is easily anticipated that the mechanism of screening of the nuclear charge against the magnetic field by the electrons also plays an important role when several electronic states interact via nonadiabatic effects — discussed in Sec. 3.2 — and in polyatomics in general. Since the dynamics at conical intersections is sensitive to the nonadiabatic couplings and magnetic fields have an impact on the latter and on the symmetry of the system, it would be interesting to study this dynamics in the presence of such fields. Surprisingly, magnetic fields can induce the appearance of conical intersections even in diatomic molecules, where such intersections are obviously absent otherwise.[49,55] In an external magnetic field, the potential surfaces of a diatomic molecule depend not only on the internuclear distance R, but also on the angle θ between the internuclear and magnetic field axes. One of the rotational degrees of freedom acquires increasing vibrational character with increasing field strength. This may lead to what is known as hindered rotation.[56–58] The potential surfaces can exhibit conical intersections in R and θ space, which have been analyzed.[49,55] Such conical intersections have been detected in accurate numerical calculations on H_2^+.[59]

6.2. *Conical Intersections and Molecular Rotations*

There is a vast number of rotational spectra which have been analyzed assuming that the Born–Oppenheimer approximation holds. In comparison, there exist only a few investigations of rotational motion in non-Born–Oppenheimer systems, where the nuclear motion takes place on coupled potential surfaces. In this case we may expect that the *vibronic coupling*, i.e. the interaction of vibrational and electronic motion, may have a strong influence on the rotational motion. It has been proposed to speak of *rovibronic* motion if the nuclear motion is governed by coupled electronic surfaces, because in this case the rotational, the vibrational, and the electronic degrees of freedom are coupled in a nontrivial manner. If only a single electronic potential surface is involved, the term *rovibrational* motion seems

appropriate, since in this case the electronic motion is separated from the vibrational and rotational motions.[60]

Experimentally, there is clear evidence for complex rovibronic spectra, see, for instance, Refs. 61 and 62. Theoretical work is available for linear molecules,[63–66] but only a few authors have considered the more general case of rotational motion in the presence of vibronic coupling in nonlinear molecules. Most of this work, see, e.g. Refs. 67–71, is on Jahn–Teller systems in the weak nonadiabatic coupling regime. A comprehensive general theory of rovibronic coupling has been given in Ref. 60 and an application to Na_3 is available.[72] Accordingly, if rotations are considered, the vibronic coupling — i.e. the Hamiltonian in the group-Born–Oppenheimer approximation (21a) in vibrational space — has to be augmented by $H_{\rm rot}$ which takes on the following appearance:[60]

$$H_{\rm rot} = H_{rv} + \sum_{\alpha} H^{\alpha}_{\rm rot} J_{\alpha} + \sum_{\alpha,\beta} H^{\alpha,\beta}_{\rm rot} J_{\alpha} J_{\beta}. \tag{53}$$

J_α are the components of the total angular momentum and the quantities H_{rv}, $H^{\alpha}_{\rm rot}$, and $H^{\alpha,\beta}_{\rm rot}$ are purely vibronic operators, which can couple the various vibronic eigenstates. Obviously, $H_{\rm rot}$ gives rise to rotational coupling between vibronic states degenerate by symmetry or close by in energy. Representing $H_{\rm rot}$ as a matrix in the space of such a manifold of vibronic states, leads to an effective matrix Hamiltonian for the rotational motion in this manifold. The situation is analogous to the common vibronic coupling, where the vibrations couple degenerate or quasidegenerate electronic states. Now, rotations couple degenerate or quasidegenerate vibronic states, giving rise to rovibronic states which may correspond to strong admixtures of electronic, vibrational and rotational motions.

The Hamiltonian (53) describes the impact of the coupling of the electronic potential surfaces on the rotational motion. But, at the same time, it also describes the coupling of the electronic states through rotations. One can even anticipate systems where the coupling between closely neighboring electronic states is mediated only through rotational motion. For instance, in a homonuclear triatomic D_{3h} molecule, the electronic states of A'_1, A'_2 and E' symmetry cannot couple to those of A''_1, A''_2 and E'' symmetry through vibrational degrees of freedom due to symmetry reasons. However, components of the total angular momentum do allow for the coupling of

electronic states with single primed symmetry to those of double primed symmetry and the Hamiltonian (53) may mediate this coupling.

The Hamiltonian (53) gives rise to a variety of interesting rovibronic phenomena which may depend on the angular momentum quantum numbers. As an example, let us briefly discuss the widespread situation of potentials with several equivalent minima and concentrate on the standard Jahn–Teller effect, where one finds two coupled electronic potential surfaces, the lower of which exhibits three equivalent minima. The Jahn–Teller vibronic coupling case is discussed in this book in Chapter 10. Typically, three nearly degenerate vibronic states, a twofold degenerate one of E symmetry and one of A symmetry, couple rovibronically in this situation. The energy splitting between the A and the E vibronic states is caused by the tunneling motion between the different minima of the potential surface. The effective Hamiltonian for the rotational motion is accordingly a 3×3 matrix. For details see Refs. 60 and 72.

We can distinguish between three different physical situations. In the first case, the tunneling splitting is much smaller than the rotational constants of the molecule. One may speak of strong localization of the vibronic levels in the minima of the surface. In this case, the effective Hamiltonian can be transformed and it separates into three independent equivalent asymmetric top rotational Hamiltonians. In the second case, the energy splitting between the E and A vibronic states is of the same order as the rotational energies. One can easily anticipate that this can cause nontrivial resonance effects, since the rotational and tunneling motions are equally fast. Indeed, this situation leads to a completely distorted pattern of rotational, or better to say, rovibronic energy levels. It is impossible to fit them to any rigid rotor or similar models. In the third case, the typical rotational energies are smaller than the splitting between the A and E vibronic levels. In this situation, the three dimensional effective Hamiltonian can be separated into a one dimensional and a two dimensional effective Hamiltonian describing the rotational motions in the A and E vibronic state, respectively. The resulting spectra are different from each other and do not correspond to those of asymmetric top rigid rotors. The classification described above partly depends on the total angular momentum quantum number J. For instance, it is possible that for small values of J case three is realized, while for high values of J the rovibronic level pattern is that of case two.

6.3. *Born–Oppenheimer Approximation for Continuum Electronic States?*

In the Born–Oppenheimer approximation, the nuclear dynamics proceeds on the potential energy surface of a single electronic state. If a group of electronic states are energetically close by, we resort to the group-Born–Oppenheimer approximation, where the nuclear dynamics takes place on the respective coupled potential surfaces. But what do we do if these electronic states are unbound, i.e. lie in the continuum, and their number is essentially infinite? It is in general an intractable problem to solve for the dynamics in this manifold of coupled continuum states. Fortunately, many elementary processes proceed via so called temporary, compound or resonant electronic states, which carry most of the information associated with the continuum states. Examples of resonant states are found in low-energy electron-molecule collisions, where a temporary anion can be formed, and in photon-molecule impact, where an inner-shell electron is ionized, forming a nonstationary electronic state which can undergo an Auger decay. In both cases, nuclear dynamics takes place in the resonant state, and this dynamics is essential for describing the underlying collision processes. Resonant states can be viewed as discrete states embedded in and interacting with the continuum,[73] and this point of view attributes to them a potential energy surface. Unlike bound electronic states, this potential surface is a complex-valued function of the nuclear coordinates, where the imaginary part is inversely proportional to the lifetime of the resonant state. Nowadays, there exist several methods which are suitable for the computation of potential surfaces of resonances. Examples are the complex rotation method,[74] the complex absorbing potential technique,[75] and the so called R-matrix approach.[76] The calculations of resonant states are in general by far more involved than those of bound electronic states.

The nuclear dynamics in an isolated resonant state can be described in analogy to that in a bound electronic state by the Born–Oppenheimer approximation using the above mentioned complex potential surface. This approximation has, however, a number of drawbacks not encountered in the case of bound states. First, the resonant state is embedded in the continuum, and this continuum of electronic states may also contribute to the nuclear dynamics and to the process to be described. In scattering processes, the contribution of the continuum is denoted as background scattering.[77]

Second, at energies close to a threshold, where the continuum begins, the density of electronic states varies strongly, and this has a severe impact on the resonant state and on the nuclear dynamics. In particular, an exchange of electronic and rovibrational energy can take place at such energies which cannot be described within the Born–Oppenheimer approximation. This situation can be remedied by extending the complex potential surface to become an energy dependent nonlocal complex potential which acts as an operator in nuclear space, see Ref. 78 for a review on this subject and Ref. 79 for a comparative study on the impact of such nonlocal potentials versus local ones.

In collisions, the relative energy of the collision partners may vary freely over a wide range and this can lead to situations which we do not encounter in the dynamics of bound electronic states. In particular, in low-energy electron-molecule collisions, the impinging electron can possess velocities similar in magnitude to those of the rovibrational motion. Then, this electron is by no means the fast particle and the nuclei the slow ones, and a basic assumption of the Born–Oppenheimer approximation does not hold. At very low collision energies, the electron can even be the slow particle. Background contributions may become relevant. Sometimes no dominating resonance is present at all and sometimes numerous resonant states contribute which are difficult to identify individually. For all these cases, the separation of nuclear and electronic motion ultimately fails. In principle, the situation can be cured if we were able to treat the nuclear motion and the motion of the slow electron on the same footing. But what about the other electrons of the system or, more precisely, can we separate the slow electron from the normally behaving molecular electrons. Indeed, it has been shown that there exists a potential — called the *dynamical optical potential* — which describes the coupled motion of the nuclei and of the slow electron.[80] This potential rigorously accounts for the many-electron nature of the target molecule, i.e. the impact of the other electrons is incorporated into this potential. The total Hamiltonian for the dynamics now consists of the kinetic energy operators of the nuclei and of the slow electron, and, of course, of the dynamical optical potential. Loosely speaking, the slow electron is treated in this approach as if it were a nuclear degree of freedom, and we have arrived again at a Born–Oppenheimer approximation appropriate for the problem at hand.

Finally, let us return to the subject of conical intersections of potential surfaces in the presence of a continuum of electronic states. We remark that bound and continuum electronic states can exhibit conical intersections. Resonant electronic states posses complex potential surfaces, and the question arises, whether these can also exhibit conical intersections. The answer is, in general, negative. Because of the complex nature of the potentials, both the real and imaginary parts of the potentials must fulfill similar conditions to those which have to be met by the real potentials of electronically bound states in order to exhibit a conical intersection, and this is much less probable. Nevertheless, this does not imply that potential surfaces of resonant states do not exhibit interesting topologies and even intersections. On the contrary. In the space of two nuclear coordinates — and this is the minimum number of coordinates needed for a conical intersection — the surfaces of bound electronic states intersect at a single point, the conical intersection point. The surfaces of resonant electronic states, on the other hand, show two points of intersection.[81] Because of the topology of these surfaces in the vicinity of these intersections, the phenomenon has been named a *square-root intersection*. The impact of this intersection on the nuclear dynamics should be similarly relevant to that of a conical intersection: the nondiabatic couplings are singular at the conical intersection point as well as at the two intersection points of the square-root intersection.[81] It should be mentioned that electron transmission spectra show that often two or more close-lying electronic resonant states are present in polyatomic molecules, see, for instance, Refs. 82 and 83.

References

1. M. Born and K. Huang, *The Dynamical Theory of Crystal Lattices* (Oxford University Press, London, 1954).
2. R. G. Wooley and B. T. Sutcliffe, *Chem. Phys. Lett.* **45**, 393 (1976).
3. N. C. Handy and A. M. Lee, *Chem. Phys. Lett.* **252**, 425 (1996).
4. L. D. Landau and E. M. Lifshitz, *The Classical Theory of Fields* (Pergamon, New York, 1971).
5. T. Pacher, L. S. Cederbaum and H. Köppel, *Adv. Chem. Phys.* **84**, 293 (1993).
6. B. Zygelman, *Phys. Rev. Lett.* **64**, 256 (1990).
7. C. Itzykson and J. B. Zuber, *Quantum Field Theory* (McGraw-Hill, New York, 1980).
8. C. A. Mead and D. G. Truhlar, *J. Chem. Phys.* **77**, 6090 (1982).

9. B. R. Johnson, J. O. Hirschfelder and K. H. Yang, *Rev. Mod. Phys.* **55**, 109 (1983).
10. P. Schmelcher, L. S. Cederbaum and H.-D. Meyer, *Phys. Rev.* **A38**, 6066 (1988).
11. C. J. Ballhausen and A. E. Hansen, *Ann. Rev. Phys. Chem.* **23**, 15 (1972).
12. H. Köppel, W. Domcke and L. S. Cederbaum, *Adv. Chem. Phys.* **57**, 59 (1984).
13. K. Huang, *Quarks, Lepton and Gauge Fields* (World Scientific, Singapore, 1982).
14. J. Moody, A. Shapere and F. Wilczek, *Geometric Phases in Physics*, eds. A. Shapere and F. Wilczek (World Scientific, Singapore, 1989).
15. A. Bohm, B. Kendrick and M. E. Loewe, *Int. J. Quant. Chem.* **41**, 53 (1992).
16. C. A. Mead, *Phys. Rev. Lett.* **59**, 161 (1987).
17. M. V. Berry, *Proc. Roy. Soc.* **A392**, 45 (1984).
18. C. A. Mead, *Rev. Mod. Phys.* **64**, 51 (1992).
19. J. W. Zwanziger, M. Koenig and A. Pines, *Ann. Rev. Phys. Chem.* **41**, 601 (1990).
20. H. C. Longuet-Higgins, *Proc. Roy. Soc.* **A344**, 147 (1975) and references therein.
21. C. A. Mead and D. G. Truhlar, *J. Chem. Phys.* **70**, 2284 (1979).
22. L. D. Landau, *Physik. Z. Sowjetunion* **2**, 46 (1932).
23. C. Zener, *Proc. Roy. Soc.* **A137**, 696 (1932).
24. E. C. G. Stückelberg, *Helv. Phys. Acta* **5**, 369 (1932).
25. W. Lichten, *Phys. Rev.* **164**, 131 (1967).
26. F. Smith, *Phys. Rev.* **179**, 111 (1969).
27. A. D. McLachlan, *Mol. Phys.* **4**, 417 (1961).
28. W. D. Hobie and A. D. McLachlan, *J. Chem. Phys.* **33**, 1695 (1960).
29. H. C. Longuet-Higgins, *Adv. Spectrosc.* **2**, 429 (1961).
30. T. Pacher, C. A. Mead, L. S. Cederbaum and H. Köppel, *J. Chem. Phys.* **91**, 7057 (1989).
31. D. R. Yarkony, *J. Chem. Phys.* **105**, 10456 (1996).
32. T. C. Thompson, D. G. Truhlar and C. A. Mead, *J. Chem. Phys.* **82**, 2392 (1985).
33. H. Köppel, Chapter 4 of this book.
34. M. Baer, *Chem. Phys. Lett.* **35**, 112 (1975).
35. M. Baer, *Mol. Phys.* **40**, 1011 (1980).
36. M. Baer and R. Englman, *Mol. Phys.* **75**, 293 (1992).
37. L. S. Cederbaum, H. Köppel and W. Domcke, *Int. J. Quant. Chem.* **S15**, 251 (1981).
38. L. S. Cederbaum, J. Schirmer and H.-D. Meyer, *J. Phys.* **A22**, 2427 (1989).
39. W. Domcke, C. Woywod and M. Stengle, *Chem. Phys. Lett.* **226**, 257 (1994).
40. C. Woywod, M. Stengle, W. Domcke, H. Flöthmann and R. Schinke, *J. Chem. Phys.* **107**, 7282 (1997).

41. H. Nakamura and D. G. Truhlar, *J. Chem. Phys.* **115**, 10353 (2001).
42. M. Born and R. Oppenheimer, *Ann. Phys.* **84**, 457 (1927).
43. R. D. Bardo and M. Wolfsberg, *J. Chem. Phys.* **68**, 2686 (1978).
44. B. T. Sutcliffe, *Methods of Computational Molecular Physics*, eds. S. Wilson and G. H. F. Diercksen (Plenum, New York, 1993).
45. C. A. Mead, *Mathematical Frontiers in Computational Chemical Physics*, ed. D. G. Truhlar (Springer, New York, 1988).
46. H. Sellers and P. Pulay, *Chem. Phys. Lett.* **103**, 463 (1984).
47. N. C. Handy, Y. Yamaguchi and H. F. Schaefer III, *J. Chem. Phys.* **84**, 4481 (1986).
48. W. Kutzelnigg, *Mol. Phys.* **90**, 909 (1997).
49. P. Schmelcher, L. S. Cederbaum and U. Kappes, *Conceptual Trends in Quantum Chemistry*, ed. E. S. Kryachko (Kluwer, Dortrecht, 1994).
50. T. Detmer, P. Schmelcher and L. S. Cederbaum, *J. Phys.* **B28**, 2903 (1995).
51. F. Gatti, C. Iung, M. Menou and X. Chapuisat, *J. Chem. Phys.* **108**, 8821 (1998).
52. S. Califano, *Vibrational States* (Wiley, New York, 1976).
53. M. Moshinsky, *Harmonic Oscillator in Modern Physics* (Gordon & Breach, New York, 1969).
54. C. Kittel, *Quantum Theory of Solids* (Wiley, New York, 1986).
55. P. Schmelcher and L. S. Cederbaum, *Phys. Rev.* **A41**, 4936 (1990).
56. D. M. Larsen, *Phys. Rev.* **A25**, 1295 (1982).
57. V. K. Khersonskij, *Astrophys. Space Sci.* **87**, 61 (1982).
58. U. Wille, *J. Phys.* **B20**, L 417 (1987).
59. U. Kappes and P. Schmelcher, *Phys. Rev.* **A53**, 3869 (1996).
60. M. Mayer and L. S. Cederbaum, *J. Chem. Phys.* **105**, 4938 (1996).
61. A. Delon, R. Georges and R. Jost, *J. Chem. Phys.* **103**, 7740 (1995).
62. W. E. Ernst and S. Rakowsky, *Phys. Rev. Lett.* **74**, 58 (1995).
63. Ch. Jungen, K.-E. J. Hallin and A. J. Merer, *Mol. Phys.* **40**, 1 (1980).
64. S. Caster and N. C. Handy, *Mol. Phys.* **52**, 1367 (1984).
65. C. Petrongolo, *J. Chem. Phys.* **89**, 1297 (1988).
66. S. Carter, N. C. Handy, P. Rosmus and G. Chambaud, *Mol. Phys.* **71**, 605 (1990).
67. M. S. Child and H. C. Longuett-Higgins, *Philos. Trans. Roy. Soc.* **A254**, 259 (1961).
68. M. S. Child and H. L. Strauss, *J. Chem. Phys.* **42**, 2283 (1965).
69. J. T. Hougen, *J. Chem. Phys.* **38**, 1167 (1963).
70. J. T. Hougen, *J. Mol. Spectrosc.* **81**, 73 (1980).
71. J. K. G. Watson, *J. Mol. Spectrosc.* **103**, 125 (1984).
72. M. Mayer, L. S. Cederbaum and H. Köppel, *J. Chem. Phys.* **104**, 8932 (1996).
73. H. Feshbach, *Ann. Phys. (New York)* **43**, 410 (1967).
74. N. Moiseyev, *Phys. Rep.* **302**, 211 (1998).

75. T. Sommerfeld, U. V. Riß, H.-D. Meyer, L. S. Cederbaum, B. Engels and H. U. Suter, *J. Phys.* **B31**, 4107 (1998).
76. B. M. Nestmann, *J. Phys.* **B31**, 3929 (1998).
77. J. R. Taylor, *Scattering Theory* (Wiley, New York, 1972).
78. W. Domcke, *Phys. Rep.* **208**, 97 (1991).
79. L. S. Cederbaum and W. Domcke, *J. Phys.* **B14**, 4665 (1981).
80. J. Brand, L. S. Cederbaum and H.-D. Meyer, *Phys. Rev.* **A60**, 2983 (1999).
81. H. Estrada, L. S. Cederbaum and W. Domcke, *J. Chem. Phys.* **84**, 152 (1986).
82. K. D. Jordan and P. Dr. Burrow, *Acc. Chem. Res.* **11**, 341 (1978).
83. M. Allan, *Chem. Phys.* **81**, 235 (1983).

CHAPTER 2

CONICAL INTERSECTIONS: THEIR DESCRIPTION AND CONSEQUENCES

David R. Yarkony
Department of Chemistry, Johns Hopkins University, Baltimore, MD 21218

Contents

1. Introduction

In the Born–Oppenheimer approximation nuclei move on the single potential energy surface created by the faster moving electrons.[1] This approximation works so well that is at the heart of the way we think about nuclear motion. Processes in which the Born–Oppenheimer approximation breaks down are known as electronically nonadiabatic processes. Despite the reverence duly accorded the Born–Oppenheimer approximation, electronically nonadiabatic processes are ubiquitous.[2] Indeed the study of nonadiabatic processes goes back almost far as the Born–Oppenheimer approximation itself.[3] It is useful to group nonadiabatic processes into

two classes. Non-Born–Oppenheimer processes[4] are those for which the breakdown of the Born–Oppenheimer approximation is so complete that the notion of a potential energy surface is not useful and electronic and nuclear motion must be treated on an equal footing. These processes usually involve very high nuclear kinetic energies. When the nuclear kinetic energy is not excessive, the notion of a potential energy surface is viable but nuclear motion cannot be restricted to a single surface. In this regime the Born–Huang or coupled electronic state approximation is used.[5] Within the coupled electronic state approximation a nonadiabatic process involves a radiationless transition between two electronic states. The propensity for such a transition is large in the vicinity of nuclear configurations where potential energy surfaces intersect.

Intersections of two, or more, potential energy surfaces are classified according to the manner in which the degeneracy is lifted. When the degeneracy is lifted linearly in displacements from the intersection, the intersection is referred to as a conical intersection. The subspace of nuclear coordinates in which the degeneracy is lifted linearly is the *branching space*[6] or *g–h space*.[7] Points of conical intersection are not isolated but are continuously connected forming seams. This *seam space* lies in the orthogonal complement of the branching space. In this space the degeneracy is lifted quadratically in nuclear displacements, if at all. Conical intersections themselves may be classified according to several criteria.

1.1. *Classification of Conical Intersections*

1.1.1. *By Electronic State Symmetry: The Noncrossing Rule*

Conical intersections can be classified according to the role played by point group symmetry in their existence. Here, we use nonrelativistic symmetry nomenclature for convenience although the discussion is equally applicable to the relativistic case.

Intersections are *symmetry-required* when the two electronic states form the components of a degenerate irreducible representation. The Jahn–Teller intersection of the two lowest electronic states in Na_3 which correspond to the components of an E irreducible representation of the point group C_{3v}, provides an example of this class of conical intersection. Conical intersections which are not required by symmetry are accidental intersections. *Accidental symmetry-allowed* (*different symmetry*) intersections correspond

to the intersection of two states of distinct spatial symmetry. The two lowest excited singlet electronic states of H–S–H, the $1^1A''$ and $2^1A''$ states, provide an example of this type of conical intersection. For C_{2v} geometries these states are of $^1A_2$ and $^1B_1$ symmetry, so that symmetry-allowed accidental conical intersections may, and in fact do, occur.[8–11] When potential energy surfaces of two states of same symmetry cross, the intersection is referred to as an *accidental same-symmetry* conical intersection. An example of a same symmetry intersection is provided by the excited 2^1A and 3^1A states of the methyl analogue of H–S–H, methyl mercaptan, CH_3–S–H. This molecule clearly does not have the C_{2v} structures that yield the symmetry-allowed accidental intersections in H–S–H, but the 2^1A and 3^1A states exhibit same symmetry conical intersections.[8,11,12]

According to the noncrossing rule (see Refs. 13 and 15) same symmetry intersections of two potential energy surfaces are permitted in a space of dimension $N^{\text{int}} - 2$ (that is, in the seam space) where N^{int} is the number of internal degrees of freedom. Thus for diatomic molecules only states of different symmetry can cross (except in the rarest of circumstances). This situation led to the widely held idea that intersections of potential energy surfaces are, usually, a consequence of point group symmetry and that, for the most part, states of the same symmetry avoid one another. Indeed the existence of same-symmetry intersections was a matter of some controversy two decades ago.[16,17] However recent computational advances have made their determination relatively straightforward and have shown that they are not at all uncommon opening new avenues of investigation.[2] Today same symmetry conical intersections are known to play a key role in electronically non-adiabatic processes that conserve total electron spin.[15,18–24]

1.1.2. *By Topography*

Conical intersections are also classified according to the shape and orientation of the double cone. Consider a line segment of length r whose polar angle is $\theta, 0 < \theta < \pi/2$. If this line segment is rotated about the z-axis it and its mirror image in the x–y plane create a *symmetric*, vertical double cone whose *pitch* or steepness is uniform and proportional to $\cos\theta$. *Asymmetry* is introduced if the tip of the line segment follows an oval rather than a circular path as it is rotated. Finally *tilt* corresponds to rotating the double cone's principal axis so that it has polar coordinates $(\theta^{\text{t}}, \phi^{\text{t}})$.

Table 1. Dimension of g–h Space (η) and of Q space (N^Q).[a]

N^{el}	H_0		H_e	
	η	N^Q	η	N^Q
even	2	2	2	2
odd	2	4	5	4
odd[b]	2	4	3	4

[a] $H_0(H_e)$ is the Coulomb (Coulomb plus spin-orbit) Hamiltonian.
[b] Spatial point group is C_s or higher.

These attributes, *pitch*, *asymmetry* and *tilt*, are convenient for discussing dynamics near conical intersections.[21,25–33]

1.1.3. *By Dimension of the Branching Space*

Seams of conical intersection can be usefully classified according to η, the dimension of the branching space with $\eta = 2, 3$ or 5 (Ref. 15) for intersections of two potential energy surfaces. Table 1 summarizes the dimension of the branching space for two potential energy surface conical intersections. $\eta = 2$ is the most common case of a two state conical intersection being applicable to the non-relativistic or Coulomb Hamiltonian (H_0) and to molecules for which N^{el}, the number of electrons, is even. Alternatively, $\eta = 2$ unless N^{el} is odd and the spin-orbit interaction cannot be neglected. In that case $\eta = 5$ in general, or $\eta = 3$ when C_s symmetry can be imposed. The origin of this change in dimension was first explained by Mead[34] and will be discussed in Sec. 3.

1.2. *Derivative Couplings*

Although points of conical intersection are quite numerous, since the seam space has dimension $N^{int} - \eta$, when viewed from the full internal coordinate space, conical intersections occupy zero volume and therefore might not be expected to influence nuclear motion. This suggestion is, emphatically, not the case. The reason for this is the derivative coupling,[35] the interaction that couples the adiabatic states. It is infinite at a conical intersection and remains large in a *volume* surrounding the seam, making it possible for conical intersections to exert considerable influence on nuclear dynamics.

1.3. *Geometric Phase Effect*

A subtle consequence of a conical intersection is the geometric phase effect. This signature property of a conical intersection went unnoticed for approximately 30 years after conical intersections were first identified.[13] The geometric phase effect modifies the nuclear Schrödinger equation. It is a non-local effect, influencing any nuclear wave packet that, in a time-dependent sense, traverses a closed loop containing the conical intersection, regardless of its distance from the intersection. The geometric phase effect was first identified by Longuet–Higgins[36] in the context of the two-state Jahn–Teller problem; incorporated into the single electronic state problem by Mead and Truhlar;[37] extended to complex-valued Hamiltonians and applied to general adiabatic processes by Berry;[38] and ultimately extended to systems with $\eta = 5$ by Avron *et al.*[39,40] see also Refs. 31 and 34.

2. Adiabatic State Representation of Nonadiabatic Processes

In this section we examine conical intersections, the derivative coupling, the geometric phase, and how they affect nonadiabatic processes. We therefore begin with an overview of these concepts and the Born–Huang approach from which they originate.

2.1. *Born–Huang Approach*

The Born–Huang approach expands Ψ_k, the total wave function for state k in a basis of N^a, in principle arbitrary, single-valued electronic wave functions

$$\Psi_k(\mathbf{x}^e, \mathbf{X}) = \sum_{i=1}^{N^a} \tilde{\Phi}_i(\mathbf{x}^e; \mathbf{X}) \chi_i^k(\mathbf{X}). \tag{1}$$

Here $\chi_i^k(\mathbf{X})$ is the component of the nuclear wave function corresponding to the ith electronic state; $\tilde{\Phi}_k(\mathbf{x}^e; \mathbf{X}) = e^{i\Omega_k(\mathbf{X})}\Phi_k(\mathbf{x}^e; \mathbf{X})$ is the single-valued electronic wave function; the semi-colon indicates a parametric dependence, $\mathbf{x}^e$ denotes the space fixed frame cartesian coordinates of the N^{el} electrons, and $\mathbf{X} \equiv (\mathbf{X}^1, \ldots, \mathbf{X}^{N^{\mathrm{nuc}}}) \equiv (X_1, \ldots, X_{3N^{\mathrm{nuc}}})$ denotes the space fixed frame, mass scaled $\mathbf{X}^k = \mathbf{X}'^k M_k^{1/2}$, cartesian coordinates of the N^{nuc} nuclei. The phase factor $\exp(i\Omega_k)$, known as the geometric phase,[36–38] is discussed below. The electronic states themselves are

expanded in a large basis:

$$\Phi_i(\mathbf{x}^e;\mathbf{X}) = \sum_{\alpha=1}^{N^{\mathrm{CSF}}} \Theta_\alpha(\mathbf{x}^e;\mathbf{X}) c_\alpha^i(\mathbf{X}). \tag{2a}$$

This approach is in principle exact provided the Φ_i are complete, and expansion (1) is convergent as $N^a \to \infty$. However, in practice the expansion in Eq. (1) must be severely truncated (N^a kept small) for the approach to be computationally viable.

2.2. *Adiabatic Electronic States*

To enable this truncation, the Φ_k are chosen to be the adiabatic states, eigenfunctions of the electronic Hamiltonian $H_e(\mathbf{x}^e;\mathbf{X})$, that is,

$$[H_e(\mathbf{x}^e;\mathbf{X}) - V_k(\mathbf{X})]\Phi_k(\mathbf{x}^e;\mathbf{X}) = 0 \tag{2b}$$

where the eigenvalue $V_k(\mathbf{X})$ is the kth potential energy surface. Using Eq. (2a), Eq. (2b) becomes

$$[\mathbf{H}^e(\mathbf{X}) - \mathbf{V}(\mathbf{X})]\mathbf{c}(\mathbf{X}) = \mathbf{0} \tag{2c}$$

where

$$H_{k,l}^e(\mathbf{X}) = \langle \Theta_k(\mathbf{x}^e;\mathbf{X}) | H_e(\mathbf{x}^e;\mathbf{X}) | \Theta_l(\mathbf{x}^e;\mathbf{X}) \rangle_{\mathbf{x}^e} \tag{2d}$$

$V_{k,l}(\mathbf{X}) = V_k(\mathbf{X})\delta_{k,l}$, and $c_\alpha^i, \alpha = 1 - N^{\mathrm{CSF}}$ is denoted $\mathbf{c}^i$. The Θ are configuration state functions (CSFs)[42,43] constructed from molecular orbitals $\phi_k(\mathbf{x}_1^e;\mathbf{X})$ determined from a state averaged multiconfigurational self-consistent field (SA-MCSCF) procedure.[44] The form of the CSF basis is discussed in Appendix A. The SA-MCSCF procedure is discussed in Chapter 3 of this volume. For some cases considered in this chapter, the $\mathbf{c}^k$ and $\mathbf{H}^e$ can be assumed real-valued. When this is not the case, that is, $\mathbf{c}^k \equiv \mathbf{c}^{k,r} + i\mathbf{c}^{k,i}, \mathbf{H}^e = \mathbf{H}^{e,r}(\mathbf{X}) + i\mathbf{H}^{e,i}(\mathbf{X})$ and the solution of Eq. (2c) is obtained by taking explicit account of its real and imaginary parts so that Eq. (2c) becomes

$$[\mathbf{H}^{e,r}(\mathbf{X}) + i\mathbf{H}^{e,i}(\mathbf{X}) - \mathrm{V}_k(\mathbf{X})\mathbf{I}][\mathbf{c}^{k,r}(\mathbf{X}) + i\mathbf{c}^{k,i}(\mathbf{X})] = \mathbf{0} \tag{3a}$$

or noting that $\mathbf{H}^{e,i}(\mathbf{X})^\dagger = -\mathbf{H}^{e,i}(\mathbf{X})$

$$\begin{pmatrix} \mathbf{H}^{e,r}(\mathbf{X}) - \mathbf{I}\mathrm{V}_k(\mathbf{X}) & -\mathbf{H}^{e,i}(\mathbf{X}) \\ \mathbf{H}^{e,i}(\mathbf{X}) & \mathbf{H}^{e,r}(\mathbf{X}) - \mathbf{I}\mathrm{V}_k(\mathbf{X}) \end{pmatrix} \begin{pmatrix} \mathbf{c}^{k,r}(\mathbf{X}) \\ \mathbf{c}^{k,i}(\mathbf{X}) \end{pmatrix} = \mathbf{0}. \tag{3b}$$

We will refer to wave functions with real-valued (complex-valued) $\mathbf{c}^k$ as real-valued (complex-valued) wave functions.

2.3. *Conical Intersections, Derivative Couplings and Geometric Phase*

2.3.1. *A Model Hamiltonian*

Before discussing the general situation, it is instructive to consider a simple example which comes from formally evaluating Eq. (2c) in the two CSF basis $\Theta_i(\mathbf{x}^e),\ i = 1, 2$. The Hamiltonian in Eq. (2c) becomes

$$\mathbf{W}(\mathbf{X}) = \begin{pmatrix} H^e_{1,1}(\mathbf{X}) & H^e_{1,2}(\mathbf{X}) \\ H^e_{1,2}(\mathbf{X}) & H^e_{2,2}(\mathbf{X}) \end{pmatrix} \equiv \mathbf{I}S(\mathbf{X}) + \begin{pmatrix} -G(\mathbf{X}) & W(\mathbf{X}) \\ W(\mathbf{X}) & G(\mathbf{X}) \end{pmatrix} \tag{4}$$

where $S(\mathbf{X}) = (H^e_{1,1}(\mathbf{X}) + H^e_{2,2}(\mathbf{X}))/2,\ G(\mathbf{X}) = (-H^e_{1,1}(\mathbf{X}) + H^e_{2,2}(\mathbf{X}))/2$ and $W(\mathbf{X}) = H^e_{1,2}(\mathbf{X})$. $\mathbf{W}$ has eigenvalues

$$V_{\pm}(\mathbf{X}) = S(\mathbf{X}) \pm \sqrt{(G(\mathbf{X})^2 + W(\mathbf{X})^2)} \tag{5a}$$

and eigenfunctions

$$\begin{aligned} \Phi_1(\mathbf{x}^e; \mathbf{X}) &= \quad \Theta_1(\mathbf{x}^e) \cos\Lambda + \Theta_2(\mathbf{x}^e) \sin\Lambda \\ \Phi_2(\mathbf{x}^e; \mathbf{X}) &= -\Theta_1(\mathbf{x}^e) \sin\Lambda + \Theta_2(\mathbf{x}^e) \cos\Lambda \end{aligned} \tag{5b}$$

where from Eqs. (B.3) and (B.12)

$$\tan 2\Lambda(\mathbf{X}) = \frac{W(\mathbf{X})}{G(\mathbf{X})}. \tag{5c}$$

$\mathbf{X}^x$ is a point of intersection provided

$$G(\mathbf{X}^x) = W(\mathbf{X}^x) = 0. \tag{6a,b}$$

Equations (6a) and (6b) define an intersection. The type of intersection depends on the derivatives of these functions. The intersection is conical, provided $\nabla G(\mathbf{X}^x) \equiv \mathbf{g}(\mathbf{X}^x) \neq 0$ and $\nabla W(\mathbf{X}^x) \equiv \mathbf{h}(\mathbf{X}^x) \neq 0$. If $\nabla G(\mathbf{X}^x) = \nabla W(\mathbf{X}^x) = 0$, but $\nabla\nabla G(\mathbf{X}^x) \neq 0$, and $\nabla\nabla W(\mathbf{X}^x) \neq 0$, the intersection is in a class that includes the Renner–Teller intersection.[45,46]

The electronic state symmetry classifications described in the Introduction are contained in the properties of G and W. The intersection is symmetry required if Eqs. (6a) and (6b) are satisfied, provided only that $\mathbf{X}^x$ has the correct symmetry. The intersection is accidental symmetry-allowed, provided Eq. (6b) is satisfied when $\mathbf{X}^x$ has the correct symmetry. The intersection is accidental same-symmetry, provided symmetry does not guarantee that Eq. (6b) is satisfied.

2.3.2. *Intersection Adapted Coordinates*

To characterize the neighborhood of $\mathbf{X}^x$ it is convenient to define intersection adapted coordinates, $x, y, w_i, i = 1\text{-}(N^{\text{int}} - 2)$, where N^{int} is the number of internal coordinates. In this cartesian coordinate system the x- and y-axes are chosen as unit vectors along the gradients $\mathbf{g}$ and $\mathbf{h}$ that is,

$$\mathbf{x} = \frac{\mathbf{g}(\mathbf{X}^x)}{g}, \quad \mathbf{y} = \frac{\mathbf{h}(\mathbf{X}^x)}{h} \tag{7a}$$

where

$$g = \|\mathbf{g}(\mathbf{X}^x)\| \quad \text{and} \quad h = \|\mathbf{h}(\mathbf{X}^x)\|. \tag{7b}$$

The pair $(\mathbf{x}, \mathbf{y})$ define the branching plane or g–h plane. The remainder of the intersection adapted coordinate system, $\mathbf{w}^i$, $i = 1\text{-}(N^{\text{int}} - 2)$, spans the seam space. These $N^{\text{int}} - 2$ mutually orthonormal vectors need only be orthogonal to the branching space. It is also convenient to define

$$\begin{aligned} s_x = \nabla S(\mathbf{X}^x) \cdot \mathbf{x}, \; s_y = \nabla S(\mathbf{X}^x) \cdot \mathbf{y} \quad &\text{and} \\ s_{w_i} = \nabla S(\mathbf{X}^x) \cdot \mathbf{w}^i, i = 1\text{-}(N^{\text{int}} - 2). \end{aligned} \tag{7c}$$

In an actual molecule, $\mathbf{x}$ and $\mathbf{y}$ correspond to molecular motions and can be described in terms of atom centered displacements. Figure 1(a) reports the $\mathbf{g}$ and $\mathbf{h}$ vectors at a conical intersection of the $1, 2^2A'$ states in BH_2.[47] In Fig. 1(a), the molecule has C_{2v} symmetry and the intersection is a symmetry-allowed $^2A_1 - {}^2B_2$ conical intersection. The $\mathbf{g}$- or $\mathbf{x}$-direction is a symmetry preserving a_1 displacement while the $\mathbf{h}$ or $\mathbf{y}$ direction is a symmetry breaking b_2 mode. This symmetry is not an intrinsic property of $\mathbf{g}$ and $\mathbf{h}$ as it would be if the two electronic states carried $^2A_1$ and $^2B_2$ irreducible representations. However, since at the conical intersection, the two degenerate electronic states can mix freely, they do not necessarily carry C_{2v} irreducible representations as they would at an arbitrary (nondegenerate) C_{2v} geometry. This symmetry of $\mathbf{x}$ and $\mathbf{y}$ can be recovered by an orthogonalization procedure discussed subsequently.

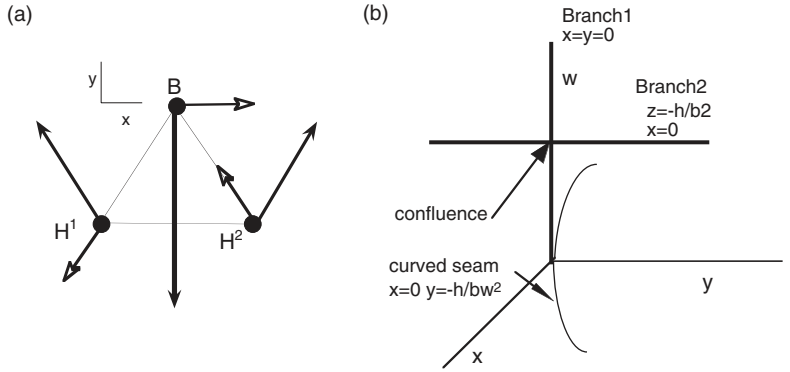

Fig. 1. (a) **g** (filled arrows) and **h** (open arrows) for a point on the $1,2^2A'$ seam of conical intersection in BH_2. (b) Two linear branches of a single state seam meet at a point of confluence (thick lines). Thin line: curved seam.

2.3.3. *Describing Conical Topographies: Linear Terms — Pitch, Asymmetry and Tilt*

Using intersection adapted coordinates, the topograghical parameters, pitch, asymmetry and tilt, described in the Introduction, can be quantified. With these definitions, **W** [Eq. (4)] becomes, through first order

$$\mathbf{W}^l(x,y,\mathbf{w}) = \left(s_x x + s_y y + \sum_{i=1}^{N^{\text{int}}-2} s_{w_i} w_i \right) \mathbf{I} + \begin{pmatrix} -gx & hy \\ hy & gx \end{pmatrix}. \tag{8}$$

Introducing polar coordinates, $x = \rho\cos\theta$ and $y = \rho\sin\theta$ and rescaling as

$$\begin{aligned} g\cos\theta &= q(\theta)\cos\lambda(\theta) \qquad & h\sin\theta &= q(\theta)\sin\lambda(\theta) \\ q(\theta)^2 &= (g\cos\theta)^2 + (h\sin\theta)^2 \end{aligned} \tag{9a}$$

so as to treat displacements along the x- and y-axes equivalently, gives

$$\begin{aligned} \mathbf{W}^l(\rho,\theta,w) = &\left[\rho(s_x\cos\theta + s_y\sin\theta) + \sum_{i=1}^{N^{\text{int}}-2} s_{w_i} w_i \right] \mathbf{I} \\ &+ \rho q(\theta) \begin{pmatrix} -\cos\lambda & \sin\lambda \\ \sin\lambda & \cos\lambda \end{pmatrix}. \end{aligned} \tag{9b}$$

$\mathbf{W}^l(\rho,\theta,\mathbf{w})$ has eigenvalues [Appendix B, Eq. (B.12b)]

$$V_\pm(\rho,\theta,\mathbf{w}) = \left[\rho(s_x\cos\theta + s_y\sin\theta) + \sum_{i=1}^{N^{\text{int}}-2} s_{w_i} w_i\right] \pm \rho q(\theta) \quad (10a)$$

$$= \left[\rho(s_x\cos\theta + s_y\sin\theta) + \sum_{i=1}^{N^{\text{int}}-2} s_{w_i} w_i\right] \pm\rho\delta_{gh}\sqrt{(1+\Delta_{gh}\cos 2\theta)} \quad (10b)$$

where $\Delta_{gh} = (g^2 - h^2)/(g^2 + h^2)$ and $\delta_{gh}^2 = (g^2 + h^2)/2$ and eigenvectors given by Eq. (5b) with $2\Lambda = \lambda$.

The s_x and s_y, Δ_{gh} and δ_{gh} describe the tilt, asymmetry and pitch of the double cone. s_x and s_y describe the tilt of the principal axis of the cone. Δ_{gh} describes the asymmetry in the pitch of the cone, which is measured by δ_{gh}. The electronic state symmetry classification of the conical intersection is reflected in these topographical parameters. The symmetry required double cone characteristic of the extensively studied Jahn–Teller problem[48,49] has $s_x = s_y = 0$, and $g = h$ by symmetry so that $q = g$ and $\Delta_{gh} = 0$. It is therefore a vertical (non-tilted) symmetric, ($\Delta_{gh} = 0$) cone. For the accidental symmetry-allowed ${}^2A_1 - {}^2B_2$ conical intersection only s_y vanishes by symmetry.

2.3.4. *Describing Conical Topographies: Second Order Terms — Branches, Confluences and Seam Curvature*

The seam space of W^l [Eq. (8)] is the set of points with $x = y = 0$. These points are isolated. By isolated we mean that there exists a small volume surrounding the seam such that the only degeneracies in that volume are the seam points themselves. While this is the case for $\mathbf{W}^l$, higher order terms can alter this situation. To illustrate, we consider the following simple extension of $\mathbf{W}^l$ which replaces W, see Eq. (4), with $W^{(c)} = hy + byw$, so that

$$\mathbf{W}^c(x,y,w) = \vartheta(x,y,w)\mathbf{I} + \begin{pmatrix} -gx & hy + byw \\ hy + byw & gx \end{pmatrix} \quad (11)$$

where $\vartheta(x,y,w)$ is the diagonal term through second order [see Eq. (60a) below] and is not of consequence here. Since W^c is now factorable,

$W^{(c)} = W^{(a)}W^{(b)} = y(h + bw)$, the single pair of conditions for a conical intersection, Eq. (6), become two independent pairs of equations

$$\text{Branch 1:} \quad G(\mathbf{X}) = 0 \text{ and } W^{(a)}(\mathbf{X}) = 0 \tag{12a}$$

$$\text{or} \quad \text{Branch 2:} \quad G(\mathbf{X}) = 0 \text{ and } W^{(b)}(\mathbf{X}) = 0. \tag{12b}$$

Branch 1 has solutions for the w-axis, that is, for $x = y = 0$ while branch 2 has solutions for the line with $x = 0, w = -h/b$ and y arbitrary. The two branches of the seam intersect when $W^{(a)}(\mathbf{X}) = W^{(b)}(\mathbf{X})$, that is, $x = 0$ with $y = 0$ and $w = -h/b$. This intersection of two branches of the same seam, pictured in Fig. 1(b), is referred as a *confluence*.[47,50,51]

As can be seen in Fig. 1(b), the seams of conical intersections considered above are straight lines in the x, y, w coordinate system. This need not be the case as the following simple example shows

$$\mathbf{W}^q(x, y, \mathbf{w}) = \vartheta(x, y, w)\mathbf{I} + \begin{pmatrix} -gx & hy + dw^2 \\ hy + dw^2 & gx \end{pmatrix}. \tag{13}$$

In this case the seam equations, Eq. (6), are satisfied for $x = 0$ and $y = -(d/h)w^2$, which is a parabola in the (w, y) plane. See Fig. 1(b). The effects of this seam curvature will be considered below.

2.3.5. *Illustrative Calculations*

The properties of a seam of conical intersection discussed above are illustrated in Figs. 2(a)–2(c). Figure 2(a) illustrates a portion of the 2 dimensional branching plane and Fig. 2(b) reports the seam (a line) for the $1^2A' - 2^2A'$ conical intersection in BH_2.[47] Figure 2(a) illustrates the conical topography in the branching plane. The connectivity is evident in Fig. 2(b) which depicts the topography along the seam. Figure 2(b) is in a sense misleading in that the wedge-like topography of the lower surface suggests a barrier on that surface in the direction of the x-coordinate. However this is not the case since there is a similar "wedge" along the y-direction so that the seam looks like, a difficult to represent, a line of mountain peaks.

The seam connectivity pictured Figs. 2(a)–2(b) is that of an isolated, single branch, seam. As shown above, more complicated connectivities exist. Seams with two or more branches are possible and these branches may intersect at confluences. A region of the $1^2A' - 2^2A'$ seam that exhibits

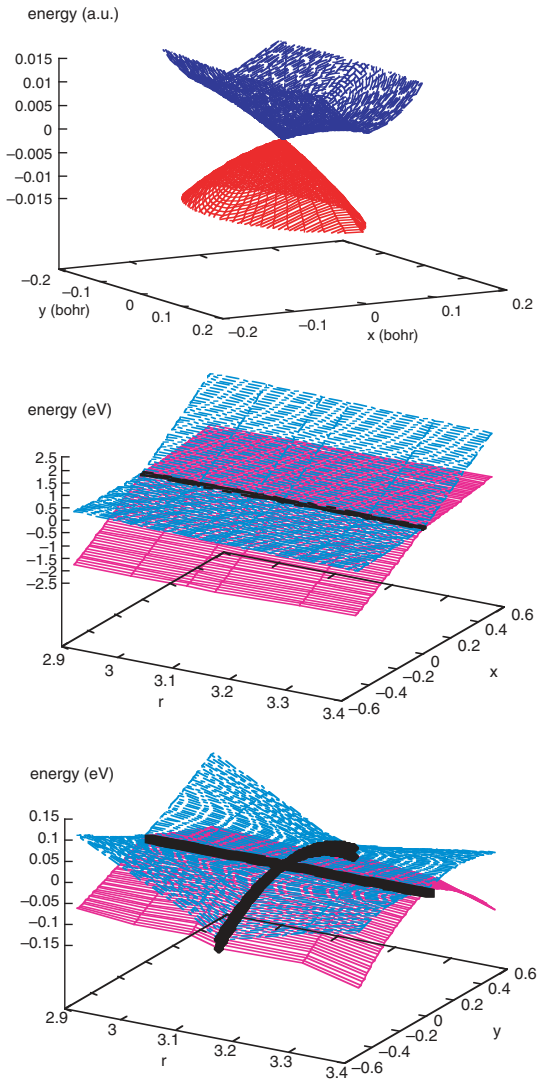

Fig. 2. BH_2: Conical intersection seams (bold lines): (a) Energy of two surfaces plotted as a function g and h coordinates, denoted x and y. (b) Energy of two surfaces plotted as function y and the seam coordinate r. (c) Energy of two surfaces plotted as function y and r, both of which are seam coordinates at the confluence.

a confluence is shown in Fig. 2(c). Clearly nuclear dynamics will be quite different for the topographies pictured in Figs. 2(b) and 2(c).

2.3.6. *Geometric Phase*

2.3.6.1. An Example

The geometric phase effect is concerned with the $\mathbf{X}$ dependence of the adiabatic electronic wave function. Consider the result of transporting a $\Phi_i(\mathbf{x}^e;\mathbf{X})$ around a small circle. The expected result is that Φ_i should return to itself, that is, Φ_i should be single-valued. That is indeed the result when the circle does not contain a conical intersection.[37] However, consider the same process applied to the eigenfunctions of $\mathbf{W}^l$, Eqs. (5b) and (5c), with $2\Lambda = \lambda$. Then since $\tan\lambda = (h/g)\tan\theta$ with $h, g > 0$ as θ increases by 2π so does λ. Therefore $\cos((\lambda + 2\pi)/2) = \cos(\lambda/2 + \pi) = -\cos(\lambda/2)$ and $\sin((\lambda + 2\pi)/2) = \sin(\lambda/2 + \pi) = -\sin(\lambda/2)$, so that

$$\Phi_i(\mathbf{x}^e;\rho,\theta + 2\pi,\mathbf{w}) = -\Phi_i(\mathbf{x}^e;\rho,\theta,\mathbf{w}),\ i = 1,2. \tag{14}$$

From Eq. (14), we see that when transported around a closed loop in nuclear coordinate ($\mathbf{X}$) space surrounding a conical intersection, both Φ_1 and Φ_2 change sign. Thus, the manifestly continuous $\Phi_i(\mathbf{x}^e;\rho,\theta,\mathbf{w})$ are double-valued, since at any point they may take on the values $\pm\Phi_i(\mathbf{x}^e;\rho,\theta,\mathbf{w})$ depending on the path. The implications of this double valuedness are discussed in Sec. 2.4 below.

2.3.6.2. Geometric Phase Effect for Real-Valued Wave Functions

The above results are actually quite general. By way of illustration here those results are re-expressed in terms of the $\mathbf{c}^k(\mathbf{X})$, the eigenvectors of $\mathbf{H}^e$ [Eq. (2c)], assuming $\mathbf{H}^e$ to be real-valued. Since $\mathbf{H}^e$ is real-valued, the $\mathbf{c}^k(\mathbf{X})$ can be chosen real-valued and are therefore determined up to the factor ± 1. This factor must be chosen to assure local continuity:

$$\mathbf{c}^k(\mathbf{X})^\dagger \cdot \mathbf{c}^k(\mathbf{X} + \boldsymbol{\varepsilon}) \to 1 \text{ as } \boldsymbol{\varepsilon} \to \mathbf{0}. \tag{15a}$$

Assume that the electronic Schrödinger equation is solved along a closed loop beginning at $\mathbf{X}^0$ and ending at $\mathbf{X}^f = \mathbf{X}^0$ and for each point on that

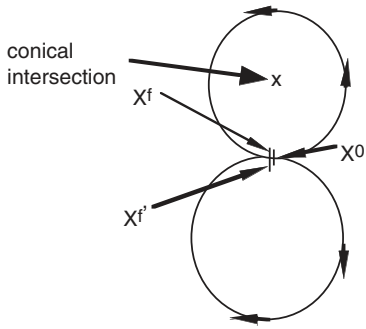

Fig. 3. Upper loop $X^0 \rightarrow X^f$ surrounds the conical intersection at **x**. Lower loop $X^0 \rightarrow X^{f\prime}$ does not enclose a conical intersection.

loop Eq. (15a) holds. Then

$$\mathbf{c}^k(\mathbf{X}^0)^\dagger \cdot \mathbf{c}^k(\mathbf{X}^f) = -1 \tag{15b}$$

$$\mathbf{c}^k(\mathbf{X}^0)^\dagger \cdot \mathbf{c}^k(\mathbf{X}^f) = 1 \tag{15c}$$

are the only possibilities. The -1 $(+1)$ result is obtained when closed loop that does (does not) contain a single point of conical intersection,[16,37,52] see Fig. 3.

There are two points to emphasize here. When a conical intersection exists, the wave functions $\mathbf{c}^k(\mathbf{X})$ that satisfy Eq. (15a) are not suitable as a basis for the Born–Huang expansion, Eq. (1), as they are double-valued, taking on either the value $\pm\mathbf{c}^k(\mathbf{X})$. To correct this deficiency, either a similarly double-valued vibrational basis must be used in Eq. (1)[53] or a phase factor $e^{i\Omega_i(\mathbf{X})}$ must be included to account for this deficiency, that is, $e^{i\Omega_i(\mathbf{X})}$ must change sign along the closed loop defined by $\mathbf{X}^0$ and $\mathbf{X}^f$. Secondly, by reducing the size of the loop in Fig. 3, Eqs. (15b) and (15c) can be used to locate a point of conical intersection.[6,54,55]

2.3.6.3. The $\eta = 3$ and 5 Cases

The geometric phase effect is more complicated for the $\eta = 5$ and $\eta = 3$ conical intersections than for the $\eta = 2$ case. In the $n = 2$ case the wave functions can be chosen real-valued. This is not the case for $\eta = 5$ or $\eta = 3$, and other limits in Eq. (15a) are possible, since neighboring wave functions will in general differ by a complex-valued phase. The $\eta = 3$ case

has been discussed in general by Berry.[38] For $\eta = 5$, the wave functions are, in general, admixtures of two orthogonal degenerate wave functions with complex-valued overlaps. This case, which has also been discussed previously,[39–41] is considered further in Sec. 3.

2.3.6.4. Geometric Phase Effect and Confluences

A point of confluence, although the intersection of two conical intersection seams, is not itself a point of conical intersection. Indeed for $\mathbf{W}^c$ [Eq. (11)], there is no geometric phase effect since

$$\Phi_k(\mathbf{x}^e; \rho, \phi + 2\pi, \mathbf{w}) = \Phi_k(\mathbf{x}^e; \rho, \phi, \mathbf{w})$$

where $x = \rho\cos\phi, z = \rho\sin\phi$.

2.3.7. *Derivative Couplings*

We will encounter (Sec. 2.4) two types of derivative couplings, $\mathbf{A}_{k.l}$. The first derivative coupling, usually referred to as just the derivative coupling, and $B_{k,l}$, the second derivative coupling, where

$$\mathbf{A}_{i,j}(\mathbf{X}) = \langle \Phi_i(\mathbf{x}^e; \mathbf{X}) | \nabla_{\mathbf{X}} \Phi_j(\mathbf{x}^e; \mathbf{X}) \rangle_{\mathbf{x}^e} \tag{16a}$$

and

$$B_{i,j}(\mathbf{X}) = \langle \nabla_{\mathbf{X}} \Phi_i(\mathbf{x}^e; \mathbf{X}) \cdot | \nabla_{\mathbf{X}} \Phi_j(\mathbf{x}^e; \mathbf{X}) \rangle_{\mathbf{x}^e}. \tag{16b}$$

Here ∇_X is a $3N^{\mathrm{Nuc}}$ component gradient with respect to the variables $\mathbf{X}$. Thus $\boldsymbol{A}(\mathbf{X})$ is a vector of matrices. When required, we will use

$$A^{\beta}_{i,j}(\mathbf{X}) = \left\langle \Phi_i(\mathbf{x}^e; \mathbf{X}) \left| \frac{\partial}{\partial X_\beta} \Phi_j(\mathbf{x}^e; \mathbf{X}) \right. \right\rangle_{\mathbf{x}^e} \tag{16a'}$$

to denote the individual components.

2.3.7.1. Derivative Couplings from Model Hamiltonians

As noted in the Introduction, perhaps the most significant property of the derivative coupling is its singular behaviour at the conical intersection. The model Hamiltonians $\mathbf{W}, \mathbf{W}^l, \mathbf{W}^q$ and $\mathbf{W}^c$ allow us to illustrate the nature of the singularity and its origin.

Inserting Φ_k, the eigenfunctions in Eq. (5b), into definition (16a), we find

$$\mathbf{A}_{1,2} = \nabla\Lambda = \frac{(\nabla W)G - (\nabla G)W}{G^2 + W^2}. \tag{17a}$$

Specializing to $\mathbf{W}^l$ in Eq. (8) gives

$$\mathbf{A}_{1,2} = \nabla\lambda/2 : A^{\rho}_{1,2} = 0 \text{ and } A^{\theta}_{1,2} = \frac{1}{2}\frac{\partial\lambda}{\partial\theta} = gh/q^2(\theta) \tag{17b}$$

or in cartesian coordinates

$$(A^x_{1,2}, A^y_{1,2}) = A^{\theta}_{1,2}\left(\frac{1}{\rho}\right)(-\sin\theta, \cos\theta). \tag{17c}$$

Thus the singularity in $\mathbf{A}_{i,j}$ is of order $(1/\rho)$ and arises from the linear terms in $\mathbf{W}^l$. Since the overlap matrix elements, $\langle\Phi_k|\Phi_l\rangle_{\mathbf{x}^e}, k, l = 1, 2$ are real-valued and the Φ_k are a complete set for the model Hamiltonian,

$$B_{1,2} = 0 \text{ and } B_{i,i} = \left(\frac{A^{\theta}_{1,2}}{\rho}\right)^2 \qquad i = 1, 2. \tag{17d}$$

In summary, as the conical intersection is approached, the first derivative coupling diverges as $A^{\theta}_{1,2}/\rho$. The second derivative coupling also becomes infinite as $(A^{\theta}_{1,2}/\rho)^2$. The implications of this singularity are discussed below.

It is also interesting to consider what happens to the derivative couplings near a confluence. The $\mathbf{W}^c$ [Eq. (11)], exhibits a confluence at $x = y = 0, w = -h/b$. The derivative coupling for its eigenstates, obtained from Eq. (17a), is given by:

$$\mathbf{A}_{1,2} = \frac{g[-\sin\theta(h + bw), \cos\theta(h + bw), (b\rho/2)\sin 2\theta]}{\rho(q^2(\theta) + f(w)(\sin\theta)^2)} \tag{18a}$$

where

$$f(w) = 2bhw + b^2w^2. \tag{18b}$$

Several points are worth noting. $A^{\omega}_{1,2}$, $\omega = x, y$ has the expected $(1/\rho)$ singularity for all $w \neq -h/b$, whereas the w component is nonsingular

$$A^{w}_{1,2} \xrightarrow[w\to 0]{} \frac{gb\sin 2\theta}{2q^2(\theta)}. \tag{18c}$$

When $w = -h/b$, $A^w_{1,2} = 0$ for $w = x, y$ for all finite ρ. Thus the derivative coupling near a confluence, the intersection of two conical intersection seams, differs qualitatively from that at an intersection itself.

To consider the effects of seam curvature, we use $\mathbf{W}^q$ [Eq. (13)] and find

$$\mathbf{A}_{1,2} = \frac{(-gh\rho\sin\theta - gdw^2, hg\rho\cos\theta, 2dwg\rho\cos\theta)}{\rho^2 q^2 + (\rho\sin\theta)w^2 2dh + d^2w^4}. \tag{19a}$$

Here it is interesting to juxtapose approaching the conical intersection in the g–h ($w = 0$) plane and along the w-axis. Approaching the conical intersection in the $w = 0$ plane, yields

$$\mathbf{A}_{1,2} = \frac{(-gh\sin\theta, hg\cos\theta, 0)}{\rho q^2}. \tag{19b}$$

Approaching the conical intersection for $\rho = 0$ along the w-axis,

$$\mathbf{A}_{1,2} \xrightarrow[\rho\to 0]{} \frac{(gdw^2, 0, 0)}{d^2w^4} \tag{19c}$$

that is, $\mathbf{A}_{1,2}$ is singular as the result of seam curvature as $w \to 0$ along the w-axis.

2.3.7.2. Derivative Couplings and the Geometric Phase

The first derivative coupling of $\mathbf{W}^l$ satisfies an interesting integral relation. Its circulation, the line integral[56] along a circle containing the conical intersection, is equal to π, that is,

$$\oint \mathbf{A}_{1,2}\cdot d\mathbf{X} = \int_0^{2\pi} A^\theta_{1,2}(\theta)d\theta = \frac{1}{2}\int_0^{2\pi}\frac{d\lambda}{d\theta}d\theta = \frac{1}{2}(2\pi) = \pi. \tag{20a}$$

This result is clearly related to the geometric phase effect noted above. However, in practical examples it must be used with some care, since the curl[57,58] of $\mathrm{A}_{k,l}$ is not guaranteed to vanish for finite ρ[37] as it does here. An alternative approach to Eq. (20a) has been recently reported[35] based

on the following exact observation:

$$\begin{aligned}\Phi_i(\mathbf{x}^e;\mathbf{X}+\delta\mathbf{X}) &= \Phi_i(\mathbf{x}^e;\mathbf{X}) + \nabla\Phi_i(\mathbf{x}^e;\mathbf{X})\cdot\delta\mathbf{X} \\ &= \Phi_i(\mathbf{x}^e;\mathbf{X}) + \sum_j \Phi_j(\mathbf{x}^e;\mathbf{X})\langle\Phi_j(\mathbf{x}^e;\mathbf{X})|\nabla\Phi_i(\mathbf{x}^e;\mathbf{X})\rangle_{\mathbf{x}^e}\cdot\delta\mathbf{X} \\ &= \Phi_i(\mathbf{x}^e;\mathbf{X}) + \sum_j \Phi_j(\mathbf{x}^e;\mathbf{X})A_{j,i}(\mathbf{X})\cdot\delta\mathbf{X} \qquad (20b)\end{aligned}$$

so that

$$\Phi(\mathbf{x}^e;\mathbf{X}^f) = \exp_T\left(\int_{\mathbf{X}^0}^{\mathbf{X}^f}\mathbf{A}\cdot\delta\mathbf{X}\right)\Phi(\mathbf{x}^e;\mathbf{X}^0). \qquad (20c)$$

Equation (20c), is a generalization of Eq. (20a) to nonclosed paths of arbitrary shape.

2.3.7.3. A Useful Approximation

B is quite costly to evaluate. Below we derive a well known approximation, useful for all but the most precise calculations. Differentiating the normalization condition $\langle\Phi_i(\mathbf{x}^e;\mathbf{X})|\Phi_j(\mathbf{x}^e;\mathbf{X})\rangle_{\mathbf{x}^e} = \delta_{ij}$ gives

$$A^*_{j,i} + A_{i,j} = 0. \qquad (21a)$$

Inserting a complete set of electronic states in Eq. (16b) gives

$$\begin{aligned}B_{i,j}(\mathbf{X}) &= \sum_k \langle\nabla_{\mathbf{X}}\Phi_i(\mathbf{x}^e;\mathbf{X})|\Phi_k(\mathbf{x}^e;\mathbf{X})\rangle_{\mathbf{x}^e}\cdot\langle\Phi_k(\mathbf{x}^e;\mathbf{X})|\nabla_{\mathbf{X}}\Phi_j(\mathbf{x}^e;\mathbf{X})\rangle_{\mathbf{x}^e} \\ &= \sum_k \mathbf{A}^*_{k,i}\cdot\mathbf{A}_{k,j} = (\mathbf{A}^\dagger\cdot\mathbf{A})_{i,j}. \qquad (21b)\end{aligned}$$

In Eq. (21b), the sum on k must extend to N^{CSF} (the complete state limit). When the sum is truncated at $N^a \ll N^{\mathrm{CSF}}$. Equation (21b) provides a commonly[59] used approximation for $B_{i,j}$. This approximation properly includes the effects of a conical intersection and is adequate for all but the most precise calculations.

2.3.7.4. Gauge Theoretic Interpretation[60]

The geometric phase can be expressed in terms of a modified momentum operator as follows:

$$\begin{aligned}\tilde{\mathbf{A}}_{i,j} &\equiv \langle e^{i\Omega_i}\Phi_i(\mathbf{x}^e;\mathbf{X})|\nabla_{\mathbf{X}} e^{i\Omega_j}\Phi_j(\mathbf{x}^e;\mathbf{X})\rangle_{\mathbf{x}^e} \\ &= \langle e^{i\Omega_i}\Phi_i(\mathbf{x}^e;\mathbf{X})|i(\nabla_{\mathbf{X}}\Omega_j)e^{i\Omega_j}\Phi_j(\mathbf{x}^e;\mathbf{X}) + e^{i\Omega_j}\nabla_{\mathbf{X}}\Phi_j(\mathbf{x}^e;\mathbf{X})\rangle_{\mathbf{x}^e} \\ &= e^{i\Delta\Omega_{ji}}[i(\nabla_{\mathbf{X}}\Omega_j)\delta_{i,j} + \mathbf{A}_{i,j}] \qquad (22a)\end{aligned}$$

where $\Delta\Omega_{ji} = \Omega_j - \Omega_i$. Equation (22a) can be written in a gauge theoretic form:[60]

$$e^{-i\Delta\Omega_{ji}}\tilde{\mathbf{A}}_{i,j} = \langle\Phi_i|[i(\nabla_{\mathbf{X}}\Omega_j) + \nabla_{\mathbf{X}}]\Phi_j\rangle_{\mathbf{x}}. \qquad (22b)$$

Thus the off diagonal first derivative coupling is determined up to a phase, while the diagonal first derivative coupling depends explicitly on the gradient of that phase. Note that here, for reasons discussed below, we have not assumed that the overlap matrix and hence the derivative couplings are real-valued. In a similar manner

$$\begin{aligned}\tilde{B}_{i,j} &\equiv \langle i(\nabla_{\mathbf{X}}\Omega_i)e^{i\Omega_i}\Phi_i(\mathbf{x}^e;\mathbf{X}) + e^{i\Omega_i}\nabla_{\mathbf{X}}\Phi_i(\mathbf{x}^e;\mathbf{X}) \\ &\quad\times|i(\nabla_{\mathbf{X}}\Omega_j)e^{i\Omega_j}\Phi_j(\mathbf{x}^e;\mathbf{X}) + e^{i\Omega_j}\nabla_{\mathbf{X}}\Phi_j(\mathbf{x}^e;\mathbf{X})\rangle_{\mathbf{x}^e} \qquad (23a) \\ &= e^{i\Delta\Omega_{ji}}[(\nabla_{\mathbf{X}}\Omega_i)(\nabla_{\mathbf{X}}\Omega_j)\delta_{ij} + B_{i,j} - i(\nabla_{\mathbf{X}}\Omega_i)A_{i,j} + i(\nabla_{\mathbf{X}}\Omega_j)A^*_{j,i}] \qquad (23b)\end{aligned}$$

which using Eq. (21a) becomes

$$\tilde{B}_{i,j} = e^{i\Delta\Omega_{ji}}[(\nabla_{\mathbf{X}}\Omega_i)\cdot(\nabla_{\mathbf{X}}\Omega_j)\delta_{ij} + B_{i,j} - i\nabla_{\mathbf{X}}(\Omega_i + \Omega_j)\cdot\mathbf{A}_{i,j} \qquad (23c)$$

or in gauge theoretic form [see Eq. (22b)].

$$e^{i\Delta\Omega_{ij}}\tilde{B}_{i,j} \equiv \langle[i(\nabla_{\mathbf{X}}\Omega_i) + \nabla_{\mathbf{X}}]\Phi_i(\mathbf{r};\mathbf{X})|(i(\nabla_{\mathbf{X}}\Omega_j) + \nabla_{\mathbf{X}})\Phi_j(\mathbf{r};\mathbf{X})\rangle_{\mathbf{r}}. \qquad (23d)$$

Thus effect of the geometric phase is the operator transformation

$$\nabla_{\mathbf{X}} \to i(\nabla_{\mathbf{X}}\Omega_j) + \nabla_{\mathbf{X}}. \qquad (24)$$

2.4. *The Nuclear Schrödinger Equation*

Additional insight into the significance of the quantities introduced above can be obtained from the nuclear Schrödinger equation in the Born–Huang approximation, which we briefly discuss below.

The Hamiltonian is $H = T_{\rm nuc} + H_e(\mathbf{x}^e; \mathbf{X})$, where

$$T_{\rm nuc} = \sum_{i=1}^{N^{\rm NUC}} \frac{\mathbf{p}_{\mathbf{X}'i} \cdot \mathbf{p}_{\mathbf{X}'i}}{2M_i} = -\sum_{i=1}^{N^{\rm NUC}} \frac{\nabla^2_{\mathbf{X}'i}}{2M_i} \equiv -\sum_{i=1}^{N^{\rm NUC}} \frac{\nabla^2_{\mathbf{X}^i}}{2}$$
$$\equiv -\frac{1}{2}\nabla^2_{\mathbf{X}} = \frac{1}{2}\mathbf{p}_{\mathbf{X}} \cdot \mathbf{p}_{\mathbf{X}} \tag{25a}$$

is the nuclear kinetic energy operator and $H_e(\mathbf{x}^e; \mathbf{X})$ is the electronic Hamiltonian. Ψ_k [Eq. (1)] satisfies the time independent Schrödinger equation

$$(H - E_k)\Psi_k = 0. \tag{25b}$$

To determine the form of the Schrödinger equation using Eq. (1), we need the effect of $T_{\rm nuc}$ on a single term in Eq. (1). This is obtained from

$$\langle \tilde{\Phi}_i(\mathbf{x}^e; \mathbf{X})\chi_i^k(\mathbf{X})|\mathbf{p}_{\mathbf{X}} \cdot \mathbf{p}_{\mathbf{X}}|\chi_j^m(\mathbf{X})\tilde{\Phi}_j(\mathbf{x}^e; \mathbf{X})\rangle$$
$$= \langle \mathbf{p}_{\mathbf{X}}[\tilde{\Phi}_i(\mathbf{x}^e; \mathbf{X})\chi_i^k(\mathbf{X})]|\mathbf{p}_{\mathbf{X}}[\chi_j^m(\mathbf{X})\tilde{\Phi}_j(\mathbf{x}^e; \mathbf{X})]\rangle \tag{26a}$$
$$= \langle [\mathbf{p}_{\mathbf{X}}\tilde{\Phi}_i(\mathbf{x}^e; \mathbf{X})\chi_i^k(\mathbf{X}) + \tilde{\Phi}_i(\mathbf{x}^e; \mathbf{X})\mathbf{p}_{\mathbf{X}}\chi_i^k(\mathbf{X})]$$
$$|[\mathbf{p}_{\mathbf{X}}\chi_j^m(\mathbf{X})\tilde{\Phi}_j(\mathbf{x}^e; \mathbf{X}) + \chi_j^m(\mathbf{X})\mathbf{p}_{\mathbf{X}}\tilde{\Phi}_j(\mathbf{x}^e; \mathbf{X})]\rangle \tag{26b}$$
$$= \langle [\mathbf{p}_{\mathbf{X}}\chi_i^k(\mathbf{X})|[\mathbf{p}_{\mathbf{X}}\chi_j^m(\mathbf{X})]\rangle\delta_{ij} \tag{26c}$$
$$+\langle \chi_i^k(\mathbf{X})[\mathbf{p}_{\mathbf{X}}\tilde{\Phi}_i(\mathbf{r}; \mathbf{X})]|[\mathbf{p}_{\mathbf{X}}\tilde{\Phi}_j(\mathbf{x}^e; \mathbf{X})]\chi_j^m(\mathbf{X})\rangle$$
$$+\langle \tilde{\Phi}_i(\mathbf{x}^e; \mathbf{X})[\mathbf{p}_{\mathbf{X}}\chi_i^k(\mathbf{X})]|[\mathbf{p}_{\mathbf{X}}\tilde{\Phi}_j(\mathbf{x}^e; \mathbf{X})]\chi_j^m(\mathbf{X})\rangle$$
$$+\langle \chi_i^k(\mathbf{X})\mathbf{p}_{\mathbf{X}}\tilde{\Phi}_i(\mathbf{x}^e; \mathbf{X})|\tilde{\Phi}_j(\mathbf{x}^e; \mathbf{X})\mathbf{p}_{\mathbf{X}}\chi_j^m(\mathbf{X})\rangle \tag{26d}$$
$$= \langle \chi_i^k\{|\mathbf{p}_{\mathbf{X}} \cdot \mathbf{p}_{\mathbf{X}}\chi_j^m(\mathbf{X})\rangle\delta_{ij} + |(\tilde{B}_{i,j}(\mathbf{X}) + \tilde{\mathbf{a}}_{i,j}(\mathbf{X})^* \cdot \mathbf{p}_{\mathbf{X}})\chi_j^m(\mathbf{X})\rangle$$
$$+|\mathbf{p}_{\mathbf{X}}[\cdot\tilde{\mathbf{a}}_{i,j}(\mathbf{X})\chi_j^m(\mathbf{X})]\rangle\} \tag{26e}$$

where $-i\boldsymbol{A} = \boldsymbol{a}$.

The above result enables the derivation of the coupled differential equations describing nuclear motion. Inserting Eq. (1) into the Schrödinger

equation (25) and projecting onto the bra $\langle\tilde{\Phi}_i(\mathbf{r};\mathbf{X})\chi_i^k(\mathbf{X})|$ gives

$$\begin{aligned}
&\left\langle \chi_i^k(\mathbf{X}) \left\{ \left| \left(\frac{\mathbf{p_X}\cdot\mathbf{p_X}}{2} + [b_{i,i}(\mathbf{X}) + V_i(\mathbf{X})] + \frac{\mathbf{a}_{i,i}(\mathbf{X})^*\cdot\mathbf{p_X}}{2} - E_m \right) \chi_i^m(\mathbf{X}) \right\rangle \right. \\
&\qquad \left. + \left| \frac{\mathbf{p_X}}{2}\cdot[\mathbf{a}_{i,i}(\mathbf{X})\chi_i^m(\mathbf{X})] \right\rangle \right\} \qquad (27) \\
&= \sum_{i\neq j} \left\langle \chi_i^k(\mathbf{X}) \left\{ \left| \tilde{b}_{i,j}(\mathbf{X})\chi_j^m(\mathbf{X}) \right\rangle + \left| \frac{1}{2}\mathbf{p_X}\cdot[\tilde{\mathbf{a}}_{i,j}(\mathbf{X})\ \chi_j^m\ (\mathbf{X})] \right\rangle \right. \\
&\qquad \left. + \left| \frac{1}{2}\tilde{\mathbf{a}}_{j,i}(\mathbf{X})^*\cdot\mathbf{p_X}\chi_j^m(\mathbf{X}) \right\rangle \right\}
\end{aligned}$$

where $\tilde{b}_{i,j} = \frac{\tilde{B}_{i,j}}{2}$. Equation (27) can be rewritten as

$$\begin{aligned}
&\left\langle \chi_i^k(\mathbf{X}) \left\{ \left| \left(\frac{\mathbf{p_X}\cdot\mathbf{p_X}}{2} + (b_{i,i}(\mathbf{X}) + V_i(\mathbf{X})) + \left(\frac{\mathbf{p_X}}{2}\cdot\mathbf{a}_{i,i}(\mathbf{X}) \right) \right. \right. \right. \\
&\qquad \left. \left. \left. + \frac{(\mathbf{a}_{i,i}(\mathbf{X}) + \mathbf{a}_{i,i}(\mathbf{X})^*)}{2}\cdot\mathbf{p_X} - E_m \right) \chi_i^m(\mathbf{X}) \right\rangle \right\} \\
&= \sum_{i\neq j} \left\langle \chi_i^k(\mathbf{X}) \left\{ \left| \tilde{b}_{i,j}(\mathbf{X})\chi_j^m(\mathbf{X}) \right\rangle + \left| \frac{1}{2}(\mathbf{p_X}\cdot\tilde{\mathbf{a}}_{i,j}(\mathbf{X}))\chi_j^m(\mathbf{X}) \right\rangle \right. \\
&\qquad \left. + \frac{1}{2} \left| (\tilde{\mathbf{a}}_{i,j}(\mathbf{X}) + \tilde{\mathbf{a}}_{j,i}(\mathbf{X})^*)\cdot\mathbf{p_X}\chi_j^m(\mathbf{X}) \right\rangle \right\} \qquad (28)
\end{aligned}$$

which in turn becomes

$$\begin{aligned}
&\left\{ \frac{\mathbf{p_X}\cdot\mathbf{p_X}}{2} + \tilde{b}_{i,i}(\mathbf{X}) + V_i(\mathbf{X}) + \left(\frac{\mathbf{p_X}}{2}\cdot\tilde{\mathbf{a}}_{i,i}(\mathbf{X}) \right) + 1/2(\tilde{\mathbf{a}}_{i,i}(\mathbf{X}) \right. \\
&\qquad \left. + \tilde{\mathbf{a}}_{i,i}(\mathbf{X})^*)\cdot\mathbf{p_X} - E_m) \right\} \chi_i^m(\mathbf{X}) \\
&= \sum_{i\neq j} \left\{ \tilde{b}_{i,j}(\mathbf{X}) + \frac{1}{2}(\mathbf{p_X}\cdot\tilde{\mathbf{a}}_{i,j}(\mathbf{X}) + (\tilde{\mathbf{a}}_{i,j}(\mathbf{X}) \right. \\
&\qquad \left. + \tilde{\mathbf{a}}_{j,i}(\mathbf{X})^*)\cdot\mathbf{p_X}) \right\} \chi_j^m(\mathbf{X}). \qquad (29)
\end{aligned}$$

Before reducing Eq. (29) to its most compact form, note that the left hand side is the single potential energy surface nuclear Schrödinger equation. The single surface solutions are coupled when the right hand side of Eq. (29) is nonvanishing, that is when the first and second derivative

couplings are nonvanishing. The diagonal second derivative coupling (the adiabatic correction) $b_{i,i}$ constitutes a positive definite, mass dependent, correction to the mass independent Born–Oppenheimer potential energy surface $V_i(X)$. From Eq. (17d), $b_{i,i} \rightarrow \infty$ as $\mathrm{X} \rightarrow \mathbf{X}^x$, thereby creating a node in the adiabatic wave function[33,61,62] at $\mathbf{X}^x$. Further discussion of this term is found in Chapter 3 of this volume.

This equation simplifies in the $\eta = 2$ case, where $\mathbf{H}^e$ is real-valued. In that case, $\tilde{\mathbf{a}}_{i,i} = \nabla\Omega_i$ and $\tilde{\mathbf{a}}_{i,j} = -ie^{i\Omega_{j,i}}A_{i,j}$. The left hand side becomes:

$$\left\{\frac{\mathbf{p_X}\cdot\mathbf{p_X}}{2} + [b_{i,i}(\mathbf{X}) + V_i(\mathbf{X})] + \left(\frac{\mathbf{p_X}}{2}\cdot\Omega_i(\mathbf{X})\right) + \nabla\Omega_i(\mathbf{X}))\cdot\mathbf{p_X} - E_m)\right\}\chi_i^m(\mathbf{X}) = 0 \tag{30}$$

or in the absense of conical intersections

$$\left\{\frac{\mathbf{p_X}\cdot\mathbf{p_X}}{2} + [b_{i,i}(\mathbf{X}) + V_i(\mathbf{X})] - E_m)\right\}\chi_i^m(\mathbf{X}) = 0. \tag{31}$$

Equation (31) is the standard nuclear Schrödinger equation in the absence of a conical intersection, while Eq. (30) evinces the changes attributable to the geometric phase effect that result from a conical intersection. This changes were termed the Molecular-Aharonov–Bohm (MAB) effect.[63,64] The $b_{i,i}$ term in Eq. (31), the adiabatic correction, modifies the Born–Oppenheimer potential energy surfaces and makes them mass dependent.

Equation (29) can be written in more compact form. Noting that from Eq. (21a) that $\tilde{\mathbf{a}}_{i,j}(\mathbf{X}) + \tilde{\mathbf{a}}_{j,i}(\mathbf{X})^* = 2\tilde{\mathbf{a}}_{i,j}(\mathbf{X})$, Eq. (30) can be rewritten in matrix form and

$$\left\{\frac{\mathbf{p_X}\cdot\mathbf{p_X}}{2}\mathbf{I} + \tilde{\mathbf{b}}(\mathbf{X}) + \mathbf{V}(\mathbf{X}) + \frac{1}{2}(\mathbf{p_X}\cdot\tilde{\mathbf{a}}(\mathbf{X})) + \tilde{\mathbf{a}}(\mathbf{X})\cdot\mathbf{p_X} - E_m\mathbf{I})\right\}\boldsymbol{\chi}^m(\mathbf{X}) = \mathbf{0}. \tag{32}$$

Provided the electronic basis is complete, according to the last equality in Eq. (21b)

$$\begin{aligned}(\mathbf{p_X}\mathbf{I} + \tilde{\mathbf{a}})^\dagger\cdot(\mathbf{p_X}\mathbf{I} + \tilde{\mathbf{a}}) &= \mathbf{p}_\mathbf{X}^\dagger\cdot\mathbf{p_X}\mathbf{I} + \tilde{\mathbf{a}}^\dagger\cdot\mathbf{p_X} + \mathbf{p_X}\cdot\tilde{\mathbf{a}} + \tilde{\mathbf{a}}^\dagger\cdot\tilde{\mathbf{a}} \\ &= \mathbf{p}_\mathbf{X}^\dagger\cdot\mathbf{p_X}\mathbf{I} + (\tilde{\mathbf{a}}^\dagger + \tilde{\mathbf{a}})\cdot\mathbf{p_X} + (\mathbf{p_X}\cdot\tilde{\mathbf{a}}) + \tilde{\mathbf{a}}^\dagger\cdot\tilde{\mathbf{a}}\end{aligned} \tag{33a}$$

can replace

$$\mathbf{p}_{\mathbf{X}}^{\dagger} \cdot \mathbf{p}_{\mathbf{X}}\mathbf{I} + (\tilde{\mathbf{a}}^{\dagger} + \tilde{\mathbf{a}}) \cdot \mathbf{p}_{\mathbf{X}} + (\mathbf{p}_{\mathbf{X}} \cdot \tilde{\mathbf{a}}) + \tilde{\mathbf{b}} \tag{33b}$$

so that Eq. (32) becomes

$$\left\{ \frac{(\mathbf{p}_{\mathbf{X}}\mathbf{I} + \tilde{\mathbf{a}})^{\dagger} \cdot (\mathbf{p}_{\mathbf{X}}\mathbf{I} + \tilde{\mathbf{a}})}{2} + \mathbf{V}(\mathbf{X}) - E_m\mathbf{I} \right\} \boldsymbol{\chi}^m(\mathbf{X}) = \mathbf{0}. \tag{34}$$

Equation (34) serves to motivate the numerical methods discussed in Chapter 3 for the evaluation of derivative couplings.

3. Perturbation Theory

The singular behaviour of the adiabatic energies, wave functions and derivative couplings near a conical intersection makes a formal analysis of that region highly desirable. This analysis is accomplished using a generalization of the perturbation theory developed by Mead in his seminal treatment of X_3 molecules.[61]

From Table 1, it is seen that there is more than one type of conical intersection. For molecules with N^{el} even (odd) $\eta = 2$ ($\eta = 3$ or 5). The origin of the differences is, as explained by Mead,[34] time reversal symmetry. For N^{el} odd (even) Φ_κ and $T\Phi_\kappa$ are (are not) linearly independent. Here T is the time reversal operator. See appendix A. Thus for odd (even) electron systems, the intersection of two potential energy surfaces requires the degeneracy of four (two) electronic states. As discussed below, this leads to the values of η reported in Table 1.

Despite this essential difference, the perturbative analyses of the individual cases have much in common. Further it will be shown that the lowest order results for $\eta = 2$ are those obtained for the model Hamiltonian $\mathbf{W}^l$ [Eq. (8a)]. Thus Sec. 2 contains most of the tools necessary to analyze the $\eta = 2$ case. For this reason, in this section, to the extent possible, we treat the most general, $\eta = 5$ case (the N^{el} odd, spin-orbit included, no symmetry case), first and then show how the simpler $\eta = 3$ case (the odd electron, spin-orbit included, C_s or greater symmetry, case) and $\eta = 2$ (the N^{el} even, spin-orbit included case and the non-relativistic case) can be recovered as limits. On the other hand, the $\eta = 5$ and 3 results are quite new compared to those for $\eta = 2$. Thus, as the subsequent presentation attests, the formalism for $\eta = 2$ is further advanced and more substantative numerical studies have been carried out.

3.1. *Crude Adiabatic Basis*

It is a nontrivial matter to determine the coordinate dependence of the eigenvalues of an $N^{\mathrm{CSF}} \times N^{\mathrm{CSF}}$ matrix in Eq. (2c) in the vicinity of a degeneracy. This task is made possible, formally, by a change of basis and computationally, by analytic gradient techniques described in Chapter 3 of this volume. We begin our analysis by constructing this change of basis.

For a conical intersection of states k, l at $\mathbf{X}^{x,k,l}$, define a crude adiabatic basis:

$$\Phi_k^c(\mathbf{x}^e; \mathbf{X}) = \sum_{a=1}^{N^{\mathrm{CSF}}} c_a^k(\mathbf{X}^{x,k,l}) \Theta_a(\mathbf{x}^e; \mathbf{X}). \tag{35}$$

Note that each point of conical intersection requires a distinct crude adiabatic basis. The eigenstates are expanded in the crude adiabatic basis

$$\Phi_k(\mathbf{x}^e; \mathbf{X}) = \sum_{l \in Q} \xi_l^k(\mathbf{X}) \Phi_l^c(\mathbf{x}^e; \mathbf{X}) + \sum_{l \in P} \Xi_l^k(\mathbf{X}) \Phi_l^c(\mathbf{x}^e; \mathbf{X}) \tag{36}$$

where Q is spanned by the functions degenerate at $\mathbf{X}^{x,k,l}$ and P is its orthogonal complement. Thus Q has dimension $N^Q = 4(2)$ for the case of an odd (even) electron molecule.

To realize the advantage of this transformation for describing $V_k(\mathbf{X})$ near an $\mathbf{X}^{x,k,l}$, we expand everything in displacements δX, from $\mathbf{X}^{x,k,l}, \delta\mathbf{X} = \mathbf{X} - \mathbf{X}^{x,k,l}$. $\mathbf{H}^e(\mathbf{X})$ is expanded to second order in the CSF basis, giving:

$$\begin{aligned} \mathbf{H}^e(\mathbf{X}) = \mathbf{H}^{\mathrm{e}}(\mathbf{X}^{x,k,l}) + \nabla_{\mathbf{X}} \mathbf{H}^{\mathrm{e}}(\mathbf{X}^{x,k,l}) \cdot \delta\mathbf{X} \\ + \frac{1}{2} \delta\mathbf{X} \cdot \nabla_{\mathbf{X}} \nabla_{\mathbf{X}} \mathbf{H}^{\mathrm{e}}(\mathbf{X}^{x,k,l}) \cdot \delta\mathbf{X}. \end{aligned} \tag{37}$$

Reexpressing $\mathbf{H}^e$ in the crude adiabatic basis gives

$$\mathbf{H}^c(\mathbf{X}) \equiv \mathbf{c}^\dagger(\mathbf{X}^{x,k,l}) \mathbf{H}^e(\mathbf{X}) \mathbf{c}(\mathbf{X}^{x,k,l}) \tag{38a}$$

$$\approx \mathbf{c}(\mathbf{X}^{x,k,l})^\dagger [\mathbf{H}^e(\mathbf{X}^{x,k,l}) + \nabla_{\mathbf{X}} \mathbf{H}^e(\mathbf{X}^{x,k,l}) \cdot \delta\mathbf{X} + 1/2 \delta\mathbf{X} \cdot \nabla_{\mathbf{X}} \nabla_{\mathbf{X}} \mathbf{H}^e(\mathbf{X}^{x,k,l}) \cdot \delta\mathbf{X}] \mathbf{c}(\mathbf{X}^{x,k,l}) \tag{38b}$$

$$\equiv V(\mathbf{X}^{x,k,l}) + H^{c,[1]}(\mathbf{X}^{x,k,l}) \cdot \delta\mathbf{X} + 1/2 \delta\mathbf{X} \cdot H^{c,[2]}(\mathbf{X}^{x,k,l}) \cdot \delta\mathbf{X} \tag{38c}$$

where $V(\mathbf{X}^{x,k,l})_{m,n} = \delta_{m,n} \mathrm{V}_m(\mathbf{X}^{x,k,l})$, and † denotes the complex conjugate transpose. $H^{c,[1]}$ is a vector (length $3N^{\mathrm{nuc}}$) of $(N^Q \times N^Q)$ matrices,

and $H^{c,[2]}$ is a $(3N^{\rm nuc} \times 3N^{\rm nuc})$ matrix of $(N^Q \times N^Q)$ matrices, where

$$\mathbf{H}^{c,[1]}_{m,n} \equiv (h_1^{m,n}, h_2^{m,n}, \ldots, h_{3N^{\rm nuc}}^{m,n}) \tag{39a}$$

$$\mathbf{H}^{c,[2]}_{m,n} \equiv (q_{1,1}^{m,n}, q_{1,2}^{m,n}, \ldots, q_{3N^{\rm nuc},3N^{\rm nuc}}^{m,n}) \tag{39b}$$

with

$$\mathbf{h}^{m,n}(\mathbf{X}) = \mathbf{c}^{m^\dagger}(\mathbf{X}^{x,k,l})[\nabla \mathbf{H}^e(\mathbf{X})]\mathbf{c}^n(\mathbf{X}^{x,k,l}) \tag{40a}$$

and finally

$$q^{m,n}_{\kappa,\kappa'}(\mathbf{X}) = \mathbf{c}^{m^\dagger}(\mathbf{X}^{x,k,l}) \left[\frac{\partial^2}{\partial X_\kappa \partial X_{\kappa'}} \mathbf{H}^e(\mathbf{X})\right] \mathbf{c}^n(\mathbf{X}^{x,k,l}). \tag{40b}$$

Next we expand $\xi(\mathbf{X}), \Xi(\mathbf{X})$ and $V_k(\mathbf{X})$, as

$$\xi^k(\mathbf{X}) = \xi^{(0),k}(\mathbf{X}^{x,k,l}) + \xi^{(1),k}(\mathbf{X}) + \xi^{(2),k}(\mathbf{X}) \tag{41a}$$

$$\Xi^k(\mathbf{X}) = \Xi^{(1),k}(\mathbf{X}) + \Xi^{(2),k}(\mathbf{X}) \tag{41b}$$

$$\mathrm{V}_k(\mathbf{X}) = \mathrm{V}_k(\mathbf{X}^{x,k,l}) + V_k^{(1)}(\mathbf{X}) + V_k^{(2)}(\mathbf{X}) \tag{42}$$

where the superscript (n) indicates the order of contribution from $\delta\mathbf{X}$. In Eq. (41b), we observed that since the crude adiabatic basis is used, $\Xi^{(0),k}(\mathbf{X}) = 0$ for $k \in Q$ This observation is key, since partitioning theory[65] can now be used to show that the degeneracy is lifted at first order, that is, linearly, in the Q-space only. It is therefore the Q-space that gives rise to the branching space. Equation (2b) can be rewritten as

$$\begin{pmatrix} {}^{QQ}\mathbf{H}^c - V_k\mathbf{I} & {}^{QP}\mathbf{H}^c \\ {}^{PQ}\mathbf{H}^c & {}^{PP}\mathbf{H}^c - V_k\mathbf{I} \end{pmatrix} \begin{pmatrix} \xi^k \\ \Xi^k \end{pmatrix} = \begin{pmatrix} \mathbf{0} \\ \mathbf{0} \end{pmatrix} \tag{43a}$$

$$\tag{43b}$$

where ${}^{AB}H^c_{i,j} = H^c_{i,j}$ provided $i \in A$ $j \in B$ and $A, B \in Q, P$. Then solving Eq. (43b) for Ξ^k and inserting into Eq. (43a) gives

$$({}^{QQ}\mathbf{H}^c + {}^{QP}\mathbf{H}^c(\mathrm{V}_k\mathbf{I} - {}^{PP}\mathbf{H}^c)^{-1\,PQ}\mathbf{H}^c - \mathrm{V}_k\mathbf{I})\boldsymbol{\xi}^k = \mathbf{0}. \tag{43c}$$

Since ${}^{QP}\mathbf{H}^c_{i,k}(\mathbf{X}^{x,k,l}) = 0 = \Xi_i^{(0),k}$, the second term in Eq. (43c) does not contribute until second order. Then using Eq. (38c) to identify the first order Hamiltonian [Appendix E, Eq. (E.3a)], the first order result is

$$(\mathbf{H}^{c,[1]} \cdot \delta\mathbf{X} - \mathbf{I}\mathrm{V}_k(\mathbf{X}))\boldsymbol{\xi}^{(0),k}(\mathbf{X}^{x,k,l}) = \mathbf{0}. \tag{44}$$

These equations are valid independent of the value of N^Q. The analytic solution of Eq. (44) with its qualifying equalities, Eqs. (39)–(40), is the lynchpin for the analysis of conical intersections.

3.2. *First Order:* $\mathbf{W}^{(1),f}$

As discussed above, the analysis begins with the $N^Q = 4, \eta = 5$ case, which is readily reduced to the $N^Q = 4, \eta = 3$ case, and ultimately reduced to the $N^Q = 2, \eta = 2$ case. We start with four adiabatic states Φ_i, Φ_j and $T\Phi_i \equiv \Phi_{Ti}, T\Phi_j \equiv \Phi_{Tj}$, degenerate at $\mathbf{X}^{x,i,j}$. Then using Eqs. (39a) and (40a), $\mathbf{H}^{c,[1]} \cdot \delta\mathbf{X}$ in Eq. (44) becomes

$$\mathbf{H}^{c,[1]} \cdot \delta\mathbf{X} = \mathbf{W}^{(1),f} = \begin{pmatrix} \mathbf{h}^{i,i} & \mathbf{h}^{i,j} & \mathbf{h}^{i,Ti} & \mathbf{h}^{i,Tj} \\ \mathbf{h}^{j,i} & \mathbf{h}^{j,j} & \mathbf{h}^{j,Ti} & \mathbf{h}^{j,Tj} \\ \mathbf{h}^{Ti,i} & \mathbf{h}^{Ti,j} & \mathbf{h}^{Ti,Ti} & \mathbf{h}^{Ti,Tj} \\ \mathbf{h}^{Tj,i} & \mathbf{h}^{Tj,j} & \mathbf{h}^{Tj,Ti} & \mathbf{h}^{Tj,Tj} \end{pmatrix} \cdot \delta\mathbf{X}. \tag{45a}$$

Simplifying Eq. (45a) is an exercise in time-reversal algebra, see Appendix A. Using Eq. (A.2b) yields the first equality below and using Eq. (A.2a′) gives the second equality

$$\begin{aligned} \mathbf{W}^{(1),f} &= \begin{pmatrix} \mathbf{h}^{i,i} & \mathbf{h}^{i,j} & \mathbf{h}^{i,Ti} & \mathbf{h}^{i,Tj} \\ \mathbf{h}^{i,j^*} & \mathbf{h}^{j,j} & \mathbf{h}^{j,Ti} & \mathbf{h}^{j,Tj} \\ -\mathbf{h}^{Ti,i^*} & -\mathbf{h}^{i,Tj^*} & \mathbf{h}^{i,i} & \mathbf{h}^{i,j^*} \\ -\mathbf{h}^{j,Ti^*} & -\mathbf{h}^{j,Tj^*} & \mathbf{h}^{i,j} & \mathbf{h}^{j,j} \end{pmatrix} \cdot \delta\mathbf{X} \\ &= \begin{pmatrix} \mathbf{h}^{i,i} & \mathbf{h}^{i,j} & 0 & \mathbf{h}^{i,Tj} \\ \mathbf{h}^{i,j^*} & \mathbf{h}^{j,j} & -\mathbf{h}^{i,Tj} & 0 \\ 0 & -\mathbf{h}^{i,Tj^*} & \mathbf{h}^{i,i} & \mathbf{h}^{i,j^*} \\ \mathbf{h}^{i,Tj^*} & 0 & \mathbf{h}^{i,j} & \mathbf{h}^{j,j} \end{pmatrix} \cdot \delta\mathbf{X}. \end{aligned} \tag{45b}$$

We then replace $\mathrm{W}^{(1),f}$ by the sum of a traceless matrix and a diagonal matrix so that

$$\mathbf{W}^{(1),f} = (\mathbf{s}^{i,j} \cdot \delta\mathbf{X})\mathbf{I} + \mathbf{H}^{(1),f} \cdot \delta\mathbf{X} \tag{46a}$$

where

$$\mathbf{H}^{(1),f} = \begin{pmatrix} -\mathbf{g}^{i,j} & \mathbf{h}^{i,j} & 0 & \mathbf{h}^{i,Tj} \\ \mathbf{h}^{i,j*} & \mathbf{g}^{i,j} & -\mathbf{h}^{i,Tj} & 0 \\ 0 & -\mathbf{h}^{i,Tj*} & -\mathbf{g}^{i,j} & \mathbf{h}^{i,j^*} \\ \mathbf{h}^{i,Tj*} & 0 & \mathbf{h}^{i,j} & \mathbf{g}^{i,j} \end{pmatrix} \tag{46b}$$

$2\mathbf{g}^{i,j} = \mathbf{h}^{i,i} - \mathbf{h}^{j,j}$ and $2\mathbf{s}^{i,j} = \mathbf{h}^{i,i} + \mathbf{h}^{j,j}$, all matrix elements are evaluated at $\mathbf{X}^{x,i,j}$ and $\mathbf{X} = \mathbf{X}^{x,i,j} + \delta\mathbf{X}$. Then Eq. (44) becomes

$$(\mathbf{W}^{(1),f} - \mathbf{I}\mathrm{V}_i(\mathbf{X}))\boldsymbol{\xi}^{(0),i}(\mathbf{X}^{x,i,j}) = \mathbf{0}. \tag{46c}$$

To orient the discussion of Eqs. (46b) and (46c), note that for $N^{\rm el}$ even the time reversed states Ti and Tj are linearly dependent with states i and j and so only the upper left 2×2 submatrix will be considered [Eq. (46g)]. For $N^{\rm el}$ odd and C_S spatial symmetry, the upper right hand 2×2 block vanishes by symmetry so the 4×4 matrix reduces to two uncoupled 2×2 matrices [Eq. (46d)]. It is essential to point out here that *all quantities in Eq. (46b) are efficiently obtained using the analytic gradient techniques* as described in Chapter 3 of this volume.

For $N^{\rm el}$ odd, in the absence of spatial symmetry, Eq. (46c) is applicable in its full generality. When C_s or higher symmetry exists, $\mathbf{h}^{i,Tj} = 0$ (Ref. 34) so that $\mathbf{W}^{(1),f}$ is replaced by $\mathbf{W}^{(1),C_s}$

$$\mathbf{W}^{(1),C_s} \equiv (\mathbf{s}^{i,j} \cdot \delta\mathbf{X})\mathbf{I} + \begin{pmatrix} \mathbf{H}^{(1),C_s} & \mathbf{0} \\ \mathbf{0} & \mathbf{H}^{(1),C_s^*} \end{pmatrix} \cdot \delta\mathbf{X} \tag{46d}$$

where

$$\mathbf{H}^{(1),C_s} = \begin{pmatrix} -\mathbf{g}^{i,j} & \mathbf{h}^{i,j} \\ \mathbf{h}^{i,j*} & \mathbf{g}^{i,j} \end{pmatrix}. \tag{46e}$$

For $N^{\rm el}$ even, only the two independent functions degenerate at $\mathbf{X}^{x,i,j}, \Phi_i$ and Φ_j, need be considered. Further $\mathbf{H}^e$ is symmetric, see Appendix A. When only H^0 is used, $\mathbf{H}^e$ is again symmetric and $\mathbf{h}^{i,Tj} = 0$ for all $\mathbf{X}$, regardless of the number of electrons. Only a single M_s conponent need be considered. In these cases Eq. (46b) reduces to

$$\mathbf{W}^{(1),nr} = (\mathbf{s}^{i,j} \cdot \delta\mathbf{X})\mathbf{I} + \mathbf{H}^{nr,(1)} \cdot \delta\mathbf{X} \tag{46f}$$

where

$$\mathbf{H}^{nr,(1)} = \begin{pmatrix} -\mathbf{g}^{i,j} & \mathbf{h}^{i,j} \\ \mathbf{h}^{i,j} & \mathbf{g}^{i,j} \end{pmatrix}. \tag{46g}$$

As discussed below $\mathbf{W}^{(1),nr}$ [Eq. (46f)] and $\mathbf{W}^l$ [Eq. (11)] are equivalent.

We now explain the origin of the values for η given in Table 1. In Appendix B, it is shown that the eigenvalues of $\mathbf{W}^{(1),m}$ for $m = f, C_s$ and nr can be written as:

$$V_{\pm}(\mathbf{X}) = (\mathbf{s}^{i,j} \cdot \delta\mathbf{X}) \pm \sqrt{\sum_{k=1}^{\eta} ([\mathbf{v}^{(k)} \cdot \delta\mathbf{X}]^2)} \tag{47}$$

where $V_- = V_i^{(1)}$ and $V_+ = V_j^{(1)}$ and $\mathbf{v}^{(1)} = \mathbf{g}^{i,j}(\mathbf{X}^{x,i,j}), \mathbf{v}^{(2)} = \text{Re } \mathbf{h}^{i,j}(\mathbf{X}^{x,i,j}) \equiv \mathbf{h}^{\mathrm{r},i,j}(\mathbf{X}^{x,i,j}), \mathbf{v}^{(3)} = \text{Im } \mathbf{h}^{i,j}(\mathbf{X}^{x,i,j}) \equiv \mathbf{h}^{\mathrm{i},i,j}(\mathbf{X}^{x,i,j})$,

and $\mathbf{v}^{(4)} = \text{Re } \mathbf{h}^{i,Tj}(\mathbf{X}^{x,i,j}) \equiv \mathbf{h}^{\mathrm{r},i,Tj}(\mathbf{X}^{x,i,j}), \mathbf{v}^{(5)} = \text{Im } \mathbf{h}^{i,Tj}(\mathbf{X}^{x,i,j}) \equiv \mathbf{h}^{\mathrm{i},i,Tj}(\mathbf{X}^{x,i,j})$. From Eq. (47), the linearly independent, nonvanishing, vectors $\mathbf{v}^{(i)}, i = 1-\eta$ lift the degeneracy in a linear manner and therefore span the branching space. Therefore $\eta = 5, 3, 2$ for $m = f$, C_s and nr. Finally from Appendix B for $m = f$ and $C_s, V_\pm$ are doubly degenerate, while for $m = nr, V_\pm$ are nondegenerate.

3.3. *Intersection-Adapted Cartesian Coordinates*

3.3.1. $\mathbf{W}^{(1),m}$ *in Intersection Adapted Coordinates*

Before determining the eigenfunctions of $\mathbf{W}^{(1),m}$, it is expedient to introduce the intersection-adapted coordinates,[6] *z, x, y, v, μ*, displacements along the $\mathbf{z} = \mathbf{g}^{i,j}(\mathbf{X}^{x,i,j})/g$, $\mathbf{x} = \mathbf{h}^{\mathrm{r},i,j}(\mathbf{X}^{x,i,j})/h^{\mathrm{r}}$, $\mathbf{y} = \mathbf{h}^{\mathrm{i},i,j}(\mathbf{X}^{x,i,j})/h^{\mathrm{i}}$, $\mathbf{v} = \mathbf{h}^{\mathrm{r},i,Tj}(\mathbf{X}^{x,i})/t^{\mathrm{r}}$, $\mu = \mathbf{h}^{\mathrm{i},i,Tj}(\mathbf{X}^{x,i,j})/t^{\mathrm{i}}$ where $g = ||\mathbf{g}^{i,j}(\mathbf{X}^{x,i,j})||$, $h^{\mathrm{r}} = ||\mathbf{h}^{\mathrm{r},i,j}(\mathbf{X}^{x,i,j})||$, $h^{\mathrm{i}} = ||\mathbf{h}^{\mathrm{i},i,j}(\mathbf{X}^{x,i,j})||$, $t^{\mathrm{r}} = ||\mathbf{h}^{\mathrm{r},i,Tj}(\mathbf{X}^{x,i,j})||$, $t^{\mathrm{i}} = ||\mathbf{h}^{\mathrm{i},i,Tj}(\mathbf{X}^{x,i,j})||$ directions respectively. With these definitions

$$\mathbf{W}^{(1),f} = (\mathbf{s}^{i,j} \cdot \delta\mathbf{X})\mathbf{I} + \mathbf{H}^{(1),f}(x, y, z, v, \mu) \tag{48a}$$

where

$$\mathbf{H}^{(1),f}(x, y, z, v, \mu) = \begin{pmatrix} -gz & h^{\mathrm{r}}x + ih^{\mathrm{i}}y & 0 & t^{\mathrm{r}}v + it^{\mathrm{i}}\mu \\ h^{\mathrm{r}}x - ih^{\mathrm{i}}y & gz & -(t^{\mathrm{r}}v + it^{\mathrm{i}}\mu) & 0 \\ 0 & -(t^{\mathrm{r}}v - it^{\mathrm{i}}\mu) & -gz & h^{\mathrm{r}}x - ih^{\mathrm{i}}y \\ t^{\mathrm{r}}v - it^{\mathrm{i}}\mu & 0 & h^{\mathrm{r}}x + ih^{\mathrm{i}}y & gz \end{pmatrix} \tag{48b}$$

$$gz = \mathbf{g}^{i,j}(\mathbf{X}^{x,i,j}) \cdot \delta\mathbf{X} \tag{49a}$$

$$h^{\mathrm{r}}x + ih^{\mathrm{i}}y = \mathbf{h}^{i,j}(\mathbf{X}^{x,i,j}) \cdot \delta\mathbf{X} \tag{49b}$$

$$t^{\mathrm{r}}v + it^{\mathrm{i}}\mu = \mathbf{h}^{i,Tj}(\mathbf{X}^{x,i,j}) \cdot \delta\mathbf{X}. \tag{49c}$$

3.4. *Intersection-Adapted Hyperspherical Coordinates*

The above Cartesian coordinates do not provide the optimal description of the conical intersection. We will show below that a set hyperspherical coordinates provides the best representation. We begin by defining spherical polar coordinates $\rho^{(1)}$, $\theta^{(1)}$, $\phi^{(1)}$, for the $\mathbf{z}, \mathbf{x}, \mathbf{y}$ ($\mathbf{g}^{i,j}$, $\mathbf{h}^{\mathrm{r},i,j}$, $\mathbf{h}^{\mathrm{i},i,j}$) axes and

polar coordinates $\rho^{(2)}$, $\phi^{(2)}$ for the $\mathbf{v}, \mathbf{w}$ ($\mathbf{h}^{\mathrm{r},i,Tj}, \mathbf{h}^{\mathrm{i},i,Tj}$) axes follows as:

$$z = \rho^{(1)} \cos\theta^{(1)} \quad x = \rho^{(1)} \sin\theta^{(1)} \cos\phi^{(1)} \quad y = \rho^{(1)} \sin\theta^{(1)} \sin\phi^{(1)} \tag{50a}$$

and

$$v = \rho^{(2)} \cos\phi^{(2)} \quad \mu = \rho^{(2)} \sin\phi^{(2)}. \tag{50b}$$

We now introduce scaling factors $h^{(1)}$, $q^{(1)}$, $q^{(2)}$,

$$h^{(1)}(\phi^{(1)})^2 = (h^{\mathrm{r}} \cos\phi^{(1)})^2 + (h^{\mathrm{i}} \sin\phi^{(1)})^2 \tag{51a}$$

$$q^{(1)}(\theta^{(1)}, \phi^{(1)})^2 = (g \cos\theta^{(1)})^2 + (h^{(1)}(\phi^{(1)}) \sin\theta^{(1)})^2 \tag{51b}$$

$$q^{(2)}(\phi^{(2)})^2 = (t^{\mathrm{r}} \cos\phi^{(2)})^2 + (t^{\mathrm{i}} \sin\phi^{(2)})^2 \tag{51c}$$

and the associated angles $\xi^{(1)}, \lambda^{(1)}, \xi^{(2)}$

$$\tan\xi^{(1)} = \frac{h^{\mathrm{i}}}{h^{\mathrm{r}}} \tan\phi^{(1)} \tag{52a}$$

$$\tan\lambda^{(1)} = \frac{h^{(1)}}{g} \tan\theta^{(1)} \tag{52b}$$

$$\tan\xi^{(2)} = \frac{t^{\mathrm{i}}}{t^{\mathrm{r}}} \tan\phi^{(2)}. \tag{52c}$$

The relations

$$\tan\theta^{(3)} = \rho^{(2)} q^{(2)} / \rho^{(1)} q^{(1)} \tag{53a}$$

$$\rho^{(3)} = (\rho^{(1)} q^{(1)})^2 + (\rho^{(2)} q^{(2)})^2 \tag{53b}$$

$$= \rho[(\rho^{(1)} q^{(1)}/\rho)^2 + (\rho^{(2)} q^{(2)}/\rho)^2] \equiv \rho\rho_s^{(3)} \tag{53c}$$

and

$$\rho = (\rho^{(2)^2} + \rho^{(1)^{(2)}})^{1/2} \tag{53d}$$

replace $\rho^{(2)}$ and $\rho^{(1)}$ with hyperspherical coordinates $\rho^{(3)}$, $\theta^{(3)}$ and the scaled hyperradius $\rho_s^{(3)}$.

In terms of the quantities in Eqs. (50)–(52):

$$\mathbf{H}^{(1),f} = \begin{pmatrix} -g\rho^{(1)}\cos\theta^{(1)} & \rho^{(1)}h^{(1)}\sin\theta^{(1)}e^{i\xi^{(1)}} & 0 & \rho^{(2)}q^{(2)}e^{i\xi^{(2)}} \\ \rho^{(1)}h^{(1)}\sin\theta^{(1)}e^{-i\xi^{(1)}} & g\rho^{(1)}\cos\theta^{(1)} & -\rho^{(2)}q^{(2)}e^{i\xi^{(2)}} & 0 \\ 0 & -\rho^{(2)}q^{(2)}e^{-i\xi^{(2)}} & -g\rho^{(1)}\cos\theta^{(1)} & \rho^{(1)}h^{(1)}\sin\theta^{(1)}e^{-i\xi^{(1)}} \\ \rho^{(2)}q^{(2)}e^{-i\xi^{(2)}} & 0 & \rho^{(1)}h^{(1)}\sin\theta^{(1)}e^{i\xi^{(1)}} & g\rho^{(1)}\cos\theta^{(1)} \end{pmatrix} \tag{54a}$$

$$\mathbf{H}^{(1),C_s} = \begin{pmatrix} -g\rho^{(1)}\cos\theta^{(1)} & \rho^{(1)}h^{(1)}\sin\theta^{(1)}e^{i\xi^{(1)}} \\ \rho^{(1)}h^{(1)}\sin\theta^{(1)}e^{-i\xi^{(1)}} & g\rho^{(1)}\cos\theta^{(1)} \end{pmatrix} \tag{54b}$$

and

$$\mathbf{H}^{(1),nr} = \begin{pmatrix} -gx & hy \\ hy & gx \end{pmatrix} = \begin{pmatrix} -g\rho\cos\theta & \rho h\sin\theta \\ \rho h\sin\theta & g\rho\cos\theta \end{pmatrix} = \rho q \begin{pmatrix} -\cos\lambda & \sin\lambda \\ \sin\lambda & \cos\lambda \end{pmatrix}. \tag{54c}$$

Note that in Eq. (54c), we have relabelled the coordinates $(z^{(1)}, x^{(1)}, y^{(1)}) \rightarrow (x = \rho\cos\theta,\ y = \rho\sin\theta)$ for consistency with Sec. 2. The second Hamiltonian in (54c) has precisely the form of the final term in Eq. (8b) so that the linear model discussed in Sec. 2 is completely general as promised. The Hamiltonian in Eqs. (54a)–(54b) form the basis of our search algorithms for locating and analyzing conical intersections with the spin-orbit interaction included.

The five coordinates, $\rho^{(3)}$, $\theta^{(3)}$, $\phi^{(2)}$, $\theta^{(1)}$, $\phi^{(1)}$ (or the appropriate subset) collectively denoted as $\boldsymbol{\omega}$, are used to describe the branching space.

3.4.1. *Eigenvalues in Terms Hyperspherical Coordinates*

From Eq. (47)

$$\begin{aligned} \sum_{k=1}^{\eta} ([\mathbf{v}^{(k)} \cdot \delta\mathbf{X}]^2) &= [\rho^{(1)}q^{(1)}]^2 + [\rho^{(2)}q^{(2)}]^2 = \rho^{(3)^2} \quad \text{for } \eta = 5 \\ &= [\rho^{(1)}q^{(1)}]^2 \quad \text{for } \eta = 3 \\ &= [\rho q]^2 \quad \text{for } \eta = 2. \end{aligned} \tag{55a}$$

Including the diagonal term for $\eta = 2$,

$$V_{\pm}^{(1),nr}(\rho,\theta,\mathbf{w}) - \left(\rho(s_x\cos\theta + s_y\sin\theta) + \sum_{i=1}^{N^{\text{int}}-2} s_{w_i} w_i\right)$$
$$= \pm\rho\sqrt{((g\cos\theta)^2 + (h\sin\theta)^2)}$$
$$= \pm\rho\delta_{gh}\sqrt{(1+\Delta_{gh}\cos 2\theta)} \tag{55b}$$

where

$$\delta_{gh}^2 = \frac{(g^2+h^2)}{2} \quad \text{and} \quad \Delta_{gh} = \frac{(g^2-h^2)}{(g^2+h^2)}. \tag{55c}$$

Equation (55b) is equivalent to Eq. (10) as promised previously.

3.5. *Orthogonal Intersection-Adapted Coordinates*

Since the $\mathbf{c}^k$, $k \in Q$, are defined only up to a unitary transformation among themselves only the branching space, rather than the individual vectors, is well defined. This flexibility can be used to determine a transformation of the degenerate electronic states that does not change the form of Eq. (46a) but causes the $\mathbf{v}^{(k)}$, $k = 1-\eta$, defined following Eq. (47), to be mutually orthogonal. The utility of this transformation should not be underestimated. The orthogonal representation provides a convenient method for making characteristic parameters, $\mathbf{v}^{(k)}$ continuous along the seam. This transformation can be used to uncover any local symmetry present at a no-symmetry conical intersection and, as illustrated in Sec. 4, it causes the $\mathbf{v}^{(k)}$ to carry the appropriate irreducible representation when symmetry is present. In the $\eta = 2$ (Ref. 66), $\eta = 3$ (Ref. 67) and $\eta = 5$ (Ref. 105) cases we have shown that the vectors defining the branching space can indeed be chosen orthogonal, without altering the form of Eq. (45b, 46d, or 46f). Appendix C discusses the derivation of these results. In particular, it is shown for $\eta = 2$ that the orthogonal $\tilde{\mathbf{g}}^{i,j}$ and $\tilde{\mathbf{h}}^{i,j}$

$$\tilde{\mathbf{g}}^{i,j} = (-\mathbf{g}^{i,j}\cos\beta + \mathbf{h}^{i,j}\sin\beta) \tag{56a}$$

and

$$\tilde{\mathbf{h}}^{i,j} = \mathbf{g}^{i,j}\sin\beta + \mathbf{h}^{i,j}\cos\beta \tag{56b}$$

where

$$\tan 2\beta = \frac{2\mathbf{g}^{i,j} \cdot \mathbf{h}^{i,j}}{\mathbf{h}^{i,j} \cdot \mathbf{h}^{i,j} - \mathbf{g}^{i,j} \cdot \mathbf{g}^{i,j}}. \tag{56c}$$

Examples of orthogonal intersection adapted coordinates are provided in Sec. 4.

3.6. *Eigenvectors*

In order to characterize the singularity in the derivative couplings an analytic expression for the eigenvectors of $\mathbf{H}^{m,(1)}$ is required. This result will also enable a discussion of the geometric phase effect and determination of an approximate diabatic basis that eliminates the singular part of the derivative coupling.[41] In Appendix C, the eigenvectors of a matrix with the general form of $\mathbf{H}^{(1),f}$ are derived. The result is expressed as a transformation $\mathbf{U}^{(f)}$ from Ψ^c_k to $\Psi^e_{k'}$, $k = i, j, Ti, Tj$, and $k' = i, Tj, j, Ti$

$$\Psi^e = \mathbf{U}^{(f)}(\Theta^{(1)}, \gamma^{(1)}, \Theta^{(2)}, \gamma^{(2)})^\dagger \Psi^c \tag{57a}$$

where

$$\mathbf{U}^{(\mathrm{tr})} = \begin{pmatrix} \mathrm{c}\Theta^{(1)}\mathrm{c}\Theta^{(2)} & \mathrm{c}\Theta^{(1)}e^{i\gamma^{(2)}}\mathrm{s}\Theta^{(2)} & e^{i\gamma^{(1)}}\mathrm{s}\Theta^{(1)}\mathrm{c}\Theta^{(2)} & e^{i(\gamma^{(1)}+\gamma^{(2)})}\mathrm{s}\Theta^{(1)}\mathrm{s}\Theta^{(2)} \\ -e^{-i\gamma^{(1)}}\mathrm{s}\Theta^{(1)}\mathrm{c}\Theta^{(2)} & -e^{-i(\gamma^{(1)}-\gamma^{(2)})}\mathrm{s}\Theta^{(1)}\mathrm{s}\Theta^{(2)} & \mathrm{c}\Theta^{(1)}\mathrm{c}\Theta^{(2)} & \mathrm{c}\Theta^{(1)}e^{i\gamma^{(2)}}\mathrm{s}\Theta^{(2)} \\ -e^{-i(\gamma^{(1)}+\gamma^{(2)})}\mathrm{s}\Theta^{(1)}\mathrm{s}\Theta^{(2)} & e^{-i\gamma^{(1)}}\mathrm{s}\Theta^{(1)}\mathrm{c}\Theta^{(2)} & -\mathrm{c}\Theta^{(1)}e^{-i\gamma^{(2)}}\mathrm{s}\Theta^{(2)} & \mathrm{c}\Theta^{(1)}\mathrm{c}\Theta^{(2)} \\ -\mathrm{c}\Theta^{(1)}e^{-i\gamma^{(2)}}\mathrm{s}\Theta^{(2)} & \mathrm{c}\Theta^{(1)}\mathrm{c}\Theta^{(2)} & e^{i(\gamma^{(1)}-\gamma^{(2)})}\mathrm{s}\Theta^{(1)}\mathrm{s}\Theta^{(2)} & -e^{i\gamma^{(1)}}\mathrm{s}\Theta^{(1)}\mathrm{c}\Theta^{(2)} \end{pmatrix} \tag{57b}$$

where c = cos and s = sin.

Using the definitions in Eqs. (52)–(54), $\Theta^{(i)} = \lambda^{(i)}/2$, $\gamma^{(i)} = \xi^{(i)}$, i=1,2, which are in turn functions of $\rho^{(1)}$, $\theta^{(1)}$, $\phi^{(1)}$ and ρ', $\phi^{(2)}$. Thus $\mathbf{H}^{(1),f}$ in Eq. (46b) is diagonalized by $\mathbf{U}^{(f)}(\lambda^{(1)}/2, \xi^{(1)}, \lambda^{(2)}/2, \xi^{(2)}) \equiv \mathbf{U}^{(p)}(\lambda^{(1)}, \xi^{(1)}, \lambda^{(2)}, \xi^{(2)})$.

It is useful to see how time reversal symmetry is reflected in $U^{(f)}$. Recall that for the time reversal adapted crude adiabatic states basis functions, the Kramers' degenerate pairs are (1,3) and (2,4), that is, $T\Phi^c_1 = \Phi^c_3$ and $T\Phi^c_2 = \Phi^c_4$, and from Eq. (36) $\Phi_k \approx \sum_{l=1}^4 \Phi^c_l U^{(p)}_{l,k}$. Then $\mathbf{U}^{(p)}$ produces two pairs of states with Kramers' degeneracy, states (1,4) and (2,3), that is, $T\Phi_1 = \Phi_4$ and $T\Phi_3 = \Phi_2$.

Again this general result can be reduced to the $\eta = 3$ case by setting $\gamma^{(2)} = \lambda^{(2)} = 0$ to give [see Eq. (C.14)]

$$\mathbf{U}^{(Cs)} = \begin{pmatrix} \cos\Theta^{(1)} & 0 & e^{i\gamma^{(1)}}\sin\Theta^{(1)} & 0 \\ -e^{-i\gamma^{(1)}}\sin\Theta^{(1)} & 0 & \cos\Theta^{(1)} & 0 \\ 0 & e^{-i\gamma^{(1)}}\sin\Theta^{(1)} & 0 & \cos\Theta^{(1)} \\ 0 & \cos\Theta^{(1)} & 0 & -e^{i\gamma^{(1)}}\sin\Theta^{(1)} \end{pmatrix} \tag{57c}$$

Equations (57b) and (57c) were derived previously in Refs. 67 and 68 respectively.

The $\eta = 2$ or nonrelativistic case is obtained by setting $\gamma^{(1)} = 0$ and $\Theta^{(1)} = \lambda/2$ and using the rows 1 and 2 and columns 1 and 3 gives

$$\mathbf{U}^{(\mathbf{nr})} = \begin{pmatrix} \cos\lambda/2 & \sin\lambda/2 \\ -\sin\lambda/2 & \cos\lambda/2 \end{pmatrix}. \tag{57d}$$

3.7. *Second Order:* $\mathbf{W}^{(2)}$

The double cone pictured in Fig. (2a) is clearly not the linear cone of Eq. (10a), rather it is curved. To describe this curvature and its impact on nuclear dynamics, it is necessary to take the perturbation theory beyond first order. From Eqs. (E.5a) and (E.5b), respectively, we have

$$V_k^{(2)} = \tilde{\xi}^{(0),k^\dagger}\mathbf{H}^{(2-\text{eff})}\tilde{\xi}^{(0),k} = (\mathbf{U}^{(p)^\dagger}\mathbf{H}^{(2-\text{eff})}\mathbf{U}^{(p)})_{k,k} \quad k = i,j \tag{58a}$$

$$\tilde{\xi}_i^{(1),j} = (\mathbf{U}^{(p)^\dagger}\mathbf{H}^{(2-\text{eff})}\mathbf{U}^{(p)})_{i,j}/(2\rho^{(2)}) \tag{58b}$$

$$\tilde{\xi}_j^{(1),i} = -(\mathbf{U}^{(p)^\dagger}\mathbf{H}^{(2-\text{eff})}\mathbf{U}^{(p)})_{j,i}/(2\rho^{(2)}) \tag{58c}$$

where $\rho^{(2)}$ is defined in Eq. (50b). Then from Eq. (58a) the Hamiltonian through second order is

$$\mathbf{W}^{(2),m} = \vartheta^{(1-2)}(\boldsymbol{\omega}, \mathbf{w})\mathbf{I} + \mathbf{H}^{(1),m} + \mathbf{H}^{(2-\text{net}),m} \tag{59a}$$

where we have removed the diagonal contribution to $\mathbf{H}^{(2-\text{eff})}$ and included it in $\vartheta^{(1-2)}(\boldsymbol{\omega}, \mathbf{w})$, the diagonal contribution through second order described below, that is, $\mathbf{H}^{(2-\text{net})} = \mathbf{H}^{(2-\text{eff})} - \vartheta^{(1-2)}(\boldsymbol{\omega}, \mathbf{w})$. Below the m superscript will be suppressed when no confusion will arise.

3.7.1. *Parametrization*

Unlike $\mathbf{H}^{(1)}, \mathbf{H}^{(2-\text{eff})}$ has contributions from both the Q-space and the P-space, so it is impractical to determine it by direct calculation. Rather it is determined from fitting the energy and/or derivative couplings to a functional form. Here we use a functional form for which the, in general, curved seam is approximated by a piecewise linear seam. Below we consider second order contributions in the branching spaces, with $\eta = 2$ and 3. For $\eta = 2$ or 3, $\mathbf{H}^{(2-\text{net})}$ can be expressed a linear combination of the Pauli matrices

$$\mathbf{H}^{(2-\text{eff})} = P(\boldsymbol{\omega}, \mathbf{w}; a)\sigma_z + P(\boldsymbol{\omega}, \mathbf{w}; b)\sigma_x + P(\boldsymbol{\omega}, \mathbf{w};\, c)\sigma_y \tag{59b}$$

where $\boldsymbol{\omega} = (x, y, z)$ or $(\rho,\, \theta,\, \phi)$, we have dropped the superscript (1) on the variables and as above, for $\eta = 2, P(\boldsymbol{\omega}, \mathbf{w}, c) = 0, \boldsymbol{\omega} = (x, y)$ or $(\rho,\, \theta)$. In the piecewise linear seam approximation

$$\begin{aligned} P(\boldsymbol{\omega}, \mathbf{w}; p) = {} & (p_1^{(\rho)} x^2 + p_2^{(\rho)} y^2 + p_3^{(\rho)} z^2 + p_4^{(\rho)} xy + p_5^{(\rho)} xz + p_6^{(\rho)} yz) \\ & + \sum_i (p_1^{(w_i)} x w_i + p_2^{(w_i)} y w_i + p_3^{(w_i)} z w_i) \end{aligned} \tag{60a}$$

and converting to polar coordinates

$$P(\boldsymbol{\omega}, \mathbf{w}; p) \equiv \rho^2 P_\rho^{(2)}(\theta, \phi; p) + \rho \sum_i w_i P_{w_i}^{(2)}(\theta, \phi; p) \tag{60b}$$

where $\vartheta^{(1-2)}$, the diagonal energy through second order is given by

$$\vartheta^{(1-2)}(\boldsymbol{\omega}, \mathbf{w}) = S(\boldsymbol{\omega}, \mathbf{w}) + P(\boldsymbol{\omega}, \mathbf{w};\, p) + N(\mathbf{w}; \mathbf{n}) \tag{60c}$$

with

$$N(\mathbf{w}, \mathbf{n}) = \sum_{i \geq j} n_{i,j} w_i w_j. \tag{60d}$$

Below we will abbreviate $P(\boldsymbol{\omega}, \mathbf{w}; p)$ by $P(p)$. For $\eta = 2, p_k^{(\rho)} = 0, k = 3, 5, 6$ and $p_3^{(w)} = 0$ for all w. Note from Eq. (60b) that P vanishes when $\rho = 0$ as required by the piecewise linear approximation.

From Eq. (58a), $\mathbf{W}^{(2)}$ is diagonalized to second order by $\mathbf{U}^{(p)}$. The second order contribution requires $\tilde{\mathbf{H}}^{(2-\text{net})} = \mathbf{U}^{(p)\dagger} \mathbf{H}^{(2-\text{net})} \mathbf{U}^{(p)}$ which is

obtained by transforming the individual Pauli matrices $\tilde{\boldsymbol{\sigma}}_w = \mathbf{U}^{(p)^\dagger}\boldsymbol{\sigma}_w\mathbf{U}^{(p)}$ [Eq. (B.5)], and combining the results to give

$$\begin{aligned}\tilde{\mathbf{H}}^{(2-\text{eff})} &= (P(a)\cos 2\Theta - P(b)\cos\gamma\sin 2\Theta - P(c)\sin\gamma\sin 2\Theta)\boldsymbol{\sigma}_z \\ &\quad +(P(a)\cos\gamma\sin 2\Theta + P(b)(\cos 2\Theta + 2\sin^2\gamma\sin^2\Theta) \\ &\quad +P(c)\sin 2\gamma\sin^2\Theta)\boldsymbol{\sigma}_x + (P(a)\sin\gamma\sin 2\Theta \\ &\quad -P(b)\sin 2\gamma\sin^2\Theta - P(c)(\cos 2\Theta + \cos^2\gamma 2\sin^2\Theta))\boldsymbol{\sigma}_y \qquad (61)\end{aligned}$$

where $\Theta = \lambda^{(1)}/2$ and $\gamma = \xi^{(1)}$. A key point here is that A, B, and C can be determined from either the coefficient of $\boldsymbol{\sigma}_z$, an energy contribution, or from a derivative coupling. The later conclusion is based on Eqs. (58b) and (61) and the analysis of the derivative coupling in Sec. 3.7.

To date, the analyses of second order terms have focused on the nonrelativistic Hamiltonian,[47] the $\eta = 2$ case, where $\gamma = 0$, and $\tilde{\mathbf{H}}^{(2-\text{net})}$ reduces to

$$\begin{aligned}\tilde{\mathbf{H}}^{(2-\text{net})} &= (P(a)\cos\lambda - P(b)\sin\lambda)\boldsymbol{\sigma}_z \\ &\quad +(P(a)\sin\lambda + P(b)\cos\lambda)\boldsymbol{\sigma}_x \\ &\equiv \rho m^0\boldsymbol{\sigma}_z + \rho m^1\boldsymbol{\sigma}_x \qquad (62a)\end{aligned}$$

$$\begin{aligned}\Delta V^{(2)}_{i,j} &= V^{(2)}_i - V^{(2)}_j \\ &= 2\rho m^0 = 2(P(a)\cos\lambda - P(b)\sin\lambda) \qquad (62b)\end{aligned}$$

$$m^1 = \rho M^{(\rho)}(\theta) + \sum_i w_i M^{(w_i)}(\theta) \qquad (62c)$$

where

$$M^{(x)} = P^{(2)}_x(a)\sin\lambda + P^{(2)}_x(b)\cos\lambda, x = \rho, w_i. \qquad (62d)$$

Equation (62b) serves to emphasize the connection to the energy. Numerical issues associated with the use of Eqs. (62a) and (62b) are discussed in Sec. 4.

3.7.2. *Confluences*

One of the most significant aspects of the second order analysis is, as was illustrated in Sec. 2, the ability to describe distinct branches of a single seam of conical intersection, and their intersection at confluences. Here we focus on the $\eta = 2$ case so that

$$\mathbf{W}^{(2)} = \vartheta^{(1-2)}(\boldsymbol{\omega}, \mathbf{w})\mathbf{I} - G(x, y, \mathbf{w})\boldsymbol{\sigma}_z + W(x, y, \mathbf{w})\boldsymbol{\sigma}_x. \qquad (63a)$$

According to the discussion in Sec. 2, multiple branches of a seam exist when W, here $W(x, y, \mathbf{w})$, is factorable. Confluences exist when each of the

factors of $W(x, y, \mathbf{w})$ vanishes. Sufficient conditions for an intersection are [see Eq. (59b)]

$$G(x, y, \mathbf{w}) = P(\boldsymbol{\omega}, \mathbf{w}; a) - gx = 0 \tag{63b}$$

$$W(x, y, \mathbf{w}) = P(\boldsymbol{\omega}, \mathbf{w}; b) + hy = 0. \tag{63c}$$

We seek conditions under which $W(x, y, \mathbf{w})$ will be factorable. Consider the frequently studied case of a symmetry-allowed conical intersection of two states of different symmetry. Assume too that the molecule has a plane of symmetry, the least restrictive case. In this case, since $\mathbf{x} \sim a'$ and $\mathbf{y} \sim a''$, where $\sim$ is read "transforms as",

$$W(x, y, \mathbf{w}) = p_3^{(\rho)} xy + \sum_{i \in a''} p_1^{(w_i)} x w_i + \sum_{i \in a'} p_2^{(w_i)} y w_i + hy. \tag{63d}$$

As a consequence of the plane of symmetry, $W_{1,2}(x, y, \mathbf{w})$ will be factorable if $w_i = 0$ for all $\mathbf{w}^i \sim a''$, that is, for molecular geometries that preserve the plane of symmetry. In this case

$$W = W^{(a)} W^{(b)} = y \left(h + p_3^{(\rho)} x + \sum_{i \in a'} p_2^{(w_i)} w_i \right) = y h^{\text{eff}}(x, \mathbf{w}) \tag{64}$$

the seam equations become, on branch $B(a), W^{(a)} = G = 0$, and, on branch $B(b), W^{(b)} = G = 0$. Note too that at the confluence, $h^{\text{eff}} = \|\mathbf{h}^{i,j}\|$ [see Eq. (54c)] vanishes. This necessary condition can be used to help locate confluences.[50,69]

The seam equations [Eqs. (63b) and (63c)] can, in turn, be solved to find the locus of the confluence. Since $G = 0$ is common to both seams, the solution space for the confluence has dimension $N^{\text{int}} - 3$. The confluence, if it exists, occurs, since $W^{(a)} = 0$, for $y = 0$, that is, for C_s geometries. Further, as the seam is described in a piecewise linear manner, confluences, X^c, are restricted to points for which $G(0, 0, w) = W^{(a)}(0, 0, \mathbf{w}) = 0$ and the w_i satisfy [on $B(b)$]

$$-\left(h + \sum_i b_2^{(w_i)} w_i \right) \Big/ b_3^{(\rho)} = 0 \,. \tag{65a}$$

Any $\mathbf{X} = (0, 0, \mathbf{w})$ satisfying Eq. (65a) can be written in terms of the $\zeta_i = -h/b_2^{(w_i)}$, the $N^{\text{int}} - 2$ primitive solutions to Eq. (65a) as

$$\mathbf{w} = (d_1 \zeta_1, \ldots, d_{N^{\text{int}}-2} \zeta_{N^{\text{int}}-2}) \quad \text{with} \quad \sum_{i=1}^{N^{\text{int}}-2} d_i = 1 \tag{65b}$$

which is a subspace of dimension $N^{\text{int}} - 3$. In Sec. 4, an iterative procedure for solving Eqs. (65a) and (65b) will be described.

In summary, we have demonstrated (a class of) confluences that is intimately related to molecular symmetry. These confluences constitute a subspace of a symmetry-allowed or different symmetry portion of the seam of conical intersection. The symmetry-allowed conical intersection has been over the years the most commonly studied type of conical intersection. Thus the comparatively recent discovery confluences would indicate that they are a rare occurrence. However, very recent work indicates instead that their only recent identification may reflect the limited data on the multidimensional character of conical intersection seams in tetra atomic and larger molecules.[51]

3.7.3. *Portion of the Wave Function not Determined by the Schrödinger Equation*

Below we will see that in order to describe the distance dependence of the derivative coupling the $\tilde{\xi}_k^{(1),m}$ are required. Perturbation theory (Appendices E and G) does not fully determine $\tilde{\xi}_m^{(1),k}$. Here we consider this point, restricting our analysis to the $\eta = 2$ and 3 cases.

In Appendix E (Eq. (E.5b)), it is seen that the $\tilde{\xi}_m^{(1),k}, k \neq m$ are determined from the perturbation theory but the $\tilde{\xi}_m^{(1),k}, k = m$ are not [Eqs. (E.2)]. In Appendix G, it is shown that the real part of $\tilde{\xi}_k^{(1),k}$ is constrained to vanish by the normalization requirement, that is, Re $\tilde{\xi}_k^{(1),k} = 0$, $k = i, j$. For real-valued wave functions ($\eta = 2$) this is sufficient since Im $\tilde{\xi}_k^{(1),k} = 0$. With this choice of phase the wave function changes sign when transported around a closed loop containing a conical interesection, see Sec. 2.3.6.2. Scaling the wave function by an appropriate $\exp i\Omega(\mathbf{X})$ makes the wave function single-valued although wave function is now complex-valued.

The situation is more complicated for the complex-valued wave functions of the $\eta = 3$ and 5 cases, where Im $\tilde{\xi}_k^{(1),k} \neq 0$ in the "nascent" wave function. Again Im $\tilde{\xi}_k^{(1),k}$ is not determined by normalization. However, it can be made to vanish by judicious choice of the overall phase, Ω_k, which is assumed to have the form, $\Omega_\kappa = \Omega_\kappa^{(0)} + \rho\Omega_\kappa^{(1)} \cdots$. Then it is shown in Appendix G that (for $\eta = 3$) to first order in $\rho, \Omega_\kappa^{(1)}$ can be chosen such that Im $\tilde{\xi}_k^{(1),k} = 0$. With this choice of $\tilde{\xi}^{(1),k}$ we can construct and analyze of the

derivative couplings near the conical intersection. As with the real-valued wave function, an alternative choice of the overall phase is required if the wave function is to be single-valued.

3.8. *Derivative Couplings*

In the vicinity of a conical intersection, the key issue for the first and second derivative coupling is the nature of the singularity. From Eq. (21b), it is sufficient to consider the first derivative term. The derivative coupling $\mathbf{A}_{k,l}(\mathbf{X})$ is given by

$$\mathbf{A}_{k,l}(\mathbf{W}) = \langle \Phi_k(\mathbf{x}^e;\mathbf{X}) \mid \nabla \Phi_l(\mathbf{x}^e;\mathbf{X}) \rangle_{\mathbf{x}^e} = {}^{\mathrm{CI}}\mathbf{A}_{k,l} + {}^{\mathrm{CSF}}\mathbf{A}_{k,l} \tag{66a}$$

where

$${}^{\mathrm{CI}}\mathbf{A}_{k,l} = \sum_{w} U^{\dagger}_{k,w}(\mathbf{X}) \nabla U_{w,l}(\mathbf{X}) \tag{66b}$$

$${}^{\mathrm{CSF}}\mathbf{A}_{k,l} = \sum_{w,w'}^{w} U^{\dagger}_{k,w}(\mathbf{X}) \mathbf{f}^{w,w'} U_{w',l}(\mathbf{X})$$

$$\mathbf{f}^{w,w'} = \langle \Phi^{\mathrm{c}}_{w}(\mathbf{x}^e;\mathbf{X}) \mid \nabla \Phi^{\mathrm{c}}_{w'}(\mathbf{x}^e;\mathbf{X}) \rangle_{\mathbf{x}^e} \tag{66c}$$

and $U_{w,k} = \xi^k_w$ for $w \in Q$, $U_{w,k} = \Xi^k_w$ for $w \in P$. Note that when the $\mathbf{A}_{k,l}(\mathbf{X})$ are complex-valued $\mathbf{A}_{k,k}(\mathbf{X})$ is non-zero. Further, since the Φ_k are determined only up to a phase

$$\langle e^{i\Omega_k(\mathbf{X})} \Phi_k(\mathbf{x}^e;\mathbf{X}) \mid \nabla e^{i\Omega_l(\mathbf{X})} \Phi_l(\mathbf{x}^e;\mathbf{X}) \rangle_{\mathbf{x}^e} = e^{-i(\Omega_k - \Omega_l)} \mathbf{A}_{k,l}(\mathbf{X}) + i\delta_{k,l} \nabla \Omega_l \tag{67}$$

and the diagonal derivative coupling, $\mathbf{A}_{k,k}(\mathbf{X})$ is only determined once that phase is specified.

3.8.1. *First Order*

The lowest order singular contributions are given, for $\Omega^{(0)}_k = 0, k = i, j$, by:

$${}^{CI}\mathbf{A}^{(1)}_{k,l} = \sum_{\alpha \in Q} \tilde{\xi}^{(0),k}_{\alpha}(\boldsymbol{\omega},\mathbf{w}) \nabla \tilde{\xi}^{(0),l}_{\alpha}(\boldsymbol{\omega},\mathbf{w}) \quad k,l \in i,j. \tag{68}$$

3.8.1.1. $\eta = 2$ (Ref. 70)

Choosing $\Omega_i = 0$, the $\tilde{\xi}_\alpha^{(0),k}$ are real-valued and given by Eq. (57d). Then $\mathbf{A}_{i,i} = \mathbf{A}_{j,j} = \mathbf{0}$ and

$$\begin{aligned}\mathbf{A}_{i,j}^{(1)} &= \nabla\lambda/2 = (A_{i,j}^{(1),x}, A_{i,j}^{(1),y}) = A_{i,j}^{(1),\theta}(1/\rho)(-\sin\theta, \cos\theta) \\ &= A_{i,j}^{(1),\theta} = gh/q^2 \end{aligned} \tag{69}$$

in accord with Eq. (17b). See Eqs. (54) and (55) for the definitions of *g*, *h*, *q*, θ and λ.

For notational simplicity, below in Eq. (70) ∇ indicates differentiation with respect to a general set of independent variables. Here it is interesting to note that in cartesian coordinates both $A_{i,j}^{(1),x}$ and $A_{i,j}^{(1),y}$ are singular, approaching ∞ as $(1/\rho)$, whereas in polar coordinates $A_{i,j}^{(1),\rho} = 0$ and $A_{i,j}^{(1),\theta}$ is nonvanishing.

3.8.1.2. $\eta = 3$ (Ref. 68)

For $\eta = 3$, the $\tilde{\xi}_\alpha^{(0),k}$ are complex-valued. Using as overall phases $\Omega_i = \exp(i\gamma^{(1)}/2), \Omega_j = \exp(-i\gamma^{(1)}/2)$ and Eq. (57c) with $\Theta^{(1)} = \lambda/2$ and $\zeta = \gamma^{(1)}/2$, gives[68]

$$A_{i,j}^{(1)} = 1/2(\nabla\lambda) + i(\nabla\zeta)(1/2)\sin\lambda \tag{70a}$$

$$A_{i,i}^{(1)} = i(\cos\lambda)/2\nabla\zeta \tag{70b}$$

$$A_{i,i}^{(1)} = -i(\cos\lambda)/2\nabla\zeta. \tag{70c}$$

The singularity in $\mathbf{A}^{(1)}$ is discussed below.

3.8.1.3. $\eta = 5$ (Ref. 41)

Choosing $\Omega_i = \Omega_j = 0$, and using Eq. (57a)

$$\mathbf{A}_{T_{j,i}}^{(1)} = e^{-i\gamma^{(2)}}(-\nabla\Theta^{(2)} + i\nabla\gamma^{(2)}/2\sin 2\Theta^{(2)}) \tag{71a}$$

$$\begin{aligned}\mathbf{A}_{j,i}^{(1)} &= e^{-i\gamma^{(1)}}(-\cos 2\Theta^{(2)}\nabla\Theta^{(1)}) \\ &\quad + i[\sin 2\Theta^{(1)}\cos 2\Theta^{(2)}\nabla\gamma^{(1)}/2]\end{aligned} \tag{71b}$$

$$\begin{aligned}\mathbf{A}_{T_{i,i}}^{(1)} &= e^{-i(\gamma^{(1)}+\gamma^{(2)})}(-\sin 2\Theta^{(2)}\nabla\Theta^{(1)}) \\ &\quad + i[\sin 2\Theta^{(1)}\sin 2\Theta^{(2)}\nabla\gamma^{(1)}/2]\end{aligned} \tag{71c}$$

$$\mathbf{A}_{i,i}^{(1)} = -i(\nabla\gamma^{(1)}\sin^2\Theta^{(1)} + \nabla\gamma^{(2)}\sin^2\Theta^{(2)}) \tag{71d}$$

$$\mathbf{A}^{(1)}_{j,j} = i(\nabla\gamma^{(1)}\sin^2\Theta^{(1)} - \nabla\gamma^{(2)}\sin^2\Theta^{(2)}) \tag{71e}$$

$$\mathbf{A}^{(1)}_{T_{j,j}} = e^{i(\gamma^{(1)}-\gamma^{(2)})}(\sin 2\Theta^{(2)}\nabla\Theta^{(1)}) + i[\sin 2\Theta^{(1)}\sin 2\Theta^{(2)}\nabla\gamma^{(1)}/2]. \tag{71f}$$

$\eta = 3$ results are obtained from Eqs. (71a)–(71e) by setting $\Theta^{(2)} = \gamma^{(2)} = 0$. In the $\eta = 3$ case, $\mathbf{A}^{(1)}_{T_{j,i}}$ vanishes, as expected, since in this case the Φ and $T\Phi$ blocks are not coupled. As in the $\eta = 2$ case, the cartesian gradients reveal the the nature of the singularity. This result is obtained by the chain rule. The details are presented in Appendix H and yield (note $A^{(1),\rho^{(2)}}_{k,l} = 0$) for $s = x, y,$ or z:

$$\begin{aligned} A^{(1),s}_{k,l} = &\left(\frac{\partial\theta^{(1)}}{\partial s}\frac{[h^{(1)}g]}{{q^{(1)}}^2} + \frac{\partial\phi^{(1)}}{\partial s}\frac{[h^{\mathrm{i}^2} - h^{\mathrm{r}^2}]}{2h^{(1)}}\sin 2\phi^{(1)}\frac{g\sin 2\theta^{(1)}}{2{q^{(1)}}^2}\right) \\ &\times\frac{A^{(1),\Theta^{(1)}}_{k,l}}{2} + \frac{\partial\phi^{(1)}}{\partial s}\frac{[h^{\mathrm{i}}h^{\mathrm{r}}]}{{h^{(1)}}^2}A^{(1),\gamma^{(1)}}_{k,l} + \frac{\rho^{(1)}{\rho_q}'}{{\rho^{(2)}}^2} \\ &\times\left(\frac{\partial\theta^{(1)}}{\partial s}\frac{[g^2 - {h^{(1)}}^2]}{2q^{(1)}}\sin 2\theta^{(1)} - \frac{\partial\phi^{(1)}}{\partial s}\frac{[h^{\mathrm{i}^2} - h^{\mathrm{r}^2}]}{2q^{(1)}}\right. \\ &\left.\times\sin 2\phi^{(1)}\sin^2\theta^{(1)} - \frac{\partial\rho^{(1)}}{\partial s}\frac{q^{(1)}}{\rho^{(1)}}\right)\frac{A^{(1),\Theta^{(2)}}_{k,l}}{2} \end{aligned} \tag{72a}$$

for $s = v$ or w:

$$\begin{aligned} A^{(1),s}_{k,l} = &\frac{\rho^{(1)}_q}{{\rho_q}'^2 + {\rho^{(1)}_q}^2}\left(\frac{\partial\phi^{(2)}}{\partial s}\rho'\frac{[t^{\mathrm{i}^2} - t^{\mathrm{r}^2}]}{2q^{(2)}}\sin 2\phi^{(2)} + \frac{\partial\rho'}{\partial s}q^{(2)}\right) \\ &\times\frac{A^{(1),\Theta^{(2)}}_{k,l}}{2} + \frac{\partial\phi^{(2)}}{\partial s}\frac{t^{\mathrm{i}}t^{\mathrm{r}}}{{q^{(2)}}^2}A^{(1),\gamma^{(2)}}_{k,l}. \end{aligned} \tag{72b}$$

Here and in Eq. (73) below, $k, l \in i, j, Ti, Tj$ and the $A^{(1),\omega}_{k,l}, \omega = \Theta^{(i)}, \gamma^{(i)}$, $i = 1, 2$, are given in Eqs. (71a)–(71e). Note that when they do not vanish, $\partial\phi^{(1)}/\partial s, \partial\theta^{(1)}/\partial s \sim 1/\rho^{(1)}, \partial\theta^{(2)}/\partial s \sim 1/\rho'$ while $\partial\rho/\partial s \sim \rho^0$, for $\rho = \rho^{(1)}$ or ρ'. Then since the conical intersection is located at $\rho^{(2)\prime} = 0$ from Eqs. (72a) and (72b), the singularities in the derivative couplings are seen

to be of the form:

$$\frac{1}{\rho'}A_{k,l}^{(1),\gamma^{(2)}}, \frac{\rho'}{\rho^{(2)^2}}A_{k,l}^{(1),\Theta^{(2)}} \text{ or } \frac{\rho^{(1)}}{\rho^{(2)^2}}A_{k,l}^{(1),\Theta^{(2)}}, \frac{1}{\rho^{(1)}}A_{k,l}^{(1),\Theta^{(1)}}, \frac{1}{\rho^{(1)}}A_{k,l}^{(1),\gamma^{(1)}} \tag{73a}$$

which reduce for $\eta = 3$ to

$$\frac{1}{\rho^{(1)}}A_{k,l}^{(1),\Theta^{(1)}}, \frac{1}{\rho^{(1)}}A_{k,l}^{(1),\gamma^{(1)}}. \tag{73b}$$

Thus in all cases the derivative coupling has a $(1/\rho^{(i)})$ singularity where $\rho^{(i)}$ depends on η as described above.

3.8.2. *Second Order*

The derivative couplings determined from the first order wave functions gives information only about the singular contribution. The next nonvanishing contribution to the derivative couplings requires consideration of higher order terms in the perturbation expansion. The electronic wave function through first order is given by Eq. (G.3b)

$$\Phi_i^e = \tilde{\Phi}_i^c + \tilde{\xi}_j^{(1),i}\tilde{\Phi}_j^c + \sum_{\alpha\neq i,j}\Xi_\alpha^{(1),i}\Phi_\alpha^c \tag{74}$$

where from Eqs. (58b) and (58c) $\xi_j^{(1),i} = -\xi_i^{(1),j^*}$. Thus writing

$$\mathbf{A}_{k,l} = \mathbf{A}_{k,l}^{(1)} + \mathbf{A}_{k,l}^{(2)} \cdots . \tag{75}$$

$\mathbf{A}^{(2)}$, the "next" nonvanishing contribution as a function of the distance from the conical intersection, comes from

$$A_{j,i}^{(2)} = \langle\tilde{\xi}_i^{(1),j}\tilde{\Phi}_i^c|\nabla\tilde{\Phi}_i^c\rangle + \langle\tilde{\Phi}_j^c|\tilde{\Phi}_j^c\nabla\tilde{\xi}_j^{(1),i}\rangle + \langle\tilde{\Phi}_j^c|\tilde{\xi}_j^{(1),i}\nabla\tilde{\Phi}_j^c\rangle \tag{76a}$$

$$A_{i,i}^{(2)} = \langle\tilde{\Phi}_i^c|(\tilde{\xi}_j^{(1),i}\nabla\tilde{\Phi}_j^c)\rangle + \langle\tilde{\xi}_j^{(1),i}\tilde{\Phi}_j^c|\nabla\tilde{\Phi}_i^c\rangle + \langle\tilde{\xi}_j^{(1),i}\tilde{\Phi}_j^c|\tilde{\Phi}_j^c\nabla\tilde{\xi}_j^{(1),i}\rangle. \tag{76b}$$

Here we have noted that the $\xi^{(1),k}$ and $\Xi^{(1),k}$ each are first order in the distance from the conical intersection.

Here we are primarily concerned with $\eta = 2$. Noting from Eq. (55a) that $\rho^{(2)} \to \rho q(\theta)$ and using Eqs. (62a) and (62b) in Eqs. (76a) and (76b) gives

$$A^{(2),x}_{j,i} = -M^{(x)}/(2q) \text{ or } 2qA^{(2),x}_{j,i} = -M^{(x)} \; x = \rho, w_i \tag{77a}$$

$$A^{(2),\theta}_{j,i} = \frac{\partial}{\partial\theta}\left[\sum_i \frac{w^i M^{(w^i)}}{2q} + \frac{\rho M^{(\rho)}}{2q}\right]. \tag{77b}$$

The second of Eqs. (77a), when combined with Eq. (77b), permits the parameters $p^{(x)}_n, x = \rho, w^i$ to be determined from derivative coupling data in the g–h plane. Equation (77b), then provides a consistency check on the parameters so determined. This approach is used in Sec. 4 as part of the algorithm for locating confluences. More details concerning the use of Eqs. (77a) and (77b) can be found in Refs. 47 and 66.

3.9. *The Geometric Phase*

As noted previously, the geometric phase was first introduced by Longuet-Higgins[36] to treat the Jahn–Teller problem, subsequently used by Mead and Truhlar[37] in the single electronic state nuclear motion problem, and ultimately generalized to arbitrary adiabatic processes in the highly influential work of Berry.[38] Both Longuet-Higgins, and Mead and Truhlar, considered $\mathbf{H}^{nr,(1)}$ [Eq. (46g)] while Berry considered $\mathbf{H}^{(1),C_s}$ [Eq. (46e)] which contains the work of Mead and Truhlar as a special case. Here we consider the more general $\mathbf{H}^{1(f)}$ [Eq. (46a)].

The scaled coordinates defined in Eqs. (D.1) and (D.2) will be used. This is equivalent to taking $g = h^{\mathrm{r}} = h^{\mathrm{i}} = t^{\mathrm{r}} = t^{\mathrm{i}} = 1$ in Eqs. (D.9a)–(D.9c), in which case in Eq. (57b) $\gamma^{(i)} = \phi^{(i)}$ and $2\Theta^{(i)} = \theta^{(i)}$ for $i = 1, 2$. A series of values of $(\rho^{(1)}, \theta^{(1)}, \phi^{(1)}, \rho', \phi^{(2)})$ defines a path in nuclear coordinate space. Along such a path when $\theta^{(1)}$ increases by 2π, $\Theta^{(1)}$ increases by π. See text following Eq. (D.7). However, this does not happen for $\Theta^{(2)}$. $\theta^{(3)}$ is derived from $\rho^{(1)}$ and $\rho^{(2)}$ using Eq. (53a). Since $\rho^{(1)}$ and $\rho^{(2)}$ are strictly positive, $\Theta^{(2)}$ returns to itself along any closed path [see Eq. (53a)]. Then from the $\Theta^{(i)}$ dependence of $\mathbf{U}^{(p)}$ in Eq. (57b), $\mathbf{U}^{(p)}$ should be multiplied by $e^{i\Theta^{(1)}}$ to make the adiabatic wave functions single-valued. These single-valued adiabatic electronic wave functions form an appropriate basis for the solution of the nuclear Schrödinger equation using single-valued nuclear wave functions.[37] Here the analytic representation of the eigenfunctions make it straightforward to guarantee single-valued wave functions. In numerical

examples, to be considered in future work, the situation is more complicated, since the two Kramers' doublets may become mixed when traversing a closed path.

Since the hamiltonian we consider is more general than that of Berry it is interesting to ask under what circumstances the geometric phase of Berry will be recovered. From Eq. (71d) for $\mathbf{A}_{i,i}$, Berry's result will be obtained provided there is no contribution from the second term. This will occur when the path has no component along $\nabla\xi^{(2)}$. Consider two paths, path 1 [path 2] with only $\phi^{(1)}[\phi^{(2)}]$ increasing from 0 to 2π. In these cases

$$\begin{aligned}\mathrm{Im}\oint A^{(0)}_{i,i}\cdot d\mathbf{X} &= -\oint \sin^2\Theta^{(i)}\nabla\gamma^{(i)}\cdot d\mathbf{X}\\ &= -\int_0^{2\pi}\sin^2\Theta^{(i)}d\phi = -2\pi\sin^2\Theta^{(i)}\\ &= -\pi(1-\cos\theta^{(i)})\end{aligned} \tag{78}$$

where $i = 1$ (2) for path 1 (path 2). For path 1, Eq. (78) is Berry's result, as for example shown in Eq. (29*c*) of Ref. 68. This occurs despite the fact that $\rho^{(2)}$ and hence $\mathbf{h}^{Tj,i}$, the coupling to the full 5 dimensional branching space, does not vanish. Path 2 is not included in Berry's treatment.

4. Numerical Examples

In this section we illustrate the ideas developed in Secs. 2 and 3 with practical results drawn from our work on nonadiabatic processes in H_2OH and HNCO. We use the S_1–S_0 seam of conical intersection in HNCO to consider issues of potential energy surface topography. In particular, we characterize the energy and derivative coupling near a conical intersection using conical parameters, derived from the $\mathbf{s}, \mathbf{g}$ and $\mathbf{h}$ vectors, efficiently determined using analytic gradient techniques described in Chapter 3 of this volume. The accuracy of this perturbative representation of the vicinity of the conical intersection is also considered. Subsequently, we illustrate how the use of *orthogonal* intersection adapted coordinates (IAC) results in conical parameters that are smoothly varying along a seam. We conclude our HNCO studies by considering the possibility that a subspace of confluences is embedded in the symmetry-allowed portion of the seam. We then consider how the inclusion of the spin-orbit interaction changes things. This analysis is based on the $^2\Sigma^+$–$^2\Pi$ portion of the $1^2A' - 2^2A'$ seam of conical

intersection in planar H_2OH. Although the dimension of the relativistic and nonrelativistic seam is different, we show how a combination of energy minimization and geometric constraints can lead to a meaningful association of relativistic and non-relativistic conical intersection points. This association is then used to compare for the nonrelativistic ($\eta = 2$) and relativistic C_s symmetry ($\eta = 3$) cases: orthogonal IAC, the energies and the conical parameters, along the seam of conical intersection for the relativistic Hamiltonian.

4.1. *Topographies and Connectivity of Seams of Conical Intersection* HNCO: The $S_0(1^1A) - S_1(2^1A)$ *Seam*

In this section, the efficient determination and compact representation of the energy and singular part of the derivative coupling[35] along the seam of conical intersection is considered. These quantities, or their diabatic equivalents, the diabatic energies, the potential couplings and the adiabatic to diabatic states transformation angle,[60,71–73] are essential to the treatment of the nuclear dynamics. In addition, we consider the locus of confluences, for this seam. These latter calculations serve to underscore the fact that as a consequence of confluences the topography of a conical intersection can change dramatically along the seam. It is essential to understand and incorporate this geometry dependence into treatments of the associated nonadiabatic process.

4.1.1. *Motivation*

The photochemistry of HNCO has been the subject of numerous recent theoretical[74–80] and experimental[81–85] studies. Following photoexcitation from S_0 to S_1, HNCO on S_1, can decay in ground state H + NCO, that is,

$$\mathrm{HNCO}(S_0) + h\nu \rightarrow \mathrm{HNCO}(S_1) \rightarrow \mathrm{HNCO}(S_0) \rightarrow \mathrm{H} + \mathrm{NCO}.$$

Since direct dissociation on S_1 is precluded by a large barrier, indirect dissociation following a radiationless transition to S_0, facilitated by a seam of conical intersections, has been suggested. For that reason the $S_0(1^1A) - S_1(2^1A)$ seam of conical intersection in HNCO has been the subject of much recent work.[51,78–80] The seam exists for both *cis* and *trans* arrangements of HNCO. The *trans* structures are relevant to the indirect photodissociation, noted above, while the *cis* structures may be relevant to the stability of a *cis* moiety on the 2^2A potential energy surface, which has yet to be

detected. In addition to a characterization of several portions of the seam, a subspace of confluences embedded in the symmetry-allowed $S_0(^1A') - S_1(^1A'')$ portion of the seam of conical intersection for *trans* HNCO will be discussed. This subspace of *trans* confluences is energetically accessible at photon energies used to photodissociate HNCO. Its significance for HNCO photodissociation will be considered.

4.1.2. *Wave Functions*

The Φ_i were approximated by restricted second order configuration interaction (SOCI)[86] wave functions based on the following partitioning of the molecular orbitals [1*a*–3*a*; 6] (4*a*–9*a*; 10) {10*a*–14*a*; 6}. Here the square brackets [ ] denote the core orbitals, kept fully occupied in the SOCI expansion; the rounded ( ) and curly { } brackets denote active spaces, $as1$ and $as2$ respectively. In each case the number of electrons in the corresponding molecular orbital set follows the semicolon. The core orbitals are the 1s orbitals of, carbon, nitrogen and oxygen. In the asymptotic NH + CO region, {10*a*–13*a*; 6} describes the NH($1\pi^2$) electrons and the CO($1\pi^4$) electrons, while in the N + HCO region {10*a*–13*a*; 6} describes H(1s) and NCO($2\pi^3, 7\sigma^2$) electrons. At higher energies, S_2 may become involved in the photochemistry. With an eye toward subsequent calculations that consider S_2, a fifth orbital (14*a*) was added to the active space. In the isocyanic acid region, the ground $^1A'$ state is dominated by the closed shell configuration $1a^2$–$11a^2$, while the open shell electron configuration $1a^2$–$10a^2 11a 12a$ dominates the $^1A''$ state.

The molecular orbitals were determined from a CAS SA-MCSCF procedure. To facilitate convergence of the SA-MCSCF procedure, in which three ^1A states were averaged with normalized weights $(0.51, 0.50.049)/0.71587$, the core and active spaces were defined, for the orbital optimizations only, as [1*a*–8*a*; 16]{9*a*′–14*a*′; 6}. Standard Dunning–Huzinaga double-zeta plus polarization (DZP) basis[87] sets, C[9*s*5*p*1*d*]/(4*s*2*p*1*d*) and H[4*s*1*p*]/(2*s*1*p*) were used in a CI treatment consisting of 3,444,355 CSF's, obtained from all single and double excitations from the two active orbital spaces.

4.1.3. *Energies and Derivative Couplings*

In the vicinity of a seam of conical intersection, the linear or conical contribution to the energy and the singular part of derivative coupling need

not be determined from *ab initio* calculations. Rather the perturbation theory of Sec. 3 can used to determine the energy and derivative coupling in terms of the magnitudes of the conical parameters, $\mathbf{s}^{k,l}, \mathbf{g}^{k,l}$, and $\mathbf{h}^{k,l}$ — Eqs. (55b) and (69) — evaluated along the seam. Below the superscripts labeling the states are omitted when no confusion will result. Here we present data illustrating this assertion and use this approach to describe the vicinity of the HNCO seam. We identify four regions of this seam, according to whether the molecule is *cis* or *trans*, *planar*(p) or nonplanar(np). The energy minimized point of conical intersection for a given set of these attributes and a given value of R(*C*–*N*) is denoted $\mathbf{R}^x(ct, x, R(C\text{–}N)) = (R(H\text{–}N), R(C\text{–}N), R(C\text{–}O), \angle\text{HNC}, \angle\text{NCO}, \angle\text{HNCO})$, where $0 \leq \angle\text{HNC}, \angle\text{NCO} \leq \pi$ and $\angle\text{HNCO} \sim 0(\pi)$ is a *cis* (*trans*) arrangement of the HNCO, and $ct = cis$ or *trans* and $x = p$ or np. This analysis benefits significantly from the use of conical parameters [Eq. (54c)] based on orthogonal intersection adapted coordinates. Energies will be expressed in cm^{-1} relative to the energy at $\mathbf{R}^{\text{eq}-\text{trans}}$, the equilibrium structure of the *trans* conformer on $S_1, V_{2^1A}(\mathbf{R}^{\text{eq}-\text{trans}}) = V_{1A''}(\mathbf{R}^{\text{eq}-\text{trans}})$ and it is convenient to define $V_x(\mathbf{R}^x) \equiv V_{2^1A}(\mathbf{R}) = V_{1^1A}(\mathbf{R})$.

4.1.3.1. Energy and Derivative Couplings from Perturbation Theory

In Eqs. (54c) and (69), the parameters $\mathbf{s}, g$ and h are used to determine the energies and derivative couplings near a point of conical intersection. Below we compare these perturbative results with those of *ab initio* calculations at $\mathbf{R}^x(trans, p, 2.95)$. Figures 4 depicts the g–h plane for this point. From this figure it is seen that the coupling mode, $\mathbf{y}$, has a'' symmetry and therefore is the unique internal a'' coordinate. The tuning mode $\mathbf{x}$ has a' symmetry and tends to decrease R(C–N) and increase $\angle$NCO.

Figure 5 demonstrates the utility of this perturbative analysis, reporting $V_i(\rho, \theta)$, $V_i^{(1)}(\rho, \theta)$ and $A^\theta(\rho\phi)$ and $A^{(1),\theta}(\rho, \theta)$ for $\rho = 0.1$ with the origin at $\mathbf{R}^x(trans, p, 2.95)$. Of primary importance is the good agreement between V_i and $V_i^{(1)}$ and, $A^\theta(\rho, \theta)$ and $A^{(1),\theta}(\rho, \theta)$, obviating the need for *ab initio* calculations in this region. Further, even at this non-infinitesimal value of ρ, $(1/\rho)A^\theta$ is > 35 times larger than any of the remaining derivative couplings, supporting their neglect. At $\mathbf{R}^x(trans, p, 2.95)$, the conical parameters are $g = 0.0540$, $h = 0.0109$, $s_x = -0.1798$ $s_y = 0.0$. Since $|s_x| \gg |s_y|, d_{gh}, V_I(\rho, \theta)$ is approximately proportional to $-\cos\theta$ which is

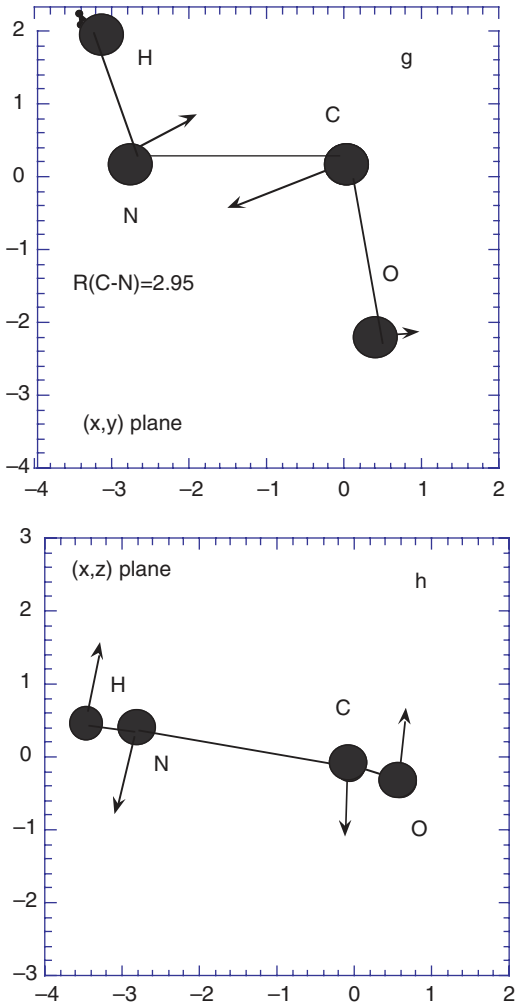

Fig. 4. HNCO: $\mathbf{g}^{1^1A,2^1A}/g$ (top panel) and $\mathbf{h}^{1^1A,2^1A}/h$ (bottom panel) for $\mathbf{R}^{x,1^1A,2^1A}(trans, p, 2.95)$ in terms of atom centered coordinates.

confirmed by Fig. 5. This point is considered further below. Interestingly, the maximum in A^θ occurs for $\theta = \pm\pi/2$, where it represents A^x. This is readily understood from Eq. (69) and the small value of h. The largest coupling near this $^1A'$-$^1A''$ conical intersection occurs not for the unique a''

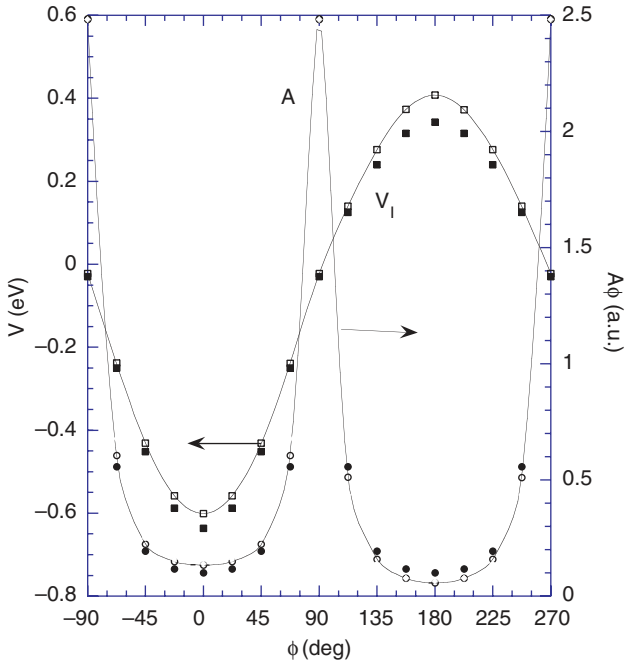

Fig. 5. HNCO: $V_K^{(1)}(\rho = 0.1, \theta)$ (filled squares), $V_K(\rho = 0.1, \theta)$ (open squares, solid line) and $A^{\phi}(\rho = 0.1, \theta)$ (open circles, solid line) $A^{(1)\phi}(\rho = 0.1, \theta)$ (filled circles) for $\mathbf{R}^{x\,1^1A,2^1A}(trans, p, 2.95)$.

mode, but for the tuning mode with a' symmetry. There is no contradiction here, since for $\theta = \pi/2$, the molecule is non-planar.

4.1.3.2. Conical Parameters Along the Seam

Figures 6(a) and 6(b) report the conical parameters s_x, s_y and g, h, respectively, obtained from orthogonal intersection adapted coordinates. If orthogonal $\mathbf{g}$ and $\mathbf{h}$ had not been used g and h would vary erratically along the path, making interpolation and extrapolation impossible. Significantly, from Figs. 6(a) and 6(b), it can be seen that although these conical parameters are by no means constant, the inequalities $s_x > g > h$, discussed above for $\mathbf{R}^x(trans, p, 2.95)$, are, in a qualitative sense, typical.

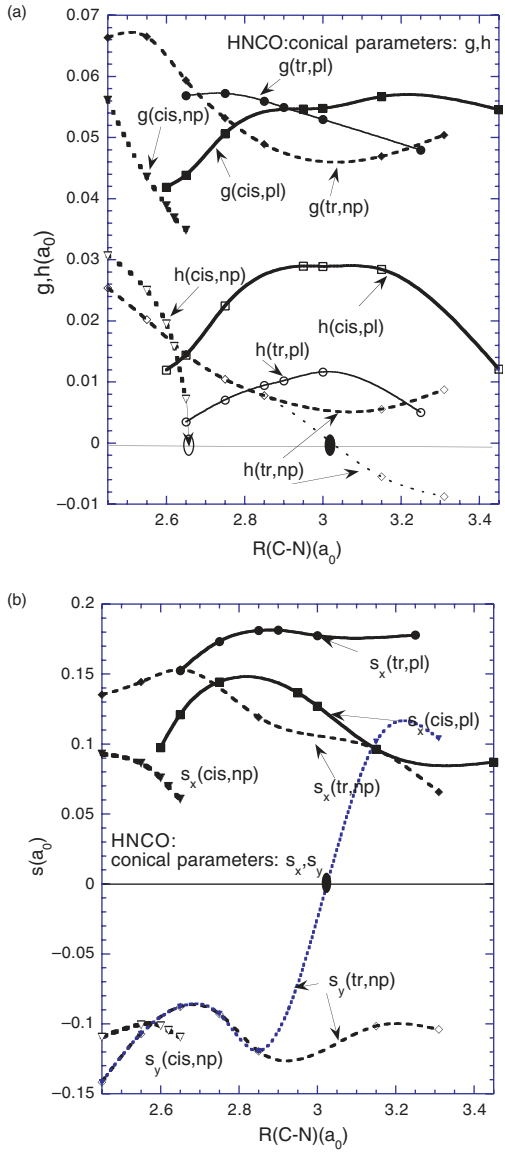

Fig. 6. HNCO: Conical parameters (a) g filled markers, h open markers. cis, pl = cis planar, squares; cis, np = cis nonplanar, triangles; tr, pl = $trans$ planar, circles; tr, np = $trans$ nonplanar, diamonds; (b) s_x, filled markers, s_y, open markers. cis, p = cis planar, squares; cis, np = cis nonplanar, triangles; tr, pl = $trans$ planar, circles; tr, np = $trans$ nonplanar, diamonds.

The topography of a conical intersection can have a profound effect on the nuclear dynamics. Time dependent wave packets can be used to study these effects.[21,25–32,88,89] We have performed such an analysis, focusing on the effects of the general strength parameter d_{gh}, the asymmetry parameter Δ_{gh}, and the parameters s_x, s_y. For $\mathbf{R}^x(trans, p, 2.95)$, $d_{gh} = 0.0275$, and $\Delta_{gh} = 0.9979$ (very asymmetric, maximum value if 1), $s_x/d_{gh} = 6.540$, and $s_y = 0$ (strongly tilted along the x-axis). Strong directional effects are predicted as a result of the large tilt and asymmetry. For the $S_1 \rightarrow S_0$ internal conversion the portion of a wave packet approaching on S_1 from the $\phi = 0(\pi)$ side will be efficiently funneled onto S_0 (deflected away from the conical intersection). The asymmetry will produce a torque that will tend to swirl the wave packet away from $\phi = 0$. These factors may be expected to limit the efficacy of the conical intersection for inducing radiationless decay.

4.1.3.3. Confluences

According to the noncrossing rule,[13] the HNCO seam of conical intersection may have both planar and non-planar portions, as reported above. In a planar tetra-atomic molecule there is only one a'' mode. Thus the $^1A'$–$^1A''$ symmetry-allowed seam of conical intersection cannot be continuously connected to the non-planar seam with both g and h non-vanishing. However these distinct portions of the same seam can intersect at a confluence since there h will vanish. Indeed, from Fig. 6(a), $h(\mathbf{R}^x) \rightarrow 0$ near $R^x(cis, p, 2.66)$ (open circle in that figure) so that a confluence is anticipated near this point. For the *trans* nuclear configurations the situation is not as clear. A confluence may exist near R(C–N) > 3.1, depending on the sign of h for R(C–N) > 3.1. Figures 6(a) and (6b) reports $h(\mathbf{R})(s_y(\mathbf{R}))$ using the two choices for the sign of h. Given the available data neither alternative is compelling. Rather than use the vanishing of h to determine whether confluences exist, an iterative procedure is used based on Eqs. (65a) and (65b).

4.1.3.3.1 *cis Confluences*

The *cis* arrangement will be used to illustrate the iterative approach to locating confluences and characterizing the subspace they span. An iteration in the procedure consists of three elementary steps. At step (k):

(i) *Construct*: At $\mathbf{R}^{(k)}$ use second order perturbation theory, Eq. (77a), to determine $\mathbf{a}^{(w)}$ and $\mathbf{b}^{(w)}$ in Eq. (59b) from the derivative couplings.

Then with the $\mathbf{b}^{(w)}$ known, Eq. (65) can be used to determine the $\zeta_m^{(k)}$, m = 1-($N^{\rm int}-2$). Our current implementation determines $\mathbf{a}^{(w)}$ and $\mathbf{b}^{(w)}$ using a least squares fit to Eq. (77a) along a closed loop in the g–h plane.

(ii) *Displace*: *Choose* $\boldsymbol{\sigma}^{(k)} = (d_1^{(k)}\zeta_1^{(k)}, \ldots, d_{N^{\rm int}-2}^{(k)}\zeta_{N^{\rm int}-2}^{(k)})$ that results in a small displacement and construct $\mathbf{R}^{(k+1)} = \boldsymbol{\sigma}^{(k)}\mathbf{w} + \mathbf{R}^{(k)}$, where $\mathbf{w}$ is the set of vectors defining the seam space at $\mathbf{R}^{(k)}$.

(iii) *Test*: At $\mathbf{R}^{(k+1)}$ determine $\Delta V, \mathbf{g}$ and $\mathbf{h}$. If ΔV is too large run one iteration of the conical intersection locator described in Chapter 3 of this volume ("relaxing") to reduce ΔV. Check for $h \sim 0$. If not $h \sim 0$, go to (i) with $\mathbf{R}^{(k+1)} \rightarrow \mathbf{R}^{(k)}$.

The iterative procedure is illustrated in Table 2. Iteration 0: Step (i) *Construct*: Starting with $\mathbf{R} = (1.936, 2.67, 2.27, 104.0, 101.3, 0.0)$, the $\mathbf{a}^{(w)}$ and $\mathbf{b}^{(w)}$ were determined from a fit to the derivative couplings along a loop with $\rho = 0.05a_0$, using Eq. (77a), see Refs. 47 and 46. Using these second order parameters, Eq. (65a) is solved to give the $\boldsymbol{\zeta}^{(0)}$. Step (ii) *Choose*: Since the representation of the seam is perturbative, its predictions at finite distances are approximations, so that neither $\Delta V_{2^1A,1^1A}$ nor h is expected to vanish exactly. However, the large $\zeta_\kappa^{(0)}$ in Table 2 are inconsistent with the perturbative nature of the equations. Instead, the linear combination given by $\boldsymbol{\sigma}^{(0)} = (z_1^{(0)}\zeta_1^{(0)}, \ldots, z_{N^{\rm int}-2}^{(0)}\zeta_{N^{\rm int}-2}^{(0)}) \cdot \mathbf{w}$ which changes principally the angles, ∠HNC and ∠NCO, was used to construct $\mathbf{R}^{(1)} = \boldsymbol{\sigma}^{(0)} + \mathbf{R}^{(0)}$

Table 2. Sequence of points on the 1^1A-2^1A seam of conical intersection of HNCO obtained from the iterative method of locating a confluence.

	R(H–N)	R(C–N)	R(C–O)	∠HNC	∠NCO	gh	$\Delta V(\mathrm{cm}^{-1})$
					Iteration 0		
$\mathbf{R}^{(0)}$	1.936	2.67	2.27	117.3	111.4	0.927(−3)	0.082
	$\zeta_i \vert i:$	1.901|1	1.369|2	1.306|3	0.379|4	$z^0 = (0.26, 0.17, 0.0, 0.57)$	
					Iteration 1		
$\mathbf{R}^{(1)}$	1.968	2.644	2.272	104.0	102.2	0.443(−3)	280
$\mathbf{R}^{(1),r}$	1.966	2.662	2.287	103.3	102.4	0.362(−3)	0.062
	$\zeta_i \vert i$	2.234|1	−1.540|2	0.119|3	0.135|4	$z^B = (0.0, 0.0, 0.5, 0.5)$	
					Iteration 2		
$\mathbf{R}^{(2)}$	2.007	2.623	2.298	101.2	106.5	0.409(−4)	309
$\mathbf{R}^{(2),r}$	1.997	2.648	2.313	100.7	106.2	0.375(−4)	4.20

with $\mathbf{R}^{(1)}$ and $\mathbf{z}^{(0)}$ given in Table 2. Step (iii) *Test:* Note that gh has decreased by a factor of two. However, ΔV has also increased substantially. ΔV is reduced to acceptable levels by running one iteration of the conical intersection search program producing the relaxed point, $\mathbf{R}^{(1),r}$. In the first iteration, choosing $\mathbf{z}^{(1)}$ as indicated in Table 2 and "relaxing", predicts $\mathbf{R}^{(2),r}$ at which gh has been lowered by an additional order of magnitude. Since the perturbation theory requires nonvanishing $\mathbf{g}$ and $\mathbf{h}$, the iterative procedure was halted at this point. A detailed study of the "converged" region is described below.

4.1.3.3.2 *trans Confluences*

We now turn to the question of confluences in the *trans* configuration. Here we focus on how Eq. (65) can be used to characterize the subspace of the symmetry-allowed seam of conical intersection spanned by the confluence. The relevant results are found in Table 3. Note that g is 100 times larger than h and slowly varying in this region. At iteration 0, with $\mathbf{R}^{(0)} \equiv \mathbf{R}^{x,\mathrm{ref}}$, gh is quite small and can be used to consider the existence of a subspace of confluences in this region.

Define $\mathbf{R}^{(Js)} = \mathbf{R}^{x,\mathrm{ref}} + s\boldsymbol{\sigma}^J \cdot \mathbf{w}$, where $\boldsymbol{\sigma}^J = (\delta_{J,1}\zeta_1, \ldots, \delta_{J,N^{\mathrm{int}}-2}\zeta_{N^{\mathrm{int}}-2})$. $\mathbf{R}^{(Js)}$ denoted $\mathbf{R}^{(J)}$ when $s = 1$ or not defined. Then at $\mathbf{R}^{(Js)}$, $J = 1, 4$, h is significantly reduced from its value at $\mathbf{R}^{x,ref}$ and $\Delta V_{2^1A,1^1A}(\mathbf{R}^{(Js)})$ is quite small. Thus $\mathbf{R}^J, J = 1$ and 4, provide good approximations to the location of two points of confluence and define a one dimensional space using Eq. (65). The largest displacement by far is along $\mathbf{R}^{(2)}$ with $\zeta_2 = 0.383$. Therefore, the appreciable reduction in h and modest increase in $\Delta V_{2^1A,1^1A}$ indicate an additional confluence along $\mathbf{w}^2$ — giving a manifold of confluences of dimension 2 — although the current specification is only approximate. On the other hand, displacement along $\mathbf{w}^3$ by ζ_3 leads to a significant lifting of the degeneracy with only marginal decrease in h. The fact that $\Delta V_{2^1A,1^1A}(\mathbf{R}^{(3)})$ is significantly greater than $\Delta V_{2^1A,1^1A}(\mathbf{R}^{x,\mathrm{ref}})$ may reflect seam curvature which mixes the $\mathbf{w}^i$ and $\mathbf{x}, \mathbf{y}$ coordinates at finite displacements from the origin, introducing a linear term into ΔV. It may also reflect the possibility that the seam space does not reach its maximum allowed dimension, introducing a quadratic term into ΔV. This point is beyond the scope of this review.

To illustrate the multidimensional character of the confluence, Table 3 reports results for the linear combination of the primitive solutions

Table 3. Analysis of the 1^1A–2^1A seam of conical intersection[a].

R(H–N)	R(C–N)	R(C–O)	∠HNC	∠NCO	h	ΔV	J(s)
				Reference			
1.946	3.146	2.242	104.0	101.3	0.881(−3)	0.92	
	$\zeta_1 = 0.111$	$\zeta_2 = 0.383$	$\zeta_3 = 0.144$	$\zeta_4 = 0.0184$			
				Displacement 1			
1.916	*3.146*	*2.246*	*99.7*	*101.2*	*0.491(−4)*	*32*	1
1.911	3.146	2.247	98.8	101.2	−0.149(−3)	43.8	1(1.2)
1.921	3.146	2.245	100.6	101.2	0.177(−3)	21.6	1(0.8)
				Displacement 2			
2.436	*3.153*	*2.243*	*96.3*	*101.4*	*0.195(−3)*	*107*	2
2.535	3.155	2.245	94.6	101.4	−0.163(−3)	152	2(1.2)
2.338	3.150	2.242	97.7	101.4	0.276(−3)	69.4	2(0.8)
				Displacement 3			
1.901	3.334	2.240	101.4	100.6	0.661(−3)	351	3
				Displacement 4			
1.953	*3.154*	*2.230*	*103.9*	*101.7*	*−0.498(−4)*	*4.5*	4
1.955	3.156	2.228	103.9	100.5	−0.302(−3)	6.77	4(1.25)
1.952	3.152	2.233	103.9	100.8	0.190(−3)	2.86	4(0.75)
1.950	3.150	2.236	104.0	101.1	0.421(−3)	1.61	4(0.5)
1.948	3.148	2.239	104.0	101.1	0.648(−3)	1.00	4(0.25)
				Displacement A			
2.024	*3.150*	*2.235*	*101.4*	*100.9*	*0.244(−4)*	*8.8*	A
1.985	3.148	2.239	102.7	101.1	0.426(−3)	2.63	A(0.5)

*All structures are *trans*. Confluences are in *italic* type face. ΔV in cm^{-1}. $\mathbf{R}^{(J)} = \mathbf{R}^{x,\mathrm{ref}} + s\boldsymbol{\sigma}^J \cdot \mathbf{w}$, where $\boldsymbol{\sigma}^J = (\delta_{J,1}\zeta_1, \ldots, \delta_{K,J}\zeta_K)$, $K{=}N^{\mathrm{int}}{-}2$. $\boldsymbol{\sigma}^A = (0.26\zeta_1,\ 0.17\zeta_2,\ 0.0\zeta_3,\ 0.57\zeta_4)$.

$\zeta_i, \sigma^A = (0.26\zeta_1, 0.17\zeta_2, 0.0\zeta_3, 0.57\zeta_4)$. From the data in Table 3, $\mathbf{R}^A = \mathbf{R}^{x,\mathrm{ref}} + \boldsymbol{\sigma}^A \cdot \mathbf{w}$ is clearly a point of confluence, as expected.

It is illuminating to compare h for the points $\mathbf{R}^{(Js)}$ (for definition). According to Eq. (65), h should vanish at $s = 1$. To this end, Table 3 reports $\pm h$ versus Js, for $J = 1, 2, 4$, that is, $\pm h$ along the direction ζ^i with steps of $s\zeta_i$. The sign of h is chosen to reflect the linear behaviour of h near $s = 1$. Consistent with the above analysis is the result that h goes through zero for $0.95 < s < 1.05$, quite close to the $s = 1$ prediction, for $J = 1, 4,\ A$ and for $s \cong 1.15$ for $J = 2$, the more approximate confluence.

4.1.4. *Implications for the $S_1 \rightarrow S_0$ Internal Conversion*

The manifold of *trans* confluences has the potential to affect HNCO internal conversion. The confluences are found for R(C–N) $\cong 3.15a_0$ (with

$J = 3$ excluded as discussed above) and R(C–O) $\cong 2.24a_0$. With R(C–O) stretched to R(C–O) $\cong 2.32$, these confluences are in close proximity geometrically, to $\mathbf{R}^x[R(\text{C–N}) = 3.15] \equiv (1.947, 3.15, 2.316, 103.3, 105.1, \pi)$, the energy minimized conical intersection with R(C–N) $= 3.15a_0$ (based on interpolation of results in Table 2 of Ref. 80). Localization along a coordinate, here R(C–O), is consistent with the reduction by one of the dimensionality of the confluence subspace relative to the different symmetry intersection subspace. Further, as $E_x(\mathbf{R}^x R(\text{C–N}) = 3.15) \approx 8500\,\text{cm}^{-1}$, these confluences are only on the order of $1500\,\text{cm}^{-1}$ above (see Table 1), the lowest energy intersections at R(C–N) $= 3.15a_0$. They are above the NCO($X^2\Pi$) + H) asymptote, which is at $9038\,\text{cm}^{-1}$, based on the experimental data in Ref. 80. Therefore for R(C–O) $\cong 2.24a_0$ (similar to its value at the equilibrium structure in the ground state and in the *trans* excited state[80]) as R(C–N) reaches $3.15a_0$, conical intersections whose energies separate very gradually along one "linear" coordinate may be accessed by the dissociating HNCO. Therefore it is important to understand the nuclear dynamics in this region and include these confluences in any detailed representation of the seam.

4.2. *Inclusion of Spin-orbit Effects.* H_2OH*: The* $\eta = 3$ *Case*

4.2.1. *Motivation*

The electronic quenching

$$\begin{aligned} &\text{OH}(A^2\Sigma^+) + \text{H}_2 \rightarrow \text{OH}(\text{X}^2\Pi) + \text{H}_2 \quad \text{Channel A} \\ &\text{OH}(A^2\Sigma^+) + \text{H}_2 \rightarrow \text{H}_2\text{O} + \text{H} \quad \text{Channel B} \end{aligned}$$

has been the subject of recent experimental studies.[90,91] These reactions are facilitated by the $1^2A'$–$2^2A'$ seam of conical intersection which can route the system to either channels A or B. $C_{\infty v}, C_{2v}$ and C_s portions of the nonrelativistic seam have been reported.[92] Here we are particularly interested in the $C_{\infty v}$ portion of the $1^2A'$–$2^2A'$ seam where the $1^2A''$ state joins the $1, 2^2A'$ states to form a $^2\Sigma^+ - {}^2\Pi$ seam of intersections. In this case the fine structure splitting of the OH moiety lifts the degeneracy obtained at the nonrelativistic ($\eta = 2$) level. Figure 7 describes the effect of the spin-orbit interaction on this degeneracy. Starting with degenerate $1^2\Pi$ and $1^2\Sigma^+$ states at $\mathbf{X}^{x,nr}$, including the spin-orbit interaction within the $^2\Pi$ manifold splits the $^2\Pi$ state into a (lower energy) $^2\Pi_{3/2}$ state

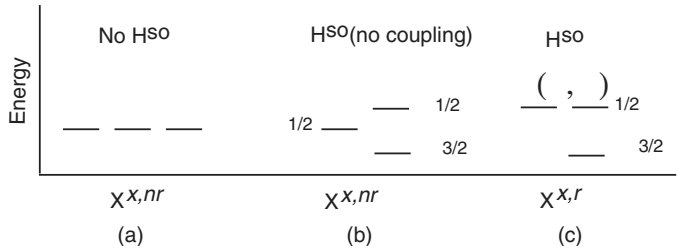

Fig. 7. H_2OH: Representation of degenerate states from nonrelativistic components. (a) Degenerate zeroth order states at $\mathbf{X}^{x,nr}$. (b) Spin-orbit interaction splits $^2\Pi$ state. (c) With full spin orbit interaction turned on, degeneracy is restored by changing geometry to $\mathbf{X}^{x,r}$.

and (higher energy) $^2\Pi_{1/2}$ state. Then, with the full spin-orbit interaction included, the molecule can distort to make either the upper pair, the $2E$ and $3E$ states, or the lower pair, the $1E$ and $2E$ states, degenerate. From Fig. 7 for $C_{\infty v}$ geometries, the $2E$–$3E$ intersection is a "same symmetry", $\Omega = 1/2, 1/2$, intersection, while the $1E$–$2E$ intersection is a different symmetry $\Omega = 3/2, 1/2$ intersection. However, both intersections are conical intersections since both $\Omega = 3/2$ and $\Omega = 1/2$ states decompose into one E' and one E'' (Kramers' doublets) when the molecule is distorted to C_s configurations. Here we consider the more computationally challenging same symmetry, $2E$–$3E$, intersection, focusing on the branching space. Points on the $2E'$–$3E'$ intersection seam were determined using the Lagrange multiplier constrained, analytic gradient driven, search algorithm, described previously[43] and in Chapter 3 of this volume. While only C_s symmetry was imposed, all points located on the $2E'$–$3E'$ seam of conical intersection, which are degenerate to $< 1\,\mathrm{cm}^{-1}$, had $C_{\infty v}$ symmetry.

4.2.2. *Wave Functions*

The nonrelativistic adiabatic wave functions, Φ_i, $i = 1, 2^2A'$, were determined at the SA-MCSCF/MRCI level. The molecular orbitals were determined from a complete active space (CAS)[93–95] SA-MCSCF procedure, employing a $(9s4p2d)$ contracted Gaussian basis set on oxygen and a $(4s2p)$ contracted set on each hydrogen, and averaging the $1^2A', 2^2A'$, and $1^2A''$ states with weights of 0.51, 0.49, and 0.50, respectively. In the SA-MCSCF procedure, the orbitals were partitioned into two subspaces, $[2a' : 4]$ and $[5a', 1a'' : 7]$, where $[ms : n]$ denotes a core space containing a

total of m orbitals of symmetry s and n electrons and $[m's : n']$ denotes an active space with m orbitals of symmetry s and n' electrons. The core space represents the oxygen $1s$ and $2s$ orbitals, whereas the active space contains the remainder of the valence orbitals derived from the oxygen $2p$ and three hydrogen $1s$ orbitals. Dynamical correlation effects were accounted for by a subsequent CI procedure in which the orbitals were repartitioned into four spaces: $[1a' : 2], \{1a' : 2\}, \{5a', 1a'' : 7\}$, and the remaining virtual orbitals. The two CI active spaces will be referred to as $AS1$ and $AS2$, respectively. The CI wave function was constructed from a CSF space that was first order with respect to these active spaces.

From these nonrelativistic wave functions, relativistic basis states were constructed using the methods in Appendix A. The resulting basis functions are

$$\begin{array}{ll} \boldsymbol{\Phi} & T\boldsymbol{\Phi} \\ \sqrt{2}\boldsymbol{\Phi}_{1E'} = \Phi_{1^2A'(1/2)} + i\Phi_{1^2A'(-1/2)} & \sqrt{2}\boldsymbol{\Phi}_{1E''} = \Phi_{1^2A'(1/2)} - i\Phi_{1^2A'(-1/2)} \\ \sqrt{2}\boldsymbol{\Phi}_{2E'} = \Phi_{2^2A'(1/2)} + i\Phi_{2^2A'(-1/2)} & \sqrt{2}\boldsymbol{\Phi}_{2E''} = \Phi_{2^2A'(1/2)} - i\Phi_{2^2A'(-1/2)} \\ \sqrt{2}\boldsymbol{\Phi}_{3E'} = \Phi_{1^2A''(1/2)} - i\Phi_{1^2A''(-1/2)} & \sqrt{2}\boldsymbol{\Phi}_{3E''} = \Phi_{1^2A''(1/2)} + i\Phi_{1^2A''(-1/2)}. \end{array}$$

Here M^S is given in parentheses for the nonrelativistic states and the $\boldsymbol{\Phi}_{iE}$ carry the $E = E'$ or E'' representations of the C_s double group. The relativistic wave functions, Φ_{kE}, $k = 1-3$ and $E = E'$ or E'', are the eigenfunctions of H^e in this basis. The spin-orbit operator is described within the Breit–Pauli approximation.[96]

Here the nonrelativistic (Coulomb, $\eta = 2$) and relativistic (Coulomb + spin-orbit, $\eta = 3$) seams of conical intersection are compared. In C_s symmetry, there are 5 symmetry preserving internal coordinates. The seam conditions, the conditions that require $\mathbf{X}$ to be a point of conical intersection, define η internal coordinates.[43] Thus there is a many-to-one association of nonrelativistic and relativistic seam points. This many-to-one association can be reduced to one-to-one association by comparing the lowest energy point of conical intersection for a fixed-value of the H^2–H^3 distance, $R(H^2 - H^3)$, see Fig. 8(a) for atom labelling. Below we show that this approach results in meaningful comparisons.

4.2.3. *Orthogonal Intersection Adapted Coordinates*

The lowest energy point on the relativistic $C_{\infty v}$ seam occurs at $\mathbf{R}^{\mathrm{mex},2E,3E} = (2.7, 2.05, 2.56)a_0$, where $\mathbf{R} = (R(\mathrm{H^1}\text{–O}), R(\mathrm{O}\text{–H}^2),$

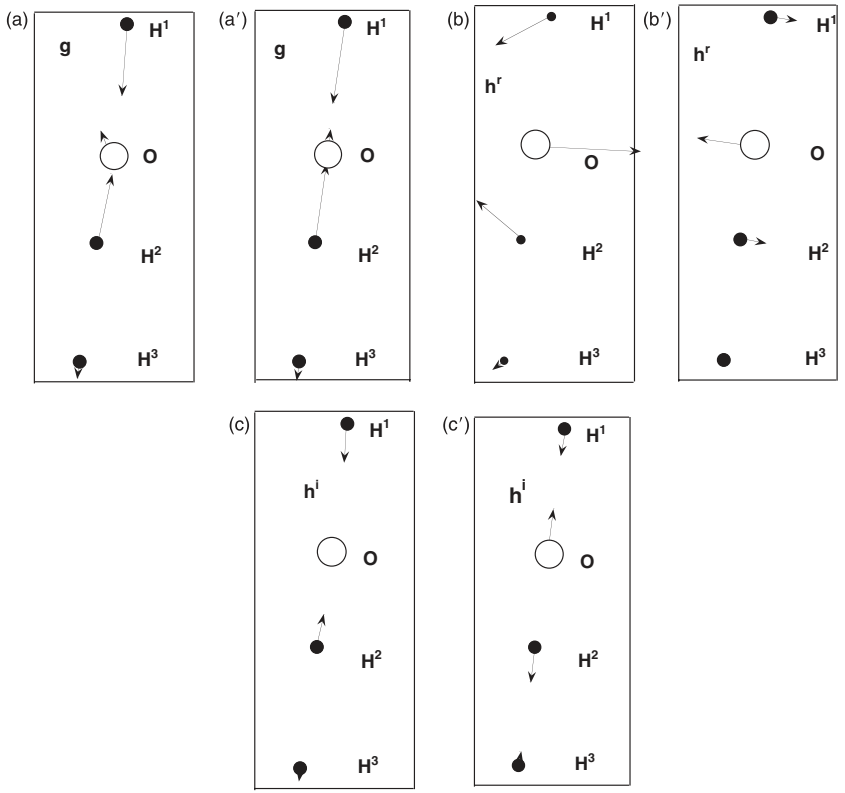

Fig. 8. H_2OH: For $\eta = 3$, the vectors $\mathbf{g}, \mathbf{h}^{\mathrm{r}}$ and $\mathbf{h}^{\mathrm{i}}$. Nascent (a, b, c) and orthogonalized (a', b', c') results at $\mathbf{R}^{x,2E,3E}(2.33)$. For orthogonal vectors, $h^{\mathrm{r}} = 0.0430, g = 0.0825$, and $h^{\mathrm{i}} = 0.000233$. All vectors are scaled by factors of 30 except the orthogonal $\mathbf{h}^{\mathrm{i}}$ which is scaled by a factor of 6000.

$R(\mathrm{H}^2\text{–}\mathrm{H}^3)$). This point is $1990\,\mathrm{cm}^{-1}$ below the $H_2 + \mathrm{OH}(A^2\Sigma^+)$ asymptote. By contrast, the minimum energy point on the $C_{\infty v}$ portion of the non-relativistic seam occurs for $\mathbf{R}^{\mathrm{mex},1^2A,2^2A} = (1.83, 2.2, 1.7)a_0$, which is $13,860\,\mathrm{cm}^{-1}$ below the $\mathrm{H}_2 + \mathrm{OH}(A^2\Sigma^+)$ asymptote.[92] This large change in geometry, reflects the nuclear coordinate dependence of the comparatively small spin-orbit matrix elements. On the other hand, while the $\eta = 3$ seam is absent from the low-energy region of the nonrelativistic seam, where it exists, the separation from the non-relativistic seam is not large.

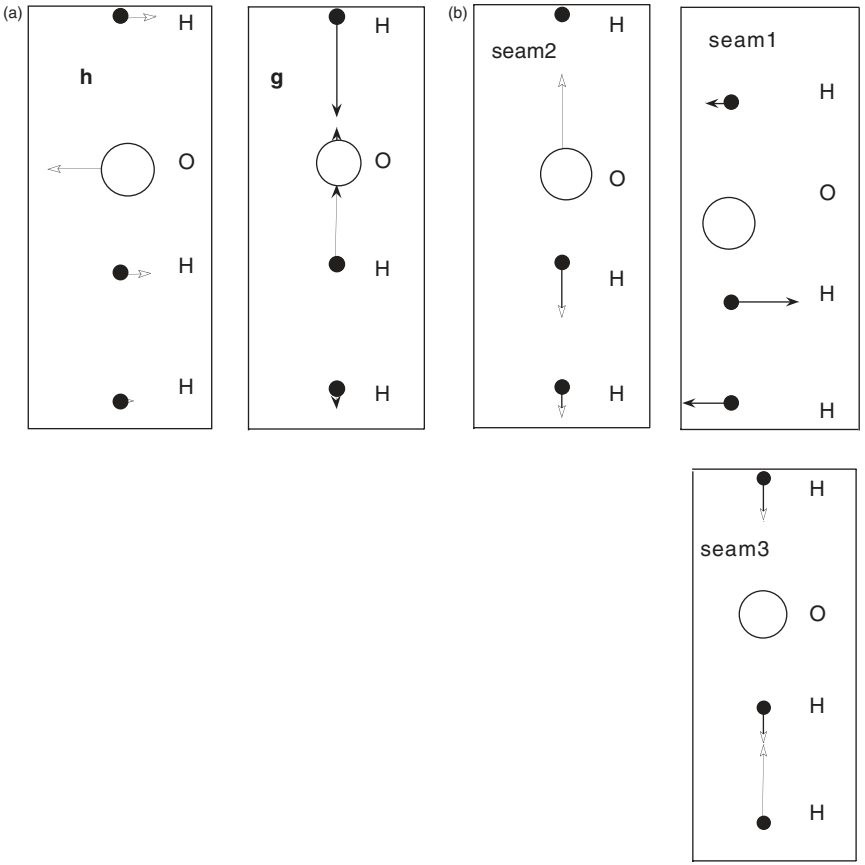

Fig. 9. H_2OH: For $\eta = 2$, (a) the orthogonal vectors $\mathbf{g}, \mathbf{h}$ and (b) seam vectors $w_i,\ i = 1-3$. Orthogonal $\mathbf{g}$ and $\mathbf{h}$ and 3 seam coordinates at $\mathbf{R}^{x,1^2A',2^2A'}(2.33)$. $g = 0.0835, h = 0.0514$. The $\mathbf{g}, \mathbf{h}$ vectors are scaled by a factor of 30. The $\mathbf{w}$ are normalized and scaled by a factor of 2.

Figures 8 and 9 compare the g–h space for the relativistic hamiltonian with the g–h plane for the nonrelativistic hamiltonian. Figure 8 reports $\mathbf{g}^{2E,3E}, \mathbf{h}^{\mathrm{r},2E,3E}$ and $\mathbf{h}^{\mathrm{i},2E,3E}$ and their orthogonalized counterparts, $\tilde{\mathbf{g}}^{2E,3E}, \tilde{\mathbf{h}}^{\mathrm{r},2E,3E}$ and $\tilde{\mathbf{h}}^{\mathrm{i},2E,3E}$ at $\mathbf{R}^{x,2E,3E} = (2.7688, 1.8790, 2.3375)$, which is typical. The nascent $\mathbf{g}^{2E,3E}$, $\mathbf{h}^{\mathrm{r},2E,3E}$ and $\mathbf{h}^{\mathrm{i},2E,3E}$ are clearly not symmetry-adapted. The orthogonalization procedure removes this deficiency, with $\tilde{\mathbf{g}}^{2E,3E}$ and $\tilde{\mathbf{h}}^{\mathrm{i},2E,3E}$ being symmetry preserving σ

displacements and $\tilde{\mathbf{h}}^{\mathrm{r},2E,3E}$ being a π displacement. Figure 9 reports $\tilde{\mathbf{g}}^{1^2A,2^2A}, \tilde{\mathbf{h}}^{1^2A,2^2A}$ and the seam coordinates $\mathbf{w}_k,\ k = 1{-}3$ for $\mathbf{R}^{x1,1^2A,2^2A} = (2.7740, 1.8732, 2.336)$. Comparing Figs. 8 and 9 illustrates the general observation that $\tilde{\mathbf{g}}^{2E,3E}$ is parallel to $\tilde{\mathbf{g}}^{1^2A,2^2A}$ and $\tilde{\mathbf{h}}^{\mathrm{r},2E,3E}$ is parallel to $\tilde{\mathbf{h}}^{1^2A,2^2A}$. This comparison clearly depends on the use of the orthogonalized vectors. $\tilde{\mathbf{h}}^{\mathrm{i},2E,3E}$ is a linear combination of the two symmetry preserving seam coordinates in Fig. 9.

Figure 10 reports additional points on the $2E'$–$3E'$ intersection seam as a function of geometrical constraint, $R(\mathrm{H}^2\text{–}\mathrm{H}^3) = \beta$. Note that $C_{\infty v}$ symmetry was not imposed. The points located on the $2E'$–$3E'$ seam of conical intersection, which are degenerate to $< 1\,\mathrm{cm}^{-1}$, all had $C_{\infty v}$ symmetry.

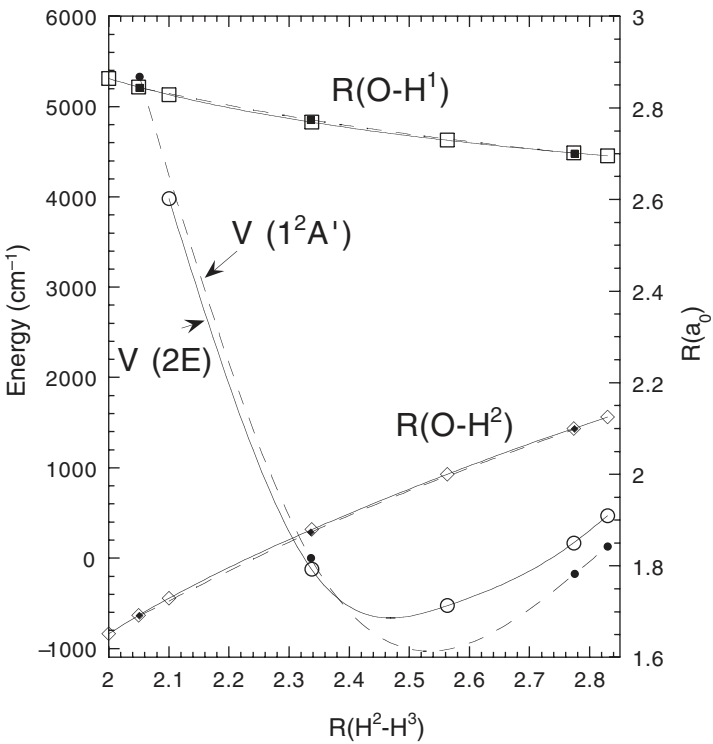

Fig. 10. The relativistic seam $\mathbf{R}^{x,ij}(R(\mathrm{H}^2\text{–}\mathrm{H}^3))$:$R(\mathrm{O}\text{–}\mathrm{H}^1)$, (empty squares), $R(\mathrm{O}\text{–}\mathrm{H}^2)$ (empty diamonds) $V_{2E'}(R(\mathrm{H}^2\text{–}\mathrm{H}^3))$ (empty circles) on the $2E$–$3E$ seam of conical intersection. Filled markers: $1^2A'$–$2^2A'$ nonrelativistic seam of conical intersection.

Figure 10 shows, that while the $\eta = 3$ seam is necessarily distinct from the non-relativistic seam, the separation is not large. In future work, it will be interesting to see how this conclusion changes as the magnitudes of the spin-orbit interactions increases. Along the non-relativistic seam the relativistic energy difference, $\Delta V_{3E,2E}(\mathbf{R}^{x,1^2A',2^2A}(R(\mathrm{H}^2\text{–}\mathrm{H}^3))$, is $\sim 70\,\mathrm{cm}^{-1}$, greater than 50% of the OH($^2\Pi$) fine structure splitting, suggesting that when heavier atoms such as chlorine, where $A^{\mathrm{so}} = \sim 780\,\mathrm{cm}^{-1}$,[97] or even bromine or iodine are involved, $\Delta V_{j,i}(\mathbf{R}^{x,IJ})$, [where I, J (i, j) denote the non-relativistic (relativistic) states] will be much larger, so that nonadiabatic

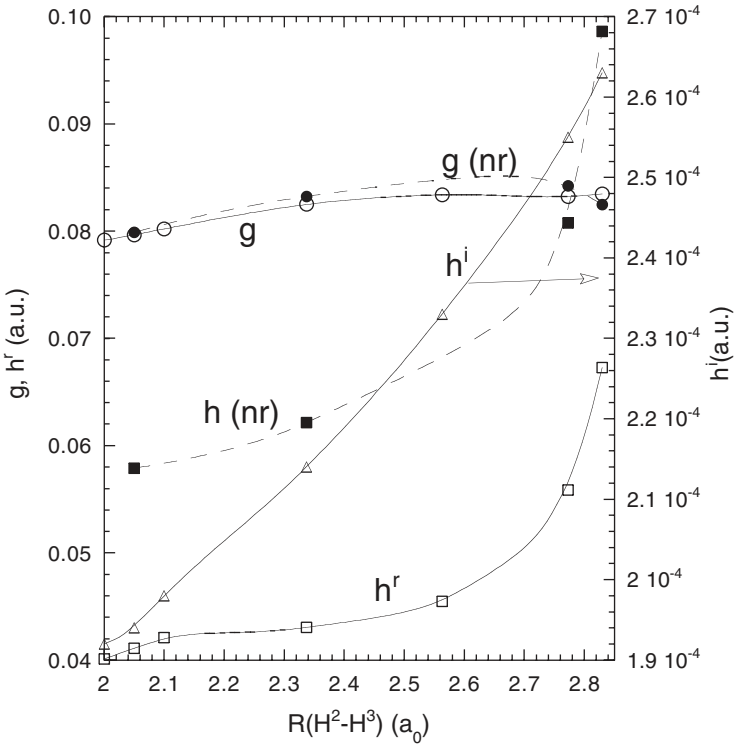

Fig. 11. Conical parameters on the relativistic seam. (a) g (open circles), h^{r} (open squares), h^{i} (open triangles). The nonrelativistic quantities, g (filled circle) and h^{r} (filled square); (b) s_w, $w = x$ (circles), y (squares), z (triangles). Filled (open) markers from nonrelativistic (relativistic) calculations.

effects may be significantly reduced at the nonrelativistic seam by the inclusion of spin-orbit coupling.

The lowest order contributions to the energy are described by the conical parameters $g^{2E,3E}, h^{\mathrm{r},2E,3E}, h^{\mathrm{i},2E,3E}$ and $s_k^{2E,3E}$, $k = x, y, z$, These parameters are reported in Figs. 11(a) and 11(b). Their continuity is attributable to the use of orthogonal intersection adapted coordinates. For comparison, Figs. 11(a) and 11(b) report the nonrelativistic quantities, $g^{1^2A',2^2A}, h^{1^2A',2^2A}$ and $\mathbf{s}^{1^2A',2^2A}$ respectively. From Fig. 11(a), it is seen that for the slowly changing $g^{2E,3E}, |g^{1^2A',2^2A} - g^{2E,3E}|/g^{1^2A',2^2A}$ is small while for the more rapidly varying $h^{\mathrm{r},2E,3E}, |h^{1^2A',2^2A} - h^{\mathrm{r},2E,3E}|/h^{1^2A',2^2A}$ is perhaps not unexpectedly, larger but still modest (< 0.4).

The relative magnitudes of $g^{2E,3E}, h^{\mathrm{r},2E,3E}, h^{\mathrm{i},2E,3E}$ and $s_k^{2E,3E}$ $k = x, y, z$ describe the orientation and shape of the double cone. The relation between these attributes and the near conical intersection dynamics has been discussed previously for nonrelativistic conical intersection. For the conical intersections encountered here, $-s_x^{2E,3E} < h^{\mathrm{r},2E,3E} (-s_z^{2E,3E} > h^{\mathrm{i},2E,3E})$, so that the cone is slightly (significantly) tilted in the $x(z)$-direction. Such a topography faciliates the downward (upward) transitions from negative $x(z)$-direction. The linear coupling in the z-direction, $h^{\mathrm{i},2E,3E}$, is however quite small, so that quadratic terms dominate except very close to the conical intersection. This will limit the role of this coordinate in inducing nonadiabatic transitions. It will be interesting to see how this changes as the size of the spin-orbit interaction increases.

5. Additional Topics

We have considered a large number of issues concerning conical intersections. Several interesting issues have not been discussed. Here we briefly mention these topics and suggest directions for future research.

5.1. *Seam Curvature and Higher Order Effects*

The degenerate perturbation method described in Sec. 3 assumes/requires that the degeneracy be lifted at first order. In this case, "first order" means that displacements exclusively in the seam space, zeroth order in displacements in the branching space [Eqs. (58)–(59)] do not lift the degeneracy. In a triatomic system, the seam would locally be a straight line perpendicular to the g–h plane, and globally the seam would be approximated by a

piecewise linear curve. We therefore refer to the perturbative description of general polyatomic molecules using the theory in Sec. 3 as the piecewise linear seam approximation. In Sec. 3.4, we showed how the piecewise linear seam approximation could be extended to higher (second) order. The higher order terms are needed to describe nonsingular parts of the derivative coupling and higher order terms in the energy. These higher order terms lead to the prediction of seams with two (or more) branches, which may intersect at confluences. The success of the iterative procedure for the location of confluences using the piecewise linear approximation described in Sec. 4 support the utility of this approximation. However, except in high symmetry molecules seam curvature is not entirely absent and it will be important to determine its significance. Initial studies in this regard have been carried out.[47] These studies considered the second order parameters determined by fitting energies and derivative couplings in the vicinity of conical intersections. Corrections for the CSF contribution were included. More studies of this type are required. In addition a theory of conical intersections that rigorously includes seam curvature is needed.

5.2. *Three State Intersections: Coalescences*

In this chapter we have considered exclusively intersections of two (perhaps two-fold degenerate) potential energy surfaces. More complicated types of intersections are possible. The seam for states k, l and that for states l, m may intersect to produce a conical intersection of three states. This situation, which we will refer to as a coalescence, is well-known when sufficient symmetry is present to require it.[48] However 3-state same symmetry conical intersections have been largely ignored, owing to their relative paucity of occurrence, attributable to their five-dimensional branching space, and hence $N^{\text{int}} - 5$ dimensional seam space.[48,99] The discovery of degeneracies of three potential energy surfaces with no-symmetry in recent work on the $3p$ Rydberg states of ethylene,[98] the excited states of allyl,[106] and most recently the accidental intersections of the lowest three states in pyrazolyl,[107] suggest that "accidental" coalescences are not rare occurrences. It will be important to determine the prevalence, and implications for nuclear dynamics, of this class of conical intersection.

Appendices

Appendix A. Time-Reversal Adapted Configuration State Functions

The N^{el}-electron CSF basis Θ^{A,S,M_s} are antisymmetrized eigenfunctions of S^2 and M_s and carry an irreducible representation A of the spatial point group. When the spin-orbit interaction is included in the Hamiltonian, it is convenient to also require that they be time-reversal adapted.[34] A basis is time reversal adapted, provided $T\Theta_a$ is in the basis whenever Θ_a is. Here T, the time reversal operator, is given by[100,101]

$$I = \prod_{j=1}^{N^{el}} (i\sigma_y K)(j), \quad \text{and} \quad \sigma_y = \begin{pmatrix} 0 & i \\ -i & 0 \end{pmatrix}. \tag{A.1}$$

σ_y is a Pauli spin matrix and K denotes complex conjugation. From Eq. (A.1), the time reversal operator, T, is an anti-unitary operator, that is, for ϕ and ψ arbitrary functions, $\langle\phi|\psi\rangle^* = \langle T\phi|T\psi\rangle$, with $T^2 = +I(-I)$ if N^{el} is even (odd). For a molecule with an odd number of electrons:

$$\langle\phi|T\phi\rangle^* = \langle T\phi|T^2\phi\rangle = -\langle T\phi|\phi\rangle = -\langle\phi|T\phi\rangle^*, \text{ so that } \langle\phi|T\phi\rangle = 0 \tag{A.2a}$$

that is, ϕ and $T\phi$ are orthogonal. Further, since T commutes with H_e, ψ and $T\psi$ are degenerate

$$\begin{aligned} \langle\phi|H_eT\psi\rangle^* &= \langle T\phi|H_eT^2\psi\rangle = -\langle T\phi|H_e\psi\rangle \\ &= -\langle\psi|H_eT\phi\rangle^*, \text{ so that } \langle\phi|H_eT\phi\rangle = 0 \end{aligned} \tag{A.2a$'$}$$

and

$$\langle\phi|H_e\psi\rangle^* = \langle T\phi|TH_e\psi\rangle = \langle T\phi|H_eT\psi\rangle. \tag{A.2b}$$

The degeneracy of Φ_i and $T\Phi_i$ is referred to as Kramers' degeneracy.[102] For a molecule with an even number of electrons, ϕ and $T\phi$ are linearly dependent and with the choice $\phi = T\phi$,

$$\langle\phi|H_e\psi\rangle^* = \langle T\phi|TH_e\psi\rangle = \langle T\phi|H_eT\psi\rangle = \langle\phi|H_e\psi\rangle. \tag{A.2c}$$

Thus in this case $\langle\phi|H_e\psi\rangle$ is real-valued. The fact that $\mathbf{H}^e$ can be chosen real-valued has important implications for the theory of conical intersections.

For odd electron molecules, the construction of a time reversal adapted basis is facilitated by the symmetry properties of the CSFs. The time reversal adapted CSF basis functions are given in terms of the Θ^{A,S,M_s} by

$$\Theta^{A,S,|M_s|,+} = \left(\Theta^{A,S,M_s} + i\Theta^{A,S,-M_s}\right)/\sqrt{2} \tag{A.3a}$$

$$\Theta^{A,S,|M_s|,-} = -i(-1)^{S+M_s}\left(\Theta^{A,S,M_s} - i\Theta^{A,S,-M_s}\right)/\sqrt{2}. \tag{A.3b}$$

From the properties of Clebsch–Gordon coefficients[103] used to construct the Θ^{A,S,M_s} in a geneological[104] manner; one shows:

$$T\Theta^{A,S,M_s} = (-1)^{S+M_s}\Theta^{A,S,-M_s} \tag{A.4a}$$

so that

$$T\Theta^{A,S,|M_s|,+} = \Theta^{A,S,|M_s|,-}; \quad T\Theta^{A,S,|M_s|,-} = -\Theta^{A,S,|M_s|,+}. \tag{A.4b}$$

From Eq. (A.4b), the space of pairs $(\Theta^{A,S,|M_s|,+}, \Theta^{A,S,|M_s|,-})$ are a time reversal adapted CSF basis.

To simplify the notation, superscripts A, S and M_s will be suppressed when no confusion will result. When point group symmetry is not an issue, A will be suppressed. To simplify the sums, we will write $\Theta_{i+\mathrm{MCSF}} = T\Theta_i, \equiv \Theta_{T_i}$ with MCSF = NCSF/2. When the Coulomb Hamiltonian is used $T\Theta^{A,S,\pm|M_s|}$ replaces $T\Theta^{A,S,|M_s|,\pm}$.

Appendix B: Eigenvalues and Eigenvectors of a 2 × 2 Hermitian Matrix

In this appendix it is shown how the transformation properties of the individual Pauli matrices can be used to facilitate diagonalization of $\mathbf{h}$, a complex hermitian Hamiltonian. The general 2 × 2 complex hermitian and linearized cases are considered. The Pauli matrices $\boldsymbol{\sigma}_w$ are given by

$$\boldsymbol{\sigma}_z = \begin{pmatrix} 1 & 0 \\ 0 & -1 \end{pmatrix} \quad \boldsymbol{\sigma}_x = \begin{pmatrix} 0 & 1 \\ 1 & 0 \end{pmatrix} \quad \boldsymbol{\sigma}_y = \begin{pmatrix} 0 & i \\ -i & 0 \end{pmatrix} \tag{B.1a}$$

and also define $2\boldsymbol{\sigma}_- = \boldsymbol{\sigma}_x + i\boldsymbol{\sigma}_y$ and $2\boldsymbol{\sigma}_+ = \boldsymbol{\sigma}_x - i\boldsymbol{\sigma}_y$

$$\boldsymbol{\sigma}_+ = \begin{pmatrix} 0 & 1 \\ 0 & 0 \end{pmatrix} \quad \boldsymbol{\sigma}_- = \begin{pmatrix} 0 & 0 \\ 1 & 0 \end{pmatrix}. \tag{B.1b}$$

B.1. *The General Case*

Let $\mathbf{h}$ have the form

$$\begin{aligned}\mathbf{h} &= \mathrm{S}\mathbf{I} + G\boldsymbol{\sigma}_z + H_x\boldsymbol{\sigma}_x + H_y\boldsymbol{\sigma}_y \\ &= \mathrm{S}\mathbf{I} + G\boldsymbol{\sigma}_z + (H_x + iH_y)\boldsymbol{\sigma}_+ + (H_x - iH_y)\boldsymbol{\sigma}_-. \end{aligned} \tag{B.2}$$

Then $\mathbf{h}$ can be diagonalized by a transformation

$$\mathbf{u} = \begin{pmatrix} \cos\Theta & e^{i\gamma}\sin\Theta \\ -e^{-i\gamma}\sin\Theta & \cos\Theta \end{pmatrix}. \tag{B.3}$$

To accomplish this, we first compute

$$\tilde{\boldsymbol{\sigma}}_w = \mathbf{u}^\dagger \boldsymbol{\sigma}_w \mathbf{u}, \quad w = x, y, z \tag{B.4}$$

and find

$$\tilde{\boldsymbol{\sigma}}_x = -\cos\gamma\sin 2\Theta\boldsymbol{\sigma}_z + (\cos 2\Theta + 2\sin^2\gamma\sin^2\Theta)\boldsymbol{\sigma}_x - \sin 2\gamma\sin^2\Theta\boldsymbol{\sigma}_y \tag{B.5a}$$

$$\tilde{\boldsymbol{\sigma}}_y = -\sin\gamma\sin 2\Theta\boldsymbol{\sigma}_z - \boldsymbol{\sigma}_x\sin 2\gamma\sin^2\Theta + (\cos 2\Theta + \cos^2\gamma 2\sin^2\Theta)\boldsymbol{\sigma}_y \tag{B.5b}$$

$$\tilde{\boldsymbol{\sigma}}_z = \cos 2\Theta\boldsymbol{\sigma}_z + \cos\gamma\sin 2\Theta\boldsymbol{\sigma}_x + \sin\gamma\sin 2\Theta\boldsymbol{\sigma}_y. \tag{B.5c}$$

Thus

$$\begin{aligned}\tilde{\mathbf{h}} - \mathrm{S}\mathbf{I} &= K_z\tilde{\boldsymbol{\sigma}}_z + K_x\tilde{\boldsymbol{\sigma}}_x + K_y\tilde{\boldsymbol{\sigma}}_y \\ &= K_z\tilde{\boldsymbol{\sigma}}_z + (K_x + iK_y)\tilde{\boldsymbol{\sigma}}_+ + (K_x - iK_y)\tilde{\boldsymbol{\sigma}}_-. \end{aligned} \tag{B.6}$$

$\mathbf{u}$ is determined by using Eqs. (B.5) and (B.2) to evaluate an off-diagonal term of $\tilde{\mathbf{h}}$

$$\begin{aligned} K_x + iK_y &= H_x\cos 2\Theta - iH_x 2\sin\gamma\sin^2\Theta e^{i\gamma} \\ &\quad + iH_y 2\cos\gamma\sin^2\Theta e^{i\gamma} + iH_y\cos 2\Theta \\ &\quad + G(\cos\gamma\sin 2\Theta + i\sin\gamma\sin 2\Theta) \qquad \text{(B.7a)} \\ &= iH_y 2\cos\gamma\sin^2\Theta e^{i\gamma} + iH_y\cos 2\Theta \\ &\quad + H_x\cos 2\Theta - iH_x 2\sin\gamma\sin^2\Theta e^{i\gamma} + Ge^{i\gamma}\sin 2\Theta \qquad \text{(B.7b)} \\ &= (H_x + iH_y)\cos 2\Theta + 2\sin^2\Theta e^{i\gamma}(-H_x i\sin\gamma + iH_y\cos\gamma) \\ &\quad + Ge^{i\gamma}\sin 2\Theta. \qquad \text{(B.7c)} \end{aligned}$$

Noting that $H_x + iH_y \equiv He^{i\xi}$, then

$$\begin{aligned} -H_x i\sin\gamma + iH_y\cos\gamma &= \frac{1}{2}(-H_x + iH_y)(i\sin\gamma + \cos\gamma) \\ &\quad +(-H_x - iH_y)(i\sin\gamma - \cos\gamma) \\ &= \frac{1}{2}(-He^{-i\xi}e^{i\gamma} - He^{i\xi}(-)e^{-i\gamma}) \\ &= \frac{1}{2}H(-e^{i(\gamma-\xi)} + e^{-i(\gamma-\xi)}). \end{aligned} \tag{B.8a}$$

the second term in Eq. (B.7c) vanishes provided $\gamma = \xi$, while the sum of the remaining terms vanishes provided

$$\tan 2\Theta = -H/G. \tag{B.8b}$$

The diagonal term, K_z, becomes

$$\begin{aligned} K_z &= (-H_y\sin\gamma - H_x\cos\gamma)\sin 2\Theta + G\cos 2\Theta \\ &= (iH_y i\sin\gamma - H_x\cos\gamma)\sin 2\Theta + G\cos 2\Theta \\ &= \sin 2\Theta(-He^{-i\xi}e^{i\gamma} - He^{+i\xi}e^{-i\gamma})/2 + G\cos 2\Theta \\ &= -H\sin 2\Theta + G\cos 2\Theta = [H^2 + G^2]^{1/2}. \end{aligned} \tag{B.8c}$$

B.2. *The Linear Hamiltonian*

A linear Hamiltonian has the form

$$\mathbf{h} = \mathrm{S}\mathbf{I} + gz\boldsymbol{\sigma}_z + h^{\mathrm{r}}x\boldsymbol{\sigma}_x + h^{\mathrm{i}}y\boldsymbol{\sigma}_y. \tag{B.2′}$$

Introducing spherical polar coordinates

$$z = \rho\cos\theta x = \rho\sin\theta\cos\phi \quad \text{and} \quad y = \rho\sin\phi\sin\theta \tag{B.9}$$

we have $H_x = \rho h^{\mathrm{r}}\sin\theta\cos\phi, H_y = \rho h^{\mathrm{i}}\sin\theta\sin\phi, G = \rho g\cos\theta$.

Since $\mathbf{h}$ is a special case of Eq. (B.2), its eigenfunctions (equivalently γ and Θ) and eigenvalues (equivalently K_z) follow Eqs. (B.8a,b,c). It is convenient to introduce scaled quantities $h^{(1)}(\phi)$, $q(\theta,\phi)$ and the associated

angles $\lambda(\theta,\phi)$, ξ, defined by [see Eqs. (50)–(51)]

$$h^{\mathrm{i}}\sin\phi = h^{(1)}(\phi)\sin\xi \quad h^{\mathrm{r}}\cos\phi = h^{(1)}(\phi)\cos\xi \tag{B.10a}$$

where

$$h^{(1)}(\phi)^2 = (h^{\mathrm{i}}\sin\phi)^2 + (h^{\mathrm{r}}\cos\phi)^2 \tag{B.10b}$$

and

$$g\cos\theta = q(\theta,\phi)\cos\lambda(\theta,\phi) \quad h^{(1)}(\phi)\sin\theta = q(\theta,\phi)\sin\lambda(\theta,\phi) \tag{B.10c}$$

with

$$q^2 = (g\cos\theta)^2 + (\sin\theta\, h^{(1)})^2. \tag{B.10d}$$

Then

$$He^{i\xi} = h^{(1)}\rho\sin\theta e^{i\xi} \tag{B.11a}$$

$$\tan 2\Theta = -H/G = \frac{-\rho h^{(1)}\sin\theta}{\rho g\cos\theta} = \frac{-\sin\lambda}{\cos\lambda} = \tan(-\lambda) \tag{B.11b}$$

$$K_z = [(\rho g\cos\theta)^2 + (\rho h^{(1)}\sin\theta^{(1)})^2]^{1/2} = \rho q. \tag{B.11c}$$

Thus

$$\tilde{\mathbf{h}} = s\mathbf{I} + \rho q(\theta,\phi)\boldsymbol{\sigma}_z \quad \text{with} \quad \Theta = -\lambda/2 \text{ and } \gamma = \xi \tag{B.12}$$

Appendix C: Eigenvalues and Eigenvectors of a 4 × 4 Hermitian Matrix in a Time Reversal Adapted Basis

Here, analytic expressions for the eigenfunctions and eigenvalues of the matrix M

$$\mathbf{M} \equiv \begin{pmatrix} \mathbf{h} & \mathbf{v} \\ \mathbf{v}^\dagger & \mathbf{h}^* \end{pmatrix} \tag{C.1a}$$

where

$$\mathbf{h} = \begin{pmatrix} -gz & h^r x + ih^i y \\ h^r x - ih^i y & gz \end{pmatrix}$$
$$\mathbf{v} = \begin{pmatrix} 0 & t^r v + it^i w \\ -(t^r v + it^i w) & 0 \end{pmatrix} \equiv \begin{pmatrix} 0 & a \\ -a & 0 \end{pmatrix} \tag{C.1b}$$

are derived. Diagonalization of $\mathbf{M}$ is accomplished in three steps. Let

$$\mathbf{U}^{(1)} = \begin{pmatrix} \mathbf{u}^{(1)} & 0 \\ 0 & \mathbf{u}^{(1)^*} \end{pmatrix} \quad \text{where } \mathbf{u}^{(1)\dagger}\mathbf{h}\mathbf{u}^{(1)} = \boldsymbol{\varepsilon}^{(1)} \tag{C.2a}$$

and

$$\varepsilon^{(1)} = \begin{pmatrix} -[(gz)^2 + (h^r x)^2 + (h^i y)^2]^{1/2} & 0 \\ 0 & [(gz)^2 + (h^r x)^2 + (h^i y)^2]^{1/2} \end{pmatrix} \tag{C.2b}$$

then

$$\begin{aligned} \mathbf{M}^{(1)} &\equiv \mathbf{U}^{(1)\dagger}\mathbf{M}\mathbf{U}^{(1)} \\ &= \begin{pmatrix} \mathbf{u}^{(1)^\dagger} & 0 \\ 0 & \mathbf{u}^{(1)^{*\dagger}} \end{pmatrix} \begin{pmatrix} \mathbf{h} & \mathbf{v} \\ \mathbf{v}^\dagger & \mathbf{h}^* \end{pmatrix} \begin{pmatrix} \mathbf{u}^{(1)} & 0 \\ 0 & \mathbf{u}^{(1)^*} \end{pmatrix} \\ &= \begin{pmatrix} \varepsilon_1 & 0 & 0 & a \\ 0 & \varepsilon_2 & -a & 0 \\ 0 & -a* & \varepsilon_1 & 0 \\ a* & 0 & 0 & \varepsilon_2 \end{pmatrix} \end{aligned} \tag{C.3}$$

where we have noted that $\mathbf{u}^{(1)\dagger}\mathbf{v}\mathbf{u}^{(1)} = \mathbf{v}$. Next reorder the transformed functions using the permutation matrix

$$\mathbf{P} = \begin{pmatrix} 1 & 0 & 0 & 0 \\ 0 & 0 & 1 & 0 \\ 0 & 0 & 0 & 1 \\ 0 & 1 & 0 & 0 \end{pmatrix} \tag{C.4}$$

which puts them in the order 1, 4, 2, 3.

$$\begin{aligned} \mathbf{M}^{(2)} &= \mathbf{P}^\dagger \mathbf{M}^{(1)} \mathbf{P} \\ &= \begin{pmatrix} \varepsilon_1 & a & 0 & 0 \\ a^* & \varepsilon_2 & 0 & 0 \\ 0 & 0 & \varepsilon_2 & -a \\ 0 & 0 & -a^* & \varepsilon_1 \end{pmatrix} \\ &\equiv (\varepsilon_1 + \varepsilon_2)/2\mathbf{I} + \begin{pmatrix} \mathbf{h}^{(2)} & \mathbf{0} \\ 0 & -\mathbf{h}^{(2)} \end{pmatrix} \end{aligned} \tag{C.5}$$

where $\varepsilon_1 + \varepsilon_2 = 0$ since $\mathbf{M}$ is traceless and

$$\begin{aligned} h^{(2)} = \begin{pmatrix} \Delta\varepsilon & a \\ a^* & -\Delta\varepsilon \end{pmatrix} \quad \Delta\varepsilon &= (\varepsilon_1 - \varepsilon_2)/2 \\ &= -[(gz)^2 + (h^{\mathrm{r}} x)^2 + (h^{\mathrm{i}} y)^2]^{1/2}. \end{aligned} \tag{C.6}$$

Finally define $\mathbf{u}^{(2)}$ such that

$$\boldsymbol{\varepsilon}^{(2)} = \mathbf{u}^{(2)\dagger}\mathbf{h}^{(2)}\mathbf{u}^{(2)} \begin{pmatrix} -(\Delta\varepsilon^2 + |a|^2)^{1/2} & 0 \\ 0 & (\Delta\varepsilon^2 + |a|^2)^{1/2} \end{pmatrix} \tag{C.7a}$$

where

$$\Delta\varepsilon^2 + |a|^2 = (gz)^2 + (h^{\mathrm{r}}x)^2 + (h^{\mathrm{i}}y)^2 + (t^{\mathrm{r}}v)^2 + (t^{\mathrm{i}}w)^2. \tag{C.7b}$$

Then

$$\mathbf{M}^{(3)} = \mathbf{U}^{(2)\dagger}\mathbf{M}^{(2)}\mathbf{U}^{(2)} = \begin{pmatrix} \boldsymbol{\varepsilon}^{(2)} & \mathbf{0} \\ \mathbf{0} & -\boldsymbol{\varepsilon}^{(2)} \end{pmatrix}, \tag{C.8a}$$

where

$$\mathbf{U}^{(2)} = \begin{pmatrix} \mathbf{u}^{(2)} & \mathbf{0} \\ \mathbf{0} & \mathbf{u}^{(2)} \end{pmatrix}. \tag{C.8b}$$

From Eqs. (C.7a) and (C.8), the pairs of roots (1, 4) and (2, 3) are degenerate. This is an example of Kramers' degeneracy. The overall transformation $\mathbf{U}$ is given by

$$\begin{aligned} U = & \begin{pmatrix} u_{11}^{(1)} & u_{12}^{(1)} & 0 & 0 \\ u_{21}^{(1)} & u_{22}^{(1)} & 0 & 0 \\ 0 & 0 & u_{11}^{(1)^*} & u_{12}^{(1)^*} \\ 0 & 0 & u_{21}^{(1)^*} & u_{22}^{(1)^*} \end{pmatrix} \begin{pmatrix} 1 & 0 & 0 & 0 \\ 0 & 0 & 1 & 0 \\ 0 & 0 & 0 & 1 \\ 0 & 1 & 0 & 0 \end{pmatrix} \\ & \times \begin{pmatrix} u_{11}^{(2)} & u_{12}^{(2)} & 0 & 0 \\ u_{21}^{(2)} & u_{22}^{(2)} & 0 & 0 \\ 0 & 0 & u_{11}^{(2)} & u_{12}^{(2)} \\ 0 & 0 & u_{21}^{(2)} & u_{22}^{(2)} \end{pmatrix} \end{aligned} \tag{C.9a}$$

$$\begin{aligned} = & \begin{pmatrix} u_{11}^{(1)} & 0 & u_{12}^{(1)} & 0 \\ u_{21}^{(1)} & 0 & u_{22}^{(1)} & 0 \\ 0 & u_{12}^{(1)^*} & 0 & u_{11}^{(1)^*} \\ 0 & u_{22}^{(1)^*} & 0 & u_{21}^{(1)^*} \end{pmatrix} \begin{pmatrix} u_{11}^{(2)} & u_{12}^{(2)} & 0 & 0 \\ u_{21}^{(2)} & u_{22}^{(2)} & 0 & 0 \\ 0 & 0 & u_{11}^{(2)} & u_{12}^{(2)} \\ 0 & 0 & u_{21}^{(2)} & u_{22}^{(2)} \end{pmatrix} \\ = & \begin{pmatrix} u_{11}^{(1)}u_{11}^{(2)} & u_{11}^{(1)}u_{12}^{(2)} & u_{12}^{(1)}u_{11}^{(2)} & u_{12}^{(1)}u_{12}^{(2)} \\ u_{21}^{(1)}u_{11}^{(2)} & u_{21}^{(1)}u_{12}^{(2)} & u_{22}^{(1)}u_{11}^{(2)} & u_{22}^{(1)}u_{12}^{(2)} \\ u_{12}^{(1)^*}u_{21}^{(2)} & u_{12}^{(1)^*}u_{22}^{(2)} & u_{11}^{(1)^*}u_{21}^{(2)} & u_{11}^{(1)^*}u_{22}^{(2)} \\ u_{22}^{(1)^*}u_{21}^{(2)} & u_{22}^{(1)^*}u_{22}^{(2)} & u_{21}^{(1)^*}u_{21}^{(2)} & u_{21}^{(1)^*}u_{22}^{(2)} \end{pmatrix}. \end{aligned} \tag{C.9b}$$

Appendix D: Representations of U

To obtain explicit expressions for the $\mathbf{u}^{(i)}$, it is convenient to introduce spherical polar coordinates ($\rho^{(1)}$, $\theta^{(1)}$, $\phi^{(1)}$), polar ($\rho^{(2)}, \phi^{(2)}$) and hyperspherical coordinates ($\rho^{(3)}, \theta^{(3)}$). Two representations will be used, a scaled coordinate system, in which displacements are energetically equivalent along each axis, and unscaled coordinate system, for which the displacement step sizes are equivalent along each axis.

D.1. *Scaled Coordinates*

$$\begin{aligned} z' &= gz = \rho^{(1)} \cos\theta^{(1)} \\ x' &= h^{\mathrm{r}} x = \rho^{(1)} \sin\theta^{(1)} \cos\phi^{(1)} \\ y' &= h^{\mathrm{i}} y = \rho^{(1)} \sin\theta^{(1)} \sin\phi^{(1)} \end{aligned} \tag{D.1}$$

and

$$v' = t^r v = \rho^{(2)} \cos\phi^{(2)} \quad w' = t^r w = \rho^{(2)} \sin\phi^{(2)} \tag{D.2}$$

so that

$$\mathbf{h} \equiv \mathbf{h}^{(1)} = \rho^{(1)} \begin{pmatrix} -\cos\theta^{(1)} & e^{i\phi^{(1)}} \sin\theta^{(1)} \\ e^{-i\phi^{(1)}} \sin\theta^{(1)} & \cos\theta^{(1)} \end{pmatrix} \quad \text{and}$$

$$\mathbf{h}^{(2)} = \begin{pmatrix} -\rho^{(1)} & \rho^{(2)} e^{i\phi^{(2)}} \\ \rho^{(2)} e^{-i\phi^{(2)}} & \rho^{(1)} \end{pmatrix}. \tag{D.3}$$

Note that the underlying coordinate axes are linearly independent but not necessarily orthogonal. See, however, Appendix F. Introducing the hyperpolar coordinates $\rho^{(3)}$, $\theta^{(3)}$ by

$$\rho^{(1)} = \rho^{(3)} \cos\theta^{(3)} \quad \text{and} \quad \rho^{(2)} = \rho^{(3)} \sin\theta^{(3)} \tag{D.4}$$

then

$$\mathbf{h}^{(2)} = \rho^{(3)} \begin{pmatrix} -\cos\theta^{(3)} & \sin\theta^{(3)} e^{i\phi^{(2)}} \\ \sin\theta^{(3)} e^{-i\phi^{(2)}} & \cos\theta^{(3)} \end{pmatrix}. \tag{D.5}$$

In these coordinates, $\rho^{(1)^2} = (gz)^2 + (h^{\mathrm{r}}x)^2 + (h^{\mathrm{i}}y)^2$ and $\rho^{(3)^2} = (gz)^2 + (h^{\mathrm{r}}x)^2 + (h^{\mathrm{i}}y)^2 + (t^{\mathrm{r}}v)^2 + (t^{\mathrm{i}}w)^2$. Further $\mathbf{h}^{(1)}$ and $\mathbf{h}^{(2)}$ have the same form

$$\mathbf{h}^{(i)} = \rho^{(i)} \begin{pmatrix} -\cos\theta^{(i)} & e^{i\phi^{(i')}} \sin\theta^{(i)} \\ e^{-i\phi^{(i')}} \sin\theta^{(i)} & \cos\theta^{(i)} \end{pmatrix} \tag{D.6}$$

and can be diagonalized by the transformation

$$\mathbf{u}^{(i)} = \begin{pmatrix} \cos\Theta^{(i)} & e^{i\gamma^{(i')}}\sin\Theta^{(i)} \\ -e^{-i\gamma^{(i')}}\sin\Theta^{(i)} & \cos\Theta^{(i)} \end{pmatrix} \tag{D.7}$$

where $\Theta^{(i)} = \theta^{(i)}/2, \gamma^{(i')} = \phi^{(i)}$, for $(i, \mathrm{i}) = (1, 1), (3, 2)$. The simple relation between the Hamiltonian parameters and those of $\mathbf{U}$ comes from the use of scaled coordinates to define the polar and spherical polar coordinates in Eqs. (C.1) and (C.2). Alternatively, one can choose unscaled coordinates as follows.

D.2. *Unscaled Coordinates*

Let

$$z = \rho^{(1)}\cos\theta^{(1)}, x = \rho^{(1)}\sin\theta^{(1)}\cos\phi^{(1)}, y = \rho^{(1)}\sin\theta^{(1)}\sin\phi^{(1)} \tag{D.8a}$$

and

$$v = \rho^{(2)}\cos\phi^{(2)}, \qquad w = \rho^{(2)}\sin\phi^{(2)}. \tag{D.8b}$$

Then define

$$h^{(1)}(\phi^{(1)})\cos\xi^{(1)} = h^{\mathrm{r}}\cos\phi^{(1)}, \qquad h^{(1)}(\phi^{(1)})\sin\xi^{(1)} = h^{\mathrm{i}}\sin\phi^{(1)} \tag{D.9a}$$

and

$$\begin{aligned} q^{(1)}(\theta^{(1)}, \phi^{(1)})\cos\lambda^{(1)} &= g\cos\theta^{(1)} \\ q^{(1)}(\theta^{(1)}, \phi^{(1)})\sin\lambda^{(1)} &= h^{(1)}(\phi^{(1)})\sin\theta^{(1)} \end{aligned} \tag{D.9b}$$

$$q^{(2)}(\phi^{(2)})\cos\xi^{(2)} = t^{\mathrm{r}}\cos\phi^{(2)}, \quad q^{(2)}(\phi^{(2)})\sin\xi^{(2)} = t^{\mathrm{i}}\sin\phi^{(2)} \tag{D.9c}$$

$$\mathbf{h} \equiv \mathbf{h}^{(1)} = \rho^{(1)}q^{(1)}\begin{pmatrix} -\cos\lambda^{(1)} & e^{i\xi^{(1)}}\sin\lambda^{(1)} \\ e^{-i\xi^{(1)}}\sin\lambda^{(1)} & \cos\lambda^{(1)} \end{pmatrix}$$

$$\mathbf{h}^{(2)} = \begin{pmatrix} -\rho^{(1)}q^{(1)} & \rho^{(2)}q^{(2)}e^{i\xi^{(2)}} \\ \rho^{(2)}q^{(2)}e^{-i\xi^{(2)}} & \rho^{(1)}q^{(1)} \end{pmatrix}. \tag{D.10}$$

Introducing the hyper polar coordinates

$$\rho^{(3)} \cos\lambda^{(3)} = \rho^{(1)} q^{(1)} \quad \text{and} \quad \rho^{(3)} \sin\lambda^{(3)} = \rho^{(2)} q^{(2)} \tag{D.11}$$

$\mathbf{h}^{(2)}$ becomes

$$\mathbf{h}^{(2)} = \rho^{(3)} \begin{pmatrix} -\cos\lambda^{(3)} & \sin\lambda^{(3)} e^{i\xi^{(2)}} \\ \sin\lambda^{(3)} e^{-i\xi^{(2)}} & \cos\lambda^{(3)} \end{pmatrix}. \tag{D.12}$$

$\mathbf{h}^{(1)}$ and $\mathbf{h}^{(2)}$ have the form of Eq. (D.6) and can be diagonalized by the transformation in Eq. (D.7) with $\Theta^{(1)} = \lambda^{(1)}/2$, $\gamma^{(1)} = \xi^{(1)}$ and $\Theta^{(2)} = \lambda^{(3)}/2$, $\gamma^{(3)} = \xi^{(2)}$. $\mathbf{U}$, Eq. (C.9b), is given by

$$\begin{pmatrix} \mathrm{c}\Theta^{(1)}\mathrm{c}\Theta^{(2)} & \mathrm{c}\Theta^{(1)} e^{i\gamma^{(2)}}\mathrm{s}\Theta^{(2)} & e^{i\gamma^{(1)}}\mathrm{s}\Theta^{(1)}\mathrm{c}\Theta^{(2)} & e^{i\gamma^{(1)}}\mathrm{s}\Theta^{(1)} e^{i\gamma^{(2)}}\mathrm{s}\Theta^{(2)} \\ -e^{-i\gamma^{(1)}}\mathrm{s}\Theta^{(1)}\mathrm{c}\Theta^{(2)} & -e^{-i\gamma^{(1)}}\mathrm{s}\Theta^{(1)} e^{i\gamma^{(2)}}\mathrm{s}\Theta^{(2)} & \mathrm{c}\Theta^{(1)}\mathrm{c}\Theta^{(2)} & \mathrm{c}\Theta^{(1)} e^{i\gamma^{(2)}}\mathrm{s}\Theta^{(2)} \\ -e^{-i\gamma^{(1)}}\mathrm{s}\Theta^{(1)} e^{-i\gamma^{(2)}}\mathrm{s}\Theta^{(2)} & e^{-i\gamma^{(1)}}\mathrm{s}\Theta^{(1)}\mathrm{c}\Theta^{(2)} & -\mathrm{c}\Theta^{(1)} e^{-i\gamma^{(2)}}\mathrm{s}\Theta^{(2)} & \mathrm{c}\Theta^{(1)}\mathrm{c}\Theta^{(2)} \\ -\mathrm{c}\Theta^{(1)} e^{-i\gamma^{(2)}}\mathrm{s}\Theta^{(2)} & \mathrm{c}\Theta^{(1)}\mathrm{c}\Theta^{(2)} & e^{i\gamma^{(1)}}\mathrm{s}\Theta^{(1)} e^{-i\gamma^{(2)}}\mathrm{s}\Theta^{(2)} & -e^{i\gamma^{(1)}}\mathrm{s}\Theta^{(1)}\mathrm{c}\Theta^{(2)} \end{pmatrix} \tag{D.13}$$

where c = cos and s = sin.

Appendix E. Degenerate Perturbation Theory

Here we collect some results from degenerate perturbation theory.[61] The degenerate states are i, j. Assume that

$$\Phi_k = \Phi_k^{(0)} + \Phi_k^{(1)} + \Phi_k^{(2)} + \cdots, \quad k = i, j \tag{E.1a}$$

$$H = H^{(0)} + H^{(1)} + H^{(2)} + \cdots, \tag{E.1b}$$

$$V_k = V_k^{(0)} + V_k^{(1)} + V_k^{(2)} + \cdots, \quad k = i, j \tag{E.1c}$$

where $\mathrm{V}_i^{(0)} = \mathrm{V}_j^{(0)}$. Then

$$(H^{(0)} - V_i^{(0)})\Phi_i^{(1)} + (H^{(1)} - V_i^{(1)})\Phi_i^{(0)} = 0 \tag{E.2a}$$

$$(H^{(0)} - V_i^{(0)})\Phi_i^2 + (H^{(2)} - V_i^{(2)})\Phi_i^{(0)} + (H^{(1)} - V_i^{(1)})\Phi_i^{(1)} = 0. \tag{E.2b}$$

Then taking the dot product of $\Phi_k^{(0)}$ with Eq. (E.2a) gives, using $k = i, j$

$$\left(QH^{(1)}Q - V_i^{(1)}\right)\Phi_i^{(0)} = 0 \tag{E.3a}$$

using $k \neq i, j$

$$P\Phi_i^{(1)} = \left(V_i^{(0)} - H^{(0)}\right)^{-1} H^{(1)}\Phi_i^{(0)} \tag{E.3b}$$

where Q projects onto the space spanned by $\Phi_i^{(0)}$ and $\Phi_j^{(0)}$, and P projects onto the orthogonal complement. The dot product of $\Phi_k^{(0)}$ $k = i, j$ with Eq. (E.2b) and using (E.3) gives

$$\left\langle \Phi_k^{(0)} \middle| \left(H^{2-\text{eff}} - V_i^{(2)}\right)\Phi_i^{(0)} \right\rangle = -(V_k^{(1)} - V_i^{(1)})\varepsilon_k^{(1),i} \tag{E.4a}$$

where $\langle \Phi_k^{(0)} | \Phi_m^{(1)} \rangle \equiv \varepsilon_k^{(1),m}$ and

$$\begin{aligned} H^{(2-\text{eff})} &= H^{(2)} + H^{(1)}\left(V_i^{(0)} - PH^{(0)}P\right)^{-1} H^{(1)} \\ &\equiv H^{(2)} + H^{(2,QPQ)}. \end{aligned} \tag{E.4b}$$

Equation (E.2b) gives the second order energy and a first order contribution to the wave function

$$V_i^{(2)} = \langle \Phi_i^{(0)} | H^{(2-\text{eff})} | \Phi_i^{(0)} \rangle \quad \text{for } k = i, j \tag{E.5a}$$

$$\varepsilon_j^{(1),i} = \langle \Phi_j^{(0)} | H^{(2-\text{eff})} | \Phi_i^{(0)} \rangle / (V_i^{(1)} - V_j^{(1)}) \quad \text{for } k = j. \tag{E.5b}$$

Appendix F: Orthogonal Intersection Adapted Coordinates

In this appendix the unitary transformation of the electronic wave functions required to make the vectors in the branching space orthogonal is discussed. Our approach will be to start from the most general, $\eta = 5$ case and recover the $\eta = 3$ and $\eta = 2$ results as special cases. Note that straightforward orthogonalization of $\mathbf{g}^{i,j}(\mathbf{X}^{x,i,j}) \equiv v^{(1)}(\mathbf{X}^{x,i,j})$, $\mathbf{h}^{\mathrm{r},i,j}(\mathbf{X}^{x,i,j}) \equiv v^{(2)}(\mathbf{X}^{x,i,j})$, $\mathbf{h}^{\mathrm{i},i,j}(\mathbf{X}^{x,i,j}) \equiv v^{(3)}(\mathbf{X}^{x,i,j})$, $\mathbf{h}^{\mathrm{r},i,Tj}(\mathbf{X}^{x,i,j}) \equiv v^{(4)}(\mathbf{X}^{x,i,j})$, and $\mathbf{h}^{\mathrm{i},i,Tj}(\mathbf{X}^{x,i,j}) \equiv v^{(5)}(\mathbf{X}^{x,i,j})$, changes the form of the Hamiltonian in Eq. (46a). Instead the orthogonalization must be accompished by a unitary transformation of the electronic states.

F.1. *Formulation*

F.1.1. $\eta = 5$

Let

$$\left(\tilde{\Phi}_i\ \tilde{\Phi}_j\ \tilde{\Phi}_{Ti}\ \tilde{\Phi}_{Tj}\right) = \left(\Phi_i\ \Phi_j\ \Phi_{Ti}\ \Phi_{Tj}\right)\mathbf{U} \quad \text{with} \quad U_{k,l} = \left\langle \Phi_k \,\middle|\, \tilde{\Phi}_l \right\rangle \quad \text{(F.1)}$$

define the transformation from the "nascent" electronic wave functions Φ, $k = i, j, Ti$ and Tj to the $\tilde{\Phi}_k$, $k = i, j, Ti$ and Tj for which the $v^{(I)}(\mathbf{X}^{x,i,j})$ are orthogonal.

A general $2n \times 2n$ unitary matrix $\mathbf{U}$ consists of $4n^2$ complex-valued matrix elements, that is $8n^2$ parameters. Viewed as column constraints, the requirement $\mathbf{U}^\dagger\mathbf{U} = I$ constitutes, (i) $2n(2n-1)/2$ orthogonality equations, $(\mathbf{U}^\dagger\mathbf{U})_{k,l} \equiv O(k,l) = O^{\mathrm{r}}(k,l) + iO^{\mathrm{i}}(k,l) = 0$, for $1 \le k < l \le 2n$, defining $2n(2n-1)$ parameters and, (ii) $2n$ normalization equations, $(\mathbf{U}^\dagger\mathbf{U})_{k,k} = N(k) = 1$, for $1 \le k \le N$, defining $2n$ parameters. Thus a total of $4n^2$ parameters are defined leaving $4n^2$ parameters undefined or free. Pairwise orthogonality of $v^{(i)}$ constitutes $\eta!/((\eta-2)!2!) = \eta(\eta-1)/2$ equations, that is, 10 for $\eta = 5$. Since here $2n = 4$, $4n^2 = 16$ and the problem appears under determined. However this is not the case, since $\mathbf{U}$ is not an arbitrary unitary matrix but connects two pairs of time reversal adapted states. Using Eq. (A.2a) in Eq. (F.1) gives:

$$U^*_{k,l} = \left\langle T\Phi_k \,\middle|\, T\tilde{\Phi}_l \right\rangle = \left\langle \Phi_{Tk} \,\middle|\, \tilde{\Phi}_{Tl} \right\rangle = U_{Tk,Tl} \quad \text{(F.2a)}$$

$$U^*_{k,Tl} = \left\langle T\Phi_k \,\middle|\, T\tilde{\Phi}_{Tl} \right\rangle = -\left\langle \Phi_{Tk} \,\middle|\, \tilde{\Phi}_l \right\rangle = -U_{Tk,l} \quad \text{(F.2b)}$$

so that

$$\mathbf{U} = \begin{pmatrix} \mathbf{u}^{(ij,ij)} & \mathbf{u}^{(ij,TiTj)} \\ -\mathbf{u}^{(ij,TiTj)^*} & \mathbf{u}^{(ij,ij)^*} \end{pmatrix} \text{ where } \mathbf{u}^{(kl,mn)} = \begin{pmatrix} u_{k,m} & u_{k,n} \\ u_{l,m} & u_{l,n} \end{pmatrix}. \quad \text{(F.3)}$$

We will refer to matrix with the form of Eq. (F.3) as T-adapted.

To incorporate time reversal symmetry, note that if $\mathbf{H}$, a T-adapted matrix, is also hermitian, then $\mathbf{h}^{(ij,ij)}(\mathbf{h}^{(ij,TiTj)})$ is hermitian (anti-symmetric). $\mathbf{h}^{(ij,ij)}$ $[\mathbf{h}^{(ij,TiTj)}]$ has $n^2[n(n-1)]$ free parameters. $\mathbf{U}\mathbf{U}^\dagger$ is both T-adapted and hermitian. Since $\mathbf{U}\mathbf{U}^\dagger = \mathbf{1}, P_n$, the number of undetermined

parameters in a general T-adapted $\mathbf{U}$ is

$$P_n = 4n^2 - n^2 - n(n-1) = n(2n+1). \tag{F.4}$$

For $n = 2$, $P_2 = 10$ precisely the number required to orthogonalize the vectors $\mathbf{v}^{(k)}(\mathbf{X}^{x,i,j})$, $k = 1 - 5$.

F.1.2. $\eta = 3$

When C_s symmetry is present there is no mixing of the $\mathbf{\Phi}$, and $T\mathbf{\Phi}$ subspaces. In that case $\mathbf{u}^{(ij,TiTj)} \equiv 0$ in Eq. (F.3), so that only $\mathbf{u}^{(ij,ij)}$, which has 4 parameters, is required. In this case three vectors define the g–h space so that their orthogonality represents 3 constraints. Therefore, there exists one additional free parameter which we take to be the requirement that $\det \mathbf{U} = 1$. Then $\mathbf{U}$ has the form

$$\mathbf{U} = \begin{pmatrix} \mathbf{u} & \mathbf{0} \\ \mathbf{0} & \mathbf{u}^* \end{pmatrix} \tag{F.5a}$$

where

$$\mathbf{u} = \begin{pmatrix} e^{i(\alpha+\gamma)/2}\cos\beta/2 & -e^{i(-\alpha+\gamma)/2}\sin\beta/2 \\ e^{-i(-\alpha+\gamma)/2}\sin\beta/2 & e^{-i(\alpha+\gamma)/2}\cos\beta/2 \end{pmatrix}. \tag{F.5b}$$

The 3 unique parameters can be determined in either the $\mathbf{\Phi}$ or $T\mathbf{\Phi}$ subspace.

F.1.3. $\eta = 2$

In this case the $\mathbf{\Phi}$ and $T\mathbf{\Phi}$ spaces are identical, $\mathbf{H}^e$ is real-valued and $\mathbf{U}$ is orthogonal rather than unitary, that is, the $T\mathbf{\Phi}$ space can be ignored. Thus $\mathbf{u}$ has the form

$$\mathbf{u} = \begin{pmatrix} \cos\beta & -\sin\beta \\ \sin\beta & \cos\beta \end{pmatrix} \tag{F.6}$$

and there is a single orthogonality equation $\mathbf{v}^{(1)} \cdot \mathbf{v}^{(2)} = 0$.

F.2. *Solutions*

To determine $\mathbf{U}$, the rotated $\mathbf{c}^i$

$$\tilde{\mathbf{c}}^i = \sum_{k=1}^{N^Q} \mathbf{c}^k \mathbf{U}_{k,i} \tag{F.7}$$

are inserted into the definitions of the $\mathbf{v}^{(i)}$. These rotated $\mathbf{v}^{(i)}$ are then required to be pairwise orthogonal.

For $\eta = 2$

$$\tilde{\mathbf{v}}^{(1)} = \left(-\mathbf{v}^{(1)} \cos 2\beta + \mathbf{v}^{(2)} \sin 2\beta\right) \tag{F.8a}$$

and

$$\tilde{\mathbf{v}}^{(2)} = \mathbf{v}^{(1)} \sin 2\beta + \mathbf{v}^{(2)} \cos 2\beta \tag{F.8b}$$

so that

$$\begin{aligned}\tilde{\mathbf{v}}^{(1)} \cdot \tilde{\mathbf{v}}^{(2)} = 0 = (\mathbf{v}^{(2)} \cdot \mathbf{v}^{(2)} - \mathbf{v}^{(1)} \cdot \mathbf{v}^{(1)}) \frac{\sin 4\beta}{2} \\ -(\mathbf{v}^{(2)} \cdot \mathbf{v}^{(1)}) \cos 4\beta\end{aligned} \tag{F.8c}$$

which gives, noting that $\mathbf{v}^{(1)} = \mathbf{g}^{i,j}$ and $\mathbf{v}^{(2)} = \mathbf{h}^{i,j}$,

$$\tan 4\beta = \frac{2\mathbf{g}^{i,j} \cdot \mathbf{h}^{i,j}}{\mathbf{h}^{i,j} \cdot \mathbf{h}^{i,j} - \mathbf{g}^{i,j} \cdot \mathbf{g}^{i,j}}. \tag{F.9}$$

For $\eta = 3$

$$\tilde{\mathbf{v}}^{(1)} = \left(-\mathbf{v}^{(1)} \cos\beta + \mathbf{v}^{(2)} \sin\beta \cos\gamma + \mathbf{v}^{(3)} \sin\beta \sin\gamma\right) \tag{F.10a}$$

$$\begin{aligned}\tilde{\mathbf{v}}^{(2)} = \mathbf{v}^{(1)} \sin\beta \cos\alpha + \mathbf{v}^{(2)} (\cos\beta \cos\gamma \cos\alpha - \sin\gamma \sin\alpha) \\ +\mathbf{v}^{(3)} (\cos\beta \sin\gamma \cos\alpha + \cos\gamma \sin\alpha)\end{aligned} \tag{F.10b}$$

$$\begin{aligned}\tilde{\mathbf{v}}^{(3)} = \mathbf{v}^{(1)} \sin\beta \sin\alpha - \mathbf{v}^{(2)} (\cos\beta \cos\gamma \sin\alpha - \sin\gamma \cos\alpha) \\ -\mathbf{v}^{(3)} (\cos\beta \cos\gamma \sin\alpha - \cos\gamma \cos\alpha).\end{aligned} \tag{F.10c}$$

Then the requirements

$$\nu_1 = \tilde{\mathbf{v}}^{(1)} \cdot \tilde{\mathbf{v}}^{(2)} = 0 \quad \nu_2 = \tilde{\mathbf{v}}^{(1)} \cdot \tilde{\mathbf{v}}^{(3)} = 0 \quad \nu_3 = \tilde{\mathbf{v}}^{(2)} \cdot \tilde{\mathbf{v}}^{(3)} = 0 \tag{F.11a,b,c}$$

yield a set of three non-linear equations. Note that $\mathbf{v}^{(1)} = \mathbf{g}^{i,j}$, $\mathbf{v}^{(2)} = \mathbf{h}^{\mathrm{r},i,j}$ and $\mathbf{v}^{(3)} = \mathbf{h}^{\mathrm{i},i,j}$, then for

$$\beta = \pi/2,\ \gamma = 0,\ \alpha = 0 \quad \mathbf{h}^{\mathrm{r},i,j} \to \tilde{\mathbf{g}}^{i,j} \quad \mathbf{g}^{i,j} \to \tilde{\mathbf{h}}^{\mathrm{r},i,j} \quad \mathbf{h}^{\mathrm{i},i,j} \to \tilde{\mathbf{h}}^{\mathrm{i},i,j} \tag{F.12a}$$

for

$$\beta = \pi/2,\ \gamma = 0, \alpha = \pi/2 \quad \mathbf{h}^{\mathrm{r},i,j} \to \tilde{\mathbf{g}}^{i,j} \quad \mathbf{h}^{\mathrm{i},i,j} \to \tilde{\mathbf{h}}^{\mathrm{r},i,j} \quad \mathbf{g}^{i,j} \to \tilde{\mathbf{h}}^{\mathrm{i},i,j} \tag{F.12b}$$

so that $\mathbf{g}^{i,j}$, $\mathbf{h}^{\mathrm{r},i,j}$ and $\mathbf{h}^{\mathrm{i},i,j}$ are interchangeable.

The solution to Eqs. (F.11a)–(F.11c) can be obtained numerically from the following Newton–Raphson procedure

$$\nu_i(\mathbf{x_n} + \delta\mathbf{x}) = \mathbf{0} = \nu_i(\mathbf{x_n}) + \nabla\nu_i(\mathbf{x_n}) \cdot \delta\mathbf{x} \quad i = 1 - 3 \tag{F.13a}$$

so that

$$\mathbf{x}_{n+1} = \mathbf{x}_n - \mathbf{F}(\mathbf{x}_n)^{-1}\boldsymbol{\upsilon}(\mathbf{x_n}) \tag{F.13b}$$

where $F_{ji} \equiv (\partial/\partial x_j)\nu_i$ is computed by divided difference and $(\mathbf{x} = \alpha, \beta, \gamma)$.

For the $\eta = 5$ case the determination of $\mathbf{U}$ using a homomorphism from the space of T-adapted $\mathbf{U}$ onto the space of rotations of 5-vectors with determinant 1 has been discussed by Han and Yarkony.[105]

Appendix G. The Phase of the Electronic Wave Function

Since each of Eq. (E.2) begins with $(H^{(0)} - V_i^{(0)})\Phi_i^{(n)}$, these equations do not determine $\langle\Phi_i^{(0)}|\Phi_i^{(n)}\rangle_{\mathbf{x}^e}$. Expansion of the normalization condition to first order gives, using the explicit form for $\Psi_i^{(1)}$ from Sec. 2

$$\begin{aligned}
&\left\langle \sum_{\alpha\in Q} \xi_\alpha^{(1),i}\tilde{\Phi}_\alpha^{(0)} + \sum_{\alpha\in P} \Xi_\alpha^{(1),i}\Phi_\alpha^{(0)} \,\middle|\, \tilde{\Phi}_i^{(0)} \right\rangle_{\mathbf{x}^e} \\
&\quad + \left\langle \tilde{\Phi}_i^{(0)} \,\middle|\, \sum_{\alpha\in Q} \xi_\alpha^{(1),i}\tilde{\Phi}_\alpha^{(0)} + \sum_{\alpha\in P} \Xi_\alpha^{(1),i}\Phi_\alpha^{(0)} \right\rangle_{\mathbf{x}^e} \\
&\quad = \xi_i^{(1),i} + \xi_i^{(1),i^*} = 2\mathrm{Re}\ \xi_i^{(1),i} = 0.
\end{aligned} \tag{G.1}$$

Thus the normalization determines only the $\mathrm{Re}\,\xi_i^{(1),i} \equiv \mathrm{Re}\langle\Phi_i^{(0)}|\Phi_i^{(1)}\rangle$. The $\mathrm{Im}\xi_i^{(1),i}$ does not effect the normalization or the energy and in a local sense is arbitrary.

For real-valued wave functions, $\mathrm{Im}\,\xi_i^{(1),i} = 0$. For the complex-valued wave functions considered here it is possible to choose the phase, to first order in ρ, such that $\mathrm{Im}\,\xi_i^{(1),i} = 0$, although this not a trivial matter as it is in the real-valued case. Here it is shown how this can be accomplished.

Expanding the phase, $\Omega_\kappa = \Omega_\kappa^{(0)}(\theta,\phi) + \rho\Omega_\kappa^{(1)}(\theta,\phi,\mathbf{w})$, in powers of ρ gives

$$\exp(i\Omega_i) = e^{i\Omega_i^{(0)}(\theta,\phi)}(1 + i\rho\Omega_i^{(1)}(\theta,\phi,\mathbf{w}) + \cdots . \tag{G.2}$$

Then since

$$\Phi_i^e(\mathbf{x}^e;\rho,\theta,\phi) = \tilde{\Phi}_i^{(0)}(\theta,\phi) + \sum_{k=i,j}(\rho\xi_k^{(1),i} + \rho^2\xi_k^{(2),i} + \cdots)\tilde{\Phi}_k^{(0)}(\theta,\phi) + \sum_{\alpha\neq i,j}(\rho\Xi_\alpha^{(1),i} + \rho^2\Xi_\alpha^{(2),i} + \cdots)\Phi_\alpha^{(0)} \tag{G.3a}$$

we have through first order

$$e^{i\Omega_i}\Phi_i^e = e^{i\Omega_i^{(0)}(\theta,\phi)}\{[1 + \rho\xi_i^{(1,\Omega),i}]\tilde{\Phi}_i^{(0)} + \rho\xi_j^{(1),i}\tilde{\Phi}_j^{(0)} + \sum_{\alpha\neq i,j}(\rho\Xi_\alpha^{(1),i})\Phi_\alpha^{(0)}\} \tag{G.3b}$$

where $\xi_i^{(1,\Omega),i} = i\mathrm{Im}\ \xi_i^{(1),i} + i\Omega_i^{(1)}$. Taking

$$\xi_i^{(1,\Omega),i} = i\mathrm{Im}\ \xi_i^{(1),i} + i\Omega_i^{(1)} = 0 \tag{G.4}$$

satisfies the condition, $\mathrm{Im}\,\xi_i^{(1),i} = 0$.

Appendix H: Evaluation of $A_{k,l}^s$ $s = x, y, z, v, w$

Before assembling the chain rule for evaluation of $A_{k,l}^s$, it is useful to begin by summarizing the relationships among the myriad of variables:

$$\begin{array}{lll} \rho^{(2)},\phi^{(2)} : v,w & \rho^{(1)},\theta^{(1)},\phi^{(1)} : x,y,z & \lambda^{(1)},q^{(1)} : \theta^{(1)},\phi^{(1)} \\ \lambda^{(2)},\rho^{(3)} : \rho^{(2)},\rho^{(1)},\theta^{(1)},\phi^{(1)},\phi^{(2)} & \xi^{(1)} : \phi^{(1)} & \xi^{(2)} : \phi^{(2)} \quad \Theta^{(i)} = \lambda^{(i)}/2 \\ \gamma^{(i)} = \xi^{(i)} & & \end{array} \tag{H.1}$$

where the colon is read (here and only here) as "depends on". Using these dependencies, the chain rule becomes

$$\begin{aligned}\frac{\partial}{\partial s} = &\left(\frac{\partial\theta^{(1)}}{\partial s}\frac{\partial\lambda^{(1)}}{\partial\theta^{(1)}} + \frac{\partial\phi^{(1)}}{\partial s}\frac{\partial\lambda^{(1)}}{\partial\phi^{(1)}}\right)\frac{\partial\Theta^{(1)}}{\partial\lambda^{(1)}}\frac{\partial}{\partial\Theta^{(1)}}\\ &+\frac{\partial\phi^{(1)}}{\partial s}\frac{\partial\xi^{(1)}}{\partial\phi^{(1)}}\frac{\partial\gamma^{(1)}}{\partial\xi^{(1)}}\frac{\partial}{\partial\gamma^{(1)}}\\ &+\left(\frac{\partial\theta^{(1)}}{\partial s}\frac{\partial\lambda^{(2)}}{\partial\theta^{(1)}} + \frac{\partial\phi^{(2)}}{\partial s}\frac{\partial\lambda^{(2)}}{\partial\phi^{(2)}} + \frac{\partial\phi^{(1)}}{\partial s}\frac{\partial\lambda^{(2)}}{\partial\phi^{(1)}}\right.\\ &\left.+\frac{\partial\rho^{(1)}}{\partial s}\frac{\partial\lambda^{(2)}}{\partial\rho^{(1)}} + \frac{\partial\rho^{(2)}}{\partial s}\frac{\partial\lambda^{(2)}}{\partial\rho^{(2)}}\right)\frac{\partial\Theta^{(2)}}{\partial\lambda^{(2)}}\frac{\partial}{\partial\Theta^{(2)}}\\ &+\frac{\partial\phi^{(2)}}{\partial s}\frac{\partial\xi^{(2)}}{\partial\phi^{(2)}}\frac{\partial\gamma^{(2)}}{\partial\xi^{(2)}}\frac{\partial}{\partial\gamma^{(2)}}\end{aligned} \tag{H.2}$$

and $A^s_{k,l}$is given by:

$$\begin{aligned}A^s_{k,l} = &\left(\frac{\partial\theta^{(1)}}{\partial s}\frac{\partial\lambda^{(1)}}{\partial\theta^{(1)}} + \frac{\partial\phi^{(1)}}{\partial s}\frac{\partial\lambda^{(1)}}{\partial\phi^{(1)}}\right)\frac{\partial\Theta^{(1)}}{\partial\lambda^{(1)}}A^{\Theta^{(1)}}_{k,l}\\ &+\frac{\partial\phi^{(1)}}{\partial s}\frac{\partial\xi^{(1)}}{\partial\phi^{(1)}}\frac{\partial\gamma^{(1)}}{\partial\xi^{(1)}}A^{\gamma^{(1)}}_{k,l}\\ &+\left(\frac{\partial\theta^{(1)}}{\partial s}\frac{\partial\lambda^{(2)}}{\partial\theta^{(1)}} + \frac{\partial\phi^{(2)}}{\partial s}\frac{\partial\lambda^{(2)}}{\partial\phi^{(2)}} + \frac{\partial\phi^{(1)}}{\partial s}\frac{\partial\lambda^{(2)}}{\partial\phi^{(1)}}\right.\\ &\left.+\frac{\partial\rho^{(1)}}{\partial s}\frac{\partial\lambda^{(2)}}{\partial\rho^{(1)}} + \frac{\partial\rho^{(2)}}{\partial s}\frac{\partial\lambda^{(2)}}{\partial\rho^{(2)}}\right)\frac{\partial\Theta^{(2)}}{\partial\lambda^{(2)}}A^{\Theta^{(2)}}_{k,l}\\ &+\frac{\partial\phi^{(2)}}{\partial s}\frac{\partial\xi^{(2)}}{\partial\phi^{(2)}}\frac{\partial\gamma^{(2)}}{\partial\xi^{(2)}}A^{\gamma^{(2)}}_{k,l}\,.\end{aligned} \tag{H.3}$$

Using the above dependencies, Eq. (D.2) becomes for $s = x, y, z$

$$\begin{aligned}A^s_{k,l} = &\left(\frac{\partial\theta^{(1)}}{\partial s}\frac{\partial\lambda^{(1)}}{\partial\theta^{(1)}} + \frac{\partial\phi^{(1)}}{\partial s}\frac{\partial\lambda^{(1)}}{\partial\phi^{(1)}}\right)\frac{A^{\Theta^{(1)}}_{k,l}}{2} + \frac{\partial\phi^{(1)}}{\partial s}\frac{\partial\xi^{(1)}}{\partial\phi^{(1)}}A^{\gamma^{(2)}}_{k,l}\\ &+\left(\frac{\partial\theta^{(1)}}{\partial s}\frac{\partial\lambda^{(2)}}{\partial\theta^{(1)}} + \frac{\partial\phi^{(1)}}{\partial s}\frac{\partial\lambda^{(2)}}{\partial\phi^{(1)}} + \frac{\partial\rho^{(1)}}{\partial s}\frac{\partial\lambda^{(2)}}{\partial\rho^{(1)}}\right)\frac{A^{\Theta^{(2)}}_{k,l}}{2}\end{aligned} \tag{H.4a}$$

and for $s = v, w$

$$A^s_{k,l} = \left(\frac{\partial\phi^{(2)}}{\partial s}\frac{\partial\lambda^{(2)}}{\partial\phi^{(2)}} + \frac{\partial\rho^{(2)}}{\partial s}\frac{\partial\lambda^{(2)}}{\partial\rho^{(2)}}\right)\frac{A^{\Theta^{(2)}}_{k,l}}{2} + \frac{\partial\phi^{(2)}}{\partial s}\frac{\partial\xi^{(2)}}{\partial\phi^{(2)}}A^{\gamma^{(2)}}_{k,l}\,. \tag{H.4b}$$

To proceed further specific relations among the variables are required. From Eqs. (B.10), we deduce

$$\begin{aligned} \tan\xi^{(1)} &= (h^{\mathrm{i}}/h^{\mathrm{r}})\tan\phi^{(1)} \\ h^{(1)}(\phi^{(1)})^2 &= (h^{\mathrm{i}}\sin\phi^{(1)})^2 + (h^{\mathrm{r}}\cos\phi^{(1)})^2 \end{aligned} \tag{H.5a}$$

$$\begin{aligned} \tan\xi^{(2)} &= t^{\mathrm{i}}/t^{\mathrm{r}}\tan\phi^{(2)} \\ q^{(2)}(\phi^{(2)})^2 &= (t^{\mathrm{i}}\sin\phi^{(2)})^2 + (t^{\mathrm{r}}\cos\phi^{(2)})^2 \end{aligned} \tag{H.5b}$$

$$\begin{aligned} \tan\lambda^{(1)} &= (h^{(1)}(\phi^{(1)})/g)\tan\theta^{(1)} \\ q^{(1)}(\theta^{(1)},\phi^{(1)})^2 &= (g\cos\theta^{(1)})^2 + (h^{(1)}(\phi^{(1)})\sin\theta^{(1)})^2 \end{aligned} \tag{H.5c}$$

$$\begin{aligned} \rho^{(3)} &= \sqrt{[(\rho^{(1)}q^{(1)} + (\rho^{(2)}q^{(2)})^2]} \quad \text{and} \\ \tan\lambda^{(2)} &= \rho^{(2)}q^{(2)}/[\rho^{(1)}q^{(1)}] \equiv \rho_q^{(2)}/\rho_q^{(1)} \end{aligned} \tag{H.5d}$$

It is convenient to begin by evaluating the s independent contributions:

$$\frac{\partial\lambda^{(1)}}{\partial\theta^{(1)}}, \frac{\partial\lambda^{(1)}}{\partial\phi^{(1)}}, \frac{\partial\xi^{(1)}}{\partial\phi^{(1)}}, \frac{\partial\lambda^{(2)}}{\partial\theta^{(1)}}, \frac{\partial\lambda^{(2)}}{\partial\phi^{(2)}}, \frac{\partial\lambda^{(2)}}{\partial\phi^{(1)}}, \frac{\partial\lambda^{(2)}}{\partial\rho^{(1)}}, \frac{\partial\lambda^{(2)}}{\partial\rho^{(2)}}, \frac{\partial\xi^{(2)}}{\partial\phi^{(2)}}$$

which follow from straightforward, albeit tedious, differentiation of Eqs. (H5.a)–(H5.d)

$$\begin{aligned} \frac{\partial\lambda^{(1)}}{\partial\theta^{(1)}} &= \frac{[h^{(1)}g]}{q^{(1)^2}} \qquad \frac{\partial\lambda^{(1)}}{\partial\phi^{(1)}} = \frac{[h^{\mathrm{i}^2} - h^{\mathrm{r}^2}]}{2h^{(1)}}\sin 2\phi^{(1)}\frac{g\sin 2\theta^{(1)}}{2q^{(1)^2}} \\ \frac{\partial\xi^{(1)}}{\partial\phi^{(1)}} &= \frac{[h^{\mathrm{i}}h^{\mathrm{r}}]}{h^{(1)^2}} \quad \frac{\partial\lambda^{(2)}}{\partial\theta^{(1)}} = \frac{-\rho^{(1)}\rho_q^{(2)}}{\rho_q^{(2)^2} + \rho_q^{(1)^2}}\frac{[h^{(1)^2} - g^2]}{2q^{(1)}}\sin 2\theta^{(1)} \\ \frac{\partial\lambda^{(2)}}{\partial\phi^{(2)}} &= \frac{\rho_q'^{(1)}}{\rho_q^{(2)^2} + \rho_q^{(1)^2}}q^{(1)}\frac{[t^{\mathrm{i}^2} - t^{\mathrm{r}^2}]}{2q^{(2)}}\sin 2\phi^{(2)} \\ \frac{\partial\lambda^{(2)}}{\partial\phi^{(1)}} &= \frac{-\rho^{(2)}\rho^{(1)}}{\rho_q^{(2)^2} + \rho_q^{(1)^2}}\frac{q^{(2)}}{q^{(1)}}\frac{[h^{\mathrm{i}^2} - h^{\mathrm{r}^2}]}{2}\sin 2\phi^{(1)}\sin^2\theta^{(1)} \\ \frac{\partial\lambda^{(2)}}{\partial\rho^{(1)}} &= \frac{-\rho^{(2)}}{\rho_q^{(2)^2} + \rho_q^{(1)^2}}q^{(2)}q^{(1)}\frac{\partial\lambda^{(2)}}{\partial\rho^{(2)}} \\ &= \frac{\rho^{(1)}}{\rho_q^{(2)^2} + \rho_q^{(1)^2}}q^{(2)}q^{(1)}\frac{\partial\xi^{(2)}}{\partial\phi^{(2)}} = \frac{t^{\mathrm{i}}t^{\mathrm{r}}}{q^{(2)^2}}. \end{aligned} \tag{H.6}$$

Using Eq. (D.5) in Eq. (D.3a) gives for $s = x, y, z$

$$\begin{aligned} A^s_{k\cdot l} = &\left(\frac{\partial\theta^{(1)}}{\partial s} \frac{[h^{(1)} g]}{q^{(1)^2}} + \frac{\partial\phi^{(1)}}{\partial s} \frac{[h^{\mathrm{i}^2} - h^{\mathrm{r}^2}]}{2h^{(1)}} \right. \\ &\left. \times \sin 2\phi^{(1)} \frac{g \sin 2\theta^{(1)}}{2q^{(1)^2}} \right) \frac{A^{\Theta^{(1)}}_{k.l}}{2} + \frac{\partial\phi^{(1)}}{\partial s} \frac{[h^{\mathrm{i}} h^{\mathrm{r}}]}{h^{(1)^2}} A^{\gamma^{(1)}}_{k.l} \\ &+ \frac{\rho^{(1)} \rho^{(2)}_q}{\rho^{(2)^2}_q + \rho^{(1)^2}_q} \left(\frac{\partial\theta^{(1)}}{\partial s} \frac{[g^2 - h^{(1)^2}]}{2q^{(1)}} \sin 2\theta^{(1)} \right. \\ &- \frac{\partial\phi^{(1)}}{\partial s} \frac{[h^{\mathrm{i}^2} - h^{\mathrm{r}^2}]}{2q^{(1)}} \sin 2\phi^{(1)} \sin^2 \theta^{(1)} \\ &\left. - \frac{\partial\rho^{(1)}}{\partial s} \frac{q^{(1)}}{\rho^{(1)}} \right) \frac{A^{\Theta^{(2)}}_{k\cdot l}}{2} \end{aligned} \tag{H.7}$$

while using Eq. (H.5) in (H.3b) gives for $s = v, w$

$$\begin{aligned} A^s_{k,l} = &\frac{\rho^{(1)}_q}{\rho^{(2)^2}_q + \rho^{(1)^2}_q} \left(\frac{\partial\phi^{(2)}}{\partial s} \rho^{(2)} \frac{[t^{\mathrm{i}^2} - t^{\mathrm{r}^2}]}{2q^{(2)}} \sin 2\phi^{(2)} + \frac{\partial\rho^{(2)}}{\partial s} q^{(2)} \right) \\ &\times \frac{A^{\Theta^{(2)}}_{k,l}}{2} + \frac{\partial\phi^{(2)}}{\partial s} \frac{[t^{\mathrm{i}} t^{\mathrm{r}}]}{q^{(2)^2}} A^{\gamma^{(2)}}_{k,l} \,. \end{aligned} \tag{H.8}$$

Acknowledgments

The calculations reported herein and the preparation of this manuscript was made possible by grants from the Air Force Office of Scientific Research, the Department of Energy and the National Science Foundation.

References

1. M. Born and J. R. Oppenheimer, *Ann. Phys. (Leipzig)* **84**, 457 (1927).
2. D. R. Yarkony, *Rev. Mod. Phys.* **68**, 985 (1996).
3. F. London, *Z. Phys.* **74**, 132 (1932).
4. N. Y. Ohrn, *Rev. Mod. Phys.* **66**, 917 (1994).
5. M. Born and K. Huang, *Dynamical Theory of Crystal Lattices* (Oxford University Press, 1954).
6. G. J. Atchity, S. S. Xantheas and K. Ruedenberg, *J. Chem. Phys.* **95**, 1862 (1991).
7. D. R. Yarkony, *Acc. Chem. Res.* **31**, 511 (1998).
8. B. Heumann, R. Duren and R. Schinke, *Chem. Phys. Lett.* **180**, 583 (1991).

9. B. Heumann, K. Weide, R. Düren and R. Schinke, *J. Chem. Phys.* **98**, 5508 (1993).
10. B. Heumann and R. Schinke, *J. Chem. Phys.* **101**, 7488 (1994).
11. N. Matsunaga and D. R. Yarkony, *J. Chem. Phys.* **107**, 7825 (1997).
12. D. R. Yarkony, *J. Chem. Phys.* **104**, 7866 (1996).
13. J. von Neumann and E. Wigner, *Physik. Z.* **30**, 467 (1929).
14. R. F. Frey and E. R. Davidson, *Advances in Molecular Electronic Structure Theory*, Ed. T. H. Dunning Jr. (JAI Press, Greenwich, Connecticut, 1990), Vol. 1.
15. D. R. Yarkony, *J. Phys. Chem.* **A105**, 6277 (2001).
16. H. C. Longuet-Higgins, *Proc. Roy. Soc. London* **A344**, 147 (1975).
17. K. R. Naqvi, *Chem. Phys. Lett.* **15**, 634 (1972).
18. J. Michl and V. Bonacic-Koutecky, *Electronic Aspects of Organic Photochemistry* (Wiley, New York, 1990).
19. M. Klessinger and J. Michl, *Excited States and the Photochemistry of Organic Molecules* (VCH, New York, 1995).
20. F. Bernardi, M. Olivucci and M. A. Robb, *Chem. Soc. Rev.* **25**, 321 (1996).
21. H. Köppel and W. Domcke, *Encyclopedia of Computational Chemistry*, Ed. P. v. R. Schleyer (Wiley, London, 1998), pp. 3166.
22. H. Steuhl, C. Bornemann and M. Klessinger, *Chem. Euro. J.* **5**, 2404 (1999).
23. A. I. Sobolewski and W. Domcke, *Chem. Phys. Lett.* **315**, 293 (1999).
24. M. A. Robb, M. Garavelli, M. Olivucci and F. Bernardi, *Rev. Comput. Chem.* **15**, 87 (2000).
25. U. Manthe and H. Köppel, *J. Chem. Phys.* **93**, 345 (1990).
26. U. Manthe and H. Köppel, *J. Chem. Phys.* **93**, 1658 (1990).
27. R. Schinke, *Photodissociation Dynamics, Spectroscopy and Fragmentation of Small Polyatomic Molecules* (Cambridge University Press, Cambridge, 1993).
28. H. Müller and H. Köppel, *Chem. Phys.* **183**, 107 (1994).
29. R. Baer, D. M. Charutz, R. Kosloff and M. Baer, *J. Chem. Phys.* **105**, 9141 (1996).
30. R. P. Krawczyk, K. Malsch, G. Hohlneicher, R. C. Gillen and W. Domcke, *Chem. Phys. Lett.* **320**, 535 (2000).
31. S. Mahapatra, H. Köppel and L. Cederbaum, *J. Phys. Chem.* **A105**, 2321 (2001).
32. G. A. Worth and L. S. Cederbaum, *Chem. Phys. Lett.* **338**, 219 (2001).
33. D. R. Yarkony, *J. Chem. Phys.* **114**, 2601 (2001).
34. C. A. Mead, *J. Chem. Phys.* **70**, 2276 (1979).
35. M. Baer, *Phys. Rep.* **358**, 75 (2002).
36. H. C. Longuet-Higgins, *Adv. Spectrosc.* **2**, 429 (1961).
37. C. A. Mead and D. G. Truhlar, *J. Chem. Phys.* **70**, 2284 (1979).
38. M. V. Berry, *Proc. Roy. Soc. London Ser.* **A392**, 45 (1984).

39. J. Avron, L. Sadun, J. Segert and B. Simon, *Phys. Rev. Lett.* **61**, 1329 (1988).
40. J. Avron, L. Sadun, J. Segert and B. Simon, *Commun. Math. Phys.* **124**, 595 (1989).
41. S. Matsika and D. R. Yarkony, *J. Phys. Chem.* **B106**, 8108 (2002).
42. D. R. Yarkony, *Atomic, Molecular and Optical Physics Handbook*, Ed. G. L. Drake (AIP, New York, 1996), pp. 357.
43. S. Matsika and D. R. Yarkony, *J. Chem. Phys.* **115**, 2038 (2001).
44. B. H. Lengsfield and D. R. Yarkony, *State-Selected and State to State Ion-Molecule Reaction Dynamics: Theory*, Part 2, Ed. M. Baer and C.-Y. Ng (John Wiley and Sons, New York, 1992), Vol. 82, pp. 1.
45. R. Renner, *Z. Phys.* **92**, 172 (1934).
46. C. Jungen and A. J. Merer, *Modern Spectroscopy: Modern Research*, Ed. K. N. Rao (Academic, New York, 1976), Vol. II.
47. S. Matsika and D. R. Yarkony, *J. Phys. Chem.* **A106**, 2580 (2002).
48. R. Englman, *The Jahn–Teller Effect in Molecules and Crystals* (Wiley-Interscience, New York, 1972).
49. I. B. Bersuker, *The Jahn–Teller Effect and Vibronic Interactions in Modern Chemistry* (Plenum, New York, 1984).
50. D. R. Yarkony, Theor. *Chem. Acc.* **98**, 197 (1997).
51. D. R. Yarkony, *J. Phys. Chem.* **A105**, 2642 (2001).
52. G. Herzberg and H. C. Longuet-Higgins, *Discus Faraday Soc.* **35**, 77 (1963).
53. A. Kuppermann, *Dynamics of Molecules and Chemical Reactions*, Ed. R. E. Wyatt and J. Z. H. Zhang (Marcel Dekker, Inc., New York, 1996), pp. 411.
54. A. J. Stone, *Proc. Roy. Soc. London* **A351**, 141 (1976).
55. S. Xantheas, S. T. Elbert and K. Ruedenberg, *J. Chem. Phys.* **93**, 7519 (1990).
56. M. Baer and R. Englman, *Chem. Phys. Lett.* **335**, 85 (2001).
57. M. Baer, *Chem. Phys. Lett.* **35**, 112 (1975).
58. M. Baer, *Chem. Phys.* **15**, 49 (1976).
59. S. Han, H. Hettema and D. R. Yarkony, *J. Chem. Phys.* **102**, 1955 (1995).
60. T. Pacher, C. A. Mead, L. S. Cederbaum, and H. Köppel, *J. Chem. Phys.* **91**, 7057 (1989).
61. C. A. Mead, *J. Chem. Phys.* **78**, 807 (1983).
62. A. J. C. Varandas and Z. R. Xu, *Chem. Phys. Lett.* **316**, 248 (2000).
63. C. A. Mead, *Chem. Phys. Lett.* **49**, 23 (1980).
64. C. A. Mead, *Chem. Phys. Lett.* **49**, 33 (1980).
65. P. O. Löwdin, *J. Mol. Spectrosc.* **10**, 12 (1963).
66. D. R. Yarkony, *J. Chem. Phys.* **112**, 2111 (2000).
67. S. Matsika and D. R. Yarkony, *J. Chem. Phys.* **115**, 5066 (2001).
68. S. Matsika and D. R. Yarkony, *J. Chem. Phys.* **116**, 2825 (2002).

69. V.-A. Glezakou, M. S. Gordon and D. R. Yarkony, *J. Chem. Phys.* **108**, 5657 (1998).
70. D. R. Yarkony, *J. Phys. Chem.* **A101**, 4263 (1997).
71. T. Pacher, L. S. Cederbaum and H. Köppel, *J. Chem. Phys.* **89**, 7367 (1988).
72. T. Pacher, L. S. Cederbaum and H. Köppel, *J. Chem. Phys.* **95**, 6668 (1991).
73. T. Pacher, L. S. Cederbaum and H. Köppel, *Adv. Chem. Phys.* **84**, 293 (1993).
74. T. A. Spiglanin and D. W. Chandler, *Chem. Phys. Lett.* **141**, 428 (1987).
75. J. E. Stevens, Q. Cui and K. Morokuma, *J. Chem. Phys.* **108**, 1452 (1998)
76. J. J. Klossika, H. Flöthmann, C. Beck, R. Schinke and K. Yamashita, *Chem. Phys. Lett.* **276**, 325 (1997).
77. J. J. Klossika and R. Schinke, *J. Chem. Phys.* **111**, 5882 (1999).
78. J. J. Klossika, H. Flöthmann, R. Schinke and M. Bittererova, *Chem. Phys. Lett.* **314**, 183 (1999).
79. R. Schinke and M. Bittererova, *Chem. Phys. Lett.* **332**, 611 (2000).
80. D. R. Yarkony, *Mol. Phys.* **99**, 1463 (2001).
81. T. A. Spiglanin, R. A. Perry and D. W. Chandler, *J. Phys. Chem.* **90**, 6184 (1986).
82. S. S. Brown, H. L. Berghout and F. F. Crim, *J. Chem. Phys.* **102**, 8440 (1995).
83. H. L. Berghout, S. S. Brown, R. Delgado and F. F. Crim, *J. Chem. Phys.* **109**, 2257 (1998).
84. W.-H. Fang, X.-Z. You and Z. Yin, *Chem. Phys. Lett.* **238**, 236 (1995).
85. M. Zyrianov, T. Droz-Georget and H. Reisler, *J. Chem. Phys.* **110**, 2059 (1999).
86. H. J. Silverstone and O. Sinanoglu, *J. Chem. Phys.* **44**, 1899 (1966).
87. T. H. Dunning and P. J. Hay, *Modern Theoretical Chemistry*, Edited by H. F. Schaefer (Plenum, New York, 1976), Vol. 3.
88. M. BenNun, T. D. Martinez and R. D. Levine, *Chem. Phys. Lett.* **270**, 319 (1997).
89. T. J. Martinez, *Chem. Phys. Lett.* **272**, 139 (1997).
90. D. T. Anderson, M. W. Todd and M. I. Lester, *J. Chem. Phys.* **110**, 1117 (1999).
91. M. I. Lester, R. A. Loomis, R. L. Schwartz and S. P. Walch, *J. Phys. Chem.* **A101**, 9195 (1997).
92. B. C. Hoffman and D. R. Yarkony, *J. Chem. Phys.* **113**, 10091 (2000).
93. P. Siegbahn, A. Heiberg, B. Roos and B. Levy, *Phys. Scr.* **21**, 323 (1980).
94. B. O. Roos, P. R. Taylor and P. E. M. Siegbahn, *Chem. Phys.* **48**, 157 (1980).
95. B. O. Roos, *Int. J. Quantum. Chem. Symp.* **14**, 175 (1980).
96. D. R. Yarkony, *Int. Rev. Phys. Chem.* **11**, 195 (1992).
97. C. E. Moore, *Atomic Energy Levels, Natl. Stand. Ref. Data Ser., Natl. Bur. Stand.* (US GPO, Washington, DC, 1971).
98. S. Matsika and D. R. Yarkony, *J. Chem. Phys.* **117**, 6907 (2002).

99. S. P. Keating and C. A. Mead, *J. Chem. Phys.* **82**, 5102 (1985).
100. L. I. Schiff, *Quantum Mechanics* (McGraw Hill, New York, 1960).
101. M. Tinkham, *Group Theory and Quantum Mechanics* (McGraw-Hill, New York, 1964).
102. H. Kramers, *Proc. Acad. Sci. Amsterdam* **33**, 959 (1930).
103. M. E. Rose, *Elementary Theory of Angular Momentum* (John Wiley and Sons, New York, 1957).
104. W. C. Swope, H. F. Schaefer III and D. R. Yarkony, *J. Chem. Phys.* **73**, 407 (1980).
105. S. Han and D. R. Yarkony, *J. Chem. Phys.* **118**, 9952 (2003).
106. S. Matsika and D. R. Yarkony, *J. Amer. Chem. Soc.* **125**, 10672 (2003).
107. S. Matsika and D. R. Yarkony, *J. Amer. Chem. Soc.* **125**, 12428 (2003).

This page intentionally left blank

CHAPTER 3

DETERMINATION OF POTENTIAL ENERGY SURFACE INTERSECTIONS AND DERIVATIVE COUPLINGS IN THE ADIABATIC REPRESENTATION

David R. Yarkony
Department of Chemistry, Johns Hopkins University, Baltimore, MD 21218

Contents

1. Introduction

1.1. *Background*

The introduction of analytic energy gradients for self-consistent field wave functions approximately 25 years ago revolutionized quantum chemistry.[1,2] With the slope of the potential energy surface known, the computational effort required to locate minima, transition states and reaction paths on those surfaces was reduced enormously. So compelling was this advance that energy gradients are considered virtually a necessity if a computational approach is to be viable. Although gradient techniques were quickly extended to correlated wave functions,[2] the focus remained almost exclusively the gradient of the energy, that is, the power of gradient technology was restricted to adiabatic processes.

An early step in bringing analytic gradient techniques to nonadiabatic quantum chemistry came in 1984 with the introduction of an algorithm for evaluating the first derivative coupling for electronic states $\Phi_i(\mathbf{x};\,\mathbf{X})$ and $\Phi_j(\mathbf{x};\,\mathbf{X})$

$$\mathbf{A}_{i,j}(\mathbf{X}) = \langle \Phi_i(\mathbf{x};\mathbf{X}) | \nabla_X \Phi_j(\mathbf{x};\mathbf{X}) \rangle_{\mathbf{x}}. \tag{1}$$

Initially only state-averaged multiconfigurational self-consistent field (SA-MCSCF) wave functions[3] could be treated but subsequently the algorithm was extended to treat general multireference configuration interaction (MRCI) wave functions.[4] Here $\mathbf{x}(\mathbf{X})$ denotes the space fixed frame coordinates of the N^{el} electrons (N^{nuc} nuclei) and Φ_I is one of N^a electronic eigenstates. $A^{\alpha}_{i,j}$ a vector ($\alpha = 1 - 3N^{\mathrm{nuc}}$) of matrices ($i, j = 1 - N^{\mathrm{a}}$) will be denoted by bold/italic type face.

Subsequently, gradient methods were used to evaluate the adiabatic correction or Born–Oppeneimer diagonal correction, $AC_{i,i}$, for SCF wave functions,[5] where

$$\begin{aligned} \mathrm{AC}_{i,i}(\mathbf{X}) &= \sum_{\alpha=1}^{N^{\mathrm{nuc}}} \frac{1}{2M_\alpha} \langle \nabla_\alpha \Phi_i(\mathbf{x};\mathbf{X}) | \nabla_\alpha \Phi_i(\mathbf{x};\mathbf{X}) \rangle_{\mathbf{x}} \\ &= \sum_{\alpha=1}^{N^{\mathrm{nuc}}} \frac{-1}{2M_\alpha} \langle \Phi_i(\mathbf{x};\mathbf{X}) | \nabla^2_\alpha \Phi_i(\mathbf{x};\mathbf{X}) \rangle_{\mathbf{x}} \end{aligned} \tag{2a}$$

and the general second derivative term, $B_{i,j}$, for MRCI wave functions,[6,7] where

$$B_{i,j}(\mathbf{X}) = \langle \nabla_X \Phi_i(\mathbf{x};\mathbf{X}) \cdot | \nabla_X \Phi_j(\mathbf{x};\mathbf{X}) \rangle_{\mathbf{x}}. \tag{2b}$$

Prior to that time, A and $B_{i,j}$ had been evaluated by divided difference techniques.[8–13]

These algorithmic advances were significant because of the importance of these quantities in the description of nonadiabatic processes. The first derivative couplings, $\mathbf{A}(\mathbf{X})$, couple adiabatic states, permitting nuclear motion to occur on more than one potential energy surface. The second derivative couplings, $\mathbf{B}(\mathbf{X})$, (i) provide mass dependent modifications to Born–Oppenheimer potential energy surfaces, (ii) couple potential energy surfaces, and (iii) are related to the existence of rigorous diabatic bases.[14] As shown in Chapter 2, $\mathbf{B}(\mathbf{X})$ is sufficient to incorporate second derivative terms into the nuclear Schrödinger equation. However some formulations of the nuclear dynamics, utilize $\mathcal{K}_{i,j} = \langle \Phi_i(\mathbf{x};\mathbf{X}) | \nabla^2 \Phi_j(\mathbf{x};\mathbf{X}) \rangle_x$. In

Sec. 7.2, it is shown how $\mathcal{K}_{i,j}$ can be evaluated using only analytic gradient techniques, provided $\mathbf{A}(\mathbf{X})$ is known with sufficient accuracy to enable divided differences.

These new algorithms made it possible to calculate the derivative couplings for general polyatomic molecules with much improved efficiency and accuracy. As discussed in Chapter 2 of this volume, the $AC_{i,i}(\mathbf{X})$ produces a mass dependent modification to a Born–Oppenheimer potential energy surface that can be inferred from measurements of ro-vibronic energy levels of the isotopomers. Indeed, using the $B_{i,i}(\mathbf{X})$ determined at the MRCI level, we[7] were able to resolve a discrepancy in the adiabatic correction for $LiH(X^1\Sigma^+)$ obtained from an analysis of experimental data,[15] and from a theoretical prediction,[16] based on highly specialized wave functions, see Sec. 8.

Despite the potential power and early successes of these techniques, the impact of analytic gradient techniques on the study of nonadiabatic chemistry was limited. However, that was to change. A harbinger of the revolution that was soon to come was the work of Koga and Morokuma[17] who, building on the work of Fletcher,[18] developed an algorithm for locating intersections of potential energy surfaces of states of different symmetry. However, it was the development of efficient, analytic gradient based, algorithms specifically designed to find conical intersections of Born–Oppenheimer[19,20] potential energy surfaces that lead to a dramatic increase in interest in nonadiabatic processes in the 1990s and spawned no less than a revolution in our perception of the significance of conical intersections. As a result of research in that period, conical intersections, once little more than a theoretical curiosity came to be recognized as essential to nonadiabatic processes.

This revolution has focused on conical intersections of two states of the same symmetry. Virtually ignored have been the intersections of three states of the same symmetry. This neglect can be attributed to the comparative paucity of these points. According to the noncrossing rule in a five-dimensional space, the set of two-state conical intersections will occupy a three-dimensional subspace while the set of all three-state intersections is a single point! Despite this low dimensional locus, recent work suggests that neglect of this class of intersections may not be justified. In particular, three-state intersections have been located for excited states in ethyl[66] and allyl[70] and for the three lowest states in pyrazolyl.[71] In this chapter the algorithm used to locate these intersections is briefly described.

1.2. *Scope*

In this chapter, the use of analytic gradient techniques to compute the quantities essential to the description of nonadiabatic processes is described. These quantities include the first and second derivative coupling matrix elements, and the energy and coupling matrix gradients needed for the search algorithms used to locate conical intersections. Section 3 discusses the algorithms used to locate conical intersections and how they exploit analytic gradient techniques. The structure of these algorithms is not dependent on the wave functions used to describe the states in question. However, the accuracy of the derived quantities is. The nature of the electronic eigenstates is the subject of Sec. 2.

Sections 4–7 describe how the requisite derivative quantities are computed. We require the derivative of a generic matrix element, $M(\mathbf{v}^1, \mathbf{v}^2) \equiv \mathbf{v}^{1\dagger}\mathbf{M}\mathbf{v}^2$ with respect to changes in nuclear coordinates. The complicating factor is that $M(\mathbf{v}^1, \mathbf{v}^2)$ will not be expressed directly as a function of these coordinates. Rather $M(\mathbf{v}^1, \mathbf{v}^2)$ will depend on the molecular orbitals and other wave function parameters, including the location of the atom centered atomic orbital basis functions. Further, the molecular orbitals must satisfy certain restrictions including the requirement that they remain orthogonal with changes in geometry. Thus the determination of the gradient of $M(\mathbf{v}^1, \mathbf{v}^2)$, $\nabla M(\mathbf{v}^1, \mathbf{v}^2)$, will require the unraveling of a complicated chain rule with the orbital orthogonality explicitly included. The explicit form of this chain rule depends on the nature of the electronic eigenstates. Section 4 describes the use of generalized density matrices formed from these eigenstates to provide a unified description of the distinct M required in this chapter. This formulation leads to a general expression for ∇M which is a central result of this chapter. In Sec. 5, the equations describing the derivative of the molecular orbitals, the coupled perturbed state-averaged MCSCF equations, are derived. These equations represent a generalization of the pioneering work of Gerrat and Mills[21,22] who considered orbitals determined from the Hartree–Fock equations. Section 6 provides the general expression for ∇M. Section 7 uses that expression to determine the first derivative quantities required to formulate the nuclear Schrödinger equation in the Born–Huang approximation as described in Chapter 2 of this volume. The second derivative nonadiabatic coupling matrix element is also determined. In Sec. 8, three numerical examples are provided, (i) the location of an energy minimized conical intersection of the nonrelativistic Hamiltonian, (ii) the location of an energy minimzed conical

intersection for an Hamiltonain with C_s symmetry and the spin-orbit interaction included, and finally an evaluation of the adiabatic correction for the $X^1\Sigma^+$ state of LiH which has been measured experimentally.[23]

2. Wave Functions

2.1. *Hamiltonians*

The electronic wave functions, Φ_k, satisfy the electronic Schrödinger equation

$$[H_e - \mathrm{V}_k(\mathbf{X})]\Phi_k(\mathbf{x};\mathbf{X}) = 0. \tag{3}$$

H_e has the form:

$$H_e = \sum_{i=1}^{N^{\mathrm{el}}} \mu^{(1)}(\mathbf{x}_i;\mathbf{X}) + \sum_{i,j=1}^{N^{\mathrm{el}}} \mu^{(2)}(\mathbf{x}_i,\mathbf{x}_j) + \mu^{(N-N)}(\mathbf{X}) \tag{4}$$

where $\mu^{(N-N)}$ is the nuclear repulsion energy, and $\mu^{(1)}$ and $\mu^{(2)}$ are one and two electron operators. Two forms for H_e will be considered: (i) the nonrelativistic or Coulomb Hamiltonian, $H_e = H_0$ where $\mu^{(1)} \rightarrow \mu^{0,(1)}$ and $\mu^{(2)} \rightarrow \mu^{0,(2)}$ with $\mu^{0,(1)}$ the one electron kinetic energy and nuclear attraction operator and $\mu^{0,(2)}$ the two electron, electron–electron repulsion operator; and (ii) the relativistic Hamiltonian, $H_e = H_0 + H_{\mathrm{so}}$, where H_0 (H_{so}) is the Coulomb (spin-orbit[24]) Hamiltonian. In the relativistic case, $\mu^{(1)}$ will include, in addition to $\mu^{0,(1)}$, the Coulumb contribution, the spin-orbit contribution, while to $\mu^{0,(2)}$ will be added the spin-same-orbit and spin-other orbit contributions. $\mu^{(1)}$ and $\mu^{(2)}$ will also be used for a general hermitian operator.

2.2. *Nonrelativistic Wave Functions*

The appropriate choice of the wave function is essential if chemically meaningful results are to be achieved. When only near equilibrium properties on the lowest potential energy surface are required, the single reference based coupled cluster wave function[25] describes that region of the potential energy surfaces to near spectroscopic accuracy. However, nonadiabatic processes require wave functions that are necessarily multireference in character. For this reason, MRCI wave functions have been the wave function of choice in this field. These wave functions are developed from molecular orbitals determined from a self-consistent field (SCF), a multiconfigurational SCF

(MCSCF) or a state-averaged-MCSCF (SA-MCSCF) procedure and are denoted M/MRCI where M = SCF, MCSCF or SA-MCSCF. In this chapter the most general option, the SA-MCSCF/MRCI wave functions, will be used.

2.2.1. *Multireference Configuration Interaction Wave Functions*

In the MRCI approach, the electronic wave functions are expanded in a basis of configuration state functions (CSFs[26]):

$$\Phi_i(\mathbf{x};\mathbf{X}) = \sum_{a=1}^{N^{\mathrm{CSF}}} c_a^i(\mathbf{X})\Theta_a(\mathbf{x};\mathbf{X}). \tag{5a}$$

The CSFs, Θ, are eigenfunctions of S^2, M^s and carry, A, an irreducible representation of G, the spatial point group in question[27]

$$\Theta_{\mathbf{b}}(\mathbf{x};\mathbf{X}) \equiv P^{S_{\mathbf{b}_0},M^S_{\mathbf{b}_0},A_{\mathbf{b}_0}} \prod_{i=1}^{N^{\mathrm{el}}} \varphi_{b_i}(\mathbf{x}_i;\mathbf{X})\sigma_{b_i}. \tag{5b}$$

They are constructed from linear combinations (accomplished using the projector P) of Slater determinants, antisymmetric products of molecular spin orbitals, $\varphi_i(\mathbf{x}_1;\mathbf{X})\sigma$, where the spin function σ may be α or β. Below, for simplicity, the vector nature of $\mathbf{b}$ will be suppressed.

The $\mathbf{c}^i(\mathbf{X})$ satisfy the configuration interaction problem

$$[\mathbf{H}^e - \mathrm{V}_k(\mathbf{X})\mathbf{I}]\mathbf{c}^k(\mathbf{X}) = \mathbf{0} \tag{6}$$

where

$$\begin{aligned} H^e_{a,b}(\mathbf{X}) &= \langle\Theta_a(\mathbf{x};\mathbf{X})|H_e\Theta_b(\mathbf{x};\mathbf{X})\rangle_{\mathbf{x}} \\ &= \sum_{m,n}\mu^{(1)}_{m,n}(\mathbf{X})\tilde{k}^{ab}_{m,n} + \sum_{m,n,k,l}\mu^{(2)}_{m,n,k,l}(\mathbf{X})\tilde{K}^{ab}_{m,n,k,l} + \mu^{(N-N)}(\mathbf{X}) \end{aligned} \tag{7a}$$

$$\mu^{(1)}_{m,n}(\mathbf{X}) = \langle\varphi_m(\mathbf{x}_1;\mathbf{X})|\mu^{(1)}(\mathbf{x}_1;\mathbf{X})|\varphi_n(\mathbf{x}_1;\mathbf{X})\rangle_{\mathbf{x}_1} \tag{7b}$$

$$\mu^{(2)}_{m,n,k,l}(\mathbf{X}) = \langle\varphi_m(\mathbf{x}_1;\mathbf{X})\varphi_n(\mathbf{x}_1;\mathbf{X})|\mu^{(2)}(\mathbf{x}_1,\mathbf{x}_2)|\varphi_k(\mathbf{x}_2;\mathbf{X})\varphi_l(\mathbf{x}_2;\mathbf{X})\rangle_{\mathbf{x}}. \tag{7c}$$

$\mu^{(1)}_{m,n}$ and $\mu^{(2)}_{m,n,k,l}$ are respectively the one-electron integrals and two-electron integrals in the molecular orbital (MO) basis, and $\widetilde{K}^{a,b}_{m,n}$ and $\tilde{k}^{a,b}_{m,n,k,l}$ are geometry independent structure factors.

2.3. *Relativistic Wave Functions*

We are concerned with molecules with N^{el} odd, referred to as odd electron molecules. The approach used in this chapter assumes that zero pair, or large component only, wave functions are used.[28] Relativistic CI wave functions are solutions of Eq. (6), constructed directly in a time-reversal adapted CSF (TRACSF) basis. For TRACSFs M^{s} is no longer a good quantum number. Instead, for each Θ_b in the basis, $T\Theta_b$ is also in the basis, where T is the time reversal operator.[29] Since T commutes with H_e, the eigenstates come in degenerate pairs, Φ_k and $T\Phi_k \equiv \Phi_{Tk}$. For a more complete discussion of time reversal symmetry and TRACSFs see Refs. 30 and 31 and Chapter 2 of this volume. The applications in this work use the truncated adiabatic states approach to approximate the relativistic wave function. In this approach, the relativistic wave functions Φ_k, $k = 1 - N^{\mathrm{a}}$ are expanded in a basis of $M^0 \ll N^{\mathrm{CSF}}$ eigenstates of H_0, the nonrelativistic Hamiltonian, which have been time reversal adapted. Analytic gradient methods for the relativistic CI or the truncated adiabatic states approach are relatively straighforward to implement, once the methods for nonrelativistic wave functions are in hand. Therefore, in this work, analytic gradient techniques are described for nonrelativistic wave functions only. For a more indepth discussion of the truncated adiabatic states approach and the implementation of analytic gradient methods, see Ref. 32.

3. Locating Conical Intersections of Born–Oppenheimer Potential Energy Surfaces

From Eqs. (46a) and (46b) in Chapter 2 of this volume the most general Hamiltonian (to first order) in the vicinity of a two state conical intersection is given by

$$\begin{aligned}\mathbf{H}^e(\mathbf{X}^{x,i,j} + \delta\mathbf{X}) &= \left[\mathbf{s}^{i,j}\mathbf{I} + \begin{pmatrix} \mathbf{g}^{i,j} & \mathbf{h}^{i,j} & 0 & \mathbf{h}^{i,Tj} \\ \mathbf{h}^{i,j^*} & -\mathbf{g}^{i,j} & -\mathbf{h}^{i,Tj} & 0 \\ 0 & -\mathbf{h}^{i,Tj^*} & \mathbf{g}^{i,j} & \mathbf{h}^{i,j^*} \\ \mathbf{h}^{i,Tj^*} & 0 & \mathbf{h}^{i,j} & -\mathbf{g}^{i,j} \end{pmatrix}\right] \cdot \delta\mathbf{X} \\ &\equiv \left[\mathbf{s}^{i,j}\mathbf{I} + \begin{pmatrix} \mathbf{H} & \mathbf{A} \\ \mathbf{A}^\dagger & \mathbf{H}^* \end{pmatrix}\right] \cdot \delta\mathbf{X} \end{aligned} \tag{8a}$$

where $\mathbf{H}$ and $\mathbf{A}$ are 2×2 matrices. $\mathbf{H}^e$, or its submatrices, see below, are the basis of the algorithms for locating a conical intersection. In describing these algorithms, it is convenient to denote

$$\mathbf{v}^{(1)} = \mathbf{g}^{i,j}, \mathbf{v}^{(2)} = \mathbf{h}^{\mathrm{r},i,j}, \mathbf{v}^{(3)} = \mathbf{h}^{\mathrm{i},i,j}, \mathbf{v}^{(4)} = \mathbf{h}^{\mathrm{r},i,Tj}, \mathbf{v}^{(5)} = \mathbf{h}^{\mathrm{i},i,Tj}. \quad (9a)$$

The space spanned by these vectors is known as the branching, or $g-h$, space. Equation (8a) is applicable to a molecule with an odd number of electrons and the spin-orbit interaction included in the Hamiltonian. When C_s (or higher) symmetry can be imposed on the molecule, $\mathbf{A}= 0$, so that $\mathbf{v}^{(4)} = \mathbf{v}^{(5)} = 0$ for all $\mathbf{X}$. Finally, when $H_e = H_0$, that is for the non-relativistic Coulomb Hamiltonian, Eq. (8a) reduces to

$$\mathbf{H}^0(\mathbf{X}^{x,i,j} + \delta\mathbf{X}) = \left[\mathbf{s}^{i,j}\mathbf{I} + \begin{pmatrix} \mathbf{g}^{i,j} & \mathbf{h}^{i,j} \\ \mathbf{h}^{i,j} & -\mathbf{g}^{ij} \end{pmatrix}\right] \cdot \delta\mathbf{X} \quad (8a')$$

The computationally intensive part of algorithms based on these Hamiltonians is the evaluation of the $\mathbf{v}^{(k)}$. It is precisely these quantities that are amenable to evaluation using analytic gradient techniques. The requisite gradients for the nonrelativistic Hamiltonian will be derived in Secs. 4–7. The gradients for relativistic Hamiltonians depend on the details of how the relativistic effects are included. A detailed discussion of this point can be found in Ref. 32. Here we assume the $\mathbf{v}^{(i)}$ are readily available.

Given the availability of the $\mathbf{v}^{(i)}$, the algorithms for the location of two-state conical intersections are formally equivalent, distinguished only by the value η, the number of linearly-independent $\mathbf{v}^{(k)}$.

Further we have shown that since for a conical intersection of three states *i, j, k*, Eq. (8a) generalizes to[66]

$$\mathbf{H}^0(\mathbf{X}^{x,i,j,k} + \delta\mathbf{X}) = \left[\mathbf{s}^{i,j,k}\mathbf{I} + \begin{pmatrix} \mathbf{g}^{i} & \mathbf{h}^{i,j} & \mathbf{h}^{i,k} \\ \mathbf{h}^{i,j} & \mathbf{g}^{j} & \mathbf{h}^{j,k} \\ \mathbf{h}^{i,k} & \mathbf{h}^{j,k} & \mathbf{g}^{k} \end{pmatrix}\right] \cdot \delta\mathbf{X}$$

where $3\mathbf{s}^{i,j,k} = \mathbf{h}^{i,i} + \mathbf{h}^{j,j} + \mathbf{h}^{k,k}$ and $\mathbf{g}^k = \mathbf{h}^{k,k} - \mathbf{s}^{i,j,k}$. The same algorithm can be used to locate intersections of three potential energy surfaces with $\eta = 5$, and the $\mathbf{v}^{(k)}$ redefined as:

$$\mathbf{v}^{(1)} = \mathbf{g}^i - \mathbf{g}^j, \quad \mathbf{v}^{(2)} = \mathbf{h}^{i,j}, \quad \mathbf{v}^{(3)} = \mathbf{h}^{i,k}, \quad \mathbf{v}^{(4)} = \mathbf{h}^{j,k}, \quad \mathbf{v}^{(5)} = \mathbf{g}^j - \mathbf{g}^k. \quad (9b)$$

Below we will describe two algorithms for locating conical intersections. The first searches in a particular branching space, while the later searches in larger spaces.

3.1. *An Algorithm Based on the Energy Difference Gradient*

In this section we will describe an algorithm for locating an intersection of two states with energetics governed by the Coulomb Hamiltonian. Near such a conical intersection the Hamiltonian in Eq. (8a′) is relevant.

3.1.1. *The Energy Difference Gradient*

Let $\mathbf{X}^{x,i,j}$ denote a point of conical intersection of states i and j, and define $\mathbf{X} = \mathbf{X}^{x,i,j} + \delta\mathbf{X}$. Then, as shown in Chapter 2 of this volume, the eigenvalues (each doubly degenerate for $\eta = 3, 5$) of $\mathbf{H}^e$ are:

$$V_{\pm}(\mathbf{X}) = (\mathbf{s}^{i,j}(\mathbf{X}^{x,i,j}) \cdot \delta\mathbf{X}) \pm \sqrt{([\mathbf{g}^{i,j}(\mathbf{X}^{x,i,j}) \cdot \delta\mathbf{X}]^2 + |\mathbf{h}^{i,j}(\mathbf{X}^{x,i,j}) \cdot \delta\mathbf{X}|^2 + |\mathbf{h}^{i,Tj}(\mathbf{X}^{x,i,j}) \cdot \delta\mathbf{X}|^2)} \tag{10a}$$

with $\mathrm{V}_i = \mathrm{V}_-$ and $\mathrm{V}_j = \mathrm{V}_+$. This can be rewritten as

$$V_{\pm}(\mathbf{X}) = \rho\left[(\mathbf{s}^{ij}(\mathbf{X}^{x,i,j}) \cdot \delta\hat{\mathbf{X}}) \pm \sqrt{\sum_{k=1}^{\eta}(\mathbf{v}^{(k)}(\mathbf{X}^{x,i,j}) \cdot \delta\hat{\mathbf{X}})(\mathbf{v}^{(k)}(\mathbf{X}^{x,i,j})^* \cdot \delta\hat{\mathbf{X}}}\right] \tag{10b}$$

where $\rho = |\delta\mathbf{X}|$, $\delta\hat{\mathbf{X}} = \delta\mathbf{X}/\rho$. The energy difference gradient is given by

$$2\mathbf{g}^{j,i}(\mathbf{X}) = \nabla(\mathrm{V}_j(\mathbf{X}) - \mathrm{V}_i(\mathbf{X})) = 2\nabla\sqrt{\sum_{k=1}^{\eta}(\mathbf{v}^{(k)}(\mathbf{X}^{x,i,j}) \cdot \delta\mathbf{X})(\mathbf{v}^{(k)}(\mathbf{X}^{x,i,j})^* \cdot \delta\mathbf{X})} \tag{11a}$$

$$= \frac{2}{\Delta V_{j,i}}\mathrm{Re}\sum_{k=1}^{\eta}(\mathbf{v}^{(k)}(\mathbf{X}^{x,i,j}) \cdot \delta\mathbf{X})\mathbf{v}^{(k)}(\mathbf{X}^{x,i,j})^* \tag{11b}$$

where $\Delta V_{j,i} = V_j - V_i$. Note from Eqs. (9) and (10b) that $\mathbf{g}^{j,i}(\mathbf{X})$ depends only on $\delta\dot{\mathbf{X}}$ rather than $\delta\mathbf{X}$ so that to first order $\Delta V_{j,i}$ can be written

$$\Delta V_{j,i}(\mathbf{X}) = \mathbf{g}^{j,i}(\mathbf{X}^{x,i,j}) \cdot \delta\mathbf{X} \approx \mathbf{g}^{j,i}(\mathbf{X}) \cdot \delta\mathbf{X} \tag{12a}$$

3.1.2. *The Algorithm*

From Eq. (12a) several interesting conclusions follow. Define $\mathbf{X}^{x,i,j} = \mathbf{X} + \delta\mathbf{X}$ and assume that $\delta\mathbf{X}$ is sufficiently small that Eqs. (8)–(10) are valid. Then requiring $\Delta V_{j,i}$ to vanish at $\mathbf{X}^{x,i,j}$, that is

$$\Delta V_{j,i}(\mathbf{X}+\delta\mathbf{X}) = \Delta V_{j,i}(\mathbf{X}) + \nabla[\Delta V_{j,i}(\mathbf{X})] \cdot \delta\mathbf{X} = \Delta V_{j,i}(\mathbf{X}) + \mathbf{g}^{j,i}(\mathbf{X}) \cdot \delta\mathbf{X} = 0 \tag{12b}$$

gives

$$\delta\mathbf{X} = -\frac{\Delta V_{j,i}\mathbf{g}^{j,i}(\mathbf{X})}{\mathbf{g}^{j,i}(\mathbf{X}) \cdot \mathbf{g}^{j,i}(\mathbf{X})}, \tag{12c}$$

which is just stepping backward by $\mathbf{g}^{j,i}(\mathbf{X}^{x,i,j}) \cdot \delta\mathbf{X}$. Thus it should be possible to locate conical intersections by following the energy difference gradient computed using nondegenerate perturbation theory. Indeed, an algorithm, based on that idea has been used to locate conical intersection seams in triatomic molecules.[33] In that algorithm $(\Delta V_{i,j})^2$ is minimized

$$\nabla(\Delta V_{i,j})^2 = 2(\Delta V_{ij})\nabla(\Delta V_{ij}) \equiv 2\mathbf{G}^{\Delta} = \mathbf{0}. \tag{13}$$

This is solved using a Newton–Raphson approach obtained by assuming that at $\mathbf{Q} + \delta\mathbf{Q}$, Eq. (13) is satisfied, that is

$$\mathbf{G}^{\Delta}(\mathbf{Q} + \delta\mathbf{Q}) = \mathbf{G}^{\Delta}(\mathbf{Q}) + \nabla\mathbf{G}^{\Delta}(\mathbf{Q}) \cdot \delta\mathbf{Q} = \mathbf{0} \tag{14a}$$

where

$$\nabla\mathbf{G}^{\Delta} = \nabla(\Delta V_{j,i})\nabla(\Delta V_{j,i}) + (\Delta V_{j,i})\nabla\nabla(\Delta V_{j,i}). \tag{14b}$$

Note that internal coordinates Q_k, $k = 1 - N^{\text{int}}$, rather than space fixed coordinates $\mathbf{X}$ are used. From Eq. (14b) near a conical intersection, since $\Delta V \to 0$, $\nabla\mathbf{G}^{\Delta} \cong \nabla(\Delta V_{j,i})\nabla(\Delta V_{j,i}) \equiv \mathbf{g}^{j,i}\mathbf{g}^{j,i}$ so that Eq. (14a) becomes

$$\mathbf{g}^{j,i}(\mathbf{Q})[\mathbf{g}^{j,i}(\mathbf{Q}) \cdot \delta\mathbf{Q}] = -\mathbf{G}^{\Delta}(\mathbf{Q}) = -\Delta V_{j,i}\mathbf{g}^{j,i}(\mathbf{Q}) \tag{15a}$$

which has as solutions

$$\delta\mathbf{Q} = -(\Delta V_{i,j}) \quad \mathbf{g}^{j,i}(\mathbf{Q})/[\mathbf{g}^{j,i}(\mathbf{Q}) \cdot \mathbf{g}^{j,i}(\mathbf{Q})] \tag{15b}$$

which is a scaled displacement along the energy difference gradient.

This approach was used to locate points on the $1,2^1A'$ seam of conical intersection in $He+H_2$.[33] In that implementation,which used $H_e = H_0$, the non-crossing rule was exploited. For $\eta = 2$ and $N^{\rm int} = 3$, the non-crossing rule gives a seam of conical intersection of dimension 1. Therefore Eq. (14) was solved with one internal coordinate Q_i fixed and the two remaining coordinates used to find the (locally) unique point at which $\Delta V = 0$. In this way the seam of conical intersection was determined as a function of Q_i.

3.2. *A Lagrange Multiplier Based Approach*

Here we are principally concerned with two-state conical intersections of H_0. However the algorithm discussed in this section is quite general, being applicable to the $N^{\rm el}$ odd with the spin-orbit interaction included case ($\eta = 5$, or 3) and three-state conical intersections of H_0 (also an $\eta = 5$ problem). This generality is illustrated in the discussion that follows.

The previous approach determines a single point on the seam of conical intersection without regard to its energy. It is therefore necessary to specify, or constrain, $N^{\rm int} - 2$ internal coordinates for each point of conical intersection, tacitly specifying the unique g–h space in which to search. This approach is therefore of limited utility for a general polyatomic molecule, owing to the large number of internal coordinates. For a more complete discussion of this idea, see Refs. 67–69. This problem can be overcome with the help of energy minimization. Rather than constraining $N^{\rm int} - 2$ internal coordinates, an energy minimized point of conical intersection of states i and j is sought subject to $N^{\rm con} \ll N^{\rm int}$ additional constraints on the internal coordinates, given by

$$K^i(\mathbf{X}) = 0, i = 1 - N^{\rm con}. \tag{16}$$

A point on the surface of conical intersection can be located as follows. Assume $\mathbf{X}$ is sufficiently close to a point of conical intersection that Eq. (8) is valid. In the adiabatic representation

$$\mathbf{U}^{-1}\mathbf{H}^e(\mathbf{X}^{x,ijk} + \delta\mathbf{X})\mathbf{U} = [\mathbf{s}^{ijk}\delta\mathbf{X}\mathbf{I} + \mathbf{E}^{ijk}] \tag{17a}$$

where $ijk = i, j$ for a two-state conical intersection.

$$E^{ijk} = \begin{pmatrix} -\varepsilon^{i,j} & 0 & 0 & 0 \\ 0 & \varepsilon^{i,j} & 0 & 0 \\ 0 & 0 & -\varepsilon^{i,j} & 0 \\ 0 & 0 & 0 & \varepsilon^{i,j} \end{pmatrix} \tag{17b}$$

with $\varepsilon^{i,j} = V_i - V_j$ for the $\eta = 5$ two-state conical intersection, and

$$E^{ijk} = \begin{pmatrix} -\varepsilon^{i,j} & 0 \\ 0 & \varepsilon^{i,j} \end{pmatrix} \tag{17c}$$

for the non-relativistic two-state conical intersection.

The Hamiltonian in Eq. (8a) will be equal to that in Eqs. (17a) and (17b), provided $\delta\mathbf{X}$ is chosen such that

$$-\mathbf{g}^{i,j} \cdot \delta\mathbf{X} = \varepsilon^{i,j} \quad \mathbf{h}^{i,j} \cdot \delta\mathbf{X} = \mathbf{0} \quad \mathbf{h}^{i,Tj} \cdot \delta\mathbf{X} = \mathbf{0}. \tag{18a}$$

or in the non-relativistic case

$$-\mathbf{g}^{i,j} \cdot \delta\mathbf{X} = \varepsilon^{i,j} \qquad \mathbf{h}^{i,j} \cdot \delta\mathbf{X} \qquad \mathbf{h}^{i,j} \text{ real-valued} \tag{18b}$$

A modified form of Eq. (18a) forms the basis of our algorithm in the case of a three-state conical intersection where

$$E^{ijk} = \begin{pmatrix} \varepsilon_i^{i,j,k} & 0 & 0 \\ 0 & \varepsilon_j^{i,j,k} & 0 \\ 0 & 0 & \varepsilon_k^{i,j,k} \end{pmatrix} \tag{17d}$$

with $\varepsilon_l^{i,j,k} = V_l - (V_i + V_j + V_k)/3$ and Eq. (18a) replaced by

$$-\mathbf{v}^{(1)} \cdot \delta\mathbf{X} = \Delta V_{i,j} \quad -\mathbf{v}^{(5)} \cdot \delta\mathbf{X} = \Delta V_{j,k} \quad \mathbf{v}^{(k)} \cdot \delta\mathbf{X} = 0 \quad k = 2,3,4 \tag{18c}$$

with $\Delta V_{m,n} = \varepsilon_m^{i,j,k} - \varepsilon_n^{i,j,k}$.

Therefore assuming that $\delta\mathbf{X}$ is sufficiently small that $\mathbf{v}^{(i)}(\mathbf{X}^{x,i,j}) \approx \mathbf{v}^{(i)}(\mathbf{X})$, Eq. (18a) or (18b) can be used to move from $\mathbf{X}$ to $\mathbf{X}^{x,i,j}$ while Eq. (18c) takes $\mathbf{X}$ to $\mathbf{X}^{x,i,j,k}$. It is to this point that we now turn.

Minimization of V_i subject to the geometric constraints, Eq. (16), and requirement that the point lies on the seam of conical intersection, Eq. (18), can be formulated using Lagrange mulipliers.[34] The desired point of conical intersection is an extremum of the following Lagrangian[20,35]

$$\begin{aligned} \mathsf{L}(\mathbf{Q}, \boldsymbol{\xi}, \boldsymbol{\lambda}) = V_i(\mathbf{Q}) + \sum_{i=1}^{N^{\text{con}}} \xi_i K^i(\mathbf{Q}) + \lambda_1 \mathbf{H}^e(\mathbf{c}^i + \mathbf{c}^j, \mathbf{c}^i - \mathbf{c}^j) + \lambda_2 \operatorname{Re} \mathbf{H}^e(\mathbf{c}^i, \mathbf{c}^j) \\ + \lambda_3 \operatorname{Im} \mathbf{H}^e(\mathbf{c}^i, \mathbf{c}^j) + \lambda_4 \operatorname{Re} \mathbf{H}^e(\mathbf{c}^i, \mathbf{c}^{Tj}) + \lambda_5 \operatorname{Im} \mathbf{H}^e(\mathbf{c}^i, \mathbf{c}^{Tj}) \end{aligned} \tag{19}$$

where $\mathbf{H}^e(\mathbf{v}^1, \mathbf{v}^2) = \mathbf{v}^{1\dagger} \mathbf{H}^e \mathbf{v}^2$. Note that $\mathbf{H}^e(\mathbf{c}^i(\mathbf{Q}) + \mathbf{c}^j(\mathbf{Q}), \mathbf{c}^i(\mathbf{Q}) - \mathbf{c}^j(\mathbf{Q})) = \mathbf{V}_i(\mathbf{Q}) - \mathbf{V}_j(\mathbf{Q}) \equiv \Delta\mathbf{V}_{i,j}(\mathbf{Q})$ and that we have switched

from $3N^{\rm nuc}$ space fixed coordinates $\mathbf{X}$ to $3N^{\rm nuc}-6$ internal coordinates, $\mathbf{Q}$. $\mathbf{Q}$, $\boldsymbol{\xi}$ and $\boldsymbol{\lambda}$ are independent variables and, as discussed above, only the first η of the λ_i are included in L. Minimization of L yields a minimum in the energy of state i, subject to the $N^{\rm con}$ geometric constraints and the requirement that $\Delta V_{i,j} = \mathbf{H}^e(\mathbf{c}^i + \mathbf{c}^j, \mathbf{c}^i - \mathbf{c}^j) = 0$. The remaining constraints, corresponding to λ_k, $k = 2-\eta$, may appear superfluous. However, this is not the case. These constraints yield the remaining $\eta-1$ vectors that are needed to define a branching space. This restriction was introduced tacitly in the algorithm in Sec. 3.1.2 by fixing one internal coordinate.

The extremum of $\mathsf{L}(\mathbf{Q},\xi,\lambda)$ is found from the requirement that its first derivative with respect to all the independent variables, $\mathbf{Q}$, ξ, λ, vanish, that is,

$$\nabla_Q \mathsf{L}(\mathbf{Q},\boldsymbol{\xi},\boldsymbol{\lambda}) = \mathbf{g}^i(\mathbf{Q}) + \sum_{k=1}^{\eta} \mathbf{v}^{(k)}(\mathbf{Q})\lambda_k + \sum_{k=1}^{N^{\rm con}} \mathbf{k}^k(\mathbf{Q})\xi_k \equiv \mathbf{L}^{\rm Q}(\mathbf{Q},\boldsymbol{\xi},\boldsymbol{\lambda}) = \mathbf{0} \tag{20a}$$

$$\frac{\partial}{\partial\lambda_k}\mathsf{L}(\mathbf{Q},\boldsymbol{\xi},\boldsymbol{\lambda}) = \Delta V_{i,j}\delta_{k,1} = 0 \tag{20b}$$

$$\nabla_\xi \mathsf{L}(\mathbf{Q}.\boldsymbol{\xi},\boldsymbol{\lambda}) = \mathbf{K}(\mathbf{Q}) = 0 \tag{20c}$$

Equations (20) are solved using a Newton–Raphson procedure. These equations have the form $\nabla F(\mathbf{X}) = 0$. A Newton–Raphson procedure to solve the equation, $\nabla F(\mathbf{X}) = 0$ is obtained by expanding:

$$\nabla F(\mathbf{X}+\delta\mathbf{X}) = \nabla F(\mathbf{X}) + \delta\mathbf{X}\cdot\nabla(\nabla F(\mathbf{X})) \tag{21a}$$

and assuming that $\nabla F(\mathbf{X}+\delta\mathbf{X}) = 0$ which gives the system of linear equations

$$\mathbf{H}\delta\mathbf{X} = -\nabla\mathbf{F}(\mathbf{X}) \tag{21b}$$

where the hessian matrix $\mathbf{H}$ is given by $\nabla\nabla\mathbf{F}$. Using Eqs. (21), Eqs. (20) yield the following set of Newton–Raphson equations:

$$\begin{pmatrix} \mathsf{L}^{Q,Q} & \mathbf{v}(\mathbf{Q})^\dagger & \mathbf{k}(\mathbf{Q})^\dagger \\ \mathbf{v}(\mathbf{Q}) & \mathbf{0} & \mathbf{0} \\ \mathbf{k}(\mathbf{Q}) & \mathbf{0} & \mathbf{0} \end{pmatrix} \begin{pmatrix} \delta\mathbf{Q} \\ \delta\boldsymbol{\lambda} \\ \delta\boldsymbol{\xi} \end{pmatrix} = - \begin{pmatrix} \mathbf{L}^Q \\ \Delta \mathrm{V}_{i,j}\mathbf{e}^1 \\ \mathbf{K}(\mathbf{Q}) \end{pmatrix} \tag{22}$$

where $\mathbf{e}^1_k = \delta_{1,k}$, $k = 1-\eta$, $\mathsf{L}^Q_l = (\partial/\partial Q_l)L$ and $\mathsf{L}^{Q,Q}_{k,l} = (\partial^2/\partial Q_k\partial Q_l)\mathsf{L}$. In our original formulation $\mathsf{L}^{Q,Q}$ is evaluated as a divided difference of $\mathbf{L}^Q$,

the gradient of L. Equation (23) below illustrates the use of a centered difference to evaluate $\mathsf{L}^{Q,Q}$

$$\frac{\partial^2}{\partial Q_k \partial Q_l}\mathsf{L}(\mathbf{Q}) \approx \frac{1}{2\varepsilon}[\mathsf{L}_l^Q(\mathbf{Q}(k,\varepsilon)) - \mathsf{L}_l^Q(\mathbf{Q}(k,-\varepsilon)] \tag{23}$$

In Eq. (23), $\mathbf{Q}(k,\varepsilon) = \mathbf{Q} + (0,0,\ldots,\varepsilon,\ldots 0)$ where ε appears in the kth position in an otherwise zero vector, and the $\boldsymbol{\xi}, \boldsymbol{\lambda}$ dependence of L and $\mathbf{L}^Q$ has been suppressed.

Equations (22) are solved iteratively. Therefore, the efficiency of the algorithm depends on the ability to rapidly determine the right hand side of Eq. (22). This is accomplished using the analytic gradient techniques discussed in this chapter. The performance of this algorithm for both non-relativistic and relativistic wave functions is discussed in Sec. 8.

The evaluation of $\mathbf{L}^{QQ}$ using Eq. (23) becomes increasingly costly as the size of the molecule increases. It is desirable to avoid explicit evaluation of $\mathbf{L}^{QQ}$, by using updating techniques to infer information about the Hessian from the gradients along the search path. To accomplish this, the functions in question must be smoothly varying along the search path. This however turns out not to be the case when searching for a conical intersection using Eq. (22) where key search parameters, the energy gradients, energy difference gradients and coupling matrix elements, vary erratically along the search path. Our numerical studies have shown that as a result of this irregular behavior while it is relatively straightforward to locate points of conical intersection, energy optimization is more costly to achieve. At first glance, this situation might seem unavoidable since it is attributable to the singular character of the conical intersection which is the object of the search. However that is not the case. We have shown that these erratic functions can be replaced by extrapolatable functions, functions that are well-behaved along the search path, and have developed a simple, yet highly effective, modification of the algorithm based on Eq. (22). This modified algorithm based on these extrapolatable functions and Hessian updating[72] significantly improves convergence to an energy-minimized point of conical intersection.

The key to this approach is the use of extrapolatable functions which are derived from two essential observations. Each point on the seam of conical intersection is characterized by a unique g–h or branching space.

For two-state intersections[69] this space, comprised of the coupling and tuning coordinates,[73] is spanned by a unique (up to transpositions and sign changes) set of mutually orthogonal vectors. These vectors turn out to be slowly varying functions of the search path and are used in solution of Eq. (18a) or (18b). The second observation concerns the formulation of the energy minimization which seeks the minimum of $\mathbf{V}_i$. The resulting gradient contribution to $\mathbf{L}^Q, \Delta\mathbf{V}_i$, behaves erratically along the search path. However we have suggested and confirmed numerically[68] that the gradient of the trace, $\mathbf{V}^{\mathrm{T}} = (\mathbf{V}_i + \mathbf{V}_j)/2$ for two-state intersections or $\mathbf{V}^{\mathrm{T}} = (\mathbf{V}_i + \mathbf{V}_j + \mathbf{V}_k)/3$ for three-state intersections is a slowly varying function of the search path.

4. Matrix Elements and Generalized Density Matrices

$\mathbf{L}^Q$ and the other gradients required in this chapter can ultimately be related to the derivative of the following matrix element in the CSF basis

$$\mathrm{M}_{a,b}(s,S;m^{(1)},m^{(2)}) = \sum_{m,n} m^{(1)}_{m,n}(\mathbf{X}) s^{ab}_{m,n} + \sum_{m,n,k,l} m^{(2)}_{m,n,k,l}(\mathbf{X}) S^{ab}_{m,n,k,l} \tag{24a}$$

where s and S are independent of geometry. $M_{a,b}(s,S;m^{(1)},m^{(2)})$ is a generalization of Eq. (7a). Its transformation to a geometry dependent basis $\mathbf{v}^i(\mathbf{X})$, $i = 1 - N^{\mathrm{CSF}}$ [linear combinations of the $\mathbf{c}^k$ in Eq. (5a), not to be confused with the $\mathbf{v}^{(i)}(\mathbf{X})$ in Eq. (9a)] gives

$$M(\mathbf{v}^i,\mathbf{v}^j;s,S;m^{(1)},m^{(2)}) = \sum_{a,b} v^i_a \; M_{a,b} \; v^j_b \tag{24b}$$

$$M(\mathbf{v}^i,\mathbf{v}^j) = \sum_{m,n} m^{(1)}_{m,n}(\mathbf{X}) \gamma^{s^{\mathbf{v}^i,\mathbf{v}^j}}_{m,n}(\mathbf{X}) + \sum_{m,n,k,l} m^{(2)}_{m,n,k,l}(\mathbf{X}) \Gamma^{S^{\mathbf{v}^i,\mathbf{v}^j}}_{m,n,k,l}(\mathbf{X}) \tag{24c}$$

where

$$\gamma^{s^{\mathbf{v}^i,\mathbf{v}^j}}_{m,n} = \sum_{a,b} v^i_a(\mathbf{X}) s^{ab}_{m,n} v^j_b(\mathbf{X}) \quad \text{and} \quad \Gamma^{s^{\mathbf{v}^i,\mathbf{v}^j}}_{m,n,k,l} = \sum_{a,b} v^i_a(\mathbf{X}) S^{ab}_{m,n,k,l} v^j_b(\mathbf{X}) \tag{24d}$$

are generalized density matrices.[36,37] The preponderance of the derivatives we require can be written as the gradient of $M(\mathbf{v}^i, \mathbf{v}^j)$ — the arguments s, S, $m^{(1)}$, $m^{(2)}$ will be suppressed when they are the $\tilde{k}, \widetilde{K}, \mu^{(1)}, \mu^{(2)}$ from Eq. (7a) — with respect to $\mathbf{X}$, where the geometry dependence of the density matrix, from the $\mathbf{v}^j$, can be ignored, that is,

$$\begin{aligned}\nabla M(\mathbf{v}^i, \mathbf{v}^j) &= \sum_{a,b} v_a^i [\nabla \mathrm{M}_{a,b}] v_b^j \\ &= \sum_{m,n} (\nabla m^{(1)}_{m,n}) \gamma^{s^{\mathbf{v}^i,\mathbf{v}^j}}_{m,n} + \sum_{m,n,k,l} (\nabla m^{(2)}_{m,n,k,l}) \Gamma^{S^{\mathbf{v}^i,\mathbf{v}^j}}_{m,n,k,l}. \end{aligned} \tag{25}$$

Before proceeding with the derivation of the working expressions for $\nabla M(\mathbf{v}^i, \mathbf{v}^j)$, it is useful to point out how and where the results will be used. Note that

$$\begin{aligned} &M(\mathbf{c}^i, \mathbf{c}^i; \tilde{k}, \widetilde{K}; \mu^{0,(1)}, \mu^{0,(2)}) = V_i \quad \text{and} \\ &\nabla M(\mathbf{c}^i, \mathbf{c}^i; \tilde{k}, \widetilde{K}; \mu^{0,(1)}, \mu^{0,(2)}) = \nabla \mathrm{V}_i \equiv \mathbf{g}^i. \end{aligned} \tag{26}$$

Table 1, summarizes the principal applications based on H_0. Note that $M(\mathbf{c}^i + \mathbf{c}^j, \mathbf{c}^i + \mathbf{c}^j) - [M(\mathbf{c}^i, \mathbf{c}^i) + M(\mathbf{c}^j, \mathbf{c}^j)] = M(\mathbf{c}^i, \mathbf{c}^j)$, and that[74] $M(\mathbf{c}^i + \mathbf{c}^j, \mathbf{c}^i - \mathbf{c}^j) = [M(\mathbf{c}^i, \mathbf{c}^i) - M(\mathbf{c}^j, \mathbf{c}^j)]$. These identities relate transition density matrices to diagonal density matrices, are useful for program documentation and can be used to avoid the explicit construction of transition density matrices which are somewhat more costly to compute than diagonal density matrices.

Table 1. Uses of generalized gradients. $\nabla M(i,j) \equiv \nabla M(\mathrm{v}^i, \mathrm{v}^j; \mu^{0,(1)}, \mu^{0,(2)}; \tilde{k}^{a,b}_{m,n}, \widetilde{K}^{a,b}_{m,n,k,l})$.

	v^i	v^j	$\nabla M(i,j)$	Use
(i)	$\mathbf{c}^i + \mathbf{c}^j$	$\mathbf{c}^i - \mathbf{c}^j$	$\mathbf{g}^{i,j} = \mathbf{g}^i - \mathbf{g}^j$	Conical intersection search, Avoided intersection search[20]
(ii)	$\mathbf{c}^i$	$\mathbf{c}^j$	$\Delta \mathrm{V}_{i,j}{}^{\mathrm{CI}}\mathbf{a}_{i,j} = \mathbf{h}^{i,j}$	Evaluate derivative coupling, Conical intersection search
(iii)	$\mathbf{c}^i + \mathbf{c}^j$	$\mathbf{c}^i + \mathbf{c}^j$	$\mathbf{g}^i + \mathbf{g}^j + 2\mathbf{h}^{i,j}$	Conical intersection search
(iv)	$\mathbf{c}^k$	$\mathbf{c}^k$	$\mathbf{g}^k$	Energy extremum search

In Eq. (25), $m^{(1)}_{k,l}$ and $m^{(2)}_{k,l,m,n}$ are in the molecular orbital basis. Therefore their gradients require the derivatives of the molecular orbitals. It is to this topic that we now turn.

5. Molecular Orbitals and Their Derivatives

The molecular orbitals, $\boldsymbol{\varphi}$, here and below assumed to be real-valued, are linear combinations of atom-centered atomic orbitals, $\boldsymbol{\alpha}(\mathbf{x}_1;\mathbf{X})$,

$$\varphi_i(\mathbf{x}_1;\mathbf{X}) = \sum_p \boldsymbol{\tau}_{p,i}(\mathbf{X})\alpha_p(\mathbf{x}_1;\mathbf{X}) \tag{27}$$

chosen to satisfy the SA-MCSCF equations. The gradient of a molecular orbital is obtained by differentiating the defining equations which in our case are the SA-MCSCF equations.

5.1. *State-Averaged Multiconfigurational Self-Consistent Field Method*

In a SA-MCSCF procedure the weighted average of the N^{wt} nonrelativistic energies with weights $\omega_k(>0)$, $k = 1 - N^{\mathrm{wt}}$, is minimized. Each wave function has the form shown in Eq. (5a)

$$\Phi^{\mathrm{MC}}_i(\mathbf{x};\mathbf{X}) = \sum_{a=1}^{N^{\mathrm{MC-CSF}}} C^i_a(\mathbf{X})\Theta_a(\mathbf{x};\mathbf{X}). \tag{28}$$

Since $N^{\mathrm{wt}} < N^{\mathrm{MC-CSF}}$, it is convenient to define as "occupied states" those states included in the state averaging, and the remaining states as "unoccupied states". The average energy can be written

$$E_{\mathrm{SAMC}}(\boldsymbol{\varphi},\mathbf{C}) = \sum_{\substack{a,b=1,N^{\mathrm{MC-CSF}} \\ i=1,N^{\mathrm{wt}}}} \omega_i C^i_a(\mathbf{X}) H^0_{a,b} C^i_b(\mathbf{X}) \equiv \sum_{i=1,N^{\mathrm{wt}}} \omega_i E^0_i(\mathbf{X}) \tag{29a}$$

$$= \sum_{a,b,i}\left[\omega_i \sum_{m,n} C^i_a \mu^{0,(1)}_{m,n} \tilde{k}^{ab}_{m,n} C^i_b + \sum_{k,l,m,n} C^i_a \mu^{0,(2)}_{k,l,m,n} \tilde{K}^{ab}_{k,l,m,n} C^i_b\right] + \mu^{(N-N)} \tag{29b}$$

$$= \sum_{a,b,i,} \sum_{m,n} \omega_i \mu^{0,(1)}_{m,n} C^i_a \tilde{k}^{ab}_{m,n} C^i_b + \sum_{k,l,m,n} \sum_{a,b,i} \omega_i \mu^{0,(2)}_{k,l,m,n} C^i_a \tilde{K}^{ab}_{k,l,m,n} C^i_b + \mu^{(N-N)}$$

$$= \sum_{m,n} \mu^{0,(1)}_{m,n}(\mathbf{X}) \gamma^{\mathrm{SAMC}}_{m,n}(\mathbf{X}) + \sum_{k,l,m,m} \mu^{0,(2)}_{k,l,m,n}(\mathbf{X}) \Gamma^{\mathrm{SAMC}}_{k,l,m,n}(\mathbf{X}) + \mu^{(N-N)}(\mathbf{X})$$

where

$$\boldsymbol{\gamma}^{\mathrm{SAMC}} = \sum_i \omega_i \boldsymbol{\gamma}^{i,i} \quad \text{and} \quad \Gamma^{\mathrm{SAMC}} = \sum_i \omega_i \boldsymbol{\Gamma}^{i,i} \tag{30a}$$

$$\gamma^{i,i}_{m,n} = \sum_{a,b} C^i_a \widetilde{K}^{ab}_{m,n} C^i_b \quad \text{and} \quad \Gamma^{i,i}_{k,l,m,n} = \sum_{a,b} C^i_a \tilde{K}^{ab}_{k,l,m,n} C^i_b \tag{30b}$$

$$\mu^{0,(1)}_{m,n}(\mathbf{X}) = \langle \varphi_m(\mathbf{x}_1;\mathbf{X}) | \mu^{0,(1)}(\mathbf{x}_1;\mathbf{X}) | \varphi_n(\mathbf{x}_1;\mathbf{X}) \rangle_{\mathbf{x}_1} \tag{30c}$$

$$\mu^{0,(2)}_{m,n,k,l}(\mathbf{X}) = \langle \varphi_m(\mathbf{x}_1;\mathbf{X}) \varphi_n(\mathbf{x}_1;\mathbf{X}) | \mu^{0,(2)}(\mathbf{x}_1,\mathbf{x}_2) | \varphi_k(\mathbf{x}_2;\mathbf{X}) \varphi_l(\mathbf{x}_2;\mathbf{X}) \rangle_{\mathbf{x}}. \tag{30d}$$

In Eq. (29a), only the dependence of $\mathrm{E_{SAMC}}$ on the variational parameters has been indicated. $\mathrm{E_{SAMC}}$ also depends, through the atomic orbital basis, on the location of the atoms and it assumes that the $\boldsymbol{\varphi}$ are orthonormal.

The SA-MCSCF equations define an optimal set of orbitals, $\boldsymbol{\varphi}^{(\mathrm{opt})}$, and expansion coefficients, $\mathbf{C}^{(\mathrm{opt})}$ as unitary transformations of an arbitrary initial set, that is,

$$\boldsymbol{\varphi}^{(\mathrm{opt})} = \boldsymbol{\varphi} e^{-\tilde{\boldsymbol{\Delta}}} \quad \varphi^{(\mathrm{opt})}_j = \sum_k \varphi_k \left(\delta_{k,j} - \tilde{\Delta}_{k,j} + 1/2 \sum_{k'} \tilde{\Delta}_{k,k'} \tilde{\Delta}_{k',j} + \cdots \right) \tag{31a}$$

and

$$\mathbf{C}^{(\mathrm{opt})} = \mathbf{C} e^{-\tilde{\zeta}} \qquad \mathbf{C}^{j,(\mathrm{opt})} = \sum_k \mathbf{C}^k \left(\delta_{k,j} - \tilde{\zeta}_{k,j} + 1/2 \sum_{k'} \tilde{\zeta}_{k,k'} \tilde{\zeta}_{k',j} + \cdots \right) \tag{31b}$$

where the antisymmetric matrix, $\tilde{\Delta}_{i,j}(\tilde{\zeta}_{i,j})$ has unique elements $\Delta_{ij}(\zeta_{ij})$ and ij denotes the compound index $(i-1)i/2+j$.

The conditions defining the MCSCF parameters, the MCSCF variational conditions,[38–40] are obtained by requiring the derivatives of $E_{\mathrm{SAMC}}(\boldsymbol{\varphi}^{(\mathrm{opt})}, \mathbf{C}^{(\mathrm{opt})})$ with respect to the unique parameters, the Δ_{ij} and ζ_{kj}, to vanish. From Eqs. (31), the derivatives can be expressed in terms of orbital and state excitations. In particular, from Eq. (31a), orbital gradients correspond to the first order terms in $\tilde{\Delta}_{k,j}$, and are expressed as a

sum of terms in which the orbital replacements $\varphi_j \rightarrow \varphi_k$, and, since $\tilde{\Delta}_{k,j}$ is antisymmetric, $\varphi_k \rightarrow -\varphi_j$ are made in Eq. (29b). The result of this orbital excitation and de-excitation is that each E_i^0 is replaced by a difference of Lagrangians ($\mathbf{L}^{i,i}$), that is,

$$\frac{\partial E_i^0}{\partial \Delta_{mn}} = L_{m,n}^{i,i} - L_{n,m}^{i,i} \tag{32a}$$

where

$$L_{m,n}^{i,i} = \sum_j 2\mu_{m,j}^{0,(1)} \gamma_{n,j}^{i,i} + \sum_{j,k,l} 4\mu_{m,j,k,l}^{0,(2)} \Gamma_{n,j,k,l}^{i,i} \tag{32b}$$

and

$$\frac{\partial}{\partial \Delta_{mn}} E_{\mathrm{SAMC}} = \sum_{k=1}^{N^{\mathrm{wt}}} \omega_k (L_{m,n}^{k,k} - L_{n,m}^{k,k}) = \sum_{k=1}^{N^{\mathrm{wt}}} \omega_k G_{m,n}^{(o)^{k,k}} \equiv G_{mn}^{(o)}. \tag{32c}$$

Similarly from Eq. (31b), the first order terms in $\tilde{\zeta}_{kj}$ give rise to a sum of terms in which a single state $\mathbf{C}^j$ is replaced by $\mathbf{C}^k$ and $\mathbf{C}^k$ by $-\mathbf{C}^j$. Thus each $\mathbf{C}^{i\dagger}\mathbf{H}^0\mathbf{C}^i$ is replaced with $\mathbf{C}^{j\dagger}\mathbf{H}^0\mathbf{C}^i + \mathbf{C}^{i\dagger}\mathbf{H}^0\mathbf{C}^j$. Equivalently this state excitation replaces density matrices with transition density matrices in Eqs. (29) giving as gradients:

$$\frac{\partial}{\partial \zeta_{ij}} E_{\mathrm{SAMC}} \equiv G_{ij}^{(\zeta)} = -2(\omega_i - \omega_j)\mathbf{C}^{j\dagger}\mathbf{H}^0\mathbf{C}^i \quad \text{for } i,j \leq N^{\mathrm{wt}} \tag{33a}$$

$$\frac{\partial}{\partial \zeta_{ij}} E_{\mathrm{SAMC}} = -2\omega_i \mathbf{C}^{j\dagger}\mathbf{H}^0\mathbf{C}^i \quad \text{for } i \leq N^{\mathrm{wt}}\ j > N^{\mathrm{wt}}. \tag{33b}$$

More details concerning the origin of these expressions can be found in Ref. 41. In the SA-MCSCF procedure there are two classes of $\tilde{\zeta}_{i,j}$, those for which both i and j are occupied states, (33a) and those with only one index in the occupied space, (33b).

Equation (33b) requires that the eigenvectors be known for both the occupied and unoccupied states. This severely limits the size of $N^{\mathrm{MC-CSF}}$.

This limitation can be overcome[39] by noting that

$$\mathbf{C}^{j\dagger}\mathbf{H}^0\mathbf{C}^i = 0 \quad \text{for } j \neq i \tag{34a}$$

is equivalent to

$$\mathbf{C}^{j\dagger}[\mathbf{H}^0 - V_i^{\mathrm{MC}}]\mathbf{C}^i = 0 \quad \text{for all j} \tag{34b}$$

which is equivalent to

$$[\mathbf{H}^0 - V_i^{\mathrm{MC}}]\mathbf{C}^i = 0 \tag{34c}$$

since the $\mathbf{C}^j$ are complete. Thus the requirement that the gradient in Eq. (33b) vanish can be written as

$$\frac{\partial}{\partial \mathbf{C}^i} E_{\mathrm{SAMC}} \equiv G_i^{(C)} = (\mathbf{H}^0 - V_i^{\mathrm{MC}})\mathbf{C}^i = 0. \tag{35}$$

Thus the mixings between the "occupied" states are represented in the eigenvector basis [Eq. (33a)] and the mixings of the "occupied" states with the "unoccupied" states are handled in the CSF basis, see Eq. (35). In this representation the SA-MCSCF variational conditions become

$$\mathbf{G}^{(\mathrm{o})}(\mathbf{X}) = \mathbf{G}^{(\zeta)}(\mathbf{X}) = \mathbf{G}^{(\mathrm{C})}(\mathbf{X}) = \mathbf{0}. \tag{36}$$

Although these equations can be solved by simple iteration, a second order or Newton–Raphson procedure is used to enable orbital derivatives to be determined, see below.

As discussed near Eq. (21), a Newton–Raphson procedure to solve the equation $\mathbf{G}(\mathbf{X}) = 0$ is obtained by expanding:

$$\mathbf{G}(\mathbf{X} + \delta\mathbf{X}) = \mathbf{G}(\mathbf{X}) + \delta\mathbf{X} \cdot \nabla(\mathbf{G}(\mathbf{X})) \tag{37a}$$

and assuming that $\mathbf{G}(\mathbf{X} + \delta\mathbf{X}) = 0$, which gives the system of linear equations

$$\mathbf{H}\delta\mathbf{X} = -\mathbf{G}(\mathbf{X}) \tag{37b}$$

where the hessian matrix $\mathbf{H}$ is given by ∇G. Here $\mathbf{X} = (\Delta, \zeta, \mathbf{C})$ and the Newton–Raphson equations for the variational parameters are

$$\begin{pmatrix} \dfrac{\partial^2 E_{\mathrm{SAMC}}}{\partial \Delta^2} & \dfrac{\partial^2 E_{\mathrm{SAMC}}}{\partial \boldsymbol{\zeta} \partial \mathbf{C}} & \dfrac{\partial^2 E_{\mathrm{SAMC}}}{\partial \Delta \partial \mathbf{C}} \\ \dfrac{\partial^2 E_{\mathrm{SAMC}}}{\partial \boldsymbol{\zeta} \partial \Delta} & \dfrac{\partial^2 E_{\mathrm{SAMC}}}{\partial \boldsymbol{\zeta}^2} & \dfrac{\partial^2 E_{\mathrm{SAMC}}}{\partial \boldsymbol{\zeta} \partial \mathbf{C}} \\ \dfrac{\partial^2 E_{\mathrm{SAMC}}}{\partial \mathbf{C} \partial \Delta} & \dfrac{\partial^2 E_{\mathrm{SAMC}}}{\partial \mathbf{C} \partial \boldsymbol{\zeta}} & \dfrac{\partial^2 E_{\mathrm{SAMC}}}{\partial \mathbf{C}^2} \end{pmatrix} \begin{pmatrix} \delta\Delta \\ \delta\zeta \\ \delta\mathbf{C} \end{pmatrix} = - \begin{pmatrix} \mathbf{G}^{(o)} \\ \mathbf{G}^{(\zeta)} \\ \mathbf{G}^{(C)} \end{pmatrix}. \tag{38}$$

The left hand side is the SA-MCSCF hessian:

$$\mathrm{H}_{\mathbf{v}^1,\mathbf{v}^2} = \frac{\partial G^{(\mathbf{v}^1)}}{\partial \mathbf{v}^2} = \frac{\partial G^{(\mathbf{v}^2)}}{\partial \mathbf{v}^1} = \frac{\partial^2 E_{\mathrm{SAMC}}}{\partial \mathbf{v}^1 \partial \mathbf{v}^2} \tag{39}$$

where we have used $\mathrm{H}_{\mathbf{v}^1,\mathbf{v}^2} \equiv \partial^2 E_{\mathrm{SAMC}}/\partial \mathbf{v}^1 \partial \mathbf{v}^2$ to represent the block of second derivatives, $\partial^2 E_{\mathrm{SAMC}}/\partial \mathrm{v}^1_m \partial \mathrm{v}^2_n$. Explicit formulae for the $\mathrm{H}_{\mathbf{v}1,\mathbf{v}2}$ can be found in Refs. 38 and 41. Since $\mathbf{H}$ depends on Δ, ζ and $\mathbf{C}$, Eq. (38) must be solved iteratively until the SA-MCSCF variational conditions, Eq. (36), are satisfied.

The second order SA-MCSCF procedure provides for rapid convergence of the SA-MCSCF equation. While this is advantageous it not essential. However, in order to determine derivative s of the molecular orbitals or their equivalents, these second order SA-MCSCF equations are essential. Below the determination of orbital derivatives is discussed.

5.2. *Coupled Perturbed State-Averaged MCSCF Equations*[42] *Orbital Derivatives*

5.2.1. *Variational and Orthogonality Contributions*

The derivatives of the molecular orbitals are obtained from the coupled-perturbed SA-MCSCF equations. These equations come from the requirement that the SA-MCSCF conditions, Eqs. (36), should be satisfied at $\mathbf{X} + \delta\mathbf{X}$, given that they are satisfied at $\mathbf{X}$, that is,

$$\mathbf{0} = \mathbf{G}^{(i)}(\mathbf{X} + \delta\mathbf{X}) = \mathbf{G}^{(i)}(\mathbf{X}) + \nabla\mathbf{G}^{(i)}(\mathbf{X}) \cdot \delta\mathbf{X} = \nabla\mathbf{G}^{(i)}(\mathbf{X}) \cdot \delta\mathbf{X}$$
$$i = o, \zeta, C. \tag{40}$$

This is simply the requirement that the gradient of Eq. (36) must vanish, $\nabla\mathbf{G}^{(i)}(\mathbf{X}) = \mathbf{0}$. These gradients, changes with respect to the nuclear coordinates, are expressed using the chain rule. A change in geometry produces changes in the CSF expansion coefficients, $\mathbf{C}^j$, in the molecular orbitals $\boldsymbol{\varphi}$.

The molecular orbitals change due to changes in the expansion coefficients $\boldsymbol{\tau}$ and in the atomic orbitals, $\boldsymbol{\alpha}$

$$\nabla\varphi_{\mathrm{j}} = \sum_p (\nabla\tau_{p,j})\alpha_p + \sum_p \tau_{p,j}\nabla\alpha_p \equiv \sum_k \mathbf{U}_{k,j}\varphi_k + \sum_p \tau_{p,j}\nabla\alpha_p \tag{41a}$$

where

$$\mathbf{U}_{j,i} = \sum_p \nabla\tau_{p,i}\langle\varphi_j(\mathbf{x}_1;\mathbf{X})|\alpha_p(\mathbf{x}_1;\mathbf{X})\rangle_{\mathbf{x}_1} \tag{41b}$$

so that $\mathbf{U}$ expresses the change in the transformation $\boldsymbol{\tau}$ in the molecular orbital basis. Therefore

$$\begin{aligned}\frac{\partial}{\partial X_\beta}\varphi_j &= \sum_m \frac{\partial U_{m\cdot j}}{\partial X_\beta}\left(\varphi_m \frac{\partial}{\partial \varphi_j}\right) + \sum_p \frac{\partial \alpha_p}{\partial X_\beta}\frac{\partial}{\partial \alpha_p} \\ &\equiv \sum_m \frac{\partial U_{m\cdot j}}{\partial X_\beta}\frac{\partial}{\partial U_{m\cdot j}} + \sum_p \frac{\partial \alpha_p}{\partial X_\beta}\frac{\partial}{\partial \alpha_p}. \end{aligned} \tag{41c}$$

Since the only geometry depend parameter in α_p is its location at $\mathbf{X_p}$, $\partial/\partial\alpha_p = \partial/\partial X_p$, which is to be distinquished from $\partial/\partial X_\beta$ on the left hand side of Eq. (41c), for which only the remaining X_γ are held constant. To complete the gradient, the changes in the $\mathbf{C}^i$ must be included. As above, these can be written

$$\frac{\partial}{\partial X_\beta} = \sum_{kl} \frac{\partial \zeta_{kl}}{\partial X_\beta}\frac{\partial}{\partial \zeta_{kl}} \tag{41d}$$

where $\partial/\partial\zeta_{kl} \equiv \partial/\partial\zeta_{k,l} - \partial/\partial\zeta_{k,l}$ and $\partial/\partial\zeta_{k,l}$ act, in the "state space", the same way $\partial/\partial U_{k,l}$ acts in the orbital space. In the mixed representation, described after Eq. (35), Eq. (41d) becomes

$$= \sum_{kl\in\text{occ}} \frac{\partial \zeta_{kl}}{\partial X_\beta}\frac{\partial}{\partial \zeta_{kl}} + \sum_{i\in\text{unocc}} \frac{\partial \mathbf{C}^i}{\partial X_\beta}\frac{\partial}{\partial \mathbf{C}^i}. \tag{41e}$$

Here and throughout the remainder of this chapter the compound summation index kl denotes a sum which extends over the unique nonredundant elements of an antisymmetric matrix. This is to be distinquished from the summation over k, l which denotes a (double) sum over all the elements in a matrix. Combining Eq. (41c) with Eq. (41e) the full gradient becomes:

$$\frac{\partial}{\partial X_\beta} = \sum_{m,n} \frac{\partial U_{m,n}}{\partial Z_\beta}\frac{\partial}{\partial U_{m,n}} + \sum_p \frac{\partial \alpha_p}{\partial X_\beta}\frac{\partial}{\partial \alpha_p} + \sum_{kl} \frac{\partial \zeta_{kl}}{\partial X_\beta}\frac{\partial}{\partial \zeta_{kl}} + \sum_i \frac{\partial \mathbf{C}^i}{\partial X_\beta}\frac{\partial}{\partial \mathbf{C}^i}. \tag{42}$$

The gradient in Eq. (42) must be taken with some care since Eq. (36) requires orthonormal molecular orbitals, that is,

$$\langle \varphi_i(\mathbf{x}_1, \mathbf{X} + \delta\mathbf{X}) | \varphi_j(\mathbf{x}_1, \mathbf{X} + \delta\mathbf{X}) \rangle_{\mathbf{x}_1} = \delta_{i,j} \tag{43a}$$

or equivalently $0 = \nabla_{\mathbf{X}} \langle \varphi_i(\mathbf{x}_1, \mathbf{X}) | \varphi_j(\mathbf{x}_1, \mathbf{X}) \rangle_{\mathbf{X}_1} \cdot \delta\mathbf{X}$. Using Eq. (27), this requirement becomes

$$\begin{aligned}
&\nabla_{\mathbf{X}} \left(\sum_{p,q} \tau_{pi}(\mathbf{X}) \langle \alpha_p(\mathbf{x}_1; \mathbf{X}) | \alpha_q(\mathbf{x}_1; \mathbf{X}) \rangle_{\mathbf{x}_1} \tau_{qj}(\mathbf{X}) \right) \\
&= \left\langle \left(\sum_k \mathbf{U}_{k,i} \varphi_k(\mathbf{x}_1; \mathbf{X}) + \sum_p \tau_{p,i} \nabla_{\mathbf{X}} \alpha_p(\mathbf{x}_1; \mathbf{X}) \right) \middle| \varphi_j(\mathbf{x}_1; \mathbf{X}) \right\rangle_{\mathbf{X}_1} \\
&\quad + \left\langle \varphi_i(\mathbf{x}_1; \mathbf{X}) \middle| \left(\sum_k \mathbf{U}_{k,j} \varphi_k(\mathbf{x}_1; \mathbf{X}) + \sum_p \tau_{p,j} \nabla_{\mathbf{X}} \alpha_p(\mathbf{x}_1; \mathbf{X}) \right) \right\rangle_{\mathbf{X}_1} \qquad (43b) \\
&= \mathbf{U}_{j,i} + \mathbf{U}_{i,j} + \left\langle \sum_p \tau_{p,i} \nabla_{\mathbf{X}} \alpha_p(\mathbf{x}_1; \mathbf{X}) \middle| \varphi_j(\mathbf{x}_1; \mathbf{X}) \right\rangle_{\mathbf{X}_1} \\
&\quad + \left\langle \varphi_i(\mathbf{x}_1; \mathbf{X}) \middle| \sum_p \tau_{p,j} \nabla_{\mathbf{X}} \alpha_p(\mathbf{x}_1; \mathbf{X}) \right\rangle_{\mathbf{X}_1} \\
&= \mathbf{U}_{j,i} + \mathbf{U}_{i,j} + \sum_p \tau_{p,i} \nabla_{\mathbf{X}} \langle \alpha_p(\mathbf{x}_1; \mathbf{X}) | \alpha_q(\mathbf{x}_1; \mathbf{X}) \rangle_{\mathbf{X}_1} \sum_q \tau_{q,j} \\
&= \mathbf{U}_{i,j}(\mathbf{X}) + \mathcal{S}_{i,j}(\mathbf{X}) + \mathbf{U}_{j,i}(\mathbf{X}) = 0 \qquad (43c)
\end{aligned}$$

where $\mathcal{S}$ and $\mathbf{S}$ are given by:

$$\begin{aligned}
\mathcal{S}_{i,j}(\mathbf{X}) &= \sum_{p,q} \tau_{p,i}(\mathbf{X}) (\nabla_{\mathbf{X}} \langle \alpha_p(\mathbf{x}_1; \mathbf{X}) | \alpha_q(\mathbf{x}_1; \mathbf{X}) \rangle_{\mathbf{x}_1}) \tau_{q,j}(\mathbf{X}) \\
&\equiv \sum_{p,q} \tau_{p,i}(\mathbf{X}) \nabla_{\mathbf{X}} \mathbf{S}_{p,q}(\mathbf{X}) \tau_{q,j}(\mathbf{X}). \qquad (43d)
\end{aligned}$$

From Eq. (43c), the requirement of orthogonality affects only the symmetric part of $\mathbf{U}$. It is incorporated by expressing $\mathbf{U}$ in terms of two matrices $\tilde{\Delta}_{i,j}$ and $\mathrm{T}_{i,j}$ such that

$$\mathrm{U}_{i,j}(\mathbf{X}) = \tilde{\Delta}_{i,j}(\mathbf{X}) + \mathrm{T}_{i,j}(\mathbf{X}) \qquad (44a)$$

where $\tilde{\Delta}_{i,j}(\mathbf{X})$ is an antisymmetric matrix, whose elements will be determined by solving the coupled-perturbed SA-MCSCF (CP-SA-MCSCF)

equations and $\mathrm{T}_{i,j}(\mathbf{X})$ has the following structure

$$\begin{aligned} \mathrm{T}_{i,j} &= -\mathcal{S}_{i,j} && \text{for } i < j \\ &= -\tfrac{1}{2}\mathcal{S}_{i,i} && \text{for } i = j \\ &= 0 && \text{for } i > j. \end{aligned} \tag{44b}$$

Equation (44a) embodies the fact that as the positions of the nuclei are changed, the orbitals evolve in response to the variational conditions and also in response to the molecular orbital orthonormality constraints. The latter contribution arises because the overlap matrix in the atomic orbital basis, $\mathbf{S}_{p,q}(\mathbf{X})$, is a function of the nuclear coordinates, $\mathbf{X}$.

We are now in a position to derive the CP-SA-MCSCF equations. Using Eqs. (42) and (44), the chain rule for $\nabla_{\mathbf{X}}$ becomes

$$\begin{aligned} \frac{\partial}{\partial X_\beta} =& \sum_{mn} \frac{\partial \Delta_{mn}}{\partial X_\beta} \frac{\partial}{\partial \Delta_{mn}} + \sum_{mn} \frac{\partial T_{mn}}{\partial X_\beta} \frac{\partial}{\partial T_{mn}} + \sum_{p} \frac{\partial \alpha_p}{\partial X_\beta} \frac{\partial}{\partial \alpha_p} \\ &+ \sum_{kl} \frac{\partial \zeta_{kl}}{\partial X_\beta} \frac{\partial}{\partial \zeta_{kl}} + \sum_{i} \frac{\partial \mathbf{C}^i}{\partial X_\beta} \frac{\partial}{\partial \mathbf{C}^i} \end{aligned} \tag{45a}$$

$$\begin{aligned} \frac{\partial}{\partial X_\beta} =& \sum_{mn} \Delta^\beta_{mn} \frac{\partial}{\partial \Delta_{mn}} + \left[\sum_{mn} T^\beta_{mn} \frac{\partial}{\partial T_{mn}} + \sum_{p} \frac{\partial \alpha_p}{\partial X_\beta} \frac{\partial}{\partial \alpha_p} \right] \\ &+ \sum_{kl} \zeta^\beta_{kl} \frac{\partial}{\partial \zeta_{kl}} + \sum_{i} \mathbf{C}^{i\beta} \frac{\partial}{\partial \mathbf{C}^i}. \end{aligned} \tag{45b}$$

Note that the terms in the square brackets involve known quantities and therefore will contribute to the inhomogeneous part of the CP-SAMCSCF equations obtained by using Eq. (45b) to differentiate Eqs. (36) and recalling the definitions in Eqs. (32c), (33a) and (35) gives

$$\begin{pmatrix} \dfrac{\partial^2 E_{\mathrm{SAMC}}}{\partial \Delta^2} & \dfrac{\partial^2 E_{\mathrm{SAMC}}}{\partial \boldsymbol{\zeta} \partial \mathbf{C}} & \dfrac{\partial^2 E_{\mathrm{SAMC}}}{\partial \Delta \partial \mathbf{C}} \\ \dfrac{\partial^2 E_{\mathrm{SAMC}}}{\partial \boldsymbol{\zeta} \partial \Delta} & \dfrac{\partial^2 E_{\mathrm{SAMC}}}{\partial \boldsymbol{\zeta}^2} & \dfrac{\partial^2 E_{\mathrm{SAMC}}}{\partial \boldsymbol{\zeta} \partial \mathbf{C}} \\ \dfrac{\partial^2 E_{\mathrm{SAMC}}}{\partial \mathbf{C} \partial \Delta} & \dfrac{\partial^2 E_{\mathrm{SAMC}}}{\partial \mathbf{C} \partial \boldsymbol{\zeta}} & \dfrac{\partial^2 E_{\mathrm{SAMC}}}{\partial \mathbf{C}^2} \end{pmatrix} \begin{pmatrix} \Delta^\alpha \\ \zeta^\alpha \\ \mathbf{C}^\alpha \end{pmatrix} = - \begin{pmatrix} \mathbf{G}^{(o)^\alpha} + \mathbf{G}^{(o)^{\mathbf{T}^\alpha}} \\ \mathbf{G}^{(\zeta)^\alpha} + \mathbf{G}^{(\zeta)^{\mathbf{T}^\alpha}} \\ \mathbf{G}^{(C)^\alpha} + \mathbf{G}^{(C)^{\mathbf{T}^\alpha}} \end{pmatrix}. \tag{46}$$

Below we will denote the right hand side by $\mathbf{G}^\alpha + \mathbf{G}^{\mathbf{T}^\alpha}$ and the hessian matrix by $\mathcal{H}$. In Eq. (46), the superscript $z = \beta$ or $\mathbf{T}^\beta$ means that in

constructing the $\mathbf{G}^{(z)}$, defined in Eqs. (32c), (33a) and (35), the $\mu^{(0),i}$ are replaced by, for β

$$\mu^{0,(1)^{\beta}}_{m,n}(\mathbf{X}) = \sum_{p,q} t_{p,i} \left[\frac{\partial}{\partial X_{\beta}} \langle \alpha_p(\mathbf{x}_1;\mathbf{X}) | \mu^{0,(1)}(\mathbf{x}_1;\mathbf{X}) | \alpha_q(\mathbf{x}_1;\mathbf{X}) \rangle_{\mathbf{x}_1} \right] t_{q,j} \tag{47a}$$

$$\mu^{0,(2)^{\beta}}_{m,n,k,l}(\mathbf{X}) = \sum_{p,qr,s} t_{r,n} t_{p,m} \times \left[\frac{\partial}{\partial X_{\beta}} \langle \alpha_p(\mathbf{x}_1;\mathbf{X}) \alpha_r(\mathbf{x}_1;\mathbf{X}) | \mu^{0,(2)}(\mathbf{x}_1;\mathbf{X}) | \alpha_q(\mathbf{x}_2;\mathbf{X}) \alpha_s(\mathbf{x}_2;\mathbf{X}) \rangle_{\mathbf{x}} \right] t_{q,k} t_{s,l} \tag{47b}$$

and for $\mathbf{T}^{\beta}$

$$\mu^{0,(1)^{\mathbf{T}^{\beta}}}_{m,n}(\mathbf{X}) = \sum_{p} [T^{\beta}_{p,m} \mu^{(0),1}_{p,n} + \mu^{(0),1}_{m,p} T^{\beta}_{p,n}] \tag{48a}$$

$$\mu^{0,(2)^{\mathbf{T}^{\beta}}}_{m,n,k,l}(\mathbf{X}) = \sum_{p} [T^{\beta}_{p,m} \mu^{(0),2}_{p,n,k,l} + \mu^{(0),2}_{m,p,k,l} T^{\beta}_{p,n} + T^{\beta}_{p,k} \mu^{(0),2}_{m,n,p,l} + \mu^{(0),2}_{m,n,k,p} T^{\beta}_{p,l}]. \tag{48b}$$

The principal computational effort in the evaluation of Eq. (46) is the construction of the gradients, $\mathbf{G}^{\beta}$, in the *molecular orbital* basis. This requires a transformation of the derivative integrals from the atomic orbital basis to the molecular orbital basis for each nuclear degree of freedom X_{β}. However, as first noted by Rice and Amos,[43] this costly step can also be avoided, since it is possible to perform the evaluation directly in the atomic orbital basis. Further, the contributions which depend on $\mathbf{T}^{\beta}(\mathbf{X})$ can be efficiently evaluated using techniques developed to compute the second derivative of the energy at the MCSCF level, see Appendix A of Ref. 41. For an alternative presentation of these ideas, see Ref. 74.

5.2.2. *Additional Constraints on the Molecular Orbitals*

In an MCSCF procedure there are generally three classes of molecular orbitals: (i) those which are doubly occupied in all CSFs, the core or inactive orbitals, (ii) those which are not occupied in any of the CSFs, the virtual orbitals, and (iii) those which are partially occupied in at least one of the CSFs, the active orbitals. The inactive or core orbitals as well as

the virtual orbitals are not uniquely defined by the MCSCF variational conditions, since a rotation among the orbitals within either of these spaces does not change the MCSCF energy. Similarly, if a complete active space (CAS)[44–46] treatment is used in the MCSCF problem, the MCSCF energy is also invariant to rotations among the active orbitals. However, in many calculations core orbitals and core-correlating orbitals are excluded from the multireference CI calculations. In some cases, limitations on computer resources necessitate further truncation of the orbitals and, perhaps, some selection of reference configurations in the CI calculation.

In these instances the multireference CI energy (but not the SA-MCSCF energy) is dependent on the definition of the individual orbitals. In this situation the orbitals in these spaces must be uniquely defined. These definitions result in new antisymmetric contributions to $\mathbf{U}^{\alpha}_{ij}$. These new contributions to $\mathbf{U}^{\alpha}(\mathbf{X})$ are obtained by differentiating the equations used to uniquely define these orbital spaces. The approach for the determination of these antisymmetric contributions from a core/virtual orbital space rotation and from an active space orbital rotation are presented in Appendices B and D of Ref. 41 respectively.

6. A Generalized Gradient

6.1. *Evaluation of* $\mathbf{g}^{i,j}$, $\mathbf{h}^{i,j}$ *and* $^{\mathbf{CI}}\mathbf{a}_{i,j}$

We are now in a position to determine $\nabla M(\mathbf{v}^i, \mathbf{v}^j; \widetilde{K}^{a,b}_{m,n}, \tilde{K}^{a,b}_{m,n,k,l}; \mu^{0,(1)}, \mu^{0,(2)})$. From Eqs. (27) and (7a)

$$\nabla M(\mathbf{v}^1, \mathbf{v}^2) = \sum_{m,n} (\nabla \mu^{(1)}_{m,n}) \gamma^{\mathbf{v}^1,\mathbf{v}^2}_{m,n} + \sum_{m,n,k,l} (\nabla \mu^{(2)}_{m,n,k,l}) \Gamma^{\mathbf{v}^1,\mathbf{v}^2}_{m,n,k,l} \tag{49a}$$

where

$$\gamma^{\mathbf{v}^1,\mathbf{v}^2}_{m,n} = \sum_{a,b} v^1_a \widetilde{K}^{ab}_{m,n} v^2_b \quad \text{and} \quad \Gamma^{\mathbf{v}^1,\mathbf{v}^2}_{m,n,k,l} = \sum_{a,b} v^1_a \widetilde{K}^{ab}_{m,n,k,l} v^2_b. \tag{49b}$$

From Eqs. (42) and (44) the derivative of $\mu^{(1)}$ and of $\mu^{(2)}$ can be expressed as

$$\begin{aligned} \nabla_{X_\alpha} \mu^{(1)}_{i,j}(\mathbf{X}) &= \mu^{(1)^{\alpha}}_{i,j}(\mathbf{X}) + \mu^{(1)^{U^{\alpha}}}_{i,j}(\mathbf{X}) \\ \nabla_{X_\alpha} \mu^{(2)}_{i,j,k,l}(\mathbf{X}) &= \mu^{(2)^{\alpha}}_{i,j,k,l}(\mathbf{X}) + \mu^{(2)^{U^{\alpha}}}_{i,j,k,l}(\mathbf{X}) \end{aligned} \tag{50}$$

where the superscript α on a quantity in the MO basis indicates that the quantity in question is constructed from the derivative of the atomic integrals, that is,

$$\mu_{i,j}^{(1)^{\alpha}}(\mathbf{X}) = \sum_{p,q} \mathbf{c}_p^{i^*} \left(\frac{\partial}{\partial X_\alpha} \mu_{p\cdot q}^{(1)} \right) \mathbf{c}_q^j \tag{51a}$$

and

$$\mu_{i,j,k,l}^{(2)^{\alpha}}(\mathbf{X}) = \sum_{p,q} \mathbf{c}_p^{i^*} \mathbf{c}_q^j \left(\frac{\partial}{\partial X_\alpha} \mu_{p\cdot q,r,s}^{(2)} \right) \mathbf{c}_r^{k^*} \mathbf{c}_s^l \tag{51b}$$

while

$$\mu_{i,j}^{(1),\mathbf{U}^{\alpha}} = \sum_m [U_{m,i}^{\alpha^*} \mu_{m,j}^{(1)} + \mu_{i,m}^{(1)} U_{m,j}^{\alpha}] \tag{52a}$$

$$\mu_{i,j,k\cdot l}^{(2),\mathbf{U}^{\alpha}} = \sum_m [U_{m,i}^{\alpha^*} \mu_{m,j,k,l}^{(2)} + \mu_{i,m,k,l}^{(2)} U_{m,j}^{\alpha} + U_{m,k}^{\alpha^*} \mu_{i,j,m,l}^{(2)} + \mu_{i,j,k,ml}^{(2)} U_{m,l}^{\alpha}]. \tag{52b}$$

Inserting Eqs. (51)–(52) into Eqs. (49) gives

$$\nabla_{X_\alpha} M(\mathbf{v}_1, \mathbf{v}_2) = G^{\alpha} + G^{\mathbf{U}^{\alpha}} \tag{53a}$$

where

$$G^{\alpha} = \sum_{m,n} (\mu_{m,n}^{\alpha,(1)}) \gamma_{m,n}^{\mathbf{v}^1,\mathbf{v}^2} + \sum_{m,n,k,l} (\mu_{m,n,k,l}^{\alpha,(2)}) \Gamma_{m,n,k,l}^{\mathbf{v}^1,\mathbf{v}^2} \tag{53b}$$

$$G^{\mathbf{U}^{\alpha}} = \sum_{m,n} L_{m,n}^{\mathbf{v}^1,\mathbf{v}^2} U_{n,m}^{\alpha} = \sum_{m,n} L_{m,n}^{\mathbf{v}^1,\mathbf{v}^2} (\tilde{\Delta}_{n,m}^{\alpha} + T_{n,m}^{\alpha}). \tag{53c}$$

In Eq. (53b), the density matrix elements, $\gamma_{m,n}^{\mathbf{v}^1,\mathbf{v}^2}$ and $\Gamma_{m,n,k,l}^{\mathbf{v}^1,\mathbf{v}^2}$, will be transformed to the atomic orbital (AO) basis in order to avoid transforming the AO derivative integrals to the MO basis for each degree of freedom. In

Eq. (53c), the Lagrangian,[42] $L_{i,j}^{\mathrm{v}^a,\mathrm{v}^b}$, has been introduced, where

$$\begin{aligned} L_{m,i}^{\mathrm{v}_a,\mathrm{v}_b} &= \sum_j (\gamma_{j,i}^{\mathbf{v}_a,\mathbf{v}_b}\mu_{m,j}^{(1)} + \gamma_{i,j}^{\mathbf{v}_a,\mathbf{v}_b}\mu_{j,m}^{(1)}) \\ &\quad + \sum_{j,k,l} (\Gamma_{i,j,k,l}^{\mathbf{v}_a,\mathbf{v}_b}\mu_{m,j,k,l}^{(2)} + \Gamma_{i,j,k,l}^{\mathbf{v}_a,\mathbf{v}_b}\mu_{j,m,k,l}^{(2)} + \Gamma_{i,j,k,l}^{\mathbf{v}_a,\mathbf{v}_b}\mu_{j,k,m,l}^{(2)} \\ &\quad + \Gamma_{i,j,k,l}^{\mathbf{v}_a,\mathbf{v}_b}\mu_{j,k,l,m}^{(2)}). \end{aligned} \tag{54}$$

Equations (53a)–(54) provide the basis for the numerical procedures used to evaluate the quantities in Table 1. Although these equations are computationally tractable, they can be further modified to reduce the overall computational effort.

6.2. *Computational Efficiencies*

In evaluating Eq. (53c), it would appear that the CP-SA-MCSCF equations must be solved for each internal degree of freedom X_α, in order to obtain Δ_{ij}^α. However, the repeated solution of the CP-SA-MCSCF equations can be avoided using the method of Handy and Schaefer.[43,47–49] The contribution from Δ_{ij}^α to Eq. (53c) can be rewritten

$$\sum_{m,n} (L_{m,n}^{\mathbf{v}^1,\mathbf{v}^2}\Delta_{n,m}^\alpha) = \sum_{ij} \{(L_{ij}^{\mathbf{v}^1,\mathbf{v}^2} - L_{ji}^{\mathbf{v}^1,\mathbf{v}^2})\}\Delta_{ij}^\alpha \equiv \sum_{ij} L_{ij}^{\mathbf{v}^1,\mathbf{v}^2}\Delta_{ij}^\alpha \tag{55a}$$

where now the sum extends only over the unique elements of Δ^α. Formally inverting Eq. (46) permits Δ_{ij}^α to be eliminated, giving:

$$\begin{aligned} \sum_{ij} L_{ij}^{\mathbf{v}^1,\mathbf{v}^2}\Delta_{ij}^\alpha &= -\mathbf{l}^{(o)\mathbf{v}_1,\mathbf{v}_2\dagger}\boldsymbol{\mathcal{H}}a^{-1}(\mathbf{G}^\alpha + \mathbf{G}^{\mathbf{T}^\alpha}) \\ &= -(\boldsymbol{\mathcal{H}}^{-1}\mathbf{l}^{(o)\mathbf{v}_1,\mathbf{v}_2})^\dagger(\mathbf{G}^\alpha + \mathbf{G}^{\mathbf{T}^\alpha}) \end{aligned} \tag{55b}$$

where

$$\mathbf{l}^{(o)\mathbf{v}_1,\mathbf{v}_2} = (\mathbf{L}^{(\mathbf{v}_1,\mathbf{v}_2)^\dagger} \quad 0 \quad 0). \tag{55c}$$

To evaluate Eq. (55a), it is sufficient to solve one equation of the form of Eq. (46), that being

$$\boldsymbol{\mathcal{H}}\mathbf{Z}^{\mathbf{v}_a,\mathbf{v}_b} = -\mathbf{l}^{(o)\mathbf{v}_a,\mathbf{v}_b} \tag{56a}$$

so that Eq. (55a) reduces to

$$\sum_{ij} L_{ij}^{\mathbf{v}^1,\mathbf{v}^2}\Delta_{ij}^\alpha = \mathbf{Z}^{\mathbf{v}_1,\mathbf{v}_2^\dagger}(\mathbf{G}^\alpha + \mathbf{G}^{\mathbf{T}^\alpha}). \tag{56b}$$

With these modifications the evaluation of a $\nabla M(\mathbf{v}^1, \mathbf{v}^2)$ requires a fraction of the time needed to determined the multireference CI wave function.

7. Computation of the Derivative Couplings

In this section the evaluation of $\mathbf{A}(\mathbf{X})$ and $\mathbf{B}(\mathbf{X})$ is considered.

7.1. *First Derivative Coupling*

From Eq. (1) evaluation of $\boldsymbol{A}$ requires, at least formally, differentiation of the wave function defined in Eq. (5a), giving:

$$\nabla_{\mathbf{X}}\Phi_i(\mathbf{x};\mathbf{X}) = \sum_{p=1}^{N^{\mathrm{CSF}}} [\nabla_{\mathbf{X}} c_p^i(\mathbf{X})\Theta_p(\mathbf{x};\mathbf{X}) + c_p^i(\mathbf{X})\nabla_{\mathbf{X}}\Theta_p(\mathbf{x};\mathbf{X})]. \tag{57}$$

Thus the first derivative nonadiabatic coupling matrix element consists of two terms

$$A_{j,i}(\mathbf{X}) = {}^{\mathrm{Cl}}\mathbf{A}_{j,i}(\mathbf{X}) + {}^{\mathrm{CSF}}\mathbf{A}_{j,i}(\mathbf{X}) \tag{58a}$$

where the CI contribution is given by

$${}^{\mathrm{CI}}\mathbf{A}_{j,i}(\mathbf{X}) = \sum_{\alpha} c_\alpha^j(\mathbf{X})(\nabla c_\alpha^i(\mathbf{X})) \tag{58b}$$

and the CSF contribution has the form

$${}^{\mathrm{CSF}}\mathbf{A}_{j,i}(\mathbf{X}) = \sum_{a,b}^{N^{\mathrm{CSF}}} c_a^j(\mathbf{X})\langle\Theta_a(\mathbf{x};\mathbf{X})|\nabla_{\mathbf{X}}\Theta_b(\mathbf{x};\mathbf{X})\rangle_{\mathbf{x}} c_b^i(\mathbf{X}). \tag{58c}$$

7.1.1. ${}^{\mathrm{CI}}\mathbf{A}_{i,j}$

From Eq. (58b), it would appear that $\nabla\mathbf{c}^i$ would be required to evaluate ${}^{\mathrm{CI}}\mathbf{A}_{j,i}$. However this is in fact not the case. Since only the projection onto the state Φ_i is actually required, Eq. (58b) for ${}^{\mathrm{CI}}\mathbf{A}_{j,i}$ can be recast in a form involving the generalized gradient $\nabla M(\mathbf{v}^{(1)}, \mathbf{v}^{(2)})$.

The coupled-perturbed CI(CP-CI) equations[50,51] provide a formal expression for $\nabla\mathbf{c}^i$. This system of linear equations is obtained by

differentiating Eq. (6) to give

$$\nabla[\mathbf{H}^e\mathbf{c}^i(\mathbf{X}) - V_i(\mathbf{X})\mathbf{c}^i(\mathbf{X})] = 0 \tag{59a}$$

so that

$$[\mathbf{H}^e - V_i(\mathbf{X})]\nabla\mathbf{c}^i(\mathbf{X}) = -[\nabla\mathbf{H}^e(\mathbf{X}) - \nabla V_i(\mathbf{X})]\mathbf{c}^i(\mathbf{X}). \tag{59b}$$

Taking the dot product of Eq. (59b) with $\mathbf{c}^j(\mathbf{X})$ gives

$${}^{\mathrm{CI}}A_{j,i}(\mathbf{X}) \equiv \mathbf{c}^j(\mathbf{X})^\dagger\nabla\mathbf{c}^i(\mathbf{X}) = [V_i(\mathbf{X}) - V_j(\mathbf{X})]^{-1}\mathbf{c}^j(\mathbf{X})^\dagger[\nabla\mathbf{H}^e(\mathbf{X})]\mathbf{c}^i(\mathbf{X}). \tag{60}$$

Note that Eq. (60) is not the Hellmann–Feynman theorem,[52,53] to which it bears a formal resemblance, since in Eq. (60) it is not the Hamiltonian *operator* $H_e(\mathbf{x};\mathbf{X})$ but rather the Hamiltonian *matrix* $\mathbf{H}^e(\mathbf{X})$ which is being differentiated. Indeed, from Eq. (49a)

$${}^{\mathrm{CI}}A_{j,i}(\mathbf{X}) = [V_i(\mathbf{X}) - V_j(\mathbf{X})]^{-1}\nabla M(\mathbf{c}^j, \mathbf{c}^i). \tag{61}$$

7.1.2. ${}^{\mathrm{CSF}}\mathrm{A}_{i,j}$

We now consider the CSF contribution to the first derivative nonadiabatic coupling matrix element. A CSF, Θ_b, is an antisymmetric, symmetry-adapted product of molecular orbitals, defined in Eq. (5b) so that its derivative has the form

$$\nabla_{\mathbf{X}}\Theta_{\mathbf{b}}(\mathbf{x};\mathbf{X}) \equiv \sum_{j=1}^{N^e} P^{S_{\mathbf{b}_0},M^{S_{\mathbf{b}_0}},A_{\mathbf{b}_0}}(\nabla_{\mathbf{X}}\varphi_{b_j}(\mathbf{x}_j;\mathbf{X}))\sigma_{b_j}\prod_{i(\neq j)=1}^{N^{\mathrm{el}}}\varphi_{b_i}(\mathbf{x}_i;\mathbf{X})\sigma_{b_i}. \tag{62}$$

Thus the overlap between a CSF and the derivative of a CSF can be represented as the matrix element of an one-electron operator,

$$\langle\Theta_a(\mathbf{x};\mathbf{X})|\nabla_{\mathbf{X}}\Theta_b(\mathbf{x};\mathbf{X})\rangle_{\mathbf{x}} = \langle\Theta_a(\mathbf{x};\mathbf{X})|\mathbf{D}\Theta_b(\mathbf{x};\mathbf{X})\rangle_{\mathbf{x}} \tag{63a}$$

where

$$D_\alpha(\mathbf{X}) = \sum_i d_\alpha(\mathbf{x_i}) \quad \text{and} \quad d_\alpha(\mathbf{x}_1)\varphi(\mathbf{x}_1;\mathbf{X}) = \frac{\partial}{\partial X_\alpha}\varphi(\mathbf{x}_1;\mathbf{X}). \tag{63b}$$

The matrix element of a one-electron operator can be obtained as the trace of the one-electron density with the appropriate integals, thus

$${}^{\mathrm{CSF}}A^\alpha_{j,i}(\mathbf{X}) = \sum_{k,l}\gamma^{j,i}_{k,l}d^\alpha_{k,l} \tag{64a}$$

where $\gamma^{j,i}_{k,l}$ is the *square* one-electron transition density matrix and $\mathbf{d}^{\alpha}(\mathbf{X})$ is an antisymmetric matrix with matrix elements

$$d^{\alpha}_{i,j} = \left\langle \varphi_i(\mathbf{x}_1;\mathbf{X}) \left| \frac{\partial}{\partial X_\alpha}\ \varphi_j(\mathbf{x}_1;\mathbf{X}) \right\rangle_{\mathbf{x}_1} . \right. \tag{64b}$$

The antisymmetry of $\mathbf{d}^{\alpha}(\mathbf{X})$ is a consequence of the orthonormality of the molecular orbitals, Eq. (43a). Here the adjective "square" has been emphasized in reference to the one-particle transition density matrix. The one particle transition density matrix is in general not symmetric, that is, the full or square matrix must be retained. However, in most electronic structure applications the associated one electron integrals, for example $\mu^{0,(1)}$, are symmetric, permitting the off-diagonal density matrix element to be stored in folded or triangular form. Since $\mathbf{d}^{\alpha}$ is not symmetric, it is necessary to construct and store the transition density matrix in its unfolded or square form.

From Eq. (64b) and (41a), $d^{\alpha}_{i,j}$ is comprised of two terms:

$$d^{\beta}_{i,j}(\mathbf{X}) = \sigma^{\beta}_{i,j} + \mathrm{U}^{\beta}_{i,j} \tag{65a}$$

$$\sigma^{\beta}_{i,j} = \sum_{p,q} \tau_{p,i}(\mathbf{X}) \langle \alpha_p(\mathbf{x}_1;\mathbf{X}) | \nabla_{X_\beta} \alpha_q(\mathbf{x}_1;\mathbf{X}) \rangle_{\mathbf{x}_1} \tau_{q,j}(\mathbf{X}) \tag{65b}$$

so that

$${}^{\mathrm{CSF}}A^{\beta}_{j,i}(\mathbf{R}) = \sum_{k,l} \gamma^{j,i}_{k,l} (\sigma^{\beta}_{k,l} + U^{\beta}_{k,l}) \tag{66}$$

which completes the construction of the first derivative nonadiabatic coupling matrix element. A study of the relative contributions to $\mathbf{A}_{k,l}$ from ${}^{\mathrm{CI}}\mathbf{A}_{k,l}$ and ${}^{\mathrm{CSF}}\mathbf{A}_{k,l}$ can be found in Ref. 54.

7.2. *Second Derivative Coupling*

In this subsection the determination of the second derivative nonadiabatic coupling matrix elements $B_{j,i}(\mathbf{X})$ is considered. Real-valued wave functions are assumed. Although the definition of $B_{j,i}(\mathbf{X})$ involves $\nabla_{\mathbf{X}}\Phi_i \cdot \nabla_{\mathbf{X}}\Phi_j$, since a change of variables in the nuclear coordinates is often required, it is

convenient to define the generalized the second derivative matrix elements $\boldsymbol{k}_{j,i}$ and $\boldsymbol{\kappa}_{j,i}$ as follows

$$\frac{\partial}{\partial X_\beta} A^\alpha_{j,i}(\mathbf{X}) = k^{\beta,\alpha}_{j,i}(\mathbf{X}) + \kappa^{\beta,\alpha}_{j,i}(\mathbf{X}) \tag{67a}$$

where

$$\begin{aligned} k^{\beta,\alpha}_{j,i}(\mathbf{X}) &= \left\langle \frac{\partial}{\partial X_\beta}\Phi_j(\mathbf{x};\mathbf{X}) \middle| \frac{\partial}{\partial X_\alpha}\Phi_i(\mathbf{x};\mathbf{X}) \right\rangle_{\mathbf{x}} \\ \kappa^{\beta,\alpha}_{j,i}(\mathbf{X}) &= \left\langle \Phi_j(\mathbf{x};\mathbf{X}) \middle| \frac{\partial^2}{\partial X_\alpha \partial X_\beta}\Phi_i(\mathbf{x};\mathbf{X}) \right\rangle_{\mathbf{x}} . \end{aligned} \tag{67b}$$

For $i = j$, $A^\alpha_{i,i}(\mathbf{X}) = 0$ for all $\mathbf{X}$, so that Eq. (67a) equation reduces to

$$k^{\beta,\alpha}_{i,i}(\mathbf{X}) = -\kappa^{\beta,\alpha}_{i,i}(\mathbf{X}). \tag{67c}$$

As discussed in Chapter 2, the $k^{\beta,\beta}_{i,i}(\mathbf{X})$ give rise to positive definite corrections to an individual Born–Oppenheimer potential energy surface. In this section we show how analytic gradient techniques can be used to evaluate $\boldsymbol{k}(\mathbf{X})$.

From Eq. (57), $\boldsymbol{k}(\mathbf{X})$ is a sum of three terms:

$$\begin{aligned} k^{\alpha,\beta}_{j,i}(\mathbf{X}) &= \left\langle \frac{\partial}{\partial X_\alpha}\Phi_j(\mathbf{x};\mathbf{X}) \middle| \frac{\partial}{\partial X_\beta}\Phi_i(\mathbf{x};\mathbf{X}) \right\rangle_{\mathbf{x}} \\ &= \left\langle \sum_a \left[\Theta_a(\mathbf{x};\mathbf{X}) \frac{\partial}{\partial X_\alpha} c^j_a(\mathbf{X}) + c^j_a \frac{\partial}{\partial X_\alpha}\Theta_a(\mathbf{x};\mathbf{X}) \right] \right| \\ &\quad \times \sum_b \left[\Theta_b(\mathbf{x};\mathbf{X}) \frac{\partial}{\partial X_\beta} c^i_b(\mathbf{X}) + c^i_b \frac{\partial}{\partial X_\beta}\Theta_b(\mathbf{x};\mathbf{X}) \right] \Bigg\rangle_{\mathbf{x}} \end{aligned} \tag{68a}$$

$$= {}^{\mathrm{CI}}k^{\alpha,\beta}_{j,i}(\mathbf{X}) + {}^{\mathrm{CSF}}k^{\alpha,\beta}_{j,i}(\mathbf{X}) + {}^{\mathrm{CSF-CI}}k^{\alpha,\beta}_{j,i}(\mathbf{X}) \tag{68b}$$

where

$${}^{\mathrm{CI}}k^{\alpha,\beta}_{j,i}(\mathbf{X}) = \sum_a \left(\frac{\partial}{\partial X_\alpha} c^j_a(\mathbf{X}) \right) \left(\frac{\partial}{\partial X_\beta} c^i_a(\mathbf{X}) \right) \tag{69a}$$

$${}^{\mathrm{CSF}}k^{\alpha,\beta}_{j,i}(\mathbf{X}) = \sum_{a,b} c^j_a(\mathbf{X}) c^i_b(\mathbf{X}) \left\langle \left(\frac{\partial}{\partial X_\alpha}\Theta_a(\mathbf{x};\mathbf{X}) \right) \middle| \left(\frac{\partial}{\partial X_\beta}\Theta_b(\mathbf{x};\mathbf{X}) \right) \right\rangle_{\mathbf{x}} \tag{69b}$$

and

$$
\begin{aligned}
{}^{\mathrm{CI-CSF}}k_{j,i}^{\alpha,\beta}(\mathbf{X}) &= \sum_{a,b,m,n}\left[\left(\frac{\partial}{\partial X_\alpha}c_a^j\right)c_b^i\tilde{k}_{m,n}^{a,b}d_{m,n}^{\beta} - c_a^j\left(\frac{\partial}{\partial X_\beta}c_b^i\right)\tilde{k}_{m,n}^{a,b}d_{m,n}^{\alpha}\right] \\
&\equiv \sum_{m,n}[\gamma_{m,n}^{j^\alpha,i}d_{m,n}^{\beta} - \gamma_{m,n}^{j,i^\beta}d_{m,n}^{\alpha}]. \qquad (69c)
\end{aligned}
$$

Here j^α indicates that $\frac{\partial}{\partial X_\alpha}\mathbf{c}^j$ is used to build the density matrix. The minus sign in Eq. (69c) arises from the previously noted antisymmetry of d_{ij}^{α}.

7.2.1. *Evaluation of* ${}^{\mathrm{CSF}}k(\mathbf{X})$

In evaluating the CSF contribution to $\boldsymbol{k}(\mathbf{X})$, ${}^{\mathrm{CSF}}\boldsymbol{k}(\mathbf{X})$, the fact that two orbitals have been differentiated must be considered. This gives rise to a contribution from the square two particle transition density matrix in addition to a contribution from the square one particle transition density matrix. In particular,

$$
{}^{\mathrm{CSF}}k_{j,i}^{\alpha,\beta}(\mathbf{X}) = \sum_{m,n}\gamma_{m,n}^{j,i}e_{m,n}^{\alpha,\beta} - \sum_{m,n,k,l}\Gamma_{m,n,k,l}^{j,i}f_{m,n,k,l}^{\alpha,\beta} \qquad (70)
$$

where

$$
f_{i,j,k,l}^{\alpha,\beta}(\mathbf{X}) = d_{i,j}^{\alpha}(\mathbf{X})d_{k,l}^{\beta}(\mathbf{X}) + d_{i,j}^{\beta}(\mathbf{X})d_{k,l}^{\alpha}(\mathbf{X}) \qquad (71a)
$$

$$
e_{m,n}^{\alpha,\beta}(\mathbf{X}) = \left\langle \frac{\partial}{\partial X_\alpha}\phi_m(\mathbf{x}_1;\mathbf{X}) \middle| \frac{\partial}{\partial X_\beta}\phi_n(\mathbf{x}_1;\mathbf{X}) \right\rangle_{\mathbf{x}_1}. \qquad (71b)
$$

Using Eq. (41a) and defining $\tau_{p,n}^{\alpha} = \frac{\partial}{\partial X_\alpha}\tau_{p\cdot n}$, gives

$$
\begin{aligned}
e_{m,n}^{\alpha,\beta}(\mathbf{X}) = &\sum_k U_{k,m}^{\alpha}U_{k,n}^{\beta} \\
&+ \sum_{p,q}\left[\tau_{p,m}\left\langle \frac{\partial}{\partial X_\alpha}\alpha_p(\mathbf{x}_1;\mathbf{X}) \middle| \frac{\partial}{\partial X_\beta}\alpha_q(\mathbf{x}_1;\mathbf{X}) \right\rangle_{\mathbf{x}_1}\tau_{q,n}\right. \\
&+\tau_{p,m}\left\langle \frac{\partial}{\partial X_\alpha}\alpha_p(\mathbf{x}_1;\mathbf{X})\,|\alpha_q(\mathbf{x}_1;\mathbf{X}) \right\rangle_{\mathbf{x}_1}\tau_{q,n}^{\beta} \\
&\left.+\tau_{p,m}^{\alpha}\left\langle \alpha_p(\mathbf{x}_1;\mathbf{X}) \middle| \frac{\partial}{\partial X_\beta}\alpha_q(\mathbf{x}_1;\mathbf{X}) \right\rangle_{\mathbf{x}_1}\tau_{q,n}\right] \qquad (71c)
\end{aligned}
$$

where use has been made of the antisymmetry of $\mathbf{d}^{\alpha}$. The fact that $f_{m,n,k,l}^{\alpha,\beta}$ is a product of one-electron integrals greatly facilitates the evaluation of

${}^{\mathrm{CSF}}k(\mathbf{X})$. In this case, all the $\mathbf{d}^{\alpha}$ needed to construct $f^{\alpha,\beta}_{m,n,k,l}$ can be held in memory so that the square two particle density matrix need not be stored. Instead, the contributions to Eq. (70) are evaluated directly. Equation (70) requires the use of the "square" two-particle transition density matrix, since the symmetry of the $f^{\alpha,\beta}_{m,n,k,l}$ with respect to the permutation of indices

$$f^{\alpha,\beta}_{m,n,k,l} = -f^{\alpha,\beta}_{n,m,k,l} = -f^{\alpha,\beta}_{m,n,l,k} = f^{\alpha,\beta}_{n,m,l,k} \tag{72}$$

is different from that of the two electron integrals $\mu^{(0),2}$.

7.2.2. *Evaluation of* ${}^{\mathrm{CI}}k$ *and* ${}^{\mathrm{CSF-CI}}k$*: the Coupled Perturbed-*CI *Equations*

The evaluation of ${}^{\mathrm{CI}}\boldsymbol{k}$ and ${}^{\mathrm{CSF-CI}}\boldsymbol{k}$ requires the derivatives of the $\mathbf{c}^i$, which are obtained by solving the coupled-perturbed CI (CP-CI) equations. Differentiating Eq. (6)

$$\nabla_{\mathbf{X}}[\mathbf{H}^e\mathbf{c}^i(\mathbf{X}) - V_i(\mathbf{X})\mathbf{c}^i(\mathbf{X})] = \mathbf{0} \tag{73}$$

gives a system of linear equations for $\nabla_{\mathbf{X}}\mathbf{c}^i(\mathbf{X})$

$$\begin{aligned}(\mathbf{H}^e - V_i(\mathbf{X}))\nabla_{\mathbf{X}}\mathbf{c}^i(\mathbf{X}) &= -[\nabla_{\mathbf{X}}\{\mathbf{H}^e - V_i(\mathbf{X})\}]\mathbf{c}^i(\mathbf{X}) \\ &= -[\mathbf{H}^{\alpha}(\mathbf{X}) + \mathbf{H}^{U^{\alpha}}(\mathbf{X}) + \nabla V_i(\mathbf{X})]\mathbf{c}^i(\mathbf{X}) \\ &= -\mathbf{P}[\mathbf{H}^{\alpha}(\mathbf{X}) + \mathbf{H}^{U^{\alpha}}(\mathbf{X})]\mathbf{c}^i(\mathbf{X}) \end{aligned} \tag{74}$$

where $\mathbf{P}$ is the projection operator,

$$\mathbf{P} = \mathbf{I} - \mathbf{c}^i\mathbf{c}^{i\dagger} \tag{75}$$

and from Eqs. (50)–(52) $\mathbf{H}^{e^{\alpha}}(\mathbf{H}^{e^{U^{\alpha}}})$ is the Hamiltonian matrix constructed from the integrals $\mu^{0,(\eta)^{\alpha}}\left(\mu^{0,(\eta)^{U^{\alpha}}}\right), \eta = 1, 2$. The use of the projector is required, since the null space of $(\mathbf{H}^e - \mathbf{I}V_i)$ is $\mathbf{c}^i$ and $(\mathbf{c}^i|\nabla\mathbf{c}^i) = 0$. The solution of the CP-CI equations requires the prior solution of the CP-SA-MCSCF equations in order to evaluate $\mathbf{U}^{\alpha}$. Given the solutions to the CP-CI equations, $\nabla_{\mathbf{X}}\mathbf{c}^i$, it is straightforward to use Eq. (69a) to construct ${}^{\mathrm{CI}}\boldsymbol{k}(\mathbf{X})$. Similarly, the evaluation of ${}^{\mathrm{CSF-CI}}\boldsymbol{k}(\mathbf{X})$ becomes analogous to the evaluation of ${}^{\mathrm{CSF}}A_{j,i}$ with

$${}^{\mathrm{CSF-CI}}k^{\alpha,\beta}_{j,i}(\mathbf{X}) = {}^{\mathrm{CSF}}A^{\beta}_{j^{\alpha},i}(\mathbf{X}) - {}^{\mathrm{CSF}}A^{\alpha}_{j,i^{\beta}}(\mathbf{X}) \tag{76}$$

where j^{α} in Eq. (67a) implies that $\frac{\partial}{\partial X_{\alpha}}\mathbf{c}^j$ replaces $\mathbf{c}^j$ in the evaluation of the transition density matrices in Eq. (66).

This completes the evaluation of $B_{i,j}$ using analytic gradient techniques. Despite the use of analytic gradient techniques, the need to solve the CP-CI equations, which scale like the CI problem, for each direction, renders the determination of **B** computationally intensive. In Sec. 8, body fixed frame wave functions are used to reduce the number of times the CP-CI equations must be solved to determine **B**.

8. Applications

In this section, the efficacy of Eq. (22) for locating a point of conical intersection in the nonrelativisitic case, using the S_0 and S_1 states of HNCO, and the relativistic case using the $1,2^2A'$, and $1^2A''$ states of OH–H_2, is considered. The adiabatic correction for the $X^1\Sigma^+$ state of LiH is presented an compared with earlier experimental and theoretical results.

8.1. *Locating Conical Intersections in the $\eta = 2$ Case*

The S_1–S_0 seam of conical intersection in HNCO is analyzed in detail in Chapter 2 of this volume and in Refs. 55 and 56. Here we illustrate the convergence of our search algorithm, Eq. (22), to a point of conical intersection. In this example, $\mathbf{L}^{Q,Q}$ is evaluated by a forward difference procedure. $\mathbf{L}^{Q,Q}$ can be approximated by a unit matrix if complete energy optimization is not required. However, if $\mathbf{L}^{Q}$, the norm of the right hand side, is to be made to vanish rapidly, $\mathbf{L}^{Q,Q}$ is required. Table 2 illustrates typical convergence with $\mathbf{L}^{Q,Q}$ evaluated by forward difference. Here it is important to note that $\Delta V_{i,j}$ is readily converged to $< 0.5\,\mathrm{cm}^{-1}$. Convergence to approximately this

Table 2. For HNCO:Convergence to $\mathbf{Q}^{\mathrm{x}}$ on planar *trans* seam with R(C–N)= $2.65a_0$ from $\mathbf{Q}^{\mathbf{x}}$ with R(C–N)= $2.85a_0$.

R(CN)	R(CO)	∠NCO	$V_x(\mathrm{cm}^{-1})$	$\Delta V(\mathrm{cm}^{-1})$	Norm
2.8500	2.3321	103.00	5907.4		0.1102E+01
2.6573	2.3645	98.800	8222.9	151.91	0.4215E−01
2.6501	2.3609	98.100	8833.9	5.9057	0.7595E−02
2.6501	2.3568	98.200	8811.3	44.898	0.8324E−02
2.6500	2.3594	98.200	8855.3	8.0157	0.5795E−02
2.6500	2.3588	98.000	8835.6	1.9092	0.2435E−02
2.6500	2.3579	98.200	8836.6	0.63871	0.8132E−03

[a]Norm is norm of right hand side of Eq. (22). $V_{\mathrm{x}} = V_i(\mathbf{Q}^{x,i,j})$.

precision is important when relativistic effects involving atoms with only moderate spin-orbit coupling, are considered, see below.

8.2. *Locating Conical Intersections in the $\eta = 3$ Case*

The results of the previous section demonstrate the convergence of our algorithm in the nonrelativistic $\eta = 2$ case. The inclusion of the spin-orbit interaction introduces new numerical challenges. Here we consider the $1,2^2A'$ conical intersection seam of H_2OH. This seam of conical intersection is relevant to the quenching of $OH(A^2\Sigma^+)$ by H_2.[57,58] Using the nonrelativistic Hamiltonian, portions of this seam of conical intersection have been identified for C_{2v}, $C_{\infty v}$ as well as C_s geometries. The C_s portion of the seam is particularly interesting, since, although it is expected to exist by the non-crossing rule, it would not be expected in the isoelectronic molecule H_2F. Thus the C_s seam represents a substituent effect.[59]

In this section we focus on the $C_{\infty v}$ portion of the seam, where, together with the $1^2A''$ state, the $1,2^2A'$ states form a $^2\Sigma^+ - {}^2\Pi$ conical intersection. The g–h space for the nonrelativistic $1,2^2A'$ conical intersection seam and its relativistic counterpart, the $2E$–$3E$ seam, defined below, have been studied in Chapter 2 of this volume. See also Refs. 32, 60–62. The nonrelativistic $C_{\infty v}$ $^2\Sigma^+ - {}^2\Pi$ symmetry-allowed conical intersection will be modified as spin-orbit coupling splits the otherwise degenerate $^2\Pi$ state. Here we use this seam of conical intersection to demonstrate convergence of our algorithm in the context of *ab initio* MRCI wave functions. This example provides a stringent test of the algorithm, since the spin-orbit interaction is relatively modest and the energy splitting changes rapidly in the region of interest.

In the computational procedure the molecule is restricted to C_s symmetry. Therefore we are considering the $\eta = 3$ case. The Hamiltonian used is:

$$\mathbf{H}^e = \begin{pmatrix} V_{1^2A'} & -iH^{so,y}_{1A'2A'} & -H^{so,x}_{1A'1A''} - iH^{so,z}_{1A'1A''} \\ iH^{so,y}_{1A'2A'} & V_{2^2A'} & -H^{so,x}_{2A'1A''} - iH^{so,z}_{2A'1A''} \\ -H^{so,x}_{1A'1A''} + iH^{so,z}_{1A'1A''} & -H^{so,x}_{2A'1A''} + iH^{so,z}_{2A'1A''} & V_{1^2A''} \end{pmatrix} \tag{77}$$

and all $H^{so,w}_{i,j}$ are real-valued functions of the nonrelativistic eigenstates. The eigenstates of $\mathbf{H}^e$ are the nE states, $n = 1-3$.

There are five internal degrees of freedom (the out of plane mode is excluded to preserve C_s symmetry) so that as many as two additional constraints may be imposed. In this example energy minimization is used in lieu of any geometric constraints. The nonrelativistic states are described at the first order configuration interaction level using a six orbital, eight electron, active space, with the oxygen $1s$ orbital kept doubly occupied. The molecular orbitals were constructed from a SA-MCSCF procedure using an extended atomic orbital basis on oxygen and hydrogen. More details concerning this description can be found in Refs. 32 and 63, and Chapter 2 of this volume.

Figure 1 considers convergence of Eq. (22) to a point of conical intersection, reporting the relativistic energy separation $\Delta V_{2E,3E}$ and the

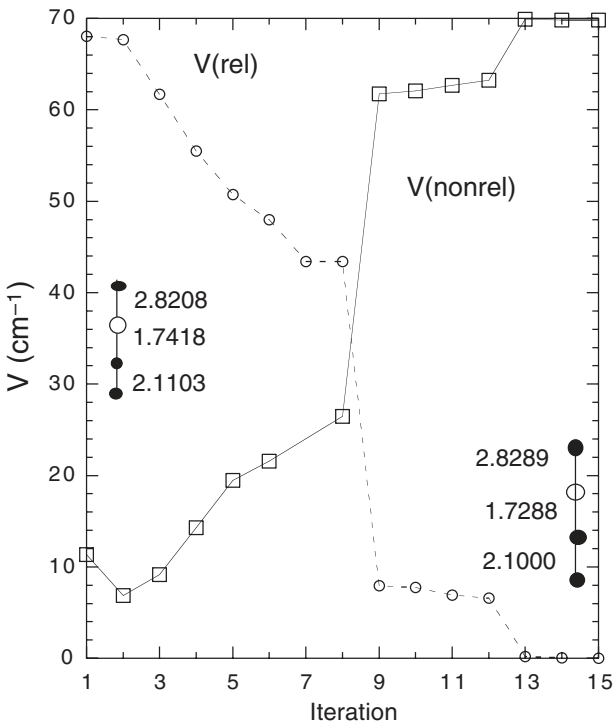

Fig. 1. $\Delta V_{3E,2E} = \Delta V(\text{rel})$ and $\Delta V_{2^2A',1^2A'} = \Delta V(\text{nonrel})$ at each iteration of the solution of Eq. (22) for OH + H_2 using multireference configuration interaction wave functions.

nonrelativistic energy separation, $\Delta V_{2^2A',1^2A'}$. The search was initiated at a structure displaced along the *nonrelativistic* seam. This structure is pictured on the left hand side of Fig. 1. At this point $\Delta V_{2^2A',1^2A'} \approx 11\,\mathrm{cm}^{-1}$ and $\Delta V_{2E,3E} \approx 70\,\mathrm{cm}^{-1}$. At the converged structure, achieved after 15 iterations, pictured on the right hand side, $\Delta V_{2E,3E} < 0.2\,\mathrm{cm}^{-1}$ while $\Delta V_{2^2A',1^2A'} \approx 70\,\mathrm{cm}^{-1}$. The large changes in $\Delta V_{2E,3E}$ between iterations 8 and 9, and 12 and 13, reflect, in part, the use of the "conjugate gradient" extrapolation described in Ref. 32. These results strongly support the utility of this search algorithm. It is worth noting that, once an initial point on a seam is found, locating additional points is facilitated by the fact that given a $\mathbf{Q}^x$ corresponding to a given set of geometrical constraints, $\mathbf{K}$, Eq. (22) can be used to predict a good starting value for a neighboring $\mathbf{Q}'^x$ corresponding to $\mathbf{K}'$. The use of Eq. (22) to predict "neighboring" points on a seam has been discussed in Ref. 64.

8.3. *The Adiabatic Correction: LiH($X^1\Sigma^+$)*

As noted in Chapter 2 of this volume, the Born–Oppenheimer diagonal correction produces a mass dependent modification of a mass independent Born–Oppenheimer potential energy surface. This modication can be inferred from experimental measurements of rovibrational levels of a series of isotopomers and can be computed directly, using the methods of this chapter. The $X^1\Sigma^+$ state of LiH is considered here. It has been the object of detailed experimental investigations[15,23] and theoretical studies, using both highly specialized wave functions[16] and the SA-MCSCF/MRCI[7] wave functions described in this chapter. Below these studies are described.

The Born–Oppenheimer diagonal correction is given in Eq. (2a). In that equation, the gradients refer to space fixed frame (SFF) coordinates. For diatomic molecules, considerable savings result from a transformation to body fixed frame (BFF) coordinates. This transformation is accomplished in two steps. The SFF coordinates are transformed to center of mass fixed frame (CMFF) coordinates and then the CMFF coordinates are transformed to BFF coordinates. The details of the transformation are beyond the scope of this review. Here we sketch the ideas involved. A detailed treatment, based on the pioneering work of Kronig,[65] can be found in Ref. 7. In particular, first the rigorously removable center of mass of the nuclei *and*

the electrons, is defined

$$\mathbf{C} = \frac{\left[\sum_{i=1}^{N^{\rm el}} m_e \mathbf{x}_i + M_1\mathbf{X}_1 + M_2\mathbf{X}_2\right]}{M^T}. \tag{78a}$$

In addition, the center of mass of the nuclei

$$\mathbf{O} = (M_1\mathbf{X}_1 + M_2\mathbf{X}_2)/M \tag{78b}$$

and internal coordinates for the electrons and nuclei are introduced

$$\mathbf{q}_k = \mathbf{x}_k - \mathbf{O};\ \mathbf{Q} = \mathbf{X}_2 - \mathbf{X}_1. \tag{78c}$$

These nonrotating coordinates take us to the CMFF. These coordinates are transformed to coordinates that rotate with the nuclei, the BFF, by

$$\begin{pmatrix} w_{k,x} \\ w_{k,y} \\ w_{k,z} \end{pmatrix} = \begin{pmatrix} -\sin\phi & \cos\phi & 0 \\ -\cos\theta\cos\phi & -\cos\theta\sin\phi & \sin\theta \\ \sin\theta\cos\phi & \sin\theta\sin\phi & \cos\theta \end{pmatrix} \begin{pmatrix} q_{k,x} \\ q_{k,y} \\ q_{k,z} \end{pmatrix} \tag{78d}$$

$$\mathrm{W} = |\mathbf{Q}| \text{ and } \mathbf{B} = (\theta, \phi)$$

where W and $\mathbf{B}$ are the spherical polar coordinates of $\mathbf{Q}$, $M = M_1 + M_2$, M_1, M_2, are the nuclear masses, $M^T = M + m_{\rm el}N^{\rm el}$ and $\mu^{-1} = M_1^{-1} + M_2^{-1}$. Then using Eq. (78) and the chain rule, $AC_{i,i}$ [Eq. (2a)] for i, a $^1\Sigma^+$ state becomes[7,11,12]

$$AC_{i,i}(\mathbf{X}) = \mathrm{MP}_{i,i}(\mathbf{X})/(2M) + L^2_{i,i}(\mathbf{X})/(2\mu W^2) + K^{\rm W}_{i,i}(\mathbf{Q})/(2M) \tag{79}$$

where [see Eq. (24b)]

$$K^W_{i,i}(\mathbf{Q}) = \frac{M_2}{M_1}k^{z_1,z_1}_{i,i} + \frac{M_1}{M_2}k^{z_2,z_2}_{i,i} - 2k^{z_1,z_2}_{i,i} \tag{80}$$

$$L^2_{i,i}(\mathbf{X}) = L^2_{x,i,i}(\mathbf{X}) + L^2_{y,i,i}(\mathbf{X}) + L^2_{z,i,i}(\mathbf{X}) \tag{81a}$$

$$L^2_{x,i,i}(\mathbf{X}) = M(\mathbf{c}^i, \mathbf{c}^i; \tilde{k}, \widetilde{K}; (\mathbf{x}_1 \times \nabla_{\mathbf{x}_1})^2, (\mathbf{x}_1 \times \nabla_{\mathbf{x}_1})(\mathbf{x}_2 \times \nabla_{\mathbf{x}_2})) \tag{81b}$$

$$MP_{i,i}(\mathbf{X}) = M(\mathbf{c}^i, \mathbf{c}^i; \tilde{k}, \widetilde{K}; \nabla^2_{\mathbf{x}_1}, \nabla_{\mathbf{x}_1} \cdot \nabla_{\mathbf{x}_2}). \tag{82}$$

Equation (79) has both computational and conceptual advantages. Conceptually, the decomposition allows us to separate the effects of internal motion from overall nuclear rotation and translation. Computationally, nine second derivatives are needed to evaluate Eq. (2a) each of which requires the

solution of the costly CP-CI equations. Since both $L^2_{w,i,i}(\mathbf{X})$ and $\mathrm{MP}_{i,i}(\mathbf{X})$ have the form of an $M(\mathbf{c}^i, \mathbf{c}^i)$ [Eq. (24b)], their evaluation, which does not require the solution of the CP-CI equations, involves little computational effort. For this reason use of BFF wave functions drastically reduces the effort required to evaluate the $AC_{i,i}$.

It will prove convenient to define the quantities $b(Z)$ for $Z = \mathrm{Li}$ and H

$$AC_{i,i} \equiv b_{i,i}({}^X\mathrm{Li}, {}^Y\mathrm{H}) \equiv b(\mathrm{Li})/M({}^x\mathrm{Li}) + b(\mathrm{H})/M({}^y\mathrm{H}). \tag{83}$$

Table 3 reports and Fig. 2 plots the contributions to the adiabatic (or Born–Oppenheimer diagonal correction) in Eq. (83). Note that the principal geometry dependence arises *not* from the internal motion contribution ($K^w_{i,i}$), but from the angular momentum contribution, $L^2_{i,i}(\mathbf{X})$. This is quite the opposite of what happens near an avoided (or conical) intersection, where $K_{i,i}$ is large (singular) and rapidly changing, see Chapter 2 in this volume and Ref. 4. Table 3 also compares the computed b(H) (JY column) with b(H) inferred from experiment (CHSW column). The agreement is quite good, supporting the validity of the geometry dependence of the decomposition discussed above.

Thus the main conclusion of this section is that, while $K^w_{i,i}$ makes the preeminent contribution to the adiabatic correction near a conical intersection away from this singular point contributions from noninternal coordinates may dominate the geometry dependence.

Table 3. Analysis of the adiabatic correction for LiH ($X^1\Sigma^+$).

R(LiH)	MP	$L2$	K	$b^{(\mathrm{H})}$			$b^{(\mathrm{Li})}$	
				JY[b]	BC[c]	CHSW[d]	JY[b]	BC[c]
2.5	124.3	58.59	24.86	6.1	5.8	12.2	7.2	7.3
3.0	123.06	52.84	25.27	0	0	0	0	0
3.5	122.04	49.63	25.17	−3.8	−3.6	−5.99	−3.7	−3.8
4.5	120.91	46.83	24.73	−8.1	−7.2	−10.8	−5.8	−6.5
5.0	120.64	46.21	24.69	−9.0	−5.5	−12.0	−4.9	−3.8
5.5	120.52	45.82	24.95	−9.5	−1.0	−12.6	−2.9	8.2
7.5	121.05	45.38	25.18	−10.6		−13.1	7.0	

[a]MP = $\mathrm{MP}_{i,i}(\mathbf{X})/(2\mathrm{M})$; $L^2 = L^2_{i,i}(\mathbf{X})/(2\mu W^2)$; $K = K^W_{i,i}(\mathbf{X})/(2M)$ for $^7\mathrm{Li}^1\mathrm{H}$ from Ref. 7.
[b]Ref. 7 relative to value at R(Li–H) = 3 a.u. of $b^{\mathrm{H}} = 72.4$ or $b^{\mathrm{Li}} = 909.7\,\mathrm{cm}^{-1}$ amu.
[c]Ref. 16 relative to value at R(Li–H) = 3 a.u. of $b^{\mathrm{H}} = 70.5$ or $b^{\mathrm{Li}} = 924.0\,\mathrm{cm}^{-1}$ amu.
[d]Ref. 23 relative to interpolated value at R(Li–H) = 3 a.u. $b^{\mathrm{H}} = 0.10\,\mathrm{cm}^{-1}$ amu.

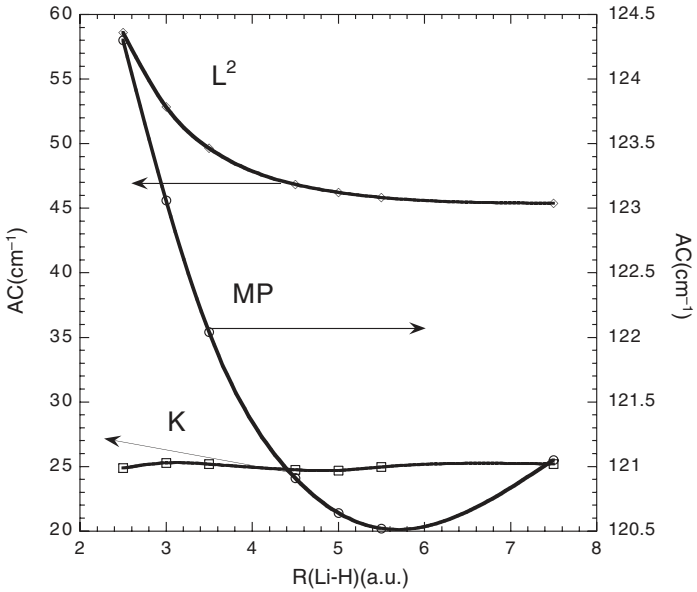

Fig. 2. Contributions to diagonal Born–Oppenheimer correction due to mass polarization (MP), angular momentum (L^2) and internal motion(K) as a function of R(Li–H).

9. Summary and Future Directions

The methods described in this chapter make the determination of the first derivative couplings and the location of points of conical intersection for two states (of the same symmetry) based on state averaged multi-configurational self-consistent field/multi-reference configuration interaction (SA–MCSCF/MRCI) wave functions quite routine. These capabilities have led to new ways of thinking about and treating nonadiabatic processes and the intersecting potential energy surfaces that describe them. The chapters that follow are ripe with examples of the new paradigms in nonadiabatic chemistry. From the perspective of this chapter, that of computational electronic structure theory, several new directions have emerged since this chapter was first prepared. Algorithms for the location of three states of the same symmetry have been introduced. Initial studies suggest that this class of conical intersection cannot be ignored. Improved implementations of the equations for locating energy minimized conical intersections of two states of the same symmetry based on extrapolatable functions will enable

much more efficient treatment of larger molecules. Finally advances in the determination of SA–MCSCF/MRCI must be noted. The examples in this chapter were limited to (a respectable) 1–5 million CSFs. However recently the COLUMBUS[75] suite of electronic structure codes has established qualitatively new standards for the state of the art. Using single processor techniques derivative couplings can be evaluated, and conical intersections located, using 100 million CSF MRCI expansions. Parallel processor techniques, which are implemented, will further extend the size of a tractable expansion. In short, a new generation of electronic structure techniques is emerging. These techniques can be expected to significantly extend the range and scope of tractable problems in nonadiabatic chemistry.

Acknowledgments

The preparation of this review and the results described herein where made possible by grants from the Air Force Office of Scientific Research, the Department of Energy and the National Science Foundation.

References

1. P. Pulay, *Modern Theoretical Chemistry*, Ed. H. F. Schaefer (Plenum Press, New York, 1977), Vol. 4.
2. Y. Yamaguchi, Y. Osamura, J. D. Goddard and H. F. Schaefer, *A New Dimension to Quantum Chemistry: Analytic Derivative Methods in ab initio Molecular Electronic Structure Theory* (Oxford University Press, Oxford, 1994).
3. B. H. Lengsfield, P. Saxe and D. R. Yarkony, *J. Chem. Phys.* **81**, 4549 (1984).
4. P. Saxe, B. H. Lengsfield and D. R. Yarkony, *Chem. Phys. Lett.* **113**, 159 (1985).
5. N. C. Handy, Y. Yamaguchi and H. F. Schaefer, *J. Chem. Phys.* **84**, 4481 (1986).
6. B. H. Lengsfield and D. R. Yarkony, *J. Chem. Phys.* **84**, 348 (1986).
7. J. O. Jensen and D. R. Yarkony, *J. Chem. Phys.* **89**, 3853 (1988).
8. R. D. Bardo and M. Wolfsberg, *J. Chem. Phys.* **67**, 593 (1977).
9. R. D. Bardo and M. Wolfsberg, *J. Chem. Phys.* **68**, 2686 (1978).
10. R. D. Bardo, L. I. Kleinman, A. W. Raczkowski and M. Wolfsberg, *J. Chem. Phys.* **69**, 1106 (1978).
11. L. I. Kleinman and M. Wolfsberg, *J. Chem. Phys.* **60**, 4740 (1974).
12. L. I. Kleinman and M. Wolfsberg, *J. Chem. Phys.* **60**, 4749 (1974).
13. R. J. Buenker, G. Hirsch, S. D. Peyerimhoff, P. J. Bruna, J. Römelt, M. Bettendorff and C. Petrongolo, *Current Aspects of Quantum Chemistry 1981*, Ed. R. Carbo (Elsevier, New York, 1982), Vol. 21, pp. 81.

14. C. A. Mead and D. G. Truhlar, *J. Chem. Phys.* **77**, 6090 (1982).
15. C. R. Vidal and W. C. Stwalley, *J. Chem. Phys.* **77**, 883 (1982).
16. D. M. Bishop and L. M. Cheung, *J. Chem. Phys.* **78**, 1396 (1983).
17. N. Koga and K. Morokuma, *Chem. Phys. Lett.* **119**, 371 (1985).
18. R. Fletcher, *Practical Methods of Optimization* (John Wiley and Sons, New York, 1981).
19. M. J. Bearpark, M. A. Robb and H. B. Schlegel, *Chem. Phys. Lett.* **223**, 269 (1994).
20. D. R. Yarkony, *Rev. Mod. Phys.* **68**, 985 (1996).
21. J. Gerratt and I. M. Mills, *J. Chem. Phys.* **49**, 1719 (1968).
22. J. Gerratt and I. M. Mills, *J. Chem. Phys.* **49**, 1730 (1968).
23. Y. C. Chen, D. R. Harding, W. C. Stwalley and C. R. Vidal, *J. Chem. Phys.* **85**, 2436 (1986).
24. D. R. Yarkony, *Int. Rev. Phys. Chem.* **11**, 195 (1992).
25. R. J. Bartlett, *Modern Electronic Structure Theory*, Ed. D. R. Yarkony (World Scientific Publishing, Singapore, 1995), Vol. 2.
26. D. R. Yarkony, *Atomic, Molecular and Optical Physics Handbook*, Ed. G. L. Drake (AIP, New York, 1996), p. 357.
27. W. C. Swope, H. F. Schaefer III and D. R. Yarkony, *J. Chem. Phys.* **73**, 407 (1980).
28. B. A. Hess and C. M. Marian, *Computational Molecular Spectroscopy*, Eds. P. Jensen and P. Bunker (John Wiley, Chichester, 2000), pp. 169.
29. L. I. Schiff, *Quantum Mechanics* (McGraw Hill, New York, 1960).
30. D. G. Truhlar, C. A. Mead and M. A. Brandt, *Adv. Chem. Phys.* **33**, 295 (1975).
31. C. A. Mead, *J. Chem. Phys.* **70**, 2276 (1979).
32. S. Matsika and D. R. Yarkony, *J. Chem. Phys.* **115**, 2038 (2001).
33. M. R. Manaa and D. R. Yarkony, *J. Chem. Phys.* **93**, 4473 (1990).
34. H. Goldstein, *Classical Mechanics* (Addison-Wesley, Massachusetts, 1950).
35. M. R. Manaa and D. R. Yarkony, *J. Am. Chem. Soc.* **116**, 11444 (1994).
36. R. McWeeny and B. T. Sutcliffe, *Methods of Molecular Quantum Mechanics* (Academic Press, London, 1969).
37. E. R. Davidson, *Reduced Density Matrices in Quantum Chemistry* (Academic Press, New York, 1976).
38. B. H. Lengsfield, *J. Chem. Phys.* **77**, 4073 (1982).
39. B. Liu and B. H. Lengsfield, *J. Chem. Phys.* **75**, 478 (1981).
40. H. J. Werner and W. Meyer, *J. Chem. Phys.* **74**, 5802 (1981).
41. B. H. Lengsfield and D. R. Yarkony, *State-Selected and State to State Ion-Molecule Reaction Dynamics: Theory*, Part 2, Eds. M. Baer and C.-Y. Ng (John Wiley and Sons, New York, 1992), Vol. 82, p. 1.
42. M. Page, P. Saxe, G. F. Adams and B. H. Lengsfield, *J. Chem. Phys.* **81**, 434 (1984).
43. J. E. Rice and R. D. Amos, *Chem. Phys. Lett.* **122**, 585 (1985).
44. P. Siegbahn, A. Heiberg, B. Roos and B. Levy, *Phys. Scr.* **21**, 323 (1980).

45. B. O. Roos, P. R. Taylor and P. E. M. Siegbahn, *Chem. Phys.* **48**, 157 (1980).
46. B. O. Roos, *Int. J. Quant. Chem. Symp.* **14**, 175 (1980).
47. N. C. Handy and H. F. Schaefer, *J. Chem. Phys.* **81**, 5031 (1984).
48. T. J. Lee and W. Allen, *J. Chem. Phys.* **87**, 7062 (1987).
49. R. Shepard, *Int. J. Quant. Chem.* **31**, 33 (1987).
50. M. R. Hoffman, D. J. Fox, J. F. Gaw, Y. Osamura, Y. Yamaguchi, R. S. Grev, G. Fitzgerald, H. F. Schaefer, P. J. Knowles and N. C. Handy, *J. Chem. Phys.* **80**, 2660 (1984).
51. B. H. Lengsfield, *Proceedings of the NATO Workshop on Geometrical Derivatives of Energy Surfaces and Molecular Properties* (Sonderborg, Denmark, 1984).
52. J. Hellmann, *Einfuhrung in die Quantenchemie* (Deuticke, Leipzig, 1937).
53. R. P. Feynman, *Phys. Rev.* **56**, 340 (1939).
54. S. Matsika and D. R. Yarkony, *J. Phys. Chem.* **A106**, 2580 (2002).
55. D. R. Yarkony, *Mol. Phys.* **99**, 1463 (2001).
56. D. R. Yarkony, *J. Phys. Chem.* **A105**, 2642 (2001).
57. M. I. Lester, R. A. Loomis, R. L. Schwartz and S. P. Walch, *J. Phys. Chem.* **A101**, 9195 (1997).
58. R. A. Loomis and M. I. Lester, *Ann. Rev. Phys. Chem.* **48**, 643 (1997).
59. D. R. Yarkony, *J. Chem. Phys.* **111**, 6661 (1999).
60. S. Matsika and D. R. Yarkony, *J. Chem. Phys.* **115**, 5066 (2001).
61. S. Matsika and D. R. Yarkony, *J. Chem. Phys.* **116**, 2825 (2002).
62. S. Matsika and D. R. Yarkony, *J. Phys. Chem.* **B106**, 8108 (2002).
63. B. C. Hoffman and D. R. Yarkony, *J. Chem. Phys.* **113**, 10091 (2000).
64. M. R. Manaa and D. R. Yarkony, *J. Chem. Phys.* **99**, 5251 (1993).
65. R. de L. Kronig, *Band Spectra and Molecular Structure* (Macmillan, New York, 1929).
66. S. Matsika and D. R. Yarkony, *J. Chem. Phys.* **117**, 6907 (2002).
67. M. Dallos, H. Lischka, R. Shepard, D. R. Yarkony and P. Szalay, *J. Chem. Phys.* (2004).
68. D. R. Yarkony, *Faraday Discussions* **127** (2004).
69. D. R. Yarkony, *J. Phys. Chem.* **A** (2004).
70. S. Matsika and D. R. Yarkony, *J. Amer. Chem. Soc.* **125**, 10672 (2003).
71. S. Matsika and D. R. Yarkony, *J. Amer. Chem. Soc.* **125**, 12428 (2003).
72. B. A. Murtagh and R. W. H. Sargent, *Computer Journal* **13**, 185 (1970).
73. H. Köppel, W. Domcke and L. S. Cederbaum, *Adv. Chem. Phys.* **57**, 59 (1984).
74. H. Lischka, M. Dallos, P. Szalay, D. R. Yarkony and R. Shepard, *J. Chem. Phys.* (2004).
75. H. Lischka, R. Shepard, I. Shavitt, R. Pitzer, M. Dallos, T. Müller, P. G. Szalay, F. B. Brown, R. Alhrichs, H. J. Böhm, A. Chang, D. C. Comeau, R. Gdanitz, H. Dachsel, C. Erhard, M. Ernzerhof, P. Höchtl, S. Irle, G. Kedziora, T. Kovar, V. Parasuk, M. Pepper, P. Scharf, H. Schiffer, M. Schindler, M. Schüler and J.-G. Zhao, *COLUMBUS, An Ab Initio Electronic Structure Program* (2003).

This page intentionally left blank

CHAPTER 4

DIABATIC REPRESENTATION: METHODS FOR THE CONSTRUCTION OF DIABATIC ELECTRONIC STATES

Horst Köppel

Theoretische Chemie, Physikalisch-Chemisches Institut, Universität Heidelberg, INF 229, D-69120 Heidelberg, Germany

Contents

1. Introduction

The concept of diabatic electronic states plays an important role in the theoretical description of strongly vibronically coupled systems. Contrary to the usual adiabatic electronic states, they are not eigenstates of the electronic Hamiltonian which thus acquires off-diagonal matrix elements in

the diabatic basis. On the other hand, the nuclear kinetic energy may be made approximately diagonal by a suitable choice of the diabatic states, and the residual off-diagonal derivative coupling terms be neglected for many practical purposes. In this chapter we address some key aspects, both conceptual and computational, of different possible choices of diabatic electronic wavefunctions.

The very notion "diabatic" was introduced by Lichten[1] into the literature and used there in the context of ion-atom collisions. It was shown that experimental results on charge exchange in He^++He collisions required several adiabatic potential energy curves, and transitions between them, for their interpretation. However, for a large range of collision energies, a single "diabatic" potential energy curved proved sufficient, which correlates with different adiabatic states in the limits of small and large internuclear distances.[1] This behavior was discussed in terms of the well-known Landau–Zener–Stückelberg theory[2,3] of avoided crossings, in which the underlying zero-order potential energy curves are a prototypical example of diabatic potential energy curves (although this notion has not been employed in that early work).

Subsequent work first continued to focus on atom–atom collision processes and also addressed the question of a proper general definition of diabatic states.[4–8] For a good overview, see the review article by O'Malley.[9] F. T. Smith was the first to give a general definition, without referring to individual systems and physical intuition, in terms of a differential equation for the adiabatic-to-diabatic transformation matrix.[6] This was derived by requiring that the derivative coupling elements should vanish in the new, diabatic electronic basis (where derivative refers to the internuclear distance, the only vibrational degree of freedom considered). Later on, Baer and coworkers considered the case of atom-diatom collisions and generalized the aforementioned differential equation to several nuclear degrees of freedom.[10–12] This leads directly to a *set* of coupled differential equations for which, however, certain conditions have to be fulfilled in order that solutions exist.[10–13] For the common case of two interacting states and three nuclear degrees of freedom this means that the *curl* of the derivative matrix element (being a vector in nuclear coordinate space) should vanish. Mead and Truhlar[13] emphasized that these conditions are generally not fulfilled and, thus, strictly diabatic electronic states do not exist in general. Exceptions are (1) the case of a single nuclear degree of freedom as for atomic

collision processes mentioned above, and (2) the case where the complete manifold of interacting states is considered in the diabatization procedure. This amounts to the choice of crude adiabatic states[14,15] which are, however, irrelevant for practical purposes, see below.

Despite this limitation the search for approximately diabatic, or quasidiabatic, states has received much attention in the literature on molecular systems. When all derivative coupling terms are given, one may, for example, transform away the whole removable part by solving an appropriate Poisson equation.[16,17] Since the *ab initio* computation of all coupling elements is an extremely tedious task in all but the smallest polyatomics, simpler construction schemes have also been followed, based on suitable properties of the electronic wavefunctions. We mention aspects of configurational change,[18–24] the behavior of the matrix elements of suitable operators,[25–28] the block diagonalization method[29–33] and others,[34–37] to be described in more detail below. As an even simpler approach, we point out the possibility of constructing (quasi)diabatic electronic states from the potential energy surfaces *alone*.[31,38–40,42] While being necessarily approximate (and possibly less accurate than other, more elaborate schemes) this proves to be a viable approach for the situation of primary interest in this book, namely that of intersecting potential energy surfaces. The knowledge of the topology of the surfaces near the subspace of degeneracy (intersection) often allows to extract the necessary information for removing the *singular part* of the derivative couplings. This elimination, on the other hand, represents the key advantage of the diabatic compared to the adiabatic electronic representation: contrary to the latter, the former wavefunctions are non-singular at conical intersections of potential energy surfaces and thus more easily to deal with, especially when performing quantum-dynamical simulations. It is precisely this difference which is at the focus of this latter approach and which leads to the notion of "regularized diabatic states".[40]

It is not the purpose of this article to give a systematic account of all aspects of the theory and construction schemes for diabatic states. Rather, after this somewhat historic introduction, we will outline salient features of the theory in Sec. 2 and refer to other chapters in this book (especially Chapter 1 by L. S. Cederbaum) and earlier review articles[31,41] for more details. Section 3 gives an overview over existing construction schemes with an attempt to characterize their respective merits and emphasis. Section 4 is devoted to a more detailed exposition of the concept of regularized diabatic

states which may be considered a promising variant for larger systems. Finally, Sec. 5 concludes with a brief summary.

2. General Theoretical Considerations

In this section we introduce the basic concept of diabatic electronic states and compare them with the adiabatic and crude adiabatic electronic wavefunctions.

2.1. *Adiabatic and Crude Adiabatic States*

We start with the set of coupled differential equations for the nuclear wavefunctions in the adiabatic representation (see Chapter 1):

$$[T_N \mathbf{1} + \mathbf{V}(\mathbf{Q}) - E\mathbf{1}]\, \boldsymbol{\chi}(\mathbf{Q}) = \boldsymbol{\Lambda} \boldsymbol{\chi}(\mathbf{Q}). \tag{1}$$

Here T_N denotes the nuclear kinetic energy, $\mathbf{V}(\mathbf{Q})$ is the diagonal matrix containing the adiabatic potential energy surfaces $V_i(\mathbf{Q})$ and $\mathbf{1}$ generally stands for the unit matrix in electronic function space. The vector $\boldsymbol{\chi}(\mathbf{Q})$ collects the vibrational wavefunctions $\chi_i(\mathbf{Q})$ of interest, and the elements Λ_{ij} of the nonadiabatic coupling matrix $\boldsymbol{\Lambda}$ can be written as:

$$\Lambda_{ij} = -\langle \Phi_i | T_N | \Phi_j \rangle + \langle \Phi_i | \boldsymbol{\nabla} | \Phi_j \rangle \, \boldsymbol{\nabla}, \tag{2}$$

where we have used $T_N = -\boldsymbol{\nabla}^2/2$ and set $\hbar = 1$ throughout. The adiabatic electronic wavefunctions Φ_i are eigenfunctions of the electronic Hamiltonian H_e according to:

$$H_e \Phi_i(\mathbf{r}, \mathbf{Q}) = V_i(\mathbf{Q})\, \Phi_i(\mathbf{Q}, \mathbf{Q}), \tag{3}$$

where H_e could include also spin-orbit coupling terms ($\mathbf{r} =$ set of electronic coordinates; $\mathbf{Q} =$ set of nuclear displacement coordinates). They enter into the expansion of the full molecular wavefunction $\Psi(\mathbf{r}, \mathbf{Q})$ according to:

$$\Psi(\mathbf{r}, \mathbf{Q}) = \sum_i \Phi_i(\mathbf{r}, \mathbf{Q})\, \chi_i(\mathbf{Q}). \tag{4}$$

For a more detailed discussion of Eq. (1), we refer to Chapter 1. At this point we only note a key property of the first derivative matrix element:

$$\mathbf{F}_{ij} = \langle \Phi_i | \boldsymbol{\nabla} | \Phi_j \rangle \tag{5}$$

appearing in Eq. (2) (note that boldface here refers to the quantities being vectors in *nuclear* coordinate space). By differentiating the eigenvalue equation (3) with respect to the nuclear coordinates, multiplying from the

left with $\Phi_j^*(\mathbf{r}, \mathbf{Q})$, $j \neq i$, and integrating over the electronic coordinates one obtains the following "off-diagonal analogue" of the Hellmann–Feynman theorem:

$$\mathbf{F}_{ij} = \frac{\langle \Phi_i | \boldsymbol{\nabla} H_e (\mathbf{r}, \mathbf{Q}) | \Phi_j \rangle}{V_j (\mathbf{Q}) - V_i (\mathbf{Q})}. \tag{6}$$

Equation (6) directly expresses the importance of near-degeneracies, and even more of intersections of potential energy surfaces, for the nuclear motion: whenever the difference $V_j - V_i$ becomes smaller than a vibrational quantum, the right hand side of Eq. (6) is expected to become large and the non-adiabatic coupling term Λ_{ij}, Eq. (2), plays a major role in Eq. (1). At conical intersections, in particular, the right hand side of Eq. (6) diverges and the $\mathbf{F}_{ij}(\mathbf{Q})$ are singular functions of the nuclear coordinates. Since the degeneracy is lifted in first order in the nuclear displacement ρ from the conical point, $\mathbf{F}_{ij}$ exhibits there a $1/\rho$ singularity. Correspondingly, the adiabatic electronic wavefunctions are discontinuous with a branch cut extending from the conical intersection point to infinity (see, for example, Ref. 42). It is this behavior which makes the adiabatic basis cumbersome to deal with numerically, especially when global potential energy surfaces are needed such as in a quantum-dynamical treatment of the nuclear motion.

To overcome the difficulty associated with this singularity, so-called "crude-adiabatic" electronic wavefunctions have been introduced into the literature.[14,15] Here, wavefunctions $\Phi_i(\mathbf{r}, \mathbf{Q}_0) \equiv \Phi_i^0$ for a fixed nuclear configuration $\mathbf{Q}_0$ are used in the expression (4) for *any* $\mathbf{Q}$ of interest:

$$\Psi (\mathbf{r}, \mathbf{Q}) = \sum_i \Phi_i (\mathbf{r}, \mathbf{Q}_0) \, \chi_i^0 (\mathbf{Q}) . \tag{7}$$

The new vibrational wavefunctions $\chi_i^0 (\mathbf{Q})$ are distinguished by the superscript from the earlier ones in Eq. (4). In a strict sense, even the atomic centers are to be kept fixed at $\mathbf{Q}_0$ when representing the electronic wavefunction at some general $\mathbf{Q}$, for example, in an *ab initio* electronic structure calculation. Correspondingly, the expression (7) is found to converge extremely slowly and the electronic energies obtained from the $\Phi_i(\mathbf{r}, \mathbf{Q}_0)$ are found to be much inferior compared to the adiabatic ones.[43,44] As a (partial) remedy of the problem, the core orbitals have been allowed to float with the instantaneous nuclear position which, nevertheless, does not improve significantly the overall situation.[43] We wish to point out, however, that expansions of the type (7) have been used frequently, especially

in Jahn–Teller (JT) theory[45,46] where $\mathbf{Q}_0$ represents a JT undistorted (i.e. high symmetry) geometry which is used to represent the Hamiltonian at a neighboring JT distorted geometry. In principle, the neighboring geometry should be infinitesimally close to the original one.[15,47] In this way many JT model Hamiltonians have been formulated which proved useful in molecular spectroscopy, dynamics and other fields (see also Chapter 10 in this book). It is evident from the above discussion that the matrix representation of the electronic Hamiltonian in the crude adiabatic basis contains also off-diagonal matrix elements (for $\mathbf{Q} \neq \mathbf{Q}_0$):

$$W_{ij} = \left\langle \Phi_i^0 | H_e | \Phi_j^0 \right\rangle , \tag{8}$$

whereas that of the nuclear kinetic energy becomes (even strictly) diagonal. Both features are close to the diabatic electronic states which are discussed next, also in relation to crude adiabatic electronic states.

2.2. *Diabatic Electronic States*

Diabatic electronic states are generally obtained by an orthogonal transformation in a *small subset* of adiabatic wavefunctions, constructed such that the off-diagonal nuclear derivative coupling becomes negligibly small (or, ideally, vanishes) in the new representation.[6,9,10] The small subset represents the strongly coupled electronic states and has to be chosen such that, for a given relevant coordinate range, all other electronic states are sufficiently far apart energetically. Confining ourselves for simplicity to a two-state problem, the adiabatic-to-diabatic transformation (ADT) matrix $\mathbf{S}$ can be written as:

$$\mathbf{S}(\mathbf{Q}) = \begin{pmatrix} \cos\alpha\,(\mathbf{Q}) & \sin\alpha\,(\mathbf{Q}) \\ -\sin\alpha\,(\mathbf{Q}) & \cos\alpha\,(\mathbf{Q}) \end{pmatrix} , \tag{9}$$

with the adiabatic-to-diabatic (ATD) mixing angle $\alpha\,(\mathbf{Q})$. In the basis of the new, diabatic wavefunctions,

$$\begin{pmatrix} \Phi_1^d \\ \Phi_2^d \end{pmatrix} = \mathbf{S}^T(\mathbf{Q}) \begin{pmatrix} \Phi_1 \\ \Phi_2 \end{pmatrix} , \tag{10}$$

the transformed first derivative matrix, i.e. the analogue of Eq. (5) in the adiabatic representation, undergoes a transformation known as *local gauge transformation*.[31] For real electronic wavefunctions the diagonal elements in Eq. (5) vanish, while the off-diagonal elements are oppositely equal,

$\mathbf{F}_{12} = -\mathbf{F}_{21}$, which also holds in the diabatic basis (effects of spin-orbit coupling are beyond the scope of this article). The transformed off-diagonal element $\mathbf{F}_{12}^{d}$ then simply reads:

$$\mathbf{F}_{12}^{d} = \boldsymbol{\nabla}\alpha\left(\mathbf{Q}\right) + \mathbf{F}_{12}. \tag{11}$$

The requirement

$$\mathbf{F}_{12}^{d} = 0 \tag{12}$$

thus leads to the following first-order differential equation for the ATD mixing angle:

$$\boldsymbol{\nabla}\alpha\left(\mathbf{Q}\right) = -\mathbf{F}_{12} = \langle\Phi_2|\boldsymbol{\nabla}|\Phi_1\rangle\,. \tag{13}$$

For one-dimensional problems Eq. (13) has been used to determine, by integration, the angle $\alpha\left(\mathbf{Q}\right)$ once the derivative matrix elements $\mathbf{F}_{12}$ are given, e.g. by an *ab initio* calculation (see, for example, Ref. 48). For the multidimensional case, a stepwise procedure has been proposed where the integration of Eq. (13) is carried out in turn along each coordinate axis.[12] However, in order that the integration does not depend on the sequence of axes chosen, and thus the result be well-defined, the following condition has to be satisfied:

$$\boldsymbol{\nabla} \times \mathbf{F}_{12} \equiv \text{curl}\ \mathbf{F}_{12} = \mathbf{0}. \tag{14}$$

Equation (14) is known as the "curl-condition" and derives from the elementary fact that the vector field $\mathbf{F}_{12}(\mathbf{Q})$ should be curl-free if expressible as the gradient of a scalar field according to Eq. (13), since one has:

$$\boldsymbol{\nabla} \times \left(\boldsymbol{\nabla}\alpha\left(\mathbf{Q}\right)\right) = \mathbf{0}. \tag{15}$$

Apart from special models, Eq. (14) is satisfied only when the whole space of interacting electronic states is considered in the ADT matrix $\mathbf{S}$ (in diatomics, with only a single nuclear degree of freedom, there is no curl-condition).[13] This, however, is contradicting the spirit of choosing a small subset of electronic states in the ADT matrix and would lead one back to the crude adiabatic basis discussed in the previous section. Therefore strictly diabatic electronic states, satisfying rigorously Eqs. (12) and (13) do not exist in the multidimensional case.[13]

Despite this limitation one may ask the question whether approximately diabatic states, satisfying Eq. (12) to a sufficient accuracy for practical

purposes, exist. With this goal in mind various construction schemes have been proposed in the literature which are surveyed in the next section. They might also be termed "quasidiabatic" states in order to indicate their approximate nature. For simplicity of nomenclature we will continue with the simpler notion "diabatic" in this article, but keep the above limitation in mind.

Another important aspect of diabatic states consists in the removability of the *singular* derivative coupling terms.[31,39,49] As mentioned above, these occur along seams of intersections between two potential energy surfaces, see Eq. (6). The curl of $\mathbf{F}_{12}$ entering Eq. (14) can be shown to involve only derivative couplings to other states, outside the manifold of intersecting states 1 and 2.[13,31,39] Therefore, it does not diverge if no intersections with other states arise and can be neglected if only singular coupling terms are of interest.[31,39,49,50] In this sense the singular derivative coupling terms constitute an important case for an isolated two-state system where rigorously diabatic states can be constructed (of course, *only* considering the singular terms). This property will be exemplified by an *ab initio* calculation[38] presented in the next section; it also underlies the concept of regularized diabatic states discussed in some detail below.

The (nearly) diagonal representation of the nuclear kinetic energy is accompanied by off-diagonal matrix elements of the potential energy in the diabatic representation. Transforming the diagonal potential energy matrix

$$\mathbf{V} = \begin{pmatrix} V_1 & 0 \\ 0 & V_2 \end{pmatrix} \tag{16}$$

from the adiabatic basis with the ADT matrix $\mathbf{S}$ according to

$$\mathbf{W}^d = \mathbf{S}^T \mathbf{V} \mathbf{S}, \tag{17}$$

one arrives at the potential energy matrix $\mathbf{W}^d$ in the diabatic basis:

$$\mathbf{W}^d = \frac{V_1 + V_2}{2} \mathbf{1} + \frac{V_1 - V_2}{2} \begin{pmatrix} \cos 2\alpha & \sin 2\alpha \\ \sin 2\alpha & -\cos 2\alpha \end{pmatrix}. \tag{18}$$

Formally, the off-diagonal appearance of $\mathbf{W}^d$ in the diabatic basis is similar to the crude adiabatic basis [as is the (nearly) diagonal form of T_N]. However, it should be kept in mind that the form of Eq. (18) refers to a small electronic subspace only, whereas all other electronic states are treated in the adiabatic representation. By contrast, the matrix $\mathbf{W}$ of Eq. (8) in the

crude adiabatic basis refers to the whole electronic function space in question and not only to small subspaces. This renders the expansion underlying Eq. (8) only slowly convergent, an undesirable feature which is *not* shared by the diabatic representation.

A connection between the crude adiabatic basis and the diabatic basis can be established, e.g. with the aid of quasi-degenerate perturbation theory.[51–53] Let the indices i and j refer to the subset (α) of strongly coupled states treated in the diabatic basis and the index n to the complementary set (β) of states coupled only weakly to these states. Then, up to the second order in the interaction between the different subsets the diabatic potential matrix $\mathbf{W}^d$ can be expressed through the crude adiabatic potential matrix $\mathbf{W}$ as follows:[42,51–53]

$$W_{ij}^d = W_{ij} + \frac{1}{2} \sum_{n \in (\beta)} \left[\frac{W_{in} W_{nj}}{W_{jj} - W_{nn}} + \frac{W_{in} W_{nj}}{W_{ii} - W_{nn}} \right]. \tag{19}$$

Suppose that the matrix elements W_{ij}, W_{in}, etc. are expanded in a Taylor series around the reference configuration $\mathbf{Q}_0$ of the crude adiabatic basis (as is frequently done in standard JT theory[45,46] and within the linear vibronic coupling scheme described in Chapter 7 of this book). Then the off-diagonal elements W_{ij} $(i \neq j)$ and W_{in} are (at most) of first order in these displacements $\delta\mathbf{Q}$. Hence, the *linear* term in W_{ij} cannot be affected by the coupling W_{in} between blocks (α) and (β) and we have:

$$W_{ij}^d = W_{ij} + \mathcal{O}\left(\delta\mathbf{Q}^T \cdot \delta\mathbf{Q}\right). \tag{20}$$

Thus the linear coupling terms are identical in the two electronic representations when taken in the rigorous sense, i.e. as deriving from an infinitesimal displacement. Of course, these coupling terms may also be taken as effective terms accounting for finite displacements; then they would differ in the two basis sets.

Finally, we point out that the above equations may be extended to comprise more than two strongly coupled electronic states. Since the overall conclusions are similar to the above ones we confine ourselves to citing some relevant literature.[10,13,31] Also, extensions have been given for the case of spin-orbit coupling when the electronic wavefunctions are necessarily complex and the relevant function space also increases.[54]

3. Construction Schemes for Diabatic Electronic States

In this section we survey some common methods used in the literature for computing (quasi)diabatic states. They are grouped into three classes, depending on the type of information upon which the construction is based.

3.1. *Derivative-Based Methods*

In this first type of methods the original proposal by Smith[6] and Baer[10–12] is followed directly, i.e. the defining differential equation (13) is solved as accurately as possible (for the two-state case). The formal solution can be written as:

$$\alpha(\mathbf{Q}) = \alpha(\mathbf{Q}_0) - \int_C \mathbf{F}_{12}(\mathbf{Q}')\,\mathbf{dQ}', \tag{21}$$

where C is a suitable contour connecting an initial (or reference) configuration $\mathbf{Q}_0$ with the nuclear configuration $\mathbf{Q}$ of interest. At some $\mathbf{Q}_0$ the mixing angle $\alpha_0 \equiv \alpha(\mathbf{Q}_0)$ has to be properly chosen; this constitutes one element of flexibility and also arbitrariness, the latter being however not relevant for practical purposes.

Equation (21) has been used routinely to determine rigorously diabatic states for diatomics where a single coordinate R exists and the integral becomes one-dimensional[48] (but note the additional appearance of angular — as opposed to radial — couplings[6]). For the multidimensional case the issue of the path-dependence of the integral in Eq. (21) exists, as already discussed above. The ATD angle $\alpha(\mathbf{Q})$ is well-defined if the integral vanishes along closed loops:

$$\oint_C \mathbf{F}_{12}(\mathbf{Q}')\,\mathbf{dQ}' = 0. \tag{22}$$

More generally, the integral may also equal a multiple of π in view of the trigonometric functions in Eq. (9), and the diabatic wavefunctions (10) still be well defined. A value of π is expected when encircling a conical intersection between potential energy surfaces in order to compensate for the singularity of the adiabatic wavefunctions (see also Chapters 1 and 7 in this book). In the ideal case, Eq. (22) is generalized as:

$$\oint_C \mathbf{F}_{12}(\mathbf{Q}')\,\mathbf{dQ}' = n\pi, \tag{23}$$

where n denotes the total number of conical points encircled by the closed loop. Yarkony[49] was probably the first to verify the accuracy to which Eq. (23) is satisfied by an *ab initio* electronic structure calculation. The example treated was the $1^2A' - 2^2A'$ seam of conical intersections of H_3 and two (small) circles were chosen, one containing the seam (at its minimum energy point), the other not. In both cases, Eq. (23) was confirmed with $n = 1$ and 0, respectively, the deviations being of the order $10^{-4} - 10^{-6}$.[49] Subsequent work on HeH_2,[28] CH_2,[55] and C_2H,[56] extended these findings. Quite naturally, Eq. (23) is satisfied to a higher accuracy for smaller loops/circles than for larger ones. The radii in case of all aforementioned calculations on H_3 were chosen as 0.1 and 0.05 a.u. In Fig. 1, we show results of calculations on CH_2, obtained with a large circle of radius $\rho = 0.5$ a.u. and taken from Ref. 55. The quantities with superscript μ relate to an alternative, property-based method which will be discussed in the next subsection. f_θ denotes the component of the derivative coupling vector along the tangent of the circular path. The ATD mixing angle obtained by integration according to Eq. (21) increases by 1.16π, when integrating from $-90°$ to $270°$.[55] This value is clearly incompatible with Eq. (23). Apparently for loops of that size the nonremovable derivative couplings play a role and strictly diabatic states do not exist. On the other hand, the results for small loops are evidenced by the perturbation theoretical result $\Theta^{(p)}$ included in the figure. This exemplifies Eq. (23) and the removability of the singular derivative couplings which dominate in the vicinity of the intersection.

We mention in passing that conditions of the form of Eq. (23) have been *postulated* by M. Baer and coworkers as necessary conditions for obtaining uniquely defined diabatic potentials.[57,58] It should be clear from the above discussion that they hold generally only for the singular derivative couplings and require careful consideration for any other cases (where they will hold only approximately).[50,59–61]

An interesting proposal has been made how to go beyond the singular coupling terms and remove *all* of the removable (i.e. also nonsingular) coupling terms.[16] This employs the decomposition, according to the Helmholtz theorem, of $\mathbf{F}_{12}(\mathbf{Q})$ into a longitudinal (removable) and a transverse (nonremovable) part:[13]

$$\mathbf{F}_{12}(\mathbf{Q}) = \mathbf{F}_{12}^{\mathrm{lon}}(\mathbf{Q}) + \mathbf{F}_{12}^{\mathrm{tra}}(\mathbf{Q}) \tag{24}$$

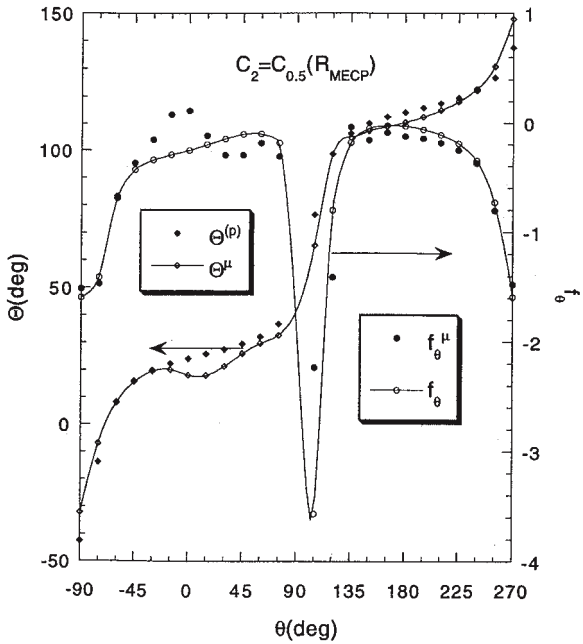

Fig. 1. Exact (f_θ) and approximate (f_θ^μ) tangential derivative coupling element for a circular path surrounding the lowest energy conical intersection between the $1^3A''$ and the $2^3A''$ states of CH_2.[55] The approximate derivative coupling is obtained by diagonalizing the dipole operator. The corresponding ATD mixing angle is denoted by Θ^μ. The analogous quantity $\Theta^{(p)}$ is obtained by perturbation theory. For more details, see text and Ref. 55.

in an obvious notation. By definition, the curl of $\mathbf{F}_{12}^{\mathrm{lon}}(\mathbf{Q})$ and the divergence of $\mathbf{F}_{12}^{\mathrm{tra}}(\mathbf{Q})$ vanish (for three relevant degrees of freedom)

$$\begin{aligned} \boldsymbol{\nabla} \times \mathbf{F}_{12}^{\mathrm{lon}}(\mathbf{Q}) &= 0, \\ \boldsymbol{\nabla} \cdot \ \mathbf{F}_{12}^{\mathrm{tra}}(\mathbf{Q}) &= 0. \end{aligned} \tag{25}$$

The defining Eq. (13) for the ATD mixing angle involves only the longitudinal part of $\mathbf{F}_{12}$ and one has:

$$\boldsymbol{\nabla} \cdot \boldsymbol{\nabla} \alpha\,(\mathbf{Q}) = \boldsymbol{\nabla} \mathbf{F}_{12}(\mathbf{Q}) = \boldsymbol{\nabla} \mathbf{F}_{12}^{\mathrm{lon}}(\mathbf{Q}). \tag{26}$$

In other words, solving the *Poisson differential equation* (26) for the mixing angle $\alpha\,(\mathbf{Q})$ does not suffer from the integration problem in Eq. (21) since the nonremovable part $\mathbf{F}_{12}^{\mathrm{tra}}$ has been eliminated from the right hand side of

Eq. (26). All the removable derivative coupling is transformed away, which is probably the most systematic way to arrive at optimum (quasi)diabatic states in general. Of course, in a given example the smallness of the residual coupling in the (quasi)diabatic basis remains to be verified and other methods could be superior when matrix elements of the derivative couplings with nuclear wavefunctions are considered.

The above scheme has first been applied by Sadygov and Yarkony[16] in a 2D study on HeH_2 and more recently by Abrol and Kuppermann[17] in a 3D study of H_3. In the latter work the whole domain of nuclear configurations relevant for reactive scattering has been treated and various boundary conditions have been compared.[17] In this way the smallness of the residual (transverse) couplings in the diabatic basis could be established and a combination of Neumann and Dirichlet boundary conditions be shown to be optimum for this purpose.

3.2. *Property-Based Methods*

The methods discussed so far are in principle the most accurate ones for constructing (quasi)diabatic states. However, they involve also the largest computational effort requiring the determination of all derivative couplings over an extended range of nuclear coordinates. Despite considerable advance in their calculation by *ab initio* electronic structure methods,[62] this is still a tedious task for all but the smallest (triatomic) systems. We therefore discuss now alternative methods, being based on the knowledge of properties of the adiabatic wavefunctions *other than* the nuclear derivative coupling matrix elements.

A key observation is that large nonadiabatic couplings are often related to *fast configurational changes* of the adiabatic electronic wavefunctions. This has been utilized already in the early literature, when constructing diabatic states for treating atomic collision problems.[1,9] A typical example would be the interaction between an ionic and a covalent configuration[9,63] in a narrow coordinate range, leading to a weakly avoided crossing. Here the fast change in character of the adiabatic wavefunctions when going from one side of the avoided crossing to the other side leads to large nonadiabatic couplings which dominate those caused by the changing coefficients of the molecular orbitals or by the floating atomic centers. The latter are often taken into account by introducing so-called electron-translation factors.[8]

A variety of methods have been proposed which all seek for reducing (or minimizing) the configurational changes of the electronic wavefunctions and thus determine the transformation from adiabatic to diabatic states. They can be further subdivided into two groups. In the first group one attempts to enforce the smoothness of a physical property, especially a one-electron property. Already in 1952, Mulliken suggested the use of dipole moments,[64] as was pursued later by Werner and Meyer[25] and others.[65,66] The quadrupole moment[26] as well as the transition dipole moment[67,68] have also been employed, by requiring that the diagonal elements be equal in the diabatic basis. More recently, Yarkony argued that (almost) any real-valued Hermitean operator, satisfying only certain limited restrictions, can be used to construct diabatic states near a conical intersection.[28] That is, the eigenfunctions of such an operator, diagonalized in the subspace of intersecting electronic states, remove all of the singular couplings at the intersection.[28] As an example, Fig. 1 includes such results for CH_2, with the operator being chosen as the dipole operator.[55] The data labelled with a superscript μ in the insert represent derivative couplings (and the ensuing ATD mixing angle) from diagonalizing the dipole operator — the residual couplings in this (quasi)diabatic basis are neglected. Despite the large radius $\rho = 0.5$ a.u. of the circular contour chosen in this case, the agreement with the full derivative couplings discussed earlier is quite good. It becomes much better for a smaller radius $\rho = 0.1$ a.u.[55] As a by-product, Fig. 1 provides also evidence that this transformation gives well-defined diabatic states, because the ATD angle integrates to π, as required, when going from $\theta = -90°$ to $270°$.

In the second group of property-based methods one enforces the smoothness of the electronic wavefunctions themselves. Hendeković and coworkers suggested to maximize the sum of the squares of the natural spin orbital occupation numbers.[18–20] Spiegelmann and Malrieu developed an effective Hamiltonian formalism[34,35] based on quasidegenerate perturbation theory[51–53] which has been improved by Cimiralia *et al.*[69] and which relates to another approach by Gadea and coworkers.[36,37,70,71] Ruedenberg and Atchity suggested and worked out the principle of configurational uniformity[21,22] which was recently extended by Nakamura and Truhlar.[24] In the Heidelberg group, the concept of block-diagonalization of the electronic Hamiltonian has been developed[29–31] and implemented,[31,72] which can be derived from a least action principle[73] and leads to optimum (quasi)diabatic

states *locally*.[31] Further remarks on this method and these attractive features are provided in Chapter 1 by L. S. Cederbaum. The block diagonalization method has been further extended within a CASSCF framework by Domcke and coworkers.[32,33] We also mention related work by Özkan and Goodman[74] and by Simah *et al.*[75]

A general issue of these latter approaches is the choice of reference states or configurations which are considered sufficiently diabatic so that their **Q**-dependence can be neglected. In the introductory remarks of this subsection these were alluded to be electronic configurations based on floating ("adiabatic") molecular orbitals so that the nonadiabatic couplings would arise only from configuration interaction (CI). Besides these CI couplings there are, however, generally also molecular orbital (MO) based derivative couplings which arise from the changing MO coefficients for different nuclear geometries (see, for example, Ref. 76). To minimize the latter, and thus facilitate the application of many of the above schemes, it may be useful to consider natural orbitals deriving from *average* density matrices, averaged over the set of strongly coupled states. These have been demonstrated to be (quasi)diabatic in many cases[77] and will thus give only CI-type couplings when used as the orbital basis (as is frequently done in CASSCF/CI-type calculations). An alternative is given by applying the block-diagonalization method[31] to the CAS orbitals and exploiting[33] the invariance of the CASSCF energies under orbital rotations. This has been shown to lead to (quasi)diabatic orbitals,[33] reducing the coupling to a CI-type problem, and global 3D *ab inito* diabatic potential energy surfaces for excited electronic states of ozone have been constructed in this way.[78]

3.3. *Energy-Based Methods*

The property-based methods described above already represent a considerable simplification in constructing diabatic states. In any wavefunction-based method the eigenvectors of the CI-type secular problem are usually computed together with the eigenvalues and, hence, the properties of interest are obtained without much additional computational effort. Without computing the residual derivative couplings in this new basis the quality of the diabatic states is, of course, not strictly under control and depends to a large extent on the physical intuition for a specific system. We now turn to an even simpler method which is inherently more approximative and relies

only on the knowledge of the adiabatic potential energy surfaces alone. This may be of particular value for not-wavefunction-based electronic structure methods which do not deliver the appropriate eigenvectors when solving the electronic structure problem.

Generally, for a two state problem, there are three elements of the diabatic potential matrix and only two adiabatic potential energy surfaces; hence a computation of the former from the latter quantities will be underdetermined. The situation changes, however, (a) when modelling the diabatic potential matrix elements in a suitable way and (b) when only the singular derivative couplings are of interest, as is relevant especially for conical intersections.

The modelling of potential energy curves has already been introduced in the early literature for atomic collision processes, within the context of the Landau–Zener approach.[2] Assuming the difference of the diagonal matrix elements (i.e. in the diabatic basis) to be a linear function of the interatomic distance and the off-diagonal element to be constant, the pertinent system parameters are readily extracted from the adiabatic potential energy surfaces. This procedure may be generalized also to a more complicated functional form of the diabatic potential matrix elements and to several degrees of freedom: for a given parametrization with a finite number of parameters one can always provide enough *ab initio* data points to enable the determination of the parameters from the latter. This holds, for example, also for the linear coupling scheme discussed in Chapter 7 of this book.

We now address the removability of the singular derivative couplings from the potential energy surfaces alone. This important aspect has been pointed out in the literature[38–40,42] and is reiterated here for the sake of clarity. We start from a diabatic basis in which the singular terms have been eliminated (see Sec. 2.2 above) and confine ourselves to two relevant degrees of freedom, x and y. The potential matrix $\mathbf{W}^{(2)}$ is expanded in a Taylor series around the conical point, defined by $x = y = 0$ and is written as:

$$\mathbf{W}^{(2)} = \begin{pmatrix} k_1 x + g_1 x^2 & \lambda y + l y^2 \\ \lambda y + l y^2 & k_2 x + g_2 x^2 \end{pmatrix}, \tag{27}$$

where a single second-order term has been included in every matrix element for the ease of notation. The conclusions below will, however, be seen to be unaffected by this simplification. The linear terms are assumed to

involve only either x or y, which is guaranteed if there is one element of symmetry.[42,79] Starting from Eq. (27), the first-order derivative coupling element between its eigenvectors (i.e. the adiabatic wavefunctions) equals the derivative of the rotation angle α of the eigenvector matrix analogous to Eq. (9). By elementary manipulations this is found to be:

$$\begin{aligned}
\frac{\partial \alpha}{\partial x} &= \frac{-L\,\dfrac{\partial D}{\partial x}}{2\,(D^2+L^2)} \\
\frac{\partial \alpha}{\partial y} &= \frac{D\,\dfrac{\partial L}{\partial y}}{2\,(D^2+L^2)} \\
D &= \frac{k_1-k_2}{2}x + \frac{g_1-g_2}{2}x^2 \\
L &= \lambda y + l y^2 \\
\delta k &= \frac{k_1-k_2}{2},
\end{aligned} \tag{28}$$

with the following leading terms around the point of intersection $x = y = 0$:

$$\begin{aligned}
\frac{\partial \alpha}{\partial x} &= \frac{1}{2}\,\frac{\left[-\lambda y + \mathcal{O}(y^2)\right]\,[\delta k + \mathcal{O}(x)]}{\delta k^2 x^2 + \lambda^2 y^2 + \mathcal{O}(x^3, y^3)} \\
&= -\frac{1}{2}\,\frac{\lambda\ \delta k\ y}{\delta V^2} + \mathcal{O}(1) \\
\frac{\partial \alpha}{\partial x} &= \frac{1}{2}\,\frac{[\lambda + \mathcal{O}(y)]\,\left[\delta k\ x + \mathcal{O}(x^2)\right]}{\delta k^2 x^2 + \lambda^2 y^2 + \mathcal{O}(x^3, y^3)} \\
&= \frac{1}{2}\,\frac{\lambda\ \delta k\ x}{\delta V^2} + \mathcal{O}(1).
\end{aligned} \tag{29}$$

Note that the denominator in Eqs. (29) is just the squared half-difference δV^2 of the adiabatic potential energy surfaces. Apparently, the leading, singular terms are determined by the leading terms of $\mathbf{W}^{(2)}$, Eq. (27). The latter can be uniquely extracted from the adiabatic potential energy surfaces by inspecting cuts along the coordinates x and y:

$$\begin{aligned}
V_{1,2}(x, y = 0) &= k_{1,2}\ x + \mathcal{O}(x^2), \\
V_{1,2}(x = 0, y) &= \pm\lambda\ y + \mathcal{O}(y^2).
\end{aligned} \tag{30}$$

Note that the uniqueness applies only to the linear terms when other second-order terms are also present in Eq. (27). We stress that the form of the

linear coupling terms in Eq. (27) holds rigorously when a symmetry element is present by which the two electronic states (as well as x and y) differ.[42,79] This constitutes, therefore, a sufficient condition for the above scheme. Finally, we note that a similar reasoning has also been presented for the case of three degrees of freedom (see Appendix of Ref. 39).

As an illustrative example, Fig. 2 shows a representative result for the $S_1 - S_2$ conical intersection in pyrazine, taken from Ref. 38. Panel (a) displays CASSCF *ab initio* potential energy surfaces in a two-dimensional coordinate space of a symmetry-preserving coordinate and a symmetry-breaking coordinate (see Ref. 38 for details). The conical intersection is seen to occur as a point of degeneracy at $Q_{10a} = 0$, $Q_{6a} = -0.54$ (in dimensionless normal coordinates). Determining the first order constants as indicated above and using the resulting first-order ATD angle α to construct diabatic states (see also next section) leads to the diabatic potential matrix elements displayed in panels (b) and (c). As expected, the degeneracy of the diabatic potentials occurs in an $(n-1)$-dimensional subspace, i.e. along a line in Fig. 2(b). All diabatic matrix elements are smooth functions of the coordinates. This holds also for the transition dipole moment presented in Fig. 3. Whereas in the adiabatic representation [Fig. 3(a)], there is the characteristic singularity at the conical intersection, this has been fully removed in the diabatic basis [Fig. 3(b)] where only a smooth dependence on the nuclear coordinates remains. Similar results have been achieved for related matrix elements.[38] This clearly illustrates the possibility of removing the singular derivative couplings at a conical intersection from energy data alone.

4. The Concept of Regularized Diabatic States

At the end of the last section it has already been pointed out that the singular derivative coupling terms can be determined from the adiabatic potential energy surfaces alone when a symmetry element is present. According to earlier reasoning it can also be eliminated by transforming to a suitable diabatic basis. In the following we describe a specific variant for this construction, focusing exclusively on the singular couplings and leading to so-called *regularized diabatic states*.[38–40]

The basic idea has already been indicated in the discussion following Eq. (27). We recall that the singular terms associated with this potential

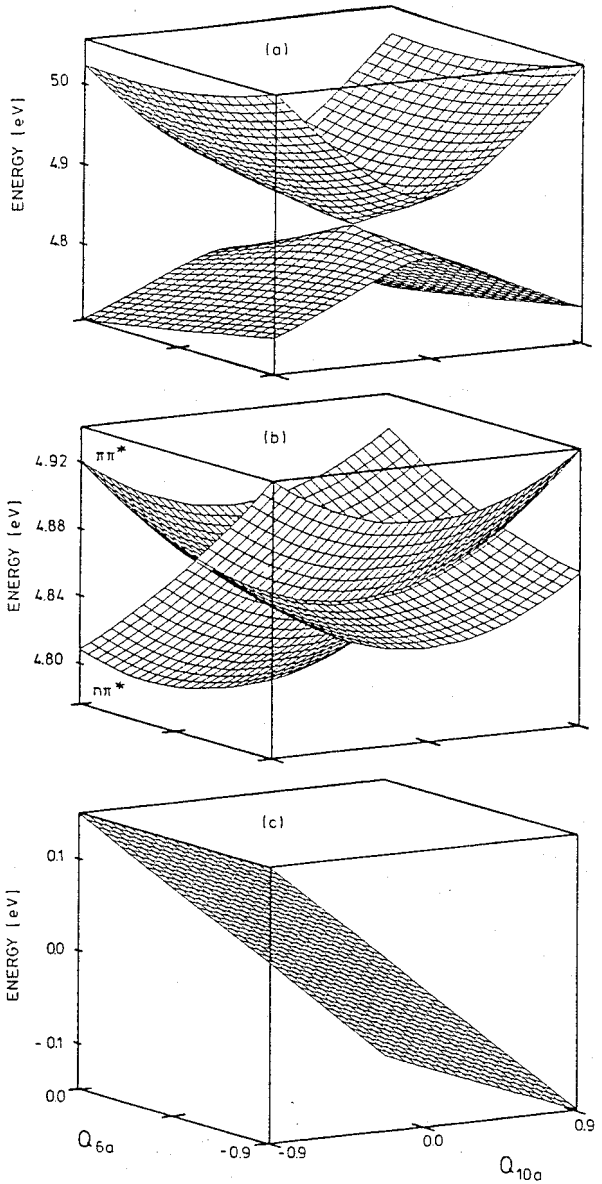

Fig. 2. Perspective drawing of the $S_1 - S_2$ conical intersection in pyrazine in the space of a symmetry-preserving (Q_{6a}) and a symmetry-lowering (Q_{10a}) normal coordinate.[38] Adiabatic surfaces are shown in (a), the diabatic diagonal elements H_{11} and H_{22} are shown in (b). The diabatic coupling element H_{12} is shown in (c).

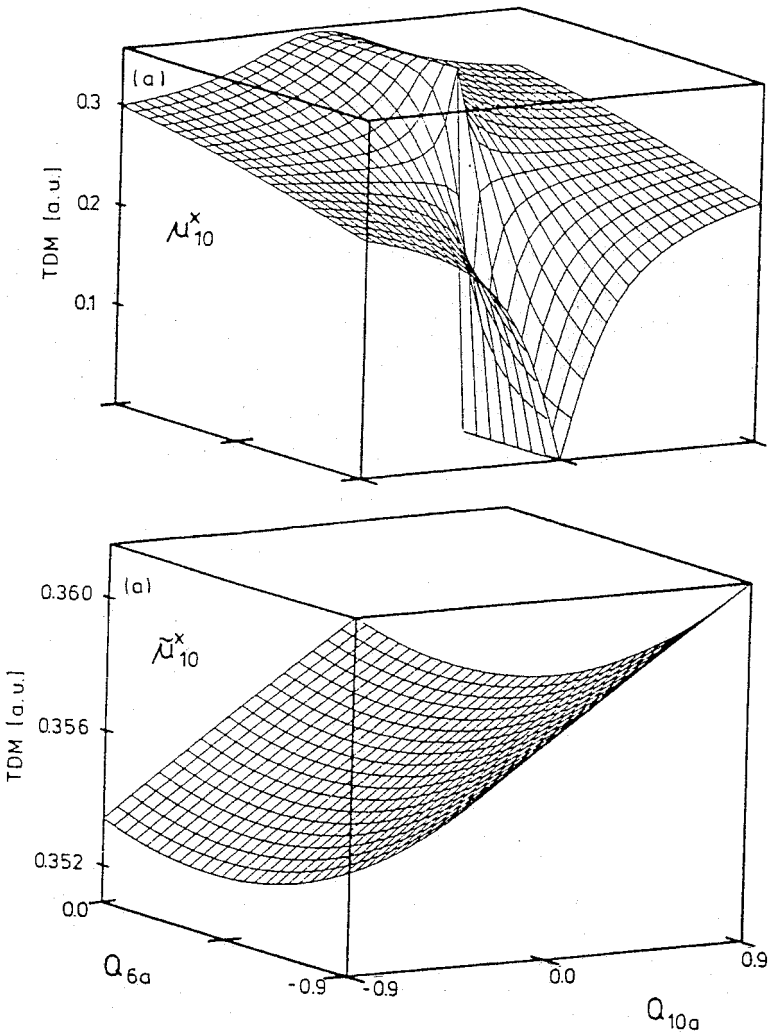

Fig. 3. x-component of the adiabatic (a) and diabatic (b) transition dipole moment for the $S_0 - S_1$ transition of pyrazine in the $Q_{6a} - Q_{10a}$ space, taken from Ref. 38.

matrix are determined by its linear part:

$$\mathbf{W}^{(1)} = \begin{pmatrix} k_1 x & \lambda y \\ \lambda y & k_2 x \end{pmatrix}, \tag{31}$$

leading to an ADT matrix $\mathbf{S}^{(1)}$:

$$\mathbf{S}^{(1)} = \begin{pmatrix} \cos\alpha^{(1)} & \sin\alpha^{(1)} \\ -\sin\alpha^{(1)} & \cos\alpha^{(1)} \end{pmatrix}, \tag{32}$$

with

$$\alpha^{(1)} = \frac{1}{2}\arctan\frac{\lambda\, y}{\delta k\, x}. \tag{33}$$

For the corresponding two-state two-mode problem the singular terms are thus eliminated by applying the ADT matrix $\mathbf{S}^{(1)}$ to the adiabatic wavefunctions with the full adiabatic potentials $V_1 \equiv V_1(x,y)$ and $V_2 \equiv V_2(x,y)$. This leads directly to the diabatic potential matrix [see also Eq. (18)] within the concept of *regularized diabatic states*:

$$\begin{aligned} \mathbf{W}_{\text{reg}} &= \frac{V_1+V_2}{2}\mathbf{1} + \frac{V_1-V_2}{2}\begin{pmatrix} \cos 2\alpha^{(1)} & \sin 2\alpha^{(1)} \\ \sin 2\alpha^{(1)} & -\cos 2\alpha^{(1)} \end{pmatrix} \\ &= \frac{V_1+V_2}{2}\mathbf{1} + \frac{V_1-V_2}{2\sqrt{\delta k^2 x^2 + \lambda^2 y^2}}\begin{pmatrix} \delta k\, x & \lambda\, y \\ \lambda\, y & -\delta k\, x \end{pmatrix}. \end{aligned} \tag{34}$$

Equation (34) has been utilized by Ref. 38 to obtain the potential matrix elements of Fig. 2 (and, analogously, the transition dipole moments of Fig. 3). The approach has been further elaborated by Refs. 39, 40 to treat also the nuclear dynamics with this scheme and to compare the result with known reference solutions, taken to be exact for this purpose. Two different cases have been considered. First, a well-known JT model Hamiltonian has been adopted in Ref. 39, representing the quadratic $E \otimes e$ JT problem:[45,46]

$$\mathcal{H}_{JT} = H_0\mathbf{1} + \begin{pmatrix} 0 & k\rho e^{-i\varphi} + \frac{g}{2}\rho^2 e^{2i\varphi} \\ \text{h.c.} & 0 \end{pmatrix}. \tag{35}$$

This serves as exact reference and is compared with a treatment where the ADT matrix of the linear problem ($g = 0$) is applied to the full adiabatic surfaces of $\mathcal{H}_{JT}$, Eq. (35). The latter leads to the approximate Hamiltonian in the regularized diabatic basis:[39]

$$\mathcal{H}_{\text{reg}} = H_0\mathbf{1} + \sqrt{1 + \frac{g}{k}\rho\cos 3\varphi + \left(\frac{g}{2k}\rho\right)^2}\begin{pmatrix} 0 & k\rho e^{-i\varphi} \\ k\rho e^{i\varphi} & 0 \end{pmatrix}. \tag{36}$$

The full and approximate JT Hamiltonians, Eqs. (35) and (36) are characterized by identical potential energy surfaces and singular derivative couplings; the non-singular coupling terms differ. They have been compared

in Ref. 39 with respect to the vibronic structure of $A \rightarrow E$ absorption spectra[45,46] where the JT dynamics is probed in a direct way. Out of results for many different parameter values, we show in Fig. 4 a comparison for $k = \sqrt{5}$ and $g = 0.4$. The quadratic coupling which is treated approximately by $\mathcal{H}_{\rm reg}$ is rather strong, leading to a strong dependence of the adiabatic potential energy surface on the azimuthal angle ϕ (they are ϕ-independent for $g = 0$);[45,46] nevertheless the exact and approximate spectra of Fig. 4 agree very well. This holds also for other parameter values reported in Ref. 39. The reason for this good agreement can be traced to the matrix elements of the derivative coupling operators with the *nuclear* wavefunctions.[39] Note that these matrix elements do not diverge because the singularity of the electronic matrix elements is cancelled by appropriate zeros of the nuclear wavefunctions at the conical intersection.[80] Nevertheless the pertinent matrix elements have been found to be strongly suppressed in the

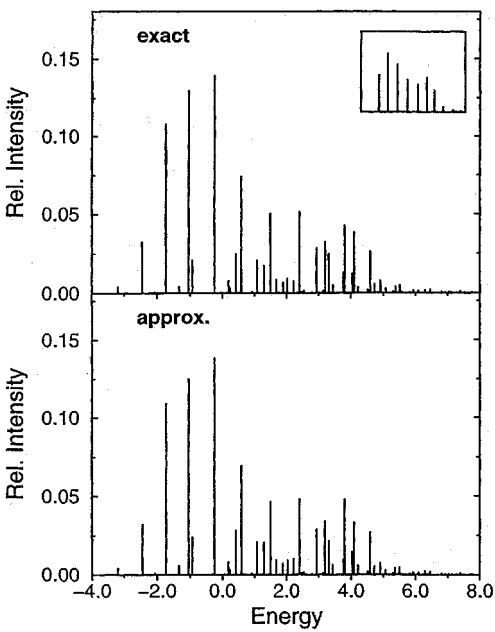

Fig. 4. Comparison of exact and approximate Jahn–Teller spectra for $k = \sqrt{5}$ and $g = 0.4$, taken from Ref. 39. The approximate spectrum is obtained by utilizing Eq. (35). The inset shows the corresponding spectrum for purely linear coupling, i.e. $g = 0$.

regularized diabatic basis.[39] This shows that the removal of the singular derivative couplings is also useful when considering matrix elements with the nuclear wavefunctions.

The concept of regularized diabatic states has been further developed and tested numerically for systems with three degrees of freedom in Ref. 40 (where also the nomenclature has been introduced). Two electronic states of different spatial symmetry with two symmetry-preserving and one symmetry-lowering coordinates have been considered, as occurs routinely in bent XY_2 molecules. For A_1/B_2 (or also A_2/B_1) electronic symmetries there may be symmetry-allowed intersections in the C_{2v} point group, whereas the states will interact for unequal bond lengths [i.e. in the C_s molecular point group, with electronic symmetries A'/A' (or A''/A'')]. Let the symmetry-lowering normal coordinate be denoted by Q_u and the "projection" of half the adiabatic energy gap $\Delta = (V_2 - V_1)/2$ onto the high-symmetry subspace by Δ_0, i.e. $\Delta_0(Q_1, Q_2, Q_u) = \Delta(Q_1, Q_2, 0)$. Then considerations analogous to the above for the 2D case lead to the following expression for the Hamiltonian within the basis of regularized diabatic states[40]

$$\mathcal{H}_{\text{reg}} = \left(T_N + \frac{V_1 + V_2}{2} \right) \mathbf{1} + \frac{\Delta}{\sqrt{\Delta_0^2 + \lambda^2 Q_u^2}} \begin{pmatrix} \Delta_0 & \lambda Q_u \\ \lambda Q_u & -\Delta_0 \end{pmatrix}. \tag{37}$$

The vibronic coupling constant λ is a measure of the strength of the interstate coupling. It can be determined either "locally" i.e. along the seam of intersections, defined by $\Delta_0 = 0$, by an equation similar to Eq. (30), or more "globally" for the entire high-symmetry subspace $Q_u = 0$ through the relation:[40]

$$\lambda = \left[\frac{1}{8} \frac{\partial^2}{\partial Q_u^2} (V_2 - V_1)^2 \right]_{Q_u=0}^{\frac{1}{2}}. \tag{38}$$

The two variants differ in the treatment of the non-singular derivative couplings but both remove the singular part fully.[40]

The scheme has been successfully applied to the photodissociation on coupled surfaces of O_3 and H_2S.[40] In both cases theoretical reference treatments are available in a diabatic electronic representation. The resulting adiabatic surfaces have been re-diabatized using Eqs. (37) and (38), and the resulting photodissociation spectra been compared to the earlier data (taken as the exact reference). For all technical details we refer to the original work.[40] In Fig. 5, we show a contour line drawing of the diabatic potential matrix elements of O_3 as a function of the bond lengths r_1 and r_2

for a fixed bond angle $\varphi = 120°$. Only one of the two diagonal matrix elements is shown because the results for the other element are very similar.[40] The agreement of the present diabatization with the exact reference, taken from Ref. 78, is seen to be very good indeed. It may therefore not be too surprising that also the photodissociation spectrum, presented in Fig. 6, closely parallels the earlier result from Ref. 81. Figure 6 also compares spectra obtained from the two different variants of determining λ (globally and

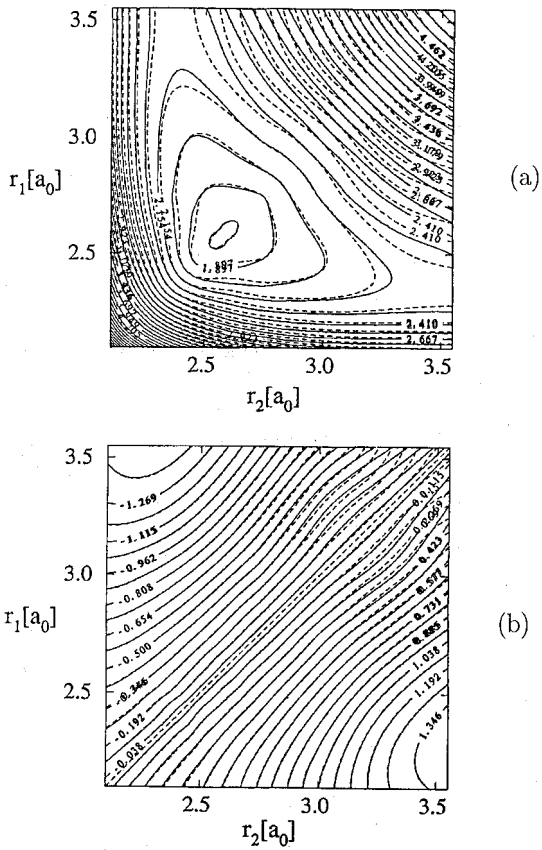

Fig. 5. Contour line drawing of a diagonal (a) and the off-diagonal (b) diabatic potential matrix element for the $1^1A''$ and $2^1A''$ states of ozone, taken from Ref. 40. The bond lengths r_1 and r_2 are varied, while the bond angle is fixed at 120°. Dashed lines represent the reference data of Woywood *et al.*,[78] full lines result from the concept of regularized diabatic states.

locally). Both are very similar, indeed, which is an indication that the different treatment of the non-singular coupling terms does not severely affect the quantum dynamical result. Finally, Fig. 7 displays the time-dependent populations of the adiabatic electronic states and confirms that the present scheme reproduces the earlier reference data[81] very well also in this respect.

The photodissociation on coupled potential surfaces of H_2S has also been treated in Ref. 40 and a similarly good agreement (with the reference data of Simah *et al.*[75]) has been obtained. As applications of the concept of regularized diabatic states we mention work on Rydberg emission spectra of H_3[82,83] and on photodetachment spectra of NO_2^-.[84] While the diabatization scheme alone cannot be tested here (due to other possible sources of error) the good agreement with experiment achieved is nevertheless considered encouraging.[83,84] Finally we emphasize that the working Eqs. (37)

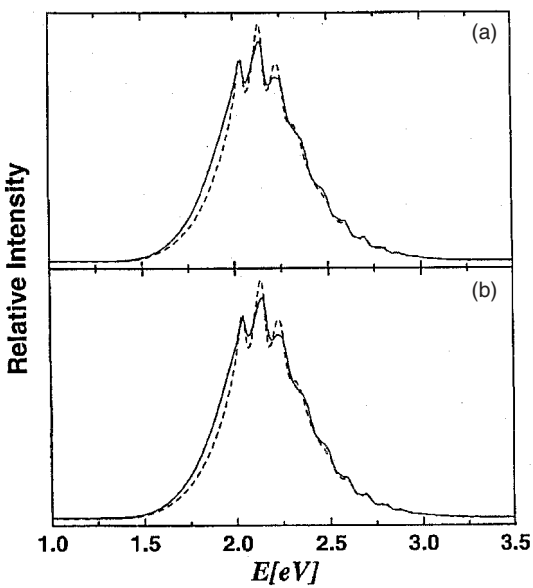

Fig. 6. Comparison of reference data (dashed lines, from Ref. 81) with results from the concept of regularized diabatic states (full lines, from Ref. 40) for the Chappuis band of ozone. In panel (a), the vibronic coupling constant λ has been determined in an extended portion of the C_{2v} subspace; in panel (b), it has been computed along the seam only. For more details see text.

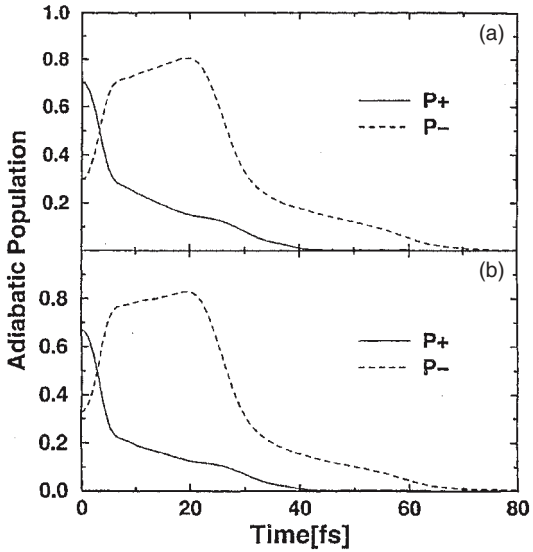

Fig. 7. Comparison of time-dependent electronic populations of upper (P_+) and lower (P_-) adiabatic states for the Chappuis band of ozone. (a) Reference data from Ref. 81. (b) Results from the concept of regularized diabatic states, from Ref. 40.

and (38) can, of course, be applied also to larger molecules, provided a symmetry element is present. In suitable cases, a modelling as described here with two symmetric (tuning) and one asymmetric (coupling) modes may be appropriate.[42] Moreover, Eqs. (37) and (38) are immediately generalized to more than two symmetric and more than one asymmetric coordinate.[40]

Let us reiterate that the computational effort associated with the construction of regularized diabatic states is very modest and does not exceed that for an uncoupled-surface nuclear dynamics calculation (apart, of course, from obtaining reliable potential energy surfaces themselves by properly treating static electron correlation effects). Therefore it is hoped that this concept will prove useful for *ab initio* quantum dynamical treatments of larger molecular systems.

5. Concluding Remarks

Diabatic electronic states represent a useful concept in theoretical studies of strongly vibronically coupled systems. They are slowly varying functions

of the nuclear coordinates and are continuous at conical intersections of potential energy surfaces. This renders them particularly useful, e.g. in quantum dynamical treatments of the nuclear motion, when global potential energy surfaces are required. Much less basis functions/grid points are needed than in the adiabatic description because no cusps, singular derivative couplings etc. are to be dealt with. Thus the numerical effort for the quantum treatment of the nuclear dynamics becomes comparable to that of an uncoupled-surface problem.

In this chapter we have reviewed some salient features of the general theory of diabatic electronic states and have surveyed some common methods used in the literature for their construction, derivative-based, property-based and energy-based. The non-existence of strictly diabatic states has been emphasized, as well as the removability of the singular derivative terms; the latter can be considered as the hallmark of conical intersections. Thus, the specific features of conical intersections can be described in the diabatic representation. Of particular use may be that, at least in the presence of a symmetry element, the singular coupling terms can be extracted from the potential energy surfaces alone, and so can be the corresponding diabatic electronic states. This idea underlies the linear vibronic coupling scheme introduced rather early into the literature, and also the more recent concept of regularized diabatic states. More elaborate schemes require the knowledge of the adiabatic electronic wave functions, possibly including the derivative coupling elements. Given all the latter, the removable derivative couplings can be eliminated by solving an appropriate Poisson equation. While this is probably the most accurate scheme in general, it is also most tedious computationally, especially for larger systems. It is of great practical value that even the (computationally simple) elimination of the singular terms alone may strongly reduce the residual coupling terms in the (quasi)diabatic electronic basis. Therefore one may hope that this idea will prove useful for a large class of molecular systems.

Acknowledgment

It is a pleasure to thank L. S. Cederbaum for a fruitful collaboration on this and other related topics.

References

1. W. Lichten, *Phys. Rev.* **131**, 229 (1963).
2. L. Landau, *Phys. Z. Sowjetunion* **2**, 46 (1932).
3. C. Zener, *Proc. Roy. Soc. Ser. A* **137**, 696 (1932).
4. W. Lichten, *Phys. Rev.* **139**, A27 (1965).
5. W. Lichten, *Phys. Rev.* **164**, 131 (1967).
6. F. T. Smith, *Phys. Rev.* **179**, 111 (1969).
7. T. G. Heil and A. Dalgarno, *J. Phys. B: Atom. Mol. Phys.* **12**, L557 (1979).
8. J. B. Delos and W. R. Thorson, *J. Chem. Phys.* **70**, 1774 (1979).
9. T. F. O'Malley, *Adv. At. Mol. Phys.* **7**, 223 (1971).
10. M. Baer, *Chem. Phys. Lett.* **35**, 112 (1975).
11. Z. H. Top and M. Baer, *J. Chem. Phys.* **66**, 1363 (1977).
12. M. Baer, *Mol. Phys.* **40**, 1011 (1980).
13. C. A. Mead and D. G. Truhlar, *J. Chem. Phys.* **77**, 6090 (1982).
14. C. J. Ballhausen and A. E. Hansen, *Ann. Rev. Phys. Chem.* **23**, 15 (1972).
15. H. C. Longuet-Higgins, *Adv. Spectrosc.* **2**, 429 (1961).
16. R. G. Sadygov and D. R. Yarkony, *J. Chem. Phys.* **109**, 20 (1998).
17. R. Abrol and A. Kuppermann, *J. Chem. Phys.* **116**, 1035 (2002).
18. J. Hendeković, *Chem. Phys. Lett.* **90**, 193 (1982).
19. J. Hendeković, *Croat. Phys. Acta* **56**, 375 (1983).
20. M. Pavlović, J. Kučar and J. Hendeković, *Int. J. Quantum Chem.* **32**, 705 (1987).
21. K. Ruedenberg and G. J. Atchity, *J. Chem. Phys.* **99**, 3799 (1993).
22. G. J. Atchity and K. Ruedenberg, *Theor. Chem. Acc.* **97**, 47 (1997).
23. G. J. Atchity, K. Ruedenberg and A. Nanayakkara, *Theor. Chem. Acc.* **96**, 195 (1997).
24. H. Nakamura and D. G. Truhlar, *J. Chem. Phys.* **115**, 10353 (2001).
25. H.-J. Werner and W. Meyer, *J. Chem. Phys.* **74**, 5802 (1981).
26. C. Petrongolo, G. Hirsch and R. J. Buenker, *Mol. Phys.* **70**, 825 (1990).
27. B. Heumann, R. Düren and R. Schinke, *Chem. Phys. Lett.* **180**, 583 (1991).
28. D. R. Yarkony, *J. Phys. Chem.* **A102**, 8073 (1998).
29. L. S. Cederbaum, H. Köppel and W. Domcke, *Int. J. Quantum Chem. Symp.* **15**, 251 (1981).
30. T. Pacher, L. S. Cederbaum and H. Köppel, *J. Chem. Phys.* **89**, 7367 (1988).
31. T. Pacher, L. S. Cederbaum and H. Köppel, *Adv. Chem. Phys.* **84**, 293 (1993).
32. W. Domcke and C. Woywod, *Chem. Phys. Lett.* **216**, 362 (1993).
33. W. Domcke, C. Woywod and M. Stengle, *Chem. Phys. Lett.* **226**, 257 (1994).
34. F. Spiegelmann and J. P. Malrieu, *J. Phys.* **B17**, 1235 (1984).
35. F. Spiegelmann and J. P. Malrieu, *J. Phys.* **B17**, 1259 (1984).
36. F. X. Gadea and M. Pelissier, *J. Chem. Phys.* **93**, 545 (1990).
37. F. X. Gadea, *Phys. Rev.* **A43**, 1160 (1991).
38. C. Woywod, W. Domcke, A. L. Sobolewski and H.-J. Werner, *J. Chem. Phys.* **100**, 1400 (1994).

39. A. Thiel and H. Köppel, *J. Chem. Phys.* **110**, 9371 (1999).
40. H. Köppel, J. Gronki and S. Mahapatra, *J. Chem. Phys.* **115**, 2377 (2001).
41. V. Sidis, *Adv. Chem. Phys.* **82**, 73 (1992).
42. H. Köppel, W. Domcke and L. S. Cederbaum, *Adv. Chem. Phys.* **57**, 59 (1984).
43. O. Atabek, A. Hardisson and R. Lefebre, *Chem. Phys. Lett.* **20**, 40 (1973).
44. J. W. C. Johnson and J. O. E. Weigang, *J. Chem. Phys.* **63**, 2135 (1975).
45. I. B. Bersuker and V. Z. Polinger, *Vibronic Interactions in Molecules and Crystals* (Springer, Heidelberg, 1989).
46. R. Englman, *The Jahn-Teller Effect in Molecules and Crystals* (Wiley, London, 1972).
47. H. A. Jahn and E. Teller, *Proc. Roy. Soc.* **A161**, 220 (1937).
48. E. F. van Dishoeck, M. C. van Hemert, A. C. Allison and A. Dalgarno, *J. Chem. Phys.* **81**, 5709 (1984).
49. D. R. Yarkony, *J. Chem. Phys.* **105**, 10456 (1996).
50. B. K. Kendrick, C. A. Mead and D. G. Truhlar, *Chem. Phys.* **277**, 31 (2002).
51. J. des Cloizeaux, *Phys. Rev.* **135**, A685 (1964).
52. B. H. Brandow, *Rev. Mod. Phys.* **39**, 771 (1967).
53. V. Kvasnicka, *Adv. Chem. Phys.* **36**, 345 (1977).
54. S. Matsika and D. R. Yarkony, *J. Chem. Phys.* **116**, 2825 (2002).
55. D. R. Yarkony, *J. Chem. Phys.* **110**, 701 (1999).
56. A. M. Mebel, A. Yahalom, R. Englman and M. Baer, *J. Chem. Phys.* **115**, 3673 (2001).
57. M. Baer and A. Alijah, *Chem. Phys. Lett.* **319**, 489 (2000).
58. M. Baer, *Chem. Phys.* **259**, 123 (2000).
59. B. K. Kendrick, C. A. Mead and D. G. Truhlar, *J. Chem. Phys.* **110**, 7594 (1999).
60. B. K. Kendrick, C. A. Mead and D. G. Truhlar, *Chem. Phys. Lett.* **330**, 629 (2000).
61. M. Baer, *Chem. Phys. Lett.* **330**, 633 (2000).
62. B. H. Lengsfield and D. R. Yarkony, *State-Selected and State to State Ion-Molecule Reaction Dynamics: Theory*, Part 2, Vol. 82 (Wiley, New York, 1992).
63. R. S. Mulliken, *Chem. Phys. Lett.* **46**, 197 (1977).
64. R. S. Mulliken, *J. Am. Chem. Soc.* **64**, 811 (1952).
65. N. S. Hush, *Progr. Inorg. Chem* **8**, 391 (1967).
66. R. J. Cave and N. D. Newton, *J. Chem. Phys.* **106**, 9213 (1997).
67. G. Hirsch, R. J. Buenker and C. Petrongolo, *Mol. Phys.* **70**, 835 (1990).
68. M. Peric, R. J. Buenker and S. Peyerimhoff, *Mol. Phys.* **71**, 673 (1990).
69. R. Cimiraglia, J. P. Malrieu, M. Persico and F. Spiegelman, *J. Phys.* **B18**, 3073 (1985).
70. T. Romero, A. Aguilar and F. X. Gadea, *J. Chem. Phys.* **110**, 6219 (1999).
71. N. Khelifi, B. Oujia and F. X. Gadea, *J. Chem. Phys.* **116**, 2879 (2002).

72. T. Pacher, H. Köppel and L. S. Cederbaum, *J. Chem. Phys.* **95**, 6668 (1991).
73. L. S. Cederbaum, J. Schirmer and H.-D. Meyer, *J. Phys. A: Math. Gen.* **22**, 2427 (1989).
74. I. Özkan and L. Goodman, *Chem. Rev.* **79**, 275 (1979).
75. D. Simah, B. Hartke and H. J. Werner, *J. Chem. Phys.* **111**, 4523 (1999).
76. M. Desouter-Lecomte, D. Dehareng and J. C. Lorquet, *J. Chem. Phys.* **86**, 1429 (1987).
77. V. M. García, M. Reguero, R. Caballol and J. P. Malrieu, *Chem. Phys. Lett.* **281**, 161 (1997).
78. C. Woywod, M. Stengle, W. Domcke, H. Flöthmann and R. Schinke, *J. Chem. Phys.* **107**, 7282 (1997).
79. H. Köppel and W. Domcke, *Encyclopedia in Computational Chemistry*, (Wiley, New York, 1998), p. 3166.
80. C. A. Mead, *J. Chem. Phys.* **78**, 807 (1983).
81. H. Flöthmann, C. Beck, R. Schinke, C. Woywod and W. Domcke, *J. Chem. Phys.* **107**, 7296 (1997).
82. S. Mahapatra and H. Köppel, *J. Chem. Phys.* **109**, 1721 (1998).
83. S. Mahapatra and H. Köppel, *Phys. Rev. Lett.* **81**, 3116 (1998).
84. S. Mahapatra, H. Köppel, L. Cederbaum, P. Stampfuss and W. Wenzel, *Chem. Phys.* **259**, 211 (2000).

CHAPTER 5

MODELING AND INTERPOLATION OF GLOBAL MULTI-SHEETED POTENTIAL ENERGY SURFACES

A.J.C. Varandas

Departamento de Química, Universidade de Coimbra
3004-535 Coimbra, Portugal

Contents

1. Introduction

The divide-and-conquer idea of separating the rapidly moving electrons from the much slower moving nuclei when treating a physical problem dates back in quantum mechanics to Born and Oppenheimer[1] (BO), and possibly even predates the publication of their key paper.[2] As a result from this separation, one hopes to get an electronic problem in which the nuclear positions can be treated as parameters and whose solutions can be used to solve the nuclear dynamics problem. The electrons provide therefore a potential (potential energy surface or, more strictly, hypersurface) which should be invariant under all uniform translations and rigid rotations of the nuclei that form the molecule. Besides enhancing the efficiency of the numerical process in the solution of Schrödinger's equation for the many-body problem, the BO approximation leads therefore to an useful physical insight.

However, nonadiabatic phenomena, in which such an approximation breaks down, are ubiquitous and occur in many important fields ranging from reaction dynamics to molecular spectroscopy and a vast number of other fields. They play a role whenever two or more electronic potential energy surfaces become degenerate or nearly-degenerate at some (finite or infinite) number of points of the molecular configurational space. It should be noted that, for triatomic or larger polyatomic systems, two adiabatic potential energy surfaces can intersect, even if the corresponding states have the same symmetry and spin multiplicity.[3–6] This stems from the fact that only two independent relations between three electronic Hamiltonian matrix elements are sufficient for the existence of a doubly-degenerate electronic energy eigenvalue. Thus, if the intersecting potential energy surfaces of

a N-atom molecule belong to different symmetry blocks of the electronic Hamiltonian, their loci of intersection have dimension $(3N-7)$, since one of the above degeneracy requirements is automatically fullfilled by symmetry; examples of these are the so-called Renner-Teller intersections in triatomic systems. However, if the two states are of the same symmetry, their intersection can occur only along a $(3N-8)$ [$(3N-7)$ in complex space[7]] hyperline as the energy is plotted against the $(3N-6)$ nuclear coordinates. As a result, electronic degeneracies between states of the same symmetry are common in nature: double-degeneracies for triatomics, triple-degeneracies also for tetratomics, and so on.

In the case of double degeneracies (the only case discussed here), such intersections are of the conical type, having the topology of a double cone. Thus, two directions can be distinguished, say x and y (these define a plane, often called g–h plane[8]) such that if one were to plot the energy in the subspace of these two geometric variables (bond lengths, angles, etc), the potential energy would have the form of a double cone in the vicinity of the degeneracy; in the remaining $(3N-8)$ directions, the energies of ground and excited states are equal. The splitting of the potential energy surfaces in the plane of x and y is therefore a linear function away from the intersection point, but close to it. Conventionally, such degeneracies can be classified as normal, when they are required by the molecular symmetry-point group, or accidental, when they are not. Examples of the former are the E-type intersections occurring in X_3-type Jahn–Teller systems[9] (see Sec. 4.1). In turn, accidental degeneracies include both symmetry-allowed ones (if permitted by the different symmetry of the involved states) and degeneracies involving states of the same symmetry, which can only occur[3–6] in triatomic and larger systems. As for the minima and saddle points on potential energy surfaces (e.g. Ref. 10), significant progress has been made with the direct location of such points on surfaces of intersection.[8,11]

In this Chapter, we focus on the modelling and interpolation of electronic manifolds, while pinpointing some topological implications of conical intersections in studies of nuclear dynamics such as the so-called geometric phase (GP) effect. Although written in the form of a review, it includes some results not reported elsewhere. Unavoidably, the material presented is biased toward our own work, although a fair coverage of other viewpoints is also presented.

2. The Many-Body Problem

Schrödinger's equation describing the complete many-body problem assumes the form

$$H_T\Omega(\mathbf{R}',\mathbf{r}') = E\Omega(\mathbf{R}',\mathbf{r}') \tag{1}$$

where H_T is the total Hamiltonian operator, $\Omega(\mathbf{R}',\mathbf{r}')$ the total molecular wave function, E the total energy, and $\mathbf{R}'$ ($\mathbf{r}'$) is the set of nuclear (electronic) coordinates in a coordinate frame fixed in the laboratory (SF frame); for simplicity, the spin coordinates of nuclei and electrons are not indicated.[12] Note that the total wave function cannot, in principle, be separated due to interactions between the nuclear and electronic degrees of freedom, although it may be separated in practice, partially or completely, depending on such interactions. In particular, the uniformity and isotropy of space may justify the separation of the translational and rotational degrees of freedom of an isolated molecule, as they can be regarded to be described by cyclic coordinates.[a] For N nuclei, this leads to $(3N-3)$ translation-free coordinates $\mathbf{R}'$, of which three coordinates (orientational or external, $\hat{\mathbf{R}}$) can be specified by a particular way of fixing a coordinate frame (BF frame) in the non-rigid assembly of particles. The remaining $(3N-6)$ internal coordinates $\mathbf{R}$ specify the geometry of the system, and it is solely in terms of these that any potential energy surface must be expressed, since it has to be invariant under all orthogonal transformations (rotation-reflections) of the particle variables in the SF frame. For example, in the case of a triatomic molecule, there are six translation-free coordinates: three describe the rotational motion, and the other three the internal vibrational motion. Examples of the latter (often also referred to as shape coordinates) are the Jacobi coordinates $[\vec{r},\vec{R},\theta \equiv \cos^{-1}(\vec{r}\cdot\vec{R}/rR)]$, the valence coordinates $(R_1,R_2,\angle\mathrm{ABC})$, and the three bond distances (R_1,R_2,R_3). In addition, linear symmetrized combinations of bond distances,

$$\begin{pmatrix} Q_1 \\ Q_2 \\ Q_3 \end{pmatrix} = \begin{pmatrix} 1/\sqrt{3} & 1/\sqrt{3} & 1/\sqrt{3} \\ 0 & 1/\sqrt{2} & -1/\sqrt{2} \\ 2/\sqrt{6} & -1/\sqrt{6} & -1/\sqrt{6} \end{pmatrix} \begin{pmatrix} R_1 \\ R_2 \\ R_3 \end{pmatrix} \tag{2}$$

[a]Even if these separations are mathematically well understood, they may pose difficulties when perceived from the point of view of separating the electronic and nuclear motions in the total Hamiltonian (Ref. 2, and references therein).

or of their squares,

$$\begin{pmatrix} \mathcal{Q} \\ \beta \\ \gamma \end{pmatrix} = \begin{pmatrix} 1 & 1 & 1 \\ 0 & \sqrt{3} & -\sqrt{3} \\ 2 & -1 & -1 \end{pmatrix} \begin{pmatrix} R_1^2 \\ R_2^2 \\ R_3^2 \end{pmatrix} \tag{3}$$

are frequently employed (the β and γ coordinates so defined should not be confused with the Euler angles below). Other internal coordinates quite often used in solving the quantum three-body nuclear problem are the hyperspherical coordinates[13–18] (ρ, θ, φ). Assuming these, and the Euler angles[19] (α, β, γ) for the orientational coordinates, one has $\mathbf{R}' = (\mathbf{R}, \hat{\mathbf{R}})$ where $\mathbf{R} = (\rho, \theta, \varphi)$ and $\hat{\mathbf{R}} = (\alpha, \beta, \gamma)$.

2.1. *Approximations and Concept of Potential Energy Surface*

In the so-called adiabatic approximation to Eq. (1), the total Hamiltonian is written as

$$H_T = -\frac{\hbar^2}{2\mu} \nabla^2_{\mathbf{R}'} + H_e(\mathbf{r}; \mathbf{R}) \tag{4}$$

where $H_e(\mathbf{r}; \mathbf{R})$ is the electronic Hamiltonian operator. The electronic wave functions and eigenvalues are defined by

$$H_e(\mathbf{r}, \mathbf{R}) \Psi_I(\mathbf{r}; \mathbf{R}) = V_I(\mathbf{R}) \Psi_I(\mathbf{r}; \mathbf{R}). \tag{5}$$

$\nabla_{\mathbf{R}'}$ is the gradient with respect to all nuclear degrees of freedom which locate the nuclei in a center-of-mass frame, and the semicolon indicates the parametric dependence of the electronic wave functions on $\mathbf{R}$. Since the latter form a complete orthonormal set, the total wave function may be written as the Born–Huang[1,20] expansion

$$\Omega(\mathbf{R}', \mathbf{r}) = \sum_I \chi_I(\mathbf{R}') \Psi_I(\mathbf{r}; \mathbf{R}) \tag{6}$$

where $\{\chi_I(\mathbf{R}')\}$ are the nuclear wave functions, and the summation includes in principle an integration over the continuum.[2]

Substitution of Eq. (6) in Eq. (1) leads to an infinite set of coupled equations which may be written in matrix form as

$$\left\{ -\frac{\hbar^2}{2\mu} \left[\mathbf{I} \nabla^2_{\mathbf{R}'} + 2\mathbf{F}(\mathbf{R}') \cdot \boldsymbol{\nabla}_{\mathbf{R}'} + \mathbf{G}(\mathbf{R}') \right] + \mathbf{V}(\mathbf{R}) - E\mathbf{I} \right\} \boldsymbol{\chi}(\mathbf{R}') = \mathbf{0} \tag{7}$$

where $\mathbf{I}$ is the appropriate identity matrix, $\boldsymbol{\chi}(\mathbf{R}')$ is a column vector whose components are the nuclear wave functions $\chi_I(\mathbf{R}')$, and the elements of the

vector matrix $\mathbf{F}(\mathbf{R}')$ and the scalar matrices $\mathbf{G}(\mathbf{R}')$ and $\mathbf{V}(\mathbf{R})$ are given by

$$\mathbf{F}_{IJ}(\mathbf{R}') = \langle \Psi_I(\mathbf{r};\mathbf{R}) | \nabla_{\mathbf{R}'} \Psi_J(\mathbf{r};\mathbf{R}) \rangle \tag{8}$$

$$G_{IJ}(\mathbf{R}') = \langle \Psi_I(\mathbf{r};\mathbf{R}) | \nabla^2_{\mathbf{R}'} \Psi_J(\mathbf{r};\mathbf{R}) \rangle \tag{9}$$

$$V_{IJ}(\mathbf{R}) = \langle \Psi_I(\mathbf{r};\mathbf{R}) | H_e | \Psi_J(\mathbf{r};\mathbf{R}) \rangle. \tag{10}$$

As usual, the bracket notation $\langle | \rangle$ implies integration over the electronic coordinates only, while $\mathbf{F}_{IJ}(\mathbf{R}')$ and $G_{IJ}(\mathbf{R}')$ are the first- and second-order nonadiabatic matrix coupling elements, respectively. By using a derivation similar to that employed for the Hellmann-Feynman theorem, it may be shown that

$$\mathbf{F}_{IJ}(\mathbf{R}') = \frac{\langle \Psi_I(\mathbf{r};\mathbf{R}) | \nabla_{\mathbf{R}'} H_e | \Psi_J(\mathbf{r};\mathbf{R}) \rangle}{V_I(\mathbf{R}) - V_J(\mathbf{R})} \qquad (I \neq J) \tag{11}$$

which illustrates the hyperbolic divergence behavior of the derivative coupling terms near the crossing seam (where $V_I = V_J$), known to be responsible for numerical computational difficulties in the adiabatic approximation. Note that the potential matrix is diagonal, in this approximation, $V_{IJ} = V_I \delta_{IJ}$, while

$$\mathbf{C} = -\frac{\hbar^2}{2\mu} \left[2\mathbf{F}(\mathbf{R}') \cdot \boldsymbol{\nabla}_{\mathbf{R}'} + \mathbf{G}(\mathbf{R}') \right] \tag{12}$$

is a nondiagonal matrix. Since the off-diagonal operators C_{IJ} induce transitions between the electronic states Ψ_I and Ψ_J, they are called operators of nonadiabaticity. In turn, $V_I = V_{II}(\mathbf{R})$ is called an adiabatic potential or sheet of the electronically adiabatic manifold. If just the Ith term is considered in Eq. (6) to represent $\Omega(\mathbf{R}', \mathbf{r})$, the motion of the nuclei can only lead to deformations of the electronic distribution and, of course, no transitions between electronic states will be allowed. The distribution of the nuclei is then described by the wave function $\chi_I(\mathbf{R}')$ in the potential $V_{II} + C_{II}$, an approximation known as the proper adiabatic approximation.[21]

Consider now an electronic basis defined with the nuclear internal coordinates clamped at $\mathbf{R} = \mathbf{R}_0$, such that $\Psi_I(\mathbf{r};\mathbf{R})$ in Eq. (6) gets replaced by the eigenfunctions $\Psi_I(\mathbf{r}) \equiv \Psi_I(\mathbf{r};\mathbf{R}_0)$ of $H_e(\mathbf{r},\mathbf{R}_0)$. Substitution of such an ansatz into Eq. (1) leads to a system of coupled differential equations similar to Eq. (7), although with some notable differences. First, the potential matrix is nondiagonal in the new basis, except at $\mathbf{R} = \mathbf{R}_0$. Second, all matrix elements of the nuclear kinetic energy operator vanish identically, since the basis functions do not depend on $\mathbf{R}$. Of course, if a complete

basis set is assumed, the eigenvalues of the potential matrix will coincide with the adiabatic potentials $V_I(\mathbf{R})$ in Eq. (5). This is called the crude Born–Oppenheimer approximation,[21] being linked to the proper adiabatic approximation by the unitary transformation of the electronic basis. Thus, they are equivalent from this point of view, although the equivalence is valid only for exact solutions. In fact, the crude BO approximation involves necessarily some power expansion of the potential energy with respect to the nuclear displacements from $\mathbf{R}_0$, and hence it is expected to have convergence properties different from those in the proper adiabatic approximation. Indeed, the crude BO approximation can break down simply due to the signficant anharmonicity of the potential energy surface. However, it is formally most convenient, since the electronic states $\{\Psi_I(\mathbf{r})\}$ form the basis of irreducible representations of the symmetry group appropriate to the nuclear configuration $\mathbf{R}_0$ (Ref. 12, and references therein).

2.2. *Geometric Phase, Adiabatic Potentials and Derivative Couplings*

As first pointed out by Longuet-Higgins,[5,6,9] the adiabatic approximation breaks down at conical intersections, since a real electronic wave function changes sign whenever traversing a nuclear path which encircles the point of degeneracy.[b] Such a geometric phase (GP) effect was placed in a wider quantum mechanical context by Berry,[24] and hence it also became known as the Berry phase effect. In fact, given the analogy with the effect of a true magnetic field confined to a narrow solenoid,[25] Mead[26] suggested the further designation "molecular Aharonov–Bohm effect". Such a sign change in the electronic wave function has important implications. In fact, since the total electronuclear wave function must be continuous and single-valued, the nuclear wave function must then also change sign to compensate the sign-change of the electronic wave function. As a result, both $\Psi_I(\mathbf{r};\mathbf{R})$ and $\chi_I(\mathbf{R}')$ are not single-valued when taken as real. However (see Appendix A), the wave functions in the Born–Huang[20] expansion can be single-valued if

[b]Reciprocally, the Longuet-Higgins[5,6,9] theorem states that if an adiabatic electronic wave function changes sign upon circulation around a closed loop in nuclear configuration space, somewhere on or inside that loop there must exist a conical intersection. Such a theorem has been used to localize at the *ab initio* level a conical intersection in LiNaK,[22] and more recently in other systems such as O_3.[23]

allowed to be complex. For example, we may write

$$\Omega\left(\mathbf{R}',\mathbf{r}\right)=\sum_{I}\chi_{I}\left(\mathbf{R}'\right)e^{iA_{I}(\mathbf{R})}\Psi_{I}\left(\mathbf{r};\mathbf{R}\right)=\sum_{I}\tilde{\chi}_{I}\left(\mathbf{R}'\right)\tilde{\Psi}_{I}\left(\mathbf{r};\mathbf{R}\right) \tag{13}$$

where $A_I\left(\mathbf{R}\right)$ is the geometric phase chosen to make the complex electronic wave function $\tilde{\Psi}_I\left(\mathbf{r};\mathbf{R}\right)$ [and hence $\Omega\left(\mathbf{R}',\mathbf{r}\right)$] be single-valued. Of course, Eq. (13) may alternatively be written as

$$\Omega\left(\mathbf{R}',\mathbf{r}\right)=\sum_{I}\tilde{\chi}_{I}\left(\mathbf{R}'\right)\Psi_{I}\left(\mathbf{r};\mathbf{R}\right) \tag{14}$$

where the complex nuclear wave functions $\{\tilde{\chi}_I\left(\mathbf{R}'\right)\}$ are now chosen to make $\Omega\left(\mathbf{R}',\mathbf{r}\right)$ be single-valued. If the ansatz in Eq. (14) is used, one obtains a set of coupled equations similar to that in Eq. (7), but with the real-valued nuclear wave functions $\chi_I\left(\mathbf{R}'\right)$ replaced by the complex ones $\tilde{\chi}_I\left(\mathbf{R}'\right)$. Furthermore, if only the diagonal matrix elements are retained (proper adiabatic approximation), one gets

$$\left\{-\frac{\hbar^{2}}{2\mu}\left[\nabla_{\mathbf{R}'}^{2}+G_{II}\left(\mathbf{R}'\right)\right]+V_{I}\left(\mathbf{R}\right)-E\right\}\tilde{\chi}_{I}\left(\mathbf{R}'\right)=0. \tag{15}$$

Alternatively, using real wave functions as in Eq. (13), one has

$$\left\{-\frac{\hbar^{2}}{2\mu}\left[\nabla_{\mathbf{R}'}+i\nabla_{\mathbf{R}'}A_{I}\left(\mathbf{R}\right)\right]^{2}+\overline{V}_{I}\left(\mathbf{R}\right)-E\right\}\chi_{I}\left(\mathbf{R}'\right)=0 \tag{16}$$

where

$$\overline{V}_{I}\left(\mathbf{R}\right)=V_{I}\left(\mathbf{R}\right)-\frac{\hbar^{2}}{2\mu}\widetilde{G}_{II}\left(\mathbf{R}'\right) \tag{17}$$

with $\widetilde{G}_{II}\left(\mathbf{R}'\right)$ assuming the form of Eq. (9), but with the electronic wave functions tilded. Note that $\widetilde{\mathbf{F}}_{II}(\mathbf{R}')=i\nabla_{\mathbf{R}'}A_I(\mathbf{R})+\mathbf{F}_{II}\left(\mathbf{R}\right)=i\nabla_{\mathbf{R}'}A_I\left(\mathbf{R}\right)$ since, for real-valued electronic wave functions,[27] $\mathbf{F}_{II}\left(\mathbf{R}\right)=\langle\Psi_I\left(\mathbf{r};\mathbf{R}\right)|\nabla_{\mathbf{R}'}\Psi_I\left(\mathbf{r};\mathbf{R}\right)\rangle=0$. In such a single-surface approach, Eqs. (15) and (16) represent the so-called generalized adiabatic approximation (also called generalized BO approximation[28,29]). As noted by Mead and Truhlar.[26,30,31] the ansatz in Eq. (13) leads to the appearance of a vector potential in the nuclear Schrödinger equation. Note that the $\mathbf{R}$-dependence of $A_I\left(\mathbf{R}\right)$ must reflect the presence of any conical intersection in accordance with the geometric phase[6,24] condition, and hence such a phase can generally be constructed only after the conical intersections have been located. Although a general approach for determining $A_I\left(\mathbf{R}\right)$ has been suggested by

Kendrick and Mead,[28] it remains a nontrivial task. An alternative approach consists of using the ansatz in Eq. (14), where the complex phase factor is absorbed in the real nuclear wave functions.[32–34] Although such an approach is especially convenient for X_3-type systems when adopting hyperspherical coordinates (since the complex phase factor concerns in principle only the φ hyperangle,[17,35]), it can be generalized[29,36,37] to the asymmetric case (see Sec. 4.1.1).

In the absence of a conical intersection, both Eq. (15) and Eq. (16) lead to the standard adiabatic nuclear Schrödinger equation

$$\left[-\frac{\hbar}{2\mu}\nabla^2_{\mathbf{R}'} + \overline{V}_i(\mathbf{R}) - E\right]\chi_I(\mathbf{R}') = 0 \tag{18}$$

which, for $I = 0$, describes the motion of the nuclei on the electronic ground state. Note that in the absence of a conical intersection, $\widetilde{G}_{II}(\mathbf{R}) = G_{II}(\mathbf{R})$, since one may choose $A_I(\mathbf{R}) = 0$.

Consider now the case of a 2×2 potential matrix $\mathbf{W}$, invariant and restricted to E space:

$$\mathbf{W} = W_{A_1}\begin{pmatrix} 1 & 0 \\ 0 & 1 \end{pmatrix} + W_x\begin{pmatrix} -1 & 0 \\ 0 & 1 \end{pmatrix} + W_y\begin{pmatrix} 0 & 1 \\ 1 & 0 \end{pmatrix} \tag{19}$$

where W_{A_1}, W_x, W_y are functions of the nuclear coordinates transforming under[c] C_{3v}, as indicated in an obvious correspondence by their subscripts ($x = r\cos\varphi$, $y = r\sin\varphi$). Thus, the energies reducing to the degenerate pair at the conical configuration are the eigenvalues of $\mathbf{W}$ given by

$$W_\pm = W_{A_1} \pm W_R \tag{20}$$

where $W_R = \left(W_x^2 + W_y^2\right)^{1/2}$. To all orders, the general form for the involved functions has been shown[38] to be

$$W_{A_1} = f_1\left[z; r^2, r^3\cos(3\varphi)\right] \tag{21}$$

$$W_x = r\cos\varphi f_3\left[z; r^2, r^3\cos(3\varphi)\right] + r^2\cos(2\varphi) f_4\left[z; r^2, r^3\cos(3\varphi)\right] \tag{22}$$

$$W_y = r\sin\varphi f_3\left[z; r^2, r^3\cos(3\varphi)\right] - r^2\sin(2\varphi) f_4\left[z; r^2, r^3\cos(3\varphi)\right] \tag{23}$$

where f_i ($i = 1-4$) are functions formally representable as a double power series in their arguments other than z, with the coefficients being constant

[c]We may consider only this subgroup of D_{3h}, since no out-of-plane bending is possible for a triatomic system. The component W_{A_2} must vanish, since $\mathbf{W}$ must be Hermitian, and in our case can be real.

or functions of z. From Eqs. (20) to (23), it follows:

$$W_{A_1} = W_{A_1}\left(z; r^2, r^3\cos 3\varphi\right) \tag{24}$$

$$W_R = r\left(f^2 + r^2 g^2 + 2rfg\cos 3\varphi\right)^{1/2} \tag{25}$$

$$\to rw\left(z; r^2, r\cos 3\varphi\right) \qquad (r \to 0) \tag{26}$$

where $f = f(z; r^2, r^3\cos 3\varphi)$, $g = g(z; r^2, r^3\cos 3\varphi)$, and w are formally analytic functions of their arguments. These equations define the correct behavior of the potential energy in the vicinity of the conical intersection, and hence may be valuable in delineating fitting forms.[38,39]

Let now $\tilde{\gamma}$ be an angle, itself a function of the nuclear coordinates, such that

$$W_x = W_R\cos\tilde{\gamma}, \;\; W_y = W_R\sin\tilde{\gamma}. \tag{27}$$

In terms of the degenerate pair of wave functions (Ψ_x, Ψ_y), we may write the two adiabatic ones (Ψ_+, Ψ_-) corresponding to the eigenvalues of Eq. (20) as

$$\Psi_+ = \Psi_x\sin(\tilde{\gamma}/2) + \Psi_y\cos(\tilde{\gamma}/2), \tag{28}$$

$$\Psi_- = \Psi_x\cos(\tilde{\gamma}/2) - \Psi_y\sin(\tilde{\gamma}/2) \tag{29}$$

which cannot be single-valued due to the appearance of $\tilde{\gamma}/2$ (note that both Ψ_+ and Ψ_- change sign when $\tilde{\gamma}$ increases by 2π). To make them single-valued, it has been suggested to use[26,30] the geometric phases $A_+(\mathbf{R}) = A_-(\mathbf{R}) = 3\varphi/2$, although other possibilities have been advocated[29,40] (see also Ref. 41). Since $\langle\Psi_+|\Psi_-\rangle = \delta_\pm$, one gets

$$\widetilde{\mathbf{F}} = \mathbf{F} = \langle\tilde{\Psi}_-|\nabla_{\mathbf{R}'}\tilde{\Psi}_+\rangle = -\langle\tilde{\Psi}_+|\nabla_{\mathbf{R}'}\tilde{\Psi}_-\rangle. \tag{30}$$

Using now Eqs. (28) to (30), one obtains

$$\mathbf{F} = \mathbf{F}^{\mathrm{lon}} + \mathbf{F}^{\mathrm{tra}} \tag{31}$$

where the curl-free longitudinal and divergence-free transverse (solenoidal) parts of the derivative coupling are given by[38]

$$\mathbf{F}^{\mathrm{lon}} = \frac{1}{2}\nabla_{\mathbf{R}'}\tilde{\gamma} \tag{32}$$

$$\mathbf{F}^{\mathrm{tra}} = \langle\Psi_x|\nabla_{\mathbf{R}'}\Psi_y\rangle \tag{33}$$

a result which is a consequence of the general Helmoltz decomposition theorem.

The longitudinal part of $\mathbf{F}$ shows a singularity at the conical intersection, but this singularity can be removed by a coordinate-dependent unitary transformation.[42] Moreover, from Eqs. (22), (23) and (27), one may write[38]

$$\tan\tilde{\gamma} = \frac{f\sin\varphi - rg\sin(2\varphi)}{f\cos\varphi + rg\cos(2\varphi)} \tag{34}$$

and defining ϵ such that $\tilde{\gamma} = \varphi + \epsilon$, one has

$$\tan\epsilon = -\frac{rg\sin(3\varphi)}{f + rg\cos(3\varphi)}. \tag{35}$$

Thus,

$$\mathbf{F}^{\text{lon}} = \frac{1}{2}\nabla_{\mathbf{R}'}\left\{\varphi - \tan^{-1}\left[\frac{rg\sin(3\varphi)}{f + rg\cos(3\varphi)}\right]\right\} \tag{36}$$

which defines the correct analytic properties of the nonadiabatic coupling near the seam of a potential energy surface exhibiting a C_{3v} conical intersection.[38,39,43,44]

Equation (32) can be solved by integration along paths in the nuclear configuration space.[45,46] The result will depend on the initial and final points of integration but not on the path chosen. Due to the GP theorem,[5,6,9] if the integration is carried out along a closed loop $\mathcal{C}$, $\tilde{\gamma}/2$ should change by[24,46,47]

$$\xi_{\tilde{\gamma}} = \oint_{\mathcal{C}} \mathbf{F}^{\text{lon}}(\mathbf{R})\, d\mathbf{R} = p\pi \tag{37}$$

where $p = 0$, if $\mathcal{C}$ does not enclose any conical intersection, and $p = 1$, if it does enclose one such an intersection.

The transverse part remains finite at the seam, and cannot generally be transformed away. However, it vanishes identically for a strictly diabatic two-state electronic basis,[d] and hence one may think of defining an

[d]It is well established that for orthonormalized wave functions such a perfect diabatization cannot generally exist for a polyatomic system.[42,45] However, a method has been suggested for constructing a strictly diabatic basis set for the two-state case by assuming non-normalized basis functions.[48]

(adiabatic-to-diabatic) angle[45,49,50] $\alpha(\mathbf{R})$ such that

$$\mathbf{F} = \nabla_{\mathbf{R}'}\alpha(\mathbf{R}) \tag{38}$$

which would be the angle[e] capable of transforming the adiabatic basis to a diabatic one, in which all the derivative couplings vanish identically. Similarly to the above, we may define a topological phase[51] as the phase accumulated by carrying out an equivalent integration of Eq. (38) along a closed path,

$$\xi_\alpha = \oint_{\mathcal{C}} \mathbf{F}\left(\mathbf{R}\right) d\mathbf{R}\,. \tag{39}$$

Since $\mathbf{F}$ does not generally satisfy Eq. (32), the result of such an integration will be path-dependent.[42] However, since the transverse part is finite (and possibly negligible, especially upon application of an optimal adiabatization[44] procedure), one may expect to have $\xi_{\tilde{\gamma}} = \xi_\alpha$. Note that the mixing angle $\gamma(\mathbf{R}) = \tilde{\gamma}/2$ that diagonalizes the potential matrix is (up to a constant) identical to $\alpha(\mathbf{R})$[40] and the geometric phase $A_I(\mathbf{R})$.[29]

3. Strategies for Multi-Sheeted Potential Energy Surfaces

Multi-sheeted potential energy surfaces are required whenever more than one possible set of electronic states are allowed per channel to break or form a polyatomic molecule. This is a situation very frequently encountered in studying chemical reactions, since the reactants and/or products are often radicals with open shells and nearly degenerate orbitals. Clearly, two distinct approaches to multi-sheeted potential energy surfaces can be envisaged. The first consists of fitting the various adiabatic potential energy surfaces which stem from the diagonalization of the electronic Hamiltonian matrix, either separately or using a multi-sheeted potential model. In the other, one fits instead the various diagonal and coupling terms of the potential matrix, each one per se; the adiabatic potentials can then be obtained by diagonalizing the fitted diabatic potential matrix. Both such approaches have merits and drawbacks. The first strategy may be more advantageous if the aim is to solve adiabatically the nuclear equations of motion, either as a single-sheet or a coupled multi-sheet problem. Of course, in this case one

[e]To avoid confusion with the Euler angle α, we indicate explicitly its dependence on $\mathbf{R}$. A similar procedure is adopted for $\gamma(\mathbf{R})$.

requires the knowledge of the derivative coupling terms, which suffer from the numerical difficulties already mentioned in Sec. 2.1. Moreover, one must ensure that the crossing seam is accurately reproduced and the adiabatic potential energy surfaces show the correct analytic properties close to the crossing seam. This cannot be ignored if the proper topological properties are to be warranted. For the 2×2 case, fits to the separate adiabatic potential energy surfaces can in principle be done either using interpolation methods or a carefully chosen global fitting form. In this case, the use of polynomial forms employing non-analytic coordinates[52] such as $q = \left(Q_2^2 + Q_3^2\right)^{1/2}$ for a X_3-type molecule may in special cases offer a method of choice. The other strategy is recommended for a diabatic treatment of the dynamics, but then a method is required to obtain the input data necessary to calibrate the elements of the diabatic potential matrix, as they cannot be obtained by solving the electronic Schrödinger equation. If *ab initio* energies are to be used, the question is how to find a similarity transformation that leads from the adiabatic to the diabatic potential matrices. In fact, strictly diabatic basis sets that fully remove the nonadiabatic coupling terms do not generally exist[42] and, for the two-state problem, the standard technique[45,50,53–55] based on the integration of Eq. (38) can be hopelessly cumbersome, because the result is path-dependent.[42] Although the use of some electronic properties (e.g. dipole matrix elements) has been suggested[8,40,46,47,56–66] to find such an adiabatic-to-diabatic transformation angle, the fact that such elements are made small does not lead to a rigorous treatment. Whatever approach is chosen, there are general requirements that are common to both modelling strategies and the single-surface problem, and it is on them that we now digress.

3.1. *General Rules*

A common starting point is to presume that the electronic Schrödinger equation has been solved at sufficiently many nuclear configurations to determine the potential energy surface (or sheets of the relevant adiabatic manifold). Although *ab initio* electronic structure calculations are becoming increasingly accurate, this poses a formidable undertaking: *ab initio* energies are calculated by pointwise solution of the electronic Schrödinger equation, while the dynamics studies require a quick and efficient method to evaluate the potential energy surface for any geometry of the nuclei. Semiempirical

methods can then be of major importance for dynamics studies. However, for systems containing a small number of light atoms, state-of-the-art *ab initio* calculations can reach sufficient accuracy to be of practical interest for direct use in molecular dynamics. In this case, interpolation schemes may be valuable to generate such data, even if some semiempirical correction is necessary to account for the unavoidable errors due to truncation of the configuration interaction expansion and incompletness of the one-electron basis sets.[67–69] Of course, direct dynamics approaches or mixed ones (direct dynamics/local interpolation methods) are unaffordable if the computational effort per point is too demanding to calculate more than a thousand points or so.

For the single-surface problem, Wright and Gray,[70] following a suggestion by Kuntz,[71] enumerated ten criteria that a potential form should satisfy to be successful:

(1) It should accurately characterize the asymptotic reactant and product molecules (or more generally any fragment of the full system).
(2) It should have the correct symmetry properties of the system.
(3) It should represent the true potential energy surface accurately in interaction regions for which experimental or nonempirical theoretical data are available (including, in principle, the very short-range and long-range regions associated with the various asymptotic channels[72,73]).
(4) It should behave in a physically reasonable manner in those parts of the interaction region for which no experimental or theoretical data are available.
(5) It should smoothly connect the asymptotic and interaction region in a physically reasonable way.
(6) The interpolating function and its derivatives should have as simple an algebraic form as possible consistent with the desired quality of the fit.
(7) It should require as small a number of data points as possible to achieve an accurate fit.
(8) It should converge to the true surface as more data become available.
(9) It should indicate where it is most meaningful to compute the data points.
(10) It should have a minimal amount of *ad hoc* or 'patched up character'.

Connor[74] noted that criteria (1)–(5) are essential (the remaining five are less essential, although highly desirable), and Schatz[75] remarked that such criteria may lead to conflicting strategies, since simplicity and accuracy are goals that are rarely met together. In an attempt to maximize accuracy and simplicity, we have advocated[72,73] the use of physically motivated forms.

Although offering the least-biased approach to potential energy surfaces, *ab initio* calculations seldom meet the standards of spectroscopic ($\leq 1\,\mathrm{cm}^{-1}$) or even chemical ($\leq 1\,\mathrm{kcal\,mol}^{-1}$) accuracy. On the other hand, vibrational-rotational spectra and kinetics data cannot generally be inverted directly to yield the potential energy surface. The only practical way available to test and improve such surfaces is therefore by comparing the calculated and experimental results, and minimize the difference between the two. Two approaches are then possible. One involves an iterative process, in which the least-squares parameters in a given potential model are, in its most sophisticated form, determined from a multiproperty fit to *ab initio* data, vibrational-rotational levels, and eventually other types of information. In this case, an *ab initio* based potential model can offer an excellent starting point for the fitting procedure, as it has recently been demonstrated[76] for SO_2. The other approach consists of merging a local potential with spectroscopic quality with a global, but less accurate, one (see Sec. 3.2.4). Both these strategies are illustrated schematically in Fig. 1, assuming, just for the sake of illustration, that the global function is of the double many-body expansion (DMBE) type to be discussed in Sec. 3.2.2.

Difficulties arise also in choosing a set of internal coordinates for a system with five atoms or more, since there are $N(N-1)$ internal coordinates but only $(3N-6)$ are independent: a set of $(3N-6)$ coordinates may then be locally complete near one configuration, but incomplete near another (for an illustration, see Ref. 77), implying that different Decius's coordinates sets should be used at those configurations. Although this may suggest that the potential energy function cannot be an analytic function of the coordinates,[2] it does not by itself show that for such systems it is impossible to find a set of internal coordinates in which the potential energy is an analytic function. In fact, a recent study on HO_4 suggests[78] that the natural coordinates in which to work may be the internuclear distances, even if they form a redundant set. Indeed, such a set has the advantage of making it easier to impose symmetry invariance under permutations.

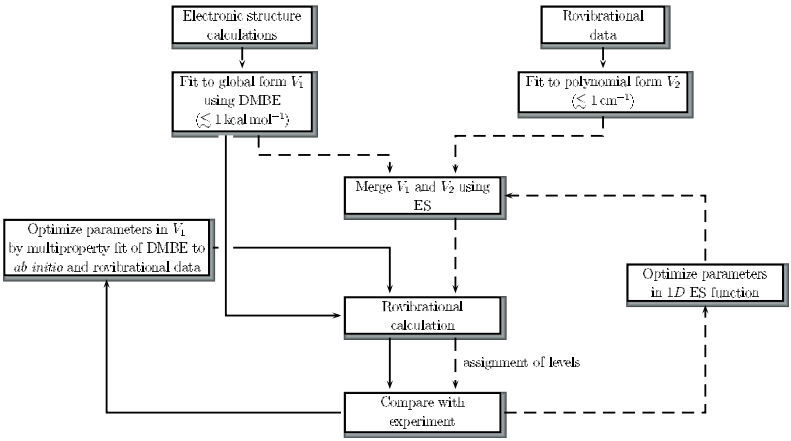

Fig. 1. Strategies for the construction of potential energy surfaces with 'near' spectroscopic accuracy. The solid lines indicate the direct fit of spectroscopic data using a DMBE form, while the dashed lines show the process followed to obtain an ES form.

Several approaches have been proposed to develop potential energy surfaces for dynamics calculations, as reviewed in a variety of places.[72,75,79–86] These methods may be categorized as global methods and local methods. In the former, the potential energy surface is determined at each point by all the data (*ab initio* points and/or other information) that are used as input for the calibration procedure. Among the global methods, we consider the following sub-categories:

- Functional forms obtained from quantum chemistry, such as those based on semiempirical valence-bond or related theories,[87–93] and many-body expansion type developments.[72,73,79,85]
- Fitting forms obtained from other motivations such as standard cubic-spline[94] methods, Morse-spline[95] and rotated Morse-spline[70] interpolation methods, reproducing kernel Hilbert space[96,97] interpolation methods, distributed approximating functionals,[98] and hybrid methods combining spline fits with simple empirical functions.[99]
- Energy-switching[100] methods based on merging forms which are reliable for different energy regimes.

In turn, the local methods determine the potential energy surface at each point based only on *ab initio* data that is available for geometries close to

that point. They include:

(1) Shepard interpolation methods;[101,102]
(2) Moving least-squares methods;[103,104]
(3) Interpolation on the fly[104] using the *ab initio* force field data obtained when doing direct reaction dynamics.[105]

Naturally, we can discuss only a subset of such methods by focusing on possible applications to multi-sheeted potential energy surfaces.

3.2. *Global Methods*

Among the global methods, two approaches are highlighted: the semi-empirical diatomics-in-molecules[91–93] (DIM) and the double many-body expansion[72,73,85] (DMBE) methods. Regarding the interpolation techniques, we focus on the global reproducing kernel Hilbert space[97] method, and the local Shepard interpolation[101,102] and moving least-squares[103,104] approaches. Inevitably, the analysis may favor approaches developed in the author's group; the reader is addressed to the original literature for more details.

3.2.1. *Diatomics-in-Molecules*

In the DIM method, originally proposed by Ellison[91] and subsquently developed by Tully [92] and Kuntz, [93] the lth electronic state is first written as the expansion $\Psi_l = \sum_m C_{ml}\Phi_m$ which runs over some finite set of polyatomic basis functions Φ_m. This leads to the eigenvalue matrix equation

$$\mathbf{HC} = \mathbf{SCE} \tag{40}$$

where $H_{mm'} = \langle \Phi_m | H_e | \Phi_{m'} \rangle$ and $S_{mm'} = \langle \Phi_m | \Phi_{m'} \rangle$ are the Hamiltonian and overlap matrix elements, respectively, and $\mathbf{E}$ is a diagonal matrix.

Then, the electronic Hamiltonian H_e is partitioned as

$$H_e = \sum_K \sum_{L>K} H_e^{KL} - (N-2) \sum_K H_e^K \tag{41}$$

where H_e^K is an atomic Hamiltonian operator that depends on the electrons and coordinates of atom K, H_e^{KL} is a diatomic Hamiltonian depending on the electrons and coordinates of atoms K and L and their interactions, and the factor $(N-2)$ corrects for the multiple counting of the atomic fragments.

In turn, the polyatomic basis functions are written as

$$\Phi_m = \mathcal{A}\phi_m^0 = \mathcal{A}A_i B_j C_k \ldots \tag{42}$$

where $\mathcal{A}$ is the n-electron antisymmetrizer, and A_i, $B_j, \ldots$ are atomic functions which are already antisymmetric with respect to interchange of any two electrons in the atom, and i, j, $k, \ldots$ label the set of atomic quantum numbers. Such wave functions are eigenfunctions of the spin ($\hat{S}^2$ and $\hat{S}_z$) and angular momentum ($\hat{L}^2$ and $\hat{L}_z$) operators, and correspond to definite values of the atomic energy. Moreover, they refer to a common space-fixed system of axis, with their transformation properties being given by

$$\hat{R}(\alpha,\beta,\gamma)|LM\rangle = \sum_{M'} R^{(L)}_{MM'}(\alpha,\beta,\gamma)|LM'\rangle \tag{43}$$

where $R^{(L)}_{MM'}(\alpha,\beta,\gamma)$ is the rotational matrix,[19] and $|LM\rangle$ a wave function with orbital angular momentum L and projection M. For triatomics, the wave functions are often defined such that they have the proper symmetry within the point group C_s. For example, for $L = 1$, they are written as

$$(P_x, P_y, P_z) = \frac{1}{\sqrt{2}}(P_1, P_0, P_{-1}) \begin{bmatrix} -1 & -1 & 0 \\ 0 & 0 & \sqrt{2} \\ 1 & -1 & 0 \end{bmatrix}. \tag{44}$$

Similarly, it is convenient to construct linear combinations of the orbitals $\{\Phi_m\}$ that are eigenfunctions of the total spin for the molecular system.

From Eqs. (41) and (42), and the fact that $\mathcal{A}$ commutes with H_e, one obtains[92]

$$H^{KL}_{mm'} = \langle\phi^0_m|H^{KL}_e|\phi^0_{m'}\rangle \tag{45}$$

$$H^{K}_{mm'} = \langle\phi^0_m|H^{K}_e|\phi^0_{m'}\rangle. \tag{46}$$

The atomic fragment matrix is easily evaluated, since H^K_e is the Hamiltonian for atom K and ϕ^0_m is a direct product of atomic eigenvectors. For atom A, one gets

$$H^A_{mm'} = \langle\phi^0_m|H^A_e|A_{i'}B_{j'}C_{k'}\ldots\rangle = E^A_{i'}\langle\phi^0_m|\phi^0_{m'}\rangle \tag{47}$$

where $m \equiv (i,j,k,\ldots)$, $m' \equiv (i',j',k',\ldots)$, and $E^A_{i'}$ are the exact atomic eigenvalues for atom A which can be obtained from atomic tables.

Similarly, by denoting the exact diatomic eigenvectors for the KL fragment by $\{\psi_\eta^{KL}\}$, and inserting $\sum_\eta |\psi_\eta^{KL}\rangle\langle\psi_\eta^{KL}|$ after the operator H^{KL} in Eq. (45), one obtains:

$$H_{mm'}^{KL} = \sum_\eta \langle\phi_m^0|\psi_\eta^{KL}\rangle E_\eta^{KL} \langle\psi_\eta^{KL}|\phi_{m'}^0\rangle \tag{48}$$

where E_η^{KL} is the exact diatomic energy eigenvalue for diatom KL, which is a function of the distance between K and L, and η specifies the set of diatomic quantum numbers. The exact diatomic eigenvectors so obtained are then expanded in terms of a complete set of atomic eigenvectors. For the case of diatomic AB, one has

$$\psi_\eta^{AB} = \sum_{ij} \langle\psi_\eta^{AB}|\mathcal{A}_{AB}A_iB_j\rangle \mathcal{A}_{AB}A_iB_j = \sum_{ij} U_{ij,\eta}^{AB} \mathcal{A}_{AB}A_iB_j \tag{49}$$

where $\mathcal{A}_{AB}$ is the $(n_A + n_B)$-electron antisymmetrizer. Substitution of ψ_η^{AB} in Eq. (48), leads now to

$$H_{mm'}^{AB} = \sum_{\eta,rs,r's'} S_{ij,rs}^{AB} U_{rs,\eta}^{AB} E_\eta^{AB} U_{\eta,r's'}^{AB\dagger} S_{r's',i'j'}^{AB\dagger} \tag{50}$$

where $S_{ij,rs}^{AB} = \langle B_jA_i|\mathcal{A}_{AB}|A_rB_s\rangle$. Being a semiempirical method, it is common to set all overlap matrices to unit matrices. Equations (47) and (50) then become

$$H_{mm'}^{A} \sim E_{i'}^{A}\delta_{ii'}\delta_{jj'}\delta_{kk'} \tag{51}$$

$$H_{mm'}^{AB} \sim \sum_\eta U_{ij,\eta}^{AB} E_\eta^{AB} U_{\eta,i'j'}^{AB\dagger}\delta_{kk'} \tag{52}$$

where $\mathbf{U}^{AB}$ is a real orthogonal matrix and the Hamiltonian matrices are symmetric. The former can be decomposed as

$$\mathbf{U}^{AB} = \mathbf{R}^{AB}\mathbf{T}^{AB} \tag{53}$$

where $\mathbf{R}^{AB}$ is a direct product of the rotation matrices (these rotate the A_i and B_j eigenvectors so that their z-axis are aligned with the internuclear axis of diatom AB), and $\mathbf{T}^{AB}$ is a spin-recoupling matrix which transforms the original coupling of spin states to one in which A couples with B. For a triatomic system, these are the well known 6-j coefficients. Often, further partitions of $\mathbf{U}^{AB}$ are convenient to impose other transformation

properties.[106] Thus, relative to the separated atoms, the diabatic potential energy surface of a triatomic system becomes

$$\mathbf{W} = \mathbf{E}^{AB} + \mathbf{R}^{BC}\mathbf{T}^{BC}\mathbf{E}^{BC}\mathbf{T}^{BC\dagger}\mathbf{R}^{BC\dagger} + \mathbf{R}^{AC}\mathbf{T}^{AC}\mathbf{E}^{AC}\mathbf{T}^{AC\dagger}\mathbf{R}^{AC\dagger} - \mathbf{H}^{A} - \mathbf{H}^{B} - \mathbf{H}^{C} \tag{54}$$

where it is assumed that the basis set corresponds to the spin coupling of the diatomic AB at first, and the axis of quantization is directed along this fragment.

3.2.2. *Double Many-Body Expansion*

The DIM approach has the appealing feature of having quantum mechanical origin, leading in principle to the exact solution of the electronic problem if complete basis sets are used. However, it has gained its greatest popularity as a semiempirical method, since it preserves in principle the correct structure of the potential matrix. Thus, one usually carries the approximations to the extreme by employing minimal basis sets and ignoring overlap between the basis functions. Eq. (48) is then no longer accurate, since the accuracy with which the matrix elements can be expressed by one-center and two-center integrals increases with basis set size.[107] A major goal would then be to correct the DIM formulation for the neglect of many-center terms and orbital overlap.

Within this spirit, we have recently shown[85] that, to second-order of approximation, Eq. (45) may be written as

$$H^{KL}_{mm'} = \sum_{\eta} \langle \phi^{0}_{m} | \psi^{KL}_{\eta} \rangle \left(E^{KL}_{\eta} + F^{KL}_{mm'} \right) \langle \psi^{KL}_{\eta} | \phi^{0}_{m'} \rangle \tag{55}$$

where

$$F^{KL}_{mm'} = \frac{\langle \psi^{KL}_{\eta} | \phi'_{m'} \rangle + \langle \phi'_{m} | \psi^{KL}_{\eta} \rangle}{\langle \psi^{KL}_{\eta} | \phi^{0}_{m'} \rangle} \tag{56}$$

and $F^{KL}_{mm'}$ is some unknown function, which may be treated as a geometry-dependent arbitrary form for each mm' matrix element of diatomic KL. Such functions may then carry adjustable parameters, which can be calibrated from a fit to accurate *ab initio* energies or empirical data. By expanding the exact diatomic eigenvectors in terms of a complete set of atomic

eigenvectors, one gets for the KL pair[85]

$$\mathbf{H}^{KL} = \mathbf{R}^{KL}\mathbf{T}^{KL}\mathbf{E}^{KL}\left(\mathbf{1}+\mathbf{F}^{KL}\right)\mathbf{T}^{KL^{\dagger}}\mathbf{R}^{KL^{\dagger}}. \tag{57}$$

For a triatomic system, the diabatic potential matrix assumes then the form

$$\begin{aligned}\mathbf{W} = {} & \mathbf{E}^{AB}\left(\mathbf{1}+\mathbf{F}^{AB}\right)+\mathbf{R}^{BC}\mathbf{T}^{BC}\mathbf{E}^{BC}\left(\mathbf{1}+\mathbf{F}^{BC}\right)\mathbf{T}^{BC^{\dagger}}\mathbf{R}^{BC^{\dagger}} \\ & +\mathbf{R}^{AC}\mathbf{T}^{AC}\mathbf{E}^{AC}\left(\mathbf{1}+\mathbf{F}^{AC}\right)\mathbf{T}^{AC^{\dagger}}\mathbf{R}^{AC^{\dagger}}-\mathbf{H}^{A}-\mathbf{H}^{B}-\mathbf{H}^{C}\end{aligned} \tag{58}$$

where $\mathbf{1}$ is a matrix of unit elements. Explicitly, one has for the ij matrix element:

$$\begin{aligned}W_{ij} = {} & E_{ij}^{AB}\left(1+F_{ij}^{AB}\right) \\ & +\sum_{k}\sum_{l}\sum_{m}\sum_{n}\Big[R_{ik}^{BC}T_{kl}^{BC}E_{lm}^{BC}\left(1+F_{lm}^{BC}\right)T_{mn}^{BC^{\dagger}}R_{nj}^{BC^{\dagger}} \\ & +R_{ik}^{AC}T_{kl}^{AC}E_{lm}^{AC}\left(1+F_{lm}^{AC}\right)T_{mn}^{AC^{\dagger}}R_{nj}^{AC^{\dagger}}\Big] \\ & -H_{ij}^{A}-H_{ij}^{B}-H_{ij}^{C}.\end{aligned} \tag{59}$$

Clearly, the DIM expression is recovered when $F_{mm'}^{KL} = 0$ for all mm' and KL.

Consider now the simplest case of interacting ^1S atoms, where the potential energy surface has dimension 1×1. Thus, it assumes the pairwise additive form

$$V(\mathbf{X}^N) = \sum_{\mathbf{X}^2\subset\mathbf{X}^N} V^{(2)}(\mathbf{X}^2)\left[1+F^{(N)}(\mathbf{X}^N)\right] \tag{60}$$

with the energies of the isolated atoms being taken as the reference energy. Note that $\mathbf{X}^n$ specifies any set of $n(n-1)/2$ interatomic distances referring to n atoms [this is a subset of $\mathbf{X}^N \equiv \left(X_1, X_2, \ldots, X_{N(N-1)/2}\right)$], and the "dressing functions" account for many-body interactions higher than two-body. By partitioning now the energy into an extended Hartree–Fock (EHF) part and a dynamical correlation (dc) part, and further developing $V_{EHF}^{(2)}(\mathbf{X}^2)F^{(N)}(\mathbf{X}^N)$ and $V_{dc}^{(2)}(\mathbf{X}^2)F^{(N)}(\mathbf{X}^N)$ as a cluster expansion, one obtains without any loss of generality

$$V(\mathbf{X}^N) = \sum_{n=2}^{N}\sum_{\mathbf{X}^n\subset\mathbf{X}^N}\left[V_{EHF}^{(n)}(\mathbf{X}^n)+V_{dc}^{(n)}(\mathbf{X}^n)\right] \tag{61}$$

which is the familiar DMBE form for single-valued potential energy surfaces. Of course, a fundamental requirement of DMBE (as well as other

formulations) is to have accurate representations of the potential energy curves for the relevant electronic states of the diatomic fragments, an issue discussed further in Appendix B. For specific forms of many-body energy terms, the reader is referred to Ref. 72.

The use of Eq. (61) to represent the potential energy surface of interacting atoms of arbitrary spin and angular momentum rests therefore on the neglect of the spin-recoupling and orientational effects. For open-shell atoms, chemical bonding may occur to form stable diatomic fragments, and hence there will be a deep minimum if the cluster expansion is truncated at the two-body level. To cancel such a minimum in part or completely, one then has to add repulsive higher-order energy terms. Other features of the potential energy surface such as crossings and avoided crossings will, of course, also be absent at the two-body level. Not surprisingly, therefore, Eq. (61) may in some cases be a poor starting point for an accurate fit of the complete adiabatic potential energy surface. For such cases, a more appropriate treatment consists of diagonalizing the potential matrix that results from Eqs. (41) and (57). Alternatively, we may use the matrix formulation proposed by Murrell *et al.*[79] for multivalued functions:

$$\mathbf{W}(\mathbf{R}) = \begin{bmatrix} W_{11}(\mathbf{R}) & W_{12}(\mathbf{R}) & \cdots & W_{1n}(\mathbf{R}) \\ W_{12}(\mathbf{R}) & W_{22}(\mathbf{R}) & \cdots & W_{2n}(\mathbf{R}) \\ \vdots & \vdots & \ddots & \vdots \\ W_{1n}(\mathbf{R}) & W_{2n}(\mathbf{R}) & \cdots & W_{nn}(\mathbf{R}) \end{bmatrix} \tag{62}$$

where the matrix elements are developed as many-body expansions or double many-body expansions involving the appropriate electronic states of the fragments. Although a correspondence between Eqs. (62) and (58) may be established only for a matrix representation of a given dimensionality, both formalisms are interelated and may in principle be calibrated from a fit to available data. Of course, difficulties in describing surface intersections in a correct quantum mechanical manner may turn out to be more critical when using Eq. (62), although such a problem may in principle be minimized if a good coverage of the molecular configuration space is provided by the *ab initio* data.

3.2.3. *Reproducing Kernel Hilbert Space*

The RKHS method proposed by Ho and Rabitz[96,108,109] provides a general approach to interpolation from a grid (not necessarily rectangular) of *ab initio* points. However, conversely to the traditional spline forms, it allows to develop interpolation functions which satisfy important boundary conditions and other constraints. For example, it may lead to smooth surfaces capable of extrapolation to the appropriate dissociation limits. Moreover, for diatomic curves, it may be chosen to satisfy the proper asymptotic dependendence on bond distance as $R \to \infty$. However, like the traditional spline methods, RKHS quickly runs into difficulties for problems with high dimensionality (tetratomic or larger systems). In the following, we survey the basic RKHS formalism by focusing on the simplest one-dimensional case. In fact, for systems with three or more dimensions, the usual strategy is to use a many-body expansion[79] of the potential energy surface and define the various multidimensional kernels from direct products of kernels developed separately for each degree of freedom.

As in all interpolation methods, one uses the potential at a given set of points $\{V(R_i)\}$ to determine the global $V(R)$. To do this while keeping $V(R)$ smooth, one imposes that $V(R)$ satisfies the reproducing property

$$V(R) = \int q(R, R')V(R')dR' \tag{63}$$

with the kernel $q(R, R')$ being determined by the order of smoothness required and the boundary conditions associated with the chosen coordinates. For a set of *ab initio* points, $V(R)$ is chosen such that Eq. (63) is exactly satisfied at each such point:

$$V(R_j) = \int q(R_j, R')V(R')dR' \qquad j = 1, \ldots, N. \tag{64}$$

The solution assumes the form

$$V(R) = \sum_{i=1}^{N} \alpha_i q(R_i, R) \tag{65}$$

where α_i are linear parameters obtained[96] by solving (directly or by singular value decomposition) the system of linear equations

$$\sum_{i=1}^{N} q(R_j, R_i)\alpha_i = V(R_j) \qquad j = 1, \ldots, N. \tag{66}$$

As an example of a reproducing kernel, Ho and Rabitz [96] suggested

$$q^{n,m}(x,x') = n^2 x_>^{-(m+1)} B(m+1,n)\ {}_2F_1\left(-n+1, m+1; n+m+1; \frac{x_>}{x_<}\right) \tag{67}$$

where $x_>$ and $x_<$ are the larger and smaller of x and x', $B(a,b)$ is the beta function, ${}_2F_1(a,b;c;z)$ is the Gauss hypergeometric function, and n and m in $q^{n,m}$ are superscripts definining the order of smoothness of the function and its asymptotic behavior (x^{-m}). For $n > 1$ (negative a), Eq. (67) reduces to the polynomial form

$$q^{n,m}(x,x') = \frac{1}{x_>^{m+1}} \sum_{k=0}^{n-1} \beta_k^{n,m} \frac{x_>^k}{x_<^k} \tag{68}$$

where the coefficients $\beta_k^{n,m}$ are implicitly given.[96] At large distances $R > R_N$, one has

$$V(R) = -\sum_{k=0}^{n-1} \frac{C_{m+k+1}^{n,m}}{R^{m+k+1}} \tag{69}$$

where

$$C_{m+k+1}^{n,m} = \beta_k^{n,m} \sum_{i=1}^{N} \alpha_i R_i^k \tag{70}$$

provides the expression for the long range coefficients. The choice $n = 2$ and $m = 5$ yields an asymptotic behavior of R^{-6}, which corresponds to the power of the leading term in the dispersion series expansion. Interpolating instead with respect to $y = R^2$ and using $(n = 2, m = 1)$, yields the form[110]

$$V(R) = -\frac{C_2^{2,1}}{R^4} - \frac{C_3^{2,1}}{R^6} \tag{71}$$

which shows only even powers in the inverse-R expansion development. However, the behavior of the potential at short distances is less satisfactory. For $R < R_1$, one obtains

$$V(R) = \sum_{k=0}^{n-1} d_k^{n,m} R^k \tag{72}$$

where

$$d_k^{n,m} = \beta_k^{n,m} \sum_{i=1}^{N} \frac{\alpha_i}{R_i^{m+k+1}} \tag{73}$$

which shows that the RKHS method extrapolates at short distance as a polynomial function of degree $n-1$. Since, as usual, n is chosen to be a small integer, the extrapolation to the repulsive wing of the potential curve (surface) can be rather poor.[110,111] This implies that the grid of *ab initio* energies must extend to rather short distances which may not be easy to do, as the calculated points often tend to be unreliable there.

3.2.4. *Energy-Switching*

Ideally, a global potential energy surface should be capable of achieving spectroscopic accuracy at regions where such an information is available. Aiming at this goal, we have proposed[100] a simple approach which is based on the switching between two forms: one (V_1), global, which provides a realistic (though not necessarily accurate) description of the surface at all regions of configuration space; the other (V_2), local, which is capable of achieving spectroscopic accuracy near the minima to which the available spectroscopic information pertains (see Fig. 1). Because the switching uses the energy as the single coordinate, the method has been named as *energy-switching*[100] (ES). Thus,

$$V_{\mathrm{ES}} = f(\Delta E)V_1(\mathbf{R}) + [1 - f(\Delta E)]V_2(\mathbf{R}) \tag{74}$$

with a convenient switching form being

$$f = \frac{1}{2}\{1 + \tanh[\gamma_E(\Delta E)\Delta E]\} \tag{75}$$

where $\Delta E = E - E_0$ is the energy difference relative to the reference energy E_0, and γ_E is some function of ΔE which is chosen to warrant the correct asymptotic limits in f.[100,112]

The ES method has been extensively tested on the water molecule, for which single-valued,[100] double-valued,[112] and triple-valued[113] potential energy surfaces of DMBE-type quality have been completed which reproduce the vibrational spectroscopy of H_2O within a few cm^{-1}. The method has also been successfully employed to obtain "spectroscopically accurate" two-valued functions for H_3^+ [114,115] and NO_2,[116] and single-valued functions

for HeHCN[117] and ArHCN.[118] Moreover, it has been used to generate an improved DMBE potential energy surface[119] for HO_3 by combining a local four-body potential fitted to accurate *ab initio* energies with one previously reported for the original DMBE function.[120] We emphasize that van der Waals molecules may provide a class of systems for which the ES method turns out to be particularly useful, given the orders of magnitude difference involved in the relevant dynamical processes.

Clearly, the ES method can only be used for adiabatic potential energy surfaces, since the spectroscopic data refers to the eigenvalues of the true Hamiltonian. One then requires some diabatization scheme to go from the diagonal adiabatic potential matrix $\mathbf{V}^{ES}$ to the complete diabatic one $\mathbf{W}^{ES}$. In principle, this may be done through numerical back-transformation

$$\mathbf{W}^{ES} = \mathbf{U}\mathbf{V}^{ES}\mathbf{U}^{\dagger} \tag{76}$$

where $\mathbf{U}$ is the orthogonal matrix which diagonalizes the original diabatic potential matrix, i.e., $\mathbf{V} = \mathbf{U}\mathbf{W}\mathbf{U}^{\dagger}$. Of course, the reliability of such a procedure stems from the premise that and ES ($\mathbf{V}^{ES}$) and global ($\mathbf{V}$) adiabatic potential energy surfaces should in principle have very similar topographies.[112]

3.3. *Local Methods*

3.3.1. *Shepard Interpolation*

In the Shepard interpolation method, the potential is written in the form

$$V(\mathbf{R}) = \sum_{i=1}^{N} \omega_i(\mathbf{R}) T_i(\mathbf{R}) \tag{77}$$

where $\mathbf{R}$ is the vector of internal coordinates, and $\omega_i(\mathbf{R})$ is the weight associated to the Taylor series expansion $T_i(\mathbf{R})$. The idea underlying such an approach is that we have *ab initio* data of sufficient density such that any geometry of interest is within the domain of convergence of Taylor series expansions about at least one point in the *ab initio* data set. Since the weights depend on the geometry, they may be viewed as switches which "turn on" whenever the *ab initio* points are suitably close to the geometry being considered. The total potential will then be just the weighted average

of Taylor expansion estimates from the nearby points. For this, the weight functions must satisfy

$$\omega_i(\mathbf{z}) \to 1 \qquad (|\mathbf{z} - \mathbf{z}(i)| \to 0) \tag{78}$$

$$\omega_i(\mathbf{z}) \to 0 \qquad (|\mathbf{z} - \mathbf{z}(i)| \to \infty) \tag{79}$$

which may be achieved with

$$\omega_i(\mathbf{z}) = \left\{ \sum_{\alpha=1}^{3N-6} [z_\alpha - z_\alpha(i)]^2 + a^2 \right\}^{-p} \tag{80}$$

once every function is properly normalized by dividing by their sum. The parameter p determines how quickly the weight function dropps off, while a is chosen such as to avoid that the weight function becomes singular at the position of each data point; for a discussion on the optimal choices of these coefficients, see Ref. 121.

A critical issue in this method is the appropriate choice of the coordinates to carry out the expansions. Collins and coworkers[122] suggested the use of $\mathbf{z} = \mathbf{R}^{-1}$, which has the advantage that a single point in Eq. (77) describes accurately the asymptotic behavior of the isolated diatomic potential.[121] In addition, Taylor series expansions in such coordinates have a much larger domain of convergence for diatomic potentials that the corresponding expansions in the coordinates themselves. Another important issue is the order of the Taylor series expansions. A high-order expansion would be expected to have an extended domain of convergence, which would imply a smaller number of points to achieve an acceptable surface. However, few *ab initio* codes provide derivatives higher than quadratic, and those which do may not be the recommended methods to describe chemical reactions. The best methods usually provide only energies and gradients, which is an handicap to the Shepard interpolation schemes that have been shown by Collins[122] to require gradient and hessian information in order to obtain reliable surfaces.

3.3.2. *Moving Least-Squares*

In this method, the potential is expanded using a set of basis functions $\{b_k(\mathbf{R})\}$ as

$$V(\mathbf{R}) = \mathbf{a}^T(\mathbf{R})\mathbf{b}(\mathbf{R}) = \sum_{k=1}^{K} a_k(\mathbf{R}) b_k(\mathbf{R}). \tag{81}$$

Thus, it has a form similar to that used in conventional least-squares approaches, but with the weights being themselves a function of $\mathbf{R}$. Also as in conventional least-squares, the parameters $a_k(\mathbf{R})$ are obtained by making stationary the functional

$$E(V) = \sum_{j=1}^{N} \omega_j(\mathbf{R}) \left[V(\mathbf{R}_j) - v_j\right]^2 \tag{82}$$

where $(\mathbf{R}_j, v_j)$ is a point to be interpolated. This leads to the following generalized normal equations

$$BW(\mathbf{R})B^T\mathbf{a}(\mathbf{R}) = BW(\mathbf{R})\mathbf{f} \tag{83}$$

where $W(\mathbf{R})$ is a diagonal matrix from all the weights

$$W = \text{diag}\left[\omega_1(\mathbf{R}), \omega_2(\mathbf{R}), \ldots, \omega_N(\mathbf{R})\right] \tag{84}$$

and B is composed by the values of the basis functions $\{b_k(\mathbf{R})\}$ at $\mathbf{R}_j$,

$$B = \begin{bmatrix} b_1(\mathbf{R}_1) & b_1(\mathbf{R}_2) & \cdots & b_1(\mathbf{R}_N) \\ b_2(\mathbf{R}_1) & b_2(\mathbf{R}_2) & \cdots & b_2(\mathbf{R}_N) \\ . & . & \cdots & . \\ b_K(\mathbf{R}_1) & b_K(\mathbf{R}_2) & \cdots & b_K(\mathbf{R}_N) \end{bmatrix}. \tag{85}$$

Clearly, for data points close to $\mathbf{R}$, the weights should be larger than for points far away. This can be accomplished by using the function in Eq. (80). Because the weights depend on position, the coefficients must be determined by solving Eq. (83) for each value of $\mathbf{R}$ where the potential is to be determined. For dynamics calculations, one often requires to know also the gradient of the potential, which requires the solution of another system of linear equations at each value of $\mathbf{R}$, namely

$$u_s(\mathbf{R}) = \mathbf{a}_s^T(\mathbf{R})\mathbf{b}(\mathbf{R}) + \mathbf{a}^T(\mathbf{R})\mathbf{b}_s(\mathbf{R}) \tag{86}$$

where the subscript s denotes the derivative with respect to the sth coordinate. In turn, $\mathbf{a}_s$ is obtained by solving the following system of linear equations

$$BW(\mathbf{R})B^T\mathbf{a}_s(\mathbf{R}) = BW_s(\mathbf{R})\left[\mathbf{f} - B^T\mathbf{a}(\mathbf{R})\right] \tag{87}$$

which has dimensions equal to the number of basis functions. Because the solution of Eq. (87) can be time consuming, it has been suggested[104] to use this procedure to calculate the gradient and hessian at each *ab initio* point, with the results being subsequently used to define a Shepard interpolation (interpolant moving least squares).

4. Case Studies

4.1. *Three-Atom Three-Electron Systems*

Restricting the analysis to a minimal polyatomic basis set, the doublet states for a three-atom three-electron (s^3) system assume the form

$$\Psi_1 = \frac{1}{\sqrt{2}}\left(|a\bar{b}c| - |\bar{a}bc|\right) \tag{88}$$

$$\Psi_2 = \frac{1}{\sqrt{6}}\left(2|ab\bar{c}| - |a\bar{b}c| - |\bar{a}bc|\right) \tag{89}$$

where the bar over an orbital in the Slater determinant denotes a beta spin for the electron of the corresponding atom (A, B, and C). The DMBE potential matrix potential assumes then the form[85]

$$\mathbf{W} = \mathbf{W}_{EHF} + \mathbf{W}_{dc} \tag{90}$$

where

$$\begin{aligned}\mathbf{W}_\Gamma = &\begin{bmatrix} {}^1V_{AB}^{(2)}\left(1+{}^1F_{\Gamma,AB}\right) & 0 \\ 0 & {}^3V_{AB}^{(2)}\left(1+{}^3F_{\Gamma,AB}\right)\end{bmatrix} \\ &+ \mathbf{T}_{BC}\begin{bmatrix} {}^1V_{BC}^{(2)}\left(1+{}^1F_{\Gamma,BC}\right) & 0 \\ 0 & {}^3V_{BC}^{(2)}\left(1+{}^3F_{\Gamma,BC}\right)\end{bmatrix}\mathbf{T}_{BC}^{-1} \\ &+ \mathbf{T}_{AC}\begin{bmatrix} {}^1V_{AC}^{(2)}\left(1+{}^1F_{\Gamma,AC}\right) & 0 \\ 0 & {}^3V_{AC}^{(2)}\left(1+{}^3F_{\Gamma,AC}\right)\end{bmatrix}\mathbf{T}_{AC}^{-1}\end{aligned} \tag{91}$$

and ${}^1V_{AB}^{(2)}$ and ${}^3V_{AB}^{(2)}$ are the Γ (= EHF, dc) components of the potential energy curves for the ground-singlet and lowest-triplet states of the diatomic AB (similarly for BC and AC). In turn, the spin recoupling matrices (determined in Appendix C) are

$$\mathbf{T}_{BC} = \frac{1}{2}\begin{pmatrix} -1 & -\sqrt{3} \\ \sqrt{3} & -1 \end{pmatrix} \qquad \mathbf{T}_{AC} = \frac{1}{2}\begin{pmatrix} 1 & \sqrt{3} \\ \sqrt{3} & -1 \end{pmatrix}. \tag{92}$$

Thus, we may also write

$$\mathbf{W}_\Gamma = \mathbf{W}_\Gamma^{(2)} + \mathbf{W}_\Gamma^{(3)} \tag{93}$$

where the two-body matrices are defined by

$$W^{(2)}_{\Gamma,11} = {}^1V^{(2)}_{\Gamma,ab} + \frac{1}{4}\left[{}^1V^{(2)}_{\Gamma,ac} + 3^3V^{(2)}_{\Gamma,ac} + {}^1V^{(2)}_{\Gamma,bc} + 3^3V^{(2)}_{\Gamma,bc}\right] \tag{94}$$

$$W^{(2)}_{\Gamma,22} = {}^3V^{(2)}_{\Gamma,ab} + \frac{1}{4}\left[3^1V^{(2)}_{\Gamma,ac} + {}^3V^{(2)}_{\Gamma,ac} + 3^1V^{(2)}_{\Gamma,bc} + {}^3V^{(2)}_{\Gamma,bc}\right] \tag{95}$$

$$W^{(2)}_{\Gamma,12} = W^{(2)}_{\Gamma,21} = \frac{\sqrt{3}}{4}\left[{}^1V^{(2)}_{\Gamma,ac} - {}^3V^{(2)}_{\Gamma,ac} - {}^1V^{(2)}_{\Gamma,bc} + {}^3V^{(2)}_{\Gamma,bc}\right] \tag{96}$$

and corresponding definitions hold for the three-body ones. For example, ${}^1V^{(3)}_{\Gamma,ab} = {}^1F_{\Gamma,ab}\,{}^1V^{(2)}_{\Gamma,ab}$, with corresponding definitions holding for the bc and ac pairs.

By defining now dressed Coulomb and exchange integrals as

$$Q_i = \frac{1}{2}\sum_{\Gamma}\left[{}^1V^{(2)}_{\Gamma,i}\left(1 + {}^1F_{\Gamma,i}\right) + {}^3V^{(2)}_{\Gamma,i}\left(1 + {}^3F_{\Gamma,i}\right)\right] \tag{97}$$

$$J_i = \frac{1}{2}\sum_{\Gamma}\left[{}^1V^{(2)}_{\Gamma,i}\left(1 + {}^1F_{\Gamma,i}\right) - {}^3V^{(2)}_{\Gamma,i}\left(1 + {}^3F_{\Gamma,i}\right)\right] \tag{98}$$

where $i = 1 - 3$ is now used to label the diatomic pair (AB, BC, AC), one gets

$$Q_i = \sum_{\Gamma}\left[Q^{(2)}_{\Gamma,i} + Q^{(3)}_{\Gamma,i}\right] \tag{99}$$

$$J_i = \sum_{\Gamma}\left[J^{(2)}_{\Gamma,i} + J^{(3)}_{\Gamma,i}\right] \tag{100}$$

where $Q^{(2)}_{\Gamma,i} = [{}^1V^{(2)}_{\Gamma,i} + {}^3V^{(2)}_{\Gamma,i}]/2$, $J^{(3)}_{\Gamma,i} = [{}^1V^{(2)}_{\Gamma,i}{}^1F_{\Gamma,i} - {}^3V^{(2)}_{\Gamma,i}{}^3F_{\Gamma,i}]/2$, and corresponding expressions apply to $Q^{(3)}_{\Gamma,i}$ and $J^{(2)}_{\Gamma,i}$. Eq. (94) to Eq. (96) may then be written as

$$W^{(n)}_{\Gamma,11} = \sum_{i=1}^{3} {}^1V^{(n)}_{\Gamma,i} - \frac{3}{2}\left[J^{(n)}_{\Gamma,j} + J^{(n)}_{\Gamma,k}\right] \tag{101}$$

$$W^{(n)}_{\Gamma,22} = \sum_{i=1}^{3} {}^3V^{(n)}_{\Gamma,i} + \frac{3}{2}\left[J^{(n)}_{\Gamma,j} + J^{(n)}_{\Gamma,k}\right] \tag{102}$$

$$W^{(n)}_{\Gamma,12} = \frac{\sqrt{3}}{2}\left[J^{(n)}_{\Gamma,j} - J^{(n)}_{\Gamma,k}\right] \tag{103}$$

which shows that $W^{(n)}_{\Gamma,11}$ correlates on dissociation with the singlet curves, while $W^{(n)}_{\Gamma,11}$ leads to the triplet ones at the same limit. Moreover, by diagonalizing Eq. (90), one obtains[85]

$$V_{\pm} = \sum_{i=1}^{3}\sum_{n=2}^{3}\sum_{\Gamma} Q^{(n)}_{\Gamma,i} \pm \frac{1}{2}\left\{\sum_{i,j=1}^{3}\left[\sum_{n=2}^{3}\sum_{\Gamma}\left(J^{(n)}_{\Gamma,i} - J^{(n)}_{\Gamma,j}\right)\right]^2\right\}^{1/2} \tag{104}$$

which, using ${}^1F_{\Gamma,i} = {}^3F_{\Gamma,i} = 0$, leads to the well known LEPS[87–90] result. In turn, if one ignores $J^{(2)}_{dc,i}$ and $J^{(3)}_{dc,i}$ and assume $J^{(3)}_{EHF,i} = 0$ for all values of i, the formalism[123] used in fitting the accurate DMBE potential energy surface[39] is recovered. By ignoring instead the partition into EHF and dc contributions and choosing appropriately the three-body energy terms, one obtains[124] the well known H_3 Porter–Karplus [125] form.

4.1.1. H_3

Figure 2 shows[f] a perspective view of the crossing seam for the H_3 DMBE potential energy surface using the coordinates (R_2, R_3, α), with the valence angle $\alpha = \angle$HHH fixed at 60°. Also indicated in dash and dash-dot are the lines corresponding to $Q_2 = 0$ and $Q_3 = 0$ (respectively), where the symmetry coordinates are defined by Eq. (2). Note that such lines intersect at the minimum of the D_{3h} degeneracy line, with the corresponding cuts of the $1\,^2E'$ and $2\,^2E'$ sheets of the potential energy surface being shown in Fig. 3. Clearly, in the vicinity of the crossing point, such lines resemble the intersection of a double cone by a plane containing the vertex of the cone. The double-cone shape itself will be recovered by relaxing the condition of a fixed Q_3. This is illustrated in Fig. 4, where we have utilized the symmetrized coordinates in Eq. (3) suitably relaxed[126] $(\beta^\star = \beta/\mathcal{Q}, \gamma^\star = \gamma/\mathcal{Q})$, such that $\mathcal{Q}$ corresponds at each point to the structure of lowest energy for that symmetry. Such coordinates can be related to the hyperspherical ones[17] (ρ, θ, φ) through the relations

$$R_1^2 = \frac{1}{2}d_1^2\rho^2\left[1 + \sin\frac{\theta}{2}\cos(\varphi + \chi_3)\right] \tag{105}$$

[f]Units conversion factors are: a.u. of energy = E_h = 27.211652 eV = 4.3598 aJ = $2.194746 \times 10^5\,\mathrm{cm}^{-1}$; a.u. of bond length= $a_0 = 0.529177\,\text{Å} = 0.529177 \times 10^{-10}$ m.

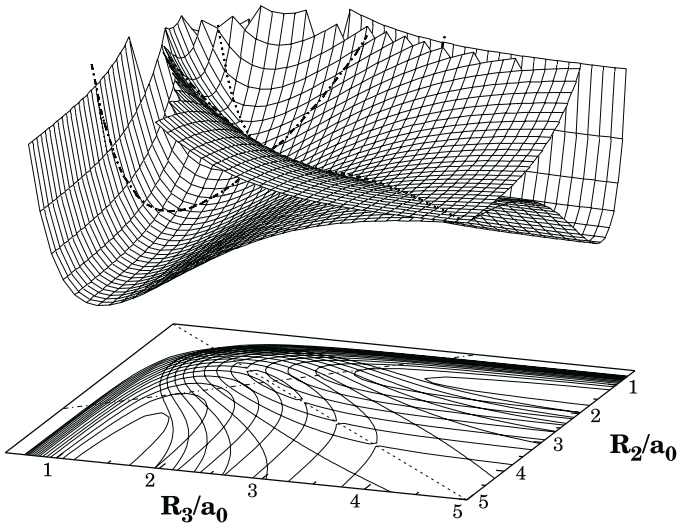

Fig. 2. Perspective view of the crossing seam for the H_3 DMBE potential energy surface using the coordinates (R_2, R_3, α), with the valence angle fixed at $\alpha = 60\,^\circ$. Also indicated in dash and dash-dot are the lines corresponding to $Q_2 = 0$ and $Q_3 = 0$, where the symmetry coordinates are defined by Eq. (2).

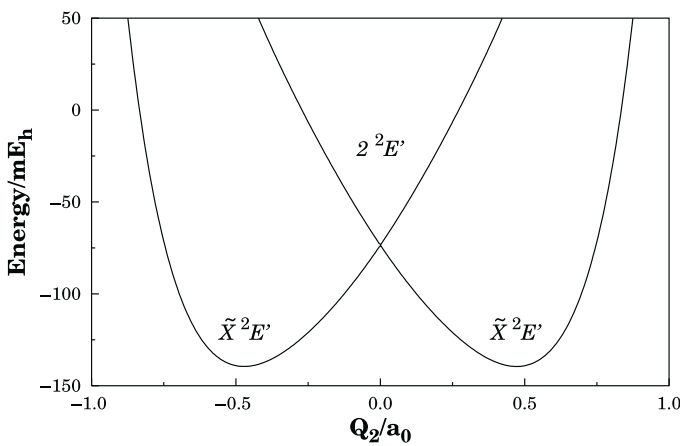

Fig. 3. Cuts on the H_3 potential energy surface corresponding to the dash-dot lines in Fig. 2.

$$R_2^2 = \frac{1}{2} d_2^2 \rho^2 \left(1 + \sin\frac{\theta}{2}\cos\varphi\right) \tag{106}$$

$$R_3^2 = \frac{1}{2} d_3^2 \rho^2 \left[1 + \sin\frac{\theta}{2}\cos(\varphi - \chi_1)\right] \tag{107}$$

where $d_i^2 = \frac{m_i}{\mu}\left(1 - \frac{m_i}{M}\right)$, $\chi_i = 2\tan^{-1}\left(\frac{m_{i+2}}{\mu}\right)$, $\mu = (m_1 m_2 m_3/M)^{1/2}$, and $M = \sum_i m_i$. Thus, the plot in Fig. 4 corresponds to a stereographic projection of the surface of an upper half sphere. The $\beta^\star$ coordinate corresponds to $\sin(\theta/2)\cos\varphi$, while $\gamma^\star$ denotes $\sin(\theta/2)\sin\varphi$. The hyperangle θ runs from zero at the north pole (center of plot) to $\pi/2$ at the equator. In turn, the hyperangle φ is measured from the positive $\beta^\star$ axis and grows on going counterclockwise. Note that the lowest point along the D_{3h} crossing seam is located at the origin of the plot and corresponds to an equilateral triangular configuration. Note also that the three equivalent saddle points for the hydrogen-atom exchange reaction lie at the outer circle of the bottom projection in Fig. 4, while the three product channels in the lower adiabatic sheet are indicated by the letters a, b, and c (primed letters are used for the corresponding channels in the upper sheet). In fact, the nuclear configurations separated by $\varphi = 2\pi/3$ are equivalent under the cyclic permutation 123. Thus, the lines in black and white indicate two paths for the adiabatic exchange of a H atom which, in principle, originate different geometric phases. This suggests that a proper consideration of the GP effect will be essential for single-surface reaction dynamics studies to attain high accuracy.

The equation describing the crossing seam can be obtained by equating the three interatomic distances. It corresponds to a straight line, where ρ is arbitrary but φ and θ have fixed values φ_s and θ_s, determined only by the nuclear masses as follows:[40]

$$\varphi_s = \tan^{-1}\left\{\frac{\cos\chi_3 - t\cos\chi_1 - (d_2/d_1)^2 + t\,(d_2/d_3)^2}{\sin\chi_3 + t\sin\chi_1}\right\} \tag{108}$$

$$\theta_s = 2\sin^{-1}\left\{\frac{(d_2/d_3)^2 - 1}{\cos(\varphi_s - \chi_1) - (d_2/d_3)^2\cos\varphi_s}\right\} \tag{109}$$

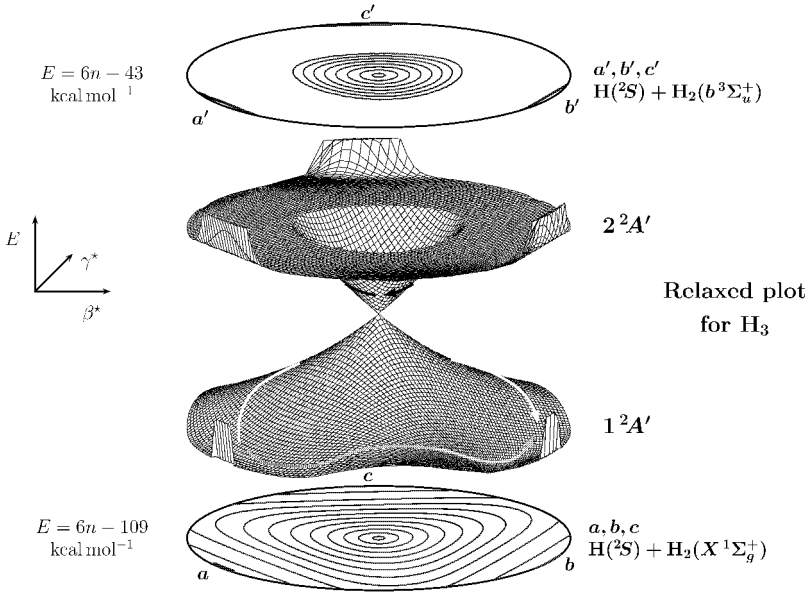

Fig. 4. Relaxed triangular plot[126] for the adiabatic DMBE potential energy surfaces of H_3 using hyperspherical coordinates. The lines in white and gray indicate two distinct paths for the adiabatic exchange of a H atom, while the line in black shows a path on the upper adiabatic sheet encircling the conical intersection. For the $1\,^2A'$ state, contours start at $-109\,\mathrm{kcal\,mol^{-1}}$ ($-0.17370\,E_h$) (the contour $n = 1$ lies close to the H + H_2 dissociation limit), and are equally spaced by $6\,\mathrm{kcal\,mol^{-1}}$ ($9.562\,mE_h$). The energy contours for the $2\,^2A'$ state are defined by $(6n - 43)\,\mathrm{kcal\,mol^{-1}}$ (note that the lowest corresponds to the central contour).

where $t = \left[(d_2/d_1)^2 - 1\right]\left[(d_2/d_3)^2 - 1\right]^{-1}$. If only two nuclear masses are equal ($m_2 = m_3$), one obtains the simplified expression

$$\theta_s = 2\sin^{-1}\left|\frac{m_2 - m_1}{m_2 + 2m_1}\right| \tag{110}$$

with φ_s being equal to π for $m_1 > m_2$, and zero for $m_1 < m_2$. If all nuclear masses are identical, one has $\theta_s = 0$ and $\varphi_s = 0$ (or π). This is the case for H_3, which is characterized by having its seam defined by $\theta_s = 0$, and hence independent of φ (or φ_s). Such a feature warrants that each path formed by varying φ from 0 to 2π in either of the two electronically adiabatic sheets (i.e. a path similar to the one shown by the green line in the upper sheet of Fig. 4) for fixed values of θ and ρ, will encircle the seam. Thus, one expects

all such paths to lead to $\xi_\alpha = \pi$ for a fixed (θ, ρ) [see Eq. (39)]. This is indeed observed,[40] implying that the DMBE potential energy surface[127] correctly describes the symmetry properties of the H_3 system.[5,6,9,22,128,129] Note that, for a circle around the seam with a small radius $d = \rho \sin\theta$ (θ or ρ are small), the dependence of A_I on φ is similar to that expected for a conical intersection ($\alpha = \varphi/2$). For larger values of d, the dependence of A_I on φ changes gradually into an equally-spaced-increasing-step-like-function which is halved by $A_I = \varphi/2$.[40]

Besides showing the correct analytic properties for a surface exhibiting a C_{3v} conical intersection,[39,43] the H_3 DMBE form then yields an accurate representation of the first-derivative coupling,[39,43] which assumes a form similar to Eq. (36) in the vicinity of the conical intersection. Specifically, assuming the transverse part to be zero over the entire configuration space, one has[39] from Eq. (38)

$$\alpha^{\mathrm{DMBE}}(\mathbf{R}) = \frac{\varphi}{2} - \tan^{-1}\left[\frac{g_0(\rho)\sin\theta\sin(3\varphi)}{f_0(\rho) + g_0(\rho)\sin\theta\cos(3\varphi) + f_1(\rho)\sin^2\theta}\right] \quad (111)$$

where $f_0(\rho)$, $g_0(\rho)$, and $f_1(\rho)$ are functions that depend only on the hyperradius. Clearly, $\alpha^{\mathrm{DMBE}}(\mathbf{R})$ is accurate close to the conical intersection as $\theta \to 0$. A three-body polynomial correction term that brings the DMBE surface (referred to as DMBE-Single-Polynomial or DSP) and derivative coupling into even closer agreement with extensive *ab initio* calculations on both doublet sheets has recently been reported.[43,44]

Finally, Eq. (110) is applicable to any AB_2-type isotopomer of H_3. Figure 5 shows the results obtained for HD_2, where the seam is defined by[40] $\theta_s = 0.5048$ rad and $\varphi_s = \pi$. Since $\theta_s \neq 0$, there are paths with constant θ and ρ which do not encircle the seam. This is the case for the loops with $\theta < \theta_s$, and hence $\xi_\alpha = 0$; the other loops lead to $\xi_\alpha = \pi$. Note that the phase factor depends on (ρ, θ, φ).[17] Note especially that the GP effect is[37,130] less relevant for HD_2 than H_3. In fact, since the conical intersection gets closer to the circle delimiting physical space with increasing θ_s, one generally expects the probability of looping around the seam to diminish with θ_s (see Fig. 5.2 of Ref. 85).

4.1.2. Li_3

The formalism derived in this section may also be used to obtain a double-sheeted potential energy surface for the alkali metal trimers. Indeed, a

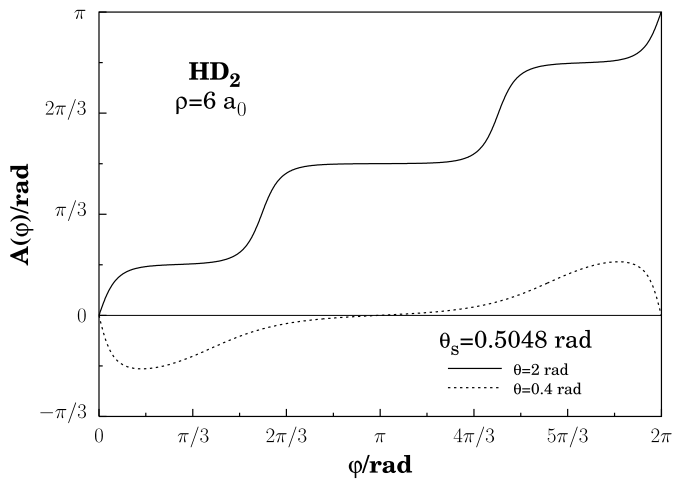

Fig. 5. Plot of the geometric phase $A(\varphi)$ for HD_2, fixed $\rho = 6\,a_0$.

reliable DMBE surface has been reported elsewhere[131,132] for Li_3 by making $J^{(3)}_{\Gamma,i} = 0$ and adding a global three-body EHF energy term to the radicand in Eq. (104). The two sheets of such a DMBE potential energy surface for Li_3 are shown in Fig. 6 as relaxed triangular plots[126] using hyperspherical coordinates. As for H_3, the lowest point along the D_{3h} conical intersection seam is located at the origin of the plot and corresponds to an equilateral triangular configuration. Clearly, the threefold symmetry gives rise to three wells which are equally spaced by 120° intervals around the origin. The minimum energy of the barrier for pseudorotation relative to the bottom of such wells (i.e. the height of the saddle points between the three wells), and the energy of the lowest point along the conical intersection seam are 0.4 and 54.2 meV (relative to $Li+Li_2$), respectively. Note that the motion along the hyperradius ρ corresponds to the symmetric stretching mode, while the motion along the $\gamma^\star$ ($\beta^\star$) axis corresponds to the bending (asymmetric stretching) mode. In turn, motion along the hyperangle φ corresponds to the pseudorotational motion.

The two sheets of the Li_3 DMBE potential energy surface have been used for detailed zero total angular momentum calculations of the bound and pseudo-bound vibrational states of Li_3 without (NGP) and with (GP) consideration of the GP effect.[12,133,134] In particular, for the lower sheet,

the calculated eigenvalues amount to 3524 and 3211, respectively for the NGP and GP cases. In fact, the full spectrum has been calculated covering the range of energies up to the threshold for $Li_2(X\,^1\Sigma_g^+) + Li$ dissociation. Of the total number of calculated NGP (GP) vibrational levels, 953 (920), 750 (817), and 1621 (1474) have been found to belong to A_1, A_2, and E symmetries in the S_3 permutational group. From their relative positioning illustrated in Fig. 7, one immediately assesses the importance of taking the GP effect into account. For example, the lowest vibrational level in the NGP calculations has A_1 symmetry, while it is of E symmetry in the GP ones, as it should be. It is also seen that the dynamical Jahn–Teller effect is, for this system, about one order of magnitude smaller than the GP effect. Moreover, a comparison of the Li_3 calculations with the only available experimental data has shown[134] good agreement. Although further studies are definitely desired, such a result seems to support the reliability of the Li_3 DMBE surface, while suggesting[12] that nonadiabatic coupling effects may play a minor role (roughly an order of magnitute smaller than the GP effect). The

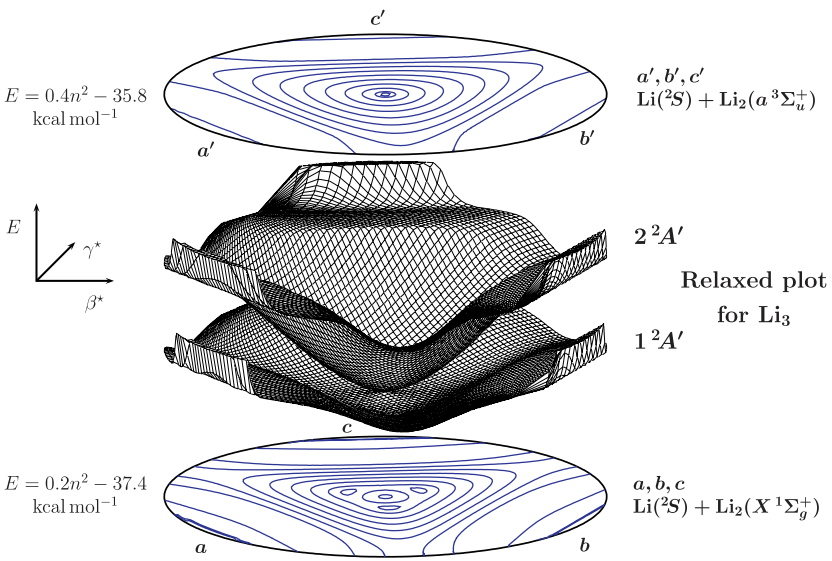

Fig. 6. Relaxed triangular plot[126] for the adiabatic DMBE potential energy surfaces of Li_3 using hyperspherical coordinates. For the $1\,^2A'$ state, contours start at $-37.4\,\mathrm{kcal\,mol^{-1}}$, with contour $n = 1$ defining the three equivalent minima. The corresponding energy labeling for the $2\,^2A'$ state is $(0.4n^2 - 35.8)\,\mathrm{kcal\,mol^{-1}}$. As in Fig. 4, the lowest contour corresponds to the one close to the vertex of the double cone.

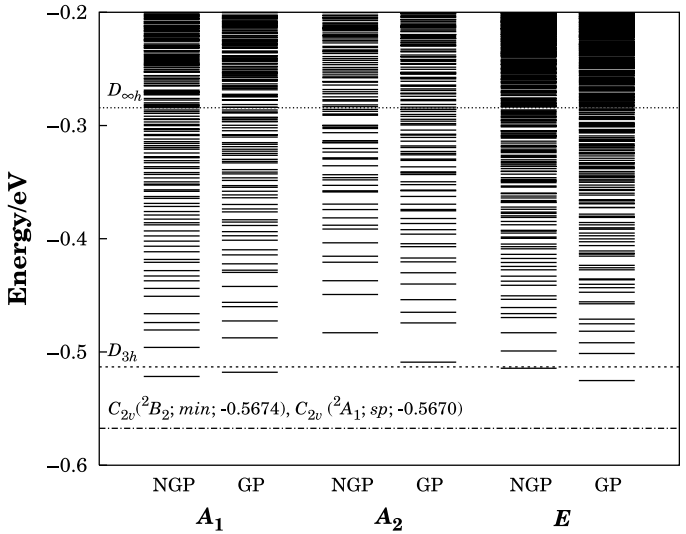

Fig. 7. Calculated vibrational levels of A_1, A_2, and E symmetries for the lowest adiabatic sheet of Li_3. The dashed, dotted, and dash-dot lines indicate the energies associated with the structures of minimum energy having $D_{\infty h}$, D_{3h}, and C_{2v} symmetries, respectively; the abbreviations "min" and "sp" stand for the three equivalent minima and saddle points of C_{2v} symmetry.

reader is referred to the original papers[133,134] for a statistical analysis of the calculated vibrational levels.

4.2. *The* NO_2 *Molecule*

The title molecule plays an important role in atmospheric chemistry[135] and combustion processes,[136] with its ground-state potential energy surface being also frequently employed as a prototype in unimolecular dissociation calculations. In this subsection, we focus on the NO_2 potential energy surfaces of $^2A'$ symmetry. Because they are outstandingly complicated, the interpretation of the visible spectrum of NO_2 poses an extremely difficult problem both to experimentalists and theoreticians. Similarly, such surfaces are crucial to study the dynamics of the reaction

$$N(^4S_u) + O_2(X\,^3\Sigma_g^-) \rightarrow NO(X\,^2\Pi) + O(^3P_g) \qquad (112)$$

which is an important source of infrared chemiluminescence in the upper atmosphere. In fact, this reaction is believed to be an important source

of vibrationally excited NO in the atmosphere, with vibrational levels up to $v = 7$ becoming populated. Note that the reaction (112) is exoergic by 1.38 eV, but thermal rate coefficient data[137] indicates an activation energy of 0.3 eV, which implies that it can occur only via energetic N atoms. Despite this requirement, studies of the equilibrium energy distribution of nitrogen atoms have established that a significant population of N atoms is created sufficiently hot to make it feasible. Note further that the first excited $^4A'$ states of NO_2 also correlate with both reactants and products of the reaction (112), although such states should only play a role for collision energies above $\sim$ 0.75 eV.[138] Thus, the title system may illustrate the scenario of difficulties encountered in modelling a manifold of adiabatic potential energy surfaces for a triatomic system with practical interest. Of course, an exhaustive review of the numerous studies carried out on that system is beyond of the scope of the present work; the reader is addressed to Refs. 139 and140, from which references to previous work may be obtained.

We begin with a brief comment on previous potential energy surfaces[139–142] for the electronic ground state of NO_2. The potential of Gilibert *et al.*[141] is based on the single-valued many-body expansion[79] formalism and the observation that $NO_2(\widetilde{X}\,^2A_1)$ may lead upon dissociation to $N(^2D_u)+O_2(X\,^3\Sigma_g^-)$ if one considers $O_2(X\,^3\Sigma_g^-)$ at its equilibrium diatomic geometry. However, if the O−O bond is allowed to relax to its experimental equilibrium geometry in $NO_2(\widetilde{X}\,^2A_1)$, $R_{OO} = 4.150\,a_0$,[143] then it may adiabatically correlate for C_{2v} geometries with $N\,(^4S_u)+O_2(c\,^3\Delta_u)$, which has an energy lower than $N(^2D_u)+O_2(X\,^3\Sigma_g^-)$ by about 2.4 eV. Such a correlation limit cannot be obtained by using the function of Gilibert *et al.*[141], nor can the deep well associated to the chemically stable $NO_2(\widetilde{X}\,^2A_1)$ species be reached. However, their analytic function has been fitted to the *ab initio* saddle point properties of Walch and Yaffe[144] for reaction (112), and has been employed in dynamics studies of the $N(^4S_u) + O_2(X\,^3\Sigma_g^-)$ reaction. In fact, the fitting procedure used by Gilibert *et al.*[141] introduced an artificial barrier of 0.55 eV, which led Duff *et al.*[145] and Sayós *et al.*[146] to report improved similar fits. These show barrier heights of 0.30 eV[145] and 0.27 eV[146] for reaction (112), which are much closer to the recommended[137] activation energy of 0.30 eV. Several dynamics studies have actually been reported[138,141,146–148] based on the above single-valued functional forms but, although Gilibert *et al.*[141] recognized that it might be possible to reach

the $\widetilde{X}\,^2A_1$ ground state of NO_2 through C_s "near-C_{2v}" configurations, none of the above surfaces allows such a possibility.

Another important topological feature, which is obviously absent from the above single-valued formulations, is the conical intersection between the two lowest $^2A'$ adiabatic potential energy surfaces. A two-valued potential energy surface, which describes such a conical intersection is due to Hirsch *et al.*[142] It is obtained by diagonalizing a 2×2 potential matrix, with the matrix elements being written as polynomial expansions in which the parameters are determined by least-squares fitting their own *ab initio* CI energies. Although such a function has been specially calibrated to model the spectroscopy of NO_2, it is unclear how accurately it describes the various channels up to dissociation. A slightly improved version of this 2×2 potential energy surface has also been reported by Mahapatra *et al.*,[139] who have carried out calculations of the whole vibrational spectra for the title system. Most recently, single-valued DMBE potential energy surfaces have been reported[140] for the two lowest $^2A'$ adiabatic potential energy surfaces of NO_2 from a fit to MR CI energies, but here too no attempt has been made to reproduce the $1\,^2A'/2\,^2A'$ conical intersection. We will return later to these two more recent works.

The minimal atomic basis set for NO_2 consists of[124]

$$\psi_1 = \mathcal{A}\,{}^3P_z\,{}^3P_y\,{}^4S_u\chi_1 \qquad \psi_2 = \mathcal{A}\,{}^3P_z\,{}^3P_y\,{}^4S_u\chi_2 \tag{113}$$

$$\psi_3 = \mathcal{A}\,{}^3P_y\,{}^3P_z\,{}^4S_u\chi_1 \qquad \psi_4 = \mathcal{A}\,{}^3P_y\,{}^3P_z\,{}^4S_u\chi_2 \tag{114}$$

$$\psi_5 = \mathcal{A}\,{}^3P_x\,{}^3P_y\,{}^4S_u\chi_1 \qquad \psi_6 = \mathcal{A}\,{}^3P_x\,{}^3P_y\,{}^4S_u\chi_2 \tag{115}$$

$$\psi_7 = \mathcal{A}\,{}^3P_y\,{}^3P_x\,{}^4S_u\chi_1 \qquad \psi_8 = \mathcal{A}\,{}^3P_y\,{}^3P_x\,{}^4S_u\chi_2 \tag{116}$$

where χ_1 and χ_2 are the appropriate doublet spin functions obtained by coupling the ^4S_u nitrogen atom with the ^3P oxygen atoms, and $\mathcal{A}$ is the antisymmetrizing operator. A similar basis set has been employed[149] to calculate the potential energy surfaces for the $^2B_2$ and $^4B_2$ electronic states of NO_2, but the results were shown to be in disagreement with *ab initio* calculations,[150] possibly due to the use of the popular Morse and Born-Meyer diatomic potentials. To improve the situation, Varandas and Voronin[124] used more accurate extended Hartree-Fock approximate correlation energy[151,152] (EHFACE2 and EHFACE2U) curves, while dressing some of them to approximately account for the three-body effects that are missing in DIM theory.

The Hamiltonian matrix assumes the form in Eq. (54), where the two oxygen atoms are A and B, and the nitrogen is atom C. In turn, the $\mathbf{R}_{BC}$ rotation matrix (antisymmetric) is defined by the following non-zero elements: $\mathbf{R}_{ii} = 1$ for $i = 1, 2, 5, 6$, $\mathbf{R}_{ii} = -\cos\theta_2$ for $i = 3, 4, 7, 8$, and $\mathbf{R}_{37} = \mathbf{R}_{48} = \sin\theta_2$. Similarly, the $\mathbf{R}_{AC}$ matrix is defined by: $\mathbf{R}_{ii} = \cos\theta_1$ for $i = 1, 2, 5, 6$, $\mathbf{R}_{ii} = 1$ for $i = 3, 4, 7, 8$, and $\mathbf{R}_{15} = \mathbf{R}_{26} = \sin\theta_1$. Moreover, the spin-recoupling matrices assume the form

$$\mathbf{T}_{BC} = \begin{pmatrix} t^{SM}_{s_{BC}s_{AB}} & 0 & 0 & 0 \\ 0 & t^{SM}_{s_{BC}s_{AB}} & 0 & 0 \\ 0 & 0 & t^{SM}_{s_{BC}s_{AB}} & 0 \\ 0 & 0 & 0 & t^{SM}_{s_{BC}s_{AB}} \end{pmatrix} \tag{117}$$

where

$$t^{SM}_{s_{BC}s_{AB}} = \frac{1}{\sqrt{6}} \begin{pmatrix} -1 & \sqrt{5} \\ \sqrt{5} & 1 \end{pmatrix} \tag{118}$$

with the corresponding $\mathbf{T}_{AC}$ matrix being similar to $\mathbf{T}_{BC}$ in Eq. (118) except for the definition of the auxiliary matrix elements that are now given by

$$t^{SM}_{s_{AC}s_{AB}} = \frac{1}{\sqrt{6}} \begin{pmatrix} -1 & -\sqrt{5} \\ -\sqrt{5} & 1 \end{pmatrix}. \tag{119}$$

In turn, the $\mathbf{H_{AB}}$ matrix assumes the form

$$\mathbf{H}_{AB} = \frac{1}{2} \begin{pmatrix} \mathbf{H}_{\Pi\Pi} & \mathbf{0} \\ \mathbf{0} & \mathbf{H}_{\Delta\Sigma} \end{pmatrix} \tag{120}$$

where the auxiliary block-diagonal matrices are defined by

$$\mathbf{H}_{\Pi\Pi} = \frac{1}{2} \begin{pmatrix} {}^3\Pi_s & 0 & {}^3\Pi_d & 0 \\ 0 & {}^5\Pi_s & 0 & -{}^5\Pi_d \\ {}^3\Pi_d & 0 & {}^3\Pi_s & 0 \\ 0 & -{}^5\Pi_d & 0 & {}^5\Pi_s \end{pmatrix} \tag{121}$$

and

$$\mathbf{H}_{\Delta\Sigma} = \frac{1}{2} \begin{pmatrix} {}^3\Delta_s & 0 & {}^3\Delta_d & 0 \\ 0 & {}^5\Delta_s & 0 & -{}^5\Delta_d \\ {}^3\Delta_d & 0 & {}^3\Delta_s & 0 \\ 0 & -{}^5\Delta_d & 0 & {}^5\Delta_s \end{pmatrix} \tag{122}$$

with $\Pi_{s,d} = \Pi_u \pm \Pi_g$ for both the triplet and quintet states, ${}^3\Delta_{s,d} = {}^3\Delta_u \pm {}^3\Sigma^-_g$, and ${}^5\Delta_{s,d} = {}^5\Sigma^-_u \mp {}^5\Delta_g$. Finally, $\mathbf{H}_{BC}$ and $\mathbf{H}_{AC}$ are diagonal matrices

defined by

$$\mathbf{H}_{BC} = \left({}^2\Pi, {}^4\Pi, {}^2\Sigma^+, {}^4\Sigma^+, {}^2\Pi, {}^4\Pi, {}^2\Pi, {}^4\Pi\right) \tag{123}$$

$$\mathbf{H}_{AC} = \left({}^2\Sigma^+, {}^4\Sigma^+, {}^2\Pi, {}^4\Pi, {}^2\Pi, {}^4\Pi, {}^2\Pi, {}^4\Pi\right). \tag{124}$$

Thus, the NO_2 DIM potential energy surfaces for the ground-state and first seven excited states of ${}^2A'$ symmetry can be obtained by diagonalizing the 8×8 Hamiltonian matrix in Eq. (54) using Eqs. (117) to (124). For C_{2v} geometries, such a DIM matrix reduces to two 4×4 matrices of ${}^2A_1$ and ${}^2B_2$ symmetries. Similarly, for $C_{\infty v}$ geometries, it factorizes into a 4×4 Π matrix and two 2×2 ones of Σ and Δ symmetries.

Figures 8 and 9 show relaxed triangular plots[126] in mass-unweighted hyperspherical coordinates (all masses are taken equal to unity) for the two lowest ${}^2A'$ adiabatic sheets of NO_2 according to a modified version[153] of the 8×8 DMBE potential energy surface reported in Ref. 124. As in previous work,[124] the parameterization has been done by dressing the ${}^{2,4}\Pi$ and ${}^5\Sigma_u^-$ diatomic curves, using simple three-body energy terms whose parameters have been adjusted by a trial-and-error procedure.[153] The notable features in Figure 8 are the deep minimum of the $1\,{}^2A'$ adiabatic sheet which is

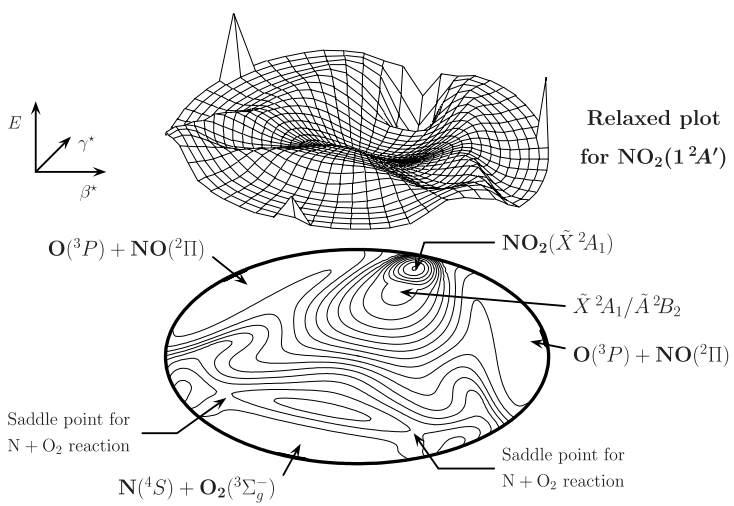

Fig. 8. Relaxed triangular plot[126] for the $1\,{}^2A'$ potential energy surface of the 8×8 NO_2 DMBE potential energy surface.[153] Contours, starting at $-0.360\,E_h$ (first countour in the NO_2 minimum), are equally spaced by $5\,mE_h$.

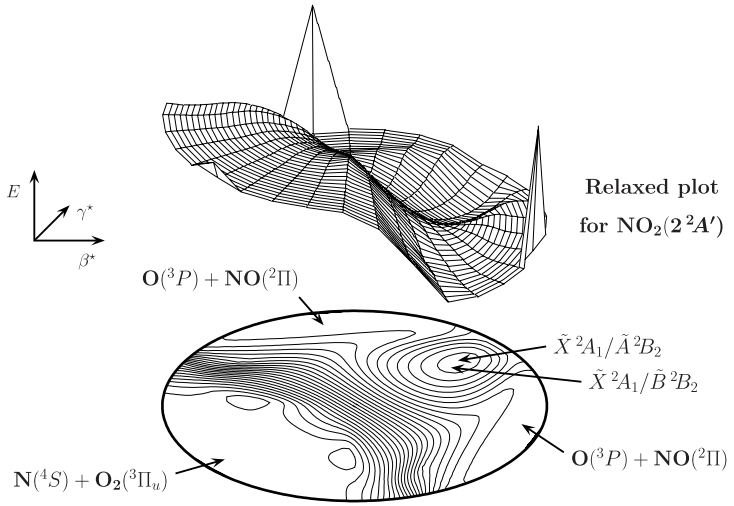

Fig. 9. As in Fig. 8 but for $NO_2(2\,^2A')$ potential energy surface.[153]

associated with the equilibrium geometry of NO_2 (this has symmetry $^2A_1$ in the C_{2v} symmetry point group), and the $1\,^2A'/2\,^2A'$ ($\widetilde{X}\,^2A_1/\widetilde{A}\,^2B_2$ in C_{2v}) conical intersection, which has been extensively studied by Leonardi *et al.*[154] and Mahapatra *et al.*[139] (see also references therein). This occurs along the C_{2v} line at ($\beta^\star = 0, \gamma^\star = 0.717$), with the corresponding structural attributes (characteristic bond length, included angle, energy above the $\widetilde{X}\,^2A_1$ minimum) at the conical intersection point of lowest energy being $R_{NO} = 2.44a_0$, $\angle ONO = 113°$, and $\Delta V = 1.637\,eV$. Clearly, such attributes deviate drastically from those of the original multivalued DMBE potential energy surface[124] ($R_{NO} = 2.58a_0$, $\angle ONO = 61°$, and $\Delta V \sim 6\,eV$), where such a crossing occurs at $\beta^\star = 0$, but only slightly off-centred at $\gamma^\star \sim 0.023$ [note that $(\beta^\star, \gamma^\star) = (0, 0)$ represents an equilateral triatomic structure]. However, they are in quite satisfactory agreement with the commonly accepted values;[155] see later. Of course, the $\widetilde{X}\,^2A_1/\widetilde{A}\,^2B_2$ conical intersection allows the reaction $N(^4S_u) + O_2(X\,^3\Sigma_g^-) \rightarrow O(^3P_g) + NO(X\,^2\Pi)$ to occur on the lowest potential energy surface of $^2A'$ symmetry. However, it is also seen that products can be formed without having to sample the deep $^2A_1$ chemical well.

Another salient feature from Fig. 8 is the high energy barrier at C_{2v} geometries for the reaction (112). This barrier has been estimated[153] from *ab initio* calculations using CASPT2 perturbation theory[g] (they have employed a FVCAS root function and a cc–AVTZ basis set[157,158]) to be about 1 eV relative to the $N(^4S) + O_2(X\,^3\Sigma_g^-)$ asymptote. Such a barrier has been approximately imposed on the $1\,^2A'$ adiabatic sheet of the novel 8×8 DMBE potential energy surface,[153] being seen from Fig. 8 that its height decreases for C_s geometries, where it reaches a minimum of 0.3 eV for a bent N − O − O structure, defined by $R_{NO} = 3.25a_0$, $R_{OO} = 2.38a_0$, and $\angle NOO = 114.2°$. Thus, the novel 8×8 DMBE potential energy surface essentially reproduces the recommended value[137] of the activation energy for the reaction (112), while the barrier location is in quite good agreement with that obtained from the *ab initio* calculations of Walch and Jaffe;[144] these predict a barrier height of 0.38 eV, with the barrier being located at a geometry defined by $R_{NO} = 3.441a_0$, $R_{OO} = 2.329a_0$, and $\angle NOO = 115.0°$. Thus, the new NO_2 multivalued DMBE potential energy surface[153] should also be useful to carry out dynamics and kinetics studies of the reaction (112).

To understand better the topology of the $^2A'$ manifold close to the conical intersection, we show in Fig. 10 energy diagrams of the four lowest states for C_{2v} [panel (a)] and "near-C_{2v}" [panel (b)] geometries of NO_2 [the C_{2v} axis was tilted in panel (b) by 1° relative to the C_{2v} angle of 90°], as a function of the distance of the N atom to the center of mass of the O − O bond, the length of which has been fixed at the calculated equilibrium geometry ($R_{OO} = 4.102\,a_0$) of the $\widetilde{X}\,^2A_1$ minimum. Several interesting features deserve attention. First, the deep chemical minimum on the $1\,^2A'$ ($\widetilde{X}\,^2A_1$) surface. Then a shallow minimum on the $1\,^2A'$ ($\widetilde{A}\,^2B_2$) surface, which is separated from the former by the $1\,^2A'/2\,^2A'$ ($\widetilde{X}\,^2A_1/\widetilde{A}\,^2B_2$) conical intersection. Interestingly, following a discussion on symmetry breaking in the NO_2 radical,[159,160] such a minimum has been characterized by Blahous III *et al.*[161] using C_s symmetry at the double-zeta plus polarization CAS level (DZP CAS) of theory. Their DZP CAS calculations predict the $^2B_2$ minimum to lie 1.06 eV above the $\widetilde{X}\,^2A_1$ one,

[g]The acronyms have their usual meaning: FVCAS denotes full valence complete active space, and CASPT2 stands for second-order Moller-Plesset perturbation theory starting from a CAS wave function.[156]

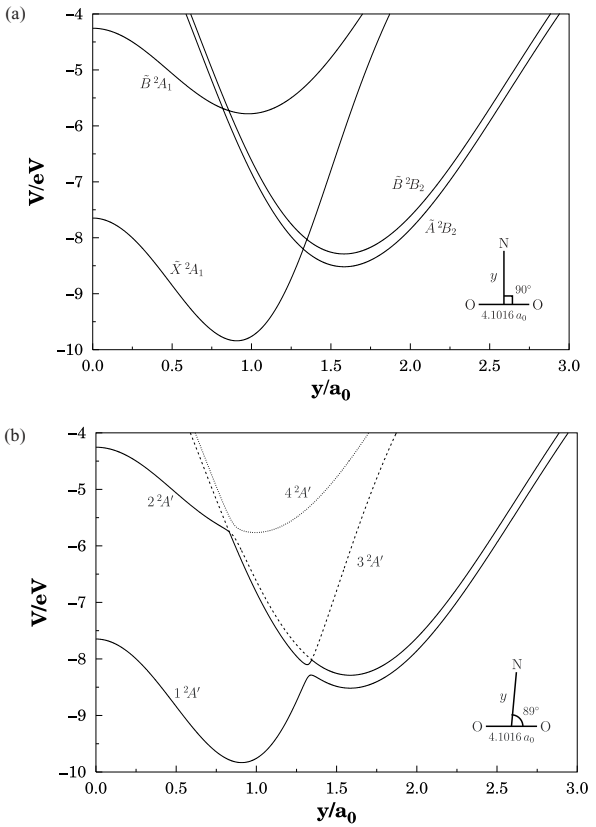

Fig. 10. Cut of lowest four $^2A'$ adiabatic potential energy surfaces along C_{2v} [panel (a)] and C_s "near-C_{2v}" [panel (b)] geometries where the attacking angle is 89°. For clarity, the two lowest $^2A'$ adiabatic potential energy surfaces are shown in solid, while the next two are indicated by the dashed and dotted lines. The O – O distance has been fixed at its value in C_{2v} equilibrium $NO_2(\widetilde{X}\,^2A')$, with (x, y) being the Cartesian coordinates of the N atom relative to the centre-of-mass of O_2.

with a geometry defined by $R_{NO} = 2.421\,a_0$ and $\angle ONO = 101.3°$, a result which compares nicely with the structural parameters of the $^2B_2$ minimum obtained from the novel multivalued DMBE surface, namely $R_{NO} = 2.59\,a_0$ and $\angle ONO = 101.8°$. Moreover, the harmonic vibrational frequencies at the DZP CAS level of theory were found to be $1391\,cm^{-1}$ (symmetric stretch), $730\,cm^{-1}$ (bending), and $359\,cm^{-1}$ (asymmetric stretch), also in good accord with the values calculated from the $1\,^2A'$ ($\widetilde{X}\,^2A_1$) sheet of

the novel 8×8 DMBE potential energy surface,[153] namely $1177\,\mathrm{cm}^{-1}$, $756\,\mathrm{cm}^{-1}$, and $386\,\mathrm{cm}^{-1}$, although a reverse assignment is found for the bending and asymmetric stretching mode frequencies. Clearly, for "near-C_{2v}" geometries, the conical intersection becomes a narrowly avoided crossing, which may act as a saddle point for connecting the $\widetilde{A}\,^2B_2$ and $\widetilde{X}\,^2A_1$ minima on the same $1\,^2A'$ potential energy surface. Its barrier height has as upper bound the height of the lowest conical intersection point, which is found to be $0.0789\,\mathrm{eV}$ ($1.8\,\mathrm{kcal\,mol}^{-1}$) relative to the minimum of the $\widetilde{A}\,^2B_2$ species. This result is in excellent agreement with the DZP CAS value of $1.8\,\mathrm{kcal\,mol}^{-1}$ predicted by Blahous III *et al.*[161]. The good agreement extends also to the predicted characteristic parameters for the lowest point of the $\widetilde{X}\,^2A_1/\widetilde{A}\,^2B_2$ conical intersection. In fact, such parameters[153] ($\Delta V = 1.637\,\mathrm{eV}, R_{\mathrm{NO}} \sim 2.44\,a_0, \angle\mathrm{ONO} \sim 113°$) are found to be in quite satisfactory agreement with the best available estimates: (1.21 ± 0.09, 2.355, 103.1),[155] (1.14, 2.379, 107.4),[64] (1.287, 2.347, 108.04),[139] and (1.420, 2.360, 110.5)[140] (the energy is relative to the bottom of the $\widetilde{X}\,^2A_1$ well). However, the $\widetilde{X}\,^2A_1/\widetilde{A}\,^2B_2$ crossing seam is probably best understood from Fig. 11, which shows a contour plot of the two lowest $^2A'$ adiabatic potential energy surfaces for C_{2v} geometries as a function of the characteristic bond length and included angle. Clearly, the locus of the $\widetilde{X}\,^2A_1/\widetilde{A}\,^2B_1$ conical intersection delimits the $\widetilde{X}\,^2A_1$ and $\widetilde{A}\,^2B_1$ minima, which lie both on the same $1\,^2A'$ adiabatic potential energy surface.

Other interesting features from Fig. 10 are the $\widetilde{X}\,^2A_1/\widetilde{B}\,^2B_2$, $\widetilde{B}\,^2A_1/\widetilde{A}\,^2B_2$, and $\widetilde{B}\,^2A_1/\widetilde{B}\,^2B_2$ intersections. They all manifest in panel (b) as narrowly avoided intersections, and hence are less clearly visible in the relevant relaxed triangular plots. Note that, no matter how small a numerical perturbation can be, it will lift the crossing in first-order, as if it were a real physical distortion of the molecular geometry at which the crossing occurs. The $\widetilde{X}\,^2A_1/\widetilde{B}\,^2B_2$ conical intersection arises at an energy just above the lowest $\widetilde{X}\,^2A_1/\widetilde{A}\,^2B_2$ conical intersection and leads to the $2\,^2A'$ adiabatic potential energy surface. This seems to encompass a minimum of $^2B_2$ symmetry (which would lie just above the $^2B_2$ minimum of the $1\,^2A'$ adiabatic potential energy surface, being higher in energy by about $0.3\,\mathrm{eV}$; see also Fig. 10), apparently in good agreement with the MRCI prediction of Reignier *et al.*[140] In fact, plots of the $2\,^2A'$ adiabatic potential energy surface obtained from the novel multivalued DMBE function[153] similar to those reported in Fig. 8 of Ref. 140 also show this "minimum". However,

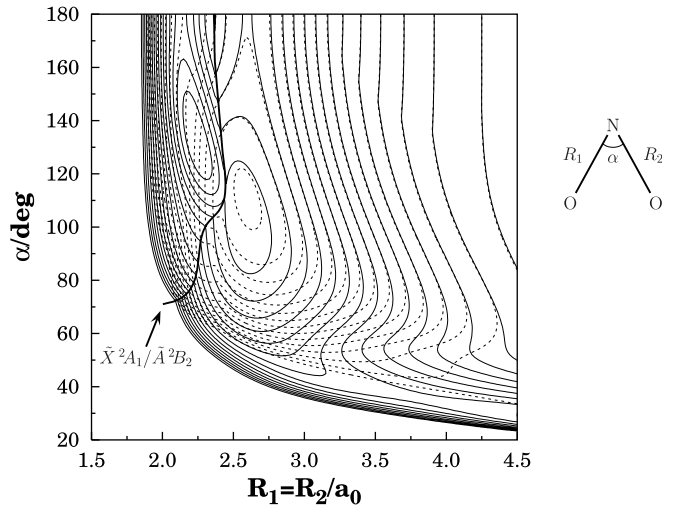

Fig. 11. Contour plot for the two lowest adiabatic sheets of $NO_2(^2A')$ DMBE potential energy surface[124] as a function of the characteristic bond length (R_{NO}) and included angle (α): (a) $1\,^2A'$, thin solid contours; (b) $2\,^2A'$, dashed contours. Contours are equally spaced by $5\,mE_h$, starting at $-0.360\,E_h$; for clarity, the contour numbers are omitted. Also shown is the $\tilde{X}\,^2A_1/\tilde{A}\,^2B_2$ intersection locus.

such a stationary point seems to be absent in Fig. 9, where the well corresponds to the upper inverted "cones" of the $\widetilde{X}\,^2A_1/\widetilde{A}\,^2B_2$ and $\widetilde{X}\,^2A_1/\widetilde{B}\,^2B_2$ conical intersections. One then wonders whether the minimum reported by Reignier *et al.*[140] also disappears when the hidden coordinate in their plots is allowed to further relax.

Regarding the minimum associated with the equilibrium $\widetilde{X}\,^2A_1$ geometry, it is found to lie 9.84 eV below the energy of the three isolated ground state atoms, which gives dissociation energies of 4.63 eV and 3.23 eV for the $N(^4S_u) + O_2(X\,^3\Sigma_g^-)$ and $O(^3P_g) + NO(X\,^2\Pi)$ product channels in exact agreement with experiment.[143] As for its geometry, the multivalued DMBE surface gives a bond length of $R_{NO} = 2.429\,a_0$, with the included angle being $\angle ONO \sim 132.2°$, also in fair agreement with the experimental values of $2.255\,a_0$ and 133.9°.[143] However, the calculated harmonic vibrational frequencies of $2508\,cm^{-1}$ (asymmetric stretch), $2626\,cm^{-1}$ (symmetric stretch), and $987\,cm^{-1}$ (bending) differ significantly from the observed frequencies[162] ($1617\,cm^{-1}$, $1320\,cm^{-1}$, and $750\,cm^{-1}$ in the above order). In turn, the optimum $D_{\infty h}$ geometry corresponding to $NO_2(^2\Pi_u)$ is found

to lie 1.47 eV above the $\widetilde{X}\,^2A_1$ minimum, with a characteristic bond length of $R_{\rm NO} = 2.13\,a_0$. Although the predicted decrease in the NO bond length of 0.11 a_0 with respect to the optimum C_{2v} geometry contrasts with experiment[163,164] (this indicates an increase by $\sim 0.07\,a_0$), the optimum energy is close to available *ab initio* results (CAS SCF: 1.8 eV[165]; MR CI: 1.5 eV;[165] MRD-CI: 1.85 eV[142]) and the experimental (1.83 eV[163,164]) value. Also located on the $1\,^2A'$ adiabatic potential energy are two shallow minima (about 0.023 eV deep) corresponding to the two equivalent peroxy structures (NOO), a feature in qualitative agreement with the bent C_1 peroxy structure predicted by Meredith *et al.*[166] Of course, the existing points of disagreement in the spectroscopic properties of the $1\,^2A'$ adiabatic potential energy surface can hopefully be fixed by combining the DMBE surface with a local spectroscopic one (Ref. 167, and references therein) using the ES method discussed in Sec. 3.2.4.[153]

We conclude this section by focusing on some recent works. One of them deals with a further simplication of the atomic basis set in the calculation of the DIM potential function. Using a subminimal basis set of four atomic basis functions, it has been shown[168] that the potential matrix can be reduced from dimension 8×8 to 2×2, while reproducing the topological features of relevance for the study of most dynamical processes of current interest. The idea has been to choose the atomic basis set such that one recovers at least the two lowest diatomic curves of the proper symmetry. For NO_2 $\left(^2A'\right)$, it amounts to consider only the basis ψ_5 to ψ_8 in Eqs. (115) and (116). The $\mathbf{H}_{ab}$ matrix assumes then the form

$$\mathbf{H}_{ab} = \frac{1}{2}\begin{pmatrix} {}^3\Delta_s & 0 & {}^3\Delta_d & 0 \\ 0 & {}^5\Delta_s & 0 & -{}^5\Delta_d \\ {}^3\Delta_d & 0 & {}^3\Delta_s & 0 \\ 0 & -{}^5\Delta_d & 0 & {}^5\Delta_s \end{pmatrix} \tag{125}$$

with ${}^3\Delta_{s,d} = {}^3\,\Delta_u \pm {}^3\,\Sigma_g^-$, and ${}^5\Delta_{s,d} = {}^5\,\Sigma_u^- \mp {}^5\,\Delta_g$. Similarly,

$$\mathbf{H}_{ac} = \left({}^2\Pi, {}^4\,\Pi, {}^2\,\Pi, {}^4\,\Pi\right) \tag{126}$$

is a diagonal matrix (a corresponding definition holds for $\mathbf{H}_{bc}$), while the spin-recoupling matrices $\mathbf{T}_{bc}$ and $\mathbf{T}_{ac}$ are given by the corresponding blocks in Eqs. (117) to (119). Diagonalization of the 4×4 Hamiltonian matrix using Eqs. (125) to (126) then leads to the first four NO_2 potential energy

surfaces of A' symmetry. In fact, such a diagonalization may be carried out analytically, leading to two pairs of roots:

$$V_{1,2} = \frac{1}{2}\left[\Delta^+(R_3) + \Pi^+(R_1) + \Pi^+(R_2)\right] \pm \frac{1}{2}\left\{\left[\Delta^-(R_3) + \frac{2}{3}\left(\Pi^-(R_1) + \Pi^-(R_2)\right)\right]^2 + \frac{5}{9}\left(\Pi^-(R_1) - \Pi^-(R_2)\right)^2\right\}^{1/2} \tag{127}$$

and

$$V_{3,4} = \frac{1}{2}\left[\Sigma^+(R_3) + \Pi^+(R_1) + \Pi^+(R_2)\right] \pm \frac{1}{2}\left\{\left[\Sigma^-(R_3) + \frac{2}{3}\left(\Pi^-(R_1) + \Pi^-(R_2)\right)\right]^2 + \frac{5}{9}\left(\Pi^-(R_1) - \Pi^-(R_2)\right)^2\right\}^{1/2} \tag{128}$$

where $\Sigma^\pm = {}^3\Sigma_g^- \pm {}^5\Sigma_u^-$, $\Pi^\pm = {}^4\Pi \pm {}^2\Pi$, and $\Delta^\pm = {}^3\Delta_u \pm {}^5\Delta_g$. Note that this approach requires to consider only the $X\,{}^3\Sigma_g^-$ and ${}^3\Delta_g$ potential energy curves of O_2, and $X\,{}^2\Pi$ and ${}^4\Pi$ for NO. For convenience, the ${}^5\Sigma_u^-$ and ${}^5\Delta_g$ states of O_2 have been added to provide extra flexibility to the final model. The crux in this approach is then the assumption that the other diatomic states can be neglected, either because they lack the proper symmetry or simply because they lie too high in energy. In fact, using the same "dressing functions", the results obtained from such a 4×4 potential matrix for NO_2 (reducible to two 2×2 problems) show a striking similarity with those obtained for the original 8×8 formulation.[124] This is an interesting result, since in reaction dynamics studies (both classical and quantum) the computational labor involved in the numerical diagonalization procedure raises as the cube of the basis set size (m^3). Moreover, only a small number of excited diatomic curves and off-diagonal terms are required for states of the same symmetry. Of course, as it also happens for the 8×8 potential matrix, there are topographical features which require some tuning before the surface can be applied for accurate dynamics calculations.

Finally, we focus briefly on the recent work of Mahapatra *et al.*,[139] and Reignier *et al.*[140] The first paper reports *ab initio* multireference configuration-interaction (MR CI) calculations of the two lowest NO_2 adiabatic potential energy surfaces of ${}^2A'$ symmetry, from which the diabatic

potential matrix has been constructed using a diabatization procedure suggested previously.[169] Such surfaces were ultimately interpolated using three-dimensional spline fits, and employed to investigate the nuclear dynamics on the two electronically coupled states by a time-dependent wave packet method. Although the approach seems to work well, it is based on the assumption that only two states are involved, which is generally a limitation. Of course, the use of splines also casts some worry on whether the approach can be extended to larger polyatomics.

Rather than attempting to obtain the diabatic potential matrix, Reignier *et al.*[140] reported separate global fits of the $1\,^2A'$ and $2\,^2A'$ adiabatic potential energy surfaces using the single-valued DMBE[72,86] formalism. The fitted surfaces provide a fairly accurate representation of their own MR CI energies, and also a realistic representation of the anisotropic $NO(^2\Pi) + O(^3P)$ long-range interaction potential, which is claimed to have an appreciable influence on dynamical features such as the density of states.[140] The emphasis has been on this channel, which is the most important one for studying the decomposition of $NO_2(\widetilde{X}\,^2A/\widetilde{A}\,^2B_2)$. Not surprisingly, therefore, the fits perform poorly at other regions of configuration space of the NO_2 molecule, in particular along the $N(^4S)+O_2(X\,^3\Sigma_g^-)$ dissociation channel, where both fits show deep spurious wells. Moreover, as admitted by the authors,[140] their separately modelled adiabatic potential energy surfaces do not describe properly the $\widetilde{X}\,^2A_1/\widetilde{A}\,^2B_2$ conical intersection, which is probably due to the difficulties anticipated in Sec. 3. Indeed, a proper matching of the surfaces along the manifold of degeneracy can be cumbersome, even if semi-numerical fitting methods are employed. At least, the question of whether the proper topological properties are reproduced cannot be answered *a priori* in this way. In summary, accurate representations of two-state manifolds exist for some X_3 systems, and some are probably well understood for heteronuclear triatomics like NO_2, although no similar understanding of electronic manifolds in larger polyatomics seems to exist.

4.3. H_3O: *A Prospective on Tetratomic Systems and Beyond*

Except for the well-known LEPS form of H_4 (Ref. 123, and references therein) and related DIM expressions[170] for s^n-type ($s=3-6$) systems, no

general global multi-sheeted potential energy surfaces have, to our knowledge, been completed for any four-atom or larger polyatomic system. In fact, although the multivalued DMBE formalism based on the "dressed-DIM" approach is general, it is far too complicated to be applied in systems with four or more atoms. Suffice it to say that the formalism is not trivial even for a general triatomic molecule, and then there are $\binom{N}{N_f}$ dissociative fragments with N_f atoms in a N-atom system: four triatomic fragments for a tetratomic system, and so on. One might then think of adopting a polyatomics-in-molecules (Ref. 171, and references therein) formalism, eventually dressed within the spirit of the "dressed-DIM" (multivalued DMBE) method discussed in the present work. However, such an approach would require the knowledge of global potential energy surfaces for the relevant electronic states of the involved triatomic (or larger polyatomic) fragments, which are generally unavailable and contain themselves subtle topological features such as the conical intersections on which we have been focusing. Thus, a simplified DMBE formalism based on a generalization of Eq. (62) may stand as the method of choice for such 'medium-size' molecules, leaving more sophisticated treatments for the triatomic fragments.

To illustrate the idea, let us examine briefly the case of the H_3O system. This plays a pivotal role in atmospheric[172] and combustion[173] chemistry, and hence has been much studied, particularly from the point of view of the H + H_2O reaction dynamics. Although several potential energy surfaces have been reported[99,174–178] for this system, none describes the conical intersection with the lowest excited state of the same symmetry (for a review that points out additional difficulties, see Ref. 99). It is the formalism relevant to overcome this problem that we tentatively highlight in the remaining of this section.

First, we assume that only two sheets are relevant to discuss the dynamics of the OH + H_2 reaction. Within such an assumption, the elements of the 2×2 potential matrix $\mathbf{W}$ will be defined by

$$W_{11}(\mathbf{R}) = E_{O(^1D)} + \sum_{i=1-3} V_{OH}^{(2)}(^2\Sigma^+; R_i) + \sum_{i=4-6} V_{H_2}^{(2)}(^1\Sigma_g^+; R_i) + V_{H_3}^{(3)}\left(2\,^2A'; \mathbf{R}_h\right) + \sum_{j=1-3} V_{H_2O}^{(3)}\left(1\,^2A'; \mathbf{R}_{wj}\right) + V_{11}^{(4)}(\mathbf{R}) \tag{129}$$

$$W_{22}(\mathbf{R}) = \sum_{i=1-3} V_{\mathrm{OH}}^{(2)}(^2\Pi; R_i) + \sum_{i=4-6} V_{\mathrm{H_2}}^{(2)}(^3\Sigma_u^+; R_i) + V_{\mathrm{H_3}}^{(3)}\left(2\,^2A'; \mathbf{R}_h\right) + \sum_{j=1-3} V_{\mathrm{H_2O}}^{(3)}\left(2\,^2A'; \mathbf{R}_{wj}\right) + V_{22}^{(4)}(\mathbf{R}) \tag{130}$$

$$W_{12}(\mathbf{R}) = W_{21}(\mathbf{R}) = \sum_{j=1-3} C(\mathbf{R}_{wj}) \sin\alpha_{wj} + V_{12}^{(4)}(\mathbf{R}) \tag{131}$$

where $E_{\mathrm{O}(^1D)}$ is the energy of the oxygen atom in its ^1D state, $\mathbf{R}_h = (R_4, R_5, R_6)$ is the subdomain of configuration space relevant to H_3, $\mathbf{R}_{w1} = (R_1, R_2, R_6)$ that of one of the H_2O fragments, and correspondingly for the other two water fragments $\mathbf{R}_{w2} = (R_2, R_3, R_4)$ and $\mathbf{R}_{w3} = (R_1, R_3, R_5)$. In turn, $V_{ij}^{(4)}(\mathbf{R})$ $(i, j = 1, 2)$ are four-body energy terms, which contain the set of parameters to be calibrated from a fit to *ab initio* data or other information on H_3O. Thus, one presumes that 2×2 potential matrices have previously been reported for the various triatomic fragments. Note that $C(\mathbf{R}_{wj})$ specifies a three-body coupling term of the form suggested in Ref. 179, and α_{wj} is the valence angle of the jth H_2O fragment. Furthermore, one may impose that the three-body energy terms for H_3 are taken from the two sheets of the DMBE potential energy surface[39] discussed in Sec. 4.1, thus ensuring that dissociation to such an accurate surface will be obtained whenever the oxygen atom is moved away from the three hydrogen ones. Similarly, the three-body terms for H_2O may be chosen such that H_3O dissociates to the H_2O ES potential energy surface[112] when a H atom is separated from the remaing triatomic fragment.

The only other requirement on dissociation refers to the diatom + diatom asymptotic limits. For this, one should bear in mind that the two relevant dissociation limits are

$$\mathrm{H_3O} \rightarrow \mathrm{OH}\left(^2\Pi\right) + \mathrm{H_2}\left(^1\Sigma_g^+\right) \tag{132}$$

$$\rightarrow \mathrm{OH}\left(^2\Sigma^+\right) + \mathrm{H_2}\left(^1\Sigma_g^+\right) \tag{133}$$

with the limit in Eq. (133) being[180] about $11\,000\,\mathrm{cm}^{-1}$ above the conical intersection, which in turn lies about $20\,000\,\mathrm{cm}^{-1}$ above the $\mathrm{OH}(X\,^2\Pi) + H_2$ asymptote. Such a conical intersection arises (see Fig. 7 of Ref. 180) for T-shaped (C_{2v}) structures when HO approaches the middle of the H_2 bond, with the H (O) atom of OH pointing to the middle of H_2 for the channel correlating with $\mathrm{OH}\left(A^2\Sigma^+\right) + \mathrm{H_2}$ $[\mathrm{OH}\left(X^2\Pi\right) + \mathrm{H_2}]$. The nuclear

configurations in the relevant g–h plane representing a circular path around the OH_3 conical intersection are illustrated in Fig. 7 of Ref. 8. Clearly, at none of the above asymptotes does one get $H_2\left({}^3\Sigma_u^+\right)$ as a dissociation product, and hence the present simplified formalism must be corrected to allow for such a behavior. This may be achieved through the replacements

$$V_{H_2}^{(2)}({}^1\Sigma_g^+) \to V_{H_2}^{(2)}({}^3\Sigma_u^+) f(\mathbf{R}) + V_{H_2}^{(2)}({}^1\Sigma_g^+)[1 - f(\mathbf{R})] \tag{134}$$

where the switching function is of the form[79]

$$f = 1 + \tanh\left[\beta(2s_i - s_j - s_k - s_{j+3} - s_{k+3})\right] \tag{135}$$

and s_i denotes a displacement from the corresponding equilibrium geometry; β is some adjustable parameter, and the indices ijk cover all cyclic permutations of 123. Note that $f \to 1$ at the $H + H_2O$ dissociation limits, but is 0 at the limit $OH\left({}^2\Pi\right) + H_2\left({}^1\Sigma_g^+\right)$. Of course, the replacements in Eq. (134) must be ensured for all permutationally equivalent channels. Moreover, the four-body energy terms must be flexible enough to allow a reliable fit of *ab initio* data in the regions of the intersection loci (Ref. 181, and references therein), and reaction paths leading to the products. Note that the surface correlating with $OH(A\,{}^2\Sigma^+) + H_2$ shows a shallow minimum corresponding to a C_{3v} H_3O intermediate, in which the oxygen atom is above the plane of the equilateral triangle formed by the three hydrogen atoms [this minimum lies[180] $\sim 1750\,\mathrm{cm}^{-1}$ above $OH(X\,{}^2\Pi) + H_2$]. Clearly, the analysis cannot be pursued prior to a fit of *ab initio* data.

4.4. *Other Systems*

A list (not exhaustive) of global multi-sheeted potential energy surfaces for the relevant manifold of electronic states of the same symmetry of some polyatomic systems is given in Table 1. Space limitations prevent any discussion of such a work, with the reader being referred to the original papers[66,106,112–115,168,182–185] for details. Much of the work published using the DIM method or some of its variants (Refs. 171,185–188, and references therein) has also been omitted.[h]

[h]The readers may have access to such a work through the internet, e.g. at the ISI Web of KNOWLEDGE homepage or, of course, via more traditional bibliography searching schemes.

Table 1. A list of systems for which multi-sheeted global potential energy surfaces have been developed

System	Method	Features	Ref.
H_3^+ ($^1A'$)	ES	Multivalued (3×3)	114,115
H_3 ($^2A'$)	DMBE	Two-valued	39
	DIM	Two-valued	124
	DMBE+correction term	Two-valued	43
H_2F ($^2A'$)	DMBE	Two-valued	182
	DIM	Two-valued	124
H_2O ($^2A'$)	ES	Two-valued	112
	ES	Multivalued (3×3)	113
C_2H ($^2A'$)	DMBE	Two-valued	66
HCN ($^2A'$)	DIM	Two-valued	184
HO_2 ($^2A''$)	DIM[a]	Multivalued (32×32)	106
	DMBE	Multivalued (18×18)	183
	DMBE	Two-valued	168
NO_2 ($^2A'$)	DMBE	Multivalued (8×8)	124
O_3 ($^1A'$)	MBE	Two-valued	192
SO_2 ($^1A'$)	MBE	Two-valued	193
HCNO (^3A)	DIM	Multivalued (45×45)	194

[a]Some of the excited states may not dissociate to accurate diatomic curves as these were taken as disposable functions to fit the data on the triatomic.

5. Concluding Remarks

Extraordinary progress has been made on the calculation of potential energy surfaces for molecular dynamics. Despite such advances in the *ab initio* theory and computational tools, chemically accurate *ab initio* potential energy surfaces are available only for systems with a few electrons. These calculations are so very time consuming that the list of such systems can hardly be substantially increased in the forthcoming few years. Thus, there is much room for methods to extrapolate to the complete basis set (Ref. 69, and references therein) limit and/or the complete basis set/full configuration interaction (exact nonrelativistic) limit (Ref. 68, and references therein). There has also been progress on modelling multi-sheeted potential energy surfaces although, not surprisingly, at a much slower pace than single-valued ones. Thus, there will also be much room for testing current strategies for multi-sheeted model potentials and developing new ones, since this is a crucial step toward the understanding of nonadiabatic chemistry in areas such as spectroscopy and reaction dynamics. Further topics include the interaction

between systems which possess by themselves a crossing seam. What happens to such seams remains to our knowledge virtually unexplored.[189–191]

In summary, after discussing the Born–Oppenheimer approximation and its generalization to systems with electronic degeneracies, the present review focused on methods for multi-sheeted global potential energy surfaces with emphasis on DMBE, since this method has led to some of the most reliable functions currently available. Although the multivalued DMBE applications completed thus far are only for triatomic systems, work on tetratomic species is currently in progress. Some topological implications of the multivaluedness have also been examined, with emphasis on the GP effect.

Acknowledgment

The author thanks his coworkers for their valuable contributions. The financial support from Fundação para a Ciência e Tecnologia, Portugal, is also appreciated.

Appendix A. The Geometric Phase

Consider an arbitrary path $\mathbf{R}(t)$. The non-stationary time-dependent electronic Schrödinger equation along such a path assumes the form

$$H_e \Psi\left(\mathbf{r};\mathbf{R}(t)\right) = i\hbar \frac{\partial \Psi\left(\mathbf{r};\mathbf{R}(t)\right)}{\partial t}. \tag{A.1}$$

Using the electronic basis set $\{\Psi_I\left(\mathbf{r};\mathbf{R}(t)\right)\}$, where

$$H_e \Psi_I\left(\mathbf{r};\mathbf{R}(t)\right) = V_I\left(\mathbf{R}(t)\right) \Psi_I\left(\mathbf{r};\mathbf{R}(t)\right) \tag{A.2}$$

the wave function may be expanded as

$$\Psi\left(\mathbf{r};\mathbf{R}(t)\right) = \sum_J c_J(t) \Psi_J\left(\mathbf{r};\mathbf{R}(t)\right) \exp\left[-\frac{i}{\hbar}\int^t V_J\left(t'\right) dt'\right] \tag{A.3}$$

where the term in the exponential is the usual dynamical phase.

From Eqs. (A.1) and (A.3), one then gets

$$i\hbar\frac{dc_I}{dt} = \sum_J c_J \left\{ H_{IJ} - V_J\delta_{IJ} - i\hbar \left\langle \Psi_I \middle| \frac{\partial \Psi_J}{\partial t} \right\rangle \exp\left[-\frac{i}{\hbar}\int^t (V_J - V_I)\, dt' \right] \right\}. \tag{A.4}$$

Neglecting now nonadiabatic coupling with states $J \neq I$ and noting that $H_{IJ} = S_{IJ} = 0$ for adiabatic basis set, one has

$$\frac{dc_I}{dt} = -\left\langle \Psi_I \middle| \frac{\partial \Psi_I}{\partial t} \right\rangle c_I \tag{A.5}$$

and hence

$$c_I = \exp\left[-\int^t \left\langle \Psi_I \middle| \frac{\partial \Psi_I}{\partial t'} \right\rangle dt' \right] = \exp\left[iA_I(t) \right] \tag{A.6}$$

where $A_I(t) = i\int^t \langle \Psi_I | \frac{\partial \Psi_I}{\partial t'} \rangle dt'$ is the geometric phase. Thus, retaining only one term in the wave function expansion, one has

$$\Psi\left(\mathbf{r}; \mathbf{R}(t)\right) = \Psi_I\left(\mathbf{r}; \mathbf{R}(t)\right) \exp\left[-\frac{i}{\hbar}\int^t V_I\left(t'\right) dt' \right] \exp\left[iA_I(t) \right] \tag{A.7}$$

which has the form expressed in Eq. (13) for the time-independent formulation.

Appendix B. Diatomic Curves: The EHFACE2U Model

Following the general DMBE strategy, the two-body energy curves assume the form

$$V^{(2)} = V_{EHF}^{(2)} + V_{dc}^{(2)} \tag{B.1}$$

where all symbols have their usual meaning. Although the simpler EHFACE2[151] model has been employed in some of the case studies reported, we describe here the more complete EHFACE2U[152] (Extended Hartree–Fock Approximate Correlation Energy model for 2-body interactions with inclusion of the United-atom limit) formulation.

First, the dynamical correlation part is written as

$$V_{dc}^{(2)} = -\sum_{n=6,8,10} C_n \chi_n(R) R^{-n} \tag{B.2}$$

where the damping dispersion functions[i] assume the form[195–197]

$$\chi_n(R) = \left[1 - \exp\left(-A_n \frac{R}{\rho} - B_n \frac{R^2}{\rho^2}\right)\right]^n \tag{B.3}$$

and A_n and B_n are the auxiliary functions[196] $A_n = \alpha_0 n^{-\alpha_1}$ and $B_n = \beta_0 \exp(-\beta_1 n)$; $\alpha_0 = 16.36606$, $\alpha_1 = 0.70172$, $\beta_0 = 17.19338$, and $\beta_1 = 0.09574$ are universal parameters (dimensionless) for all isotropic interactions. In turn, the scaling parameter is defined by $\rho = (5.5 + 1.25R_0)$, where $R_0 = 2(\langle r_X^2\rangle^{1/2} + \langle r_Y^2\rangle^{1/2})$ with $\langle r_X^2\rangle$ ($\langle r_Y^2\rangle$) being the expectation value of the squared radii for the outermost electrons in atom X(Y).[198] Thus, all coefficients in $V_{dc}^{(2)}$ are in principle obtained *a priori* from theoretical or semi-empirical data.

In turn, the V_{EHF} component of the potential assumes the form[152]

$$V_{EHF}^{(2)} = -DR^{-1}\left(1 + \sum_{i=1}^{N} a_i r^i\right)\exp[-\gamma(r)r] + V_{exc}^{asym}(R)\chi_{exc}(R) \tag{B.4}$$

where $\gamma(r) = \gamma_0[1+\gamma_1 \tanh(\gamma_2 r)]$, $r = R - R_m$ is the displacement from the equilibrium geometry, and D, $a_i (i = 1-N)$ and $\gamma_i (i = 1-2)$ are parameters usually determined from a least-squares fitting procedure to RKR and/or other available data. Moreover, V_{exc}^{asym} is the asymptotic exchange energy. Except for this, all the numerical coefficients in $V_{EHF}^{(2)}$ are usually obtained from a fit to accurate *ab initio* energies or spectroscopic information referring to the complete potential. For numerical values of the parameters in specific interactions, the reader is referred to the original papers cited in Sec. 4.

Appendix C. Spin Wave Functions and Recoupling Matrices for H_3

Consider first the spin states of the various species involved: $s = \frac{1}{2}$, $m_s = \pm\frac{1}{2}$ for H; $s = 0, 1$, $m_s = 0, \pm 1$ for H_2; $s = \frac{1}{2}$, $m_s = \pm\frac{1}{2}$ for H_3. By

[i]These should not be confused with nuclear wave functions in Eq. (6). Similarly, ρ and $\gamma(r)$ should not be confused with similar symbols used in the main text.

considering

$$|S,M\rangle = \sum_{m_\mathrm{a} m_\mathrm{b}} C^{SM}_{s_\mathrm{a} m_\mathrm{a}, s_\mathrm{b} m_\mathrm{b}} |s_\mathrm{a}, m_\mathrm{a}\rangle |s_\mathrm{b}, m_\mathrm{b}\rangle \tag{C.1}$$

one gets for the AB spin functions:

$$|1,1\rangle = C^{1,1}_{\frac{1}{2}\frac{1}{2},\frac{1}{2}\frac{1}{2}} \left|\frac{1}{2}\frac{1}{2}\right\rangle \left|\frac{1}{2}\frac{1}{2}\right\rangle = \mathrm{ab} \tag{C.2}$$

$$|1,0\rangle = C^{1,0}_{\frac{1}{2}\frac{1}{2},\frac{1}{2}\frac{\overline{1}}{2}} \left|\frac{1}{2}\frac{1}{2}\right\rangle \left|\frac{1}{2}\frac{\overline{1}}{2}\right\rangle + C^{1,0}_{\frac{1}{2}\frac{\overline{1}}{2},\frac{1}{2}\frac{1}{2}} \left|\frac{1}{2}\frac{\overline{1}}{2}\right\rangle \left|\frac{1}{2}\frac{1}{2}\right\rangle = \frac{1}{\sqrt{2}} \left(\mathrm{a\overline{b}} + \mathrm{\overline{a}b}\right). \tag{C.3}$$

Moreover, for H_3, one obtains:

$$\begin{aligned}\chi_1 =& C^{\frac{1}{2},\frac{1}{2}}_{\frac{1}{2}\frac{1}{2},10} \left|\frac{1}{2}\frac{1}{2}\right\rangle |10\rangle + C^{\frac{1}{2}\frac{1}{2}}_{\frac{1}{2}\frac{1}{2},1\overline{1}} \left|\frac{1}{2}\frac{1}{2}\right\rangle |1\overline{1}\rangle + C^{\frac{1}{2}\frac{1}{2}}_{\frac{1}{2}\frac{\overline{1}}{2},11} \left|\frac{1}{2}\frac{\overline{1}}{2}\right\rangle |11\rangle \\ =& \frac{1}{\sqrt{6}} \left(2\mathrm{ab\overline{c}} - \mathrm{a\overline{b}c} - \mathrm{\overline{a}bc}\right)\end{aligned} \tag{C.4}$$

$$\chi_2 = C^{\frac{1}{2},\frac{1}{2}}_{\frac{1}{2}\frac{1}{2},00} \left|\frac{1}{2}\frac{1}{2}\right\rangle |00\rangle = \frac{1}{\sqrt{2}} \left(\mathrm{a\overline{b}c} - \mathrm{\overline{a}bc}\right). \tag{C.5}$$

In turn, the spin recoupling matrices for BC and AC are defined by:

$$\phi_i = \sum_{k=1}^{2} t_{ki} \chi_k \tag{C.6}$$

which, for diatomic BC, leads to

$$|s_\mathrm{a} s_\mathrm{b} s_\mathrm{c}; s_\mathrm{bc} SM\rangle = \sum_{s_\mathrm{ab}} t^{SM}_{s_\mathrm{bc} s_\mathrm{ab}} |s_\mathrm{a} s_\mathrm{b} s_\mathrm{c}; s_\mathrm{ab} SM\rangle \tag{C.7}$$

where

$$t_{s_\mathrm{bc} s_\mathrm{ab}} = (-1)^{s_\mathrm{a}+s_\mathrm{b}+s_\mathrm{c}+S} \sqrt{(2s_\mathrm{ab}+1)+(2s_\mathrm{bc}+1)} \begin{Bmatrix} s_\mathrm{a} & s_\mathrm{b} & s_\mathrm{ab} \\ s_\mathrm{c} & S & s_\mathrm{bc} \end{Bmatrix} \tag{C.8}$$

which leads to

$$\mathbf{T}_{bc} = \frac{1}{2} \begin{pmatrix} -1 & -\sqrt{3} \\ \sqrt{3} & -1 \end{pmatrix}. \tag{C.9}$$

Similarly, one has for diatomic AC:

$$\mathbf{T}_{ac} = \frac{1}{2} \begin{pmatrix} 1 & \sqrt{3} \\ \sqrt{3} & -1 \end{pmatrix} \tag{C.10}$$

Appendix D. Note Added in Proof

The main body of this article dates to May 2002, when the work described in Sec. 4.2 for the NO_2 molecule was far from completion.[153] Apart from minor corrections, we have decided at the proof stage to maintain the text in its original form, addressing the reader to the paper[116] where the completed 8×8 DMBE potential energy surface for $NO_2(^2A')$ has been published. Not surprisingly, small changes are observed, although they should not be of concern for the purposes of the present work. In that publication,[116] we have also conveyed near spectroscopic accuracy to the ground-state sheet $(1^2A')$ of the NO_2 potential energy surface in the vicinity of the deep potential well by merging it with a spectroscopically determined[167] Taylor-series-expansion type form via a novel multiple ES scheme. After this work has been completed, a paper by Kurkal *et al.*[199] reporting global potential energy surfaces for the ground (1^2A_1) and the first excited (1^2B_2) electronic states of NO_2 has also appeared. In this paper, about 5000 *ab initio* points have been calculated at the internally contracted MR CI level using the standard correlation consistent polarized quadruple (cc − pVQZ) atomic basis set. The calculated dissociation energy corresponding to $NO_2 \rightarrow NO + O$ and other features of the surfaces are found to be in close agreement with experimental values. Not surprisingly therefore, the structure and energy parameters of the two electronic states of NO_2 tabulated in Ref. 199 show good agreement with the corresponding attributes of the DMBE/ES[116] potential energy surface. Note that the fundamental frequencies and energies of low lying bound states have also been reported[116,199] for the two surfaces from quantum dynamics calculations, with the results showing reasonably good agreement. Since the grid of calculated *ab initio* points is dense enough, they have adopted an interpolation with a three-dimensional cubic spline rather than an analytical representation of the NO_2 potential energy surface. However, as the authors themselves have pointed out,[199] their chosen coordinates are not well suited to describe the $N + O_2$ channel. In particular, this is found[199] to be 1.30 eV above the $O + NO$ channel, which underestimates the experimental value by 0.1 eV. Thus, the accuracy of their surface for reaction dynamics studies remains to be shown. We should mention in this context that the lowest adiabatic sheet of the DMBE/ES[116] potential energy surface has recently been employed for dynamics and kinetics studies[200] of the

reaction $N(^4S_u) + O_2(X^3\Sigma_g^-) \rightarrow NO + O$ and its reverse, with the calculated thermal rate coefficients being found to be in good agreement with the recommended values over a wide range of temperatures. A final remark goes to a recent paper[201] where a new scheme is presented to allow an accurate representation of a double-sheeted potential energy surface using standard single-valued DMBE theory. According to this new approach, the degeneracy of the two sheets along the conical intersection line is guaranteed by construction. Such a method has been applied to the lowest triplet state of $H_3^+(a^3E')$ for which the lowest vibrational levels have also been calculated.

References

1. M. Born and J. R. Oppenheimer, *Ann. Phys.* **84**, 457 (1927).
2. B. T. Sutcliffe, in *Lecture Notes in Chemistry*, Ed. A. F. Sax (Springer, Berlin, 1999), Vol. 71, p. 61.
3. J. von Neumann and E. Wigner, *Phys. Z.* **30**, 467 (1929).
4. E. Teller, *J. Phys. Chem.* **41**, 109 (1937).
5. G. Herzberg and H. C. Longuet-Higgins, *Faraday Discuss. Chem. Soc.* **35**, 77 (1963).
6. H. C. Longuet-Higgins, *Proc. R. Soc. London* **A344**, 147 (1975).
7. T. F. George, K. Morokuma and Y.-W. Lin, *Chem. Phys. Lett.* **30**, 54 (1975).
8. D. R. Yarkony, *J. Phys. Chem.* **100**, 18612 (1996).
9. H. C. Longuet-Higgins, *Adv. Spectrosc.* **2**, 429 (1961).
10. Y. Yamaguchi, Y. Osamura, J. D. Goddard and H. F. Schaeffer, *New Dimension to Quantum Chemistry: Analytic Derivative Methods in* ab initio *Molecular Electronic Structure Theory* (Oxford University Press, Oxford, 1994).
11. M. J. Bearpark, M. A. Robb and H. B. Schlegel, *Chem. Phys. Lett.* **223**, 269 (1994).
12. A. J. C. Varandas and Z. R. Xu, in *Adv. Chem. Phys.*, Eds. M. Baer and G. D. Billing (Wiley, New York, 2002), Vol. 124, p. 659.
13. R. C. Whitten and F. T. Smith, *J. Math. Phys.* **9**, 1103 (1968).
14. B. R. Johnson, *J. Chem. Phys.* **73**, 5051 (1980).
15. B. R. Johnson, *J. Chem. Phys.* **79**, 1906 (1983).
16. B. R. Johnson, *J. Chem. Phys.* **79**, 1916 (1983).
17. A. J. C. Varandas and H. G. Yu, *J. Chem. Soc. Faraday Trans.* **93**, 819 (1997).
18. J. Zúñiya, A. Bastida and A. Requena, *J. Chem. Soc. Faraday Trans.* **93**, 1681 (1997).
19. D. A. Varshalovich, A. N. Moskalev and V. K. Khersonskii, *Quantum Theory of Angular Momentum* (World Scientific, Singapore, 1988).

20. M. Born and K. Huang, *Dynamical Theory of Crystal Lattices* (Oxford, London, 1954).
21. I. B. Bersuker and V. Z. Polinger, *Vibronic Interactions in Molecules and Crystals* (Springer-Verlag, Berlin, 1989).
22. A. J. C. Varandas, J. Tennyson and J. N. Murrell, *Chem. Phys. Lett.* **61**, 431 (1979).
23. S. S. Xantheas, S. T. Elbert and K. Ruedenberg, *J. Chem. Phys.* **93**, 7519 (1990).
24. M. V. Berry, *Proc. R. Soc.* **A392**, 45 (1984).
25. Y. Aharonov and B. Bohm, *Phys. Rev.* **115**, 485 (1959).
26. C. A. Mead, *Chem. Phys.* **49**, 23 (1980).
27. R. Jackiw, *Comments At. Mol. Phys.* **21**, 71 (1988).
28. B. K. Kendrick and C. A. Mead, *J. Chem. Phys.* **102**, 4160 (1995).
29. A. J. C. Varandas and Z. R. Xu, *J. Chem. Phys.* **112**, 2121 (2000).
30. C. A. Mead and D. G. Truhlar, *J. Chem. Phys.* **70**, 2284 (1979).
31. C. A. Mead, *J. Chem. Phys.* **72**, 3839 (1980).
32. Y.-S. M. Wu, B. Lepetit and A. Kuppermann, *Chem. Phys. Lett.* **186**, 319 (1991).
33. Y.-S. M. Wu and A. Kuppermann, *Chem. Phys. Lett.* **201**, 178 (1993).
34. A. Kuppermann and Y.-S. M. Wu, *Chem. Phys. Lett.* **213**, 636 (1993).
35. G. D. Billing and N. Marković, *J. Chem. Phys.* **99**, 2674 (1993).
36. Z. R. Xu and A. J. C. Varandas, *Int. J. Quantum Chem.* **80**, 454 (2000).
37. Z. R. Xu and A. J. C. Varandas, *J. Phys. Chem.* **105**, 2246 (2001).
38. T. C. Thompson and C. A. Mead, *J. Chem. Phys.* **82**, 2408 (1985).
39. A. J. C. Varandas, F. B. Brown, C. A. Mead, D. G. Truhlar and N. C. Blais, *J. Chem. Phys.* **86**, 6258 (1987).
40. Z. R. Xu, M. Baer and A. J. C. Varandas, *J. Chem. Phys.* **112**, 2746 (2000).
41. B. Kendrick, C. A. Mead and D. G. Truhlar, *Chem. Phys. Lett.* **277**, 31 (2002).
42. C. A. Mead and D. G. Truhlar, *J. Chem. Phys.* **77**, 6090 (1982).
43. R. Abrol, A. Shaw, A. Kuppermann and D. R. Yarkony, *J. Chem. Phys.* **115**, 4640 (2001).
44. R. Abrol and A. Kuppermann, *J. Chem. Phys.* **116**, 1035 (2002).
45. M. Baer, *Chem. Phys. Lett.* **35**, 112 (1975).
46. D. R. Yarkony, *J. Chem. Phys.* **105**, 10456 (1996).
47. D. R. Yarkony, *J. Phys. Chem.* **A101**, 4263 (1997).
48. E. S. Kryachko and A. J. C. Varandas, *Int. J. Quantum Chem.* **89**, 255 (2002).
49. M. Baer, *Mol. Phys.* **40**, 1011 (1980).
50. T. Pacher, L. S. Cederbaum and H. Köppel, *Adv. Chem. Phys.* **84**, 293 (1993).
51. R. Englman and M. Baer, *J. Phys. Condens. Matt.* **11**, 1059 (1999).

52. A. J. C. Varandas and J. N. Murrell, *Faraday Discuss. Chem. Soc.* **62**, 92 (1977).
53. M. Baer, *Chem. Phys.* **15**, 49 (1976).
54. Z. H. Top and M. Baer, *Chem. Phys.* **25**, 1 (1977).
55. Z. H. Top and M. Baer, *J. Chem. Phys.* **66**, 1363 (1977).
56. W. Lichten, *Phys. Rev.* **131**, 229 (1965).
57. H. Werner and W. Meyer, *J. Chem. Phys.* **74**, 5802 (1981).
58. D. R. Yarkony, *Rev. Mod. Phys.* **68**, 985 (1996).
59. G. Parlant, J. Rostas, G. Taieb and D. R. Yarkony, *J. Chem. Phys.* **93**, 6403 (1990).
60. G. Hirsch, R. J. Buenker and C. Petrongolo, *Mol. Phys.* **70**, 835 (1990).
61. S. Han, H. Hettema and D. R. Yarkony, *J. Chem. Phys.* **102**, 1955 (1995).
62. N. Matsunaga and D. R. Yarkony, *Mol. Phys.* **93**, 79 (1998).
63. E. S. Kryachko and D. R. Yarkony, *Theor. Chem. Acc.* **100**, 154 (1998).
64. R. F. Salzgeber, V. Mandelshtam, C. Schlier and H. S. Taylor, *J. Chem. Phys.* **109**, 937 (1998).
65. E. S. Kryachko and D. R. Yarkony, *Int. J. Quantum Chem.* **76**, 235 (2000).
66. M. Boggio-Pasqua, A. I. Voronin, P. Halvick, J. C. Rayez and A. J. C. Varandas, *Mol. Phys.* **98**, 1925 (2000).
67. F. B. Brown and D. G. Truhlar, *Chem. Phys. Lett.* **117**, 307 (1985).
68. A. J. C. Varandas, *J. Chem. Phys.* **90**, 4379 (1989).
69. A. J. C. Varandas, *J. Chem. Phys.* **113**, 8880 (2000).
70. J. S. Wright and S. K. Gray, *J. Chem. Phys.* **69**, 67 (1978).
71. P. J. Kuntz, in *Dynamics of Molecular Collisions, Part B*, Ed. W. Miller (Plenum, New York, 1976), p. 53.
72. A. J. C. Varandas, *Adv. Chem. Phys.* **74**, 255 (1988).
73. A. J. C. Varandas, in *Trends in Atomic and Molecular Physics*, Ed. M. Yáñez (Universidad Autonoma de Madrid, Madrid, 1990), p. 113.
74. J. N. L. Connor, *Comput. Phys. Comm.* **17**, 117 (1979).
75. G. C. Schatz, *Rev. Mod. Phys.* **61**, 669 (1989).
76. A. J. C. Varandas and S. J. P. Rodrigues, *Spectrochim. Acta* **A58**, 629 (2002).
77. M. A. Collins and D. F. Parsons, *J. Chem. Phys.* **99**, 6756 (1993).
78. A. J. C. Varandas and L. Zhang, *Chem. Phys. Lett.* **331**, 474 (2000).
79. J. N. Murrell, S. Carter, S. C. Farantos, P. Huxley and A. J. C. Varandas, *Molecular Potential Energy Functions* (Wiley, Chichester, 1984).
80. N. Sathyamurthy, *Comput. Phys. Rep.* **3**, 1 (1985).
81. D. G. Truhlar, R. Steckler and M. S. Gordon, *Chem. Rev.* **87**, 217 (1987).
82. A. J. C. Varandas, *J. Mol. Struct. Theochem* **166**, 59 (1988).
83. R. Jaquet, in *Lecture Notes in Chemistry*, Ed. A. F. Sax (Springer, Berlin, 1999), Vol. 71, p. 97.
84. G. C. Schatz, in *Lecture Notes in Chemistry*, Eds. A. Laganá and A. Riganelli (Springer, Berlin, 2000), Vol. 75, p. 15.

85. A. J. C. Varandas, in *Lecture Notes in Chemistry*, Ed. A. Laganá and A. Riganelli (Springer, Berlin, 2000), Vol. 75, p. 33.
86. A. J. C. Varandas, *Int. Rev. Phys. Chem.* **19**, 199 (2000).
87. F. London, *Z. Electrochem.* **35**, 552 (1929).
88. H. Eyring and M. Polanyi, *Z. Phys. Chem. Abt.* **12**, 279 (1931).
89. S. Sato, *J. Chem. Phys.* **23**, 592 (1955).
90. S. Sato, *J. Chem. Phys.* **23**, 2465 (1955).
91. F. O. Ellison, *J. Am. Chem. Soc.* **85**, 3540 (1963).
92. J. C. Tully, *Adv. Chem. Phys.* **42**, 63 (1980).
93. P. J. Kuntz, in *Atom-Molecule Collision Theory*, Ed. R. Bernstein (Plenum, New York, 1979), p. 79.
94. N. Sathyamurthy and L. M. Raff, *J. Chem. Phys.* **63**, 464 (1975).
95. H. Koizumi, G. C. Schatz and J. M. Bowman, *J. Chem. Phys.* **95**, 4130 (1992).
96. T.-S. Ho and H. Rabitz, *J. Chem. Phys.* **104**, 2584 (1996).
97. T.-S. Ho, T. Hollebeek, H. Rabitz, L. B. Harding and G. C. Schatz, *J. Chem. Phys.* **105**, 10472 (1996).
98. A. Frishman, D. K. Koffman and D. J. Kouri, *J. Chem. Phys.* **107**, 804 (1997).
99. G. s. Wu, G. C. Schatz, G. Lendvay, D.-C. Fang and L. B. Harding, *J. Chem. Phys.* **113**, 3150 (2000).
100. A. J. C. Varandas, *J. Chem. Phys.* **105**, 3524 (1996).
101. K. C. Thompson, M. J. T. Jordan and M. A. Collins, *J. Chem. Phys.* **108**, 564 (1998).
102. T. Ishida and G. C. Schatz, *Chem. Phys. Lett.* **298**, 285 (1998).
103. P. Lancaster and K. Salkauskas, *Curve and Surface Fitting* (Academic Press, London, 1986).
104. T. Ishida and G. C. Schatz, *Chem. Phys. Lett.* **314**, 369 (1999).
105. A. J. C. Varandas and P. E. Abreu, *Chem. Phys. Lett.* **293**, 261 (1998).
106. B. K. Kendrick and R. Pack, *J. Chem. Phys.* **102**, 1994 (1995).
107. M. B. Faist and J. T. Muckerman, *J. Chem. Phys.* **71**, 225 (1979).
108. T. Hollebeek, T.-S. Ho and H. Rabitz, *Ann. Rev. Phys. Chem.* **46**, 169 (1999).
109. T. Ho, T. Hollebeek, H. Rabitz, S. D. Chao, R. T. Skodje, A. S. Zyubin and A. M. Mebel, *J. Chem. Phys.* **116**, 4124 (2002).
110. P. Soldán and J. M. Hutson, *J. Chem. Phys.* **112**, 4415 (2000).
111. P. Jimeno, A. I. Voronin and A. J. C. Varandas, *J. Mol. Spectrosc.* **192**, 86 (1998).
112. A. J. C. Varandas, *J. Chem. Phys.* **107**, 867 (1997).
113. A. J. C. Varandas, A. I. Voronin and P. J. S. B. Caridade, *J. Chem. Phys.* **108**, 7623 (1998).
114. R. Prosmiti, O. L. Polyansky and J. Tennyson, *Chem. Phys. Lett.* **273**, 107 (1997).

115. O. L. Polyansky, R. Prosmiti, W. Klopper and J. Tennyson, *Mol. Phys.* **98**, 261 (2000).
116. A. J. C. Varandas, *J. Chem. Phys.* **119**, 2596 (2003).
117. W. Ansari and A. J. C. Varandas, *J. Phys. Chem.* A **106**, 9338 (2002).
118. A. J. C. Varandas, S. P. J. Rodrigues and P. A. J. Gomes, *Chem. Phys. Lett.* **297**, 458 (1998).
119. H. G. Yu and A. J. C. Varandas, *Chem. Phys. Lett.* **334**, 173 (2001).
120. A. J. C. Varandas and H. G. Yu, *Mol. Phys.* **91**, 301 (1997).
121. T. Ishida and G. C. Schatz, *J. Chem. Phys.* **107**, 3558 (1997).
122. M. A. Collins, *Adv. Chem. Phys.* **93**, 389 (1996).
123. A. J. C. Varandas, *Int. J. Quantum Chem.* **32**, 563 (1987).
124. A. J. C. Varandas and A. I. Voronin, *Mol. Phys.* **95**, 497 (1995).
125. R. N. Porter and M. Karplus, *J. Chem. Phys.* **40**, 1105 (1964).
126. A. J. C. Varandas, *Chem. Phys. Lett.* **138**, 455 (1987).
127. A. J. C. Varandas and H. G. Yu, *Chem. Phys. Lett.* **259**, 336 (1996).
128. H. C. Longuet-Higgins, U. Öpik, M. H. L. Pryce and R. A. Sack, *Proc. R. Soc.* **A244**, 1 (1958).
129. M. S. Child and H. C. Longuet-Higgins, *Phil. Trans. R. Soc. London* **A254**, 259 (1961).
130. Z. R. Xu and A. J. C. Varandas, *Int. J. Quantum Chem.* **83**, 279 (2001).
131. A. J. C. Varandas and A. A. C. C. Pais, *J. Chem. Soc. Faraday Trans.* **89**, 1511 (1993).
132. A. A. C. C. Pais, R. F. Nalewajski and A. J. C. Varandas, *J. Chem. Soc. Faraday Trans.* **90**, 1381 (1994).
133. A. J. C. Varandas, H. G. Yu and Z. R. Xu, *Mol. Phys.* **96**, 1193 (1999).
134. A. J. C. Varandas and Z. R. Xu, *Int. J. Quantum Chem.* **75**, 89 (1999).
135. K. Yoshino, J. R. Esmond and W. H. Parkinson, *Chem. Phys.* **221**, 169 (1997).
136. T. C. Corcoran, E. J. Beiting and M. O. Mitchell, *J. Mol. Spectrosc.* **154**, 119 (1992).
137. D. L. Baulch, C. J. Cobos, R. A. Cox, G. Hayman, T. Just, J. A. Kerr, T. Murrells, M. J. Pilling, J. Troe, R. W. Walker and J. Warnatz, *J. Phys. Chem. Ref. Data* **23**, 873 (1994).
138. N. Balakrishnan and A. Dalgarno, *Chem. Phys. Lett.* **302**, 485 (1999).
139. S. Mahapatra, H. K. and L. S. Cederbaum, P. Stampfuß and W. Wenzel, *Chem. Phys.* **259**, 211 (2000).
140. D. Reignier, T. Stoecklin, A. Voronin and J. C. Rayez, *Phys. Chem. Chem. Phys.* **3**, 2726 (2001).
141. M. Gilibert, A. Aguilar, M. González and R. Sayós, *Chem. Phys.* **172**, 99 (1993).
142. G. Hirsch, R. J. Buenker and C. Petrongolo, *Mol. Phys.* **73**, 1085 (1991).
143. W. C. Bowman and F. C. De Lucia, *J. Chem. Phys.* **77**, 92 (1979).
144. S. P. Walch and R. L. Jaffe, *J. Chem. Phys.* **86**, 6946 (1987).

145. J. W. Duff, F. Bien and D. E. Paulsen, *Geophys. Res. Lett.* **21**, 2043 (1994).
146. R. Sayós, J. Hijazo, M. Gilibert and M. González, *Chem. Phys. Lett.* **284**, 101 (1998).
147. M. Gilibert, A. Aguilar, M. González and R. Sayós, *Chem. Phys.* **178**, 287 (1993).
148. D. Bose and G. V. Candler, *J. Chem. Phys.* **107**, 6136 (1997).
149. C. W. Wilson Jr., *J. Chem. Phys.* **62**, 4843 (1975).
150. P. A. Benioff, G. Das and A. C. Wahl, *J. Chem. Phys.* **67**, 2449 (1977).
151. A. J. C. Varandas and J. D. Silva, *J. Chem. Soc. Faraday Trans. 2* **82**, 593 (1986).
152. A. J. C. Varandas and J. D. Silva, *J. Chem. Soc. Faraday Trans.* **88**, 941 (1992).
153. A. J. C. Varandas (unpublished work); see Ref. 116, and Appendix D.
154. E. Leonardi, C. Petrongolo, V. Keshari, G. Hirsch and R. J. Buenker, *Mol. Phys.* **82**, 553 (1994).
155. J. C. D. Brand, K. J. Cross and A. R. Hoy, *Can. J. Phys.* **57**, 428 (1979).
156. B. O. Roos, K. Andersson, M. P. Fülsher, P.-A. Malmquist, L. Serrano-Andrès, K. Pierloot and M. Merchán, *Adv. Chem. Phys.* **XCIII**, 219 (1996).
157. T. H. Dunning, Jr., *J. Chem. Phys.* **90**, 1007 (1989).
158. D. E. Woon and T. H. Dunning Jr., *J. Chem. Phys.* **103**, 4572 (1995).
159. C. F. Jackels and E. R. Davidson, *J. Chem. Phys.* **64**, 2908 (1976).
160. C. F. Jackels and E. R. Davidson, *J. Chem. Phys.* **65**, 2941 (1976).
161. C. P. Blahous, B. F. Yates, Y. Xie and H. F. Schaefer, *J. Chem. Phys.* **93**, 8105 (1990).
162. A. Delon and R. Jost, *J. Chem. Phys.* **95**, 5686 (1991).
163. W. J. Lafferty and R. L. Sams, *J. Mol. Spectrosc.* **66**, 478 (1977).
164. J. L. Hardwick and J. C. D. Brand, *Can. J. Phys.* **54**, 80 (1976).
165. H. Katagiri and S. Kato, *J. Chem. Phys.* **99**, 8805 (1993).
166. C. Meredith, R. D. Davy, G. E. Quelch and H. F. Schaefer III, *J. Chem. Phys.* **94**, 1317 (1991).
167. J. H. Schryber, O. L. Polyansky, P. Jensen and J. Tennyson, *J. Mol. Spectrosc.* **185**, 234 (1997).
168. A. J. C. Varandas and A. I. Voronin (unpublished work).
169. A. Thiel and H. Köppel, *J. Chem. Phys.* **110**, 9371 (1999).
170. A. Gelb, K. D. Jordan and R. Silbey, *Chem. Phys.* **9**, 175 (1975).
171. C. W. Eaker and C. A. Parr, *J. Chem. Phys.* **64**, 1322 (1976).
172. T. E. Graedel and P. J. Crutzen, *Atmospheric Change* (Freeman, New York, 1993).
173. J. Warnatz, U. Maas and R. W. Dibble, *Combustion: Physical and Chemical Fundamentals, Experiments, Pollutant Formation* (Springer-Verlag, Berlin Heidelberg, 1996).
174. G. C. Schatz and H. Elgersma, *Chem. Phys. Lett.* **73**, 21 (1980).
175. A. D. Isaacson, *J. Chem. Phys.* **107**, 3832 (1997).

176. G. Ochoa and D. C. Clary, *J. Phys. Chem.* **A102**, 9631 (1998).
177. K. C. Thompson and M. A. Collins, *J. Chem. Soc. Faraday Trans.* **93**, 871 (1997).
178. M. Alagia, N. Balucani, P. Casavecchia, D. Stranges, G. G. Volpi, D. C. Clary, A. Kliesch and H.-J. Werner, *Chem. Phys.* **207**, 389 (1996).
179. J. N. Murrell, S. Carter, I. M. Mills and M. F. Guest, *Mol. Phys.* **42**, 605 (1981).
180. M. I. Lester, R. A. Loomis, R. L. Schwartz and S. P. Walch, *J. Phys. Chem.* **101**, 9195 (1997).
181. S. Matsika and D. R. Yarkony, *J. Chem. Phys.* **115**, 5066 (2001).
182. G. Lynch, R. Steckler, D. W. Schwenke, A. J. C. Varandas, D. G. Truhlar and B. C. Garrett, *J. Chem. Phys.* **94**, 7136 (1991).
183. A. J. C. Varandas and A. I. Voronin, *J. Phys. Chem.* **99**, 15846 (1995).
184. A. J. C. Varandas, A. I. Voronin and P. Jimeno, *J. Chem. Phys.* **107**, 10014 (1997).
185. A. K. Belyaev, A. S. Tiukanov and W. Domcke, *Phys. Rev. A* **65**, 012508 (2002).
186. A. A. Wu, *Mol. Phys.* **38**, 843 (1979).
187. I. Last and M. Baer, *J. Chem. Phys.* **75**, 288 (1981).
188. C. A. Eaker, *J. Chem. Phys.* **93**, 8073 (1990).
189. M. Baer, R. Englman and A. J. C. Varandas, *Mol. Phys.* **97**, 1185 (1999).
190. M. Baer, A. J. C. Varandas and R. Englman, *J. Chem. Phys.* **111**, 9493 (1999).
191. A. J. C. Varandas, A. I. Voronin and I. Borges Jr., *Chem. Phys. Lett.* **331**, 285 (2000).
192. S. Carter, I. M. Mills, J. N. Murrell and A. J. C. Varandas, *Mol. Phys.* **45**, 1053 (1982).
193. J. N. Murrell, W. Craven, M. Vincent and Z. H. Zhu, *Mol. Phys.* **56**, 839 (1985).
194. A. J. C. Varandas and A. I. Voronin, (unpublished work).
195. A. J. C. Varandas and J. Brandão, *Mol. Phys.* **45**, 857 (1982).
196. A. J. C. Varandas, *J. Mol. Struct. Theochem* **120**, 401 (1985).
197. A. J. C. Varandas, *Mol. Phys.* **60**, 527 (1987).
198. J. P. Desclaux, *At. Data Nucl. Data Tables* **12**, 311 (1973).
199. V. Kurkal, P. Fleurat-Lessard and R. Schinke, *J. Chem. Phys.* **119**, 1489 (2003).
200. P. J. S. B. Caridade and A. J. C. Varandas, *J. Phys. Chem. A* (in press).
201. A. J. C. Varandas, A. Alijah and M. Cernei, *Chem. Phys.* (in press).

CHAPTER 6

CONICAL INTERSECTIONS AND ORGANIC REACTION MECHANISMS

Annapaola Migani and Massimo Olivucci

Dipartimento di Chimica dell'Università di Siena, via Aldo Moro I-53100 Siena, Italy

Contents

1. Introduction: The Search for the Photochemical Funnel

With their seminal 1935 work on the structure of potential-energy surfaces, Eyring,[1] Evans and Polany[2] were able to define the exact nature of the "activated complex" or "transition state" for ordinary (thermal) chemical reactions. The molecular structure of a transition state describes the spatial arrangement of the atoms corresponding to the highest point (**TS**) on the potential-energy surface that has to be overcome by the reactant to form the product. This discovery not only provided the basic "conceptual tool" for understanding chemical reactivity, but also indicated the way for getting, through quantum chemical calculations, information on the molecular structure of the transition state. If the **TS** structure is known, the full reaction path can be determined by computing the minimum-energy path [(MEP), see dashed line in Fig. 1]: the curve that connects the **TS** (a saddle point on the potential-energy surface) with the energy minima associated with the reactant ($\mathbf{Min}_1$) and the product ($\mathbf{Min}_2$). The successful development of quantum chemistry packages and the availability of increasingly fast computers in recent years have made the computational investigation of thermal reaction paths a routine practice in the modern chemical laboratory.

Until the early 1990s, the systematic computation of photochemical reaction paths was unpractical if not impossible. In a photochemical reaction, the reactant is an electronically excited-state molecule or complex $\mathbf{M}^*$, while the product is a ground-state species. Thus, in order to describe a photochemical reaction, one must first establish the nature of the spatial arrangement of the atoms corresponding to the point where $\mathbf{M}^*$ decays from the excited-state potential-energy surface to the ground state and initiates product formation. Loosely, this critical molecular structure plays the role of the "transition state" for a photochemical process.[3]

The classic view of unsensitized (i.e. singlet) photochemical reactions is mainly due to the 1969 computational work of Van der Lugt and Oosterhoff[4] on the photochemistry of butadienes. As illustrated in Fig. 2(a), these authors proposed that decay of $\mathbf{M}^*$ takes place at an excited-state energy minimum corresponding to an *avoided crossing* of the excited- and ground-state potential-energy surfaces. However, experimental evidence such as the

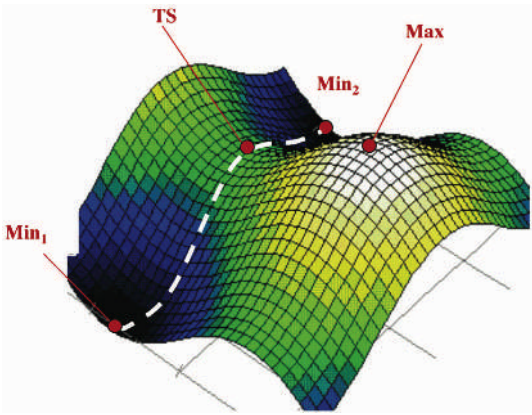

Fig. 1. Schematic representation of the structure of the potential-energy surface for a thermal chemical reaction. The dashed curve indicates the minimum-energy path. **Min$_1$** and **Min$_2$** are local energy minima corresponding to reactants and products. **TS** is a saddle point corresponding to the transition structure. **Max** is a local maximum.

lack of fluorescence from such a minimum indicated that the decay must be extremely fast, which can only occur when the energy gap between excited and ground state is within a few kcal mol^{-1}. On the other hand, the calculations available at that time, which, as stressed in Fig. 2(b), were forced to assume the conservation of molecular symmetry along the reaction path, predicted quite sizable energy gaps.[4,5] In these conditions $\mathbf{M}^*$ would rapidly equilibrate and the excited-state decay would occur on a time scale close to that of fluorescence (i.e. allowing many vibrational oscillations) as in standard internal conversion processes.

In 1966 and 1972, Zimmerman,[6] Michl[7–10] and, in 1974, Salem[11–13] were the first to suggest, independently, that certain photoproducts originate by decay of the excited-state species $\mathbf{M}^*$ through a conical intersection (**CI**) of the excited- and ground-state potential-energy surfaces. Zimmerman and Michl used the term "funnel" for this feature that corresponds, in contrast to the Van der Lugt and Oosterhoff computations, to a *real* crossing of two potential-energy surfaces. The same idea was proposed by Edward Teller[14] in 1969. Teller made two general observations:

(a) in a polyatomic molecule, the non-crossing rule, which is rigorously valid for diatomics, fails and two electronic states, even if they have the same symmetry, are allowed to cross at a conical intersection.

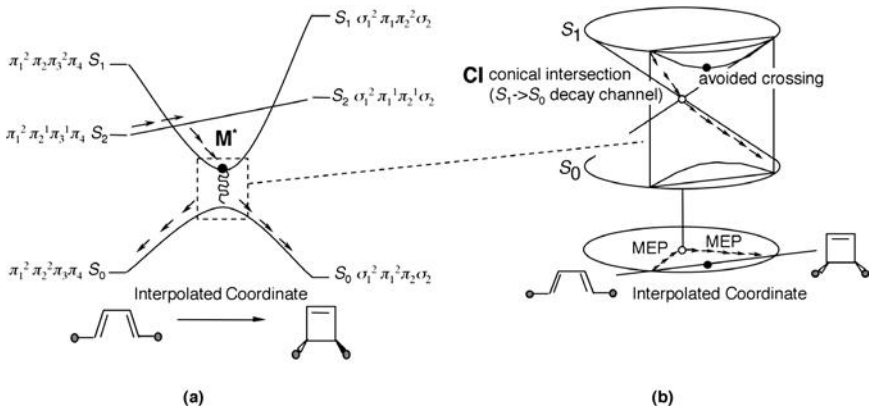

Fig. 2. The relationship between (a) the Van der Lugt–Oosterhoff model and (b) a model (see Sec. 2.1) based on MEP computations for the photochemical electrocyclization of buta-1,3-diene. The Van der Lugt–Oosterhoff model is based on an *assumed* (interpolated) reaction coordinate and suggests that the photochemical funnel corresponds to an avoided crossing at $\mathbf{M}^*$ (see dashed frame). MEP computations yield a different, but *unbiased* coordinate, corresponding to the steepest-descent path from the excited-state reactant. The reaction coordinate characterizing such a path leads to a conical intersection between the excited (S_1) and ground (S_0) states. The framed region in part (b) indicates the position of the Van der Lugt–Oosterhoff avoided crossing in the conical intersection region.

(b) radiationless decay from the upper to the lower intersecting state occurs within a few vibrational periods when the system "travels" in the vicinity of such intersection points.[15]

On the basis of these observations, Teller proposed that conical intersections provide a very fast decay channel from the lowest excited states of polyatomics that would explain the lack of fluorescence from the excited state. Despite the fact that the ideas of Teller, Zimmerman, Michl and Salem represented an important refinement of the avoided crossing model,[4,5] *conical intersections were thought to be extremely rare or inaccessible* (i.e. located too high in energy) in organic compounds and thus were disregarded for many years.

At the end of the 1980s, improved *ab initio* quantum chemical methodologies became available which were suitable for computing, in a balanced way, excited- and ground-state potential-energy surfaces. In particular, the *ab initio* CASSCF method[16] had an analytical gradient which could be

employed for efficient geometry optimization (the search for the structure corresponding to energy minima and transition states) taking into account the complete set of the $3N - 6$ nuclear degrees of freedom of the reacting system (N is the number of atoms). It was thus obvious that with this new methodology it was possible to overcome the limits (i.e. symmetry constraints and pre-defined reaction coordinates) used in the Van der Lugt and Oosterhoff[4] and Devaquet[5] calculations [see Fig. 2(b)].

A first application[17,18] of the *ab initio* CASSCF method in 1990 to the photoinduced cycloaddition of two ethylene molecules showed that:

(i) a conical intersection exists right at the bottom of the first excited-state energy surface.
(ii) the molecular structure of the conical intersection is related to the observed photoproducts and stereochemistry of the reaction.

Therefore it appeared possible that conical intersections could, contrary to the common belief, be frequent (if not ubiquitous) in organic systems. Further, they may constitute the photochemically relevant decay channel.

Despite the hypothesis of Zimmerman[6] and Michl[7−10] as well as few encouraging computational results by Michl and coworkers[19,20] and by ourselves[17,18] one has to reckon that there is no general theorem supporting the existence of low-lying (i.e. accessible in ordinary experimental conditions) conical intersections in organic chromophores. *The only way to prove the validity of the hypothesis stated above was a painstaking systematic search for properties (i)–(ii) in different classes of organic chromophores.* Thus, in 1992 Bernardi, Robb and one of the authors started a long-term project, focusing on a systematic investigation of the basic organic chromophores: alkenes, isolated and conjugated dienes, polyenes, arenes, enones, azoalkanes and others (see Sec. 3.1). The results showed that, in all cases, it is possible to locate a low-lying conical intersection with a structure related to the observed photoproducts. Furthermore, for a number of species it was possible to compute the entire excited-state reaction path (see also Sec. 2.1) starting at the ground-state equilibrium geometry (the Franck–Condon structure **FC**) and ending at the low-lying conical intersection **CI**.

Due to the recent availability of suitable computational methods in standard quantum chemistry packages (e.g. GAUSSIAN[21]), the computation of conical intersections of organic chromophores and, to a certain extent,

the computation of excited-state reaction paths are becoming a standard practice among computational chemists. As a consequence, the amount of structural data on conical intersections and, thus, on the mechanism of the critical step of different classes of organic photochemical reactions are rapidly increasing. In this context, the present book chapter has two main objectives. The first is a discussion of the main mechanistic results that have been achieved in the field. The second is a presentation of the conical intersections detected in a number of basic organic chromophores. These objectives are the subject of Secs. 2 and 3, respectively.

2. Mechanistic Results

2.1. *General Structure of the Photochemical Reaction Path*

In Sec. 1 we have stressed that, in a statistically significant number of cases, a conical intersection plays the role of the photochemical funnel. However, the discovery of a conical intersection structure in a reactive organic molecule does not guarantee that such a structure corresponds to the photochemical funnel or that the computed conical intersection is involved in the reaction at all. A rigorous evidence for the involvement of a conical intersection in a photochemical process can be provided through the computation of the photochemical reaction path. The result of such a computation for the fairly complex organic molecule **1**[22] (a Z polyeniminium cation) undergoing a photoinduced Z/E isomerization to produce the E form **2**, is given in Fig. 3.

In the figure we show that a photochemical reaction path is defined and computed in terms of a set of connected minimum-energy paths.[23] In particular, the path starting at the **FC** structure **1** on the potential-energy surface of the spectroscopic excited state and ending at the photoproduct energy minimum **2** located on the ground-state energy surface is constructed by joining two MEPs. A first MEP (full squares) connects the **FC** point to the conical intersection (**FC**→**CI**). A second MEP (open squares) connects the conical intersection to the photoproduct (**CI**→Photoproduct). A third MEP (full circles) can be computed that starts at **CI** and describes the *photochemical* reactant reconstitution process (**CI**→Reactant) responsible for partial return of the photoexcited species to the original ground-state minimum. In the same figure, we also show that it is possible to

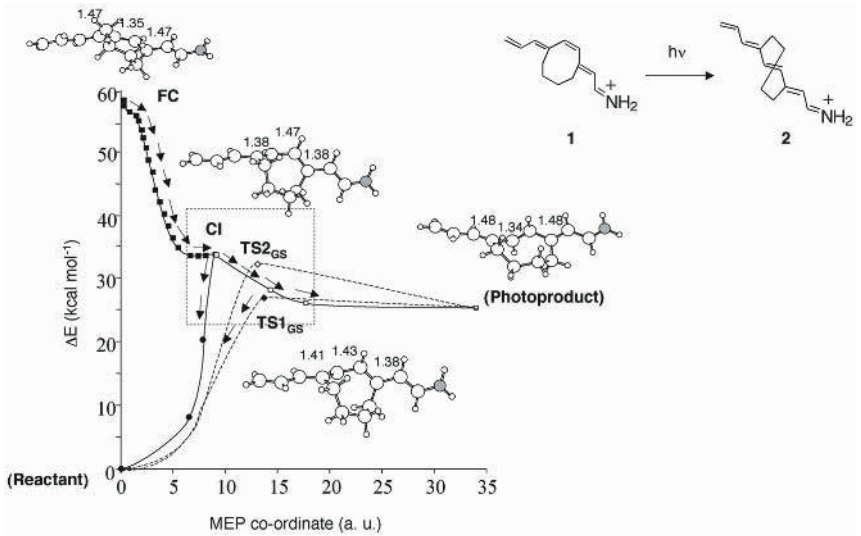

Fig. 3. Computed photochemical reaction path for the Z/E isomerization of 4-*Z*-nona-2,4,6,8-tetraeniminium cation derivative **1** featuring a 4-*Z* double bond embedded in an eight-membered-ring. The values of the relevant structural parameters are given in Å.

compute the thermal reaction pathways describing the evolution of the primary photoproduct towards secondary products. In the specific case, this evolution describes the reactant reconstitution via two different transition structures (open and full diamonds). Of course, these transition structures (**TS1**$_{GS}$ and **TS2**$_{GS}$ in Fig. 3) define two additional ground-state MEPs.

The computed set of MEPs can, in principle, provide a full description of the direct and indirect photochemical reactivity of the system. The analysis of the reaction coordinate associated to each MEP provides information on the spatial/geometrical relationship between the MEPs and, effectively, on the multidimensional structure of the chemically relevant part of the excited- and ground-state energy surfaces. The same analysis also reveals the nature of the molecular modes involved in the reactivity process. In certain favorable cases, such as that of the Z/E photoisomerization discussed above, this structural information can be condensed in a two-dimensional cross-section of the intersecting surfaces displaying the topography of the excited- and ground-state energy surfaces, respectively. Such a representation is given in Fig. 4.

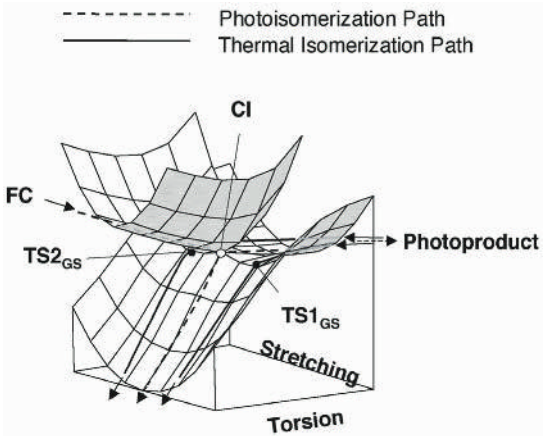

Fig. 4. Three-dimensional representation of the topography of the excited- and ground-state potential-energy surfaces in the framed region (see dashed rectangle) of Fig. 3. Although one of the two coordinates is referred to as "torsion", it does not really correspond to the change of a dihedral angle, but to a "local" torsional distortion of the central segment of the molecule. Indeed, it can be described as a coupled pyramidalization at the C_3 and C_6 centers of the carbon skeleton.

As extensively discussed in other chapters of this book, a conical intersection is characterized by *two* "special" molecular modes forming the so-called "branching"[24] or "g, h"[25] plane. A molecular structure deformation along this plane lifts the excited-/ground-state energy degeneracy. Furthermore, the ground- and excited-state wavefunctions undergo a dramatic change as the molecular structure is changed along a closed loop lying on the branching plane and comprising the conical intersection. In particular, these wavefunctions exchange their character along the loop. One will therefore have regions of the ground-state energy surface with an electronic structure that correlates with that of the excited state at **FC** and *vice versa.* A detailed analysis of the structure of the branching plane and of the behavior of the wavefunctions of the excited and ground state in the region of the conical intersection can be used to provide information on the nature of the "reactive" process mediated by the **CI**.

In Fig. 5 we plot the branching plane vectors ($\mathbf{X}_1$ and $\mathbf{X}_2$) at the conical intersection of **1**. It is apparent that in this molecule $\mathbf{X}_1$ and $\mathbf{X}_2$ describe either a "local" torsional deformation of the central segment of the molecule (this second mode can be more rigorously described as coupled

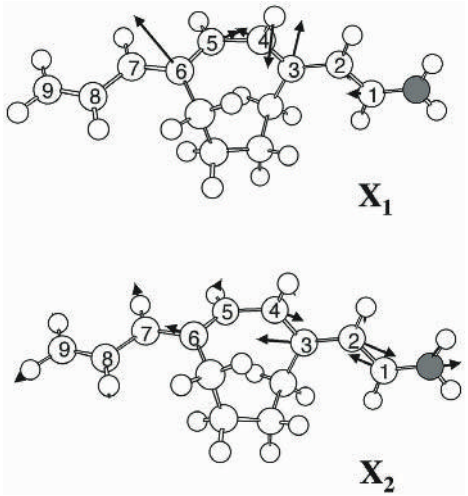

Fig. 5. Branching (or g, h) plane vectors for the **CI** structure of Fig. 3. The $\mathbf{X}_1$ and $\mathbf{X}_2$ vectors correspond to the derivative coupling[24] (or non-adiabatic coupling) and gradient difference[24] vectors between the S_1 and S_0 states.

pyramidalization (wagging) modes at the C_3 and C_6 centers of the π-chain) or a stretching deformation (a double-bond expansion and single-bond contraction mode) of the N=C_1–C_2=C_3–C_4=C_5–C_6= chain segment. As illustrated in Scheme 1 (here and throughout the text, conical intersections will be denoted with the χ symbol), simple structural considerations suggest that evolution of the conical intersection structure along the $\mathbf{X}_2$ and $-\mathbf{X}_2$ directions would ultimately yield two structures which may be represented by (resonance) formulas with inverted single and double bonds and with the positive charge shifted from the nitrogen to the C_9 position (indeed these deformations lead to the two transition structures $\mathbf{TS1_{GS}}$ and $\mathbf{TS2_{GS}}$ of Figs. 3 and 4). Similarly, structural deformation along the $\mathbf{X}_1$ and $-\mathbf{X}_1$ directions yields structures that can be represented by formulas with the Z and E central double bond, respectively. Obviously these two structures will be more stable than the 90° twisted structure generated by motion along $\mathbf{X}_2$**,** since in this case the deformation allows for reconstitution of the central double bond (i.e. the reactant and the primary photoproduct in Fig. 3). For this reason, the analysis of the branching plane suggests that upon decay from **CI** the molecule will generate the Z and E stereoisomers.

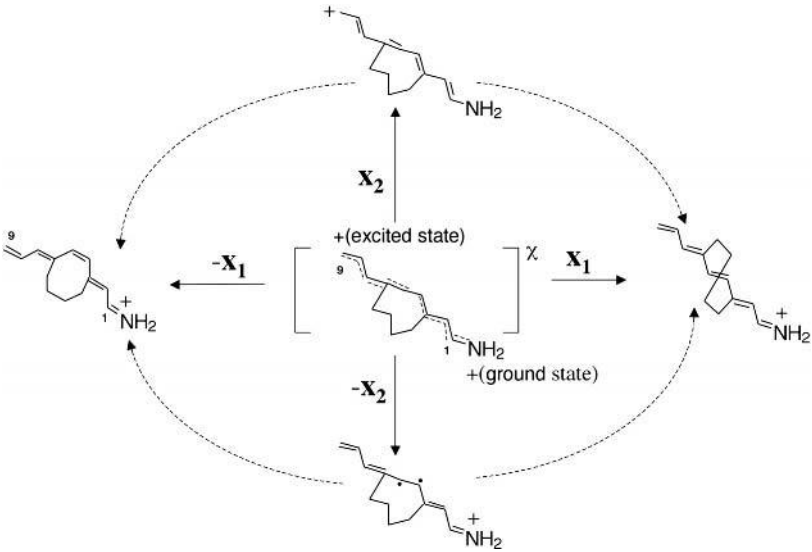

Scheme 1

Notice that the position of the positive charge of **1** is not the same along the four possible directions. Furthermore, notice that at the **CI** where the excited- and ground-state energies are degenerate, the positive charge (i.e. the electronic distribution) is very different in the excited and ground state as shown in Scheme 1. These electronic features will now be discussed.

As mentioned above, the analysis of the wavefunction, taken together with the analysis of the branching plane, provides the basis for the rationalization of the electronic structure of the part of the ground-state energy surface (see Fig. 4) comprising the reactant and product valleys and the transition structures connecting them. Notice that the topography of this region is conceptually related to the topography of the moat of the Mexican hat of Jahn–Teller-type intersections discussed elsewhere in this book. The result of such an analysis for chromophore **1** is shown in Scheme 2, where the wavefunction is analyzed in terms of point charges of the C_9–C_8–C_7–C_6–C_5– and –C_4–C_3–C_2–C_1–N fragments. It is clear from the scheme that **1**, **2** and $\mathbf{TS1_{GS}}$ exhibit the same type of electronic structure. This can be described by a resonance formula with the charge located on the nitrogen atom. On the other hand, $\mathbf{TS2}_{GS}$ clearly shows a different electronic structure, where the positive charge has partially migrated to the

C_9–C_8–C_7–C_6–C_5– fragment. The structure is thus characterized by a large contribution of a different resonance formula. The two types of charge distribution correlate with those computed for the ground and excited states of **FC** (at **FC** the charge is mainly located on the –C_4–C_3–C_2–C_1–N fragment in the ground state, but is shifted to the C_9–C_8–C_7–C_6–C_5– fragment in the excited state) and with those of the two intersecting states at **CI** (at **CI** the 99% of the charge is located on the –C_4–C_3–C_2–C_1–N fragment in one state, but is located on the C_9–C_8–C_7–C_6–C_5– fragment in the other state). The energy equality between the covalent and ionic configurations at **CI** has been explained for the model system prop-2-eniminium cation by Bonačić-Koutecký and Michl.[26] While the change from one type of electronic structure to the other occurs along a loop centered on the **CI**, this change is usually not smooth. In fact, the intramolecular charge-transfer process that characterizes the change occurs in a rather restricted region of the branching plane. For **1** this region corresponds, schematically, to the area comprised between the two dashed lines in Scheme 2.

As reported in other parts of the book, a conical intersection point is, in general, part of a subspace of conical intersection points. This is usually a $3N-8$ dimensional subspace (N is the number of atoms of the molecule)

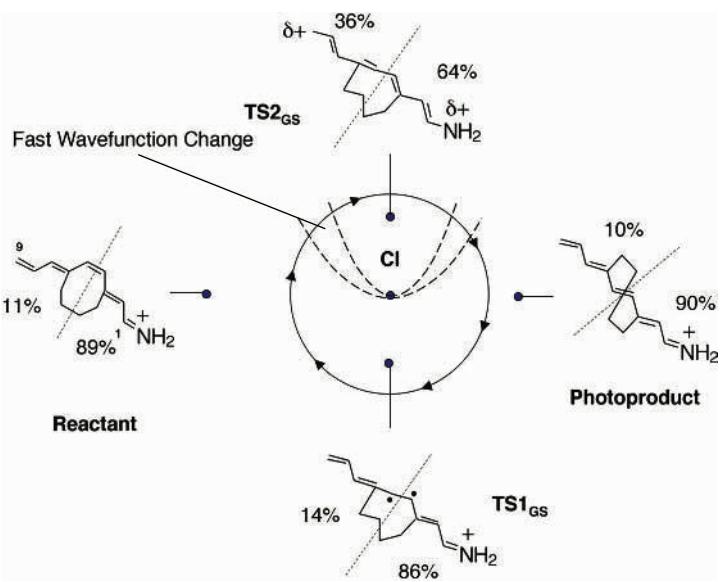

Scheme 2

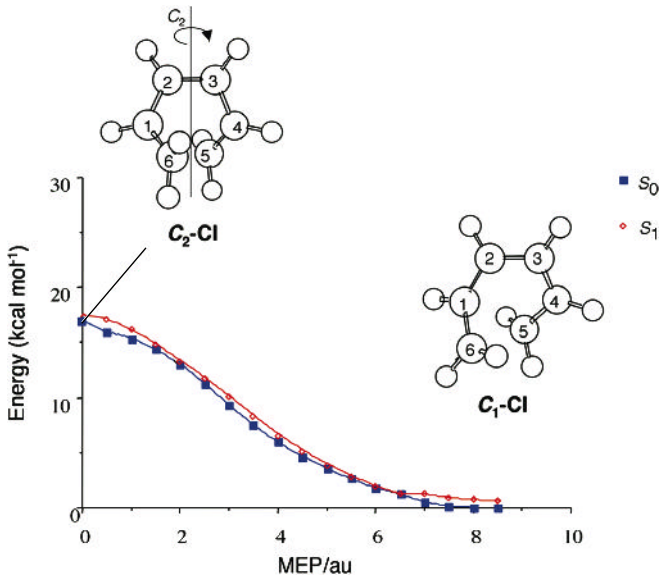

Fig. 6. MEP along the intersection space of cyclohexa-1,3-diene. The 2^1A_1 excited-state energies are labelled with open diamonds, while the 1^1A_1 ground-state energies are labelled with full squares (the labels 2^1A_1 and 1^1A_1 refers to the symmetric (left) conical intersection structure). Adapted from Ref. 27.

called the intersection space[24] (or seam of intersection[25]) and it is, locally, orthogonal to the two-dimensional branching plane. Recently, it has become possible to obtain information on the structure of the low-lying region of the intersection space of organic molecules through constrained MEP computations that yield paths residing entirely on the intersection space.[27] Such a MEP may connect a higher-energy conical intersection structure to a lower-energy conical intersection, provided that these intersections belong to the same pair of potential-energy surfaces. An example is reported in Fig. 6 for the case of the cyclohexa-1,3-diene molecule.

From inspection of the figure, it is apparent that a continuum of conical intersection points connects a higher-energy conical intersection with C_2 symmetry C_2-**CI**) to a lower-energy asymmetric conical intersection C_1-**CI**). It has been independently shown via conical intersection optimization[27–29] that the asymmetric intersection is the lowest-energy minimum of the intersection space in the chemically relevant region. The

mapping of low-lying segments of the intersection space by means of MEP computations provides information on the family of low-lying molecular structures that, if achieved during the excited-state motion of the reactant, could provide efficient access to the ground state.

It must be stressed that excited-state relaxation/reaction paths (such as the **FC→CI** path of Fig. 3) do not necessarily hit the lowest-energy point belonging to the intersection space. Thus the actual decay may occur in a region removed from the lowest-energy conical intersection located via direct optimization methods (see also Sec. 3.1). One of these cases is reported in Fig. 7, where it is shown that the relaxation path of the penta-2,4-dienimminium cation (a minimal model of the retinal protonated Schiff base chromophore) ends at a conical intersection with a ca. 70° (**CI**$_{70\circ}$) twisted structure, while the lowest-energy intersection (**CI**$_{92\circ}$) located on the intersection space has a 92° twisted structure.[30] Notice that in this situation the main locus of excited-state (S_1) decay is predicted to be **CI**$_{70\circ}$.

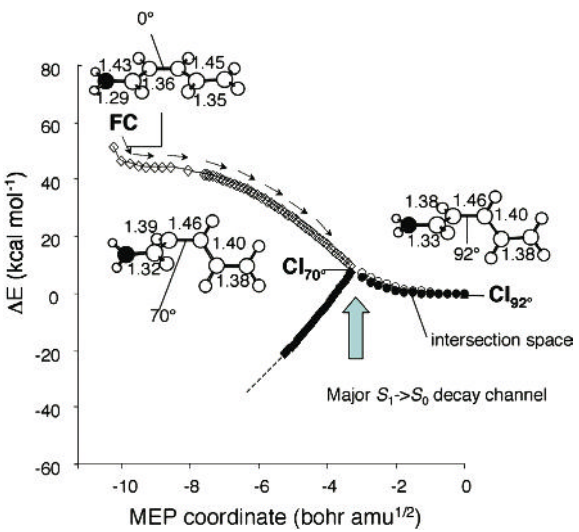

Fig. 7. The excited-state reaction path of the penta-2,4-dienimminium cation intercepts the conical intersection point **CI$_{70\circ}$** located ca. 5 kcal mol^{-1} above the minimum-energy conical intersection **CI$_{92\circ}$**. **FC→CI$_{70\circ}$** MEP (S_1 open diamonds and S_0 full diamonds), **CI$_{70\circ}$→CI$_{92\circ}$** MEP (S_1 open circles and S_0 full circles). The values of the relevant structural parameters are given in Å and degrees.

In Sec. 3 we will mainly concentrate on the discussion of the structure (both geometrical, electronic and topographical) of the chemically relevant (low-lying) conical intersections that have been documented in a number of basic organic chromophores. As we will further point out in Sec. 3.1, the majority of these structures have been computed via conical intersection optimizations and do not strictly correspond to the conical intersection points located at the very bottom of the excited-state path. Nevertheless, their general features are representative of the chemically relevant segment of the intersection space and can be used for the mechanistic rationalization of different photoinduced molecular processes.

2.2. *Bond Making, Bond Breaking, Group Exchange, Electron Transfer*

The elementary events occurring during chemical reactions are bond making, bond breaking, group (and atom) exchange, electron (and charge) transfer. A first basic result of the extensive computational investigation of organic compounds is the demonstration of the existence of conical intersections that mediate *all* types of chemical events. Thus, in Fig. 8 we report the structure of three conical intersections that mediate bond making, bond breaking and group exchange, respectively.

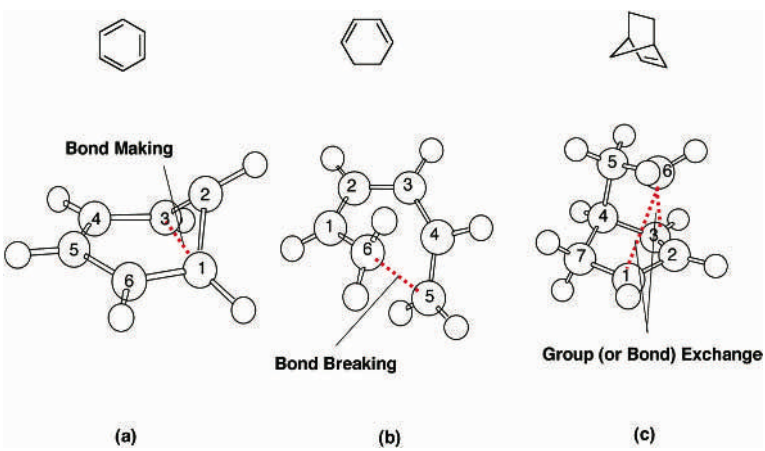

Fig. 8. Conical intersections in (left to right) benzene, cyclohexa-1,3-diene and bicyclo[2.2.1]hept-2-ene (norbornene).

The molecular structures of Fig. 8 may appear unusual. However, it must be noticed that in all structures specific σ-bond and/or π-bond lengths are far from their equilibrium values. This basic feature reinforces the idea (see Sec. 1) that these structures can be thought as the "photochemical analogue" of transition structures. Analysis of the geometry, π-electron distribution and branching plane vectors reveals the nature of the photochemical event mediated by the computed conical intersection structure. In Scheme 3, we display the structure of the branching plane for the conical intersection between the first singlet excited state and the ground state of benzene[31] (see also Sec. 3.3.4). It is clear from $\mathbf{X}_1$ that this intersection mediates a σ-bond-making process between the centers $C_1$and C_3, leading to the formation of a bicyclic biradical species ($-\mathbf{X}_1$ leads to benzene reconstitution). This species is prefulvene, the postulated intermediate leading to fulvene[32] and benzvalene.[31] In contrast, evolution along the $\mathbf{X}_2$ and $-\mathbf{X}_2$ vectors leads to two distorted Kekulè structures (i.e. unstable cyclohexatrienes) that must revert to benzene upon further relaxation. The branching plane shown in Scheme 4 is associated with the conical intersection of cyclohexa-1,3-diene given in Fig. 8(b) (the chromophore of steroids such as ergosterol and 7-dehydrocholesterol).[27–29] Inspection of the highly distorted structure of the intersection indicates that this mediates a C_5–C_6

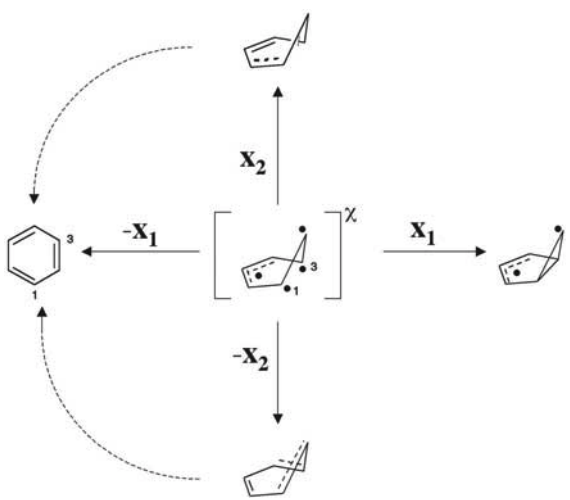

Scheme 3

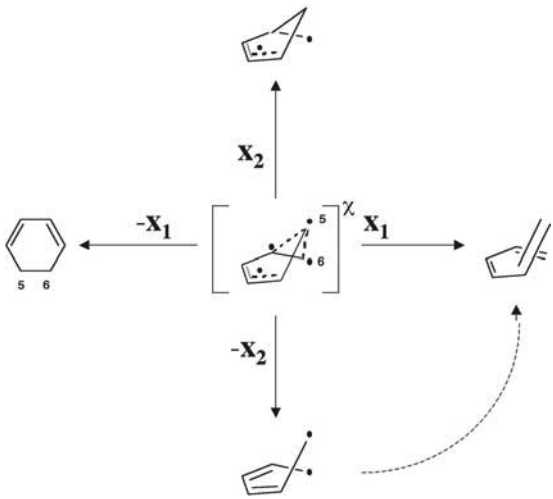

Scheme 4

σ-bond-breaking event, leading to ring opening. Indeed, evolution along $\mathbf{X_1}$ leads to the acyclic photoproduct hexa-1,3,5-triene chain in a *s-cis*,*Z*,*s-cis* conformation. In contrast to benzene, evolution along the $\mathbf{X_2}$ vector leads to the methylenecyclopentenyl biradical intermediate that is a precursor of a bicyclic compound (a bicyclo[3.1.0]hex-2-ene). On the other hand, evolution along the $-\mathbf{X}_2$ vector leads to an unstable acyclic biradical structure that must relax to *s-cis*,*Z*,*s-cis*-hexa-1,3,5-triene. The structure of Fig. 8(c) provides an example where the conical intersection mediates an intramolecular group transfer (more precisely an intramolecular [1,3]-sigmatropic shift) in norbornene.[33,34] Notice that this process is characterized by simultaneous σ-bond breaking at C_1–C_6 and σ-bond making at C_6–C_3. In Scheme 5, we report the structure of the branching plane of this reaction as well as a plot of the $\mathbf{X_1}$ and $\mathbf{X_2}$ vectors.

Evolution along $\mathbf{X}_1$ and $-\mathbf{X}_1$ leads to the [1,3]-sigmatropic shift product bicyclo[3.2.0]hept-2-ene and to the original norbornene, respectively. On the other hand, evolution along $\mathbf{X_2}$ leads to a [1,2]-sigmatropic shift product, corresponding to a bicyclic biradical species (which may further evolve to generate a tricyclic product). In contrast, evolution along $-\mathbf{X}_2$ leads to an unstable biradical, where the two unpaired electrons reside on an allyl and an ethyl moiety, respectively, and are apart from each other.

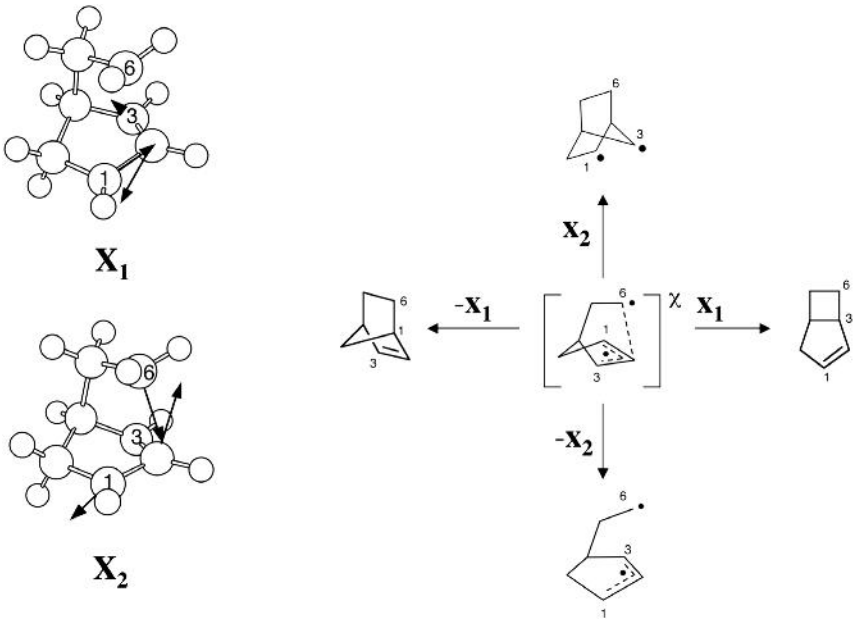

Scheme 5

A different category of conical intersections mediates photoinduced electron- and charge-transfer processes (i.e. photoinduced redox reactions). The first example is given by a bimolecular reaction between a $^1n - \pi^*$ azoalkane (pyrazoline) and a chlorinated hydrocarbon (CH_2Cl_2),[35,36] where decay at a conical intersection leads to simultaneous production of radical and ion pairs. Reaction path computations show that, after excited-state hydrogen atom transfer from CH_2Cl_2 to pyrazoline, the path intercepts a conical intersection with a nearly formed N–H bond. The structure of the associated branching plane is shown in Fig. 9(a). Distortion along $\mathbf{X_1}$ leads to production of a radical pair, while distortion along $-\mathbf{X_1}$ leads to production of an unstable ion pair (see discussion in Ref. 36). In analogy with the branching plane of Scheme 1, evolution towards the $\mathbf{X_2}$ and $-\mathbf{X_2}$ directions leads to two equivalent ground-state transition structures which feature a distorted pyrazoline ring. In Fig. 9(b), we show the result of wavefunction analysis (in terms of fragment charges) along a loop [see dashed arrows in Fig. 9(a)] centered on the conical intersection. It is clear that at $\omega = 0°$ one has an ion-pair region, where the charge on the azoalkane and chlorinated

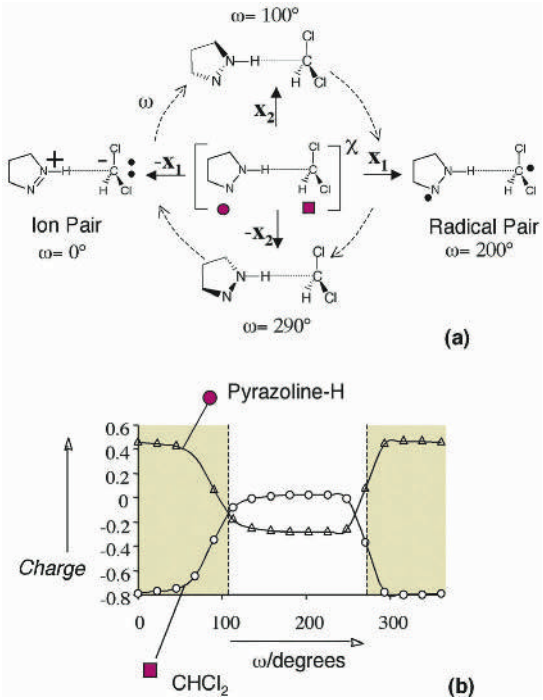

Fig. 9. (a) Structure of the branching plane for the conical intersection mediating the hydrogen-atom transfer from methylene chloride to an ^1n-π^* azoalkane (pyrazoline). (b) Analysis of the fragment charges along a circle (dashed arrows) centered on the conical intersection. The ω angle describes the progression along the circle starting at the ion-pair structure ($-\mathbf{X}_1$ direction). Data from Ref. 36.

hydrocarbon are positive and negative, respectively. In contrast, for values of ω around 200° one has a nearly neutral pair. The regions of the two transition states are instead characterized by a sharp change of the electronic distribution (i.e. an electron-transfer process) in the chlorinated hydrocarbon → azoalkane direction at $\omega = 100°$ and in the azoalkane → chlorinated hydrocarbon direction at $\omega = 290°$. Reaction path analysis shows, consistently with the experimental observations on diazabicyclo[2.2.2]oct-2-ene (DBO) + chloroform, that both the radical and ion pairs are transient species and revert back to the original reactant. As we will see in the next section, this constitutes a case of unsuccessful photochemistry.

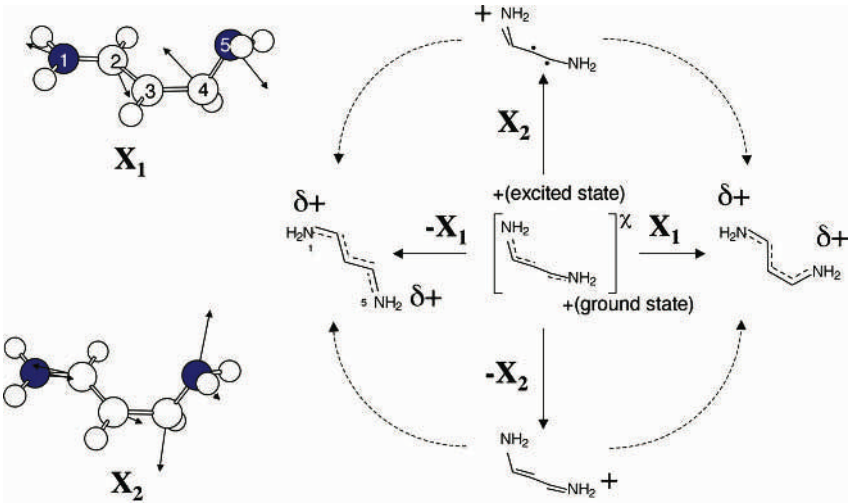

Fig. 10. The conical intersection of cyanine dyes is characterized by two electronic states that differ in the position of a positive charge. The intersection mediates a charge-transfer process in the $\mathbf{X}_2$ direction of the branching plane dominated by stretching deformations and Z/E isomerization in the $\mathbf{X_1}$ direction. The same situation occurs in polyenal protonated Schiff bases (see Scheme 1).

The conical intersection seen in Fig. 3 for a protonated polyene Schiff base is an example of a conical intersection between two electronic states that differ for the position of one positive charge. It is thus obvious that such an intersection is not only related to a Z/E photoisomerization process, but also to a charge transfer along the conjugated backbone. Indeed, such a charge transfer occurs along $\mathbf{X_2}$. A related example is that of carbocyanine dyes. The conical intersection found for a short carbocyanine model is given in Fig. 10 together with the associated branching plane vectors.[37] These are strictly related with the vectors seen in Fig. 5. In particular, $\mathbf{X_1}$ is related to the coupled pyramidalization of three centers of the conjugated chain and $\mathbf{X_2}$ is a stretching.

2.3. *Chemical Reaction, Quenching and Deactivation*

Conical intersections, whose structure appears to mediate (locally) a chemical event such as the ones described in the previous section, do not necessarily take part in a truly *successful* chemical reaction.[38] Computations

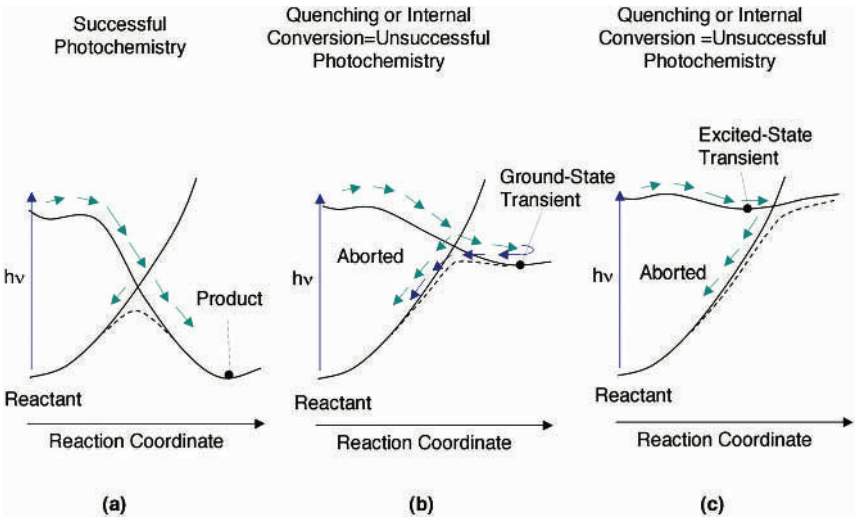

Scheme 6

of excited-state reaction pathways such as those described for the electron transfer in Sec. 2.2 show that, in certain organic materials, an intersection is the hub of the molecular mechanism for light energy wastage such as quenching and internal conversion processes. In both these events, the energy of the photon is converted to ground-state vibrational energy with no net permanent change in the original molecular structure. In Scheme 6 we show the three basic types of photochemical reaction paths found in organic chromophores. Path (a) corresponds to that of a successful photochemical reaction, where a finite percentage of the absorbed photon energy is used to produce a different chemical species. This type of path operates, for example, in the reactions mediated by the intersections seen in Fig. 8 and discussed in Sec. 2.2. In path (b), we show a case where the production of an excited- or ground-state *short-lived* new chemical species is achieved, but then this species is immediately converted to the original material and no net chemical reaction is accomplished. Finally, path (c) illustrates a case where there is no formation of ground-state photoproduct. In this case, the photochemical reaction is simply aborted at the conical intersection point. In Fig. 11, we show a conical intersection structure loosely belonging to path (b). This regards the case of the quenching of the fluorescence of ^1n-π^* azoalkanes as DBO.[39] This molecule is quenched when it interacts

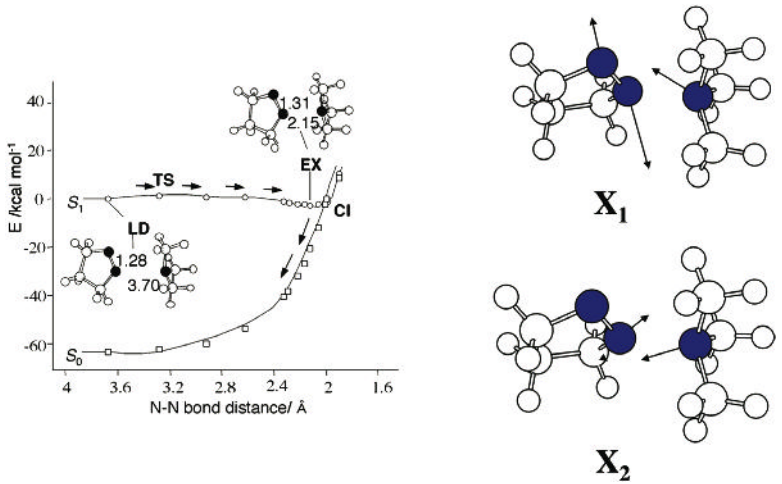

Fig. 11. Conical intersection for intermolecular charge transfer between ^1n-π^* pyrazoline and trimethylamine. Excited-state path (open circles), ground-state relaxation path (open squares). **LD** is a weak covalent complex, **TS** indicates the position of the barrier, **EX** is the exciplex. The values of the relevant structural parameters are given in Å. Adapted from Ref. 39.

with electron donors such as amines. In Fig. 11, we report the computed photochemical reaction pathway for the intermolecular charge transfer from a photoexcited ^1n-π^* pyrazoline (taken as a model of DBO) to an amine (trimethylamine). Notice that the excited-state branch of the reaction path is dominated by the decrease in distance between the reactant moieties. This process, which is controlled by a small excited-state barrier, leads to the formation of an exciplex located in the close vicinity of a conical intersection. The geometrical structure of the conical intersection and the vectors of the branching plane are given in the same figure. Notice that $\mathbf{X_1}$ is dominated by the out-of-plane deformation of the pyrazoline ring, and $\mathbf{X_2}$ is dominated by the interfragment distance. While, in principle, the reaction could lead to formation of an ion pair, this process is aborted immediately after the exciplex formation where already 0.3 electrons have been transferred from the amine to the azoalkane.

In the example above, the quenching occurs with the intervention of an unstable excited-state species. A different quenching process that involves the formation of an unstable ground-state species that readily reverts to

the reactant via a thermal reaction [thus conforming closely to path (b) of Scheme 6] is given in Fig. 9 of Sec. 2.2. In fact, the quenching of ^1n-π^* pyrazoline occurs via hydrogen abstraction, leading to formation of a transient radical pair.[35,36] This transient reverts efficiently to the reactant pair.

The conical intersections of Fig. 12 are responsible for the efficient internal conversion of azulene from its first excited state.[40,41] This process occurs according to path (c). The two intersections belong to the same intersection space that, in the region of interest (i.e. the lowest energy region), is spanned by a ring-flipping deformation. This mode simply interconnects the intersections of C_{2v} and C_S symmetries. On the other hand, an analysis of the shape of the branching plane vectors reveals that $\mathbf{X_1}$ is dominated by a transannular bond contraction and $\mathbf{X_2}$ is dominated by a stretching deformation. Notice that both intersections involve the formation of a transannular double bond ($\mathbf{X_1}$ direction in Scheme 7). However, this "chemical event" is aborted and the molecule relaxes back to the original structure.

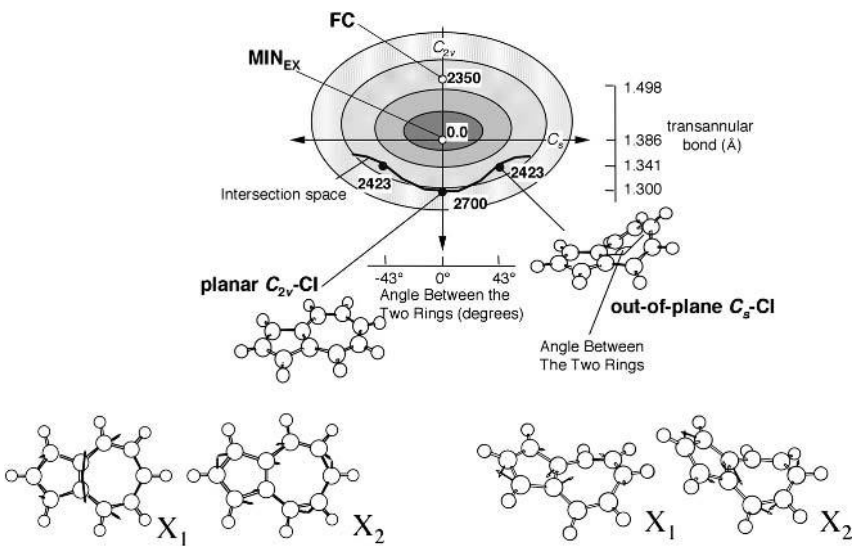

Fig. 12. Conical intersections ($\boldsymbol{C_{2v}}$**-CI** and $\boldsymbol{C_s}$**-CI**) driving the internal conversion of azulene. $\mathbf{MIN_{EX}}$ is the azulene S_1 energy minimum. **FC** is the Franck–Condon structure. Comparison of the $\mathbf{X_1}$ and $\mathbf{X_2}$ vectors associated with the two conical intersections indicates that they belong to the same intersection space.

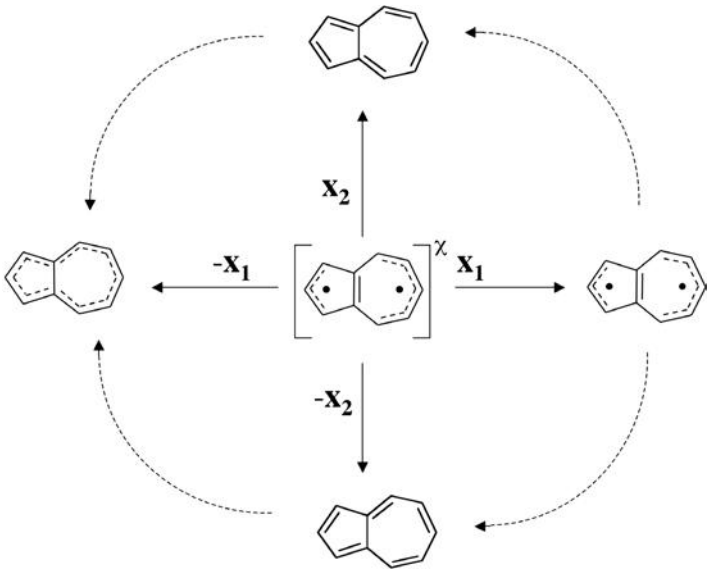

Scheme 7

3. Classification of Conical Intersections in Organic Compounds

3.1. *Tracing and Recording Conical Intersections*

As mentioned in Sec. 1, a long-term project was started in the early 1990s for the search of conical intersections in organic compounds. Between 1992 and 2000, the potential-energy surfaces of ca. 25 different organic chromophores were mapped to search for photochemically relevant conical intersections. These compounds belong to one of the following classes:

Chromophores with one Double Bond (or two Isolated Double Bonds)
Chromophores with conjugated double-bonds
Chromophores with a Carbonyl Group or a Conjugated Carbonyl Group
Azo-Chromophores
Models of the Retinal Chromophore (Schiff Bases)
Model Photochromic Compounds and Dyes
Aromatic Chromophores and Related Compounds
Polysilanes

Such a systematic investigation could not be carried out without the development of novel computational tools. The first tool developed was a method (the CIO method) for the unbiased search and optimization of low-lying conical intersection points between pairs of potential-energy surfaces.[42] Other novel tools were designed and implemented to compute the excited- and ground-state branches of photochemical reaction paths (the IRD method in Ref. 43) and most recently to compute "photochemical" semi-classical surface hopping trajectories (SHT),[40,44,45] and Ehrenfest trajectories,[46] i.e. trajectories that start on the excited-state energy surface and continue along the ground-state surface in the region of the conical intersection. With the help of these tools, a complete computational strategy was defined to compute the entire photochemical reaction path.[47–49] The traditional (e.g. stationary point search, vibrational frequency and intrinsic reaction coordinate computations) and the new mapping methods used in our project are schematically summarized in Fig. 13.

While, as already mentioned above, the *ab initio* CASSCF method has been considered the reference quantum chemical methodology for locating conical intersections in organic compounds, in principle any quantum chemical method including model Hamiltonians, semi-empirical and *ab initio* configuration interaction methods, can be used to trace conical intersections. This is mainly due to the fact that conical intersections are topological features of the potential-energy surfaces and usually do not disappear as a function of the level of theory used. However, it is clear that their relative energy and geometrical structure may not be realistic if a low level of theory is used. It is useful to mention that parameterized effective Hamiltonian methods (e.g. the MMVB method[50]) have been developed that can be used to trace conical intersections in hydrocarbon chromophores with an accuracy close to that of CASSCF.

The results of the project described above strongly support the hypothesis that low-lying conical intersections are ubiquitous in organic molecules.[51] During the last years, different research groups have been focused on the computational investigation of organic chromophores and the number of novel conical intersection structures of organic materials reported in the literature is currently growing. Below, we will not attempt to assemble an exhaustive classification of all conical intersections found, but we will limit ourselves to a survey of the conical intersection structures found for a number of important classes of organic chromophores.

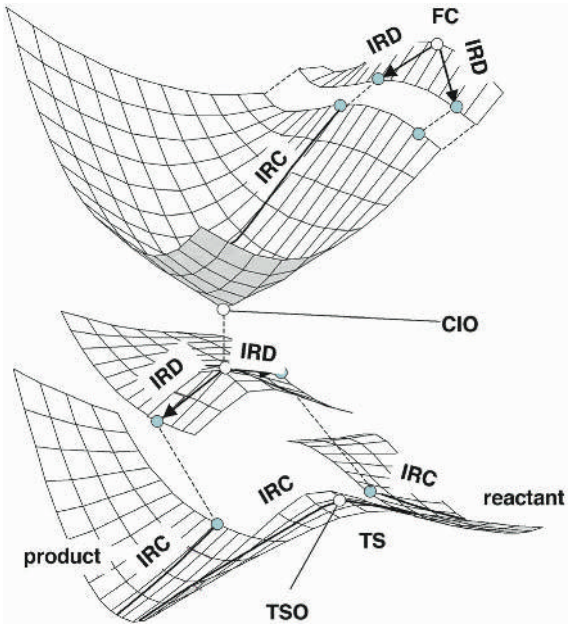

Fig. 13. The computational methods used for constructing a photochemical reaction path. The full path is computed by joining different MEPs, each one providing information on a specific part of the excited- or ground-state potential-energy surface. The **IRD** method is used to compute the steepest relaxation directions departing from the **FC** point (excited-state relaxation) or **CI** (ground-state relaxation). The **IRC** method is used to compute the steepest-descent line defined by the computed **IRD**s. The **CIO** method is used to compute the lowest-energy conical intersection point directly. With **TSO** we indicate the standard transition structure optimization procedure.

3.2. *Types of Classification*

Thermal organic reactions are often classified in terms of the molecular and electronic structure of their transition state or reactive intermediate (which is often taken as a model of the transition state). Thus, for instance, one has the S_N2 transition state for concerted bimolecular nucleophilic substitution reactions; one has the E_2 and E_1 transition states in elimination reactions, etc. Given the transient nature of the transition states, the use of quantum chemical methodologies is essential for the determination of their detailed geometrical and electronic structure. Furthermore, the computation of the associated transition vectors provides information on the reactive mode

Table 1. List of photochemical reactions where a conical intersection structure has been shown to be related to the structure of the photoproducts.

Reaction	Ref. Number
Ring-opening and Ring-closure	28,29,52–59
[1,2]-, [1,3]-Sigmatropic Shifts	53,60
Di-π-methane Rearrangement	61
Oxadi-π-methane Rearrangement	62
Valence Isomerization of Aromatics	31,63
[2+2], [4+2] and [4+4] Cycloadditions	64–66
Bicyclization of Dienes	67
Cis/trans Isomerization	58,68–73
Deazetization	74–76
Hydrogen Transfer	35,77
Charge Transfer	39
Paterno–Büchi	78
Polysilane Fragmentation	79

and therefore on the expected products. The same type of concept can be applied to photochemical organic reactions. In fact, these can be classified by computing the geometrical, electronic, and branching plane structures of the associated conical intersections. As reported in Table 1, in a number of cases, *the structure of the conical intersections has been shown to be related to the structure of the observed photoproducts* of a specific successful photochemical reaction.

As seen in Sec. 2.3, conical intersections that mediate unsuccessful chemical reactions have been shown to provide the decay channel associated with processes that are usually thought to occur through a photophysical mechanism (e.g. controlled by the Fermi Golden Rule[80]) such as the radiationless deactivation and/or quenching processes. Furthermore, important organic chromophores have been demonstrated to undergo either photochemical reactions or internal conversion processes on an extremely fast (usually sub-picosecond) time scale (i.e. emission is not observed from the excited state, since the time scale of the reaction is faster than the radiative lifetime).

In Scheme 8, we show the structures of the path for a standard photochemical reaction [Scheme 8(a)] and for an ultrafast photochemical reaction [Scheme 8(b)]. The fact that these processes occur on an ultrafast time

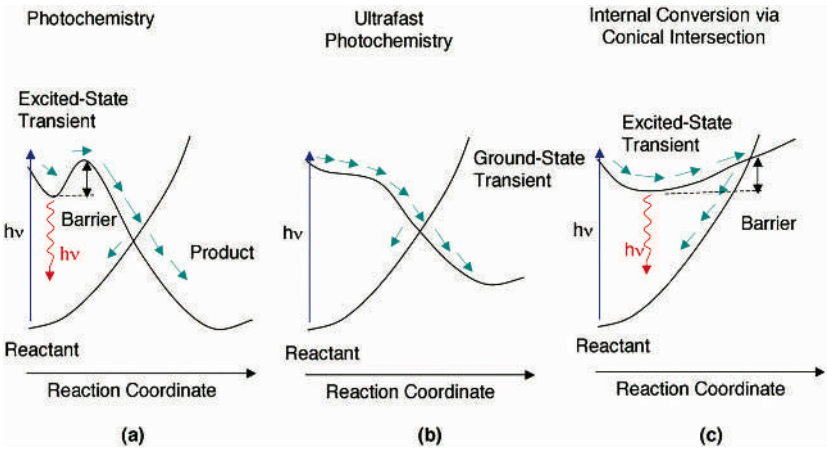

Scheme 8

Table 2. List of ultrafast photochemical processes whose excited-state path is characterized by a small or negligible barrier.

Ultrafast Radiationless Decay	Ref. Number
Polyenes and Polyene Schiff Bases	81–83
Benzene	31
Azulene	40
Fulvene	45
Indacene	84
Cyanine	37
Styrene	85

scale is explained by the fact that the computed excited-state paths are barrierless or feature a negligible energy barrier. In these systems, evolution towards the conical intersection funnel is not restrained. The same type of feature has been documented for ultrafast internal conversion processes [see Scheme 8(c)], where the unsuccessful chemical process leading to decay is, again, controlled by a small or negligible barrier. A list of these types of reactions is given in Table 2.

The computational investigation of the reactions and chromophores relative to the references of Tables 1 and 2 would constitute, together with additional results from our and other research groups, the basis for a systematic

presentation of computed conical intersection structures. Given the length limitations, it will be not possible to implement such a presentation in the present chapter. Nevertheless in Sec. 3.3 we present a selection of results (Scheme 9) that, in our view, complement those already given above in providing an overview of recent case studies. This presentation has been designed to:

(i) Focus on the chemical role played by the conical intersection. Thus, for the computational aspects (e.g. the level of theory used in the computation) the reader shall refer to the cited literature.

(ii) Despite the fact that a number of conical intersections have now been located for processes involving higher excited states (e.g. S_2/S_1 intersections), here we limit ourselves to a discussion of S_1/S_0 conical intersections. Conical intersections between states of other spin multiplicities (e.g. T_2/T_1) also exist, but will not be systematically described.

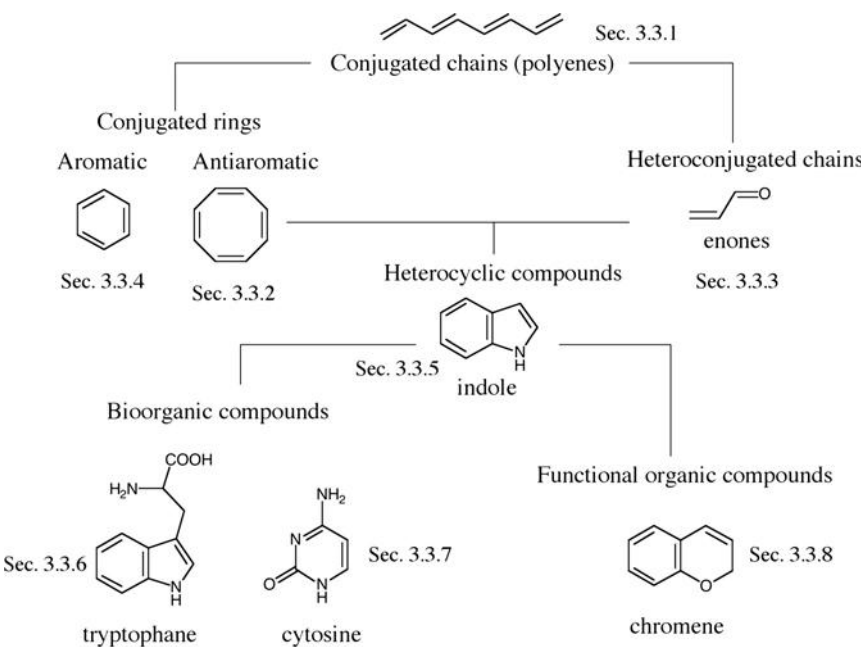

Scheme 9

(iii) Although crossings between states of different spin multiplicity (e.g. T_1/S_0) are chemically very important, they do not correspond to conical intersections and thus will not be discussed.

3.3. *Basic Organic and Bioorganic Chromophores*

3.3.1. *Conjugated Dienes and Polyenes*

Buta-1,3-diene represents the simplest conjugated polyene. There are three states involved in the photochemistry and photophysics of polyenes.[55,57,81] In fact, these chromophores are initially excited to the S_2 state (1^1B_2 and 1^1B_u states for polyenes with C_S and C_{2h} symmetry, respectively), then they relax (through a S_2/S_1 conical intersection) to a low-lying doubly excited covalent S_1 state (2^1A_1 and 2^1A_g states for C_S and C_{2h} symmetry, respectively). Further relaxation along S_1 leads to barrierless decay to the ground-state via a S_1/S_0 conical intersection. The S_1/S_0 conical intersections (Fig. 14) accessed from *s-cis*- and *s-trans*-buta-1,3-dienes are characterized by the same sharp –$(CH)_3$– "kink" in the carbon backbone:[55,81,86,87] the two C–C bonds of the –C_2–C_3–C_4 segment are twisted and the C_2–C_3–C_4 bending angle is decreased, resulting in the pyramidalization of the –C_2–C_3–C_4 segment central carbon. In Scheme 10 we show that the electronic structure of the kink is characterized by three uncoupled π-electrons arranged at the vertex of a triangle defined by the C_2, C_3, and C_4 atoms. The C_2–C_3–C_4 kink is loosely coupled to an isolated π-electron located at the terminal methylene group $C_{(1)}H_2$. The structure of the branching plane is similar to that described in Scheme 3 for the prefulvenic conical

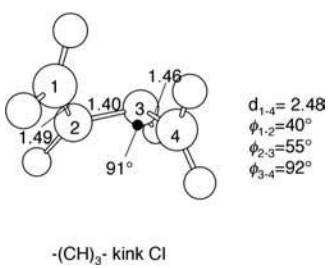

Fig. 14. The –$(CH)_3$– kink intersection of *s-cis*-buta-1,3-diene. ϕ_{1-2}, ϕ_{2-3}, ϕ_{3-4} describe the torsion about the C_1–C_2, C_2–C_3 and C_3–C_4 bonds, respectively. The values of the relevant structural parameters are given in Å and degrees.

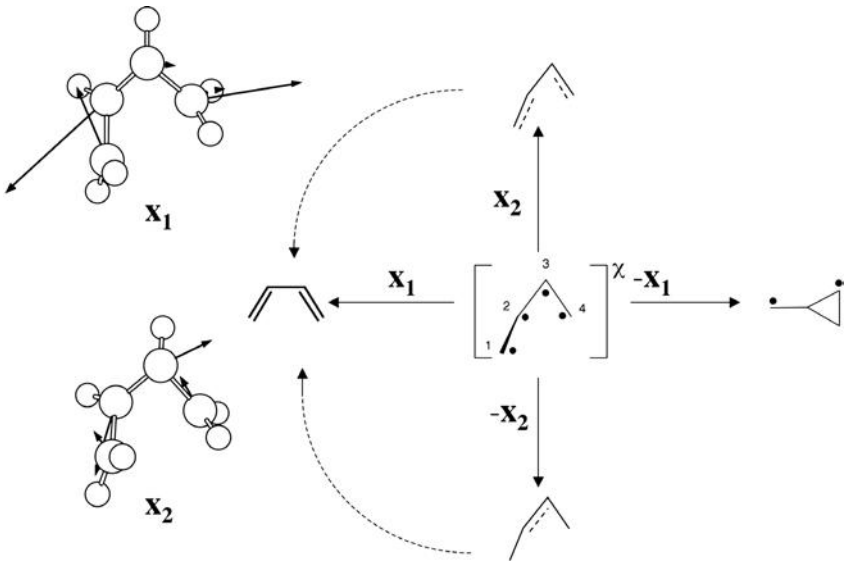

Scheme 10

intersection of benzene. It is clear from the $\mathbf{X_1}$ vector that the intersection mediates a σ-bond-making process between the C_2 and C_4 centers to generate a biradical species. This species is the precursor of bicyclobutane. Alternatively, motion along the $\mathbf{X_2}$ and $-\mathbf{X_2}$ directions leads to two highly distorted butadiene structures that must revert to the parent molecule upon further relaxation.

In longer polyenes, the $-(CH)_3-$ kink intersection is a common feature of the S_1 state as documented for *s-cis,Z,s-cis-*, *s-trans, Z,s-trans-*, and *all-trans*-hexa-1,3,5-triene[28,68,81,88] (see Fig. 15 for the latter conformer) and for *all-trans*-octa-1,3,5,7-tetraene,[81,82] *all-trans*-dodeca-1,3,5,7,9,11-hexaene,[83] as well as for the allyl, pentadienyl, heptatrienyl polyene radicals.[81] In Fig. 15(a), we compare the structure of the $-(CH)_3-$ units of six all-trans conjugated hydrocarbons, three polyenes (butadiene, hexatriene, and octatetraene) and three polyene radicals (allyl, pentadienyl, and heptatrienyl). The comparison of these structures with that of buta-1,3-diene seen in Fig. 14 reveals that each structure contains the same triangular arrangement of the carbon skeleton that we have already discussed above. In longer polyenes, there is the possibility of several conical intersections with the kink located at different positions in the chain. For example,

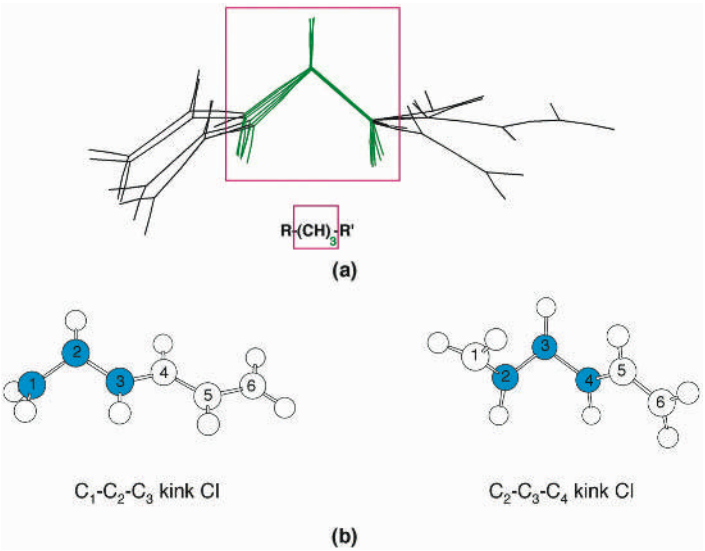

Fig. 15. (a) Superimposed $-(CH)_3-$ kinks of six all-trans conjugated hydrocarbons: three polyenes (butadiene, hexatriene, and octatetraene) and three polyene radicals (allyl, pentadienyl and heptatrienyl). Adapted from Ref. 81. (b) Structures of the conical intersections of *all-trans*-hexa-1,3,5-triene. (left) the $-(CH)_3-$ kink corresponds to the $C_1-C_2-C_3-$ segment, (right) the $-(CH)_3-$ kink corresponds to the $-C_2-C_3-C_4$ segment. The shaded atoms indicate the position of the kink. The data are from Ref. 88.

Fig. 15b shows that in *all-trans*-hexa-1,3,5-triene there are two distinct kinked S_1/S_0 conical intersections, one with the $-(CH)_3-$ kink located at the $C_2-C_3-C_4$ position mediating simultaneous Z/E and *s-cis/s-trans* isomerizations, and the other with the kink located at the $C_1-C_2-C_3$ position, mediating simultaneous *s-cis/s-trans* isomerization and methylene twisting. The conical intersection of benzene,[31,89–92] displaying the typical $-(CH)_3-$ kink arrangement, has already been reported in Fig. 8(a) of Sec. 2.2. The $-(CH)_3-$ kink intersection has been recognized in other aromatic systems such annulene,[63] styrene,[85,93] stilbene[94] and azabenzenes[90–92,95] and pyrrole,[96] and antiaromatic molecules such as cyclo-1,3,5,7-octatetraene[97] (see below).

3.3.2. *Cyclocta-1,3,5,7-tetraene*

Cyclooctatetraene is formally an antiaromatic compound. Its ground-state structure is far for being planar and displays a tub conformation with four

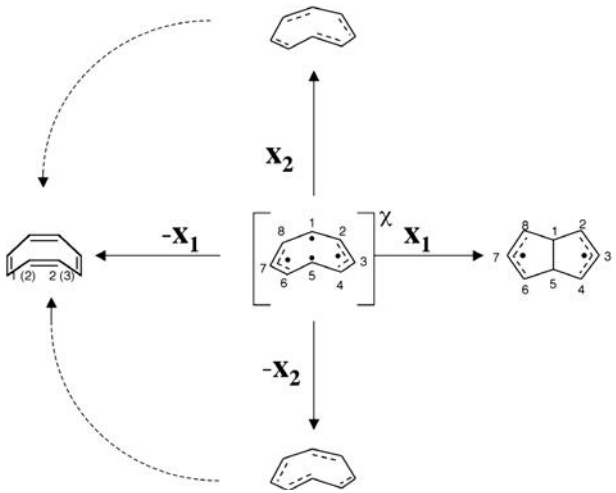

Scheme 11

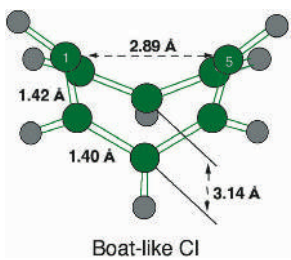

Fig. 16. Structure of the "boat-like" conical intersection of cyclocta-1,3,5,7-tetraene. This intersection mediates semibullvalene formation and double-bond/single-bond shifting. The values of the relevant structural parameters are given in Å and degrees. Data from Refs. 97 and 98.

moderately interacting localized double bonds (left structure in Scheme 11). In contrast, the S_1 excited-state minimum is a planar structure that correlates with S_3 at **FC**.[97] The vertical S_3 state is described in terms of the molecular orbitals involved in the electronic excitation as a doubly excited state $^1\pi^{*2}$ that it is totally symmetric (2^1A_1 in the D_{2d} group that applies to the ground-state cyclooctatetraene tub form) as the ground state (1^1A_1). There are two tetraradical S_1/S_0 conical intersections. One corresponds to the –$(CH)_3$– kink intersection of the same type as the previously discussed intersection of linear conjugated hydrocarbons (e.g. butadiene and longer

polyenes in Sec. 3.3.1)[97,98] and aromatic compounds such as benzene [see Fig. 8(a) discussed in Sec. 2.2]. While for benzene there is only one low-energy tetraradical pattern involving three adjacent unpaired electrons (i.e. the kink, see Scheme 3) and an allyl radical, in cyclooctatetraene, due to its larger size, a new and more stable tetraradical type configuration is possible that corresponds to a boat-like conical intersection (Fig. 16). Here, there are two unpaired facing electrons on the C_1 and C_5 centers, plus two delocalized allyl radicals (Scheme 11). Obviously, this configuration is more stable than the kink one and correspondingly the boat-like intersection is the lowest-energy crossing point. A tetraradical tetrahedral structure can be also found in the higher-energy C_2 symmetric intersection in cyclohexa-1,3-diene seen in Fig. 6 of Sec. 2.1. The main geometric feature is the C_1–C_5 transannular bond distance (2.89 Å). In Scheme 11, we show that the structure of the branching plane is similar to that previously documented for benzene. The geometry, the electronic distribution, and the branching plane vectors clearly indicate that this conical intersection mediates a σ-bond formation process between C_1 and C_5. Indeed, motion along $\mathbf{X_1}$ leads to the formation of a bicyclic biradical product (bicyclo[3.3.0]octadienyl biradical) which is the precursor of semibullvalene. On the other hand, evolution along the $\mathbf{X_2}$ and $-\mathbf{X}_2$ vectors leads to two unstable structures with alternating single/double bonds that relax towards the parent molecule or its double-bond-shifted isomer.

3.3.3. *Conjugated Enones*

The simplest conjugated enone is acrolein. In Fig. 17 we show the structure of the branching plane of the ^1n-π^* S_1/S_0 conical intersection of *s-cis*-acrolein.[58] The conical intersection structure features inverted single and double-bonds with a 90° twisted terminal methylene. $\mathbf{X_1}$ describes a stretching deformation that corresponds to double-bond expansion and single-bond contraction. In contrast, $\mathbf{X_2}$ corresponds to a CO stretching coupled to terminal CH_2 torsion. Evolution along the $\mathbf{X_2}$ and $-\mathbf{X_2}$ directions would yield two structures that correspond to the four-membered-ring oxetene and ground-state reactant, respectively. Since the conical intersection structure has the CH_2 moiety twisted, the cis/trans isomerization product could be formed by terminal CH_2 forward rotation. Evolution along the $\mathbf{X_1}$ and $-\mathbf{X_1}$ directions would yield two unstable structures that may be

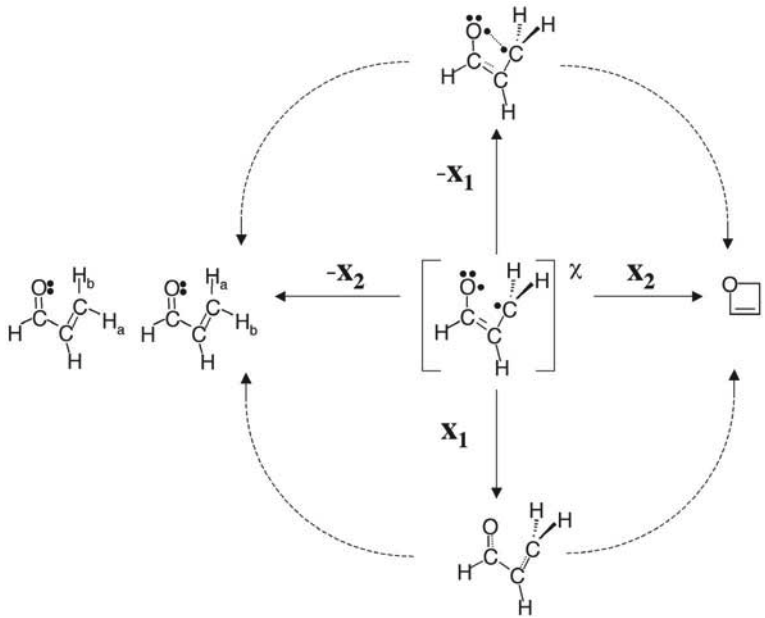

Fig. 17. The conical intersection for cyclization and Z/E isomerization of *s-cis*-acrolein and the corresponding branching plane structure. Data from Ref. 58.

represented by formulas with inverted single and double bonds and correspond to ground-state cyclization transition states. These unstable structures should revert to acrolein and to oxetene. In Sec. 3.3.8 we shall see that a similar intersection has been located for photoinduced ring opening of benzopyran.

3.3.4. *Benzene and [18]annulene*

Benzene displays a symmetric (C_s symmetry) S_1/S_0 conical intersection between states that correlate with the $^1E_{2g}$ state (S_2 in the FC region) and the ground state of the planar equilibrium structure.[31,89–92] In Scheme 12, we show that the electronic character of the anti-aromatic (i.e. difference of the two Kekulé structures indicated with a dashed circle) S_1 surface ($^1B_{2u}$) changes along the S_1 reaction path due to an avoided crossing between the S_2 and S_1 states.[31] The S_2 ($^1E_{2g}$) state can be described by a combination of quinoid (Dewar type) and antiquinoid spin couplings. As seen in Fig. 8(a)

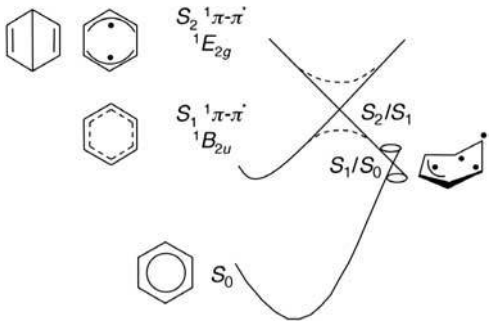

Scheme 12

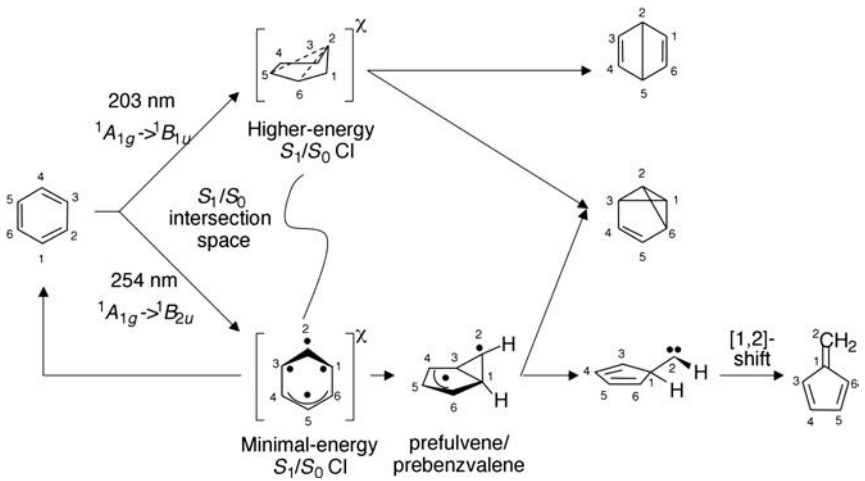

Fig. 18. The photochemistry of benzene. The curve connecting the two conical intersections in the centre of the scheme indicates that the two structures belong to the same intersection space. Data from Refs. 31 and 32.

of Section 2.2, the benzene S_1/S_0 intersection structure is characterized by the same $-(CH)_3-$ "kink" feature found in polyene hydrocarbons. In fact, one –CH– unit is raised out of the original plane of the ring and pyramidalized, yielding a highly distorted allyl radical moiety with a small C–C–C bending angle (the distance between the carbons at position 1 and 3 is ca. 2.0 Å, and corresponds to a closing cyclopropanyl σ-bond). The remaining part of the molecule corresponds to a planar allyl radical moiety with a geometry that is very close to that of the equilibrium allyl radical.

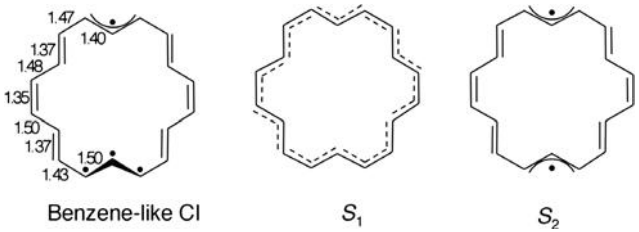

Scheme 13

This intersection is usually referred to as the "prefulvenic" intersection. As shown in Scheme 12, the intersection is accessible from: (i) the S_1 state by surmounting an energy barrier related to the S_1/S_2 avoided crossing (see dashed curves), and (ii) from the S_2 state through a barrierless path involving a higher-energy S_2/S_1 conical intersection.

The photochemistry of benzene leading to formation of benzvalene, fulvene, and Dewar benzene is summarized in Fig. 18 and rationalized by the branching plane of Scheme 3 in Sec. 2.2. The four quasi-unpaired electrons (see minimal-energy CI) can recouple in two different ways, leading to the reactant or to a ground-state prefulvene biradical intermediate. This species in turn isomerizes to benzvalene. We have found that the prefulvene structure does not correspond to a minimum, but to a transition state connecting two slightly distorted structures named prebenzvalene.[31] Another photoproduct observed upon irradiation of benzene is fulvene. In Fig. 18 we also report a plausible low-energy pathway for the thermal conversion of prefulvene (or prebenzvalene) to fulvene involving the formation of 1,3-cyclopentadienylcarbene via C_2–C_3 bond breaking followed by [1,2]-H shift to yield fulvene.[32] Calculations show that Dewar benzene is a product of S_2 photochemistry (at vertical geometries S_2 is $^1B_{1u}$, but it soon acquires the character of the E_{2g} state as motion along the reaction path occurs). This is due to the fact that the molecule moves downhill on the S_2 surface to an S_2/S_1 conical intersection and reaches the S_1 surface at a higher energy S_1/S_0 conical intersection (see Fig. 18) belonging to the same intersection space of the prefulvenic intersection with a geometry that potentially mediates either Dewar benzene or benzvalene formation.

A benzene-like intersection exists also for [18]annulene (Scheme 13) that, similarly to benzene, obeys to the Hückel $4n + 2$ aromaticity rule.[63] In fact, the annulene S_1/S_0 intersection has a $-(CH)_3-$ "kink" feature, a

3-electron allyl center and 6 fully formed double bonds. While in principle the reaction could lead to formation of a cross-ring σ-bond, this process is simply aborted at the conical intersection point and radiationless decay leads exclusively to the reactant reconstitution [see path (c) in Scheme 6]. In analogy to benzene, in [18]annulene the S_1 ($^1B_{2u}$) and relaxed S_2 states correspond to the anti-aromatic (i.e. difference of the two Kekulé structures) and antiquinoid structures, respectively.

3.3.5. *Indole*

The relevant potential-energy surfaces for photochemically induced H-detachment in indole are shown in Fig. 19(a).[99,100] The key role in this

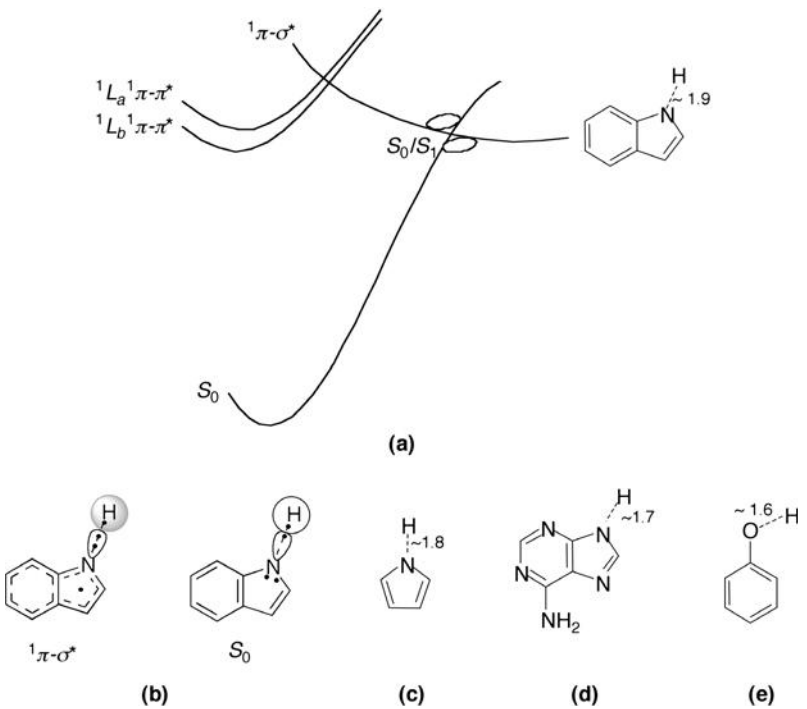

Fig. 19. Schematic representation of the potential-energy profiles of the $^1\pi$-σ^*, ^1L_b and ^1L_a, $^1\pi$-π^* excited states and ground state for the NH group hydrogen-atom detachment of indole. The $^1\pi$-σ^* state is repulsive. The values of the relevant structural parameters are given in Å. Data from Refs. 99 and 100.

picture is played by the $^1\pi$-σ^* excited state, which has a repulsive potential-energy function relative to the in-plane stretching of the N–H bond and intersects in turn the ^1L_b and ^1L_a excited states of $^1\pi$-π^* character and the ground state that instead are bound. The resulting multiple conical intersections can provide the mechanism for efficient internal conversion to the ground state. The $^1\pi$-σ^* S_1/S_0 intersection is planar and occurs at a dissociating NH distance of ∼1.9 Å. Since the intersection has been located under a symmetry constraint and not by applying the CIO method, the existence of lower-energy intersections of lower symmetry cannot be excluded. This intersection provides a mechanism for repopulation of the ground-state parent molecule or dissociation to ground-state radical and H atom. The diagram in Fig. 19(a) derives from two important properties of the electronic structure of the $^1\pi$-σ^* excited state. First, the $^1\pi$-σ^* state is antibonding relative to the NH bond. Initially, the $^1\pi$-σ^* excited state is described by a Rydberg-like configuration due to the diffuse character of the σ^*-orbital, which resembles the 3*s* hydrogen orbital. However, a stretching of the NH bond leads to a collapse of the antibonding σ^*-orbital towards the 1*s* orbital of hydrogen. Accordingly, as shown in Fig. 19(b), the N–H bond in the $^1\pi$-σ^* state is described by a configuration consisting of a linear array of two orbitals containing three electrons, two forming a lone pair on the N atom and one localized in the 1*s* orbital of the detaching hydrogen. Since the ground state and $^1\pi$-π^* states are bound (two electrons in the NH σ-bond), stretching the NH bond lowers the $^1\pi$-σ^* energy and raises the corresponding S_0 and $^1\pi$-π^* energies, bringing the states to cross. Second, the crossings are enforced by symmetry. The $^1\pi$-σ^* state is of $^1A''$ symmetry, while the $^1\pi$-π^* and the S_0 states are of $^1A'$ symmetry in the C_s group, and therefore the intersections are symmetry-allowed intersections of $^1A''$ and $^1A'$ states.

The existence of a conical intersection of the lowest $^1\pi$-σ^* state with the ground state is a general property of planar aromatic systems containing hydroxy or azine groups. The H-detachment intersection has been documented along the N–H stretch coordinate in (c) pyrrole, and (d) 9H tautomer of adenine (Fig. 19).[99−101] A similar conical intersection mediating O–H cleavage has been identified in phenol [Fig. 19(e)].[100]

3.3.6. *Tryptophan*

In zwitterionic tryptophan (the amino acid chain contains an ammonium group and a carboxylate anion), in addition to the S_1/S_0 H-detachment

intersection of the indole chromophore discussed above, there is a S_1/S_0 intersection that arises from the interaction between the amino acid chain and the indole chromophore and is held to be responsible for the $^1\pi$-π^* fluorescence quenching (Fig. 20).[102] The two paths may in fact coexist on the same multidimensional potential-energy surface along different geometric coordinates. Reaction-path computations show that after hydrogen transfer from the amino acid chain to the indole chromophore, the path intercepts a conical intersection along the amino acid chain decarboxylation coordinate with the C–C σ-bond linking the amino acid chain to the

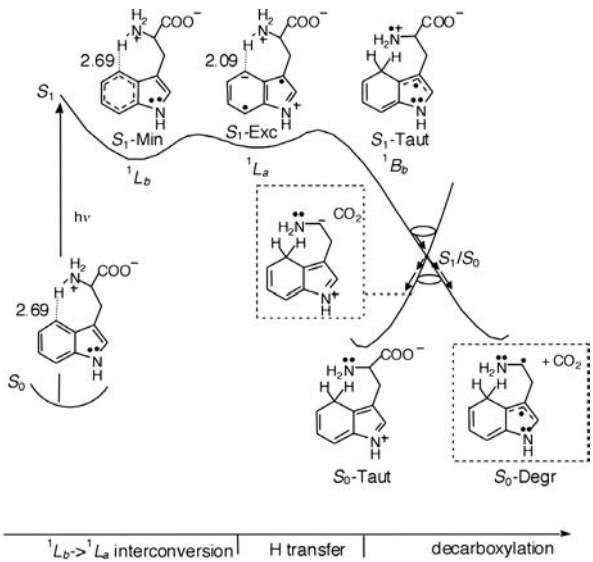

Fig. 20. Schematic representation of the reaction coordinate for tryptophan fluorescence quenching induced by hydrogen transfer and aborted decarboxylation. The electronic nature of the S_1 surface changes character along the S_1 path due to two avoided crossings between S_1 and S_2. The first one occurs between the covalent ^1L_b state and the ionic ^1L_a state along the reaction coordinate that interconverts the S_1-Min and S_1-Exc minima. The second one occurs between the ionic ^1L_a state and the biradical ^1B_b state along the tautomerization coordinate that leads to the excited-state tautomerized form S_1-Taut. This point does not corresponds to a minimum on the potential-energy surface and it is found that evolution along a decarboxylation coordinate leads to a S_1/S_0 conical intersection, where efficient radiationless decay to the ground state takes place. The values of the relevant structural parameters are given in Å. Data from Ref. 102.

indole chromophore nearly broken (1.74 Å). Thus, the amino acid chain acts not only as the hydrogen donor, but is involved in another step of the reaction, namely the decarboxylation process. In Fig. 9(a), we have seen that in azoalkanes the decay at the intermolecular H-transfer intersection leads to simultaneous production of radical and ion pairs. In tryptophan, the decay at the conical intersection leads to simultaneous formation of a zwitterionic and biradical species (framed structures). Distortion along $\mathbf{X_1}$ that corresponds to the stretching of the C–C bond involved in the decarboxylation process leads to production of the biradical species, while distortion along $-\mathbf{X_1}$ leads to production of the zwitterionic species. The zwitterionic species can be derived from the biradical species by means of an electron transfer from the side chain to the indole chromophore. The zwitterionic species is a transient species and relaxes toward the ground-state tautomerized form. This is an additional case of unsuccessful photochemistry, where the second part of the quenching mechanism corresponds to an aborted decarboxylation process and conforms to the case depicted in Scheme 6(c). The tautomerized form in turn reverts to the untautomerized form via back-proton transfer from the chromophore to the side chain on the ground-state surface.

3.3.7. *Cytosine*

Figure 21 shows two intersections that occur in the amino keto tautomer of cytosine. The azine and carbonyl functionalities introduce two low-lying ^1n-π^* excited states, one involving the nitrogen lone pair and the other the oxygen lone pair. Each state gives a conical intersection with the ground state.[103] In the ^1n_O-π^* S_1/S_0 intersection (excitation involves the oxygen

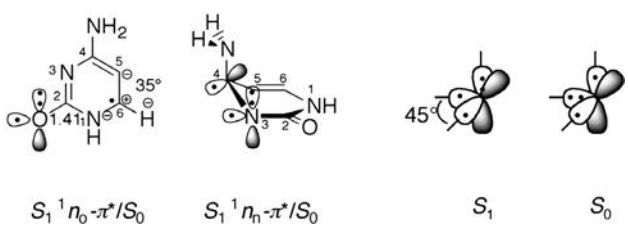

Fig. 21. Conical intersections in the amino keto tautomer of cytosine. The values of the relevant structural parameters are given in Å and degrees. Data from Ref. 103.

lone pair, n_O) the C–O bond is stretched to 1.41 Å and C_6 is significantly pyramidalized (the deviation from planarity, calculated as the difference between 360° and the sum of the three bending angles is 35°). This intersection is similar to the acrolein intersection that features a stretched C–O bond and a twisted terminal methylene (see Sec. 3.3.3). A type of reasoning similar to that employed in acrolein can indeed be used to rationalize the degeneracy in cytosine. The S_0 and S_1 states correspond to two biradical configurations ($n_O p_C / p_O p_C$) that can be interconverted by swapping the relative occupancies of the n_O- and p_O-orbitals. When the unpaired electrons are completely uncoupled, the two arrangements, one with two electrons in the n_O-orbital and one electron in the p_O-orbital and the other with reversed occupancies, are energetically equivalent. The decoupling between the biradical centers requires C–O bond stretching and pyramidalization in cytosine, while it is achieved by means of C–O bond stretching and methylene twisting in acrolein. However, one should bear in mind that the intersection is associated with two different reaction coordinates for the two molecules and describes a photochemical process in acrolein and a purely photophysical process in cytosine.

The geometry of the ^1n_o-π^* S_1/S_0 intersection has not been confirmed upon inclusion of dynamical correlation.[104] At the ^1n_o-π^* S_1/S_0 crossing geometry of Fig. 21 the lowest excited state becomes $^1\pi$-π^* while ^1n_o-π^* corresponds to S_2. As the C–O bond distance is stretched further from 1.41 to 1.43 Å, a $^1\pi$-π^* S_1/S_0 crossing is reached.[104] This type of situation arises because the $^1\pi$-π^* and ^1n_o-π^* states are close in energy and their order is altered upon inclusion of dynamical correlation. A precise location of the two S_1/S_0 crossings (i.e. ^1n_o-π^* S_1/S_0 and $^1\pi$-π^* S_1/S_0) would require a conical intersection optimization procedure that includes dynamical correlation.[96]

The ^1n_N-π^* S_1/S_0 intersection (the excitation involves the oxygen lone pair, n_N) features out-of-the plane distortion of the C_4 ring atom and resembles the prefulvenic conical intersection, although, strictly speaking, it can not be classified as a prefulvenic intersection, because there is no tendency to form a partial cross σ-bond between the C_3 and C_5 pair of neighboring atoms. The S_1 state and S_0 state have both one electron in the C_4 p-orbital raised out of the plane, so that it is rotated of ∼45° relative to the original molecular plane (see Newman projection). At this geometry, the electronic configurations, one with two electrons in the n_N-orbital and one electron

in the p_N-orbital (S_0 state) and the other with swapped occupancies of the n_N- and p_N- orbitals (S_1 state), are degenerate.

3.3.8. *Benzopyran*

An *s-cis*-acrolein-like S_1/S_0 conical intersection arising from the degeneracy between the ^1n-π^* excited and ground states has also been found to occur along the photochemical ring-opening coordinate involving C–O bond cleavage in benzopyran (Fig. 22).[59] The geometry is acyclic, with the C–O σ-bond fully broken (2.35 Å). While the *s-cis*-acrolein intersection has the O–C–C–C dihedral angle close to 0° and the terminal CH_2 moiety twisted of ∼90°, the benzopyran intersection has a spiral-like structure with some degree of torsion about the C_2–C_3, C_3–C_4, C_4–C_5 bonds. In acrolein, the radical centers are separated by two sp^2-carbons, whereas in benzopyran

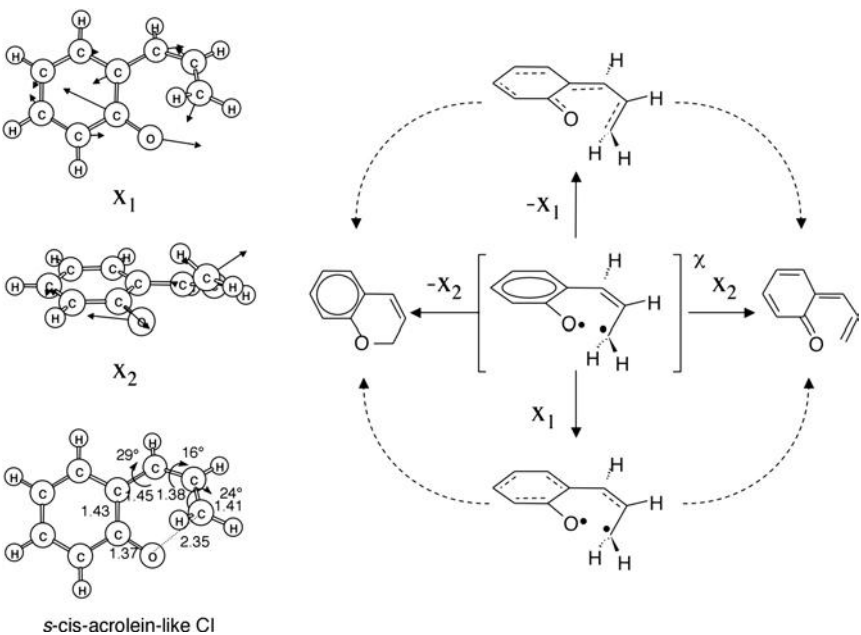

Fig. 22. The S_1/S_0 conical intersection mediating the photochemical ring-opening of benzopyran together with the $\mathbf{X}_1$ and $\mathbf{X}_2$ vectors. (right) Schematic representation of the branching plane structure. The values of the relevant structural parameters are given in Å and degrees. Data from Ref. 59.

by four sp^2-carbons. Benzopyran is a suitable model to describe the excited reaction coordinate for the ring opening of benzospiropyran.[59] The benzene moiety acts as an antenna, absorbing light energy that in turn is transferred to the carbonyl-group along the ring-opening coordinate. At **FC** the S_1 state is described by a benzene-like anti Kekulé state, whereas at the intersection S_1corresponds to a ^1n-π^* carbonyl-group-like state. In Fig. 22, we report the branching plane vectors. The $\mathbf{X_2}$ vector clearly corresponds to the C–O bond breaking mode. Distortion along $-\mathbf{X_2}$ leads to the cyclic benzopyran product; evolution along $\mathbf{X_2}$ leads to the acyclic 6-allylidene-cyclohexa-2,4-dienone system. $\mathbf{X_1}$ describes an asymmetric stretching coordinate. Evolution along the $\mathbf{X_1}$ and $-\mathbf{X_1}$ directions yields two structures that may be represented by formulas with inverted single and double bonds. These unstable structures should revert to benzopyran and to the acyclic molecule.

4. Conclusions

Above we have given an (not exhaustive) overview of the present knowledge of the geometrical, electronic and branching plane structure of the conical intersections associated with different classes of organic compounds. This knowledge could potentially provide the basis for the rationalization, systematic classification and design of photochemical organic reactions. It is our hope that the current and future increase in the amount of available computational results in the field of excited-state organic molecules will prompt a more complete classification and comprehension of these features that are already been taught in advanced organic chemistry courses.[105] On the other hand, the importance of the progress in this field has been recently reckoned by the European Commission for the Research.[106] Very obviously, the knowledge of conical intersections appears to be a key step for the rational design of molecules capable to either exploit or waste the photon energy (see for instance Ref. 38).

The extension of this knowledge to bioorganic chemistry[107] and organometallic chemistry[108] is only in its early stage. The major difficulty for the search and classification of conical intersections in these systems is related to the larger molecular size and extension of the π-systems. This calls not only for faster computers, but also for improved as well as new methodologies. These may include: (i) methodologies that

allow the treatment of larger π-systems in CASSCF computations, (ii) methodologies for computing the dynamic correlation energy corrections at a lower computational cost such as the CAS-DFT[109] or TD-DFT[110] and (iii) suitable QM/MM hybrid methodologies that allow for excited-state computations[111] and conical intersection search in proteins (e.g. in rhodopsins, fluorescent proteins and others).

A different research field awaiting further methodological development and testing is that of solvent effects in photochemical reactions. It is clear that this type of investigation will only be possible when it will be possible to compute the structure of conical intersections in solution. All intersections discussed above have been computed in isolated conditions and for organic ions (e.g. PSB, cyanines and radical cations) in absence of the couterion. It would be therefore mandatory, for the many cases where the experimental observations are carried out in solution, to further develop methodologies[112] and computational strategies allowing such an investigation.

The search of conical intersections both in solution and in proteins represents remarkable applicative research targets for modern quantum chemical methodologies. However, it must be stressed that the understanding of the exact nature and structure of the intersection space (i.e. the $\leq 3N-8$ dimensional space spanned by a family of conical intersection) is still very poorly understood. Regions where two such spaces cross, leading to a lower dimensional intersection space (but higher dimensional branching space), have been demonstrated for simple molecular systems.[113] In the authors' opinion, the knowledge of such structural/topological features of a pair of intersecting potential-energy surfaces and their relationship with photochemical reaction paths in organic chromophores represents a fundamental research topic. In principle, photochemical properties such as the time scale, quantum yield, stereoselectivity and substituent effects may well be affected by the structure of the intersection space.

Finally, the development of methodologies for the computation of non-adiabatic trajectories in sizable organic molecules at a level of theory that ensures qualitatively correct force fields represents another fundamental research target.[114] In fact, while the qualitative aspects of the dynamics of organic chromophores can be derived by the mapping of the excited- and ground-state reaction coordinates (e.g. as illustrated in Fig. 13), the evaluation of the reaction time scale, quantum yields as well as the direct

comparison with time-resolved spectroscopic measurements can only be carried out when direct-dynamics data become available.

Acknowledgments

Funds have been provided by the Università di Siena (Progetto di Ateneo A.A. 00/02 and A.A. 02/04). The authors are grateful to the HFSP (RG 0229/2000-M) for a grant to A. Migani. We wish to thank the "Cineca" for granted calculation time used to refine a few results given in this chapter on their computers. Many thanks to Elena Porciatti for help with the literature search.

References

1. H. Eyring, *Chem. Rev.* **17**, 65 (1935).
2. M. Evans and M. Polanyi, *Trans. Faraday Soc.* **31**, 875 (1935).
3. F. Bernardi, M. Olivucci and M. A. Robb, *Chem. Soc. Rev.* **25**, 321 (1996).
4. W. T. A. M. Van Der Lugt and L. J. Oosterhoff, *J. Am. Chem. Soc.* **91**, 6042 (1969).
5. D. Grimbert, G. Segal and A. Devaquet, *J. Am. Chem. Soc.* **97**, 6629 (1975).
6. H. E. Zimmerman, *J. Am. Chem. Soc.* **88**, 1566 (1966).
7. J. Michl, *J. Mol. Photochem.* **4**, 243 (1972).
8. J. Michl, *J. Mol. Photochem.* **4**, 257 (1972).
9. J. Michl, *Topics Curr. Chem.* **46**, 1 (1974).
10. J. Michl, *Pure App. Chem.* **41**, 507 (1975).
11. L. Salem, *J. Am. Chem. Soc.* **96**, 3486 (1974).
12. L. Salem, C. Leforestier, G. Segal and R. Wetmore, *J. Am. Chem. Soc.* **97**, 479 (1975).
13. W. G. Dauben, L. Salem and N. J. Turro, *Accts. Chem. Res.* **8**, 41 (1975).
14. E. Teller, *Isr. J. Chem.* **7**, 227 (1969).
15. Later estimates showed that the decay may occur within one vibrational period, see H. Köppel, L. S. Cederbaum, W. Domcke and S. S. Shaik, *Angew. Chem. Int. Ed.* **22**, 210 (1983).
16. B. O. Roos, in *Ab Initio Methods in Quantum Chemistry-II*, Ed. K. P. Lawley (John Wiley & Sons Ltd., Chichester, 1987), p. 399.
17. F. Bernardi, S. De, M. Olivucci and M. A. Robb, *J. Am. Chem. Soc.* **112**, 1737 (1990).
18. F. Bernardi, M. Olivucci and M. A. Robb, *Acc. Chem. Res.* **23**, 405 (1990).
19. W. Gerhartz, R. D. Poshusta and J. Michl, *J. Am. Chem. Soc.* **98**, 6427 (1976).
20. W. Gerhartz, R. D. Poshusta and J. Michl, *J. Am. Chem. Soc.* **99**, 4263 (1977).

21. M. J. Frisch, G. W. Trucks, H. B. Schlegel, G. E. Scuseria, M. A. Robb, J. R. Cheeseman, V. G. Zakrzewski, J. A. Montgomery Jr., R. E. Stratmann, J. C. Burant, S. Dapprich, J. M. Millam, A. D. Daniels, K. N. Kudin, M. C. Strain, O. Farkas, J. Tomasi, V. Barone, M. Cossi, R. Cammi, B. Mennucci, C. Pomelli, C. Adamo, S. Clifford, J. Ochterski, G. A. Petersson, P. Y. Ayala, Q. Cui, K. Morokuma, D. K. Malick, A. D. Rabuck, K. Raghavachari, J. B. Foresman, J. Cioslowski, J. V. Ortiz, A. G. Baboul, B. B. Stefanov, G. Liu, A. Liashenko, P. Piskorz, I. Komaromi, R. Gomperts, R. L. Martin, D. J. Fox, T. Keith, M. A. Al-Laham, C. Y. Peng, A. Nanayakkara, C. Gonzalez, M. Challacombe, P. M. W. Gill, B. Johnson, W. Chen, M. W. Wong, J. L. Andres, C. Gonzalez, M. Head-Gordon, E. S. Replogle and J. A. Pople, *"Gaussian 98" , Revision A.7*, (Gaussian Inc., Pittsburgh PA, 1998).
22. L. De Vico, M. Garavelli, F. Bernardi and M. Olivucci, submitted for publication.
23. M. A. Robb, M. Garavelli, M. Olivucci and F. Bernardi, in *Reviews in Computational Chemistry*, Eds. K. B. Lipkowitz and D. B. Boyd (Wiley-VCH: John Wiley and Sons Inc., New York, Chichester, 2000), p. 87.
24. G. J. Atchity, S. S. Xantheas and K. Ruedenberg, *J. Chem. Phys.* **95**, 1862 (1991).
25. D. R. Yarkony, *J. Phys. Chem. A* **105**, 6277 (2001).
26. V. Bonačić-Koutecký, J. Koutecký and J. Michl, *Angew. Chem. Int. Ed.* **26**, 170 (1987).
27. M. Garavelli, C. S. Page, P. Celani, M. Olivucci, W. E. Schmid, S. A. Trushin and W. Fuss, *J. Phys. Chem. A* **105**, 4458 (2001).
28. P. Celani, S. Ottani, M. Olivucci, F. Bernardi and M. A. Robb, *J. Am. Chem. Soc.* **116**, 10141 (1994).
29. M. Garavelli, P. Celani, M. Fato, M. J. Bearpark, B. R. Smith, M. Olivucci and M. A. Robb, *J. Phys. Chem. A* **101**, 2023 (1997).
30. A. Migani, M. A. Robb and M. Olivucci, *J. Am. Chem. Soc.* **125**, 2804 (2003).
31. I. J. Palmer, I. N. Ragazos, F. Bernardi, M. Olivucci and M. A. Robb, *J. Am. Chem. Soc.* **115**, 673 (1993).
32. J. Dreyer and M. Klessinger, *Chem. Eur. J.* **2**, 335 (1996).
33. S. Wilsey, K. N. Houk and A. H. Zewail, *J. Am. Chem. Soc.* **121**, 5772 (1999).
34. S. Wilsey and K. N. Houk, *J. Am. Chem. Soc.* **122**, 2651 (2000).
35. W. M. Nau, G. Greiner, J. Wall, H. Rau, M. Olivucci and M. A. Robb, *Angew. Chem. Int. Ed.* **37**, 98 (1998).
36. A. Sinicropi, R. Pogni, R. Basosi, M. A. Robb, G. Gramlich, W. M. Nau and M. Olivucci, *Angew. Chem. Int. Ed.* **40**, 4185 (2001).
37. A. Sanchez-Galvez, P. Hunt, M. A. Robb, M. Olivucci, T. Vreven and H. B. Schlegel, *J. Am. Chem. Soc.* **122**, 2911 (2000).

38. A. Sinicropi, W. N. Nau and M. Olivucci, *Photochem. Photobiol. Sci.* **1**, 537 (2002).
39. A. Sinicropi, U. Pischel, R. Basosi, W. M. Nau and M. Olivucci, *Angew. Chem. Int. Ed.* **39**, 4582 (2000).
40. M. J. Bearpark, F. Bernardi, S. Clifford, M. Olivucci, M. A. Robb, B. R. Smith and T. Vreven, *J. Am. Chem. Soc.* **118**, 169 (1996).
41. M. Olivucci and M. A. Robb, paper in preparation.
42. I. N. Ragazos, M. A. Robb, F. Bernardi and M. Olivucci, *Chem. Phys. Lett.* **197**, 217 (1992).
43. O. Celani, M. A. Robb, M. Garavelli, F. Bernardi and M. Olivucci, *Chem. Phys. Lett.* **243**, 1 (1995).
44. B. R. Smith, M. J. Bearpark, M. A. Robb, F. Bernardi and M. Olivucci, *Chem. Phys. Lett.* **242**, 27 (1995).
45. M. J. Bearpark, F. Bernardi, M. Olivucci, M. A. Robb and B. R. Smith, *J. Am. Chem. Soc.* **118**, 5254 (1996).
46. S. Klein, M. J. Bearpark, B. R. Smith, M. A. Robb, F. Bernardi and M. Olivucci, *Chem. Phys. Lett.* **292**, 259 (1998).
47. F. Bernardi, M. Olivucci and M. A. Robb, *Isr. J. Chem.* **33**, 265 (1993).
48. F. Bernardi, M. Olivucci and M. A. Robb, *Pure Appl. Chem.* **67**, 17 (1995).
49. M. A. Robb, F. Bernardi and M. Olivucci, in *ECCC I. 1st European Conference on Computational Chemistry*, Eds. F. Bernardi and J.-L. Rivail (AIP Press, 1995), p. 87.
50. F. Bernardi, M. Olivucci and M. A. Robb, *J. Am. Chem. Soc.* **114**, 1606 (1992).
51. M. Olivucci, *La Chimica e L'Industria* **84**, 44 (2002).
52. F. Bernardi, M. Olivucci and M. A. Robb, *J. Am. Chem. Soc.* **114**, 2752 (1992).
53. F. Bernardi, M. Olivucci, M. A. Robb and G. Tonachini, *J. Am. Chem. Soc.* **114**, 5805 (1992).
54. F. Bernardi, M. Olivucci, I. N. Ragazos and M. A. Robb, *J. Am. Chem. Soc.* **114**, 8211 (1992).
55. M. Olivucci, I. N. Ragazos, F. Bernardi and M. A. Robb, *J. Am. Chem. Soc.* **115**, 3710 (1993).
56. M. Olivucci, F. Bernardi, S. Ottani and M. A. Robb, *J. Am. Chem. Soc.* **116**, 2034 (1994).
57. P. Celani, F. Bernardi and M. Olivucci, *J. Chem. Phys.* **102**, 5733 (1995).
58. M. Reguero, M. Olivucci, F. Bernardi and M. A. Robb, *J. Am. Chem. Soc.* **116**, 2103 (1994).
59. P. Celani, F. Bernardi, M. Olivucci and M. A. Robb, *J. Am. Chem. Soc.* **119**, 10815 (1997).
60. I. Rossi, F. Bernardi, M. Olivucci and M. A. Robb, *J. Phys. Chem.* **99**, 6757 (1995).

61. M. Reguero, F. Bernardi, H. Jones, M. Olivucci, I. N. Ragazos and M. A. Robb, *J. Am. Chem. Soc.* **115**, 2073 (1993).
62. S. Wilsey, M. J. Bearpark, F. Bernardi, M. Olivucci and M. A. Robb, *J. Am. Chem. Soc.* **118**, 176 (1996).
63. M. J. Bearpark, F. Bernardi, S. Clifford, M. Olivucci, M. A. Robb and T. Vreven, *Mol. Phys.* **89**, 37 (1996).
64. S. Clifford, M. J. Bearpark, F. Bernardi, M. Olivucci, M. A. Robb and B. R. Smith, *J. Am. Chem. Soc.* **118**, 7353 (1996).
65. M. J. Bearpark, M. Deumal, M. A. Robb, T. Vreven, N. Yamamoto, M. Olivucci and F. Bernardi, *J. Am. Chem. Soc.* **119**, 709 (1997).
66. M. Deumal, M. J. Bearpark, B. R. Smith, M. Olivucci, F. Bernardi and M. A. Robb, *J. Org. Chem.* **63**, 4594 (1998).
67. M. Garavelli, B. Frabboni, M. Fato, P. Celani, F. Bernardi, M. A. Robb and M. Olivucci, *J. Am. Chem. Soc.* **121**, 1537 (1999).
68. M. Olivucci, F. Bernardi, P. Celani, I. Ragazos and M. A. Robb, *J. Am. Chem. Soc.* **116**, 1077 (1994).
69. M. Garavelli, P. Celani, F. Bernardi, M. A. Robb and M. Olivucci, *J. Am. Chem. Soc.* **119**, 6891 (1997).
70. T. Vreven, F. Bernardi, M. Garavelli, M. Olivucci, M. A. Robb and H. B. Schlegel, *J. Am. Chem. Soc.* **119**, 12687 (1997).
71. M. Garavelli, F. Bernardi, M. A. Robb and M. Olivucci, *J. Mol. Struct. (Theochem)* **463**, 59 (1999).
72. M. Garavelli, T. Vreven, P. Celani, F. Bernardi, M. A. Robb and M. Olivucci, *J. Am. Chem. Soc.* **120**, 1285 (1998).
73. R. Gonzales-Luque, M. Garavelli, F. Bernardi, M. Merchan, M. A. Robb and M. Olivucci, *Proc. Natl. Acad. Sci. USA* **97**, 9379 (2000).
74. N. Yamamoto, F. Bernardi, A. Bottoni, M. Olivucci, M. A. Robb and S. Wilsey, *J. Am. Chem. Soc.* **116**, 2064 (1994).
75. N. Yamamoto, M. Olivucci, P. Celani, F. Bernardi and M. A. Robb, *J. Am. Chem. Soc.* **120**, 2391 (1998).
76. F. Bernardi, M. Olivucci, M. A. Robb, T. Vreven and J. Soto, *J. Org. Chem.* **65**, 7847 (2000).
77. W. M. Nau, G. Greiner, H. Rau, M. Olivucci and M. A. Robb, *Ber. Bunsenges. Phys. Chem.* **102**, 486 (1998).
78. I. J. Palmer, I. N. Ragazos, F. Bernardi, M. Olivucci and M. A. Robb, *J. Am. Chem. Soc.* **116**, 2121 (1994).
79. A. Venturini, T. Vreven, F. Bernardi, M. Olivucci and M. A. Robb, *Organometallics* **14**, 4953 (1995).
80. J. Michl and V. Bonacic-Koutecky, *Electronic Aspects of Organic Photochemistry* (Wiley, New York, 1990).
81. P. Celani, M. Garavelli, S. Ottani, F. Bernardi, M. A. Robb and M. Olivucci, *J. Am. Chem. Soc.* **117**, 11584 (1995).

82. M. Garavelli, P. Celani, N. Yamamoto, F. Bernardi, M. A. Robb and M. Olivucci, *J. Am. Chem. Soc.* **118**, 11656 (1996).
83. M. Garavelli, B. R. Smith, M. J. Bearpark, F. Bernardi, M. Olivucci and M. A. Robb, *J. Am. Chem. Soc.* **122**, 5568 (2000).
84. M. J. Bearpark, P. Celani, F. Jolibois, M. Olivucci, M. A. Robb and F. Bernardi, *Mol. Phys.* **96**, 645 (1999).
85. M. J. Bearpark, M. Olivucci, S. Wilsey, F. Bernardi and M. A. Robb, *J. Am. Chem. Soc.* **117**, 6944 (1995).
86. S. Sakai, *Chem. Phys. Lett.* **287**, 263 (1998).
87. S. Sakai, *Chem. Phys. Lett.* **319**, 687 (2000).
88. M. Garavelli, P. Celani, F. Bernardi, M. A. Robb and M. Olivucci, *J. Am. Chem. Soc.* **119**, 11487 (1997).
89. S. Kato, *J. Chem. Phys.* **88**, 3045 (1988).
90. A. L. Sobolewski and W. Domcke, *Chem. Phys. Lett.* **180**, 381 (1991).
91. W. Domcke, A. L. Sobolewski and C. Woywod, *Chem. Phys. Lett.* **203**, 220 (1993).
92. A. L. Sobolewski, C. Woywod and W. Domcke, *J. Chem. Phys.* **98**, 5627 (1993).
93. M. J. Bearpark, *J. Phys. Chem. A* **101**, 8395 (1997).
94. M. J. Bearpark, F. Bernardi, S. Clifford, M. Olivucci, M. A. Robb and T. Vreven, *J. Phys. Chem. A* **101**, 3841 (1997).
95. M. Chachisvilis and A. H. Zewail, *J. Phys. Chem. A* **103**, 7408 (1999).
96. C. S. Page and M. Olivucci, *J. Comput. Chem.* **24**, 298 (2002).
97. M. Garavelli, F. Bernardi, A. Cembran, O. Castano, L. M. Frutos, M. Merchan and M. Olivucci, *J. Am. Chem. Soc.* **124**, 13770 (2002).
98. M. Garavelli, F. Bernardi, V. Moliner and M. Olivucci, *Angew. Chem. Int. Ed.* **40**, 1466 (2001).
99. A. L. Sobolewski and W. Domcke, *Chem. Phys. Lett.* **315**, 293 (1999).
100. A. L. Sobolewski, W. Domcke, C. Dedonder-Lardeux and C. Jouvet, *Phys. Chem. Chem. Phys.* **4**, 1093 (2002).
101. A. L. Sobolewski and W. Domcke, *Chem. Phys.* **259**, 181 (2000).
102. L. Blancafort, D. Gonzales, M. Olivucci and M. A. Robb, *J. Am. Chem. Soc.* **124**, 6398 (2002).
103. N. Ismail, L. Blancafort, M. Olivucci, B. Kohler and M. A. Robb, *J. Am. Chem. Soc.* **124**, 6818 (2002).
104. M. Merchan and L. Serrano-Andrés, *J. Am. Chem. Soc.* **125**, 8108 (2003).
105. F. A. Carey and R. J. Sundberg, *Advanced Organic Chemistry* (Kluwer Academic/Plenum Publishers, New York, London, 2000).
106. http://www.cordis.lu/descartes/prize_thisyear02e.htm
107. G. A. Worth and L. S. Cederbaum, *Chem. Phys. Lett.* **338**, 219 (2001).
108. S. A. Trushin, W. Fuss and W. E. Schmid, *Chem. Phys.* **259**, 313 (2000).
109. P. A. Malmqvist, Mediterranean Seminar on Computational Chemistry for Complex Systems, Palermo, Italy, 2002.

110. F. Furche and R. Ahlrichs, *J. Chem. Phys.* **117**, 7433 (2002).
111. S. Hayashi and I. Ohmine, *J. Phys. Chem. B* **104**, 10678 (2000).
112. M. Cossi and V. Barone, *J. Chem. Phys.* **112**, 2427 (2000).
113. S. Matsika and D. R. Yarkony, *J. Phys. Chem. A* **116**, 2580 (2002).
114. G. A. Worth and M. A. Robb, in *The Role of Degenerate States in Chemistry*, Eds. M. Baer and G. D. Billing (Wiley-Interscience, Hoboken, N.J., 2002), p. 355.

PART II

Conical Intersections in Photoinduced and Collisional Dynamics

This page intentionally left blank

CHAPTER 7

THE MULTI-MODE VIBRONIC-COUPLING APPROACH

Horst Köppel,* Wolfgang Domcke,† and Lorenz S. Cederbaum*

* *Theoretical Chemistry, Institute of Physical Chemistry, University of Heidelberg, 69120 Heidelberg, Germany*

† *Institute of Physical and Theoretical Chemistry, Technical University of Munich, 85747 Garching, Germany*

Contents

1. Introduction

The concept "vibronic coupling" subsumes all phenomena which arise from the mixing of several electronic states (or components of degenerate electronic states) by nuclear displacements. Vibronic-coupling effects become important whenever there is a degeneracy or near-degeneracy of electronic states. Vibronic-coupling effects are ubiquitous in the electronic spectroscopy of highly symmetric polyatomic molecules as well as crystals, the Jahn–Teller effect being the most widely known example.[1,2] In this case the electronic degeneracy or near-degeneracy arises as a consequence of symmetry. The concept of vibronic coupling is of much wider relevance, however, and applies to essentially all polyatomic systems in excited electronic states. The dynamics at conical intersections, in particular, involves a strong mixing of electronic and vibrational degrees of freedom and thus is generically of "vibronic" character.

Vibronic-coupling theory has been a well established area of research since many years. The basic elements of the theory are the concept of diabatic electronic states, the normal-mode description of vibrational motion, and the application of symmetry selection rules to derive appropriate model Hamiltonians. The applications of vibronic-coupling theory cover the full range of molecular spectroscopy, including, in particular, optical absorption and emission and photoelectron spectroscopy. Typical spectroscopic phenomena associated with vibronic interactions are the appearance of nominally forbidden electronic bands, the excitation of nontotally symmetric modes, or unusual and complex vibronic fine structures of electronic spectra. A fairly comprehensive and up-to-date exposition of vibronic-coupling theory is provided by the monograph of Bersuker and Polinger.[3]

Traditionally, vibronic-coupling Hamiltonians have been considered as heuristic models, involving certain parameters, the values of which had to be determined by the fitting of observed spectra. More recently, the advent of large-scale computing has lead to new developments in vibronic-coupling theory. Owing to considerable progress in *ab initio* electronic-structure theory, it is now possible to compute all relevant parameters such as harmonic vibrational frequencies and vibronic coupling constants from first principles, even for somewhat larger polyatomic systems. Although vibronic-coupling parameters derived from *ab initio* calculations may often not be sufficiently accurate for a quantitative calculation of spectra, these data generally provide a very useful first guess, which subsequently may be refined to improve the agreement with the experiment.

Vibronic-coupling dynamics, that is, the solution of the Schrödinger equation for vibronic-coupling Hamiltonians, represents another area where modern computational techniques have been fruitfully applied. The computation of spectra of systems with several vibronically active vibrational modes generally requires the diagonalization of very large, but sparse, Hamiltonian matrices. Iterative diagonalization methods such as the Lanczos algorithm[4] are ideally suited for this purpose, as they do not require the Hamiltonian matrix to be stored in computer memory. Vibronic eigenvalue problems involving up to 10^9 vibronic basis states have been treated with such techniques.

Strong vibronic coupling of degenerate or nearly degenerate states can lead to an essentially complete mixing of zero-order electronic states as well as very dense and irregular vibronic line spectra. When considered in the time domain, such systems exhibit radiationless electronic decay (internal conversion) at femtosecond time scales.[5,6] To describe such phenomena, it is computationally advantageous to solve the time-dependent Schrödinger equation directly in the time domain, employing an appropriate finite-basis representation and one of many available numerical propagators[7] for first-order differential equations. Here again explicit storage of the Hamiltonian matrix can be avoided by a direct coding of the matrix-vector product. With such techniques, the femtosecond dynamics of complex systems involving many millions of vibronic basis states have become accessible to computation.

The combination of modern electronic-structure theory with efficient numerical techniques for the solution of the vibronic Schrödinger equation

represents a powerful tool for the analysis of complex electronic spectra as well as ultrafast electronic decay processes in polyatomic molecules. In this chapter we give a brief exposition of the basic concepts of vibronic-coupling theory and its application to conical intersections. More detailed and comprehensive descriptions can be found in several monographs[1,3,8–10] and review articles.[5,6,11,12] We emphasize the *ab initio* determination of vibronic-coupling parameters and the numerical treatment of multi-mode vibronic-coupling dynamics in the time as well as the frequency domain. A few applications will be briefly reviewed which illustrate the present state of the art in this area.

2. Vibronic-Coupling Hamiltonians

2.1. *General Concepts*

The basic elements of the description of non-Born–Oppenheimer dynamics in either the adiabatic or diabatic representations have been outlined in Chapters 1–4. The point of departure of the present discussion are the coupled equations in the diabatic representation

$$(T_N + W_{nn}(\mathbf{R}) - E)\,\chi_n(\mathbf{R}) = \sum_{m\neq n} W_{nm}(\mathbf{R})\chi_m(\mathbf{R}) \tag{1}$$

where

$$W_{nm}(\mathbf{R}) = \int d\mathbf{r}\Phi_n^*(\mathbf{r},\mathbf{R})[T_E + U(\mathbf{r},\mathbf{R})]\Phi_m(\mathbf{r},\mathbf{R}) \tag{2}$$

are matrix elements of the electronic Hamiltonian in the diabatic basis. Eq. (1) is equivalent to the following representation of the molecular Hamiltonian in a basis of diabatic electronic states

$$H = \sum_n |\,\Phi_n\rangle\,[T_N + W_{nn}(\mathbf{R})]\langle\,\Phi_n| + \sum_{n\neq m} |\,\Phi_n\rangle W_{nm}(\mathbf{R})\langle\Phi_m\,|. \tag{3}$$

We refer to Chapter 4 for a detailed discussion on the definition and explicit construction of diabatic states. The diabatic representation is generally advantageous for the computational treatment of the nuclear dynamics if the adiabatic potential-energy surfaces exhibit degeneracies such as conical intersections. Moreover, the diabatic representation often reflects more clearly than the Born–Oppenheimer adiabatic representation the essential physics of curve crossing problems and is thus very useful for the construction of appropriate model Hamiltonians for polyatomic systems.

An essential aspect in the construction of model Hamiltonians for chemical dynamics is the choice of the nuclear coordinates **R**. The form of the electronic potential-energy as well as the kinetic-energy expression depends on the choice of coordinates; coordinate systems may be selected to simplify either the construction of potential-energy (PE) functions or the construction of the kinetic-energy operator. For classical trajectory calculations, where the computational cost scales only linearly with the dimension, Cartesian or mass-weighted Cartesian coordinates are the obvious choice, since the kinetic-energy expression is trivial. In quantum-mechanical treatments, the computational cost grows much more rapidly with the dimension of the problem, and the elimination of translation and overall rotation is usually essential. It appears thus natural to formulate the Hamiltonian in internal coordinates as defined, for example, by Wilson *et al.*[13] Bond length/bond angle internal coordinates are best suited for the modeling of the PE function. Their drawback is the possibly very complicated form of the quantum-mechanical nuclear kinetic energy operator.[14–16]

The construction of appropriate kinetic-energy operators and PE functions simplifies considerably if we can assume that no large-amplitude motions are involved. In this case we can define a suitable reference geometry of the system (for example, the equilibrium geometry of the electronic ground state) and adopt internal displacement coordinates to describe vibrations of moderate amplitude about the reference geometry. It is then a standard procedure to introduce normal coordinates by the simultaneous diagonalization of the kinematic matrix (taken at the reference geometry) and the matrix of force constants for the electronic ground state.[13] The normal coordinates are defined by

$$\mathbf{q} = \mathbf{L}^{-1}\delta\,\mathbf{R} \tag{4}$$

where $\delta\mathbf{R}$ is the $3N-6$ ($3N-5$ for linear molecules) dimensional vector of internal displacement coordinates (changes of bond lengths and bond angles) for an N-atomic molecule, and $\mathbf{L}$ is the L-matrix of the well-known Wilson FG-matrix method.[13] It is convenient to introduce dimensionless normal coordinates via

$$Q_i = (\omega_i/\hbar)^{1/2} q_i \tag{5}$$

where ω_i is the harmonic vibrational frequency of the ith normal mode. In the harmonic approximation, which implies the expansion of the electronic

ground-state PE up to second order in the displacements as well as the approximation of the metric tensor by its value at the equilibrium geometry,[13] the kinetic-energy and PE operators of the electronic ground state take the simple form

$$T_N = -\frac{1}{2}\sum_i \hbar\omega_i \partial^2/\partial Q_i^2 \tag{6}$$

$$V_0 = \frac{1}{2}\sum_i \hbar\omega_i Q_i^2. \tag{7}$$

We proceed by expanding the diabatic excited-state PE functions and coupling elements in terms of normal-mode displacements:

$$W_{nn}(\mathbf{Q}) = W_0(\mathbf{Q}) + E_n + \sum_i \kappa_i^{(n)} Q_i + \sum_{ij} \gamma_{ij}^{(n)} Q_i Q_j + \cdots \tag{8}$$

$$W_{nn'}(\mathbf{Q}) = W_{nn'}(0) + \sum_i \lambda_i^{(nn')} Q_i + \cdots \tag{9}$$

where

$$\kappa_i^{(n)} = (\partial W_{nn}/\partial Q_i)_0 \tag{10}$$

$$\lambda_i^{(nn')} = (\partial W_{nn'}/\partial Q_i)_0 \tag{11}$$

$$\gamma_{ij}^{(n)} = \frac{1}{2}[(\partial^2 W_{nn}/\partial Q_i \partial Q_j)_0 - \hbar\omega_i \delta_{ij}]. \tag{12}$$

Here E_n denotes the vertical excitation energy of the nth excited electronic state. The $\kappa_i^{(n)}$ represent the gradients of the excited-state potential functions at the equilibrium geometry of the ground state and are referred to as first-order intra-state electronic-vibrational coupling constants. The $\lambda_i^{(nn')}$ are correspondingly called first-order inter-state coupling constants. The second-order intra-state coupling constants $\gamma_{ij}^{(n)}$ are responsible for the so-called Duschinsky rotation of the normal modes in the excited state. For simplicity, we have included in Eq. (9) only the linear term in the Taylor expansion of the off-diagonal diabatic PE matrix elements. The effect of bilinear inter-state couplings has been discussed, for example, in Refs. 102 and 113.

Combining Eqs. (6)–(9), the molecular Hamiltonian takes the form

$$H = \sum_n |\Phi_n\rangle h_n \langle\Phi_n| + \sum_{n\neq n'} |\Phi_n\rangle [W_{nn'}(0) + \sum_i \lambda_i^{(nn')} Q_i] \langle\Phi_{n'}| \qquad (13)$$

with

$$h_n = h_0 + E_n + \sum_i \kappa_i^{(n)} Q_i + \sum_{ij} \gamma_{ij}^{(n)} Q_i Q_j \qquad (14)$$

$$h_0 = \sum_i \frac{1}{2} \hbar\omega_i (-\partial^2/\partial Q_i^2 + Q_i^2). \qquad (15)$$

In practical applications of the theory, the computational problem is simplified by restricting the electronic Hilbert space to just two or three electronic states of interest, e.g. the ground state and two excited states. A further significant simplification arises from symmetry selection rules. It follows from the definition (10) that the first-order intra-state coupling constants $\kappa_i^{(n)}$ can be nonzero only for totally symmetric modes. $W_{nn'}(0)$ is zero if Φ_n and $\Phi_{n'}$ transform according to different irreducible representations. The first-order inter-state coupling constant $\lambda_i^{(nn')}$ is nonzero only for modes which transform according to the irreducible representation Γ_Q which fulfils

$$\Gamma_n \times \Gamma_Q \times \Gamma_{n'} \supset \Gamma_A \qquad (16)$$

where Γ_n, $\Gamma_{n'}$ are the irreducible representations of the electronic states and Γ_A denotes the totally symmetric representation. In molecules with high symmetry these selection rules strongly restrict the number of nonzero electronic-vibrational coupling parameters.

The interaction of the molecular system with the radiation field is described in the dipole approximation

$$H_{\mathrm{int}}(t) = -\sum_{n>m} |\Phi_n\rangle \vec{E}(t) \cdot \vec{\mu}_{nm} \langle\Phi_m|. \qquad (17)$$

The $\vec{\mu}_{nm}$ are electronic transition dipole moments, defined as matrix elements of the electronic dipole operator with diabatic states

$$\vec{\mu}_{nm} = \langle\Phi_n|\vec{\mu}|\Phi_m\rangle \qquad (18)$$

and $\vec{E}(t)$ is the external electric field. Since the electronic basis functions $|\Phi_n\rangle$, $|\Phi_m\rangle$, are diabatic, $\vec{\mu}_{nm}$ is a slowly varying function of the nuclear

coordinates and can thus be expanded in a rapidly converging Taylor series

$$\vec{\mu}_{nm}(\mathbf{Q}) = \vec{\mu}_{nm}(0) + \sum_i \left(\frac{\partial \vec{\mu}_{nm}}{\partial Q_i} \right)_0 Q_i + \cdots . \tag{19}$$

It should be stressed that for multidimensional curve crossing problems the low-order Taylor expansions (8), (9) and (19) are justified only in the diabatic electronic representation. In the adiabatic representation, curve crossings generally lead to rapid variations of potential-energy functions and transition dipole moments, rendering a low-order Taylor expansion of these functions in terms of nuclear coordinates meaningless.

Model Hamiltonians constructed according to Eqs. (13)–(15) are particularly well suited for the calculation of low-resolution absorption spectra, photoelectron spectra and resonance-Raman spectra of polyatomic molecules. As is well known,[17–19] these spectra are largely determined by the short-time dynamics in the excited state, which in turn is governed by the shape of the PE functions within the so-called Franck–Condon zone of the optical transition. In this limited range of nuclear geometries, the multidimensional PE functions are generally well approximated by the Taylor expansions of Eqs. (8) and (9).

2.2. *Specific Models*

The presumably most widely known example of vibronic coupling is the Jahn–Teller effect of a doubly degenerate electronic state, that is, the coupling of the two components of the degenerate state by a doubly degenerate vibrational mode.[1–3,8–11] The symmetry selection rule for this type of vibronic coupling, the so-called $E \times E$ Jahn–Teller effect, is[20]

$$(E)^2 \supset E \tag{20}$$

i.e. the symmetrized product of the E representation has to contain the E representation itself. This condition is fulfilled in point groups with at least one three-fold symmetry axis.[20]

The $E \times E$ Jahn–Teller model comprises two diabatic electronic states (the two components of the degenerate electronic state) and two vibrational degrees of freedom (the two components of the degenerate vibrational mode), which transform as x and y under three-fold rotations. It is convenient to introduce complex electronic basis states and complex vibrational

coordinates

$$|\Phi_{\pm}\rangle = \frac{1}{\sqrt{2}}(|\Phi_x\rangle \pm i|\Phi_y\rangle) \tag{21}$$

$$Q_{\pm} = Q_x \pm iQ_y = \rho e^{\pm i\varphi} \tag{22}$$

The $E \times E$ Jahn–Teller Hamiltonian then takes the well-known form[1–3]

$$H = |\Phi_+\rangle h_0 \langle\Phi_+| + |\Phi_-\rangle h_0 \langle\Phi_-| + \{|\Phi_+\rangle \left(\kappa\rho e^{i\varphi} - \frac{1}{2}g\rho^2 e^{-2i\varphi}\right) \langle\Phi_-| + h.c.\}. \tag{23}$$

Here

$$h_0 = -\frac{\hbar\omega}{2\rho^2}\left(\rho\frac{\partial}{\partial\rho}\rho\frac{\partial}{\partial\rho} + \frac{\partial^2}{\partial\varphi^2}\right) + \frac{1}{2}\hbar\omega\rho^2 \tag{24}$$

is the Hamiltonian of the two-dimensional isotropic harmonic oscillator, and κ and g are the linear and quadratic Jahn–Teller coupling constants, respectively.

The adiabatic potential-energy surfaces are obtained by diagonalizing the Hamiltonian (23) in the fixed-nuclei limit ($T_N = 0$). For vanishing quadratic coupling ($g = 0$), this yields

$$V_{\pm} = \frac{1}{2}\hbar\omega\rho^2 \pm \kappa\rho. \tag{25}$$

The potentials (25), often referred to as "mexican hat", represent the prototype of a conical intersection. The azimuthal symmetry of the adiabatic potentials reflects the existence of a constant of motion of the linear Jahn–Teller problem, the so-called vibronic angular momentum[1,2]

$$J = \hbar\left(-\frac{1}{2} + \frac{1}{i}\frac{\partial}{\partial\varphi}\right)|\Phi_+\rangle\langle\Phi_+| + \hbar\left(\frac{1}{2} + \frac{1}{i}\frac{\partial}{\partial\varphi}\right)|\Phi_-\rangle\langle\Phi_-| \tag{26}$$

which commutes with H of Eq. (23).

For nonvanishing quadratic Jahn–Teller coupling, the adiabatic potentials $V_{\pm}$ exhibit the threefold symmetry of the point group. The lower sheet, in particular, exhibits three equivalent local minima which are separated by three equivalent saddle points.[1–3]

The seemingly simple $E \times E$ Jahn–Teller model exhibits a surprisingly rich variety of dynamical phenomena. The Hamiltonian (23) and its eigenvalues and eigenfunctions have been discussed in several comprehensive reviews and monographs.[1–3,8–12] The richness of dynamical phenomena

arises from the presence of both strong non-Born–Oppenheimer coupling (the derivative couplings diverge at the point of intersection of the adiabatic energy surfaces) as well as strong anharmonic distortions of the adiabatic potential surfaces.

Most systems exhibiting the Jahn–Teller effect possess more than one degenerate vibrational mode (the exception are triatomic systems, such as H_3, Li_3, etc.). The Hamiltonian is then given by

$$H = \sum_j H_j \tag{27}$$

where each H_j describes Jahn–Teller coupling by a degenerate mode according to Eq. (23). It is important to realize that the H_j, acting in a two-dimensional electronic Hilbert space, do not commute with each other. The multi-mode Jahn–Teller effect is thus a nontrivial extension of the single-mode $E \times E$ Jahn–Teller effect. The dynamics of two-mode or few-mode Jahn–Teller systems has been analyzed, for example, in Refs. 5, 21 and 22. It has been found that strong Jahn–Teller activity of several modes leads to particularly strong inter-mode energy transfer and irreversible electronic decay dynamics on ultrafast time scales.[5,12,23,24] These aspects are discussed in more detail in Chapter 10.

In systems with triply degenerate states, both doubly as well as triply degenerate modes are generally Jahn–Teller active, resulting in the $T \times T$, $T \times E$ or, more generally, the $T \times (T + E)$ Jahn–Teller effects. For a discussion of the corresponding Hamiltonians and their energy-level spectra we refer to the literature.[1−3,8−11]

Another vibronic-coupling phenomenon which is frequently encountered in highly symmetric polyatomic molecules is the interaction of a doubly degenerate electronic state with a nearby nondegenerate electronic state via a degenerate vibrational mode, usually referred to as pseudo-Jahn–Teller coupling. The electronic Hilbert space of the pseudo-Jahn–Teller problem is three-dimensional (given by the two components of the degenerate state as well as the nondegenerate state). The corresponding vibronic-coupling Hamiltonian can be set up in the same manner as in the $E \times E$ Jahn–Teller case.[5,25,26] Again, the Hamiltonians referring to different pseudo-Jahn–Teller-active vibrational modes do not commute. The multi-mode pseudo-Jahn–Teller effect is therefore a nontrivial generalization of the single-mode case.[23,24] In Chapter 10 the vibronic dynamics of the benzene cation will be

discussed as an example of combined multi-mode Jahn–Teller and pseudo-Jahn–Teller effects.

According to the Jahn–Teller theorem,[20] linear polyatomic molecules in degenerate electronic states (Π, Δ, etc.) do not exhibit the first-order coupling which applies for nonlinear molecules in degenerate electronic states. The coupling of the components of a Π electronic state via the degenerate bending mode occurs in second order of the bending normal mode and is referred to as the Renner effect.[27–29] The vibronic coupling of a degenerate (Π) with a nearby nondegenerate (Σ) electronic state, however, occurs in first order of the bending displacement.[30,31] The $(\Pi+\Sigma)\times\Pi$ vibronic problem is in fact isomorphic to the $(E+A)\times E$ pseudo-Jahn–Teller problem.[5]

So far we have considered systems with relatively high symmetry at the reference geometry (usually the equilibrium geometry of the closed-shell electronic ground state), such that there exist degenerate electronic states and degenerate vibrational modes. The degeneracy in these cases is a consequence of the molecular symmetry. High symmetry is not a prerequisite, however, for conical intersections of adiabatic PE surfaces to occur. There are now well-documented examples of conical intersections which are not due to the existence of a symmetry operation, see Chapter 2.

The most frequently encountered type of conical intersection is partly induced by symmetry in the following sense. Let us consider a molecular system that possesses at least one nontrivial symmetry element, e.g. a plane of reflection (C_s point group), and thus at least two irreducible representations (A' and A'' in the case of the C_s point group). Consider two electronic states transforming according to different irreducible representations. In this case, the Hamiltonian (13) takes the form

$$\begin{aligned} H = h_0 &+ |\Phi_1\rangle \left(E_1 + \sum_{i=1}^{N_t} \kappa_i^{(1)} Q_i \right) \langle \Phi_1| + |\Phi_2 \left(E_2 + \sum_{i=1}^{N_t} \kappa_i^{(2)} Q_i \right) \langle \Phi_2| \\ &+ \{ |\Phi_1\rangle \left(\sum_{j=1}^{N_c} \lambda_j Q_j \right) \langle \Phi_2| + \text{h.c.} \} \end{aligned} \tag{28}$$

$$h_0 = \frac{\hbar}{2} \sum_{i=1}^{N_t} (-\omega_i \partial^2 / \partial Q_i^2 + \omega_i Q_i^2) + \frac{\hbar}{2} \sum_{j=1}^{N_c} (-\omega_j \partial^2 / \partial Q_j^2 + \omega_j Q_j^2) \tag{29}$$

where we have neglected second-order electronic-vibrational couplings for simplicity. The normal coordinates $Q_i, i = 1 \ldots N_t$, are totally symmetric. Displacements in these coordinates "tune" the energy gap $|E_2 - E_1|$ of the two electronic states and generally lead to intersections of the PE functions, which are allowed by symmetry. These vibrational modes have therefore been termed "tuning modes".[5] The normal coordinates $Q_j, j = 1 \ldots N_c$, are of the symmetry species determined by the selection rule (16). They are responsible for electronic inter-state coupling and have therefore been termed "coupling modes".[5] The coupling modes lift accidental electronic degeneracies induced by the tuning modes in first order and thus convert the surface intersections in the subspace of the tuning modes into conical intersections. A well documented example of a conical intersection described by a Hamiltonian of the type (28) is provided by the $S_1(n\pi^*)$ and $S_2(\pi\pi^*)$ excited states of pyrazine, see below.

2.3. *Ab initio Determination of Electronic-Vibrational Coupling Parameters*

Modern electronic-structure theory provides all tools which are required to determine the parameters entering vibronic-coupling Hamiltonians from first principles.

We consider systems with a closed-shell electronic ground state and adopt the equilibrium geometry of the electronic ground state as the reference geometry. The equilibrium geometry and the harmonic force field in Cartesian displacement coordinates can routinely be obtained for electronic-structure models for which analytic derivatives of the energy are available, e.g. restricted Hartree–Fock (RHF) augmented by second-order Møller–Plesset perturbation theory (MP2). Geometry optimization and normal-mode analysis at the MP2 level employing basis sets of at least double-zeta-plus-polarization (DZP) quality are nowadays feasible for reasonably large polyatomic systems. Modern variants of density-functional theory appear also suitable for this purpose and will allow the treatment of even larger systems.

Let us next consider the computation of intra-state coupling constants $\kappa_i^{(n)}$, $\gamma_{ij}^{(n)}$ defined in Eqs. (10) and (12) as first and second derivatives of the excitation energy with respect to ground-state normal coordinates.

For this purpose an electronic-structure model is required which accurately describes excited electronic states. The most widely applicable zeroth-order model for excited electronic states is provided by the complete-active-space self-consistent-field (CASSCF) method.[32] The CASSCF method is able to provide a balanced description of several excited states and fully accounts for quasi-degeneracy effects. The dynamical correlation energy, which is neglected in the CASSCF approximation, can be taken into account by a multi-reference configuration-interaction (MRCI) calculation[33] or by many-body perturbation theory based on the CASSCF reference.[34] Alternative electronic-structure models which have been found useful for excited states and ionized states are the equation-of-motion coupled-cluster (EOMCC)[35] and many-body Green's function (MBGF)[36] methods, respectively. It should be noted that the computation of the $\kappa_i^{(n)}$, $\gamma_{ij}^{(n)}$, being defined as derivatives of the energy at a single geometry, is a much simpler task than a geometry optimization of the excited state.

The computation of the inter-state coupling constants $\lambda_j^{(nn')}$, being defined as first derivatives of off-diagonal elements of the electronic Hamiltonian in the diabatic representation (see Eq. (11)), appears at first sight to be more difficult. It can be shown, however, by analyzing the adiabatic PE functions associated with the vibronic-coupling Hamiltonian (13) that the $\lambda_j^{(nn')}$ can be determined from second derivatives of the adiabatic energies with respect to the nontotally symmetric coordinate Q_j. For an electronic two-state system, the following simple formula results[5]

$$\lambda_j^{(1,2)} = \left[\frac{1}{8} \frac{\partial^2}{\partial Q_j^2} |V_1(\mathbf{Q}) - V_2(\mathbf{Q})|^2 \right]_0^{1/2} . \tag{30}$$

A reliable electronic-structure model which provides a balanced description of the electronic states of interest is required for the computation of inter-state vibronic coupling constants. In particular, artifactual symmetry-breaking effects in the electronic wave function[37] should be avoided. For excited electronic states, a CASSCF/MRCI description with appropriately chosen active space is generally to be recommended. For ionized states, the OVGF method,[36] the ADC(3) method[38] or the EOM-CC method[35] have been found to be appropriate tools.

3. Multi-Mode Vibronic Dynamics

In this section we consider various observables associated with Hamiltonians of the type of Eqs. (13)–(15) and discuss methods for their numerical determination. These quantities are useful in characterizing the system dynamics and making contact with experiment. Both time-independent and time-dependent aspects are addressed in turn.

3.1. *Time-Independent Approach*

3.1.1. *Vibronic Eigenvalue Problem and Spectra*

In the time-independent approach, the object of primary importance is the spectral intensity distribution for an electronic transition into the vibronically interacting manifold. According to Fermi's golden rule it can be written as

$$P(E) = \frac{2\pi}{\hbar} \sum_{\nu} |\langle \Psi_i | \hat{T} | \Psi_\nu \rangle|^2 \delta(E - E_\nu + E_i). \tag{31}$$

Here $\hat{T}$ denotes the transition operator and E the energy transferred to the system (e.g. the photon energy in optical absorption). The initial state $|\Psi_i\rangle$ (with energy E_i) can, but need not, belong to the set $|\Psi_\nu\rangle$ of vibronic states (with energies E_ν) which constitute the set of final states given by the solutions of the vibronic Hamiltonian. In the applications to be discussed below, $|\Psi_i\rangle$ will be the zero vibrational level of the electronic ground state which is assumed to be vibronically uncoupled from the excited states.

By making use of a well-known integral representation of the Dirac delta-function $\delta(x)$ appearing in Eq. (31), this equation can be rewritten in the following compact form

$$P(E) = \int \mathrm{d}t e^{i(E+E_i)t/\hbar} \langle \Psi_i | \hat{T} e^{-iHt/\hbar} \hat{T}^\dagger | \Psi_i \rangle. \tag{32}$$

Equation (32) does not exhibit explicitly the final states and energies, but rather is expressed in terms of the pertinent vibronic Hamiltonian H of Sec. 2. Through the Fourier integral it is related to the time-dependent approach of Sec. 3.2. Its use has been advocated especially by Heller and coworkers who demonstrated its efficiency when combined, e.g. with the Gaussian wavepacket approach.[17]

The spectrum, Eq. (31), can be computed immediately once the eigenvalue problem of the vibronic Hamiltonian H has been solved. Except for

special cases, the latter task requires numerical techniques. To this end the state vector is expanded in a direct-product basis of suitable harmonic-oscillator wavefunctions

$$|\Psi_\nu\rangle = \sum_{i,n_1,n_2,\ldots,n_k} a^{(\nu)}_{i,n_1,n_2,\ldots,n_k} |\Phi_i\rangle |n_1\rangle |n_2\rangle \cdots |n_k\rangle. \tag{33}$$

Here the subscripts $1 \ldots k$ characterize the relevant set of vibrational modes appearing in the Hamiltonian, Eq. (13), and the expansion coefficients $a^{(\nu)}_{i,n_1,n_2\ldots n_k}$ are to be determined numerically. For each mode I the choice of the basis functions $\{|n_I\rangle\}$ is, in principle, free (as far as equilibrium position and frequency, for example, are concerned). However, it is usually advantageous to choose the eigenfunctions of the unperturbed Hamiltonian h_0 of Eq. (15) as basis functions. Although other alternatives may lead to a more compact expansion, requiring less basis functions in Eq. (33), this choice offers a significant computational advantage.

When the eigenfunctions of h_0 are taken as basis functions, the vibronic secular matrix is highly sparse, i.e. most of the matrix elements are zero. The degree of sparsity increases with the number of modes considered. For f vibrational modes, and with typically n basis functions per mode, the fraction R of non-zero entries per row or column is

$$R \approx (2f+1)n^{-f}. \tag{34}$$

In addition, the non-zero elements follow a simple pattern, both by position in the matrix and by value. This behaviour has been termed "structured sparsity"[39] and greatly facilitates the computations. It is a direct consequence of the concept of the low-order Taylor expansion introduced in Sec. 2 and becomes particularly pronounced for its simplest variant, the linear vibronic-coupling scheme, cf. Eq. (28).

Despite these simplifications, the solution of the *full* eigenvalue problem

$$\sum_m (H_{nm} - E_\nu \delta_{nm}) a^{(\nu)}_m = 0 \tag{35}$$

often represents a formidable numerical task. For typical parameter values, 10–30 basis functions per mode are needed to obtain converged results, leading to 10^6–10^9 basis functions for vibronic systems with 5 or 6 vibrational modes. The computation of all eigenvalues and eigenvector components would be hopelessly time-consuming on present-day computers. Fortunately, two essential simplifications arise when calculating the spectral

intensity profile, Eq. (31). First, only those eigenstates are relevant which enter with a notable spectral intensity

$$I_\nu = |\langle \Psi_i | \hat{T} | \Psi_v \rangle|^2. \tag{36}$$

In practice, this may be only a small fraction of all eigenstates, especially in multi-mode problems. Secondly, the I_ν may be calculated directly, without computing all eigenvector components in Eq. (33), see below. Moreover, if there are many dense-lying eigenvalues in a certain energy interval, not all individual states may be of interest but only a smoothed spectral envelope

$$P_\delta(E) = P(E) \otimes L_\delta(E) \tag{37}$$

where "$\otimes$" denotes convolution and $L_\delta(E)$ stands, e.g. for a Lorentzian of suitable width δ. There exists a computational tool nearly ideally suited to deal with this situation, the Lanczos algorithm.[4] With this algorithm, described in the next subsection, the structured sparsity of the Hamiltonian matrix can be fully exploited.

3.1.2. *Lanczos Algorithm*

Consider some initial state $|p_0\rangle$ and define the state vector $|p_1\rangle$ by the relations

$$\begin{aligned} |q_1\rangle &= H|p_0\rangle - \langle p_0|H|p_0\rangle |p_0\rangle \\ |p_1\rangle &= q_1 / \sqrt{\langle q_1 | q_1 \rangle}. \end{aligned} \tag{38}$$

Here H may be any hermitean operator of interest, but in our case is identified with the vibronic Hamiltonian. Given these states, one may start the following three-term recurrence relations, also called Lanczos iteration[4,40]

$$\begin{aligned} |q_{i+1}\rangle &= H|p_i\rangle - \langle p_i|H|p_i\rangle - \sqrt{\langle q_i | q_i \rangle} |p_{i-1}\rangle \\ |p_{i+1}\rangle &= |q_{i+1}\rangle / \sqrt{\langle q_{i+1} | q_{i+1} \rangle}. \end{aligned} \tag{39}$$

This generates a sequence of states $|p_0\rangle$, $|p_1\rangle$, $|p_2\rangle, \ldots$ spanning the so-called Krylov subspace of H.

Straightforward algebra shows that these states are orthonormal. The matrix elements T_{ij} of the Hamiltonian read

$$\begin{aligned} T_{ii} &= \langle p_i|H|p_i\rangle \\ T_{i,i+1} &= T_{i+1,i} = \sqrt{\langle q_{i+1}|q_{i+1}\rangle} \\ T_{i,j} &= 0 \qquad \text{for } |i-j|>1. \end{aligned} \tag{40}$$

This means that in this new basis the Hamiltonian takes the form of a tridiagonal matrix. The matrix elements are generated automatically during the recursion process, Eq. (39).

For our purposes we identify

$$|p_0\rangle = \hat{T}^\dagger|\Psi_i\rangle \tag{41}$$

and use the basis-set expansion (33) to represent the Kylov subspace as the sequence of (column) vectors $\mathbf{p}_0$, $\mathbf{p}_1$, $\mathbf{p}_2 \ldots$. Likewise, the coefficients $a_m^{(\nu)}$ are combined into a column vector $\mathbf{a}^{(\nu)}$. With Eq. (40) we have

$$\begin{aligned} \mathbf{P}_m^\dagger \mathbf{H} \mathbf{P}_m &= \mathbf{T}^{(m)} \\ \mathbf{P}_m &= (\mathbf{p_0}, \mathbf{p_1}, \ldots, \mathbf{p}_m) \end{aligned} \tag{42}$$

where $\mathbf{T}^{(m)}$ denotes the $m\times m$ tridiagonal matrix with elements, Eq. (40), resulting from performing m Lanczos iterations according to Eqs. (38) and (39). Let $\mathbf{x}_\nu^{(m)}$be the eigenvector of $\mathbf{T}^{(m)}$ with eigenvalue $E_\nu^{(m)}$. Then $\mathbf{P}_m\mathbf{x}_\nu^{(m)}$represents the corresponding eigenstate of the original Hamiltonian and its spectral intensity becomes

$$\begin{aligned} I_\nu^{(m)} &= |\mathbf{p}_0^\dagger \mathbf{P}_m \mathbf{x}_\nu^{(m)}|^2 \\ &= \mathbf{p}_0^\dagger(\mathbf{p}_0, \mathbf{p}_1, \ldots, \mathbf{p}_m)\mathbf{x}_\nu^{(m)}|^2 \\ &= |(1,0,0,\ldots,0)\mathbf{x}_\nu^{(m)}|^2 \\ &= |x_\nu^{(m)}(1)|^2. \end{aligned} \tag{43}$$

Owing to the orthogonality of the $\mathbf{p}_i$, and by virtue of the choice of $|p_0\rangle$, Eq. (41), it is only the *first* component $x_\nu^{(m)}(1)$ of the eigenvectors of the tridiagonal matrix that determines the spectral intensity.[41] This result is very relevant, since with standard algorithms the various eigenvector components of tridiagonal matrices are computed *separately*.[42] Thus, by simple modifications of existing library routines, the required information can be obtained with negligible additional effort as compared to eigenvalue-only calculations.

Summarizing, the calculation of the spectrum (31) with the aid of the Lanczos algorithm proceeds in three steps.

(i) Select a basis-set representation, Eq. (36), and perform a suitable number m of Lanczos iteration steps (38) and (39) with the initial state, Eq. (41). Only matrix-vector multiplications are to be performed. Therefore, the secular matrix need not be built explicitly, and its structured sparsity can be exploited efficiently in the vector-update routine. Nevertheless, this is the most time-consuming step.
(ii) Diagonalize the resulting tridiagonal matrix $\mathbf{T}^{(m)}$ and obtain the first eigenvector components along with the eigenvalues.
(iii) Take these energies and the residues according to Eq. (43) to obtain the vibronic line spectrum. If desired, compute the spectral envelope according to Eq. (37).

The approximate nature of the solutions of $\mathbf{T}^{(m)}$ deserves further comments. If the number m of Lanczos iteration steps is equal to the dimension M of the secular matrix and if exact arithmetic is assumed, then the matrix $\mathbf{P}_M$, Eq. (42), is orthogonal. At the $(M+1)$th step the iteration terminates. In finite precision, this turns out to be not the case, due to a global loss of orthogonality of the vectors $\mathbf{p}_m$.[4] This numerical instability has prevented the use of the Lanczos algorithm for a long time. Later it was recognized that the Lanczos algorithm nevertheless converges to the correct solutions, starting at the edges of the spectrum.[4,43] Here, convergence is achieved even for a small number of iterations, $m \ll M$. There exist also criteria for distinguishing correct from spurious eigenvalues.[4] Even more important for our purposes, the spectral envelope (for moderate resolution) converges rapidly ($m \ll M$), even though dense-lying eigenvalues are not converged individually.[44] The latter fact can be attributed to the close relationship between the Lanczos procedure and the method of moments.[45,46]

In the applications, we are interested in individual eigenstates mostly in the low-energy part of the spectrum, while for higher energies it is more the spectral envelope that matters. For both of these pieces of information, the Lanczos algorithm converges particularly fast. In representative applications typically 10^3–10^4 Lanczos steps are found to be sufficient, even though the dimension of the secular matrix may be 10^8 or more.

The first application of the Lanczos procedure to quantum molecular dynamics appears to have been a study on the $T \times T$ Jahn–Teller effect.[47]

Shortly later, it has been used by O'Brian and coworkers and by the Heidelberg group for the $E \times E$ Jahn–Teller effect[48,49] and related multimode systems.[50,51] Of course, the advantages of the method are related to the multimode nature of the system and can likewise be exploited for single-surface problems. The latter type of applications has been advocated especially by Wyatt and coworkers,[52] who called the method recursive-residue-generation method (RRGM). In their early work, the tridiagonal matrix was diagonalized twice (the second time without the first row and column), and the information on the residues has been extracted from the comparison of eigenvalues. We have shown above (and have made use of this fact since a long time) that the second diagonalization can actually be avoided and the residues be computed with negligible additional effort.

3.2. *Time-Dependent Approach*

Additional insight into the vibronic dynamics can be achieved by performing time-dependent calculations. The latter allow for a more direct visualization of the coupled electronic and nuclear motions. Moreover, given only the spectrum, Eq. (31), or a small number of resonance Raman amplitudes, the information obtained from the time-dependent wavefunction differs also in principle from that of stationary spectra.

3.2.1. *Observables of the Time-Dependent Dynamics*

Let us consider the time evolution of an initial wavepacket $\Psi(0) \equiv \Psi(t = 0)$ created by optical excitation out of an initial state Ψ_i. With the transition operator $\hat{T}$ as in Eqs. (31) and (32) we have

$$|\Psi(0)\rangle = \hat{T}^{\dagger}|\Psi_i\rangle \tag{44}$$

i.e. the same initial state as in Eq. (41) for the Lanczos iteration scheme. Equation (44) corresponds, for example, to optical excitation by an ideally short laser pulse.[6] If the dependence of the electronic matrix elements of $\hat{T}$ on the nuclear coordinates is negligible, this amounts to vertically lifting the nuclear wavefunction of the electronic ground state to the excited-state PE surface. In practice, the initial state will be the zero vibrational level of the electronic-ground state potential surface. The latter is usually vibronically uncoupled from the excited state manifold and taken to be described

in the harmonic approximation. Then $|\Psi(0)\rangle$ is simply a product of Gaussians (with appropriate widths) centred at the ground-state equilibrium geometry.

Evolving under the influence of the vibronic Hamiltonian H, the time-dependent wavepacket $|\Psi(t)\rangle$ will change in position, shape and electronic composition. A generally used, though necessarily incomplete, measure of these changes is provided by the so-called autocorrelation function (see, for example, Refs. 53 and 54)

$$\Phi(t) = \langle\Psi(0)|\Psi(t)\rangle = \langle\Psi(0)|e^{-iHt/h}|\Psi(0)\rangle. \tag{45}$$

By definition, $\Phi(t)$ represents the probability amplitude that, after a finite evolution time t, the system is still in the same state as at time $t = 0$. Referring back to Eq. (32), we see that $\Phi(t)$ and the spectral intensity distribution $P(E)$ are related by Fourier transformation and thus contain the same information on the system dynamics. The square $|\Phi(t)|^2$ is also known as survival probability and provides a measure of nonradiative decay processes occurring on picosecond or nanosecond time scales.[53,54]

To proceed, we note that the initial state $|\Psi(0)\rangle$ usually represents a coherent state on the excited-state potential surface (because of the assumed broadband excitation). Moreover, as emphasized in Sec. 2 above, the strong nonadiabatic coupling effects at conical intersections may lead to a pronounced mixing of vibrational levels of the upper and lower of the intersecting surfaces. For these reasons, it is appropriate to introduce the overall *electronic population* $P_i(t)$ (of electronic state i) as a direct and natural measure of the internal-conversion dynamics on strongly coupled surfaces.[5,6] The population of electronic state $|\Phi_i\rangle$ is defined as the expectation value of the projection operator

$$\hat{P}_t^d = |\Phi_i^d\rangle\langle\Phi_i^d| \tag{46}$$

with the full time-dependent wavefunction $|\Psi(t)\rangle$, i.e.

$$\hat{P}_t^d(t) = \langle\Psi(t)|\hat{P}_t^d|\Psi(t)\rangle. \tag{47}$$

In Eq. (46) the diabatic electronic representation has been employed. Of course, adiabatic electronic populations $P_t^a(t)$ may be defined in a completely analogous manner. These electronic population probabilities and their behavior for typical conical intersection models are further discussed in Chapter 9.

Owing to the strong coupling of electronic and nuclear motions, the vibrational dynamics also exhibits nontrivial features at conical intersections. Observables which directly reflect the nuclear motion are, for example, the expection values of the position and momentum operators of individual normal modes[55]

$$Q_i(t) = \langle \Psi(t) | \hat{Q}_i | \Psi(t) \rangle \tag{48}$$

$$P_i(t) = \langle \Psi(t) | \hat{P}_i | \Psi(t) \rangle. \tag{49}$$

In the absence of vibronic coupling, $Q_i(t)$ and $P_i(t)$ are simply periodic functions of time for the harmonic diabatic potentials of Eq. (8). The vibronic coupling introduces an effective damping of the vibrational amplitudes and a noisy behaviour of the mean values for longer times, in a very similar way as already mentioned for the electronic populations.[55] The vibrational dephasing process is accompanied by a drastic broadening of the wavepacket, so that the significance of the "trajectories" $Q_i(t)$ should not be overinterpreted for longer times. These aspects are discussed in more detail in Chapter 9.

3.2.2. *Integration of the Time-Dependent Schrödinger Equation*

In the above discussion we have tacitly assumed that the full time-dependent state vector $|\Psi(t)\rangle$ is known. As in the case of the spectrum, this in general requires numerical techniques. To this end we introduce a basis-set expansion similar to Eq. (33)

$$|\Psi(t)\rangle = \sum_{i,n_1,\ldots,n_k} a_{i,n_1,\ldots,n_k}(t) |\Phi_i\rangle |n_1\rangle \cdots |n_k\rangle \tag{50}$$

with time-dependent expansion coefficients $a_{i,n_1,\ldots,n_k}(t)$. Inserting Eq. (50) into the time-dependent Schrödinger equation

$$i\hbar \partial/\partial t |\Psi(t)\rangle = H |\Psi(t)\rangle \tag{51}$$

immediately leads to the following set of coupled first-order differential equations

$$i\hbar \dot{\mathbf{a}}(t) = \mathbf{H}\mathbf{a}(t). \tag{52}$$

Here the dot denotes differentiation with respect to time, $\mathbf{a}(t)$ stands for the vector of expansion coefficients $a_{i,n_1,\ldots,n_k}(t)$, and $\mathbf{H}$ represents the Hamiltonian matrix.

Equation (52) can be solved with various integration schemes which are available in the literature and have increasingly been employed for chemical dynamics problems in the last decade. In general, there are no specific aspects in this task related to inter-surface coupling. Therefore, we confine ourselves to a very brief discussion of several relevant integration techniques and our computational experiences with some of them.

We may distinguish between all-purpose integrators suitable also for nonlinear differential equations and for time-dependent Hamiltonians and others, specifically designed for time-independent Hamiltonians with the formal solution

$$\mathbf{a}(t) = \exp(-iHt/\hbar)\mathbf{a}(0). \tag{53}$$

Prominent representatives of the first class are predictor-corrector schemes,[56] the Runge–Kutta method,[7] and the Bulirsch–Stoer method.[57] Among the more specific integrators we mention, apart from the simple Taylor-series expansion of the exponential in Eq. (53), the Cayley (or Crank–Nicholson) scheme,[58] finite differencing techniques, especially those of second or fourth order (SOD and FOD, respectively),[59–61] the split-operator method[62] and, in particular, the Chebychev[63] and the short-time iterative Lanczos (SIL)[64] integrators. Some of these latter integration schemes are norm-conserving (namely Cayley, split-operator and SIL) and thus accumulate only phase errors; the SOD and FOD integrators are conditionally stable (i.e. up to a maximum time step), while the Taylor series and Chebychev integrators are unstable.

Besides stability, accuracy is the other important criterion characterizing an integration scheme. Here, the Chebychev integrator is unique because of the high order of the polynomial approximation achieved, which also overcomes the aforementioned stability problems.[63] On the other hand, if the time-dependent wavefunction $|\Psi(t)\rangle$ is needed for many intermediate times, and if very high accuracy is not important, usually the SIL method is recommended in the literature.[65]

In our early work on multimode vibronic dynamics, a fourth-order predictor-corrector method[56] has been used to integrate the time-dependent Schrödinger equation. Later, FOD schemes[61] and a fourth-order Runge–Kutta method[66] have also been employed. These techniques proved to be superior to the predictor-corrector method; for example, the FOD scheme was found to be ∼3–5 times faster than the SOD integrator[61] (the latter

being at least as efficient as the predictor-corrector method). More recently, the SIL scheme has been successfully implemented[67,68] for vibronic problems, exceeding in turn the FOD integrator by a factor of ∼3 in speed. In many of these latter implementations a variable time step size has been provided to achieve a predefined accuracy of the wavefunction.[66,67]

All the applications mentioned in the preceding paragraph have dealt with propagation with time-independent, purely intramolecular Hamiltonians. Many of these integration schemes can also be used with time-dependent Hamiltonians, provided the time step is chosen sufficiently small. This will generally reduce the efficiency of higher-order and sophisticated techniques more than that of simpler schemes, which require a small time step from the outset. In our work with externally driven vibronic-coupling systems, we found the Runge–Kutta method and the Bulirsch–Stoer method with judicious step-size control particularly efficient and reliable.[69−71]

To conclude this section, we mention another class of integrators, called symplectic, which have gained increasing interest quite recently.[72,73] These rely on the formal equivalence between the time-dependent Schrödinger equation and the classical Hamilton equations of motion for the real and imaginary parts of the components of the state vector.[74] By this analogy, symplectic integrators for the solution of the classical equations of motion can be transferred to the quantal problem. Modifications have been proposed to tailor them for this latter use.[75] Symplectic integrators combine an efficiency similar to the SIL method with minimal storage requirements (only two (complex) state vectors need be kept in memory). This experience by Gray *et al.*[75] is confirmed by first results on vibronically coupled systems.[24] It makes symplectic integrators a very attractive tool for multimode vibronic-coupling problems, since often many basis functions are needed in the expansion, Eq. (50), and storage limitations may be a crucial aspect.

The expansion (50) of the time-dependent state vector in terms of time-independent basis functions becomes impractical for vibronic-coupling problems with more than about 7 vibrational modes, especially if one or several modes possess large coupling parameters or if the excess energy is very large. For such more demanding applications the MCTDH scheme, which is based on an expansion of the time-dependent state vector in terms of variationally determined time-dependent basis functions,[76] has proven

to be a powerful tool. The application of the MCTDH method to vibronic-coupling problems is described in detail in Chapter 14.

4. Representative Applications

The spectroscopy and photophysical dynamics of numerous systems exhibiting conical intersections have been treated within the multi-mode vibronic-coupling approach, see[5,6,77,78] for reviews. The first investigations of the dynamics and spectroscopy of non-symmetry-induced conical intersections (that is, conical intersections which are not of the Jahn–Teller type) have been performed by the Heidelberg group for certain polyatomic cations, employing the linear vibronic-coupling formalism with *ab initio* determined vibronic coupling constants.[50,79–81] Multi-mode vibronic-coupling systems involving degenerate vibrational modes (Jahn–Teller and pseudo-Jahn–Teller effects) are discussed in Chapter 10. Aspects of the photophysical dynamics of conical intersections are analyzed in some detail in Chapters 9 and 14. We limit ourselves in this chapter to a brief discussion of electronic spectra (absorption, resonance Raman and photoelectron spectra) of multi-mode vibronic-coupling systems. The techniques for the calculation of spectra are further elaborated and exemplified in Chapter 16.

As mentioned above, vibronic-coupling model Hamiltonians constructed by low-order Taylor expansions of the diabatic PE functions in terms of normal coordinates are particularly suitable for the calculation of low-resolution spectra of polyatomic molecules. In resonance Raman spectroscopy, for example, the usually extremely fast electronic dephasing in polyatomic systems limits the time scale for the exploration of the excited-state PE surface by the nuclear wave packet to about 10 fs.[17,82,83] In this limited range of nuclear geometries accessible to the wave packet, the multi-dimensional diabatic PE surfaces are generally well approximated by low-order Taylor expansions. The same argument applies for low-resolution absorption and photoelectron spectra.[18,19] For this reason, even the simplest version of the multi-mode vibronic-coupling approach, the so-called linear coupling model,[5] can be surprisingly successful in reproducing the vibronic structures of optical or photoelectron spectra associated with conical intersections which are located within or near the Franck–Condon zone of the optical transition. Moreover, the Lanczos algorithm represents a tool which is specifically tailored to the calculation of spectral band shapes.

The combination of the linear-coupling model with the Lanczos algorithm allows for an extremely efficient computation of even very complex vibronic spectra.

4.1. *Photoelectron Spectra of Triatomics:* NO_2 *and* O_3^+

The NO_2 molecule has a long-standing history as an example of a notoriously complex low-energy electronic absorption spectrum. For an overview over the large amount of work prior to 1978, see the monograph by Hsu, Monts and Zare.[84] More recent experimental work has been carried out, in particular, by Jost *et al.*, as described, e.g., in Refs. 85 and 86 and references cited therein. The low-energy absorption spectrum of NO_2 arises from the dipole-allowed transition from the $\widetilde{X}^2A_1$ ground state to the $\widetilde{A}^2B_2$ first excited electronic state. Early *ab initio* calculations[87,88] have revealed that a conical intersection between the $^2A_1$ and $^2B_2$ PE surfaces is involved. The intersection occurs at a bond angle of $\sim$105°, to be compared with the equilibrium bond angles of the $\widetilde{X}^2A_1$ state ($\sim$133°) and of the $\widetilde{A}^2B_2$ state ($\sim$101°). The intersection is located at an energy slightly above the minimum energy of the $\widetilde{A}$ state.

The data of these early *ab initio* calculations have been used to develop a PE model within the linear vibronic-coupling scheme, employing all three nonseparable nuclear degrees of freedom[5,51]. The complex line structure of the $\widetilde{X}^2A_1 - \widetilde{A}^2B_2$ absorption system could be satisfactorily reproduced and the origin of the complexity could unambiguously be traced back to the conical intersection between the $^2A_1$ and $^2B_2$ PE surfaces.[5,51] A one-by-one reproduction of spectral lines was not possible within this simple model and will be difficult to achieve even with more elaborate treatments of this system that have been developed more recently[89] (see also Chapter 16).

In view of these results, the vibrational structure of the second band of the photodetachment spectrum of NO_2^- appears surprising. The photodetachment spectrum exhibits a regular, apparently single-mode progression which has been assigned to the bending mode of $NO_2(\widetilde{A}^2B_2)$.[90] It is an important difference to the visible absorption spectrum mentioned above that the equilibrium geometry of NO_2^- corresponds to a bond angle of $\sim$117° which is between that of the $\widetilde{A}$ state of NO_2 and the $\widetilde{X}$ state of NO_2. Therefore, the photodetachment process probes the level structure of the $^2B_2$ state closer to its energetic minimum than the $\widetilde{X} - \widetilde{A}$ absorption process.

A comparison between the measured[90] and calculated[91] second band of the photodetachment spectrum of NO_2^- is shown in Fig. 1. The theoretical line spectrum has been generated by employing the linear vibronic-coupling model with parameters determined by *ab initio* calculations which are more accurate than those previously available.[91] Subsequently, the line spectrum has been convoluted with Lorentzians of suitable width to account for the finite experimental resolution and thermal line broadening effects. The experimental spectral envelope is seen to be very well reproduced by the theory. The theory predicts, moreover, a sub-structure of vibronic lines under most of the peaks of the spectral envelope, which could not be resolved experimentally.

The vibronic sub-structure shown in Fig. 1 is an important result and reflects the coupling between the $\widetilde{A}^2B_2$ and $\widetilde{X}^2A_1$ vibrational levels caused

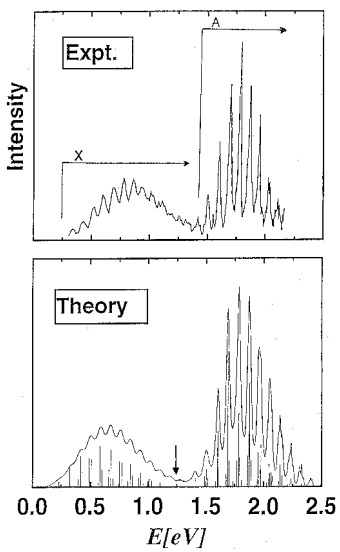

Fig. 1. Comparison of experimental[90] and theoretical[91] photodetachment spectra of NO_2^-. The zero of the energy scale corresponds to the minimum of the $\widetilde{X}^2A_1$ potential energy surface of NO_2. Only the higher-energy band corresponding to the $\widetilde{A}^2B_2$ state of NO_2, is discussed in the text. The theoretical line spectrum has been convoluted by Lorentzians of an energy-dependent width of 8–14 meV HWHM to account for finite instrumental resolution and rotational broadening. The arrow in the theoretical spectrum indicates the minimum energy of the seam of conical intersection.

by the conical intersection. The coupling is relatively weak, which causes the vibronic levels to form "clumps" of lines, each clump being associated with a single zero-order bending vibrational level of the $\widetilde{A}^2B_2$ state. Compared to the earlier calculation of the visible absorption spectrum, the coupling constant λ is substantially smaller (0.087 eV rather than 0.28 eV). This reduction can be traced primarily to the new and more accurate *ab initio* calculations underlying the simulation of the photodetachment spectrum. In addition, also the different probing of the conical intersection may play a role: due to the smaller equilibrium bond angle of NO_2^- mentioned above, the seam of intersection is probed closer to its energetic minimum by the photodetachment process than in the case of the absorption spectrum.[90,92] As more accurate calculations confirm, the vibronic coupling constant is indeed varying substantially along the seam.[92]

The type of vibronic coupling effects displayed in Fig. 1 is unusually weak for conically intersecting PE surfaces. A more generic scenario emerges when we consider the isoelectronic system O_3^+ which is also characterized by an $\widetilde{X}^2A_1$ ground and $\widetilde{A}^2B_2$ first excited electronic state.[93]. The equilibrium bond angles of these two states are $\sim$130° and $\sim$105°, respectively, and the vertical $\widetilde{X}^2A_1$ energy gap for the photoionization process is $\sim$0.2 eV, compared to $\sim$1.1 eV for NO_2^-/NO_2.

Figure 2 shows a comparison between the experimental[94] and theoretical first band of the photoelectron spectrum of O_3 which corresponds to the transition to the interacting manifold of the $\widetilde{X}^2A_1$ and $\widetilde{A}^2B_2$ states of O_3^+.[95] In the theoretical spectrum, final states of $A_1(B_2)$ vibronic symmetries are indicated by dashed (full) lines to distinguish the different vibronic contributions. It is seen that for low vibronic energies there is a regular series of lines corresponding to the bending vibrational mode.[95] The regularity is lost for energies above $\sim$12.8 eV, where the minimum of the seam of conical intersection between the $\widetilde{X}^2A_1$ and $\widetilde{A}^2B_2$ PE surfaces occurs.[95] For these higher energies, the nonadiabatic coupling effects lead to a complete reordering of the spectral lines, resulting in an irregular spectral envelope which matches the experiment at least qualitatively quite well. Additional calculations for $\lambda = 0$ give a very regular series of lines throughout the spectral band.[95] This shows that the vibronic coupling effects are much stronger in the photoelectron spectrum of O_3 than in the photodetachment spectrum of NO_2^- (as is evidenced also by the ratio $\lambda_{O_3^+}/\lambda_{NO_2} \approx 1.4$). They are, in fact, much closer to the other examples discussed in the following.

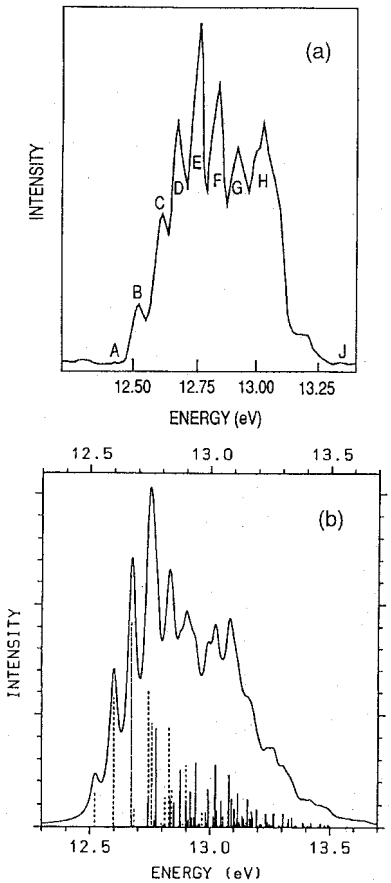

Fig. 2. (a) Experimental photoelectron spectrum of O_3 as recorded by Dyke *et al.*[94] (b) Calculated first (composite) band of the photoelectron spectrum of O_3 using *ab initio* values of the coupling parameters.[95] The linear-plus-quadratic coupling scheme and a difference of the vertical ionization potentials of 0.24 eV has been used in the computation. Final states of $A_1(B_2)$ vibronic symmetries are indicated by dashed (full) lines. The theoretical line spectrum has been convoluted with a Lorentzian of width 0.02 eV HWHM to account for finite experimental resolution.

In concluding this subsection, we mention that both systems have been treated also by more elaborate calculations beyond the linear-plus-quadratic vibronic-coupling model. The vibronic dynamics of O_3^+ has been studied using anharmonic C_{2v} PE surfaces,[95] while in case of NO_2 global

anharmonic (i.e. also for C_s nuclear conformations) PE surfaces have been employed in the vibronic calculation.[92] In the latter example, diabatic electronic states have been constructed using the concept of regularized diabatic states (see Chapter 4). For both examples the spectra obtained with the comparatively simple multi-mode vibronic-coupling approach agree rather well with those obtained with more accurate descriptions of the PE surfaces. This finding underlines the usefulness of the LVC scheme for an efficient modeling of the overall spectral features of vibronically coupled systems.

4.2. *The Photoelectron Spectrum of Allene*

Allene ($H_2C{=}C{=}CH_2$) is an interesting species as the first member of the cumulene series and as a representative of the less common point group D_{2d}. In the D_{2d} point group the degeneracy of electronic states is not lifted, as is usually the case, by degenerate modes of E symmetry, but by nondegenerate modes of B_1 and B_2 symmetry.[20] This so called $E \times B$ Jahn–Teller effect is described by the Hamiltonian of Eqs. (13)–(15), where the modes of B_2 symmetry (v_5, v_6, v_7 in allene) possess non-vanishing intra-state linear coupling constants (κ), while the modes of B_1 symmetry (v_4 in allene) possess non-vanishing inter-state linear coupling constants (λ).

It has been shown by an early vibronic-coupling model calculation[96] that the unusual band shape of the first band in the photoelectron spectrum of allene[97], corresponding to the $\widetilde{X}^2E$ state of the allene cation, can be qualitatively explained by a two-mode $E{\times}B$ Jahn–Teller effect. More recent high resolution recordings of the photoelectron spectrum of allene[98,99] have stimulated more comprehensive and accurate *ab initio* calculations of the vibronic-coupling parameters and more extensive simulations of the multi-mode dynamics.[100–102] Here we restrict ourselves to a brief discussion of the relatively simple $E \times B$ Jahn–Teller effect in the electronic ground state of $C_3H_4^+$. The more complex multi-mode Jahn–Teller and pseudo-Jahn–Teller effects of the multiply intersecting excited states of the allene cation are discussed in Chapters 10 and 14.

Ab initio calculations[100,101] have identified the torsional mode v_4 (B_1 symmetry) and the asymmetric stretching mode v_6 (B_2 symmetry) as the only active modes in the $\widetilde{X}^2E$ ground state of the allene cation. Figure 3 displays the potential energies of the $\widetilde{X}^2E$, $\widetilde{A}^2E$ and $\widetilde{B}^2B_2$ states of $C_3H_4^+$ (calculated in Koopmans' approximation[100]) as a function of these two

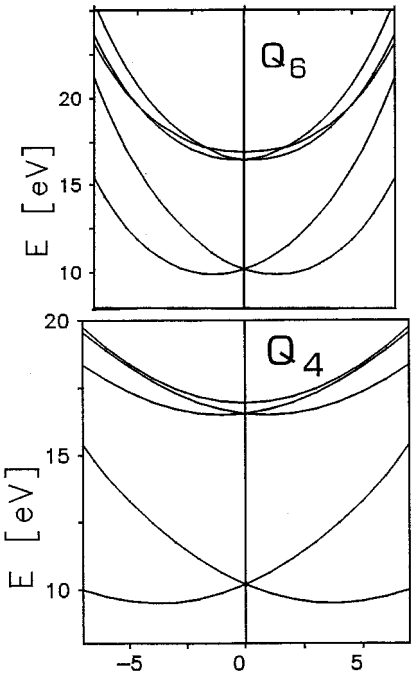

Fig. 3. Potential energies of the $\widetilde{X}^2E, \widetilde{A}^2E$ and $\widetilde{B}^2B_2$ states of the allene cation as a function of the normal coordinates Q_6 (asymmetric stretch, upper panel) and Q_4 (torsion, lower panel), calculated in Koopmans' approximation.[100]

normal modes. The lifting of the degeneracy of the $\widetilde{X}^2E$ state by distortion of the molecule along both v_4 and v_6 is clearly discernible. It is also seen that the $\widetilde{X}^2E$ state can approximately be considered as an isolated electronic state, while the $\widetilde{A}^2E$ and $\widetilde{B}^2B_2$ states are closely spaced and their PE functions exhibits crossings both along Q_4 and Q_6 as well as other normal coordinates.[100−102]

The calculated vibronic structure of the $\widetilde{X}^2E$ photoelectron band[100] is compared in Fig. 4 with the experimental recording.[98] To obtain this nearly quantitative agreement with experiment, it has been necessary to adjust the *ab initio* calculated vibronic-coupling constants and the vibrational frequencies of the cation.[100] The low-energy part of the spectrum is dominated by an extended progression in the torsional mode v_4. This regular progression is associated with the lower adiabatic energy surface

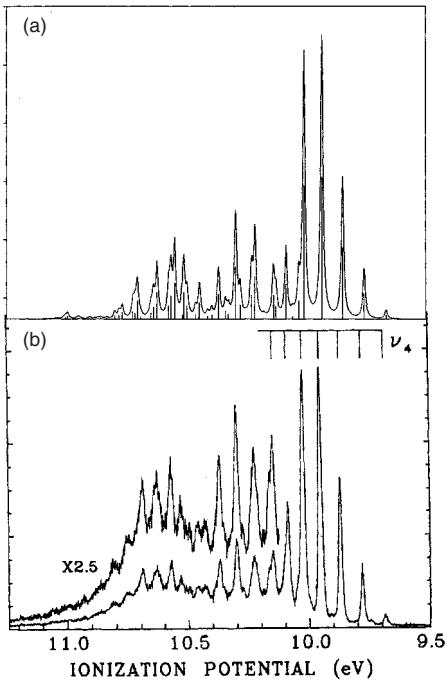

Fig. 4. The $\widetilde{X}^2E$ band in the photoelectron spectrum of allene. (a) Calculated spectrum including two (v_4+v_6) Jahn–Teller active modes. (b) Experimental high-resolution spectrum[98] (reproduced from Ref. 100).

(cf. Fig. 3). The progression completely breaks down at the energetic location of the conical intersection. At higher energies we observe a much denser and rather irregular vibronic line structure, reflecting a strong nonseparability of the v_4 and v_6 Jahn–Teller active modes. In this relatively simple case, the conical intersection is thus spectroscopically identifiable by the transition from a regular to an irregular vibronic line spectrum.

4.3. *Absorption, Resonance Raman and Photoelectron Spectra of Pyrazine*

The $S_1[^1B_{3u}(n\pi^*)]$ and $S_2[^1B_{2u}(\pi\pi^*)]$ excited states of pyrazine represent a classic example of vibronic coupling in aromatic systems.[103] The gas-phase absorption spectrum of pyrazine exhibits typical features of such

systems, namely a well-resolved vibronic structure in the lower energy band, corresponding to the $S_1 - S_0$ transition, and a largely structureless spectral profile for the $S_2 - S_0$ transition.[104] The S_2 state is characterized by a lack of detectable emission, implying a fluorescence quantum yield $\Phi < 10^{-5}$.[104]

Earlier theoretical work on the excited-state dynamics of pyrazine focused on the vibronically induced anharmonic couplings in the S_1 state,[105] on the interactions between *gerade* and *ungerade* $n\pi^*$ states[106] or on selected PE functions[107] and electron-vibrational coupling parameters.[108] In a series of papers the Munich group has characterized the S_2 and S_1-state PE surfaces in the conformational subspace relevant for the short-time photophysics following the $S_2 - S_0$ and $S_1 - S_0$ transitions.[109,110] In the course of this work, the treatment has steadily improved, as regards the accuracy of the electronic-structure calculation as well as the number and description of the vibrational modes considered. The most accurate calculations are based on the CASSCF/MRCI method with a basis set of DZP quality.[111]

These computations establish conclusively that there is a seam of low-energy conical intersections, primarily in the Q_1, Q_{6a}, Q_{10a} subspace of normal-coordinate space. Here, ν_1 and ν_{6a} are two of the five totally symmetric normal modes, while ν_{10a} is the (single) mode of appropriate symmetry ($B_{3u} \times B_{2u} = B_{1g}$) to couple the S_1 and S_2 excited states in first order. Two other totally symmetric modes, ν_{8a} and ν_{9a}, turn out to be of secondary importance, while the coupling strength of the remaining mode of this symmetry, ν_2, is found to be negligible.[111] The existence of a conical intersection has already been inferred from lower-level *ab initio* data,[106] as well as from a combination of semiempirical calculations and adjustments of parameters to reproduce the spectral profile.[109] This conical intersection dominates the short-time photophysics of S_1 and S_2-excited pyrazine, as documented below for absorption and resonance Raman spectra.

The absorption spectrum of the $S_2 - S_0$ and $S_1 - S_0$ electronic transitions of pyrazine has been calculated at various levels of sophistication.[105,109–113] The most elaborate treatment of the Munich group relies on the CASSCF/MRCI data mentioned above and includes seven vibrational modes, ν_1, ν_4, ν_{6a}, ν_{8a}, ν_{9a}, ν_{10a} and ν_{14}.[112] The Heidelberg group has gone beyond this 7-mode model by including all 24 vibrational modes of pyrazine[113] within a linear-plus-quadratic vibronic-coupling model, employing the MCTDH method[76] for the solution of the time-dependent

Schrödinger equation (see also Chapter 14). The linear vibronic coupling approach, Eq. (28), has been shown to be appropriate for the totally symmetric modes ν_1, ν_{6a}, ν_{8a}. Consequently, it has been adopted for these modes in the calculation of the spectrum. For the coupling mode ν_{10a}, the significant reduction of vibrational frequency in the excited states has been accounted for.[112] The two additional non-totally symmetric modes, ν_4 and ν_{14}, are characterized by relatively large diagonal quadratic coupling constants γ_{ii}, Eq. (12). The resulting secular problem of dimension 1.360.800 (per vibronic symmetry) has been solved with the aid of the Lanczos algorithm to yield the stick spectrum shown in Fig. 5(b). Convolution with Lorentzians of fwhm $\approx 0.04\,\text{eV}$ leads to the envelope which is also included in the drawing and may be compared with the experimental gas-phase absorption profile[104] in Fig. 5(a).

The calculated envelope matches the experimental result in almost every detail. It should be mentioned that all parameters, except for an empirical dephasing time[114] have been determined by *ab initio* calculations (the

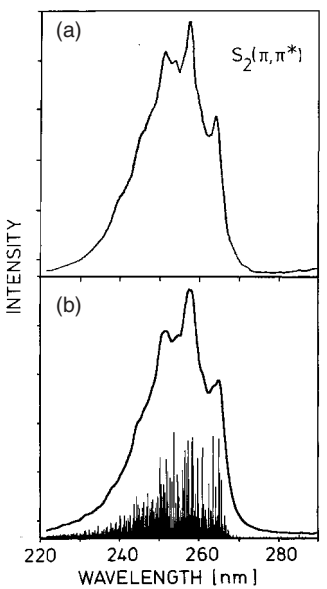

Fig. 5. Experimental (a) and calculated (b) absorption spectrum of the $S_2(\pi\pi^*)$ state of pyrazine. The stick spectrum in (b) represents the vibronic energy levels and absorption intensities of the seven-mode vibronic-coupling model. The envelope has been obtained by including a phenomenological line broadening (reproduced from Ref. 112).

vertical electronic energy gap Δ has been adjusted slightly, from 0.83 to 0.846 eV). This demonstrates that the *ab initio* calculations provide a correct picture of the short-time dynamics in the S_2 state. While the line structure in the lower energy-band (S_1) is sparse and regular, and allows for the assignment of approximate vibrational quantum numbers, the line structure of the S_2 state (Fig. 5) is very complex and irregular. (This impression of an inspection by eye can actually be quantified by a statistical analysis of energy levels and spectral intensities[115].) The irregular line structure results from the fact that the vibrational levels of the upper adiabatic energy surface have completely dissolved into the dense manifold of excited levels of the lower surface, whereby many mixed vibronic eigenstates share the spectral intensity of a few zero-order levels (of the upper surface). The strong mixing reflects the large nonadiabatic coupling elements in the vicinity of the intersection and the pronounced anharmonicity of the PE surfaces. This is a typical finding which characterizes the dynamics on conically intersecting PE surfaces and has been found also for other systems.[5] It can only be correctly described by nonperturbative numerical techniques.

Resonance Raman (RR) spectra yield valuable additional information on the excited-state dynamics and allow for a further test of the theoretical model. RR excitation profiles and spectra can be computed via a straightforward generalization of the Lanczos algorithm to allow for several initial states (namely, all those states where RR transitions are sought for). This amounts to a block-Lanczos or band-Lanczos procedure, both of which are well established in the literature.[4] Alternatively, RR amplitudes may be obtained through Fourier transformation of appropriate cross-correlation functions which can be directly extracted from the time-dependent wavepacket $\Psi(t)$.[17,114]

Figure 6 displays calculated (b) and observed (a) RR spectra of pyrazine for an excitation wavelength $\lambda = 266\,\text{nm}$ close to the origin of the S_2 band.[112] Several modes are found to be excited besides the dominating modes ν_1 and ν_{6a}. Interestingly, the coupling mode ν_{10a} hardly shows up in the S_2 RR spectrum, in marked contrast to the preresonant S_1 Raman spectrum, obtained with $\lambda = 337\,\text{nm}$.[112] The overall features of the S_2 RR spectrum are similar for other excitation wavelengths; this holds also for the generally very satisfactory agreement between theory and experiment.[112] This confirms that the vibronic-coupling model[111,112] yields an authentic

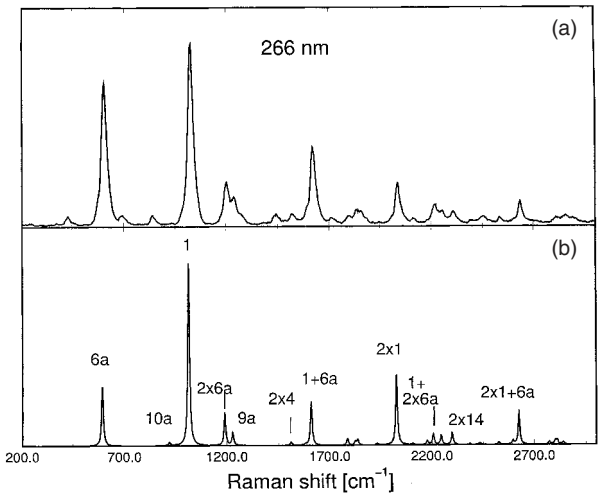

Fig. 6. Experimental (a) and calculated (b) resonance Raman spectra of pyrazine, obtained for an excitation wave length of 266 nm, close to the onset of the $S_2(\pi\pi^*)$ absorption band (reproduced from Ref. 112).

description of the primary photophysical processes of pyrazine in the S_1 and S_2 excited states.

Interestingly, a conical intersection very similar to that of the $S_1(n\pi^*)$ and $S_2(\pi\pi^*)$ neutral excited states has been found for the n^{-1} and π^{-1} hole states of the pyrazine cation.[116] A linear vibronic-coupling model has been constructed for the n^{-1} and π^{-1} states of the pyrazine cation employing many-body Green's function methods for the calculation of the vibronic-coupling parameters.[116] The *ab initio* calculated photoelectron spectrum of the $\widetilde{X}^2A_g(n^{-1})$ and $\widetilde{A}^2B_{1g}$ (π^{-1}) states is compared in Fig. 7 with the experimental photoelectron spectrum of pyrazine.[117] Similar to the case of the $S_2(\pi\pi^*)$ spectrum in Fig. 5, the line spectrum of the higher $\widetilde{A}^2B_{1g}$ state is very dense, reflecting the dissolution of the $\widetilde{A}$ adiabatic energy levels into the manifold of levels of the lower $\widetilde{X}$ surface. In the experimental low-resolution spectrum, this effect is reflected by a noticeable broadening of the apparent vibrational structure (Fig. 7). Correspondingly, the population of the $\widetilde{A}$ state decays to the $\widetilde{X}$ state on a femtosecond time scale, as has been discussed for a number of related examples (cf. Chapter 9).

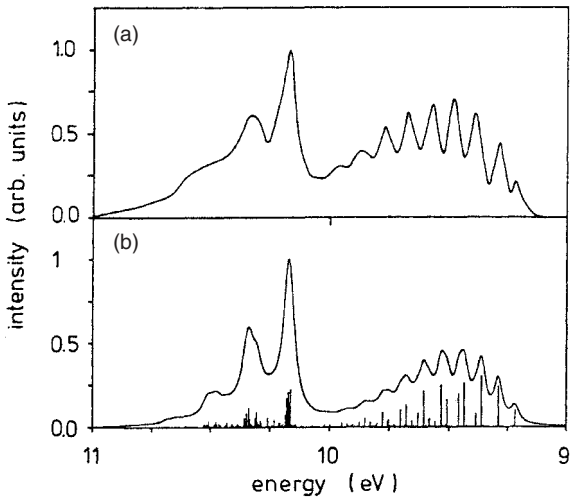

Fig. 7. Experimental[117] HeI UV photoelectron spectrum of pyrazine (a) and calculated spectrum (b), showing the $\widetilde{X}^2A_g$ and $\widetilde{A}^2B_{1g}$ bands. The envelope in (b) represents the convolution of the theoretical spectrum with a typical experimental resolution function (reproduced from Ref. 116).

4.4. *Absorption Spectra of Trans-Butadiene and Trans-Hexatriene*

Understanding the mechanistic details of the photochemistry of polyenes has been a challenge since many years.[118,119] It is known that the smallest members of the polyene series, butadiene and hexatriene, exhibit strongly homogenously broadened $S_0 \rightarrow {}^1B(\pi\pi^*)$ absorption spectra[120] and are completely nonfluorescent.[119] Recent femtosecond time-resolved pump-probe ionization experiments have confirmed the extremely short lifetime of the ${}^1B(\pi\pi^*)$ state in butadiene and hexatriene.[121–123] These experimental findings suggest that the spectroscopy and photophysical dynamics of the ${}^1B(\pi\pi^*)$ states of butadiene and hexatriene are dominated by a directly accessible conical intersection.

The investigation of the electronic structure of excited states of polyenes has a long history[118] which cannot be reviewed here. It suffices to say that modern methods of electronic-structure theory, in particular multi-reference configuration-interaction and multi-reference perturbation methods, allow the determination of the vertical excitation energies of valence and Rydberg

excited states of small polyenes with reasonable accuracy, see, e.g. Ref. 124 and references therein. Conical intersections and photochemical reaction pathways have been explored at the CASSCF level[125−128] and a qualitative picture of the internal conversion process to the electronic ground state via two conical intersections has been developed for butadiene and hexatriene[129−134] (see also Chapter 9).

The available electronic-structure data indicate the existence of a conical intersection of the optically allowed $1^1B(\pi\pi^*)$ state with the dark 2^1A_g state in the vicinity of the Franck-Condon zone of the $S_0 \rightarrow {}^1B$ transition of *trans*-butadiene and *trans*-hexatriene. Accurate calculations of excited-state PE functions of *trans*-butadiene have been performed with the CASPT2 method in order to determine the precise location of this intersection and to determine the relevant coupling modes.[135,136] On the basis of these *ab initio* data, a vibronic-coupling model has been constructed which includes the most relevant vibronically active and Condon active vibrational modes.[135] It has been found that only one normal mode of B_u symmetry, the in-plane bending mode ν_8, is involved in the $1^1B_u - 2^1A_g$ inter-state coupling, while six of the nine totally symmetric modes exhibit nonnegligible activity as tuning modes.

The details of the vibronic dynamics calculations employing the Lanczos algorithm as well as time-dependent wave packet propagation methods are described in Ref. 135. Figure 8 shows the comparison of the calculated ${}^1B_u(\pi\pi^*)$ absorption spectrum with the experimental UV absorption spectrum of jet-cooled *trans*-butadiene.[120] The stick spectrum represents the vibronic energy levels and absorption intensities of the seven-mode vibronic-coupling model. The envelope has been obtained by inclusion of a phenomenological electronic dephasing time of 15 fs. The strong coupling of the 1^1B_u state with the adiabatically lower-lying dark 2^1A_g state is reflected by the dense and irregular vibronic level structure. It is seen that the calculated envelope is in quantitative agreement with the experimental spectrum. The physical mechanisms responsible for the surprisingly short electronic dephasing time have not yet been definitively established. It is likely that a very fast decay of the 2^1A_g state via a conical intersection with the 1^1A_g ground state is mainly responsible for the ultrafast decay of the autocorrelation function.[121]

The calculations predict a decay of the population probability of the ${}^1B_u$ state of *trans*-butadiene on a time scale of 30 fs[135] which is in excellent

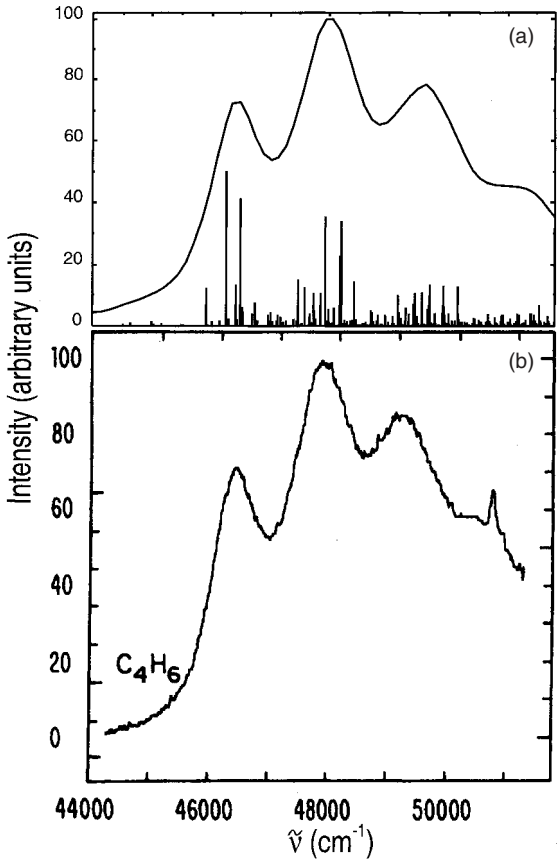

Fig. 8. Calculated (a) and experimental (b) UV absorption spectrum of the $^1B_u(\pi\pi^*)$ state of trans-butadiene. The envelope in (a) has been obtained with the inclusion of a phenomenological optical dephasing time of 15 fs (reproduced from Ref. 135).

agreement with recent direct experimental measurements, which yielded 40 fs and 35 fs, respectively.[121,122] These results demonstrate that first-principles calculations of the time-scale of ultrafast internal conversion through a conical intersection are nowadays feasible.

While the $1^1B_u - 2^1A_g$ conical intersection in *trans*-butadiene can be reasonably accurately modeled within the multi-mode vibronic-coupling approach, this is not the case for the $2^1A_g - 1^1A_g$ conical intersection. Several large-amplitude deformations, in particular out-of-plane torsion and

pyramidization of CH_2 groups, are involved in the reaction path leading to this intersection.[129−133] The treatment of the internal-conversion process from the 2^1A_g state to the electronic ground state is thus beyond the scope of the multi-mode vibronic-coupling approach.

Similar *ab initio* based calculations of absorption and RR spectra have been performed by Woywod *et al.* within the multi-mode vibronic-coupling framework for *trans*-hexatriene and *cis*-hexatriene.[137,138] As an example of these results, we show in Fig. 9 the calculated $S_0 \rightarrow {}^1B_u(\pi\pi^*)$ absorption spectrum[137] in comparison with the experimental spectrum of jet-cooled *trans*-hexatriene.[120] The vibronic calculation involved eight modes, two inter-state coupling modes of B_u symmetry, five tuning modes of A_g symmetry, and one mode of A_u symmetry which exhibits strong intra-state quadratic coupling.[137] The *ab initio* calculated vertical $1^1B_u - 2^1A_g$ energy gap Δ is 0.5 eV. An electronic dephasing time of 90 fs has been assumed to obtain the envelope of the theoretical spectrum.

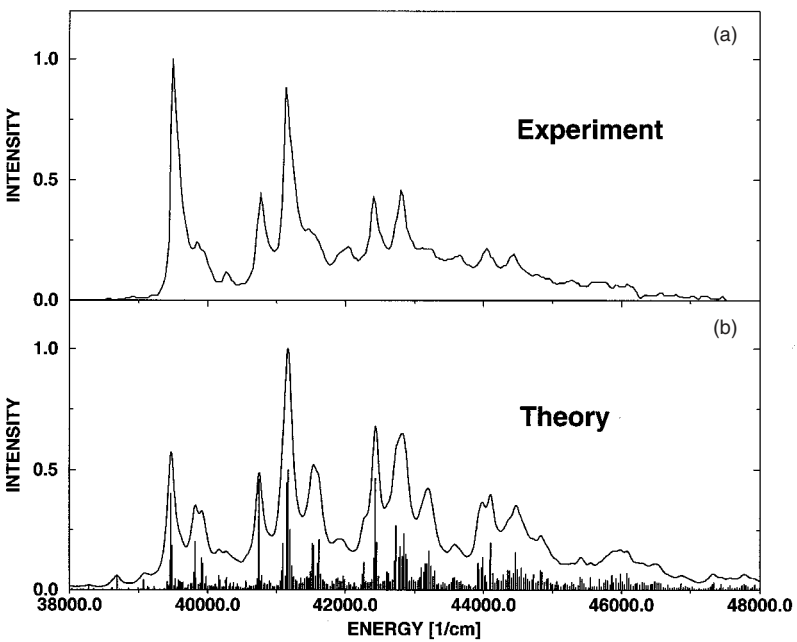

Fig. 9. Experimental (a) and calculated (b) UV absorption spectra of the ${}^1B_u(\pi\pi^*)$ state of *trans*-hexatriene (reproduced from Ref. 137).

It is seen that the calculated envelope is in good agreement with experiment, although the progression in the high-frequency C–C stretch mode is somewhat overestimated (see[137] for a discussion of details of the spectra). Figure 9b again shows the high density of vibronic levels which arises from the dissolution of the ^1B_u adiabatic energy levels in the dense manifold of levels of the lower-lying dark 2^1A_g state. The corresponding population decay time of the $^1B_u(\pi\pi^*)$ state has been estimated to be of the order of 100 fs.[137]

5. Conclusions

We have outlined the concepts, the technical aspects and typical applications of the multi-mode vibronic-coupling approach. This approach allows a comparatively simple and computationally highly efficient description of the photophysical dynamics and spectroscopy of conical intersections. The advantages of this approach are its conceptual and technical simplicity and wide applicability. The latter aspect is documented by numerous successful applications of the multi-mode vibronic-coupling model to a wide variety of molecular systems, from triatomics to medium-size polyatomics.[5,6,77,78] Ground-state normal modes and Taylor expansions of diabatic excited-state potential energies are universal concepts and can routinely be constructed for essentially any stable molecule. The treatment of the vibronic dynamics, in either the time-dependent or the time-independent formalism, is highly efficient. With the MCTDH scheme, in particular, an impressive number of nonseparable vibrational degrees of freedom can be included, as demonstrated by recent benchmark calculations (see Chapter 14).

The multi-mode vibronic-coupling approach is restricted, on the other hand, to cases where the photoinduced nuclear dynamics is restricted to a limited region of configuration space. In this sense, the approach is a useful tool for the microscopic first-principles modeling of photophysical relaxation dynamics, but it is not applicable for the description of photochemical dynamics (isomerization or dissociation) triggered by conical intersections. In the latter case, a global modeling of the potential-energy surfaces is necessary at least in some of the nuclear degrees of freedom. Alternatively, so-called direct-dynamics methods with "on the fly" computation of the electronic potential energies[139–141] may be employed.

References

1. R. Englman, *The Jahn–Teller Effect in Molecules and Crystals* (Wiley, New York, 1972).
2. H. C. Longuet–Higgins in *Advances in Spectroscopy*, Vol. II, Ed. H. W. Thompson (Interscience, New York, 1961).
3. I. B. Bersuker and V. Z. Polinger, *Vibronic Interactions in Molecules and Crystals* (Springer, Berlin, 1989).
4. J. K. Cullum and R. A. Willoughby, *Lanczos Algorithms for Large Symmetric Eigenvalue Problems,* Vol. I (Birkhäuser, Basel, 1985).
5. H. Köppel, W. Domcke and L. S. Cederbaum, *Adv. Chem. Phys.* **57**, 59 (1984).
6. W. Domcke and G. Stock, *Adv. Chem. Phys.* **100**, 1 (1997).
7. W. H. Press, B. P. Flannery, S. A. Teukolsky and W. T. Vetterling, *Numerical Recipes* (Cambridge UP, Cambridge, 1987).
8. I. B. Bersuker, *The Jahn–Teller Effect and Vibronic Interactions in Modern Chemistry* (Plenum Press, New York, 1984).
9. G. Fischer, *Vibronic Coupling* (Academic Press, New York, 1984).
10. Y. E. Perlin and M. Wagner, Eds., *The Dynamical Jahn–Teller Effect in Localized Systems* (North-Holland, Amsterdam, 1984).
11. M. D. Sturge, *Solid State Phys.* **20**, 91 (1967).
12. R. L. Whetten, G. S. Ezra and E. R. Grant, *Ann. Rev. Phys. Chem.* **36**, 277 (1985).
13. E. B. Wilson, J. C. Decius and P. C. Cross, *Molecular Vibrations* (McGraw-Hill, New York, 1955).
14. B. Podolsky, *Phys. Rev.* **32**, 812 (1928).
15. N. C. Handy, *Mol. Phys.* **61**, 207 (1987).
16. J.H. Frederick and C. Woywod, *J. Chem. Phys.* **111**, 7255 (1999).
17. E. J. Heller, *Acc. Chem. Res.* **14**, 368 (1981).
18. L. S. Cederbaum and W. Domcke, *J. Chem. Phys.* **64**, 603 (1976).
19. R. Schinke, *Photodissociation Dynamics* (Cambridge UP, Cambridge, 1993).
20. H. A. Jahn and E. Teller, *Proc. Roy. Soc. (London)* **A161**, 220 (1937).
21. J. R. Fletcher, M. C. M. O'Brien and S. N. Evangelou, *J. Phys.* **A13**, 2035 (1980).
22. T. J. Sears, T. A. Miller and V. E. Bondybey, *J. Chem. Phys.* **74**, 3240 (1981).
23. H. Köppel, L. S. Cederbaum and W. Domcke, *J. Chem. Phys.* **89**, 2023 (1988).
24. M. Döscher and H. Köppel, *Chem. Phys.* **225**, 93 (1997).
25. M.H. Perrin and M. J. Gouterman, *J. Chem. Phys.* **46**, 1019 (1967).
26. M.Z. Zgierski and M. Pawlikowski, *J. Chem. Phys.* **70**, 3444 (1979).
27. R. Renner, *Z. Physik* **92**, 172 (1934).
28. Ch. Jungen and A. J. Merer, *Mol. Phys.* **40**, 1 (1980).

29. M. Peric, S. D. Peyerimhoff and R. J. Buenker, *Int. Rev. Phys. Chem.* **4**, 85 (1985).
30. H. Köppel, W. Domcke and L. S. Cederbaum, *J. Chem. Phys.* **74**, 2945 (1981).
31. S. Carter, I. M. Mills and R. N. Dixon, *J. Mol. Spectrosc.* **106**, 411 (1984).
32. B. O. Roos, *Adv. Chem. Phys.* **69**, 399 (1987).
33. H. J. Werner, *Adv. Chem. Phys.* **69**, 1 (1987).
34. K. Andersson, P.-A. Malmquist and B. O. Roos, *J. Chem. Phys.* **96**, 1218 (1992).
35. J. F. Stanton and R. J. Bartlett, *J. Chem. Phys.* **98**, 7029 (1993).
36. L. S. Cederbaum and W. Domcke, *Adv. Chem. Phys.* **36**, 205 (1977).
37. E. R. Davidson and W. T. Borden, *J. Phys. Chem.* **87**, 4783 (1983).
38. W. von Niessen, J. Schirmer and L. S. Cederbaum, *Comput. Phys. Rep.* **1**, 57 (1984).
39. J. E. Castillo and R. E. Wyatt, *J. Comput. Phys.* **59**, 120 (1985).
40. C. Lanczos, *J. Res. Natl. Bur. Stand.* **45**, 255 (1950).
41. E. Haller and H. Köppel, in *Large Scale Eigenvalue Problems*, Eds. J. Cullum and R. A. Willoughby (Elsevier, Amsterdam, 1986), p. 163.
42. J. H. Wilkinson and C. Reinsch, *Linear Algebra*, Vol. II (Springer, Berlin, 1971).
43. C. C. Page, *J. Inst. Math. Appl.* **10**, 373 (1972); ibid. **18**, 341 (1976).
44. R. Haydock, *Solid State Phys.* **35**, 215 (1980).
45. Y. V. Varobyev, *Method of Moments in Applied Mathematics* (Gordon & Breach, New York, 1965).
46. R. R. Whitehead, in *Moment Methods in Many-Fermion Systems*, Eds. B. J. Dalton *et al.* (Plenum, New York, 1980).
47. N. Sakamoto and S. Muramatsu, *Phys. Rev. B* **17**, 868 (1978).
48. M. C. M. O'Brien and S. N. Evangelou, *J. Phys. C* **13**, 611 (1980).
49. E. Haller, L. S. Cederbaum and W. Domcke, *Mol. Phys.* **41**, 1291 (1980).
50. H. Köppel, L. S. Cederbaum and W. Domcke, *J. Chem. Phys.* **77**, 2014 (1982).
51. E. Haller, H. Köppel and L. S. Cederbaum, *J. Mol. Spectrosc.* **111**, 377 (1985).
52. R. E. Wyatt, *Adv. Chem. Phys.* **73**, 231 (1989).
53. K. F. Freed, *Topics Appl. Phys.* **15**, 23 (1976).
54. P. Avouris, W. M. Gelbart and M. A. El-Sayed, *Chem. Rev.* **77**, 793 (1977).
55. R. Schneider, W. Domcke and H. Köppel, *J. Chem. Phys.* **92**, 1045 (1990).
56. F. B. Hildebrand, *Introduction to Numerical Analysis* (McGraw-Hill, New York, 1974).
57. J. Stoer and R. Burlisch, *Einführung in die Numerische Mathematik II* (Springer, Berlin, 1978).
58. E. A. McCullough and R. E. Wyatt, *J. Chem. Phys.* **51**, 1253 (1969).
59. A. Askar and A. S. Cakmak, *J. Chem. Phys.* **68**, 2794 (1978).

60. C. Leforestier, *Chem. Phys.,* **68**, 2794 (1978).
61. U. Manthe and H. Köppel, *J. Chem. Phys.* **93**, 345 (1990).
62. M. D. Feit, J. A. Fleck and A. Steiger, *J. Comput. Phys.* **47**, 412 (1982).
63. H. Tal-Ezer and R. Kosloff, *J. Chem. Phys.* **81**, 3967 (1984).
64. T. J. Park and J. C. Light, *J. Chem. Phys.* **85**, 5870 (1986).
65. C. Leforestier *et al.*, *J. Comput. Phys.* **94**, 59 (1991).
66. L. Seidner and W. Domcke, *Chem. Phys.* **186**, 27 (1994).
67. U. Manthe and H. Köppel, *Chem. Phys. Lett.* **178**, 36 (1991).
68. A. Ferretti, G. Granucci, A. Lami, M. Persico and G. Villani, *Chem. Phys.* **104**, 5517 (1996).
69. M. Seel and W. Domcke, *J. Chem. Phys.* **95**, 7806 (1991).
70. J. Schön and H. Köppel, *Chem. Phys. Lett.* **231**, 55 (1994).
71. L. Seidner, G. Stock and W. Domcke, *J. Chem. Phys.* **103**, 3998 (1995).
72. P. B. Visscher, *Comput. Phys.* **5**, 596 (1991).
73. S. K. Gray and J. M. Verosky, *J. Chem. Phys.* **100,** 5011 (1994).
74. F. Strocchi, *Rev. Mod. Phys.* **38,** 36 (1966).
75. S. K. Gray and D. E. Manolopoulos, *J. Chem. Phys.* **104**, 7099 (1996).
76. M.H. Beck, A. Jäckle, G. A. Worth and H.-D. Meyer, *Phys. Rep.* **324**, 1 (2000).
77. H. Köppel and W. Domcke, in *Encyclopedia of Computational Chemistry*, Ed. P.v.R. Schleyer (Wiley, New York, 1998) p. 3166.
78. H. Köppel, *Z. Phys. Chemie* **200**, 3 (1997).
79. L. S. Cederbaum, W. Domcke, H. Köppel and W. von Niessen, *Chem. Phys.* **26**, 169 (1977).
80. W. Domcke, H. Köppel and L. S. Cederbaum, *Mol. Phys.* **43**, 212 (1981).
81. L. S. Cederbaum, H. Köppel and W. Domcke, *Int. J. Quant. Chem. Symp.* **15**, 215 (1981).
82. P. J. Reid, M. K. Lawless, S. D. Wickham and R. A. Mathies, *J. Phys. Chem.* **98**, 5597 (1994).
83. A. B. Myers, R. A. Mathies, D. J. Tannor and E. J. Heller, *J. Chem. Phys.* **77**, 3857 (1982).
84. D. K. Hsu, D. L. Monts and R. N. Zare, *Spectral Atlas of* NO_2 (Academic Press, New York, 1978).
85. B. Kirmse, A. Delon and R. Jost, *J. Chem. Phys.* **108**, 6638 (1998).
86. A. Delon and R. Jost, *J. Chem. Phys.* **110**, 4300 (1999).
87. G. D. Gillispie, A. U. Khan, A. C. Wahl, R. P. Hosteny and M. Krauss, *J. Chem. Phys.* **63**, 3425 (1975).
88. C. F. Jackels and E. R. Davidson, *J. Chem. Phys.* **64**, 2908 (1976).
89. F. Leonardi and C. Petrongolo, *J. Chem. Phys.* **106**, 10066 (1997).
90. A. Weaver, R. B. Metz, S. E. Bradforth and D. M. Neumark, *J. Chem. Phys.* **90**, 2070 (1989).
91. S. Mahapatra, H. Köppel and L. S. Cederbaum, *J. Chem. Phys.* **110,** 5691 (1999).

92. S. Mahapatra, H. Köppel and L. S. Cederbaum, *Chem. Phys.* **259**, 211 (2000).
93. T. Schmelz, G. Chambaud, P. Rosmus, H. Köppel, L. S. Cederbaum and H. J. Werner, *Chem. Phys. Lett.* **183**, 209 (1991).
94. J. M. Dyke, L. Golob, N. Jonathan, A. Morris and M. Okuda, *J. Chem. Soc. Faraday Trans. 2*, **70**, 1828 (1974).
95. H. Müller, H. Köppel and L. S. Cederbaum, *J. Chem. Phys.* **101**, 10263 (1994).
96. L. S. Cederbaum, W. Domcke and H. Köppel, *Chem. Phys.* **33**, 319 (1978).
97. D. W. Turner, C. Baker, A. D. Baker and C. R. Brundle, *Molecular Photoelectron Spectroscopy* (Wiley, New York, 1970).
98. Z. Z. Yang, L. S. Wang, Y. T. Lee, D. A. Shirley, S.Y. Huang and W. A. Lester Jr., *Chem. Phys. Lett.* **171**, 9 (1990).
99. P. Baltzer, B. Wannberg, M. Lundqvist, L. Karlsson, D. M. P. Holland, M. A. McDonald and W. von Niessen, *Chem. Phys.* **196**, 551 (1995).
100. C. Woywod and W. Domcke, *Chem. Phys.* **162**, 349 (1992).
101. S. Mahapatra, L. S. Cederbaum and H. Köppel, *J. Chem. Phys.* **111**, 10452 (1999).
102. S. Mahapatra, G. A. Worth, H.-D. Meyer, L. S. Cederbaum and H. Köppel, *J. Phys. Chem. A* **105**, 5567 (2001).
103. K. K. Innes, I. G. Ross and W. R. Moomaw, *J. Mol. Spectrosc.* **132**, 492 (1988).
104. I. Yamazaki, T. Murao, T. Yamanaka and K. Yoshihara, *Faraday Discuss. Chem. Soc.* **75**, 395 (1983).
105. N. Heider and S. F. Fischer, *Chem. Phys.* **88**, 209 (1984).
106. D. A. Kleier, R. L. Martin, W. R. Wadt and W. R. Moomaw, *J. Am. Chem. Soc.* **104**, 60 (1982).
107. A. L. Sobolewski and R. Cerminski, *Chem. Phys.* **130**, 123 (1989).
108. E. Venuti and G. Marconi, *Chem. Phys.* **125**, 1 (1988).
109. R. Schneider and W. Domcke, *Chem. Phys. Lett.* **150**, 235 (1988).
110. L. Seidner, G. Stock, A. L. Sobolewski and W. Domcke, *J. Chem. Phys.* **96**, 5298 (1992).
111. C. Woywod, W. Domcke, A. L. Sobolewski and H.-J. Werner, *J. Chem. Phys.* **100**, 1400 (1994).
112. G. Stock, C. Woywod, W. Domcke, T. Swinney and B. T. Hudson, *J. Chem. Phys.* **103**, 6851 (1995).
113. A. Raab, G. A. Worth, H.-D Meyer and L. S. Cederbaum, *J. Chem. Phys.* **110**, 936 (1999).
114. G. Stock and W. Domcke, *J. Chem. Phys.* **93**, 5496 (1990).
115. T. Zimmermann, L. S. Cederbaum, H.-D. Meyer and H. Köppel, *J. Phys. Chem.* **91**, 4446 (1987).
116. L. Seidner, W. Domcke and W. von Niessen, *Chem. Phys. Lett.* **205**, 117 (1993).

117. C. Fridh, L. Åsbrink, B. Ö. Jonsson and E. Lindholm, *Internat. J. Mass Spec. Ion Phys.* **8**, 101 (1972).
118. B. S. Hudson, B. E. Kohler and K. Schulten, in *Excited States*, Ed. E. C. Lim (Academic Press, New York, 1982) Vol. 6, p.1.
119. B. E. Kohler, *Chem. Rev.* **93**, 41 (1993).
120. D. G. Leopold, R. D. Pendley, J. L. Roebber, R. J. Hemley and V. Vaida, *J. Chem. Phys.* **81**, 4218 (1984).
121. W. Fuß, W. E. Schmid and S. A. Trushin, *Chem. Phys. Lett.* **342**, 91 (2001).
122. F. Assenmacher, M. Gutmann, G. Hohlneicher, V. Stert and W. Radloff, *PCCP* **3**, 2981 (2001).
123. D. R. Cyr and C. C. Hayden, *J. Chem. Phys.* **104**, 771 (1996).
124. J. Lappe and R. J. Cave, *J. Phys. Chem.* **A104**, 2294 (2000).
125. M. Aoyagi, Y. Osamura and S. Iwata, *J. Chem. Phys.* **83**, 1140 (1985).
126. F. Zerbetto and M.Z. Zgierski, *J. Chem. Phys.* **93**, 1235 (1990).
127. K. Nakayama, H. Nakano and K. Hirao, *Int. J. Quant. Chem.* **66**, 157 (1998).
128. S. Sakai, *Chem. Phys. Lett.* **319**, 687 (2000).
129. M. Olivucci, F. Bernardi, P. Celani, I. Ragazos and M. A. Robb, *J. Am. Chem. Soc.* **116**, 1077 (1994).
130. P. Celani, F. Bernardi, M. Olivucci and M. A. Robb, *J. Chem. Phys.* **102**, 5733 (1995).
131. M. Garavelli, P. Celani, M. Fato, M. J. Bearpark, B. R. Smith, M. Olivucci and M. A. Robb, *J. Phys. Chem.* **A101**, 2023 (1997).
132. M. Garavelli, P. Celani, F. Bernardi, M. A. Robb and M. Olivucci, *J. Am. Chem. Soc.* **119**, 11487 (1997).
133. M. Ito and I. Ohmine, *J. Chem. Phys.* **106**, 3159 (1997).
134. S. Zilberg and Y. Haas, *J. Phys. Chem.* **A103**, 2364 (1999).
135. R. P. Krawczyk, K. Malsch, G. Hohlneicher, R. C. Gillen and W. Domcke, *Chem. Phys. Lett.* **320**, 535 (2000).
136. B. Ostojic and W. Domcke, *Chem. Phys.* **269**, 1 (2001).
137. C. Woywod, W. C. Livinghood and J. H. Frederick, *J. Chem. Phys.* **112**, 613, 626 (2000).
138. C. Woywod, W. C. Livinghood and J. H. Frederick, *J. Chem. Phys.* **114**, 1631, 1645 (2001).
139. M. Ben-Nun and T. J. Martinez, *Chem. Phys. Lett.* **298**, 57 (1998).
140. S. Klein, M. J. Bearpark, B. R. Smith, M. A. Robb, M. Olivucci and F. Bernardi, *Chem. Phys. Lett.* **292**, 259 (1998).
141. G. Granucci, M. Persico and A. Toniolo, *J. Chem. Phys.* **114**, 10608 (2001).

This page intentionally left blank

CHAPTER 8

MODEL STUDIES OF THE DYNAMICS AT CONICAL INTERSECTIONS

A. Lami* and G. Villani

Istituto per i Processi Chimico-Fisici del CNR,
Area della Ricerca del CNR di Pisa,
Via Moruzzi 1, I-56124 Pisa, Italy
**lami@ipcf.cnr.it*

Contents

1. Introduction

The continuous progress in Theoretical and Computational Chemistry produced, in the last years, a growing amount of accurate information on conical intersections (CIs) occurring in molecules of chemical interest, and then encouraged the treatment of specific cases. However, in our opinion, the "exact" numerical study of simpler model systems remains a necessary preliminary step to unravel various general aspects of the complex dynamics of such strongly non-adiabatic systems. Before illustrating some representative examples, it is worthwhile to spend a few words to clarify what we mean here by model systems. These are essentially built up choosing the simplest Hamiltonian sharing with actual systems the essential features of the problem under study (in our case the CI), while disregarding the details that are of course necessary if the scope is to reproduce the output of an experiment on a given molecule, but are judged non-essential for a basic understanding of the process. Thus, the accent here is on general features that may give some interpretative rules, beyond specific examples. There are a number of general points that can be elucidated looking at model systems and we will proceed discussing a few of them, also with the aim of underlining the origin of their interest. In the following, we focus on the dynamics around the conical intersection, assuming that the initial excitation is obtained by a light pulse so short that it is seen as a Dirac δ-function by the nuclei (which means that, if the transition dipole is constant, a vertical excitation is achieved) but sufficiently long (and thus not too broad in energy) to be selective as far as the electronic state is concerned.

2. Basic Concepts and Simple Interpretation Schemes

The dynamical behavior of strongly non-adiabatic multimode systems exhibits complex features that can perhaps be better understood by trying first to underline the aspects that they share with simple one-dimensional models basically derived from scattering theory. To this purpose we introduce a minimal model for the CI and then discuss the limit of validity of an interpretation scheme grounded on the Landau–Zener formula as well as of a simple one-dimensional time-dependent model obtained by treating quantum-mechanically only the coupling mode.

2.1. *The Minimal Model for a CI*

As is well known, the minimal model for a CI involves two purely (i.e. completely independent on nuclear coordinates) diabatic states with identical but displaced (both vertically along the energy axis and horizontally along a vibrational coordinate) harmonic surfaces.[1] The minimum number of vibrational modes required to have a CI is two: the totally symmetric mode Q (tuning mode) that is involved in the shift of the equilibrium position, and the so-called coupling mode Q_c, which is a symmetry-breaking coordinate responsible for the electronic coupling (which is taken as linear in Q_c). In the usual mixed representation (operator for the nuclear terms and matrix for the electronic part) it is written, using dimensionless normal coordinates:

$$H = \begin{pmatrix} H_{11} & H_{12} \\ H_{21} & H_{22} \end{pmatrix} \tag{1}$$

with:

$$H_{11} = \frac{\hbar\omega}{2} Q^2 + g_1 Q + \frac{\hbar\omega_c}{2} Q_c^2 - \hbar\omega \frac{\partial^2}{\partial Q^2} - \hbar\omega_c \frac{\partial^2}{\partial Q_c^2} \tag{2a}$$

$$H_{22} = \Delta E + \frac{\hbar\omega}{2} Q^2 + g_2 Q + \frac{\hbar\omega_c}{2} Q_c^2 - \hbar\omega \frac{\partial^2}{\partial Q^2} - \hbar\omega_c \frac{\partial^2}{\partial Q_c^2} \tag{2b}$$

$$H_{12} = H_{21} = \lambda f(Q, Q_c) Q_c. \tag{2c}$$

The parameters g_1 and g_2 are simply related to the equilibrium positions Q_{1m}, Q_{2m} of the two diabatic surfaces along the tuning coordinate and could be reduced to a single parameter by placing the zero of Q just in the middle of them. Here, however, we prefer to maintain this notation, reserving the minimum at $Q = 0$ to the ground state, which might not coincide with state $|1\rangle$.

The above two-state, two-mode model Hamiltonian can be easily generalized to include more tuning and coupling modes (and electronic states, if necessary) as well as higher-order terms in both the intrastate and interstate coupling. It has been successfully used in the last twenty years, mainly by the Heidelberg and Munich groups,[1–3] to study several low-energy CI's in molecules, as discussed in Chapter 7, both from the point of view of cw spectra and of time-resolved non-linear spectroscopy.

The function $f(Q, Q_c)$, which is assumed to be symmetric in both coordinates, is often taken as the identity. It has been introduced here for generality, since we will explore in the following the consequences of the fact

that the diabatic coupling is actually damped out as one moves away from the conical intersection point.

The time-dependent Schrödinger equation:

$$i\hbar\frac{\partial}{\partial t}\begin{pmatrix}\chi_1(Q,Q_c,t)\\ \chi_2(Q,Q_c,t)\end{pmatrix} = H\begin{pmatrix}\chi_1(Q,Q_c,t)\\ \chi_2(Q,Q_c,t)\end{pmatrix} \tag{3}$$

can be numerically solved, opening the way to the computation of any time-resolved quantity. We do not examine here the various available techniques, just recalling that all the "exact" results shown below have been obtained through a Lanczos propagation scheme[3,4] (with Householder orthogonalization[5]) working with a basis set built as tensorial product of diabatic electronic states and harmonic oscillator states for each mode.[4]

Figure 1 gives a pictorial representation of the diabatic (a) and adiabatic (b) surfaces for the model two-mode CI utilized for several computations discussed in the following. The third panel (c) gives a cross-section along the tuning coordinate Q at $Q_c = 0$ and also reports the numbering of the different initial conditions for the excited wavepacket used in the calculations presented and discussed in the following. As is clear from the adiabatic surfaces, the interstate coupling λ is large enough to develop a double minimum along the coupling coordinate. The crossing has been placed at the minimum of the upper diabatic surface, a position which makes the CI well accessible for various initial conditions.

2.2. *The Vibronic Model*

When studying the photochemical/photophysical behavior of large molecules, one finds that, whenever a CI is present and accessible, the decay from the initially excited PES to a lower one occurs in a few femtoseconds. From a chemical point of view, the most interesting situations are those in which reactive channels are open both on the surface directly reached by excitation and on the one populated by internal conversion through the CI. This means that the wavepacket moves into regions where any mode separation breaks down and then rapidly spreads out. In practice, also in the absence of a true continuum giving rise to energy dissipation (as for channels leading to isomerizations), a kind of irreversibility arises, in such a way that the excited wavepacket has rarely the possibility of experiencing more than a single passage through the CI, in contrast with what happens for low-energy CIs, when no reactive channels are open. The above motivates

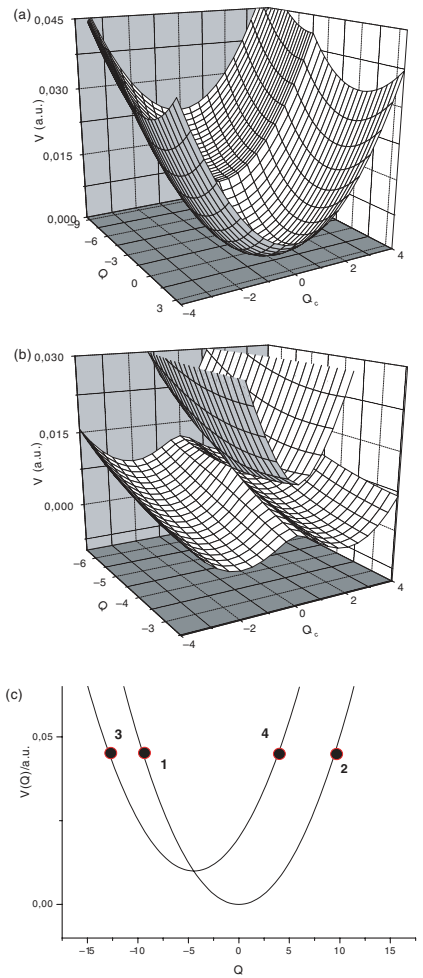

Fig. 1. The figure shows the CI for the two-mode model Hamiltonian [Eqs. (1) and (2)]. The parameters are: $\omega = 0.001$, $\omega_c = 0.003873$, $g_1 = 0$, $g_2 = 1.02873$, $\lambda = 0.00787196$, $\Delta E = 0.02$ are all in a.u., while the coordinates are dimensionless. (a) A view of the diabatic surfaces. In order to put in evidence the intersection, the upper diabatic surface is plotted for values of $Q < Q_{2m}$ (the minimum of the excited diabatic state), while the lower for $Q > Q_{2m}$. (b) The adiabatic surfaces. (c) The sections of the two diabatic surfaces at $Q_c = 0$. The numbered points refer to various initial conditions for the excited wavepacket, as discussed in the text.

the interest for simple generalizations of the Landau–Zener formula to give a reasonable estimate of the transition probability after a single passage through the CI.

The Landau–Zener formula is a scattering solution to the problem of crossing between two diabatic curves, derived by assuming that the nuclei follow a classical trajectory.[6,7] The diabatic curves are linearized around the crossing point, which translates into an electronic energy gap varying linearly with time. The transition probability P is:

$$P_{LZ}(1 \to 2) = 1 - e^{-\gamma}\,;\, \gamma = \frac{2\pi\lambda^2}{V\Delta F} \tag{4}$$

where λ is the coupling, V the velocity at the crossing point, and ΔF is the difference of the slopes at the same point. Equation (4) refers to a constant coupling between diabatic potential energy curves and as such cannot directly applied to the conical intersection problem.

Let us take as an example the two-mode model system depicted in Fig. 1, exhibiting a CI at the bottom of the upper diabatic surface. We may interpret Fig. 1 as referring to a pair of excited states while leaving as undetermined the equilibrium position of the electronic ground state (not shown), which is assumed, for simplicity, to share the same frequencies. Different initial positions [numbered points in Fig. 1(c)] of the excited wavepacket on both diabatic surfaces will then be considered in the following, to mimic not only different minima of the ground state, but also different dipole selection rules (only one diabatic state is assumed to be bright).

As a first attempt, one may take the displacement along the tuning coordinate, Q, as a parameter and assume that each level of the coupling oscillator gives rise to a distinct diabatic curve with its crossings, as shown in Fig. 2.[8] The "good" crossings are those between levels for which $\Delta v_c = \pm 1$ and to each one is associated a different coupling: for example the levels $|v_c\rangle$ and $|v_c - 1\rangle$ experience a coupling $\lambda\langle v_c|Q_c|v_c - 1\rangle = \lambda\sqrt{v_c}$ (here $f(Q, Q_c)$ is taken as 1, for simplicity). Let us take as an example the initial condition numbered as 1 in Fig. 1(c). As should be clear from Fig. 2, the relevant crossings are $1_0 \to 2_1 \to 1_2$, where e.g. 1_0 is the ground vibrational level of the coupling oscillator in the lower diabatic state, here numbered 1. Applying the Landau–Zener formula, the following total probability of remaining in the initial electronic state 1 is obtained:

$$P_1^{VM} = 1 - P_{LZ}(1_0 \to 2_1) + P_{LZ}(1_0 \to 2_1)\, P_{LZ}(2_1 \to 1_2) = 1 - e^{-2\gamma} + e^{-3\gamma}. \tag{5}$$

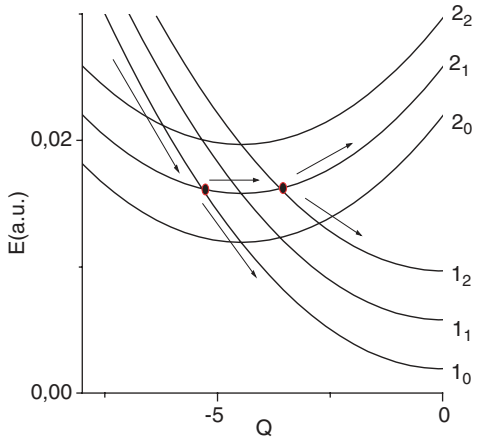

Fig. 2. The figure shows how the CI of Fig. 1 can be visualized in one dimension as a sequence of crossings among diabatic states, each one referring to a different vibrational level of the coupling oscillator. The points are placed at the crossings which are relevant for the initial condition number 1 [see Fig. 1(c)], while the arrows indicate possible paths.

Such a vibronic model (VM), which also accounts for the repopulation of the initial diabatic state due to back-crossings, gives a good estimate of the first-passage transition probability (FPTP) for small values of the coupling parameter as illustrated in Fig. 3,[8] showing the VM and the exact results obtained by a Lanczos propagation . In order to check the influence of the damping function in the interstate coupling, we have investigated both the case of a purely linear coupling (i.e. $f(Q, Q_c) = 1$) and that of a gaussian damping: $f(Q, Q_c) = \exp[-\alpha Q_c^2 - \beta(Q - Q_{CI})^2]$, where $Q_{\rm CI}$ is the point at which the CI occurs along the Q axis (see caption for further details). Basically, the figure demonstrates that, for the damped case, the VM gives a good estimate of the FPTP, at least for small values of the coupling parameter λ. Further calculations, not reported here, show that the agreement is excellent for the whole range of parameters when the initial wavepacket is on the lower adiabatic state, as for the case numbered 3 in Fig. 1(c). In the case of a purely linear interstate coupling, there is still a qualitative agreement, which is however much more sensitive to the coupling strength. In general, one may say that, as expected, the coupling threshold after which the one-dimensional representation looses its validity it is much lower for the case without damping. The comparison between the

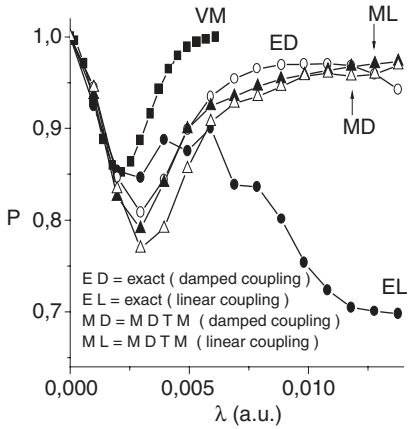

Fig. 3. The figure shows the behavior of the probability of remaining in the initial diabatic state (i.e. P = 1-FPTP) for the conical intersection of Fig. 1 (whose parameters are specified in the caption). The initial condition corresponds to the case 1 of Fig. 1(c). The exact results are compared with those obtained using the MTDM for both damped ($\alpha = 0.33541$, $\beta = 0.590397$) or purely linear interstate coupling. The VM results (see text) are also shown.

exact calculations performed using a purely linear coupling and a damped linear coupling clearly shows that, after a given threshold, the decay is very sensitive to the tails of the coupling function and then, for such cases, some additional care has to been devoted to its computation, going beyond simple linear or quadratic expansions.

2.3. *The Time-Dependent One-Dimensional Model*

Going up in a hierarchy of simple approximating schemes, one may substitute Q with the classical trajectory of the center of the vertically excited wavepacket along the initial diabatic curve, $Q_{\rm cl}(t)$. The following time dependent Schrödinger equation is obtained:

$$i\hbar\frac{\partial}{\partial t}\begin{pmatrix}\chi_1(Q_c,t)\\ \chi_1(Q_c,t)\end{pmatrix} = H_M(t)\begin{pmatrix}\chi_1(Q_c,t)\\ \chi_1(Q_c,t)\end{pmatrix} \tag{6}$$

where $H_M(t)$ is obtained from the Hamiltonian [Eqs. (1) and (2)], by dropping the kinetic energy along the tuning mode and replacing Q with $Q_{\rm cl}(t)$.[9−11] Neglecting the kinetic energy of the tuning mode is not due here to the fact that it is negligible, of course. It may be regarded as a constraint:

the jumps from a surface to the other have to be vertical and have to conserve the kinetic energy along the Q coordinate. In other words, according to this elementary model, which will be referred as the mono-dimensional time-dependent model (MTDM), the motion along Q simply results in a time-dependent energy gap to be taken into account when describing the quantum mechanical mode Q_c (the coupling becomes also time-dependent, if it is damped along Q). The probability of remaining in the initial diabatic state (1-FPTP) from the numerical solution of Eq. (6) is also reported in Fig. 3 together with the exact quantum result. As one can see, the MTDM gives excellent results for the case of damped coupling. When no damping is present, the range of validity is restricted, albeit the correct behavior is qualitatively reproduced up to a coupling strength of nearly 0.006 au. The results of further numerical investigations, not reported here, show that the damping along the tuning mode is more crucial than the one along the coupling mode. This may be attributed to the fact that the damping restricts the coordinate range where the jumps take place, thus reducing the spreading of the wavepacket along the Q coordinate and making the motion more classical.

3. Exact Time-Dependent Results

The numerical solution of the time-dependent Schrödinger equation opens the way to the calculation of several time-dependent quantities which may be utilized for analyzing the dynamics, as, for example, the mean value of position and momenta, the average energy for each mode, the entropy production and the coherences in reduced density matrices obtained tracing out the electronic or the vibrational degree of freedom.[2,12] The effects of relaxing the simplifying assumption of identical frequencies in both diabatic states have been also investigated.[13] Time-dependent observables directly related to linear and nonlinear optical experiments (e.g. pump and probe, photon echo and photoelectron spectra) can also be evaluated, as widely discussed in Ref. 2 and in Chapters 7 and 17 of this book. While the short-time behavior can be often be rationalized, as before, in terms of trajectories along the tuning modes, even when dealing with pump and probe spectroscopy,[14] the dynamics becomes very complex at longer times, even for the simple two-mode model of Fig. 1. Figure 4, showing a few snapshots of the excited wavepacket for the case (4) of Fig. 1(c), gives a

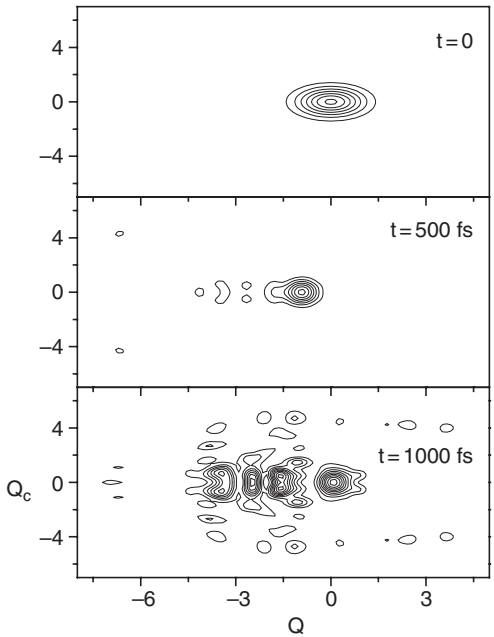

Fig. 4. Contour plots showing snapshots at $t = 0$, $t = 500\,\text{fs}$ and $t = 1000\,\text{fs}$, of the evolving wavepacket for the case (4) of Fig. 1(c).

pictorial example of this complexity. The initially localized wavepacket is strongly perturbed at any passage through the CI region and acquires a complex nodal structure. In the remaining part of this section, for reason of space, we limit ourselves to present a few examples of numerical results illustrating selected aspects of the dynamics.

3.1. *Diabatic vs. Adiabatic Populations*

As illustrated also in other Chapters of this book (see especially Chapters 3), the transformation from the adiabatic wavefunctions computed by *ab initio* methods to diabatic ones, is often the first task to be accomplished when approaching the study of the dynamics around a CI.[15] The main historical reason for the preference given to the diabatic representation was the problem of the divergence of the coupling between adiabatic surfaces, as illustrated for example in the review of Ref. 1. This computational difficulty seems to have been overcome, judging from the increasing

popularity of adiabatic surfaces, preferred in approximate methods as the "surface hopping"[16] or the "multiple spawning" approach[17] since it gives rise to a more localized coupling.

When one deals with molecular systems exhibiting an irreversible behavior, i.e. as discussed before, there is a single passage through the CI region, the problem of the utility of adiabatic vs. diabatic populations is not relevant, since initially (i.e. in the region containing the vertically excited wavepacket) diabatic and adiabatic states coincide (hence $P_{\mathrm{d1}} = P_{\mathrm{a1}}, P_{\mathrm{d2}} = P_{\mathrm{a2}}$), while after the passage they are simply exchanged ($P_{\mathrm{d1}} = P_{\mathrm{a2}}, P_{\mathrm{d2}} = P_{\mathrm{a1}}$). In other cases, the two kinds of populations are not simply related, and the emphasis given to one or the other depends then uniquely on the possibility of relating them to observables. As discussed, for example, in Chapter 16 of this book, the dipole matrix elements between the ground state and the pair of crossing diabatic states are usually directed along different axis, which means that for an oriented molecule it would be possible to excite selectively one or the other diabatic state. Quite often, however, the modulus of the transition moment is also very different, so that one may consider, to a good approximation, that one is bright and the other dark (this is certainly true if one of them is the ground state). If, say, state 1 is bright then the total (i.e. frequency integrated) fluorescence emitted at a given time can be computed as a sum of probabilities of emission from the evolving wavepacket to all the lower levels. To be more realistic, one should however take into account that actual experimental methods, e.g. the up-conversion technique, work opening a time window for the revelation of emitted photons.[2,18]

Let us indicate with g the electronic ground state and with 1 and 2 the two crossing diabatic states. Using as vibrational basis set the harmonic oscillator states of the ground state, the doorway state at time t is:

$$|d(t)\rangle = \sum_{n1,n2} \left(c_{1;n1,n2}(t)|1;n1,n2\rangle + c_{2;n1,n2}(t)|2;n1,n2\rangle\right) \tag{7}$$

and the probability of emission to the ground electronic state at time t is:

$$P_e(t) \propto \sum_{n1,n2} \left|\langle g;n1,n2|\hat{\mu}|\psi(t)\rangle\right|^2 = \mu^2 \sum_{n1,n2} \left|c_{1;n1,n2}(t)\right|^2 = \mu^2 P_1(t) \tag{8}$$

where $\hat{\mu} = \mu(|g\rangle\langle 1| + \mathrm{h.c.})$ and μ is a constant.

The above shows that, in the Condon approximation, which is rigorously valid in the purely diabatic basis set adopted in Eqs. (1) and (2), the total

fluorescence monitors the population of the bright diabatic state and is then a significant quantity, especially if one takes into account that the recording of fluorescence is a widely used tool to get information on the excited states. From a numerical point of view, the diabatic populations are directly obtained from propagation, when working in the diabatic basis:

$$P_1^d(t) = \langle \psi(t) \,|\, 1 \rangle \langle 1 \,|\, \psi(t) \rangle = \sum_{n_1, n_2} |c_{1;n_1,n_2}(t)|^2; \tag{9}$$

while the adiabatic ones must be obtained by a multidimensional numerical integration over nuclear coordinates (which then requires working on a grid of points), as briefly sketched below:

$$\begin{aligned} A_1(Q, Q_c, t) &= \langle \phi_1^a \mid \psi(Q, Q_c, t) \rangle_r \\ &= \sum_{\alpha, n_1, n_2} S_{1\alpha}(Q, Q_c) c_{\alpha;n_1,n_2}(t) \chi_{n_1}(Q) \varphi_{n2}(Q_c); \\ P_1^{ad}(t) &= \iint dQ dQ_c |A_1(Q, Q_c, t)|^2 \end{aligned} \tag{10}$$

where the bracket with the subscript r indicates integration over electronic coordinates and $\mathbf{S}$ is the diabatic-adiabatic transformation 2×2 matrix, depending on nuclear coordinates. The amount of numerical computations for obtaining adiabatic populations becomes rapidly very heavy when including more vibrational modes, and efficient algorithms must be used for this purpose.[19–21]

The previous discussion on the close relation between the population of the bright diabatic state and the intensity of the fluorescence concerned the case where the state reached by the radiative decay is a third one (the ground state, in our example). As pointed out by Meyer and Köppel,[22] in the case where the spontaneous emission takes place between the two coupled states one may relate the fluorescence to the population of the upper adiabatic state.

3.2. *Some Numerical Results and their Interpretation*

Figure 5 shows some computed adiabatic/diabatic populations for the two-mode model system illustrated in Fig. 1. They are intended to illustrate different typologies concerning the ground-state equilibrium position with respect to the crossing surfaces,[23] a point which will be further discussed in the next section. What we do, in practice, is to select the different initial

conditions depicted in Fig. 1(c) and report them in each of the panels. The various cases have been also identified by Uu, Ul, Lu, Ll where the capital letter identifies the initial diabatic state, as far as its minimum is concerned (U = upper, L = lower), while the lower case letter is to characterize the initial adiabatic state (u = upper, l = lower). Hence, for example, Ul means that at $t = 0$ the wavepacket is on the upper lying diabatic state but on the lower adiabatic state, which means that, initially, its vertical jump to the other diabatic surface needs energy. Let us leave to the next section the detailed interpretation of what happens in the first period T of the tuning oscillator (about 150 fs). Here we notice that, as shown from the adiabatic populations, there is a clear tendency to a trapping on the lower adiabatic surface. If the wavepacket is placed initially on the lower adiabatic state (case Ul or Ll) it tends to remain there, while if it starts on the upper adiabatic state (Lu or Uu) it goes rapidly down. In this latter case, if the wavepacket crosses the CI with high kinetic energy, as in our example, then some pronounced (damped) oscillations may be seen, but on the average the adiabatic population transfer is still massive.

The corresponding diabatic population of the bright state (i.e. the time-dependent total fluorescence) exhibits always an oscillatory behavior, which is however more pronounced for an almost purely adiabatic situation, as for Ul and Ll.

As a demonstration of the interpretative capability of the MTDM (which can be viewed as a time-dependent version of the VM model), let us compare the behavior of the diabatic populations in cases Ul and Ll, which correspond both to placing the initial wavepacket on the lower adiabatic surface. Looking at the corresponding panels of Fig. 5, one may see that for the Ul initial conditions the damping of the oscillations is slower and more regular than for the Ll case. This effect cannot be attributed to the different velocity of the wavepacket at the CI point, since as can be easily checked by looking at Fig. 1(c), the corresponding classical trajectories arrive at the CI with identical velocity. The difference between the two cases can be easily qualitatively explained in terms of the MTDM introduced in Sec. 2.3. In fact, looking at the time-dependent energies of the levels of the coupling oscillator, Fig. 6, one may see that in the Ul case (3) the only active crossing during the first passage is that between the 2_0 and the 1_1 levels (the same notation as in Sec. 2.2 is used), giving rise to a population transfer, which is then partially reversed during the second passage (here a second active

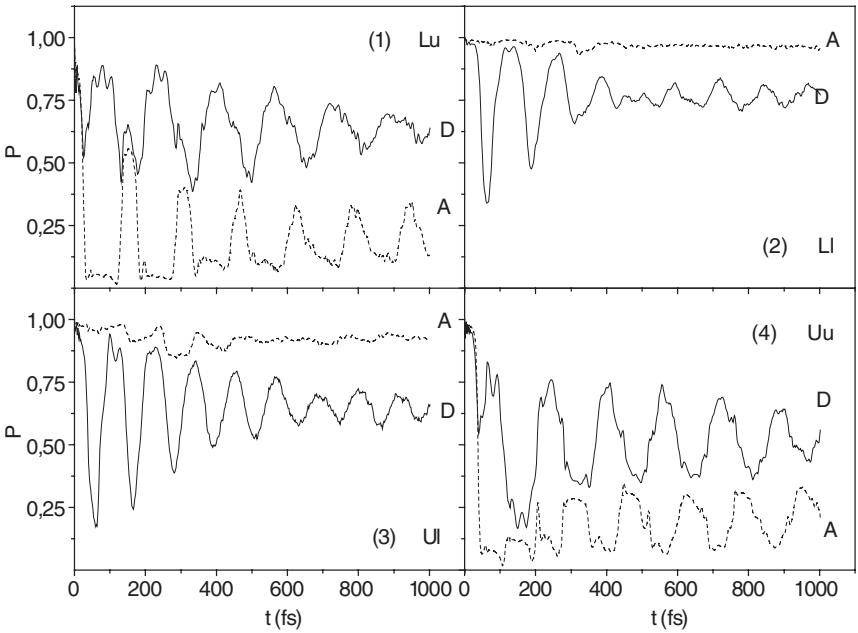

Fig. 5. The computed diabatic (D) and adiabatic (A) populations for the two-mode CI of Fig. 1. The numbering of the four panels refers to the initial conditions shown in Fig. 1(c). The letters indicate the relative position along the energy scale of diabatic and adiabatic surfaces at the initial point, as explained in the text.

crossing appears between 1_1 and 2_2). In the *Ll* case (2) there are instead two different possibilities at the first passage, giving rise to more paths and then to a complex dynamical pattern, which is reflected in the behavior of the diabatic populations.

An extensive theoretical/computational study of the time-dependent behavior of diabatic and adiabatic populations for three well-known examples of low-energy conical intersections, the $C_2H_4^+$, pyrazine and NO_2 molecules, has been performed by Köppel *et al.*,[21,24] who used a three-mode version of the Hamiltonian in Eqs. (1) and (2) (two tuning oscillators) and investigated also the role of the coupling parameter λ. It is interesting to compare their results with the general considerations illustrated above. First of all, we notice that according to the previous classification all the three are *Uu* cases (i.e. the vertically excited wavepacket starts initially on the upper adiabatic surface, on the side originating from the upper diabatic

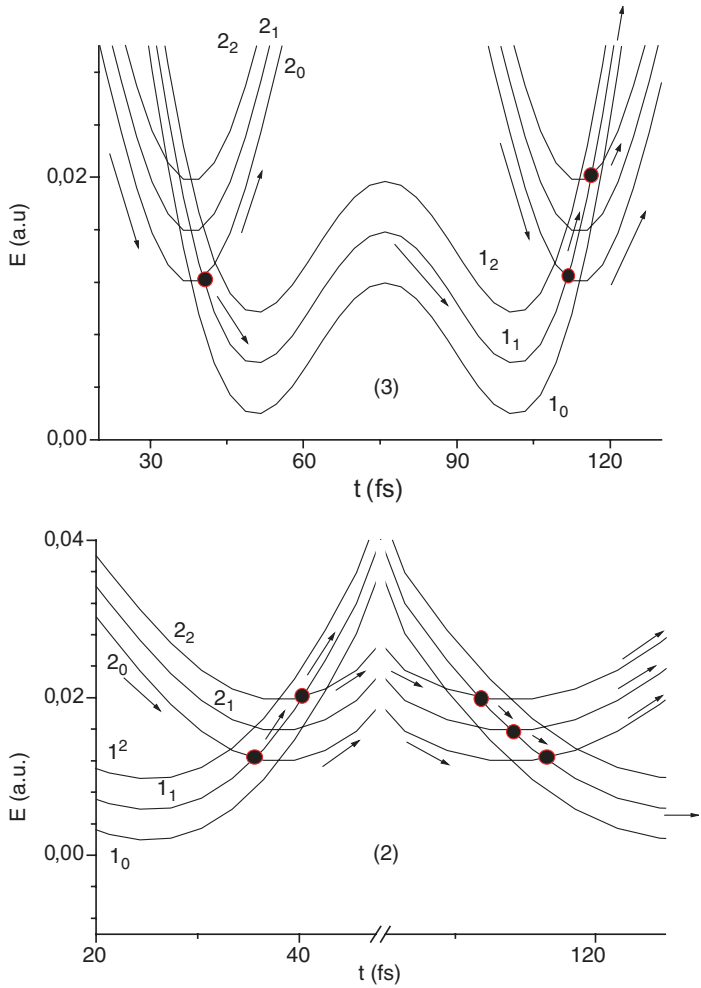

Fig. 6. The time-dependent energies of the first three vibrational levels of the coupling oscillator on the two diabatic surfaces according to the MTDM (see text). The numbering in the two panels refers to the initial conditions of Fig. 1(c). As explained in the text, the plotted energies are obtained considering that the motion along the tuning oscillator is a classical trajectory on the initial diabatic surface. As in Fig. 2, the points are placed at the crossing which are relevant for the selected initial condition, while the arrows indicate possible paths.

surface). The figures reported in Ref. 24 show that for all three the decay of the population of the upper adiabatic state is rapid. Already after the first passage the decay is almost complete, albeit some small amplitude oscillations persist. These are more pronounced for NO_2, which can be explained taking into account that this is the case in which the wavepacket travels across the conical intersection with higher kinetic energy. This favors the permanence on the initial diabatic state (hence the transition to the lower adiabatic state) at the first passage, but does the same at the second passage (which means that it may jump back to the excited adiabatic states). It is also worthwhile to remind here that more recent calculations on NO_2 with improved surfaces show that the oscillations are very pronounced in the adiabatic populations, while they are practically absent in the diabatic ones.[25,26]

As a general trend, one observes that, when the coupling is sufficiently strong, increasing the number of tuning oscillators increases the adiabaticity, i.e. the wavepacket jumps rapidly down and then tends to get trapped on the lower adiabatic surface. This is beautifully illustrated from the various calculations on the benchmark example of pyrazine by the Munich and Heidelberg groups, with an increasing number of modes. If only the coupling mode (v_{10a}) is considered, there is practically no decay of the population of the initial adiabatic state, while the inclusion of a tuning mode (v_{6a}) gives rise to a fast decay with some small amplitude persistent oscillations.[2] The further inclusion of an additional tuning mode (v_1) strongly suppresses the oscillations,[2] while model calculations on systems with four[27] or more modes[28] show that the adiabatic population relaxes to zero. A look at the behavior of the dipole autocorrelation function obtained via approximate computations with all the 24 modes of pyrazine (through a path-integral[29,30] or a self-consistent, time-dependent Hartree approach[31]) can only give an indirect confirmation of a general trend, since the direct evaluation of adiabatic populations cannot be attempted.

The role of the coupling strength may be better understood by looking at the spreading of the wavepacket along the coupling oscillator as a function of the coupling. After a threshold value, which can be estimated to be $\lambda \geq 3\hbar\omega_c$,[21] two well-separated minima appear in the lower adiabatic surface, on opposite sides of the CI. These minima, which act as a trap for the wavepacket, are sufficiently far away from the CI, in such a way that the effective non-adiabatic coupling is strongly reduced. The interstate coupling then basically determines the time behavior of diabatic

and adiabatic populations. At low values of λ (diabatic regime), the diabatic populations vary smoothly, while the adiabatic ones exhibit an oscillatory behavior, while at the opposite limit (adiabatic regime), the reverse is observed. In the middle region, both populations have more or less pronounced oscillations.

3.3. *Initial Conditions and the Geometric Setup of Surfaces*

Since, as previously discussed, the population of the bright diabatic state can be monitored by looking at the time-dependent fluorescence signal, it is useful to check if one can extract in this way some information on the relative position of the crossing surfaces with respect to the ground state minimum, which may be of value when there are no reliable computations at our disposal. What happens during the first period of the tuning oscillator is particularly interesting, since it may be often analyzed in terms of a pair of modes, the coupling mode and a single tuning mode suitably chosen to reproduce the initial motion of the wavepacket on the bright diabatic state (hence it may be a collective coordinate, in the case of several tuning modes). It is also interesting to notice that, due to the short time of propagation, it is possible to use approximate arguments as the previously discussed MTDM, to rationalize the results of calculations. In fact, as discussed in Ref. 23, the general behavior after the first passage is reproduced quite well from the MTDM, while also the behavior after the first period is reproduced in its main features. Two general rules emerge from the perusal of the first period behavior of diabatic populations, which applies, for $\lambda > \omega_c$, when the crossing between the two diabatic surfaces occurs not far from the minimum of the upper one (in our example it is just at the minimum) and the initial conditions are such that the vertically excited wavepacket travels through the CI with a sufficient kinetic energy. These rules are:

(a) after the first passage, the wavepacket is found prevalently on the lower adiabatic surface, no matter where it was initially;
(b) after the first period of the tuning oscillator, the population of the initial diabatic state is almost completely recovered for cases Ul and Ll while it is distributed between the two states in the cases Uu and Lu.

The rule (a) is particularly interesting for the Ll, case, since the population remains basically trapped on the lower adiabatic surface. This, in turn,

implies that strong non-adiabatic effects can be observed, for example in the absorption spectrum, without a corresponding radiationless decay. This has been predicted by Müller and Köppel for the $^1B_1 \rightarrow {}^1A_2$ transition in SO_2.[32]

Rule (b) can be useful as a guide to interpret time-dependent fluorescence following femtosecond excitation in system with a CI. As a first possibility, we consider that of a CI of the bright state with the (dark) ground state. It is clear that the only relevant case is Uu, which means that already at the end of the first period of the tuning oscillator a significant decay of the fluorescence signal is observed. Hence, extrapolating, one expects a rapid fluorescence decay. The case where both the crossing diabatic states are excited is by far richer, since all the four cases of Fig. 1(c) can be realized. By the same arguments, one can argue that a rapidly damped fluorescence signal may be interpreted as an indication that the geometric setup is either due to Uu or Lu (i.e. the wavepacket is initially on the excited adiabatic surface), while a fluorescence exhibiting persistent oscillations may support a Ul or Ll disposition (initial wavepacket on the lower adiabatic surface). This could be the case of some triphenylmethane dyes[33] and charge transfer complexes.[34]

4. Model Studies of Photoisomerization Occurring via a CI

Diabatic states are smoothly dependent on nuclear coordinates, which means that they basically refer to the same electronic structure, i.e. in a chemical sense no bond rearrangement occurs when nuclei move. This is, instead, what may happen when a pair of diabatic surfaces cross each other, with a probability depending on the kinematics of the nuclear wavepacket as well as on the diabatic coupling strength. If the latter is too strong, then the wavepacket moves along the adiabatic surface, i.e. jumps from a diabatic surface to the other. The above practically means that there is not really a competition between different channels. The latter often happens, instead, at CI's, since they are loci of points where not only the diabatic surfaces intersect but also the diabatic coupling vanishes. In fact, in recent years, there has been a growing amount of accurate *ab initio* computations showing that CI's are often associated with the opening of competing photochemical channels.[35,36] It is then useful to investigate simple dynamical models of chemical reactions occurring at a CI. This can

be accomplished by extending the previous basically harmonic model to include a large amplitude (and then necessarily not harmonic) tuning mode. Having in mind the cis-trans isomerization of ethylene derivatives, in which the near degeneracy of S_0 and S_1 states is basically obtained by a twisting around the double bond, Seidner and Domcke[27] investigated numerically the following model Hamiltonian (for up to four modes):

$$H = \begin{pmatrix} H_{11} & \lambda Q_c \\ \lambda Q_c & H_{22} \end{pmatrix} \tag{11}$$

$$\begin{aligned} H_{\alpha\alpha} &= E_\alpha + \left[V^{(\alpha)}(\phi) - \frac{\hbar^2}{2I_\phi} \frac{\partial^2}{\partial \phi^2} \right] + \left[\frac{\omega_c}{2} Q_c^2 - \hbar\omega_c \frac{\partial^2}{\partial Q_c^2} \right] \\ &\quad + \sum_j \left(\frac{1}{2} \omega_j Q_j^2 + g_j^{(\alpha)} Q_j - \hbar\omega_j \frac{\partial^2}{\partial Q_j^2} \right) \end{aligned} \tag{12}$$

where ($\alpha = 1, 2$).

In the above equation, ϕ is the torsional angle describing twisting, I_ϕ its reduced moment of inertia and $V^{(\alpha)}(\phi)$ is the corresponding periodic potential for the diabatic state α. (For simplicity, frequencies have been considered identical for the two diabatic states). The basic aspects of the problem can be recovered by considering only the leading terms in the Fourier expansion of $V^{(\alpha)}(\phi)$:

$$V^{(\alpha)} = A^{(\alpha)} + \frac{1}{2} B^{(\alpha)} [1 - \cos(n\phi)], \tag{13}$$

where $A^{(\alpha)}$ and $B^{(\alpha)}$ are constants and $n = 1, 2$ (giving rise to a $2\pi/n$ periodic system).

The numerical results from the wavepacket propagation[2,27] illlustrate dramatically the complete and irreversible spreading of the torsional wavepacket in all the accessible coordinate region, which can be attributed not only to the possibility of jumping from a diabatic surface to the other, but also to the dephasing induced by the strong mode-mode coupling present in the adiabatic surfaces, close to the CI region. The numerical investigation also clearly shows that, despite the irreversible behavior, the torsional wavepacket does not localize at the minima of the lower adiabatic surface. This is essentially due to the fact that the irreversibility is mainly due to vibrational dephasing, while there is no significant energy flow out of the torsional mode. Hence the model is not useful to investigate the problem of branching between isomers.

4.1. *How to Deal with Irreversibility?*

As previously mentioned, including more and more tuning modes is a way for introducing irreversibility. The problem is that exact quantum mechanical calculations cannot be performed when the number of nuclear degrees of freedom becomes too large, since the computational effort scales as n^2, where n is the total number of vibronic states needed. It is to remember that, due to the fact that the basis set is built up as a tensor product, if one adds a further oscillator, requiring m states, the total number of states is multiplied by m. Various strategies can be elaborated to overcome this problem through approximate calculations, as recently reviewed.[2] Among the most effective approaches, we mention that of treating exactly the two or three most relevant modes, while making recourse to a time-dependent Hartree approach for the other tuning oscillators, as in the two-state two-oscillator modeling of rhodopsin by Hahn and Stock.[37,38] Taking a single configuration and considering a harmonic bath, the evolving wavepacket is built by a product of gaussian wavepackets, expressed in terms of classical trajectories, momenta and actions.[39] This approximate approach scales as f and then offers interesting computational opportunities, as demonstrated by the 25-mode model of rhodopsin built up by the authors, and the further inclusion of a bath of hundred harmonic oscillators, introduced to simulate the coupling with the protein environment.[38]

A different way for dealing with dissipation in the case of the benchmark example of pyrazine has been explored in Ref. 40. The authors consider two relevant modes, the coupling mode Q_{6a} and a single tuning mode, Q_{10a}, and project out the others, working with a multilevel Redfield master equation for the reduced density matrix in the eigenstate basis set. Their numerical results show that the population decay becomes bimodal. The fast component, mainly due to the two modes included, remains quite insensitive to the coupling with the bath of other modes. These, instead, are quite effective in suppressing the tails of oscillations and driving towards zero the population of the adiabatic excited state. The diabatic population of the initially excited diabatic state, instead, never goes to zero in this example.

4.2. *The Solvent Role: A Stochastic Model for CT Associated with Large Amplitude Motions*

The irreversibility may arise from the coupling to a manifold of other modes, some of which may be intramolecular, while others may involve the solvent.

This is typically the case for the torsional motion which can dissipate its high initial energy to overcome the friction of solvent molecules. The purely quantum mechanical approach considered above is not suitable for dealing with many modes, for computational reasons. One possibility is to switch to a stochastic model. As an example, let us consider the case of the negative ion of a molecule obtained joining two identical moieties (as a biphenyl or another diaryl species) in which the extra electron can jump between the two subunits (aromatic rings)[41,42] and consider the following model with two diabatic states and two modes (which is essentially the model introduced by Fulton and Gouterman several years ago to treat the excited states of symmetrical dimers[43]):

$$H = \begin{pmatrix} H_{11} & th\ \cos(\phi) \\ th\ \cos(\phi) & H_{22} \end{pmatrix} \tag{14}$$

where:

$$\begin{aligned} H_{11} &= \hat{T}(\phi, Q_1, Q_2) + \frac{\hbar\omega}{2}Q_1^2 - \lambda Q_1 + \frac{\hbar\omega}{2}Q_2^2\,, \\ H_{22} &= \hat{T}(\phi, Q_1, Q_2) + \frac{\hbar\omega}{2}Q_1^2 + \frac{\hbar\omega}{2}Q_2^2 - \lambda Q_2\,, \end{aligned} \tag{15}$$

and:

$$\hat{T}(\phi, Q_1, Q_2) = -\frac{\hbar^2}{2I_\phi}\frac{\partial^2}{\partial\phi^2} - \hbar\omega\frac{\partial^2}{\partial Q_1^2} - \hbar\omega\frac{\partial^2}{\partial Q_2^2}. \tag{16}$$

Here ϕ is the coordinate describing the torsion of one ring with respect to the other and triggering the electron hopping, th, while Q_1 and Q_2 are identical modes of the two moieties, whose equilibrium position depends on the extra charge. Introducing the symmetric and antisymmetric coordinates $Q_{s,a} = \frac{1}{\sqrt{2}}(Q_1 \pm Q_2)$ reduces the problem to two dimensions. The symmetric coordinate, in fact, is identically displaced in the two states and can then be disregarded, since it does not play any role in the dynamics. The next step consists in introducing symmetric and antisymmetric electronic (diabatic) states to get the following transformed Hamiltonian:

$$H' = \begin{pmatrix} \hbar\frac{\omega_a}{2}Q_a^2 - \frac{\hbar^2}{2I_\phi}\frac{\partial^2}{\partial\phi^2} + th\cos(\phi) & \lambda Q_a \\ \lambda Q_a & \hbar\frac{\omega_a}{2}Q_a^2 - \frac{\hbar^2}{2I_\phi}\frac{\partial^2}{\partial\phi^2} - th\cos(\phi) \end{pmatrix} \tag{17}$$

which has now the familiar form of a conical intersection problem (the CI point is at $\phi = \pm\pi/2,\ Q_a = 0$). If $\lambda \ll \hbar\omega_a$, one can assume that the dynamics along the Q_a coordinate involves only the vibrational ground state, as far

as the diabatic ground state is concerned, and the first excited state for the diabatic excited state. Hence, the diabatic coupling can be approximately be taken to be a constant, which transforms the above two-dimensional problem into a one-dimensional one involving an avoided crossing between two adiabatic curves.

The dynamics following the vertical excitation of the vibrational ground state wavepacket localized near $\phi = 0$ up to the excited adiabatic curve has been studied by a fully quantum mechanical approach.[42] The result (see Fig. 7) is that the population remains trapped in the excited state, which can be interpreted as due to the fact that the wavepacket travels too quickly through the region where the non adiabatic coupling is stronger (i.e. near $\phi = \pm 90°$). This is due to the absence of nuclear degrees of freedom capable of accepting the high energy of the torsion. This is precisely the role of the solvent, which can be mimicked through a stochastic approach. This can be accomplished by admitting that the process can be described by a probability distribution for the torsional coordinate, $P(\phi, t)$, whose time-space behavior is determinded by a Fokker–Planck equation.[44] The above means that it undergoes a diffusive motion in the presence of the external force due to the potential energy along ϕ in the excited adiabatic state $E(\phi)$. The occurrence of transitions (here assumed to be irreversible) to the lower adiabatic state is described by a ϕ-dependent rate $k(\phi)$, which can be estimated from exact quantum mechanical calculations on the initial-time behavior of a wavepacket sharply localized at each value of ϕ.[42] The Fokker–Planck equation:

$$\frac{\partial P(\phi,t)}{\partial t} = \left\{ D_R \frac{\partial}{\partial \phi} \left[\frac{1}{k_B T} \frac{\partial E(\phi)}{\partial \phi} + \frac{\partial}{\partial \phi} \right] - k(\phi) \right\} P(\phi, t) \qquad (18)$$

can be solved numerically by expanding the probability distribution in a suitable basis set. The numerical results (Fig. 7) show that now the excited-state population decays, with some time delay depending on the value assumed for the diffusion constant (i.e. for a given molecular system, on the solvent). This delay is clearly due to the time required to reach the region where the non-adiabatic coupling is stronger. It is also interesting to notice[42] that if the torsion is blocked, for example by a saturated chain connecting the rings, the excited state does not decay appreciably. The above is also a suggestive, albeit qualitative, explanation of the fact that apparently similar dye anions have a fluorescence quantum yields close to unity if the

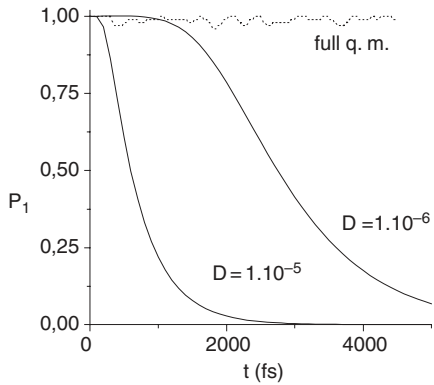

Fig. 7. The time-dependent population of the upper adiabatic state, as computed from the Fokker–Planck equation (see text) for two different values of the diffusion constant D at $T = 298\,\mathrm{K}$. The other parameters in Eq. (17) are: $I_\phi = 5.0154\,10^5$ a.u. (a typical value for the reduced momentum of inertia of a substituted benzene ring); $\omega_a = 1500\,\mathrm{cm}^{-1}$; $\lambda = 100\,\mathrm{cm}^{-1}$. The exact, full quantum mechanical result for the case without coupling to the solvent is also reported.

rings are rigid, while they undergo an efficient radiationless decay if there is the possibility of large amplitude torsions.[45,46]

The question concerning the adiabatic versus the diabatic picture, discussed in Sec. 3.1, can be enriched by arguments that come into play when dealing with the problem of the interaction with the surroundings and its role for the dynamics around a conical intersection. In some cases, it appears that the solvent has mainly the role of a viscous medium which damps the large-amplitude motions that would be present in the free molecule. It is clear that in such cases the adiabatic representation is privileged, since a large fraction of the kinetic energy is rapidly lost. In many other cases, however, the diabatic picture is more convenient, for computational as well as physical reasons. This happens, for example, for CIs related to charge-transfer processes in polar solvents. The interaction, in fact, depends essentially on the dipole moment (we do not consider here specific interactions such as the hydrogen bond), which as almost every observable whose character is mainly electronic, is better described in terms of diabatic states. So, if the system under study is one in which the jump from a diabatic state to the other is associated with a large dipole change (as in the charge-transfer systems having special interest in biological systems and in material

science), one expects that the solvent results in fluctuations of the diabatic electronic energies. It is then clear that in such cases the role of the solvent can be better modeled in terms of diabatic states. It is interesting to notice that, in a sense, every time the system is interrogated about its electronic state, either by an external electromagnetic field (which may be the vacuum field, in the case of spontaneous emission) or by a static field (due to a polar solvent), its response is in terms of diabatic states. This is of course an important physical point in favor of the diabatic representation.

5. Concluding Remarks

We hope that the present contribution, albeit limited to a restricted range of arguments and examples, may have convinced the reader of the important role played by the investigation of simple model systems in our understanding of the dynamics at a CI. There are several important points, of course, that have been either only marginally touched or ignored, for reasons of space. Among those that merit further attention, we want to mention the role of the external medium, which may be crucial especially in large and biological molecules, and the development of qualitative methods to predict the location of CIs in organic molecules of photochemical interest,[47,48] which may be of great help also for experimentalists. The general understanding of the role of the topological features of the CI,[49] as well as of the crossing of seams of different symmetry,[50] which may deeply influence the wavepacket propagation in high-symmetry molecular systems, are also goals that can be pursued through model calculations.

Acknowledgment

We wish to thank Dr. Alessandro Ferretti for the many animated and stimulating discussions on the whole subject of conical intersections.

References

1. H. Köppel, W. Domcke, and L. S. Cederbaum, *Adv. Chem. Phys.* **57**, 59 (1984).
2. W. Domcke and G. Stock, *Adv. Chem. Phys.* **100**, 1 (1997).
3. H. Köppel and W. Domcke, *Encyclopedia of Computational Chemistry*, Eds. P. von Ragué Schleyer *et al.* (Wiley, N.Y., 1998).
4. A. Ferretti, A. Lami and G. Villani, *Chem. Phys.* **196**, 447 (1995).

5. G. H. Golub and C. F. Van Loan, *Matrix Computations* (North Oxford Academic, London, 1986).
6. L. D. Landau, *Phys. Zts. Sowiet*, **2**, 46 (1932).
7. C. Zener, *Proc. Roy. Soc.* **A137**, 696 (1932).
8. A. Ferretti, G. Granucci, A. Lami, M. Persico and G. Villani, *J. Chem. Phys.* **104**, 5517 (1996).
9. A. Ferretti, A. Lami and G. Villani, *J. Chem. Phys.* **106**, 934 (1997).
10. A. Ferretti, A. Lami and G. Villani, *J. Chem. Phys.* **107**, 3948 (1997).
11. P. Cattaneo and M. Persico, *J. Phys. Chem.* **A101**, 3454 (1997).
12. R. Schneider, W. Domcke and H. Köppel, *J. Chem. Phys.* **92**, 1045 (1990).
13. A. Ferretti, A. Lami and G. Villani, *J. Chem. Phys.* **109**, 9002 (1998).
14. A. Lami, Conference Proceeding of: *Atoms, Molecules and Quantum Dots in Laser Fields: Fundamental Processes*, Eds. N. Bloembergen, N. K. Rahman and A. Rizzo (SIF, Bologna, 2001) p. 145.
15. M. Baer, *Phys. Rep.* **358**, 75 (2002).
16. J. C. Tully, *J. Chem. Phys.* **93**, 1061 (1990).
17. T. J. Martínez, M. Ben-Nun and R. D. Levine. *J. Phys. Chem.* **101**, 6389 (1997), and references therein.
18. F. Santoro, C. Petrongolo and A. Lami, *J. Chem. Phys.* **113**, 4073 (2000).
19. D. O. Harris, G. G. Engerholm and W. D. Gwinn, *J. Chem. Phys.* **43**, 1515 (1965).
20. J. C. Light, I. P. Hamilton and J. V. Lill, *J. Chem. Phys.* **82**, 1400 (1985).
21. U. Manthe and H. Köppel, *J. Chem. Phys.* **93**, 345 (1990); ibid **93**, 1658 (1990).
22. H. D. Meyer and H. Köppel, *J. Chem. Phys.* **81** 2605 (1984).
23. A. Ferretti, A. Lami and G. Villani, *J. Chem. Phys.* **111**, 916 (1999).
24. R. Schneider, W. Domcke and H. Köppel, *J. Chem. Phys.* **92**, 1045 (1990).
25. F. Santoro, C. Petrongolo, G. Granucci, M. Persico, *Chem. Phys.* **259**, 193 (2000).
26. S. Mahapatra, H. Köppel, L. S. Cederbaum, P. Stampfuss, W. Wentzel, *Chem. Phys.* **259**, 211 (2000).
27. L. Seidner and W. Domcke, *Chem. Phys.* **186**, 27 (1994).
28. G. Stock, *J. Chem. Phys.* **103**, 10015 (1995).
29. S. Krempl, M. Winterstetter, H. Plöhn and W. Domcke, *J. Chem. Phys.* **100**, 926 (1994).
30. S. Krempl, M. Winterstetter and W. Domcke, *J. Chem. Phys.* **102**, 6499 (1995).
31. G. A. Worth, H.-D. Meyer and L. S. Cederbaum, *J. Chem. Phys.* **109**, 3518 (1998).
32. H. Müller and H. Köppel, *Chem. Phys.* **183**, 107 (1994).
33. A. Mokhtari, A. Chebira and J. Chesnoy, *J. Opt. Soc. Am.* **B7**, 1551 (1990).
34. I. V. Rubitsov and K. Yoshihara, *J. Phys. Chem.* **101**, 6938 (1999).

35. M. Garavelli, P. Celani, M. Fato, M. J. Bearpark, B. R. Smith, M. Olivucci and M. A. Robb, *J. Phys. Chem.* **101**, 2023 (1997).
36. F. Bernardi, M. Olivucci and M. A. Robb, *J. Photochem. Photobiol.* **A105**, 365 (1997).
37. S. Hahn and G. Stock, *J. Phys. Chem.* **B104**, 1146 (2000).
38. S. Hahn, G. Stock, *Chem. Phys.* **259**, 297 (2000).
39. E. J. Heller, *J. Chem. Phys.* **62**, 1544 (1975).
40. A. Kühl and W. Domcke, *Chem. Phys.* **259**, 227 (2000).
41. A. Ferretti, A. Lami and G. Villani, *Chem. Phys.* **259**, 201 (2000).
42. A. Ferretti, A. Lami and G. Villani, *Adv. Quant. Chem.* **36**, 283 (1999).
43. R. L. Fulton and M. Gouterman, *J. Chem. Phys.* **35**, 1059 (1961); ibid **41**, 2280 (1964).
44. N. G. Van Kampen, *Stochastic Processes in Physics and Chemistry*, (North-Holland, Amsterdam, 1981).
45. Y. Nagasawa, Y. Ando, D. Kataoka, H. Matsuda, H. Kiyasaka and T. Okada, *J. Phys. Chem.* **A106**, 2024 (2002) and references therein.
46. M. M. Martin, P. Plaza, P. Changenet and Y. H. Meyer, *J. Photochem. Photobiol.* **A105**, 197 (1997).
47. Y. Haas and S. Zilberg, *J. Photochem. Photobiol.* **A144**, 221 (2001) and references therein.
48. W. Fuß, Y. Haas and S. Zilberg, *Chem. Phys.* **259**, 273 (2000).
49. D. R. Yarkony, *J. Chem. Phys*, **114**, 2601 (2001).
50. D. R. Yarkony, *J. Phys. Chem.* **A105**, 6277 (2001).

CHAPTER 9

GENERIC ASPECTS OF THE DYNAMICS AT CONICAL INTERSECTIONS: INTERNAL CONVERSION, VIBRATIONAL RELAXATION AND PHOTOISOMERIZATION

Wolfgang Domcke

Institute of Physical and Theoretical Chemistry,
Technical University of Munich,
D-85747 Garching, Germany

Contents

1. Introduction

In this chapter we survey characteristic features of time-dependent quantum wave-packet dynamics on conically intersecting potential-energy (PE) surfaces. The focus will be on the fully microscopic description of nontrivial dynamical processes such as ultrafast internal conversion and photoisomerization, as well as vibrational energy redistribution and dephasing. The quantum dynamics calculations discussed in this chapter are

partly based on generic simplified models of conically intersecting surfaces, and partly on *ab initio* surfaces for specific systems. We shall exclude from the present discussion more or less direct photodissociation processes on conically intersecting PE surfaces of small systems, e.g. triatomics. Direct photodissociation dynamics on coupled surfaces is discussed in Chapter 11.

Early attempts to treat the dynamics at conical intersections were based on the Landau–Zener–Stückelberg approach.[1−3] While the Landau–Zener–Stückelberg model[4,5] provides a transparent picture for one-dimensional avoided-crossing situations, its generalization to multi-dimensional nuclear motion is nontrivial, and no quantitative results for electronic population probabilities or transition rates have been obtained in these early studies.

In an alternative approach, exact (numerical) time-dependent quantum wave-packet methods have been employed since the early eighties of the last century to explore the dynamics of *ab-initio*-based models of conical intersections, see Refs. 6–8 for reviews. It has been found by these calculations that the fundamental dissipative processes of population and phase relaxation at femtosecond time scales are clearly expressed already in few-mode systems, if a directly accessible conical intersection of the PE surfaces is involved. The results strongly support the idea that conical intersections provide the microscopic mechanism for ultrafast relaxation processes in polyatomic molecules.[6−8] More recently, these calculations have been extended to describe photodissociation[9−11] and photoisomerization[12,13] processes associated with conical intersections. The latter are particularly relevant for our understanding of the elementary mechanisms of photochemistry.[14]

It is suggested by these studies of representative models that ultrafast internal conversion through a conical intersection typically involves only a few strongly coupled vibrational modes, even in larger molecules with many vibrational degrees of freedom. The ultrafast internal-conversion process thus results in a pronounced nonequilibrium distribution of the vibrational energy. The coupling of the active modes of the conical intersection with the many inactive modes and possibly the environment will cause vibrational energy redistribution, typically on a subpicosecond time scale. Several attempts have been described in the recent literature to account for this phenomenon. One possibility is the solution of

the time-dependent Schrödinger equation for truly multidimensional systems, employing efficient numerical techniques (see Chapter 14). Using the MCTDH method,[15] Meyer and collaborators have computed the absorption spectrum of the S_1-S_2 conical intersection in pyrazine for a vibronic-coupling model which includes all 24 vibrational modes of this molecule.[16] Alternatively, the Feynman path-integral formalism has been adapted for the study of vibronic-coupling models of arbitrary dimension.[17] Computationally efficient classical or semi-classical models of electronically nonadiabatic dynamics have been developed and applied to the investigation of the effect of vibrational energy redistribution on the electronic decay dynamics at conical intersections (see Chapter 15). Finally, the well-known system-bath formulation and reduced density-matrix theory[18] can be used to describe the effect of a dissipative environment on the dynamics at a conical intersection.[19] The latter relatively simple approach is adequate when the relaxation effects caused by the system-bath interaction are slow relative to the ultrafast dynamics driven by the active modes of the conical intersection and if the bath correlation time is short.

Although much progress has been made in recent years with *ab initio* electronic-structure theory and the efficient interpolation of multidimensional potential functions, the selection of the relevant coordinates, the construction of a diabatic representation (see Chapter 4) and the analytic modeling of potential functions of conical intersections in polyatomic molecules (see Chapter 5) represent major bottlenecks in the theoretical treatment of photochemical dynamics. In principle, one can try to avoid these bottlenecks by evaluating the potentials and the derivative couplings at every point where they are required in a classical or quantum dynamical calculation. Several attempts combining this "on the fly" approach with classical surface-hopping trajectory calculations or similar trajectory-based methods for conical intersections have been reported in the recent literature.[20–23] Serious obstacles encountered in this type of approach are the immense cost of these calculations, if reasonably accurate *ab initio* methods are to be employed, the phase problem of electronic wave functions in the presence of intersections, and the development of quantitatively accurate surface-hopping prescriptions. Nevertheless, the development of full-dimensional on-the-fly methods for the dynamics at conical intersections will continue to be an active area of research in the future.

2. Time-Dependent Quantum Wave-Packet Dynamics and Reduced Density-Matrix Dynamics

The dynamics of an isolated molecular system, prepared in a nonstationary state $|\Psi(0)\rangle$ by a short laser pulse, is governed by the time-dependent Schrödinger equation

$$i\hbar\,\partial/\partial t|\Psi(t)\rangle = H_M|\Psi(t)\rangle \tag{1}$$

where $H_M = T_N + H_{el}$ is the molecular Hamiltonian, T_N being the nuclear kinetic-energy operator.

The most straightforward numerical technique for the solution of Eq. (1) is based on the expansion of the state vector $|\Psi(t)\rangle$ in a complete set of time-independent basis functions. Such a complete basis can be constructed as the direct product of diabatic electronic basis states $\{|\Phi_n\rangle\}$ and suitable orthonormal states $\{|\chi_{\nu j}\rangle\}$ for each nuclear degree of freedom (see Chapter 7)

$$|\Psi(t)\rangle = \sum_n \sum_{\nu_1\nu_2\ldots} C_{n,\nu_1,\nu_2,\ldots}(t)|\Phi_n\rangle|\chi_{\nu 1}\rangle|\chi_{\nu 2}\rangle\cdots \tag{2}$$

This expansion converts the time-dependent Schrödinger Eq. (1) into a set of coupled first-order differential equations

$$i\hbar\dot{\boldsymbol{C}}(t) = \boldsymbol{H}\boldsymbol{C}(t), \tag{3}$$

where $\boldsymbol{C}(t)$ is the vector of expansion coefficients in Eq. (2) and $\boldsymbol{H}$ is the corresponding matrix representation of the Hamiltonian. Equation (3) can be solved by a variety of standard or specialized numerical algorithms.[24–26]

There are various options concerning the choice of basis functions or grid representations of the wave function or combinations of both (the so called discrete-variable representation). For a discussion of these technical aspects we refer to Chapters 7, 11, 13 and 14 and earlier literature.[6,7,26,27]

As mentioned in the introduction, only few vibrational degrees of freedom are usually actively involved in the ultrafast dynamics at the conical intersection. To account for the effect of energy transfer from the active modes to the many inactive modes of the polyatomic molecule or a condensed-phase environment, the reduced-density-matrix formalism may

be employed. The molecular Hamiltonian is written as

$$H_M = H_S + H_B + H_{SB}, \tag{4}$$

where H_S represents a few-mode model of a conical intersection, H_B stands for a harmonic vibrational bath, and H_{SB} is the (usually bilinear) system-bath coupling. The standard approximations of quantum relaxation theory[18] yield an effective equation of motion for the reduced density operator, defined as

$$\sigma(t) = \mathrm{tr}_B\{\rho(t)\}, \tag{5}$$

where $\rho(t)$ is the full time-dependent density operator and tr_B denotes the trace over the bath variables. In the eigenstate representation of the system Hamiltonian

$$H_s|\Psi_\nu\rangle = E_\nu|\Psi_\nu\rangle, \tag{6}$$

the resulting equation of motion reads[18]

$$\dot{\sigma}_{\mu\nu}(t) = -i\omega_{\mu\nu}\sigma_{\mu\nu}(t) + \sum_{\kappa\lambda} R_{\mu\nu\kappa\lambda}\sigma_{\kappa\lambda}(t) \tag{7}$$

with $\omega_{\mu\nu} = (E_\mu - E_\nu)/\hbar$. The first term of the rhs of Eq. (7) describes the time evolution of the isolated system, while the Redfield tensor $\boldsymbol{R}$ accounts for the effects of the environment. The elements of $\boldsymbol{R}$ are determined by matrix elements of the system-bath coupling operator and Laplace transforms of the bath correlation functions.[18] The procedure of the numerical solution of Eq. (7) is analogous to the solution of Eq. (3) (see Ref. 19 for more details).

3. Electronic Decay Dynamics

The quantity of primary interest for the description of radiationless electronic transitions is the time-dependent population probability of excited electronic states. The population $P_n^d(t)$ of the nth diabatic electronic state is defined as the expectation value of the projection operator

$$\hat{P}_n^d = \left|\Phi_n^d\right\rangle\left\langle\Phi_n^d\right|, \tag{8}$$

i.e.

$$P_n^d(t) = \langle\Psi(t)|\hat{P}_n^d|\Psi(t)\rangle. \tag{9}$$

The superscript "d" refers to the fact that the projector (8) is defined in the diabatic electronic representation. Alternatively, we may consider the

time-dependent population of adiabatic electronic states, i.e.

$$P_n^a(t) = \langle \Psi(t) | \hat{P}_n^a | \Psi(t) \rangle, \tag{10}$$

$$\hat{P}_n^a = |\Phi_n^a\rangle\langle\Phi_n^a|. \tag{11}$$

Equivalently, these electronic population probabilities may be expressed as the integral of the nuclear probability density over all nuclear degrees of freedom, i.e.

$$P_n^d(t) = \int dR_1 \int dR_2 \int dR_3 \cdots |\Psi_n^d(R_1, R_2, R_3, \ldots, t)|^2, \tag{12}$$

$$P_n^a(t) = \int dR_1 \int dR_2 \int dR_3 \cdots |\Psi_n^a(R_1, R_2, R_3, \ldots, t)|^2, \tag{13}$$

where

$$\Psi_n^d(t) = \langle \Phi_n^d \mid \Psi(t) \rangle \quad \text{and} \quad \Psi_n^a(t) = \langle \Phi_n^a \mid \Psi(t) \rangle.$$

From Eqs. (12) and (13) it is obvious that the electronic populations are just the diagonal elements of the electronic reduced density matrix, defined as the trace of the complete density matrix over the nuclear degrees of freedom.

Since $\hat{P}_n^d$ commutes with the molecular Hamiltonian in the absence of electronic inter-state couplings, $P_n^d(t)$ becomes a constant of motion in this limit. Correspondingly, $P_n^a(t)$ becomes a constant of motion if the nonadiabatic coupling operators are neglected. The populations $P_n(t)$ are thus a direct measure of nonadiabatic transitions in either the diabatic or the adiabatic representation.[6]

In the case of open-system dynamics, assuming weak coupling of the conical intersection with an environment, the time evolution of the system is determined by the Redfield Eq. (7) for the reduced density matrix. In this case, the time-dependent population probabilities of diabatic and adiabatic states are given by

$$P_n^d(t) = \mathrm{tr}\Big\{ \hat{P}_n^d \sigma(t) \Big\}, \tag{14}$$

$$P_n^a(t) = \mathrm{tr}\Big\{ \hat{P}_n^a \sigma(t) \Big\}. \tag{15}$$

Given either the coefficient vector $\boldsymbol{C}(t)$ [representing the time-dependent wave function in the direct-product basis according to Eq. (2)] or the reduced density matrix $\sigma(t)$ (representing the reduced density operator in

the system eigenstate basis), the population probabilities of adiabatic or diabatic electronic states can straightforwardly be calculated.

The transition rate out of the electronic state n (in either the diabatic or adiabatic representation) is given by

$$k_n(t) = -\dot{P}_n(t)/P_n(t). \tag{16}$$

In a nonperturbative treatment of radiationless decay, $P_n(t)$ is generally not simply an exponential function; the nonperturbative rate $k_n(t)$ is thus time-dependent. It should be stressed that $P_n(t)$ and thus $k_n(t)$ can be measured explicitly, at least in principle, in a femtosecond time-resolved experiment. There is thus no need to invoke a long-time limit or to perform an average over time to obtain time-independent rates.

The population probabilities $P_n(t)$ defined in Eqs. (8)–(13) should not be confused with the population probabilities which have been considered in the extensive earlier literature on radiationless transitions in polyatomic molecules, see Refs. 28 and 29 for reviews. There the population of a single "bright" (i.e. optically accessible from the electronic ground state) zero-order Born–Oppenheimer (BO) level is considered. Here, in contrast, we define the electronic population as the sum of all vibrational level populations within a given (diabatic or adiabatic) electronic state. These different definitions are adapted to different regimes of time scales of the system dynamics. If nonadiabatic interactions are relatively weak, and radiationless transitions relatively slow, the concept of zero-order BO levels is useful; the populations of these levels can be prepared and probed using suitable laser pulses (typically of nanosecond duration). If the nonadiabatic transitions occur on femtosecond time scales, the preparation of individual zero-order BO levels is no longer possible. The total population of an electronic state then becomes the appropriate concept for the interpretation of time-resolved experiments.[30,31]

A particularly well studied example of radiationless decay through a conical intersection is the intersection of the $S_1(n\pi^*)$ and $S_2(\pi\pi^*)$ excited-state PE surfaces of pyrazine. In this molecule of high symmetry (D_{2h}), the out-of-plane mode of B_{1g} symmetry is the single normal mode which can couple the $^1B_{3u}(n\pi^*)$ and $^1\mathrm{B}_{2u}(\pi\pi^*)$ electronic states in first order. This one-dimensional vibronic-coupling problem[32] is converted into a conical intersection by the totally symmetric tuning modes ν_1 (ring stretching) and $\nu_{6\mathrm{a}}$ (ring bending), which induce symmetry-allowed intersections of

the $S_1(n\pi^*)$ and $S_2(\pi\pi^*)$ PE surfaces.[33,34] In this particular case the diabatic PE surfaces can be modeled rather accurately by a three-dimensional vibronic-coupling model, employing low-order Taylor expansions in terms of ground-state normal coordinates[6] as discussed in Chapter 7.

Improved and extended versions of this conical intersection model involving four or seven nuclear degrees of freedom have been developed.[35–37] Raab *et al.* extended these vibronic-coupling models to include all 24 normal modes of pyrazine.[16] These models have served as testbeds for the development and application of novel techniques for the treatment of multi-dimensional nonadiabatic dynamics.[38–43]

Figure 1 shows two alternative two-dimensional perspective views of the adiabatic PE surfaces of this intersection, calculated at the CASSCF level.[36] The PEs as functions of the coupling coordinate Q_{10a} and the tuning coordinate Q_1 are shown in Fig. 1(a). Figure 1(b) gives the PEs as a function of Q_{10a} and the second tuning coordinate Q_{6a}. The intersection space is a line in this three-dimensional model; it becomes an (N-2)-dimensional hypersurface in N-dimensional models. The S_1-S_2 conical intersection in pyrazine can be classified as a *nonreactive* conical intersection, since the nuclear motion remains bounded in the vicinity of the initially prepared geometry (the equilibrium geometry of the electronic ground state). Excitation of the $S_2(\pi\pi^*)$ state thus induces photophysical dynamics (internal conversion to the $S_1(n\pi^*)$ surface), but not photochemical dynamics. Conical intersections of this type have been identified and characterized in the ethylene cation,[44] the butatriene cation,[45] the ozone cation,[46] the pyrazine cation,[47] and in NO_2.[48–51]

We assume preparation of the $S_2(\pi\pi^*)$ diabatic state at $t = 0$ by an ideally short laser pulse. The ground-state vibrational wave packet is thus placed vertically on the S_2 surface. The time-dependent population probability of the thus prepared diabatic S_2 state in the three-mode model is given by the full curve in Fig. 2. It exhibits an initial decay on a time scale of ≈ 20 fs, followed by quasi-periodic recurrences of the population, which are damped on a time scale of a few hundred femtoseconds. Beyond ≈ 500 fs the S_2 population probability becomes quasi-stationary, fluctuating statistically around its long-time limit of ≈ 0.33. The dotted curve in Fig. 2 shows the time-dependent population of the adiabatic S_2 state. $P_2^a(t)$ is seen to decay even faster than $P_2^d(t)$ and to attain an asymptotic value of ≈ 0.1. 90% of the population thus relax to the S_1 state, and this happens essentially

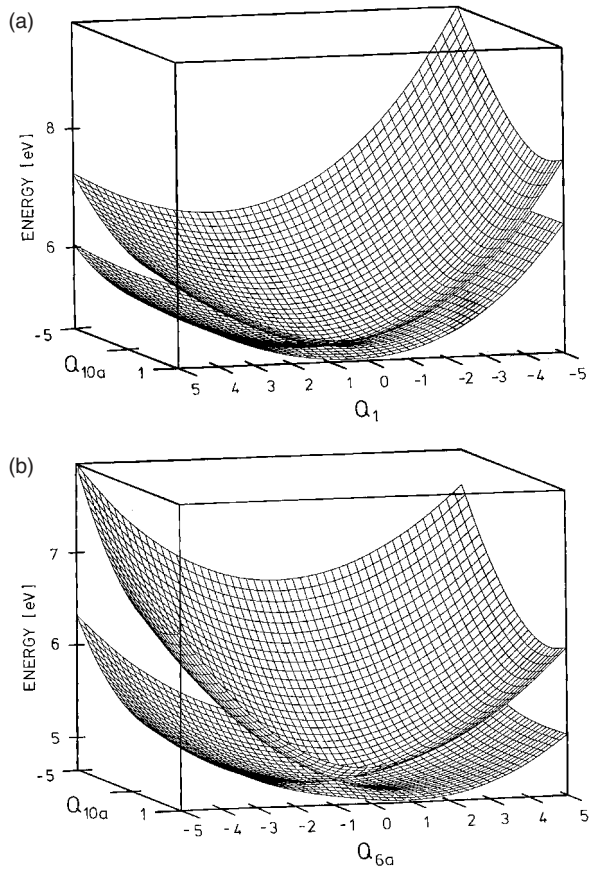

Fig. 1. (a) Conical intersection of the adiabatic S_1 and S_2 PE surfaces of pyrazine in the two-dimensional space spanned by the totally symmetric tuning coordinate Q_1 and the coupling coordinate Q_{10a}. (b) Conical intersection of the adiabatic S_1 and S_2 PE surfaces in the two-dimensional space spanned by Q_{6a} and the coupling coordinate Q_{10a}. The surfaces have been calculated at the CASSCF level.[36]

within a single vibrational period of the system. The higher asymptotic value of P_2^d can qualitatively be interpreted as representing the admixture or the upper diabatic state in the wave packet which has relaxed to the minimum of the lower adiabatic surface.[74] Note that the difference between adiabatic and diabatic population probabilities is significant, underscoring the necessity of a precise definition of the electronic population probability and transition rate in cases of ultrafast electronic decay. The question

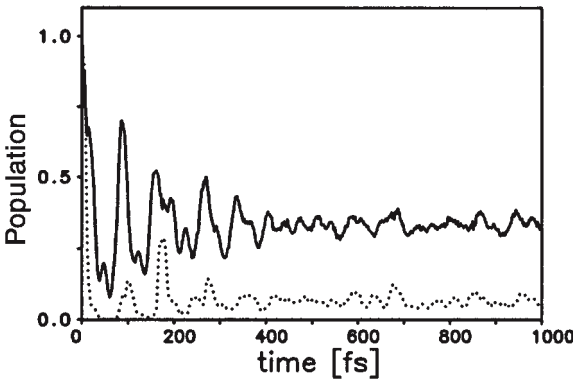

Fig. 2. Diabatic (solid line) and adiabatic (dotted line) population probability of the S_2 state for the three-mode S_1-S_2 conical intersection model of pyrazine.

of the detectability of electronic populations by femtosecond pump-probe spectroscopy is discussed in Chapter 17.

It is instructive to consider the development of the electronic decay dynamics with increasing number of nuclear degrees of freedom for this representative model. Figure 3 compares the adiabatic S_2 population probability of a one-dimensional model (coupling mode ν_{10a} only, upper panel), a two-dimensional model (ν_{10a} and tuning mode ν_{6a}, middle panel) and a three-dimensional model (ν_{10a} and two tuning modes, ν_{6a} and ν_1, lower panel). Inclusion of the coupling mode alone does not lead to any significant electronic population dynamics because of the relatively large vertical energy gap of the S_1 and S_2 states (0.9 eV). The tuning mode ν_{6a} induces a low-lying crossing of the S_1 and S_2 potentials and thus leads, together with ν_{10a}, to the formation of a conical intersection (cf. Fig. 1). It is seen that the two-dimensional conical intersection causes an ultrafast ($\sim$30 fs) initial decay of the S_2 population, followed by large irregular fluctuations. Inclusion of the second tuning mode ν_1 leads to even faster initial decay and a strong suppression of the population fluctuations. Very similar results have been obtained for a variety of systems with conical intersections, e.g. $C_2H_4^+$,[44] $C_6H_6^+$ [52] and NO_2.[50,51] In all cases that have been studied in detail, it has been found that a minimum of three strongly coupled nuclear degrees of freedom is required to obtain ultrafast irreversible decay of the electronic population.

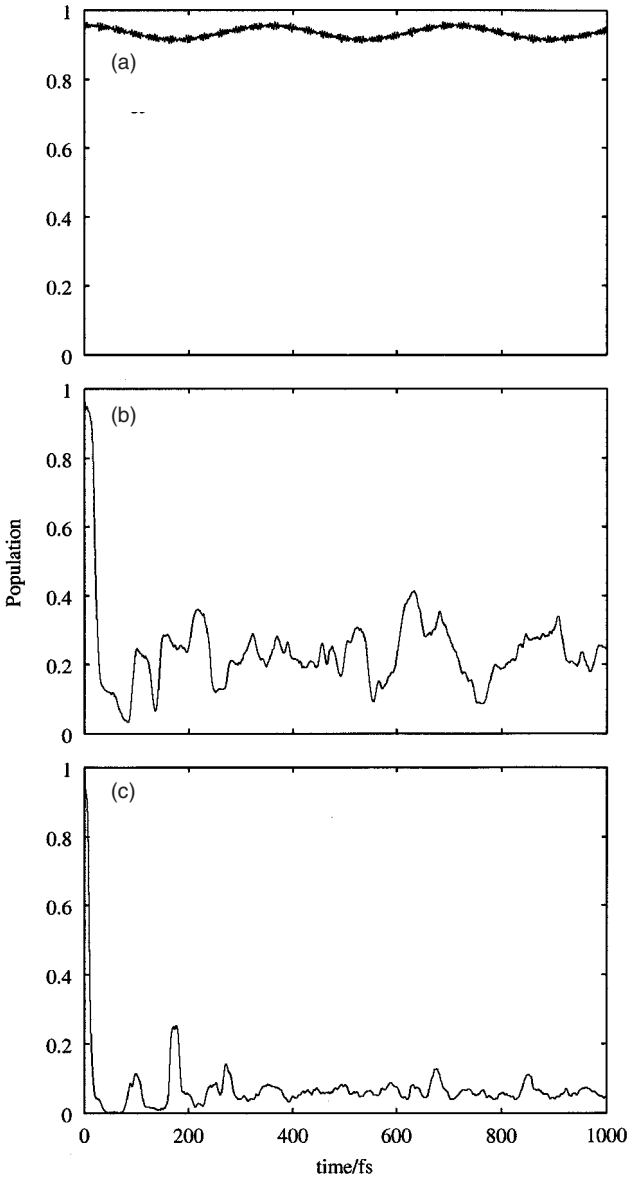

Fig. 3. Adiabatic S_2 population probability for (a) the one-dimensional (ν_{10a}), (b) the two-dimensional (ν_{10a}, ν_{6a}), and (c) the three-dimensional (ν_{10a}, ν_{6a}, ν_1) models of S_1-S_2 vibronic coupling in pyrazine.

It should be stressed that we are discussing here numerically exact results obtained by the solution of the time-dependent Schrödinger equation for an isolated system. No assumptions or approximations leading to decay or dissipation have been introduced. The time evolution of the wave function $\Psi(t)$ is thus fully reversible. The obviously irreversible time evolution of the electronic population probabilities in Figs. 2 and 3 arises from the reduction process, that is, the integration over part of the system [in this case, the nuclear degrees of freedom, cf. Eqs. (12) and (13)].

As a second example, we consider a model of a conical intersection which involves large-amplitude motion along a reaction coordinate. Examples of considerable interest in organic photochemistry and in biophysical chemistry are photoreactions triggered by the twisting of $C{=}C$ double bonds, e.g. in polyenes and in chromophores involved in the process of vision. It has often been conjectured that such ultrafast photoreactions should proceed through conical intersections.[14] A few attempts have been undertaken to construct PE models for such processes.[12,13] A generic model of a photochemical funnel induced by a torsional reaction coordinate φ and a coupling coordinate Q_{c} is displayed in Fig. 4. It is clear that this type of intersection governs simultaneously internal-conversion dynamics to the ground state as well as photochemical dynamics (*cis-trans* isomerization). The application of such models for the simulation of the photochemical dynamics of the retinal chromophore in Rhodopsin has recently been discussed by Hahn and Stock.[53]

Figure 5 shows, in analogy to Fig. 3, the development of the electronic decay dynamics of such a reactive conical-intersection model with increasing number of degrees of freedom (the detailed specification of the model can be found in Ref. 12). The time-dependent population $P_1^a(t)$ of the upper adiabatic surface is shown, assuming instantaneous electronic excitation from the lower to the upper surface at $t = 0$. As in the pyrazine model, no electronic decay occurs when only the coupling mode ν_{c} is included (not shown in Fig. 5). Figure 5a gives the result when the torsional mode is included in addition to ν_{c}, and thus the conical intersection shown in Fig. 4 is formed. A fast ($\approx 50\,\mathrm{fs}$) initial decay of $P_1^a(t)$ is observed, followed by large irregular fluctuations of the electronic population. In the three-mode model, an additional harmonic tuning mode has been included.[12] The result is a significant qualitative change of the electronic population dynamics (Fig. 5b). The irregular fluctuations of $P_1^a(t)$ have virtually disappeared

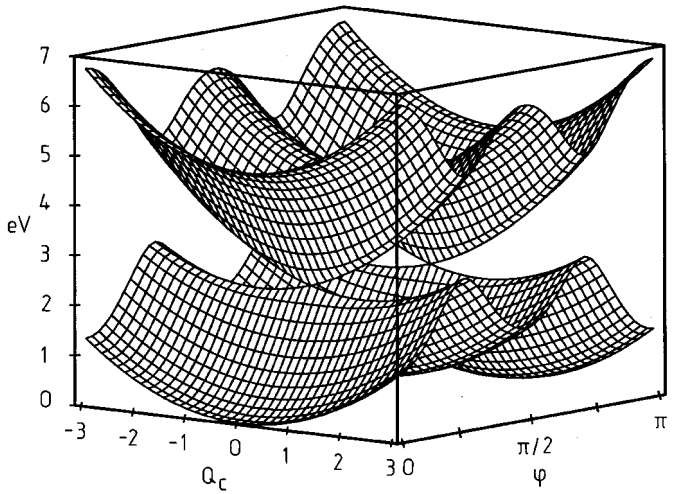

Fig. 4. Adiabatic PE surfaces of the photoisomerization model in the two-dimensional space spanned by the torsional angle φ (reaction coordinate) and the coupling coordinate Q_c.

in the three-dimensional model. $P_1^a(t)$ exhibits an ultrafast initial decay ($\approx$50 fs), followed by a slower transient decay ($\approx$200 fs) and small statistical fluctuations around a long-time limit of $\approx$0.3. In the four-dimensional model [Fig. 5(c)] an additional low-frequency tuning mode has been included.[12] The statistical fluctuations are now completely suppressed and $P_1^a(t)$ drops to a long-time limit below 0.2. Within the first 500 fs, in particular, the electronic population dynamics of the four-mode model is nearly identical with that of the three-mode model, indicating a fast convergence of the ultrafast electronic decay dynamics with respect to the number of nuclear degrees of freedom.

Although the conical intersection illustrated in Fig. 4 is hardly more than a toy model, it exhibits some of the features which are believed to be essential in the photochemistry of polyenes according to *ab initio* investigations of the singlet PE surfaces of ethylene, *cis* and *trans* butadiene and hexatriene.[54–61] The situation in real systems is more complex, since at least three electronic states and additional large-amplitude motions (e.g. pyramidization and H atom migration) are involved.[54–60] Despite the oversimplification of the model, Fig. 5 highlights the possibility of a fully

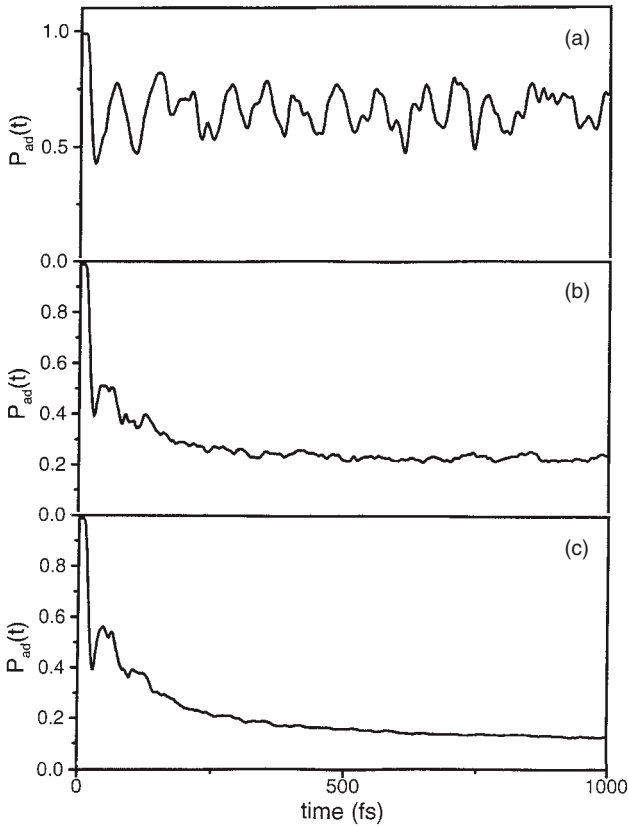

Fig. 5. Time evolution of the population probability of the upper (S_1) adiabatic electronic state of the photoisomerization model with (a) two degrees of freedom (torsion, coupling mode), (b) three degrees of freedom (torsion, coupling mode, tuning mode), and (c) four degrees of freedom (torsion, coupling mode, two tuning modes).

microscopic explanation of the ultrashort excited-state lifetimes of ethylene and butadiene.[62–65]

As a third characteristic example of a conical intersection, we consider the intersection of the PE surfaces of the $\widetilde{A}^2\Sigma_g^+$and $\widetilde{X}^2\Pi_u$ states of the acetylene cation. In this case, the *cis* and *trans* bending modes have been found to induce the intersection and to govern the electronic decay dynamics.[66] The most relevant cuts of the *ab initio* calculated PE surfaces of $C_2H_2^+$ (CASSCF/CASPT2 level) are shown in Fig. 6. Despite

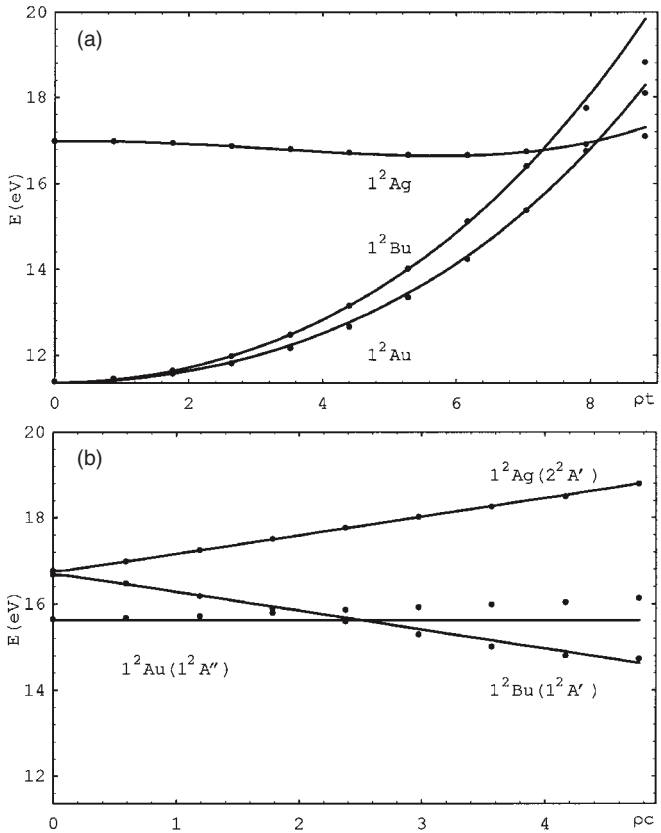

Fig. 6. (a) Trans-bending PE functions of the $\widetilde{X}^2\Pi_u$ and $\widetilde{A}^2\Sigma_g^+$ electronic states of $C_2H_2^+$, calculated at the CASPT2 level[66] with fixed C–H and C–C bond lengths. Dots represent CASPT2 energies, the lines are analytic fits.[66] (b) *Cis*-bending PE functions of $C_2H_2^+$, for fixed C–H and C–C distances and a trans-bending angle of 82°, corresponding to the point of intersection of the ^2A_g and ^2B_u PE functions in (a).

the unusually large vertical energy gap of nearly 6 eV, the extremely flat PE of the $\tilde{A}^2\Sigma_g^+$ state as a function of the *trans*-bending mode leads to an energetically accessible crossing with the lower-lying $\widetilde{X}^2\Pi_u$ state [Fig. 6(a)]. The accidental degeneracy of the ^2A_g and ^2B_u states at the crossing is lifted by the *cis*-bending mode, see Fig. 6(b). The degenerate *trans*-bending and *cis*-bending modes are the dominant tuning and coupling modes, respectively, in this system.[66]

The $\widetilde{A}^2\Sigma_g^+$ diabatic electronic population probability obtained for a six-dimensional model (only the antisymmetric C–H stretching mode has been excluded)[66] is shown in Fig. 7 for $C_2H_2^+$(a) and $C_2D_2^+$(b). Figure 7 represents a nice example of "ballistic" wave-packet motion and electronic decay. $P_\Sigma(t)$ remains essentially equal to unity until wave packet motion in the *trans*-bending mode reaches the conical intersection, which happens at ≈20 fs for $C_2H_2^+$ and ≈30 fs for $C_2D_2^+$. Then an ultrafast decay of the $^2\Sigma_g^+$ population occurs within about 20 fs. After about 40 (50) fs the decay process is finished in $C_2H_2^+$($C_2D_2^+$). The weak oscillations of the population surviving at longer times reflect oscillations of the symmetric CH stretching mode. The incompleteness of the electronic decay in this example as well as the previous examples reflects a lack of vibrational energy redistribution on the lower adiabatic PE surfaces as a consequence of the harmonic modeling of the diabatic PE surfaces. Vibrational energy redistribution processes are inefficient in these models once the wave packet has left the vicinity of the conical intersection.

A possibility to overcome this limitation of the above conical-intersection models, at least in a qualitative manner, is to consider anharmonic couplings of the active degrees of freedom of the conical intersection with a large manifold of spectroscopically inactive vibrational modes. The effect of such a coupling with an environment has been investigated for the pyrazine model in the weak-coupling limit (Redfield theory) in Ref. 19. The simplest ansatz for the system-bath interaction, which is widely employed in quantum relaxation theory[67] assumes a coupling term which is bilinear in the system and bath operators

$$H_{SB} = H_{SB}^{(c)} + H_{SB}^{(t)} \tag{17a}$$

$$H_{SB}^{(c)} = \sum_j g_j^{(c)}(b_c^\dagger a_j + b_c a_j^\dagger) \tag{17b}$$

$$H_{SB}^{(t)} = \sum_j g_j^{(t)}(b_t^\dagger a_j + b_t a_j^\dagger). \tag{17c}$$

Here $a_j(a_j^\dagger)$ are creation and annihilation operators of the bath mode of frequency ω_j and $b_c(b_t)$ are annihilation operators of a coupling and a tuning mode, respectively. The so-called rotating-wave approximation (RWA) has been invoked in Eq. (17), neglecting terms of the type ba and $b^\dagger a^\dagger$. The effect of the bath on the system dynamics is completely determined by the

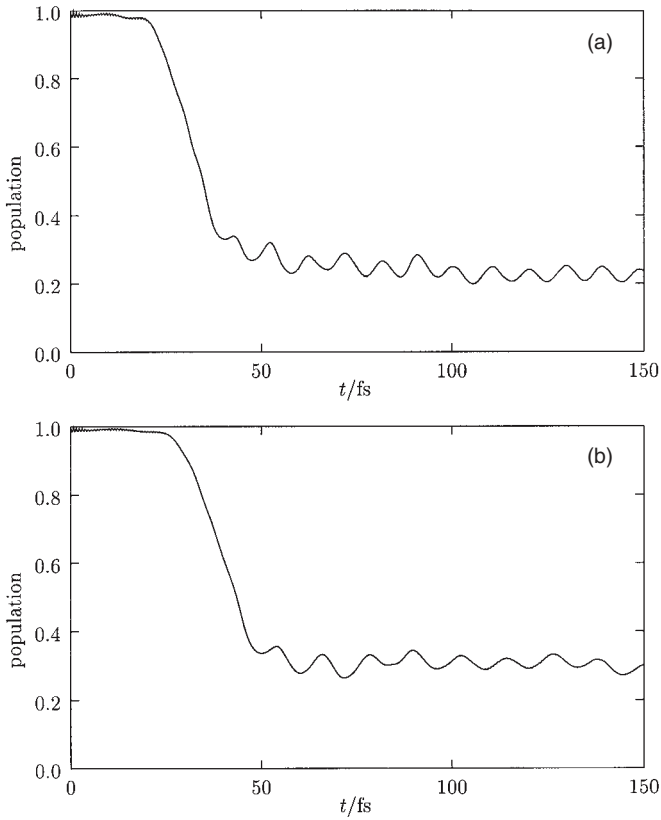

Fig. 7. Calculated time-dependent population probability of the diabatic $\widetilde{A}^2\Sigma_g^+$ state of (a) $C_2H_2^+$ and (b) $C_2D_2^+$.

spectral function

$$J_n(\omega) = 2\pi \sum_j \left(g_j^{(n)}\right)^2 \delta\Big(\omega - \omega_j\Big), \quad n = c, t \tag{18}$$

for each mode. In the numerical studies, $J_n(\omega)$ has been modeled by a so-called Ohmic spectral function[67]

$$J_n(\omega) = \eta_n \omega e^{-\omega/\omega_0^{(n)}}. \tag{19}$$

Here η_n is a dimensionless parameter representing the system-bath coupling strength for mode n and $\omega_0^{(n)}$ is a cut-off frequency which determines the bath relaxation time (see Ref. 19 for more details).

The effect of environmental vibrational damping on the electronic decay dynamics of the three-mode pyrazine model (cf. Fig. 2) is shown in Fig. 8. Diabatic (a) and adiabatic (b) S_2 population probabilities are shown for $\eta = 0$ (isolated system), $\eta = 0.01$ and $\eta = 0.05$. In all cases the coupling with the environment is rather weak, as required for the application of Redfield theory. The temperature of the bath has been set to zero; thermal effects play no significant role because of the large excess energy becoming available in the internal-conversion process. It is seen that vibrational damping lowers, as expected, the long-time limit of the population of the upper electronic state. Inspection of Fig. 8b reveals that moderate damping ($\eta = 0.05$) is sufficient to induce a complete decay of $P_2^a(t)$ to zero within about 200 fs. The result is a typical bimodal decay of the excited-state population, consisting of an ultrafast (≈ 10 fs) initial decay driven by the active modes of the conical intersection, followed by a slower (≈ 1 ps) decay, reflecting vibrational energy relaxation on the lower adiabatic surface.

4. Vibrational Energy Redistribution and Dephasing

Ultrafast internal-conversion processes involve a complex interplay of electronic and nuclear motions. The visualization of time-dependent wave packets (see below) is a possible way of revealing this interplay. Alternatively, we may consider time-dependent expectation values of appropriate operators which reflect the most relevant properties of the nuclear dynamics.

As is well known in nonequilibrium statistical mechanics, it is necessary to distinguish between energy-transfer processes and phase-relaxation processes in the description of the dynamics of complex systems. To monitor the coherence of vibrational motion, we may consider the expectation values of the position and momentum operators

$$\langle R_i \rangle_t = \langle \Psi(t) | R_i | \Psi(t) \rangle \tag{20}$$

$$\langle P_i \rangle_t = \langle \Psi(t) | P_i | \Psi(t) \rangle. \tag{21}$$

Here R_i is the vibrational coordinate and P_i the conjugate momentum of the ith mode. Note that the definition [Eqs. (20) and (21)] implies the trace over

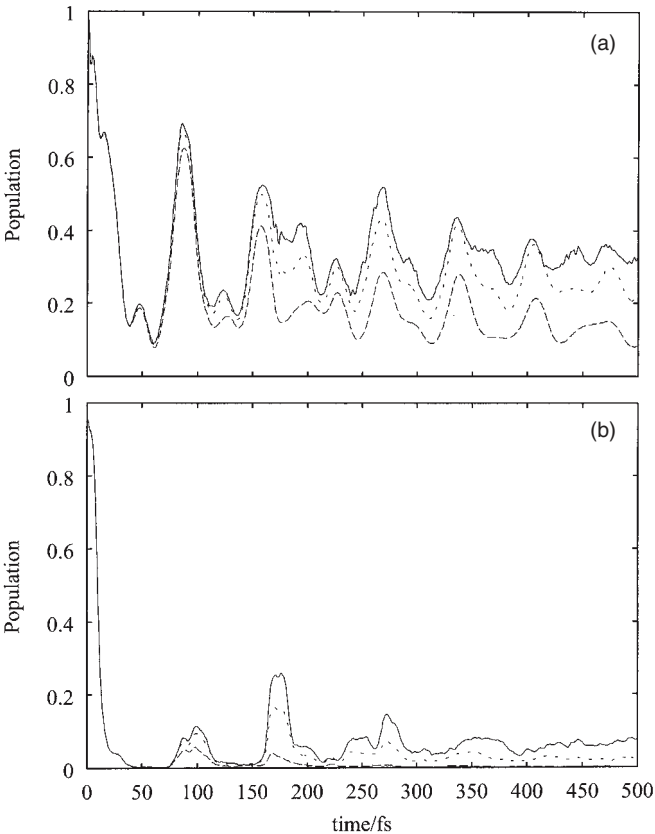

Fig. 8. Diabatic (a) and adiabatic (b) population probability of the S_2 state of the pyrazine model coupled to a harmonic bath, for three values of the system-bath coupling strength. Full line: isolated conical intersection ($\eta = 0$); dotted line: weak system-bath coupling ($\eta = 0.01$); dashed line: moderate system-bath coupling ($\eta = 0.05$).

the electronic subsystem. We thus do not differentiate the nuclear dynamics with respect to individual electronic surfaces. For uncoupled harmonic systems in the absence of environmental dissipation, the expectation values $\langle Q_i \rangle_t$, $\langle P_i \rangle_t$ of normal coordinates and momenta evolve periodically in time, corresponding to undamped coherent vibrational motion. In vibronically coupled systems, on the other hand, the oscillation of $\langle Q_i \rangle_t$ and $\langle P_i \rangle_t$ is typically damped on femtosecond time scales. Figure 9 shows this phenomenon for the tuning modes ν_1 and ν_{6a} of the three-mode pyrazine model. The

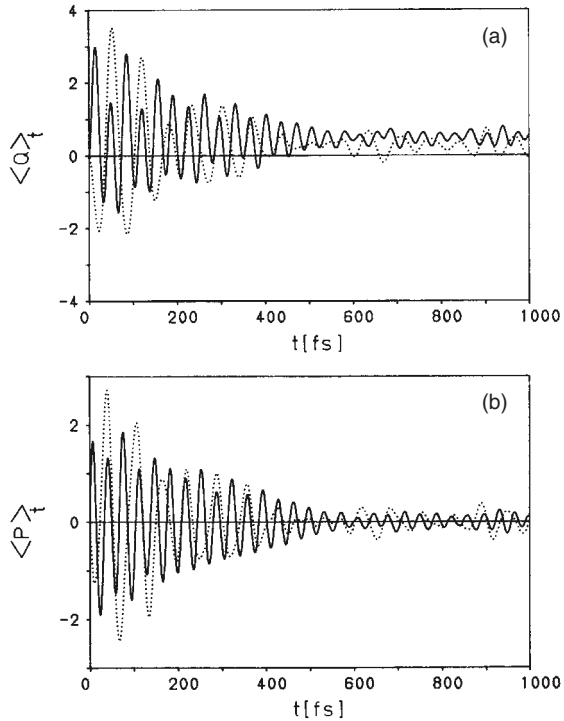

Fig. 9. Time evolution of the expectation values of (a) position and (b) momentum of the tuning modes ν_1 (solid line) and ν_{6a}(dotted line) of the three-mode pyrazine model.

same phenomenon has been found for the harmonic tuning modes of three- and four-dimensional photoisomerization models.[12] It should be pointed out that the decay of the amplitude of $\langle Q_i \rangle_t$ and $\langle P_i \rangle_t$ is not related to the dissipation of vibrational energy (in fact the energy of the tuning modes increases during the internal-conversion process owing to the interconversion of electronic energy into vibrational energy, see below). The damping of the amplitude seen in Fig. 8 rather reflects a vibrational dephasing process, that is, the loss of phase coherence of the initially prepared vibrational wave packet. This femtosecond vibrational dephasing process, which is faster than typical vibrational relaxation processes in isolated electronic states of polyatomic molecules,[68] is another manifestation of the pronounced mode-mode coupling effects in systems with conically intersecting PE surfaces.

As discussed in detail in Ref. 34, the vibrational dephasing process represents the origin of the irreversible time evolution of the electronic population (Fig. 2). The initial quasi-periodic recurrences of $P_2^d(t)$ reflect the driving of electronic population by initially coherent vibrational motion in the tuning modes ν_1 and ν_{6a}. The vibrational dephasing process destroys the coherence of vibrational motion and thus irreversibly traps the electronic populations.

Let us next consider vibrational energy relaxation. To characterize these processes, we shall consider the energy content of individual nuclear degrees of freedom. The definition of individual mode energies is to some extent arbitrary, since there exists, in general, no unique decomposition of the total vibrational energy into single-mode contributions. The concept of time-dependent vibrational energy expectation values for individual modes can nevertheless be very useful for a qualitative analysis of ultrafast internal-conversion processes.[34,69] For the precise definition of the energy content of tuning and coupling modes of conical-intersection models constructed by Taylor expansions in normal modes, including photochemically reactive modes, we refer to Sec. IV.C of Ref. 7.

Figure 10 shows the expectation values of the vibrational energy for the three modes ν_1, ν_{6a}, and ν_{10a} of the pyrazine model. The rapid initial increase of $\langle E_i \rangle_t$, in particular for the modes ν_{6a} and ν_{10a}, shows that the interconversion of electronic to vibrational energy occurs essentially on the time scale of a single vibrational period. After about 500 fs the mode energies become stationary. In this model, as well as in other few-mode vibronic-coupling models, we do not find equipartition of vibrational energy in the long-time limit. It can be expected that additional coupling mechanisms not included in the model will ultimately lead to complete equilibration of the vibrational energy in real systems. The model calculations nevertheless provide a hint that vibrational energy equilibration may be incomplete in internal-conversion processes at subpicosecond time scales. Recent experimental observations for several systems support this idea, see e.g. Refs. 70–72.

The vibrational energy expectation values for the three-mode nonadiabatic photoisomerization model[12] are shown in Fig. 11. In this case the large electronic excess energy (5.0 eV) is initially stored in the torsional mode. It is seen that energy is transferred from the highly excited torsional mode to the other modes on a 100 fs time scale. Again, the energy

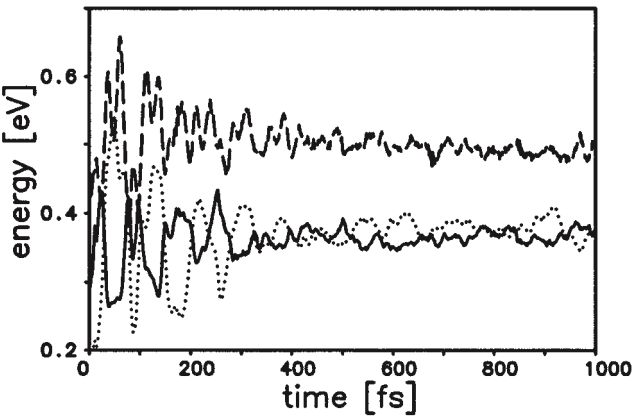

Fig. 10. Time evolution of the expectation values of vibrational energies of the three modes ν_1 (solid line), ν_{6a} (dotted line), and ν_{10a} (dash-dotted line) of the pyrazine model.

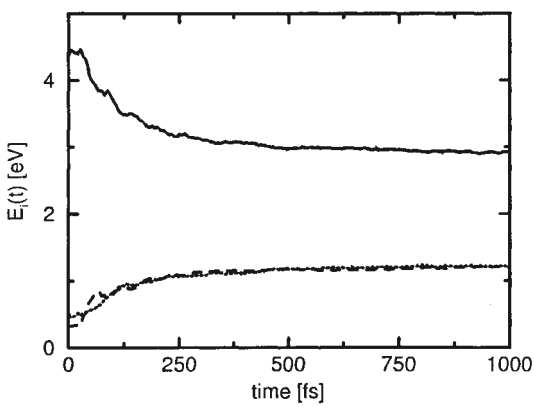

Fig. 11. Time-dependent energy content of the torsional mode (solid line), the coupling mode (dashed line), and the tuning mode (dotted line) of the three-dimensional photoisomerization model.

equilibration remains incomplete in this model. It would be interesting to investigate these energy redistribution processes for more realistic three- or four-dimensional photoisomerization models to see the effect of additional anharmonic as well as kinematic couplings.

5. Wave Packets and Vibrational Probability Densities

The numerical techniques briefly described in Sec. 2 yield the time-dependent coefficient vector $\boldsymbol{C}(\mathrm{t})$. Given $\boldsymbol{C}(\mathrm{t})$, the component of the wave packet on the nth diabatic surface

$$\Psi_n^d(R_1, R_2, R_3, \ldots, t) = \langle R_1|\langle R_2|\langle R_3| \cdots \left\langle \Phi_n^d \;\middle|\; \Psi(t) \right\rangle \tag{22}$$

can immediately be constructed

$$\Psi_n^d(R_1, R_2, R_3, \ldots, t) = \sum_{\nu_1\nu_2\nu_3\ldots} C_{n,\nu_1\nu_2\nu_3\ldots}(t)$$

$$\chi_{\nu_1}(R_1)\chi_{\nu_2}(R_2)\chi_{\nu_3}(R_3)\cdots . \tag{23}$$

For interpretative purposes, we shall also be interested in the projections of the wave packet on adiabatic electronic states, that is

$$\Psi_n^a(R_1, R_2, R_3, \ldots, t) = \langle R_1|\langle R_2|\langle R_3| \cdots \langle \Phi_n^a \mid \Psi(t)\rangle. \tag{24}$$

Since

$$|\Phi_n^a\rangle = \sum_i X_{ni}(R_1, R_2, R_3, \ldots)\big|\Phi_i^d\big\rangle, \tag{25}$$

where $\mathbf{X}$ is the diabatic-to-adiabatic transformation matrix, it is possible to calculate the adiabatically projected wave packets from the diabatic projections. To effect the transformation, one needs the representation of $X_{ni}(R_1, R_2, R_3\ldots)$ in the direct-product basis. Exploiting the fact that the necessary transformations can be performed sequentially for each mode, the construction of adiabatically projected wave packets is feasible for systems with up to four modes, see Refs. 12, 73 and 74 for details.

For systems with just one or two degrees of freedom, the explicit consideration of time-dependent wave packets as defined in Eqs. (22) and (24) can be illuminating. The book by Schinke on photodissociation dynamics, for example, contains nice examples.[10] If the problem involves three or more nuclear degrees of freedom, on the other hand, a reduced description, which condenses the information carried by the wave packet, is desirable. Such reduced descriptions are obtained by integrating the probability density over part of the degrees of freedom. The relevance of reduced descriptions for complex systems is based on the fact that an experimental measurement will not yield the complete quantum mechanical wave function, but rather partially integrated information, e.g. the population of an electronic state or

the population of a particular isomer. The very concept of an isomerization reaction of a complex molecule, for example, implies a reduced description.

Let, for example, R_1 denote the reaction coordinate of interest in a multi-dimensional system. The corresponding reduced probability density is defined as

$$P_n(R_1,t) = \int dR_2 \int dR_3 \cdots |\Psi_n(R_1,R_2,R_3,\ldots,t)|^2. \tag{26}$$

$P_n(R_1,t)$ carries the information on the spatial distribution of the wave packet with respect to R_1 on the nth electronic surface.

In the case of a reduced density-matrix description of the system dynamics,[19] the reduced probability density of coordinate R_1 is given by

$$P_n(R_1,t) = \int dR_2 \int dR_3 \cdots \sigma_{nn}(R_1,R_2,\ldots;R_1,R_2,\ldots;t), \tag{27}$$

where $\sigma(R_1,R_2,\ldots;R_1^{'},R_2^{'},\ldots;t)$ is the vibrational coordinate representation of the reduced density matrix, defined via

$$\begin{aligned}\sigma_{nn'}&(R_1,R_2,\ldots;R_1^{'},R_2^{'},\ldots;t)\\ &= \sum_{\nu\mu} \langle R_1|\langle R_2|\cdots\langle\Phi_n \mid \mu\rangle\sigma_{\mu\nu}(t)\langle\nu \mid \Phi_n^{'}\rangle|R_1^{'}\rangle|R_2^{'}\rangle\cdots .\end{aligned} \tag{28}$$

$P_n(R_1,t)$ of Eq. (27) gives the probability density of vibrational coordinate R_1 in the nth electronic state, averaged both over the degrees of freedom of the bath as well as the remaining vibrational modes of the conical intersection.

Figure 12 shows the projected vibrational probability density $P_n^a(Q_{6a},t)$ of the tuning mode ν_{6a} of the pyrazine model (cf. Fig. 1) for the first 200 fs. It is seen that the wave packet prepared on the upper (S_2) surface at $t=0$ hardly has time to respond to the gradient of the S_2 surface after its preparation. Within a fraction of a vibrational period, the wave packet is quantitatively transferred to the S_1 surface. There it experiences a significant gradient in the opposite direction, resulting in large coherent oscillations in the mode ν_{6a}. A similar result is obtained for the second tuning mode ν_1.[19] The coherence of the wave-packet motion in the tuning modes is thus not destroyed by the initial ultrafast internal-conversion process. The effect of weak environmental damping on the wave-packet dynamics has been investigated in Ref. 19.

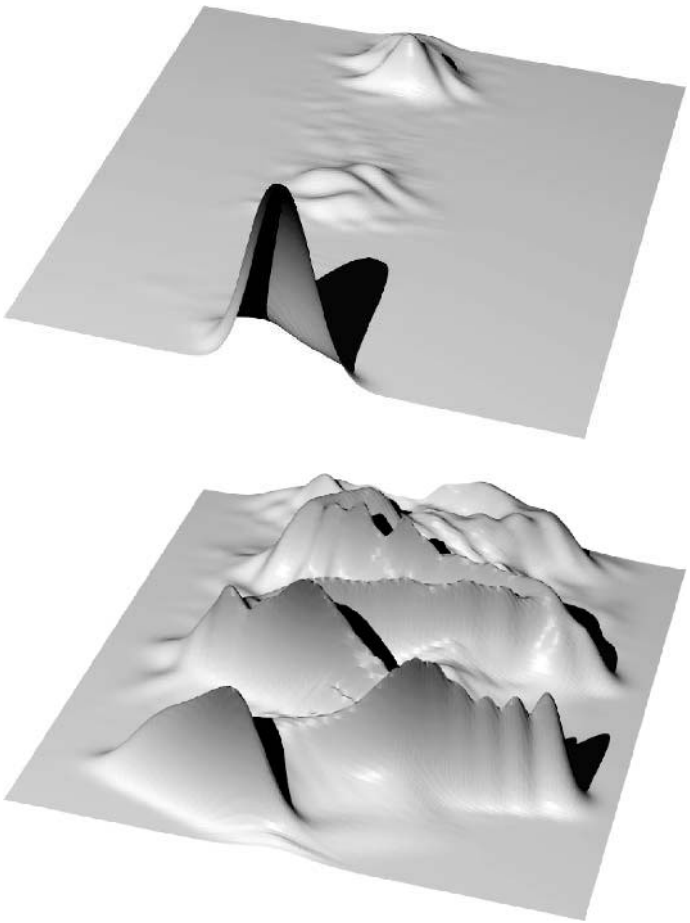

Fig. 12. Projected probability density of the tuning mode ν_{6a} in the S_2 (upper frame) and S_1 (lower frame) adiabatic electronic states for the three-dimensional pyrazine model. The normal coordinate axis extends from –7.0 to 7.0, the time axis from zero to 200 fs (from front to back).

The wave-packet dynamics of the coupling mode is very different, as can seen in Fig. 13. In this case the initially prepared wave packet experiences no gradient on the S_2 surface. It is rather squeezed (that is, it becomes more localized) as the conical intersection is approached by motion in the tuning modes. When the conical intersection is reached, the wave packet instantaneously appears on the lower surface, where it spreads rapidly as a

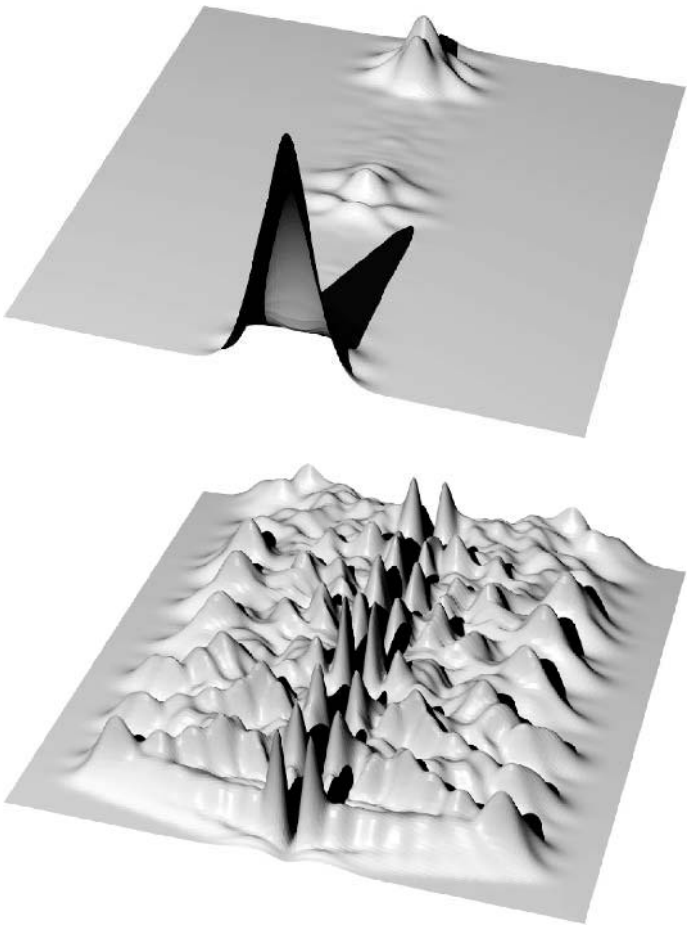

Fig. 13. Projected probability density of the coupling mode ν_{10a} in the S_2 (upper frame) and S_1 (lower frame) adiabatic electronic states for the three-dimensional pyrazine model. The normal coordinate axis extends from –7.0 to 7.0, the time axis from zero to 200 fs (from front to back).

consequence of the flatness of this surface. After reflection from the outer walls, a complicated interference pattern results.

It should be noted that $P_k^a(Q_{10a}, t)$ exhibits a maximum at $Q_{10a} = 0$ on the S_2 surface, but a zero (a node of the wave function) on the S_1 surface. In the present model this is a consequence of symmetry (the nontotally

symmetric character of ν_{10a}). In a qualitative sense the phenomenon is generic, however, reflecting the topography of the adiabatic PE surfaces. The wave packet is focused into the conical intersection when moving on the upper part of the cone, while it is pushed away from the intersection when moving on the lower part of the cone.[75] This explains the unidirectionality of the internal-conversion process on the femtosecond time scale.

From this analysis of the wave-packet dynamics of the S_1-S_2 conical intersection of pyrazine as well as similar studies for other conical intersections[12,75] the following qualitative picture of the mechanism of a conical intersection emerges. As schematically shown in Fig. 14, the relevant dynamical phenomena are (i) focusing of the initial wave packet towards the apex of the cone due to the convex shape of the upper (S_1) adiabatic surface, (ii) first transition through the intersection which leads to the lower (S_0) surface with high probability, (iii) deflection of the recurring wave packet by the concave shape of lower (S_0) adiabatic surface, which prevents return of the wave packet to the upper surface, and (iv) vibrational energy relaxation involving one or more additional (accepting) modes or a dissipative environment, which lowers the energy content of the active modes below the energy of the point of intersection and ensures the irreversibility of the process.

6. Photochemical Dynamics

Finally, we consider the characterization of chemically reactive dynamics. To define reactant/product population probabilities and corresponding

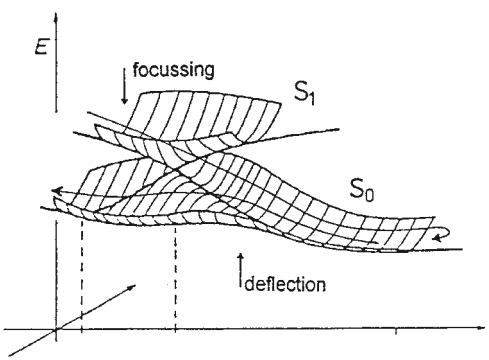

Fig. 14. Qualitative picture of the mechanism of a conical intersection.

transition rates, we have to introduce imaginary hypersurfaces separating the configuration spaces of reactants and products. As an example, consider the photoisomerization model repeatedly referred to above, which involves a single "reactive" torsional degree of freedom with minima of the S_0 PE surface at $\varphi = 0$ and $\varphi = \pi$, which may be defined as the "*trans*" and "*cis*" conformations of the molecule (see Fig. 4). Projection operators defining the "*trans*" ($-\pi/2 < \varphi < \pi/2$) and "*cis*" ($\pi/2 < \varphi < 3\pi/2$) conformations are thus

$$\hat{P}_{trans} = \theta(\pi/2 - \varphi)\theta(\varphi + \pi/2), \tag{29}$$

$$\hat{P}_{cis} = \theta(3\pi/2 - \varphi)\theta(\varphi - \pi/2). \tag{30}$$

The time-dependent "*trans*" and "*cis*" population probabilities are then given by

$$P_{trans}(t) = \langle \Psi(t)|\hat{P}_{trans}|\Psi(t)\rangle, \tag{31}$$

$$P_{cis}(t) = \langle \Psi(t)|\hat{P}_{cis}|\Psi(t)\rangle. \tag{32}$$

Nonperturbative time-dependent transition rates can be defined analogously to Eq. (14). To characterize a photochemical process in more detail, we may furthermore consider the joint probability of populating a given electronic state as well as a given conformer, for example,

$$P^d_{n,trans}(t) = \langle \Psi(t)|\hat{P}^d_n\hat{P}_{trans}|\Psi(t)\rangle. \tag{33}$$

Figure 15(a) shows, as an illustration, the time-dependent *trans* population probability for the three-dimensional photoisomerization model, assuming excitation of the *trans* conformer at $t = 0$ to the inverted S_1 surface (cf. Fig. 4). Figure 15(b) shows, for comparison, $P_{trans}(t)$ for the one-dimensional model (torsion only). In the one-dimensional case, the wave packet relocalizes periodically at the *trans* conformation and $P_{trans}(t)$ oscillates quasi-periodically. In the three-dimensional case, the torsional quasi-periodicity is destroyed already during the first passage through the conical intersection and $P_{trans}(t)$ quickly becomes stationary (the transient oscillations in Fig. 15 arise from the harmonic tuning mode). As expected for this completely symmetric system, asymptotically we have $P_{trans} = P_{cis} = 0.5$. Although this model is somewhat academic, it clearly reveals the fundamental difference between reversible torsional motion in the one-dimensional case and irreversible photoisomerization in the three-dimensional case. A model with more interesting *cis/trans* population

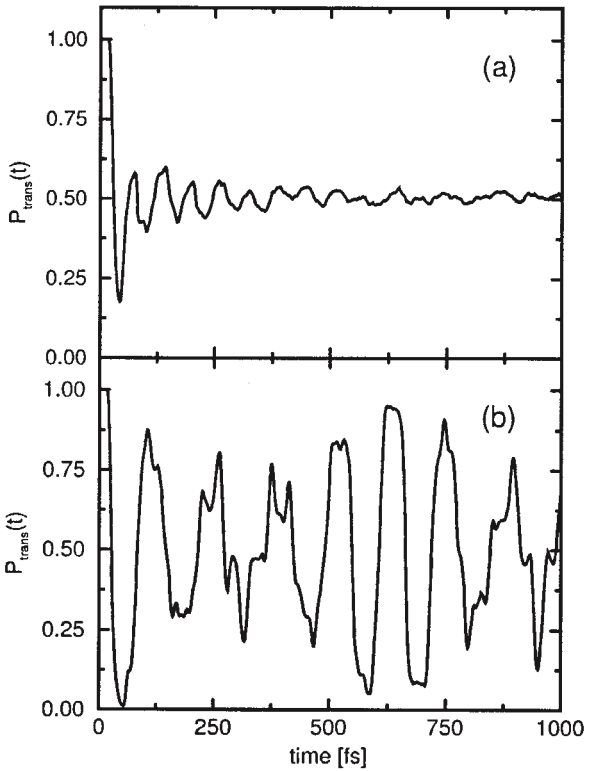

Fig. 15. (a) Time-dependent population probability of the *trans* conformer, obtained for the three-dimensional photoisomerization model. (b) The *trans* population probability of the one-dimensional model (torsional mode only).

dynamics has been considered in Refs. 13 and 76 in the context of real-time detection of photoisomerization dynamics.

7. Conclusions

The examples collected for this survey of femtosecond nonadiabatic dynamics at conical intersections illustrate the interesting interplay of coherent vibrational motion, vibrational energy relaxation and electronic transitions within a fully microscopic quantum mechanical description. It is remarkable that irreversible population and phase relaxation processes are so clearly developed in systems with just three or four nuclear degrees of freedom.

This makes first-principles quantum dynamical studies of ultrafast electronic decay processes possible and thus opens the perspective of unraveling in detail the most elementary steps of photochemical dynamics in polyatomic molecules.

It should be stressed that the wave-packet picture of photophysical relaxation and photochemical reaction dynamics described in this chapter is substantially different from the traditional concepts in this area. In contrast to the established picture of radiationless transitions in terms of interacting tiers of zero-order molecular eigenstates,[28,29] the dynamics is rationalized in terms of local properties of PE surfaces such as slopes, barriers and surface intersections, a view which now becomes widely accepted in photochemistry.[14] This picture is firmly based on *ab initio* electronic-structure theory, and the molecular relaxation dynamics is described on the basis of quantum mechanics, replacing previously prevailing kinetic models[77,78] of electronic decay processes. Such a more detailed and rigorous description of elementary photochemical processes appears timely in view of the rich and specific information on ultrafast chemical processes which is provided by modern time-resolved spectroscopy.[79–81]

References

1. E. Teller, *J. Phys. Chem.* **41**, 109 (1937).
2. E. E. Nikitin, in *Chemische Elementarprozesse,* Ed. H. Hartmann (Springer, Berlin, 1968), p.70.
3. M. Desouter-Lecomte, D. Dehareng, B. Leyh-Nihant, M. T. Praet, A. J. Lorquet and J. C. Lorquet, *J. Chem. Phys.* **89**, 214 (1985).
4. L. D. Landau, *Phys. Z. Sowjetunion* **2**, 46 (1932).
5. C. Zener, Proc. Roy. Soc. (London) **A137**, 696 (1932).
6. H. Köppel, W. Domcke and L. S. Cederbaum, *Adv. Chem. Phys.* **57**, 59 (1984).
7. W. Domcke and G. Stock, *Adv. Chem. Phys.* **100**, 1 (1997).
8. H. Köppel and W. Domcke, in *Encyclopedia of Computational Chemistry*, Ed. P. v. R. Schleyer (Wiley, New York, 1998), p. 3166.
9. U. Manthe, H. Köppel and L. S. Cederbaum, *J. Chem. Phys.* **95**, 1708 (1991).
10. R. Schinke, *Photodissociation Dynamics* (Cambridge University Press, UK, 1993).
11. H. Guo and G. C. Schatz, *J. Chem. Phys.* **92**, 1634 (1990).
12. L. Seidner and W. Domcke, *Chem. Phys.* **186**, 27 (1994).
13. S. Hahn and G. Stock, *J. Phys. Chem.* **B104**, 1146 (2000).

14. M. Klessinger and J. Michl, *Excited States and Photochemistry of Organic Molecules* (VCH, New York, 1995).
15. M. H. Beck, A. Jäckle, G. A. Worth and H.-D. Meyer, *Phys. Rep.* **324**, 1 (2000).
16. A. Raab, G. Worth, H.-D. Meyer and L. S. Cederbaum, *J. Chem. Phys.* **110**, 936 (1999).
17. S. Krempl, H. Winterstetter and W. Domcke, *J. Chem. Phys.* **102**, 6499 (1995).
18. K. Blum, *Density Matrix Theory and Applications* (Plenum Press, New York, 1981).
19. A. Kühl and W. Domcke, *J. Chem. Phys.* **116**, 263 (2002).
20. P. Cattaneo and M. Persico, *Chem. Phys. Lett.* **289**, 160 (1998).
21. M. Ben-Nun and T. J. Martinez, *Chem. Phys. Lett.* **298**, 57 (1998).
22. M. Ben-Nun, J. Quenneville and T. J. Martinez, *J. Phys. Chem.* **104**, 5161 (2000).
23. G. Granucci, M. Persico and A. Toniolo, *J. Chem. Phys.* **114**, 10608 (2001).
24. W. H. Hess, B. P. Flannery, S. A. Teukolsky and W. T. Vetterling, *Numerical Recipes* (Cambridge University Press, UK, 1987).
25. C. Leforestier *et al.*, *J. Comput. Phys.* **94,** 59 (1991).
26. R. Kosloff, in *Numerical Grid Methods and their Application to Schrödinger's Equation*, Ed. C. Cerjan (NATO ASI Series C 412, Kluwer, Dordrecht, 1993).
27. J. C. Light and T. Carrington, Jr., *Adv. Chem. Phys.* **114,** 263 (2000).
28. K. F. Freed, in *Radiationless Processes*, Ed. F. K. Fong (Springer, Berlin, 1976), p. 23.
29. E. S. Medvedev and V. I. Osherov, *Radiationless Processes in Polyatomic Molecules* (Springer, Berlin, 1995).
30. W. Domcke and H. Köppel, *Chem. Phys. Lett.* **140**, 133 (1987).
31. G. Stock, R. Schneider and W. Domcke, *J. Chem. Phys.* **90**, 7184 (1989).
32. K. K. Innes, I. G. Ross and W. R. Moomaw, *J. Mol. Spectrosc.* **132**, 492 (1988).
33. R. Schneider and W. Domcke, *Chem. Phys. Lett.* **150**, 235 (1988).
34. R. Schneider, W. Domcke and H. Köppel, *J. Chem. Phys.* **92**, 1045 (1990).
35. L. Seidner, G. Stock, A. L. Sobolewski and W. Domcke, *J. Chem. Phys.* **96**, 5298 (1992).
36. C. Woywod, W. Domcke, A. L. Sobolewski and H.-J. Werner, *J. Chem. Phys.* **100**, 1400 (1994).
37. G. Stock, C. Woywod, W. Domcke, T. Swinney and B. Hudson, *J. Chem. Phys.* **103**, 6851 (1995).
38. G. Stock, *J. Chem. Phys.* **103**, 10015 (1995).
39. M. Müller and G. Stock, *J. Chem. Phys.* **107**, 6230 (1997).
40. J.-Y. Fang and S. Hammes-Schiffer, *J. Phys. Chem.* **A103**, 9399 (1999).
41. M. Thoss, W. H. Miller and G. Stock, *J. Chem. Phys.* **112**, 10282 (2000).
42. T. Gerdts and U. Manthe, *Chem. Phys. Lett.* **295**, 167 (1998).

43. G. A. Worth, H.-D. Meyer and L. S. Cederbaum, *J. Chem. Phys.* **109**, 3518 (1998).
44. H. Köppel, L. S. Cederbaum and W. Domcke, *J. Chem. Phys.* **77**, 2014 (1982).
45. L. S. Cederbaum, W. Domcke, H. Köppel and W. von Niessen, *Chem. Phys.* **26**, 169 (1977).
46. H. Müller, H. Köppel and L. S. Cederbaum, *J. Chem. Phys.* **101**, 10263 (1994).
47. L. Seidner, W. Domcke and W. von Niessen, *Chem. Phys. Lett.* **205**, 117 (1993).
48. E. Haller, H. Köppel and L. S. Cederbaum, *J. Mol. Spectrosc.* **111**, 377 (1985).
49. E. Leonardi, C. Petrongolo, G. Hirsch and R. J. Buenker, *J. Chem. Phys.* **105**, 9051 (1996).
50. F. Santoro and C. Petrongolo, *J. Chem. Phys.* **110**, 4419 (1999).
51. S. Mahapatra, H. Köppel, L. S. Cederbaum, P. Stampfuß and W. Wenzel, *Chem. Phys.* **259**, 211 (2000).
52. H. Köppel, L. S. Cederbaum and W. Domcke, *J. Chem. Phys.* **89**, 2023 (1988).
53. S. Hahn and G. Stock, *Chem. Phys.* **259**, 297 (2000).
54. M. Ben-Nun and T. J. Martinez, *Chem. Phys.* **259**, 237 (2000).
55. L. Freund and M. Klessinger, *Int. J. Quantum Chem.* **70**, 1023 (1998).
56. M. Aoyagi, Y. Osamura and S. Iwata, *J. Chem. Phys.* **83**, 1140 (1985).
57. M. Ito and I. Ohmine, *J. Chem. Phys.* **106**, 3159 (1997).
58. F. Bernardi, M. Olivucci and M. A. Robb, *Chem. Soc. Rev.* **1996**, 321.
59. B. Ostojic and W. Domcke, *Chem. Phys.* **269**, 1 (2001).
60. M. Garavelli, F. Bernardi, M. Olivucci, T. Vreven, S. Klein, P. Celani and M. A. Robb, *Faraday Discuss.* **110**, 51 (1998).
61. C. Woywod, W. D. Livinghood and J. H. Frederick, *J. Chem. Phys.* **112**, 613 (2000).
62. P. Farmanara, V. Stert and W. Radloff, *Chem. Phys. Lett.* **288,** 518 (1998).
63. J. M. Mestdagh, J. P. Visticot, M. Elhanine and B. Soep, *J. Chem. Phys.* **113**, 237 (2000).
64. W. Fuß, W. E. Schmid and S. A. Trushin, *Chem. Phys. Lett.* **342**, 91 (2001).
65. F. Assenmacher, M. Gutmann, G. Hohlneicher, V. Stert and W. Radloff, *PCCP* **3**, 2981 (2001).
66. R. C. Gillen, B. Ostojic and W. Domcke, *Chem. Phys.* **272**, 1 (2001).
67. U. Weiss, *Quantum Dissipative Systems* (World Scientific, Singapore, 1999).
68. V. E. Bondybey, *Annu. Rev. Phys. Chem.* **35**, 591 (1984).
69. H. Köppel, *Chem. Phys.* **77**, 359 (1983).
70. R. J. Sension, S. T. Repinec, A. Z. Szarka and R. M. Hochstrasser, *J. Chem. Phys.* **98**, 6291 (1993).

71. S. K. Doorn, R. B. Dyer, P. O. Stoutland and W. H. Woodruff, *J. Am. Chem. Soc.* **115**, 6398 (1993).
72. S. Hogiu, W. Werncke, M. Pfeiffer, J. Dreyer and T. Elsaesser, *J. Chem. Phys.* **113**, 1587 (2000).
73. X. P. Jiang, R. Heather and H. Metiu, *J. Chem. Phys.* **90**, 2555 (1991).
74. U. Manthe and H. Köppel, *J. Chem. Phys.* **93**, 345 (1990).
75. U. Manthe and H. Köppel, *J. Chem. Phys.* **93**, 1658 (1990).
76. L. Seidner, G. Stock and W. Domcke, *J. Chem. Phys.* **103**, 3998 (1995).
77. B. Bagchi, G. R. Fleming and D. V. Oxtoby, *J. Chem. Phys.* **78**, 735 (1983).
78. M. Tachiya and S. Murata, *J. Am. Chem. Soc.* **116**, 2434 (1994).
79. A. H. Zewail, *Femtochemistry-Ultrafast Dynamics of the Chemical Bond* (World Scientific, Singapore, 1994).
80. D. A. Wiersma, Ed., *Femtosecond Reaction Dynamics* (North Holland, Amsterdam, 1994).
81. F. C. De Schryver, D. De Feyter and G. Schweitzer (Eds.) *Femtochemistry* (Wiley-VCH, Weinheim, 2001).

This page intentionally left blank

CHAPTER 10

JAHN–TELLER AND PSEUDO-JAHN–TELLER INTERSECTIONS: SPECTROSCOPY AND VIBRONIC DYNAMICS

Horst Köppel

Theoretische Chemie, Physikalisch-Chemisches Institut, Universität Heidelberg, Im Neuenheimer Feld 229, D-69120 Heidelberg, Germany

Contents

1. Introduction

In 1934 L. Landau and E. Teller had a scientific discussion about the role which degeneracy of electronic energy levels plays for the coupling with the nuclear vibrations of a polyatomic molecule. Landau argued that "in a degenerate electronic state the symmetry on which the degeneracy is based ... will in general be destroyed".[1,2] Teller managed to convince Landau that, at least for the particular case of linear molecules, his doubts were unfounded. (This was just the case treated before by Teller's student R. Renner[3]). Nevertheless, the discussion with Landau prompted subsequent work by Teller with H. A. Jahn which showed that in virtually all other cases L. Landau was right, and lead to the formulation of the now-famous Jahn–Teller theorem: a molecule in an orbitally degenerate state is unstable unless the degeneracy is accidental or the nuclei lie on a straight line.[4]

The essence of the proof consists in the demonstration that, for any realization of any molecular point group, there exist asymmetric vibrational modes that lift the degeneracy in first order and cause the stationary point to occur at a configuration of reduced symmetry. Since there are always at least two of these "Jahn–Teller active" vibrational degrees of freedom, the potential energy surfaces take the shape of a double cone at the symmetric configuration and thus constitute there a conical intersection. To the knowledge of the author, this is the first time that this topology has been treated in the literature, even if only implicitly (but see Ref. 5). From a modern perspective, it therefore constitutes a prototype example of a conical intersection, also termed Jahn–Teller (JT) intersection.

It is the purpose of this article to survey some key aspects of JT theory and its extensions, as they relate to the focus of this book and to the title of this chapter, namely, the quantum dynamics at JT intersections. A comprehensive review of general JT theory and its applications is far beyond the scope of this chapter, and we refer the interested reader to a number of monographs[1,6,7] and review articles[8–11] on the field. Suffice it to say that much of the theory deals with structural aspects of the JT distortion, that is, with the topology of the adiabatic potential energy surfaces, the stationary points occurring at a reduced symmetry and their manifestation, e.g. in ESR and NMR spectroscopy. Also, many of the applications are concerned with impurities or cooperative effects occurring in the solid state. For the

vast amount of literature on these topics we collectively refer to the above books and review articles and references cited therein (especially in Refs. 6 and 10).

In the present survey, we focus instead on dynamical aspects of the JT effect and their manifestations in electronic spectra of polyatomic molecules. More specifically, we will deal with electronic transitions from a nondegenerate (initial) electronic state into a degenerate (final) electronic state in which the JT effect is operative. When the nondegenerate state has its minimum at the symmetric conformation (as is usually the case), the center of the Franck–Condon (FC) zone coincides with the locus of the JT intersection, where the two potential energy surfaces are degenerate by symmetry. In agreement with general reasoning (see Chapters 1, 7 and 9 of this book) this is just the locus of strong nonadiabatic coupling effects, which are thus explored most directly by this type of spectral transitions. The comparison with other situations, where the FC zone center is displaced from the intersection, can thus give insight into the importance which this factor has on the vibronic dynamics. In addition to nonadiabatic coupling effects we will also touch upon aspects of the geometric phase which has found interest within JT theory as well (see also Chapter 12).

A natural extension of the theory applies to systems where the electronic states are not degenerate, but sufficiently close in energy so that similar interactions may play a role. This has been termed pseudo-Jahn–Teller effect in the literature[7,10] and in the widest sense would comprise any vibronic coupling system as treated, for example, in Chapter 7. To keep the nomenclature more specific, we prefer here (as in our earlier work[11–13]) to restrict the term pseudo-Jahn–Teller (PJT) to systems where a doubly degenerate state is energetically close and coupled to another (often nondegenerate) electronic state. In either case, the PJT induced distortion is not "spontaneous", i.e. a threshold for the coupling strength is to be exceeded in order that the energetic minimum of the lower surface occurs at a configuration of lower symmetry. From the point of view of surface intersections the more specific nomenclature adopted here implies three interacting potential energy surfaces which may lead to triple intersections and intersecting seams of conical intersections. These interesting features will also be covered below, from the general point of view as well as in relation to individual examples. We thus hope to provide a coherent overview

of different system types, and also emphasize the importance of simultaneous JT + PJT interactions in actual molecular systems. Likewise, we will consider older and more recent applications in order to provide a (partial) historical perspective, although in the examples we will focus on work done by the Heidelberg group.

2. Vibronic Model Systems for *E* States

2.1. *General*

The derivation of JT Hamiltonians follows general principles of vibronic coupling theory, several of which have, in fact, first been formulated within JT theory.[1,14] Generally, the concept of diabatic electronic states is employed, where the nuclear kinetic energy can be taken diagonal to a sufficiently good approximation and the pertinent off-diagonal coupling terms arise from the potential energy operator (for a more detailed exposition of the concept of diabatic states, see Chapter 4). More specifically, the components of the degenerate electronic states at the high-symmetry reference configuration are used as an electronic basis *also for displaced*, lower-symmetry nuclear configurations. The JT Hamiltonian is then represented as a matrix with respect to this basis, and the matrix elements are usually expanded in a Taylor series for small displacements Q_i $(i = 1, \ldots, n)$ from the reference configuration:[1,7]

$$\mathcal{H}_{\alpha\alpha'}{}^{JT} = H_0\delta_{\alpha\alpha'} + \sum_i \frac{\partial V_{\alpha\alpha'}}{\partial Q_i} Q_i + \sum_{i,j} \frac{\partial^2 V_{\alpha\alpha'}}{\partial Q_i \partial Q_j} Q_i Q_j + \mathcal{O}\left(Q^3\right). \qquad (1)$$

Here $V_{\alpha\alpha'}$ $(\alpha, \alpha' = 1, \ldots, m)$ denote the matrix elements of the potential energy operator in the electronic basis chosen, and the derivatives are to be taken at the symmetric conformation $Q_i = Q_j = 0$ $(i, j = 1, \ldots, n)$. The term H_0 includes the zero-order element of the expansion, i.e. the degenerate electronic energy at the high-symmetry nuclear configuration, and the "JT-unperturbed" vibrational Hamiltonian. The latter is usually written in the harmonic approximation, comprising all relevant vibrational degrees of freedom. It represents vibrational motion on the arithmetic mean of the JT split potential energy surfaces. In practice, this part of the Hamiltonian is often equated with the vibrational Hamiltonian of the initial, nondegenerate electronic state of the electronic transition under investigation.

The similarity of the Hamiltonian (1) and the vibronic coupling Hamiltonian discussed in Chapter 7 will be noted and reflects the virtually identical underlying concepts. The only essential difference is that the relative sizes and signs of the derivatives of $V_{\alpha\alpha'}$ within a degenerate electronic manifold are fixed by symmetry in the JT case. Also, the degeneracy itself, being a conical intersection for finite first derivatives $\partial V_{\alpha\alpha'}/\partial Q_i$, occurs for $Q_i = Q_j = 0$, i.e. it is not accidental, but again fixed by symmetry. Finally, the symmetries of the linearly JT-active normal modes are determined by the requirement that their irreducible representations Γ_{vib} are contained in the decomposition of the symmetrized direct product of the irreducible representation Γ_{el} of the electronic state according to[1,4,7]

$$(\Gamma_{el})^2 \supset \Gamma_{\text{vib}} \,. \tag{2}$$

Equation (2) is the analogue of related selections rules discussed in Chapter 7. In the following, these general statements will be exemplifed for various prototype cases involving twofold degenerate electronic states. While extensions to include additional (nondegenerate) states will also be discussed, the reader is referred to the literature for symmetry-induced threefold (and higher) electronic degeneracies.

2.2. *The Single-Mode $E \otimes e$ Jahn–Teller Effect*

Let us consider a system with a doubly degenerate electronic state and a threefold principal rotation axis. Then there are always doubly degenerate vibrational modes that are (linearly) JT-active, that is, the derivatives $\partial V_{\alpha\alpha'}/\partial Q_i$ do not vanish for their (Cartesian) displacement components Q_x and Q_y. By elementary symmetry considerations the corresponding 2×2 JT matrix Hamiltonian in first order is found to be[1,14,15]

$$\mathcal{H}^{E\otimes e} = H_0\mathbf{1} + k \begin{pmatrix} Q_x & Q_y \\ Q_y & -Q_x \end{pmatrix} . \tag{3}$$

Putting the electronic energy at the origin $Q_x = Q_y = 0$ to be zero, the term H_0 reduces to the Hamiltonian of the isotropic two-dimensional harmonic oscillator (with frequency ω). $\mathbf{1}$ denotes the 2×2 unit matrix.

Equation (3) is the well-known Hamiltonian of the (linear) $E \otimes e$ JT effect which has been amply studied in the literature (see, for example, Refs. 1, 7 and 11 and references therein). Diagonalization of the potential

energy part leads to the famous "Mexican hat" potential energy surfaces

$$V_{\pm} = \frac{\omega}{2}\rho^2 \pm k\rho\,, \tag{4}$$

$$\rho^2 = Q_x^2 + Q_y^2\,. \tag{5}$$

These rotationally symmetric surfaces are depicted schematically in Fig. 1 and characterized there by the JT stabilization energy

$$E_{JT} = \frac{k^2}{2\omega}\,, \tag{6}$$

occurring at the optimum distortion

$$\rho_0 = k/\omega\,. \tag{7}$$

The so-called pseudorotational angle ϕ is defined as

$$\phi = \arctan\left(Q_y/Q_x\right). \tag{8}$$

The corresponding eigenvector matrix reads

$$\mathbf{S} = \begin{pmatrix} \cos\left(\phi/2\right) & -\sin\left(\phi/2\right) \\ \sin\left(\phi/2\right) & \cos\left(\phi/2\right) \end{pmatrix}, \tag{9}$$

where the two columns represent the expansion coefficients of the adiabatic wave functions in the diabatic electronic basis. Transforming the complete

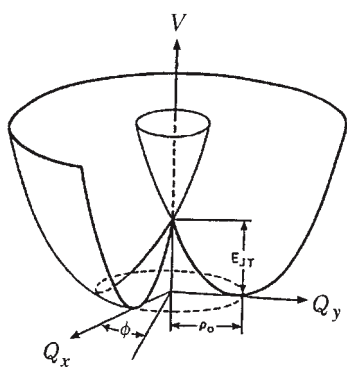

Fig. 1. Perspective drawing of the $E \otimes e$ JT intersection arising for linear coupling (Mexican hat). The rotationally symmetric double cone is located in the figure centre. Also indicated in the figure are the Cartesian displacement coordinates Q_x and Q_y of the JT active mode, the pseudorotational angle ϕ and the energy gain E_{JT} occurring for the optimum distortion ρ_0.

Hamiltonian (3) to the adiabatic basis leads to

$$\mathbf{H}_{ad}^{E\otimes e} = \mathbf{S}^{\dagger}\mathbf{H}^{E\otimes e}\mathbf{S} = H_0\mathbf{1} + \begin{pmatrix} V_+ & 0 \\ 0 & V_- \end{pmatrix} + \mathbf{\Lambda}, \tag{10}$$

with the nonadiabatic coupling operator

$$\mathbf{\Lambda} = \frac{\omega}{2\rho^2}\begin{pmatrix} \frac{1}{4} & i\frac{\partial}{\partial\phi} \\ i\frac{\partial}{\partial\phi} & \frac{1}{4} \end{pmatrix}, \tag{11}$$

which is seen to diverge at the origin $\rho = 0$, where the two adiabatic potential energy surfaces exhibit the JT intersection.

The singularity of the nonadiabatic couplings at the locus of intersection derives from general principles discussed in other places in this book (see, for example, Chapters 1 and 7). The vibronic secular problem corresponding to the Hamiltonian (3) has been solved, and electronic absorption spectra for an optical transition from a nondegenerate state into the coupled surfaces of Fig. 1 been computed numerically by Longuet-Higgins *et al.*[15] This represents the first study of its kind in the literature.

For weak-coupling systems, characterized by $k \lesssim \omega$, the JT stabilization energy is too small to support vibrational motion below the conical intersection at $E = 0$, and the vibronic motion is nonadiabatic throughout, i.e. it proceeds on both potential energy surfaces simultaneously, owing to the operator $\mathbf{\Lambda}$ in Eq. (10). For strong-coupling cases, characterized by $k \gg \omega$, there is a profound difference in the vibronic motion and spectral line structure between $E < 0$ and $E > 0$. This is illustrated in Fig. 2 for $A \rightarrow E$ electronic transitions for two values of E_{JT} ($\omega = 1$). For $E < 0$, i.e. energies below the conical intersection, there is a single vibrational progression which can be ascribed to FC transitions to the lower adiabatic surface V_- of Eq. (4). For $E > 0$, there is a series of quasi-resonances (so-called "Slonczewski-resonances"[16–19]) each manifesting itself as a peak in the spectral envelope, although the individual lines are sharp and represent the — necessarily discrete — vibronic eigenstates of the Hamiltonian (3). Each of these quasi-resonances corresponds to a single vibrational level of the upper adiabatic surface V_+ of Eq. (4), as is schematically indicated in the lowest panel of Fig. 2. The formation of the *broad* resonances and the redistribution of the spectral strength over the participating vibronic eigenstates represents the *strong* nonadiabatic coupling effects caused by the operator $\mathbf{\Lambda}$ in Eq. (10) (recall the singular strength of the elements of $\mathbf{\Lambda}$ at $\rho = 0$,

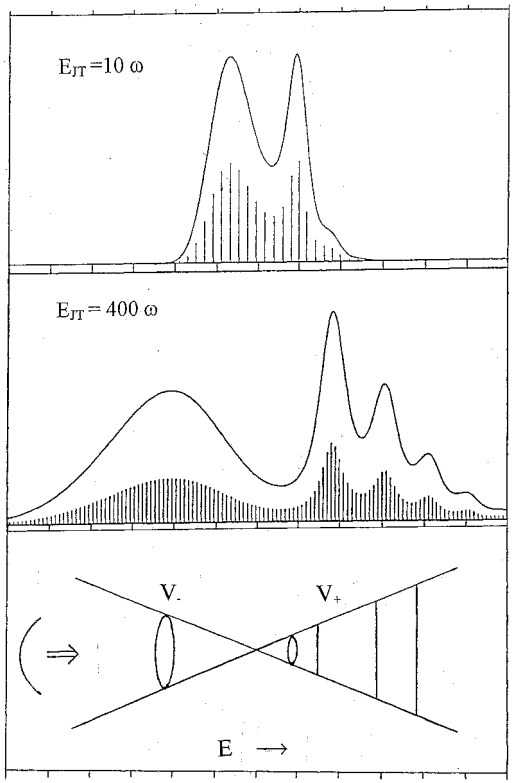

Fig. 2. Vibronic $E \otimes e$ JT spectra for two different values of E_{JT}, Eq. (6). The electronic transition is from a nondegenerate, JT-undistorted state to the JT-distorted final state as indicated schematically in the lowest panel of the figure. Here the Mexican hat potential energy surfaces are represented roughly by the double cone, with the upper-cone vibrational levels indicated by the three straight lines (for $E_{JT} = 400\omega$).

already pointed out above.) The regular structure of the individual lines, on the other hand, is accidental and reflects the rotational symmetry of the potential surfaces, Eq. (4). The accidental symmetry is mathematically expressed by the existence of a vibronic angular momentum operator

$$\mathbf{J} = l_{vib}\mathbf{1} + \begin{pmatrix} 1/2 & 0 \\ 0 & -1/2 \end{pmatrix}, \tag{12}$$

which commutes with $\mathbf{H}$,

$$\left[\mathbf{H}^{E\otimes e}, \mathbf{J}\right] = 0\,. \tag{13}$$

Here, l_{vib} is the vibrational angular momentum operator associated with the two-dimensional harmonic oscillator H_0 of Eq. (3). The eigenvalues j of the operator $\mathbf{J}$ are half-odd integers ($\hbar = 1$). The spectra of Fig. 2 are characterized by $j = \pm 1/2$, because the initial vibrational level is the ground state with $l_{vib} = 0$. We mention in passing that the width of the Slonczewski resonances — and thus the strength of the nonadiabatic interaction — is greatly reduced for $j > 1/2$.[20] This is easily understood in terms of an increased centrifugal barrier for finite l_{vib}, which reduces the probability density of the system near $\rho = 0$ where the elements of $\mathbf{\Lambda}$ in Eq. (11) diverge.

When the quadratic coupling terms in Eq. (3) are included, the rotational symmetry of the potential surfaces in Eq. (4) is lost and replaced by a threefold symmetry inherent to systems with a threefold rotation axis. Consequently, j ceases to be a good quantum number and the spectra of the linear $E \otimes e$ JT system for individual j become "mixed". This inherently two-dimensional vibronic motion leads to a complicated, erratic line structure (see, for example, Ref. 21) as is typical for other, less symmetric conical intersections discussed throughout this book. The above statements about adiabatic and nonadiabatic behavior for $E < 0$ and $E > 0$, and the formation of *broad* quasi-resonances arising from the upper cone vibrational levels, are not affected by the inclusion of quadratic coupling terms.

For sufficiently large coupling strength, $k/\omega > 1$, the vibronic motion near the bottom of the lower adiabatic potential energy surface of the $E\otimes e$ JT system can be described in the Born-Oppenheimer approximation, but the so-called geometric phase[22–24] comes into play as an unusual feature influencing the vibronic motion. Its origin is embodied in the trigonometric functions appearing in the adiabatic eigenvector matrix $\mathbf{S}$, Eq. (9), and leading to

$$\mathbf{S}(\phi + 2\pi) = -\mathbf{S}(\phi)\,. \tag{14}$$

The adiabatic electronic wave functions thus change sign when encircling the conical intersection in Fig. 1 in a closed loop. To compensate this double-valued behavior of the electronic wave functions, Longuet-Higgins *et al.*

required also the nuclear wave functions to show the same behavior and thus make the total wave function single-valued.[15] This results in half-odd integer values of the vibrational angular momentum in the adiabatic basis and thus to a *different* eigenvalue spectrum than usual. (It should be mentioned that this is consistent with the vibronic angular momentum **J**, Eq. (12), becoming a purely vibrational angular momentum in the adiabatic basis.[12]) In later work, Mead and Truhlar pointed out the possibility of multiplying the adiabatic eigenvectors with suitable complex phase factors to make them single-valued functions of the nuclear coordinates.[25,26] This leads again to integer vibrational angular momentum quantum numbers, but at the expense of introducing an additional vector potential term in the nuclear equation of motion. While the latter procedure is more general from a systematic point of view, in the $E \otimes e$ JT case it yields the same eigenvalue spectrum as obtained with double-valued, real electronic wave functions.[25,26]

The geometric phase is an important feature of general conical intersections. While originally formulated as a sign change of the adiabatic electronic wave functions when encircling the intersection in a closed loop[27] it was later put on a more general footing by M. Berry[23] as a consequence of adiabatic traversal of a hermitean Hamiltonian in some external parameter space. A more detailed treatment of these geometric phase effects is given in Chapter 12. We conclude by mentioning that the geometric phase plays an important role also for quadratic JT coupling systems, where it leads to a reversed ordering of the tunnelling-induced singlets and doublets, i.e. of the delocalized nuclear wave functions deriving from the tunnelling between the three equivalent minima of V_-.[28] For extremely strong quadratic coupling, on the other hand, three additional conical intersections affect the low-energy vibronic motion and cancel the geometric phase effects.[29,30]

2.3. *Influence of Additional Modes*

The above rather comprehensive presentation of the single-mode $E \otimes e$ JT effect serves as a reference for the discussion of related and more general systems. These will be discussed more briefly, focussing on their similarities and differences with respect to the prototype case. We start with the inclusion of additional vibrational modes.

2.3.1. *Additional e Vibrational Modes*

Additional e modes are included in the Hamiltonian (3) by replacing the corresponding single-mode terms by summations over all relevant vibrations, e.g.

$$kQ_x \to \sum_i k_i Q_x^i\,, \quad kQ_y \to \sum_i k_i Q_y^i\,, \tag{15}$$

in a self-explanatory notation (and an analogous extension in the zero-order Hamiltonian H_0). Since virtually all molecules exhibiting the $E \otimes e$ JT effect possess several e modes (except for equilateral X_3 systems) this generalization is of immediate relevance. Although the total JT stabilization energy E_{JT} is additive, i.e.

$$E_{JT} = \sum_i \frac{k_i^2}{2\omega_i} \equiv \sum_i E_{JT}^{(i)}\,, \tag{16}$$

the Hamiltonians $\mathbf{H}_i^{E\otimes e}$ for the various modes do not commute ($i \neq j$):

$$\left[\mathbf{H}_i^{E\otimes e}, \mathbf{H}_j^{E\otimes e}\right] \neq 0\,. \tag{17}$$

Thus, the eigenvalue problems of the individual Hamiltonians cannot be solved separately. Rather, the multi-mode vibronic secular matrix has to be diagonalized as a whole[11] (see Chapter 7 for a discussion of the corresponding numerical techniques).

The non-separability of the vibrational modes is illustrated in Fig. 3 through the strong dependence of the JT potential energy surfaces for one of the interacting modes on the coordinates of the other mode (taken as a parameter). Whereas in Fig. 3(a) (zero displacement of the second mode) the potential surface for mode 1 exhibits the familiar Mexican-hat shape, for increasing displacements as in Figs. 3(b) and 3(c) there is an increasing distortion and the rotational symmetry is lost.[31]

To account for the low-energy vibronic structure of multi-mode $E \otimes e$ systems, a cluster model has been introduced by O'Brien *et al.*[32] This is an effective one-mode description which correctly reproduces the multi-mode stabilization energy, Eq. (16). For the description of multi-mode JT band shapes, on the other hand, another effective one-mode model is more appropriate, which may be called "effective single-mode" Hamiltonian.[33] The idea consists in performing a rotation in normal-coordinate space such that the coupling terms, Eq. (15), are represented by a *single* mode in

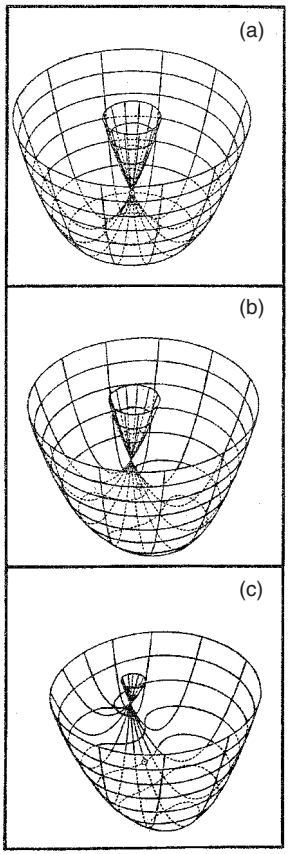

Fig. 3. Perspective drawing of potential energy surfaces for the two-mode $E \otimes e$ JT effect. The coordinates of one mode represent the variables, while the coordinates of the other mode are taken as parameters, increasing from (a) (where they are zero) to (c). Adapted from Ref. 31.

the new vibrational basis.[34] This leads to the following effective coupling constant and frequency for this mode[33,35]

$$k_{eff} = \left\{ \sum_i k_i^2 \right\}^{1/2} , \tag{18}$$

$$\omega_{eff} = \left\{ \sum_i k_i^2 \omega_i \right\} \Big/ \left\{ \sum_i k_i^2 \right\} . \tag{19}$$

The other modes are coupled only by bilinear terms resulting from the transformation of the unperturbed Hamiltonian H_0, and they become decoupled in the limiting case of equal frequencies. The spectral moments are correctly reproduced up to third order by this approach and the bandshapes of multi-mode JT systems are accurately reproduced in this way for a large range of system parameters.[33]

2.3.2. *Influence of a_1 Vibrational Modes*

Totally symmetric (or a_1) vibrational modes are included in first order by adding a term

$$k_g Q_g \mathbf{1} \tag{20}$$

to the Hamiltonian (3) and similarly augmenting H_0 (the subscript g indicates the "gerade" property for all symmetry operations). By virtue of the unit matrix $\mathbf{1}$, this term commutes with the e-mode coupling terms in Eq. (3) and both types of modes are thus separable. For this reason, a_1 modes are usually omitted from JT treatments and included in the computation of optical spectra, if needed at all, by convolution.

The situation may change, however, when second-order coupling terms are included.[36] Then there exist also bilinear coupling terms, involving the products $Q_x Q_g$ or $Q_y Q_g$ in the Hamiltonian (3). Formally these are obtained by the substitution

$$k \rightarrow k + bQ_g \tag{21}$$

in Eq. (3), where b denotes the bilinear coupling constant. These terms should be included in a complete second-order treatment, and b may be expected to be of a similar order of magnitude as the quadratic JT coupling constant. Their inclusion leads to a modification of the various stationary points and the JT barrier heights by the a_1 mode(s). Moreover, the various conical intersections of the quadratic $E \otimes e$ JT model system exhibit a different dependence on Q_g and turn into a set of intersecting seams of conical intersections.[36]

For finite values of b, the $E \otimes (e + a)$ JT spectrum is generally no longer given by convolution of the individual-mode spectra. For sufficiently different values of the vibrational frequencies, a vibrationally adiabatic decoupling procedure has been formulated and investigated, where the coupling

constant of the lower-frequency mode takes an effective value, obtained by averaging over the higher-frequency motion.[36] This improves the agreement with the full calculation drastically and can reproduce the results of the latter very accurately[36] — an application to a real molecular system (the methoxy radical) will be mentioned in Sec. 3.1.

2.4. *The $E \otimes b$ Jahn–Teller Effect*

In systems with two- and fourfold rotation axes, the $E \otimes e$ JT effect, discussed so far, is not operative. In the corresponding (sometimes called tetragonal) point groups, the decomposition of the symmetrized direct product $(E)^2$ of an irreducible representation E with itself reads

$$\begin{aligned}(E)^2 &= A_1 + B_1 + B_2\,, \quad \text{for } C_{4v}, D_4, D_{2d}, D_{4h}\,;\\ &= A + 2B\,, \quad \text{for } C_4, C_{4h}, S_4\,.\end{aligned} \tag{22}$$

According to the symmetry selection rule, Eq. (2), the irreducible representations of the JT active modes have to be contained in the decomposition of $(E)^2$. In the above point groups these are therefore vibrational modes of B ($B_{1,2}$), rather than E, symmetry. We emphasize that such molecules will often have E vibrational modes and that these may be pseudo-Jahn–Teller (rather than Jahn–Teller) active, see below.

In first order, totally symmetric modes are again separable from the JT problem. The generic $E \otimes b$ JT Hamiltonian is set up by including only a single B_1 and B_2 vibrational mode:[7,37–39]

$$\mathbf{H}^{E\otimes b} = H_0\mathbf{1} + \begin{pmatrix} k_1 Q_1 & k_2 Q_2 \\ k_2 Q_2 & -k_1 Q_1 \end{pmatrix}. \tag{23}$$

Here, the vibrational normal coordinate Q_1 (Q_2) transforms according to the B_1 (B_2) irreducible representation, with the corresponding coupling constant denoted k_1 (k_2), and H_0 collects the pertinent harmonic oscillator Hamiltonians. The adiabatic potential energy surfaces $V_\pm$ read as follows

$$V_\pm = \frac{\omega_1}{2}Q_1^2 + \frac{\omega_2}{2}Q_2^2 \pm \sqrt{k_1^2 Q_1^2 + k_2^2 Q_2^2}\,, \tag{24}$$

where the energy at $Q_1 = Q_2 = 0$ has again been put to be zero. Equation (24) describes a conical intersection which has now an elliptical (rather than circular) shape and is thus more similar to general (i.e. non-JT) intersections discussed, for example, in Chapter 7. The stationary points of the

lower surface V_- occur at

$$Q_1^{(0)} = \pm\frac{k_1}{\omega_1}\,; \qquad Q_2^{(0)} = 0 \tag{25}$$

and

$$Q_1^{(0)} = 0\,; \qquad Q_2^{(0)} = \pm\frac{k_2}{\omega_2}\,. \tag{26}$$

It depends on the relative magnitude of the respective JT stabilization energies

$$E_1^{JT} = -\frac{k_1^2}{2\omega_1}\,, \tag{27}$$

$$E_2^{JT} = -\frac{k_2^2}{2\omega_2}\,, \tag{28}$$

which pair of stationary points represent the global minima and which represents the saddle points of V_-. The overall appearance of $V_\pm$ is reminiscent of the potential surfaces of the linear-plus-quadratic $E \otimes e$ JT effect, but with a twofold, rather than threefold, symmetry. On the other hand, in the special case of equal frequencies and coupling constants, $\omega_1 = \omega_2$ and $k_1 = k_2$, the Hamiltonian of the *linear* $E \otimes e$ JT effect and its rotationally symmetric potential energy surfaces are recovered from Eqs. (23) and (24).

The vibronic problem of the Hamiltonian (23) is easily solved in closed form if either $k_1 = 0$ or $k_2 = 0$; in this case the potential surfaces (24), taken as *diabatic* surfaces, represent displaced harmonic oscillators and lead to a Poisson distribution for the vibronic line structure of electronic spectra.[1,7] In the general case, $k_1.\ k_2 \neq 0$, numerical techniques are required to solve the vibronic secular problem (see Chapter 7). The resulting vibronic line strucure shows similar features as discussed above for the $E \otimes e$ JT effect. Since there is no constant of the motion like the vibronic angular momentum $\mathbf{J}$, Eq. (12), the motion is genuinely two-dimensional and thus more similar to the quadratic, rather than linear, $E \otimes e$ coupling case of Sec. 2.1. Thus, it displays the generic behavior also found for other, less symmetric (non-JT) systems discussed in Chapter 7. We conclude by pointing out that in many examples like the allene radical cation, discussed in Sec. 3.1, there will be more than a single B_1 and B_2 vibrational mode. These additional modes are all nonseparable, thus rendering the vibronic dynamics inherently more complex.

2.5. *The Pseudo-Jahn–Teller Effect*

The discussion so far has been confined to an isolated doubly degenerate (E) electronic state. This idealization will not always be applicable to a real molecular system, where couplings to other electronic states may play a role. As a simple generalization we will therefore consider now the interaction of an E electronic state with a nondegenerate state, characterized by the symmetry label A. The intra-state (JT) interaction within the E state will initially be suppressed for clarity.

The general principles for the construction of the vibronic Hamiltonian and the symmetry selection rules are the same as indicated above and discussed in more detail in Chapter 7. The previous distinction between trigonal and tetragonal point groups does not play a role, and the first-order coupling is always accomplished by doubly degenerate (e) vibrational modes. In an analogous notation as in Eq. (3), the Hamiltonian for the linear $(E + A) \otimes e$ pseudo-Jahn–Teller effect is found to be[11,40,41]

$$\mathcal{H} = H_0\mathbf{1} + \begin{pmatrix} E_E & 0 & \lambda Q_x \\ 0 & E_E & \lambda Q_y \\ \lambda Q_x & \lambda Q_y & E_A \end{pmatrix}. \tag{29}$$

Here E_E and E_A denote the E and A state energies for the undistorted nuclear configuration ($Q_x = Q_y = 0$) and $\mathbf{1}$ represents the 3×3 unit matrix.

The Hamiltonian (29) shares many features with the general vibronic coupling problem for two nondegenerate electronic states, discussed in Chapter 7. We note that the notion "pseudo-Jahn–Teller" interaction has also been used in the chemical, rather than spectroscopic literature, for this latter situation. We adhere to the more precise definitions of the spectroscopic literature and reserve the term "pseudo-Jahn–Teller" (PJT) for systems where one of the interacting states as well as the coupling mode are degenerate. We also note that, as for general vibronic coupling systems, the totally symmetric modes are nonseparable from the PJT problem and play an important role already in first order. They are neglected in Eq. (29) for simplicity but are included in most of the examples discussed in Sec. 3.

The adiabatic eigenvectors corresponding to Eq. (29) involve either the asymmetric (potential surface V_0) or symmetric (potential surfaces V_+ and V_-) linear combinations of the E component basis states. The eigenvalues

are

$$V_0 = \frac{\omega}{2}\left(Q_x^2 + Q_y^2\right) + E_E\,,$$
$$V_\pm = \frac{\omega}{2}\left(Q_x^2 + Q_y^2\right) + \frac{E_E + E_A}{2} \pm \sqrt{\left(\frac{E_E - E_A}{2}\right)^2 + \lambda^2\left(Q_x^2 + Q_y^2\right)}\,. \tag{30}$$

It depends on the sign of $E_E - E_A$ whether V_+ or V_- correlates with the E state for $Q_x = Q_y = 0$ and becomes degenerate there with the "unperturbed" surface V_0. For small $\rho^2 = Q_x^2 + Q_y^2$ and $E_E \neq E_A$ the rotationally symmetric surfaces (30) depend quadratically on the displacement amplitude. The intersection of the E-type potential energy surfaces (V_0 and either V_+ or V_-) is therefore not of the conical type and also called a *glancing* intersection[27,42] A glancing intersection is characteristic of the Renner–Teller effect in linear molecules.[3,50,51] There is no geometric phase effect for glancing intersections[29,43] and there is not necessarily an instability of the high-symmetry configuration $Q_x = Q_y = 0$. Rather, the lower surface V_- may have its minimum at a distorted structure $\rho_0 \neq 0$ with

$$\rho_0^2 = \lambda^2/\omega^2 - \Delta^2/\lambda^2\,, \tag{31}$$

provided that $\lambda^2 > \omega\Delta$, $\Delta = |E_E - E_A|/2$.[11] In other words, since a threshold coupling is to be exceeded, there is, unlike the JT case, no spontaneous distortion.

The potential energy surfaces (30) may exhibit the interesting topology of a triple conical intersection[41,43,44] displayed in Fig. 4. This occurs for $E_E = E_A$, when all surfaces are degenerate at $\rho = 0$, and the degeneracies are all lifted in first order in ρ. The equality $E_A = E_E$ will not be a rare exception, because of the existence of totally symmetric modes which modulate the $E - A$ energy gap and often cause an $E - A$ surface crossing. In the $Q_x - Q_y$ subspace depicted in Fig. 4, the JT-type geometric phase is absent, because the angular dependence of the adiabatic eigenvectors of Eq. (29) does not depend on the $E - A$ energy gap.[11,43] Pictorially speaking, the geometric phase of the two conical intersections, which each of the surfaces undergoes with the other two, may be imagined to cancel each other.

Figure 5 demonstrates the profound impact which the presence or the absence of the geometric phase may have on the time-dependent wave

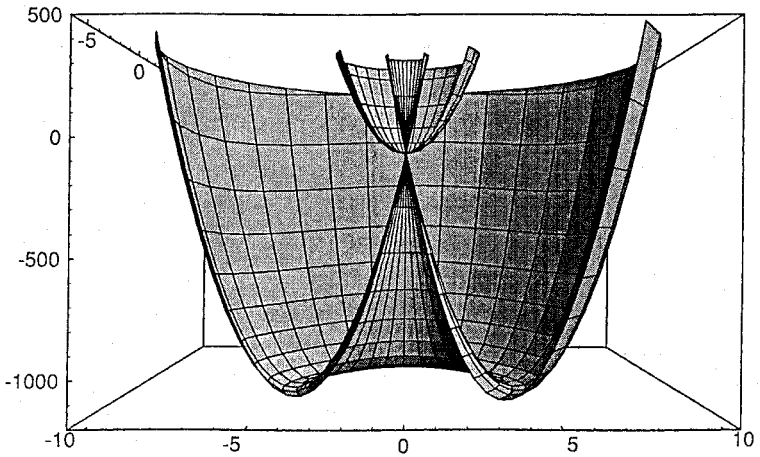

Fig. 4. Perspective drawing of a triple conical intersection arising for the PJT potential energy surfaces of Eq. (30). While the upper and lower surfaces (V_+ and V_-) are identical to the Mexican hat surfaces of Fig. 1, the additional surface (V_0) represents the unperturbed harmonic oscillator potential. For more details see text.

packet dynamics on intersecting surfaces: whereas the left-hand panels are for the triple intersection (or PJT) case without geometric phase effects, the right-hand panels depict results for the conical intersection (or JT) case exhibiting the geometric phase effect. The system parameters are chosen such that the lower surfaces V_- are identical and that nonadiabatic coupling effects to the higher-energy surface(s) are negligible in both systems[45] (see Ref. 46 and Sec. 3.3 below for more information on the system chosen). The initial wave packets are identical Gaussians located on the lower surface and on the positive Q_y axis for initial time $t = 0$. At later times they are seen to broaden and gradually enircle the intersection at $Q_x = Q_y = 0$. In the lower half-plane there is constructive/destructive interference as the two parts of either wave packet start to overlap on the lower Q_y axis. For longer times (lowest panels) this causes a *completely different* interference structure of the two wave packets due to geometric phase effects.

The anomalous symmetry effects caused by the geometric phase are generic to the quantum dynamics at conical intersections and are further discussed in Chapter 12. The probably most intuitive way to rationalize these effects consists in noting that the two electronic states in the upper

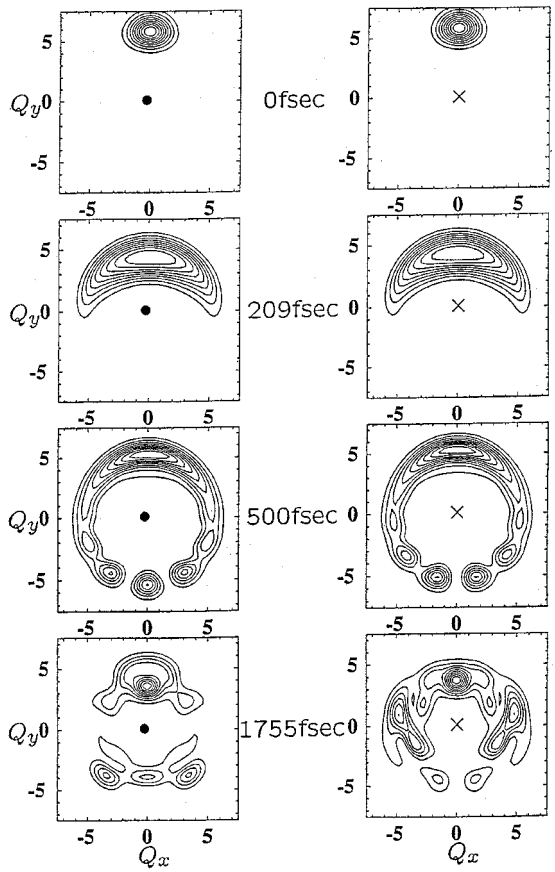

Fig. 5. 2D contour line diagrams of snapshots of time-dependent wave packets surrounding an intersection (occurring at $Q_x = Q_y = 0$). The latter is a two-state JT intersection in the right hand column and a triple, or PJT, intersection in the left-hand column of panels. The presence or absence of the geometric phase causes a different nodal pattern of the wave packets near the negative Q_y axis, and a globally different behavior of the wave packets for long times (see lowest panels, from Ref. 46).

and lower half-planes of Fig. 5 ($Q_y > 0$ and $Q_y < 0$) have opposite symmetry behavior with respect to the reflection $Q_x \rightarrow -Q_x$ (in case of E states for equilateral X_3 systems, for example, these have A_1 and B_2 symmetries in the C_{2v} subgroup relevant to $Q_y \neq 0$). The corresponding nuclear wave functions must also have the same (e.g. A_1 and B_2) symmetries as the

electronic wave functions, thus differing in the two half-planes $Q_y > 0$ and $Q_y < 0$. This explains the phenomenon observed in Fig. 5.

In real applications, the Hamiltonian (29) generally has to be extended to account for the intra-state (JT) couplings within the E state. Three different cases can be distinguished. In trigonal point groups with a single E irreducible representation, the same set of modes will be JT and PJT active. Then the extension of Eq. (29) will consist in adding the coupling terms of Eq. (3) for the same mode(s). In trigonal point groups with different E irreducible representations (say, E_1 and E_2), the E_2 vibrational modes are JT active and, depending on the system under study, either E_2 or E_1 modes are PJT active. In the latter case, the Hamiltonians (3) and (29) for both sets of modes have to be added. Finally, in tetragonal point groups, the JT active (B_1/B_2) vibrational modes are always different from the PJT active (E) modes. Then, Eq. (29) is to be augmented by the Hamiltonian (23) for the $E \otimes b$ JT effect. In all cases there will arise a complex set of seams of conical intersections comprising different pairs of potential energy surfaces, and possible intersections of these seams may also occur.

As an illustration, Fig. 6 depicts a set of three intersections occurring in the benzene radical cation. One is of the conical type, whereas at the other two crossings no interaction occurs, at least not in the subset of coordinates chosen for the drawing. The situation changes, however, in different vibrational subspaces, which underlines the complex topology of the surfaces in the pertinent higher-dimensional coordinate space.[12]

Finally, we add that the Hamiltonian (29) also describes Σ-Π vibronic coupling in linear molecules,[48] for example in HCN^{+}[47] and $C_2H_2^{+}$.[49] Its generalization to include purely intra-state vibronic coupling consists in adding the so-called Renner–Teller coupling terms.[50,51]

3. Representative Examples

3.1. *Brief General Overview*

In this subsection, we give a very condensed overview over molecular JT and PJT systems, ordered with increasing size (and, partly, complexity) of the system. This is primarily intended as a guide to the considerable amount of literature in the field.

The probably simplest class of JT systems are regular (equilateral triangular) X_3 systems. Focussing on cases with a single active, or valence,

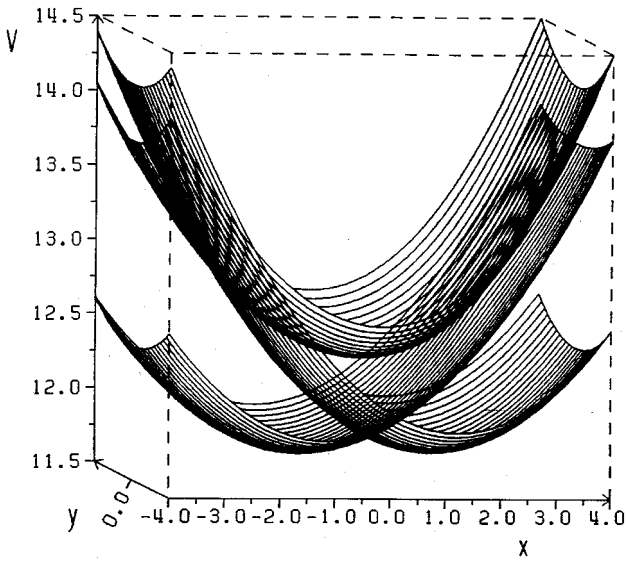

Fig. 6. Perspective drawing of three different (JT and PJT) intersections occurring in the benzene cation (from Ref. 12). The $x(y)$-coordinate represents a JT(PJT)-active mode. The right-hand intersection is conical in the drawing, while for the other two crossings the coordinate space is to be augmented to reveal the conical intersection. See Ref. 12 for more details.

electron, we have X = H, Li – Rb, and the electronic ground state at the D_{3h} configuration is of ^2E symmetry and thus JT unstable. The smallest metal trimers (X = Li – K) have been studied theoretically as regards their electronic and geometrical structure.[52–55] The dynamical JT effect has been identified in the two-photon ionization and stimulated emission spectra of Li_3[56] and Na_3,[57,58] also in excited electronic states.[59,60] The issue of the geometric phase played a major role[43,44,61,123] and led to its first unambiguous identification in the A-state of Na_3.[62] For a higher excited electronic manifold of Na_3, see a later subsection in this chapter. In a similar vein, ultraviolet absorption, dispersed fluorescence and two-photon ionization spectra of Al_3, Cu_3,[63,64] Ag_3,[65] and Au_3[66] have been reported and analysed in terms of JT models, and pertinent potential energy surfaces have been computed *ab initio*.[67–69]

As next larger systems with a threefold symmetry axis, we mention NH_3, BF_3, NO_3, and their radical cations. The first excited state of NH_3^+

is a prominent example of a strong two-mode JT effect, which has been analysed using *ab initio* calculated coupling constants;[70] recently this work has been extended to take also the PJT coupling to the ground state into account[71] which modifies the ^2E spectral envelope and leads to intensity borrowing effects in the ground state as well as absence of detectable emission in NH_3^+. Two-mode JT and PJT calculations have also been reported for BF_3^+ in relation to the vibronic line structure of the photoelectron spectrum.[31] Apart from "standard" JT spectra, also intensity borrowing effects and a two-mode-driven PJT instability of the ground state of BF_3^+ have been identified. The latter is very small in the ground state of NO_3,[72] but significant JT coupling effects have been established for electronically excited, as well as ionic, states of this species.[73,74]

A natural extension is provided by regular XY_3Z systems, with X and Z lying on the threefold symmetry axis of the (equilateral) Y_3 moiety. This comprises, in particular, the methoxy family of radicals (CH_3O, CD_3O, CH_3S, CF_3O, CF_3S) and metal monomethyl radicals MCH_3 (M = Mg, Ca, Zn, Cd), which are all covered comprehensively in the review article by Barckholtz and Miller.[9] Suffice it to say that the methoxy radical and its derivatives are among the best-studied JT-active radicals; we confine ourselves to mentioning some key experimental[75–77] and theoretical[78,79] studies. A complete second-order analysis of the three-mode JT effect in CH_3O, based on large-scale *ab initio* computations, has been performed by Höper *et al.*[79] This has recently been extended to demonstrate the importance of bilinear JT coupling terms, mixing a_1 and e vibrational modes, on photoelectron spectral intensities as well as spin-orbit splittings[80] (see also Sec. 2.3.2). As a closely related system we mention CH_3F^+.[127]

Examples of the less common tetragonal point groups (see Sec. 2.4) are the "odd-numbered" cumulenes C_3H_4 and C_5H_4 and their radical cations. Here the terminal CH_2-groups lie in perpendicular planes, giving rise to the $E \otimes b$ JT effect. The latter has been established for the ground states of the radical cations[81] and been reconsidered and extended to excited electronic states[82] of $C_3H_4^+$. Simultaneous PJT interaction with a higher excited state of $C_3H_4^+$ has also been analysed theoretically.[83,84] For more details, see Chapters 7 and 14.

Further examples for tetragonal point groups are the cyclic molecules cyclobutane (CB), cyclobutadiene (CBD), and their radical cations. Depending on whether CB is planar or puckered, the pertinent point group

is D_{4h} or D_{2d},[85] while CBD is a classic example for a PJT distorted square, leading to a rectangular shape (point group D_{2h}, see, for example, Ref. 86). Both radical cations are characterized by an ^2E ground state at the square planar (D_{4h}) configuration, which is thus JT unstable.[85,87] The JT effect manifests itself in the PE spectral envelope[88,89] and in the (highly anharmonic) potential energy surfaces, which have been explored in a number of *ab initio* calculations.[85,90]

The smaller related species cyclopropane (point group D_{3h}) represents a well-known case of the $E \otimes e$ JT effect in the radical cation. It displays the characteristic double-peaked PE spectral profile[91] and has been characterized *ab initio* in terms of its JT distorted structures[92,93] and in terms of its spectral profile.[155] Similarly well studied is the next larger analogue, the cyclopentadienyl radical,[94,95] especially since the recent, combined experimental and theoretical analysis of T. Miller and coworkers.[96,97]

As a final prominent class of molecules we emphasize benzene and benzenoid cations. There has been a large amount of work on halogenated systems, especially $C_6H_3F_3^+$ and $C_6F_6^+$, where the multi-mode JT effect in the electronic ground state could be measured through emission spectra in the radical cation (see, for example, Refs. 98–100). A wealth of detailed information emerged on the JT and related coupling parameters, also on related systems[101,102] and aided by *ab initio* calculations.[103] More recently, also the parent ion, $C_6H_6^+$, has been measured through high-resolution spectroscopic techniques[104] which have been combined very recently with *ab initio* calculations to arrive at a nearly quantitative characterization of the system parameters.[105] For a more detailed discussion of $C_6H_6^+$, comprising also PJT interactions and excited electronic states, we refer to Sec. 3.4 below.

Although the above list is far from complete, it gives nevertheless a representative selection of JT-active molecular systems with doubly degenerate electronic states. Concerning triply degenerate states, which are beyond the scope of this survey, we mention the ground state of the methane radical cation[106,107] and the tetrahedral systems P_4, As_4, and Sb_4, where JT activity has been documented in ground and excited states of the radical cations (of E and T symmetry).[108,109] A combined JT-plus-PJT approach has also been applied to P_4^+, involving five coupled potential energy surfaces (interacting $E + T$ states).[110] We conclude by pointing to the upsurge of interest in the JT effect in icosahedral systems caused by the discovery of the fullerenes and documented, for example, in Refs. 10 and 111.

3.2. *Triatomic Hydrogen*

Formally, triatomic hydrogen represents the smallest member of the series of X_3 systems mentioned above, with X possessing a single active (or valence) electron. H_3 obviously constitutes the smallest JT-active system at all. However, as an important difference to the examples of Li_3 and Na_3, the ground state potential energy surface of H_3 is repulsive and H_3 therefore does not occur as a stable molecule. Nevertheless, at the equilateral triangular configuration the electronic ground state is of $^2E'$ symmetry, JT-unstable, and the ground state surface therefore correlates with the lower sheet of the $E\otimes e$ Mexican-hat double cone discussed in Sec. 2.2. The details of this topology have first been investigated in the pioneering work of Porter Stevens, and Karplus.[112] The impact of the geometric phase, associated with this JT intersection, on the H + H_2 reactive scattering process (which proceeds on the electronic ground state surface of H_3) has first been investigated by Kuppermann and coworkers.[113,114] For a general survey of this prototype reactive scattering process see, for example, Refs. 115 and 116. For a detailed discussion of the geometric phase issue we refer to Chapter 12.

A direct way of probing the conical intersection of H_3 ($\widetilde{X}^2E'$) are Rydberg emission spectra.[117,118] Here the initial electronic state has (approximately) D_{3h} geometry. The conical intersection in the final (ground) electronic state thus falls into the FC zone of the electronic transition. The situation is depicted in the upper panel of Fig. 7 which shows the potential energy surfaces of initial and final electronic states as a function of the distance between one H-atom and the centre of the H_2 moiety (for perpendicular approach and fixed r_{H-H} distance as indicated in the panel). The conical intersection is represented by the curve crossing at $R = \sqrt{3}r/2 \approx 1.42$ au and seen to coincide with the maximum of the initial state wave function which is also included in the drawing.

In order to simulate the experimental emission spectrum (panel c) we have performed 3D wave-packet dynamical calculations[119,120] using Jacobi coordinates and the so-called DMBE potential energy surfaces of Varandas *et al.*[121] The result (for $J = 0$) is displayed in panel b and seen to match the experiment[117,118] quite well. It should be noted that the weak lines superimposed on the double-hump structure are not significant; they arise from impurities (in experiment) or from convergence problems (in the theoretical result). There is thus a continuous, nearly structureless spectrum, both for the short- and long-wavelength hump. The two humps can

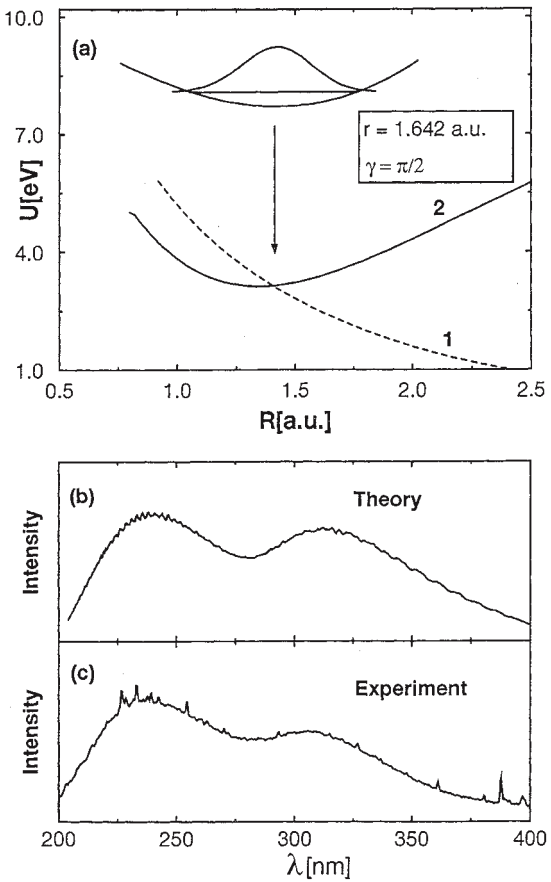

Fig. 7. Potential energy curves (panel a) and theoretical and experimental spectral profiles (panels b, c) for the Rydberg emission spectra of D_3. As revealed by panel a, the initial, upper electronic state is characterized by a near-equilateral triangular shape and the transition directly probes the curve crossing (conical intersection) in the ground state occurring for $R = r\sqrt{3}/2$ (see the arrow). The experimental and theoretical spectra are from Refs. 117 and 120, respectively.

be associated with the lower and upper sheet of the JT-split potential energy surfaces, respectively. While for the lower surface this behavior is not surprising in view of its repulsive nature, it is remarkable for the upper surface, since the latter is probed near its minimum and well below its dissociation limit of 4.74 eV (three-particle breakup[121]). Indeed, companion calculations performed for the *uncoupled* adiabatic surfaces reproduce the

smooth, short-wavelength hump corresponding to the repulsive lower surface, but give a series of *discrete* lines (instead of the long-wavelength hump) corresponding to the bound upper surface.[122] These lines represent mostly excitation of the breathing mode owing to the different bond lengths of H_3 in the initial and final states.[120] Remember that for the standard $E \otimes e$ JT model the nonadiabatic coupling effects lead to the formation of resonances (Slonczewski resonances) as discussed in relation to Fig. 2 above. In the case of H_3 ($\widetilde{X}^2E'$), this broadening is so strong and the resonances are overlapping so heavily that none can be identified in the spectrum of Fig. 7(b). Therefore this prototype JT system also serves as a representative example of the thorough redistribution of spectral intensity due to JT nonadiabatic interactions.

In order to obtain additional insight into the effects of these interactions, we have also studied the electronic population dynamics in this coupled electronic manifold. The case of broadband excitation has been considered (similar to the FC transition of the emission spectrum) as well as state-specific properties.[119] In the latter case the upper uncoupled-surface vibrational levels have been computed first and then been used as initial wavepackets in coupled-surface calculations. The resulting electronic populations of the upper adiabatic state are collected in Fig. 8; the inset gives the quantum numbers of the different initial vibrational levels. One recognizes the *extremely short* timescale of only $\approx 3-6$ fs on which the population decay (i.e. the internal conversion process from the upper to the lower JT-split surface) takes place. Upon closer inspection there is a mode-specificity which can be explained in terms of the nodal properties of the initial wavefunction: the vibrational levels with the (somewhat) slower decay have a nodal line along the seam of conical intersections which reduces the nonadiabatic coupling effects slightly.[119] A similar, extremely fast decay has been deduced from the (more phenomenological) analysis of the experimental spectrum.[118] These decay times are among the fastest known for internal conversion processes. We conclude that this smallest JT system highlights the profound impact which conical intersections can have on the system dynamics.

3.3. *The Sodium Trimer in the B-State*

As mentioned earlier, the sodium trimer represents a well-known example for the $E \otimes e$ JT effect in the ground as well as in several excited electronic

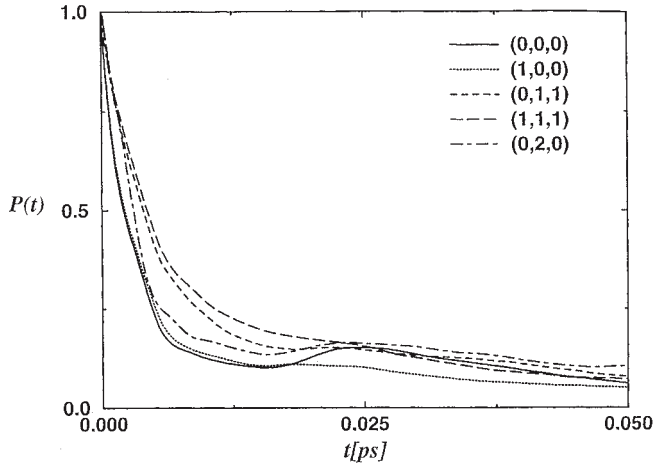

Fig. 8. Adiabatic electronic populations of the higher JT sheet of the ground state manifold of H_3, as obtained from 3D wavepacket dynamical calculations.[119] Five different upper-cone vibrational states are employed in the calculation as initial states, which are indicated through the different line types (see legend for their assignment). The extremely fast decay, with lifetimes of only 3–6 fs, demonstrates the exceedingly strong nonadiabatic coupling effects in this system. This amounts to a very large homogeneous (lifetime) broadening of these levels which causes them to be "absent" in the spectra of Fig. 7. Note the mode-specificity of the lifetimes (see text).

states. It is, therefore, not surprising that an electronic excitation spectrum of Na_3 (so-called B-band of the two-photon-ionization spectrum) has been interpreted in terms of JT activity in the final electronic state.[61] More specifically, the excited state has been anticipated to possess $^2E'$ symmetry at the D_{3h} configuration and the vibronic motion has been interpreted as large amplitude pseudorotational motion, i.e. as a concerted near-circular motion of the 3 atoms around the D_{3h} reference point. This is illustrated by the central panel of Fig. 9, which shows a high-frequency progression corresponding to the bending mode of Na_3 in the C_{2v} configuration (radial motion in Fig. 1) and a low-frequency, non-equidistant series of lines corresponding to the pseudorotational motion (angular motion in Fig. 1). Assuming low-energy motion around a JT intersection at the origin like in Fig. 1, the latter motion would be adiabatic, but subject to the geometric phase effect.

This is indeed the result of the original analysis of the experimental spectrum which was based on the linear + quadratic $E \otimes e$ JT model.[61]

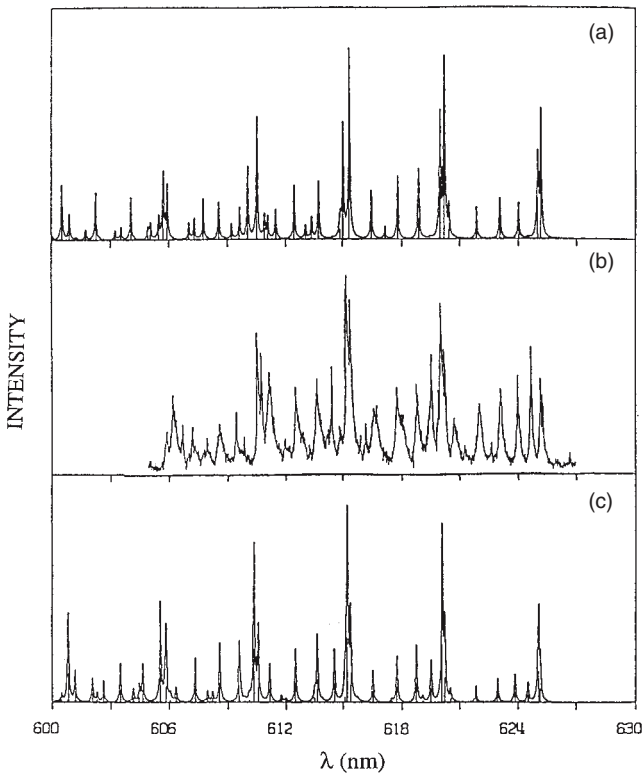

Fig. 9. Comparison of experimental and calculated vibronic structures for the B-band of Na_3. Upper and lower panel: computed vibronic structures employing a JT (a) and a pure PJT (c) approach. Central panel (b): experimental recording from Ref. 61.

Subsequent *ab initio* calculations by Cocchini *et al.*, however, laid the ground for a different scenario which consists of accidentally small linear JT couplings and a significant PJT interaction with a nearby nondegenerate (at the D_{3h} configuration) electronic state.[44] Remember that according to Sec. 2.4 there is *no* geometric phase effect in such a situation.

This question provided the motivation for a simple 2D model description of the *B*-band, focussing exclusively on the PJT interaction; for comparison, also the earlier JT-type approach was reconsidered.[43] The vibronic Hamiltonians are given by Eqs. (3) and (29), respectively, augmented by the appropriate quadratic coupling constants. The two coupling constants

were adjusted in either approach within a realistic range (the $E-A$ energy gap was constrained to be zero in the PJT case to avoid a bias in the comparison, and because the $E-A$ energy gap is small and changes sign within the relevant range of the breathing mode coordinate[44]). The resulting JT and PJT spectra are included and compared to the experimental recording in Fig. 9. By and large, the agreement with experiment is similarly good in either case: both the high-frequency and the low-frequency progressions are qualitatively reproduced. A closer inspection reveals that the details of the PJT line-structure reproduce the experimental findings better than do the JT results. Although this evidence alone may not be conclusive, the PJT approach is clearly supported by the *ab initio* calculation[44] and later high-resolution spectra of Ernst and Rakowski.[123] Thus, the $Na_3(B)$ system is *not* an example of the geometric phase effect.

The absence of the geometric phase allows a FC type description and the use of standard wavepacket propagation on a single potential energy surface. The Berlin groups have performed 3D *ab initio* quantum dynamical treatments of cw spectra and (low intensity) fs pump-probe signals.[124–126] Valuable additional insight into the system dynamics could be obtained by these calculations. We have presented here $Na_3(B)$ as a PJT system since the above comparison (Fig. 9) shows that generally care is needed in deducing the system dynamics from experiment alone in the case of complex spectra, without guidance from *ab initio* data. In particular, vibronic energy levels, and even spectral intensities (see Fig. 9), can be quite insensitive to the differences in the system dynamics. The results of time-dependent wavepacket calculations, using the same parameters as in the theoretical JT and PJT spectra of Fig. 9, have been contrasted in the earlier Fig. 5. Here, for longer times the JT and PJT wavepackets look *entirely different*, although the corresponding spectra of Fig. 9 are rather similar. Of course, this difference is related to the well-known fact that low-resolution cw spectra probe primarily the short-time system dynamics. It has indeed been shown that fs pump-probe signals are more sensitive to the difference between JT and PJT couplings,[46] and a possible strategy to detect this difference in a three-pulse-experiment has been proposed.[128] We also mention related work by Cina and coworkers on a direct detection of geometric phase effects by femtosecond pump-probe interferometry.[129]

More information on the PJT nonadiabatic interactions is encoded in the higher-energy B'-band of Na_3 which probes a higher-energy surface of

the PJT-coupled manifold.[61] This system also has been studied recently by us using the same approach, and good agreement with available experimental data has been achieved.[130] A higher-resolution experimental spectrum would be desirable to shed more light on the various mode-mode and nonadiabatic coupling mechanisms operative in this band.

3.4. *The Benzene Radical Cation*

The benzene radical cation (Bz^+) represents a prototype organic radical cation and has been studied extensively in the literature, both theoretically and experimentally. We mention early and more recent studies of its electronic structure,[131–135] the photoelectron spectrum of benzene,[136–140] including its vibrational structure and the high-resolution ZEKE spectra,[104] dissociation and MATI spectra,[141,142] as well as studies on fluorescence[143,144] and fragmentation[145,146] dynamics. Many of these are dominated by vibronic effects which occur in a rich variety in this species.

Benzene has D_{6h} symmetry in its electronic ground state and the doubly degenerate ionic states are thus subject to the $E \otimes e$ JT effect. Since Koopman's theorem is valid for the lower electronic states of Bz^+, their ordering is given by that of the orbital energies of neutral benzene, which reads

$$(\text{core})(2a_{1g})^2(2e_{1u})^4(2e_{2g})^4(3a_{1g})^2(2b_{1u})^2(1b_{2u})^2(3e_{1u})^4(1a_{2u})^2(3e_{2g})^4(1e_{1g})^4$$

Besides the $^2E_{1g}$ ground state of Bz^+, the JT effect is thus operative also in low-lying excited states such as the $^2E_{2g}$ and $^2E_{1u}$ states of Bz^+. In addition, PJT coupling effects and related vibronic interactions may occur between *different* (degenerate or nondegenerate) electronic states. In the following we give an outline of the resulting vibronic dynamics, including our (as of this writing) recent studies of multi-state vibronic coupling effects. Unless otherwise stated, the work will refer to the undeuterated species, $C_6H_6^+$.

Benzene has four e_{2g} vibrational modes ($\nu_{15} - \nu_{18}$ in Herzberg numbering) which are linearly JT active according to the decomposition of the symmetrized direct products

$$(E_{1g})^2 = (E_{2g})^2 = (E_{1u})^2 = (E_{2u})^2 = A_{1g} + E_{2g} \tag{32}$$

The pertinent coupling constants have been determined with *ab initio* methods in a number of papers.[105,132,133,147,148] Unequivocally, the C–H

stretching mode ν_{15} has been found to have negligible JT activity in the $\widetilde{X}^2E_{1g}$ ground state, while the other three degenerate modes are found to be moderately JT active. Also, the ordering $D_{18} > D_{16} > D_{17}$ for the linear coupling parameters $D_i = k_i^2/2\omega_i^2$ (i =16–18) is in mutual agreement in the literature.

In Fig. 10 we depict the vibronic structure of the $\widetilde{X}$ band of the PE spectrum as obtained with the coupling constants of Ref. 148 (upper panel). The 3-mode JT problem has been solved with the Lanczos algorithm and the resulting line spectrum been convoluted with Lorentzians of width FWHM = 20 meV to account for finite resolution. The experimental result of Ref. 140 is included in the figure for comparison (lower panel) and is seen to agree nicely with the calculation. Very similar agreement has been obtained before,[147] based on similar *ab initio* methods and comparing with the earlier experimental recording of Ref. 138. The low-energy vibronic structure in Fig. 10 can be assigned to the CCC-bending mode ν_{18}, while beyond ∼9.4 eV there are strong mode-mixing effects. We note that also the symmetric CC-stretching mode ν_2 (we use Herzberg numbering throughout) is excited, leading to the line at ∼9.37 eV.

The above conclusions are corroborated by similar results for $C_6D_6^+$.[147] We note that all coupling parameters D_i (i = 16–18) are of order unity, implying nonadiabatic nuclear motion proceeding on both JT-split potential energy surfaces simultaneously. Since the studies of Refs. 147 and 148 are confined to the linear coupling approximation, there exists a (collective) rotational symmetry of the potential energy surfaces around the D_{6h} configuration. Including quadratic coupling terms leads to two sets of stationary points of D_{2h} symmetry, corresponding to an either compressed or elongated shape, and it depends on the sign of the quadratic coupling constant which set represents the equivalent minima or saddle points. Such an analysis has been initiated based on high-resolution ZEKE spectra[104] (see also Ref. 103) and been extended recently in the careful work of Ref. 105. While the earlier analysis has been performed in terms of a single JT active mode, leading to a barrier height of only ∼8 cm^{-1},[104] all JT active modes have been included by Applegate and Miller[105] and an even smaller barrier height been obtained (by calculation of contributions from different modes). Similar results have been obtained by Ref. 156. Therefore, it can be concluded that the vibronic motion in the $\widetilde{X}^2E_{1g}$ state of Bz^+ is nonadiabatic and highly fluxional.[104]

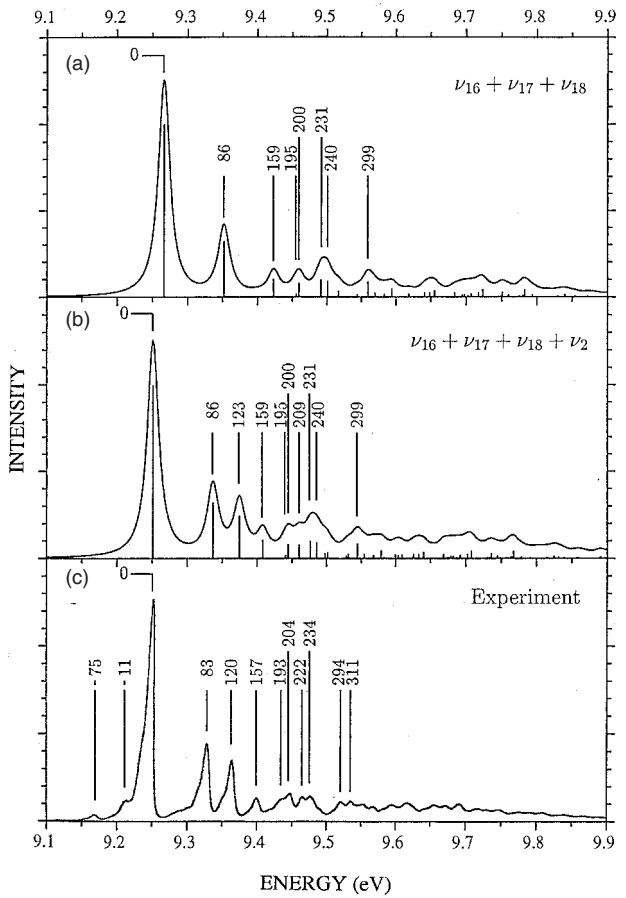

Fig. 10. Comparison of theoretical (panels (a,b)) and experimental (panel (c)) first bands of the photoelectron spectrum of benzene. The final state is the $\tilde{X}\,^2E_{1g}$ ground state of the cation. The JT activity of the modes ν_{16}, ν_{17} and ν_{18} is displayed by panel (a), the excitation of the symmetric CC-stretching mode ν_2 is included in panel (b). The experiment[140] is characterized, in addition, by hot bands near 9.2 eV and (probably) 9.3 eV, which are not accounted for in the calculation, performed for $T = 0$.

A JT-plus-PJT vibronic coupling approach has been applied to describe the close-lying $\widetilde{B}-\widetilde{C}$ bands corresponding to the $^2E_{2g}-^2A_{2u}$ states of Bz^+, respectively.[12,149] Here, the three-mode JT Hamiltonian of Eqs. (3) and (15) has been augmented by the two-mode extension of the PJT Hamiltonian,

Eq. (29). The PJT couplings are provided by the modes ν_{19} and ν_{20}. The PJT coupling constants have been determined by *ab initio* methods.[12,148] The results are shown in Fig. 11 and compared to the experimental recording of Baltzer *et al.* (see insert). The two different contributions are drawn separately to reveal the different sources of spectral intensity in the lower and higher-energy ranges. The former, being dominated by E_{2g} vibronic symmetry, is characterized mainly by a 3-mode JT effect quite similar to the $\widetilde{X}\,^2E_{1g}$ ground state (see Refs. 12 and 149 for details). The energy range around 12.1–12.7 eV, deriving its spectral intensity mostly from the $^2A_{2u}$ state, is characterized by a very dense level structure with highly irregular line positions and intensities. The peaks of the envelope do not represent zero-order vibrational levels but rather accidental agglomerations of spectral intensity.

In a time-domain description, the dense and erratic line structure of the $^2A_{2u}$ state corresponds to an ultrafast electronic population decay, that is, a femtosecond $\widetilde{C}\,^2A_{2u} \rightarrow \widetilde{B}\,^2E_{2g}$ internal conversion process of an initial wavepacket which has been placed on the $\widetilde{C}$ state potential energy surface by a FC-type transition.[12] Both phenomena reflect the strong nonadiabatic coupling effects triggered by a conical intersection between the $\widetilde{B}$ and $\widetilde{C}$ state potential energy surfaces. The situation is illustrated by the earlier Fig. 6 which shows the "additional" conical intersection in its center right hand part. Remember that this conical intersection, which may be called PJT-induced, complements the JT intersection at the origin in Fig. 6. Both lead to intersecting seams of conical intersections and to nonadiabatic coupling effects between different pairs of (component) electronic states: whereas in the low-energy region of Fig. 11 the vibronic dynamics is nonadiabatic only in the JT-coupled (i.e. E_{2g}) electronic function space, the high-energy vibronic motion is also subject to strong $E_{2g} - A_{2u}$ nonadiabatic interactions. This highlights the additional complexity which is caused by the interplay between JT and PJT coupling mechanisms.

There is further evidence pointing to an even richer variety of vibronic phenomena in Bz^+. From the experimental side, no Bz^+ fluorescence could be detected although the transition $\widetilde{C}\,^2A_{2u} \rightarrow \widetilde{X}\,^2E_{1g}$ is dipole-allowed (and the $\widetilde{C}$ state is below the threshold for fragmentation).[143,144] This has been interpreted in terms of a sub-picosecond nonradiative transition of the $\widetilde{B} - \widetilde{C}$ excited state manifold to the $\widetilde{X}$ ground state of Bz^+.[150] Of course, this phenomenon is not accounted for by the aforementioned IC processes

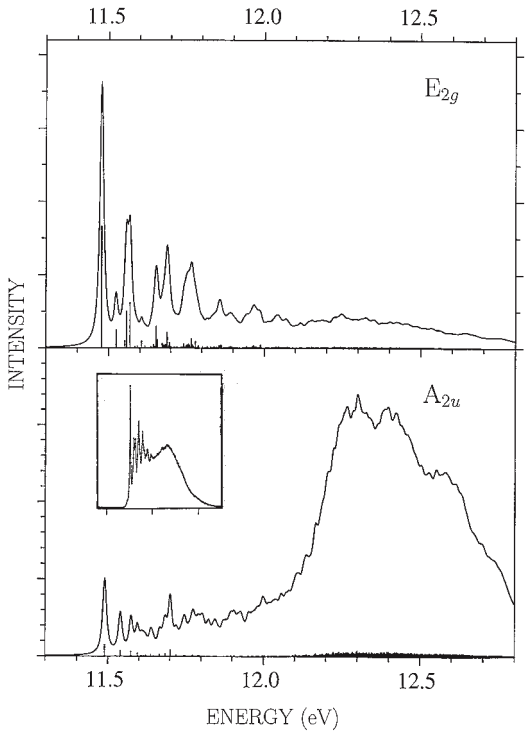

Fig. 11. Calculated vibronic structure of the $\widetilde{B}\,^2E_{2g} - \widetilde{C}\,^2A_{2u}$ band of the PE spectrum of benzene. The two contributing vibronic symmetries are drawn separately to reveal the different sources of spectral intensity. The insert shows the experimental recording of Ref. 140.

which take place *within* the $\widetilde{B} - \widetilde{C}$ electronic manifold. Also, the authors of Ref. 144 estimated the dependence of the pertinent potential energy surfaces on the totally symmetric coordinates (the latter being the dominant "accepting modes" in standard non-radiative decay theory[151,152]). No low-energy curve crossing or conical intersection was found which would have provided a mechanism for the fast $\widetilde{C} - \widetilde{B} \rightarrow \widetilde{X}$ non-radiative transition. Finally we mention indirect evidence that the fragmentation of highly excited Bz^+, with an internal energy of ~5 eV, proceeds through the $\widetilde{X}\,^2E_{1g}$ state.[145,146] This points to efficient coupling mechanisms involving also the higher-energy $\tilde{D}\,^2E_{1u}$ and $\widetilde{E}\,^2B_{2u}$ electronic states.

We have investigated the potential energy surfaces of Bz^+ in an enlarged nuclear configuration space and indeed found a whole variety of additional conical intersections.[148,149] These comprise also upper and lower JT-split potential energy surfaces of *different* (at the D_{6h} geometry) degenerate electronic states of Bz^+, i.e. they are triggered by the multimode JT effect in these states. This is a novel finding (see also Ref. 150) which is indicated schematically in Fig. 12. The effective coordinate Q_{eff} chosen here represents a linear combination of all linearly active vibrational modes (e_{2g} and a_{1g}) and is meant to give an overall impression of the conical intersections in the $\widetilde{X}\,^2E_{1g} - \widetilde{E}\,^2B_{2u}$ electronic manifold. Although the potential energy curves rely on the linear coupling model, the additional intersections have been confirmed by various single-point coupled-cluster calculations in the ν_{16} and ν_{18} normal coordinate subspaces. Of course, also the pertinent coupling constants entering Fig. 12 have been determined by *ab initio* calculations, partly with the use of analytical gradient methods.[148]

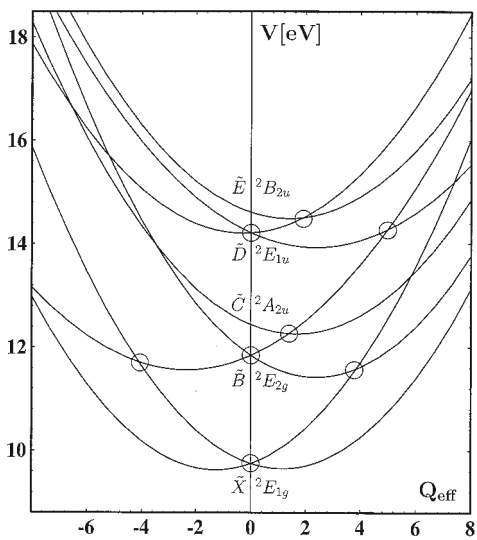

Fig. 12. Representative cut through the potential energy surfaces of the $\widetilde{X}\,^2E_{1g} - \widetilde{E}\,^2B_{2u}$ states of the benzene radical cation. An effective coordinate has been used, which is a linear combination of all linearly active normal modes and has been chosen so as to reveal the various low-energy curve crossings (conical intersections) qualitatively correctly. These are indicated by the open circles and comprise JT intersections (at $Q_{\text{eff}} = 0$) as well as PJT intersections (at $Q_{\text{eff}} \neq 0$).

Figure 12 opens the fascinating perspective of a whole sequence of ultrafast IC processes for highly excited Bz^+. We have undertaken extensive wavepacket-dynamical calculations for this system, comprising (so far) up to five coupled potential energy surfaces and eight vibrational degrees of freedom.[149] From the electronic structure point of view, the calculations are based on the extensive *ab initio* calculations mentioned above and on a careful group-theoretical analysis of the underlying multi-state vibronic coupling terms.[148] This includes, in particular, the relative signs of the various JT coupling constants in the different electronic states. The actual wavepacket propagation has been performed with the powerful MCTDH method[153] which is described, in relation to vibronic coupling problems, in Chapter 14.

As two representative results from Ref. 149 we present in Fig. 13 the time-dependent electronic populations for the coupled $\widetilde{X} - \widetilde{B} - \widetilde{C}$ states of Bz^+. In the full calculation of Fig. 13(a) the degeneracies of all vibrational modes and electronic states are treated correctly, amounting to five strongly coupled potential surfaces and eight nonseparable nuclear degrees of freedom. The number of underlying "primitive" time-independent basis functions is $\sim 10^{11}$ and is reduced to $\sim 10^6$ time-dependent single-particle basis functions by the MCTDH contraction effect (see Chapter 14). The $\widetilde{B}$ and $\widetilde{C}$ state populations exhibit a similar short-time behavior as described above on account of the $\widetilde{B}-\widetilde{C}$ conical intersection, namely, a $\widetilde{C}$ state population decay in $\sim$20 fs followed by damped recurrences with a period of $\sim$33 fs (corresponding to the CC-stretching mode ν_2). At longer times, however, the combined $\widetilde{C} + \widetilde{B}$ population drops considerably below unity in favor of that of the $\widetilde{X}$ state of Bz^+. This finding, and the associated timescale of $\sim$200 fs, provides a natural explanation for the absence of detectable emission from the $\widetilde{C} - \widetilde{B}$ states. From the theoretical point of view, the gradual, kinetic-type increase of the $\widetilde{X}$ state population is remarkable, since the calculation is fully microscopic, without any phenomenological damping. The effective damping obtained here even surpasses related phenomena observed earlier for two state-three mode vibronic coupling systems (see Chapter 7).

A similar modelling has been performed for the coupled higher-energy $\widetilde{B} - \tilde{D} - \widetilde{E}$ manifold of states.[13,149] An intriguing combination of $\sim$20 fs and $\sim$200 fs IC processes has been obtained which can be traced to an overall similar behavior of the potential energy surfaces (see Fig. 12). For both sets of states the influence of the lower-energy state ($\widetilde{X}$ and $\widetilde{B}$, respectively) on

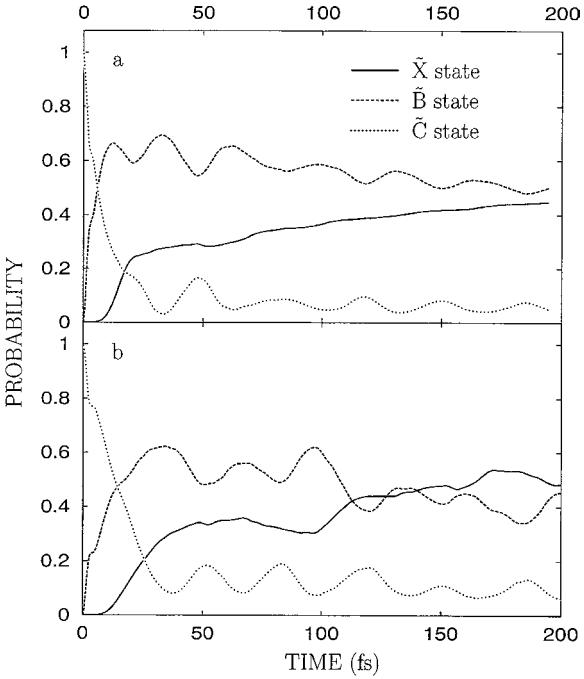

Fig. 13. Time-dependent electronic populations of the $\widetilde{X}$, $\widetilde{B}$ and $\widetilde{C}$ states of Bz^+ obtained from wavepacket dynamical calculations. The *ab initio* parameters of Ref. 148 and the MCTDH wavepacket propagation method[153] have been employed in the study. The initial wavepacket is defined by a FC transition to the $\widetilde{C}$ state potential energy surface; it is seen to undergo a stepwise transition to the $\widetilde{B}$ and then to the $\widetilde{X}$ state of the cation. The respective time constants are approximately 20 fs and 200 fs. (a) Calculation with degenerate vibrational modes and electronic states. (b) Analogous calculation, but suppressing these degeneracies. Apparently, this simpler calculation reproduces the full result of panel (a) quite well. For more details see text.

the spectral profile of the higher-energy electronic manifold has been quantitatively assessed.[149] All these results are novel findings in view of the complexity and number of conical intersections treated quantum-dynamically. They also provide a route to understanding the fragmentation dynamics of highly excited Bz^+. In that vein, Fig. 13(b) shows the results of companion calculations similar to Fig. 13(a), but suppressing the vibrational and electronic degeneracies. The result of this much simpler calculation is seen to reproduce the full result of Fig. 13(a) quite well. Such a simplified

treatment could be employed to model the dynamics for the entire $\widetilde{X} - \widetilde{E}$ sequence of intersections displayed in Fig. 12.

Summarizing, we hope to have demonstrated that Bz^+ represents a fascinating example of combined JT and PJT coupling effects leading to a genuinely complex, multi-mode and multi-state vibronic dynamics.

4. Concluding Remarks

In this Chapter, I have attempted to provide a brief overview over JT theory and its applications to molecular problems. Particular emphasis has been put on the relation of the JT effect to the focus of this book, namely, conical intersections and the associated vibronic dynamics. A variety of systems has been treated involving a doubly degenerate (E) state, mostly in trigonal, but also in tetragonal symmetry, and possibly interacting with a nondegenerate (A) state. Besides a very condensed survey of applications in molecular spectroscopy, three representative examples have been discussed in more detail, involving 2, 3 or up to 5 coupled surfaces in the quantum-dynamical treatment (H_3, $Na_3(B)$ and $C_6H_6^+$). The strong nonadiabatic coupling effects above the minimum energy of the conical intersection manifest themselves as an irregular line structure and as a femtosecond electronic population decay, as is typical also for other systems treated in this book.

As pointed out in the introduction, the JT theorem constitutes one of the first developments in the literature relating to conical intersections (even if only implicitly). On the other hand, JT systems like Bz^+ play a key role in modern work extending the frontiers of vibronic coupling theory. In this sense, the JT effect is of continuous importance in the field. From a systematic point of view, JT intersections represent one of three basic symmetry types of conical intersections (symmetry-enforced, symmetry-allowed and fully accidental). While in the last case, discussed especially in Chapters 2, 3 and 6, the locus of degeneracy of potential energy surfaces is truely accidental (determined by the specific system), the symmetry-allowed intersections, treated e.g. in Chapters 7–9, are characterized by the vanishing of *one* symmetry-lowering coordinate, so that the crossing is again symmetry-allowed in the remaining *sub*-space (owing to different symmetries of the electronic states). The JT intersections, on the other hand, are enforced to occur by the vanishing of *two* symmetry-lowering

coordinates, namely those of the JT-active mode(s). In the language of Ref. 154, the intersection space is thus predetermined to be located in the high-symmetry molecular point group, with the branching space given as its orthogonal complement. Note, however, that the latter holds only for a single JT-active, or e, vibrational mode. For several JT-active modes, linear combinations of their coordinates will generally exist such that the off-diagonal coupling terms like in Eq. (1) may vanish, although the individual displacements are nonzero. This observation, which is formulated here as a general prediction without further discussion, may lead to other interesting, though complicated seams of JT intersections. It is thus to be expected that the JT and PJT effects will provide fruitful areas of research also in the future, both from the point of view of basic theory as well as regarding specific examples.

References

1. R. Englman, *The Jahn–Teller Effect in Molecules and Crystals* (Wiley, New York, 1972).
2. E. Teller, preface in Ref. 1.
3. R. Renner, *Z. Phys.* **92**, 172 (1934).
4. H. A. Jahn and E. Teller, *Proc. Roy. Soc.* **A161**, 220 (1937).
5. E. Teller, *J. Chem. Phys.* **41**, 109 (1937).
6. I. Bersuker (editor), *The Jahn–Teller Effect. A Bibliographic Review* (IFI/Plenum, New York, 1984).
7. I. B. Bersuker and V. Z. Polinger, *Vibronic Interactions in Molecules and Crystals* (Springer Verlag, Heidelberg, 1989).
8. M. D. Sturge, *The Jahn–Teller Effect in Solids*, in *Solid State Physics*, Eds. F. Seitz, D. Turnball and H. Ehrenreich, Vol. **20** (Academic Press, New York, 1967).
9. T. A. Barckholtz and T. A. Miller, *Int. Rev. Phys. Chem.* **17**, 435 (1998).
10. I. Bersuker, *Chem. Rev.* **101**, 1067 (2001).
11. H. Köppel, W. Domcke and L. S. Cederbaum, *Adv. Chem. Phys.* **57**, 59 (1984).
12. H. Köppel, L. S. Cederbaum and W. Domcke, *J. Chem. Phys.* **89**, 2023 (1988).
13. M. Döscher and H. Köppel, *Chem. Phys.* **225**, 93 (1997).
14. H. C. Longuet-Higgins, *Adv. Spectrosc.* **2**, 420 (1961).
15. H. C. Longuet-Higgins, U. Öpik, M. H. Pryce and R. A. Sack, *Proc. Roy. Soc.* **A244**, 1 (1958).
16. J. C. Slonczewski, *Phys. Rev.* **131**, 1596 (1963).
17. J. C. Slonczewski and V. L. Moruzzi, *Physics* **3**, 237 (1967).

18. H. Köppel, L. S. Cederbaum and W. Domcke, *Mol. Phys.* **41**, 669 (1980).
19. M. C. M. O'Brien and S. N. Evangelou, *Solid State Commun.* **36**, 29 (1980).
20. H. Köppel, unpublished results.
21. A. Thiel and H. Köppel, *J. Chem. Phys.* **110**, 9371 (1999).
22. H. C. Longuet-Higgins, *Proc. Roy. Soc.* **A344**, 147 (1975).
23. M. V. Berry, *Proc. Roy. Soc. London* **A392**, 45 (1984).
24. C. A. Mead, *Rev. Mod. Phys.* **64**, 51 (1992).
25. C. A. Mead and D. G. Truhlar, *J. Chem. Phys.* **70**, 2284 (1979).
26. C. A. Mead, *Chem. Phys.* **49**, 23 (1980).
27. G. Herzberg and H. C. Longuet-Higgins, *Discuss. Faraday Soc.* **35**, 77 (1963).
28. F. S. Ham, *Phys. Rev. Lett.* **58**, 725 (1987).
29. J. W. Zwanziger and E. R. Grant, *J. Chem. Phys.* **87**, 2954 (1987).
30. H. Koizumi and I. Bersuker, *Phys. Rev. Lett.* **83**, 3009 (1999).
31. E. Haller, H. Köppel, L. S. Cederbaum, W. von Niessen and G. Bieri, *J. Chem. Phys.* **78**, 1359 (1983).
32. M. C. M. O'Brien and S. N. Evangelou, *J. Phys.* **C13**, 611 (1980).
33. L. S. Cederbaum, E. Haller and W. Domcke, *Solid State Commun.* **35**, 879 (1980).
34. Y. Toyozawa and M. Inoue, *J. Phys. Soc. Jpn.* **21**, 1663 (1966).
35. E. Haller, L. S. Cederbaum and W. Domcke, *Mol. Phys.* **41**, 1291 (1980).
36. R. Meiswinkel and H. Köppel, *Chem. Phys.* **129**, 463 (1989).
37. M. S. Child, *Mol. Phys.* **3**, 601 (1960).
38. C. J. Ballhausen, *Theor. Chim. Acta* **3**, 368 (1965).
39. B. M. Hofmann and M. A. Ratner, *Mol. Phys.* **35**, 901 (1978).
40. M. H. Perrin and M. Gouterman, *J. Chem. Phys.* **46**, 1019 (1967).
41. J. H. van der Waals, A. M. D. Berghuis and M. S. de Groot, *Mol. Phys.* **13**, 301 (1967).
42. T. Carrington, *Discuss. Farad. Soc.* **53**, 27 (1972).
43. R. Meiswinkel and H. Köppel, *Chem. Phys.* **144**, 117 (1990).
44. F. Cocchini, T. H. Upton and W. Andreoni, *J. Chem. Phys.* **88**, 6068 (1988).
45. J. Schön and H. Köppel, *J. Chem. Phys.* **103**, 9292 (1995).
46. J. Schön and H. Köppel, *Chem. Phys. Lett.* **231**, 55 (1994).
47. H. Köppel, L. S. Cederbaum, W. Domcke and W. von Niessen, *Chem. Phys.* **37**, 303 (1979).
48. H. Köppel, W. Domcke and L. S. Cederbaum, *J. Chem. Phys.* **74**, 2945 (1981).
49. R. C. Gillen, B. Ostojić and W. Domcke, *Chem. Phys.* **272**, 1 (2001).
50. Ch. Jungen and A. J. Merer, in *Molecular Spectroscopy: Modern Research*, Ed. K. N. Rao (Academic Press, New York, 1976), Vol. 2, p. 127.
51. M. Perić, B. Ostojić and J. Radić-Perić, *Phys. Rep.* **290**, 283 (1997).
52. R. L. Martin and E. R. Davidson, *Mol. Phys.* **35**, 1713 (1978).
53. W. Gerber and E. Schumacher, *J. Chem. Phys.* **69**, 1692 (1978).

54. J. L. Martins, R. Car and J. Buttet, *J. Chem. Phys.* **78**, 5646 (1983).
55. T. C. Thompson *et al.*, *J. Chem. Phys.* **82**, 5597 (1985).
56. Ph. Dugourd, J. Chevaleyre, M. Broyer, J. P. Wolf and L. Wöste, *Chem. Phys.* **175**, 555 (1990).
57. M. Broyer, G. Delacrétaz, P. Labastie, J. P. Wolf and L. Wöste, *J. Phys. Chem.* **91**, 2626 (1987).
58. M. Broyer *et al.*, *Phys. Rev. Lett.* **62**, 2100 (1989).
59. J.-P. Wolf, G. Delacrétaz and L. Wöste, *Phys. Rev. Lett.* **63**, 1946 (1989).
60. H.-G. Krämer, M. Keil, C. B. Suarez, W. Demtröder and W. Meyer, *Chem. Phys. Lett.* **299**, 212 (1999).
61. G. Delacrétaz *et al.*, *Phys. Rev. Lett.* **56**, 2598 (1986).
62. H. von Busch *et al.*, *Phys. Rev. Lett.* **81**, 4584 (1998).
63. M. D. Morse, J. B. Hopkins, P. R. R. Langridge-Smith and R. E. Smalley, *J. Chem. Phys.* **79**, 5316 (1983).
64. J. W. Zwanziger, R. L. Whetten and E. R. Grant, *J. Phys. Chem.* **90**, 3298 (1986).
65. A. M. Ellis, E. S. J. Robles and T. A. Miller, *Chem. Phys. Lett.* **201**, 132 (1993).
66. G. A. Bishea and M. D. Morse, *J. Chem. Phys.* **95**, 8779 (1991).
67. D. G. Truhlar, T. C. Thompson and C. A. Mead, *Chem. Phys. Lett.* **127**, 287 (1986).
68. K. Balasubramanian and M. Z. Liao, *J. Chem. Phys.* **86**, 5587 (1987).
69. H. Basch, *Chem. Phys. Lett.* **136**, 289 (1987).
70. E. Haller, L. S. Cederbaum, W. Domcke and H. Köppel, *Chem. Phys. Lett.* **72**, 247 (1980).
71. C. Woywod, S. Scharfe, R. Krawczyk, W. Domcke and H. Köppel, *J. Chem. Phys.* **118**, 5880 (2003).
72. M. Mayer, L. S. Cederbaum and H. Köppel, *J. Chem. Phys.* **100**, 899 (1994).
73. A. Weaver, D. W. Arnold, S. E. Bradforth and D. M. Neumark, *J. Chem. Phys.* **94**, 1740 (1991).
74. M. Nooijen, unpublished results; W. Eisfeld *et al.*, to be published.
75. A. Geers, J. Kappert, F. Temps and T. J. Sears, *J. Chem. Phys.* **98**, 4297 (1993).
76. Y.-Y. Lee, G.-H. Wann and Y.-P. Lee, *J. Chem. Phys.* **99**, 9465 (1993).
77. D. L. Osborn *et al.*, *Chem. Phys. Lett.* **292**, 651 (1998).
78. T. A. Barckholtz and T. A. Miller, *J. Phys. Chem.* **A103**, 2321 (1999).
79. U. Höper, P. Botschwina and H. Köppel, *J. Chem. Phys.* **112**, 4132 (2000).
80. J. Schmidt-Klügmann, H. Köppel, S. Schmatz and P. Botschwina, *Chem. Phys. Lett.* **369**, 21 (2003).
81. L. S. Cederbaum, W. Domcke and H. Köppel, *Chem. Phys.* **33**, 319 (1978).
82. C. Woywod and W. Domcke, *Chem. Phys.* **162**, 349 (1992).
83. S. Mahapatra, L. S. Cederbaum and H. Köppel, *J. Chem. Phys.* **111**, 10452 (1999).

84. S. Mahapatra, G. A. Worth, H.-D. Meyer, L. S. Cederbaum and H. Köppel, *J. Phys. Chem.* **A105**, 5567 (2001).
85. P. Jungwirth, P. Čársky and T. Bally, *J. Am. Chem. Soc.* **115**, 5776 (1993).
86. G. Maier, *Angew. Chem. Int. Ed. English.* **27**, 309 (1988).
87. W. T. Borden, E. R. Davidson and D. Feller, *J. Am. Chem. Soc.* **103**, 5725 (1981).
88. D. W. Kohn and P. Chen, *J. Amer. Chem. Soc.* **115**, 2844 (1993).
89. P. Bischof, E. Haselbach and E. Heilbronner, *Angew. Chem. Int. Ed. English.* **9**, 953 (1970).
90. M. Roeselová, T. Bally, P. Jungwirth and P. Čársky, *Chem. Phys. Lett.* **234**, 395 (1995).
91. K. Kimura *et al.*, *Handbook of HeI Photoelectron Spectra of Fundamental Organic Molecules* (Japan Scientific Societies Press, 1981).
92. E. Haselbach, *Chem. Phys. Lett.* **7**, 428 (1970).
93. K. Müller-Dethlefs and J. B. Peel, *J. Chem. Phys.* **111**, 10550 (1999).
94. T.-K. Ha, R. Meyer and H. H. Günthard, *Chem. Phys. Lett.* **69**, 510 (1980).
95. L. Yu *et al.*, *J. Chem. Phys.* **92**, 4263 (1988).
96. B. E. Applegate, T. A. Miller and T. A. Barckholtz, *J. Chem. Phys.* **114**, 4855 (2001).
97. B. E. Applegate, A. J. Bezant and T. A. Miller, *J. Chem. Phys.* **114**, 4869 (2001).
98. C. Cossart-Magos, D. Cossart and S. Leach, *Mol. Phys.* **37**, 793 (1979).
99. D. Klapstein *et al.*, *Mol. Phys.* **51**, 413 (1984).
100. T. A. Miller and V. E. Bondybey, in *Molecular Ions: Spectroscopy, Structure and Chemistry*, Eds. T. A. Miller and V. E. Bondybey (North-Holland, Amsterdam, 1983), p. 201.
101. T. Sears, T. A. Miller and V. E. Bondybey, *J. Chem. Phys.* **72**, 6070 (1980).
102. C. Cossart-Magos, D. Cossart and S. Leach, *Chem. Phys.* **41**, 363 (1979).
103. K. Raghavachari, T. A. Miller and V. E. Bondybey, *J. Chem. Phys.* **79**, 1387 (1983).
104. R. Lindner, K. Müller-Dethlefs, E. Wedum, K. Haber and E. R. Grant, *Science* **271**, 1698 (1996).
105. B. E. Applegate and T. A. Miller, *J. Chem. Phys.* **117**, 10654 (2002).
106. M. Reeves and E. Davidson, *J. Chem. Phys.* **95**, 6551 (1991).
107. D. Keela and Z. Vager, *J. Chem. Phys.* **102**, 8424 (1995).
108. L.-S. Wang, B. Niu, Y. T. Lee, D. A. Shirley, E. Ghelichkhani and E. R. Grant, *J. Chem. Phys.* **93**, 6318 (1990).
109. L.-S. Wang, B. Niu, Y. T. Lee, D. A. Shirley, E. Ghelichkhani and E. R. Grant, *J. Chem. Phys.* **93**, 6327 (1990).
110. R. Meiswinkel and H. Köppel, *Chem. Phys. Lett.* **201**, 449 (1993).
111. C. C. Chancey and M. C. M. O'Brien, *The Jahn–Teller Effect in C_{60} and other Icosahedral Complexes* (Princeton University Press, NJ, 1997).

112. R. N. Porter, R. M. Stevens and M. Karplus, *J. Chem. Phys.* **49**, 5163 (1968).
113. A. Kuppermann and Y.-S. Wu, *Chem. Phys. Lett.* **205**, 577 (1993).
114. Y.-S. Wu and A. Kuppermann, *Chem. Phys. Lett.* **235**, 105 (1995).
115. W. H. Miller, *Ann. Rev. Phys. Chem.* **41**, 245 (1990).
116. F. Fernandéz and R. N. Zare, *Ann. Rev. Phys. Chem.* **53**, 67 (2002).
117. R. Bruckmeier, Ch. Wunderlich and H. Figger, *Phys. Rev. Lett.* **72**, 2250 (1994).
118. D. Azinovic *et al.*, *Phys. Rev.* **58**, 1115 (1998).
119. S. Mahapatra and H. Köppel, *J. Chem. Phys.* **109**, 1721 (1998).
120. S. Mahapatra and H. Köppel, *Phys. Rev. Lett.* **81**, 3116 (1998).
121. A. J. C. Varandas *et al.*, *J. Chem. Phys.* **86**, 6258 (1987).
122. S. Mahapatra and H. Köppel, *Chem. Phys. Lett.* **306**, 387 (1999).
123. W. E. Ernst and S. Rakowski, *Phys. Rev. Lett.* **74**, 58 (1995).
124. J. Gaus *et al.*, *J. Chem. Phys.* **97**, 12509 (1993).
125. B. Reischl, R. de Vivie-Riedl, S. Rutz and E. Schreiber, *J. Chem. Phys.* **104**, 8857 (1996).
126. R. de Vivie-Riedl, J. Gaus, V. Bonačić-Koutecký, J. Manz, B. Reischl-Lenz and P. Saalfrank, *Chem. Phys.* **223**, 1 (1997).
127. S. Mahapatra, V. Vallet, C. Woywod and H. Köppel, *Chem. Phys.* (2004), to be published.
128. J. Schön and H. Köppel, *J. Phys. Chem.* **A103**, 8579 (1999).
129. J. A. Cina, T. J. Smith, Jr. and V. Romero-Rochín, *Adv. Chem. Phys.* **83**, 1 (1993).
130. I. Bâldea and H. Köppel, to be published.
131. W. von Niessen, L. S. Cederbaum and W. P. Kraemer, *J. Chem. Phys.* **65**, 1378 (1976).
132. N. O. Lipari, C. B. Duke and L. Pietronero, *J. Chem. Phys.* **65**, 1165 (1976).
133. P. Pulay, G. Fogarasi and J. E. Boggs, *J. Chem. Phys.* **74**, 3999 (1981).
134. H.-G. Weikert, H.-D. Meyer, L. S. Cederbaum and F. Tarantelli, *J. Chem. Phys.* **104**, 7122 (1996).
135. M. S. Deleuze, A. B. Trofimov and L. S. Cederbaum, *J. Chem. Phys.* **115**, 5859 (2001).
136. L. Asbrink, E. Lindholm and O. Edquist, *Chem. Phys. Lett.* **5**, 609 (1970).
137. A. W. Potts, W. C. Price, D. G. Streets and T. A. Williams, *Farad. Discuss. Chem. Soc.* **54**, 168 (1972).
138. L. Karlsson, L. Mattsson, R. Jadrny, T. Bergmark and K. Siegbahn, *Phys. Scr.* **14**, 230 (1976).
139. L. Mattson, L. Karlsson, R. Jadrny and K. Siegbahn, *Phys. Scr.* **16**, 221 (1977).
140. P. Baltzer, L. Karlsson, B. Wannberg, G. Öhrwall, D. M. P. Holland, M. A. Mac Donald, M. A. Hayes and W. von Niessen, *Chem. Phys.* **224**, 95 (1997).

141. K. Walter, R. Weinkauf, U. Boesl and E. W. Schlag, *Chem. Phys. Lett.* **155**, 8 (1989).
142. J. G. Goode, J. Hofstein and P. M. Johnson, *J. Chem. Phys.* **107**, 1703 (1997).
143. J. P. Maier, *Kinetics of Ion-Molecule Reactions* (Plenum Press, New York, 1979), p. 437.
144. O. Braitbart, E. Castellucci, G. Dujardin and S. Leach, *J. Phys. Chem.* **87**, 4799 (1983).
145. T. Baer, G. D. Willet, D. Smith and J. S. Phillips, *J. Chem. Phys.* **70**, 4076 (1979).
146. H. Kühlewind, A. Kiermeier and H. J. Neusser, *J. Chem. Phys.* **85**, 4427 (1986).
147. J. Eiding, R. Schneider, W. Domcke, H. Köppel and W. von Niessen, *Chem. Phys. Lett.* **177**, 345 (1991).
148. M. Döscher, H. Köppel and P. G. Szalay, *J. Chem. Phys.* **117**, 2645 (2002).
149. H. Köppel *et al.*, *J. Chem. Phys.* **117**, 2657 (2002).
150. H. Köppel, *Chem. Phys. Lett.* **205**, 361 (1993).
151. K. F. Freed, *Topics Appl. Phys.* **15**, 23 (1976).
152. P. Avouris, W. M. Gelbart and M. A. El-Sayed, *Chem. Rev.* **77**, 793 (1977).
153. M. H. Beck, A. Jäckle, G. A. Worth and H.-D. Meyer, *Phys. Rep.* **324**, 1 (2000).
154. G. J. Atchity, S. S. Xantheas and K. Ruedenberg, *J. Chem. Phys.* **95**, 1862 (1991).
155. T. Venkatesan, S. Mahapatra, L. S. Cederbaum and H. Köppel *J. Chem. Phys.* (2004), to be published.
156. H. Köppel, I. Baldea and P. Szalay, *Adv. Quantum Chem.* **44**, 199 (2003).

CHAPTER 11

QUANTUM MECHANICAL STUDIES OF PHOTODISSOCIATION DYNAMICS USING ACCURATE GLOBAL POTENTIAL ENERGY SURFACES

Reinhard Schinke

Max-Planck-Institut für Strömungsforschung, D-37073 Göttingen, Germany

Contents

1. Introduction

In a typical photodissociation experiment, a molecule is excited with a laser from the ground electronic state, $\tilde{X}$, to an excited electronic state, for example $\tilde{A}$, as illustrated in Fig. 1.[1,2] For molecules consisting of more than two atoms, the potential curves in Fig. 1 represent one-dimensional cuts through potential energy surfaces (PES), which depend on as many coordinates, Q_i, as there are internal degrees of freedom, e.g. three for a triatom. The observables are the absorption cross section, $\sigma_{\rm abs}(E)$, and the distribution of the internal product states, $P_\alpha(E)$, where α is an abbreviation for the

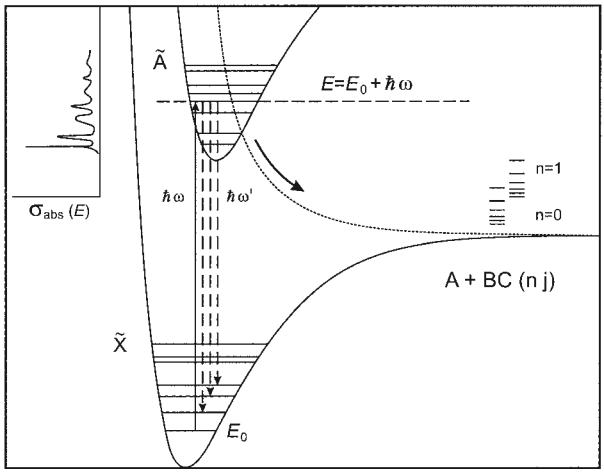

Fig. 1. Illustration of a photodissociation process ($\tilde{X} \rightarrow \tilde{A}$) including a non-adiabatic transition from a bound excited state to a repulsive excited state. ω' indicates the emission frequency and $\sigma_{\mathrm{abs}}(E)$ is the absorption cross section.

possible quantum states of the products like vibrational states (n), rotational states (j) or electronic states. The absorption cross section provides information about the dynamics in the upper state primarily in the region around the Franck–Condon (FC) point. The product state distributions, on the other hand, depend also on the dynamics in the exit channel. Even though the time the molecule spends in the inner region of the upper-state PES may be very short, light can be spontaneously emitted.[3] The dispersed fluorescence intensity defines the third observable, the Raman cross section $\sigma_{\mathrm{R}}^{(i)}(E)$, where i denotes the particular vibrational state in the ground electronic state. $\sigma_{\mathrm{R}}^{(i)}(E)$ depends on the dynamics between the FC region and the exit channel and, loosely speaking, reflects the route along which the molecule breaks apart.[4] All observables depend on the energy $E = E_0 + \hbar\omega$. Measuring these quantities for many photon energies $\hbar\omega$, yields a complete picture of the dissociation process. Alternatively, one can perform measurements in the time domain by first exciting the molecule with a short laser and then probing the status of the dissociating molecule with a second short pulse after a well defined delay time.[5–8]

In many situations, the molecule cannot dissociate in the initially excited electronic state because the energy is not sufficient. However, if

this state is coupled to a repulsive state, the molecule can "hop" over to this repulsive state and dissociate on its PES as illustrated in Fig. 1. The coupling between the two states is provided by those terms which are neglected in the Born–Oppenheimer (BO) electronic Hamiltonian, e.g. spin-orbit interaction, or neglected in the expression for the kinetic energy operator of the nuclei, that is the coupling elements $F_{i,j} = \langle \Phi_i | \partial / \partial Q | \Phi_j \rangle$ and $G_{i,j} = \langle \Phi_i | \partial^2 / \partial Q^2 | \Phi_j \rangle$. In the first case one speaks about "intersystem crossing" and transitions induced by the second possibility are termed "internal conversion". Non-Born–Oppenheimer transitions often occur at conical intersections. The strength of the coupling strongly influences the lifetime of the excited complex and therefore, according to the time-energy uncertainty relation, the resolution of features in the absorption spectrum. Nonadiabatic transitions also leave hallmarks in the product state distributions as well as the Raman cross section. Figure 1 represents only one particular case. It is, of course, also possible that two or more states are initially excited by the photon or that all states are repulsive.

Nonadiabatic transitions, in general, and conical intersections, in particular, are very important in photochemistry and photophysics.[9] Dissociation on a single PES is more the exception rather than the rule. Generally speaking, couplings between different BO states become increasingly more important at higher energies, when the density of electronic states increases. Rigorous quantum mechanical treatments of nonadiabatic effects in photodissociation are quite demanding. They require, in the diabatic representation, knowledge of three functions, i.e. the two diagonal potentials W_{11} and W_{22} and the off-diagonal coupling potential W_{12}. In addition, the two transition dipole functions are needed, which adds up to five functions, each depending on all internal coordinates.

In this chapter we will describe some examples of nonadiabatic transitions during the breakup of a small molecule. We will consider only investigations in which reasonably realistic PES and coupling elements are used. The many calculations in which model potentials have been employed will not be considered here; they may be covered in other chapters of this book, e.g. Chapters 8 and 9.

The present contribution is structured in the following way: In Sec. 2 the basic equations are summarized and numerical methods will be briefly mentioned. The processes are distinguished according to whether the dissociation is direct or delayed; in the latter case the absorption spectrum

shows structures, which can be narrow as well as diffuse. Direct processes are described in Sec. 3. Delayed processes with the spectral features in σ_{abs} mainly representing symmetric stretch or mainly bending motion will be reviewed in Secs. 4 and 5, respectively. Molecules dissociating due to Renner–Teller coupling, a special kind of non-BO effect which is somehow related to conical intersections, are discussed in Sec. 6. An outlook to future work, Sec. 7, will end this chapter.

2. Basic Equations and Numerical Aspects

In this chapter it is assumed that the pulse by which the molecule is excited is long, i.e. of the order of nanoseconds, and weak, so that the light/molecule interaction can be treated by first-order perturbation theory (Fermi's Golden Rule).[1,10] These are the conditions under which photodissociation experiments commonly are performed. The dynamical modeling of experiments with short and strong pulses is more complicated and requires different tools[8,11] (see the Chapters 17 and 18 in this book).

Photodissociation processes can be studied in the time-independent as well as the time-dependent picture.[1] In the first approach, one solves the time-independent Schrödinger equation for the nuclear motion at a fixed energy E. The correct boundary conditions for large separations between the products are fulfilled and different wave functions are obtained for each quantum state α of the products.[12] In the second approach, the time-dependent Schrödinger equation for the nuclear motion is solved for a wave packet $\chi(t)$ with the appropriate initial condition for time $t = 0$. Both approaches are equivalent, provided the Hamiltonian is time-independent.

The most rigorous description of nonadiabatic effects in molecules is provided by the adiabatic representation. However, that requires knowledge of all derivative coupling matrix elements,

$$F_{12}^{(i)} = \left\langle \Phi_1^{(a)} \left| \frac{\partial}{\partial Q_i} \right| \Phi_2^{(a)} \right\rangle \quad \text{and} \quad G_{12}^{(i)} = \left\langle \Phi_1^{(a)} \left| \frac{\partial^2}{\partial Q_i \partial Q_{i'}} \right| \Phi_2^{(a)} \right\rangle, \quad (1)$$

where $\Phi_1^{(a)}$ and $\Phi_2^{(a)}$ are the two coupled *adiabatic* electronic wave functions and the Q_i denote the various internal coordinates. These elements are difficult to calculate and difficult to represent by analytical functions. For this reason, to our knowledge, all of the computational studies of nonadiabatic transitions in real molecules with more than one internal degree of freedom use the diabatic representation described in detail in Chapter 4. The

diabatic electronic wave functions, $\Phi_1^{(d)}$ and $\Phi_2^{(d)}$, are obtained from the adiabatic ones by a unitary transformation, such that the derivative coupling matrix elements — in the new representation — are negligibly small. In contrast to the adiabatic wave functions, the diabatic ones are not eigenfunctions of the electronic Hamiltonian H_e, i.e. the matrix $\langle \Phi_k^{(d)} | H_e | \Phi_{k'}^{(d)} \rangle$ is not diagonal. In the adiabatic representation the different electronic states are coupled through the derivative coupling matrix elements, Eq. (1), while the diabatic states are coupled through the off-diagonal matrix elements of H_e, i.e. W_{12} and W_{21}. In this chapter we will only discuss the diabatic representation. Moreover, we will concentrate on the time-dependent approach, because this is the approach employed in most applications.

Let us assume that the molecule is promoted from the ground electronic state, with initial wave function $\tilde{\chi}_0$ and energy E_0, to two coupled excited states. The corresponding wave packets are denoted by $\chi_1(t)$ and $\chi_2(t)$. For simplicity of the notation, the dependence on the coordinates is omitted. The wave packets describing the motion in the excited states are solutions of the two-state time-dependent Schrödinger equation

$$\begin{aligned} i\hbar \frac{\partial}{\partial t} \chi_1(t) &= [T_n + W_{11}]\, \chi_1(t) + W_{12}\, \chi_2(t)\,, \\ i\hbar \frac{\partial}{\partial t} \chi_2(t) &= [T_n + W_{22}]\, \chi_2(t) + W_{21}\, \chi_1(t)\,, \end{aligned} \tag{2}$$

where T_n is the kinetic energy operator of the nuclear degrees of freedom and W_{ij} are the diabatic matrix elements; the superscript referring to the diabatic representation is also omitted in what follows. Equations (2) must be solved subject to the initial conditions

$$\chi_i(0) = \mu_i\, \tilde{\chi}_0\,, \tag{3}$$

with μ_i being the transition dipole moment function between the ground electronic state and the ith diabatic excited electronic state. Transitions between the two states are due to the off-diagonal elements W_{12} and W_{21}. Methods for propagating wave packets have been amply described in the literature[1,7,8,13–15] and therefore they are not discussed here.

During the propagation of the wave packets one calculates the autocorrelation function $S(t)$ defined as

$$S(t) = \sum_{i=1,2} \langle \chi_i(0) | \chi_i(t) \rangle\,. \tag{4}$$

The autocorrelation function is a very useful quantity, because it reflects the dynamics of the wave packets, that is how fast they depart from the region, where they were launched, how often they recur to the place of birth, for how long the wave packets remain compact and localized and on which timescale the bonds are broken.[1,4,16] Eventually, when the entire wave packet has left the interaction region, i.e. when all molecules are dissociated, $S(t)$ becomes zero. Even though the initial wave packet is a real function, it becomes complex, because the time evolution operator is complex. Thus, $S(t)$ is a complex function and fulfills the symmetry relation

$$S(-t) = S(t)^* \,, \tag{5}$$

where the star indicates the complex conjugate of $S(t)$. According to the time-energy uncertainty relation, the absorption spectrum is obtained by Fourier transformation of the autocorrelation function, i.e.[1]

$$\sigma_{\mathrm{abs}}(E) \propto E_{\mathrm{photon}} \int_{-\infty}^{+\infty} dt\, e^{iEt/\hbar}\, S(t)\,. \tag{6}$$

Here, E_{photon} is the photon energy and $E = E_0 + E_{\mathrm{photon}}$.

With the help of the basic properties of the Fourier transformation, the behavior of the absorption spectrum can be interpreted in terms of the time-dependence of the autocorrelation function. For example, the overall width of $\sigma_{\mathrm{abs}}(E)$ is related to the width of $|S(t)|$ around $t = 0$. Periodic structures in the autocorrelation function with period ΔT, so-called "recurrences", which occur whenever a part of the evolving wave packet returns back to the FC region, lead to structures in the spectrum with energy spacing $\Delta E = 2\pi\hbar/\Delta T$.[4] These structures can be interpreted as "resonances", quasi-bound states embedded in the continuum.[1,17] They reflect the internal vibrational excitation of the molecule. The longer the lifetime of the molecule in the inner region of the PES, the more recurrences appear and therefore the narrower are the resonances. If there is no recurrence, the spectrum is structureless. Resonances are characterized by their position on the energy axis and by their full width at half maximum, Γ, with the lifetime of the resonance given by $\tau = \hbar/\Gamma$. In order to determine the lifetimes of very long lived resonance states by Fourier transformation of the autocorrelation function, the wave packet has to be propagated for a time at least $\Delta t \approx h/\Gamma = 2\pi\tau$. Significantly shorter propagation times are needed when the widths are directly extracted from the autocorrelation function by

using harmonic inversion techniques.[18,19] In the time-dependent approach the entire spectrum can be obtained from a single wave packet propagation.

Raman emission spectra can be calculated in a manner similar to Eq. (6) for the absorption spectrum.[3,20,21] The main difference is the replacement of the autocorrelation function by the so-called cross-correlation function, which also can be obtained from the propagation of a single wave packet, respectively two when two interacting states are involved. Finally, also the partial dissociation cross sections for producing the fragments in a particular set of quantum states, denoted by α, can be calculated from the evolving wave packet according to[1]

$$\sigma_\alpha(E) \propto E_{\text{photon}} \frac{m}{\hbar k_\alpha} \lim_{t\to\infty} \left|\langle e^{ik_\alpha R}\phi_\alpha|\chi(t)\rangle\right|^2, \tag{7}$$

where m is the reduced mass appropriate for the dissociation of ABC $\rightarrow$ A+BC and R is the intermolecular A$-$BC distance, k_α is the corresponding wave number, and the ϕ_α are the wave functions describing the quantum states of the products. Several practical and efficient ways for calculating the partial cross sections have been derived.[22,23] The product state distributions are defined by

$$P_\alpha(E) = \frac{\sigma_\alpha(E)}{\sigma_{\text{abs}}(E)}\,. \tag{8}$$

Product state distributions are routinely measured.[1,2] They often reveal details of the dissociation mechanism, which is particularly true when the fragmentation proceeds through a conical intersection.

3. Direct Dissociation

If the upper-state PESs are purely repulsive, the dissociation process is direct and the excited molecule breaks apart on a very short timescale. No barrier hinders the fragmentation and the wave packet does not recur to the location where it originally started at $t = 0$. The autocorrelation function shows no recurrences and, consequently, the absorption spectrum is featureless.[1]

The photodissociation of ICN in the $\tilde{A}$ band is an illustrative example of fast dissociation, which has been studied thoroughly; see Refs. 24 and 25 for reviews of the many theoretical and experimental studies. Despite the short fragmentation time, the dissociation of ICN is a very complicated process, because five different electronic states are involved. The gross features

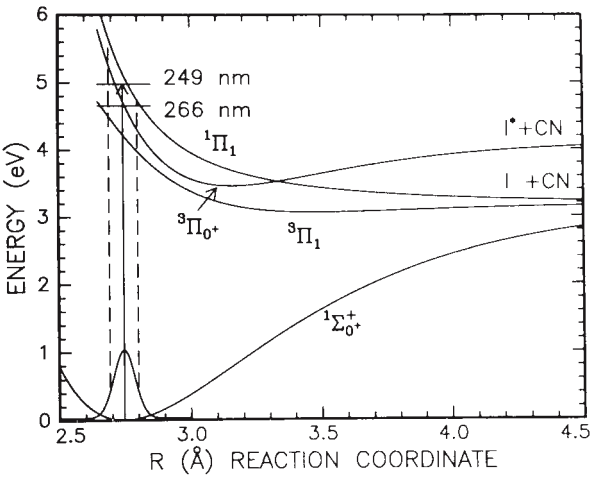

Fig. 2. Potential energy curves relevant for excitation of ICN in the $\tilde{A}$ continuum. Reprinted, with permission of the American Institute of Physics, from Ref. 33.

are reasonably well understood, while details are still waiting for rigorous theoretical descriptions and explanations.[25]

The ground state is linear and has $^1\Sigma^+_{0^+}$ symmetry in the linear configuration. There are three electronic states that are excited by photons in the range of 210 to 320 nm (Fig. 2): $^3\Pi_1$, $^3\Pi_{0^+}$ and $^1\Pi_1$. In C_s symmetry the two Π_1 states split into A' and A'' Renner–Teller components, so that five electronic states are involved. At I–CN distances near the FC region all the five excited states are strongly bent with minima around 50°–60°.[24] In terms of increasing energy the states are labeled $2A''$, $3A'$, $4A'$, $4A''$, and $5A'$, respectively. In linear geometry, the $^3\Pi_{0^+}$ and the $^1\Pi_1$ states cross at large internuclear separations, far away from the FC point. For bent geometries, this crossing becomes an avoided crossing between the $4A'$ and the $5A'$ PESs as seen in Fig. 3. The dissociation products are CN($X^2\Sigma^+$) and iodine atoms either in the ground state, I($^2P_{3/2}$), or in the excited state, I*($^2P_{1/2}$). The products can be reached on several adiabatic and nonadiabatic dissociation routes, which may give rise to interesting interference effects.

The quantities of interest are the absorption cross section,[26] the I/I* ratio,[25,26] the rotational distribution of the CN diatoms,[27,28] the vibrational excitation of CN, and various vector properties like angular anisotropy and

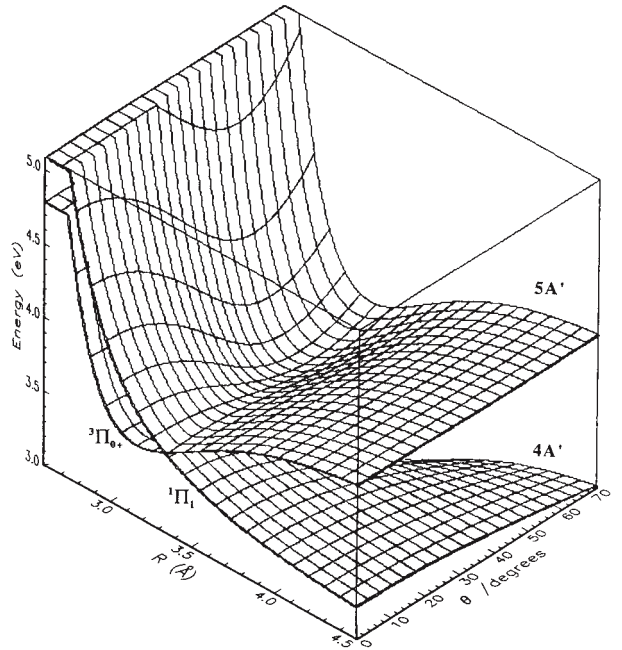

Fig. 3. Three-dimensional plot of the adiabatic PESs of the states $4A'$ and $5A'$ of ICN, which emerge from the states $^3\Pi_{0^+}$ and $^1\Pi_1$, respectively, when ICN is bent. Reprinted, with permission of the American Institute of Physics, from Ref. 33.

rotational alignment parameters.[29,30] The absorption spectrum is the sum of three contributions, each being structureless as anticipated for a fast dissociation process.[31] The I/I* ratio goes through a maximum value near the center of the $\tilde{A}$ band. Because the CN minimum distance does not change significantly along the dissociation path, CN is preferentially produced in the lowest vibrational state. The excited electronic states are bent and thus CN experiences a more or less strong torque while ICN breaks apart, with the result that the CN molecules are produced in high rotational states. The CN rotational distribution corresponding to the I channel is highly inverted with a maximum at around $j \approx 50$. CN produced in the I* channel is less inverted with the maximum occurring at smaller rotational states.

The photodissociation of ICN had been investigated in numerous theoretical studies in order to explain the experimental findings. For a collection

of relevant publications see Ref. 24. However, as pointed out by Amatatsu *et al.*,[24] although particular aspects of the measurements were reproduced, these studies did not lead to a fully consistent picture of the dissociation process. The failures were very likely due to the limitation to only two electronic states and/or the inaccuracy of the empirical PESs used in the calculations. A new era in the study of the photodissociation of ICN followed the calculation of all five excited-state PESs by *ab initio* electronic structure (*spin-orbit configuration interaction*) calculations by Morokuma and coworkers.[24,32] For example, these calculations predicted for the first time, in contrast to earlier assumptions, that all five PESs are bent. Diabatic PESs were also determined.

Amatatsu *et al.*[24] employed the five PES and the transition dipole moment functions in classical trajectory calculations. The transition between the $4A'$ and $5A'$ surfaces was treated by the surface hopping technique. In view of the complexity of the dissociation process, remarkable agreement with many of the experimental data was achieved, at least qualitatively. Wang and Qian[33] slightly modified the PESs of Amatatsu *et al.*[24] and performed similar classical trajectory calculations including nonadiabatic processes. They obtained even better agreement with experiment. Figure 4 shows the comparison of the measured and the calculated rotational state distributions for the I and the I* channel for two photolysis wavelengths. Following the pioneering work of Amatatsu *et al.*, their surfaces were subsequently used by several authors in fully quantum mechanical time-dependent[31,34] and time-independent[35,36] calculations. However, the overall agreement with experimental data did not seem to improve much.

As mentioned above, the most interesting question concerns the contributions of different paths leading to one particular product channel. For example, a high rotational state of CN formed in coincidence with I* may have followed a diabatic path from the $4A'$ ($^3\Pi_{0^+}$) state or an adiabatic path from the $5A'$ ($^1\Pi_1$) state. The diabatic path originates from a parallel transition and the adiabatic one begins with a perpendicular transition, i.e. they start in different electronic states. On the other hand, CN in the I channel can be formed in three different ways, the two already mentioned and the uncoupled path from the A'' component of the $^1\Pi_1$ state. In a pioneering experiment, Costen *et al.*[25] determined the various contributions by using different polarizations for exciting ICN and carefully measuring the

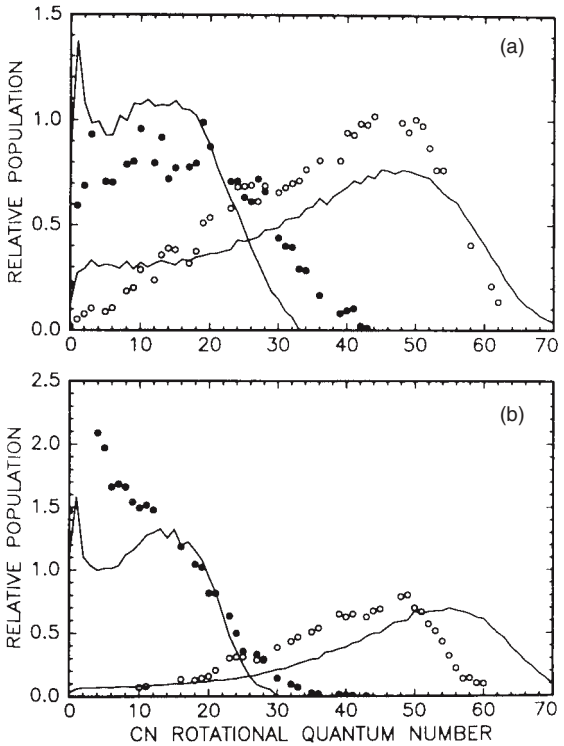

Fig. 4. (a) The 249 nm experimental CN rotational distributions for both I (open circles) and I* (filled circles) channels in comparison with the calculated distributions. (b) The same as in (a), but for 266 nm. The experimental data are from Refs. 27 and 28. Reprinted, with permission of the American Institute of Physics, from Ref. 33.

bipolar moments which characterize the CN velocity and angular momentum anisotropy. These measurements have been performed for several CN rotational states and different wavelengths. It is seen how the contributions gradually vary with CN rotational state and excitation energy and this yields a very detailed picture of the dissociation dynamics. A satisfactory theoretical description of this "map" is a great challenge for dynamical theory.

The photodissociation of methyl iodide, $CH_3I \rightarrow CH_3 + I$, in the $\tilde{A}$ band with iodine produced either in its ground state $^2P_{3/2}$ or the excited state $^2P_{1/2}$ is a prototypical system for molecular photodissociation.[37] Brief overviews of the many experimental and theoretical studies are found in

Refs. 38–40. It is very similar to the photodissociation of ICN in that the relevant PESs are steeply repulsive and a conical interaction localized between the FC region and the exit channel largely influences the outcome of the fragmentation process. In principle, three excited states are involved; they are, in order of increasing energy, $^3Q_1$, $^3Q_0$, and $^1Q_1$. All the three PESs are repulsive, with the consequence that the absorption spectra are structureless. However, the cross sections for $^3Q_1$ and $^1Q_1$ are almost negligibly small compared to the $^3Q_0$ absorption cross section and therefore it is reasonable to assume, in contrast to ICN, that only one electronic state is originally populated.

The $^3Q_0$ state correlates with I^*, whereas the other two states correlate with I in its ground state. Thus, if non-adiabatic coupling were absent, only excited iodine atoms would be produced. That is, however, not what is observed experimentally:[41] With increasing photolysis energy more and more ground-state iodine atoms are produced. The quantum yield for I^* is about 0.5 at long wavelengths and nearly one at the blue end of the absorption spectrum. The transition occurs in the region of a conical intersection between the $^1Q_1$ and $^3Q_0$ states. The influence of the nonadiabatic transition is also intriguingly manifested by the emission spectrum of the dissociating CH_3I molecule.[42] The fraction of photons emitted via a perpendicular transition moment, i.e. which originate from the $^1Q_1$ state, continually increases with the number of quanta in the C–I stretch mode. This indicates that the probability for the non-adiabatic transition from $^3Q_0$ to $^1Q_1$ increases with the separation from the FC point towards the fragment channel.

In early theoretical studies the photodissociation of CH_3I was treated as an effective two-mode system with CH_3 considered as one particle.[43–46] As with ICN, a new era began with *ab initio* calculations performed by Morokuma and coworkers[39,47] on a reasonably high level of electronic structure theory. These authors determined six- and nine-dimensional adiabatic and diabatic PESs, which were used in classical surface hopping trajectory calculations. Hammerich *et al.*[38] performed large-scale five-dimensional wave packet calculations using these PESs. As concluded by Eppink and Parker:[40] "One *caveat* of the *ab initio* surfaces is that they do not successfully reproduce the experimental absorption spectrum, which peaks to the red side of and is broader than the spectrum predicted by the theoretical treatments. ... Furthermore, the predicted I^* quantum yields of the most

advanced (9D) study are significantly higher than those determined experimentally ... A quantitative prediction from theory is thus not expected from these studies, but the general trends should still be valid." The most recent (three-mode) calculations only partly correct these shortcomings.[48]

Indeed, the general dissociation dynamics is qualitatively well described. For example, the product state distributions of the CH_3 umbrella mode are quite different in the I^* and the I channels (Fig. 5). While the

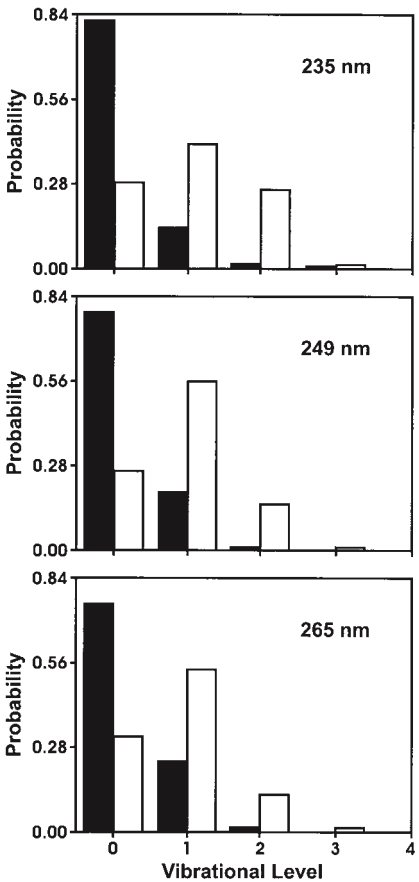

Fig. 5. CH_3 umbrella vibrational distribution for the I^* (black boxes) and I (white boxes) channels following the photodissociation of CH_3I in the $\tilde{A}$ continuum for three different wavelengths. Reprinted, with permission of the American Institute of Physics, from Ref. 38.

distribution for the I* channel is maximal for the lowest vibrational state and quickly falls off with increasing excitation, the distribution for the I channel is inverted. This difference, which is in accord with the most recent measurements,[40] has been attributed to an abrupt change of the methyl group from pyramidal to planar at the seam of the conical intersection.[39] On the other hand, the excitation of the symmetric C–H stretch found experimentally[40] is not reproduced in any of the calculations. Thus, as for the dissociation of ICN, there is still need for high-level theoretical investigations.

4. Delayed Dissociation — Symmetric Stretch Excitation

Because of the C_{2v} symmetry, conical intersections are typical for ABA type molecules like H_2O. Here, we will discuss in detail two examples, the photodissociation of H_2S in the first absorption band and the photodissociation of O_3 in the Chappuis band, which both have been studied in numerous experimental and theoretical investigations. If the two HS distances, R_{H_1S} and R_{H_2S}, are varied symmetrically, the ground electronic state has $^1A_1$ symmetry and the first two excited electronic singlet states are of $^1A_2$ and $^1B_1$ symmetry. With photons only the $^1B_1$ state can be accessed — in C_{2v} symmetry. The excited states are close in energy as shown in Fig. 6. Because these states have different symmetries, the corresponding one-dimensional potential curves (or two-dimensional potential surfaces if also the HSH bending angle, α, is included) are allowed to cross and actually cross twice, at small and at large HS distances. The general behavior of the crossings depends markedly on the angle. The inner crossing for the ground-state equilibrium angle, $\alpha_e \approx 92°$, occurs right in the FC region, that is, the photon promotes H_2S to the region, where the two electronic states cross in C_{2v} symmetry.

In C_s symmetry, i.e. when the two HS distances are not equal, the two excited electronic states have the same symmetry, namely $^1A''$, and the two PESs are not allowed to cross any longer. Thus, the crossing points on the C_{2v} line $R_{H_1S} = R_{H_2S}$ are indeed conical intersections. The lower adiabatic state, $1^1A''$, is dissociative, whereas the upper one, $2^1A''$, is bound at the photon energies of interest. The special feature of H_2S is that the motion in the excited states starts close to one of the conical intersections, where the coupling between the two states is, for obvious reasons, largest, with the result that the population transfer is very rapid.

Three-dimensional studies of the photodissociation of H_2S in the first absorption band using *ab initio* PESs have been first performed by

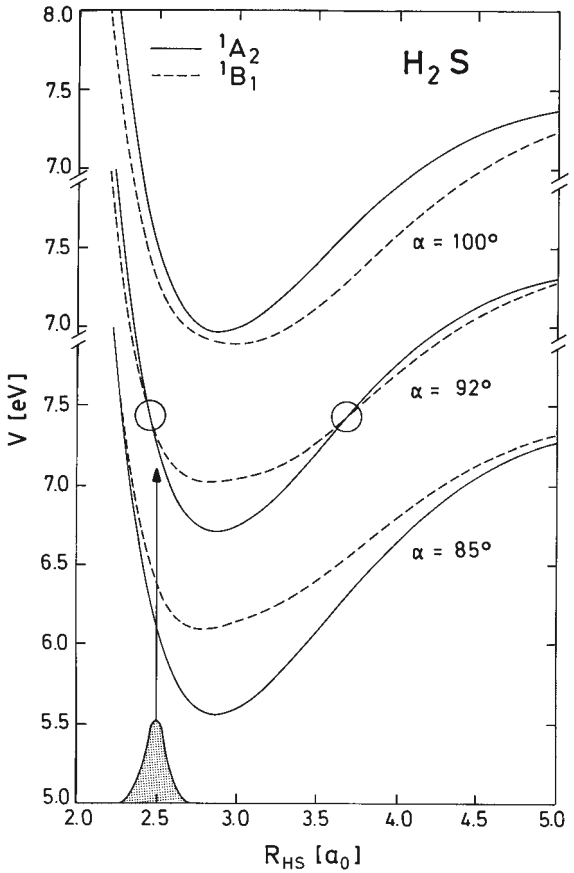

Fig. 6. One-dimensional potential energy curves for the two excited states, $^1A_2$ and $^1B_1$, of H_2S. The two HS separations, R_{HS}, are varied symmetrically. Note the different vertical axes for the different HSH bond angles α. The wave function in the ground electronic state is indicated on the horizontal axis and the circles for $\alpha = 92°$ mark the two conical intersections. Reprinted, with permission of the American Institute of Physics, from Ref. 49.

Heumann *et al.*[49,50] Later, Hartke, Werner and coworkers[51,52] performed similar studies with improved PESs. Both studies have been performed in the diabatic representation and the nuclear dynamics has been treated in the time-dependent picture. Because the potentials and couplings determined in the later study are more accurate, we will present mainly results

from Hartke, Werner, and coworkers. However, the basic picture emerging from both studies is very similar.

One-dimensional cuts of the adiabatic and diabatic potentials along the dissociation coordinate are depicted in Fig. 7 together with the mixing angle θ and the nonadiabatic derivative coupling matrix element F_{12}. The latter should be approximately equal to the derivative of θ and the results in Fig. 7 confirm this. The nonadiabatic derivative coupling element is strongly localized near the conical intersection. On the other hand, the mixing angle near the avoided crossing is approximately zero, i.e. the mixing of the two diabatic states is minimal in the vicinity of the C_{2v} line. Asymptotically, θ does not approach zero nor $\pm 90^\circ$ but some constant value in between. That means that the diabatic potentials do not approach the adiabatic ones as the molecule dissociates. At first glance, this behavior appears to be unphysical. However, the diabatic states are not eigenstates of the electronic Hamiltonian and one also must take into account the coupling W_{12} between them; though it becomes constant as one HS distance becomes large, it is not zero. In the adiabatic picture, the coupling between the adiabatic states is localized at the region of the avoided crossing (maximum of the derivative coupling element) and zero asymptotically. On the other hand, in the diabatic picture the coupling is small near the C_{2v} symmetry line ($\theta \approx 0$) but large asymptotically ($\theta \neq 0$). The consequence for the wave packet propagation is that the probability amplitude of being in the one or the other diabatic state rapidly oscillates in the exit channel. This may be numerically inconvenient, but it does not pose any real problem. In order to determine the product state distributions, it is necessary to transform to the adiabatic states.

Three-dimensional plots of the diabatic potentials as functions of either two distances and fixed bending angle, or one distance and the angle with the other distance being fixed, are depicted in Fig. 8. The diabatic potentials are allowed to cross and that is clearly seen in Fig. 8. In what follows we will denote by $A\,(B)$ the state, which in C_{2v} corresponds to the $^1A_2\,(^1B_1)$ state. State B is the binding state and A is the dissociative one. Within the diabatic representation the absorption and dissociation processes can be viewed in the following way: In C_{2v} symmetry, the transition dipole moment with the ground electronic state is finite for state B and exactly zero for state A. Therefore, initially mainly ($\approx$90%) the B state is populated and the A state is only marginally excited. However, the coupling between

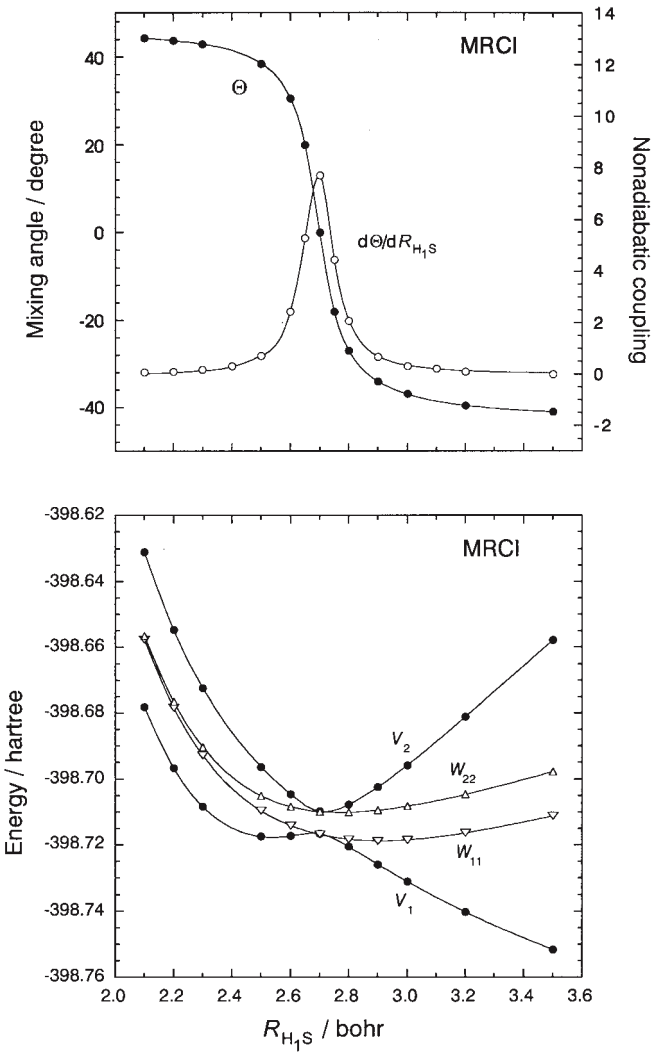

Fig. 7. Upper panel: Diabatic mixing angle θ (full circles, left-hand axis) for H_2S and the derivative of the mixing angle with respect to one of the HS distances, R_{H_1S} (open circles, right-hand axis). The HSH angle is 92° and the other HS distance is 2.7 Bohr. The line going through the open circles is the corresponding nonadiabatic coupling matrix element calculated by finite differences from the adiabatic electronic wave functions. Lower panel: Adiabatic energies (full circles, V_1 and V_2) and diabatic diagonal potential energies (open triangles, W_{11} and W_{22}). The other coordinates are the same as in (a). Redrawn, with permission of the American Institute of Physics, from Ref. 51.

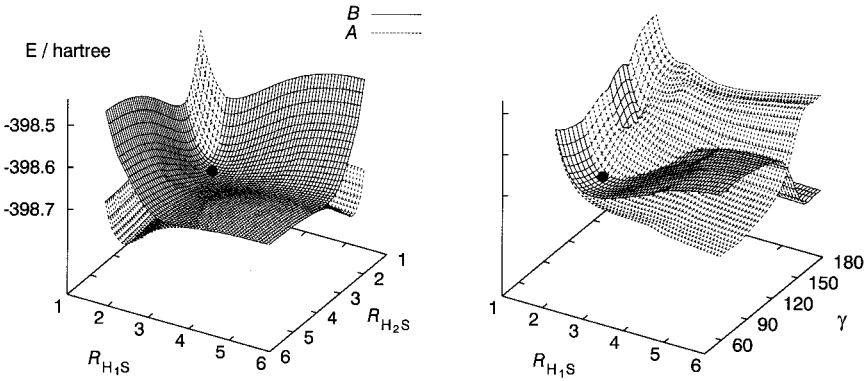

Fig. 8. Diabatic potential energy surfaces for the A (dashed lines) and B (solid lines) states of H_2S as functions of the two HS bond distances for fixed angle $\alpha = 92°$ (left-hand panel) and as functions of one HS bond distance and α with the other HS bond distance fixed at $2.5a_0$ (right-hand panel). The black circles indicate the position of the Franck–Condon point where the motion on the upper-state potential energy surfaces starts. Redrawn, with permission of the American Institute of Physics, from Ref. 51.

the two states is strong when the molecule moves away from the symmetry line and the probability is very quickly redistributed. After about 20 fs most of the molecules are in the repulsive A state and dissociate and after 50 fs, or so, the fragmentation process is over. The autocorrelation function exhibits only a single recurrence at ∼28 fs with an amplitude of about 0.01 (compared to 1 at $t = 0$). This recurrence reflects vibrational motion along the symmetric stretch coordinate. A small part of the wave packet in the binding B state is "trapped" for one symmetric stretch period. Because the coupling to the A state is strong, the lifetime in the binding state is very small, the recurrence is tiny, and only a single recurrence occurs.

Nevertheless, the small recurrence causes structures on top of a broad absorption spectrum (Fig. 9). These very diffuse structures with spacings $\Delta E \approx 2\pi\hbar/\Delta T$ reflect the initial motion of the wave packet along the symmetric stretch coordinate.[4,16,53] The first structure at long wavelengths corresponds to the lowest symmetric stretch level of the binding state, $v_{ss} = 0$, the second one to $v_{ss} = 1$, etc. The experimental spectrum[54] is compared to two calculated spectra. In both cases the theoretical spectrum is shifted by 2.02 nm to smaller wavelengths in order to account for a small error of the vertical excitation energy. In the second calculation, the FC point is

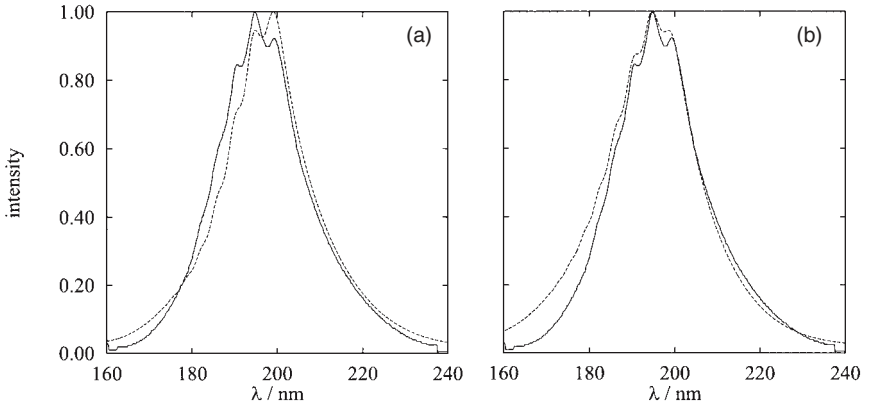

Fig. 9. Comparison of the experimental (solid line, Ref. 54) and calculated (dashed line) absorption spectrum for H_2S. In the right-hand panel (b) the initial wave packet is shifted by $0.05a_0$ along the symmetric stretch coordinate to smaller R_{HS} values in order to artificially modify the intensities of the diffuse structures. Redrawn, with permission of the American Institute of Physics, from Ref. 51.

additionally shifted to smaller HS separations. This artificial modification also affects the relative amplitudes of the diffuse structures. On the whole, the agreement is satisfactory — if one takes into account that two three-dimensional PESs, a three-dimensional coupling element, and two transition dipole moment functions are involved. In particular, the overall shape and the diffuseness of the structures are reasonably reproduced.

The distribution of the HS vibrational states has been measured by several groups.[55–57] The probability is largest for $v_{HS} = 0$, for all wavelengths. However, as the wavelength increases a broad tail with relatively small probabilities grows in, both in the experimental and in the calculated distributions. As discussed by Heumann *et al.*,[49] this tail is the consequence of the particular dissociation mechanism with two states being involved. Trajectories, if we think classically, which "hop" very early from the binding to the repulsive state lead primarily to the lowest HS vibrational state. The later the trajectories "hop" to the lower PES, the more elongated are the two HS distances and the more is the HS fragment vibrationally excited. An interesting relationship between the fraction, f_{vib}, of the available energy partitioned into HS product vibration and the first diffuse resonance maximum has been observed by Wilson *et al.*:[57] With decreasing wavelength

f_{vib} first increases, reaches a maximum at the first peak in the absorption spectrum and then decreases again.

The rotational product state distributions of HS, depicted in Fig. 10, can be described in terms of the FC mapping model.[1] Along the dissociation path the two PESs do not depend much on the bending angle so that the torque exerted on the HS fragment is weak. As a consequence, the HS rotational distribution can be viewed as the angular momentum representation of the angular part of the initial H_2S wave function in the ground electronic state, which is essentially a Gaussian in α. Fourier transformation of a Gaussian yields a Gaussian in the j space centered around $j \sim 0$ and that is exactly what is seen in Fig. 10. The angular function for D_2S in the

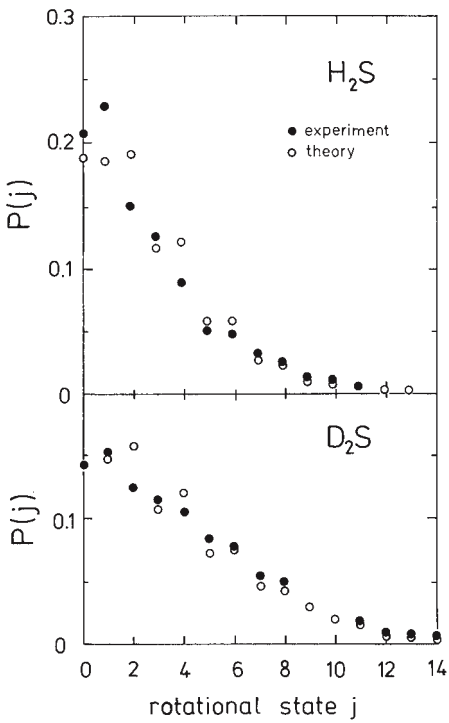

Fig. 10. Comparison of calculated and measured (Ref. 58) rotational state distributions in the dissociations of H_2S and D_2S. Reproduced, with permission of the American Institute of Physics, from Ref. 49.

ground state is narrower than for H_2S and consequently, the rotational distribution for DS is significantly broader. The calculated distributions agree well with the measured ones.[58,59]

Finally, the emission spectrum of the dissociating H_2S molecule has been studied, both experimentally[60,61] and theoretically,[50,52] for several wavelengths in the region of the maximum of the absorption spectrum. The Raman intensities reflect the motion of the dissociating molecule in the excited electronic states and therefore the main goal of emission studies is to infer from the intensity pattern information about this motion.[3] As already discussed above, the predominant motion in the first few femtoseconds after excitation is symmetric stretching and therefore it is not surprising to find excitation of high symmetric stretch states in the ground electronic state, with up to seven quanta. The bending mode is also excited in a short progression. Most striking, however, is the pronounced wavelength dependence of the Raman spectrum,[61] which is qualitatively ascribed to the coupled motion on two PESs. Since the motion in the upper states begins in the region of the conical intersection, where the coupling is naturally strong, it is not unexpected to find that small changes in λ can lead to significant changes in the intensity pattern. In contrast to the absorption process, which is of first order in the light/matter interaction, the Raman process is of second order[1] and "phases" are more important, especially when two coupled wave packets evolving in different states are involved, and the "phases" depend on the total energy. This is one possible explanation why the calculations, both the older ones of Heumann and Schinke[50] and the more refined ones by Skouteris *et al.*,[52] do not describe all details in full satisfaction. In the photodissociation of water in the first absorption band, on the other hand, a process which evolves only on a single PES but otherwise is similar to H_2S, the variation of the emission intensity with wavelength is much less spectacular — and experiment and theory agree nicely.[62]

The dissociation of ozone following excitation in the Chappuis band is in many respects similar to the photodissociation of H_2S. Although all three atoms are identical, O_3 in the ground as well as the two excited states has C_{2v} symmetry. When the separations between the two end atoms, on the one hand, and the central atom, on the other, are symmetrically varied, the two lowest excited singlet states, $^1A_2$ and $^1B_1$, are very close in energy with two crossings, one close to the FC point and one at larger O–O

separations. The corresponding potential diagram (cf. Fig. 2 of Ref. 63) is similar to Fig. 6 for H_2S. In C_s symmetry, the two states are the first and the second singlet state with A'' symmetry, $1^1A''$ and $2^1A''$. The adiabatic PESs and transition dipole moment functions have been calculated by *ab initio* methods by Woywod *et al.*[64] These authors also determined the diabatic potentials and couplings in a way similar to H_2S.[51] Time-dependent wave packet calculations have been performed by Flöthmann *et al.*[63]

As for H_2S, the excitation and dissociation process can be described in the following way: excitation of the binding state, fast probability transfer to the dissociative state and dissociation on the repulsive PES. However, compared to H_2S, the lifetime in the excited state is longer, leading to several recurrences in the autocorrelation function, shown in Fig. 11, and therefore to a more complicated absorption spectrum, depicted in Fig. 12. The main recurrence around 40 fs is, like in H_2S, caused by symmetric stretch motion in the binding state. Because the lifetime of O_3 in the binding state is longer than for H_2S, there are two additional recurrences in the symmetric stretch mode, at 80 and at 120 fs, respectively. A second period of about 6–7 fs is clearly seen on top of the first recurrence at 40 fs. It is due to excitation of the anti-symmetric stretch motion.[63] For two reasons, this period is so much smaller than the symmetric stretch period. First, the corresponding force constant in this degree of freedom is considerably larger and, second, because of symmetry, only the states with even quantum numbers, $v_{as} = 0, 2, \ldots$, are excited, whereas this symmetry constraint does not apply for the symmetric stretch mode. There is a third period somehow hidden in the autocorrelation function, the one corresponding to the bending degree of freedom. However, this period is roughly twice the symmetric stretch period and therefore not clearly discernible "by eye", although the Fourier transformation to the energy domain makes it visible. By the time the recurrences due to bending motion were to leave a hallmark in the autocorrelation function, $|S(t)|$ has already deceased to zero.

The diffuse structures in the absorption spectrum of ozone in the Chappuis band, shown in Figs. 12 (b) and (c), has likewise puzzled experimentalists and theorists for a long time.[65] The recurrence structures of the autocorrelation function provide a reasonable explanation, although not all details are perfectly reproduced by the calculations. The main structures reflect excitation of the symmetric stretch motion, just like for H_2S.

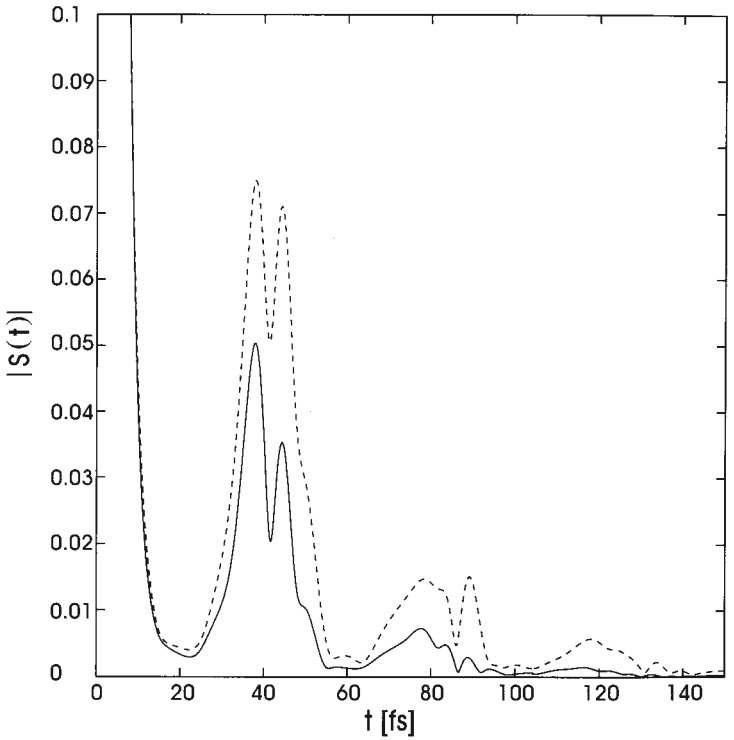

Fig. 11. Modulus of the autocorrelation function for ozone excited in the Chappuis band. The results of two different calculations are presented. In the first calculation (solid curve) the original potential energy surfaces are used, whereas in the second calculation one of the diabatic potentials is shifted by $-0.1\,\mathrm{eV}$ in order to modify the coupling strength (dashed curve). Reprinted, with permission of the American Institute of Physics, from Ref. 63.

A difference with respect to H_2S is that the spectrum is actually a superposition of two spectra, one with $v_{as} = 0$, located around $17\,000\,\mathrm{cm}^{-1}$, and a second one with $v_{as} = 2$ centered around $22\,000\ \mathrm{cm}^{-1}$. This is more clearly revealed by the second derivative of $\sigma(E)$ with respect to E in the lower trace in Fig. 12 (a). In the region from $18\,000$–$20\,000\,\mathrm{cm}^{-1}$ the two spectra overlap, which makes the diffuse structures in this energy region even more diffuse and difficult to interpret. The structures caused by the bending motion are hardly seen in the calculated spectrum, although they show up in $\sigma''(E)$ at higher excitation energies. They are, however, quite

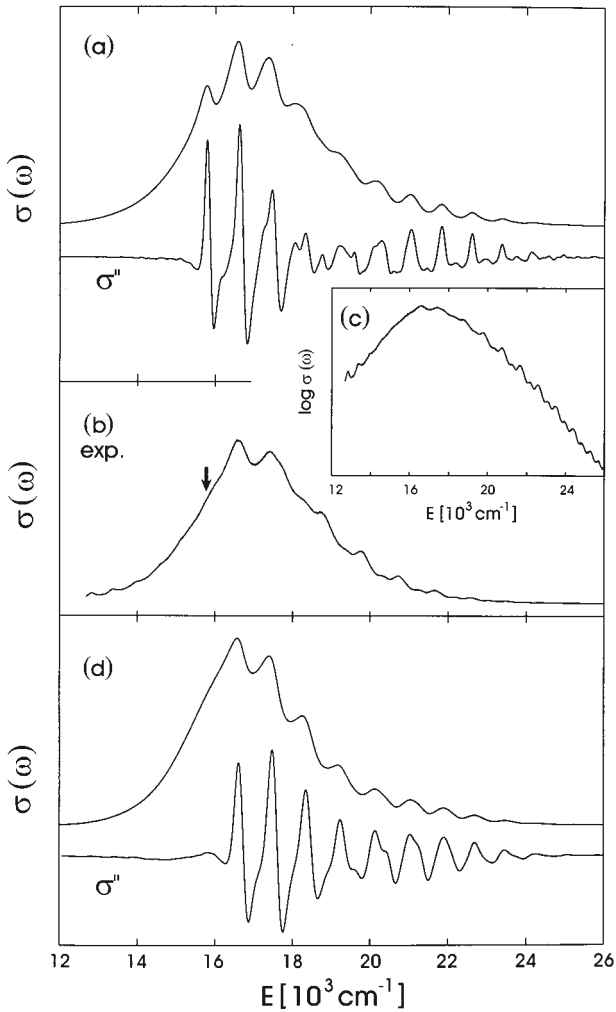

Fig. 12. (a) Calculated absorption spectrum for ozone in the Chappuis band. The lower trace, σ'', is the second derivative with respect to energy. (b) Measured absorption spectrum, Ref. 65. (c) Logarithm of the experimental spectrum. (d) Theoretical spectrum calculated with a slightly different potential and FC point. Reprinted, with permission of the American Institute of Physics, from Ref. 63.

clearly seen in the high-energy part of the experimental spectrum when plotted on a logarithmic scale [Fig. 12(c)]. The theoretical explanation was confirmed by new measurements.[66] All structures would become more pronounced and therefore more easily assignable, if the lifetime in the excited state were longer, that is, if the nonadiabatic coupling were weaker.

The final vibrational distributions of the O_2 fragments are similar to those for HS in the dissociation of H_2S. They are maximal for $n = 0$ and then rapidly fall off.[67] A broader maximum with very small probability exists at higher vibrational numbers. The agreement with the experimental data[68] is satisfactory. In contrast to H_2S, the diatomic fragments are produced in high rotational states.[67,68] When O_2 and O separate the repulsive force acts mainly along the bond between the two nearest oxygen atoms (repulsive model[1]), which generates a strong torque around the center-of-mass of O_2. In H_2S, on the other hand, the center-of-mass of HS is almost identical with the S atom and therefore the torque is very small.

5. Delayed Dissociation — Bending Excitation

While in the previous section the bending motion plays only a minor role, in the present section we will discuss systems for which excitation of the angular mode is essential. A common situation in triatomic molecules is a conical intersection for linear geometries as the result of the crossing of a Σ and a Π state along the dissociation coordinate. If the motion in the excited state originates in a bent geometry, then bending motion is required to reach this conical intersection. An illustrative example, which has been extensively studied over the past two decades, both experimentally and theoretically, is the photodissociation of water in the second ($\tilde{B}$) band. Because of lack of space, we will discuss only the most essential features of this dynamically interesting process involving three electronic states.

The electronic states involved can be briefly described in the following way. At linear H–O–H geometry there is a binding Σ state, $1^1\Sigma^+$, which leads to electronically excited $OH(A^2\Sigma)$, and a repulsive Π state, $1^1\Pi$, which correlates with $OH(X^2\Pi)$. The two potential curves cross around an O–H separation of about $3.2\,a_0$, when the other O–H bond distance is in the range of $1.8\,a_0$. When water bends, the $1^1\Sigma^+$ becomes the ground electronic state, $\tilde{X}^1A'$, with an equilibrium angle of 104°, and the Π state splits into the states $\tilde{A}^1A''$ and $\tilde{B}^1A'$, which form a Renner–Teller (RT) pair. The lower

RT state, $\tilde{A}^1A''$, is also bent, with an equilibrium angle similar to the one in the ground state. Because it has A'' symmetry, there is no avoided crossing with the other two states, which have A' symmetry, and the corresponding PES is purely repulsive. The upper RT state, $\tilde{B}^1A'$, is linear and due to the conical intersection, respectively avoided crossing, with the ground electronic state, it has a deep potential well at linear geometries and relatively large O–H separations. The topology of the three PES's is schematically illustrated in Fig. 13. Photoexcitation of the $\tilde{A}^1A''$ state gives rise to the first absorption band with a maximum around 165–170 nm. The fragmentation in this state is direct and fast and evolves on a single PES. For a summary of the many experimental and theoretical investigations, see the overview by Engel *et al.*[62]

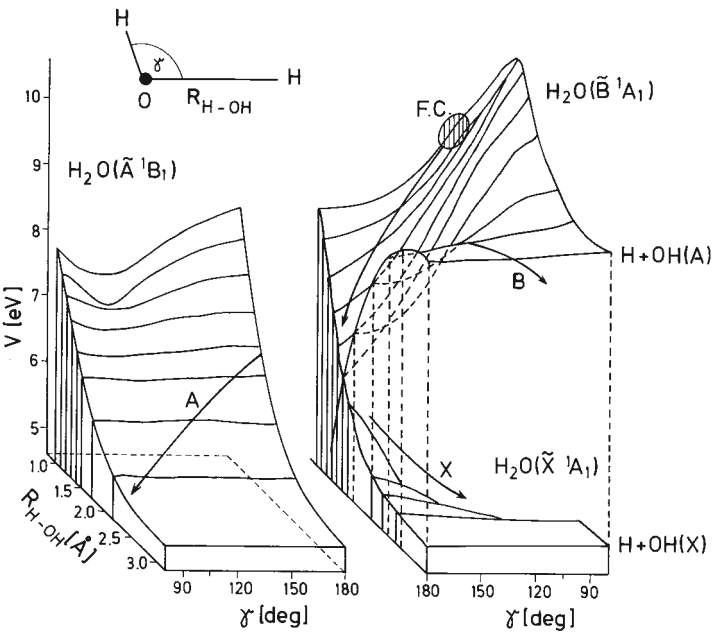

Fig. 13. Schematic illustration of the three potential energy surfaces, $\tilde{X}$, $\tilde{B}$, and $\tilde{A}$, involved in the photodissociation of water in the $\tilde{A}$ and the $\tilde{B}$ band. The shaded area (F.C.) marks the Franck–Condon region where the motion on the $\tilde{B}$-state potential energy surface starts. The arrows labelled B, A, and X indicate the routes of the classical trajectories or the corresponding wave packets. Reprinted, with permission of the American Institute of Physics, from Ref. 75.

The dissociation in the second absorption band, following excitation of the $\tilde{B}^1A'$ state with a maximum around 125–130 nm, is more involved. Briefly, excitation promotes H_2O to the $\tilde{B}$-state PES far away from the equilibrium of this state; the angular displacement, 104° compared to 180°, is particularly large. Thus, after being released, the wave packet immediately slides down the steep slope toward the potential minimum and reaches the linear configuration. Here, the molecule can follow three different routes: (1) It stays on the $\tilde{B}$-state PES, climes up the other side of the well and eventually dissociates leading to excited $OH(A^2\Sigma)$. (2) It "hops" to the ground-state PES and dissociates there to yield OH in the $X^2\Pi$ ground state. (3) The molecule can also make a transition to the $\tilde{A}$ state, which is the other state of the RT pair, and dissociate on its repulsive PES to yield ground-state OH. In the first case, the high rotational excitation of OH gained in the first part of the fragmentation process is partly lost when the molecule leaves the deep potential well and reaches the $H + OH(A)$ plateau;[69] nevertheless, the OH products are created in relatively high rotational states. The final state distributions of $OH(A^2\Sigma)$ can be obtained from $A - X$ fluorescence spectra.[70] When the molecule makes a transition to the ground electronic state, the rotational excitation of OH is continued beyond the linear configuration[69] and the $OH(X^2\Pi)$ fragment is produced in very high rotational states with a sharply inverted distribution peaking near the energetic cutoff.[71–73] The vibrational-rotational distribution of $OH(X^2\Pi)$ has been measured by the H-atom Rydberg "tagging" time-of-flight technique, which was pioneered by Welge and co-workers.[71]

Theoretical descriptions of the dissociation of water in the second absorption band have gradually improved over the past two decades. In the earliest calculations, merely the $\tilde{B}$-state PES was taken into account,[74–77] and the potential surfaces were not of high quality. Weide and Schinke[75] presented an ultra-simple model to include the $\tilde{B} \rightarrow \tilde{X}$ transition near collinear geometries: When the trajectory reached linearity, it was continued either on the upper or on the lower state. Although this surface hopping model was very crude, it could rationalize the rotational state distributions of $OH(A)$ as well as $OH(X)$, in qualitative agreement with the experimental results available at that time.[71] Later, the theoretical descriptions were refined by taking two states into account.[72] Finally, the three relevant adiabatic potentials, $\tilde{X}$, $\tilde{A}$ and $\tilde{B}$, were determined by high-level electronic structure calculations by two groups and diabatic potentials were also constructed.[78,79]

With these accurate PESs available, rigorous quantum mechanical dynamics calculations have been performed, taking simultaneously into account all three states and the couplings between them and all nuclear degrees of freedom.[80] These calculations, for the first time, allowed detailed comparisons with the many experimental data and provided valuable insight into the complex dissociation dynamics. In the following we discuss some of the highlights of the comparisons between experiment and theory.

Figure 14 depicts the measured absorption spectrum[81] in comparison with the calculated[80] one. The experimental spectrum consists of a broad background, which is indicative of fast dissociation, and a rather regular progression of diffuse structures superimposed to the background. The general shape of the calculated spectrum is similar, with the exception that it shows more narrower structures, especially near the maximum. It has been argued that averaging of all rotational states of water populated at room temperature, rather than using only $J = 0$ and 1 as was done in the calculations, may wash out the narrower structures and so yield better agreement with experiment. The structures are relatively broad resonances above the dissociation threshold of the $\tilde{B}$ state.[17] In the time-dependent picture of photodissociation they are caused by a long progression of small-amplitude recurrences in the autocorrelation function. These recurrences are due to a small part of the wave packet, which remains in the well of the $\tilde{B}$-state

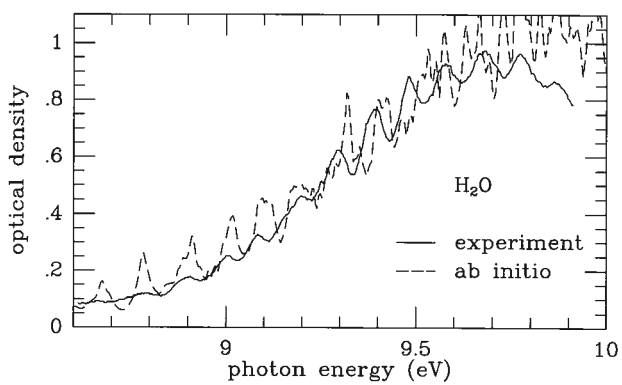

Fig. 14. Comparison of the measured (solid line) and the calculated (dashed line) absorption spectrum of H_2O in the second absorption band. Redrawn, with permission of the American Institute of Physics, from Ref. 80.

PES for a long time, i.e. which does not dissociate either on the upper or on the lower PES. As discussed by Weide *et al.*,[76] the short-time dynamics of the wavepacket which does not quickly dissociate is governed by a periodic classical orbit that basically performs bending motion in the deep potential well. For a more detailed discussion of diffuse structures and periodic classical orbits, see Ref. 1. Thus, in contrast to H_2S and the excitation of ozone in the Chappuis band, the diffuse structures are due to bending excitation rather than due to excitation of the symmetric stretch mode. Because the equilibrium angles in the two electronic states are so drastically different, the progression is long.

The branching ratios for forming OH in the excited state, A, or in the ground state, X, depend, apart from resonance-like structures as also seen in the absorption spectrum, smoothly on the excitation energy.[80] For low energies above the OH(A) threshold, the branching ratio is small for OH(A) and almost unity for OH(X). However, as the excess energy increases, the first one increases and the latter decreases. Simultaneously, the branching ratio for the third dissociation channel, $O(^3P) + 2H$, also rises; however, even one electron Volt above the OH(A) threshold it is only 20%. The calculated results agree reasonably well with the experimental data of Mordaunt *et al.*[72]

The rotational state distributions of the OH($A^2\Sigma$) product molecules have been measured by Fillion *et al.*[82] for a series of excitation wavelengths and several vibrational states of OH. They are compared to the results of quantum mechanical calculations using two different sets of PESs.[82] Some of the distributions are depicted in Fig. 15. They are inverted, with a maximum occurring close to the highest state that is energetically accessible. As the excess energy increases, the maximum shifts to higher rotational states. Likewise, the maximum occurs at successively lower states with increasing vibrational excitation. The agreement with the two sets of calculated rotational distributions is in general good. The smaller, more irregular structures, which are probably the result of interferences, are less well reproduced. An interesting effect, termed "single rotational product propensity", has been observed experimentally and explained in terms of an adiabatic dissociation model.[83] It is found that under certain conditions a single rotational state can have a probability of about 50%.

The rotational distributions of OH($X^2\Pi$) are even more inverted (Fig. 16).[84] They have pronounced maxima around $N = 45$, which

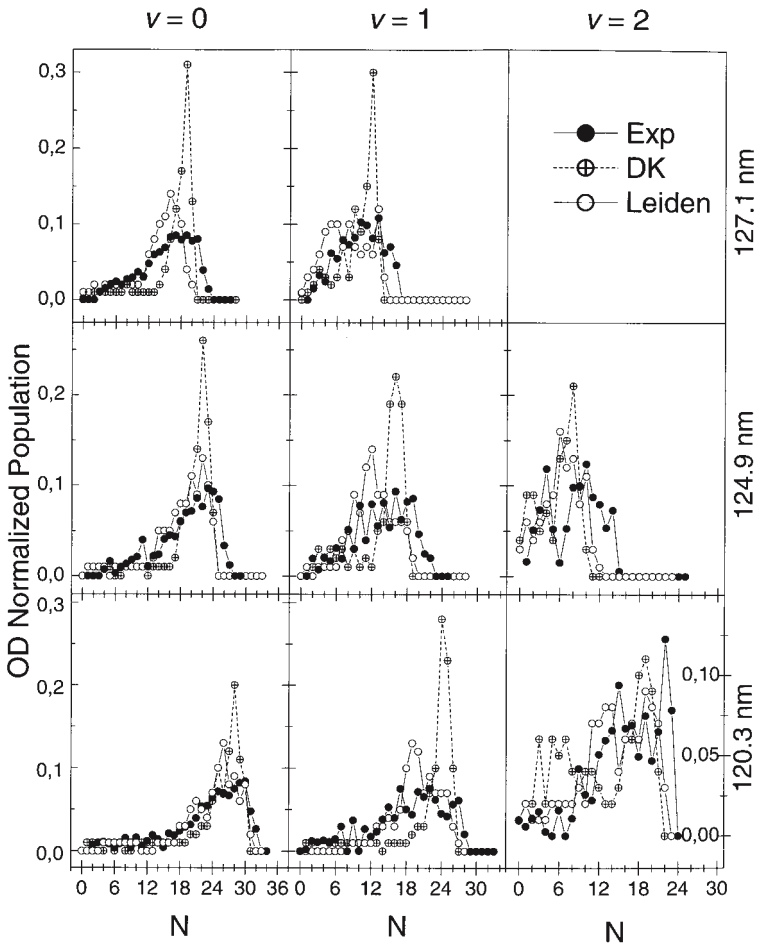

Fig. 15. OD($A^2\Sigma^+$) rotational population distributions for vibrational quantum numbers $v = 0, 1$, and 2. The experimental (Exp) results are compared to quantum mechanical calculations using the potential energy surfaces of Dobbyn and Knowles[78] (DK) and of the Leiden group[79] (Leiden). Reprinted, with permission of the American Chemical Society, from Ref. 82.

corresponds to about 32 000 cm^{-1} or 75% of the available energy. This is certainly an extreme case of rotational excitation and contrasts the very weak rotational excitation following photodissociation of water in the first absorption band.[62] The additional release of electronic energy, that is the

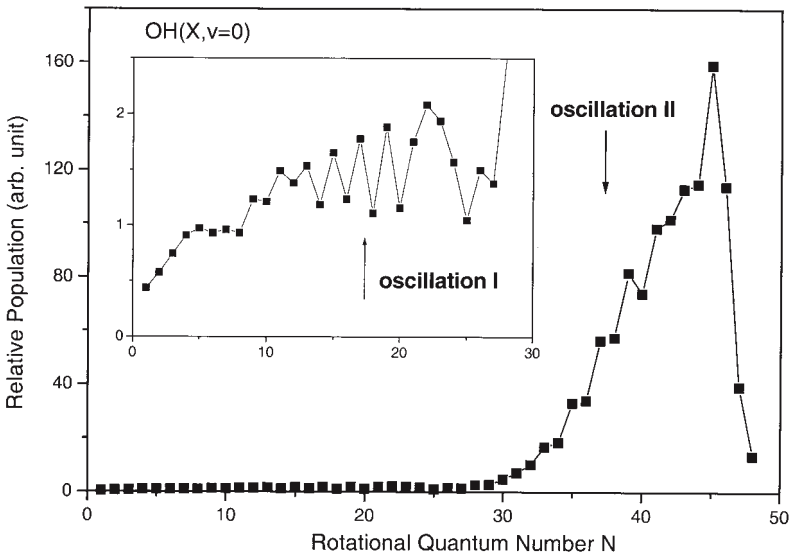

Fig. 16. The total rotational state distribution of OH($X^2\Pi$) in vibrational state $v = 0$ from the photodissociation at 121.6 nm. Reprinted, with permission of the American Institute of Physics, from Ref. 84.

difference between $E_{\mathrm{OH}(A)}$ and $E_{\mathrm{OH}(X)}$ is one reason. Another reason is of dynamical origin:[75] The rotational excitation which the OH entity experiences on the excited-state PES up to the linear geometry is continued in the second half of the dissociation in the ground electronic state. The measured distribution clearly shows two regions with pronounced odd-even oscillations. These oscillations have been attributed to interferences between two pathways for "hopping" to the ground electronic state: through the conical intersection in linear H–O–H geometry and a similar conical intersection for linear O–H–H.[85]

Also the vibrational state distributions of both electronic states of OH have been determined.[73,84] The distribution for OH($A^2\Sigma$) is maximal for $n = 0$ and then smoothly decays to zero around $n = 3$. The distribution for OH($X^2\Pi$) is different; the majority of OH(X) molecules are formed in $n = 0$. However, there is a long tail with small probability extending to very high vibrational states, $n \approx 10$, in good agreement with the calculations.[80] There are more interesting dynamical details in the photodissociation of water in the second band. Because of lack of space we have to refer to the

original literature. Finally, we mention that the fully quantum mechanical 3D multiple-surface calculations have been compared to equivalent classical trajectory surface-hopping calculations.[86] Although the classical results generally agree well with the quantum results, some serious deficiencies of the former were detected.

A process which bears some similarities with the photodissociation of water in the $\tilde{B}$ state is the photodissociation of ammonia in the $\tilde{A}$ band,[87] $NH_3(\tilde{X}^1A_1') + \hbar\omega \rightarrow NH_3(\tilde{A}^1A_2'') \rightarrow H + NH_2(\tilde{X}^2B_1)$. The $\tilde{A}$ band system is dominated by a progression of diffuse structures of the out-of-plane vibration, ν_2. All of these levels lie above the $H + NH_2(\tilde{X}^2B_1)$ asymptote, but they are temporarily trapped by the effects of a small barrier in each of the three equivalent exit channels. Dissociation occurs through a combination of tunnelling, internal vibrational energy distribution in the $\tilde{A}$ state and internal conversion to the ground electronic state. Very detailed spectroscopic experiments have been performed by Mordaunt *et al.*[88,89]

Relevant for the present chapter is the existence of a conical intersection of the $\tilde{A}$ and $\tilde{X}$ PESs in the exit channel, beyond the barrier, and the effect it has on the product state distributions. For planar ammonia the excited state correlates with ground-state products and the ground state correlates with excited products $H + NH_2(\tilde{A}^2A_1)$. However, if the symmetry is lowered, i.e. when ammonia is not planar, both surfaces belong to the same representation and the intersection becomes an avoided crossing. NH_3 in the lower state is non-planar and therefore the wave packet in the excited state starts its dissociative motion on the upper-state PES on the slope of the potential well in the $\tilde{A}$ state. After the barrier region has been crossed the dissociating molecule is "funneled" towards the conical intersection at the planar geometry and the NH_2 product experiences strong internal excitation — particularly rotation about the a inertial axis. The excitation is continued, as in the dissociation of water, on the ground-state PES yielding strong rotational excitation of the $NH_2(\tilde{X})$ product. Elaborate wave packet calculations including both electronic states have been performed by Dixon[90] including three degrees of freedom: HNH bending, stretching of the third NH bond and the out-of-plane coordinate. The PESs have been calculated by Polák *et al.*[91] within the diatom-in-molecule (DIM) approach. The highly inverted K_a rotational state distributions of $NH_2(\tilde{X})$ as well as the state-dependent anisotropy parameter, β, are accurately reproduced by these calculations.

Recently, more experimental work on the dissociation of ammonia, focussing on the partitioning of the internal energy of the $NH_2(\tilde{A})$ products, has become available.[92,93] Bach *et al.*[94,95] have investigated the influence of vibrational excitation of ammonia in the ground state on the dissociation products and lifetimes. Detailed theoretical descriptions of these large sets of experimental data are desired.

Another molecule with strong non-adiabatic coupling caused by a conical intersection is NO_2, whose rovibronic spectrum is known to be very complex;[96,97] for references see, for example, Ref. 98. NO_2 has been a benchmark molecule for spectroscopy and unimolecular dissociation for a long time. The ground electronic state, $\tilde{X}^2A_1$, is coupled with the $\tilde{A}^2B_2$ excited electronic state through the asymmetric stretching vibrational mode already at low energy, about 10 000 cm^{-1} above the well of the $\tilde{X}$ state. At higher energies, there are additional crossings with other electronic states, but the one between the $\tilde{X}$ and the $\tilde{A}$ state is believed to have the strongest influence on the spectrum of NO_2 for energies below the $O(^3P) + NO(X^2\Pi)$ dissociation threshold. The equilibrium angles in the two states are quite different, 134° in the ground state and 102° in the excited state, and the conical intersection occurs at intermediate angles of about 108° (Ref. 99). Thus, excitation with photons in the range of 25 000 cm^{-1}, i.e. near the dissociation energy, promotes NO_2 to the steep slope of the $\tilde{A}$ state PES, far away from the equilibrium of this PES. As a consequence, the wave packet performs large-amplitude bending motion which shows up as a pronounced progression in the (low-resolution) absorption spectrum.[100,101] When the wave packet swings through the region of the conical intersection, which is located between the two wells, the two states mix and probability is transferred from the $\tilde{A}$ state, where the motion started, to the ground state. This mixing is very strong and already after 100 fs the probabilities in the two states are about equal.[99] If the energy is sufficiently high, the molecule can dissociate in the ground electronic state to yield the products $O(^3P)$ and $NO(X^2\Pi)$. The dissociation rate is much smaller than the mixing rate between the two electronic states, and therefore the internal vibrational energy distribution on the lowest PES is the rate determining step for the dissociation.[102,103]

The mixing between the $\tilde{X}$ and the $\tilde{A}$ state has been studied in numerous theoretical studies. Parts of the corresponding PESs have been calculated by Hirsch and Buenker[104] and diabatic surfaces have been constructed.

However, these PESs, which have been used in many dynamics calculations, have not been constructed for dissociation studies and therefore cover only a rather limited region of the entire configuration space. Extensions to cover also the O+NO exit channel must be considered with caution.[105] The more recent electronic structure calculations of Mahapatra *et al.*[99] cover the region up to about $3a_0$ in the dissociation coordinate. Although this range is larger than in the older PES calculations, it still does not allow to investigate the fragmentation process. These authors calculated the photodetachment spectrum for NO_2^- and obtained good agreement with experiment.[106] Global potential energy surfaces, which do extend to the products region, recently have been constructed by Reignier *et al.*[107] However, they did not construct diabatic PESs and did not consider the non-adiabatic coupling.

Because of the strong vibronic interaction and the high density of vibrational states, which is the result of the large dissociation energy and the three heavy atoms involved, the dynamics of NO_2 at energies high above the conical intersection, especially near the dissociation limit, is irregular. Therefore, taking into account only the lowest adiabatic PES, is an appropriate model. Indeed, quantum calculations using exclusively the $\tilde{X}$ state PES provide dissociation rates in good overall agreement with experimental rates as well as time-resolved, non-exponential decay curves.[103]

The photodissociation of $CH_2(\tilde{X}\,^3B_1)$ through the coupled $2\,^3A''$ and $3\,^3A''$ states also involves strong excitation of the bending mode.[108,109] In C_{2v}, these states have $^3B_1$ and $^3A_2$ electronic symmetry. In the diabatic picture, the B state, which in C_{2v} corresponds to the $^3B_1$ state, is preferentially excited, whereas the A state, which correlates with the $^3A_2$ state, is only marginally excited. However, the conical intersection occurs right in the region of the FC point,[109,110] and therefore probability transfer is fast. The B state is bound for excitation energies up to 7.3 eV; at higher energies dissociation into H atoms and excited $CH(A^2\Delta)$ products is possible. Below 7.3 eV the molecule can dissociate only via the A state, which can break apart into both $H + CH(a^4\Sigma)$ and $C(^3P) + H_2$. Upon photo-excitation the main part of the wave packet immediately dissociates on the A-state PES which gives rise to a broad absorption cross section. However, a small part of the wave packet is temporarily trapped in the B state leading to more or less sharp resonance structures on the red side of the spectrum.[108,109] The B state is linear while the ground state is strongly bent (134°). Therefore, it is plausible to assume that bending motion in the deep well of the B state

is predominantly excited. The spectrum on the blue side of the maximum is almost structureless.

6. Renner–Teller Induced Dissociation

Renner–Teller (RT) coupling is a particular case of the breakdown of the Born–Oppenheimer approximation.[111] It is the result of the interaction between the two components of a degenerate electronic state: $\Pi, \Delta, \ldots$ etc. Let us consider an example, HCO. The lowest doublet state for linear HCO has $^2\Pi$ symmetry and is doubly degenerate; the projection of the electronic angular momentum on the linear HCO axis has the eigenvalues $\lambda = \pm 1$. If HCO is bent, the degeneracy is lifted, and the resulting two states have $^2A'$ and $^2A''$ symmetry, respectively. The first one is bent and is the ground electronic state; the other state is linear and is the first excited doublet state. Excitation with a photon promotes HCO from the ground state to the first excited state, at geometries far away from the equilibrium of the upper state. As a consequence, the wave packet immediately slides toward the linear geometry, where the two states are degenerate. Whenever the wave packet reaches linearity, part of the wave packet belonging to the $^2A''$ state is promoted to the lower state. Since the excitation energy is well above the H + CO threshold, HCO quickly dissociates on the ground state PES into H and CO.

The lifetime in the upper state, and therefore the widths of the resonances in the absorption spectrum, depend directly on the RT coupling strength: the stronger the coupling, the shorter is the lifetime. HCO is an example for a bent/linear RT pair and the probability transfer is quite effective, because the molecule freely swings through the linear configuration where the RT coupling is localized. Bending excitation decreases the net probability for the molecule to spend time in the interaction region and thus the lifetime increases.[112] HNO, on the other hand, is an example of a bent/bent RT pair, i.e. both states are bent (Fig. 17). In this case, the probability to penetrate into the linear regime is relatively small, the RT coupling is weak, and consequently the lifetime is long.[113] In contrast to HCO, bending excitation increases the RT coupling and therefore decreases the lifetime.

Although the RT effect is, strictly speaking, not identical with the coupling between two states at a conical intersection, there are nevertheless

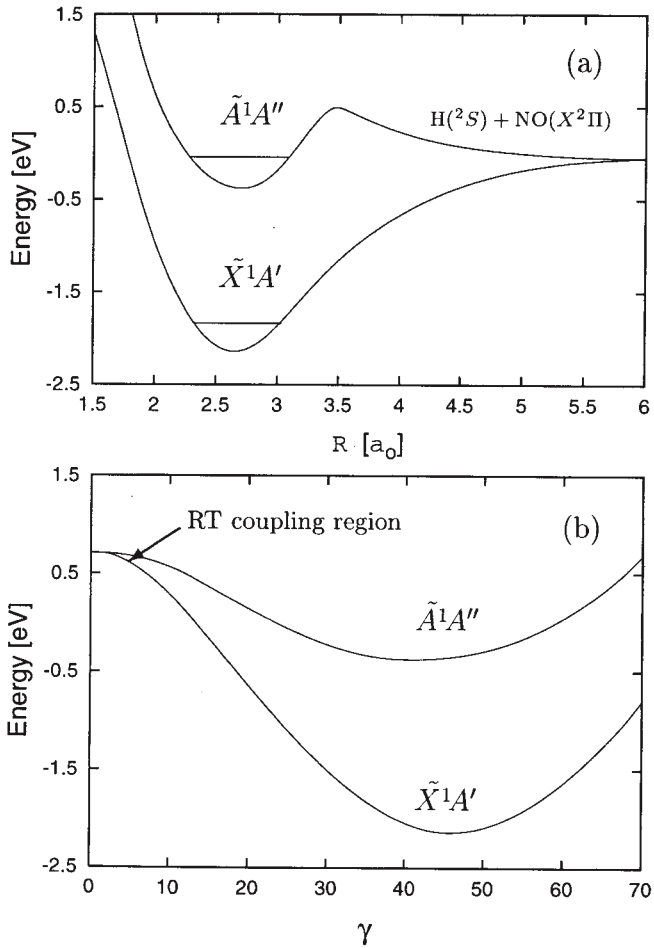

Fig. 17. One-dimensional cuts through the $\tilde{X}^1A'$ and $\tilde{A}^1A''$ potential energy surfaces along the Jacobi dissociation coordinate R (a) and the Jacobi bending angle γ (b). The potential is minimized in the other two coordinates. $\gamma = 0$ corresponds to linear HNO. The horizontal lines in (a) indicate the two zero-point energies. Reprinted, with permission of the American Institute of Physics, from Ref. 113.

important similarities. For example, the interaction between the two electronic states is localized, where they are degenerate; outside this region the two states are almost decoupled. Moreover, both processes are most conveniently described in a diabatic representation. Renner–Teller induced

dissociation is an important effect in molecular dynamics, especially photodissociation. However, to our knowledge, there are only few theoretical studies on global PESs including all degrees of freedom. Because the RT coupling is absent for non-rotating molecules, the calculations must be performed for $J \neq 0$. Although such calculations are certainly more involved than calculations for $J = 0$, they do not present a real problem. In the following we will briefly discuss two examples, HCO and HNO, which nicely illustrate how the lifetime in the excited state varies with the particular vibrational-rotational excitation.

Calculations of the RT induced fragmentation of HCO($^2A''$) have been performed in the time-dependent[114,115] as well as the time-independent[116] approach. In the first case, one propagates two coupled wave packets and determines the autocorrelation function $S(t)$, which shows a long sequence of recurrences caused by the excited bending motion in the $^2A''$ state. Fourier transformation of $S(t)$ yields the absorption cross section, which in the present case consists of several progressions of narrow absorption lines, i.e. resonances, with widths Γ. These widths depend on the vibrational states and thus reflect, how the coupling to the dissociative state varies with the degree of vibrational excitation. The calculations are performed in a diabatic scheme, in which the off-diagonal elements are proportional to the potential energy difference of the $^2A'$ and $^2A''$ states, $V_{A''} - V_{A'}$. Thus, like in the case of a conical intersection, the coupling in the diabatic representation is zero, where the two adiabatic states are degenerate, and it is large, where the adiabatic states are well separated. In the time-independent approach, the resonance widths are directly calculated by introduction of an absorbing complex potential in the H+CO exit channel.[116] The corresponding Hamilton matrix is complex symmetric with complex eigenvalues $E_0 - i\Gamma/2$.

In Fig. 18 we depict Γ for three different progressions as function of the bending quantum number v_2. As rationalized above, the resonance width decreases with increasing v_2. The agreement with the measured[117–119] widths is satisfactory. The structures for low values of v_2 are probably due to mixings with particular resonance states belonging to the ground electronic state (see also below). The RT coupling operator is proportional to K, the projection quantum number of the total angular momentum on the CO axis. As a consequence, the widths grow roughly quadratically with K, as has been observed experimentally and theoretically. The strong bending excitation in the upper electronic state survives when the molecule dissociates

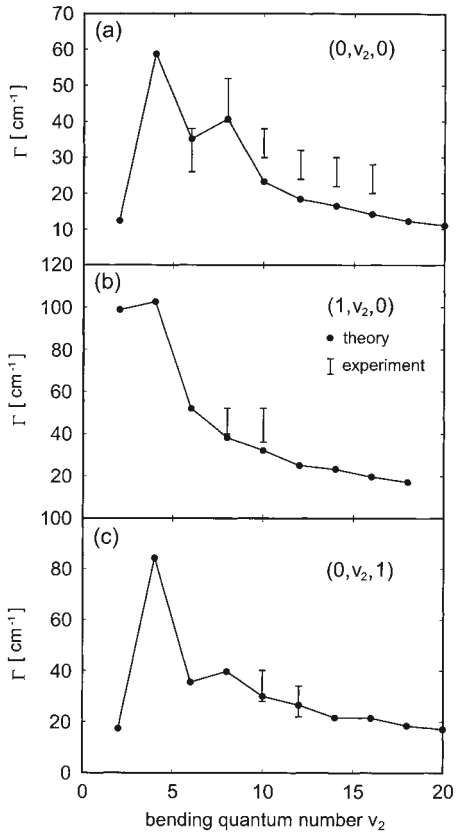

Fig. 18. Dependence of the HCO($^2A''$) predissociation rate Γ on the bending quantum number v_2 for three progressions: $(0, v_2, 0)$ (a), $(1, v_2, 0)$ (b), and $(0, v_2, 1)$ (c). v_1 and v_3 are the HC and the CO stretching quantum numbers, respectively. In all cases $J = K = 1$. The error bars indicate the experimental results of Loison *et al.*[117] Reprinted, with permission of the American Institute of Physics, from Ref. 116.

on the ground-state PES, with the result that the CO fragments are highly rotationally excited.[115,120]

The widths for the predissociation of the $^1A''$ state of HNO are much smaller than the widths shown for HCO in Fig. 18, typically smaller than $1\,\mathrm{cm}^{-1}$; they depend markedly on the particular vibrational state and the K rotational quantum number (see Ref. 113). The widths depend, of course, also on the total rotational angular momentum quantum number J. However, because the term in the kinetic energy operator responsible for the

RT coupling is independent of J, one anticipates only a marginal variation, as has been actually found for several states. Nevertheless, there are also other cases for which Γ shows a distinct J dependence. One example, state (0,1,1) and $K = 3$, is shown in Fig. 19. The three quantum numbers refer to the H–N stretching mode, the N–O mode, and the bending mode, respectively. The resonance width exhibits a variation with J which is reminiscent of anharmonic mixing with a "dark" state, as it is often found in molecular spectroscopy.[121] In the present case, the "bright" state $(0, 1, 1|K = 3)$ of the excited electronic state couples to a "dark" state, which mainly belongs to the ground electronic state. According to Fig. 17, the vibrational states belonging to the $^1A''$ state are embedded in the continuum of the $^1A'$ electronic state. The continuum of the ground state itself consists of resonance states. Many are very broad and overlap, but some of them are reasonably narrow and have a distinct nodal structure. It is one of the latter with which the bright state interacts and mixes. Since the rotational constants are different for the two interacting states — their wave functions have completely different nodal structures — the energy mismatch and therefore the degree of mixing varies with J: As J increases the two states are tuned in and out resonance and this is reflected by the resonance width of the bright state. Because the width of the dark state is considerably larger, the width of the bright state is noticeably enhanced when the mixing is optimal, i.e. when the energy gap is close to zero, as seen in the inset of Fig. 19. The mixing between the two resonance states occurs over an energy range comparable to the width of the dark state.

This kind of resonance effect has also been observed in the spectroscopic experiment of Pearson *et al.*,[122] however, for different vibrational states and different J's than in the calculations.[113] In order to quantitatively reproduce these effects, the PESs of the ground and the excited state must be extremely accurate and the vertical separation between them must also be precise. The mixing between resonances and the tuning of the resonance via rotational excitation, for example, is a generic effect, when two electronic states are coupled, irrespective of the nature of the coupling.

7. Outlook

The transition between different electronic states is an important phenomenon in molecular photodissociation processes. It is more the rule than the exception; the validity of the Born–Oppenheimer approximation, that

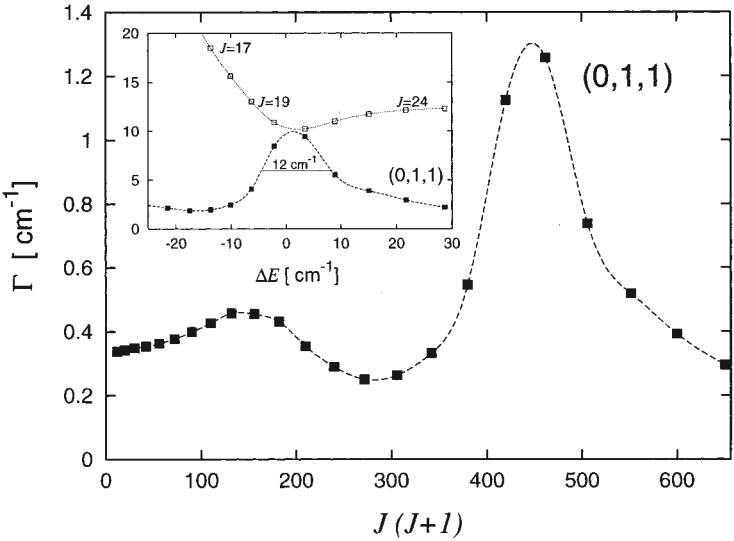

Fig. 19. The linewidth of state (0,1,1) of HNO($^1A''$) as a function of $J(J+1)$ for $K = 3$. The inset shows the width as function of the energy mismatch, ΔE, between the "bright" state (0,1,1) and the "dark" state belonging to the ground electronic state. The width of the "bright" state is multiplied by 7.5. See the text for more details. Reprinted, with permission of the American Institute of Physics, from Ref. 113.

is nuclear motion on a *single* potential energy surface as in the dissociation of water via excitation in the $\tilde{A}$ state, is exceptional. A nonadiabatic transition occurring near a conical intersection is only one, but an important example.

Due to the limitations of computational capacity, theoretical investigations before the nineties of the last century were mainly based on model studies using simple PES and coupling elements. Also, often the number of degrees of freedom were reduced in order to make dynamical studies feasible. As a result of the development of efficient computer codes, both to calculate potential surfaces and to solve the Schrödinger equation for the nuclear motion on these potentials, and the drastic increase of computer power, it is nowadays possible to accurately describe photodissociation processes involving more than one electronic state. Especially the development of easy-to-use diabatization schemes and their implementation in quantum chemical program packages has greatly advanced the study of nonadiabatic

processes. Thus, the rigorous treatment of two coupled electronic states for a triatomic molecule, including low rotational states, is not a serious problem today. Several examples have been described in this chapter.

However, this does not imply that the calculations are without complications. The construction of accurate PESs is still a formidable task, especially if several surfaces have to be calculated simultaneously. The dynamics in general and the non-adiabatic transitions in particular may crucially depend on fine details of the electronic structure calculations, such as the location of the conical intersection in the multi-dimensional coordinate space or its energy. The dissociations of ICN or HNO, discussed in Secs. 3 and 6, are good examples to illustrate this point. Although the effects are qualitatively well described by the calculations, finer details of the experimental observations are not in quantitative agreement. In the latter example, two PES with an accuracy of the order of approximately $50\,\mathrm{cm}^{-1}$ were needed; moreover, the vertical separation of these two potentials should have a similar exactness. It is doubtful whether this goal can be achieved in the near future.

Although several triatomic molecules, involving nonadiabatic transitions at conical intersections, have been theoretically described in detail, there are still examples for which — in view of the many experimental data available — high-level calculations are needed. One example is the predissociation of high-lying Rydberg states of H_3. For a comprehensive list of references see Ref. 123. Electronically excited H_3 can dissociate into $H + H_2$ or three hydrogen atoms. The lifetime and the vibrational-rotational product distribution of H_2 depend sensitively on the particular rovibronic state of the parent molecule.[123,124] Recently, also the correlation among the fragments in the three-body breakup has been investigated.[125,126] Although a number of calculations have been aimed in interpreting these data,[127–131] we think that more rigorous descriptions are still needed.

Rigorous descriptions of nonadiabatic transitions in molecules with more than three atoms are, for several reasons, much more complicated than for triatoms. First, the dimensionality is considerably higher and therefore more energy points are required to construct global PESs. As an unavoidable consequence, the accuracy of the electronic structure calculations has to be lower. Second, the dynamical calculations become much more demanding. Exact quantum mechanical calculations are possible with more than three degrees of freedom, as has been demonstrated by Hammerich

et al.[38] for the dissociation of CH_3I using the Multi-Configuration Time-Dependent-Hartree (MCTDH) method (see also Chapters 14 and 15 in this book). But, these calculations are demanding although the dissociation of CH_3I in the first absorption band is a comparatively "simple" reaction, because the "lifetime" is extremely short.

A photodissociation process involving a polyatomic molecule and a conical intersection is the fragmentation of HNCO via the first absorption band, which has been intensively studied in several laboratories.[132–135] The interest for this reaction partly results from the possibility that two dissociation channels of similar energy are accessible: HN+CO and H+NCO. The latter channel has a lower threshold, but is blocked by a high barrier.[136] Therefore, at low excess energies HNCO can dissociate only via a non-adiabatic transition to the ground electronic state. The conical intersection, where this transition can occur, has been localized by extensive *ab initio* calculations.[137–140] The first triplet state is also involved in the dissociation process. Thus, a complete description requires two singlet PESs and one triplet PES, each being a function of six variables, and the corresponding coupling matrix elements. This is a great challenge for dynamical theory. However, in view of the many detailed experimental data available, it appears worthwhile to tackle this problem.

Acknowledgments

The author gratefully acknowledges financial support by the Deutsche Forschungsgemeinschaft through the Sonderforschungsbereich 357 "Molekulare Mechanismen unimolekularer Reaktionen".

References

1. R. Schinke, *Photodissociation Dynamics* (Cambridge University Press, Cambridge, 1993).
2. H. Sato, *Chem. Rev.* **101**, 2686 (2001).
3. B. R. Johnson, C. Kittrell, P. B. Kelly and J. L. Kinsey, *J. Phys. Chem.* **100**, 7743 (1996).
4. E. J. Heller, *Acc. Chem. Res.* **14**, 368 (1981).
5. A. H. Zewail, *Faraday Discuss. Chem. Soc.* **91**, 207 (1991).
6. A. H. Zewail, in *Femtosecond Chemistry*, Eds. J. Manz and L. Wöste (Verlag Chemie, Weinheim, 1995).

7. J. Manz, in *Femtochemistry and Femtobiology: Ultrafast Dynamics at Atomic Scale Resolution*, Eds. V. Sundström (Imperial College, London, 1997).
8. W. Domcke and G. Stock, *Adv. Chem. Phys.* **100**, 1 (1997).
9. L. J. Butler, *Ann. Rev. Phys. Chem.* **49**, 125 (1998).
10. R. Loudon, *The Quantum Theory of Light* (Oxford University Press, Oxford, 1983).
11. V. Engel, *Comput. Phys. Comm.* **63**, 228 (1991).
12. G. G. Balint-Kurti and M. Shapiro, in *Photodissociation and Photionization*, Ed. K. P. Lawley (Wiley, New York, 1985).
13. R. B. Gerber, R. Kosloff and M. Berman, *Comput. Phys. Rep.* **5**, 59 (1986).
14. V. Mohan and N. Sathyamurthy, *Comput. Phys. Rep.* **7**, 213 (1988).
15. N. Balakrishnan, C. Kalyanaraman and N. Sathyamurthy, *Phys. Rep.* **280**, 79 (1997).
16. E. J. Heller, in *Potential Energy Surfaces and Dynamics Calculations*, Ed. D. G. Truhlar (Plenum Press, New York, 1981).
17. R. Schinke, H.-M. Keller, M. Stumpf and A. J. Dobbyn, *J. Phys.* **B28**, 3081 (1995).
18. G.-J. Kroes, M. R. Wall, J. W. Pang and D. Neuhauser, *J. Chem. Phys.* **106**, 1800 (1997).
19. V. A. Mandelshtam and H. S. Taylor, *J. Chem. Phys.* **106**, 5085 (1997).
20. S. Y. Lee and E. J. Heller, *J. Chem. Phys.* **71**, 4777 (1979).
21. D. Tannor and E. J. Heller, *J. Chem. Phys.* **77**, 202 (1982).
22. R. Heather and H. Metiu, *J. Chem. Phys.* **86**, 5009 (1987).
23. G. G. Balint-Kurti, R. N. Dixon, C. C. Marston and A. J. Mulholland, *Comput. Phys. Commun.* **63**, 126 (1991).
24. Y. Amatatsu, S. Yabushita and K. Morokuma, *J. Chem. Phys.* **100**, 4894 (1994).
25. M. L. Costen, S. W. North and G. E. Hall, *J. Chem. Phys.* **111**, 6735 (1999).
26. W. P. Hess and S. R. Leone, *J. Chem. Phys.* **86**, 3773 (1987).
27. I. Nadler, D. Mahgerefteh, H. Reisler and C. Wittig, *J. Chem. Phys.* **82**, 3885 (1985).
28. J. F. Black, J. R. Waldeck and R. N. Zare, *J. Chem. Phys.* **92**, 3519 (1990).
29. M. A. O'Halloran, H. Joswig and R. N. Zare, *J. Chem. Phys.* **87**, 303 (1987).
30. E. Hasselbrink, J. R. Waldeck and R. N. Zare, *Chem. Phys.* **126**, 191 (1989).
31. J. Qian, D. J. Tannor, Y. Amatatsu and K. Morokuma, *J. Chem. Phys.* **101**, 9597 (1994).
32. S. Yabushita and K. Morokuma, *Chem. Phys. Lett.* **175**, 518 (1990).
33. Y. Wang and C. X. W. Qian, *J. Chem. Phys.* **100**, 2707 (1994).
34. H. Wei and T. Carrington, Jr., *J. Chem. Phys.* **105**, 141 (1996).
35. J. M. Bowman, R. C. Mayrhofer and Y. Amatatsu, *J. Chem. Phys.* **101**, 9469 (1994).
36. F. N. Dzegilenko, J. M. Bowman and Y. Amatatsu, *Chem. Phys. Lett.* **264**, 24 (1997).

37. A. J. R. Heck and D. W. Chandler, *Ann. Rev. Phys. Chem.* **46**, 335 (1995).
38. A. D. Hammerich, U. Manthe, R. Kosloff, H.-D. Meyer and L. S. Cederbaum, *J. Chem. Phys.* **101**, 5623 (1994).
39. Y. Amatatsu, S. Yabushita and K. Morokuma, *J. Chem. Phys.* **104**, 9783 (1996).
40. A. T. J. B. Eppink and D. H. Parker, *J. Chem. Phys.* **110**, 832 (1999).
41. A. T. J. B. Eppink and D. H. Parker, *J. Chem. Phys.* **109**, 4758 (1998).
42. K. Q. Lao, M. D. Person, P. Xayariboun and L. J. Butler, *J. Chem. Phys.* **92**, 823 (1990).
43. M. Shapiro and R. Bersohn, *J. Chem. Phys.* **73**, 3810 (1980).
44. H. Guo and G. C. Schatz, *J. Chem. Phys.* **93**, 393 (1990).
45. H. Guo, *J. Chem. Phys.* **96**, 6629 (1992).
46. C. Rist and M. H. Alexander, *J. Chem. Phys.* **98**, 6196 (1993).
47. Y. Amatatsu, K. Morokuma and S. Yabushita, *J. Chem. Phys.* **94**, 4858 (1991).
48. D. Xie, H. Guo, Y. Amatatsu and R. Kosloff, *J. Phys. Chem.* **A104**, 1009 (2000).
49. B. Heumann, K. Weide, R. Düren and R. Schinke, *J. Chem. Phys.* **98**, 5508 (1993).
50. B. Heumann and R. Schinke, *J. Chem. Phys.* **101**, 7488 (1994).
51. D. Simah, B. Hartke and H.-J. Werner, *J. Chem. Phys.* **111**, 4523 (1999).
52. D. Skouteris, B. Hartke and H.-J. Werner, *J. Phys. Chem.* **A105**, 2458 (2001).
53. R. T. Pack, *J. Chem. Phys.* **65**, 4765 (1976).
54. L. C. Lee, X. Wang and M. Suto, *J. Chem. Phys.* **86**, 4353 (1987).
55. X. Xie, L. Schnieder, H. Wallmeier, R. Boettner, K. H. Welge and M. N. R. Ashfold, *J. Chem. Phys.* **92**, 1608 (1990).
56. R. E. Continetti, B. A. Balko and Y. T. Lee, *Chem. Phys. Lett.* **182**, 400 (1991).
57. S. H. S. Wilson, J. D. Howe and M. N. R. Ashfold, *Mol. Phys.* **88**, 841 (1996).
58. B. R. Weiner, H. B. Levene, J. J. Valentini and A. P. Baronavski, *J. Chem. Phys.* **90**, 1403 (1989).
59. M. N. R. Ashfold, L. Schnieder and K. H. Welge, *Faraday Discuss. Chem. Soc.* **91**, 128 (1991).
60. R. J. Brudzynski, R. J. Sension and B. Hudson, *Chem. Phys. Lett.* **165**, 487 (1990).
61. P. W. Browning, E. Jensen, G. C. G. Waschewsky, M. R. Tate, L. J. Butler and J. Hessler, *J. Chem. Phys.* **101**, 5652 (1994).
62. V. Engel, V. Staemmler, R. L. Vander Wal, F. F. Crim, R. J. Sension, B. Hudson, P. Andresen, S. Hennig, K. Weide and R. Schinke, *J. Phys. Chem.* **96**, 3201 (1992).

63. H. Flöthmann, C. Beck, R. Schinke, C. Woywod and W. Domcke, *J. Chem. Phys.* **107**, 7296 (1997).
64. C. Woywod, M. Stengle, W. Domcke, H. Flöthmann and R. Schinke, *J. Chem. Phys.* **107**, 7282 (1997).
65. S. M. Anderson and K. Mauersberger, *J. Geophys. Res.* **100**, 3033 (1995).
66. K. Bogumil, J. Orphal, J. P. Burrows and J. M. Flaud, *Chem. Phys. Lett.* **349**, 241 (2001).
67. H. Flöthmann, R. Schinke, C. Woywod and W. Domcke, *J. Chem. Phys.* **109**, 2680 (1998).
68. H. B. Levene, J.-C. Nieh and J. J. Valentini, *J. Chem. Phys.* **87**, 2583 (1987).
69. K. Kühl and R. Schinke, *Chem. Phys. Lett.* **158**, 81 (1989).
70. M. P. Docker, A. Hodgson and J. P. Simons, in *Molecular Photodissociation Dynamics*, Eds. M. N. R. Ashfold and J. E. Baggott (The Royal Society of Chemistry, London, 1987).
71. H. J. Krautwald, L. Schnieder, K. H. Welge and M. N. R. Ashfold, *Faraday Discuss. Chem. Soc.* **82**, 99 (1986).
72. D. H. Mordaunt, M. N. R. Ashfold and R. N. Dixon, *J. Chem. Phys.* **100**, 7360 (1994).
73. S. A. Harich, X. Yang, D. W. H. Hwang, J. J. Lin, X. Yang and R. N. Dixon, *J. Chem. Phys.* **114**, 7830 (2001).
74. E. Segev and M. Shapiro, *J. Chem. Phys.* **77**, 5604 (1982).
75. K. Weide and R. Schinke, *J. Chem. Phys.* **87**, 4627 (1987).
76. K. Weide, K. Kühl and R. Schinke, *J. Chem. Phys.* **91**, 3999 (1989).
77. B. Heumann, K. Kühl, K. Weide, R. Düren, B. Hess, U. Meier, S. D. Peyerimhoff and R. Schinke, *Chem. Phys. Lett.* **166**, 385 (1990).
78. A. J. Dobbyn and P. J. Knowles, *Mol. Phys.* **91**, 1107 (1997).
79. R. van Harrevelt and M. C. van Hemert, *J. Chem. Phys.* **112**, 5777 (2000).
80. R. van Harrevelt and M. C. van Hemert, *J. Chem. Phys.* **112**, 5787 (2000).
81. H.-T. Wang, W. S. Felps and S. P. McGlynn, *J. Chem. Phys.* **67**, 2614 (1977).
82. J. H. Fillion, R. van Harrevelt, J. Ruiz, M. Castillejo, A. H. Zanganeh, J. L. Lemaire, M. C. van Hemert and F. Rostas, *J. Phys. Chem.* **A105**, 11414 (2001).
83. S. A. Harich, X. F. Yang, X. Yang, R. van Harrevelt and M. C. van Hemert, *Phys. Rev. Lett.* **87**, 263001 (2001).
84. S. A. Harich, D. W. H. Hwang, X. Yang, J. J. Lin, X. Yang and R. N. Dixon, *J. Chem. Phys.* **113**, 10073 (2000).
85. R. N. Dixon, D. W. H. Hwang, X. F. Yang, S. A. Harich, J. J. Lin and X. Yang, *Science* **285**, 1249 (1999).
86. R. van Harrevelt, M. C. van Hemert and G. C. Schatz, *J. Phys. Chem.* **A105**, 11480 (2001).
87. R. N. Dixon, *Mol. Phys.* **68**, 263 (1989).
88. D. H. Mordaunt, M. N. R. Ashfold and R. N. Dixon, *J. Chem. Phys.* **104**, 6460 (1996).

89. D. H. Mordaunt, R. N. Dixon and M. N. R. Ashfold, *J. Chem. Phys.* **104**, 6472 (1996).
90. R. N. Dixon, *Mol. Phys.* **88**, 949 (1996).
91. R. Polaḱ, I. Paidarová and P. J. Kuntz, *Int. J. Quantum Chem.* **62**, 659 (1997).
92. J. P. Reid, R. A. Loomis and S. R. Leone, *J. Phys. Chem.* **A104**, 10139 (2000).
93. J. P. Reid, R. A. Loomis and S. R. Leone, *J. Chem. Phys.* **112**, 3181 (2000).
94. A. Bach, J. M. Hutchison, R. J. Holiday and F. F. Crim, *J. Chem. Phys.* **116**, 4955 (2002).
95. A. Bach, J. M. Hutchison, R. J. Holiday and F. F. Crim, *J. Chem. Phys.* **116**, 9315 (2002).
96. A. Delon, R. Jost and M. Lombardi, *J. Chem. Phys.* **95**, 5701 (1991).
97. A. Delon, R. Jost and M. Jacon, *J. Chem. Phys.* **114**, 331 (2001).
98. S. A. Reid and H. Reisler, *J. Phys. Chem.* **100**, 474 (1996).
99. S. Mahapatra, H. Köppel, L. S. Cederbaum, P. Stampfuß and W. Wenzel, *Chem. Phys.* **259**, 211 (2000).
100. B. Kirmse, A. Delon and R. Jost, *J. Geophys. Res.* **102**, 16089 (1997).
101. A. Delon, R. Georges, B. Kirmse and R. Jost, *Faraday Discuss.* **102**, 117 (1996).
102. S. I. Ionov, G. A. Bruckner, C. Jaques, Y. Chen and C. Wittig, *J. Chem. Phys.* **99**, 3420 (1993).
103. B. Kirmse, B. Abel, D. Schwarzer, S. Yu. Grebenshchikov and R. Schinke, *J. Phys. Chem.* **A104**, 10374 (2000).
104. G. Hirsch, R. J. Buenker and C. Petrongolo, *Mol. Phys.* **73**, 1085 (1991).
105. R. F. Salzgeber, V. Mandelshtam, C. Schlier and H. S. Taylor, *J. Chem. Phys.* **110**, 3756 (1999).
106. A. Weaver, R. B. Metz, S. E. Bradforth and D. M. Neumark, *J. Chem. Phys.* **90**, 2070 (1989).
107. D. Reignier, T. Stoecklin, P. Halvick, A. Voronin and J. C. Rayez, *Phys. Chem. Chem. Phys.* **3**, 2726 (2001).
108. G.-J. Kroes, M. C. van Hemert, G. D. Billing and D. Neuhauser, *Chem. Phys. Lett.* **271**, 311 (1997).
109. G.-J. Kroes, M. C. van Hemert, G. D. Billing and D. Neuhauser, *J. Chem. Phys.* **107**, 5757 (1997).
110. D. R. Yarkony, *J. Chem. Phys.* **104**, 2932 (1996).
111. G. Herzberg *Molecular Spectra and Molecular Structure III. Electronic Spectra and Electronic Structure of Polyatomic Molecules* (Van Nostrand, Princeton, 1967).
112. R. N. Dixon, *Mol. Phys.* **54**, 333 (1985).
113. J. Weiß and R. Schinke, *J. Chem. Phys.* **115**, 3173 (2001).
114. E. M. Goldfield, S. K. Gray and L. B. Harding, *J. Chem. Phys.* **99**, 5812 (1993).

115. A. Loettgers, A. Untch, H.-M. Keller, R. Schinke, H.-J. Werner, C. Bauer and P. Rosmus, *J. Chem. Phys.* **106**, 3186 (1997).
116. J. Weiß, R. Schinke and V. A. Mandelshtam, *J. Chem. Phys.* **113**, 4588 (2000).
117. J.-C. Loison, S. H. Kable, P. L. Houston and I. Burak, *J. Chem. Phys.* **94**, 1796 (1991).
118. D. W. Neyer, X. Luo, I. Burak and P. L. Houston, *J. Chem. Phys.* **102**, 1645 (1995).
119. D. W. Neyer and P. L. Houston, in *The Chemical Dynamics and Kinetics of Small Radicals*, Eds. K. Liu and A. Wagner (World Scientific, Singapore, 1994).
120. D. W. Neyer, S. H. Kable, J.-C. Loison, P. L. Houston, I. Burak and E. M. Goldfield, *J. Chem. Phys.* **97**, 9036 (1992).
121. H. Lefebvre-Brion and R. W. Field, *Perturbations in the Spectra of Diatomic Molecules* (Academic Press, Orlando, 1986).
122. J. Pearson, A. J. Orr-Ewing, M. N. R. Ashfold and R. N. Dixon, *J. Chem. Phys.* **106**, 5850 (1997).
123. U. Müller and P. C. Cosby, *J. Chem. Phys.* **105**, 3532 (1996).
124. I. Mistrík, R. Reichle, H. Helm and U. Müller, *Phys. Rev.* **A63**, 042711 (2001).
125. U. Müller, Th. Eckert, M. Braun and H. Helm, *Phys. Rev. Lett.* **83**, 2718 (1999).
126. M. Braun, M. Beckert and U. Müller, *Rev. Sci. Instrum.* **71**, 4535 (2000).
127. A. E. Orel and K. C. Kulander, *J. Chem. Phys.* **91**, 6086 (1989).
128. J. L. Krause, K. C. Kulander, J. C. Light and A. E. Orel, *J. Chem. Phys.* **96**, 4283 (1992).
129. I. F. Schneider and A. E. Orel, *J. Chem. Phys.* **111**, 5873 (1999).
130. M. Tashiro and S. Kato, *Chem. Phys. Lett.* **354**, 14 (2002).
131. M. Tashiro and S. Kato, *J. Chem. Phys.* **117**, 2053 (2002).
132. M. Zyrianov, A. Sanov, Th. Droz-Georget and H. Reisler, *J. Chem. Phys.* **110**, 10774 (1999).
133. H. L. Berghout, F. F. Crim, M. Zyrianov and H. Reisler, *J. Chem. Phys.* **112**, 6678 (2000).
134. H. L. Berghout, S. Hsieh and F. F. Crim, *J. Chem. Phys.* **114**, 10835 (2001).
135. R. A. Brownsword, M. Hillenkamp, T. Laurent, R. K. Vatsa and H.-R. Volpp, *J. Chem. Phys.* **106**, 4436 (1997).
136. J.-J. Klossika and R. Schinke, *J. Chem. Phys.* **111**, 5882 (1999).
137. A. L. Kaledin, Q. Ciu, M. C. Heaven and K. Morokuma, *J. Chem. Phys.* **111**, 5004 (1999).
138. J.-J. Klossika, H. Flöthmann, R. Schinke and M. Bittererová, *Chem. Phys. Lett.* **314**, 182 (1999).
139. R. Schinke and M. Bittererová, *Chem. Phys. Lett.* **332**, 611 (2000).
140. D. R. Yarkony, *Mol. Phys.* **99**, 1463 (2001).

This page intentionally left blank

CHAPTER 12

GEOMETRIC PHASE EFFECTS IN CHEMICAL REACTION DYNAMICS

Brian K. Kendrick
Theoretical Division (T-12, MS-B268),
Los Alamos National Laboratory,
Los Alamos, New Mexico 87545

Contents

1. Introduction

The standard theoretical treatment of chemical reaction dynamics is based on the separation of the total molecular motion into fast and slow parts. The fast motion corresponds to the motion of the electrons and the slow motion corresponds to the motion of the nuclei. The theoretical foundation for the separation of the electronic and nuclear motion was first developed by Born and Oppenheimer.[1] In this approach, the total molecular wave function is expanded in terms of a set of electronic eigenfunctions which depend parametrically on the nuclear coordinates. The expansion coefficients are the

nuclear motion wave functions which satisfy a matrix Schrödinger equation which includes off-diagonal coupling matrix elements with respect to the electronic quantum numbers. The smallness of the electronic mass (m_e) relative to the nuclear mass (m_N) is used to obtain an asymptotic expansion of the total molecular wave function, energy, and other quantities of interest in terms of the small parameter $\kappa = (m_e/m_N)^{1/4}$.[2–5] To lowest order in κ, the off-diagonal coupling terms can often be ignored for low-energy collisions and nondegenerate electronic states. In this case, the total molecular wave function can be expressed in terms of a single electronic state (usually the ground state). Thus, to a good approximation, the dynamics of the nuclear motion is governed by an effective Schrödinger equation, whose potential energy surface is determined by solving the Schrödinger equation for the ground electronic state at each nuclear geometry. This one-state approximation is often referred to as the "Born–Oppenheimer approximation" and has been the foundation for the modern theory of electronically adiabatic processes.

For high-energy collisions or degenerate electronic states, the Born–Oppenheimer approximation breaks down and more than one electronic state must be included. High-energy collisions give rise to electronically non-adiabatic processes (i.e. collision processes which change the electronic quantum numbers).[6] Another situation, for which the standard Born–Oppenheimer method becomes inadequate, is when a conical intersection occurs between the ground and an excited electronic state. Conical intersections can alter the nuclear dynamics even for low-energy collisions for which the one-state approximation is still valid. In this chapter, we will consider the modifications to the standard Born–Oppenheimer method which are required in order to account for the effects of conical intersections on the nuclear dynamics for low-energy collisions.

In 1963, Herzberg and Longuet-Higgins[7] showed that a real adiabatic electronic wave function changes sign (i.e. it is a double-valued function) when the nuclear coordinates traverse a closed path which encircles a conical intersection. In order for the total molecular wave function to remain single-valued, a compensating sign change must also occur in the nuclear motion wave function. Furthermore, for molecules with two or more identical nuclei, the sign change must be accounted for in order for the total molecular wave function to satisfy the correct Bose–Fermi statistics under an interchange of any two identical nuclei. In 1979, Mead and Truhlar[8,9]

discussed two approaches for including the sign change in the nuclear motion wave function. In one approach, a real double-valued electronic wave function is used and the correct nuclear motion wave functions are obtained by solving the standard Schrödinger equation for the nuclear motion, but with double-valued boundary conditions. In the second approach, a *complex* single-valued electronic wave function is used and the correct nuclear motion wave functions are obtained by solving a generalized Schrödinger equation for the nuclear motion with single-valued boundary conditions. The complex single-valued electronic wave function is obtained by multiplying the real double-valued electronic wave function by a complex phase factor which is a function of the nuclear coordinates. This phase factor changes sign for any closed path which encircles a conical intersection, so that the complex electronic wave function is single-valued. The electronic Schrödinger equation is unchanged by the phase transformation, so that the complex single-valued electronic wave function satisfies the same eigenvalue equation as the real double-valued electronic wave function. However, the Schrödinger equation for the nuclear motion acquires a vector potential (i.e. the momentum operator $\mathbf{p} \rightarrow \mathbf{p} - \mathbf{A}$). This vector potential comes from the gradient operator with respect to the nuclear coordinates acting on the complex phase factor. The vector potential is non-trivial (i.e. it cannot be transformed or gauged away by using a single-valued phase transformation) and is mathematically equivalent to that of a "magnetic solenoid" centered at the conical intersection. The resulting Schrödinger equation for the nuclear motion is identical to that of a charged particle moving in the presence of a magnetic solenoid. If the nuclear motion wave function has significant amplitude along the entire minimum energy pathway encircling a conical intersection, significant interference effects will occur which can significantly alter the nuclear dynamics. These effects can occur for relatively small collision energies which are much smaller than the energy of the conical intersection. The collision energy only needs to be larger than all of the potential energy barriers which may occur along the minimum energy pathway encircling the conical intersection. Mead later called this effect the "molecular Aharonov–Bohm effect".[10] In 1984, Berry[11] considered a general quantum system with parametric time dependence undergoing a cyclic adiabatic time evolution. He showed that the sign change which occurs in the "molecular Aharonov–Bohm effect" is a special case of the more general geometric phase often referred to as "Berry's phase". Berry's influential

paper generated much theoretical and experimental interest in this effect which continues to this day.

Section 2.1 presents the generalized Born–Oppenheimer equation for the nuclear motion which takes into account the geometric phase effects due to a conical intersection. Section 2.2 reviews the recently developed numerical methodology for solving the generalized Born–Oppenheimer equation. Section 2.3 reviews several applications of this methodology in chemical reaction dynamics. In particular, $H+O_2$ inelastic scattering and $H+H_2$, $D+H_2$, and $H + D_2$ reactive scattering are discussed. The effects of the geometric phase are investigated by solving both the standard and generalized Born–Oppenheimer equations for the nuclear motion and comparing the results. The effects of the geometric phase in reaction probabilities, resonance spectra, integral, and differential cross sections are investigated as a function of total energy and total angular momentum (J). Section 3 presents some conclusions regarding the importance of geometric phase effects in chemical reaction dynamics.

2. The Generalized Born–Oppenheimer Method

2.1. *Theory*

The molecular Schrödinger equation is given by

$$H\,\Psi = E\,\Psi\,, \tag{1}$$

where Ψ is the total molecular wave function, H the total molecular Hamiltonian, and E the total energy. We restrict our present treatment to triatomic molecules so that there are six nuclear coordinates relative to the center of mass. Three of these six are internal coordinates which are functions of the three internuclear distances. The remaining three are angular coordinates which specify the orientation of the body-frame relative to the space-frame and are usually taken to be the three Euler angles. The six nuclear coordinates are denoted as $\mathbf{R} = (\mathrm{x}, \hat{x})$, where x and $\hat{x}$ denote the three internal and three angular coordinates, respectively.

After separating out the center of mass motion, we can express H in space-frame coordinates as

$$H \equiv -\frac{\hbar^2}{2\mu}\,\nabla^2 + H_e(\mathbf{R})\,, \tag{2}$$

where ∇^2 is the six-dimensional Laplacian with respect to the six nuclear coordinates $\mathbf{R}$, μ is the three body reduced mass $\mu \equiv (m_\mathrm{A}\, m_\mathrm{B}\, m_\mathrm{C}/(m_\mathrm{A} + m_\mathrm{B} + m_\mathrm{C}))^{1/2}$, and $H_e(\mathbf{R})$ is the electronic Hamiltonian which depends parametrically on the nuclear coordinates.

We neglect all electronic angular momentum (spin and orbital) so that the space-frame electronic eigenfunctions (Φ_n) depend parametrically on the three internal nuclear coordinates x and can be chosen real orthogonal with real eigenvalues (V_n)[12]

$$H_e(\mathbf{R})\, \Phi_n(\mathbf{r};\mathrm{x}) = V_n(\mathrm{x})\, \Phi_n(\mathbf{r};\mathrm{x})\,, \tag{3}$$

where $\mathbf{r}$ denotes all of the electronic coordinates. From now on, we assume that accurate solutions to Eq. (3) are available or can be readily calculated.

The total molecular wave function can be expanded in terms of the electronic eigenfunctions

$$\Psi = \sum_{n=0}^{N} \chi_n(\mathbf{x}) \Phi_n(\mathbf{r};\mathrm{x}) \psi^{\mathcal{N}}\,, \tag{4}$$

where the expansion coefficients $\chi_n(\mathbf{x})$ are the nuclear motion wave functions, and $\psi^{\mathcal{N}}$ is the nuclear spin wave function. The number of electronic states N is in general infinite. Fortunately, for low collision energies, the smallness of the Born–Oppenheimer parameter κ allows one to truncate this infinite sum to some finite number N. If one substitutes Eq. (4) into Eq. (1), multiplies on the left by $\Phi_n(\mathbf{r};\mathrm{x})$, integrates over $\mathbf{r}$ and uses Eq. (3), one obtains the following matrix equation for the nuclear motion wave function $(n = 0, 1, 2, \ldots, N)$[13–15]

$$\sum_{m=0}^{N} \left[\frac{\hbar^2}{2\mu} \sum_{k=0}^{N} (-i\delta_{nk}\nabla - \mathbf{A}_{nk}(\mathrm{x})) \cdot (-i\delta_{km}\nabla - \mathbf{A}_{km}(\mathrm{x})) + \varepsilon_{nm}(\mathrm{x}) \right] \chi_m(\mathbf{x}) = E\chi_\mathrm{n}(\mathbf{x}), \tag{5}$$

where the vector nonadiabatic coupling matrix elements are given by[13–16]

$$\mathbf{A}_{nm}(\mathrm{x}) = i\langle \Phi_n(\mathrm{x}) | (\nabla \Phi_m(\mathrm{x})) \rangle\,. \tag{6}$$

The effective scalar potential is given by[13–15,17]

$$\varepsilon_{nm}(\mathrm{x}) = V_n(\mathrm{x})\delta_{nm} - \frac{\hbar^2}{2\mu}\sum_{l\neq n,m}\langle\Phi_n(\mathrm{x})|(\nabla\Phi_l(\mathrm{x}))\rangle\cdot\langle\Phi_l(\mathrm{x})|(\nabla\Phi_m(\mathrm{x}))\rangle\,. \quad (7)$$

The scalar potential given in Eq. (7) contains contributions which involve derivative coupling matrix elements between the electronic subspace of interest and the excited electronic states. These contributions have the effect of a small correction (proportional to κ^4) to the potential energy $V_n(\mathrm{x})$. From now on, we ignore these small corrections and take $\varepsilon_{nm}(\mathrm{x}) = V_n(\mathrm{x})\delta_{nm}$.

For low collision energies and a non-degenerate ground electronic state, we can truncate the sum in Eq. (4) to only one term. This case is often referred to as the "Born–Oppenheimer approximation" and the molecular wave function is given by

$$\Psi \approx \chi_0(\mathbf{x})\Phi_0(\mathbf{r};\mathrm{x})\psi^{\mathcal{N}}\,, \quad (8)$$

where $n = 0$ denotes the ground electronic state. For degenerate electronic states or high collision energies, more terms in the sum over n must be included. From now on, we assume that Eq. (8) is valid and drop the subscript on the nuclear and electronic wave functions with the understanding that they denote the ground electronic state. The Born–Oppenheimer Eq. (5) for the nuclear motion becomes

$$\Big[-\frac{\hbar^2}{2\mu}\nabla^2 + V(\mathrm{x})\Big]\chi(\mathbf{x}) = E\chi(\mathbf{x})\,. \quad (9)$$

In the derivation of Eq. (9), we used the fact that $\langle\Phi(\mathrm{x})|\nabla|\Phi(\mathrm{x})\rangle = 0$ which is straightforward to prove by differentiating the normalization equation $\langle\Phi(\mathrm{x})|\Phi(\mathrm{x})\rangle = 1$ and using the fact that $|\Phi(\mathrm{x})\rangle$ is real.

We denote the d-dimensional internal nuclear parameter space by $\mathcal{M}$ ($d = 3$ for triatomics) and the subspace of $\mathcal{M}$ for which a conical intersection occurs by $\mathcal{D} \subset \mathcal{M}$. The subspace $\mathcal{D}$ is of dimension $d-2$, and for triatomic molecules it is a one-dimensional curve in the three-dimensional nuclear parameter space $\mathcal{M}$.[7,18] Two conditions, $u(\mathrm{x}) = 0$ and $v(\mathrm{x}) = 0$, define the subspace $\mathcal{D}$, and these can be expressed in terms of any two diagonal cofactors of the matrix $\mathbf{w}(\mathrm{x}) \equiv \mathbf{H}_e(\mathrm{x}) - \mathbf{I}V_0(\mathrm{x})$, where $\mathbf{H}_e$ is the electronic Hamiltonian and V_0 is the ground state eigenvalue.[19] In an infinitesimal

region near $\mathcal{D}$, the relevant part of the electronic Hamiltonian is a 2×2 matrix of the form[8,18]

$$H_e(\mathrm{x}) = -\begin{pmatrix} \delta u & \delta v \\ \delta v & -\delta u \end{pmatrix} = -r \begin{pmatrix} \cos\eta & \sin\eta \\ \sin\eta & -\cos\eta \end{pmatrix}, \tag{10}$$

where $\delta u(\mathrm{x})$ and $\delta v(\mathrm{x})$ are infinitesimal displacements from the origin in the two-dimensional Cartesian space spanned by $u\mathbf{e}_u$ and $v\mathbf{e}_v$ (see Fig. 1). The polar coordinates are denoted by (r, η), where r is the radial distance from the origin in uv space and η is the azimuthal angle around the origin. The two eigenvalues of Eq. (3) are $V_{\pm}(\mathrm{x}) = \pm r$ which correspond to the upper and lower cones in Fig. 1. The two corresponding eigenvectors are given by

$$\Phi^+ = \begin{pmatrix} -\sin\frac{\eta}{2} \\ \cos\frac{\eta}{2} \end{pmatrix}, \qquad \Phi^- = \begin{pmatrix} \cos\frac{\eta}{2} \\ \sin\frac{\eta}{2} \end{pmatrix}. \tag{11}$$

It is clear that, due to the half-angle functional dependence upon the azimuthal angle η, these eigenvectors change sign (i.e. are double-valued) for any closed path in the nuclear parameter space for which η changes by 2π. Equation (11) is valid only in the infinitesimal region near the conical intersection. However, the sign change (double-valuedness) exists *globally*. That is, any closed path in $\mathcal{M}$ which encircles $\mathcal{D}$ (no matter how far away from $\mathcal{D}$) results in a sign change in the adiabatic ground state real electronic eigenvector.[20] The *global* expression for the angle η is given by $\eta(\mathrm{x}) \equiv \tan^{-1}(v(\mathrm{x})/u(\mathrm{x}))$, which is in general a complicated function of the

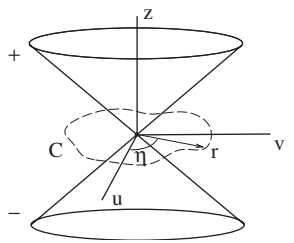

Fig. 1. Perspective plot of a two-dimensional slice of a potential energy surface near a conical intersection. The degeneracy point is located at the origin in the uv plane. The radial distance from the intersection is denoted by r and the azimuthal angle around the intersection denoted by η. The adiabatic ground state real electronic wave function changes sign for any closed path in uv space which encircles the origin (such as the dashed curve C).

three internal nuclear coordinates.[21] Recently, techniques have been developed to compute $\eta(\mathrm{x})$ for a general polyatomic molecule.[19] However, for triatomic molecules (such as H_3, HO_2, and Na_3) a suitable functional form for $\eta(\mathrm{x})$ can often be derived analytically.[8,12] It is important to realize that the functional forms of $u(\mathrm{x})$ and $v(\mathrm{x})$ are not unique. Hence, $\eta(\mathrm{x})$ is not unique. The only requirement is that $\eta(\mathrm{x})$ change by 2π for *any* closed path in $\mathcal{M}$ which encircles $\mathcal{D}$. This freedom in choosing η is called "gauge freedom" and different choices for η are related by $U(1)$ gauge transformations.[8,12,18,19,22]

Following Mead and Truhlar,[8] we multiply the real adiabatic electronic wave function by a complex phase

$$\Phi^{\mathcal{C}}(\mathbf{r};\mathrm{x}) \equiv \exp\left(i\frac{l}{2}\eta(\mathrm{x})\right)\Phi(\mathbf{r};\mathrm{x})\,, \tag{12}$$

where l is an *odd integer* and $\eta(\mathrm{x})$ is the azimuthal angle discussed above which changes by 2π for any nuclear motion which encircles a conical intersection. The complex phase factor cancels the sign change from the real electronic wave function $\Phi(\mathbf{r};\mathrm{x})$, giving rise to a complex *single-valued* electronic wave function $\Phi^{\mathcal{C}}(\mathbf{r};\mathrm{x})$. It is straightforward to show that the different choices for l are related by gauge transformations.[8] Hence, the choice of l is a matter of convenience, although larger values of l cause the numerical calculations to converge more slowly.[12,22]

Using Eq. (12) and repeating the same steps which lead to Eq. (9), we obtain the generalized Born–Oppenheimer equation for the nuclear motion[8,12–15,18,23]

$$\left[\frac{\hbar^2}{2\mu}(-i\nabla - \mathbf{A}(\mathrm{x}))^2 + V(\mathrm{x})\right]\chi^{\mathcal{C}}(\mathbf{x}) = E\chi^{\mathcal{C}}(\mathbf{x})\,, \tag{13}$$

where the nuclear motion wave function $\chi^{\mathcal{C}}(\mathbf{x})$ is *single-valued* and $\mathbf{A}(\mathrm{x})$ is the vector potential defined as

$$\mathbf{A}(\mathrm{x}) \equiv i\langle\Phi^{\mathcal{C}}(\mathrm{x})|(\nabla\Phi^{\mathcal{C}}(\mathrm{x}))\rangle\,. \tag{14}$$

Substituting Eq. (12) into Eq. (14), we can write the vector potential as

$$\mathbf{A}(\mathrm{x}) = -\frac{l}{2}\nabla\eta(\mathrm{x})\,. \tag{15}$$

Equation (15) has the same mathematical form as the vector potential of a magnetic solenoid located at the conical intersection.[8–10,18] By taking the curl of Eq. (15), we find that the corresponding "magnetic field" is zero

everywhere except at the conical intersection, where it has a delta function singularity

$$\mathbf{B}(\mathrm{x}) \equiv \nabla \times \mathbf{A}(\mathrm{x}) = -l\pi\delta(\mathrm{x})\mathbf{e}_z\,, \tag{16}$$

where $\mathbf{e}_z$ points along the z axis perpendicular to the uv-plane with the conical intersection located at the origin (see Fig. 1).[8–10,18] Equation (16) has the same mathematical form as the magnetic field of an infinitely thin and infinitely long magnetic solenoid centered at the conical intersection. Of course, the vector potential of Eq. (15) and its associated magnetic field given by Eq. (16) do not represent a real magnetic field. They come from the diagonal derivative coupling term which couples the nuclear and electronic motion [see Eq. (14)].

The geometric phase (β_g) can be expressed as the line integral of $\mathbf{A}$ along a closed path $\mathcal{C}$ in $\mathcal{M}$ which encircles the degeneracy subspace $\mathcal{D}$[8–11,18]

$$\beta_g = \oint_C \mathbf{A}\cdot \mathrm{d}\mathbf{l}\,. \tag{17}$$

By using Stokes's theorem, we can express the line integral of $\mathbf{A}$ as a surface integral of $\mathbf{B}$ which shows that the geometric phase (β_g) is equal to the "flux" of the "magnetic field" through the surface S enclosed by C

$$\beta_g = \int_S \mathbf{B}\cdot \mathrm{d}\mathbf{s}\,. \tag{18}$$

Upon substituting Eq. (15) into Eq. (17) or Eq. (16) into Eq. (18), we find that $\beta_g = -l\pi$ which corresponds to a phase factor of $\exp(-l\pi) = -1$. Thus, the sign change associated with a conical intersection can be given a geometrical interpretation. Equations (17) and (18) can be generalized to higher dimensions using the language of differential geometry. Equation (17) can be expressed as the line integral of a connection 1-form along the closed path $\mathcal{C}$ and the phase factor $\exp(i\beta_g)$ the associated holonomy. Similarly, Eq. (18) can be expressed as the surface integral of a curvature 2-form over the surface S enclosed by $\mathcal{C}$.[11,18,24–28]

2.2. *Numerical Techniques*

Although the generalized Born–Oppenheimer, Eq. (13), was first derived in 1979, numerical techniques for solving this equation were developed only recently. Part of this delay is due to the singular nature of the vector

potential, which exhibits a r^{-1} singularity where r denotes the radial distance from the conical intersection. Thus, until recently, geometric phase effects were included in quantum reactive scattering calculations by solving the standard Schrödinger Eq. (9), but with double-valued boundary conditions. For example, the H_3 molecule contains a conical intersection which occurs for equilateral triangle (D_{3h}) geometries. If one uses symmetrized hyperspherical coordinates, then double-valued boundary conditions are relatively straightforward to implement for this molecule by choosing the angle η (see Fig. 1) equal to the azimuthal angle ϕ of the 2D hypersphere. Thus, geometric phase effects can be included in the calculations by solving the standard Born–Oppenheimer Eq. (9), but expanding the solutions in terms of a double-valued basis set such as $\exp[i(m+1/2)\phi]$ (where m is an integer). This is the approach used by Kuppermann and coworkers.[29,30] However, for other coordinate systems, more complicated molecules, or when the conical intersection is not located at the symmetry point of the hyperspherical coordinates, the double-valued boundary conditions can be difficult to implement. For these more complicated cases, the vector potential approach, which is based on solving the generalized Born–Oppenheimer Eq. (13) with single-valued boundary conditions, is often more convenient. In 1994, Wu, Wyatt, and D'Mello[31] included geometric phase effects in scattering calculations for a model X_3 system using the vector potential approach. The motivation for using the vector potential approach in their calculations was that double-valued boundary conditions are difficult to implement in Jacobi coordinates. The development of numerical methods for using the vector potential approach to include geometric phase effects in quantum reactive scattering calculations for a real molecule occurred in 1996.[12,22] This methodology uses symmetrized hyperspherical coordinates and is capable of treating multiple conical intersections located at arbitrary points on the 2D hypersphere. In the first applications using this method, the location of a conical intersection on the 2D hypersphere was taken to be independent of hyper-radial coordinate ρ.[12,22] In this case, the angle η is a function of the two hyperangles (θ, ϕ). The method was later generalized so that it can also treat the dependence of η on ρ.[32] The vector potential approach has been applied to low-energy inelastic scattering of $H + O_2(v,j) \rightarrow H + O_2(v',j')$,[12,22,32,33] to quantum reactive scattering of $H + D_2(v,j) \rightarrow HD(v',j') + D$,[34] $D + H_2(v,j) \rightarrow HD(v',j') + H$,[35,36]

$H + H_2(v, j) \rightarrow H_2(v', j') + H$,[35] and to bound state calculations of HO_2[32] and Na_3.[33,37]

As mentioned above, our theoretical approach is based on symmetrized hyperspherical coordinates x = (ρ, θ, ϕ).[38–41] The radial coordinate ρ corresponds to a symmetric stretch motion, the polar angle θ represents a bending type motion, where $\theta = \pi/2$ corresponds to linear geometries and $\theta = 0$ corresponds to T-shaped arrangements (equilateral triangles for equal mass nuclei), and the azimuthal angle ϕ corresponds to an internal kinematic rotation (i.e. a pseudo-rotational motion). The body-frame z axis is chosen perpendicular to the plane of the triatomic molecule, and the body-frame x and y axes are chosen to lie along the instantaneous principal axes of inertia (i.e. the Q and q vectors of Ref. 42, respectively). The orientation of the body-frame relative to the space-frame is given by the three Euler angles, so that the collective set of six coordinates is given by $\mathbf{R} = (\rho, \theta, \phi, \alpha, \beta, \gamma)$. The Schrödinger equation for the nuclear motion is solved in two steps.[42] In the first step, the radial variable ρ is partitioned into a large number of "sectors" and the five dimensional surface (angular) differential equation is solved with ρ fixed at the center of each sector. This step is independent of the scattering energy. The surface solutions are used to compute the potential coupling and overlap matrices which appear in the coupled-channel (CC) radial equations. In the second step, the CC radial equations are solved at each scattering energy using a log-derivative propagation technique.[43,44] Once we have solved the CC radial equations, we apply the boundary conditions to the log-derivative matrix at large ρ to obtain the scattering matrix $\mathbf{S}$.[34,42]

The five dimensional surface function solutions are expanded in terms of a hybrid basis set consisting of a Discrete Variable Representation (DVR)[45–47] in the hyperangle θ, a Finite Basis Representation (FBR) in the azimuthal angle ϕ, and the appropriate set of normalized Wigner $\tilde{D}(\alpha, \beta, \gamma)$ functions.[48] The hybrid basis set accurately treats *both* of the Eckart[49] singularities which occur in the kinetic energy operator at the north pole and equator of the 2D hypersphere in (θ, ϕ) for all values of total angular momentum J (see Ref. 48 for details). This basis set also allows for an accurate treatment of geometric phase effects and is highly parallelizable.[34,50] The surface function Hamiltonian is diagonalized in parallel using a parallel implementation of the Implicitly Restarted Lanzcos Method (IRLM).[51–53]

A careful choice of the numerical quadrature scheme and a large set of quadrature points are required in order to obtain accurate matrix elements of the vector potential terms in Eq. (13).[12] The singularities in the terms involving $\mathbf{A}^2$ are the most troublesome, since they involve r^{-2}. The volume element cancels one of the r^{-1} singularities, but the integration of the remaining r^{-1} singularity gives rise to a divergent logarithmic function. Fortunately, the potential energy surface $V(\mathrm{x})$ is highly repulsive near a conical intersection, so that, for low collision energies, the nuclear motion wave function has essentially zero amplitude near the conical intersection. Thus, the problem with the singular $\mathbf{A}^2$ terms can be handled by introducing a cutoff so that when $\mathbf{A}^2 > A_{\mathrm{cut}}$, we set $\mathbf{A}^2 = A_{\mathrm{cut}}$. The cutoff allows the numerical integrals to converge. The cutoff parameter A_{cut} is determined from convergence studies and is increased until the solutions become insensitive to it.[12,32,34]

2.3. *Applications*

The methodology for solving the generalized Born–Oppenheimer equation described above was first applied to the inelastic scattering of $\mathrm{H} + \mathrm{O}_2(v, j) \rightarrow \mathrm{H} + \mathrm{O}_2(v', j')$ at low collision energies and zero total angular momentum (i.e. $J = 0$).[12,22,32,33] The ground state electronic potential energy surface for the HO_2 molecule contains a conical intersection which occurs for T-shaped (C_{2v}) geometries. It also contains two conical intersections which occur for linear geometries. The minimum energy pathway around each of the linear conical intersections exhibits a barrier of about 0.42 eV relative to the asymptotic $\mathrm{H} + \mathrm{O}_2$ potential well.[54] Thus, for total scattering energies below 0.42 eV, the nuclear motion wave function will not have appreciable amplitude along the entire minimum energy pathway around the linear conical intersections, and the effects of the geometric phase associated with these intersections can be ignored. However, the minimum energy pathway around the C_{2v} conical intersection contains no barrier.[54] Thus, the nuclear motion wave function can have significant amplitude along the entire minimum energy pathway around this intersection, even for very low scattering energies near threshold. The C_{2v} conical intersection in HO_2 gives rise to a geometric phase which alters the symmetry of the nuclear motion wave function, causing it to simultaneously exhibit both even and odd symmetry (with respect to an interchange of

the two identical nuclei of ^{16}O).[12,32,55] Thus, the correct nuclear motion wave functions exhibit even symmetry across the C_{2v} saddle point and odd symmetry across the C_{2v} symmetry line for H–O_2 geometries (see Fig. 5 in Ref. 12 and the discussion of symmetry in Refs. 55 and 56). The odd symmetry for H–O_2 correlates to the odd rotational levels of O_2 (due to Bose statistics only the odd rotational levels of O_2 are physically allowed).[57] In order to quantify the effects of the geometric phase due to the C_{2v} conical intersection, two sets of calculations were performed. One set included the geometric phase by using the vector potential approach (i.e. by solving the generalized Born–Oppenheimer Eq. (13)). The other set did not include the geometric phase and solved the standard Born–Oppenheimer Eq. (9). Both sets of calculations implemented single-valued boundary conditions on the nuclear motion wave function. Significant differences between the two sets of calculations were observed. The transition probabilities were computed as a function of total energy. Many of the probabilities which include the geometric phase were found to be shifted in energy (i.e. "out-of-phase") with respect to those which did not include the geometric phase.[22] The geometric phase also lowered the average $J = 0$ cumulative transition probability for the lowest vibrational transition by 35%.[32] Significant differences were also seen in the resonance spectrum. The geometric phase altered many of the resonance energies and lifetimes. In addition, new resonances appeared when the geometric phase was included, which were not present in the spectrum calculated without the geometric phase. Similarly, many of the resonances in the spectrum calculated without the geometric phase were missing in the spectrum which included the geometric phase.[22,32] Gauge invariance was also tested by performing a third set of calculations which solved the generalized Born–Oppenheimer Eq. (13) but with $l = 2$ [see Eq. (15)]. The $l = 2$ results do not include geometric phase effects and should be identical to the results based on solving the standard Born–Oppenheimer Eq. (9) with single-valued boundary conditions (i.e. the $l = 0$ case). As expected, excellent agreement was observed between the $l = 2$ and $l = 0$ calculations for the resonance spectrum and transition probabilities which indicates that the calculations are well converged and that gauge invariance is satisfied.[22,32] In summary, the geometric phase significantly alters the results of the calculations on H + O_2 inelastic scattering and it must be included in the theoretical treatment in order to obtain the correct results.

The vector potential approach was recently extended to include non-zero total angular momentum.[34] It was then used to perform quantum reactive scattering calculations for the $H + H_2$, $D + H_2$, and $H + D_2$ reactions, both with and without the geometric phase.[34–36] The H_3 molecule contains a conical intersection which occurs between the ground and first excited electronic states for equilateral (D_{3h}) nuclear geometries. The minimum energy of this intersection is quite high (2.7 eV relative to the bottom of the H_2 well) so that, for low collision energies, the Born–Oppenheimer approximation is valid and the nuclear dynamics can be accurately calculated using a single (ground state) electronic potential energy surface. However, due to the low potential energy barrier (0.42 eV) between the different nuclear arrangements, the nuclear motion wave function can have significant amplitude along the entire minimum energy pathway around the conical intersection, even for relatively low collision energies. Thus, a correct theoretical treatment of the $H + H_2$ reaction (and its isotopic variants) must include geometric phase effects.

The quantum reactive scattering calculations for the $H + D_2(v, j) \rightarrow HD(v', j') + D$ reaction were done for each value of total angular momentum $J = 0 - 5$ and inversion parity $P = \pm$ at 126 values of total energy in the range 0.4–2.4 eV.[34] The entire set of calculations were performed on two different potential energy surfaces for H_3: the Boothroyd–Keogh–Martin–Peterson (BKMP2)[58] and the Liu–Siegbahn–Truhlar–Horowitz (LSTH).[59] The scattering results on each surface are quite similar. In mass scaled symmetrized hyperspherical coordinates, the D_{3h} conical intersection for HD_2 is located at $\theta = 14.478°$ and $\phi = \pi$ for all values of ρ. Since the nuclei of the two D atoms in HD_2 are spin-1 Bosons,[57] the total molecular wave function [Ψ of Eq. (8)] must be symmetric under a permutation ($\mathcal{P}$) of the two identical nuclei. Since the nuclear spin is $S = 1$, we have a total of $(2S+1)^2 = 9$ nuclear spin states with $(2S + 1)(S + 1) = 6$ being symmetric and $(2S + 1)S = 3$ being antisymmetric. The symmetric states have the larger statistical weight and are called *ortho*-D_2. The antisymmetric states are called *para*-D_2. Since the ground electronic state of H_2 is a $^1\Sigma_g^+$ state,[60] we know that asymptotically (i.e. for large ρ) the electronic wave function for H–D_2 is symmetric. Since the total wave function must be symmetric and the electronic wave function is symmetric, we know that for *ortho* (*para*)-D_2 the nuclear motion wave function (Ψ) must be symmetric (antisymmetric) for H–D_2. Thus, for *ortho*-D_2 the symmetry of the nuclear motion wave

function must be even across the C_{2v} symmetry line for H–D_2 geometries (i.e. to the right of the conical intersection in Fig. 2 of Ref. 34). Since the geometric phase causes the electronic wave function to be double-valued, the electronic wave function exhibits odd symmetry across the C_{2v} symmetry line which lies to the left of the conical intersection in Fig. 2 of Ref. 34. This implies that the nuclear motion wave function must also be double-valued and exhibit odd symmetry to the left of the conical intersection, so that Bose statistics is satisfied. For *para*-D_2, the symmetry arguments are reversed.

The reaction probabilities for $H + D_2$ were computed as a function of total energy for each value of J^P. Many of the reaction probabilities which include the geometric phase exhibit an "out-of-phase" behavior relative to those which do not include the geometric phase for total energies above about 1.6 eV (see Figs. 7 and 8 of Ref. 34). This "out-of-phase" behavior alternates "phase" with even and odd values of J. When the contributions from even and odd values of J are added together to obtain the partial integral and differential cross sections, all of the geometric phase effects completely cancel out (see Fig. 10 of Ref. 34). No geometric phase effects were observed in any of the state-to-state partial integral and differential cross sections summed over the first six values of J for all 126 values of total energy (see Figs. 9, and 11–15 of Ref. 34). The cancellation of the geometric phase effects when even and odd values of J are added together appears to be related to the alternating symmetry of the surface function solutions with respect to even and odd values of J. The alternating symmetry causes the differences between the surface function energies computed with and without the geometric phase to alternate sign with respect to even and odd values of J (see Fig. 3 of Ref. 34). Since the cancellation of all geometric phase effects in the partial integral and differential cross sections appears to be due to symmetry, it was concluded in Ref. 34 that the cancellation should be independent of the potential energy surface and should continue to hold for higher values of J. This would imply that there are no geometric phase effects in fully converged integral and differential cross sections. The cancellation of all geometric phase effects would explain why fully converged quantum reactive scattering calculations for the $H + D_2$ reaction which ignore geometric phase effects[50,61–67] are in excellent agreement with recent high resolution molecular beam experiments.[64,65,68,69]

The quantum reactive scattering calculations for the $D + H_2(v, j) \rightarrow HD(v', j') + H$ reaction were done for each value of total angular momentum

$J = 0 - 34$ and inversion parity $P = \pm$ at 48 values of total energy in the range 0.4–2.32 eV.[35,36] The Boothroyd–Keogh–Martin–Peterson (BKMP2)[58] potential energy surface for H_3 was used. In mass scaled symmetrized hyperspherical coordinates, the D_{3h} conical intersection for DH_2 is located at $\theta = 11.537°$ and $\phi = 0$ for all values of ρ. Since the nuclei of the two H atoms in DH_2 are spin-1/2 fermions,[57] the total molecular wave function [Ψ of Eq. (8)] must be antisymmetric under a permutation ($\mathcal{P}$) of the two identical nuclei. Since the nuclear spin is $S = 1/2$, we have a total of $(2S+1)^2 = 4$ nuclear spin states with $(2S+1)(S+1) = 3$ being symmetric and $(2S+1)S = 1$ being antisymmetric. The symmetric states have the larger statistical weight and are called *ortho*-H_2. The antisymmetric states are called *para*-H_2. Since the ground electronic state of H_2 is a $^1\Sigma_g^+$ state,[60] we know that asymptotically (i.e. for large ρ) the electronic wave function for D–H_2 is symmetric. Since the total wave function must be antisymmetric and the electronic wave function is symmetric, we know that for *ortho* (*para*)-H_2 the nuclear motion wave function (Ψ) must be antisymmetric (symmetric) for D–H_2. Thus, for *ortho* (*para*)-H_2 the nuclear motion wave function is antisymmetric (symmetric) across the C_{2v} symmetry line to the right of the conical intersection. As mentioned above, the geometric phase alters the symmetry of the real electronic wave function for D–H_2 so that it is antisymmetric across the C_{2v} symmetry line to the left of the conical intersection. This change in symmetry is a direct consequence of the wave function's double-valuedness. Thus, in order for the total molecular wave function to satisfy Fermi statistics, the nuclear motion wave function for *ortho* (*para*)-H_2 must be symmetric (antisymmetric) across the C_{2v} symmetry line to the left of the conical intersection.

Many of the state-to-state reaction probabilities for D+H_2 which include the geometric phase were also found to exhibit an "out-of-phase" behavior as a function of scattering energy relative to those which do not include the geometric phase.[35,36] For example, Fig. 2 plots the reaction probabilities for $D + H_2$ ($v = 1$, $j = 0$) $\rightarrow$ $HD(v' = 0, j' = 0) + H$ as a function of total energy for all $J \leq 19$. We note that for zero initial rotational angular momentum (i.e. $j = 0$), the only non-zero reaction probabilities are for even $J + P$. The solid curves and data points do not include the geometric phase. The short dashed curves and open squares include the geometric phase and are based on the vector potential approach. At high energies, significant "out-of-phase" behavior occurs between the results which include

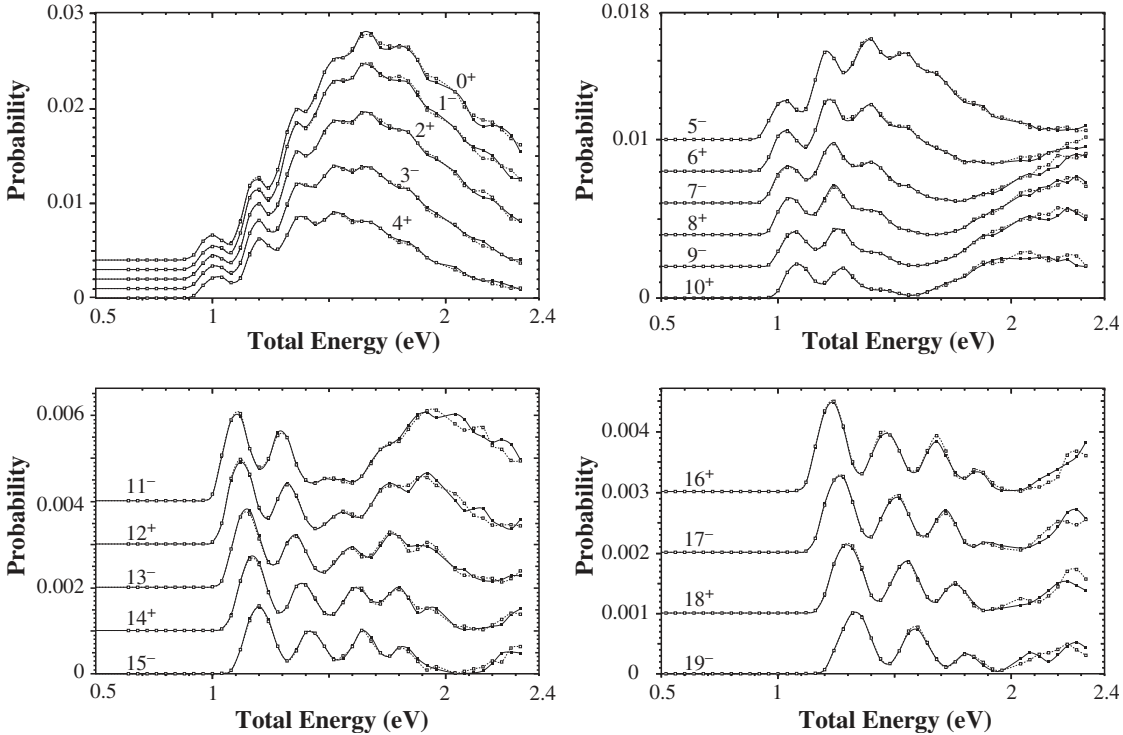

Fig. 2. Reaction probabilities for D + $H_2(v = 1, j = 0) \rightarrow HD(v' = 0, j' = 0)$ + H are plotted as a function of total energy for all values of $J \leq 19$. The solid curves and data points do not include the geometric phase. The short dashed curves and open squares include the geometric phase. The numbers labeling each set of curves denote the value of J^P. The curves are shifted to make viewing easier. The flat part of the curves near 0.5 eV corresponds to zero probability and indicates the value of the shift. The data points are calculated values and the curves are a cubic spline fit.

the geometric phase and those which do not. The "out-of-phase" behavior alternates "phase" with respect to even and odd J. Compare the solid and dashed curves for $J = 0 - 3$ near 2.15 eV. For $J = 0$ the dashed curve is above the solid curve and for $J = 1$ the dashed curve is below the solid curve. Similar behavior occurs for $J = 2$ and 3. More alternating "out-of-phase" behavior can be seen for other energies and values of J (especially for $E_{\text{tot}} > 1.9$ eV and $J \geq 16$). The alternating "out-of-phase" behavior in the reaction probabilities appears to be related to the alternating symmetry of the Wigner D functions with respect to even and odd J. When the contributions from even and odd values of J are added together to obtain fully converged integral and differential cross sections, all of the geometric phase effects completely cancel out.[35,36] For example, Figs. 3 and 4 plot the degeneracy averaged rotational distribution and differential cross sections for $D + H_2$ $(v = 0, j = 0) \rightarrow HD(v' = 0, j') + H$ at $E_{\text{tot}} = 1.25$ eV summed over all values of $J \leq 34$, respectively. There are two sets of curves in Figs. 3 and 4. The solid curves and data points do not include the geometric phase. The short dashed curves and open squares include the geometric phase. In

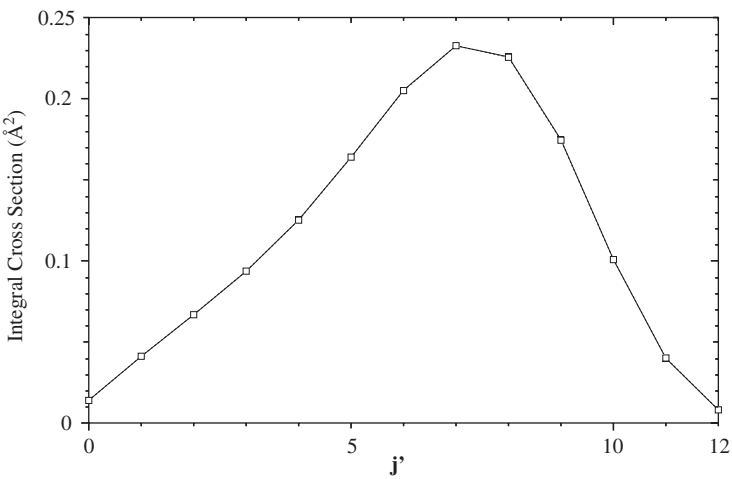

Fig. 3. The degeneracy averaged rotational distribution is plotted for $D + H_2(v = 0, j = 0) \rightarrow HD(v' = 0, j') + H$ at $E_{\text{tot}} = 1.25$ eV summed over all $J \leq 34$. Two curves are plotted. The solid curve and data points do not include the geometric phase. The short dashed curve and open squares include the geometric phase. The geometric phase results lie directly on top of the results which ignore the geometric phase.

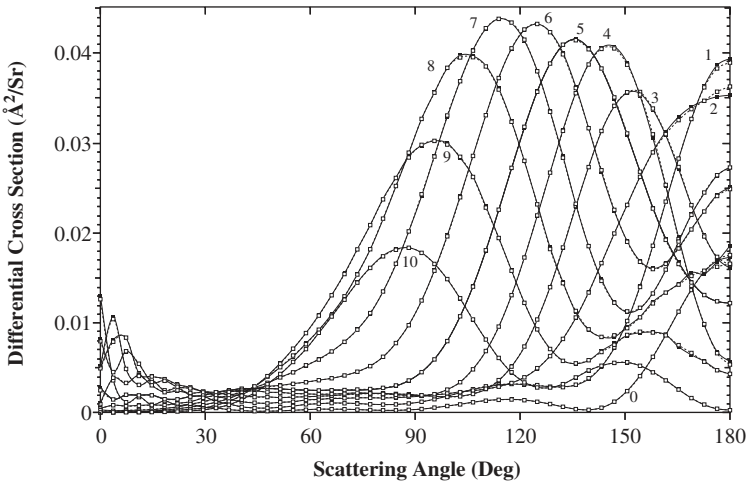

Fig. 4. The degeneracy averaged differential cross sections are plotted for $D + H_2(v = 0, j = 0) \rightarrow HD(v' = 0, j') + H$ at $E_{tot} = 1.25\,eV$ summed over all $J \leq 34$. The number next to each curve labels the value of j'. The solid curves and data points do not include the geometric phase. The short dashed curves and open squares include the geometric phase. The geometric phase results are almost identical to the results which ignore the geometric phase.

both figures, the results which include the geometric phase are essentially identical to those which do not include the geometric phase (i.e. the open squares cover the solid squares).

Figures 5 and 6 plot the degeneracy averaged rotational distribution and differential cross sections for $D + H_2$ $(v = 1, j = 1) \rightarrow HD$ $(v' = 1, j') + H$ at $E_{tot} = 1.8\,eV$ summed over all values of $J \leq 34$, respectively. There are two sets of curves in Figs. 5 and 6. The solid curves and data points do not include the geometric phase. The short dashed curves and open squares include the geometric phase. In Fig. 5 the results which include the geometric phase are identical to those which do not include the geometric phase (i.e. the open squares cover the solid squares). Figure 5 also contains two additional curves which include the geometric phase but are summed over $J \leq 33$ and 32. These curves correspond to the short dashed curves with the smaller open squares. The results which are summed over $J = 32$, 33, and 34 are nearly the same which indicates that this rotational distribution is converged with respect to the sum over J. In Fig. 6 the results which

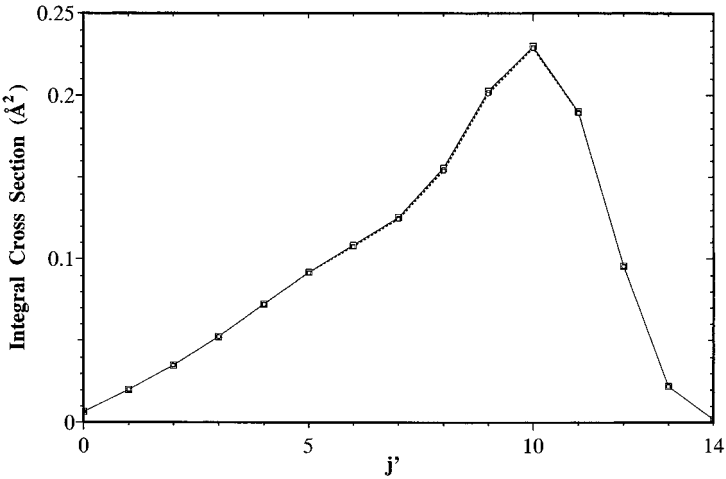

Fig. 5. The degeneracy averaged rotational distribution is plotted for D + $H_2(v = 1, j = 1) \rightarrow HD(v' = 1, j') + H$ at $E_{tot} = 1.8\,eV$ summed over all $J \leq 34$. The solid curve and data points do not include the geometric phase. The short dashed curve and open squares include the geometric phase. The geometric phase results lie directly on top of the results which ignore the geometric phase. The two short dashed curves with the smaller open squares include the geometric phase but are summed over all $J \leq 32$ and 33. These results are nearly the same as those summed over all $J \leq 34$ which indicates convergence.

include the geometric phase are very similar to those which do not include the geometric phase. Some small "out-of-phase" behavior can be seen which increases in amplitude as j' is increased. Based on our convergence studies for other initial and final states and values of total energy, we suspect that the increasing amplitude of the "out-of-phase" behavior in Fig. 6 with increasing j' is due to the lack of convergence of these differential cross sections with respect to the sum over J. We expect that another four or six values of J will be required to fully converge all of the differential cross sections in Fig. 6. We also expect that the amplitude of the "out-of-phase" behavior for $j' > 6$ will decrease as the sum over J is increased to its fully converged value.

Figure 7 plots the degeneracy averaged differential cross section for D + H_2 $(v = 1, j = 1) \rightarrow HD$ $(v' = 1, j' = 8) + H$ at $E_{tot} = 1.8\,eV$. There are four sets of curves in Fig. 7. The solid curves and data points do not include the geometric phase. The short dashed curves and open squares include

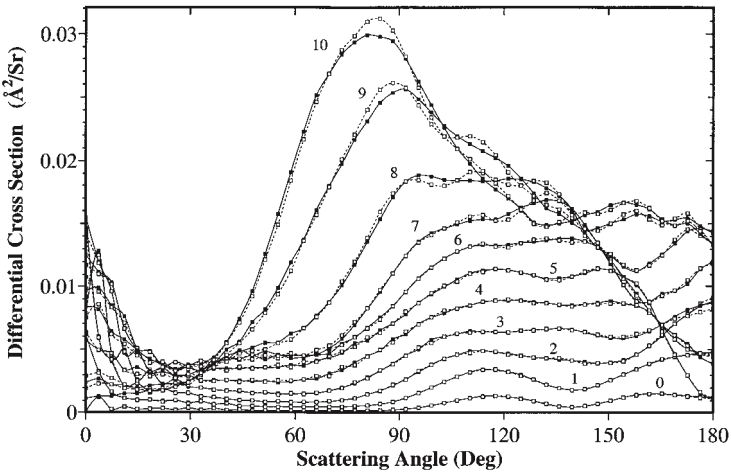

Fig. 6. The degeneracy averaged differential cross sections are plotted for D + $H_2(v = 1, j = 1) \rightarrow$ HD $(v' = 1, j')$ + H at $E_{\text{tot}} = 1.8\,\text{eV}$ summed over all $J \leq 34$. The number next to each curve labels the value of j'. The solid curves and data points do not include the geometric phase. The short dashed curves and open squares include the geometric phase. The geometric phase results are very similar to those which ignore the geometric phase. Some small "out-of-phase" behavior can be seen which increases in amplitude as j' is increased (see text for discussion and Fig. 7).

the geometric phase. The thick curves and large data points correspond to summing over all $J \leq 34$. The thinner curves and smaller data points correspond to summing over all $J \leq 33$. The differences between the thin and thick curves indicates the level of convergence. The main features of the cross section appear to be well converged between about $\theta = 50°$ and $\theta = 160°$. Larger differences occur in the forward $\theta = 0°$ and backward $\theta = 180°$ scattering regions. The amplitude of the "out-of-phase" behavior between the solid and short dashed curves in the region between $\theta = 90°$ and $\theta = 130°$ is similar to the differences between the thin and thick curves in this region.

The cancellation of the geometric phase effects in both the integral and differential cross sections with respect to the sum over J occurs for all of the energies and all of the initial and final states that we have looked at. Some small amplitude "out-of-phase" behavior is seen in some of the differential cross sections but these differences are typically quite small (usually less than 5%). We estimate that our calculations are accurate to within a few

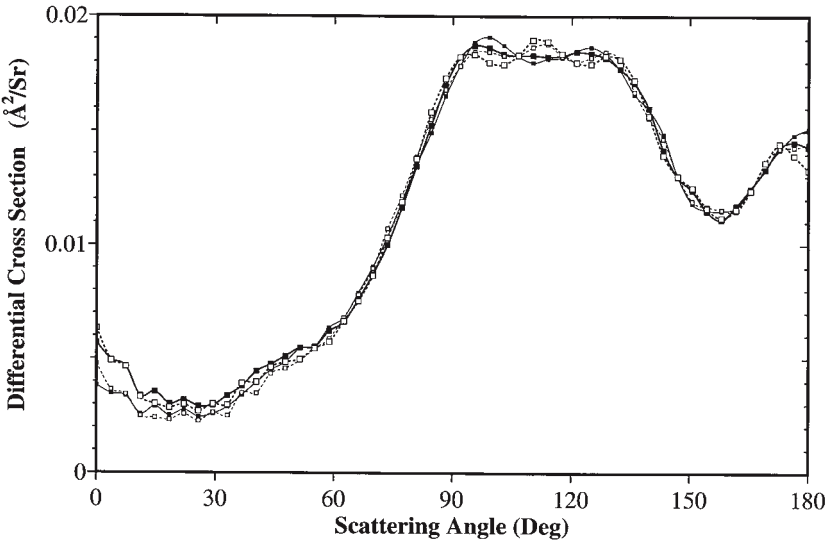

Fig. 7. The degeneracy averaged differential cross section is plotted for $D + H_2(v = 1, j = 1) \rightarrow HD(v' = 1, j' = 8) + H$ at $E_{tot} = 1.8\,eV$. The solid curves and data points do not include the geometric phase. The short dashed curves and open squares include the geometric phase. The thicker curves and larger data points are summed over all $J \leq 34$. The thinner curves and smaller data points are summed over all $J \leq 33$. The small differences between the results which are summed over all $J \leq 34$ and 33 indicate the level of convergence (see text for discussion).

percent. Thus, for all of the initial and final states and values of total energy that we have considered, most of the differences between the differential cross sections computed with and without the geometric phase are about the same as the numerical uncertainties in our calculations. We conclude that there are no significant geometric phase effects in the fully converged integral and differential cross sections for the $D + H_2$ reaction at all of the energies that we have considered.

The geometric phase calculations for $D + H_2$ were done using both the double-valued basis set approach and the vector potential approach. As expected, the results and conclusions using these two methods are the same. The double-valued basis set approach is based on the same scattering codes which were used to obtain fully converged integral and differential cross sections for the $H + D_2$ reaction without the geometric phase.[50] The double-valued basis set approach is implemented by changing one line of

code which replaces the basis set $\exp(im\phi)$ with $\exp(i(m + 1/2)\phi)$. The $D + H_2$ calculations confirm that the cancellation of the geometric phase effects with respect to the sum over J holds for fully converged integral and differential cross sections. Since the cancellation appears to be due to symmetry, we expect that it will probably occur for other $A + B_2$ systems as well (such as $H + D_2$ and $H + O_2$).

The quantum reactive scattering calculations for the $H + H_2(v, j) \rightarrow H_2(v', j') + H$ reaction were done at 96 values of total energy in the range 0.5–2.42 eV for each value of total angular momentum $J = 0 - 10$.[35] The Boothroyd–Keogh–Martin–Peterson (BKMP2)[58] potential energy surface for H_3 was used. Since the masses of the three atoms are all equal, the D_{3h} conical intersection is located at $\theta = 0$. The nuclei of H_3 are spin-1/2 fermions. Thus, the total molecular wave function [Ψ of Eq. (8)] must be antisymmetric under a permutation ($\mathcal{P}$) of any two identical nuclei. Since the nuclear spin is $S = 1/2$, we have a total of $(2S + 1)^3 = 8$ nuclear spin states. Due to the 3-fold symmetry of H_3 the nuclear spin states can be classified using the irreducible representations of the permutation group S_3. The irreducible representations of S_3 are A_1 (symmetric), A_2 (antisymmetric), and E (doubly degenerate). The number of spin states of A_1, A_2, and E symmetry are given by $(2S + 1)(2S + 3)(S + 1)/3 = 4$, $(2S+1)(2S-1)S/3 = 0$, and $(2S+1)(S+1)8S/3 = 4$, respectively.[33,70] Since the E representation is two dimensional, there are two distinct spin states of E symmetry and each one consists of two components which makes a total of four. The two components in each spin state are labeled by $\pm m_s$ (the z component of the total nuclear spin). The nuclear motion wave function (Ψ) can also be classified using the irreducible representations of the permutation group S_3. Since the ground state of H_2 is a $^1\Sigma_g^+$ state,[60] we know that asymptotically (i.e. for large ρ) the electronic wave function for H–H_2 is symmetric. Thus, for the A_1 (symmetric) nuclear spin states, we must choose the nuclear motion wave function (Ψ) to be of A_2 symmetry (i.e. antisymmetric) for H–H_2 so that the total wave function is antisymmetric. Similarly, for the E nuclear spin states, we must choose the nuclear motion wave function (Ψ) to be of E symmetry for H–H_2. The two distinct nuclear spin states of E symmetry combine with each doubly-degenerate nuclear motion wave function of E symmetry to form two symmetric and two antisymmetric functions. Only the two antisymmetric functions are physically allowed. Since the real electronic wave function for H_3 is symmetric for

H–H_2, we know that it is symmetric across the symmetry line which extends radially outward from the origin at $\phi = 0$ (i.e. to the right of the conical intersection). It is also symmetric across the two symmetry lines which extend radially outward from the origin at $\phi = \pm 120°$. The geometric phase alters the symmetry of the real electronic wave function for H_3, so that it is also antisymmetric across the symmetry line which extends radially outward from the origin at $\phi = \pm\pi$ (i.e. to the left of the conical intersection). By symmetry, it is also antisymmetric across the two symmetry lines which extend radially outward from the origin at $\phi = \pm 60°$. The antisymmetric behavior is a direct consequence of the wave function's double-valuedness. In order to satisfy Fermi statistics for all nuclear geometries, the product of the nuclear motion wave function and nuclear spin wave function must also be double-valued and be antisymmetric across the symmetry lines at $\phi = 0$, $\phi = +120°$, and $\phi = -120°$. The product must also be symmetric across the symmetry lines at $\phi = \pi$, $\phi = +60°$, and $\phi = -60°$.

Significant geometric phase effects occur in many of the reaction probabilities for $H + H_2$, especially for total energies above about 1.9 eV.[35] For example, Fig. 8 plots the reaction probability for $H + H_2$ ($v = 0$, $j = 1$) $\rightarrow$ $H_2(v' = 1,\ j' = 2) + H$ and zero total angular momentum ($J = 0$) as a function of total energy. Significant differences occur between the results which include the geometric phase (the solid curve and squares) and those which do not (the dashed curve and open squares) for energies above about 1.9 eV. The dashed curve and open squares include the geometric phase and are based on the vector potential approach with $l = 3/2$. The long-dashed curve and Xs also include the geometric phase, but are based on the double-valued basis set approach. The double-valued basis set approach uses the same computer codes that were used in the calculations which *do not* include the geometric phase. The only difference is one line of code which replaces the basis set $\exp(im\phi)$ with $\exp(i(m+3/2)\phi)$. As expected, the results based on the double-valued basis set approach are in good agreement with those based on the vector potential approach. Gauge invariance is also verified by performing the calculations using the vector potential approach but with $l = 9/2$ and $l = 6/2$. The $l = 9/2$ results are related to those with $l = 3/2$ by a gauge transformation. The dashed curve and open triangles in Fig. 8 are the results using $l = 9/2$. As expected, good agreement is observed between the $l = 9/2$ and $l = 3/2$ reaction probabilities. The $l = 6/2$ results are related to those with $l = 0$ by a gauge

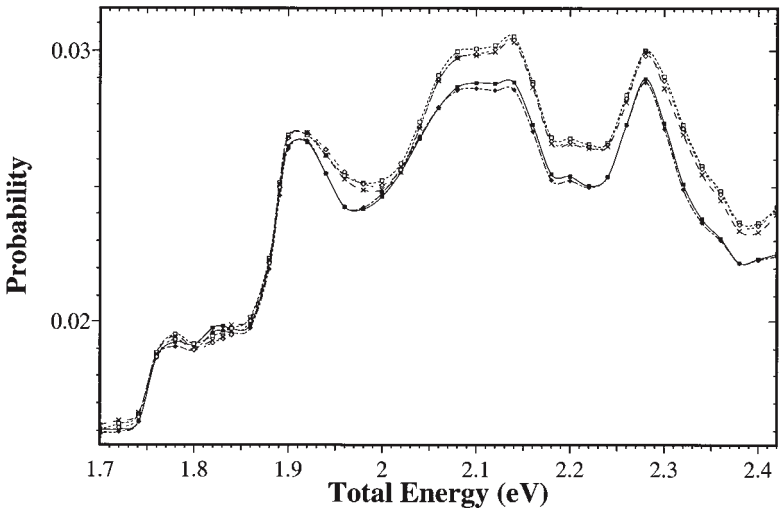

Fig. 8. The reaction probability for H + $H_2(v = 0, j = 1) \rightarrow H_2(v' = 1, j' = 2)$ + H and zero total angular momentum ($J = 0$) is plotted as a function of energy. The solid curve and solid squares do not include the geometric phase. The short dashed curve and open squares include the geometric phase and are based on the vector potential approach with $l = 3/2$. The short dashed curve and open triangles also include the geometric phase and are based on the vector potential approach but are computed with $l = 9/2$. The long dashed curve and Xs also include the geometric phase but are based on the double-valued basis set approach. The short-long dashed curve and solid triangles do not include the geometric phase but are computed using the vector potential approach with $l = 6/2$. The data points are calculated values and the curves are a cubic spline fit.

transformation and correspond to doing the calculations without the geometric phase. The short-long dashed curve and solid triangles in Fig. 8 are the results using $l = 6/2$. As expected, good agreement is observed between the $l = 6/2$ and $l = 0$ reaction probabilities. Gauge invariance and the good agreement between the double-valued basis set approach and the vector potential approach are also observed for other initial and final states and nonzero values of J.

Figure 9 plots the degeneracy averaged partial integral cross sections for $H + H_2(v = 0, j = 0) \rightarrow H_2(v' = 1, j' = 0 - 3)$ + H as a function of energy and include all $J \leq 10$. The solid curve and solid squares do not include the geometric phase. The short dashed curve and open squares include the geometric phase and are based on the vector potential approach. For the

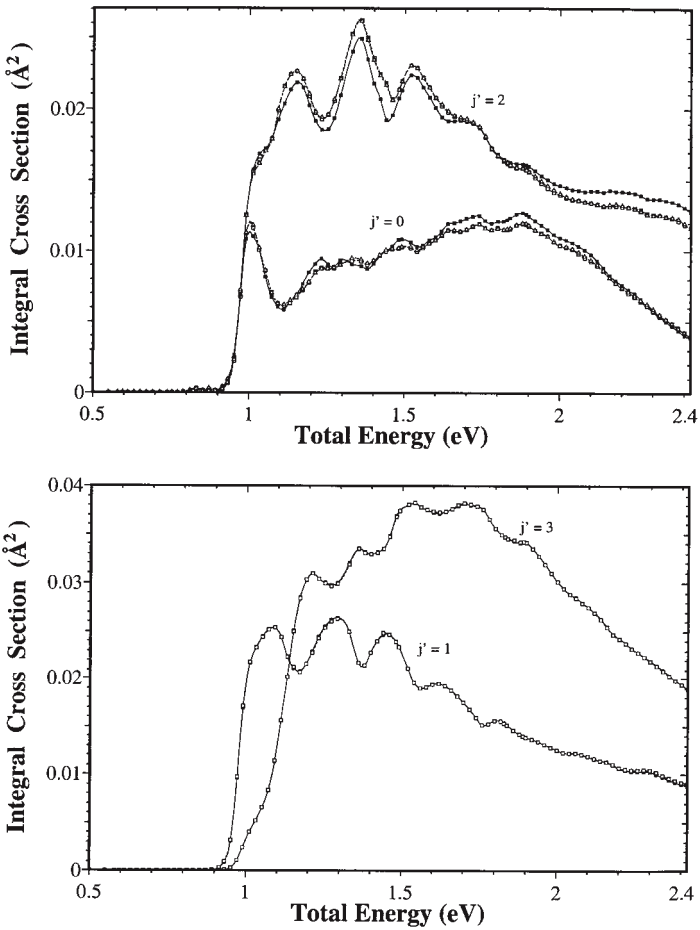

Fig. 9. Degeneracy averaged partial integral cross sections for H + $H_2(v = 0, j = 0) \rightarrow H_2(v' = 1, j' = 0 - 3)$ + H summed over all $J \leq 10$ are plotted as a function of energy. The solid curve and solid squares do not include the geometric phase. The short dashed curve and open squares include the geometric phase and are based on the vector potential approach. The short dashed curve and open triangles are based on the calculations which ignore the geometric phase but are computed using the opposite sign for the interference terms between reactive and non-reactive contributions, for the *para* → *para* transitions. The data points are calculated values and the curves are a cubic spline fit.

para → *ortho* transitions there are no significant differences between the cross sections computed with and without the geometric phase. However, for the *para* → *para* transitions, significant differences occur between the cross sections computed with and without the geometric phase, even for relatively low energies. These differences are due to the change in the sign of the interference terms between the reactive and nonreactive contributions.[35] This can be verified by doing the calculations *without* the geometric phase, but changing the sign on the interference terms. The short-long dashed curve and open triangles are based on the calculations which ignore the geometric phase, but use the opposite sign on the interference terms. We see that the short-long dashed curve and open triangles are essentially identical to the results which include the geometric phase (the short dashed curve and open squares).

Figure 10 plots the degeneracy averaged partial differential cross sections for $H+H_2(v=0, j=0) \rightarrow H_2(v'=1, j'=0-3) + H$ at $E_{\rm tot} = 1.8\,{\rm eV}$ and include all $J \leq 10$. The solid curve and solid squares do not include the geometric phase. The short dashed curve and open squares include the geometric phase and are based on the vector potential approach. For the *para* → *ortho* transitions there are no significant differences between the differential cross sections computed with and without the geometric phase. However, for the *para* → *para* transitions, significant "out-of-phase" behavior occurs between the differential cross sections computed with and without the geometric phase. These differences are due to the change in the sign of the interference terms between the reactive and nonreactive contributions. This can be verified by doing the calculations *without* the geometric phase, but using the opposite sign on the interference terms. The short-long dashed curve and open triangles are based on the calculations which ignore the geometric phase, but use the opposite sign on the interference terms. We see that the short-long dashed curve and open triangles are essentially identical to the results which include the geometric phase (the short dashed curve and open squares).

3. Conclusions

We reviewed the fundamental theory for including the geometric phase in quantum reactive scattering calculations based on a single adiabatic electronic potential energy surface. Two methods were discussed. In one

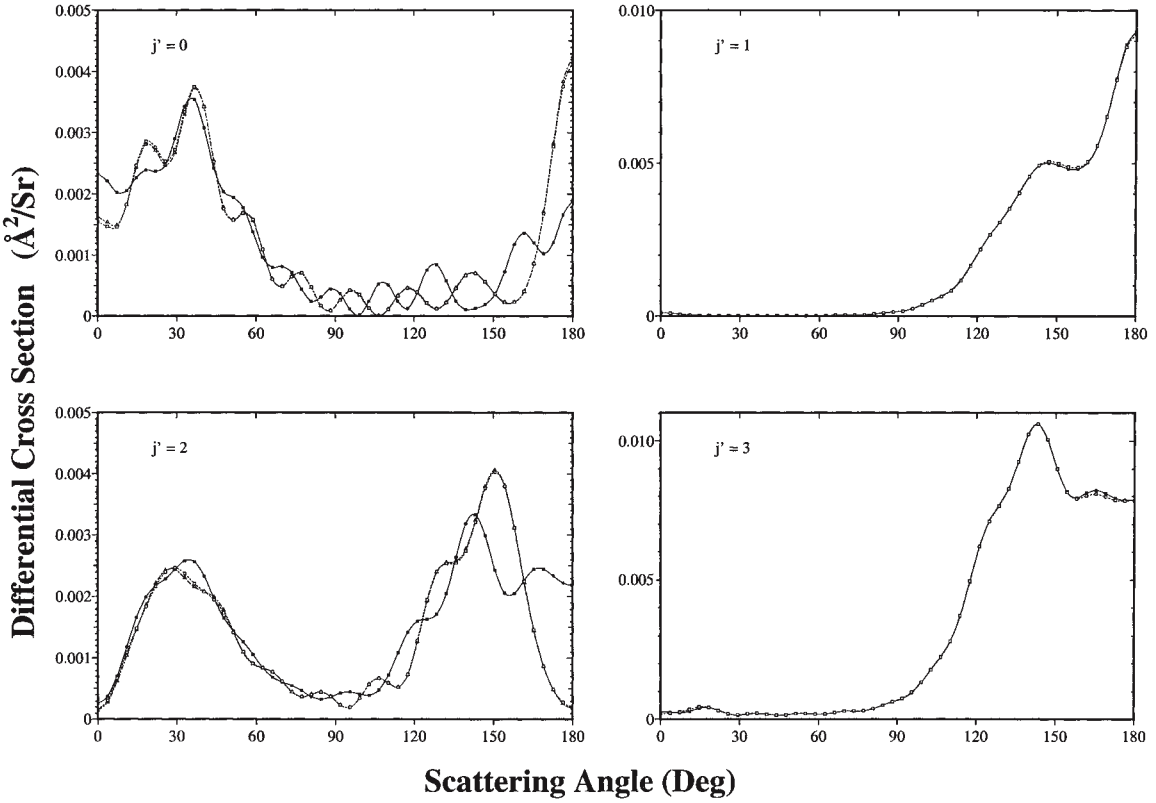

Fig. 10. Degeneracy averaged partial differential cross sections for $H + H_2(v = 0, j = 0) \rightarrow H_2(v' = 1, j' = 0-3) + H$ summed over all $J \leq 10$ at $E_{tot} = 1.8\,eV$. The solid curve and solid squares do not include the geometric phase. The short dashed curve and open squares include the geometric phase and are based on the vector potential approach. The short-long dashed curve and open triangles are based on the calculations which ignore the geometric phase but are computed using the opposite sign for the interference terms between reactive and non-reactive contributions, for the *para* → *para* transitions.

approach, the standard Born–Oppenheimer equation for the nuclear motion is solved, but with double-valued boundary conditions. In the second approach, a generalized Born–Oppenheimer equation for the nuclear motion is solved using single-valued boundary conditions. The generalized Born–Oppenheimer equation for the nuclear motion contains a vector potential which has the same mathematical properties as that of a magnetic solenoid centered at the conical intersection. Either approach is valid and will give the same results for the physical observables. In different situations, one approach may be more convenient to implement than the other.

We discussed the recently developed numerical methodology for solving the generalized Born–Oppenheimer equation for the nuclear motion. This methodology is based on symmetrized hyperspherical coordinates and can be used for both quantum reactive scattering and bound state calculations. Several applications using this methodology were discussed. In particular, the low-energy inelastic scattering of $H + O_2$ and the quantum reactive scattering of $H + H_2$, $D + H_2$, and $H + D_2$ were discussed. The geometric phase alters the symmetry of the nuclear motion wave function, causing it to simultaneously exhibit both even and odd symmetry under an interchange of any two identical nuclei. This change in symmetry gives rise to an "out-of-phase" behavior in the transition probabilities for $H + O_2$ and the reaction probabilities for $H + D_2$ and $D + H_2$. It also alters many of the lifetimes and energies of the resonances in $H + O_2$. In the $H + D_2$ reaction, the effects of the geometric phase completely cancel out in the partial integral and differential cross sections at *all* energies when the contributions from even and odd values of $J \leq 5$ are added together. This cancellation appears to be related to the alternating symmetry of the Wigner D functions with respect to even and odd J. Similarly, in the $D+H_2$ reaction, the effects of the geometric phase completely cancel out in the *fully converged* integral and differential cross sections at *all* energies when the contributions from even and odd values of $J \leq 34$ are added together. Significant geometric phase effects are seen in the reaction probabilities for $H + H_2$ at high energies. For *para* $\rightarrow$ *ortho* and *ortho* $\rightarrow$ *para* transitions, the effects of the geometric phase completely cancel out in the partial integral and differential cross sections at *all* energies when the contributions from even and odd values of $J \leq 10$ are added together. However, for *para* $\rightarrow$ *para* and *ortho* $\rightarrow$ *ortho* transitions, significant geometric phase effects appear in the partial integral

and differential cross sections summed over all $J \leq 10$, even for relatively low energies. These large geometric phase effects are due to the change in sign of the interference terms between the reactive and non-reactive contributions to the cross sections. This sign change is a direct consequence of the double-valuedness of the real adiabatic electronic wave function which changes sign under a cyclic permutation of the three identical nuclei in H_3.[9] The calculations for $D + H_2$ and $H + H_2$ which include the geometric phase were done using both the double-valued basis set approach and the vector potential approach. As expected, these two methods give the same results and conclusions.

The effects of the geometric phase at low energies for the *para* $\rightarrow$ *para* and *ortho* $\rightarrow$ *ortho* transitions in $H + H_2$ were first predicted by Mead[9] in 1980. He showed that the geometric phase changes the sign of the interference terms between the reactive and non-reactive contributions to the cross sections. Thus, significant geometric phase effects can occur whenever the interference between reactive and non-reactive processes is important. Mead claimed that, for low energies, the effects of the geometric phase can be treated by doing the calculations without the geometric phase, but computing the cross sections with the opposite sign on the interference terms. However, for high energies, an accurate calculation based on the double-valued basis set approach or the vector potential approach is required. Our results indicate that Mead's procedure is probably accurate even for high energies. All other geometric phase effects in the cross sections appear to cancel out when summed over J.

We conclude that the effects of the geometric phase in chemical reaction dynamics can be important for chemical reactions which contain three or more identical nuclei. For these reactions, the geometric phase can significantly alter the integral and differential cross sections whenever the interference between reactive and non-reactive processes is important. Furthermore, it appears that the effects of the geometric phase for these reactions can be taken into account by simply applying Mead's procedure. However, more work is needed in order to investigate the importance of the geometric phase in chemical reaction dynamics when more than one conical intersection is present (such as in the $H + O_2 \rightarrow OH + O$ reaction). Because of its fundamental nature, the $H + H_2$ reaction is an excellent candidate for both theoretical and experimental studies. The differential cross sections for the *para* $\rightarrow$ *para* and *ortho* $\rightarrow$ *ortho* transitions in the $H + H_2$ reaction are

probably the best candidates for an experimental confirmation of geometric phase effects in a chemical reaction.

Acknowledgments

This work was done under the auspices of the U.S. Department of Energy under Project No. 20020015ER of the Laboratory Directed Research and Development program at Los Alamos under contract W-7405-ENG-36. Computer time on an SGI Origin 2000 at the Advanced Computing Laboratory at Los Alamos was provided by the Institutional High Performance Computing Initiative at Los Alamos.

References

1. M. Born and R. Oppenheimer, *Ann. Phys.* **84**, 457 (1927).
2. M. Born and K. Huang, *The Dynamical Theory of Crystal Lattices* (Oxford University Press, London, 1954).
3. C. J. Ballhausen and A. E. Hansen, *Ann. Rev. Phys. Chem.* **23**, 15 (1972).
4. C. A. Mead in *Mathematical Frontiers in Computational Chemical Physics*, Eds. D. G. Truhlar (Springer-Verlag, New York, 1988), pp. 1–17.
5. L. S. Cederbaum, *The Born–Oppenheimer Approximation and Beyond*, Chapter 1 of this book.
6. For a recent review see: A. W. Jasper, B. K. Kendrick, C. A. Mead and D. G. Truhlar in *Modern Trends in Chemical Reaction Dynamics* (World Scientific, Singapore, 2003).
7. G. Herzberg and H. C. Longuet-Higgins, *Discuss. Faraday Soc.* **35**, 77 (1963).
8. C. A. Mead and D. G. Truhlar, *J. Chem. Phys.* **70**, 2284 (1979).
9. C. A. Mead, *J. Chem. Phys.* **72**, 3839 (1980).
10. C. A. Mead, *Chem. Phys.* **49**, 23 (1980).
11. M. V. Berry, *Proc. R. Soc. London* **A392**, 45 (1984); in *Geometric Phases in Physics*, Eds. A. Shapere and F. Wilczek (World Scientific, Singapore, 1989); *Phys. Today* **43**(12), 34 (1990).
12. B. Kendrick and R. T. Pack, *J. Chem. Phys.* **104**, 7475 (1996).
13. A. Bohm, B. Kendrick and M. Loewe, *Int. J. Quantum Chem.* **41**, 53 (1992).
14. A. Bohm, B. Kendrick, M. Loewe and L. J. Boya, *J. Math. Phys.* **33**, 977 (1992).
15. B. K. Kendrick, C. A. Mead and D. G. Truhlar, *Chem. Phys.* **277**, 31 (2002).
16. We note that $\mathbf{A}_{nm} = i\mathbf{F}_{nm}$ where $\mathbf{F}_{nm}$ is defined in Eq. (2.9b) of Ref. 5.
17. We note that $\varepsilon_{nm} = W^{(g)}_{nm}$ where $W^{(g)}_{nm}$ is defined in Eq. (3.7b) of Ref. 5.
18. C. A. Mead, *Rev. Mod. Phys.* **64**, 51 (1992).
19. B. Kendrick and C. A. Mead, *J. Chem. Phys.* **102**, 4160 (1995).

20. The global nature of the sign change can be understood topologically by realizing that within the adiabatic approximation the degeneracy manifold $\mathcal{D}$ effectively "punches a hole" in $\mathcal{M}$ so that the effective nuclear parameter space $\mathcal{M} - \mathcal{D}$ is *not* simply connected. Thus, a vector potential of the form $\mathbf{A} = (-l/2)\nabla\eta(x)$ (l odd integer) is *not* a pure gauge and therefore gives rise to a geometric phase which can lead to physical effects.
21. The full 2π range for η is determined from the signs of the $v(x)$ and $u(x)$ functions which appear in the $\tan^{-1}$ function.
22. B. Kendrick and R. T. Pack, *J. Chem. Phys.* **104**, 7502 (1996).
23. See also Eq. (3.9) of Ref. 5.
24. B. Simon, *Phys. Rev. Lett.* **51**, 2167 (1983).
25. A. Bohm, L. J. Boya and B. Kendrick, *Phys. Rev.* **A43**, 1206 (1991).
26. A. Bohm, L. J. Boya and B. Kendrick, *J. Math. Phys.* **33**, 2528 (1992).
27. B. Schutz, *Geometrical Methods of Mathematical Physics* (Cambridge University Press, New York, 1988).
28. C. Nash and S. Sen, *Topology and Geometry for Physicists* (Academic Press, San Diego, California, 1983).
29. B. Lepetit and A. Kuppermann, *Chem. Phys. Lett.* **166**, 581 (1990).
30. Y. S. M. Wu, A. Kuppermann and B. Lepetit, *Chem. Phys. Lett.* **186**, 319 (1991).
31. X. Wu, R. E. Wyatt and M. D'Mello, *J. Chem. Phys.* **101**, 2953 (1994).
32. B. Kendrick and R. T. Pack, *J. Chem. Phys.* **106**, 3519 (1997).
33. B. Kendrick, *Int. J. Quantum Chem.* **64**, 581 (1997).
34. B. K. Kendrick, *J. Chem. Phys.* **112**, 5679 (2000); **114**, 4335(E) (2001).
35. B. K. Kendrick, *J. Phys. Chem.* **A107**, 6739 (2003).
36. B. K. Kendrick, *J. Chem. Phys.* **118**, 10502 (2003).
37. B. Kendrick, *Phys. Rev. Lett.* **79**, 2431 (1997).
38. F. T. Smith, *J. Chem. Phys.* **31**, 1352 (1959); *Phys. Rev.* **120**, 1058 (1960).
39. A. J. Dragt, *J. Math. Phys.* **6**, 533 (1965).
40. W. Zickendraht, *Ann. Phys.* **35**, 18 (1965).
41. R. C. Whitten and F. T. Smith, *J. Math. Phys.* **9**, 1103 (1968).
42. R. T. Pack and G. A. Parker, *J. Chem. Phys.* **87**, 3888 (1987), and references therein.
43. B. R. Johnson, *J. Comput. Phys.* **13**, 445 (1973); *J. Chem. Phys.* **67**, 4086 (1977).
44. F. Mrugała and D. Secrest, *J. Chem. Phys.* **78**, 5954 (1983).
45. J. C. Light, I. P. Hamilton and J. V. Lill, *J. Chem. Phys.* **82**, 1400 (1985).
46. Z. Bačić, R. M. Whitnell, D. Brown and J. C. Light, *Comput. Phys. Comm.* **51**, 35 (1988).
47. Z. Bačić, J. D. Kress, G. A. Parker and R. T. Pack, *J. Chem. Phys.* **92**, 2344 (1990), and references therein.
48. B. K. Kendrick, R. T. Pack, R. B. Walker and E. F. Hayes, *J. Chem. Phys.* **110**, 6673 (1999).

49. C. Eckart, *Phys. Rev.* **46**, 383 (1934); *ibid.* **47**, 552 (1935).
50. B. K. Kendrick, *J. Chem. Phys.* **114**, 8796 (2001).
51. R. B. Lehoucq, D. C. Sorensen and P. Vu, ARPACK: Fortran Subroutines for solving large scale eigenvalue problems, Release 2.1, available from netlib@ornl.gov in the scalapack directory.
52. K. J. Maschoff and D. C. Sorensen, in *Proceedings of the PARA96 Conference, Lingby, Denmark*, Eds. J. Wasniewski, J. Dongarra, K. Madsen and D. Olesen, Springer Lecture Notes in Computer Science (Springer, New York, 1996) Vol. 1184.
53. R. B. Lehoucq, D. C. Sorensen and C. Yang, *ARPACK Users' Guide* (SIAM, Philadelphia, PA, 1998).
54. B. Kendrick and R. T. Pack, *J. Chem. Phys.* **102**, 1994 (1995).
55. V. J. Barclay, C. E. Dateo, I. P. Hamilton, B. Kendrick, R. T. Pack and D. W. Schwenke, *J. Chem. Phys.* **103**, 3864 (1995).
56. J. Schön and H. Köppel, *J. Chem. Phys.* **103**, 9292 (1995).
57. G. Herzberg, *Molecular Spectra and Molecular Structure* (Van Nostrand Reinhold, New York, 1955), Vol. I.
58. A. I. Boothroyd, W. J. Keogh, P. G. Martin and M. R. Peterson, *J. Chem. Phys.* **104**, 7139 (1996).
59. P. Siegbahn and B. Liu, *J. Chem. Phys.* **68**, 2457 (1978); D. G. Truhlar and C. J. Horowitz, *ibid.* **68**, 2466 (1978); **71**, 1514E (1979).
60. K. P. Huber and G. Herzberg, *Molecular Spectra and Molecular Structure* (Van Nostrand Reinhold, New York, 1979), Vol. 4.
61. M. J. D'Mello, D. E. Manolopoulos and R. E. Wyatt, *J. Chem. Phys.* **94**, 5985 (1991).
62. S. L. Mielke, D. G. Truhlar and D. W. Schwenke, *J. Phys. Chem.* **98**, 1053 (1994).
63. M. J. D'Mello, D. E. Manolopoulos and R. E. Wyatt, *Science* **263**, 102 (1994).
64. F. J. Aoiz, L. Bañares, M. J. D'Mello, V. J. Herrero, V. Sáez Rábanos, L. Schnieder and R. E. Wyatt, *J. Chem. Phys.* **101**, 5781 (1994).
65. L. Bañares, F. J. Aoiz, V. J. Herrero, M. J. D'Mello, B. Niederjohann, K. Seekamp-Rahn, E. Wrede and L. Schnieder, *J. Chem. Phys.* **108**, 6160 (1998).
66. D. C. Clary, *Science* **279**, 1879 (1998).
67. M. P. de Miranda, D. C. Clary, J. F. Castillo and D. E. Manolopoulos, *J. Chem. Phys.* **108**, 3142 (1998).
68. K. Seekamp-Rahn, *Untersuchung der Wasserstoffaustauschreaktion* $H + D_2(v = 0, j) \rightarrow HD(v', j') + D$ *in gekreuzten Molekularstrahlen*, Dissertation zur Erlangung des Doktorgrades der Fakultät für Physik der Universität Bielefeld, (1996).
69. E. Wrede and L. Schnieder, *J. Chem. Phys.* **107**, 786 (1997).
70. D. M. Dennison, *Rev. Mod. Phys.* **3**, 280 (1931).

This page intentionally left blank

CHAPTER 13

QUANTUM REACTION DYNAMICS ON COUPLED MULTI-SHEETED POTENTIAL ENERGY SURFACES

Susanta Mahapatra

School of Chemistry,
University of Hyderabad,
Hyderabad 500 046, India
smsc@uohyd.ernet.in

Contents

1. Introduction

The coupling between electronic potential energy surfaces (PESs) through nuclear vibrational degrees of freedom is a generic feature of polyatomic molecules. Such a coupling, commonly referred to as *vibronic coupling*, initiates a wide variety of new phenomena in molecular dynamics.[1,2] Particularly, *conical intersections* of PESs in this context are most common in polyatomic molecular systems and have made considerable impact,[3–8] which is attested by the appearance of many articles in the present book.

Conical intersections are characterized by a degeneracy of two PESs in an $(N-2)$-dimensional vibrational subspace (N being the total number of vibrational degrees of freedom) of the molecule and a lifting of the degeneracy in first-order with respect to nuclear displacement coordinates out of the degeneracy space. The locus of this degeneracy is called a *seam*, on which the derivative matrix elements of the electronic wave functions with respect to the nuclear coordinates (known as nonadiabatic coupling) diverge and the nonadiabatic effects can become very strong.[4]

The existence of conical intersections of the electronic PESs leads to a complete break-down of the well-known Born–Oppenheimer (BO) or adiabatic approximation.[9,10] As a result, it is necessary to monitor the nuclear motions simultaneously on more than one electronic PES in a nuclear dynamical study, which amounts to solving highly complex coupled differential equations. In an adiabatic electronic basis, the coupling between the electronic states is caused by the off-diagonal elements of the nuclear kinetic energy operator. These off-diagonal elements form a part of the nonadiabatic coupling matrix Λ and diverge at the point of intersection of the electronic states.[4] The elements of the matrix Λ are given by[4,6,10,11]

$$\Lambda_{ij} = -\int d\mathbf{r}\Phi_i^*(\mathbf{r},\mathbf{R})\left[T_n, \Phi_j(\mathbf{r},\mathbf{R})\right], \tag{1}$$

where Φ represents the electronic states, T_n the nuclear kinetic energy operator and $\mathbf{r}$ and $\mathbf{R}$ collectively denote the electronic and nuclear coordinates, respectively. In terms of the first- and second-order derivative couplings, Λ_{ij} can be written as (for Cartesian coordinates)[4,11]

$$\Lambda_{ij} = -\sum_k \frac{\hbar^2}{M_k} F_{ij} \frac{\partial}{\partial R_k} - \sum_k \frac{\hbar^2}{2M_k} G_{ij}, \tag{2}$$

where M_k are nuclear masses and

$$F_{ij} = \langle \Phi_i(\mathbf{r}) | \nabla_{\mathbf{k}} | \Phi_j(\mathbf{r}) \rangle \,, \tag{3}$$

$$G_{ij} = \langle \Phi_i(\mathbf{r}) | \nabla^2_{\mathbf{k}} | \Phi_j(\mathbf{r}) \rangle \,, \tag{4}$$

in which $\nabla_{\mathbf{k}} \equiv \partial / \partial R_k$. The quantity Λ_{ij} is Hermitian and represents the nonadiabatic coupling effects in the adiabatic electronic representation. Note that F_{ij} is anti-Hermitian and G_{ij} is non-Hermitian. The elements G_{ii} constitute the diagonal part of Λ and F_{ij} describes the off-diagonal derivative coupling terms (for real electronic wave functions). In the usual BO approximation, Λ is set to zero altogether. If the diagonal G_{ii} elements are retained only, then one arrives at what is known as the Born–Huang (BH) representation.[10]

The derivative matrix elements F_{ij} can be expressed according to the well-known Hellmann–Feynman type of relation as[4]

$$F_{ij} = \langle \Phi_i | \nabla | \Phi_j \rangle = \frac{\langle \Phi_i | \nabla H_e(\mathbf{r}, \mathbf{R}) | \Phi_j \rangle}{V_i(\mathbf{R}) - V_j(\mathbf{R})} \,, \tag{5}$$

where H_e defines the electronic Hamiltonian for fixed nuclear coordinates. At the degeneracy of the two surfaces, $V_i(\mathbf{R}) = V_j(\mathbf{R})$, and the F_{ij} exhibit a singular behavior. As a result, the electronic wave function becomes discontinuous and the energy has a *cusp* like behavior at such points, making the adiabatic representation unsuitable for the numerical simulation of the dynamics. In order to deal with this situation, one resorts to a diabatic electronic representation, where these diverging kinetic energy coupling elements are transformed into smooth potential energy couplings and thereby the discontinuity of the adiabatic representation is avoided.[12–14] The diabatic molecular states are constructed by a unitary transformation of the corresponding adiabatic electronic states. The Hamiltonian in the diabatic representation $\mathcal{H}^d$ can be obtained from that in the adiabatic representation $\mathcal{H}^{ad}$ through the following unitary transformation

$$\mathcal{H}^d = \mathbf{S} \mathcal{H}^{ad} \mathbf{S}^\dagger = T_n \mathbf{1} + \mathbf{W}. \tag{6}$$

Here $\mathbf{S}$ defines the orthogonal transformation matrix. For a 2×2 Hamiltonian $\mathbf{S}$ is given by

$$\mathbf{S} = \begin{pmatrix} \cos\alpha & \sin\alpha \\ -\sin\alpha & \cos\alpha \end{pmatrix}, \tag{7}$$

where α represents the adiabatic-to-diabatic transformation angle and $\Psi^d = \mathbf{S}\Psi^{ad}$. In doing so, the diverging kinetic couplings of Eq. (5) are transformed into the smooth potential coupling [off-diagonal elements of $\mathbf{W}$ in Eq. (6)] and thereby the discontinuity of the adiabatic representation is avoided. Various approximate schemes are proposed in the literature to construct (quasi) diabatic electronic states for polyatomic molecular systems (see, for example, the reviews in Refs. 15–17 and Chapter 3).

The study of molecular dynamics on conically intersecting PESs has mainly focused on the spectroscopy of bound molecular systems, in particular, optical and photoelectron spectroscopy. The typical scenario that emerged from these studies is an ultrafast decay of the excited molecular states, a seemingly diffuse line structure in the corresponding electronic transition,[4,6] and also geometric phase (GP) effects.[18] It is only recently that attention has been paid to the possible implications of conical intersections on photodissociation,[19] reactive scattering[20–27] and photochemical transitions[5,8] (also see the related Chapters 6, 11 and 12 in this book). Unlike the spectroscopy of bound molecular systems, where small-amplitude molecular vibrations are of major significance, in order to deal with the photodissociation and reactive scattering dynamics, it is important to describe the large-amplitude molecular vibrations and the asymptotic behavior of molecular PESs. Much of the complexity in the treatment of the dissociation of a molecule on multi-sheeted PESs arises from the difficulty in constructing suitable diabatic electronic potentials of reasonable accuracy.

The effect of conical intersections on the state-specific and state-to-state reactive and nonreactive scattering attributes was demonstrated with the aid of an extended two coordinate quasi Jahn–Teller (JT) model.[28] In recent years, the photodissociation dynamics of triatomic molecules, for example O_3 and H_2S, have been studied by calculating the diabatic electronic states and their couplings employing an *ab initio* approach.[19] The reactive scattering dynamics of insertion reactions, for example, $C + H_2$,[20] $O + H_2$,[21–23] $Cl + HCl$,[24] $N + H_2$,[25] $S + H_2$[26] and $N + O_2$,[27] where surface coupling is believed to play an important role, have been studied (also see the review article in Ref. 29). In the following, we consider our recent work[30] on the thermal reactive scattering of a bimolecular system on a conically intersecting manifold of two electronic states and describe the multi-state quantum flux operator formalism within a time-dependent wave packet (WP) approach. This formalism is applied to the $H + H_2$ exchange

reaction in order to calculate the initial state-selected and energy-resolved reaction probabilities. These nonadiabatic reaction probabilities are compared with the adiabatic ones obtained only with the lower adiabatic sheet of its double-sheeted potential energy surface and the differences are analyzed and discussed.

2. Theory

In the following we consider a bimolecular A + BC type of reaction occurring on the conically intersecting manifold of two electronic states. The initial state-selected and energy-resolved reaction probabilities are calculated through the quantum flux operator and a time-dependent WP approach. The formalism describes the representation of the flux operator in a two-state adiabatic as well as a diabatic basis, and calculation of state-selected reaction probabilities in both basis sets. The initial WP pertinent to the reactants is prepared in the adiabatic electronic representation (as in the case of all previous studies) and time-propagated in the coupled diabatic manifold. Finally the scattering attributes are analyzed in both the adiabatic as well as diabatic electronic basis and the identity of the results is confirmed by applying this formalism to the $H + H_2$ exchange reaction as a reference.

In what follows, we use the mass-scaled reactant channel body-fixed Jacobi coordinates R, r, γ in order to describe the A + BC collisions for the total angular momentum $J = 0$ (planar collisions). The two Jacobi distances are denoted as R (distance of A from the center-of-mass of BC) and r (BC internuclear distance; not to be confused with the electronic coordinates as stated in the introduction), respectively. The Jacobi angle (angle between $\vec{R}$ and $\vec{r}$) is denoted by γ. The body-fixed z axis is defined to be parallel to $\vec{R}$ and BC lies in the (x, z) plane.

2.1. *The Flux Operator*

The quantum flux operator $\hat{F}$ measures the probability current density. The latter satisfies the continuity equation resulting from the invariance of the norm of the wave packet in the coordinate basis. For a stationary wave function, the probability density is independent of time and the flux is constant across any fixed hypersurface. In reaction dynamics the flux operator is most generally defined in terms of a dividing surface Θ which

is a function of a suitable coordinate (the convenient choice is the reaction coordinate) that separates the products from the reactants[31]

$$\hat{F} = \frac{i}{\hbar}[\mathcal{H}, \Theta]\,. \tag{8}$$

In the present case an obvious choice for Θ is given by

$$\Theta = h(r - r_d), \tag{9}$$

where h is the heaviside step function which equals unity for positive argument and zero otherwise. r_d is to be chosen far out in the product channel to ensure the asymptotic motion for all $r \geq r_d$. Since Θ depends only on coordinates, the electronic part of $\mathcal{H}$ commutes with it, therefore Eq. (8) becomes

$$\hat{F} = \frac{i}{\hbar}[T_n, \Theta]\,. \tag{10}$$

The two-state flux operator described below is derived from Eq. (10) in a diabatic as well as in an adiabatic electronic basis. We note that the flux operator is Hermitian and its other properties are well documented in the literature.[32] We note that the flux operator $\hat{F}$ should not be confused with the derivative coupling elements F_{ij} introduced in Eq. (2).

2.2. *Diabatic Electronic Representation*

2.2.1. *The Hamiltonian*

The diabatic Hamiltonian for the coupled manifold of two electronic states of the A + BC system can be written as

$$\begin{aligned}\mathcal{H}^d &= T_n + \mathcal{H}_e, \\ &= T_n \begin{pmatrix} 1 & 0 \\ 0 & 1 \end{pmatrix} + \begin{pmatrix} w_{11} & w_{12} \\ w_{21} & w_{22} \end{pmatrix},\end{aligned} \tag{11}$$

where T_n and $\mathcal{H}_e$ are the nuclear and the electronic parts of the Hamiltonian matrix. w_{11} and w_{22} are the energies of the two diabatic electronic states coupled by the potential matrix elements $w_{12} = w_{21}$. T_n, in terms of R, r, γ

and for the total angular momentum $J = 0$ is given by[33]

$$T_n = \frac{1}{2\mu}\left[P_R^2 + P_r^2\right] + \frac{\mathbf{j}^2}{2I},$$
$$= -\frac{\hbar^2}{2\mu}\left[\frac{\partial^2}{\partial R^2} + \frac{\partial^2}{\partial r^2}\right] - \frac{\hbar^2}{2I}\frac{1}{\sin\gamma}\frac{\partial}{\partial\gamma}\left(\sin\gamma\frac{\partial}{\partial\gamma}\right). \quad (12)$$

Here P_R and P_r are the momentum operators corresponding to the respective Jacobi distances. $\mathbf{j}$ is the BC rotational angular momentum operator associated with the Jacobi angle γ. The quantity μ defines the three-body uniform reduced mass, $\mu = \sqrt{m_\mathrm{A} m_\mathrm{B} m_\mathrm{C}/(m_\mathrm{A} + m_\mathrm{B} + m_\mathrm{C})}$ (where m_X is the mass of the nuclei X), and I is the three-body moment of inertia $I = \mu R^2 r^2/(R^2 + r^2)$.

2.2.2. *The Flux Operator and Reaction Probability*

In a diabatic representation, the kinetic energy operator T_n is diagonal [Eq. (11)]; therefore the flux operator [Eq. (10)] possesses the same property in this representation. Substituting T_n from Eq. (12) into Eq. (10) and applying some straightforward algebra, the non-zero diagonal elements of the flux operator are given by

$$\hat{f}_{11} = \hat{f}_{22} = \frac{-i\hbar}{2\mu}\left[\frac{\partial}{\partial r}\delta(r - r_d) + \delta(r - r_d)\frac{\partial}{\partial r}\right]. \quad (13)$$

The reaction probability is defined as the expectation value of this flux operator in the basis of energy normalized time-independent reactive scattering wave function evaluated at the dividing surface.[31,34–38] We write this wave function in the diabatic electronic basis as

$$|\Phi^d(R, r_d, \gamma, E)\rangle = \begin{pmatrix} |\phi_1^d(R, r_d, \gamma, E)\rangle \\ |\phi_2^d(R, r_d, \gamma, E)\rangle \end{pmatrix}, \quad (14)$$

where ϕ_1^d and ϕ_2^d correspond to the wave function components on the diabatic state 1 and 2, respectively. The initial state i (corresponding to a specific vibrational v and rotational j state of the reagent BC) selected and energy resolved reaction probability (summed over the final states f (v', j')

of the product AB) is given by

$$P_i^R(E) = \sum_f |S_{fi}^R|^2 = \langle \Phi^d(R, r_d, \gamma, E)|\hat{F}^d|\Phi^d(R, r_d, \gamma, E)\rangle \,. \tag{15}$$

The quantity S_{fi}^R in the above equation is the reactive scattering matrix from an initial state (i) of the reactant to a final state (f) of the product. In terms of the component diabatic wave functions [Eq. (14)], the above equation can be rewritten as

$$\begin{aligned} P_i^R(E) &= \sum_{k=1}^{2} \langle \phi_k^d(R, r_d, \gamma, E)|\hat{f}_{kk}|\phi_k^d(R, r_d, \gamma, E)\rangle \,, \\ &= \frac{\hbar}{\mu} \sum_{k=1}^{2} \mathrm{Im}\left[\left\langle \phi_k^d(R, r_d, \gamma, E) \left| \frac{\partial \phi_k^d(R, r_d, \gamma, E)}{\partial r} \right\rangle \right]\right|_{r=r_d} . \end{aligned} \tag{16}$$

The quantity on the right hand side of the above equation is integrated over the entire range of R and γ. The energy-normalized time-independent reactive scattering wave function is calculated along the dividing surface at $r = r_d$ as

$$|\phi_k^d(R, r_d, \gamma, E)\rangle = \frac{|\psi_k^d(R, r_d, \gamma, E)\rangle}{\kappa_E}. \tag{17}$$

The function $|\psi_k^d(R, r_d, \gamma, E)\rangle$ is obtained by Fourier transforming the time-evolved WP $|\psi_k^d(R, r, \gamma, t)\rangle$ along the dividing surface

$$|\psi_k^d(R, r_d, \gamma, E)\rangle = \frac{1}{\sqrt{2\pi}} \int_{-\infty}^{+\infty} e^{iEt/\hbar} |\psi_k^d(R, r, \gamma, t)\rangle dt|_{r=r_d}. \tag{18}$$

The quantity κ_E in Eq. (17) is the weight of the translational component $F(R)$ [see Eq. (35)] contained in the initial wave packet for a given total energy E

$$\kappa_E = \left(\frac{\mu}{2\pi\hbar k}\right)^{1/2} \int_{-\infty}^{+\infty} F(R) e^{ikR} dR \,, \tag{19}$$

where $k = \sqrt{2\mu(E - \epsilon_{vj})}/\hbar$, with ϵ_{vj} being the initial ro-vibrational energy of the BC molecule.

2.3. *Adiabatic Electronic Representation*

2.3.1. *The Hamiltonian*

The electronic part of the Hamiltonian is diagonal in the adiabatic electronic representation and the off-diagonal elements of the nuclear part describe the nonadiabatic coupling between the two states. The adiabatic Hamiltonian matrix can be obtained from the diabatic one of Eq. (11) via the transformation matrix $\mathbf{S}$ [cf. Eq. (7)] as

$$\begin{aligned}\mathcal{H}^{ad} &= \mathbf{S}^{\dagger}\mathcal{H}^{d}\mathbf{S}, \\ &= T_n\mathbf{1} + \mathbf{S}^{\dagger}\left[T_n, \mathbf{S}\right] + \begin{pmatrix} V_- & 0 \\ 0 & V_+ \end{pmatrix}, \end{aligned} \tag{20}$$

where T_n represents the nuclear kinetic energy operator given in Eq. (12). The nonadiabatic coupling matrix is therefore given by

$$\Lambda = -\mathbf{S}^{\dagger}\left[T_n, \mathbf{S}\right]. \tag{21}$$

The elements of Λ are described by Eq. (2). Using the diabatic Hamiltonian matrix of Eq. (11) and the transformation matrix $\mathbf{S}$ of Eq. (7), after some rigorous algebra the following adiabatic Hamiltonian is obtained:[4,30,39]

$$\begin{aligned}\mathcal{H}^{ad} = T_n &\begin{pmatrix} 1 & 0 \\ 0 & 1 \end{pmatrix} + \begin{pmatrix} V_- & 0 \\ 0 & V_+ \end{pmatrix} + \left[\frac{\hbar^2}{2\mu}(\alpha_R'^2 + \alpha_r'^2) + \frac{\hbar^2}{2I}\alpha_\gamma'^2\right]\begin{pmatrix} 1 & 0 \\ 0 & 1 \end{pmatrix} \\ &+ \left[\frac{\hbar^2}{2\mu}\left(\alpha_R'' + 2\alpha_R'\frac{\partial}{\partial R} + \alpha_r'' + 2\alpha_r'\frac{\partial}{\partial r}\right)\right. \\ &\left. + \frac{\hbar^2}{2I}\left(\alpha_\gamma'' + 2\alpha_\gamma'\frac{\partial}{\partial \gamma} + \alpha_\gamma'\cot\gamma\right)\right]\begin{pmatrix} 0 & -1 \\ 1 & 0 \end{pmatrix}, \end{aligned} \tag{22}$$

where $\alpha_x' = \partial\alpha/\partial x$ and $\alpha_x'' = \partial^2\alpha/\partial x^2$. In the right hand side of Eq. (22) the third term corresponds to the diagonal Born-Huang term Λ^0 [G_{ii} elements of Eq. (2)][10] and the fourth term corresponds to the off-diagonal derivative coupling term [written in terms of F_{ij} in Eq. (2)].

2.3.2. *The Flux Operator and Reaction Probability*

In order to calculate the reaction probability in the two-state adiabatic electronic basis, the flux operator needs to be represented in this basis. As the quantity Θ in the flux operator depends only on the reaction coordinate

(here r), the r-dependent part of the nuclear kinetic energy operator is of only relevance in Eq. (10). It can be seen from Eq. (22) that the nuclear kinetic energy operator is non-diagonal and its r-dependent part is given by

$$T_r^{ad} = \frac{-\hbar^2}{2\mu} \begin{pmatrix} \dfrac{\partial^2}{\partial r^2} - \alpha_r'^2 & \left(\alpha_r'' + 2\alpha_r' \dfrac{\partial}{\partial r}\right) \\ -\left(\alpha_r'' + 2\alpha_r' \dfrac{\partial}{\partial r}\right) & \dfrac{\partial^2}{\partial r^2} - \alpha_r'^2 \end{pmatrix}. \tag{23}$$

Since T_r^{ad} is non-diagonal, the flux operator will have the same property in the adiabatic electronic basis. On substituting T_r^{ad} in Eq. (10) one arrives at the same expression as in Eq. (13) for the diagonal elements ($\hat{f}_{11}$ and $\hat{f}_{22}$) of the flux operator in the adiabatic basis, and its off-diagonal elements take the following form:[30]

$$\hat{f}_{12} = -\hat{f}_{21} = \frac{-i\hbar\alpha_r'}{\mu}\delta(r - r_d)\,. \tag{24}$$

Defining the energy normalized time-independent reactive scattering wave function in the adiabatic electronic basis as

$$|\Phi^{ad}(R, r_d, \gamma, E)\rangle = \begin{pmatrix} |\phi_-^{ad}(R, r_d, \gamma, E)\rangle \\ |\phi_+^{ad}(R, r_d, \gamma, E)\rangle \end{pmatrix}, \tag{25}$$

where ϕ_-^{ad} and ϕ_+^{ad} represent the two components of this wave function on V_- and V_+, respectively, the reaction probability in this basis is given by

$$\begin{aligned} P_i^R(E) &= \left\langle \Phi^{ad}(R, r_d, \gamma, E)|\hat{F}|\Phi^{ad}(R, r_d, \gamma, E)\right\rangle, \\ &= \frac{\hbar}{\mu}\Bigg[\mathrm{Im}\left\langle \phi_-^{ad}(R, r_d, \gamma, E)\middle|\frac{\partial\phi_-^{ad}(R, r_d, \gamma, E)}{\partial r}\right\rangle \\ &\quad + \mathrm{Im}\left\langle \phi_+^{ad}(R, r_d, \gamma, E)\middle|\frac{\partial\phi_+^{ad}(R, r_d, \gamma, E)}{\partial r}\right\rangle \\ &\quad + \mathrm{Im}\langle\phi_-^{ad}(R, r_d, \gamma, E)|\alpha_r'|\phi_+^{ad}(R, r_d, \gamma, E)\rangle \\ &\quad - \mathrm{Im}\langle\phi_+^{ad}(R, r_d, \gamma, E)|\alpha_r'|\phi_-^{ad}(R, r_d, \gamma, E)\rangle\Bigg]. \end{aligned} \tag{26}$$

The wave functions ϕ_-^{ad} and ϕ_+^{ad} can be obtained in an analogous way as described for ϕ_1^d and ϕ_2^d. Since α_r' is a real quantity, the last two terms of

Eq. (26) are complex conjugate to each other and therefore $P_i^R(E)$ becomes

$$P_i^R(E) = \frac{\hbar}{\mu}\Bigg[\mathrm{Im}\left\langle \phi_-^{ad}(R,r_d,\gamma,E)\middle|\frac{\partial\phi_-^{ad}(R,r_d,\gamma,E)}{\partial r}\right\rangle + \mathrm{Im}\left\langle \phi_+^{ad}(R,r_d,\gamma,E)\middle|\frac{\partial\phi_+^{ad}(R,r_d,\gamma,E)}{\partial r}\right\rangle + 2\mathrm{Im}\langle\phi_-^{ad}(R,r_d,\gamma,E)|\alpha_r'|\phi_+^{ad}(R,r_d,\gamma,E)\rangle\Bigg]. \quad (27)$$

Contrary to the analogous expression [Eq. (16)] in the diabatic basis, the result [Eq. (27)] contains also off-diagonal electronic contributions. These are expected to play an important role when both channels, corresponding to V_- and V_+, are open. If only V_- is open, then only the first of the three terms on the right hand side of Eq. (27) contributes to the reaction probability. Even in this case, however, both terms in the diabatic analogue of Eq. (16) may play a role, because adiabatic and diabatic surfaces need not coincide asymptotically.[19]

3. Illustrative Example: The $H + H_2$ Exchange Reaction

3.1. *General Consideration*

The prototypical hydrogen exchange reaction

$$H + H_2 \rightarrow H_2 + H \quad (R1)$$

is one of the cornerstones in our understanding of the microscopic details of the chemical reaction dynamics [for example, see Ref. 40 and references therein]. The ground electronic state of triatomic hydrogen is degenerate by symmetry with its first excited electronic state at the D_{3h} equilibrium configuration and forms a conical intersection.[41] This is the simplest representative of a $(E \times \epsilon)$-JT conical intersection.[41,42] While the lower adiabatic sheet of this double-sheeted electronic state is of repulsive nature and the reactive scattering process occurs on it, the upper adiabatic sheet supports bound states in the absence of any coupling with the lower one. The conical intersection in the ground electronic manifold of H_3 is probed in a Rydberg emission experiment,[43] which was further corroborated in a detailed theoretical study[44] indicating an extremely fast relaxation from the upper adiabatic sheet driven by the nonadiabatic coupling associated with the conical intersection.

The effect of the conical intersection on the reactive scattering dynamics of (R1) has been studied by Kuppermann and coworkers.[45,46] In these studies, this effect is incorporated in the dynamical calculations in terms of the GP change of the adiabatic electronic wave function when encircling the conical intersection in a closed path on the lower adiabatic sheet. The two sheets of the PES and the nonadiabatic coupling between them are not explicitly considered in these studies. Their findings show that the differential cross sections of the $H + D_2$ ($v = 0$) exchange reaction at a collision energy of 1.29 eV agree well with the experimental results when the GP effect is considered.[46] In a later study Schnieder *et al.*[47] have reproduced the fully state-resolved measurements of ultrahigh resolution without taking the GP effects into account. In view of the fact that the minimum of the seam of conical intersections in H_3 occurs at $\sim$2.74 eV, it is not clear if any noticeable GP effects will show up in its dynamics much below this energy. Kendrick[48] has performed very accurate quantum mechanical calculations and found no noticeable GP effects on the dynamics of this reaction. Very recently a combined experimental and WP theoretical study has been reported on the system and the experimental results were reproduced without inclusion of the GP effects in the theoretical formulation.[49]

We have studied for the first time the state-selected scattering dynamics of (R1) by extending the quantum flux operator formalism (as described above) to two interacting electronic states.[30] The reaction probabilities were reported for energies up to the onset of the three-body dissociation of H_3 and our results did not indicate any noticeable effects of the conical intersection on the state-specific dynamics of this system for $J = 0$. The coupled-state results can be essentially reproduced by adding the diagonal correction term in the uncoupled-surface calculations. These findings in a way extend the recent studies on this system by going to higher energies and incorporating GP effects and the nonadiabatic couplings in a coherent fashion. Furthermore, the formalism illustrated above can be efficiently applied to reactions that bear strong signatures of nonadiabatic effects. The details of the calculations for H_3 are described in the following.

3.2. *Potential Energy Surface*

The repulsive lower adiabatic sheet of the ground electronic state of H_3 has been reported by several groups with improved accuracy.[50–52] However,

until recently the double many-body expansion (DMBE) PES has been the only PES[51] available for the system which globally represents both the lower and the upper adiabatic sheets of the double-sheeted ground electronic manifold of H_3 and thus offers the possibility to study theoretically the nonadiabatic effects associated with the conical intersection. We note that the DMBE PES relies on the analytic continuation approach for the upper adiabatic sheet. Recently extensive *ab initio* calculations of the double-sheeted ground electronic manifold of H_3 and their nonadiabatic couplings were performed by Yarkony.[53] These *ab initio* points have been subsequently utilized by Kuppermann and coworkers[54,55] and been represented in a diabatic electronic basis. In our study we used the DMBE PES[51] and a suitable diabatization scheme (see below) to calculate the reaction probability in the coupled electronic manifold. We also note that we have accessed the accuracy of the analytic continuation approach of the DMBE surface by an explicit comparison of the various stationary points and the long-range behavior of this surface with the new *ab initio* results of Yarkony.[53] The topography of the conical intersection in the double-sheeted ground electronic surface of H_3 is shown in Fig. 1.

The elements of the diabatic electronic Hamiltonian matrix in Eq. (11) are obtained by diabatizing the adiabatic electronic Hamiltonian matrix through the following similarity transformation:

$$\begin{aligned}\begin{pmatrix} w_{11} & w_{12} \\ w_{21} & w_{22} \end{pmatrix} &= \mathbf{S} \begin{pmatrix} V_- & 0 \\ 0 & V_+ \end{pmatrix} \mathbf{S}^\dagger \\ &= \frac{V_+ + V_-}{2} \mathbf{1} + \frac{\mathbf{V}_+ - \mathbf{V}_-}{\mathbf{2}} \begin{pmatrix} -\cos\chi & \sin\chi \\ \sin\chi & \cos\chi \end{pmatrix}, \end{aligned} \tag{28}$$

with ($\chi = 2\alpha$). Here $\mathbf{1}$ is a 2×2 unit matrix and $\mathbf{S}$ is given in Eq. (7). The quantities V_- and V_+ are the potential energies of the lower and the upper adiabatic sheets of the DMBE PES of H_3,[51] respectively. The angle χ is identified with the pseudorotation angle, defined as the direction of the ϵ-type displacement in its two-dimensional vibrational space of the D_{3h} point group.[51,56] This method of diabatization was tested numerically with a second-order model ($E \times \epsilon$)-JT Hamiltonian by Thiel and Köppel.[56] It was shown that with this scheme of diabatization the singular derivative coupling terms are eliminated and the matrix elements of the residual derivative couplings become vanishingly small.[56] We also applied this scheme successfully in our earlier investigations on the Rydberg emission spectrum of H_3.[44]

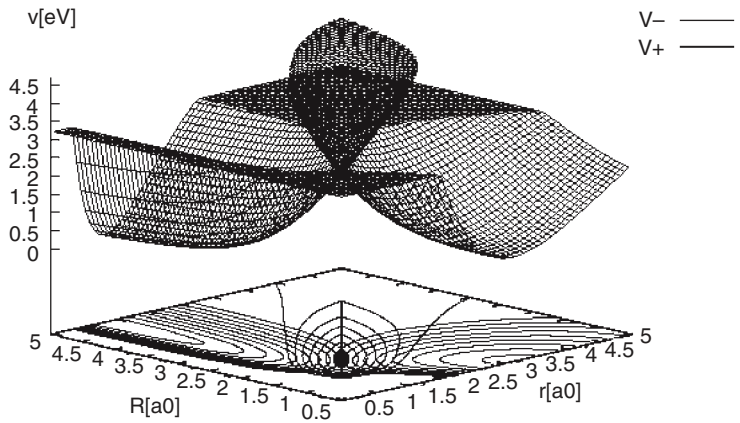

Fig. 1. Three-dimensional perspective plot of the adiabatic potential energy surfaces of the double-sheeted ground electronic state of H_3 in the (R, r) plane for $\gamma = \pi/2$, corresponding to the C_{2v} arrangements of the three nuclei. The contour line diagram is included in the base of the plot. The spacing between the successive contour lines is 0.3 eV. The potential energies are obtained from the DMBE PES[51] and the lower (V_-) and the upper (V_+) adiabatic sheets are shown by the thin and thick solid curves, respectively. The conical intersection of the two surfaces should not be realized as an isolated point as apparently revealed by the perspective plot, rather, it represents a seam of intersections occurring for $R = \sqrt{3r}/2$ which is more clearly indicated by the thick solid line on the contour plot. The energetic minimum on this seam occurring at ~ 2.74 eV for the D_{3h} configuration of H_3 is shown by the dot.

Very recently, Köppel and coworkers have extended this scheme to a more general situation.[57]

3.3. *Diagonal Correction to the Adiabatic Hamiltonian*

The adiabatic–diabatic mixing angle α is a complicated function of the Jacobi coordinates and an evaluation of Λ in these coordinates is cumbersome. This can be better accomplished in the $(E \times \epsilon)$-JT coordinates ρ_{JT} and χ. The latter are identified as the radius of the JT displacement and the pseudo-rotation angle (introduced above), respectively. These coordinates can be expressed in terms of the dimensionless normal coordinates (cartesian) of the ϵ-type vibration (Q_x and Q_y) of the D_{3h} point group as

$$\rho_{JT} e^{i\chi} = Q_x + iQ_y \,. \tag{29}$$

In these coordinates the BH term is given by[56,58]

$$\Lambda^0(\tilde{\alpha}) = \frac{\omega_\epsilon \hbar}{8}\left[\left(\frac{\partial\tilde{\alpha}}{\partial\rho_{JT}}\right)^2 + \frac{1}{\rho_{JT}^2}\left(\frac{\partial\tilde{\alpha}}{\partial\chi}\right)^2\right], \tag{30}$$

where ω_ϵ is the frequency of the degenerate vibration and $\tilde{\alpha} = 2\alpha$. Within the linear coupling scheme $\tilde{\alpha} = \chi$ [Eq. (28)] and does not depend on ρ_{JT} and therefore Eq. (30) is given by

$$\Lambda^0 = \frac{\omega_\epsilon \hbar}{8\rho_{JT}^2}\,. \tag{31}$$

In terms of the mass-weighted coordinate q_{JT} to be used below, Eq. (31) reads

$$\Lambda^0 = \frac{\hbar^2}{8m_{\mathrm{H}}q_{JT}^2}\,. \tag{32}$$

3.4. *Computational Details*

We now discuss the necessary details of the computational aspects to obtain the reaction probability by the scheme developed above. In the following we proceed with the coupled-surface calculations; the uncoupled-surface calculations follow from them in an elementary way. The time-dependent Schrödinger equation (TDSE) is solved numerically in the diabatic electronic representation on a grid in the (R, r, γ) space using the matrix Hamiltonian in Eq. (11). For an explicitly time-independent Hamiltonian the solution reads

$$\Psi^d(R, r, \gamma, t) = \exp\left[\frac{-i\mathcal{H}^d t}{\hbar}\right]\Psi^d(R, r, \gamma, 0)\,. \tag{33}$$

Here $\Psi^d(R, r, \gamma, 0)$ is the initial wave function pertinent to the reactants in the diabatic electronic representation and $\Psi^d(R, r, \gamma, t)$ is the wave function at time t.

The initial wave function pertinent to the $H + H_2$ reacting system is prepared in the asymptotic reactant channel and is written as a product of the translational wave function $F(R)$ for the motion along R and the ro-vibrational wave function $\Phi_{vj}(r)$ of the H_2 molecule. We locate the wave function initially on the repulsive lower adiabatic sheet (V_-) of the DMBE

PES.[51] In the present case for, $J = 0$, it is given by

$$\Psi^{ad}(R, r, \gamma, 0) = F(R)\Phi_{vj}(r)\sqrt{\frac{2j+1}{2}}P_j(\cos\gamma)\begin{pmatrix}1\\0\end{pmatrix}. \tag{34}$$

We choose a minimum uncertainty Gaussian wave packet (GWP) for $F(R)$:

$$F(R) = \left(\frac{1}{2\pi\delta^2}\right)^{1/4}\exp\left[-\frac{(R-R_0)^2}{4\delta^2} - ik_0(R-R_0)\right]. \tag{35}$$

The quantity δ is the width parameter of the GWP, and R_0 and k_0 correspond to the location of its maximum in the coordinate and momentum space, respectively. The functions $\Phi_{vj}(r)$ along with the normalized Legendre polynomials ($P_j(\cos\gamma)$) represent the ro-vibrational eigenfunction corresponding to a (v, j) state of the H_2 molecule. The functions $\Phi_{vj}(r)$ are obtained by solving the eigenvalue equation of the free H_2 molecule:

$$\left[-\frac{\hbar^2}{2\mu'}\frac{d^2}{dr'^2} + V(r') + \frac{j(j+1)\hbar^2}{2\mu' r'^2}\right]\Phi_{vj}(r') = \epsilon_{vj}\Phi_{vj}(r'). \tag{36}$$

Here μ' is the reduced mass of the H_2 molecule, ϵ_{vj} the energy eigenvalue, $r'[= r(\mu/\mu')^{1/2}]$ the unscaled internuclear distance, and $V(r')$ is the potential energy of the H_2 molecule obtained from the DMBE PES by setting $R \to \infty$. We used the sine-DVR approach of Colbert and Miller[59] to solve the above eigenvalue equation.

The initial wave function defined in Eq. (34) is transformed to the diabatic representation by using the **S** matrix [Eq. (7)] prior to its propagation. In the diabatic representation the initial wave function can be written in the vector notation as

$$\Psi^d(R, r, \gamma, 0) = \psi_1^d(R, r, \gamma, 0)\begin{pmatrix}1\\0\end{pmatrix} + \psi_2^d(R, r, \gamma, 0)\begin{pmatrix}0\\1\end{pmatrix}, \tag{37}$$

where $\binom{1}{0}$ and $\binom{0}{1}$ indicates the first and the second diabatic electronic state with energy w_{11} and w_{22}, respectively. Note that these are different from the ones introduced in Eq. (34). ψ_1^d and ψ_2^d are the nuclear wave functions in the respective electronic states, depending on the set of Jacobi coordinates. In order to follow the nuclear dynamics, the TDSE [Eq. (33)] is solved with the above initial diabatic wave function. The exponential time evolution operator in Eq. (33) is evaluated by dividing the time axis into N

segments of length Δt. The exponential operator at each time step is then approximated by the split-operator method,[60]

$$\exp\left[\frac{-i\mathcal{H}^d\Delta t}{\hbar}\right] = \exp\left[\frac{-i\mathcal{H}^{el}\Delta t}{2\hbar}\right]\exp\left[\frac{-i\mathbf{j}^2\Delta t}{4I\hbar}\mathbf{1}\right]\exp\left[\frac{-iT(R,r)\Delta t}{\hbar}\mathbf{1}\right] \times \exp\left[\frac{-i\mathbf{j}^2\Delta t}{4I\hbar}\mathbf{1}\right]\exp\left[\frac{-i\mathcal{H}^{el}\Delta t}{2\hbar}\right] + O[(\Delta t)^3]\,, \tag{38}$$

where $T(R,r) = (P_R^2 + P_r^2)/2\mu$ is the total radial kinetic energy operator. $\mathbf{1}$ represents the 2×2 unit matrix. The electronic Hamiltonian $\mathcal{H}^{el}$ can be decomposed into

$$\mathcal{H}^{el} = \begin{pmatrix} w_{11} & 0 \\ 0 & w_{22} \end{pmatrix} + w_{12}\begin{pmatrix} 0 & 1 \\ 1 & 0 \end{pmatrix}. \tag{39}$$

Since the diagonal and the off-diagonal parts of $\mathcal{H}^{el}$ do not commute with each other, the propagator containing it in Eq. (38) is further written as

$$e^{-i\mathcal{H}^{el}\Delta t/2\hbar} = e^{-i\begin{pmatrix} w_{11} & 0 \\ 0 & w_{22} \end{pmatrix}\Delta t/4\hbar}\; e^{-iw_{12}\begin{pmatrix} 0 & 1 \\ 1 & 0 \end{pmatrix}\Delta t/2\hbar}\; e^{-i\begin{pmatrix} w_{11} & 0 \\ 0 & w_{22} \end{pmatrix}\Delta t/4\hbar}. \tag{40}$$

The exponent containing the off-diagonal matrix elements is now expressed in terms of the 2×2 Pauli matrix

$$e^{-iw_{12}\begin{pmatrix} 0 & 1 \\ 1 & 0 \end{pmatrix}\Delta t/2\hbar} = \begin{pmatrix} \cos(w_{12}\Delta t/2\hbar) & -i\sin(w_{12}\Delta t/2\hbar) \\ -i\sin(w_{12}\Delta t/2\hbar) & \cos(w_{12}\Delta t/2\hbar) \end{pmatrix}. \tag{41}$$

Equation (38) is used in conjunction with the fast Fourier transform method[61] to evaluate the action of the exponential containing the radial kinetic energy operator and the discrete variable representation method[62] to evaluate the exponential containing the rotational kinetic energy operator ($\mathbf{j}^2/2I$) on the wave function. The coordinate grid consists of equally spaced points R_l and r_m along the Jacobi distances R and r, respectively. The grid along the Jacobi angle γ is chosen as the nodes of a n-point Gauss–Legendre quadrature (GLQ).[63]

We have constructed a grid consisting of $128\times 64\times 48$ points in the R_l, r_m, γ_n space with R ranging between 0.10 and $15.34a_0$ and r between 0.50 and $8.06a_0$. The grid along γ is defined by the 48-point GLQ. The initial WP is prepared at $R_0 = 10.5a_0$ and the width parameter of the GWP, δ is chosen to be $0.16a_0$. The WP is time propagated with a step size Δt

of 0.1347 fs for a total time of 413.76 fs. The analysis line at the product channel is fixed at $r_d = 4.1a_0$. In order to avoid unphysical reflections or wrap arounds of the fast moving components of the WP at the grid boundaries, it is multiplied by a damping function[64] at each time step which is activated outside the dividing line at $r = 4.70a_0$ in the product channel and also in the asymptotic reactant channel at $R = 11.74a_0$.

The time dependence of the adiabatic electronic populations can be calculated either by using the **S** matrix [Eq. (7)] or by defining suitable adiabatic projection operators. The **S** matrix is a double-valued function of the coordinates and possesses a branch point at the conical intersection. This problem is circumvented by using adiabatic projectors in the diabatic electronic representation[4,39,65]

$$\begin{aligned} P_{\mp}^{ad} &= \mathbf{S} \begin{pmatrix} 1 & 0 \\ 0 & 0 \end{pmatrix} \mathbf{S}^{\dagger} \\ &= \frac{1}{2} - \frac{1}{2(\Delta^2 + w_{12}^2)^{1/2}} \begin{pmatrix} -\Delta & w_{12} \\ w_{12} & \Delta \end{pmatrix}, \\ P_{+}^{ad} &= 1 - P_{-}^{ad}, \end{aligned} \tag{42}$$

where $\mp$ refers to the lower and the upper adiabatic sheet, respectively. Δ is one-half of the energy gap between the two diabatic surfaces. The expectation values of the above projectors define the electronic populations in the respective electronic states.

3.5. *Results and Discussion*

We now show and discuss the results of initial state-specific and energy resolved reaction probabilities of (R1), applying the formalism and the computational strategy illustrated above. The reaction probabilities are calculated with an energy spacing of 9×10^{-3} eV. The convergence of the results is checked with respect to the numerical grid parameters.

The total reaction probability (summed over all open vibrational (v') and rotational (j') states of the product H_2 at a given energy) of $H + H_2$ ($v = 0, j = 0$) calculated in the diabatic electronic picture through Eq. (16) as a function of the total energy E is plotted in Fig. 2. The probability values shown by the short- and long-dashed lines are obtained by analyzing the reactive flux on the two component diabatic electronic states w_{11} and w_{22}, respectively [represented by the first and the second term of

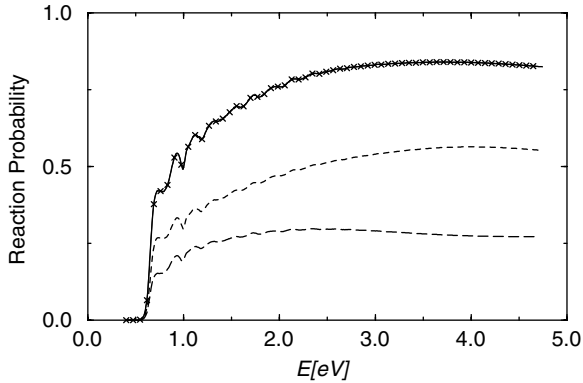

Fig. 2. Total reaction probability for the $H + H_2(v = 0, j = 0) \rightarrow H_2(\sum v', \sum j') + H$ exchange reaction in three dimensions and for total angular momentum $J = 0$, plotted as a function of total energy E (H,H_2 translational + H_2 ro-vibrational). The energy E is measured relative to the H_2 potential minimum. The reaction probabilities obtained on the two diabatic electronic states w_{11} and w_{22} [cf. Eq. (16)] are shown by the short- and long-dashed lines, respectively. The sum total of these diabatic probabilities (indicated by crosses) on a coarse energy grid is superimposed on the adiabatic coupled-surface probabilities (indicated by the solid line, see, Fig. 3 below).

Eq. (16)]. The sum of these two components is indicated by the crosses and is superimposed on the coupled-surface results shown as a solid line. The latter are obtained by analyzing the reactive flux in the adiabatic electronic picture and from the first term of Eq. (27) (also see Fig. 3 below). For clarity of presentation, we show the crosses on a coarse grid of energy values. It is clear from Fig. 2 that the second and the third terms of Eq. (27) do not contribute to the reaction probability of $H + H_2(v = 0, j = 0)$ in the energy range of the present investigations. This is, because, on the upper adiabatic surface, product H_2 is asymptotically prepared in its $^3\Sigma_u$ state which has its minimum at $E \sim 4.74\,\text{eV}$,[51] at the onset of the three-body dissociation. Therefore, in the present investigation this channel remains energetically closed and does not contribute to the reaction probability. This is numerically checked further from the reaction probabilities obtained from the second term of Eq. (27). They are all zero until the fourth decimal place, which shows that the second and the third terms are zero individually, not just their sum. Despite a difference in the magnitude of the reaction probabilities, the two component diabatic probability curves exhibit similar resonance structures.

The same reaction probability of $H + H_2$ ($v = 0$, $j = 0$) calculated in the adiabatic electronic picture is shown in Fig. 3. The coupled-surface results (also shown in Fig. 2 for comparison) are shown by the solid line. The uncoupled (lower adiabatic)-surface results without and with the diagonal correction are shown by the short- and long-dashed lines, respectively. The energy distribution of the initial translational GWP is shown in the inset. It can be seen that the translational components of the initial WP cover a broad range of energies from the onset of the reaction threshold at $E = 0.55\,\text{eV}$ to the three-body dissociation limit at $E = 4.74\,\text{eV}$. Therefore, the reaction probabilities in that range of energies can be reliably obtained with this WP. The coupled-surface results are obtained by analyzing the reactive flux in the adiabatic picture through Eq. (27). As mentioned above, only the first term of Eq. (27) contributes to the reaction probability. The resonance structures and their energetic locations are same in the coupled- and uncoupled-surface results. The difference between the coupled- and uncoupled-surface (without the diagonal correction) results is 2–3% at low energies. At high energies this difference increases only slightly. The minimum of the seam of conical intersections of H_3 occurs at $\sim 2.74\,\text{eV}$.[51] Therefore, the coupled-surface results are expected to differ more from the uncoupled ones beyond this energy. However, it can be seen from Fig. 3 that the impact of the conical intersection on the $H_2(v = 0, j = 0)$ reaction probabilities is negligibly small. The small deviations become even smaller when including the diagonal correction.

In order to better understand the similarity between the coupled- and the uncoupled-surface results, we show the time evolution of the electronic populations in Fig. 4. The initial WP corresponds to $H_2(v = 0, j = 0)$ and is again prepared in the asymptotic reactant channel of the lower adiabatic sheet. [It is transformed to the diabatic representation using the **S**-matrix of Eq. (7) prior to propagation]. As can be seen from Fig. 4, we obtain a 0.71/0.29 population of the two component diabatic electronic states (shown by the dashed and solid lines) at $t = 0$. Therefore, the diabatic potentials do not approach the asymptotic adiabatic states of $H + H_2$ but represent a mixture of them.

A similar kind of behavior of the diabatic electronic states has been found, e.g. for the ozone and hydrogen disulphide molecules.[19] This may be a surprising feature of the diabatization procedure but, in practice, is often unavoidable. However, since the adiabatic states are well separated

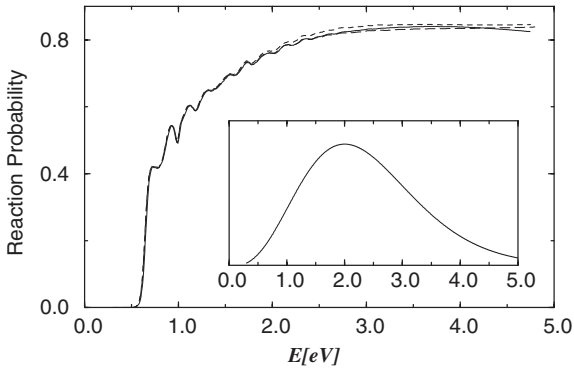

Fig. 3. Same as in Fig. 2, the coupled-surface results [obtained through Eq. (27)] are shown by the solid line. The uncoupled-surface results with (long-dashed lines) and without (short-dashed lines) the diagonal BH correction are also shown. The energy distribution of the initial translational GWP is shown in the inset.

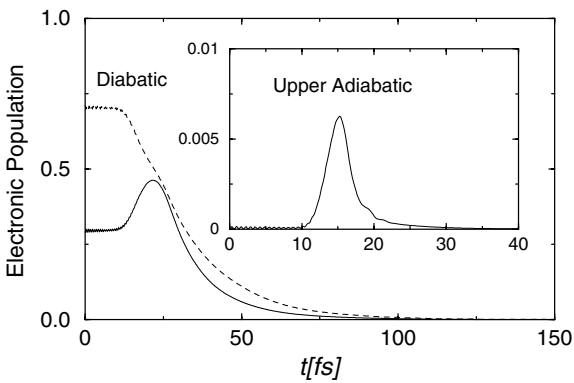

Fig. 4. Time dependence of the electronic populations for the exchange process of Fig. 3. The populations of the two component diabatic electronic states w_{11} and w_{22} are shown by the dashed and solid lines, respectively. The electronic populations approach zero at longer times because of the damping of the WP at the grid edges. The population of the upper adiabatic electronic state (V_+) is shown in the inset.

asymptotically, preparing an initial WP on the adiabatic electronic state and propagating it in the diabatic electronic representation and finally transforming it back to the adiabatic states before analysis, is expected to have only little relevance of this "artifact" on the dynamics. The coincidence of the reaction probabilities obtained in the diabatic and the adiabatic

picture (see Fig. 2) also adds evidence to this remark. The population of the upper adiabatic electronic state is shown in the inset of Fig. 4. The population of this state reaches a maximum value of $\sim 6.25 \times 10^{-3}$ after ~ 15 fs. Therefore, only $\sim 0.625\%$ of the WP traverses to the upper adiabatic cone during the course of the entire dynamics. This can hardly have any major impact on the dynamics. The minimum energy path for the $H + H_2$ reactive scattering process occurs at the collinear arrangement of the three nuclei which is far away from the seam of conical intersections, occurring at the D_{3h} arrangements of the three nuclei. The classical barrier height of the collinear saddle point on the lower adiabatic sheet is ~ 0.42 eV, whereas the minimum of the seam of conical intersections occurs at ~ 2.74 eV at the equilateral triangular geometry.[51] Apparently, also for higher energies a major part of the reactive flux is directed via the low-energy transition state conformation. A similar numerical observation has been made earlier in a bound-state calculation of electronically excited states of SO_2 by Müller and Köppel.[66]

We also performed a detailed analysis of the probabilities obtained with vibrationally excited H_2. Our findings are similar to those discussed above: the difference between the coupled- and uncoupled-surface results is very small. We notice that for vibrationally excited H_2 a relatively larger fraction of the WP traverses to the upper adiabatic sheet during the reaction. For instance, $\sim 1\%$ and $\sim 1.6\%$ of the WP traverse to the upper cone during the reaction for $v = 1$ and $v = 2$, respectively. Also, the population maximum occurs at a slightly later propagation time upon vibrational excitation.[30]

4. Summary and Outlook

We have presented a brief account of the reactive scattering dynamics occurring on a multi-sheeted PES. The reaction dynamics of bimolecular systems occurring on a single PES is well studied in the literature. In this account, effort is made to include the surface crossings and the associated nonadiabatic couplings in the formalism — the importance of which in a reactive scattering process is being increasingly realized in recent years.

We particularly focused on a conically intersecting manifold of two electronic states and described the quantum flux operator formalism within a time-dependent WP approach to calculate the initial state-specific and energy resolved reaction probabilities. The flux operator is represented in the two-state diabatic as well as adiabatic representation. While the

representation of the flux operator is diagonal in the diabatic electronic basis, it contains off-diagonal elements (arising from the off-diagonal kinetic coupling elements) in the adiabatic electronic basis. The initial WP is prepared on an adiabatic electronic state and is propagated in a suitable diabatic electronic representation. One needs to resort to the latter representation in order to avoid the diverging (at the seam of intersections of the potential energy surfaces) nonadiabatic coupling elements appearing in the adiabatic electronic basis. The final analysis of the reactive flux is carried out both in the adiabatic and in the diabatic electronic representations and the identity of the results were confirmed.

With the aid of the above formalism we reported the state-selected and energy resolved total reaction probabilities of the $H+H_2$ exchange reaction (R1) on the DMBE PES. The coupled-surface results differ only slightly from the corresponding uncoupled (single) surface ones, and the former at high energies can essentially be reproduced by the uncoupled-surface calculation, including the diagonal correction to the BO Hamiltonian. The resonance structures and their energetic locations are found to be similar in both the coupled- and uncoupled-surface results. The sum of the reaction probabilities obtained in the diabatic representation [Eq. (16)] equals to that obtained in the adiabatic picture considering only the first term of Eq. (27). On the upper adiabatic sheet, H_2 is produced in its $^3\Sigma_u$ state and the energetic minimum of this state occurs at the onset of the three-body dissociation ($\sim$4.74 eV) Therefore, in the energy range of the present investigations, the last two terms of Eq. (27) do not contribute to the reaction probability.

The minimum energy path for the $H + H_2$ exchange process occurs at the collinear arrangement of the three nuclei, which is far away from the seam of conical intersections occurring at the D_{3h} configuration. Beyond the minimum of the seam of conical intersections occurring at $\sim$2.74 eV, the noncollinear collisions might be expected to make significant contributions in the reactive scattering dynamics. However, the region of the space covered by the configuration of the three nuclei for which the two surfaces are nearly degenerate is very small and any slight deviation form these configurations leads to a significant energy splitting of the two surfaces. We find only a very small fraction the WP (less than 2%) traversing the upper adiabatic cone during the course of the reaction. Therefore, no dramatic effects of the conical intersections on the reaction probability are unveiled by the present investigations.

Unlike in the above situation, where surface couplings have been shown to have only minor effects on the dynamics, they may have quite significant roles in other situations, e.g. in the dynamics of $H + O_2$[22,23] and $N + O_2$[27] reactions. Investigations of the dynamics of $H + O_2$ reaction by Gray and coworkers[22] have indicated that the inclusion of the coupling between its two low-lying $^1A'$ surfaces yields reaction cross-section in better agreement with the experiment than the uncoupled-surface result at 56 meV collision energy. In a subsequent study Aoiz *et al.*[23] have reiterated this point in a combined experimental and theoretical study and found that the experimental results at 56 meV collision energy can be essentially reproduced by resorting to adiabatic calculations on the ground $1^1A'$ PES. The $2^1A'$ surface has a barrier of ~ 0.1 eV relative to the reactants and the conical intersections of the $1^1A'$-$2^1A'$ electronic states occur at the product side of the barrier.[21,22] Therefore, any possible contribution of the nonadiabatic coupling in the $H + O_2$ reaction dynamics is only expected beyond the collision energy of 0.1 eV. More theoretical and experimental works are necessary in order to resolve this issue. The $N + O_2$ reaction, on the other hand, appears to be far more complex.[27] Several low-lying doublet and quartet electronic states and multiple conical intersections are reported to be involved in the C_{2v} insertion mechanism of the reaction.[27] A study of the dynamics of this reaction including these conical intersections and the associated nonadiabatic couplings is worthwhile and is expected to lead to a better understanding of the impact of conical intersections in bimolecular reactive scattering.

Acknowledgments

The author is indebted to Professors H. Köppel and L. S. Cederbaum for their interest in this work and a fruitful collaboration which resulted in the first publication (Ref. 30) on this subject. Thanks are due to Professors W. Domcke and H. Köppel for their kind invitation and encouragement to contribute this chapter in the present book. This study is supported in part by a grant from the department of science and technology, New Delhi under the fast track scheme. S. M. is a receipient of the Friedrich Wilhelm Bessel Forschungspreis of the Alexander von Humboldt Stiftung.

References

1. I. B. Bersuker, *The Jahn-Teller Effect and Vibronic Interactions in Modern Chemistry* (Plenum Press, New York, 1984); G. Fischer, *Vibronic Coupling*

(Academic Press, New York, 1984); I. B. Bersuker and V. Z. Polinger, *Vibronic Interactions in Molecules and Crystals* (Springer-Verlag, Berlin, 1989).
2. H. Köppel and W. Domcke, in *Encyclopedia of Computational Chemistry*, Ed. P. v. R. Schleyer (Wiley, New York, 1998), p. 3166.
3. E. Teller, *J. Phys. Chem.* **41**, 109 (1937); G. Herzberg and H. C. Longuet-Higgins, *Discuss. Faraday Soc.* **35**, 77 (1963); T. Carrington, *Discuss. Faraday Soc.* **53**, 27 (1972); *Acc. Chem. Res.* **7**, 20 (1974); E. R. Davidson, *J. Am. Chem. Soc.* **99**, 397 (1977).
4. H. Köppel, W. Domcke and L. S. Cederbaum, *Adv. Chem. Phys.* **57**, 59 (1984).
5. F. Bernardi, M. Olivucci and M. Robb, *Chem. Soc. Reviews* **25**, 321 (1996).
6. W. Domcke and G. Stock, *Adv. Chem. Phys.* **1**, 100 (1997).
7. D. R. Yarkony, *Acc. Chem. Res.* **31**, 511 (1998).
8. *Chemical Physics* **2000**, 259, 121-337 (Special issue on Conical Intersections).
9. M. Born and J. R. Oppenheimer, *Ann. Phys. (Leipzig)* **84**, 457 (1927).
10. M. Born and K. Huang, *Dynamical Theory of Crystal Lattices* (Oxford University Press, New York, 1954).
11. B. H. Lengsfield and D. R. Yarkony, *Adv. Chem. Phys.* **82**, 1 (1992).
12. W. Lichten, *Phys. Rev.* **131**, 229 (1963); F. T. Smith, *Phys. Rev.* **179**, 111 (1969); T. F. O'Malley, *Adv. At. Mol. Phys.* **7**, 223 (1971).
13. M. Baer, *Chem. Phys. Lett.* **35**, 112 (1975); *Chem. Phys.* **15**, 49 (1976).
14. C. A. Mead and D. G. Truhlar, *J. Chem. Phys.* **77**, 6090 (1982).
15. V. Sidis, *Adv. Chem. Phys.* **82**, 73 (1992).
16. M. Baer, *Adv. Chem. Phys.* **82**, 187 (1992).
17. T. Pacher, L. S. Cederbaum and H. Köppel, *Adv. Chem. Phys.* **84**, 293 (1993).
18. R. Meiswinkel and H. Köppel, *Chem. Phys.* **144**, 117 (1990); *Z. Phys D* **19**, 63 (1991); H. Köppel and R. Meiswinkel, *Z. Phys.* **D32**, 153 (1994); J. Schön and H. Köppel, *Chem. Phys. Lett.* **231**, 55 (1994); M. Mayer, L. S. Cederbaum and H. Köppel, *J. Chem. Phys.* **104**, 8932 (1996); W. E. Ernst and S. Rakowsky, *Z. Phys.* **D26**, 270 (1993); *Phys. Rev. Lett.* **74**, 58 (1995); T. Baumert, R. Thalweiser, V. Weiss and G. Gerber, *Z. Phys.* **D26**, 131 (1993); H. von Busch, V. Dev, H.-A. Eckel, S. Kasahara, J. Wang, W. Demtröder, P. Sebald and W. Meyer, *Phys. Rev. Lett.* **81**, 4584 (1998); F. Cocchini, T. H. Upton and W. Andreoni, *J. Chem. Phys.* **88**, 6068 (1988); B. Kendrick, *Phys. Rev. Lett.* **79**, 2431 (1997); M. Keil, H.-G. Krämer, A. Kundell, M. A. Baig, J. Zhu, W. Demtröder and W. Meyer, *J. Chem. Phys.* **113**, 7414 (2000).
19. C. Woywod, M. Stengle, W. Domcke, H. Flöthmann and R. Schinke, *J. Chem. Phys.* **107**, 7282 (1997); H. Flöthmann, C. Beck, R. Schinke, C. Woywod and W. Domcke, *J. Chem. Phys.* **107**, 7296 (1997); G. Theodorakopoulos and I. D. Petsalakis, *Chem. Phys. Lett.* **178**, 475 (1991); D. Simah, B. Hartke and H. J. Werner, *J. Chem. Phys.* **111**, 4523 (1999); D. Skouteris, B. Hartke and H.-J. Werner, *J. Phys. Chem.* **A105**, 2458 (2001).

20. A. Bergeat, L. Cartechini, P. Casavecchia and G. G. Volpi, *Proc. 16th Int. Conf. on Molecular Energy Transfer* (Assisi, Italy), p. 51.
21. K. Drukker and G. C. Schatz, *J. Chem. Phys.* **111**, 2451 (1999); Y.-T. Hsu, K. Liu, L. A. Pederson and G. C. Schatz, *J. Chem. Phys.* **111**, 7931 (1999); M. R. Hoffmann and G. C. Schatz, *J. Chem. Phys.* **113**, 9456 (2000); X. Liu, J. J. Lin, S. Harich, G. C. Schatz and X. Yang, *Science* **289**, 1536 (2000).
22. S. K. Gray, G. G. Balint-Kurti, G. C. Schatz, J. J. Lin, X. Liu, S. Harich and X. Yang, *J. Chem. Phys.* **113**, 7330 (2000).
23. F. J. Aoiz, L. Bañares, J. F. Castillo, V. J. Herrero, B. Martínez-Haya, P. Honvault, J. M. Launay, X. Liu, J. J. Lin, S. A. Harich, C. C. Wang and X. Yang, *J. Chem. Phys.* **116**, 10692 (2002).
24. T. W. Whiteley, A. J. Dobbyn, J. N. L. Connor and G. C. Schatz, *Phys. Chem. Chem. Phys.* **2**, 549 (2000).
25. M. Alagia, N. Balucani, L. Cartechini, P. Casavecchia, G. G. Volpi, L. A. Pederson, G. C. Schatz, G. Lendvay, L. B. Harding, T. Hollebeck, T.-S. Ho and H. Rabitz, *J. Chem. Phys.* **110**, 8857 (1999); T. Takayanagi, Y. Kurosaki and K. Yokoyama, *Chem. Phys. Lett.* **321**, 106 (2000).
26. S.-H. Lee and K. Liu, *J. Phys. Chem.* **A102**, 8637 (1998); H. Shiina, A. Miyoshi and H. Matsui, *J. Phys. Chem.* **A102**, 3556 (1998); A. S. Zyubin, A. M. Mebel, S. D. Chao and R. T. Skodje, *J. Chem. Phys.* **114**, 320 (2001).
27. R. Sayós, C. Oliva and M. González, *J. Chem. Phys.* **117**, 670 (2002); M. González, C. Oliva and R. Sayós, *J. Chem. Phys.* **117**, 680 (2002).
28. R. Baer, D. M. Charutz, R. Kosloff and M. Baer, *J. Chem. Phys.* **105**, 9141 (1996).
29. P. Casavecchia, *Rep. Prog. Phys.* **63**, 355 (2000).
30. S. Mahapatra, H. Köppel and L. S. Cederbaum, *J. Phys. Chem.* **A105**, 2321 (2001).
31. W. H. Miller, *J. Phys. Chem.* **102**, 793 (1998) and references therein.
32. T. J. Park and J. C. Light, *J. Chem. Phys.* **88**, 4897 (1988).
33. J. Tennyson and B. T. Sutcliffe, *J. Chem. Phys.* **77**, 4061 (1972).
34. D. Neuhauser and M. Baer, *J. Chem. Phys.* **91**, 4651 (1989); D. Neuhauser, M. Baer, R. S. Judson and D. J. Kouri, *J. Chem. Phys.* **93** 312 (1990).
35. D. H. Zhang and J. Z. H. Zhang, *J. Chem. Phys.* **99**, 5615 (1993); **100**, 2697; 5631 (1994).
36. U. Manthe, *Chem. Phys. Lett.* **241**, 497 (1995).
37. N. Balakrishnan, C. Kalyanaraman and N. Sathyamurthy, *Phys. Rep.* **280**, 79 (1997); M. Beck, A. Jäckle, G. A. Worth and H.-D. Meyer, *Phys. Rep.* **324**, 1 (2000); G. Nyman and H.-G. Yu, *Rep. Prog. Phys.* **63**, 1001 (2000).
38. S. Mahapatra, *Phys. Chem. Chem. Phys.* **2**, 671 (2000).
39. U. Manthe and H. Köppel, *J. Chem. Phys.* **93**, 345 (1990).
40. F. Fernández-Alonso and R. N. Zare, *Ann. Rev. Phys. Chem.* **53**, 67 (2002).
41. R. N. Porter, R. M. Stevens and M. Karplus, *J. Chem. Phys.* **49**, 5163 (1968).
42. R. Englman, *The Jahn–Teller Effect in Molecules and Crystals* (Wiley-Interscience, New York, 1972).

43. R. Bruckmeier, Ch. Wunderlich and H. Figger, *Phys. Rev. Lett.* **72**, 2250 (1994).
44. S. Mahapatra and H. Köppel, *J. Chem. Phys.* **109**, 1721 (1998); *Phys. Rev. Lett.* **81**, 3116 (1998); *Faraday Discuss.* **110**, 248 (1998).
45. Y.-S. M. Wu, A. Kuppermann and B. Lepetit, *Chem. Phys. Lett.* **186**, 319 (1991); Y.-S. M. Wu and A. Kuppermann, *ibid.* **201**, 178 (1993); A. Kuppermann and Y.-S. M. Wu, *ibid.* **205**, 577 (1993).
46. Y.-S. M. Wu and A. Kuppermann, *Chem. Phys. Lett.* **235**, 105 (1995); A. Kuppermann and Y.-S. M. Wu, *Chem. Phys. Lett.* **241**, 229 (1995).
47. L. Schnieder, K. Seekamp-Rahn, J. Borkowski, E. Wrede, K. Welge, F. J. Aoiz, L. Bañares, M. J. D'Mello, V. J. Herrero, V. Sáez Rábanos and R. E. Wyatt, *Science* **269**, 207 (1995); E. Wrede, L. Schnieder, K. H. Welge, F. J. Aoiz, L. Bañares, J. F. Castillo, B. Martínez-Haya and V. J. Herrero, *J. Chem. Phys.* **110**, 9971 (1999).
48. B. K. Kendrick, *J. Chem. Phys.* **112**, 5679 (2000).
49. S. C. Althorpe, F. Fernández-Alonso, B. D. Bean, J. D. Ayers, A. E. Pomerantz, R. N. Zare and E. Wrede, *Nature* **416**, 67 (2002).
50. P. Siegbahn and B. Liu, *J. Chem. Phys.* **68**, 2466 (1978); D. G. Truhlar and C. J. Horowitz, *J. Chem. Phys.* **68**, 2466 (1978).
51. A. J. C. Varandas, F. B. Brown, C. A. Mead, D. G. Truhlar and N. C. Blais, *J. Chem. Phys.* **86**, 6258 (1987).
52. A. I. Boothroyd, W. J. Keogh, P. G. Martin and M. R. Peterson, *J. Chem. Phys.* **104**, 7139 (1996).
53. D. R. Yarkony, private communication.
54. R. Abrol, A. Shaw, A. Kuppermann and D. R. Yarkony, *J. Chem. Phys.* **115**, 4640 (2001).
55. R. Abrol and A. Kuppermann, *J. Chem. Phys.* **116**, 1035 (2002).
56. A. Thiel and H. Köppel, *J. Chem. Phys.* **110**, 9371 (1999).
57. H. Köppel, J. Gronki and S. Mahapatra, *J. Chem. Phys.* **115**, 2377 (2001).
58. J. Schön and H. Köppel, *J. Chem. Phys.* **103**, 9292 (1995).
59. D. T. Colbert and W. H. Miller, *J. Chem. Phys.* **96**, 1982 (1992).
60. M. D. Feit, J. A. Fleck, Jr. and A. Steiger, *J. Comp. Phys.* **47**, 412 (1982).
61. D. Kosloff and R. Kosloff, *J. Comput. Phys.* **52**, 35 (1983).
62. Z. Bačić and J. C. Light, *Ann. Rev. Phys. Chem.* **40**, 469 (1989); F. Quéré and C. Leforestier, *J. Chem. Phys.* **92**, 247 (1990); G. C. Corey and D. Lemoine, *J. Chem. Phys.* **97**, 4115 (1992).
63. W. H. Press, B. P. Flannery, S. A. Teukolsky and W. T. Vetterling, *Numerical Recipes: The Art of Scientific Computing* (Cambridge University Press, Cambridge, 1986), p. 125.
64. S. Mahapatra and N. Sathyamurthy, *J. Chem. Soc. Faraday Trans.* **93**, 773 (1997).
65. U. Manthe and H. Köppel, *J. Chem. Phys.* **93**, 1658 (1990).
66. H. Müller and H. Köppel, *Chem. Phys.* **183**, 107 (1994).

This page intentionally left blank

CHAPTER 14

MULTIDIMENSIONAL DYNAMICS INVOLVING A CONICAL INTERSECTION: WAVEPACKET CALCULATIONS USING THE MCTDH METHOD

G. A. Worth

Dept. of Chemistry,
King's College London,
The Strand, London, WC2R 2LS, UK

H.-D. Meyer and L. S. Cederbaum

Theoretical Chemistry,
University of Heidelberg,
INF 229, 69120 Heidelberg, Germany

Contents

1. Introduction

The time-evolution of a molecular system through a conical intersection is multi-dimensional in nature, i.e. its description cannot be reduced to a single reaction coordinate. In addition to this, such processes are inherently quantum mechanical due to the mixing of electronic states as the intersection is traversed, and a powerful quantum dynamics method is required to treat these, often large, systems accurately.

The most intuitive way of obtaining a numerically exact solution of the time-dependent Schrödinger equation is to use standard wave packet propagation methods. These represent the evolving system wave function using basis set expansion techniques or grid representations.[1–3] Unfortunately, the standard methods are restricted by an exponential increase in the computational resources required with the number of degrees of freedom treated. Therefore, usually no more than 4–6 nuclear modes can be included. Systems in which vibronic coupling plays a role are often much larger than this. To treat these systems using the standard methods, it is then necessary to turn to reduced dimensionality models, in which only a few degrees of freedom are explicitly included, and the remainder either ignored or included in a phenomenological manner.

An alternative is to use approximative methods and include all degrees of freedom. In this chapter we discuss and apply the multi-configuration time-dependent Hartree (MCTDH) method.[4–6] At the present time, this method is the only one that can treat reliably, with controllable accuracy, the multi-mode dynamics of polyatomic systems like the ones discussed below. By using a time-dependent basis set that adapts with the evolving wave packet, the MCTDH algorithm extends wave packet propagation to larger systems. Importantly, calculations converge to the numerically exact solution, and so the error introduced by the approximative nature of the method can be controlled. Using MCTDH, conically intersecting systems with up to 24 degrees of freedom have been studied.

Importantly, the vibronic coupling model Hamiltonian described in detail in Sec. 2 is of a form that allows the full efficiency of the method to be realized. This combination of model and propagation technique thus allows us to study completely and in detail the multidimensional molecular dynamics through a conical intersection.

As well as providing an overview of the MCTDH method and the vibronic coupling Hamiltonian, results will be presented in this chapter that highlight the features of three photo-physical systems in which vibronic coupling plays a crucial role. Here it will become clear that in some cases many degrees of freedom are required for a faithful description of the system dynamics through a conical intersection, and for these the MCTDH method is able to provide accurate information.

2. Vibronic Coupling Hamiltonian

The existence of a conical intersection within or close to the Franck–Condon zone has very dramatic effects on the dynamics and hence on the spectra of polyatomic molecules. Usually, the density of spectral lines becomes very high and only the envelope, rather than the individual line, is of interest. This allows one to concentrate on short-time dynamics. For a reliable treatment of the dynamics it is important to describe the vicinity of the Franck–Condon point accurately. However, as only short-time dynamics is required, the interaction potential away from the Franck–Condon point may be of lesser accuracy.

The adiabatic potential energy surfaces in the vicinity of a conical intersection usually exhibit a rather complicated form, i.e. they are strongly anharmonic and may show double or multiple minima. In contrast to the adiabatic surfaces, the diabatic ones often show an astonishingly simple structure and may — for the region of interest — be well approximated by simple harmonic potentials. Combined with the fact that the diabatic coupling is well behaved, non-singular, and of potential type, this makes the diabatic representation extremely attractive.

We are interested in the study of absorption or ionisation spectra of small polyatomic molecules. Before the absorption of a photon (or the collision with an electron) the molecule is assumed to be in its electronic and vibrational ground state (we ignore rotation). We use the dimensionless normal coordinates of the ground state throughout and write the ground

state Hamiltonian in harmonic approximation as

$$H_{GS} = T_n + \sum_{i=1}^{f} \frac{\omega_i}{2} Q_i^2 \,, \tag{1}$$

$$T_n = -\sum_{i=1}^{f} \frac{\omega_i}{2} \frac{\partial^2}{\partial Q_i^2} \tag{2}$$

where f denotes the number of degrees of freedom and ω_i is the ith normal mode frequency (we use units in which $\hbar = 1$). The ground state is assumed to be well separated from all other electronic states. After excitation, however, the electronic structure is described by a set of close lying, interacting states. The vibronic Hamiltonian for this set of states reads

$$H = T_n + \mathbf{W}(\mathbf{Q}) \,. \tag{3}$$

Assuming — for sake of simplicity — that there are only two interacting excited states of relevance, and developing the diabatic potential energy matrix $\mathbf{W}$ in a power series around the equilibrium position of the ground state, keeping only terms up to second order, one arrives at

$$\begin{aligned} H = T_n \mathbf{1} + \sum_{i=1}^{f} \frac{\omega_i}{2} Q_i^2 \mathbf{1} + \begin{pmatrix} \epsilon_1 & 0 \\ 0 & \epsilon_2 \end{pmatrix} + \sum_{i \in G_1} \begin{pmatrix} \kappa_i^{(1)} & 0 \\ 0 & \kappa_i^{(2)} \end{pmatrix} Q_i \\ + \sum_{(i,j) \in G_2} \begin{pmatrix} \gamma_{i,j}^{(1)} & 0 \\ 0 & \gamma_{i,j}^{(2)} \end{pmatrix} Q_i Q_j + \sum_{i \in G_3} \begin{pmatrix} 0 & \lambda_i \\ \lambda_i & 0 \end{pmatrix} Q_i \\ + \sum_{(i,j) \in G_4} \begin{pmatrix} 0 & \mu_{i,j} \\ \mu_{i,j} & 0 \end{pmatrix} Q_i Q_j \,. \end{aligned} \tag{4}$$

The first two terms reproduce the ground state Hamiltonian, but located on the diagonal of the electronic 2×2 matrix. The two energies ϵ_1 and ϵ_2 are the vertical excitation energies. The next four sums describe the linear and the bilinear coupling terms.

Due to symmetry considerations, the sums run only over restricted sets of modes. G_1 is the set of totally symmetric modes:

$$G_1 : \quad \Gamma_i \supset \Gamma_A \,, \tag{5}$$

where Γ_i is the irreducible representation of the normal–mode coordinate Q_i and Γ_A the totally symmetric representation. These modes provide the

linear intra-state coupling. They are called *tuning modes*, as they modulate the energy gap between the two states.

G_2 is the set of pairs of modes that supplies the bilinear and quadratic on-diagonal couplings:

$$G_2 : \quad \Gamma_i \times \Gamma_j \supset \Gamma_A \,. \tag{6}$$

The parameters $\gamma_{i,j}^{(s)}$ account for frequency shifts and for the so-called Duschinsky rotation.[7]

G_3 is the set of modes which provide linear coupling between the two interacting states:

$$G_3 : \quad \Gamma_i \times \Gamma_1 \times \Gamma_2 \supset \Gamma_A \,, \tag{7}$$

where Γ_1 and Γ_2 are the irreducible representations of the two electronic states considered. These modes account for the linear inter-state coupling. They are called *coupling modes*, as they couple the two electronic states. Finally, G_4 is the set of all pairs of off-diagonal coupling modes which bilinearly enter the Hamiltonian:

$$G_4 : \quad \Gamma_i \times \Gamma_j \times \Gamma_1 \times \Gamma_2 \supset \Gamma_A \,. \tag{8}$$

When only linear coupling terms are included, i.e. when γ and μ are set to zero, one arrives at the so-called linear vibronic coupling (LVC) model.

A high symmetry of the molecule does not only help to (sometimes dramatically) reduce the number of parameters, it also provides a solid basis for the vibronic coupling model Hamiltonian. When the two interacting electronic states are of different symmetry (as assumed here), the inter-state coupling must be an odd function of the coupling coordinate. Hence, there can be no constant or quadratic terms, only linear or bilinear ones are allowed. The vibronic coupling Hamiltonian was first derived by Cederbaum *et al.*[8,9] and is more fully described in a review article by Köppel *et al.*[10] and in Chapter 7 of this book.

Quantum chemistry supplies us with the adiabatic potential energy surfaces V_i, and — at considerably higher cost — with the nonadiabatic coupling elements. Fortunately, the latter are not needed when determining the parameters of the vibronic coupling Hamiltonian, the knowledge of the adiabatic potential energy surfaces alone is sufficient. The parameters of the vibronic coupling Hamiltonian are determined by comparing the adiabatic potential energy surfaces obtained by diagonalising the diabatic model potential with those obtained by quantum chemistry. The most simple and

most direct way is to require that the lowest order derivatives agree at the Franck–Condon point, $\mathbf{Q} = 0$. This readily yields for the linear parameters:

$$\kappa_i^{(s)} = \frac{\partial V_s}{\partial Q_i}|_{\mathbf{Q}=0}\,, \tag{9}$$

$$\lambda_i^2 = \frac{1}{8}\frac{\partial^2}{\partial Q_i^2}\left[V_2(\mathbf{Q}) - V_1(\mathbf{Q})\right]^2|_{\mathbf{Q}=0}\,. \tag{10}$$

The equations for the parameters of the bilinear and quadratic terms are more complicated. They are discussed, e.g. in Ref. 11.

It has been found that the determination of the parameters may become unstable when going beyond the linear model. Much more convenient is then to determine the parameters by a least-squares fit, i.e. to minimize the function[12]

$$L(\kappa,\lambda,\gamma,\mu) = \sum_{n=1}^{M_1} w_n^{(1)}\left[V_1^{\mathrm{mod}}(\epsilon_1,\epsilon_2,\kappa,\lambda,\gamma,\mu;\mathbf{Q}_n) - V_1(\mathbf{Q}_n)\right]^2 + \sum_{n=1}^{M_2} w_n^{(2)}\left[V_2^{\mathrm{mod}}(\epsilon_1,\epsilon_2,\kappa,\lambda,\gamma,\mu;\mathbf{Q}_n) - V_2(\mathbf{Q}_n)\right]^2. \tag{11}$$

Here $\kappa,\lambda,\gamma,\mu$ stand for all the coupling constants and $V_{1,2}^{\mathrm{mod}}$ denote the adiabatic surfaces obtained by diagonalising the potential part of the vibronic coupling Hamiltonian, Eq. (4). There is some unavoidable arbitrariness in this approach, as the points $\mathbf{Q}_n$ and their weights $w_n^{(s)}$ have to be chosen. However, the least-squares approach is to be preferred when more than linear coupling terms are included.

Finally, we remark that one may replace the low-order polynomials by other functions, if those functions would better describe the particular molecule under discussion. For example, the inter-state coupling mode of molecules like ethylene, allene, or butatriene is the torsion of the two CH_2 end-groups. To correctly reproduce the periodicity of this degree of freedom one may replace λQ by $\alpha\sin(\beta Q)$, where $\alpha\beta = \lambda$ and where Q is the normal mode coordinate representing the torsion.[12]

3. Multiconfiguration Time-Dependent Hartree (MCTDH)

3.1. *Introduction*

Wave packet propagation methods are an essential tool for understanding the molecular dynamics underlying many physical phenomena, especially

those that occur on an ultrafast (sub-picosecond) time scale. The standard method is the numerically exact solution of the time-dependent Schrödinger equation, representing the wavepacket and Hamiltonian in an appropriate basis. The method is, however, restricted by the numerical resources required, which grow exponentially with the number of degrees of freedom, and studies of systems with more than six degrees of freedom are in general impossible.

In an attempt to remove this obstacle, approximate methods exemplified by the time-dependent Hartree (TDH) method have been developed. Here, the wave function is represented as a Hartree product of one-dimensional functions, and, as a result, the equations of motion for the wave packet are a set of coupled one-dimensional equations. The effort required is thus significantly reduced, but at the cost that the correlation between the degrees of freedom is no longer treated correctly. For strongly correlated systems like the vibronic coupled ones, TDH completely fails.

The multi-configuration time-dependent Hartree (MCTDH) method[4–6,13,14] combines the benefits of these two extremes. As the name implies, the wave function is described by an expansion in Hartree products (configurations). Using this wave function ansatz and solving the time-dependent Schrödinger equation by a variational method leads to a set of coupled equations of motion for the expansion coefficients and for the functions used to build the Hartree products. The latter are known as *single-particle functions* (SPFs). In the limit of convergence with respect to the number of configurations included, the results become numerically exact. An important feature of the method is that, due to its variational character, small sets of SPFs are in general sufficient to produce good results. The MCTDH method thus requires considerably less effort and memory than the standard one.

3.2. *Equations of Motion*

The MCTDH method is to a large extent defined through its *ansatz* for the wave function[4–6,13]

$$\Psi(Q_1,\ldots,Q_f,t)=\sum_{j_1=1}^{n_1}\cdots\sum_{j_f=1}^{n_f}A_{j_1\ldots j_f}(t)\prod_{\kappa=1}^{f}\varphi_{j_\kappa}^{(\kappa)}(Q_\kappa,t)\,, \tag{12}$$

where f denotes the number of degrees of freedom, $Q_1, \ldots, Q_f$ are the nuclear coordinates, the $A_{j_1 \ldots j_f}$ denote the MCTDH expansion coefficients, and the $\varphi_{j_\kappa}^{(\kappa)}$ are the n_κ expansion functions for each degree of freedom κ, the SPFs.

We simplify the notation by introducing the composite index J

$$J = (j_1, j_2, \ldots, j_f)\,, \tag{13}$$

and the configuration

$$\Phi_J = \prod_{\kappa=1}^{f} \varphi_{j_\kappa}^{(\kappa)}, \tag{14}$$

which is known as a *Hartree product*. The MCTDH wave function is thus a superposition of Hartree products. This explains the name of the method. Alternatively, one may interpret Eq. (12) as an expansion of the wave function in a time-dependent product basis. Since the basis set functions follow the wave packet, one may expect that the numbers, n_κ, of SPFs, needed to ensure convergence, are rather small. The SPFs are given only numerically, and in a practical calculation they thus have to be represented in an underlying — so-called primitive — basis set

$$\varphi_{j_\kappa}^{(\kappa)}(Q_\kappa, t) = \sum_{l=1}^{N_\kappa} c_{l j_\kappa}^{(\kappa)}(t) \chi_l^{(\kappa)}(Q_\kappa)\,.$$

MCTDH will be of advantage if $n_\kappa < N_\kappa$ $(\kappa = 1, \ldots, f)$. The primitive basis functions $\chi_l^{(\kappa)}$ are in practice often replaced by a discrete variable representation (DVR) grid,[6,15,16] and we use the word *grid* as synonymous with *primitive basis*.

The equations of motion for the coefficients and the SPFs are derived from the Dirac–Frenkel variational principle[17,18]

$$\langle \delta\Psi | H - i\partial/\partial t | \Psi \rangle = 0\,. \tag{15}$$

As the coefficients and the SPFs are time-dependent, there are some ambiguities in the equations of motions which must be lifted by imposing constraints. The simplest set of constraints reads

$$\langle \varphi_j^{(\kappa)}(t) | \dot{\varphi}_l^{(\kappa)}(t) \rangle = 0\,. \tag{16}$$

These constraints minimise the motion of the SPFs and keeps them orthonormal. For a discussion of other constraints see Refs. 5 and 6. Employing the above constraints, the equations of motion read[5,6]

$$i\dot{A}_J = \sum_L \langle \Phi_J | H | \Phi_L \rangle A_L \,, \tag{17}$$

$$i\dot{\varphi}_j^{(\kappa)} = \sum_{l,m} \left(1 - P^{(\kappa)}\right) \left(\rho^{(\kappa)^{-1}}\right)_{jl} \langle \mathbf{H} \rangle_{lm}^{(\kappa)} \varphi_m^{(\kappa)} \tag{18}$$

where

$$P^{(\kappa)} = \sum_{j=1}^{n_\kappa} \left|\varphi_j^{(\kappa)}\right\rangle \left\langle\varphi_j^{(\kappa)}\right| \tag{19}$$

denotes the projector on the space spanned by the SPFs for the κth degree of freedom, and

$$\rho_{jl}^{(\kappa)} = \left\langle \Psi_j^{(\kappa)} | \Psi_l^{(\kappa)} \right\rangle \tag{20}$$

and

$$\langle \mathbf{H} \rangle_{jl}^{(\kappa)} = \left\langle \Psi_j^{(\kappa)} \middle| H \middle| \Psi_l^{(\kappa)} \right\rangle \tag{21}$$

denote a *density matrix* and a matrix of *mean-fields*, respectively. Here

$$\Psi_l^{(\kappa)} = \left\langle \varphi_l^{(\kappa)} \middle| \Psi \right\rangle_\kappa \tag{22}$$

denotes a *single–hole function*. Obviously, $\Psi_l^{(\kappa)}$ depends on all coordinates except the κ's one. The mean-fields are thus one-dimensional operators, acting solely on the κ's degree of freedom.

The MCTDH equations of motion (17) and (18) are a fairly complicated set of coupled non-linear differential equations. (Note that $\dot{A}$ depends on φ through $\langle \Phi_J | H | \Phi_L \rangle$ and $\dot{\varphi}$ depends on A through ρ and $\langle \mathbf{H} \rangle$). However, there are fewer equations compared to the set of linear differential equations of the standard method, i.e by simply employing directly the primitive product basis set. In fact, the number of equations is often smaller by several orders of magnitude. This is what makes MCTDH both small (in terms of memory requirement) and fast.

3.3. *Representation of the Hamiltonian*

The solution of the MCTDH equations of motion requires the evaluation of the Hamiltonian matrix $\langle \Phi_J | H | \Phi_L \rangle$ and the mean fields $\langle \mathbf{H} \rangle$ at each time step of the integration. These are formally f and $f-1$ dimensional integrals. Doing the integrals by multi-dimensional quadrature over the primitive grid points would slow down MCTDH such that it would not be competitive.

The multi-dimensional integrations can be circumvented if the Hamiltonian is written as a sum of products of single-particle operators,

$$H = \sum_{r=1}^{s} c_r \prod_{\kappa=1}^{f} h_r^{(\kappa)}, \tag{23}$$

with expansion coefficients c_r. Using Eq. (23) the matrix elements can be expanded as

$$\langle \Phi_J | H | \Phi_L \rangle = \sum_{r=1}^{s} c_r \prod_{\kappa=1}^{f} \left\langle \varphi_{j_\kappa}^{(\kappa)} \middle| h_r^{(\kappa)} \middle| \varphi_{l_\kappa}^{(\kappa)} \right\rangle, \tag{24}$$

and similarly for the mean fields (see Refs. 5 and 6). Note that only one-dimensional integrals are used now. Fortunately, the vibronic-coupling Hamiltonian, derived in the previous section, is precisely of form (23) with comparatively few expansion terms. This makes MCTDH very well adapted for solving the vibronic coupling dynamical problem.

For the general case, we remark that the kinetic energy operator normally has the required form (23), but the potential energy operator often does not. It then may be fitted to the product form. A convenient, systematic, and efficient approach to obtain an optimal product representation is described in Refs. 6 and 19. We finally note that there are other methods which evaluate the Hamiltonian matrix elements efficiently without relying on a product expansion (23). Most notable here is the CDVR method of Manthe.[20]

The building of the mean fields is still the most time consuming part of MCTDH. To reduce the effort, the mean fields are evaluated not at every integrator time step, but at larger (so called *update*) time steps. This *constant mean field* (CMF) integration scheme is described in Refs. 6 and 21. The use of CMF speeds up the calculation by typically a factor of 10.

3.4. *Nonadiabatic Systems*

It was implicitly assumed in the discussion so far that the motion of the molecular nuclei is determined by a single Born–Oppenheimer potential energy surface. However, in vibronic coupling systems, there are several coupled electronic states of importance. The MCTDH algorithm hence has to be extended to deal with more than one electronic state.

The most direct way to accomplish this is to choose one extra degree of freedom, the κ_eth say, to represent the electronic manifold.[22,23] The coordinate Q_{κ_e} then labels the electronic states, taking only discrete values $Q_{\kappa_e} = 1, 2, \ldots, \sigma$, where σ is the number of electronic states under consideration. The number of SPFs for such an electronic mode is set to the number of states, i.e. $n_{\kappa_e} = \sigma$. The equations of motion (17) and (18) remain unchanged, treating nuclear and electronic modes on the same footing. This is called the *single-set formulation*, since only one set of SPFs is used for all the electronic states.

Contrary to this, the *multi-set formulation* employs different sets of SPFs for each electronic state.[24,25] In this formulation, the wave function Ψ and the Hamiltonian H are expanded in the set $\{|\alpha\rangle\}$ of electronic states:

$$|\Psi\rangle = \sum_{\alpha=1}^{\sigma} \Psi^{(\alpha)} |\alpha\rangle \tag{25}$$

and

$$H = \sum_{\alpha,\beta=1}^{\sigma} |\alpha\rangle H^{(\alpha\beta)} \langle\beta| \,, \tag{26}$$

where each state function $\Psi^{(\alpha)}$ is expanded in MCTDH form (12). The derivation of the equations of motion corresponds to the single-set formalism, except that extra state labels have to be introduced on the various quantities such as mean fields and density matrices. The equations of motion now read

$$i\dot{A}_J^{(\alpha)} = \sum_{\beta=1}^{\sigma} \sum_{L} \langle \Phi_J^{(\alpha)} | H^{(\alpha\beta)} | \Phi_L^{(\beta)} \rangle A_L^{(\beta)} \,, \tag{27}$$

$$i\dot{\varphi}_j^{(\alpha,\kappa)} = \sum_{lm\beta} \left(1 - P^{(\alpha,\kappa)}\right) \left(\rho^{(\alpha,\kappa)^{-1}}\right)_{jl} \langle \mathbf{H} \rangle_{lm}^{(\alpha\beta,\kappa)} \varphi_m^{(\beta,\kappa)} \,, \tag{28}$$

with mean-fields

$$\langle H\rangle_{jl}^{(\alpha\beta,\kappa)} = \langle \Psi_j^{(\alpha,\kappa)} | H^{(\alpha\beta)} | \Psi_l^{(\beta,\kappa)} \rangle \,. \tag{29}$$

The superscripts α and β denote to which electronic state the functions and operators belong. A fuller derivation of these equations is given in Refs. 6, 21 and 25.

The single-set formulation is to be preferred when the different electronic states have a similar form. The well known spin-boson model is in this category.[26] When the motion on the different electronic states is very different, the multi-set formulation becomes the appropriate choice. The smaller number of SPFs needed for convergence then over-compensates the overhead of the multi-set formulation. For vibronically coupled systems, we have always chosen the multi-set formulation.

3.5. *Mode Combination*

The importance of the memory requirements for large systems can be easily seen by looking at what would be needed for studying the dynamics of the pyrazine molecule ($C_4H_4N_2$). This system has 25 degrees of freedom (24 vibrational modes and a set of electronic states). Although in a study which we have performed[14] the mean grid length for the degrees of freedom was only $N \approx 7.4$, the corresponding direct product grid consists of about 10^{21} points, making the use of the standard method totally infeasible. Unfortunately, the MCTDH method as presented above, using a set of SPFs per degree of freedom, is also unable to treat this system on a workstation: the program requires memory equivalent to approximately 12 wave function vectors, double precision complex, and so with only 5 SPFs for each of the four strongly coupled modes and only 2 SPFs per mode for the remaining degrees of freedom the calculation would need $5^4 \times 2^{21} \times 12 \times 16$ Bytes ≈ 234 GB.

The memory requirements can, however, be reduced, if SPFs are used that describe a set of degrees of freedom, rather than just one. The wave function ansatz, Eq. (12), is then rewritten as a multi-configuration over p generalised "particles",

$$\Psi(q_1,\ldots,q_p,t) = \sum_{j_1=1}^{\tilde{n}_1} \cdots \sum_{j_p=1}^{\tilde{n}_p} A_{j_1\ldots j_p}(t) \prod_{\kappa=1}^{p} \varphi_{j_\kappa}^{(\kappa)}(q_\kappa,t) \,, \tag{30}$$

where $q_\kappa = (Q_i, Q_j, \ldots)$ is the set of coordinates combined together in a single particle, described by $\tilde{n}_\kappa$ functions, termed *multi-mode* SPFs to distinguish them from the usual *single-mode* SPFs.

By combining d degrees of freedom together to form a set of $p = f/d$ particles, the memory requirement reads

$$\text{memory} \sim p\tilde{n}N^d + \tilde{n}^p\,, \tag{31}$$

where $\tilde{n}$ is the number of multi-mode functions needed for the new particles. The first and second term of Eq. (31) represent the space taken by the SPFs and the coefficients, respectively. This equation holds as well for the uncombined case when setting $p = f, d = 1$ and $\tilde{n}_\kappa = n_\kappa$. For large systems, the second term of Eq. (31) dominates. Thus, if

$$\tilde{n} < n^d\,, \tag{32}$$

i.e. the number of multi-mode functions is less for a multi-dimensional particle than the product of single-mode functions needed for the separate degrees of freedom, there can be a large saving in memory required.

The inequality (32) will in general be fulfilled. This comes from the fact that the number of SPFs required is related to the strength of coupling between the particle and the rest of the system. By combining modes, this coupling is reduced as the coupling between the combined degrees of freedom is now treated within the SPFs for the combined mode. For example, consider a system with a set of coupled modes. The coupling will lead to a wave function which is poorly described by a Hartree product, and many single-mode SPFs would be needed. Going to the extreme and combining all the degrees of freedom together into one particle, only one SPF will be required: the standard numerically exact wave function.

To summarize, if only single-mode functions are used, i.e. $d = 1$, the memory requirement is dominated by the number of A-coefficients, n^f. By combining degrees of freedom together, this number can be reduced, but at the expense of longer product grids required to describe the now multi-mode SPFs. At the extreme of all degrees of freedom combined together, one arrives at N^f. Between these two extremes, however, there is an optimally small amount of memory required. Similar considerations apply to the numerical effort. For a fuller discussion see Ref. 6. Combining modes is not recommended for small systems, unless two degrees of freedom are very strongly coupled.[27] For large systems however, the effect is very

significant, and enables the 24 nuclear degrees of freedom pyrazine system to be studied.[11,14,28] More recently, it was even possible to study a 80 mode spin-boson model with the MCTDH method[26] using highly combined SPFs.

4. Examples of Dynamics

4.1. *Spectral Intensities*

In this section, results are presented from MCTDH wavepacket propagation calculations[29] on systems involving a conical intersection. The accuracy of the method is such that all results can be taken as complete quantum dynamical calculations, while the power is seen in that calculations with up to 24 vibrational modes have been made, allowing calculations to be made without resorting to drastic approximations. Photophysical systems from three molecules will be looked at: butatriene, allene and pyrazine.

The property of interest here is a spectrum, either an absorption spectrum (pyrazine) or photoelectron spectrum (butatriene and allene). The spectrum $\sigma(\omega)$ is calculated by Fermi's golden rule:[8]

$$\sigma(\omega) = a(\omega) \sum_n |\langle \Psi_n^f | \hat{T} | \Psi_0^i \rangle|^2 \delta \left(\omega + E_0^i - E_n^f \right) . \tag{33}$$

Here, the final states $\{|\Psi_n^f\rangle\}$ represent eigenstates of the Hamiltonian with energies E_n^f, and $\hat{T}$ denotes the appropriate transition operator. The initial state $|\Psi_0^i\rangle$ (with energy E_0^i) is the electronic and vibrational ground state of the molecule. The pre-factor $a(\omega)$ is proportional to ω for absorption spectra, but is taken constant for ionization spectra.

The spectrum is conveniently evaluated by Fourier transform of the autocorrelation function. To this end, one defines the initial state of the propagation by

$$\Psi(0) = \hat{T} |\Psi_0^i\rangle . \tag{34}$$

As we assume a vertical transition (Condon approximation), $\Psi(0)$ is the ground-state wave packet placed on an excited or ionic diabatic potential energy surface. The autocorrelation function is defined as

$$C(t) = \big\langle \Psi(0) \big| \Psi(t) \big\rangle = \big\langle \Psi^*(t/2) \big| \Psi(t/2) \big\rangle \tag{35}$$

where the second form is only valid for a real initial wave function and a symmetric Hamiltonian. These requirements are fulfilled here and the

second form is particularly useful in conjunction with the MCTDH method, as it reduces the required length of propagation by a factor of two.

The absorption (or ionization) cross-section can now be expressed as

$$\sigma(\omega) = a(\omega)\pi^{-1}\mathrm{Re}\int_0^\infty C(t)e^{i(\omega+E_0^i)t}dt\,. \tag{36}$$

To compensate for the finite time of the propagation, the autocorrelation must be multiplied by a function which ensures that it goes to zero at the end of the propagation. If this is not done, spurious structures (known as Gibbs phenomenon) will be seen in the spectrum. We choose the function

$$g(t) = \cos\left(\frac{\pi t}{2T}\right)\theta\left(1-\frac{|t|}{T}\right) \tag{37}$$

for this task, where T is the length of the propagation, and θ is the Heaviside step function. In order to compare the calculated spectrum with the experimental one, it may also be necessary to multiply the autocorrelation function with a damping factor

$$f(t) = \exp(-t/\tau) \tag{38}$$

where τ is a time constant describing a phenomenological broadening of the spectrum due to, e.g. spectral resolution. This is equivalent to convoluting the spectrum with a Lorentzian function of full width at half-maximum (FWHM) of $\Gamma[\mathrm{eV}] \approx 1.31/\tau[\mathrm{fs}]$.

4.2. *The Butatriene Cation $\tilde{X}/\tilde{A}$ Manifold*

The first demonstration[8] of the dramatic effects which a conical intersection may have on the dynamics of a molecular system was given through the computation of the photoelectron spectrum of butatriene (C_4H_4). The measured spectrum[30] of the ground ($\tilde{X}$) and first excited ($\tilde{A}$) electronic states of the cation of this planar molecule is shown in Fig. 1(a). Two intense peaks are seen, which lie at the energies expected for the two electronic states. Unexpectedly, between these peaks is also a structured region, which is due to the strong vibronic coupling between these states. The calculation could reproduce the measured spectrum and, in particular, the so called "mystery band", i.e. the intensity between the two main peaks. As the "mystery band" is not understandable in an adiabatic picture, this early study vividly proved the importance of nonadiabatic effects caused by a conical intersection when computing spectra.

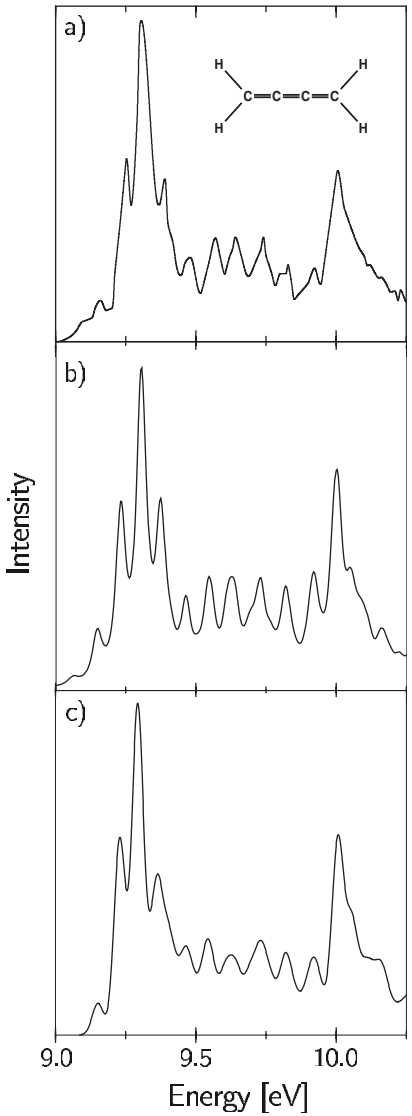

Fig. 1. The $\tilde{X}/\tilde{A}$ spectrum of the butatriene radical cation. (a) Experimental results from Ref. 30. (b) 2-mode model from Ref. 10. (c) 18-mode model from Ref. 12. The model spectra are the Fourier Transform of the autocorrelation function calculated using the MCTDH wavepacket propagation method. A damping function of $\tau = 55\,\text{fs}$ has been used.

The molecule has D_{2h} symmetry and the states of the cation are $\tilde{X}^2B_{2g}$ and $\tilde{A}^2B_{3u}$. Thus, from the symmetry arguments of the vibronic coupling model, the linear coupling is due to modes with A_u symmetry, of which butatriene has only one, the ν_5 torsional motion. Four modes of A_g symmetry are present and able to be tuning modes, but the ν_{14} central C–C stretch dominates, with a coupling constant an order of magnitude larger than the coupling constants of the other modes.

Using this information, a two-dimensional vibronic coupling model Hamiltonian, Eq. (4), has been set up and parametrised using *ab initio* calculated data.[8,10] Figure 2 shows the adiabatic potential energy surfaces for these states in the space of the two dominant vibrational modes. These surfaces are the eigenvalues of the diabatic potential matrix, **W**, in Eq. (3). In Fig. 2(a) the vibronic coupling has been set to zero. Two inter-penetrating wells are seen, representing the uncoupled oscillators, shifted along the symmetric vibrational coordinate. In Fig. 2(b), the effect of including the interstate coupling is obvious: the lower well has broadened and split into a double well. The upper and lower surfaces also now meet at a point, the conical intersection.

The spectrum from this two-dimensional model is shown in Fig. 1(b). The spectrum has been broadened by multiplying the autocorrelation function with Eq. (38) with a time constant of 35 fs. This is equivalent to convoluting the peaks in the spectrum with a fairly broad Lorentzian with 40 meV FWHM. The agreement with the experimental spectrum is very good: proof that the central band is due to a breakdown of the Born–Oppenheimer approximation by vibronic coupling.

To see the effect of the vibrational modes which have been neglected in this 2-mode model, an 18-mode model Hamiltonian has also been parametrised including all the vibrational modes, and coupling coefficients up to second order (quadratic and bilinear).[12] The spectrum from this 18-mode model is shown in Fig. 1(c). Little change is seen, showing that in this case the two modes previously identified dominate the dynamics. This will be shown not to be the case in other systems.

Although the 2-mode model can reproduce the experiment astonishing well, it can do so only by using effective coupling constants. To reproduce the experiment, the coupling constants had to be manually adjusted and differ from the *ab initio* values by factors between 1.3 and 1.5. In contrast, the 18-mode model used the un-modified *ab initio* values for all coupling

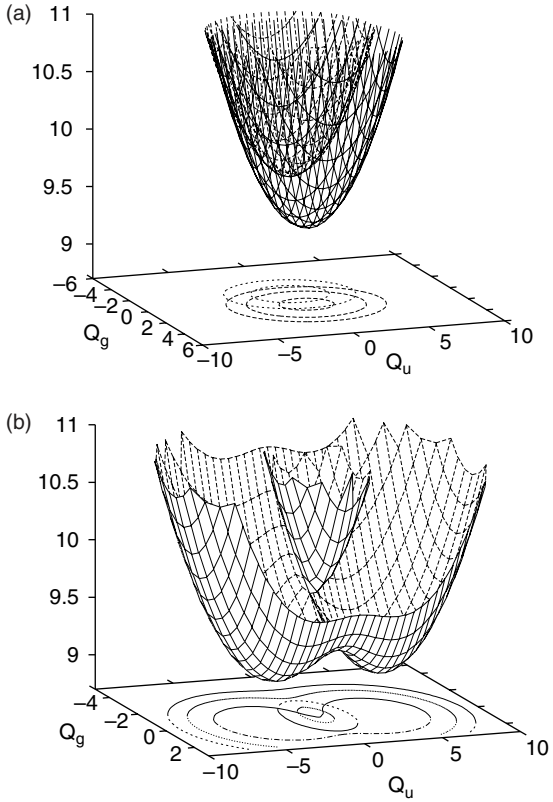

Fig. 2. The adiabatic potential energy surfaces for the $\tilde{X}/\tilde{A}$ states of the butatriene radical cation. (a) in the absence of vibronic coupling. (b) including vibronic coupling. Q_u is the unsymmetric normal mode corresponding to the $\nu_5(a_u)$ torsional mode, and Q_g is the symmetric normal mode corresponding to the ν_{14} central C–C stretching vibration.

constants except for the linear interstate coupling constant λ. The latter was increased by 19% with respect to the *ab initio* data. (See Ref. 12 for details). The rather large changes required for the parameters of the 2-mode model indicate that here the two modes act as effective modes, partially accounting for the neglected modes through their modified parameters.

As this system can be described by a 2-mode model, we are able to plot the complete nuclear wave function as it evolves in time, and this provides a base against which other systems can be compared. In Fig. 3, the time-evolution of the system density is shown in the diabatic picture.

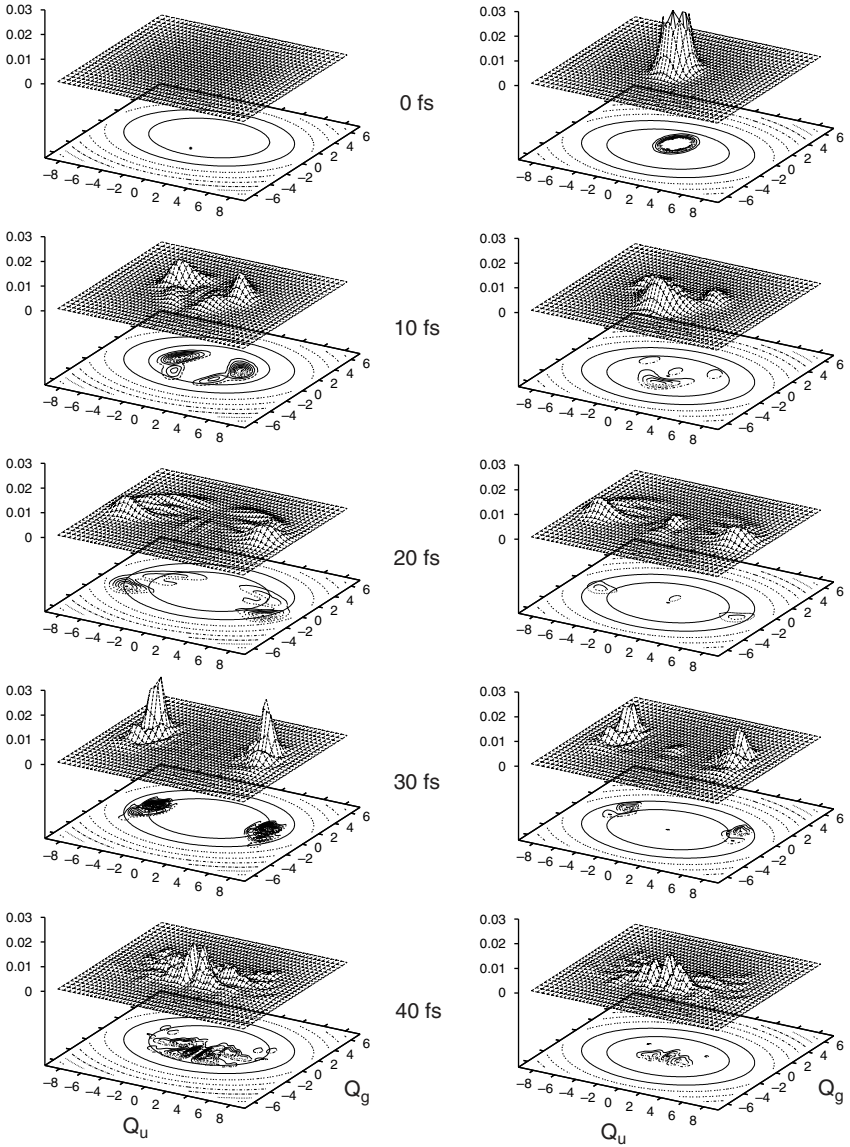

Fig. 3. The time evolution of a wavepacket through the conical intersection between the $\tilde{X}/\tilde{A}$ PES of the butatriene radical cation in the diabatic picture. The location of the conical intersection is indicated by a thick point in the uppermost plot. Left: first surface, right: second surface.

The initial wave packet is the ground state vibrational eigenfunction, a Gaussian function centred around $\mathbf{Q} = 0$, projected onto the upper state. Initial motion remains in this state, moving across the upper well, until the conical intersection is reached. At this point, which is reached after only a few femtoseconds, density is transferred to the lower state, appearing on two sides of the cone. The density on both surfaces then travels around the respective minima, and returns to the intersection after 40 fs, when interstate crossing (in both directions) occurs once more. In this undamped two-mode system, this pattern is repeated ad infinitum.

In Fig. 4, the time-evolution of a wavepacket is shown again, but this time in the adiabatic picture. As the conical intersection lies within the Condon region, the excitation results in a small occupation of the lower adiabatic state besides mainly occupying the upper. Following the evolution of the packet on the upper surface, the cone in Fig. 2(b), the density quickly disappears, and is transferred to the lower state within 30 fs. The dynamics on the lower surface is more complicated, but similar to that in the diabatic picture, with the density again flowing around the minimum, coming away from two sides of the intersection. After 40 fs the density returns to the intersection point and some re-crossing to the upper state is seen.

4.3. *The Allene Cation $\tilde{A}/\tilde{B}$ Manifold*

Despite its chemical similarity to butatriene, allene (C_3H_4) has a very different set of electronic states due to the fact that the ground state equilibrium structure is D_{2d}, with the CH_2 groups perpendicular to one another. The ground state of the cation is doubly degenerate, $\tilde{X}^2E$, and forms an example of the relatively rare $E \otimes \beta$ Jahn–Teller interaction.[31,32] An even more interesting system is found in the next band of the photoelectron spectrum, which is shown in Fig. 5(a). At low energies a set of ordered peaks are seen, with the structure being washed out at high energies. This band in fact contains two states, the close lying $\tilde{A}^2E$ and $\tilde{B}^2B_2$ states.[33] The $\tilde{A}^2E$ is again a $E\otimes\beta$ Jahn–Teller state, which then further interacts with the $\tilde{B}^2B_2$ state via pseudo-Jahn–Teller coupling. This system provides a challenge for dynamics calculations, as all fifteen vibrational modes couple in first order.

Early calculations focused on the low energy $\tilde{A}^2E$ band structure.[32] Here the four doubly degenerate vibrations can be ignored, as they do not couple these states. Of the remaining seven modes, the most strongly

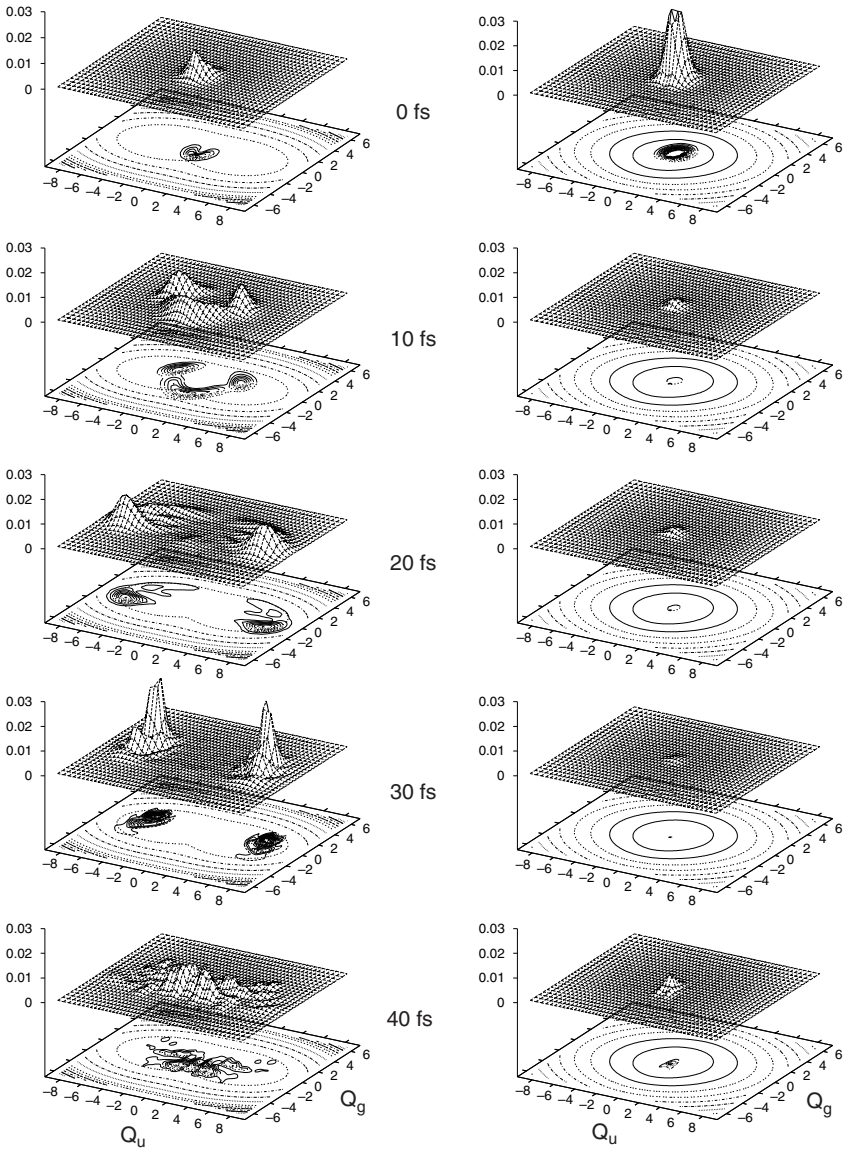

Fig. 4. The time evolution of a wavepacket through the conical intersection between the $\tilde{X}/\tilde{A}$ PES of the butatriene radical cation in the adiabatic picture. The location of the conical intersection is indicated by a thick point in the uppermost plot. Left: lower surface, right: upper surface.

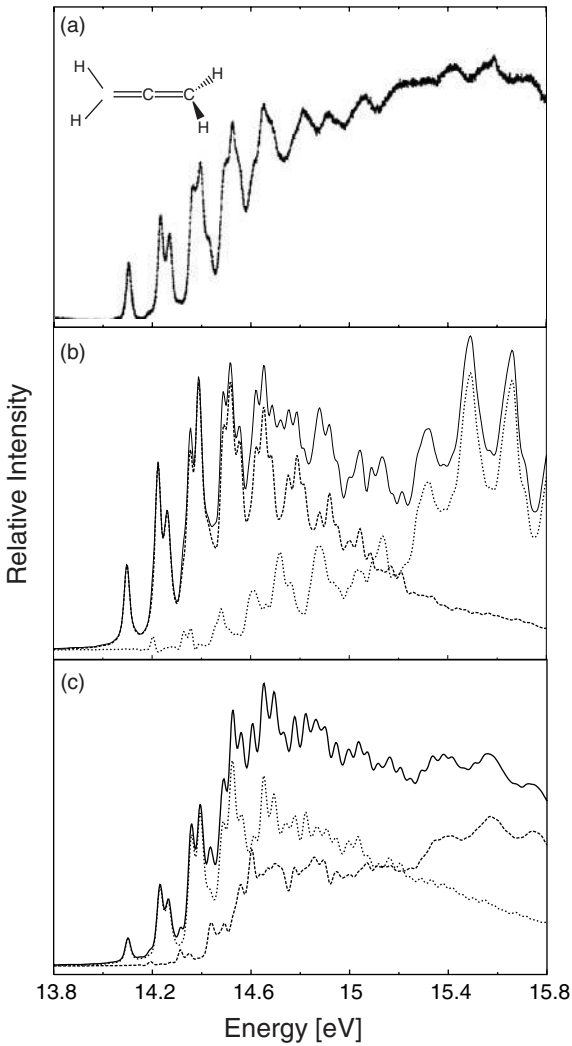

Fig. 5. The $\tilde{A}/\tilde{B}$ spectrum of the allene radical cation. (a) Experimental results from Ref. 33. (b) 10-mode model from Ref. 34. (c) 15-mode model from Ref. 35. The model spectra are the Fourier Transform of the autocorrelation function calculated using the MCTDH wavepacket propagation method. A damping function of $\tau = 50\,\text{fs}$ has been used.

coupled of each symmetry type were taken to provide a 3-mode model with the ν_4 (B_1), ν_7 (B_2), and ν_2 (A_1) modes. The first two of these provide the Jahn–Teller active modes, coupling the degenerate electronic states. From inspection of the orbitals, the B_1 torsional mode provides the off-diagonal coupling and B_2 the on-diagonal coupling. The A_1 mode is also activated by excitation from the neutral ground state, and appears on the diagonal of the Hamiltonian. The coupling constant is, however, the same for both states by symmetry. After adjustment of the parameters, this model is able to adequately describe the experimental spectrum.

A later study[34] added the pseudo-Jahn–Teller coupling to the $\tilde{B}^2B_2$ state to this model. This resulted in a 10-mode model, the spectrum of which is shown in Fig. 5(b). The two parts of the spectrum are plotted separately to show that the peaks at either end can be assigned to each state, with the overlap in the middle forming a structureless band.

Including all 15 vibrational modes, however, was not possible within the linear model in a satisfactory manner. In particular, inclusion of the ν_3 (A_1) mode provided problems, as it is also significantly coupled to the excitation. The problem was traced to the lack of second-order coupling. On calculating these parameters, it was found that the ν_2 and ν_3 modes were strongly coupled, and undergo Duschinsky rotation. No correction of the first order terms was then required and the resulting spectrum from the 15-mode model is shown in Fig. 5(c).[35]

How this second order model changes the interpretation of the spectrum arising from the Jahn–Teller active $\tilde{A}$ band is made clear in Fig. 6. In (a) the spectrum obtained from a 2-mode model with the adjusted parameters of Ref. 32 is shown. The progression of peaks is in good agreement with the experimental spectrum, and these can then be assigned to the ν_7 and ν_2 vibrations, and overtones of these. Figure 6(b) shows the same spectrum from the three most important modes from the second order model. The interpretation here is that the lower peak is due to a combination of ν_2 and ν_3 vibrations, while the higher peak is from ν_7. This interpretation is more satisfactory, as it fits the *ab initio* data better. Moreover, the inclusion of ν_3 and — to a lesser extent — of all the other neglected modes significantly increases the density of states, leading to an enhanced spectral intensity in the vicinity of 15 eV (see Fig. 5).

In Fig. 7 the time evolution of the diabatic state populations in the $\tilde{A}/\tilde{B}$ manifold are plotted. In (a) the results are shown after excitation

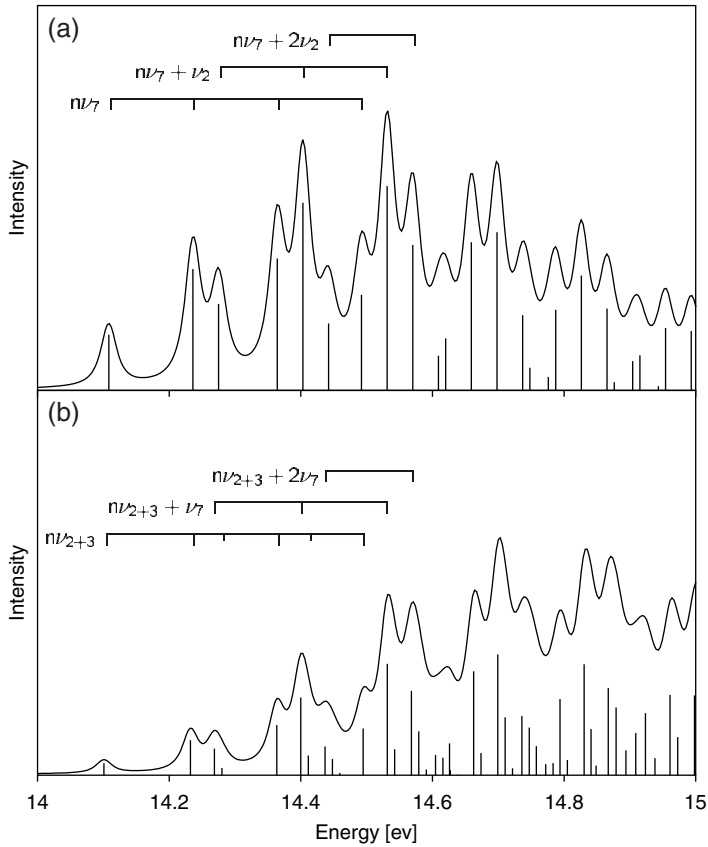

Fig. 6. The spectrum of the Jahn–Teller split $\tilde{A}^2E$ state of the allene radical cation using different reduced dimensionality models. (a) A linear 2-mode model including the vibrational modes ν_2 and ν_7 with parameters adjusted to fit the spectrum. (b) A 2nd order 3-mode model including the vibrational modes ν_2, ν_3 and ν_7.

takes place from the neutral ground state to the B_2 state. The population is seen to rapidly decay, transferring to the lower energy E state within 20 fs. Weak recurrences are then seen with a time period of 50 fs.

In Fig. 7(b) the population is shown after excitation to one component of the E state. Population transfer takes place initially to the B_2 state before being transferred on to the other E component. This process continues in an oscillatory fashion with a frequency of approximately 25 fs, which corresponds to the frequency of the ν_2 mode. This process is in fact a

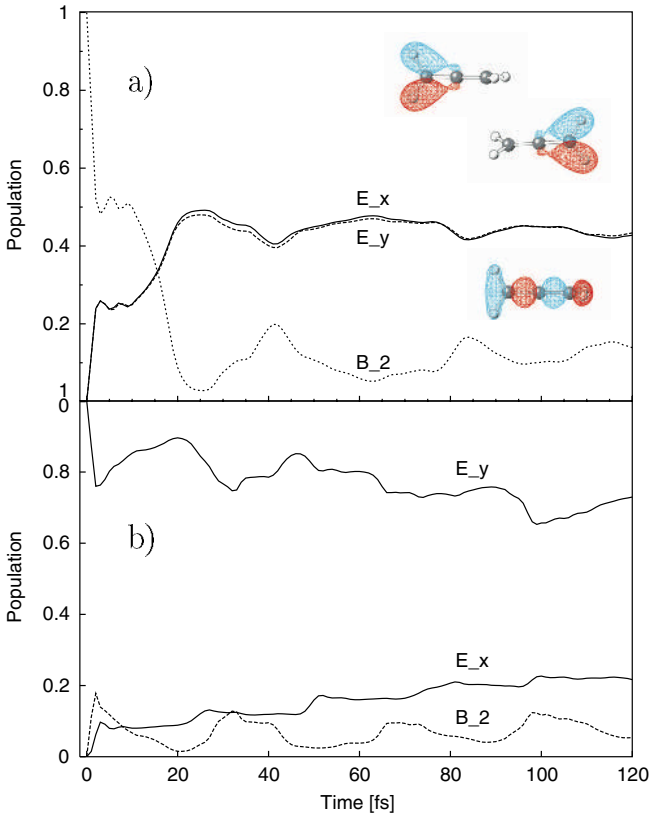

Fig. 7. The time evolution of state population transfer in the $\tilde{A}/\tilde{B}$ manifold of the allene radical cation after excitation to (a) the $\tilde{B}(B_2)$ and (b) the $\tilde{X}(E_y)$ diabatic state.

step-wise electron transfer process.[36] The orbitals of the states are plotted in Fig. 7(a), and it can be seen that excitation to a component of the E state corresponds to removing an electron from one end of the molecule. Population transfer corresponds to transferring electron density from the other end to fill this hole. The B_2 state, which has density all along the conjugated system, thus plays a role in this transfer.

4.4. *The Pyrazine S_1/S_2 Manifold*

A classic example of the effect of a conical intersection on the photophysics of a molecule is found in the absorption spectrum of the pyrazine

molecule.[37,38] In contrast to the S_1 (B_{3u}) band, which has a well defined vibronic structure, the S_2 (B_{2u}) state gives rise to a very broad band with little structure. This is reproduced in Fig. 8(a).

Using the vibronic coupling model, a conical intersection has been identified and characterized.[39] In the linear model, there is one coupling mode, ν_{10a} with B_{1g} symmetry, and five possible tuning modes with A_g symmetry. The spectrum from a linear 4-mode model, which ignores the two weakest coupled tuning modes, is shown in Fig. 8(b), and is seen to agree very well with the experimental one. To obtain this spectrum, however, a large phenomenological broadening has been added, with the spectrum being convoluted with a broad Lorentzian of 37 meV FWHM ($\tau = 35$ fs in Eq. (38)).

In Fig. 8(c) the spectrum is shown from a second order model, which includes all 24 modes.[11] Here a damping function with a time-constant of 150 fs is sufficient for good agreement with the experimental spectrum, equivalent to the broadening due to the spectrometer. Thus, while the major features of the spectrum can be accounted for by the 4-mode model, its envelope can only be explained by including all the modes.

This calculation was a formidable task. Alone setting up the Hamiltonian, which involved calculating and testing 102 coupling constants, was very time consuming. 24 vibrational modes and 2 coupled electronic states is well beyond the reach of standard wave packet methods. This was possible only by using the MCTDH method, with the refinements of combined modes, and the multi-set formulation. Even so, 2 771 440 configurations were required for good quality results, and the propagation of 150 fs required 650 MB and 485 h on a Cray T90 vector computer. In contrast, the 4-mode model required 20 min and 16 MB on an IBM RS/6000 power 2 workstation.

4.5. *The Pyrazine Molecule Viewed as a System Coupled to a Bath*

One question that arises in the pyrazine study is as to whether it is really necessary to accurately describe the 20 weakly-coupled modes, or could a weakly coupled bath lead to the same result, namely a seemingly homogeneous broadening of the 4-mode model spectrum. A model in which the 4-mode linear model is coupled to a weak bath has thus also been set up.[40] The bath modes are coupled linearly to each state, and provide pathways

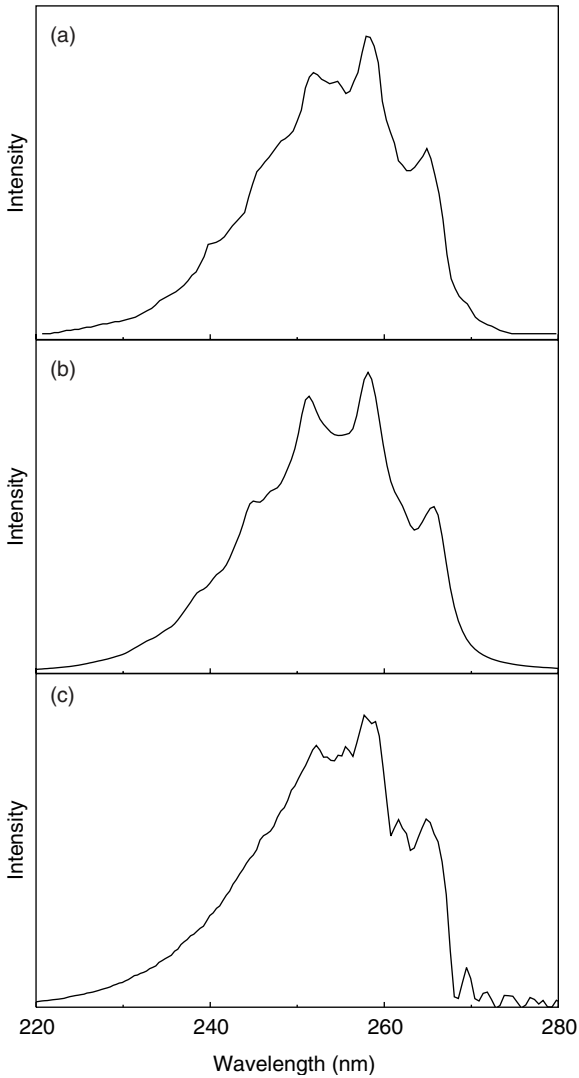

Fig. 8. The S_2 absorption spectrum of the pyrazine molecule (a). Experimental results from Ref. 37. (b) 4-mode model from Ref. 39. (c) 24-mode model from Ref. 11. The model spectra are the Fourier Transform of the autocorrelation function calculated using the MCTDH wave packet propagation method. A damping function of $\tau = 30\,\text{fs}$ has been used in (b) and $\tau = 150\,\text{fs}$ in (c).

for the dephasing of the wavepacket. We have studied this model using the MCTDH method,[14] with which it was possible to perform accurate quantum dynamical calculations including up to 20 bath modes.

These calculations demonstrate the scaling of the MCTDH method with system size. The computer resources required are summarized in Table 1. For comparison, it is indicated how many MCTDH particles (effective degrees of freedom in the calculation) were used, and how many configurations were required. Both memory requirements and CPU-time required increase rapidly: not exponentially, however, but roughly like dimension to the third power. For a 120 fs propagation, this 4-mode model, which is slightly different from that used above, required 4 MB and 6 min, while the system coupled to 20 bath modes required 687 MB and 3100 min (≈52 h). Even so, the 24-mode calculations are easy to perform on a normal workstation. The much longer time required for the 24-mode second-order pyrazine model calculations discussed above is due to the large number of terms in the Hamiltonian required.

The spectra from the 4-mode model coupled to 0, 5, 10, and 20 bath modes are plotted in Figs. 9(a)–(d). The addition of the bath clearly results in the structure of the spectrum being washed out. The experimental spectrum is, however, not obtained. The effect of the bath modes is made clear in Figs. 10(a)–(d), in which the absolute values of the autocorrelation function for the 4-mode system with 0, 5, 10, and 20 bath modes is plotted. Just the strongest 5 bath modes lead to a significant damping of the oscillations in the function. This is simply due to the extra volume of phase-space available

Table 1. Summary of computer resources required for calculations made using the MCTDH method on a 4-mode model of the S_1 and S_2 states of the pyrazine molecule after excitation to the S_2 state, and coupled to harmonic oscillator baths of varying size.[14] The degrees of freedom (no. of bath modes + 4) were combined together into the no. of particles listed, and the no. of configurations required for converged calculations are given. The wave packet was propagated for 120 fs.

Bath Modes	MCTDH Particles	Configurations	Memory (MB)	CPU Time[a] (min)
0	4	10 575	3.7	6.3
5	4	74 024	48.9	185.0
10	5	142 350	52.5	196.9
20	7	3 759 552	686.5	3095.6

[a] On an IBM RS/6000 power2 workstation.

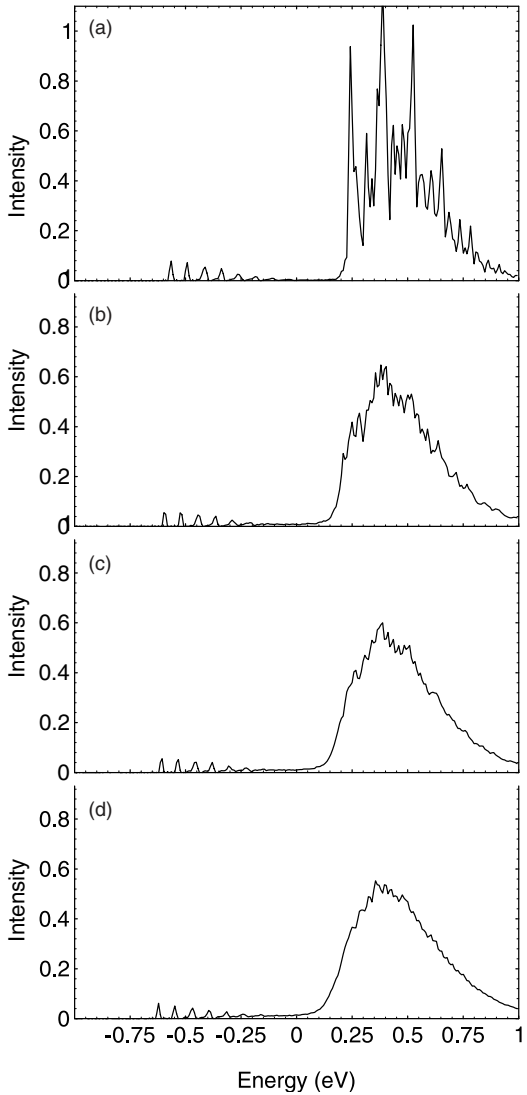

Fig. 9. The effect of a bath on the spectrum of the 4-mode model for the S_1/S_2 manifold of the pyrazine molecule after initial excitation to the S_2 state. Taken from Ref. 14. (a) No bath present. (b) 5 bath modes. (c) 10 bath modes. (d) 20 bath modes. The spectra are calculated from the Fourier Transform of the autocorrelation function. No phenomenological broadening has been added, but a cutoff function is used to remove artefacts due to the finite time-length (240 fs) of the autocorrelation function.

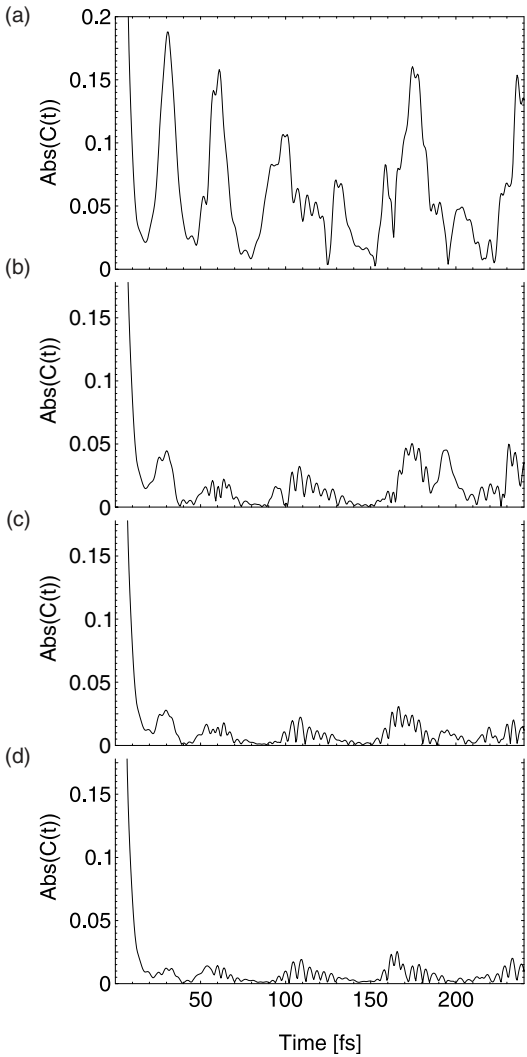

Fig. 10. The effect of a bath on the autocorrelation function of the 4-mode model for the S_1/S_2 manifold of the pyrazine molecule after initial excitation to the S_2 state. Taken from Ref. 14. (a) No bath present. (b) 5 bath modes. (c) 10 bath modes. (d) 20 bath modes.

in which the wavepacket dissipates, and thus dephases. It is clear from this plot that the bath model chosen does not lead to a homogenous broadening of the spectrum, as extra structure is also added (see for example the first peak). Interestingly, even with the 20-mode bath a definite beat-like structure is present, and it is as if the bath is filtering the spectrum — while the wave packet at most frequencies is dephased, certain frequencies survive.[28]

Figure 11 shows the time-evolution of the population of (a) diabatic and (b) adiabatic S_2 states. In all cases, the population decays sharply during the first 40 fs. After approximately 80 fs, a recurrence occurs, and population is transferred back from the S_1 to the S_2 state. The adiabatic populations exhibit a faster, and more complete, population transfer. The recurrence is also much smaller. In both diabatic and adiabatic pictures, the presence of the bath increases the rate and amount of transfer. With 10 bath modes, the population of the adiabatic S_2 state goes very nearly to zero over this time-scale. The 20 bath mode model adiabatic state populations could not be calculated due to the technical problem of the diabatic — adiabatic transformation for a system of this size.

We finally mention that the system/bath picture for studying the pyrazine spectrum has been adopted by two other publications.[41,42] There, however, the bath was treated implicitly by dissipative operators of the Lindblad type.

5. Conclusions

A very useful starting point for the study of non-adiabatic processes, which are common in photochemistry and photophysics, is the vibronic coupling model Hamiltonian. The model is based on a Taylor expansion of the potential surfaces in a diabatic electronic basis, and it is able to correctly describe the dominant feature resulting from vibronic coupling in polyatomic molecules: a conical intersection. The importance of such intersections is that they provide efficient non-radiative pathways for electronic transitions. Not only is the position and shape of the intersection described by the model, but it also predicts which nuclear modes of motion are coupled to the electronic transition which takes place as the system evolves through the intersection.

The modes involved to first order, i.e. including coupling terms linear in the nuclear coordinates, are the coordinates of the correct symmetry

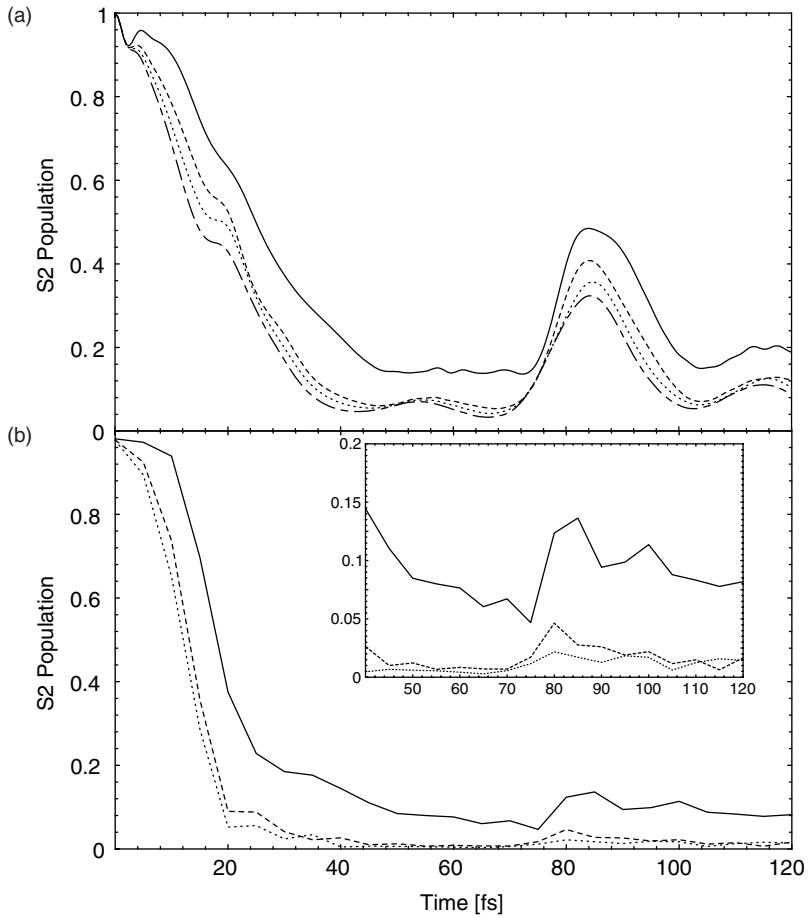

Fig. 11. The effect of a bath on the rate of inter-state crossing in the 4-mode model of the pyrazine S_1/S_2 manifold of the pyrazine molecule after initial excitation to the S_2 state. Taken from Ref. 14. (a) diabatic state population. (b) adiabatic state population. Full line: 0 bath oscillators. Dashed line: 5 bath oscillators. Dotted line: 10 bath oscillators. Dash-dot line 20 bath oscillators (diabatic state only).

required to couple the electronic states, as well as the totally symmetric coordinates, which modulate the energy gap. These are often only a few modes in total, and may provide a reasonable description of the major physics of the system. Neglecting further the most weakly coupled modes, this can result in small, 2, 3 or 4 mode models, which can then be treated

using standard wave packet methods to obtain a full quantum mechanical solution of the problem.

To second order, however, all degrees of freedom are involved. Even for small molecules (5–12 atoms, say) these systems are no longer accessible to standard quantum dynamics methods. Here, the MCTDH method becomes an essential tool. MCTDH is an efficient wave packet propagation method, accurate, yet flexible, and applicable to a wide range of problems. Its ability to include more degrees of freedom than conventional wave packet methods is of particular importance in the study of the multi-dimensional dynamics associated with nonadiabatic processes. Using this method, we have been able to treat a number of typical nonadiabatic systems completely up to second order, i.e. including all degrees of freedom.

Our calculations show that these second order terms are important for a quantitative description of nonadiabatic systems. This is demonstrated in the pyrazine S_1/S_2 system, where a reduced 4-mode model provides a qualitative picture with the main peaks of the spectrum in the correct places. The addition of second order terms and all degrees of freedom, results in the correct spectral envelope also being produced by the model. Also in the allene $\tilde{A}/\tilde{B}$ system, the second order terms are required, not only for the correct description of the Duschinsky rotation in the excited state, but also for the high spectral density between the two bands. Even in the butatriene $\tilde{X}/\tilde{A}$ system, in which second order terms play a minor role in the description of the spectral band, the inclusion of these terms means that the *ab initio* data could be taken with minimal adjustment, whereas a reduced dimensionality model required significant adjustment of the expansion parameters.

Using the MCTDH method, we have thus been able to provide full-dimensionality calculations on the quantum dynamics of a molecular system passing through a conical intersection. These calculations not only give insight into the factors required for the description of such systems, but also provide benchmarks for comparison with results from more approximate methods.

Let us summarize the major points:

- The vibronic coupling Hamiltonian provides a realistic model for accurately describing the short-time multi-mode dynamics in nonadiabatic systems.

- The computations have shown that a multi-mode treatment is essential for correctly describing the dynamics in the presence of a conical intersection.
- The advent of MCTDH has made it possible to solve the (second-order) vibronic coupling Hamiltonian of small to medium sized molecules (5–12 atoms, say), including *all* internal degrees of freedom. In fact, it is the combination of the vibronic coupling model with MCTDH which is numerically so successful. The vibronic coupling model provides a realistic multi-mode Hamiltonian, and this Hamiltonian is, from its *ansatz*, in the product form advantageous for MCTDH. MCTDH then solves the dynamics problem accurately and efficiently.

References

1. *Time-dependent Methods for Quantum Dynamics*, Ed. K. C. Kulander (Elsevier, Amsterdam, 1991).
2. *Numerical Grid Methods and their Application to Schrödinger's Equation*, Ed. C. Cerjan (Kluwer Academic Publishers, Dordrecht, 1993).
3. R. Kosloff, *Ann. Rev. Phys. Chem.* **45**, 145 (1994).
4. H.-D. Meyer, U. Manthe and L. S. Cederbaum, *Chem. Phys. Lett.* **165**, 73 (1990).
5. U. Manthe, H.-D. Meyer and L. S. Cederbaum, *J. Chem. Phys.* **97**, 3199 (1992).
6. M. H. Beck, A. Jäckle, G. A. Worth and H.-D. Meyer, *Phys. Rep.* **324**, 1 (2000).
7. F. Duschinsky, *Acta Physicochim. URSS* **7**, 551 (1937).
8. L. S. Cederbaum, W. Domcke, H. Köppel and W. von Niessen, *Chem. Phys.* **26**, 169 (1977).
9. L. S. Cederbaum and W. Domcke, *Adv. Chem. Phys.* **36**, 205 (1977).
10. H. Köppel, W. Domcke and L. S. Cederbaum, *Adv. Chem. Phys.* **57**, 59 (1984).
11. A. Raab, G. Worth, H.-D. Meyer and L. S. Cederbaum, *J. Chem. Phys.* **110**, 936 (1999).
12. C. Cattarius, G. A. Worth, H.-D. Meyer and L. S. Cederbaum, *J. Chem. Phys.* **115**, 2088 (2001).
13. H.-D. Meyer, in *The Encyclopedia of Computational Chemistry*, Ed. P. v. R. Schleyer *et al.* (John Wiley and Sons, Chichester, 1998), Vol. 5, pp. 3011–3018.
14. G. A. Worth, H.-D. Meyer and L. S. Cederbaum, *J. Chem. Phys.* **109**, 3518 (1998).
15. J. C. Light, I. P. Hamilton and J. V. Lill, *J. Chem. Phys.* **82**, 1400 (1985).

16. J. C. Light, in *Time-Dependent Quantum Molecular Dynamics*, Eds. J. Broeckhove and L. Lathouwers (Plenum, New York, 1992), pp. 185–199.
17. P. A. M. Dirac, *Proc. Cambridge Philos. Soc.* **26**, 376 (1930).
18. J. Frenkel, *Wave Mechanics* (Clarendon Press, Oxford, 1934).
19. A. Jäckle and H.-D. Meyer, *J. Chem. Phys.* **109**, 3772 (1998).
20. U. Manthe, *J. Chem. Phys.* **105**, 6989 (1996).
21. M. H. Beck and H.-D. Meyer, *Z. Phys.* **D42**, 113 (1997).
22. U. Manthe and A. D. Hammerich, *Chem. Phys. Lett.* **211**, 7 (1993).
23. A. D. Hammerich *et al.*, *J. Chem. Phys.* **101**, 5623 (1994).
24. J.-Y. Fang and H. Guo, *J. Chem. Phys.* **101**, 5831 (1994).
25. G. A. Worth, H.-D. Meyer and L. S. Cederbaum, *J. Chem. Phys.* **105**, 4412 (1996).
26. H. Wang, *J. Chem. Phys.* **113**, 9948 (2000).
27. M. Ehara, H.-D. Meyer and L. S. Cederbaum, *J. Chem. Phys.* **105**, 8865 (1996).
28. G. A. Worth, H.-D. Meyer and L. S. Cederbaum, *Chem. Phys. Lett.* **299**, 451 (1999).
29. G. A. Worth, M. H. Beck, A. Jäckle and H.-D. Meyer, The MCTDH Package, Version 8.2, (2000). See http://www.pci.uni-heidelberg.de/tc/usr/mctdh/.
30. F. Brogli *et al.*, *Chem. Phys.* **4**, 107 (1974).
31. L. S. Cederbaum, W. Domcke and H. Köppel, *Chem. Phys.* **33**, 319 (1978).
32. C. Woywood and W. Domcke, *Chem. Phys.* **162**, 349 (1992).
33. P. Baltzer *et al.*, *Chem. Phys.* **196**, 551 (1995).
34. S. Mahapatra, L. S. Cederbaum and H. Köppel, *J. Chem. Phys.* **111**, 10452 (1999).
35. S. Mahapatra *et al.*, *J. Phys. Chem.* **A105**, 5567 (2001).
36. G. Worth and L. Cederbaum, *Chem. Phys. Lett.* **348**, 477 (2001).
37. I. Yamazaki, T. Murao, T. Yamanaka and K. Yoshihara, *Faraday Discuss. Chem. Soc.* **75**, 395 (1983).
38. K. K. Innes, I. G. Ross and W. R. Moonaw, *J. Mol. Spec.* **132**, 492 (1988).
39. C. Woywod, W. Domcke, A. L. Sobolewski and H.-J. Werner, *J. Chem. Phys.* **100**, 1400 (1994).
40. S. Krempl, M. Winterstetter, H. Plöhn and W. Domcke, *J. Chem. Phys.* **100**, 926 (1994).
41. T. Gerdts and U. Manthe, *J. Chem. Phys.* **106**, 3017 (1997).
42. A. Raab and H.-D. Meyer, *J. Chem. Phys.* **112**, 10718 (2000).

This page intentionally left blank

CHAPTER 15

MIXED QUANTUM-CLASSICAL DESCRIPTION OF THE DYNAMICS AT CONICAL INTERSECTIONS

Gerhard Stock

Institute of Physical and Theoretical Chemistry,
J. W. Goethe University,
Marie-Curie-Str. 11, D-60439 Frankfurt, Germany
stock@theochem.uni-frankfurt.de

Michael Thoss

Institute of Physical and Theoretical Chemistry,
Technical University of Munich,
D-85748 Garching, Germany
michael.thoss@ch.tum.de

Contents

1. Introduction

The description of quantum-mechanical processes through a mixed quantum-classical (MQC) formulation has attracted considerable interest for more than seventy years. The reason for this is easy to understand: As the numerical effort of a quantum-mechanical basis-set calculation increases exponentially with the number of nonseparable degrees of freedom (DoF), a straightforward quantum computation is restricted to only a few vibrational DoF of a polyatomic system. Classical mechanics, on the other hand,

scales linearly with the number of DoF; however it only represents a reasonable description of microscopic dynamics in the case that the corresponding action integral is large compared to $\hbar$, i.e. for heavy particles. Hence the strategy of MQC models is to combine the advantages of both methods, thus describing the dynamics of the "classical DoF" (e.g. the motion of heavy nuclei) in a classical framework and invoke quantum mechanics only for the description of the dynamics of the "quantum DoF" (e.g. the motion of electrons and protons). In this review, we will focus on the application of MQC methods to describe non-Born–Oppenheimer dynamics mediated by a conical intersection.

The first MQC formulation was proposed by Mott,[1] who considered the excitation of atoms in collision reactions. Inspired by the work of Born and Oppenheimer,[2] he described the dynamics of the electrons through an expansion of the total wave function in adiabatic electronic wave functions, while the motion of the heavy nuclei was considered in a classical manner. As the electronic dynamics is evaluated along the classical path of the nuclei, this ansatz is often referred to as *classical-path* approximation. While the classical-path approximation describing the reaction of the quantum DoF to the dynamics of the classical DoF is common to most MQC formulations, there are several ways to describe the "back-reaction" of the classical DoF to the dynamics of the quantum DoF. One way is to employ Ehrenfest's theorem[3] and calculate the effective force on the classical trajectory through a mean potential that is averaged over the quantum DoF.[4–16] As most MQC formulations, the resulting mean-field trajectory method employs a *quasiclassical* approximation for the heavy-particle DoF, i.e. the quantum nature of the initial state of the classically treated subsystem is simulated through quasiclassical sampling of the corresponding probability distribution.[17–19] In contrast to a true *semiclassical* description (i.e. in the sense of the Van–Vleck–Gutzwiller formulation[20]), possible quantum-mechanical interferences between individual classical paths are therefore not included.

1.1. *Classification of Methods*

In general, a MQC description may be derived by starting with a quantum-mechanically exact formulation for the complete system and performing a partial classical limit for the heavy-particle DoF. This procedure is not

unique, however, since it depends on the particular quantum formulation chosen as well as on the specific way to achieve the classical limit. In the *mean-field trajectory* method explained above, for example, the wavefunction formulation of quantum mechanics is adopted and the Ehrenfest classical limit is performed for the heavy-particle DoF. Alternatively, one may consider the Liouville equation of the density operator and perform a classical limit within the Wigner representation for the heavy-particle DoF. This leads to the *quantum-classical Liouville* description which has recently received considerable attention.[21–34] Furthermore, one may start with a path-integral formulation and treat the heavy-particle DoF by the stationary-phase approximation, thus yielding Pechukas' theory.[35] Quite recently, also the hydrodynamic or Bohmian formulation of quantum mechanics has been used as a starting point for a MQC description.[36–38] It should be made clear at the outset that the MQC formulations differ greatly, depending on whether the problem is approached via the wavefunction, density-operator, path-integral, or hydrodynamic formulation of quantum mechanics.

A different way to combine classical and quantum mechanics is the "connection approach," which was proposed independently by Landau,[39] Zener,[40] and Stückelberg[41] and has later been adopted and generalized by many authors.[42–50] In this formulation, nonadiabatic transitions of classical trajectories are described in terms of a connection formula of the semiclassical WKB wave functions associated with the two coupled electronic states. While the true semiclassical evaluation of these formulations has mostly been concerned with one-dimensional problems, the intuitively appealing picture of trajectories hopping between coupled potential-energy surfaces gave rise to a number of quasiclassical implementations of this idea.[51–68] In the popular *surface-hopping* scheme of Tully and coworkers,[51–53] classical trajectories are propagated on a single adiabatic potential-energy surface until, according to some "hopping criterion", a transition probability $p_{1\to 2}$ to another potential-energy surface is calculated and, depending on the comparison of $p_{1\to 2}$ with a random number, the trajectory "hops" to the other adiabatic surface. The many existing variants of the method mainly differ in choice and degree of sophistication of the hopping criteria. In recent years, the term "surface hopping" and its underlying ideas have also been used in the stochastic modeling of a given deterministic differential equation, e.g. the quantum-classical Liouville equation.[29–32]

Recently, a conceptionally different way to couple the dynamics of quantum and classical DoF has been proposed, the so-called *mapping* approach.[69–71] In this formulation the problem of a classical treatment of discrete quantum DoF is bypassed by transforming the discrete quantum variables to continuous variables. Based on Schwinger's theory of angular momentum,[72] the mapping of discrete DoF to continuous DoF is achieved through the representation of spin operators by boson operators. To illustrate the concept, consider a molecular system comprising N_{el} electronic states and N_{vib} vibrational modes: The basic idea is to (i) map the N_{el} discrete DoF onto N_{el} continuous DoF and (ii) solve the resulting dynamical problem of $N_{\mathrm{el}} + N_{\mathrm{vib}}$ continuous DoF employing standard classical or semiclassical methodology. On a purely classical level, the formalism has been shown to recover the classical electron analog model of Meyer and Miller.[73–76] The "Langer-like modifications"[77] that were empirically introduced in this model could be identified as a zero-point energy term that accounts for quantum fluctuations in the electronic DoF.[71,78] This in practice quite important feature was found to be the main difference between the classical mapping formulation and standard quantum-classical mean-field models. On a semiclassical level, the mapping goes beyond the original classical electron analog model, because it is exact for an N-level system and unambiguously defines the Hamiltonian as well as the boundary (or initial) conditions of the semiclassical propagator.[69,70] Employing an initial-value representation for the semiclassical propagator,[79–86] the formulation has recently been applied to a variety of systems with nonadiabatic dynamics.[69–71,78,87–97] Furthermore, the approach allows us to study the classical phase space of a nonadiabatically coupled system and also to introduce classical periodic orbits of such a system.[98–101]

In summary, we have made an attempt to classify existing MQC strategies in formulations resulting from (i) a partial classical limit, (ii) a connection ansatz, and (iii) a mapping formalism. In this overview, we shall focus on essentially classical formulations that may be relatively easily applied to multidimensional surface-crossing problems. On the other hand, it should be noted that there also exists a number of essentially quantum-mechanical formulations which at some point use classical ideas. A well-known example are formulations that combine quantum-mechanical time-dependent perturbation theory with a classical evaluation of the resulting correlation functions, e.g. Golden Rule type formulations.[102,103] Furthermore, several

workers have suggested time-dependent quantum propagation schemes that employ Gaussian wave packets as a time-dependent basis set.[104–108] For example, Martinez and coworkers have developed such a method ("multiple spawning") that borrows ideas from surface-hopping and is designed to be effectively interfaced with quantum-chemical methods, thus providing an *ab initio* molecular dynamics description of nonadiabatic photochemical processes.[105–107]

1.2. *Application to the Dynamics at Conical Intersections*

Since the validity of an approximate description depends to a large extent on the specific physical application under consideration, one may ask whether a MQC strategy appears promising to describe the dynamics at conical intersections. As discussed in this book, the electronic and vibrational relaxation dynamics associated with conical intersections exhibits several characteristic features, which represent a hard challenge for an approximate theoretical description: (i) The dynamics is caused by strong intramolecular interactions that cannot be accounted for in a perturbative manner (ii) Due to the large anharmonicity of the adiabatic potential-energy surfaces, the vibrational motion is highly correlated, thus hampering the application of simple self-consistent-field schemes. Within the limits of the underlying classical approximation, these requirements are fulfilled by a MQC formulation which is a nonperturbative description and also fully includes the correlation between the individual DoF. In fact, a MQC description appears to be one of the few approximations that may be expected to work. Furthermore, it should be stressed that a classical (and therefore local) description is readily combined with an "on-the-fly" *ab initio* evaluation of the potential-energy.[106,107,109–114] Nonadiabatic *ab initio* molecular dynamics methods are one of the few promising strategies to explore excited-state potential-energy surfaces of multidimensional system in an unbiased manner.

Let us briefly review what MQC methods have so far been applied to the dynamics at conical intersections. Here the surface-hopping method has been the most popular approach,[54,60–62,115] in particular in combination with an on-the-fly *ab initio* evaluation of the potential-energy.[109–114] Furthermore, various self-consistent-field methods have been employed to describe internal-conversion dynamics associated with a conical intersection, including the mean-field trajectory method, the classical electron

analog model, and the quasiclassical mapping formulation.[14,71,78,116] Since there is no sampling problem due to oscillating phases, all these method are readily implemented and typically converge for a moderate number of trajectories ($\approx 10^2 - 10^4$). Because of rapidly oscillating phases and the representation of nonlocal operators, however, the numerical propagation of the quantum-classical Liouville equation represents a significantly more tedious problem. Hence only a few workers have considered the dynamics at conical intersections with this approach.[33,34]

Due to the development of efficient initial-value representations of the semiclassical propagator, recently there has been considerable progress in the semiclassical description of multidimensional quantum processes.[79–86] Considering the semiclassical description of nonadiabatic dynamics, only the mapping approach,[69,70] and the equivalent formulation that is obtained by requantizing the classical electron analog model of Meyer and Miller,[87] appears to be amenable to a numerical treatment via an initial-value representation.[89,92,97] Other semiclassical formulations such as Pechukas' path-integral formulation[35] and the various connection theories[42–50] have been conceptionally illuminating, but so far of limited computational value.

1.3. *Outline of the Chapter*

The goal of this review is to critically compare — from both a conceptional and a practical point of view — various MQC strategies to describe non-Born–Oppenheimer dynamics. Owing to personal preferences, we will focus on the modeling of ultrafast bound-state processes following photoexcitation such as internal-conversion and nonadiabatic photoisomerization. To this end, Sec. 2 introduces three model problems: Model I represents a three-mode description of the $S_1 - S_2$ conical intersection in pyrazine.[117] Model II accounts for the ultrafast $\widetilde{C} \to \widetilde{B} \to \widetilde{X}$ internal-conversion process in the benzene cation,[118,119] and Model III represents a three-mode description of ultrafast photoisomerization triggered by a conical intersection.[120] Allowing for exact quantum-mechanical reference calculations, all models have been used as benchmark problems to study approximate descriptions.

The remaining sections are devoted to a discussion of the various MQC methods. Among other issues, we consider the ability of a method to (i) account for the branching of trajectories, (ii) account for the electronic phase coherence, (iii) correctly describe the vibrational motion on coupled

PESs, and (iv) obey the principle of microreversibility. Section 3 describes in some detail the mean-field trajectory method and also discusses its connection to time-dependent self-consistent-field schemes. The surface-hopping method is considered in Sec. 4, which discusses various motivations of the ansatz as well as several variants of the implementation. Section 5 gives a brief account on the quantum-classical Liouville description and considers the possibility of an exact stochastic realization of its equation of motion. The mapping formalism, its relation to other formulations, and its quasi-classical implementation is introduced in Sec. 6. Section 7 is concerned with the semiclassical description of nonadiabatic quantum mechanics. Section 8 summarizes our results and concludes with some general remarks.

2. Models

2.1. *Model Hamiltonian*

In what follows, we introduce the model Hamiltonian pertaining to the molecular systems under consideration. As has been discussed in detail in previous chapters of this book, a curve-crossing problem can be formulated in the adiabatic as well as in a diabatic electronic representation. Depending on the system under consideration and on the specific method used, both representations have been employed in mixed quantum-classical (MQC) approaches. While the diabatic representation is advantageous to model potential-energy surfaces in the vicinity of an intersection and has been used in mean-field type approaches, other MQC approaches such as the surface-hopping method usually employ the adiabatic representation.

Adopting diabatic electronic basis states $|\Phi_k^d\rangle$, the molecular model Hamiltonian can be written as[121,122]

$$H = T_n + \sum_{k,k'} \left|\Phi_k^d\right\rangle W_{kk'} \left\langle\Phi_{k'}^d\right| . \tag{1}$$

Here the $W_{kk'}$ represent the electronic matrix elements of the diabatic potential matrix and T_n is the nuclear kinetic-energy operator. We wish to consider molecular models describing (i) photophysical processes in which the molecular system undergoes electronic relaxation through internal conversion mediated by conical intersections and (ii) photochemical processes in which the molecular system additionally changes its chemical identity (e.g. through isomerization).

To account for the first kind of process, we employ the linear vibronic coupling model, where the diabatic potential matrix elements $W_{kk'}$ are approximated by a Taylor expansion with respect to the electronic ground-state equilibrium geometry[121,122] (see Chapter 7). In lowest order we thus obtain (throughout the article, we set $\hbar \equiv 1$)

$$T_n = \frac{1}{2} \sum_j \omega_j P_j^2, \tag{2}$$

$$W_{kk} = E_k + \frac{1}{2} \sum_j \omega_j Q_j^2 + \sum_j \kappa_j^{(k)} Q_j, \tag{3}$$

$$W_{kk'} = W_{kk'}(0) + \sum_j \lambda_j^{(kk')} Q_j, \quad k \neq k', \tag{4}$$

where ω_j is the vibrational frequency and Q_j, P_j are the dimensionless position and momentum of the jth vibrational mode. E_k denotes the vertical transition energy of the diabatic state $|\Phi_k^d\rangle$ and $\kappa_j^{(k)}$ represents the gradient of the exited-state diabatic potential-energy surface at the ground-state equilibrium geometry. The vibronic-coupling constants $\lambda_j^{(kk')}$ are given by the gradients of $W_{kk'}(x)$. In all the models considered in this paper we have $W_{kk'}(0) = 0$ due to symmetry reasons, resulting in a *conical intersection* of the corresponding adiabatic potential-energy surfaces.

To account for photochemical processes, we adopt a simple model recently proposed by Seidner and Domcke for the description of *cis-trans* isomerization processes.[120] In addition to the normal-mode expansion above, they introduced a Hamiltonian exhibiting torsional motion, the diabatic matrix elements of which are given as

$$h_{kk}^{\mathrm{R}} = -\frac{1}{2I} \frac{\partial^2}{\partial \varphi^2} + \frac{1}{2} W_k^{\mathrm{R}} (1 - \cos(n\varphi)). \tag{5}$$

Here φ represents the torsional coordinate, I denotes the moment of inertia, and W_k^{R} is the first coefficient of the Fourier series expansion of the isomerization potential of periodicity $n\pi$.

Introducing adiabatic electronic states $|\Phi_k^a\rangle$ the model Hamiltonian in the adiabatic representation can then be written as[121,122]

$$H = \sum_{k,k'} |\Phi_k^a\rangle \left[(T_n + V_k)\delta_{k,k'} + \Lambda_{kk'} \right] \langle \Phi_{k'}^a | \,. \tag{6}$$

Here, V_k denotes the adiabatic Born–Oppenheimer potential-energy surfaces which are obtained by diagonalizing the diabatic potential matrix

defined above. The non-Born–Oppenheimer operator

$$\Lambda_{kk'} = -\sum_j \omega_j \left(iF^{(j)}_{kk'} P_j + \frac{1}{2} G^{(j)}_{kk'} \right) \tag{7}$$

is given in terms of the nonadiabatic coupling matrices of first and second order

$$F^{(j)}_{kk'} = \left\langle \Phi^a_k \left| \frac{\partial}{\partial Q_j} \right| \Phi^a_{k'} \right\rangle, \tag{8}$$

$$G^{(j)}_{kk'} = \left\langle \Phi^a_k \left| \frac{\partial^2}{\partial Q_j^2} \right| \Phi^a_{k'} \right\rangle. \tag{9}$$

2.2. *Observables of Interest*

The various aspects of photoinduced nonadiabatic dynamics are reflected by different time-dependent observables. Following a brief introduction of the observables of interest, we discuss how these quantities are evaluated in a MQC simulation.

In general, the time evolution of the molecular system is governed by the Liouville–von Neumann equation

$$i\dot{\rho}(t) = [H, \rho(t)], \tag{10}$$

where H represents the molecular Hamiltonian defined in Eqs. (1) or (6) and $\rho(t)$ is the density operator. The time-dependent expectation value of the observable $\widehat{A}$ is then given by

$$A(t) = \mathrm{Tr}\{\rho(t)\widehat{A}\} = \mathrm{Tr}\{\rho(0)\widehat{A}(t)\}, \tag{11}$$

where $\mathrm{Tr}\{\ldots\}$ represents the quantum-mechanical trace over all degrees of freedom of the system and $\widehat{A}(t)$ denotes the operator $\widehat{A}$ in the Heisenberg representation. Assuming that at time $t = 0$ the molecular system is photoexcited from the electronic ground state (e.g. $|\Phi_0\rangle$) to an upper state (e.g. $|\Phi_2\rangle$) by an ultrashort laser pulse, the initial state is given as

$$\rho(0) = |\Phi_2\rangle|\mathbf{0}\rangle\langle\mathbf{0}|\langle\Phi_2|, \tag{12}$$

where $|\mathbf{0}\rangle$ denotes the vibrational ground state in $|\Phi_0\rangle$.[122] In a MQC calculation the trace operation in the Heisenberg representation is replaced by a quantum-mechanical trace ($\mathrm{Tr_q}$) over the quantum degrees of freedom and

a classical trace (i.e. a phase-space integral over the initial positions $\mathbf{R}_0$ and momenta $\mathbf{P}_0$) over the classical degrees of freedom. This yields

$$A(t) = \int d\mathbf{R}_0 \int d\mathbf{P}_0 \, \mathrm{Tr_q}\{\rho(\mathbf{R}_0, \mathbf{P}_0) A[\mathbf{R}(t), \mathbf{P}(t)]\}, \tag{13}$$

where $\rho(\mathbf{R}_0, \mathbf{P}_0)$ denotes a phase-space representation of the vibrational initial state.[17–19] For example, to represent the ground state $|0\rangle\langle 0|$ of a one-dimensional harmonic oscillator $H = \frac{1}{2}\omega(P^2 + R^2)$, one may employ the Wigner distribution [123]

$$\rho(R_0, P_0) = \frac{1}{\pi} e^{-P_0^2 - R_0^2}. \tag{14}$$

Alternatively one may change to classical action-angle variables n, q (using the transformation $R = \sqrt{2N+1}\sin q$, $P = \sqrt{2N+1}\cos q$, $q \in [0, 2\pi]$[17,18]) and consider initial conditions with fixed action $N_0 = \frac{1}{2}$

$$\rho(N_0) = \delta\left(N_0 - \tfrac{1}{2}\right), \tag{15}$$

reflecting the zero-point energy of the harmonic oscillator.

As a first example, let us consider the time-dependent mean position of a normal mode Q_j of the system. In a MQC calculation, this observable is directly given by the quasiclassical average over the nuclear trajectories $Q_j^{(r)}(t)$, i.e.

$$\langle Q_j(t)\rangle_C = \frac{1}{N_{\mathrm{traj}}} \sum_{r=1}^{N_{\mathrm{traj}}} Q_j^{(r)}(t) \tag{16}$$

where the phase-space integral over the classical initial conditions in Eq. (13) has been approximated by a sum over N_{traj} trajectories with equal weights. Similarly, the corresponding mean momenta and other vibrational quantities such as normal-mode energies are readily evaluated.

The time evolution of a photoisomerization process can be visualized by considering the time-dependent probability of finding the system in either the *cis* or the *trans* conformation.[120,122] Assuming a π-periodic torsional potential as used in Model III below, we assign a torsional angle φ between $-\pi/2$ and $\pi/2$ to the *cis* conformation and a torsional angle between $\pi/2$ and $3\pi/2$ to the *trans* conformation, resulting in the projectors

$$\begin{aligned} P_{\mathrm{trans}} &= \Theta(|\varphi| - \pi/2), \\ P_{\mathrm{cis}} &= \mathbf{1} - P_{\mathrm{trans}}, \end{aligned} \tag{17}$$

where Θ denotes the Heaviside step function and φ is restricted to $-\pi/2 \leq \varphi \leq 3\pi/2$.

To describe the electronic relaxation dynamics of a photoexcited molecular system, it is instructive to consider the time-dependent population of an electronic state, which can be defined in a diabatic or the adiabatic representation.[122] The population probability of the diabatic electronic state $\left|\Phi_k^d\right\rangle$ is defined as the expectation value of the diabatic projector

$$\begin{aligned} P_k^{\mathrm{dia}}(t) &= \mathrm{Tr}\{\hat{P}_k^{\mathrm{dia}}\rho(t)\}, \\ \hat{P}_k^{\mathrm{dia}} &= \left|\Phi_k^d\right\rangle\left\langle\Phi_k^d\right|. \end{aligned} \tag{18}$$

In a MQC simulation such as a mean-field-trajectory or a surface-hopping calculation, the population probability of the diabatic state $\left|\Phi_k^d\right\rangle$ is given as the quasiclassical average over the squared modulus of the diabatic electronic coefficients $d_k(t)$ defined in Eq. (21). This yields

$$\begin{aligned} P_k^{\mathrm{dia}}(t) &= \langle d_k^*(t) d_k(t)\rangle_C \\ &= \frac{1}{N_{\mathrm{traj}}} \sum_{r=1}^{N_{\mathrm{traj}}} |d_k^{(r)}(t)|^2. \end{aligned} \tag{19}$$

In complete analogy, the adiabatic population probability is defined as the expectation value of the adiabatic projector $\hat{P}_k^{\mathrm{ad}} = |\Phi_k^a\rangle\langle\Phi_k^a|$, and is quasiclassically given as average over the squared modulus of the adiabatic electronic coefficients $a_k(t)$ defined in Eq. (24).

Finally, in the semiclassical formulation introduced in Sec. 7 it is of interest to calculate the autocorrelation function

$$J(t) = \left\langle \mathbf{0} \left| \left\langle \Phi_2 \left| e^{-iHt} \right| \Phi_2 \right\rangle \right| \mathbf{0} \right\rangle, \tag{20}$$

the Fourier transform of which yields the electronic absorption spectrum.

2.3. *Model Systems*

In order to discuss various aspects of a MQC treatment of photoinduced electronic and vibrational relaxation dynamics mediated by conical intersections, we consider three different kinds of molecular models, each representing a specific challenge for a MQC modeling. Here, we introduce the specifics of these models and discuss the characteristics of their nonadiabatic dynamics. The molecular parameters of the models are collected in Tables 1–3.

Table 1. Parameters of Model I representing a three-mode model of the $S_1 - S_2$ conical intersection in pyrazine.[117] All quantities are given in eV.

	E_k	ω_1	$\kappa_1^{(k)}$	ω_{6a}	$\kappa_{6a}^{(k)}$	ω_{10a}	λ
$\|\Phi_1^d\rangle$	3.94	0.126	0.037	0.074	−0.105	0.118	0.262
$\|\Phi_2^d\rangle$	4.84	0.126	−0.254	0.074	0.149	0.118	

Table 2. Parameters of Model II representing a three-state five-mode model of the ultrafast $\tilde{C} \rightarrow \tilde{B} \rightarrow \tilde{X}$ internal-conversion process in the benzene cation.[118,119] All quantities are given in eV.

	E_k	ω_2	$\kappa_2^{(k)}$	ω_{16}	$\kappa_{16}^{(k)}$	ω_{18}	$\kappa_{18}^{(k)}$	ω_8	$\lambda_8^{(12)}$	ω_{19}	$\lambda_{19}^{(23)}$
$\|\Phi_1^d\rangle$	9.65	0.123	−0.042	0.198	0.246	0.075	0.125	0.088	0.164	0.12	0.154
$\|\Phi_2^d\rangle$	11.84	0.123	−0.042	0.198	0.246	0.075	0.1	0.088		0.12	
$\|\Phi_3^d\rangle$	12.44	0.123	−0.301	0.198	0	0.075	0	0.088		0.12	

Table 3. Parameters of Model III which represents a three-mode model exhibiting nonadiabatic photoisomerization.[130] The torsional potentials are characterized by the reciprocal moment of inertia I^{-1} and the potential parameters E_k and W_k. All quantities are given in eV.

	E_k	I^{-1}	W_k	ω_t	$\kappa^{(k)}$	ω_c	λ
$\|\Phi_1^d\rangle$	0.0	1.11×10^{-3}	4.5	0.2	0.0	0.17	0.34
$\|\Phi_2^d\rangle$	5.0	1.11×10^{-3}	−4.5	0.2	0.3	0.17	

2.3.1. *Model I: $S_2 \rightarrow S_1$ Internal Conversion in Pyrazine*

Model I represents a three-mode model of the $S_1(n\pi^*)$ and $S_2(\pi\pi^*)$ electronic states of pyrazine,[117] which has been adopted by several authors as a standard example of ultrafast electronic relaxation.[14,124–126] Taking into account a single coupling mode (ν_{10_a}) and two totally symmetric modes (ν_1, ν_{6a}), Domcke and coworkers have identified a low-lying conical intersection of the two lowest excited singlet states of pyrazine, which has been shown to trigger internal conversion and a dephasing of the vibrational

motion on a femtosecond time scale.[124] A variety of theoretical investigations, including quantum wave-packet studies,[124,125] absorption and resonance Raman spectra,[127] as well as time-resolved pump-probe spectra[122,128] have been reported for this system. Exhibiting complex electronic and vibrational relaxation dynamics, the model provides a stringent test for an approximate description.

Let us briefly discuss the characteristics of the nonadiabatic dynamics exhibited by this model. Assuming an initial preparation of the S_2 state by an ideally short laser pulse, Fig. 1 displays in thick lines the first 500 fs of the quantum-mechanical time evolution of the system. The population probability of the diabatic S_2 state shown in panel (b) exhibits an initial decay on a timescale of ≈ 20 fs, followed by quasi-periodic recurrences of the population, which are damped on a timescale of a few hundred femtoseconds. Beyond ≈ 500 fs (not shown) the S_2 population probability becomes quasi-stationary, fluctuating statistically around its asymptotic value of $\approx$0.3. The time-dependent population of the adiabatic S_2 state, displayed in panel (a), is seen to decay even faster than the diabatic population — essentially within a single vibrational period — and to attain an asymptotic value of $\approx$0.05. The finite asymptotic value of P_2^{ad} is a consequence of the restricted phase space of the three-mode model. The population P_2^{ad} is expected to decay to zero for systems with many degrees of freedom.

The vibrational dynamics of the model is illustrated in panels (c) and (d) of Fig. 1, showing the expectation values of the momenta of the tuning modes ν_1 and ν_{6a}, respectively. It is seen that the oscillations of the two modes are damped on a timescale of a few hundred femtoseconds. As has been discussed in detail in Ref. 124, this damping reflects the strong nonadiabatic coupling of the system which causes a large anharmonicity of the lower adiabatic potential-energy surface. It should be pointed out that the decay of the amplitude of $\langle p \rangle_t$ is not related to the dissipation of vibrational energy but rather reflects a vibrational pure dephasing process.

2.3.2. *Model II: $\tilde{C} \rightarrow \tilde{B} \rightarrow \tilde{X}$ Internal-Conversion Process in the Benzene Cation*

Recently, an *ab initio*-based model of the ultrafast $\widetilde{C} \rightarrow \widetilde{B} \rightarrow \widetilde{X}$ internal-conversion process in the benzene cation (Bz^+) has been proposed by Köppel, Domcke, and Cederbaum.[118,119] The diabatic potential matrix

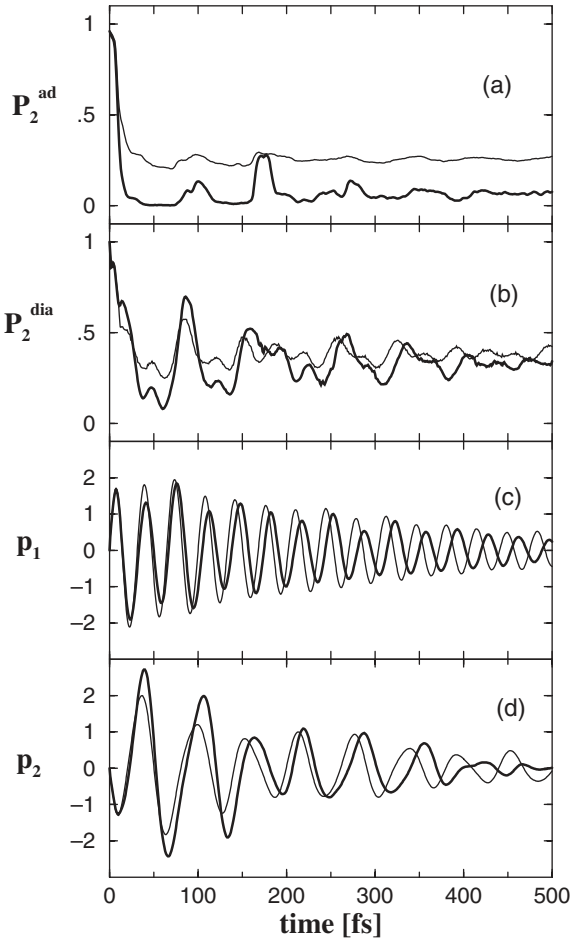

Fig. 1. Quantum-mechanical (thick lines) and mean-field-trajectory (thin lines) calculations obtained for Model I describing the $S_2 \rightarrow S_1$ internal-conversion process in pyrazine. Shown are the time-dependent population probabilities $P_2^{\mathrm{ad}}(t)$, $P_2^{\mathrm{dia}}(t)$ of the initially prepared adiabatic and diabatic electronic state, respectively, as well as the mean momenta $p_1(t)$, $p_2(t)$ of the two totally symmetric modes ν_1 and ν_{6a} of the model.

elements of the Hamiltonian have been approximated by a quadratic Taylor expansion in normal coordinates of the electronic ground state of neutral benzene. The resulting model system has been shown to give rise to multidimensional conical intersections of the corresponding adiabatic

potential-energy surfaces. Model II is obtained by taking into account the five most important vibrational modes ($\nu_2, \nu_8, \nu_{16}, \nu_{18}$, and ν_{19} in Herzberg numbering) and ignoring the degeneracy of the $\widetilde{X}$ and $\widetilde{B}$ electronic states as well as of the modes $\nu_{16}, \nu_{18}, \nu_{19}$.

Köppel[119] has performed exact time-dependent quantum wave-packet propagations for this model, the results of which are depicted in Fig. 2(a). He showed that the initially excited $\widetilde{C}$ state decays irreversibly into the $\widetilde{X}$ state within ≈250 fs. The decay is nonexponential and exhibits a pronounced beating of the $\tilde{C}$ and $\tilde{B}$ state populations. This model will allow us to test MQC approaches for multistate systems with several conical intersections.

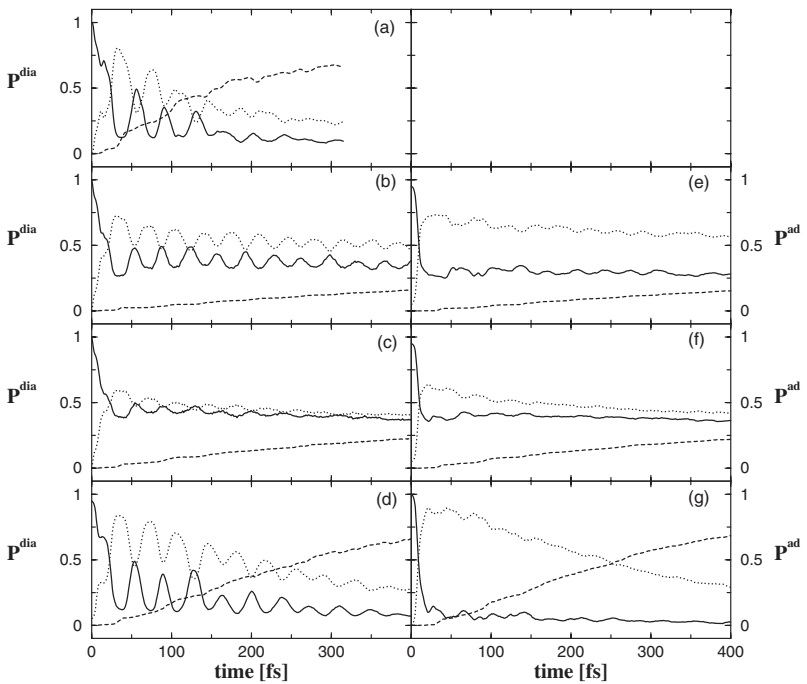

Fig. 2. Diabatic (left) and adiabatic (right) population probabilities of the $\widetilde{C}$ (full line), $\widetilde{B}$ (dotted line), and $\widetilde{X}$ (dashed line) electronic states as obtained for Model II representing a three-state five-mode model of the benzene cation. Shown are (a) exact quantum calculations of Ref. 119, as well as mean-field-trajectory results [panels (b),(e)] and surface-hopping results [panels (c),(d),(f),(g)]. The latter are obtained either directly from the electronic coefficients [(c),(f)] or from binned coefficients [(d),(g)].

2.3.3. *Model III: Nonadiabatic Photoisomerization*

As last example of a molecular system exhibiting nonadiabatic dynamics caused by a conical intersection we consider a model that recently has been proposed by Seidner and Domcke to describe ultrafast *cis-trans* isomerization processes in unsaturated hydrocarbons.[120] Photochemical reactions of this type are known to involve large-amplitude motion on coupled potential-energy surfaces,[129] thus representing another stringent test for a MQC description which is complementary to Models I and II. A number of theoretical investigations, including quantum wavepacket studies,[120,122,130] time-resolved pump-probe spectra,[130–132] and various MQC simulations[62,133] have been reported for this system. The model considered here includes three nuclear degrees of freedom consisting of a large-amplitude torsional motion, a vibronically active mode which couples the electronic ground state and the excited state, and a totally symmetric mode which modulates the energy gap of the interacting states.

Figure 3 shows the quantum-results (thick full lines) for time-dependent population probabilities $P_2^{\mathrm{ad}}(t)$, $P_2^{\mathrm{dia}}(t)$ of the initially prepared (a) adiabatic and (b) diabatic electronic state, respectively, as well as (c) the probability $P_{\mathrm{cis}}(t)$ that the system remains in the initially prepared *cis* conformation. The results illustrate the interplay of isomerization dynamics and internal-conversion dynamics of Model III: The ultrafast photoisomerization process as monitored by the probability $P_{\mathrm{cis}}(t)$ is seen to directly result in a highly effective internal-conversion process as monitored by the adiabatic population $P_2^{\mathrm{ad}}(t)$. It is noted that the isomerization process and the decay of the diabatic population is virtually completed after 100 fs. The long-time values of $\approx\frac{1}{2}$ for $P_{\mathrm{cis}}(\infty)$ and $P_2^{\mathrm{dia}}(\infty)$ is a consequence of the symmetric torsional potential chosen in Model III (cf. Table 3). The adiabatic population probability, on the other hand, decays to its long-time value of 0.25 within ≈400 fs, thus reflecting the redistribution of vibrational energy occurring on this time scale.[120]

3. Mean-Field Trajectory Method

3.1. *Classical-Path Approximation*

As explained in the Introduction, most mixed quantum-classical (MQC) methods are based on the classical-path approximation, which describes the reaction of the quantum degrees of freedom (DoF) to the dynamics of

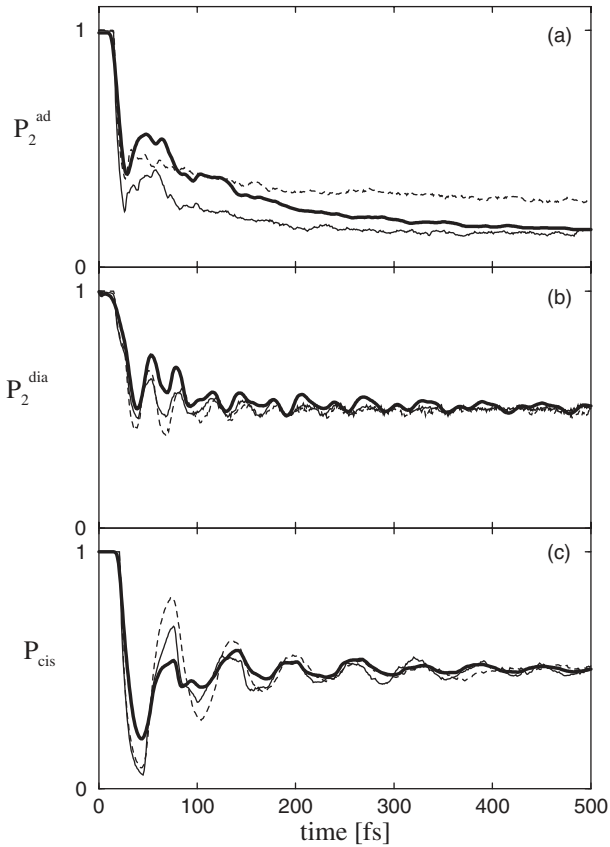

Fig. 3. Time-dependent simulations of the nonadiabatic photoisomerization dynamics exhibited by Model III, comparing results of the mean-field-trajectory method (dashed lines), the surface-hopping approach (thin lines), and exact quantum calculations (full lines). Shown are the population probabilities of the initially prepared (a) adiabatic and (b) diabatic electronic state, respectively, as well as (c) the probability $P_{\rm cis}(t)$ that the system remains in the initially prepared *cis* conformation.

the classical DoF. Let us first consider a diabatic electronic representation and expand the time-dependent molecular wave function $|\Psi(t)\rangle$ in terms of diabatic basis states $|\Phi_k^d\rangle$

$$|\Psi(t)\rangle = \sum_k d_k(\mathbf{R},t)\,\left|\Phi_k^d\right\rangle, \tag{21}$$

where $d_k(\mathbf{R},t)$ denotes the vibrational wave function pertaining to the diabatic state $|\Phi_k^d\rangle$. Insertion of Eq. (21) into the time-dependent Schrödinger equation yields the equations of motion in the diabatic representation

$$i\dot{d}_k = \sum_{k'} W_{kk'} d_{k'}. \tag{22}$$

Equation (22) is still exact. To introduce the classical-path approximation, we assume that the nuclear dynamics of the system can be described by classical trajectories, that is, the position operator $\widehat{\mathbf{R}}$ is approximated by its mean value, i.e. the trajectory $\mathbf{R}(t)$. As a consequence, the quantum-mechanical *operators* of the nuclear dynamics (e.g. $W_{kk'}(\mathbf{R})$) become classical *functions* which depend parametrically on $\mathbf{R}(t)$. In the same way, the nuclear *wave functions* $d_k(\mathbf{R},t)$ become complex-valued *coefficients* $d_k(\mathbf{R}(t),t)$. As the electronic dynamics is evaluated along the classical path of the nuclei, the approximation thus accounts for the reaction of the quantum DoF to the dynamics of the classical DoF.

In order to introduce the classical-path approximation in the adiabatic electronic representation, we expand the total wave function in terms of adiabatic basis states

$$|\Psi(t)\rangle = \sum_k a_k(\mathbf{R},t)|\Phi_k^a\rangle. \tag{23}$$

In complete analogy to the diabatic case, the equations of motion in the adiabatic representation are then obtained by inserting the ansatz (23) into the time-dependent Schrödinger equation for the adiabatic Hamiltonian (6)

$$\begin{aligned} \dot{a}_k &= \sum_{k'} A_{kk'} a_{k'} \\ A_{kk'} &= -i(V_k \delta_{k,k'} + \Lambda_{kk'}). \end{aligned} \tag{24}$$

As long as no approximation is introduced, it is clear that the equations of motion are equivalent in the diabatic and adiabatic representations. This is no longer true, however, once the classical-path approximation is employed; the resulting classical-path equations of motion in the adiabatic representation are *not equivalent* to the diabatic equations of motion. Depending on whether the approximation is employed in the diabatic or in the adiabatic representation, the resulting classical-path Hamiltonian contains identical first-order nonadiabatic couplings but different

second-order nonadiabatic couplings.[62] The existence of several possibilities always raises the question on the "best" approximation. The numerical studies reported below suggest that the mean-field trajectory simulations for the model Hamiltonian (1) are best performed in a diabatic representation; employing the classical-path approximation in the adiabatic representation was found to lead to numerical instabilities in the vicinity of the intersection of the electronic potential-energy surfaces. The surface-hopping simulations, on the other hand, are best performed in the adiabatic representation. This appears to be the natural choice, since the surface-hopping model is defined in the adiabatic representation.

3.2. *Mean-Field Trajectory Scheme*

The classical-path approximation introduced above is common to most MQC formulations and describes the reaction of the quantum DoF to the dynamics of the classical DoF. The back-reaction of the quantum DoF onto the dynamics of the classical DoF, on the other hand, may be described in different ways. In the mean-field trajectory (MFT) method (which is sometimes also called Ehrenfest model, self-consistent classical-path method, or semiclassical time-dependent self-consistent-field method) considered in this section, the classical force $F = \dot{P}_j$ acting on the nuclear DoF R_j is given as an average over the quantum DoF

$$\dot{P}_j = -\left\langle \Psi(t) \left| \frac{\partial H}{\partial R_j} \right| \Psi(t) \right\rangle, \tag{25}$$

where the wave function $|\Psi(t)\rangle$ and the molecular Hamiltonian H may be defined in a diabatic as well as in the adiabatic representation. Adopting, for example, a diabatic electronic representation, the nuclear MFT equations of motion read

$$\dot{P}_j = -\sum_{k,k'} d_k^* d_{k'} \frac{\partial W_{kk'}(\mathbf{R})}{\partial R_j}, \tag{26}$$

i.e. the classical DoF propagate according to a mean-field potential, the value of which is weighted by the instantaneous populations of the different quantum states. A MFT calculation thus consists of the self-consistent solution of the time-dependent Schrödinger equation (22) for the quantum DoF and Newton's equation (26) for the classical DoF. To represent the initial state (12) of the molecular system, the electronic DoF $d_k(0)$ as well as the

nuclear DoF $R_j(0)$ and $P_j(0)$ are sampled from a quasiclassical phase-space distribution.[17–19] For example, the vibrational initial state may be represented by a Wigner distribution (14), while the initial electronic coefficients may be determined by $d_k(0) = \delta_{k2}e^{iq}$, q being an arbitrary phase.[134]

3.3. *Results*

To illustrate the quality of the MFT method, let us first consider Model I describing the $S_2 - S_1$ conical intersection in pyrazine. Figure 1 compares quantum-mechanical and MFT results obtained for the adiabatic and diabatic electronic population probabilities $P_2^{\mathrm{ad}}(t)$ and $P_2^{\mathrm{dia}}(t)$ as well as for the mean momenta of the two totally symmetric modes of the model. Generally speaking, the results are in qualitative agreement, in particular, the ultrafast initial decay of the adiabatic population and the oscillations of the diabatic population are quite well described by the MFT method. The electronic relaxation dynamics for longer time, however, is not reproduced. The oscillations of the diabatic population are too strongly damped and the final value of the adiabatic population is too large. As will be discussed in detail in Sec. 6.3, this deficiency of the method is related to the fact that the MFT approach treats electronic and nuclear DoF on an unequal dynamical footing. The comparison of the MFT and quantum results obtained for the mean momenta of the two vibrational modes v_1 and v_{6a} demonstrates that the MFT method is able to describe the dephasing of the vibrational motion caused by the internal conversion process. For longer times, however, the quality of the MFT result deteriorates. In particular, there is a mismatch of the phase of the oscillations.

Let us next turn to Model II representing the $\tilde{C} \to \tilde{B} \to \tilde{X}$ internal-conversion process in the benzene cation. Figure 2 demonstrates that this (compared to the electronic two-state Model I) more complicated process is difficult to describe with a MFT ansatz. Although the method is seen to catch the initial fast $\tilde{C} \to \tilde{B}$ decay quite accurately and can also qualitatively reproduce the oscillations of the diabatic populations of the $\tilde{C}$- and $\tilde{B}$-state, it essentially fails to reproduce the subsequent internal conversion to the electronic $\tilde{X}$-state. In particular, the MFT method predicts a too slow population transfer from the $\tilde{C}$- and $\tilde{B}$-state to the electronic ground state.

Finally, Fig. 3 displays the results for Model III, describing ultrafast photoisomerization triggered by a conical intersection. Similarly as found

for Model I, the MFT method is seen to reproduce the initial fast decay of the adiabatic population as well as the coherent oscillations of the diabatic population, but has problems to describe the long-time decay of the adiabatic population correctly. The probability P_{cis} that the system remains in the initially prepared *cis*-conformation is also seen to be in quite good agreement with the quantum result. This finding demonstrates the ability of the MFT method to qualitatively describe the nonadiabatic dynamics in the presence of highly anharmonic potential-energy surfaces.

3.4. *Discussion*

The MFT equation of motion (25) can be derived in many ways, including the WKB approximation,[4] the eikonal method,[7] a (semi)classical time-dependent self-consistent field ansatz,[11–14] density-matrix approaches,[8–10] and the classical limit of algebraic quantization.[23] Depending on the specific approach used, slightly different MFT schemes may result. For example, the classical force can be described either by the average of the quantum force as in Eq. (25) or by the derivative of the average quantum potential.[15,16]

While most derivations focus on the equation of motion, an equally important aspect of the MFT method is the correct representation of the quantum-mechanical initial state. It is well known that the classical limit of quantum dynamics in general is represented by an ensemble of classical orbits.[17–19,135] Hence it is not appropriate to use a single classical trajectory but it is necessary to average over many trajectories, the initial conditions of which are chosen to mimic the quantum nature of the initial state of the classically treated subsystem. Interestingly, it turns out that several misconceptions concerning the theory and performance of the MFT method are rooted in the assumption of a single classical trajectory.

First, it is noted that it is this sampling that makes the MFT method quite different from the quantum-mechanical time-dependent self-consistent-field (TDSCF) approach. It is well known that the MFT equation of motion for a single trajectory may be derived as an classical approximation to the single-configuration TDSCF ansatz.[11–14] To derive the MFT method including the correct quasiclassical averaging, however, the derivation needs to start from a multiconfiguration-type TDSCF ansatz and furthermore has to assume a rapid randomization of the nuclear phases.[13,14] Because of the ensemble average, the quasiclassical MFT method contains

"static" correlation, and actually may perform qualitatively better than a quantum-mechanical single-configuration TDSCF ansatz. This effect was explicitly shown in the case of Model I,[126] where the quantum TDSCF approximation was found to completely fail to account for the long-time behavior of the electronic dynamics, which is at least qualitatively reproduced by the MFT results reported above. This is because the standard TDSCF ansatz neglects all correlations between the dynamical DoF, whereas the MFT treatment may account for some correlation due to the sampling of the initial state.

Furthermore, a related and common criticism of the MFT method is that a mean-field approach cannot correctly describe the branching of wavepackets at crossings of electronic states.[52,55,66] This is true for a *single* mean-field trajectory, however, not so for an ensemble of trajectories. In this context it may be stressed that an *individual* trajectory of an ensemble does not even possess a physical meaning — only the average does.

Employing a correct quasiclassical average, the numerical results obtained above for the Models I and III have clearly demonstrated that the MFT method qualitatively reproduces the electronic population dynamics and therefore — at least in principle — is able to account for the branching of trajectories in a nonadiabatic calculation. The failure of the MFT method to describe the long-time dynamics of the three-state Model II has a quite different origin. It is related to the fact that the MFT approach treats electronic and nuclear DoF on an unequal dynamical footing. This becomes clear within the mapping approach introduced in Sec. 6, where it is shown that the MFT method can be derived from the classical mapping formulation if the initial quantum fluctuations of the electronic and nuclear DoF are treated in a different way.

Let us finally discuss to what extend the MFT is able to (i) obey the principle of microreversibility, (ii) account for the electronic phase coherence, and (iii) correctly describe the vibrational motion on coupled potential-energy surfaces. Although the MFT equations of motion and their solutions are invariant with respect to the symmetry operation of time reversal, it is a well-known flaw of the MFT propagation to violate quantum microreversibility. It should be noted that this property of the MFT scheme is not caused by the classical-path approximation, but is common to any approximate TDSCF description. The problem is most easily rationalized in the case of a scattering reaction occurring in a two-state curve-crossing

system. Assuming for illustrative purposes that the electronic transition probability is small, the forward trajectory mainly propagates on the electronic $|\Phi_1\rangle$ surface, while the back trajectory mainly propagates on the electronic $|\Phi_2\rangle$ surface, thus leading to different dynamics and transition probabilities (see, e.g. the discussion in Ref. 62).

A further important property of a MQC description is the ability to correctly describe the time evolution of the electronic coefficients. A proper description of the electronic phase coherence is expected to be particularly important in the case of multiple curve-crossings which are frequently encountered in bound-state relaxation dynamics.[122] Within the limits of the classical-path approximation, the MFT method naturally accounts for the coherent time evolution of the electronic coefficients. This conclusion is clearly supported by the numerical results for the transient oscillations of the electronic population, which were reproduced quite well by the MFT method. Similarly, it has been shown that the MFT method in general does a good job in reproducing coherent nuclear motion on coupled potential-energy surfaces.

4. Surface-Hopping Method

As explained in the Introduction, one needs to distinguish the following kinds of "surface hopping" (SH) methods: (i) Semiclassical theories based on a connection ansatz of the WKB wave function,[39–50] (ii) stochastic implementations of a given deterministic multistate differential equation, e.g. the quantum-classical Liouville equation,[29,31,32] and (iii) quasiclassical models such as the well-known SH schemes of Tully and others.[51–68] In this chapter, we focus on the latter type of SH method, which has turned out to be the most popular approach to describe nonadiabatic dynamics at conical intersections.

4.1. *General Idea*

The quasiclassical SH model employs the simple and physically appealing picture in which a molecular system always evolves on a *single adiabatic* potential-energy surface (PES). When the trajectory reaches an intersection of the electronic PESs, the transition probability $p_{k\to k'}$ to the other PES is calculated according to some hopping criterion and, depending on the comparison of $p_{k\to k'}$ with a random number, the trajectory "hops" to

the other adiabatic surface. Contrary to the mean-field trajectory scheme, where the trajectories evolve on an *averaged* electronic PES [cf. Eq. (25)], the SH equations of motion for the nuclear degrees of freedom therefore assume the simple form

$$\begin{aligned} \dot{R}_j &= \omega_j P_j, \\ \dot{P}_j &= -\frac{\partial V_k}{\partial R_j}, \end{aligned} \tag{27}$$

where V_k denotes the adiabatic PES on which the trajectory currently evolves. In order to conserve the energy of the classical system during an electronic transition, the momenta of the nuclei have to be adjusted after every hop. We note in passing that SH simulations are performed in the adiabatic representation, because (i) the picture of instantaneous hops only appears plausible for highly localized interactions between the PESs such as the nonadiabatic kinetic-energy couplings, and (ii) a single adiabatic PES is expected to represent the coupled-surfaces problem better than a single diabatic one.

Since the hopping procedure accounts for the coupling of electronic and nuclear degrees of freedom, the key problem of the SH approach is to establish a dynamically consistent hopping criterion and momentum adjustment. As already mentioned, any rigorous way to derive such a formulation leads to complicated equations of motion that in general are quite cumbersome to implement (see, e.g. Sec. 5.2). Many workers have therefore developed simple but practical models of SH.[51–68] Here the most popular formulation is the "fewest switches" algorithm proposed by Tully.[52] Since a detailed description can be found in many papers (see, e.g. Refs. 52, 53, 66 and 67), in the following only the main idea of this method is outlined.

4.2. *Theory and Numerical Implementation*

As a starting point, we consider the Schrödinger equation (24) in the adiabatic classical-path approximation. This equation can be recast in a density-matrix notation by

$$\dot{\rho}_{kk} = 2\mathrm{Re} \sum_{k'} A_{kk'} \rho_{kk'}, \tag{28}$$

where the electronic density-matrix elements are given as $\rho_{kk'}(t) = a_k^*(t) a_{k'}(t)$, and $k, k' = 1, 2$. Introducing a time step Δt which is small

enough that the change $\Delta\rho_{kk}$ of the diagonal matrix elements can be approximated by

$$\Delta\rho_{kk} = \dot{\rho}_{kk}\Delta t, \tag{29}$$

the basic assumption is that the populations ρ_{kk} change according to the master equation

$$\Delta\rho_{kk} = -\sum_{k'} p_{k\to k'}\rho_{kk} + \sum_{k'} p_{k'\to k}\rho_{k'k'}. \tag{30}$$

By combining Eqs. (28)–(30), the electronic transition probability $p_{1\to 2}$ is readily derived as

$$p_{1\to 2} = 2\mathrm{Re}\; A_{21}\Delta t\; \rho_{21}/\rho_{11}. \tag{31}$$

Similarly, the transition probability $p_{2\to 1}$ is obtained by exchanging the indices "1" and "2".

The formulation outlined above allows for a simple stochastic implementation of the deterministic differential equation (28). Starting with an ensemble of trajectories on a given adiabatic PES V_k, at each time step Δt (i) we compute the transition probability $p_{k\to k'}$, (ii) compare it to a random number $\zeta \in [0,1]$, and (iii) perform a hop if $p_{k\to k'} > \zeta$. In the case of a pure N-level system (i.e. in the absence of nuclear dynamics), the assumption (30) holds in general, and the stochastic modeling of Eq. (28) is exact. Considering a vibronic problem with coordinate-dependent $A_{kk'}$, however, it can be shown that the electronic transition probability depends in a complicated and nonlocal way on the nuclear dynamics (cf. Sec. 5.2). In this case, the stochastic model represents an approximation to the true dynamics.

As a consistency test of the stochastic model, one can check whether the percentage $N_k(t)$ of trajectories propagating on the adiabatic PES V_k is equal to the corresponding adiabatic population probability $P_k^{\mathrm{ad}}(t)$. In a SH calculation, the latter quantity may be evaluated by an ensemble average over the squared modulus of the adiabatic electronic coefficients [cf. Eq. (19)], i.e.

$$P_k^{\mathrm{ad}}(t) = \langle a_k^*(t)a_k(t)\rangle_C. \tag{32}$$

To obtain a similar expression for $N_k(t)$, we introduce "binned" adiabatic coefficients $\tilde{a}_k(t)$, i.e.

$$\tilde{a}_k(t) = \begin{cases} 1 & \text{if trajectory evolves on } V_k \\ 0 & \text{otherwise.} \end{cases} \tag{33}$$

Hence the percentage $N_k(t)$ of trajectories propagating on the adiabatic PES V_k can be written as

$$N_k(t) = \langle \tilde{a}_k^*(t)\tilde{a}_k(t)\rangle_C. \tag{34}$$

Combining these equation, the consistency condition of the stochastic model reads

$$\langle a_k^*(t)a_k(t)\rangle_C = \langle \tilde{a}_k^*(t)\tilde{a}_k(t)\rangle_C. \tag{35}$$

As is shown below, the simple SH model in general does not satisfy this relation.

Besides the hopping criterion, one furthermore needs to establish a rule that ensures the energy conservation of the classical system during an electronic transition. Assuming that the positions of the nuclei do not change during an instantaneous hopping process, we need to find a procedure which allows us to calculate the momenta of the trajectory on the new electronic PES. Semiclassical analyzes[42,44,47] suggest that the momenta are adjusted in the direction of the nonadiabatic coupling $\mathbf{F}_{kk'} = \langle \Phi_k|\nabla|\Phi_{k'}\rangle$, thus yielding the ansatz

$$\mathbf{P}' = \mathbf{P} + \sigma \mathbf{F}_{kk'}, \tag{36}$$

where the parameter σ is assumed to be real and identical for all momenta. Employing the condition of energy conservation, we obtain a quadratic equation for σ

$$c_{kk'}\sigma^2 + b_{kk'}\sigma + (V_{k'} - V_k) = 0, \tag{37}$$

where we have used the abbreviations $c_{kk'} = \sum_j \frac{1}{2}\omega_i |F^j_{kk'}|^2$ and $b_{kk'} = \sum_j \omega_j P_j F^j_{kk'}$.

To obtain a unique and consistent matching condition for the vibrational momenta in a hopping process, a single and real solution of Eq. (37) is required. If the equation possesses two real roots, one may choose the solution with the smaller modulus. Problems arise, however, if there is no real solution to Eq. (37). This case may occur for transitions from a lower to a higher electronic state whereby there is less kinetic energy (in direction of the nonadiabatic coupling) available than the potential-energy difference $V_{k'} - V_k$ requires. Hence the hopping process has to be rejected although the electronic equations of motion (28) suggest an electronic transition. Since the situation is quite similar to quantum-mechanical tunneling, the rejected hops have been referred to as *classically forbidden electronic transitions*.[62]

The breakdown of the SH scheme in the case of classically forbidden electronic transitions should not come as a surprise, but is a consequence of the rather simplifying assumptions [i.e. Eqs. (30) and (36)] underlying the SH model. On a semiclassical level, classically forbidden transitions may approximately be described within an initial-value representation (see Sec. 7) or by introducing complex-valued trajectories.[42] On the quasiclassical level considered here, however, there is no rigorous way to solve the problem. This has spurred a large number of ideas to fix the situation. The standard proposal is to "reflect" the trajectory when a surface hop is rejected, that is, to reverse the component of momentum in direction of the nonadiabatic coupling vector.[47,53] Other proposals include the combination of mean-field and SH ideas,[55–58] the resetting of electronic coefficients,[61] and the introduction of a position adjustment[50] or a time uncertainty[59] during a hop. Based on detailed numerical studies of the dynamics at a conical intersection, Müller and Stock[62] suggested the minimal solution of simply ignoring forbidden hops (see below).

4.3. *Results and Discussion*

As first example, we again consider Model I describing a two-state three-mode model of the $S_1(n\pi^*)$ and $S_2(\pi\pi^*)$ states of pyrazine. Figure 4(a) shows the quantum-mechanical (thick line) and the SH (thin lines) results for the population probability $P_2^{\mathrm{ad}}(t)$ of the initially prepared adiabatic electronic state $|\Phi_2\rangle$. As explained above, there are two ways to evaluate the adiabatic population in a SH calculation: One may either evaluate the adiabatic population from the electronic coefficients [Eq. (32)], or one may employ the binned adiabatic coefficients defined in Eq. (33) and calculate the percentage of trajectories $N_k(t)$ propagating on the adiabatic surface V_k [Eq. (34)]. According to Eq. (35), the results of both calculations should coincide if the SH model provides a consistent description of the nonadiabatic dynamics. Figure 4(a) clearly demonstrates that this is not the case. Although the general appearance (i.e. ultrafast initial decay to an approximately constant value) is roughly the same for both quantities, they are seen to differ significantly after only $\approx 20\,\mathrm{fs}$.

As discussed above, this discrepancy may be caused by classically forbidden electronic transitions, i.e. cases in which a proposed hopping process is rejected due to a lack of nuclear kinetic energy. Figure 4(c) supports this

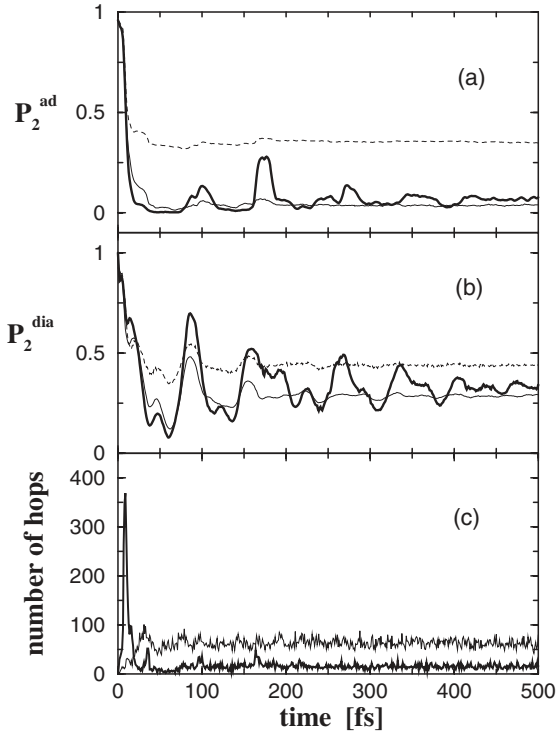

Fig. 4. Time-dependent population probability of the upper (a) adiabatic and (b) diabatic electronic state of Model I. The quantum-mechanical results (thick lines) are compared to SH results obtained directly from the electronic coefficients (dashed lines) and to SH results obtained from binned coefficients (thin solid lines), reflecting the percentage $N_2(t)$ of trajectories propagating on the upper adiabatic surface. (c) Absolute number of successful (thick line) and rejected (thin line) surface hops occurring in the SH calculation.

idea by showing the absolute numbers of successful (thick line) and rejected (thin line) surface hops. In accordance with the initial decay of the adiabatic population, the number of successful surface hops is largest during the first 20 fs. For larger times, the number of rejected hops exceeds the number of successful surface hops. This behavior clearly coincides with the onset of the deviations between the two classically evaluated curves $N_k(t)$ and $P_k^{\mathrm{ad}}(t)$. We therefore conclude that the observed breakdown of the consistency relation (35) is indeed caused by classically forbidden electronic transitions.

In direct analogy to the adiabatic case, the classical diabatic population probability is given by

$$P_k^{\mathrm{di}}(t) = \langle d_k^*(t) d_k(t) \rangle_C, \tag{38}$$

where the diabatic electronic coefficients $d_k(t)$ may be calculated from the adiabatic electronic coefficients $a_k(t)$ employing the transformation between the two representations. Figure 4(b) compares the SH results obtained for the diabatic population (dashed line) to the quantum-mechanical reference data (thick line). Similar as in the adiabatic case, the diabatic population calculated from the electronic coefficients can only roughly match the quantum results. Inspired by the finding that the quantity $N_k(t)$ provides a better approximation of the adiabatic population probability, we have also evaluated the "binned" diabatic population

$$\tilde{P}_k^{\mathrm{di}}(t) = \langle \tilde{d}_k^*(t) \tilde{d}_k(t) \rangle_C, \tag{39}$$

where the diabatic coefficients $\tilde{d}_k(t)$ have been calculated from the binned adiabatic coefficients $\tilde{a}_k(t)$. Interestingly, it is seen that the quantum results are reproduced much better by this approximation. In fact, in all simulations performed for conical intersections, it has been found that the binned quantities $N_k(t)$ and $\tilde{P}_k^{\mathrm{di}}(t)$ provide the better approximation to the corresponding quantum-mechanical population probabilities. If not noted otherwise, henceforth we will always consider binned electronic population probabilities.

To obtain a more comprehensive picture of the performance of the SH method for Model I, Fig. 5 compares quantum (thick lines) and SH (thin lines) results for the adiabatic and diabatic population probabilities as well as for the mean momenta of the two totally symmetric modes of the model. Let us first consider the results obtained for the standard SH algorithm[52] shown on the left side, and focus on the vibrational dynamics of the system. The SH calculations of the momenta are seen to qualitatively match the quantum-mechanical results, although the classical approximation exaggerates the damping of the coherent vibrational motion. Interestingly, the onset of the deviations between quantum and classical results again coincides with the onset of rejected hops displayed in Fig. 4(b). This finding indicates that the adjustment of momenta performed in this case might not be appropriate. In fact, we have found that the SH results improve significantly, if one simply omits the momentum adjustment in the case of

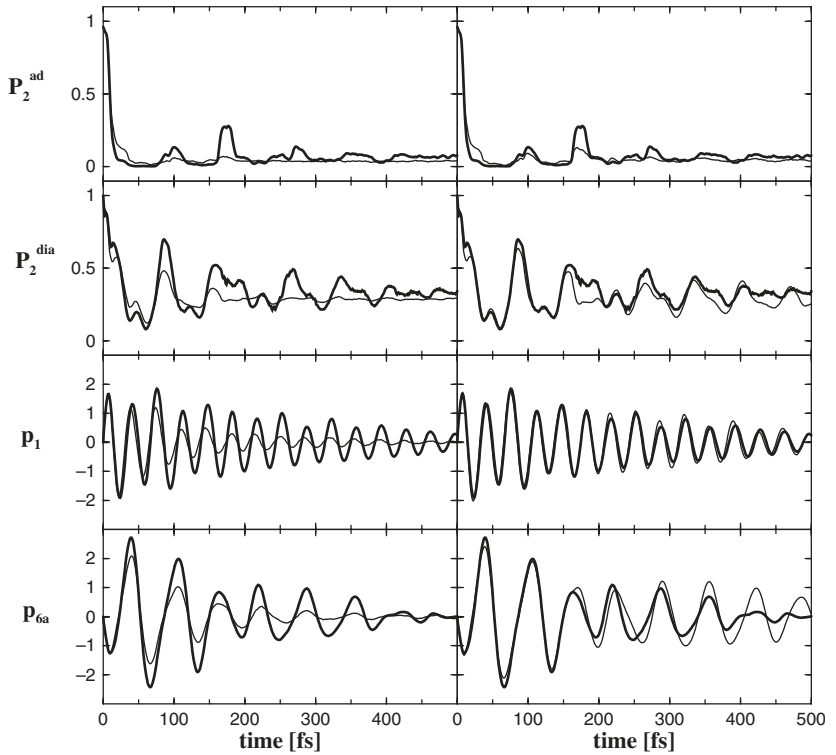

Fig. 5. Quantum-mechanical (thick lines) and SH (thin lines) calculations obtained for Model I describing the $S_2 \rightarrow S_1$ internal-conversion process in pyrazine. Shown are the time-dependent population probabilities $P_2^{\mathrm{ad}}(t)$, $P_2^{\mathrm{dia}}(t)$ of the initially prepared adiabatic and diabatic electronic state, respectively, as well as the mean momenta of the two totally symmetric modes ν_1 and ν_{6a}. The SH calculations used the standard algorithm of Tully[52] (left panels) as well as a modified algorithm described in Ref. 62 (right panels).

a rejected hop. A comparison of the results obtained by the thus modified SH algorithm (right panels) and the standard algorithm (left panels) reveals that all time-dependent observables are reproduced much better by the modified algorithm. In particular, the vibrational momenta of the quantum calculation and the modified SH calculation are in excellent agreement, thus suggesting that the vibrational dephasing associated with the internal-conversion process in pyrazine is mainly caused by the anharmonicity of the lower adiabatic PES. As the modified algorithm has been found

to yield better results for *all* model systems considered,[62] it has been used in all remaining calculations.

Let us turn to Model II describing the $\tilde{C} \rightarrow \tilde{B} \rightarrow \tilde{X}$ internal-conversion of the benzene cation. Figure 2 shows the diabatic population probabilities pertaining to the three electronic states as obtained from (a) the quantum-mechanical calculation of Köppel,[119] (b) the mean-field trajectory method described in Sec. 3, (c) the SH method using Eq. (38), and (d) the SH method using Eq. (39). Furthermore, the corresponding adiabatic population probabilities are shown at the right-hand-side of Fig. 2, although a quantum-mechanical calculation of this observable is not available. Again, we observe that only the binned SH results match the quantum reference data. It is interesting to note that the standard SH results shown in panel (c) are quite similar to the mean-field trajectory results in that they essentially fail to reproduce the internal conversion to the electronic $\tilde{X}$-state. As both SH populations are obtained from the same simulation, this finding is somewhat disturbing, although the binned results in (d) look quite promising.

Finally, let us consider Model III describing ultrafast nonadiabatic *cis-trans* photoisomerization. Figure 3 compares quantum (thick line), mean-field (dashed line), and SH (thin line) results of the (a) adiabatic and (b) diabatic population as well as (c) of the probability $P_{\text{cis}}(t)$ that the system remains in the initially prepared *cis* conformation. Again, binned electronic population probabilities and no momentum adjustment for classically forbidden transitions are employed in the SH calculations. Similar to the mean-field calculations, the SH simulations are able to qualitatively reproduce the main features of the nonadiabatic photoisomerization, including initial decay, oscillatory transients as well as long-time limits. It may be noted that, similar to Model I, the adiabatic relaxation dynamics of Model III is relatively simple, thus facilitating a modeling by the SH method. On the other hand, the simulations for Model III convincingly demonstrate that the SH technique is able to account for nonadiabatic relaxation dynamics in the presence of highly anharmonic PESs.

5. Quantum-Classical Liouville Description

5.1. *General Idea*

The dynamics of classical as well as of quantum systems can be described by a Liouville equation for the time-dependent density. In quantum-mechanics,

the Liouville equation for the density operator $\hat{\rho}(t)$ reads

$$\frac{\partial}{\partial t}\hat{\rho}(t) = -\frac{i}{\hbar}[\hat{H}, \hat{\rho}(t)], \tag{40}$$

where $\hat{H} = \hat{H}(\hat{q}, \hat{p})$ is the quantum Hamiltonian depending on position and momentum operators $\hat{q}$ and $\hat{p}$, respectively and $[\hat{A}, \hat{B}] = \hat{A}\hat{B} - \hat{B}\hat{A}$ denotes the usual quantum commutator. In order to obtain the classical limit of Eq. (40), one may introduce a quantum-mechanical phase-space representation of the operators such as the Wigner–Weyl formulation.[123] Retaining only the classical ($\hbar = 0$) terms, the resulting equation of motion reads

$$\frac{\partial}{\partial t}\rho(t) = \{H, \rho(t)\}, \tag{41}$$

where $\rho(t) = \rho(q, p, t)$ is the Wigner density function, $H = H(q, p)$ is the classical Hamiltonian, and $\{A, B\} = \partial_q A \partial_p B - \partial_p A \partial_q B$ denotes the classical Poisson bracket.

The similar appearance of the quantum and classical Liouville equations has motivated several workers to construct a mixed quantum-classical Liouville (QCL) description.[21–34] Hereby a partial classical limit is performed for the heavy-particles dynamics, while a quantum-mechanical formulation is retained for the light particles. The quantities $\rho(t)$ and H in the mixed QC formulation are then operators with respect to the electronic degrees of freedom, described by some basis states $|\phi_n\rangle$, and classical functions with respect to the nuclear degrees of freedom with coordinates $\mathbf{R} = \{R_j\}$ and momenta $\mathbf{P} = \{P_j\}$, for example,

$$\rho(t) = \sum_{nm} \rho_{nm}(\mathbf{R}, \mathbf{P}, t)|\phi_n\rangle\langle\phi_m|. \tag{42}$$

The standard proposal for the Liouville equation for this QC density operator is

$$\frac{\partial}{\partial t}\rho(t) = [H, \rho(t)]_{QC}, \tag{43}$$

$$[A, B]_{QC} = -i/\hbar[A, B] + \tfrac{1}{2}\{A, B\} - \tfrac{1}{2}\{B, A\}, \tag{44}$$

where $[.,.]_{QC}$ denotes the QC bracket that contains the quantum commutator $[.,.]$ in (40) and the classical Poisson bracket $\{.,.\}$ in (41) as limiting cases. Equation (43) can be derived via a number of approaches, for example, by requiring certain axioms for the QC bracket to be satisfied,[22] by

replacing nuclear commutators by Poisson brackets and nuclear anticommutators by products of operators,[25] and by performing the partial classical limit in the Wigner phase-space representation.[24,27,28,30]

Although the QC bracket (44) is not unique and there has been some discussion on the overall consistency of the approach,[23,24,27] the QCL formulation appears to be a quite promising formulation. As shown below, the QCL description naturally provides a correct treatment of electronic coherences and of the momentum change associated with an electronic transition, and is therefore not plagued by the obvious inconsistencies arising in simpler MQC approaches. Furthermore, since the classical Wigner approximation is exact for quadratic Hamiltonians, it is easy to show that the QCL equation is actually *exact* in the case of the linear vibronic-coupling Hamiltonian of Model I (2), describing a multimode model of a conical intersection.

The latter observation, however, indicates that the general solution of the QCL equation may require a similar effort as the solution of an exact quantum-mechanical description. In fact, the numerical implementation of the partial differential equation (43) is only straightforward if the density is represented by some sort of a grid in phase space. The grid may be fixed[25,30] or moving in phase space, for example, via Gaussian wave packets.[26,31] Similar to a full quantum calculation, however, the numerical effort for these strategies appears to scale exponentially with the number of quantum *and* classical degrees of freedom. To obtain a numerical method that is directly applicable to truly multidimensional systems, it therefore is desirable to employ a stochastic scheme involving a Monte-Carlo sampling of local classical trajectories.[29,32–34] Such an approach has to cope with two major complications, that is, the representation of nonlocal phase-space operators and the convergence of the sampling procedure which is cumbersome due to complex-valued trajectories with rapidly oscillating phases. The latter is related to the so-called dynamical sign problem which is well known from real-time path-integral[136] and time-dependent semiclassical[86] calculations.

To give an impression of the virtues and shortcomings of the QCL approach and to study the performance of the method when applied to the dynamics at conical intersections, in the following we briefly introduce the QCL working equation in the adiabatic representation, describe a recently proposed stochastic trajectory implementation of the resulting QCL equation,[34] and apply this numerical scheme to Model I, which describes the $S_2 \rightarrow S_1$ internal conversion in pyrazine.

5.2. *Theory and Numerical Implementation*

Performing a partial Wigner transformation with respect to the nuclear variables, the molecular Hamiltonian can be written as

$$H(\mathbf{R},\mathbf{P}) = \sum_j \frac{P_j^2}{2M_j} + h(\mathbf{R}), \tag{45}$$

where the nuclear coordinates $\mathbf{R}$ and momenta $\mathbf{P}$ are now classical degrees of freedom and $h(\mathbf{R}) = T_r + V(\mathbf{r},\mathbf{R})$ is the electronic Hamiltonian comprising the electronic coordinates $\mathbf{r}$. Adopting the adiabatic electronic representation with basis states $\{|\Phi_n^a(\mathbf{R})\rangle\}$, the electronic Hamiltonian $h(\mathbf{R})$ is diagonal in this representation

$$h(\mathbf{R})|\Phi_n^a(\mathbf{R})\rangle = V_n(\mathbf{R})|\Phi_n^a(\mathbf{R})\rangle, \tag{46}$$

with $V_n(\mathbf{R})$ being the nth adiabatic potential-energy surface. The corresponding electronic matrix elements of the partial Wigner transformed density operator $\rho(\mathbf{R},\mathbf{P},t)$ are given by

$$\rho_{nm}(\mathbf{R},\mathbf{P},t) = \langle\Phi_n^a(\mathbf{R})|\rho(\mathbf{R},\mathbf{P},t)|\Phi_m^a(\mathbf{R})\rangle. \tag{47}$$

For notational convenience, in the following we will usually drop the dependency on the nuclear variables $\mathbf{R},\mathbf{P}$.

By inserting Eqs. (45)–(47) into the QCL equation (43), the equations of motion for the QC density matrix in the adiabatic representation can be written in the following suggestive form[28]

$$\frac{\partial}{\partial t}\rho_{nn'} = \sum_{m,m'} \left(\mathcal{L}^Q_{nn',mm'} + \mathcal{L}^C_{nn',mm'} + \mathcal{L}^{QC}_{nn',mm'}\right)\rho_{mm'}, \tag{48}$$

where

$$\mathcal{L}^Q_{nn',mm'} = -i/\hbar(V_n - V_{n'})\delta_{nm}\delta_{n'm'}, \tag{49}$$

$$\mathcal{L}^C_{nn',mm'} = \sum_j \left(-\frac{P_j}{M_j}\frac{\partial}{\partial R_j} + \frac{\partial}{\partial R_j}\frac{1}{2}\left(V_n + V_{n'}\right)\frac{\partial}{\partial P_j}\right)\delta_{nm}\delta_{n'm'}, \tag{50}$$

account for the pure quantum-mechanical and the pure classical time evolution of the density matrix, respectively. Hereby, the quantum part $\mathcal{L}^Q$ introduces the phase $(V_n - V_{n'})/\hbar$ to the off-diagonal matrix elements of the density matrix, while the classical part $\mathcal{L}^C$ describes standard Newtonian dynamics with respect to the adiabatic potential energy $(V_n + V_{n'})/2$. It is

noted that the evaluation of the equations of motion (48) requires the propagation of classical trajectories in diagonal and off-diagonal matrix elements of the electronic density matrix. This is in contrast to usual surface-hopping methods based on a wave-function ansatz.[65–67] These formulations do not explicitly account for the coherences $\rho_{n\neq m}(t)$ and therefore only require the propagation of classical trajectories in diagonal potential-matrix elements V_{nn}.

The quantum-classical part of the Liouville operator

$$\mathcal{L}^{QC}_{nn',mm'} = -\sum_j \frac{P_j}{M_j}\, F^{(j)}_{nm} \left(1 + \sum_i S^{(i)}_{nm} \frac{\partial}{\partial P_i}\right) \delta_{n'm'}(1 - \delta_{nm}\delta_{n'm'}) \; + \text{h.c.}, \tag{51}$$

$$S^{(i)}_{nm} = \frac{(V_n - V_m)}{2\sum_j F^{(j)}_{nm}\, P_j/M_j}\, F^{(i)}_{nm} \tag{52}$$

accounts for the non-Born–Oppenheimer transitions of the system which are induced by the first-order nonadiabatic couplings $F^{(j)}_{nm} = \langle \Phi_n | \partial/\partial R_j | \Phi_m \rangle$. Note that in a standard quantum-mechanical formulation only the first part of $\mathcal{L}^{QC}$ appears, that is, the term $\propto PF_{nm}$. In this case, P and F_{nm} represent nonlocal quantum operators with respect to the nuclear degrees of freedom, while in the QC case P and F_{nm} are classical functions. Here the nonlocal nature of the nonadiabatic transition is accounted for by the term $\propto S_{nm}\partial/\partial P$, which affects a momentum change of the classical trajectory. This shift of nuclear momenta associated with the transition between adiabatic potential-energy surfaces has been discussed in various semiclassical theories of nonadiabatic processes.[42–50]

It is noted that the momentum derivatives of the coupling elements (51) represent one of the main obstacles of a practical trajectory-based evaluation of the QCL equation, because these terms require the knowledge of the function in question not only at a particular point in phase space but at the same time also at nearby points. As a remedy, we may restrict ourselves to the limit of small momentum changes $S_{nm}/P \ll 1$ and approximate $1 + S_{nm}P \approx \exp(S_{nm}\partial/\partial P)$. Since $e^{S\partial/\partial p} f(p) = f(p + S)$, the approximation reduces the action of the differential operator to a simple shift of momenta. We note that this approximation resembles the usual momentum-jump ansatz employed in various surface-hopping methods.[65–67] As has been discussed in Sec. 4, however, the latter formulations typically

require the conservation of nuclear energy during an electronic transition, which gives rise to the problem of classically forbidden transitions. The QCL formulation, on the other hand, does not conserve the energy of an *individual* trajectory but the energy of the trajectory *average*.[30]

For the numerical implementation of the QCL equation, the Liouville operator $\mathcal{L}$ is decomposed into a zero-order part $\mathcal{L}_0$ which is easy to evaluate and a nonadiabatic transition part $\mathcal{L}^{QC}$ whose evaluation is difficult. In order to facilitate the treatment of multidimensional systems, Santer *et al.* have introduced a stochastic algorithm which uses a Monte-Carlo sampling of local classical trajectories.[34] In this formulation, the QC density matrix $\rho_{nm}(\mathbf{R}, \mathbf{P}, t)$ is represented by a set of "random walkers," where each random walker carries the information of its phase-space position $(\mathbf{R}, \mathbf{P})$, its density $P_{nm}(t)$ and phase $\sigma_{nm}(t)$, as well as of its weight $W_{nm}(t)$. A stochastic realization of the $\mathcal{L}_0$ propagation process is then straightforward: One first samples positions and momenta from the given initial phase-space distributions $\rho_{nm}(\mathbf{R}, \mathbf{P}, t = 0)$, thus determining the densities $P_{nm}(0)$. Furthermore, the initial weights and phases are chosen to correctly represent the initial state of the density matrix. To describe the evolution of the system within a time step δt due to the action of $\mathcal{L}_0 = \mathcal{L}^Q + \mathcal{L}^C$, the density matrix element ρ_{nm} (i) accumulates a phase $\exp(-i/\hbar(V_n - V_m)\delta t)$ which is represented by the phase function $\sigma_{nm}(t)$, and (ii) is subject to propagation in phase space driven by $e^{-i/\hbar\mathcal{L}^C\delta t}$, which affects the densities P_{nm}, but leaves the weights W_{nm} unchanged. As described in Ref. 34, the stochastic realization of the off-diagonal operator $\mathcal{L}^{QC}$ is somewhat more involved. Causing transitions between the different components of the density matrix, this operator can be viewed as a branching or hopping term, which also modifies the weights $W_{nm}(t)$.

Within the momentum-jump approximation, the algorithm described in Ref. 34 provides an in principle *exact stochastic realization* of the QCL equation. Similar to path-integral[136] and semiclassical[86] propagation methods, however, the Monte-Carlo evaluation of the QCL equation is plagued by the so-called dynamical sign problem, which is caused by exponentially increasing weights accompanied by rapidly varying phases. As a consequence, the signal-to-noise ratio of the sampling deteriorates in the course of propagation, or in other words, the sampling effort increases exponentially in time. A well-known strategy to overcome this fundamental problem is to reorganize the sum over complex paths in a way that facilitates this canceling. In

our example this effect can be achieved by generating new random walkers at each surface hop: Whenever a hop is requested in the algorithm, a copy of the random walker is made. While the original walker stays on the potential-energy surface, the copy starts out on the new surface, whereby its phase and momenta are updated. Finally, the copy is added to the collection of random walkers already present, where the weights are adjusted accordingly. Proceeding this way, one may expect that at any time a sufficiently large number of random walkers is present to yield a reliable description of the density matrix. We note that the concept of generating new random walkers at curve crossings is quite similar to the "spawning" scheme suggested by Martinez and coworkers.[105–107]

5.3. *Results*

Employing the stochastic trajectory scheme outlined above to various avoided-curve-crossing problems, Ref. 34 has presented detailed numerical studies on the accuracy and efficiency of the algorithm which appeared to be quite promising. Because of the divergence of the nonadiabatic couplings, however, it may be expected that a conical intersection represents a much more challenging task for the QCL approach. So far, only two groups have reported first computational results, that is, an explicit phase-space density propagation of a two-mode model[33] and a stochastic trajectory study of the conical intersection in pyrazine (i.e. our Model I),[34] which will be briefly discussed in the following.

Let us first consider the population probability of the initially excited adiabatic state as shown in Fig. 6. Within the first 20 fs, the quantum-mechanical result is seen to decay almost completely to zero. The result of the QCL calculation matches the quantum data only for about 10 fs and is then found to oscillate around the quantum result. A closer analysis of the calculation shows that this flaw of the QCL method is mainly caused by large momentum shifts associated with the divergence of the nonadiabatic couplings $F_{nm}^{(j)} = \langle \Phi_n^a | \partial / \partial R_j | \Phi_m^a \rangle$. We therefore chose to resort to a simpler approximation and require that the energy of each individual trajectory is conserved. Employing this scheme, the corresponding QCL result for the adiabatic population matches at least qualitatively the quantum data.

Due to the large level density of the lower-lying adiabatic electronic state, the chances of a back transfer of the adiabatic population are quite

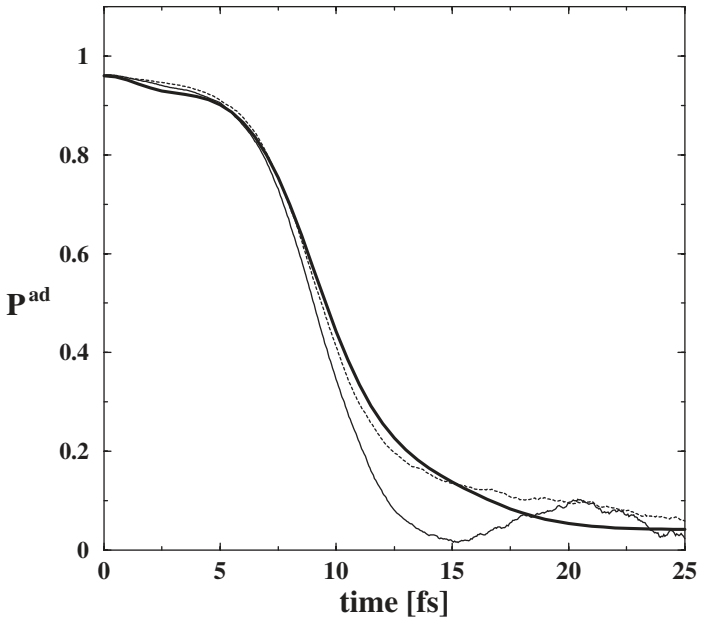

Fig. 6. Initial decay of the adiabatic population probability obtained for Model I. Compared are quantum results (thick line) and standard (thin full line) and energy-conserving (dotted line) quantum-classical Liouville results.

small for a multidimensional molecular system. To a good approximation, one may therefore assume that subsequent to an electronic transition a random walker will stay on the lower adiabatic potential-energy surface.[125] This observation suggests a physically appealing computational scheme to calculate the time evolution of the system for longer times. First, the initial decay of the adiabatic population is calculated within the QCL approach up to a time t_0, when the system is (almost) completely localized in the lower adiabatic electronic state $|\Phi_1^a\rangle$. In a second step, we take the resulting phase-space distribution $\rho_{11}(\mathbf{R}, \mathbf{P}, t_0)$ as initial state for a standard quasi-classical trajectory propagation on the lower adiabatic potential-energy surface. While the adiabatic electronic population is constant by construction, the scheme yields diabatic electronic quantities as well as observables of the nuclear motion such as the time-dependent mean positions and momenta.

As an example, Fig. 7 shows the diabatic electronic population probability for Model I. The quantum-mechanical results (thick line) are reproduced

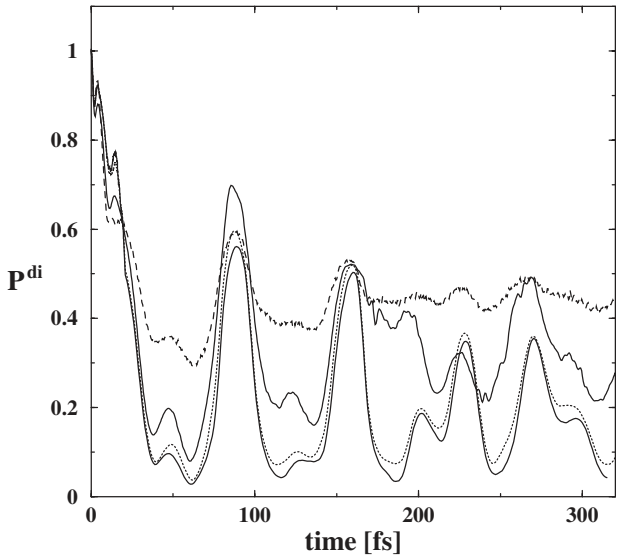

Fig. 7. Diabatic electronic population probability obtained for Model I. Compared are quantum results (thick line) and standard (thin full line) and energy-conserving (dotted line) quantum-classical Liouville results, as well as results from standard surface-hopping calculations (dashed line).

well by the QCL calculations, which have assumed a "localization time" of $t_0 = 20\,\text{fs}$. The results obtained for the standard QCL (thin full line) and the energy-conserving QCL (dotted line) are of similar quality, thus indicating that the phase-space distribution $\rho_{11}(\mathbf{R}, \mathbf{P})$ at $t_0 = 20\,\text{fs}$ is similar for the two schemes. Also shown in Fig. 7 are the results obtained for a standard surface-hopping calculation (dashed line), which largely fail to match the beating of the quantum reference.

We conclude that the QCL description represents a promising approach to the treatment of multidimensional curve-crossing problems. The density-matrix formulation yields a consistent treatment of electronic populations *and* coherences, and the momentum changes associated with an electronic transition can be directly derived from the formalism without the need of *ad hoc* assumptions. Employing a Monte-Carlo sampling scheme of local classical trajectories, however, we have to face two major complications, that is, the representation of nonlocal phase-space operators and the sampling problem caused by rapidly varying phases. At the present time, the

QCL calculations performed for conical intersections cannot yet compete in accuracy and efficiency with more established methods. Recalling, though, that all numerical implementations of the QCL equation have been suggested within the last few years,[26,29–34] it is clear that the QCL approach still holds a large potential to be discovered.

6. Mapping Approach

By definition, a mixed quantum-classical method treats the various degrees of freedom (DoF) of a system on a different dynamical footing, e.g. quantum mechanics for the electronic DoF and classical mechanics for the nuclear DoF. As was discussed above, some of the problems with these methods are related to inconsistencies inherent in this mixed quantum-classical ansatz. To avoid these problems, recently a conceptually different way to incorporate quantum mechanical DoF into a semiclassical or quasiclassical theory has been proposed, the so-called mapping approach.[69–71] In this formulation, the problem of a classical treatment of discrete DoF such as electronic states is bypassed by transforming the discrete quantum variables to continuous variables. In this section we briefly introduce the general concept of the mapping approach and discuss the quasiclassical implementation of this method as well as applications to the three models introduced above. The semiclassical version of the mapping approach is discussed in Sec. 7.

6.1. *Theoretical Formulation*

Let us consider a N-level system described by the Hamiltonian

$$H = \sum_{n,m} h_{nm} |\Phi_n\rangle\langle\Phi_m| . \tag{53}$$

The basic idea of the mapping approach is to change from the discrete representation employed in Eq. (53) to a continuous representation. There are several ways to do so, most of them are based on the representation of spin operators by boson operators.[137] Well-known examples of such mappings are the Holstein–Primakoff transformation,[138] which represents a spin system by a single nonlinear boson DoF, and Schwinger's theory of angular momentum,[72] which represents a spin system by two independent boson DoF.

As has been shown in Ref. 69, a general N-state system can be mapped on N continuous DoF, which are described by the harmonic-oscillator

creation and annihilation operators $a_n, a_m^\dagger$ with commutation relations $[a_n, a_m^\dagger] = \delta_{nm}$ and basis states $|n_1, \ldots, n_N\rangle$. The mapping relations for the operators and basis states are given by

$$|\Phi_n\rangle\langle\Phi_m| \mapsto a_n^\dagger a_m, \tag{54}$$

$$|\Phi_n\rangle \mapsto |0_1 \ldots 1_n \ldots 0_N\rangle. \tag{55}$$

According to Eq. (54), the Hamiltonian (53) in the continuous "oscillator representation" reads

$$\mathcal{H} = \sum_{n,m} h_{nm} a_n^\dagger a_m. \tag{56}$$

It is easy to show that the mapping of the operators (54) preserves the commutation relations and leads to the exact identity of the electronic matrix elements of the propagator

$$\langle\Phi_n|e^{-iHt}|\Phi_m\rangle = \langle 0_1 \ldots 1_n \ldots 0_N|e^{-i\mathcal{H}t}|0_1 \ldots 1_m \ldots 0_N\rangle. \tag{57}$$

As is stated by Eq. (57), the Hamiltonians (53) and (56) are fully equivalent when used as generators of quantum-mechanical time evolution. It is noted that the mapping (54) only represents an identity if it is restricted to the oscillator subspace with a single excitation [Eq. (55)]. In the quantum-mechanical formulation, this feature does not cause any problems, since it is clear from Eq. (56) that the system will always remain in this subspace. As discussed below, however, this virtue does not in general apply for the classical counterpart of the Hamiltonian (56).

To apply the formalism to vibronically coupled systems, we identify the $|\Phi_n\rangle$ with electronic states and the h_{nm} with operators of the nuclear dynamics. Hereby, the adiabatic as well as a diabatic electronic representation may be employed. In a diabatic representation, we have [cf. Eq. (1)]

$$h_{nm} = T(\mathbf{P})\delta_{nm} + W_{nm}(\mathbf{R}). \tag{58}$$

Introducing furthermore "Cartesian" electronic variables $x_n = (a_n^\dagger + a_n)/\sqrt{2}$, $p_n = i(a_n^\dagger - a_n)/\sqrt{2}$, the molecular Hamiltonian in the diabatic oscillator representation can be written as

$$\mathcal{H} = T(\mathbf{P}) - \frac{1}{2}\sum_n W_{nn}(\mathbf{R}) + \frac{1}{2}\sum_{n,m}(x_n x_m + p_n p_m) W_{nm}(\mathbf{R}). \tag{59}$$

Here, for notational convenience, we have assumed that $W_{nm} = W_{nm}^\dagger$. We would like to emphasize that the mapping to the continuous Hamiltonian

(59) does not involve any approximation, but merely represents the discrete Hamiltonian (58) in an extended Hilbert space. The quantum dynamics generated by both Hamilton operators is thus equivalent. The Hamiltonian (59) describes a general vibronically coupled molecular system, whereby both electronic and nuclear DoF are represented by continuous variables. Contrary to Eq. (53), the quantum-mechanical system described by Eq. (59) therefore has a well-defined classical analog.

6.2. *Classical Dynamics*

Since the mapping Hamiltonian (59) has a well defined classical analog, the semiclassical or quasiclassical evaluation of general nonadiabatic problems is in principle a straightforward matter. The transition from quantum to classical mechanics can be performed by changing from the Heisenberg *operators* obeying Heisenberg's equations to the corresponding classical *functions* obeying Hamilton's equations

$$\dot{p}_n = -\frac{\partial \mathcal{H}}{\partial x_n}, \qquad \dot{x}_n = \frac{\partial \mathcal{H}}{\partial p_n}, \tag{60}$$

$$\dot{P}_j = -\frac{\partial \mathcal{H}}{\partial R_j}, \qquad \dot{R}_j = \frac{\partial \mathcal{H}}{\partial P_j}, \tag{61}$$

where now $\mathcal{H}$ denotes the classical Hamiltonian function corresponding to the Hamiltonian operator (59).

In addition to the equations of motion one needs to specify a procedure to evaluate the observables of interest. Within a quasiclassical trajectory approach, the expectation value of an observable A is given by Eq. (13). For example, the expression for the electronic population probability, which is defined as the expectation value of the electronic occupation operator, reads

$$\begin{aligned} P_n(t) &= \left\langle \frac{1}{2}(x_n^2 + p_n^2 - 1) \right\rangle_C \\ &= \int d\mathbf{x} \int d\mathbf{p} \int d\mathbf{R} \int d\mathbf{P} \rho_{\mathrm{el}}(\mathbf{x}, \mathbf{p}) \rho_{\mathrm{vib}}(\mathbf{R}, \mathbf{P}) \frac{1}{2}(x_n^2 + p_n^2 - 1). \end{aligned} \tag{62}$$

As has been discussed in Sec. 3, the initial phase-space distribution ρ_{vib} for the nuclear DoF R_j and P_j may be chosen from the action-angle (15) or the Wigner (14) distribution of the initial state of the nuclear DoF. To specify the electronic phase-space distribution ρ_{el}, let us assume that the system is

initially in the electronic state $|\Phi_n\rangle$. According to Eq. (55), the electronic state $|\Phi_n\rangle$ is mapped onto $N_{\rm el}$ harmonic oscillators, whereby the nth oscillator is in its first excited state while the remaining $N_{\rm el}-1$ oscillators are in their ground state. The initial density operator is thus given by

$$\rho_{el} = |0_1 \ldots 1_n \ldots 0_{N_{\rm el}}\rangle\langle 0_1 \ldots 1_n \ldots 0_{N_{\rm el}}|. \tag{63}$$

The initial electronic distribution $\rho_{\rm el}(\mathbf{X},\mathbf{P})$ thus factorizes in $N_{\rm el}$ harmonic-oscillator distributions, which may be sampled, for example, from the Wigner distribution of $\rho_{\rm el}$. While this is known to work well for the ground state of the harmonic oscillator, the Wigner distribution pertaining to the first excited state may become negative, which can give rise to unphysical results. To avoid this well-known problem, it has proven advantageous to again change to classical action-angle variables n_k, q_k [cf. Eq. (15)] and assume a constant initial action n_k for all trajectories.[78]

6.3. *Relation to Other Formulations*

The mapping approach outlined above has been designed to furnish a well-defined classical limit of nonadiabatic quantum dynamics. The formalism applies in the same way at the quantum-mechanical, semiclassical (see Sec. 7), and quasiclassical level, respectively. Most important, no additional assumptions but the standard semiclassical and quasiclassical approximations are needed to get from one level to another. Most of the established mixed quantum-classical methods such as the mean-field-trajectory method or the surface-hopping approach do invoke additional assumptions. The comparison of the mapping approach to these formulations may therefore (i) provide insight into the nature of these additional approximation and (ii) indicate whether the conceptual virtues of the mapping approach may be expected to result in practical advantages.

Let us first consider the relation to the mean-field trajectory method discussed in Sec. 3. To make contact to the classical limit of the mapping formalism, we express the complex electronic variables d_n [cf. Eq. (22)] in terms of their real and imaginary parts, i.e. $d_n = (x_n + ip_n)/\sqrt{2}$. Furthermore, we introduce the mean-field Hamiltonian function $H_{\rm MF}$, which may

be defined as

$$H_{\mathrm{MF}} = \langle \Psi(t)|H|\Psi(t)\rangle = T(\mathbf{P}) + \frac{1}{2}\sum_{n,m}(x_n x_m + p_n p_m)W_{nm}(\mathbf{R}). \tag{64}$$

As first noted by Dirac[139] the canonical equations of motion for the real variables x_n, p_n with respect to H_{MF} are completely equivalent to Schrödinger's equation (22) for the complex variables d_n. Moreover, it is clear that the time evolution of the nuclear DoF [Eq. (26)] can also be written as Hamilton's equations with respect to H_{MF}. Similarly to the equations of motion for the mapping formalism [Eqs. (60) and (61)], the mean-field equations of motion for both electronic and nuclear DoF can thus be written in canonical form.

There is, however, an important conceptional difference between the two approaches. On the quasiclassical level, this difference simply manifests itself in the initial conditions chosen for the electronic DoF. Let us consider an electronic two-level system which is initially assumed to be in the electronic state $|\Phi_1\rangle$. In the mean-field formulation, the initial conditions are $|d_1(0)| = 1$, $|d_2(0)| = 0$. Changing to action-angle variables [cf. Eq. (15)], the electronic initial distribution in (62) thus is given by $\rho_{\mathrm{el}} = \delta(n_1 - 1)\delta(n_2)$. In the mapping formalism, on the other hand, the initial electronic state $|\Phi_1\rangle$ is represented by the first oscillator being in its first excited state and the second oscillator being in its ground state [cf. Eq. (63)]. This corresponds to the electronic action-angle initial distribution $\rho_{\mathrm{el}} = \delta\left(n_1 - \frac{3}{2}\right)\delta\left(n_2 - \frac{1}{2}\right)$, stating that, just like the nuclear DoF, the electronic DoF hold zero-point energy. Since the two-level system to be described, of course, does not hold zero-point energy, the zero-point energy $\frac{1}{2}(W_{11} + W_{22})$ of the two oscillators needs to be subtracted from the Hamiltonian. In fact, comparing the corresponding Hamiltonian functions $\mathcal{H}$ [Eq. (59)] and H_{MF} [Eq. (64)], it is found that

$$\mathcal{H} = H_{\mathrm{MF}} - \frac{1}{2}\sum_{n} W_{nn}(\mathbf{R}), \tag{65}$$

thus assuring that the total energy is the same in both formulations.

What is the origin for the difference between the two formulations? In the mapping approach, we perform a quantum-mechanically exact transformation and subsequently employ the classical approximation to the

complete system. As explained above, this results in harmonic-oscillator initial conditions and in the zero-point energy correction (65), which originates from nonvanishing commutators $[x_n, p_n] = i\hbar$.[69,70] As a consequence, the classical limit of the mapping formalism accounts for the dynamics of both quantum and classical DoF in a completely equivalent way. The mean-field trajectory method, on the other hand, is based on a partial classical limit for the nuclear DoF and, therefore, treats electronic and nuclear DoF differently with respect to their initial conditions (quantum-like initial conditions for the electronic DoF, quasiclassical initial conditions for the nuclear DoF). As shown in Sec. 6.5, this seemingly minor aspect may in fact completely determine the outcome of the classical modeling of nonadiabatic dynamics.

The general idea of an equivalent classical treatment of electronic and nuclear DoF was first suggested in the "classical electron-analog" models of McCurdy, Meyer and Miller.[73–76] Exploiting various quantum-classical analogies, these authors constructed classical-path-like Hamiltonian functions similar to (64), thus treating the dynamics of electrons and nuclei on the same dynamical footing of classical mechanics. There exists a close connection between these classical models and the classical limit of the mapping approach. In particular, the classical electron analog model may be considered as the classical limit of the mapping formalism. The main difference between the two theories is of conceptual nature: While the formulation of Meyer and Miller is a *classical model*, the mapping approach is an exact quantum-mechanical formulation that allows for a well-defined classical limit. This difference becomes evident at the semiclassical level of the theory. Starting from an exact quantum-mechanical formulation, the mapping approach unambiguously defines the classical Hamiltonian as well as the boundary (or initial) conditions of the semiclassical propagator. The classical electron analog model, on the other hand, is based on a model ansatz and is therefore not unique. For example, the theory does not determine the boundary conditions of the semiclassical propagator and "Langer-like modifications" need to be invoked to the off-diagonal elements of the Hamiltonian function to achieve meaningful semiclassical quantization conditions.[75,77] In recent works on the semiclassical description of nonadiabatic dynamics,[87–89,92,93] Miller and coworkers use a modified formulation of their original model,[75] which is identical to the classical limit of the mapping approach proposed in Ref. 69. For a detailed discussion of the

common and diverse features of the two formulations, we refer to Refs. 70 and 71.

6.4. *Zero-Point Energy Problem*

Within the mapping approach, the electronic states are represented by products of harmonic-oscillator states, where one of the oscillators is in the first excited state and all others are in the ground state. Quantum-mechanically, the dynamics is restricted to this subspace with one quantum of excitation. In the classical limit of the mapping approach, however, this dynamical constraint is not necessarily fulfilled. The explanation for this failure of the classical formulation is given by the well-known zero-point energy (ZPE) problem of classical mechanics.[140] In quantum mechanics, each oscillator mode must hold an amount of energy that is larger or equal to the ZPE of this mode. In a classical trajectory calculation, on the other hand, energy can flow among the modes without this restriction. Since according to Eq. (62) the population probability of an electronic state is directly proportional to the mean energy content of the corresponding electronic oscillator, $P_n(t) \propto \langle \frac{1}{2} W_{nn}(x_n^2 + p_n^2 - 1) \rangle$, this unphysical flow of ZPE may result in negative population probabilities. To illustrate the problem, Fig. 8 shows the adiabatic and diabatic population for Model I obtained with the mapping approach. It is seen that the overall agreement with the quantum results is of the same quality for the mean-field trajectory method and the mapping approach. Due to the ZPE problem, however, the latter may result in negative values of the adiabatic population.

The problem of an unphysical flow of ZPE is not a specific feature of the mapping approach, but represents a general flaw of quasiclassical trajectory methods. Numerous approaches have been proposed to fix the ZPE problem.[140] They include a variety of "active" methods (i.e. the flow of ZPE is controlled and (if necessary) manipulated during the course of individual trajectories) and several "passive" methods which, for example, discard trajectories not satisfying predefined criteria. However, most of these techniques share the problem that they manipulate *individual* trajectories, whereas the conservation of ZPE should correspond to a virtue of the *ensemble average* of trajectories.

Recently, Stock and Müller have proposed an alternative strategy to tackle the ZPE problem.[71,78,141] The theory is based on the observation

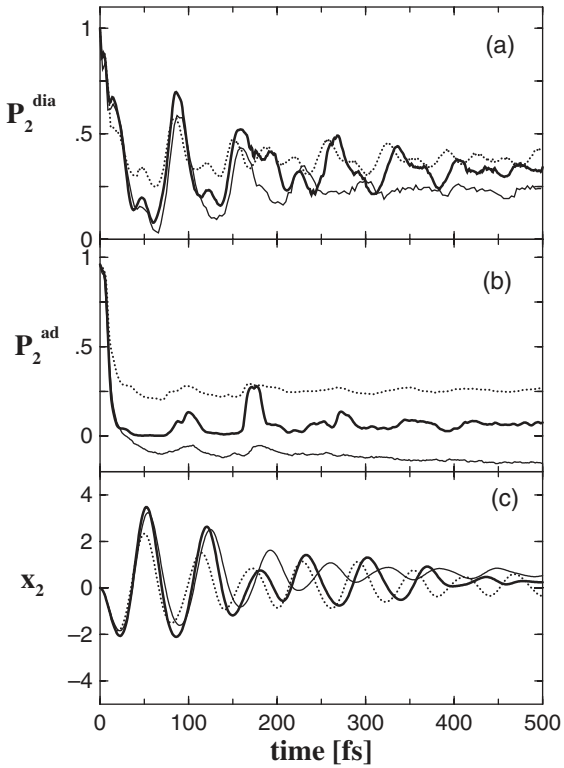

Fig. 8. Time-dependent (a) diabatic and (b) adiabatic electronic excited-state populations and (c) vibrational mean positions as obtained for Model I. Shown are results of the mean-field trajectory method (dotted lines), the quasiclassical mapping approach (thin full lines), and exact quantum calculations (thick full lines).

that the unphysical flow of ZPE is a consequence of the fact that the classical phase-space distribution may enter regions of phase space that correspond to a violation of the uncertainty principle. To restrict the classically accessible phase space according to the rules of quantum mechanics, it has been proposed to invoke quantum corrections to the classical calculation. At the simplest level of the theory, these corrections have been shown to correspond to including only a fraction γ ($0 \leq \gamma \leq 1$) of the full ZPE into the classical calculation. To study the effect of this modification on the mapping description, we note that in this formalism the electronic ZPE appears in (i) the quasiclassical description of the initial electronic state,

e.g. $\rho_{\rm el} = \delta[n_1 - (1+\gamma/2)]\delta(n_2 - \gamma/2)$, (ii) in the electronic projectors $\frac{1}{2}(p_n^2 + x_n^2 - \gamma)$, and (iii) in the Hamiltonian

$$\mathcal{H} = T(\mathbf{P}) + \sum_n \frac{1}{2}(p_n^2 + x_n^2 - \gamma) W_{nn}(\mathbf{R}) + \sum_{n>m} (x_n x_m + p_n p_m) W_{nm}(\mathbf{X}). \quad (66)$$

A value of $\gamma = 1$ corresponds to the original mapping formulation which takes into account the full amount of ZPE. If, on the other hand, all electronic ZPE is neglected, i.e. $\gamma = 0$, the mapping approach becomes equivalent to the mean-field trajectory method.

To determine the optimal value of quantum correction γ, several criteria have been proposed, which all are based on the idea that an appropriate classical theory should correctly reproduce long-time limits of the electronic populations. (Since the populations are proportional to the mean energy of the corresponding electronic oscillator, this condition also conserves the ZPE of this oscillator.) Employing phase-space theory, it has been shown that this requirement leads to the condition that the state-specific level densities

$$N_k(E) = \mathrm{Tr}\{|\Phi_k\rangle\langle\Phi_k|\Theta(E - \mathcal{H})\} \quad (67)$$

should be the same for the quantum-mechanical description and its classical approximation.[78,141] Although this is a rigorous criterion, unfortunately, it is not a very practical one since the quantum-mechanical state-specific level density in general is not easy to calculate. On a somewhat more approximate level, one may also require that the total integral level density (or level number)

$$N(E) = \mathrm{Tr}\{\Theta(E - \mathcal{H})\} \quad (68)$$

should be equivalent in the classical and quantum-mechanical description.[71] While this criterion may not yield the optimal quantum correction, nonetheless, it has been shown to cure the ZPE problem. We note in passing that there also have been several attempts to obtain analytical expressions for the quantum correction which, however, mostly apply to idealized model systems.[141–143]

Considering the practical application of the mapping approach, it is most important to note that the quantum correction can also be determined in cases where no reference calculations exist. That is, if we *a priori* know the long-time limit of an observable, we can use this information to

determine the quantum correction. For example, a multidimensional molecular system is for large times expected to completely decay in its adiabatic ground state, i.e.

$$P_k^{\mathrm{ad}}(\infty) = \delta_{k0}. \tag{69}$$

Performing several trajectory calculations with varying values of γ, the optimal quantum correction is thus obtained from the requirement (69).

It is interesting to note that the latter criterion implies that the ground-state level density completely dominates the total level density, i.e. that $N_0(E) \approx N(E)$. Hence the assumption (69) of complete decay into the adiabatic ground state is equivalent to the criterion that the classical and quantum total level densities should be equivalent. Furthermore, it is clear that this criterion determines the upper limit of γ. This is because larger values of the quantum correction would result in ground-state population larger than one (or negative excited-state populations).

6.5. *Results*

It is instructive to first consider how the classical approximation of the total level density, $N_C(E)$, depends on the amount of electronic ZPE included. Figure 9(a) compares $N_C(E)$ as obtained for Model I in the limiting cases $\gamma = 0$ and 1 (thin solid lines) to the exact quantum-mechanical density $N(E)$ (thick line). The classical level density is seen to be either much higher (for $\gamma = 1$) or much lower (for $\gamma = 0$) than the quantum result. Since the integral level density can be considered as a simple measure of the overall phase-space volume occupied by the system, this finding reflects directly the ZPE problem: Including no ZPE in the classical calculation, we have $N_C(E) \ll N(E)$ and therefore insufficient relaxation (see Fig. 8). Including the full ZPE, we have $N_C(E) \gg N(E)$ and therefore exaggerated relaxation due to unphysical flow of ZPE. Also shown are two intermediate cases, $\gamma = 0.44$ (dashed line) and $\gamma = 0.68$ (dotted line). The latter value of γ has been chosen to reproduce the quantum level density around $E = 5\,\mathrm{eV}$ and indeed provides a quite accurate approximation.

The corresponding normalized state-specific level densities $N_1(E)/N(E)$ are displayed in Fig. 9(b). Again, the limiting cases $\gamma = 0$ and 1 under- and overestimate the quantum data, respectively, while the intermediate value of $\gamma = 0.44$ (dashed line) provides a good approximation of the quantum

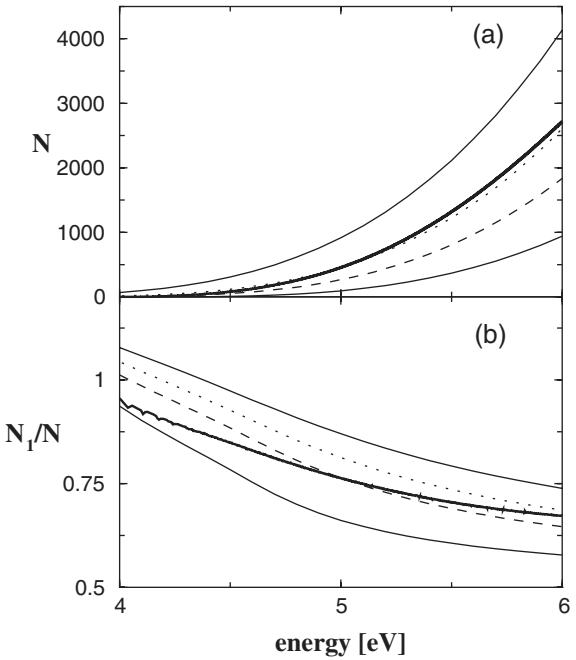

Fig. 9. (a) Total integral level density $N(E)$ and (b) normalized state-specific level density $N_1(E)/N(E)$ as obtained for Model I. Thick lines show exact quantum-mechanical results, thin lines display classical results for the limiting cases $\gamma = 0$, 1 (full lines) and the intermediate cases $\gamma = 0.44$ (dashed lines) and $\gamma = 0.68$ (dotted lines).

results. It is noted, however, that requiring optimal agreement of the state-specific level density results in a lower ZPE correction as requiring optimal agreement of the total level density.

Let us now study to what extent the ZPE-corrected mapping formulation is able to describe the nonadiabatic relaxation dynamics of our model problems. Beginning with Model I, Fig. 10 again shows the (a) diabatic and (b) adiabatic populations as well as (c) the mean position of the totally-symmetric vibrational modes ν_{6a}. The ZPE-corrected mapping results for $\gamma = 0.44$ (thin solid lines) and the corresponding quantum results (thick lines) are seen to be in quite good overall agreement. In particular, it is found that for large times both the classical and the quantum diabatic population fluctuate around the same value of $P_2^{\mathrm{dia}}(\infty) \approx 0.3$. This reconfirms our assertion that the agreement of the classical and the quantum

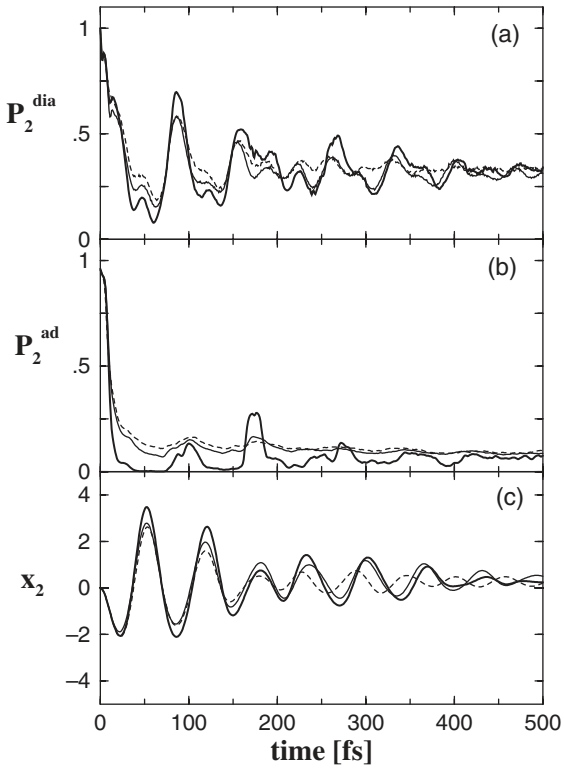

Fig. 10. Same as Fig. 8, except ZPE-corrected mapping results are shown for $\gamma = 0.44$, whereby action-angle (full lines) and Wigner (dashed lines) initial conditions have been employed.

state-specific level densities results in the equivalent long-time values of the classical and quantum diabatic population. Most importantly, it is seen that the ZPE-corrected results also reproduce the entire time evolution of the electronic and vibrational observable under consideration. In particular, the data nicely match the coherent transients of the diabatic population and the vibrational motion.

We note in passing that the results above have been obtained with action-angle initial conditions for the electronic DoF. Employing Wigner initial conditions with $\gamma = 0.44$, similar results are obtained (dashed lines in Fig. 10), although the coherent beating of the signals is reproduced only

qualitatively. Within the mapping approach, action-angle initial conditions generally have been found superior to Wigner initial conditions.[78]

Employing the alternative criterion that requires the agreement of the classical and the quantum-mechanical total level density, we have also calculated the time-dependent observables for the quantum correction $\gamma = 0.68$ (data not shown). The overall quality of the data is quite similar to the data shown above, although the overall relaxation is somewhat exaggerated. As expected from the discussion above, we obtained $P_2^{\mathrm{ad}}(\infty) = 0$, that is, the requirement of a correct total level density coincides with the criterion (69).

We proceed with the discussion of Model II, representing the $\widetilde{C} \rightarrow \widetilde{B} \rightarrow \widetilde{X}$ internal-conversion process in the benzene cation. Figure 11 shows quantum mechanical results (a) as well as various mapping results obtained for different values of the ZPE. As was discussed in Sec. 3, the mean-field trajectory method, corresponding to the mapping approach without ZPE (i.e. $\gamma = 0$), essentially fails to describe the long-time relaxation of the population of the electronic $\widetilde{C}$ and $\widetilde{B}$-states [see panels (b) and (e)]. Taking into account the full ZPE (i.e. $\gamma = 1$) shown in panels (c) and (f), on the other hand, results in a quite good agreement with the quantum results for short times. For longer times, however, the overall relaxation is exaggerated and both the adiabatic and the diabatic population of the $\widetilde{C}$ state have negative values, indicating an unphysical flow of ZPE. It is noted that, due to the higher number of electronic states and the larger excess energy of the initial state, the ZPE problem in Model II is considerably more severe than in Model I. For example, a detailed analysis showed that the mean-field trajectory method ($\gamma = 0$) predicts a level number which is about a factor of 50 smaller than the corresponding level number of the ZPE-corrected mapping result.[71]

In the case of Model II, neither the state-specific nor the total quantum-mechanical level densities are available. To determine the optimal value of the ZPE correction, therefore criterion (69) was applied, which yielded $\gamma = 0.6$. The mapping results thus obtained (panels d and g) are seen to reproduce the quantum result almost quantitatively. It should be noted that this ZPE adjustment assures that the adiabatic population probabilities remain within $[0, 1]$ and at the same time also yields the best agreement with the quantum diabatic populations.

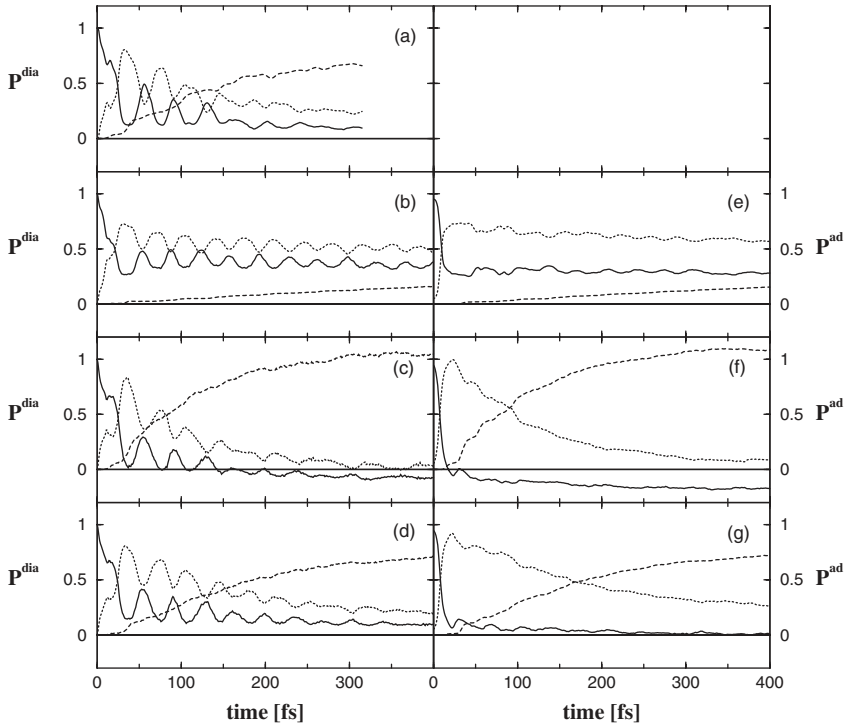

Fig. 11. Diabatic (left) and adiabatic (right) population probabilities of the $\widetilde{C}$ (full line), $\widetilde{B}$ (dotted line), and $\widetilde{X}$ (dashed line) electronic states as obtained for Model II representing a three-state five-mode model of the benzene cation. Shown are (a) exact quantum calculations of Ref. 119, as well as mean-field-trajectory results [panels (b),(e)], and quasiclassical mapping results including the full [panels (c),(f)] and 60% [panels (d),(g)] of the electronic zero-point energy, respectively.

The excellent performance of the mapping formulation for this model encouraged us to consider an extended model of the benzene cation, for which no quantum reference calculations are available.[144] The model comprises 16 vibrational DoF and five coupled potential-energy surfaces, thus accounting for the degeneracy of the electronic states $\widetilde{X}$ and $\widetilde{B}$.[119] Assuming again a complete decay into the adiabatic ground state, a ZPE correction of $\gamma = 0.33$ was determined. Figure 12 displays the diabatic and adiabatic population dynamics of this model. As may be expected, the inclusion of the additional DoF results in a faster dephasing of the coherent

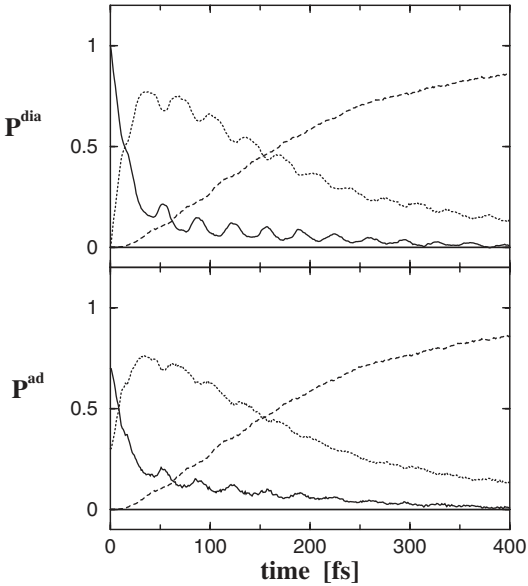

Fig. 12. Diabatic and adiabatic population probabilities of the $\widetilde{C}$ (full line), $\widetilde{B}$ (dotted line), and $\widetilde{X}$ (dashed line) electronic states as obtained for a five-state 16-mode model of the benzene cation.

beating and in an even more efficient internal-conversion process. Very recent quantum-mechanical studies of Köppel and coworkers employing a refined five-state model including eight vibrational modes reconfirm these findings.[145]

Finally, we consider Model III, which describes an ultrafast photoinduced isomerization process. Figure 13 shows quantum mechanical results as well as results of the ZPE-corrected mapping approach for three different observables: the adiabatic and diabatic population of the excited state, and P_{cis}, the probability that the system remains in the initially prepared *cis*-conformation. A ZPE correction of $\gamma = 0.5$ has been used in the mapping calculation, based on the criterion to reproduce the quantum mechanical long-time limit of the adiabatic population. It is seen that the ZPE-corrected mapping approach represents an improvement compared to the mean-field trajectory method (cf. Fig. 3), in particular for the adiabatic population. The influence of the ZPE correction on the dynamics of the observables is, however, not as large as in the two other models.

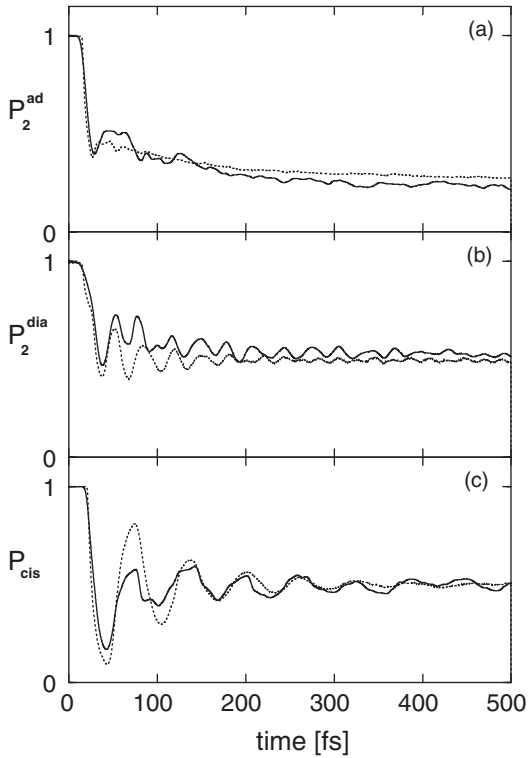

Fig. 13. Time-dependent simulations of the nonadiabatic photoisomerization dynamics exhibited by Model III, comparing results of the ZPE-corrected classical mapping approach (dotted lines) and exact quantum calculations (full lines). Shown are the population probabilities $P_2^{\rm ad}(t)$, $P_2^{\rm dia}(t)$ of the initially prepared adiabatic (a) and diabatic (b) electronic state, respectively, as well as the probability $P_{\rm cis}(t)$ that the system remains in the initially prepared *cis* conformation (c).

Two further mapping studies of nonadiabatic photoisomerization dynamics may be mentioned. Coupling the two-state three-mode Model III considered above to a bath of 100 harmonic modes, the vibrational cooling of the three-mode system (modeling a "chromophore") due to the additional modes (mimicking the solvent) has been studied.[133] It was found that the overall relaxation and the quantum yield of the photoreaction depends to a large extent on the specific system-bath coupling under consideration. Employing the recently introduced concept of vibronic periodic orbits of a nonadiabatic system,[98–100] a very recent investigation showed

that coherent features of the nonadiabatic photoisomerization dynamics may be interpreted in terms of a few quasiperiodic orbits of the classical mapping system.[101]

6.6. *Discussion*

Although the mapping approach provides an in principle consistent classical description of nonadiabatic dynamics, the formulation has been shown to suffer seriously from the ZPE problem. This finding should not come as a surprise, since in the mapping formalism the electronic oscillators are constrained to the ground and first excited state [cf. Eq. (54)], therefore representing a hard challenge for a classical description. In contrast to a semiclassical theory discussed in Sec. 7, there is no rigorous solution to the ZPE problem on the quasiclassical level. Nevertheless, based on the phase space theory developed in Refs. 78 and 141 a quantum correction γ was introduced which affects a reduction of the electronic ZPE included in the calculation. Employing this correction, the quasiclassical mapping formulation was shown to provide an accurate description of the electronic and vibrational relaxation dynamics of all three model problems considered. Generally speaking, the mapping calculations represent a significant improvement over the mean-field trajectory results and are of similar quality as the surface-hopping calculations. Since all these methods in some sense over-stress the classical limit (e.g. ZPE excitation in the mapping approach, classically forbidden transitions in surface-hopping calculations), however, it is not easy to predict which method will perform better for a given problem.

We have discussed several ways to determine the optimal value of the quantum correction γ. Apart from the rigorous conditions associated with the state-specific and total level densities of the system, we have also established the quite useful criterion (69), which assumes that a multidimensional system at large times localizes in its adiabatic ground state. Experience shows that in most two-state problems associated with a multidimensional conical intersection a value of $\gamma = 0.5$ provides a fairly good description of the nonadiabatic relaxation dynamics. It is interesting to note that this rule of the thumb was first established in an empirical analysis of the classical electron analog model,[14] i.e. without knowing anything about the exact mapping relations or the crucial role of ZPE in this approach.

7. Semiclassical Description of Nonadiabatic Quantum Dynamics

All approaches for the description of nonadiabatic dynamics discussed so far invoke simple quasiclassical approximations to treat the dynamics of the nuclear degrees of freedom. As a consequence, these methods are in general not able to describe processes or observables for which quantum effects of the nuclear degrees of freedom are important. Such processes include nuclear tunneling, interference effects in wave-packet dynamics as well as the conservation of zero-point energy. In contrast to purely classical approximations, semiclassical methods are in principle capable of describing quantum effects.

A semiclassical description is well established when both the Hamilton operator of the system and the quantity to be calculated have a well-defined classical analog. For example, there exist several semiclassical methods for calculating the vibrational autocorrelation function on a single excited electronic surface, the Fourier transform of which yields the Franck–Condon spectrum.[83,84,104,146] In particular, semiclassical methods based on the initial-value representation of the semiclassical propagator,[79–86] which circumvent the cumbersome root-search problem in boundary-value based semiclassical methods, have been successfully applied to a variety of systems (see, for example, the reviews Refs. 85, 86 and references therein). These methods cannot directly be applied to nonadiabatic dynamics, though, because the Hamilton operator for the vibronic coupling problem [Eq. (1)] involves discrete degrees of freedom (discrete electronic states) which do not possess an obvious classical counterpart.

The mapping procedure introduced in Sec. 6 results in a quantum-mechanical Hamiltonian with a well-defined classical limit, and therefore extends the applicability of the established semiclassical approaches to nonadiabatic dynamics. The thus obtained semiclassical version of the mapping approach, as well as the equivalent formulation that is obtained by requantizing the classical electron analog model of Meyer and Miller, have been applied to a variety of systems with nonadiabatic dynamics in the recent years.[69–71,78,87–97] It appears that this approach is so far the only fully semiclassical method that allows a numerical treatment of truly multidimensional nonadiabatic dynamics at conical intersections.

Following a brief introduction of the basic concepts of semiclassical dynamics, in particular the semiclassical propagator and its initial-value

representation, we discuss in this section the application of the semiclassical mapping approach to nonadiabatic dynamics. Based on numerical results for the $S_1 - S_2$ conical intersection in pyrazine, we discuss advantages and problems of this semiclassical method.

7.1. *Semiclassical Propagator*

To introduce the basic concept of a semiclassical propagator, let us consider a n-dimensional quantum system with Hamiltonian H, which is assumed to possess a well-defined classical analog. In order to obtain the semiclassical approximation to the transition amplitude $K_t(f|i)$ between the initial state $|i\rangle$ and the final state $|f\rangle$, the amplitude is expressed in terms of the coordinate-dependent propagator $K_t(\mathbf{q}'|\mathbf{q})$

$$\begin{aligned} K_t(f|i) &\equiv \langle f|e^{-iHt}|i\rangle \\ &= \int \mathrm{d}\mathbf{q}' \int \mathrm{d}\mathbf{q} \langle f|\mathbf{q}'\rangle K_t(\mathbf{q}'|\mathbf{q})\langle \mathbf{q}|i\rangle, \end{aligned} \tag{70}$$

which then is evaluated within the semiclassical Van Vleck–Gutzwiller approximation[20]

$$K_t^{\mathrm{VVG}}(\mathbf{q}'|\mathbf{q}) = \sum_{\mathrm{traj}} \frac{e^{iS_t - i\pi\nu/2}}{\sqrt{\det(2\pi i \partial \mathbf{q}'/\partial \mathbf{p})}}. \tag{71}$$

Here the sum runs over all trajectories that start from point $\mathbf{q}_0 = \mathbf{q}$ at time $t = 0$ and end up at point $\mathbf{q}_t = \mathbf{q}'$ at time t, S_t is the classical action along such a trajectory, and the monodromy matrix elements $\partial \mathbf{q}'/\partial \mathbf{p}$ account for the dependency of the trajectory $\mathbf{q}_t$ with respect to its initial momentum $\mathbf{p}_0$. The Maslov-index ν counts the zeroes of the Van Vleck determinant. The evaluation of the semiclassical Van Vleck–Gutzwiller propagator (71) amounts to the solution of a boundary-value problem. That is, given a trajectory characterized by the position $\mathbf{q}(t) = \mathbf{q}_t$ and momentum $\mathbf{p}(t) = \mathbf{p}_t$, we need to find the roots of the equation $\mathbf{q}_t = \mathbf{q}_t(\mathbf{q}_0, \mathbf{p}_0)$. To circumvent this cumbersome root-search, one may rewrite the propagator as an initial-value problem.[79–86] As a consequence, the semiclassical propagator is given as a phase-space integral over the initial conditions $\mathbf{q}_0$, $\mathbf{p}_0$, which is amenable to a Monte-Carlo evaluation. For this reason, semiclassical initial-value representations are regarded as the key to the application of semiclassical methods to multidimensional systems.

Most of the applications of initial-value representation methods in recent years have employed the Herman–Kluk (coherent-state) representation of the semiclassical propagator,[80] which for a general n-dimensional system can be written as

$$\left(e^{-iHt}\right)_{HK} = \int \frac{d\mathbf{q}_0 d\mathbf{p}_0}{(2\pi)^n} |\mathbf{q}_t \mathbf{p}_t\rangle C_t e^{iS_t} \langle \mathbf{q}_0 \mathbf{p}_0|, \tag{72}$$

where $(\mathbf{p}_0, \mathbf{q}_0)$ are initial momenta and coordinates for classical trajectories, $\mathbf{p}_t = \mathbf{p}_t(\mathbf{p}_0, \mathbf{q}_0)$ and $\mathbf{q}_t = \mathbf{q}_t(\mathbf{p}_0, \mathbf{q}_0)$ are the classically time-evolved phase space variables and S_t is the classical action integral along the trajectory. The pre-exponential factor C_t is given by

$$C_t(\mathbf{p}_0, \mathbf{q}_0) = \sqrt{\det\left[\frac{1}{2}\left(\alpha^{\frac{1}{2}}\frac{\partial \mathbf{q}_t}{\partial \mathbf{q}_0}\alpha^{-\frac{1}{2}} + \alpha^{-\frac{1}{2}}\frac{\partial \mathbf{p}_t}{\partial \mathbf{p}_0}\alpha^{\frac{1}{2}} - i\alpha^{\frac{1}{2}}\frac{\partial \mathbf{q}_t}{\partial \mathbf{p}_0}\alpha^{\frac{1}{2}} + i\alpha^{-\frac{1}{2}}\frac{\partial \mathbf{p}_t}{\partial \mathbf{q}_0}\alpha^{-\frac{1}{2}}\right)\right]}. \tag{73}$$

It involves a combination of the elements of the monodromy matrix

$$\mathbf{M}_t = \begin{pmatrix} \dfrac{\partial \mathbf{p}_t}{\partial \mathbf{p}_0} & \dfrac{\partial \mathbf{p}_t}{\partial \mathbf{q}_0} \\ \dfrac{\partial \mathbf{q}_t}{\partial \mathbf{p}_0} & \dfrac{\partial \mathbf{q}_t}{\partial \mathbf{q}_0} \end{pmatrix}. \tag{74}$$

In the above expression α denotes a n-dimensional diagonal matrix, with element α_j being the width parameter for the coherent state of the jth dimension. The coordinate space representation of an n-dimensional coherent state is the product of n one-dimensional minimum uncertainty wave packets

$$\langle \mathbf{x}|\mathbf{pq}\rangle = \prod_{j=1}^{n} \left(\frac{\alpha_j}{\pi}\right)^{1/4} e^{-\frac{\alpha_j}{2}(x_j - q_j)^2 + ip_j(x_j - q_j)}. \tag{75}$$

Within the applicability of the semiclassical approximation, the propagator (72) is rather insensitive to the particular value of the width parameters α_j, but this parameter can of course affect the numerical efficiency of the calculation. In the numerical studies presented below, we have chosen the width α_j as the width of the harmonic ground state of the jth vibrational mode. In the dimensionless units used here this choice corresponds to $\alpha_j = 1$ for all degrees of freedom.

The calculation of the Herman–Kluk propagator for multidimensional nonseparable systems is a challenging task because it involves a multidimensional integral over an oscillating integrand. In addition, the preexponential factor C_t can become large for chaotic trajectories. Therefore, it is rather difficult to converge the integral for longer times using simple Monte-Carlo integration schemes. Several smoothing techniques have been proposed to overcome this well-known problem of semiclassical propagators.[83,84,97,147–150] The basic idea of these techniques is to integrate out the local oscillations analytically, using a linearization of the integrand over a small phase-space cell. In the numerical results reported below we have adopted the method of Walton and Manolopoulos.[84] This method combines the Herman–Kluk propagator with the cellular dynamics algorithm of Heller.[81] It is based on the Filinov[151,152] or stationary-phase Monte-Carlo method.[153]

7.2. *Nonadiabatic Dynamics*

The mapping procedure introduced in Sec. 6 results in a quantum-mechanical Hamiltonian with a well-defined classical limit, thus rendering the semiclassical evaluation a straightforward matter. To illustrate the concept let us consider the transition amplitude $\langle\Phi_f^d|\langle\mathbf{v}_f|e^{-iHt}|\mathbf{v}_i\rangle|\Phi_i^d\rangle$. The semiclassical mapping approach consists of two steps: First, one uses the quantum mechanical identity between the discrete and the continuous representation of the Hamiltonian [cf. Eqs. (53) and (59)]

$$\begin{aligned}&\langle\Phi_f^d|\langle\mathbf{v}_f|e^{-iHt}|\mathbf{v}_i\rangle|\Phi_i^d\rangle\\&\quad=\langle 0_1,\ldots,1_f,\ldots,0_{N_{\mathrm{el}}}|\langle\mathbf{v}_f|e^{-i\mathcal{H}t}|\mathbf{v}_i\rangle|0_1,\ldots,1_i,\ldots,0_{N_{\mathrm{el}}}\rangle.\end{aligned}\tag{76}$$

Subsequently, any of the well-established semiclassical approximations for the quantum propagator $e^{-i\mathcal{H}t}$ can be employed to obtain a semiclassical approximation for the transition amplitude. Employing, for example, the Herman–Kluk propagator, the semiclassical approximation for this transition amplitude is given by

$$\begin{aligned}&\langle\Phi_f^d|\langle\mathbf{v}_f|e^{-iHt}|\mathbf{v}_i\rangle|\Phi_i^d\rangle_{HK}\\&\quad=\int\frac{d\mathbf{x}_0d\mathbf{p}_0}{(2\pi)^{N_{\mathrm{el}}}}\int\frac{d\mathbf{R}_0d\mathbf{P}_0}{(2\pi)^{N_{\mathrm{vib}}}}\langle 0_1,\ldots,1_f,\ldots,0_{N_{\mathrm{el}}}|\mathbf{x}_t\mathbf{p}_t\rangle\\&\qquad\times\langle\mathbf{v}_f|\mathbf{R}_t\mathbf{P}_t\rangle C_te^{iS_t}\langle\mathbf{R}_0\mathbf{P}_0|\mathbf{v}_i\rangle\langle\mathbf{x}_0\mathbf{p}_0|0_1,\ldots,1_i,\ldots,0_{N_{\mathrm{el}}}\rangle.\end{aligned}\tag{77}$$

In contrast to the quasiclassical approaches discussed in the previous sections of this review, Eq. (77) represents a description of nonadiabatic dynamics which is "semiclassically exact" in the sense that it requires only the basic semiclassical Van Vleck–Gutzwiller approximation[20] to the quantum propagator. Therefore, it allows the description of electronic and nuclear quantum effects.

An alternative way to obtain a semiclassically exact description for systems involving discrete quantum degrees of freedom is based on the spin-coherent state representation. In particular, the spin-coherent state path integral has been used to investigate the semiclassical description of spin systems.[154–158] As has been discussed in detail in Ref. 70 there exists a close connection between these approaches and the semiclassical mapping approach. For example, the mapping approach can be used to derive a semiclassical spin-coherent state propagator.[70]

To conclude this section, we would like to mention some technical details of the semiclassical calculation. The various elements of the semiclassical expression (77) are obtained in the following way: The phase-space integral is evaluated using standard importance-sampling Monte-Carlo schemes. Thereby, as was mentioned above, filtering techniques are employed to facilitate the integration over the oscillating integrand (for details see Ref. 92). The classical action and the monodromy matrix for each trajectory $(\mathbf{q}_t, \mathbf{p}_t) = (\mathbf{x}_t, \mathbf{R}_t, \mathbf{p}_t, \mathbf{P}_t)$ are obtained by solving the differential equations

$$\frac{dS_t}{dt} = \mathbf{p}_t \cdot \dot{\mathbf{q}}_t - \mathcal{H}, \tag{78}$$

$$\frac{d}{dt}\mathbf{M}_t = \begin{pmatrix} -\dfrac{\partial^2 \mathcal{H}}{\partial \mathbf{q} \partial \mathbf{p}} & -\dfrac{\partial^2 \mathcal{H}}{\partial \mathbf{q} \partial \mathbf{q}} \\ \dfrac{\partial^2 \mathcal{H}}{\partial \mathbf{p} \partial \mathbf{p}} & \dfrac{\partial^2 \mathcal{H}}{\partial \mathbf{p} \partial \mathbf{q}} \end{pmatrix} \mathbf{M}_t \tag{79}$$

along the trajectory.[159] The calculation of the pre-exponential factor C_t involves a complex square root, Eq. (73) , the correct branch of which is determined by requiring continuity of C_t.[83] In particular for larger systems, it is thereby advantageous to combine some of the phase factors of C_t and e^{iS_t}, in order to avoid the calculation of the pre-exponential factor for very small time intervals.[160]

7.3. *Results*

The semiclassical approach outlined above has been applied to various nonadiabatic systems with avoided crossings including nonadiabatic bound-state dynamics of several spin-boson type models with up to three vibrational modes,[69,70] a series of scattering-type test problems,[87] a model for laser driven population transfer between two adiabatic potential-energy surfaces.[90] To our knowledge, so far only three applications to systems with conical intersections have been reported: the photodissociation of ozone[89] and ICN,[96] and the photoinduced nonadiabatic dynamics of pyrazine at the $S_1 - S_2$ conical intersection.[92,97] In this section we will discuss the results obtained for the latter system. While the simulations of the pyrazine system discussed in the previous sections of this review have employed a three-mode model (Model I), the semiclassical simulations we will present here are based on two different models: a four-mode model and a model including all 24 normal modes of the pyrazine molecule.

Let us first consider the four-mode model of the $S_1 - S_2$ conical intersection in pyrazine which was developed by Domcke and coworkers.[161] In addition to the three modes considered in Model I, it takes into account another Condon-active mode (ν_{9a}). Figure 14 shows the modulus of the autocorrelation function [cf. Eq. (20)] of this model after photoexcitation to the S_2 electronic state. The exact quantum results (full line) are compared to the semiclassical results (dotted line). The autocorrelation function exhibits a fast initial decay, reflecting the initial displacement of the wave packet on the S_2 surface. The suppression of the ensuing recurrences (which is absent for the uncoupled system, i.e. $W_{12} = 0$)[124] reflects the ultrafast electronic dephasing in the S_2 electronic state of pyrazine. This dephasing process is incomplete due to the limited density of states of the four-mode model. It is seen that the semiclassical result reproduces all essential features of the autocorrelation function up to 100 fs. Both the first two recurrences and the high frequency modulations are well described. Upon closer inspection, one recognizes that the fine structure of the autocorrelation function is better reproduced than the overall damping of the amplitude, e.g. the semiclassical result underestimates the damping of the first reoccurrence and has too small an amplitude for times $t > 80$ fs. The former deviation is related to the nonunitarity of the semiclassical approximation[162] and can be corrected to some extent by normalizing the data (see below). The latter deviation is

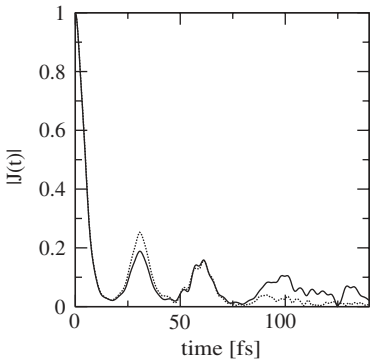

Fig. 14. Modulus of the autocorrelation function for the four-mode model of pyrazine. The full line is the quantum result and the dotted line is the semiclassical result.

presumably a result of the filtering technique used in the calculation, which tends to exaggerate the damping of the autocorrelation function for longer times.

The S_2 absorption spectrum is displayed in Fig. 15. Panel (a) compares the semiclassical and the quantum result and panel (b) shows the experimental data from Ref. 163. Both theoretical results have been obtained by Fourier transformation of the autocorrelation function. Thereby a phenomenological dephasing constant $T_2 = 30\,\mathrm{fs}$ has been included to reproduce the homogeneous width of the experimental spectrum. The absorption spectrum shows a diffuse S_2 band with irregularly spaced structures, which cannot be assigned in terms of normal modes in the S_2 state.[122,124] The weak tail in the energy region of the S_1 state represents the well-known phenomenon of vibronic-intensity borrowing. It is seen that the semiclassical and the exact quantum results are in very good agreement in both parts of the spectrum. It is interesting to compare this semiclassical result with a calculation performed by Stock and Miller some time ago for the same model using a quasiclassical approach (i.e. without semiclassical phase information) based on the classical electron analog model.[164] Although this classical method was able to reproduce the global features of the absorption spectrum, it was not capable of reproducing the finer structure. In contrast, the semiclassical method describes these fine structures very well,

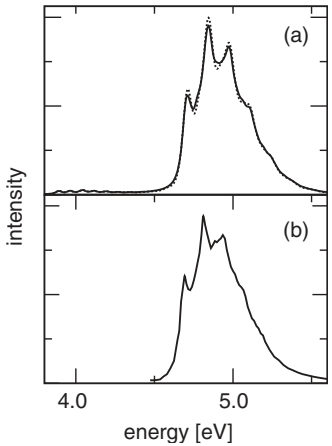

Fig. 15. Absorption spectrum of pyrazine in the energy region of the $S_1 - S_2$ conical intersection. Shown are (a) quantum mechanical (full line) and semiclassical (dotted line) results for the four-mode model (including a phenomenological dephasing constant of $T_2 = 30\,\text{fs}$), and (b) the experimental data.[163]

demonstrating that the inclusion of phase information (and hence quantum interference) is important to describe the absorption spectrum in this system correctly.

The ultrafast initial decay of the population of the diabatic S_2 state is illustrated in Fig. 16 for the first 30 fs. Since the norm of the semiclassical wave function is only approximately conserved, the semiclassical results are displayed as rough data (dashed line) and normalized data (dotted line) [i.e. $P_2^{\text{norm}} = P_2/(P_1 + P_2)$]. The normalized results for the population are seen to match the quantum reference data quantitatively. It should be emphasized that the deviation of the norm shown in Fig. 16 is not a numerical problem, but rather confirms the common wisdom that a two-level system as well as its bosonic representation is a prime example of a quantum system and therefore difficult to describe within a semiclassical theory. Nevertheless, besides the well-known problem of norm conservation, the semiclassical mapping approach clearly reproduces the nonadiabatic quantum dynamics of the system. It is noted that the semiclassical results displayed in Fig. 16 have been obtained without using filtering techniques. Due to the highly chaotic classical dynamics of the system, therefore, a very large number of trajectories ($\approx 2 \times 10^7$) is needed to achieve convergence, even over

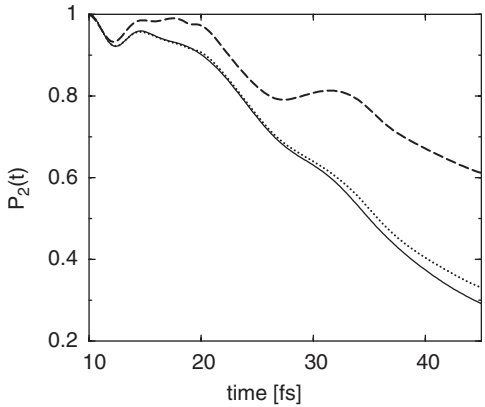

Fig. 16. Initial decay of the diabatic population of the S_2 state for the four-mode pyrazine model. Compared are quantum (full line), semiclassical (dashed line) and normalized semiclassical (dotted line) results.

the relatively short timescale of 30 fs. To improve the convergence and to facilitate the calculation of the population for longer times, effective filtering techniques or more sophisticated semiclassical techniques such as the forward-backward initial-value representation[165–167] need to be employed.

Within the four-mode model, the experimental absorption spectrum can only be obtained by including a rather large phenomenological dephasing parameter $T_2 = 30$ fs. Recently, Raab *et al.* have reported multiconfiguration time-dependent Hartree calculations[168,169] based on a model Hamiltonian which takes into account all the 24 normal modes of the pyrazine molecule.[170] Figure 17 displays the modulus of the autocorrelation function for the 24-mode model. The semiclassical results are compared with the results of Raab *et al.*[170] The comparison with the 4-mode model (Fig. 16) shows that the inclusion of the remaining 20 modes leads to a damping of the recurrences of the autocorrelation function. The semiclassical result is seen to reproduce the quantum result rather well up to 70 fs. In particular, the calculation is seen to well reproduce the damping of the first recurrence due to the inclusion of the additional modes. This is in contrast to more classical methods, such as the quasiclassical implementation of the mapping approach. As we have discussed in Sec. 6, this failure to describe the correct relaxation behaviour is related to an incorrect treatment of the zero-point energy in the classical implementation. The results in Fig. 17

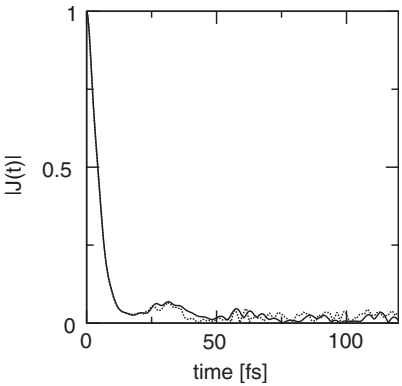

Fig. 17. Modulus of the autocorrelation function for the 24-mode pyrazine model. The full line is the quantum result[170] and the dotted line is the semiclassical result.

demonstrate that the semiclassical method is capable of describing this effect correctly without requiring further zero-point energy modifications.

Finally, Fig. 18 shows the absorption spectrum for the 24-mode model. As was done by Raab *et al.*,[170] we have included a phenomenological dephasing time of $T_2 = 150\,\text{fs}$ to model the experimental broadening due to finite resolution and rotational motion. It can be seen that the inclusion of all 24 normal modes of the pyrazine molecule leads to a shape of the spectrum which is in good agreement with the experimental result [Fig. 15(b)]. The semiclassical result is seen to be in fairly good agreement with the quantum result. The spurious structure in the semiclassical spectrum is presumably due to the rather high statistical error.

To conclude, the results presented in this section demonstrate that the semiclassical implementation of the mapping approach is able to describe the ultrafast dynamics in the pyrazine system. In particular, it is capable of describing the correct relaxation dynamics as well as the structures of the absorption spectrum. The former is related to a correct treatment of the zero-point energy, the latter reflects the correct inclusion of quantum interference effects. The ability to describe these quantum effects is in contrast to the quasiclassical implementation of the mapping approach discussed in Sec. 6. The semiclassical version of the mapping approach should, therefore, also be well suited to describe time-resolved nonlinear spectra.

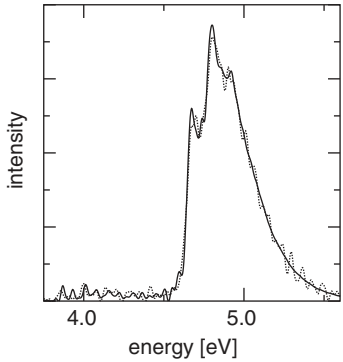

Fig. 18. Absorption spectrum for the 24-mode pyrazine model. The full line is the quantum result[170] and the dotted line is the semiclassical result. In both spectra a phenomenological dephasing constant of $T_2 = 150\,\mathrm{fs}$ was used.

Although this result is quite encouraging, it should be mentioned that the required numerical effort for the semiclassical calculation is rather large. We have found that even though the required CPU time seems to have a better scaling (with respect to the number of nuclear degrees of freedom) in the semiclassical approach then in the quantum multiconfiguration time-dependent Hartree method, it is still comparable in the case of the 24-mode model. There are two main reasons for the rather large numerical effort in the semiclassical calculation: (i) Although we have used an integral conditioning (filtering) technique, the oscillatory nature of the integrand still requires a large number ($\approx 10^7$) of trajectories to converge the Monte-Carlo integration for longer times.[171] (ii) Due to the calculation of the pre-exponential factor, the numerical effort per trajectory has a unfavorable $(2 + N_{\mathrm{vib}})^3$ scaling. Both problems need to be addressed further to make the semiclassical approach a practical method for the treatment of complex molecular systems.

8. Conclusions

In this review we have considered mixed quantum-classical (MQC) methods to describe non-Born–Oppenheimer dynamics at conical intersections. We have started with an attempt to classify existing MQC strategies in formulations resulting from a partial classical limit, from a connection ansatz, and from a mapping formalism. Focusing on methods that have been applied

to conical intersections, we have restricted the discussion to the mean-field trajectory method, the surface-hopping model, the quantum-classical Liouville equation, as well as the quasiclassical and semiclassical version of the mapping approach. Since many of the existing works on MQC theory are closely related, we have tried to point out some of these connections. In particular, we have discussed the relation of the mean-field trajectory method with the quantum-mechanical time-dependent self-consistent field ansatz (Sec. 3.4), the connection of empirical surface-hopping models with the stochastic implementation of the quantum-classical Liouville equation (Sec. 5.2), and the relation of the mapping approach with the mean-field trajectory method and the classical electron analog model (Sec. 6.3).

To obtain a comprehensive picture of the performance of the various MQC approaches, we have considered three model problems involving conical intersections, where each model represents a specific challenge for an approximate description. The detailed computational studies have shown that the practical applicability of MQC methods depends largely on whether the MQC formulation merely requires a simple quasiclassical average to calculate the observables of interests, or whether phase-space integrals involving rapidly oscillating phases need to be evaluated for this purpose. The first group comprises the mean-field trajectory method, the surface-hopping model, and the quasiclassical version of the mapping approach. The second group includes the quantum-classical Liouville description and the semiclassical mapping formulation. While the latter formulations suffer from the dynamical sign problem, the first group of methods may employ standard Monte-Carlo sampling techniques. This yields converged results for typically $10^2 - 10^4$ trajectories and allows for the treatment of molecular systems with a large number of degrees of freedom.

At present, the surface-hopping method is the most popular approach to describe nonadiabatic dynamics at conical intersections. The model employs the simple and physically appealing picture in which a molecular system always evolves on a *single adiabatic* potential-energy surface. Nonadiabatic transitions are realized in this approach via instantaneous hops of the trajectories between the coupled potential-energy surfaces according to some hopping criterion. As discussed in Sec. 4.2, there is no algorithm that provides both a practical and dynamically consistent stochastic realization of the Schrödinger equation in the classical-path approximation. Nevertheless, it has been found that the surface-hopping method gives an at least

qualitative description of the dynamics in all cases considered. We have proposed a modified version of Tully's algorithm which was shown to give significantly better results than the standard method. In particular, it has been shown that it is important to use "binned" electronic population probabilities.

The mean-field trajectory method represents the simplest and in general most widely used MQC approach. Applied to models involving a single conical intersection, the method has been shown to afford a qualitative description of the nonadiabatic dynamics. Although the overall quality of the results deteriorates at longer times, the mean-field trajectory method appropriately describes the branching of trajectories at a surface crossing as well as the electronic and vibrational coherences associated with this process. On the other hand, it was found that the method largely fails to account for the correct branching of trajectories in the case of multiple conical intersections. To explain these findings, a detailed discussion has been given in Secs. 3.4 and 6.3, which also tries to clarify several common misconceptions concerning the theory and the performance of the mean-field trajectory method.

The mapping approach consists of (i) a quantum-mechanically exact transformation of the electronic states of the system to harmonic oscillators and (ii) a subsequent classical (or semiclassical) approximation to the *complete* system. As a consequence, the classical limit of the mapping formalism accounts for the dynamics of both quantum and classical degrees of freedom in a completely equivalent way. The mean-field trajectory method, on the other hand, is based on a *partial* classical limit for the nuclear degrees of freedom. Therefore, it treats electronic and nuclear degrees of freedom differently with respect to their initial conditions, i.e. quantum-like initial conditions for the electronic degrees of freedom and quasiclassical initial conditions for the nuclear degrees of freedom. Correcting for this inconsistency, the mapping formulation is able to describe the nonadiabatic dynamics of all model problems considered rather well. Since the equations of motion of both methods are quite similar, the mapping formulation furthermore explains some of the failures of the mean-field trajectory method.

Although the mapping approach provides an in principle consistent classical description of nonadiabatic dynamics, the formulation has been shown to suffer seriously from the zero-point energy problem. This is because in the mapping formalism the electronic oscillators are constrained to the ground

and first excited state, therefore representing a hard challenge for a classical description. Although on a quasiclassical level there is no rigorous solution to the zero-point energy problem, a quantum correction was introduced which affects a reduction of the electronic zero-point energy included in the calculation. Employing this correction, the quasiclassical mapping formulation was shown to provide an accurate description of the electronic and vibrational relaxation dynamics of all three model problems considered. Generally speaking, the zero-point energy-corrected mapping calculations represent a significant improvement over the mean-field trajectory results and are of similar quality as the surface-hopping calculations. Since both methods in some sense over-stress the classical limit (e.g. zero-point energy excitation in the mapping approach, classically forbidden transitions in surface-hopping calculations), however, it is not easy to predict which method will perform better for a given problem.

A conceptually more consistent treatment of nonadiabatic quantum dynamics can be obtained by either the quantum-classical Liouville formulation or the semiclassical version of the mapping approach. In particular, it has been shown that the quantum-classical Liouville equation is actually exact for the linear vibronic-coupling model considered here. The numerical deviations of this MQC description and the quantum-mechanical reference calculations therefore merely point out the numerical problems of a trajectory-based Monte-Carlo implementation of the Liouville equation. While the quantum-classical Liouville equation is based on a partial classical limit for the nuclear degrees of freedom, the semiclassical version of the mapping approach, on the other hand, employs a semiclassical treatment of both nuclear and electronic degrees of freedom. Hence the approach accounts for electronic and nuclear quantum phenomena in a natural manner, including, e.g. effects of quantum coherence and zero-point energy. Unlike the quasiclassical version of the mapping approach, its semiclassical version is therefore not plagued by the zero-point energy problem and is well suited for the simulation of stationary and time-resolved optical spectra.

At present the practical applicability of the quantum-classical Liouville description and the semiclassical version of the mapping approach is limited because of the dynamical sign problem. As both methods have been proposed only in the last few years, however, they still hold a great potential for improvement. Finally it is noted that all methods considered in this review can in principle be interfaced with an "on-the fly" *ab initio*

evaluation of the potential energy, thus resulting in a practical scheme to perform nonadiabatic *ab initio* molecular-dynamics simulations.

Acknowledgments

A major part of this review is based on results obtained by former graduate students, in particular, Stefan Dilthey, Uwe Müller, and Mark Santer, to whom we wish to express our gratitude for a fruitful and pleasant collaboration. Numerous discussions with our colleague Uwe Manthe are gratefully acknowledged. Furthermore, we want to thank our academic teachers Wolfgang Domcke and William H. Miller for introducing us to the exciting field of conical intersections and semiclassical theories. This work has been supported by the Deutsche Forschungsgemeinschaft and the Fonds der Chemischen Industrie.

References

1. N. F. Mott, *Proc. Cambridge Phil. Soc.* **27**, 553 (1931).
2. M. Born and R. Oppenheimer, *Ann. Physik Leipzig* **84**, 457 (1927).
3. P. Ehrenfest, *Z. Phys.* **45**, 455 (1927).
4. W. Thorson, J. Delos and S. Boorstein, *Phys. Rev.* **A4**, 1052 (1971); **6**, 709 (1972).
5. G. D. Billing, *Chem. Phys. Lett.* **30**, 391 (1975).
6. D. Diestler, *J. Chem. Phys.* **78**, 2240 (1983).
7. D. A. Micha, *J. Chem. Phys.* **78**, 7138 (1983).
8. H. J. C. Berendsen and J. Mavri, *J. Chem. Phys.* **99**, 8637 (1993).
9. R. Kosloff and A. Hammerich, *Faraday Discuss.* **91**, 239 (1991).
10. J. Fang and C. C. Martens, *J. Chem. Phys.* **104**, 3684 (1996).
11. R. B. Gerber, V. Buch and M. A. Ratner, *J. Chem. Phys.* **77**, 3022 (1982).
12. P. Jungwirth and R. B. Gerber, *Chem. Rev.* **99**, 1583 (1999).
13. G. Stock, *J. Chem. Phys.* **103**, 1561 (1995).
14. G. Stock, *J. Chem. Phys.* **103**, 2888 (1995).
15. P. Bala, B. Lesyng and J. A. McCammon, *Chem. Phys. Lett.* **219**, 259 (1994).
16. F. A. Bornemann, P. Nettesheim and C. Schütte, *J. Chem. Phys.* **105**, 1074 (1996).
17. L. M. Raff and D. L. Thompson, in *Theory of Chemical Reaction Dynamics*, Ed. M. Baer (Chemical Rubber, Boca Raton, Florida, 1985), Vol. 3.
18. R. Schinke, *Photodissociation Dynamics* (University Press, Cambridge, 1993).
19. *Quantum and Classical Dynamics in Condensed Phase Simulations*, Eds. B. J. Berne, G. Ciccotti and D. F. Coker (World Scientific, Singapore, 1998).

20. M. C. Gutzwiller, *Chaos in Classical and Quantum Mechanics* (Springer, New York, 1990).
21. I. V. Aleksandrov, *Z. Naturforsch.* **36a**, 902 (1981).
22. W. Boucher and J. Traschen, *Phys. Rev.* **D37**, 3522 (1988).
23. A. Anderson, *Phys. Rev. Lett.* **74**, 621 (1995).
24. O. V. Prezhdo and V. V. Kisil, *Phys. Rev.* **A56**, 162 (1997).
25. C. C. Martens and J. Fang, *J. Chem. Phys.* **106**, 4918 (1997).
26. A. Donoso and C. C. Martens, *J. Phys. Chem.* **A112**, 4291 (1998).
27. J. Caro and L. L. Salcedo, *Phys. Rev.* **A60**, 842 (1999).
28. R. Kapral and G. Cicotti, *J. Chem. Phys.* **110**, 8919 (1999).
29. S. Nielsen, R. Kapral and G. Cicotti, *J. Chem. Phys.* **112**, 6543 (2000).
30. C. Schütte, ZIP-preprint SC-99-10 (2000).
31. I. Horenko, C. Salzmann, B. Schmidt and C. Schütte, *J. Chem. Phys.* **117**, 11075 (2002).
32. C.-C. Wan and J. Schofield, *J. Chem. Phys.* **112**, 4447 (2000).
33. C.-C. Wan and J. Schofield, *J. Chem. Phys.* **116**, 494 (2002).
34. M. Santer, U. Manthe and G. Stock, *J. Chem. Phys.* **114**, 2001 (2001).
35. P. Pechukas, *Phys. Rev.* **181**, 174 (1969).
36. J. Burant and J. Tully, *J. Chem. Phys.* **112**, 6097 (2000).
37. E. Gindensperger, C. Meier and J. Beswick, *J. Chem. Phys.* **113**, 9369 (2000); **116**, 8 (2001).
38. O. Prezhdo and C. Brooksby, *Phys. Rev. Lett.* **86**, 3215 (2001).
39. L. D. Landau, *Z. Sowjetunion U.R.S.S.* **2**, 46 (1932).
40. C. Zener, *Proc. Roy. Soc.* **A137**, 696 (1932).
41. E. C. G. Stückelberg, *Helv. Phys. Acta* **5**, 369 (1932).
42. W. H. Miller and T. F. George, *J. Chem. Phys.* **56**, 5637 (1972).
43. E. E. Nikitin, *Theory of Elementary Atomic and Molecular Processes in Gases* (Clarendon, Oxford, 1974).
44. M. F. Herman, *J. Chem. Phys.* **81**, 754, 764 (1984); **103**, 8081 (1995).
45. F. J. Webster, P. J. Rossky and R. A. Friesner, *Comput. Phys. Commun.* **63**, 494 (1991).
46. R. G. Littlejohn and W. G. Flynn, *Phys. Rev. Lett.* **66**, 2839 (1991).
47. D. F. Coker and L. Xiao, *J. Chem. Phys.* **102**, 496 (1995).
48. J. Bolte and S. Keppler, *Phys. Rev. Lett.* **81**, 1987 (1998).
49. C. Zhu and H. Nakamura, *J. Chem. Phys.* **106**, 2599 (1997).
50. C. Zhu, Y. Teranishi and H. Nakamura, *Adv. Chem. Phys.* **117**, 127 (2001).
51. J. C. Tully and R. K. Preston, *J. Chem. Phys.* **55**, 562 (1971).
52. J. C. Tully, *J. Chem. Phys.* **93**, 1061 (1990).
53. S. Hammes-Schiffer and J. Tully, *J. Chem. Phys.* **101**, 4657 (1994).
54. N. C. Blais, D. Truhlar and C. A. Mead, *J. Chem. Phys.* **89**, 6204 (1988).
55. P. Kuntz, *J. Chem. Phys.* **95**, 141 (1991).
56. O. Prezhdo and P. J. Rossky, *J. Chem. Phys.* **107**, 825 (1997).
57. D. Sholl and J. Tully, *J. Chem. Phys.* **109**, 7702 (1998).

58. Y. L. Volobuev, M. Hack, M. Topaler and D. Truhlar, *J. Chem. Phys.* **112**, 9716 (2000).
59. A. W. Jasper, S. N. Stechmann and D. G. Truhlar, *J. Chem. Phys.* **116**, 5424 (2002).
60. A. Ferretti, G. Granucci, A. Lami, M. Persico and G. Villani, *J. Chem. Phys.* **104**, 5517 (1996).
61. J.-Y. Fang and S. Hammes-Schiffer, *J. Phys. Chem.* **A103**, 9399 (1999).
62. U. Müller and G. Stock, *J. Chem. Phys.* **107**, 6230 (1997).
63. A. I. Krylov and R. B. Gerber, *J. Chem. Phys.* **105**, 4626 (1996).
64. V. Batista and D. Coker, *J. Chem. Phys.* **106**, 6923 (1997).
65. S. Chapman, *Adv. Chem. Phys.* **82**, 423 (1992).
66. D. F. Coker, in *Computer Simulation in Chemical Physics*, Eds. M. P. Allen and D. J. Tildesley (Kluwer Academic, Dordecht, 1993), p. 315.
67. J. C. Tully, *Faraday Discuss.* **110**, 407 (1998).
68. M. Hack and D. Truhlar, *J. Phys. Chem.* **104**, 7917 (2000).
69. G. Stock and M. Thoss, *Phys. Rev. Lett.* **78**, 578 (1997).
70. M. Thoss and G. Stock, *Phys. Rev.* **A59**, 64 (1999).
71. U. Müller and G. Stock, *J. Chem. Phys.* **108**, 7516 (1998).
72. J. Schwinger, in *Quantum Theory of Angular Momentum*, Eds. L. C. Biedenharn and H. V. Dam (Academic, New York, 1965).
73. W. H. Miller and C. W. McCurdy, *J. Chem. Phys.* **69**, 5163 (1978).
74. C. W. McCurdy, H.-D. Meyer and W. H. Miller, *J. Chem. Phys.* **70**, 3177 (1979).
75. H.-D. Meyer and W. H. Miller, *J. Chem. Phys.* **70**, 3214 (1979).
76. H.-D. Meyer and W. H. Miller, *J. Chem. Phys.* **71**, 2156 (1979); **72**, 2272 (1980).
77. M. F. Herman and R. Currier, *Chem. Phys. Lett.* **114**, 411 (1985).
78. U. Müller and G. Stock, *J. Chem. Phys.* **111**, 77 (1999).
79. W. H. Miller, *J. Chem. Phys.* **53**, 3578 (1970).
80. M. F. Herman and E. Kluk, *Chem. Phys.* **91**, 27 (1984).
81. E. J. Heller, *J. Chem. Phys.* **94**, 2723 (1991).
82. G. Campolieti and P. Brumer, *J. Chem. Phys.* **96**, 5969 (1992).
83. K. G. Kay, *J. Chem. Phys.* **100**, 4377 (1994); **101**, 2250 (1994).
84. A. R. Walton and D. E. Manolopoulos, *Mol. Phys.* **87**, 961 (1996).
85. M. A. Sepúlveda and F. Grossmann, *Adv. Chem. Phys.* **96**, 191 (1996).
86. W. H. Miller, *J. Phys. Chem.* **A105**, 2942 (2001).
87. X. Sun and W. H. Miller, *J. Chem. Phys.* **106**, 6349 (1997).
88. X. Sun, H. Wang and W. H. Miller, *J. Chem. Phys.* **109**, 7064 (1998).
89. V. S. Batista and W. H. Miller, *J. Chem. Phys.* **108**, 498 (1998).
90. F. Grossmann, *Phys. Rev.* **A60**, 1791 (1999).
91. E. Rabani, S. A. Egorov and B. J. Berne, *J. Phys. Chem.* **A103**, 9539 (1999).
92. M. Thoss, W. H. Miller and G. Stock, *J. Chem. Phys.* **112**, 10282 (2000).

93. E. A. Coronado, J. Xing and W. Miller, *Chem. Phys.* **349**, 521 (2001).
94. S. Bonella and D. Coker, *J. Chem. Phys.* **114**, 7778 (2001).
95. S. Bonella and D. F. Coker, *Chem. Phys.* **268**, 189 (2001).
96. V. S. Batista and P. Brumer, *J. Phys. Chem.* **A105**, 2591 (2001).
97. H. Wang, D. E. Manolopoulos and W. Miller, *J. Chem. Phys.* **115**, 6317 (2001).
98. S. Dilthey and G. Stock, *Phys. Rev. Lett.* **87**, 140404 (2001).
99. S. Dilthey, B. Mehlig and G. Stock, *J. Chem. Phys.* **116**, 69 (2002).
100. S. Dilthey and G. Stock, *J. Phys. Chem.* **A**106, 8483 (2002).
101. B. Balzer, S. Dilthey, S. Hahn, M. Thoss and G. Stock, *J. Chem. Phys.* **119**, 4202 (2003).
102. B. Berne and G. D. Harp, *Adv. Chem. Phys.* **17**, 63 (1970).
103. S. Egorov, K. F. Everitt and J. L. Skinner, *J. Phys. Chem.* **A103**, 9494 (1999).
104. E. J. Heller, *J. Chem. Phys.* **75**, 2923 (1981).
105. T. J. Martinez, M. Ben-Nun and R. D. Levine, *J. Chem. Phys.* **100**, 7884 (1996).
106. M. Ben-Nun and T. J. Martínez, *Chem. Phys. Lett.* **298**, 57 (1998).
107. M. Ben-Nun, J. Quenneville and T. J. Martínez, *J. Phys. Chem.* **A104**, 5161 (2000).
108. D. Shalashilin and M. Child, *J. Chem. Phys.* **115**, 5367 (2001).
109. T. Vreven, F. Bernardi, M. Garavelli, M. Olivucci, M. A. Robb and H. B. Schlegel, *J. Am. Chem. Soc.* **119**, 12687 (1997).
110. M. Garavelli, F. Bernardi, M. Olivucci, M. J. Bearpark, S. Klein and M. A. Robb, *J. Phys. Chem.* **A105**, 11496 (2001).
111. M. Hartmann, J. Pittner and V. Bonačić-Koutecký, *J. Chem. Phys.* **114**, 2123 (2001).
112. G. Granucci, M. Persico and A. Toniolo, *J. Chem. Phys.* **114**, 10608 (2001).
113. P. Cattaneo and M. Persico, *J. Am. Chem. Soc.* **123**, 7638 (2001).
114. N. L. Doltsinis and D. Marx, *Phys. Rev. Lett.* **88**, 166402 (2002).
115. M. Topaler, T. Allison, D. Schwenke and D. Truhlar, *J. Chem. Phys.* **109**, 3321 (1998).
116. H.-D. Meyer, *Chem. Phys.* **82**, 199 (1983).
117. R. Schneider and W. Domcke, *Chem. Phys. Lett.* **150**, 235 (1988).
118. H. Köppel, L. Cederbaum and W. Domcke, *J. Chem. Phys.* **89**, 2023 (1988).
119. H. Köppel, *Chem. Phys. Lett.* **205**, 361 (1993).
120. L. Seidner and W. Domcke, *Chem. Phys.* **186**, 27 (1994).
121. H. Köppel, W. Domcke and L. S. Cederbaum, *Adv. Chem. Phys.* **57**, 59 (1984).
122. W. Domcke and G. Stock, *Adv. Chem. Phys.* **100**, 1 (1997).
123. E. Wigner, *Phys. Rev.* **40**, 749 (1932).
124. R. Schneider, W. Domcke and H. Köppel, *J. Chem. Phys.* **92**, 1045 (1990).
125. U. Manthe and H. Köppel, *J. Chem. Phys.* **93**, 345, 1658 (1990).

126. M. Durga Prasad, *Chem. Phys. Lett.* **194**, 27 (1992).
127. G. Stock and W. Domcke, *J. Chem. Phys.* **93**, 5496 (1990).
128. G. Stock, R. Schneider and W. Domcke, *J. Chem. Phys.* **90**, 7184 (1989).
129. J. Michl and V. Bonačić-Koutecký, *Electronic Aspects of Organic Photochemistry* (Wiley, New York, 1990).
130. L. Seidner, G. Stock and W. Domcke, *Chem. Phys. Lett.* **228**, 665 (1994).
131. L. Seidner, G. Stock and W. Domcke, *J. Chem. Phys.* **103**, 3998 (1995).
132. S. Hahn and G. Stock, *J. Phys. Chem.* **B104**, 1146 (2000).
133. G. Stock, *J. Chem. Phys.* **103**, 10015 (1995).
134. For the applications considered it was found that it virtually makes no difference whether the phase q is sampled from the intervall $[0, 2\pi]$ or chosen as $q = 0$ for each trajectory.
135. See, for example, the discussions in Ref. 13 and in L. E. Ballentine, Y. Yang and J. P. Zibin, *Phys. Rev.* **A50**, 2854 (1994).
136. C. H. Mak and R. Egger, *Adv. Chem. Phys.* **93**, 39 (1996).
137. J. P. Blaizot and E. R. Marshalek, *Nucl. Phys.* **A309**, 422 (1978).
138. T. Holstein and H. Primakoff, *Phys. Rev.* **58**, 1098 (1940).
139. P. A. M. Dirac, *Proc. Roy. Soc.* (London) **A114**, 243 (1927).
140. For a general discussion and an overview of existing methods see, for example, Y. Guo, D. L. Thompson and T. D. Sewell, *J. Chem. Phys.* **104**, 576 (1996).
141. G. Stock and U. Müller, *J. Chem. Phys.* **111**, 65 (1999).
142. A. A. Golosov and D. R. Reichman, *J. Chem. Phys.* **114**, 1065 (2001).
143. S. Dilthey and G. Stock, *Israel J. Chem.* **42**, 203 (2002).
144. U. Müller, PhD thesis, Technical University Munich, unpublished (1999).
145. H. Köppel, M. Döscher, I. Baldea, H.-D. Meyer and P. G. Szalay, *J. Chem. Phys.* **117**, 2657 (2002).
146. M. Ovchinnikov and V. A. Apkarian, *J. Chem. Phys.* **108**, 2277 (1998).
147. B. W. Spath and W. H. Miller, *J. Chem. Phys.* **104**, 95 (1996).
148. B. E. Guerin and M. F. Herman, *Chem. Phys. Lett.* **286**, 361 (1998).
149. Y. Elran and K. G. Kay, *J. Chem. Phys.* **110**, 8912 (1999).
150. B. R. McQuarrie and P. Brumer, *Chem. Phys. Lett.* **319**, 27 (2000).
151. V. S. Filinov, *Nucl. Phys.* **B271**, 717 (1987).
152. N. Makri and W. H. Miller, *Chem. Phys. Lett.* **139**, 10 (1987).
153. J. D. Doll, D. L. Freeman and T. L. Beck, *Adv. Chem. Phys.* **78**, 61 (1994).
154. W.-M. Zhang and D. H. Feng, *Phys. Rep.* **252**, 1 (1995).
155. J. R. Klauder, *Phys. Rev.* **D19**, 2349 (1979).
156. E. Ercolessi, G. Morandi, F. Napoli and P. Pieri, *J. Math. Phys.* **37**, 535 (1996).
157. A. Alscher and H. Grabert, *J. Phys.* **A32**, 4907 (1999).
158. A. Lucke, C. H. Mak and J. T. Stockburger, *J. Chem. Phys.* **111**, 10843 (1999).

159. Bonella and Coker have recently proposed a slightly different semiclassical implementation of the mapping approach,[95] where a part of the mapping Hamiltonian that does not depend on the electronic variables is not included in the equation of motion for the trajectories but added as a phase factor to the action, thereby improving the stability of the numerical integration.
160. H. Wang, M. Thoss, K. Sorge, R. Gelabert, X. Gimenez and W. H. Miller, *J. Chem. Phys.* **114**, 2562 (2001).
161. C. Woywod, W. Domcke, A. L. Sobolewski and H.-J. Werner, *J. Chem. Phys.* **100**, 1400 (1994).
162. For a discussion of the nonunitarity of the semiclassical approximation in the context of nonadiabatic dynamics see, for example, Ref. 70.
163. I. Yamazaki, T. Murao, T. Yamanaka and K. Yoshihara, *Faraday Discuss.* **75**, 395 (1983).
164. G. Stock and W. H. Miller, *Chem. Phys. Lett.* **197**, 396 (1992).
165. N. Makri and K. Thompson, *Chem. Phys. Lett.* **291**, 101 (1998).
166. X. Sun and W. H. Miller, *J. Chem. Phys.* **110**, 6635 (1999).
167. M. Thoss, H. Wang and W. H. Miller, *J. Chem. Phys.* **114**, 9220 (2001).
168. M. H. Beck, A. Jäckle, G. A. Worth and H.-D. Meyer, U. Manthe and L. S. Cederbaum, *Chem. Phys. Lett.* **165**, 73 (1990).
169. M. H. Beck, A. Jäckle, G. A. Worth and H.-D. Meyer, *Phys. Rep.* **324**, 1 (2000).
170. A. Raab, G. A. Worth, H.-D. Meyer and L. S. Cederbaum, *J. Chem. Phys.* **110**, 936 (1999).
171. Wang *et al.* have recently repeated the calculation for the 24-mode pyrazine model employing an improved filtering technique, thereby reducing the number of trajectories required to obtain convergence by almost two orders of magnitude.[97]

This page intentionally left blank

PART III

Detection and Control of Chemical Dynamics at Conical Intersections

This page intentionally left blank

CHAPTER 16

ABSORPTION, EMISSION, AND PHOTOELECTRON CONTINUOUS-WAVE SPECTRA

A. Lami*, C. Petrongolo† and F. Santoro*‡[a]

*Istituto per i Processi Chimico-Fisici del CNR,
Area della Ricerca del CNR di Pisa,
Via Moruzzi 1, I-56124 Pisa, Italy
‡f.santoro@ipcf.cnr.it

†Dipartimento di Chimica,
Università di Siena,
via A. Moro, I-53100 Siena, Italy

Contents

[a]Corresponding author.

1. Introduction

In this chapter, we deal with conical-intersection (CI) effects on continuous-wave (CW) spectra, i.e. with static molecular properties. Nevertheless, some overlap with dynamical studies of other chapters will clearly appear, because time-independent and time-dependent methods are linked by Fourier transforms.

CIs among adiabatic potential energy surfaces (PES) cause the breakdown of the Born–Oppenheimer (BO) approximation, and have thus a deep impact on molecular states and CW spectra. In general, the corresponding nonadiabatic (NA) interactions mix different vibrational manifolds, increase by far the line density, and in CW spectra they give highly irregular line and intensity distributions, which do not follow simple vibrational progressions or approximated selection rules. Besides energy and intensity, also other observables can be strongly affected. Therefore, CI spectra can be much more complex than what is expected on the basis of the number of active vibrational modes.

The BO representation is very useful for understanding CI effects, because we may know which BO states are mixed by NA couplings and to what extent. We can thus obtain the energies of the NA states and their compositions in terms of the BO species, whose properties and features are clearly understood. In principle, this knowledge enlightens CI effects on any

molecular property and process, except on those caused by strong external interactions.

Even without NA interactions, the normal mode approximation breaks down as the energy increases, because the PES becomes anharmonic and vibrational mixings do not allow us to assign good vibrational quanta. In general, the spectrum becomes more and more complex, and regular level progressions are less and less recognizable. A CI complicates further the spectrum, perturbing the level spacing and mixing the vibrational states $\chi_{1\alpha}$ and $\chi_{2\beta}$ belonging to two coupled electronic species Φ_1 and Φ_2. The mixing of $\chi_{1\alpha}$ and $\chi_{2\beta}$ increases when they are nearly degenerate and with the strength of their NA interaction. When this mixing is strong, electronic and vibrational quantum numbers are meaningless, and radiative selection rules hold only in the NA-state representation. Since the energy gap between the Φ_1 and Φ_2 PES minima is usually large, NA interactions can mix very different states $\chi_{1\alpha}$ and $\chi_{2\beta}$, leading to NA states with very complex nodal structures, which further increase the difficulty of assign good vibrational quanta. The resulting NA spectrum is generally very diffuse, dense, and complex, and without regular progressions.

CIs can also have an indirect, yet important effect on spectra, giving radiative access to highly excited, dark vibrational states that *per se* lack of regular progressions and reliable assignments. This happens in the common case of an electronic excitation $\Phi_0 \rightarrow \Phi_1$, where Φ_1 interacts with a third and dark electronic species Φ_2, and the PES minima of the interacting states have a large energy gap ($E_2^{\min} \ll E_1^{\min}$).

2. Theory of CW-Spectra

2.1. *Electric-Dipole Transitions*

The formulas for the CW absorption, emission and photoelectron spectra can be directly derived making use of the scattering formalism. The derivation grounded on the time-dependent formalism is, however, more intuitive and useful in order to understand the various approximations introduced. Furthermore, it is naturally related to modern computational techniques based on the wavepacket propagation, which have revealed very helpful also in evaluating time-independent observables.

We treat the electromagnetic field in second quantization and adopt the dipole approximation, which is well suited for molecules whose dimension

is negligible with respect to the wavelength.[1,2] The total Hamiltonian is then written as (H_M and H_R are the molecular and the field Hamiltonians, respectively, V is the interaction and the molecule is placed at the origin):

$$H = H_M + H_R + V = H_0 + V$$

where

$$H_R = \hbar\omega a_\omega^+ a_\omega; \quad V = -\mathbf{E}\boldsymbol{\mu}; \quad \mathbf{E} = \boldsymbol{\varepsilon} i R(a_\omega - a_\omega^+); \; R = \left(\frac{2\pi\hbar\omega}{L^3}\right)^{1/2}, \tag{1}$$

L^3 is the quantization volume and $\boldsymbol{\varepsilon}$ the polarization. Both the dipole $\boldsymbol{\mu}$ and the electric field $\mathbf{E}$ are given in the space-fixed frame and a single mode has been taken. In order to ensure that at the initial time t_0 as well as at the time t the field is off, we can imagine that the interaction term is multiplied by a suitable time-dependent switching function. Since we are interested here in the limits $t_0 \to -\infty$, $t \to \infty$, we really need an infinitely slowly varying switching function whose role is then simply that of ensuring convergence of integrals. In dealing with spontaneous emission we will also introduce the second quantization representation for the vacuum field.

The mean value of a given observable is computed at the lowest possible perturbative order in the exciting field. The standard perturbative expansion can be derived recursively from:

$$|\psi^{(0)}(t)\rangle = U_0(t-t_0)|\psi(t_0)\rangle; \quad |\psi^{(n)}(t)\rangle = -\frac{i}{\hbar}\int_{t_0}^{t} dt' U_0(t-t')V|\psi^{(n-1)}(t')\rangle, \tag{2}$$

where $U_0(t) = \exp(-iH_0 t/\hbar)$.

The first observable we are interested in is the rate of energy absorption from the external field ($n_\omega = a_\omega^+ a_\omega$ is the number of quanta with frequency ω):

$$W_{\text{abs}}(\omega) = -\hbar\omega\frac{d}{dt}\langle\psi(t)|n_\omega|\psi(t)\rangle = -i\omega\langle\psi(t)|[H, n_\omega]|\psi(t)\rangle \tag{3}$$

which, after evaluating the commutator, becomes:

$$W_{\text{abs}}(\omega) = R\omega\langle\psi(t)|\boldsymbol{\mu}\boldsymbol{\varepsilon}(a_\omega - a_\omega^+)|\psi(t)\rangle. \tag{4}$$

Looking at Eq. (2), one easily realizes that the leading term in the evaluation of Eq. (4) is first-order (i.e. in Eq. (4) we have to make the replacements $|\psi(t)\rangle \to |\psi^{(0)}(t)\rangle$ and $\langle\psi(t)| \to \langle\psi^{(1)}(t)|$ or the same with the *bra* for the zero-order and the *ket* for the first order term). Assuming that the initial

molecule $\otimes$ field state $|\Psi_g; n\rangle$ is an eigenstate of H_0, the above translates into:

$$W_{\text{abs}}(\omega) = -\omega \frac{R^2}{\hbar} \cos^2(\theta) \int_{t_0}^{t} dt_1 \left\langle \Psi_g; n_\omega \right| \exp\left[\frac{i}{\hbar}(E_g + n\hbar\omega)(t - t_1)\right] \times \mu a_\omega^+ U_0(t - t_1) \mu a_\omega \left| \Psi_g; n_\omega \right\rangle + \text{c.c.} \tag{5}$$

where $\boldsymbol{\mu\varepsilon} = \mu \cos(\theta)$, θ being the angle between the dipole and the field (we are considering here a non-rotating molecule).

Changing the variable to $t' = t - t_1$, and performing the integral one has

$$W_{\text{abs}}(\omega) = -\frac{4\pi\hbar\omega^2}{3L^3}(n_\omega + 1)\,\text{Im}[\langle\Psi_g|\mu G_M(E_g + \hbar\omega)\mu|\Psi_g\rangle], \tag{6}$$

where $G_M(E) = (E - H_M + i\eta)^{-1}$ and $\eta \to 0^+$.

In deriving Eq. (6) we have taken into account that the propagation from t_1 to t happens in the subspace with $(n_\omega - 1)$ photons and have also performed the average over the molecular orientation (non aligned molecules), which gives a factor 1/3. Dividing by the photon energy density $n_\omega\hbar\omega/L^3$ and taking account that for any light source $(n_\omega + 1) \approx n_\omega$, we get the following rate of energy absorption per unit radiant energy density due to 1 molecule:

$$W^u_{\text{abs}} = -\frac{4}{3}\pi\omega\,\text{Im}[\langle\Psi_g|\mu G_M(E_g + \hbar\omega)\mu|\Psi_g\rangle]. \tag{7}$$

At this stage, there is no more trace of the field polarization and so no other average is needed to treat unpolarized sources (i.e. the absorption of randomly oriented molecules does not depend on the polarization of the light).

The molar extinction coefficient k, which is related to the decrease of intensity I when the light travels through an absorbing medium, is given by $k = W^u_{\text{abs}}\ N/c$ where N is Avogadro's number and c the light speed. The absorbance A simply differs by the use of the logarithm in base 10: $A = W^u_{\text{abs}} \cdot N/(c \cdot \ln 10)$.

The absorption cross section, defined as the rate of photon absorption per molecule and per unit radiant energy flux, can be obtained from Eq. (7) taking into account that if n_ω photons pass through $1\,\text{cm}^2$ in 1 sec and they

are all contained in a volume $c \cdot 1\,\mathrm{s} \cdot 1\,\mathrm{cm}^2$, then:

$$\sigma_{\mathrm{abs}}(\omega) = -\frac{4\pi\omega}{3c}\mathrm{Im}\langle\Psi_g|\mu G_M(E_g + \hbar\omega)\mu|\Psi_g\rangle. \tag{8}$$

Looking at Eq. (8) and introducing the spectral representation of the resolvent, one can see that, if the eigenstates $|\Psi_j\rangle$ of H_{m} are known, the absorption spectrum can be computed straightforwardly as a sum of sharp lines, which may be transformed into lorentzians (gaussians) to simulate homogeneous (inhomogeneous) broadening:

$$\sigma_{\mathrm{abs}}(\omega) = \frac{4\pi^2\omega}{3c}\sum_j |\mu_{jg}|^2\delta(E_g + \hbar\omega - E_j), \tag{9}$$

where the index j runs over molecular eigenstates.

Alternatively, the absorption spectrum can be computed in an eigenstate-free context, if one is able to propagate the doorway state, by:

$$\sigma_{\mathrm{abs}}(\omega) = \frac{4\pi\omega}{3\hbar c}\mathrm{Re}\left[\int_0^\infty dt\langle\Psi_g|\mu U_0(t)\mu|\Psi_g\rangle e^{(i(E_g+\hbar\omega)t)/\hbar}e^{-\Gamma^2t^2}\right], \tag{10}$$

which is identical with Eq. (9) if one drops the phenomenological damping factor resulting in a gaussian line broadening. It is worthwhile to remind here that if the BO approximation works, then Eq. (10) requires propagation on a single PES, while in presence of strong nonadiabatic interactions two (or more) surfaces may be needed. This is just the case of conical intersections which we discuss in this chapter.

The derived relations for light absorption can also be used to calculate a photoelectron spectrum under CW excitation, which is the counting rate of ejected electrons for a given light frequency $\overline{\omega}$, as a function of their kinetic energy $E_{kin} = k^2/2m_e$ (at time $t \to \infty$). We write it as $W_{pe}^{\overline{\omega}}(k)$ to remember that it depends on the light frequency $\overline{\omega}$. It clearly coincides with the rate of disappearance of photons, i.e. $W_{pe}^{\overline{\omega}}(k) = W_{\mathrm{abs}}^{u}(\overline{\omega})/\hbar\overline{\omega}$ [see Eq. (7)]. It must be noticed, however, that the emission of electrons instead of photons has a certain number of advantages and may result in a very high resolution, as in the zero kinetic energy (ZEKE) photoelectron spectroscopy.[3]

Let us start from Eq. (8) and take into account that now at the energy $E_g + \overline{\omega}$ the spectrum is continuous. The continuous eigenstates can be build up in different ways as far as the asymptotic behavior of the outgoing electron is concerned. Since we are not concerned here with the problem of the

angular distribution of photoelectrons, we simply label continuous eigenstates generically as $|\Psi_n; k\rangle$ to indicate that they give rise to a molecular ion in the vibronic state $|\Psi_n\rangle$ with energy E_n and an ejected electron with energy $k^2/2m_e$. Neglecting the discrete part of the spectrum (as well as the continua involving multiple ionizations) one has (the normalization is $\langle\Psi_n; k|\Psi_{n'}; k'\rangle = \delta_{nn'}\delta(k-k')$):

$$G_M(E) \simeq \sum_{nv} \int_0^\infty \frac{|\Psi_n; k\rangle\langle\Psi_n; k|}{E - E_n - k^2/2m_e + i\eta} dk, \tag{11}$$

which gives

$$\sigma_{pe}^{\overline{\omega}}(k) = \frac{4\pi^2\overline{\omega}}{3c} \sum_n |\langle\Psi_g|\mu|\Psi_n; k\rangle|^2 \; \delta(E_g + \hbar\overline{\omega} - E_n - k^2/2m_e). \tag{12}$$

Equation (12) shows that the calculation of a photoelectron spectrum may proceed exactly as that of an absorption spectrum, as far as one is able to evaluate the required matrix elements or to propagate the doorway state [Eq. (12) can be recast in a time-dependent formalism proceeding as previously illustrated for the absorption spectrum]. In passing we notice that many progresses have been achieved in the last years in the computation of accurate photoelectron spectra, i.e. of the matrix elements $\langle\Psi_g|\mu|\Psi_n; k\rangle$ with a variety of methods ranging from the Green function approach to the use of discretized basis to simulate the continuum.[4] If one can reasonably assume that the scattering states can be well described by anti-symmetrized products of ionic states and continuum orbitals for the ejected electron (as for high photon energy, in the "sudden limit") things become much simpler, as discussed for example in Ref. 5, since, in the time dependent approach, the problem reduces to the propagation of a vibrational wavepacket for the ion.

For treating observables involving spontaneously emitted photons, the Hamiltonian involving the light source and the molecule must be extended to include the vacuum field:

$$H = H_M + H_R + H_S + V + V_S = H_0 + V + V_S, \tag{13}$$

$$H_S = \hbar \sum_{\boldsymbol{\varepsilon}_S, \mathbf{k}_S} \omega_S a^+_{\boldsymbol{\varepsilon}_S \mathbf{k}_S} a_{\boldsymbol{\varepsilon}_S \mathbf{k}_S},$$

$$V_S = -i \sum_{\boldsymbol{\varepsilon}_S, \mathbf{k}_S} \boldsymbol{\mu}\boldsymbol{\varepsilon}_S R_S (a_{\boldsymbol{\varepsilon}_S \mathbf{k}_S} - a^+_{\boldsymbol{\varepsilon}_S \mathbf{k}_S}). \tag{14}$$

Spontaneous Raman scattering involves the counting rate of spontaneously emitted photons at frequency ω_s, after an excitation at frequency ω i.e., proceeding as above ($n_{\boldsymbol{\varepsilon}_S,\mathbf{k}_S} = a^+_{\boldsymbol{\varepsilon}_S,\mathbf{k}_S} a_{\boldsymbol{\varepsilon}_S,\mathbf{k}_S}$):

$$W_{RS}(\omega,\omega_S) = \frac{d}{dt}\left\langle \psi(t) \left| \sum_{\boldsymbol{\varepsilon}_S \mathbf{k}_S} n_{\boldsymbol{\varepsilon}_S \mathbf{k}_S} \right| \psi(t) \right\rangle = \frac{i}{\hbar} \sum_{\boldsymbol{\varepsilon}_S \mathbf{k}_S} R_S \boldsymbol{\mu}\boldsymbol{\varepsilon}_S (a_{\boldsymbol{\varepsilon}_S \mathbf{k}_S} - a^+_{\boldsymbol{\varepsilon}_S \mathbf{k}_S}), \tag{15}$$

where the polarization of the spontaneously emitted photon may differ from that of the absorbed photon. One may easily check that this time the lowest-order contribution is third order and involves $|\psi^{(1)}(t)\rangle$ and $|\psi^{(2)}(t)\rangle$. Writing down the corresponding integrals and performing integrations in the limit $t_0 \to -\infty$ one obtains after some algebra:

$$W_{RS}(\omega,\omega_S) = \frac{8 n_\omega \pi^3 \hbar\omega}{L^6} \sum_{\boldsymbol{\varepsilon}_S \mathbf{k}_S, p} \omega_S |\chi_{pg}(\omega)|^2 \delta(E_g + \hbar\omega - E_q - \hbar\omega_S), \tag{16}$$

where

$$\chi_{qg}(\omega) = \sum_p \langle \Psi_q | \boldsymbol{\varepsilon}_S \boldsymbol{\mu} | \Psi_p \rangle \langle \Psi_p | \boldsymbol{\varepsilon}\boldsymbol{\mu} | \Psi_g \rangle [(E_g + \hbar\omega - E_p + i\Gamma_p)^{-1} + (E_g - \hbar\omega - E_p + i\Gamma_p)^{-1}]. \tag{17}$$

In the derivation we have neglected the possibility of overlapping molecular resonances[6] (i.e. we have assumed that there are not couples of eigenstates so close in energy that they can emit identical photons). Furthermore, a width Γ_p has been attributed to the excited state $|\Psi_p\rangle$, which accounts for its finite lifetime due to spontaneous emission or other decay mechanisms. The first term in Eq. (17) is dominant when $E_g + \hbar\omega \approx E_p$, i.e. for resonant Raman (RR) scattering.

Let us now put, as above, $\boldsymbol{\varepsilon}_{\mathbf{k}_S}\boldsymbol{\mu} = \mu\cos(\theta_S)$, $\boldsymbol{\varepsilon}\boldsymbol{\mu} = \mu\cos(\theta)$, introduce the density of photon modes in the cavity by the substitution $\sum_{\mathbf{k}_S} \to L^3 \int d\omega_S \omega_S^2 / 2\pi^2 c^3$, and perform the double average $\langle\cos^2(\theta)\rangle\langle\cos^2(\theta_S)\rangle$ which gives $(1/3)\cdot(1/3)$. The sum over the two independent polarization vectors gives a further factor 2, leading to the following differential emission rate for spontaneous photons (no matter for their polarization):

$$\frac{dW_{RS}(\omega,\omega_S)}{d\omega_S} = \frac{8 n_\omega \pi \hbar \omega \omega_S^3}{9 c^3 L^3} \sum_q |\chi_{qg}(\omega)|^2 \ \delta(E_g + \hbar\omega - E_q - \hbar\omega_S). \tag{18}$$

The differential (with respect to frequency) Raman scattering cross section is obtained by dividing Eq. (18) by the laser photon flux $F = n_\omega c/L^3$:

$$\frac{d\sigma_{RS}(\omega,\omega_S)}{d\omega_S} = \frac{1}{F}\frac{dW(\omega,\omega_S)}{d\omega_S} = \frac{8\pi\hbar\omega\omega_S^3}{9c^4}\sum_q |\chi_{qg}(\omega)|^2\,\delta(E_g+\hbar\omega-E_q-\hbar\omega_S) \tag{19}$$

where $d\sigma_{RS}(\omega,\omega_S)$ is the number of photons spontaneously emitted in the range $\omega_S, \omega_S + d\omega_S$ per unit of time and of laser photon flux. Equation (19) can be generalized to the case of an initial distribution over molecular states $|\Psi_j\rangle$, whose population is P_j to give:

$$\left\langle \frac{d\sigma_{RS}(\omega,\omega_S)}{d\omega_S} \right\rangle = \frac{8\pi\hbar\omega\omega_S^3}{9c^4}\sum_{q,j} P_j|\chi_{qj}(\omega)|^2\;\delta(E_j+\hbar\omega-E_q-\hbar\omega_S). \tag{20}$$

As for the case of light absorption, Eq. (20) has a time dependent counterpart which can be exploited by noticing that Eq. (17) can be rewritten as:

$$\chi_{qg}(\omega) = \int_0^\infty dt\langle\Psi_q|\boldsymbol{\varepsilon}_S\boldsymbol{\mu}e^{-iH_M t}\boldsymbol{\varepsilon}\boldsymbol{\mu}|\Psi_g\rangle e^{\frac{i}{\hbar}(E_g+\hbar\omega)t-\Gamma t}. \tag{21}$$

The above means that, albeit we started from a third-order term, we can practically evaluate the weight of each peak appearing in the Raman scattering and corresponding to a given molecular final state by propagating the doorway state $\boldsymbol{\varepsilon}\boldsymbol{\mu}|\Psi_g\rangle$ and Fourier transforming its overlap with the state $\boldsymbol{\varepsilon}_S\boldsymbol{\mu}|\Psi_q\rangle$ (notice that the width now must be identical for each intermediate state $|\Psi_p\rangle$).[7] The exponential damping is often replaced by a gaussian damping for mimicking inhomogeneous broadening.

The Raman scattering (which is called resonance fluorescence when the final molecular state $|\Psi_q\rangle$ is identical to the initial one $|\Psi_g\rangle$) is not, however, the only process resulting in spontaneous photon emission. If one repeats the above treatment in a density matrix formalism[8,9] and allows for intermediate state dephasing, one obtains, for resonant excitation, a fluorescence contribution. In practice, in this case the doorway state is really (not virtually) excited and becomes populated for a significant time interval, as pointed out by Lee and Heller.[7] The system becomes then sensitive to any phase-disturbing perturbation.[10] As a consequence, due to dephasing, the scattering is no more a purely coherent two-photon process, and the Raman emission competes with a relaxed component which is usually called fluorescence. The fluorescence is then simply the spontaneous emission from populated excited states, which have completely lost the memory of the

way they have been excited. From a spectroscopic point of view, it gives rise to broader bands, since now the initial state is an excited state, whose initial energy is not precisely defined, according to the time-energy Heisenberg uncertainty, due to various relaxation processes. The fluorescence from a given state $|\Psi_j\rangle$, whose intensity is proportional to its population, decays usually exponentially and is characterized by its lifetime $\tau_j^F = 1/\Gamma_j^F$, where

$$\Gamma_j^F = \sum_{\mathbf{k}_S} \frac{W^{em}(\omega_S)}{\hbar\omega_S} = \frac{4\pi^2}{3L^3} \sum_l \sum_{\boldsymbol{\varepsilon}_S \mathbf{k}_S} |\langle\Psi_j|\mu|\Psi_l\rangle|^2 \omega_S \delta(E_j - \hbar\omega_S - E_l) \quad (22)$$

is the photon emission rate. The second equality in Eq. (22) stands because W^{em} is essentially the same quantity as W^{abs} in Eq. (6), but instead of dealing with a single laser mode containing n_ω photons we have to consider all the initially empty ($n_\omega = 0$) cavity modes. The sum over modes and polarizations can be carried out as described above Eq. (18) to give:

$$\Gamma_j^F = \sum_l \Gamma_{j\to l}^F; \quad \Gamma_{j\to l}^F = \frac{4\omega_{jl}^3}{3\hbar c^3} |\langle\Psi_j|\mu|\Psi_l\rangle|^2; \quad \omega_{jl} = \frac{E_j - E_l}{\hbar}, \qquad (23)$$

which partitions the emission rate of a given state into contributions due to transitions to all the lower lying levels.

2.2. *Matrix Elements*

The eigenstates $\Psi_n^{JMS\Sigma p}$ of a spinless molecular Hamiltonian are labeled by the quantum numbers n for the energy, J and M for the square of the total angular momentum $\mathbf{J}$ and the SF component J_z^{SF}, S and Σ for the square of the total electronic spin $\mathbf{S}$ and the body-fixed (BF) component S_z, and $p = \pm$ for the parity. Employing the Wigner–Eckart theorem and the symmetry properties of the SF $\boldsymbol{\mu}$ components, the general selection rules for the matrix elements $\langle\Psi_{n'}^{J'M'S'\Sigma'p'}|\mu|\Psi_{n'}^{JMS\Sigma p}\rangle$ are:[11]

$$\begin{aligned}
&\Delta J = 0 \text{ (not for } J = 0) \text{ or } \pm 1,\\
&\Delta M = 0 \ (\mu_z^{SF} \text{ ; not for } \Delta J = M = 0) \text{ or } \pm 1 \ (\mu_x^{SF}, \mu_y^{SF}),\\
&\Delta S = \Delta\Sigma = 0, \text{ and the matrix elements do not depend on } \Sigma,\\
&p' = -p. \qquad (24)
\end{aligned}$$

If Φ_i are adiabatic or diabatic electronic states, the $\boldsymbol{\mu}$ matrix elements in the $\Psi_n^{JMS\Sigma p}$ representation depend[12] on the BF electronic moments

$\mu^b_{i'i}(\boldsymbol{Q}) = \langle \Phi_{i'}|\mu_b|\Phi_i\rangle_q$, where $b = x$, y, or z, $\boldsymbol{Q}$ are vibrational coordinates, and we integrate on the electronic coordinates $\boldsymbol{q}$. These moments fulfill the point-group selection rules and can be also classified in the permutation-inversion group,[13] thus obtaining further information. If Γ_{ir} label indeed the irreducible representations of the latter group, $\mu^b_{i'i}$ belongs to the representation $\Gamma_{i'} \otimes \Gamma_b \otimes \Gamma_i$ that must contain at least one allowed Γ_{ir} of an arbitrary function $F(\boldsymbol{Q})$, otherwise $\mu^b_{i'i}$ vanishes identically. For example, in a triatomic AB_2 molecule, the matrix element of μ_z between A_1 and B_2 electronic states belongs to B_2, i.e. is anti-symmetric under the permutation of the identical B nuclei. In particular, this symmetry behavior implies that $\langle A_1|\mu_z|B_2\rangle$ vanishes at C_{2v} point-group geometries.

The inclusion of the molecular rotation often makes CI spectra overwhelmingly complex. Because most CI effects are fully exploited at a vibronic level, it is useful to consider experiments on jet-cooled molecular beams, where the rotational effects are strongly reduced. In this case, we are interested only in vibronic band origins of a rovibronic spectrum and we can neglect the molecular rotation altogether. The hypothetical vibronic spectrum with $J = 0$ depends on the matrix elements

$$\langle \Psi_{n'}|\mu_b|\Psi_n\rangle \approx \sum_{i'}\sum_{i}\sum_{\alpha'}\sum_{\alpha}\langle \Psi_{n'}|\Phi_{i'}\chi_{i'\alpha'}\rangle\langle \chi_{i'\alpha'}|\mu^b_{i'i}|\chi_{i\alpha}\rangle\langle \Phi_i\chi_{i\alpha}|\Psi_n\rangle, \tag{25}$$

where n labels both the energy and the parity, and $\chi_{i\alpha}$ are Born–Oppenheimer (BO) vibrational states belonging to the electronic state Φ_i. These matrix elements rule both BO and NA transitions, as those associated with avoided-crossing, CI, or Jahn–Teller (JT) couplings.

For optical transitions, we omit the very small matrix elements $\langle \chi_{i\alpha'}|\mu^b_{ii}|\chi_{i\alpha}\rangle$, diagonal in the electronic indices, and we employ the Franck–Condon (FC) approximation for the transition electronic moments,

$$\mu^b_{i'i} \approx \text{constant with respect to } \boldsymbol{Q}, \qquad \text{any } b, i', \text{ and } i; i' \neq i. \tag{26}$$

Equation (26) implies that all non-vanishing transition electronic moments $\mu^b_{i'i}$ $(i' \neq i)$ belong to the totally symmetric Γ_{ir} of the molecular symmetry group, and that we are considering small oscillations or diabatic electronic

states that depend weakly on $\boldsymbol{Q}$.[14] Within the FC model, Eq. (25) reads

$$\begin{aligned}\langle\Psi_{n'}|\mu_b|\Psi_n\rangle &\approx \sum_{i'(\neq i)}\sum_i \mu^b_{i'i}\sum_{\alpha'}\sum_{\alpha}\langle\Psi_{n'}|\Phi_{i'}\chi_{i'\alpha'}\rangle\langle\chi_{i'\alpha'}|\chi_{i\alpha}\rangle\langle\Phi_i\chi_{i\alpha}|\Psi_n\rangle \\ &= \sum_{i'(\neq i)}\sum_i \mu^b_{i'i}\sum_{\alpha}\langle\Psi_{n'}|\Phi_{i'}\chi_{i\alpha}\rangle\langle\Phi_i\chi_{i\alpha}|\Psi_n\rangle. \qquad (27)\end{aligned}$$

Equations (25) and (27) explain the intensity borrowing effects of the exact spectra with respect to the FC ones: the $\langle\chi_{i'\alpha'}|\mu^b_{i'i}|\chi_{i\alpha}\rangle$ selection rules in Eq. (25) are less demanding than the $\langle\chi_{i'\alpha'}|\chi_{i\alpha}\rangle$ ones in Eq. (27), and thus some weak lines of exact spectra are forbidden in the FC approximation.

Let us consider a FC μ_b transition between the vibrational states $\chi_{1\alpha}$ of an isolated electronic state Φ_1, which fulfills the BO approximation, and the NA species $\Psi_{n'}$ associated with two interacting electronic states Φ_2 and Φ_3,

$$\Phi_1 \xrightarrow{\mu_b} \Phi_2/\Phi_3. \qquad (28)$$

The BO species Φ_1 may be one of the coupled ones, Φ_2 and Φ_3, and the JT theorem implies that Φ_1 belongs to a one-dimensional Γ_{ir}. For example, we may consider one-photon absorption from, or fluorescence to the lowest vibrational states of the ground electronic species, which are usually well below the NA states. Eq. (27) thus becomes

$$\langle\Psi_{n'}|\mu_b|\Phi_1\chi_{1\alpha}\rangle \approx \sum_{i'(\neq 1)}\mu^b_{i'1}\langle\Psi_{n'}|\Phi_{i'}\chi_{1\alpha}\rangle. \qquad (29)$$

We shall now assume that Φ_2 and Φ_3 undergo a CI in the adiabatic representation, that they are not the components of a degenerate JT state, and that μ_b induces a selective electronic transition between Φ_1 and only one of the coupled states Φ_2 and Φ_3. This means that either μ^b_{21} or μ^b_{31} is different from zero for a given μ_b component, i.e. that one of the coupled states is bright, while the other is dark under μ_b. This is a very common feature of CI spectra, which is often required by symmetry. It occurs, e.g., in molecular spectra of NO_2,[15] H_2S,[16] NH_2,[17] H_2O^+,[18] SO_2,[19] and pyrazine,[20] and in photoelectron spectra of HCN,[21] C_2H_4,[14] C_4H_4,[14] and five-member ring

molecules.[5] Assuming that Φ_2 is the bright state, Eq. (29) then simplifies as

$$\begin{aligned}\langle\Psi_{n'}|\mu_b|\Phi_1\chi_{1\alpha}\rangle &\approx \mu_{21}^b\langle\Psi_{n'}|\Phi_2\chi_{1\alpha}\rangle \\ &\approx \mu_{21}^b\sum_{\alpha'}\langle\Psi_{n'}|\Phi_2\chi_{2\alpha'}\rangle\langle\chi_{2\alpha'}|\chi_{1\alpha}\rangle, \\ &\qquad \mu_b \text{ couples only } \Phi_1 \text{ and } \Phi_2. \end{aligned} \tag{30}$$

This equation shows clearly the well-known FC principle of a vertical transition of the $\chi_{1\alpha}$ vibrational state from the potential surface of Φ_1 to the potential surface of the bright state Φ_2. It is interesting to contrast the matrix element of Eq. (30) with that resulting when the BO approximation holds also for the state Φ_2,

$$\langle\Phi_2\chi_{2\alpha'}|\mu_b|\Phi_1\chi_{1\alpha}\rangle \approx \mu_{21}^b\langle\chi_{2\alpha'}|\chi_{1\alpha}\rangle. \tag{31}$$

We see that a band intensity of a BO spectrum depends on the FC factors $|\langle\chi_{2\alpha'}|\chi_{1\alpha}\rangle|^2$, whereas the corresponding intensity of a CI spectrum is shared by several NA states $\Psi_{n'}$ that have a large $|\langle\Psi_{n'}|\Phi_2\chi_{2\alpha'}\rangle|^2$ weight. Taking also into account interference effects in the sum of Eq. (30), we may state the following propensity rules, which are the main signatures of CI effects in molecular spectra. A CI absorption spectrum is more diffuse, more irregular, and weaker than a BO spectrum. In general, vibrational progressions are much more irregular in NA spectra and fluorescence lifetimes are strongly lengthened by NA couplings.

2.3. *Methods of Calculation*

As we saw in Sec. 2.1, CW spectra can be calculated by time-independent (TI) or time-dependent (TD) methods. In an adiabatic electronic representation, the vibronic couplings diverge along the CI locus. Therefore, a diabatic electronic representation strongly simplifies the calculations, coupling the electronic species with well-behaved potential terms.

In general, theoretical studies of triatomic[16,22–24] and tetra-atomic molecules employ analytical PESs carefully fitted to large grids of *ab initio* data points, and curvilinear vibrational coordinates, to take into account large-amplitude motions. On the other hand, larger polyatomic molecules are investigated with simple polynomial PES, whose parameters are obtained from *ab initio* data, and with normal coordinates, possibly considering only the active ones. Finite basis representations[25] (FBR),

discrete variable representations[26] (DVR), or coordinate grids and Fourier transforms[27] are employed.

TI methods calculate the spectrum diagonalizing the Hamiltonian matrix **H**, or some matrix derived by **H**. Because of memory-storage requirements and the unfavorable scaling with the dimension of the basis set, conventional tridiagonalizations are only employed in small molecules and with well-optimized FBRs. The nonorthogonal[14,24,28,29] or orthogonalized[24,30] Lanczos algorithm is widely employed when the dimensions are too large for conventional diagonalizations. TD methods obtain the spectrum by Fourier transforming suitable correlation functions, and hence rely on effective wavepacket propagation.[31] The recent method by Mandelshtam and Taylor,[32] based on a low-storage Chebyshev iteration/filter-diagonalization, can be included among TD approaches.

The assignment of the individual spectral lines requires the knowledge of the corresponding eigenstates, and TI methods are more directly applicable to this problem. When the number of states is too large, the main lines of the spectrum can be identified via TI or TD methods, and only the corresponding states can be calculated by a filter diagonalization.[33] An alternative strategy renounces to assign the single lines of the high-resolution spectrum, and try to assign the bands of a lower resolution spectrum by small Lanczos expansions, whose pseudo-eigenstates carry all the required information.[24]

3. Interpretation of Nonadiabatic Spectra

The interpretation of a NA spectrum can be tackled at several levels. The theoretical approach has the power to inquire separately the effect of any particular interaction, by alternatively switching it on and off. On the other hand, the approximations of the calculations can prevent a one-to-one comparison of the theoretical and experimental lines, and theoretical results must be frequently regarded as models of real systems. Luckily, a rough experiment-theory agreement is often sufficient. For example, the overall influence of the CI couplings on a spectrum can be simply proved showing that a NA calculation gives a spectrum that resembles much more the experimental one than a BO calculation. This has been carried out for many polyatomic molecules.[5,14,34]

Detailed interpretations of high-resolution NA spectra follow two main routes: a level-by-level analysis and a statistical approach. In the following

two subsections, we present a general description of these approaches and their application to the X^2A'/A^2A' CI in NO_2.

3.1. *Level-by-Level Analysis*

A detailed, level-by-level analysis is the ultimate route for assigning spectra and investigating NA effects, but it is a very difficult task, both experimentally and theoretically. This analysis relies indeed on the approximate separation of the rotational, vibrational, and electronic motions, i.e. on the canonical model of the molecular structure that is based on the Eckart conditions, on the BO approximation, and on the normal-mode approach. These models lose progressively their meaning when strong NA interactions mix the molecular motions as CIs do.

A typical two-state CI increases by about an order of magnitude the number of bright levels with respect to the BO model, since the BO selection rules are not longer valid, and NA mixings can mask the vibrational progressions. Even omitting the rotation, both the electronic and the vibrational character should be assigned to each NA state. This task is experimentally solved employing selection rules, expectation values of some observables, Dunham expansions, and approximate FC factors. Deviations from the expected BO and Dunham behaviors hint at NA interactions. On the other hand, theoreticians can assign the bands calculating both NA states and levels, analyzing their expansion coefficients in the BO basis, and assigning approximate vibrational quanta from the nodal structure of the wavefunctions and from Dunham expansions.

The NO_2 molecule is probably the best-known CI example. The potential energy surfaces (PES) of the ground X^2A' and first excited A^2A' adiabatic electronic states intersect in C_{2v} symmetry,[15] where they belong to the $^2A_1$ and $^2B_2$ species, respectively. The minimum crossing energy is $8374\,cm^{-1}$ above the X^2A' vibrationless level.[22] Owing to this low intersection energy, NA effects begin at about $9500\,cm^{-1}$ and have a deep impact on bound states and resonances, on optical spectra, and on internal and collision dynamics, from the near infrared up to and beyond the first dissociation limit at $25\,129\,cm^{-1}$.[35] Considering also the small molecular dimensions that allow highly accurate investigations, NO_2 has been the subject of a lot of experimental and theoretical work. For example, Delon *et al.*[36]

have observed absorption and fluorescence spectra of jet cooled NO_2, and Santoro, Petrongolo, *et al.* (SP)[24,37] have calculated these spectra with a NA formalism. We here review some results by SP who employed a diabatic electronic representation $^2A_1/^2B_2$, an optimized FBR, and conventional or Lanczos eigensolvers, and refer the reader to the original literature for technical details. Owing to the symmetry of the vibronic basis, A_1 (B_2) NA states are represented in the space of the a_1 (b_2) and b_2 (a_1) vibrational states of the electronic species $^2A_1$ and $^2B_2$, respectively.

We show in Fig. 1 the beginning and development of the NA effects, plotting the correlations between the vibrational and the NA states up to $\sim 12\,000\,\mathrm{cm}^{-1}$. We also report the vibrational quanta for the symmetric stretch, the bending, and the anti-symmetric stretch, v_1, v_2, and v_3 respectively, the weights of the main vibrational states, and the weight w_{2n} of the $^2B_2$ electronic state. The CI couplings perturb slightly the $^2A_1$ vibrational states below 9500 cm^{-1} and then strongly couple the $^2A_1$ $(0,11,1)$ and $^2B_2$ $(0,0,0)$ states, giving a first strongly mixed B_2 NA state at $9534\,\mathrm{cm}^{-1}$. The $^2A_1$ $(0,11,1)$ and $^2B_2$ $(0,0,0)$ vibrational weights are equal to 25% and 51%, respectively, and the w_{2n} is equal to 53%. The NA interactions are gradual and selective, because they mix close lying vibrational species of the electronic states, mainly highly excited $^2A_1$ bending states of b_2 (a_1) symmetry and low lying $^2B_2$ states of a_1 (b_2) symmetry. The large Δv_2 value of the coupled vibrational states reflects the different equilibrium bond angles of the electronic states (≈ 32 degrees).[22] Up to about $12\,000\,\mathrm{cm}^{-1}$, 8 A_1 and 19 B_2 NA states are mixed (with $w_{2n} > 10\%$), of a total of 189 and 140 states for the two symmetries, respectively. Note that several $^2A_1$ vibrational states are practically unmixed, whereas all the $^2B_2$ vibrational states are strongly coupled with many $^2A_1$ partners. This result is consistent with the larger $^2A_1$ density of states with respect to the $^2B_2$ one.

Experimental and theoretical energies and band assignments have already been compared.[23,38] We here report only a further comparison that has been made possible by recent measurements. Biesheuvel *et al.*[39] have estimated the $^2A_1$ electronic character, $w_{1n} = 1 - w_{2n}$, of 29 rovibronic states Ψ_n between 11 211 and $13\,680\,\mathrm{cm}^{-1}$, by measuring the Fermi-contact constants σ_n and obtaining the mean values $\overline{w}_1 = 61\%$ and $\overline{\sigma} = 86\,\mathrm{MHz}$. Leonardi *et al.*[22] found 24 B_2 strongly mixed NA states, which are nearby the vibronic bands of Ref. 39, and have $\overline{w}_1 = 71\%$ and $\overline{\sigma} = 102\,\mathrm{MHz}$. The $\overline{\sigma}$ value has been obtained from $\sigma_n \approx \sigma_1 w_{1n} + \sigma_2 w_{2n}$,

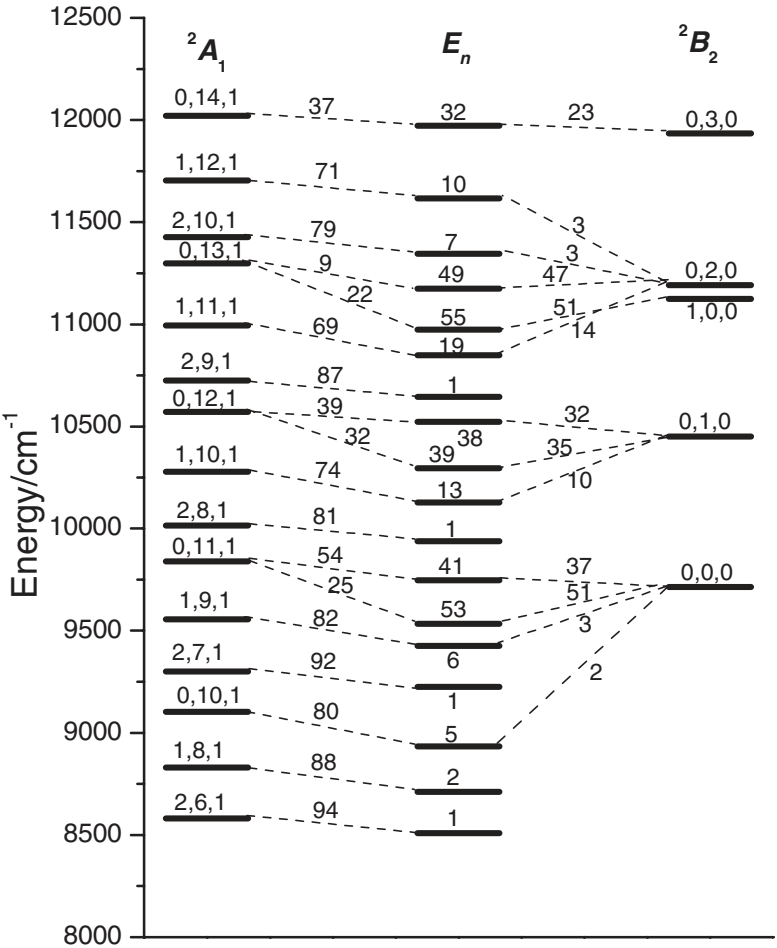

Fig. 1. Correlation between the BO vibrational and NA NO_2 levels. The $^2A_1$ and $^2B_2$ BO levels are labeled by the (v_1, v_2, v_3) vibrational quanta. The NA levels are marked by the total weight w_{2n} of the $^2B_2$ electronic state. Dashed lines connect a BO and a NA level and the numbers upon them indicate the contribution of the former to the latter.

with $\sigma_1(^2A_1) = 147.3\,\mathrm{MHz}$ and $\sigma_2(^2B_2) = -10\,\mathrm{MHz}$.[39] The calculations overestimate by ∼16% the weight of the electronic ground state and the Fermi-contact constant in this energy range, where the mean error of the calculated levels with respect to the observed ones is $73\,\mathrm{cm}^{-1}$.

3.2. *Statistical Approach*

A complementary perspective in the analysis of a spectrum is furnished by a statistical approach, first developed in nuclear physics[40] but then applied also to molecular systems.[14,41] There is an interesting connection between the spectral statistical properties and the classical dynamics of a system.[42] The quantum levels of systems which are classically integrable, i.e. those having a constant of motion for each degree of freedom, are uncorrelated in the semi-classical limit (with the exception of systems of harmonic oscillators) and resemble a random sequence.[43] These spectra of levels are called regular. On the other side, the levels of quantum systems which are the counterparts of classical systems with no good constant of motion, are strongly correlated, and their spectra are called irregular and are well reproduced by the eigenvalues of real random matrices[42,44,45] (the Gaussian orthogonal ensemble, GOE). Because of these connections with classical dynamics, spectral statistics has been utilized to come to a definition of quantum chaos, and irregular spectra are sometimes called chaotic spectra.

Spectral analysis is applied to the complete set of levels E_i of a molecule in a given energy range which share the same set of good quantum numbers (as symmetry and spin). To have results that can be contrasted with some universal limits, the secular variation, i.e. the average variation of the integrated density of levels $N(E)$ with the energy E, must be eliminated. This can be accomplished in several ways,[41,46] for example by the mapping $E_i \rightarrow \varepsilon_i = \overline{N}(E_i)$, which defines the new unfolded energies ε_i as the value of a polynomial fit $\overline{N}(E)$ to $N(E)$ at the energy E_i. Several statistical measures have been utilized in literature to study spectral characteristics. Here we discuss only the nearest neighbor spacing distribution (NNSD),[40] referring the reader to the literature for a more complete discussion of the subject.[14,40]

The normalized NNSD, namely $P(S)$, is the distribution function of spacings S between adjacent energy levels. It is related to the conditional probability $P_2(S)dS$ to find a level in the interval $[\varepsilon + S, \varepsilon + S + dS]$ when there is a level at ε and no level in the interval $[\varepsilon, \varepsilon + S]$. For a random, uncorrelated sequence (regular systems), $P_2(S)$ is a constant, and we get a Poisson distribution $P(S) = \exp(-S)$ (from now on the mean spacing $\overline{S} = 1$), while for a linear repulsion of the energy levels, $P_2(S) \propto S$, and we get the Wigner distribution $P(S) = (\pi S/2)\exp(-\pi S^2/4)$.

The levels of a GOE ensemble (and hence those of irregular systems) have a NNSD distribution very close to the Wigner one. Notice that while the Poisson distribution is maximal at $S = 0$ (no level repulsion), the Wigner distribution vanishes at $S = 0$ (there is level repulsion). An intermediate behavior can be described in different ways. Considering also a non-linear repulsion, $P_2(S) \propto S^{q_B}$, Brody[40] computed the distribution

$$P_B(q_B; S) = \alpha S^{q_B} \exp(-\beta S^{1+q_B}), \tag{32}$$

where $\beta = \Gamma[(2 + q_B)/(1 + q_B)]$ and $\alpha = (1 + q_B)\beta$. Berry and Robnik[47] obtained a different expression,

$$P_{BR}(q_{BR}; S) = \left[1 - q_{BR}^2 + \frac{\pi q_{BR}^3 S}{2} - (1 - q_{BR})^2 R(q_{BR} S)\right] \cdot \exp\left[-(1 - q_{BR})S - \frac{\pi q_{BR}^2 S^2}{4}\right], \tag{33}$$

where $R(z) = 1 - \exp(\pi z^2/4) erfc(2\sqrt{\pi}/2)$, and q_{BR} is the chaotic fraction of the total classical phase space domain at the energy E under investigation. Both in the case of Eqs. (32) and (33), the Poisson and Wigner distributions are obtained as particular cases for values of the free parameter (q_B and q_{BR}) of 0 and 1 respectively. By fitting Eqs. (32) and (33) to the actual NNSD of the system under investigation, the best q_B and q_{BR} values are obtained that are quantitative indices of the degree of irregularity of the spectrum, though with some different physical meaning as reported above, and some care as q_{BR} approaches very slowly to zero.[42]

The NNSD deals with short-range correlations. The analysis of long-range correlations is also very interesting in NA systems and it has been often performed by the $\overline{\Delta}_3$ statistics, which we do not describe for lack of space. The theoretical foundations are presented in Refs. 48 and 49, and Refs. 50 and 51 report some applications to molecular NA systems. Sophisticated techniques based numerical recognition patterns[52] and correlation diagrams[53] have been recently reported in literature but, to our knowledge, they have not yet been applied to spectra with significant NA effects.

To show the statistical approach at work, we discuss the result of the analysis of 1226 B_2 NA levels of NO_2 calculated by us from 10 000 cm^{-1}, where CI effects begin, up to 22 000 cm^{-1}. We employed a diabatic electronic representation, an optimized FBR, and a nonorthogonal Lanczos recursion.[24] The computed NNSD is shown in Fig. 2, and the q_B and q_{BR}

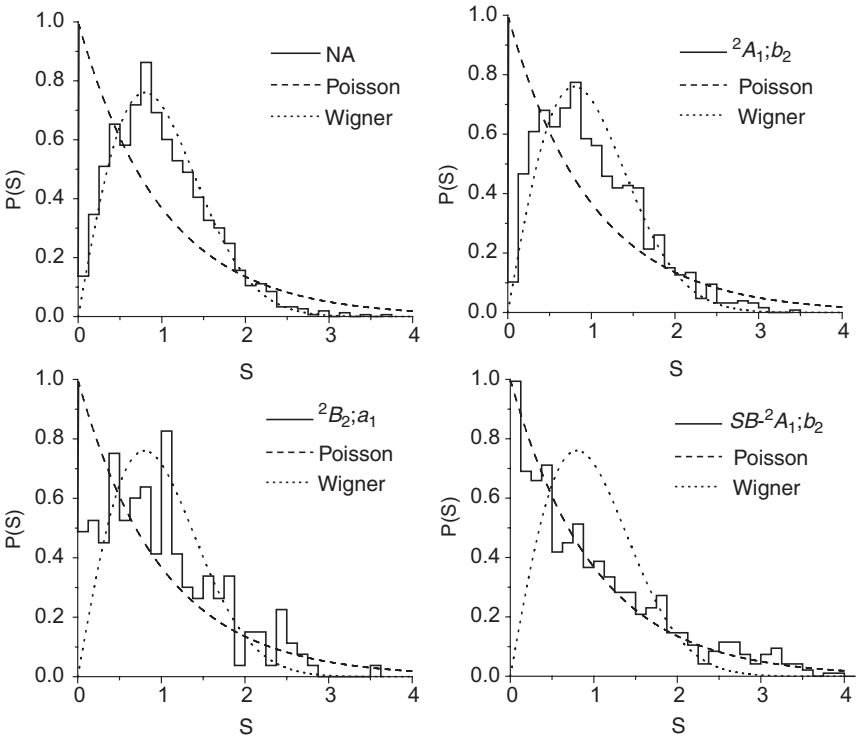

Fig. 2. NNSD statistics of set of levels of NO_2 of B_2 symmetry . (a) NA levels NA; (b) BO levels $^2A_1;b_2$ of the $^2A_1$ electronic species; (c) BO levels $^2B_2;a_1$ of the $^2B_2$ electronic species; (d) SB-$^2A_1;b_2$ levels of the $^2A_1$ electronic species obtained neglecting the stretch-bend couplings.

parameters obtained from a fit of Eqs. (32) and (33), together with the second $\langle S\rangle^2$ and third $\langle S\rangle^3$ moments and the standard deviation σ, are reported in Table 1. The data point out a behavior very close to the GOE limit. The analysis of the $\overline{\Delta}_3$ statistics not reported here for lack of space, agrees with this conclusion.[51]

To investigate the dependence of the spectrum irregularity with the energy, we divided the spectrum in half-overlapping sets of 200 levels and we best fitted the q_{BR} value to the computed NNSD, attributing the resulting degree of irregularity to the average energy spanned by the considered subset: q_{BR} increases monotonically up to 1.0 at $18\,500\,\mathrm{cm}^{-1}$, then

shows a small decrease to 0.9 at about $20\,000\,\mathrm{cm}^{-1}$, reaching back 1.0 at $22\,000\,\mathrm{cm}^{-1}$.[51]

The statistical features of the computed levels have been compared with those of several experimental sets[51] from $14\,645\,\mathrm{cm}^{-1}$ to $19\,360\,\mathrm{cm}^{-1}$ and the fine agreement suggests they are accurate enough to be used for further investigation of the causes of the spectrum irregularity. This was possible by theoretically switching off selectively different coupling terms in the molecular Hamiltonian, generating new sets of levels and computing the NNSD of each of them. Table 1 and Fig. 2 compare the statistics of the B_2 NA levels with that of the diabatic B_2 BO states in both electronic states ($^2A_1; b_2$ and $^2B_2; a_1$) and with that of the levels obtained by neglecting the stretch-bend couplings in the $^2A_1$ ground diabatic potential ($SB\text{-}^2A_1; b_2$). It is shown that the $^2A_1; b_2$ set is slightly less irregular than the NA one, whereas the $^2B_2; a_1$ spectrum is more regular. The NNSD of the $SB\text{-}^2A_1; b_2$ levels is, on the contrary, close to the Poisson statistics and hence almost regular. These findings point out that the spectral chaos is due both to the vibronic coupling between the two diabatic electronic states and to the stretch-bend couplings on the ground diabatic surface. It is interesting to stress that the vibronic coupling acts at several levels: on one hand, it brings into the spectrum the irregularity due to the stretch-bend couplings of the highly-excited dark $^2A_1; b_2$ vibrational levels, on the other hand, it is strong enough to oppose the possible decrease of correlation (which would make the spectrum more regular), due to the overlapping of the two different $^2A_1; b_2$ and $^2B_2; a_1$ sets, and to cause, on the contrary, an overall increase of

Table 1. NNSD parameters of the B_2 levels of NO_2 in the $10\,000$–$22\,000\,\mathrm{cm}^{-1}$ range. M is the number of levels; $\langle S\rangle^2$ and $\langle S\rangle^3$ are the second and third moment, respectively, in mean spacing units, σ is the standard deviation, q_B and q_{BR} are the Brody and Berry–Robnik parameters as defined in Eqs. (32) and (33) respectively.

	M	$\langle S\rangle^2$	$\langle S\rangle^3$	σ	q_B	q_{BR}
Poisson		2	6	1	0	0
Wigner		1.27	1.91	0.52	1	1
NA	1226	1.32	2.12	0.57	0.85	0.96
$^2A_1; b_2$	1013	1.37	2.30	0.61	0.68	0.90
$^2B_2; a_1$	214	1.47	2.69	0.69	0.42	0.74
$SB\text{-}^2A_1; b_2$	766	1.78	4.19	0.88	0.00	0.26

the spectral irregularity. The conclusions reported here retain their validity, even when the statistical study is performed after dividing the energy range in the two sub-ranges 10 000–16 500 cm^{-1} and 16 500–22 000 cm^{-1}.[51]

4. Discussion of Selected CW Spectra

The literature on CW spectra deeply affected by the existence of a CI is too wide to be reviewed in this chapter. Instead of trying a complete exposition of the literature results, we will pursue a different task, trying to elucidate the main features of these effects through a discussion of few interesting and prototypical examples from the literature and our own laboratory research. The cited works are preferably chosen among the more recent ones to give the reader a flavor of the great activity in this field and the state-of-the-art capabilities.

4.1. *Absorption Spectra*

The main CI effects on an absorption spectrum are an increased density of the lines and a partial or total loss of regular progressions. The impact of a CI on a particular absorption spectrum is ruled by several factors, as the strength of the NA interactions, the location of the CI with respect to the FC region, and the characteristics of the interacting electronic states. As an example of the third factor, we cite that when one of the two coupled states is dark and dissociative, the spectrum shows very diffuse bands, as in the case of the $^1A_1 \rightarrow {}^1B_1/{}^1A_2$ absorption of H_2S[16] and O_3,[23,54] where the $^1B_1$ state is bound and $^1A_2$ is repulsive. Below, we discuss in some detail the spectra of NO_2 and O_3 and of some larger polyatomic molecules.

4.1.1. *NO_2*

In agreement with Eq. (9), the intensities of the NO_2 diabatic (NA coupling neglected) or NA cold absorption spectra have been approximated as $\varepsilon_{2\alpha}|\langle\Phi_2\chi_{2\alpha}|\mu_y|\Phi_1\chi_{1,0}\rangle|^2$ or $E_n|\langle\Psi_n|\mu_y|\Phi_1\chi_{1,0}\rangle|^2$, respectively.[24,55] Here Φ_1 and Φ_2 are the $^2A_1$ and $^2B_2$ electronic states, $\varepsilon_{2\alpha}$ are the $^2B_2$ vibrational levels and E_n are NA levels, $\chi_{1,0}$ is the $^2A_1$ vibrational ground state, and the dipole matrix elements are given in Eqs. (30) and (31) within the FC approximation with $\mu_{21}^y = 1$ au. For symmetry reasons, only B_2 states are populated. Figure 3 contrasts the calculated diabatic and NA spectra with

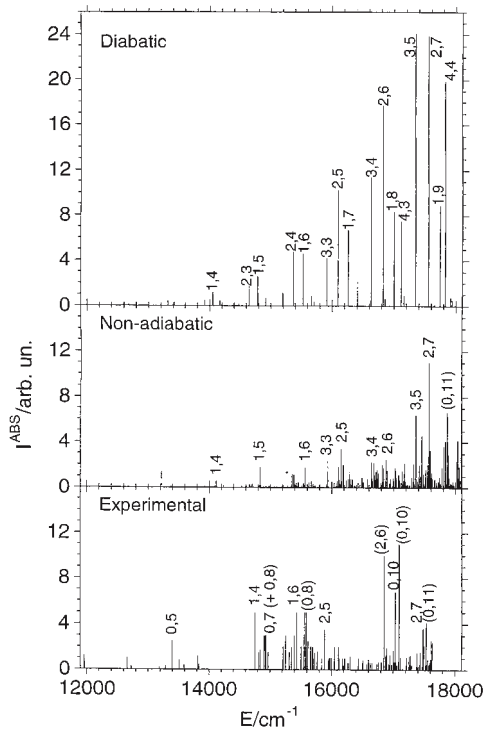

Fig. 3. NO_2 absorption spectrum. Comparison of the experimental spectrum with the theoretical diabatic (NA coupling neglected) and NA spectra. The lines are labeled by the v_1, v_2 quantum numbers ($v_3 = 0$). The uncertain assignments are in parentheses.

those observed[36] in the 12 000–18 000 cm^{-1} energy range, and reports the $^2B_2$ $(v_1, v_2, 0)$ assignments of some bands.

Owing to the Fermi resonance between the $^2B_2$ symmetric stretching and bending modes,[38,56] all the spectra show long $^2B_2$ $(v_1, v_2, 0)$ vibrational progressions, which are grouped in polyads with quantum number $v = 2v_1 + v_2$. The diabatic and NA parts of Fig. 3 show clearly the CI effects on the spectrum. The diabatic spectrum is regular and strong, and its $^2B_2$ vibrational progressions and polyads are clearly recognizable up to high energy. On the contrary, the NA spectrum is much more irregular, diffuse, and weak. The density of NA bright states is by far larger than that of the diabatic species, and the intensity of a diabatic band is distributed among many NA states, with a clear borrowing effect.[55]

The NO_2 example shows the usefulness of assigning even approximated electronic and vibrational quanta for understanding CI absorption spectra. The absorbing NA states are built by a manifold of dark and highly excited $^2A_1$ BO states, which cannot be assigned, and by very few, bright, and low-lying $^2B_2$ BO states, which can be identified and approximately assigned. The knowledge of the $^2B_2$ character of the NA states allows us to study the indirect mixing of the bright $^2B_2$ BO states and polyads, due to the common coupling to the $^2A_1$ BO species, the intensity borrowing effects, and the destruction of the regular $^2B_2$ vibrational progressions in the NA spectrum.

Above 17 000 cm^{-1}, the CI effects are so strong that the $^2B_2$ vibrational progressions and polyads begin to overlap, giving rise to a rather chaotic NA spectrum.[55] Small spectral regularities persist, however, even above 18 000 cm^{-1}. By analyzing the polyad interactions,[24] we estimate a maximum spectral irregularity in the energy range 17 800–19 700 cm^{-1} due to the mixed polyads 12–14, and this is in fine agreement with the results of the statistical analysis reported in Sec. 3.2.

Figure 3 shows that NA and experimental data agree only qualitatively. This result is mainly due to the employed PESs, because the removal of the FC approximation does not improve the calculated spectrum.[57] In general, the theoretical coupling is larger than that inferred from the experimental data. The calculations thus favor $^2B_2$ $v_1 - v_2$ couplings and $^2B_2$ vibrational mixings at high energy. On the contrary, the model underlying the experimental assignments relies on separated v_1 and v_2 modes and on a single $^2B_2$ component. The comparison of the six bands, whose $^2B_2$ $(v_1, v_2, 0)$ assignments are equal in Refs. 55 and 36, gives a quantitative measure of the features of the calculations: the mean energy error of the theoretical bands is 237 cm^{-1}, ($\sim$ 1.5%), and the calculated mean intensity is 14% smaller than that observed (4.3 *vs.* 5.0 a.u.).

4.1.2. *O_3*

The absorption spectrum of O_3 is characterized by the diffuse Chappuis band between 14 000 and 24 000 cm^{-1} that has been attributed to the existence of the $1^1A''/2^1A''$ ($1^1A_2/1^1B_1$ in C_{2v}) CI very close to the zero-point energy of the two surfaces.[54] The 1^1B_1 state is bound and carries most of the oscillator strength, while 1^1A_2 is dissociative. This is the cause for the diffuse structure of the band. Because of the dissociative nature of the problem, the theoretical spectrum has been computed through

time-dependent methods using Jacobi coordinates and expressing the wavefunction on FBR/DVR for the angular coordinate and a grid of points for the other two coordinates. The very interesting characteristics of the spectrum is that the band structure looks irregular at energies $<19\,000\,\mathrm{cm}^{-1}$, while at higher energies it shows two regular progressions $(v_1, 0, 2)$ and $(v_1, 1, 2)$ respectively, assigned both experimentally[54] and theoretically.[23] Thus, unlike the case of NO_2, the CI effects are localized in the energy domain. It has been argued that this happens since the upper adiabatic surface, $2^1A''$, whose vibrational levels after neglecting the NA coupling still account for most of the features of the spectrum, is much narrower than the ground surface along the anti-symmetric stretching coordinate. Because of that, the optical excitation populates also the high lying vibrational levels of $2^1A''$ with an excited (even by symmetry) number of quanta in this mode, prevalently $v_3 = 2$. These states have a small probability density close to C_{2v} geometries, where the CI takes place, and are hence little influenced by it, explaining the regularity of the high-energy part of the band. This is not the case for NO_2, whose strongest states in absorption have $v_3 = 0$, i.e. their maximum probability density is in C_{2v} and they are strongly perturbed by the CI.

4.1.3. *Larger Polyatomic Molecules*

While the work on triatomics allows the computation of large *ab initio* grids in the full-coordinate space, a different approach must be pursued for larger polyatomics. Remarkable theoretical success in reproducing experimental spectra has been obtained with the model first proposed by Köppel *et al.,*[14] where the diabatic PESs of the different states are multi-dimensional paraboloids shifted along the totally-symmetric tuning modes and linearly coupled by the non-totally symmetric modes of the right symmetry (quadratic terms have been added in some cases). Computations taking into account a large number of vibrational modes have been recently performed. A well known example is the $S_0 \rightarrow S_1/S_2$ spectrum of pyrazine,[20] well reproduced by Lanczos calculations with a three-state, four-mode (harmonic) model.

A recent computation concerns the absorption and Raman spectrum of *trans*-butadiene[58] computed by a TD approach. The two lowest valence excited states of *trans*-butadiene are the 1^1B_u (HOMO $\rightarrow$ LUMO), which

is bright, and the 2^1A_g (HOMO $-$ 1 $\rightarrow$ LUMO, HOMO $\rightarrow$ LUMO + 1, HOMO^2 $\rightarrow$ LUMO^2), which is dark. Their relative position with respect to a vertical excitation from the ground state has been debated for a long time (there is some agreement now that the 1^1B_u state is the lower). The observation that the absorption spectrum is quite diffuse and there is no detectable fluorescence, points towards a fast radiationless decay. An accurate theoretical investigation[58] performed by help of CASSCF and CASPT2 with respect to the CASSCF reference, resulted in a set of parameters that characterizes the CI between the 1^1B_u and the 2^1A_g states, located not far from the equilibrium position of the ground state. Only the in-plane modes were considered, which gives rise to eight coupling modes and nine tuning modes. The authors computed the absorption spectrum and the resonance Raman spectrum at 217.9 mm (see Sec. 4.3.4) by wavepacket propagation, as discussed in Sec. 2. Figure 4 taken from Ref. 58 reports their nice results which agree well with the experimental one if a very rapid phenomenological dephasing time of 15 fs is included, which, according to the authors, serves also to mimic the role of the missing out-of-plane modes as well as the $2^1A_g/1^1A_g$ CI.

Very recently, by a three electronic-states eight harmonic-modes model and time-dependent methods based on a Runge–Kutta–Merson propagation, the absorption spectrum $S_0 \rightarrow S_1/S_2$ of *cis*-1,3,5-hexatriene (CHT) has been satisfactorily reproduced.[34] Some differences with the analogous spectrum of the *trans*-isomer have been rationalized in terms of the strong NA coupling modes existing in the *cis*-isomer. The longer dephasing time T_2 for the spectrum of CHT with respect to the analogous spectrum of pyrazine,[20] in contrast with the larger number of coupling modes (3 to be compared with 1) and an activity coefficient[34] for the strongest coupling mode, larger about two times in CHT than in pyrazine, has been ascribed to the different location of the S_1/S_2 CI in the two molecules, in pyrazine being closer to the minimum of the S_2 PES than in CHT.

4.2. *Photoelectron Spectra*

Many photoelectron (PE) spectra showing clear marks of a CI among the ionic PESs have been measured and calculated. We mention ethylene,[14] butatriene,[14] allene,[14] BF_3,[14] and HCN,[14] pyrazine,[59] and vinylbromide.[60] In the next subsections we discuss in some detail an interesting comparison

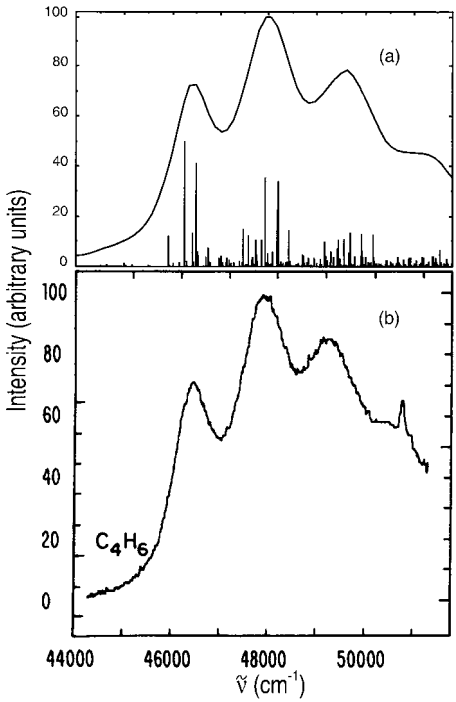

Fig. 4. Calculated (a) and experimental (b) UV absorption spectrum of *trans*-butadiene, reproduced with permission from Ref. 58.

of the CI effects on the PE spectra of furan, pyrrole, and thiophene, and the pseudo-JT (PJT) effect on the PE spectrum of allene.

4.2.1. *Furan, Pyrrole and Thiophene*

The vibronic structure of the valence photoelectron spectra of furan, pyrrole and tiophene due to π-electrons have been computed in Ref. 5 by the linear vibronic coupling model[14] and compared with high-resolution spectra. The *ab initio* calculations were performed utilizing ground-state geometries and vibrational frequencies optimized at the MP2 level, while the parameters for the intrastate and interstate coupling, due to totally symmetric (tuning modes) and non-totally symmetric (coupling modes), respectively, were evaluated by the outer-valence Green function method.

The photoionization from the π_3 or the π_2 MOs leaves the ion in the $^2A_2$ or $^2B_1$ states, respectively. These give rise to a CI that manifests itself in the lack of a vibrational structure in pyrrole and thiophene (CI near the minimum of the upper, $^2B_1$ surface) and by line broadening in furan (CI at higher energy). The agreement between experimental and computed spectra is excellent, as witnessed from Figs. 5 and 6 for furan and thiophene, taken from Ref. 5 (the figure for pyrrole shows a similar agreement and it is not reported for lack of space). The analysis of the data concerning the nontotally symmetric (b_2) coupling modes, as well as the tuning modes, shows that the increasing effectiveness of the CI in perturbing the spectra with respect to the case of uncoupled surfaces (indicated in Figs. 5 and 6 as Poisson distribution) from furan, to pyrrole, to thiophene is not due to a different interstate coupling strength. The latter is in fact moderate and similar for all three. It is instead the role of tuning modes which is prominent, since they are displaced in such a way that the CI moves towards the bottom of the upper surface, going from furan to thiophene.

4.2.2. *Allene*

When a molecule has doubly degenerate symmetry species, three adiabatic electronic states can intersect conically. Three-state CIs can occur e.g. for Σ and Π states of linear molecules or for non-degenerate and degenerate states in other point groups, as in the PJT effect.[14] These multiple CIs cause a huge increase of NA effects.

Recently, Mahapatra *et al.*[61] have simultaneously investigated the JT and PJT effects in the PE spectrum of allene, C_3H_4, which belongs to the D_{2d} point group. In the $C_3H_4^+$ ion, the A^2E JT coupling is due to b_1 (v_4) and b_2 (v_5–v_7) vibrational modes, and the A^2E/B^2B_2 PJT interaction is governed by e modes (v_8–v_{11}). These authors have considered FC absorption from the ground state of C_3H_4 to the three coupled states of $C_3H_4^+$, and have employed a diabatic-electronic and a harmonic-oscillator representation of a linear vibronic Hamiltonian. By taking into account eight normal modes, they have calculated the allene PE spectrum via a TI Lanczos recursion.

The calculated NA PE spectrum is in very good agreement with that observed between 13.8 and 15.8 eV. The minimum energy crossing among the A^2E and B^2B_2 states is at ∼15.05 eV, and the NA spectrum below

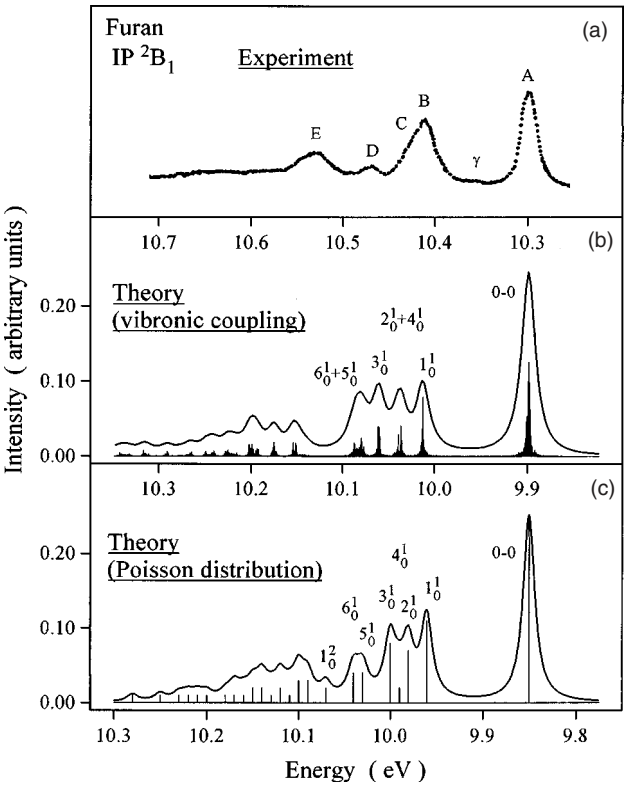

Fig. 5. $^2B_1$ photoelectron band in furan: (a) experiment, (b) nonadiabatic calculation, (c) ideal diabatic case in which the NA couplings are switched off. Reproduced with permission from Ref. 5.

this energy has rather regular A^2E vibrational progressions of the non-degenerate modes v_2 and v_7. On the other hand, the spectrum at higher energies is due to the A^2E/B^2B_2 PJT effect induced by the degenerate modes v_8 and v_{eff}, where the latter is an effective mode that merges v_9 and v_{10}. This high-energy NA spectrum is by far more diffuse and irregular than the diabatic spectrum. The huge increase of the spectral density and the absence of any vibrational progression above 15.05 eV clearly show the deep impact of this three-state CI on the PE spectrum.

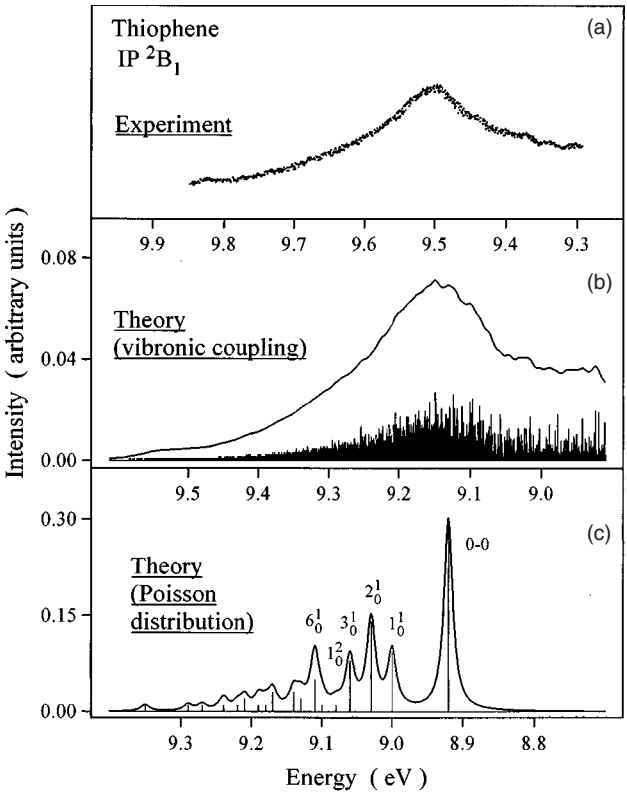

Fig. 6. $^2B_1$ photoelectron band in tiophene: (a) experiment, (b) nonadiabatic calculation, (c) ideal diabatic case in which the NA couplings are switched off. Reproduced with permission from Ref. 5.

4.3. *Emission Spectra*

The separation between fluorescence and resonance Raman (RR) emission, as described in Sec. 2.1, is well established theoretically, but it is difficult to attain experimentally. In most of the papers, total emission spectra are reported, without an estimate of the importance of the two separate contributions. Because of that, in this Section we discuss together both phenomena, enlightening the differences when possible.

CIs strongly affect the emission processes, quenching for example the quantum yield of fluorescence in pyrazine[62] and lengthening the radiative

lifetimes in NO_2.[37] The effect of a CI perturbing the final states of the emission process is seen in JT systems. Emission spectra in cases of $(E \times \varepsilon)$ JT spectra of bound states show a double-humped envelope.[63,64] Such an envelope has been seen also in the emission spectra of Rydberg-excited H_3 radicals,[65] even if the lower adiabatic sheet is unstable with respect to dissociation. The existence of two different maxima, $9600\,\mathrm{cm}^{-1}$ apart, has been attributed by model calculations[66] to the double-sheeted nature of the ground PES. Very recently, a new theoretical method for the calculation of the JT spectroscopic parameters have been proposed in literature and applied with success to the study of the dispersed fluorescence of the methoxy radical and other CX_3Y radicals[67] and of the cyclopentadienyl radical.[68]

CIs can effectively alter the emission spectra also by perturbing the initial emitting states of the transition. In the following, we discuss some typical features of the phenomenon in NO_2, pyrazine, H_2S and *trans*-butadiene.

4.3.1. *NO_2*

The NO_2 molecule gives us the possibility to discuss in a detailed example of the CI effect on laser-induced fluorescence (LIF) and laser-induced dispersed fluorescence (LIDF) spectra. They have been observed by the Grenoble group[36] and calculated by our group.[37] We here discuss some results of the calculations, comparing diabatic and NA spectra for enlightening CI effects, and contrasting theoretical and experimental results. LIF lifetimes (τ_n^F) and intensities I_n^{LIF} have been calculated assuming a photon excitation from the ground state, $\Phi_1\chi_{1,0}$, to B_2 NA states, Ψ_n, which then radiate down to A_1 $\Psi_{n'}$ species. The LIF intensities are equal to

$$I_n^{LIF} \propto I_n^{ABS}(1 - e^{-t/\tau_n^F}), \tag{34}$$

where τ_n^F are the radiative lifetimes (see Sec. 2.1), I_n^{ABS} are the absorption intensities (see Sec. 4.1.1), and $t = 10\,\mu\mathrm{s}$ is the acquisition time.

Like the absorption spectrum, CI interactions strongly influence the NO_2 fluorescence properties. As we have seen in Sec. 3.1, the absorption from $\Phi_1\chi_{1,0}$ populates preferably NA states Ψ_n with large $^2B_2$ $(v_1, v_2, 0)$ character. The vibronic couplings between these bright vibrational states and the dark species $^2A_1$ (v_1, v_2, v_3) lower the Ψ_n radiative rates $\Gamma^F_{n\to n'}$ [Eq. (23)] and therefore increase the lifetimes τ_n^F. The accurate calculations[37] thus confirm that the lifetimes of the intense bands

are strongly lengthened by CI couplings, as has been pointed out several years ago by Douglas[69] and Bixon and Jortner.[70] On the other hand, and quite interesting, explicit calculations[37] show that $^2B_2$ vibrational mixings $(0,0,v_3)/(v_1,v_2,0)$ decrease τ_n^F of weak bands with high $^2B_2$ $(0,0,v_3)$ character, because the bright $^2B_2$ $(v_1,v_2,0)$ vibrational states have short lifetimes. It is however difficult to observe experimentally this effect, because these bands are weak in absorption and in LIF spectra.

We compare in Fig. 7 calculated and observed[56] LIF spectra between 11 600 and 13 900 cm^{-1}, showing also some $^2B_2$ $(v_1,v_2,0)$ assignments.[36,37] Similar to the absorption spectrum, the LIF NA bands are about three times weaker than the diabatic ones. Contrary, however, to the absorption

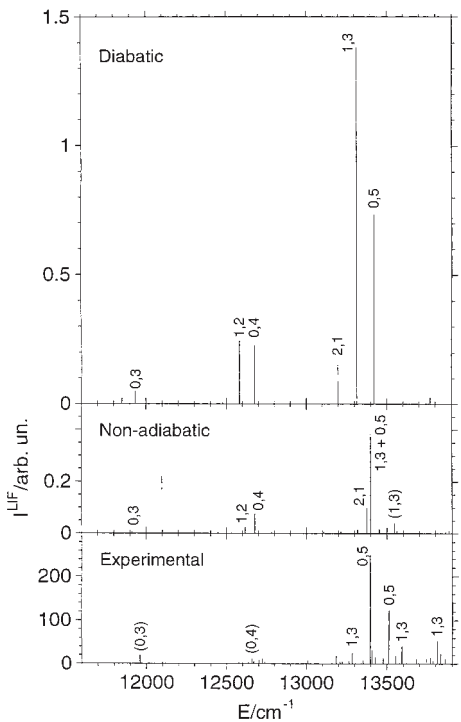

Fig. 7. NO_2 LIF spectrum for a 10 µs acquisition time. Comparison of the experimental spectrum with the theoretical diabatic (NA coupling neglected) and NA spectra. The lines are labeled by the v_1, v_2 quantum numbers ($v_3 = 0$). The uncertain assignments are in brackets.

spectrum, the number of bright NA states in LIF is about equal to that of the diabatic states, because the large τ_n^F of many NA bands lower the $(1 - e^{-t/\tau_n^F})$ term in Eq. (34). We have calculated 11 diabatic and 107 NA states in the energy range of Fig. 7: among them, six diabatic species have medium or large LIF intensities, but only five of the NA states have comparable intensities. The comparison between theory and experiment is good for the strongest band, but it degrades somewhat for the weaker ones. The calculated strongest band is at $13\,398\,\mathrm{cm}^{-1}$ and has a mixed $^2B_2$ character, namely $(1,3,0) + (0,5,0)$ with weights equal to 28% and 5%, respectively. Probably this result reflects an overestimation of the coupling of the diabatic PES. Delon *et al.*[36] assign their observed band at $13\,395\,\mathrm{cm}^{-1}$ as $^2B_2$ $(0,5,0)$, because their model does not take into account that two different $^2B_2$ vibrational states can contribute to the same vibronic species up to $\sim 17\,600\,\mathrm{cm}^{-1}$.

4.3.2. *Pyrazine*

The S_1 and S_2 electronic states of pyrazine are coupled by a widely studied CI. Here we report some results by Stock and Domcke[62] as a nice example, in which the effect of the CI on fluorescence and resonance Raman have been analyzed separately. By a three electronic-states three harmonic-modes model,[62] it has been shown that the CI has a clear effect on the excitation profiles of the molecule, i.e. on spectra which record the total emission intensity (or the RR contribution alone) as a function of the exciting frequency, whose envelopes are much more irregular and with broad and blurred peaks than those obtained switching off the NA couplings. The effect of the CI is evident also considering the dispersed emission (fluorescence + RR) of the molecule upon monocromatic excitation at the center of the S_2 absorption band. The results are reported in Fig. 8 for the case of the real system (a) and an ideal diabatic system (b) for which the NA coupling has been switched off. While the blue part of the spectra is due to Raman-like lines, the red part is due to the fluorescence and is much more pronounced in the real system than in the uncoupled one. This happens because NA couplings populate highly excited vibrational states of S_1 which, because of the favorable FC factors, make preferential transitions toward excited vibrational states of the S_0 surface. The dashed curve in Fig. 8 shows that the effect is not washed out by

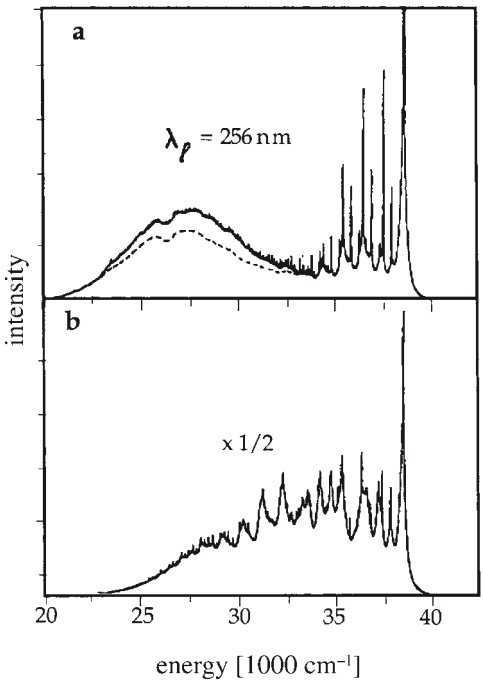

Fig. 8. Dispersed emission (resonance Raman + fluorescence) of pyrazine after an excitation at 256 nm (the center of the S_2 absorption band): (a) nonadiabatic system, emission from both S_1 and S_2 states (full line), and from S_2 only (dashed line); (b) idealized diabatic system (NA coupling neglected). Published with permission from Ref. 62.

neglecting the $S_1 \rightarrow S_0$ oscillator strength and this suggests a contribution to the red-shifted fluorescence due to S_2 vibrational states populated by the indirect coupling to the S_1 manifold. Similar results have been reported for the NO_2 molecule, showing that the NA coupling causes large shifts in the dispersed fluorescence.[71] In general, in pyrazine the impact of the S_1/S_2 CI is larger on fluorescence than on RR emission. Anyway, it is worth to notice that in other systems, as in the case of the RR spectrum of *cis*-1,3,5-hexatriene, a better agreement with experiment has been obtained by computations which properly describe the strong S_1/S_2 vibronic coupling.[34]

4.3.3. H_2S

The emission of H_2S upon tunable excitation in the first excitation band around 200 nm has been measured[72] and theoretically investigated[16] and clearly shows how emission spectra can reveal the excited dynamics of a molecule. At these energies, the vertical excitation accesses the zone of the inner one of two $1^1A''/2^1A''$ CIs. The system is properly described in a diabatic representation with a bright $^1B_1$ and a dark (in C_{2v}) dissociative $^1A_2$ state. Upon excitation, the wavepacket feels a force along the symmetric stretch on the $^1B_1$ PES. On the contrary, the motion in $^1A_2$ on involves also the anti-symmetric stretch, due to the dissociative nature of the PES, and the bending, due to its flatness with respect to this coordinate. The consequence of the NA couplings on the experimental emission spectra of the molecule excited in the range 199–203 nm are striking.[72] The spectra drastically vary also in this short-energy region. They show emission to excited symmetric-stretch states, due to the motion on the $^1B_1$ PES, but also emission to excited bending and/or anti-symmetric stretch states, putting into evidence a motion on the coupled $^1A_2$ PES due to the NA interaction.

4.3.4. *trans-Butadiene*

The resonance Raman spectrum of *trans*-butadiene at 217.9 mm has been computed in Ref. 58 by the TD approach, including the same dephasing time of 15 fs used for the absorption spectrum. Some details of the calculation have been presented in the Sec. 4.1.3 devoted to absorption spectra. In Fig. 9 the comparison between the theoretical and experimental results shows that nice agreements are now possible also for rather large molecules. The prominent role of the C=C stretching is evident, while the most important coupling mode ($v_8^{b_u}$), is not seen due to the dark nature of the 2^1A_g state. The remaining lines are due to the fundamentals of the other in-plane modes (the out-of plane modes have not been considered) as well as some combination bands.

5. Conclusions

In this chapter, we discussed CI effects on CW spectra, presenting briefly the theory and some computational methods, stressing the BO model for

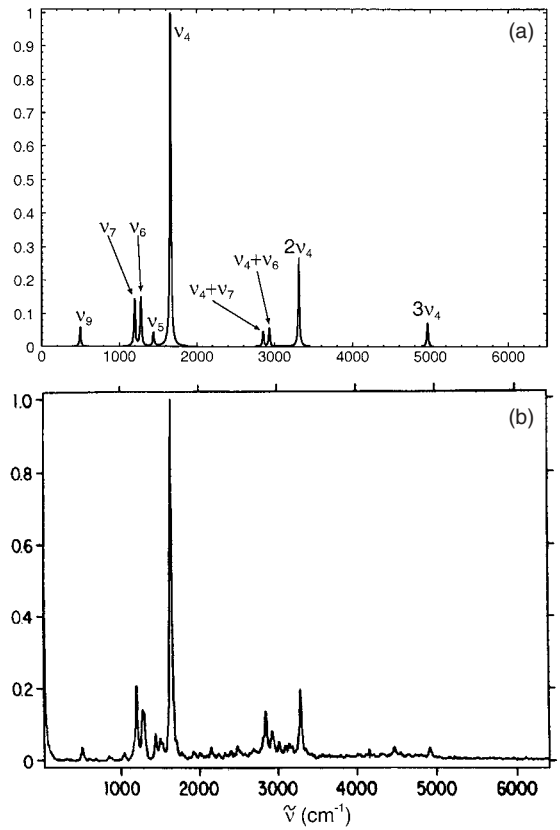

Fig. 9. Calculated (a) and experimental (b) resonance Raman spectra of *trans*-butadiene excited at 217.9 nm. Published with permission from Ref. 58.

understanding CI spectra, and reporting some typical examples. The interpretation of NA spectra can be performed at four theoretical levels, of increasing difficulty, which give more and more detailed information.

(1) Calculations without and with NA couplings. They allow to evaluate the impact of these couplings, to rationalize the differences, and to assign the gross spectral features also in large molecules that prevent a detailed analysis.

(2) Low-resolution spectrum analysis and comparison with experiment. The main BO components are assigned through small Lanczos expansions when high-resolution studies are impossible.

(3) High-resolution statistical analysis of the levels. This step is linked to studies on classical chaos, gives the degree of irregularity of a spectrum, and points out the couplings that cause that irregularity. It provides a different perspective from the level-by-level analysis, and is useful when the level-by-level comparison with experiment is prevented by the inaccuracy of the calculations.

(4) High-resolution level-by-level analysis. We can assign the main BO components of NA states corresponding to the strongest spectral bands, and analyze the interactions among BO states and polyads. This level gives the ultimate understanding of a spectrum, and is very effective when few low-excited BO bright states, coupled to many dark BO species, build up the NA states. However, it is very demanding for its computational costs, because relies on the calculation of BO vibrational states and on the assignment of their quanta. Therefore, it is restricted to small molecules.

Both absorption and photoelectron CI spectra show a noticeable increase of the line density and a partial or total loss of regular progressions. This has been discussed for NO_2, O_3, *trans*-butadiene, furan, pyrrole, thiophene, and allene. The role of the CI location has been stressed in the five-member ring molecules and comparing 1,3,5 *cis*-hexatriene and pyrazine. It comes out that a noticeable increase of the NA effects occurs when the CI is close to the PES minimum of the bright electronic state. The NO_2 and O_3 cases show that the impact of a CI can extend to all the spectrum or be confined in an energy domain. CIs show clear marks on the emission of a molecule, affecting quantum yields and radiative lifetimes. Emission toward JT states gives a typical double-maximum spectrum, while fluorescence from CI states results in complex and irregular spectra and can show large red-shifts in dispersed spectra as suggested for NO_2 and pyrazine. LIF spectra sum up the CI effects on absorption and emission processes. Finally, resonance Raman spectra are very useful to study the dynamics of the excited states, as discussed for H_2S.

As the interest of the researchers is shifting toward the role of CIs in photochemical systems, theoretical developments will be necessary to work out Hamiltonians and computational techniques to treat multidimensional systems with large-amplitude motions and dissipative channels. Detailed interpretations of CI effects in photochemistry will call for more sophisticated and innovative approaches, because the ones utilized up to now are suitable for small molecules. Whether CW spectra analysis is a suitable tool

for studying CI effects on these systems and can provide complementary information to time-resolved studies will be a matter of exploration in the near future.

Acknowledgments

F. Santoro and C. Petrongolo acknowledge the support by MIUR. C. Petrongolo thanks the hospitality of the IPCF-CNR in Pisa.

References

1. W. Heitler, *The Quantum Theory of Radiation* (Dover Publications, Inc., New York, 1984).
2. A. S. Davydov, *Quantum Mechanics*, 2nd. Edn. (Pergamon, Oxford, 1976).
3. K. Müller-Dethlefs, E. W. Schlag, E. R. Grant, K. Wang and B.V. McKoy, *Adv. Chem. Phys.* **XC**, 1 (1995).
4. I. Cacelli, V. Carravetta, A. Rizzo and R. Moccia, *Phys. Rep.* **205**, 283 (1991).
5. A. B. Trofimov and H. Köppel, *J. Chem. Phys.* **109**, 1025 (1998).
6. A. Nitzan and J. Jortner, *J. Chem. Phys.* **57**, 2870 (1972).
7. S.-Y. Lee and E. J. Heller, *J. Chem. Phys.* **71**, 4777 (1979).
8. R. M. Hochstrasser and F. A. Novak, *Chem. Phys. Lett.* **53**, 3 (1978).
9. S. Mukamel, *Principles of Nonlinear Optical Spectroscopy* (Oxford University Press, New York, 1995).
10. F. A. Novak, J. M. Friedman and R. M. Hochstrasser, in *Laser and Coherence Spectroscopy*, Ed. J. I. Steinfeld (Plenum Press, New York, 1978).
11. G. Herzberg, *Molecular Spectra and Molecular Structure* Vol. III (Van Nostrand Reinhold Company, New York, 1966).
12. L. Landau and E. Lifchitz, *Mécanique Quantique* (Éditions MIR, Moscow, 1974), p. 518.
13. P. R. Bunker, *Molecular Symmetry and Spectroscopy* (Academic Press, New York, 1979).
14. H. Köppel, W. Domcke and L. S. Cederbaum, *Adv. Chem. Phys.* **57**, 59 (1984).
15. G. D. Gillispie, A. U. Khan, A. C. Wahl, R. P. Hostiny and M. Krauss, *J. Chem. Phys.* **63**, 3425 (1975).
16. B. Heumann and R. Schinke, *J. Chem. Phys.* **101**, 7488 (1994).
17. R. J. Buenker, M. Peric, S. D. Peyerimhoff and R. Marian, *Mol. Phys.* **43**, 987 (1981).
18. D. Dehareng, X. Chapuisat, J.-C. Lorquet, C. Galloy and G. Raseev, *J. Chem. Phys.* **78**, 1246 (1983).
19. H. Müller and H. Köppel, *Chem. Phys.* **183**, 107 (1994).
20. C. Woywod, W. Domcke, A. L. Sobolewski and H.-J. Werner, *J. Chem. Phys.* **100**, 1400 (1994).

21. U. Manthe, H. Köppel and L. S. Cederbaum, *J. Chem. Phys.* **95**, 1708 (1991).
22. E. Leonardi, C. Petrongolo, G. Hirsch and R. J. Buenker, *J. Chem. Phys.* **105**, 9051 (1996).
23. H. Flöthmann, C. Beck, R. Schinke, C. Woywod and W. Domcke, *J. Chem. Phys.* **107**, 7296 (1997).
24. F. Santoro and C. Petrongolo, *Adv. Quantum Chem.* **36**, 323 (2000).
25. S. Carter and N. C. Handy, *Mol. Phys.* **57**, 175 (1986).
26. Z. Bačić and J. C. Light, *J. Chem. Phys.* **85**, 4594 (1986).
27. R. Kosloff in *Dynamics of Molecules and Chemical Reactions*, Eds. R. E. Wyatt and J. Z. H. Zhang (Marcel Dekker, Inc., New York, 1996).
28. J. K. Cullum and R. A. Willoughby, *Lanczos Algorithms for Large Symmetric Eigenvalue Computations* (Birkhäuser, Boston, 1985).
29. R. E Wyatt and C. Iung in *Dynamics of Molecules and Chemical Reactions*, Eds. R. E. Wyatt and J. Z. H. Zhang (Marcel Dekker, Inc., New York, 1996).
30. G. H. Golub and C. F. Van Loan, *Matrix Computations* (North Oxford Academic, London, 1986).
31. C. Leforestier, R. H. Bisseling, C. Cerjan, M. D. Feit, R. Friesner, A. Guldberg, A. Hammerich, G. Jolicard, W. Karrlein, H.-D. Meyer, N. Lipkin, O. Roncero and R. Kosloff, *J. Comput. Phys.* **94**, 59 (1991).
32. V. A. Mandelshtam and H. S. Taylor, *J. Chem. Phys.* **107**, 6756 (1997).
33. R. Wyatt, *J. Chem. Phys.* **103**, 8433 (1995).
34. C. Woywod, W. C. Livingood and J. H. Frederick, *J. Chem. Phys.* **114**, 1645 (2001)
35. R. Jost, J. Nygard, A. Pasinski and A. Delon, *J. Chem. Phys.* **105**, 1287 (1996).
36. A. Delon, R. Jost and M. Jacon, *J. Chem. Phys.* **114**, 331 (2001), and references therein.
37. F. Santoro and C. Petrongolo, *J. Chem. Phys.* **111**, 9651 (1999), and references therein.
38. L. Leonardi and C. Petrongolo, *J. Chem. Phys.* 106, 10066 (1997).
39. C. A. Biesheuvel, J. Bulthuis, M. H. M. Janssen, S. Stolte and J. G. Snijders, *J. Chem. Phys.* **109**, 9701 (1998).
40. A. Brody, J. Flores, J. B. French, P. A. Mello, A. Pandey and S. S. M. Wong, *Rev. Mod. Phys.* **53**, 385 (1981).
41. A. Delon, R. Jost and M. Lombardi, *J. Chem. Phys.* **95**, 5701 (1991).
42. Th. Zimmermann, L. S. Cederbaum, H.-D. Meyer and H. Köppel, *J. Phys. Chem.* **91**, 4446 (1987).
43. M. V. Berry and M. Tabor, *Proc. Roy. Soc. London* **A356**, 375 (1977).
44. P. Pechukas, *Phys. Rev. Lett.* **51**, 943 (1983).
45. M. V. Berry, *Proc. R. Soc. London* **A400**, 229 (1985).
46. E. Haller, H. Köppel and L. S. Cederbaum, *Chem. Phys. Lett.* **101**, 215 (1983).
47. M. V. Berry and M. Robnik, *J. Phys.* **A17**, 2413 (1984).

48. F. J. Dyson and M. L. Mehta, *J. Math. Phys.* **4**, 701 (1963).
49. M. Feingold and S. Fishman, *Physica* **D25**, 181 (1987).
50. A. Delon, R. Georges and R. Jost, *J. Chem. Phys.* **103**, 1732 (1995).
51. F. Santoro, *J. Chem. Phys.* **109**, 1824 (1998).
52. J. P. O'Brien, M. P. Jacobson, J. J. Sokol, S. L. Coy and R. W. Field, *J. Chem. Phys.* **108**, 7100, (1998).
53. J. P. Rose and M. E. Kellman, *J. Chem. Phys.* **105**, 7348 (1996).
54. K. Bogumil, J. Orphal, J. P. Burrows and J. M. Flaud, *Chem. Phys. Lett.* **349**, 241 (2001).
55. R. Brandi, F. Santoro and C. Petrongolo, *Chem. Phys.* **225**, 55 (1997).
56. A. Delon and R. Jost, *J. Chem. Phys.* **110**, 4300 (1999).
57. D. Belmiloud and M. Jacon, *Int. J. Quantum Chem.* **70**, 475 (1998).
58. R. P. Krawczyk, K. Malsch, G. Hohlneicher, R. C. Gillen and W. Domcke, *Chem. Phys. Lett.* **320**, 535 (2000).
59. S. Hahn and G. Stock, *Phys. Chem. Chem. Phys.* **3**, 2331 (2001).
60. A. Hoxha, R. Locht, B. Leyh, D. Dehhareng, K. Hottmann and H. Baumgärtel, *Chem. Phys.* **256**, 239 (2000).
61. S. Mahapatra, L. S. Cederbaum and H. Köppel, *J. Chem. Phys.* **111**, 10452 (1999).
62. G. Stock and W. Domcke, *J. Chem. Phys.* **93**, 5496 (1990).
63. R. Engleman, *The Jahn-Teller Effect in Molecules and Crystals* (Wiley-Interscience, New York, 1972).
64. I. B. Bersuker and V. Z. Polinger, *Vibronic Interactions in Molecules and Crystals* (Springer-Verlag, Berlin, 1989).
65. R. Bruckmeier, Ch. Wunderlich and H. Figger, *Phys. Rev. Lett.* **72**, 2250 (1994).
66. S. Mahapatra and H. Köppel, *J. Chem. Phys.* **109**, 1721 (1998).
67. T. A. Barckholtz and T. A. Miller, *J. Phys. Chem.* **A103** 2321 (1999).
68. B. E. Applegate, T. A. Miller and T. A. Barckholtz, *J. Chem. Phys.* **114**, 4855 (2001).
69. A. E. Douglas, *J. Chem. Phys.* **45**, 1007 (1966).
70. M. Bixon and J. Jortner, *J. Chem. Phys.* **50**, 3284 (1969).
71. F. Santoro, *Theor. Chem. Acc.* **104**, 203 (2000).
72. P. W. Browning, E. Jensen, G. C. G. Waschewsky, M. R. Tate, L. J. Butler and J. P. Hessler, *J. Chem. Phys.* **101**, 5652 (1994).

CHAPTER 17

FEMTOSECOND TIME-RESOLVED SPECTROSCOPY OF THE DYNAMICS AT CONICAL INTERSECTIONS

Gerhard Stock

Institute of Physical and Theoretical Chemistry,
J.W. Goethe University
D-60439 Frankfurt, Germany

Wolfgang Domcke

Institute of Physical and Theoretical Chemistry,
Technical University of Munich
D-85748 Garching, Germany

Contents

1. Introduction

In the chapters of Part II of this book it has been demonstrated for a variety of examples that conical intersections can provide the mechanism for extremely fast chemical processes, e.g. photodissociation, photoisomerization and internal conversion to the electronic ground state. Time-dependent quantum wave-packet calculations have established that radiationless transitions between electronic states can take place on a time scale of the order of 10 fs, if a conical intersection is directly accessible after preparation of the wave packet in the excited state, see, e.g. Chapters 8–11 and 14–15. In view of these findings and the omnipresence of conical intersections in polyatomic molecules (cf. Chapter 6), it is now widely accepted that conical intersections are of fundamental importance for the understanding of the reaction mechanisms in photochemistry and photobiology.[1–7]

On the experimental side, dramatic progress has been made during the last few decades with the generation and shaping of ultrafast light pulses, see, e.g. Refs. 8 and 9. With the availability of pulses as short as a few femtoseconds, an ultimate goal has been achieved: Essentially any chemical process can be resolved in real time by an appropriately designed pump-probe-type measurement. This applies, in particular, also for ultrafast internal conversion processes. In fact, the detection of exceptionally fast radiationless decay processes appears at present to be the only way to establish by purely experimental means the existence of a conical intersection.

While femtosecond pump-probe experiments readily yield information on the time scales of the processes under investigation, the interpretation of these experiments is a nontrivial problem and is strongly dependent on theoretical support. Given the experimental data alone, it is generally not possible to decide how many electronic states and vibrational modes are involved and what type of dynamics (e.g. intra- or intermolecular dynamics, electronic decay or vibrational relaxation) is observed. Moreover, the signals usually depend in a complex manner both on the chemical dynamics as well as on laser pulse properties. In order to establish unambiguously the connection between the experimental signals that are measured and the molecular dynamics that is to be observed, it is necessary to perform theoretical simulations which take into account both the dynamics of the molecular system as well as the properties of the laser fields involved in the preparation and detection processes.

In principle, the theory of nonlinear spectroscopy with femtosecond laser pulses is well developed. A comprehensive and up-to-date exposition of nonlinear optical spectroscopy in the femtosecond time domain is provided by the monograph of Mukamel.[10] For additional reviews, see Refs. 7 and 11–14. While many theoretical papers have dealt with the analysis or prediction of femtosecond time-resolved spectra, very few of these studies have explicitly addressed the dynamics associated with conical intersections. In the majority of theoretical studies, the description of the chemical dynamics is based on rather simple models of the system that couples to the laser fields, usually a few-level system or a set of harmonic oscillators. In the case of condensed-phase spectroscopy, dissipation is additionally introduced by coupling the system to a thermal bath, either at a phenomenological level or in a more microscopic manner via reduced density-matrix theory.[15–20] For these simple models of the chemical dynamics, it is straightforward to evaluate analytically the multi-time response functions and to perform the numerous time integrations and Fourier transforms required for the calculation of the signal.[10] The description of chemical dynamics associated with conical intersections, on the other hand, is considerably more challenging, requiring numerical time-dependent wave-packet or density-matrix propagations involving several (typically at least three) strongly nonseparable vibrational degrees of freedom and thus very large basis sets. The construction of multi-time response functions and the evaluation of the multiple time integrals then becomes a very tedious and time-consuming procedure.[21,22]

As will be outlined in more detail below, the much higher complexity of the dynamics at conical intersections calls for a new strategy for the calculation of absorption and emission signals, which differs from the established formalism of nonlinear optics, based on higher-order (typically third-order) perturbation theory in the laser-matter interaction.[10,23] Independently of the strength of the perturbation, higher-order perturbation theory becomes unwieldy if the propagator of the unperturbed system (in the present case, the field-free chemical system) cannot be evaluated in a simple manner. This is definitely the case for the multi-mode nonadiabatic dynamics at conical intersections and distinguishes such systems from few-level models or harmonic oscillators. It has indeed been found that a nonperturbative formulation, in which the laser-matter interaction is included in the solution of the time-dependent Schrödinger equation or Liouville–von-Neumann equation, in the general case becomes computationally more tractable than the perturbative formalism.[24–27]

In this chapter we briefly review both the perturbative as well as nonperturbative formalism for the calculation of femtosecond time-resolved spectra, focusing on the detection of the photophysical and photochemical dynamics at conical intersections. To set the stage for a general discussion of the potential of modern time-resolved spectroscopy, we begin with a brief overview of the spectroscopic techniques, which are particularly suitable in the present context.

2. Preparation and Detection of Nonstationary States

There exists a large variety of spectroscopic techniques that employ ultrashort laser pulses. These methods may differ, for example, in the detection mechanism and in the number and properties of laser fields, and will in general monitor different aspects of the dynamics of the molecular system. Most of these experiments are of the pump-probe (PP) type, that is, the molecular system is prepared by a first laser pulse (the "pump") into a nonstationary state, the time evolution of which is interrogated by a time-delayed second laser pulse (the "probe"). It is important to distinguish between resonant and nonresonant electronic excitation of the system. In the latter case, it is not possible to establish a *population* in the excited electronic state which survives the duration of the pump field. As a consequence, nonresonant excitation gives only rise to "Raman-like" emission, which is known

to essentially reflect the dynamics in the electronic ground state.[10,23] Being mainly interested in the observation of excited-state dynamics, we therefore focus on resonant excitation of the molecule, which results in both resonance-Raman as well as stimulated-emission contributions to the overall signal. Various aspects of electronic excitation by a pulsed laser field have been discussed, for example, in Refs. 28 and 29.

While the *preparation* of the system by an ultrashort laser pulse is common to most femtosecond experiments, there exists a wealth of different techniques to *probe* the dynamics initiated by the pump. Let us consider a standard two-pulse PP experiment and let us assume that at $t = 0$ the system has been excited by the first pulse into the nonstationary state $|\Psi_{\mathrm{P}}\rangle$. In order to probe the dynamics of the excited-state wave function $|\Psi_{\mathrm{P}}(t)\rangle = e^{-iH_M t/\hbar}|\Psi_{\mathrm{P}}\rangle$, the second pulse is used to project the evolving state $|\Psi_{\mathrm{P}}(t)\rangle$ onto a known final state $|\psi_{\mathrm{f}}\rangle$. A major criterion to distinguish the probe mechanisms is thus given by the kind of final states $|\psi_{\mathrm{f}}\rangle$ involved in the experiment. Possible choices for the electronic part of $|\psi_{\mathrm{f}}\rangle$ are the electronic ground state (through time-resolved fluorescence spectroscopy[30–33]), higher-lying electronic states (through excited-state absorption[34]), and the cationic ground state as well as high Rydberg states (through pulsed ionization with ion or photoelectron detection[35–46]). Alternatively, one may measure transient infrared absorption or resonance-Raman spectra of the sample.[47,48] In the case of reactive systems, it is often advantageous to probe the dynamics of the products (instead of the parent molecule), which may be accomplished, for example, through excited-state absorption with subsequent detection of the laser-induced fluorescence.[34]

While experimental considerations are beyond the scope of this chapter (various PP techniques have been extensively discussed, e.g. in Refs. 34, 43, 46, 49 and 50), we wish to address some theoretical issues concerning the choice of the detection mechanism. First note that, to facilitate a microscopic interpretation of the PP signals, *the final state must be well known*. This is often the case for the electronic and ionic ground states, but generally not so for the excited states of polyatomic molecules. Second, it is clear that each final electronic state is associated with different Franck–Condon factors and selection rules, i.e. depending on the specific system under consideration, each probe mechanism will monitor different aspects of the dynamics. Finally, it should be stressed that in general different detection techniques also monitor different dynamical processes. For example,

transient transmittance spectroscopy reflects both ground-state dynamics (via impulsive resonance Raman scattering) as well as excited-state dynamics (via stimulated-emission and excited-state absorption). Time-resolved fluorescence spectroscopy, on the other hand, exclusively monitors the dynamics of the initially prepared excited state, thus facilitating the interpretation of the experimental data.

Besides various detection *mechanisms* (e.g. stimulated emission or ionization), there exist moreover numerous possible detection *schemes*. For example, we may either directly detect the emitted polarization ($\propto \mathbf{PP}^*$, so-called homodyne detection), thus measuring the decay of the *electronic coherence* via the photon-echo effect, or we may employ a heterodyne detection scheme ($\propto \mathbf{EP}^*$), thus monitoring the time evolution of the *electronic populations* in the ground and excited electronic states via resonance Raman and stimulated emission processes. Furthermore, one may use polarization-sensitive detection techniques (transient birefringence and dichroism spectroscopy[51,52]), employ frequency-integrated (see, e.g. Ref. 53) or dispersed (see, e.g. Ref. 54) detection of the emission, and use laser fields with definite phase relation.[55] On top of that, there are modern coherent multi-pulse techniques, which combine several of the above mentioned options. For example, phase-locked heterodyne-detected four-pulse photon-echo experiments[56] make it possible to monitor all three time evolutions inherent to the third-order polarization, namely, the electronic coherence decay induced by the pump field, the dynamics of the system occurring after the preparation by the pump, and the electronic coherence decay induced by the probe field. For a theoretical survey of the various spectroscopic detection schemes, see Ref. 10.

In this chapter, we will focus on the discussion of experiments that directly monitor the time-evolution of the electronic excited-state dynamics. In particular, we shall consider transient transmittance, time-resolved fluorescence, and time-resolved ionization spectroscopy. This is because these techniques have the potential to directly observe the ultrafast photochemical excited-state processes triggered by conical intersections.

2.1. *Transient Transmittance*

We are concerned with the interaction of a molecular system with the pulsed electric field $\mathbf{E}(\mathbf{x}, t)$. Within the electric dipole approximation, the response

of the molecular system to the field $\mathbf{E}(\mathbf{x},t)$ is completely described by the electric polarization $\mathbf{P}(\mathbf{x},t)$, which is defined as the expectation value of the electronic dipole moment of the system.[23] $\mathbf{E}(\mathbf{x},t)$ is considered as a classical field

$$\mathbf{E}(\mathbf{x},t) = \sum_{i=1,2} \mathbf{E}_i(\mathbf{x},t), \tag{1}$$

$$\mathbf{E}_i(\mathbf{x},t) = \boldsymbol{E}_i(\mathbf{x},t)\exp(i\mathbf{k}_i\mathbf{x}) + c.c., \tag{2}$$

$$\boldsymbol{E}_i(\mathbf{x},t) = \boldsymbol{\epsilon}_i E_i(\mathbf{x},t), \tag{3}$$

$$E_i(\mathbf{x},t) = \mathcal{E}_i(\mathbf{x},t)e^{-i\omega_i t}, \tag{4}$$

consisting of the pump field $\boldsymbol{E}_1$ and the probe field $\boldsymbol{E}_2$, which are characterized by wave vector $\mathbf{k}_i$, laser frequency ω_i, polarization vector $\boldsymbol{\epsilon}_i$, and pulse envelope function $\mathcal{E}_i$. We use Roman type-setting for real fields (e.g. $\mathbf{E}$, $\mathbf{P}$), italics for complex fields ($\boldsymbol{E}$, $\boldsymbol{P}$), and calligraphics for the corresponding envelope functions ($\mathcal{E}$, $\mathcal{P}$).

The experimental PP signal is usually defined as the difference between the transmittance of the probe pulse with and without the preparation of the sample by the pump pulse.[10] To calculate the electric field of the probe pulse after passing the sample, we need to consider the propagation of the probe in the nonlinearly polarized medium. Assuming that the spatial extent of the pulse is large compared to its wavelength, we may invoke the slowly varying envelope approximation. This reduces the second-order wave equation for the probe field $\mathbf{E}_2$ to a first-order differential equation for the corresponding envelope function $\mathcal{E}_2$[23]

$$\left(\frac{\partial}{\partial z} + \frac{1}{v}\frac{\partial}{\partial t}\right)\mathcal{E}_2(z,t) = \frac{2\pi i\omega_2}{nc}\mathcal{P}(z,t), \tag{5}$$

where $n = v/c$ is the refractive index of the medium and it has been assumed that the pulses propagate along the z-axis. It should be noted that the nonlinear polarization $\mathcal{P}(z,t)$ is itself a function of the local probe field $\mathcal{E}_2(z,t)$ in the sample. To properly describe the propagation of the classical field $\mathcal{E}_2(z,t)$ through the medium characterized by $\mathcal{P}(z,t)$, we thus have to solve the coupled field-matter equations in a self-consistent way.[57]

In many practical cases, however, it is justified to neglect pulse-propagation effects and ignore the time-derivative at the left-hand side of Eq. (5). The situation furthermore simplifies considerably if one assumes an *optically thin sample*, that is, the incident electric field that induces the

polarization passes, by definition, through the medium unchanged. Hence the total electric field at the end of the sample ($z = l$) is simply given as a sum of the incident field and the polarization

$$\mathcal{E}_2(l,t) = \mathcal{E}_2(0,t) + \frac{2\pi i\omega_2 l}{nc}\mathcal{P}(0,t). \tag{6}$$

Note that the first two approximations employed (classical external field and dipole approximation) are usually well justified in molecular physics, whereas the slowly varying envelope approximation may approach the limits of validity in the case of femtosecond pulses with optical frequencies. The validity of the assumption of an optically thin sample, i.e. the complete neglect of pulse propagation effects, depends on the specific experiment under consideration. To simplify the notation, we henceforth suppress the **x**-dependence of polarizations and fields, and also drop the prefactor of the polarization in Eq. (6).

From classical electrodynamics it is well known that the rate of dissipated energy of an electric field $\mathbf{E}(t)$ in a medium that is characterized by its polarization $\mathbf{P}(t)$ is given by $\mathbf{E}(t) \cdot \dot{\mathbf{P}}(t)$.[23] Assuming a photodetector at the end of the sample that counts all photons being emitted in $\mathbf{k}_2$ direction, the PP signal is proportional to the total energy dissipated (or gained) by the probe pulse in the medium

$$I = \int_{-\infty}^{\infty} dt \dot{\mathbf{E}}_2(t) \cdot \widetilde{\mathbf{P}}(t). \tag{7}$$

Here $\widetilde{\mathbf{P}}(t) = \mathbf{P}_{\text{pump on}} - \mathbf{P}_{\text{pump off}}$ denotes the difference of the polarizations radiating along $\mathbf{k}_2$ with and without the preparation of the sample by the pump pulse, and we have performed a partial integration. The sign convention is such that the signal is negative for absorption (disappearance of photons) and positive for emission (creation of photons). The signal (7) depends on the pulse delay time Δt as well as on the properties of the laser pulses (e.g. pulse durations τ_i and laser frequencies ω_i), and may be considered as a time- and frequency-dependent signal $I_{\text{In}}(\omega_2, \Delta t)$ when recorded as a function of Δt and the probe carrier frequency ω_2. As (7) is (inherently) integrated over all emission frequencies, it will be referred to as *integral* PP signal. It is instructive to rewrite the integral PP spectrum (7) as

$$I_{\text{In}}(\omega_2, \Delta t) = 2\omega_2 \,\text{Im} \int_{-\infty}^{\infty} dt \mathbf{E}_2(t) \widetilde{\mathbf{P}}^*(t), \tag{8}$$

where we have employed the slowly-varying envelope approximation and the rotating-wave approximation,[58] thus neglecting $\dot{\mathcal{E}}_2$ contributions and terms with rapidly oscillating ($\propto e^{2i\omega_2 t}$) integrands, respectively. Although both approximations may approach the limits of validity in the case of intense femtosecond laser pulses with optical frequencies, it has been found in numerical studies that deviations between the complete signal (7) and the approximated signal (8) are usually minor.[59]

In order to obtain the spectrum of the emitted field, the probe pulse is frequency resolved by a spectrometer after it has passed the sample (see, e.g. Ref. 54). Because the PP signal is measured as the time-integrated energy rate (cf. Eq. (7)), the corresponding spectrum may be considered as stationary, although it inherently depends on the delay time Δt. Contrary to the case of time-resolved fluorescence (see next Section), the effects of the spectrometer therefore need not to be considered in the theoretical description, and we may define the *dispersed* PP signal as the intensity of the Fourier transform of the total emitted field (6), yielding[10,11]

$$I_{\mathrm{D}}(\omega, \Delta t) = 2\omega \,\mathrm{Im}\, \mathbf{E}_2(\omega)\widetilde{\mathbf{P}}^*(\omega), \tag{9}$$

where

$$\mathbf{E}_2(\omega) = \int_{-\infty}^{\infty} dt e^{i\omega t}\mathbf{E}_2(t), \tag{10}$$

$$\widetilde{\mathbf{P}}(\omega) = \int_{-\infty}^{\infty} dt e^{i\omega t}\widetilde{\mathbf{P}}(t) \tag{11}$$

denote the Fourier transform of the incident probe field and the polarization, respectively. Combining the definitions (7)–(11), it is easily verified that integration of the dispersed PP signal (9) over all emission frequencies ω again yields the integral PP signal (7). It should be noted that the experimental transmittance spectrum is often alternatively defined by normalizing the dispersed PP spectrum (9) to the intensity of the incident field,[11,54] which makes it possible to express the PP spectrum in terms of an exponential law

$$\begin{aligned} I_{\mathrm{D}}(\omega, \Delta t) &= |\mathbf{E}_2(\omega)|^2 e^{-\Gamma(\omega,\Delta t)l}, \\ \Gamma(\omega, \Delta t) &= \frac{4\pi\omega}{nc}\,\mathrm{Im}\,\widetilde{\mathbf{P}}(\omega)/\mathbf{E}_2(\omega). \end{aligned} \tag{12}$$

It is interesting to note that the simultaneous time and frequency resolution of the *dispersed* transmittance spectrum $I_{\mathrm{D}}(\omega, \Delta t)$ is not limited by the well-known time-frequency uncertainty principle. This is because the frequency

resolution of this signal is determined by the polarization decay time [cf. Eq. (11)], which is independent of the pulse duration, which represents the time resolution. In the case of the *integral* transmittance spectrum, on the other hand, time and frequency resolution are Fourier limited. This is because the duration of the pulses defines the duration of the measurement, which in turn determines the frequency resolution of the experiment.[60]

The definitions of the dispersed transmittance spectrum $I_{\mathrm{D}}(\omega, \Delta t)$ [Eq. (9)] and the integral transmittance spectrum $I_{\mathrm{In}}(\omega_2, \Delta t)$ [Eq. (7)] connect these experimental signals to the macroscopic polarization difference $\widetilde{\mathbf{P}}(t)$. Because we have neglected all pulse propagation effects, both the incident electric fields and the polarization are approximated by plane waves in $\mathbf{x}$-space, i.e. the macroscopic polarization is simply given by an orientational average over the microscopic polarizations of the individual molecules in a unit volume. Describing the molecular system as an electronic two-state system, the orientational averaging of $\widetilde{\mathbf{P}}(t)$ simply amounts to the multiplication with a constant, i.e. the macroscopic and microscopic polarizations are proportional to each other. Assuming, on the other hand, a model system with several ($\geq$3) electronic states with more than one optically allowed transition, the averaging process in general depends on the relative orientations of the individual transition dipole moments. In this case it is necessary to explicitly perform the orientational average.[61]

2.2. *Time-Resolved Fluorescence*

With the development of fluorescence upconversion techniques,[30] which nowadays provide femtosecond time resolution,[31–33,56] it is also possible to directly measure the time evolution of the spontaneous emission following the excitation of the sample by the pump pulse. In this method, the fluorescence is collected and focused onto a nonlinear crystal, where it is superposed with the probe beam in order to perform upconversion. Time resolution is achieved because the probe pulse creates a "time gate" for the spontaneous emission, i.e. the fluorescence is only measured within the duration of the probe. Frequency resolution is achieved by subsequently dispersing the upconverted signal in a monochromator. Although fluorescence detection provides less photon yield than stimulated techniques, it has the desirable feature to exclusively monitor the time evolution in the initially excited electronic states (cf. the discussion above).

There exist two major approaches to the theoretical description of the time and frequency gated spontaneous emission (TFG SE). In the first approach, the TFG SE spectrum is defined as the rate of emission of photons of a certain frequency within a definite time interval. The influence of the measuring device is not taken into account in this formulation.[19,62–65] Starting from this definition, one obtains an ideal (bare) TFG SE spectrum, which is not guaranteed to be positive, however. For instance, for certain parameters of the Brownian oscillator model, the spectrum can attain negative values.[66] Moreover, the time and frequency resolutions of this ideal spectrum are not limited by the fundamental time-frequency uncertainty principle. This underlines the necessity to develop a more comprehensive theory, in which both a spectrometer and a time-gating device enter the description from the outset.

This is the characteristic feature of the second group of approaches, in which the TFG SE is taken to be proportional to the integrated intensity of the total emitted field which has passed through a spectrometer and a temporal gating device.[67,68] Following the guidelines developed in Ref. 67, the TFG SE has been investigated by a number of authors.[69–72] The explicit consideration of the TFG process adds, however, additional complexity to the problem, and it is therefore not surprising that most papers deal with one-dimensional dissipation-free systems, which allows the description of the material dynamics in terms of the eigenvalues and eigenfunctions of the Hamiltonian. Cina and coworkers have formulated a theory which is intermediate between the two approaches.[66] These authors have investigated the influence of the time gate on the intensity and anisotropy of the spontaneous emission, while the frequency resolution was tacitly assumed to be perfect. Mukamel and coworkers have developed a general description, which ensures a correct inclusion of the TFG process for any material system under study.[73,74] The passage to an ideal gate also has been briefly discussed by these authors.

The total intensity of the temporally gated and spectrally filtered field at the position $\mathbf{r}$ in the far-field region is given by the general expression[67]

$$S_{st}(t_0,\omega_0) \propto \int_{-\infty}^{\infty} dt \int_{-\infty}^{\infty} dt' \int_{-\infty}^{\infty} dt'' E_t(t';t_0) E_t^*(t'';t_0) \times F_s(t-t',\omega_0)\, F_s^*(t-t'',\omega_0)\, \langle \mathbf{E}(\mathbf{r},t')\mathbf{E}^*(\mathbf{r},t'')\rangle. \quad (13)$$

Here $E_t(t;t_0)$ is the time-gate function which is strongly peaked near the gating time $t \sim t_0$, the function $F_s(t-t',\omega_0)$ is responsible for the spectral filtering near the central frequency ω_0, and $\langle \mathbf{E}(\mathbf{r},t')\mathbf{E}^*(\mathbf{r},t'')\rangle$ is the correlation function of the emitted field. It is clear from this definition that the TFG SE spectrum is always positive, in contrast to its bare counterpart.

It is straightforward to show that the light emitted by a collection of independent dipoles in the far-field region is proportional to the second derivative of the optically induced polarization[75]

$$\mathbf{E}(\mathbf{r},t) = -\frac{2\pi}{c^2 r}\frac{d^2}{dt^2}\mathbf{P}(\mathbf{r},t-\tau_r). \tag{14}$$

Here c is the speed of light, and $\tau_r \equiv r/c$ is the retardation time. Integrating the correlation function of the emitted light over a small solid angle on the sphere of radius r, one arrives at the expression

$$\langle \mathbf{E}(\mathbf{r},t')\mathbf{E}(\mathbf{r},t'')^*\rangle \propto \frac{d^2}{dt'^2}\frac{d^2}{dt''^2}\langle \mathbf{P}(t'-\tau_r)\mathbf{P}(t''-\tau_r)\rangle. \tag{15}$$

In order to derive the TFG SE signal from this definition, it is standard practice in the literature to neglect the retardation effects ($\tau_r \equiv 0$) and to invoke the slowly-varying-envelope approximation, i.e. $\partial_t^2\mathbf{P}(t) \approx -\omega^2\mathbf{P}(t)$, where ω is the carrier frequency. This is tantamount to the assumption

$$\langle \mathbf{E}(\mathbf{r},t')\mathbf{E}(\mathbf{r},t'')^*\rangle \propto \langle \mathbf{P}(t')\mathbf{P}(t'')\rangle. \tag{16}$$

The TFG SE signal is thus expressed in terms of the time-gate and frequency filtering functions and the optically induced polarization.

2.3. *Time-Resolved Ionization and Fragment Detection*

The majority of femtosecond time-resolved PP experiments is performed in the condensed phase and is based on the detection of photons. For these experiments, the calculation of the nonlinear electric polarization represents the central task of the theoretical description. While femtosecond time-resolved measurements with detection of photons are possible also in the gas phase, e.g. by the detection of laser-induced fluorescence (LIF)[34,76,77] or with background-free four-wave-mixing schemes,[14,78] the detection of charged particles (i.e. photoelectrons or ions) has the advantage of the extremely high collection efficiency. By mass-selected detection of the ions, additional information on the photoinduced fragmentation

processes can be obtained.[79,80] Femtosecond time-resolved photoelectron spectroscopy[41–46] has been shown to be a particularly versatile tool for the exploration of ultrafast excited-state processes in molecules and clusters. It has been demonstrated that in simple systems such as diatomic molecules a complete time-resolved mapping of the vibrational wave-packet dynamics is possible.[81,82] Photoelectron-ion coincidence experiments with femtosecond time resolution have opened the field of femtochemistry of size-selected clusters.[83]

To model these experiments, one usually identifies the count rate of the detector with the field-induced populations of the electronic or ionic states under consideration. To give an example for product detection through the measurement of the LIF, let us consider the pioneering NaI experiment of Zewail and coworkers.[34,76,77] In this experiment, the photoinduced predissociation of NaI is observed through two-photon excitation and subsequent monitoring of the LIF of the sodium fragment. Assuming that the LIF emission is directly proportional to the field-induced population in the excited electronic state $|\psi_{\mathrm{Na^*I}}\rangle$, the LIF signal is given by[84,85]

$$I_{\mathrm{LIF}}(\Delta t) = \langle \Psi_{\mathrm{PP}}(t)|\psi_{\mathrm{Na^*I}}\rangle\langle\psi_{\mathrm{Na^*I}}|\Psi_{\mathrm{PP}}(t)\rangle, \tag{17}$$

where $|\Psi_{\mathrm{PP}}(t)\rangle$ denotes the wave function of the molecular system after the interaction with the pump and probe fields, and Δt represents the delay time between the two pulses. The calculation of the LIF signal via Eq. (17) depends on the knowledge of the potential-energy surface of the excited state and, moreover, relies on the assumption that competing excitation pathways involving different electronic states can be excluded. Although straightforward in principle, the interpretation of LIF experiments therefore requires detailed information on the excited states of the molecular system.

The simplest signal to be measured in a time-resolved photoionization experiment is the total ion yield following the action of pump and probe pulses. It is given by the integral population of the ionization continua in the limit $t \to \infty$.[24,86]

$$I_{\mathrm{Ion}}(\Delta t) = \sum_l \int_0^\infty dE_k \langle \Psi(t \to \infty)|\psi_l^{(k)}\rangle\langle\psi_l^{(k)}|\Psi(t \to \infty)\rangle. \tag{18}$$

Here $|\Psi(t)\rangle$ is the time-dependent wave-function of the system and $|\psi_l^{(k)}\rangle$ denotes a continuum state with a free electron of energy E_k.

Alternatively, the energy spectrum of the photoelectrons may be measured. This signal is represented by the population probability density of the ionization continua[24]

$$I_{\mathrm{Ion}}(E_k, \Delta t) = \sum_l \langle \Psi(t \to \infty) | \psi_l^{(k)} \rangle \langle \psi_l^{(k)} | \Psi(t \to \infty) \rangle. \tag{19}$$

In the limiting case of $E_k \to 0$, Eq. (19) describes the zero-kinetic-energy (ZEKE) photoelectron signal. ZEKE photoelectron spectroscopy[87] is a background-free technique with high frequency-resolution, which recently has been combined with PP techniques with picosecond[37] and femtosecond[41–46] time resolution.

Even more detailed information, in particular on the electronic character of the excited-state wave function, can be obtained by time, energy and angle-resolved photoelectron spectroscopy.[27,88,97] In this case, the signal can be expressed in terms of the coefficients of the partial-wave decomposition of the continuum amplitude $\langle \psi_l^{(k)} | \Psi(t \to \infty) \rangle$.[89]

3. Calculation of Spectra: Perturbative Approach

3.1. *Absorption and Emission of Photons*

Adopting a diabatic electronic representation, the Hamiltonian of a molecular system, which interacts with a time-dependent classical electric field $\mathbf{E}(t)$, can be written as[7]

$$H(t) = H_M + H_{\mathrm{int}}(t), \tag{20}$$

$$H_M = \sum_k |\Phi_k^d\rangle h_k \langle \Phi_k^d| + \sum_{k \neq k'} \left|\Phi_k^d\right\rangle W_{kk'} \left\langle \Phi_{k'}^d\right|, \tag{21}$$

$$\begin{aligned} H_{\mathrm{int}}(t) &= -\boldsymbol{\mu} \cdot \mathbf{E}(t) \\ &= -\sum_{k \neq k'} |\Phi_k^d\rangle \boldsymbol{\mu}_{\boldsymbol{kk'}} \cdot \mathbf{E}(t) \langle \Phi_{k'}^d| + \mathrm{h.c.} \end{aligned} \tag{22}$$

Initially, i.e. before the interaction with the laser field, the molecular system is assumed to be in its electronic and vibrational ground state $|\Psi_0\rangle$ (throughout this section $\hbar = 1$)

$$|\Psi^{(0)}(t)\rangle = e^{-iH_M t} |\Psi_0\rangle. \tag{23}$$

By solving the time-dependent Schrödinger equation

$$i \frac{\partial}{\partial t} |\Psi(t)\rangle = H(t) |\Psi(t)\rangle, \tag{24}$$

we obtain the overall polarization $\mathbf{P}(t)$ as the quantum-mechanical expectation value of the dipole operator

$$\begin{aligned}\mathbf{P}(t) &= \langle\Psi(t)|\boldsymbol{\mu}|\Psi(t)\rangle \\ &= 2\,\mathrm{Re}\sum_{k\neq k'}\langle\Psi(t)|\Phi_k^d\rangle\boldsymbol{\mu}_{\boldsymbol{kk'}}\langle\Phi_{k'}^d|\Psi(t)\rangle. \end{aligned} \tag{25}$$

Within the electric dipole approximation, the response of the molecular system to an electric field is completely described by the electric polarization $\mathbf{P}(t)$, which therefore represents the central quantity of interest for the calculation of spectroscopic signals. For simplicity, we want to restrict ourselves to model systems with a single dipole-allowed electronic transition (say, the $|\Phi_0^d\rangle - |\Phi_2^d\rangle$ transition).

In this subsection, we employ standard time-dependent perturbation theory with respect to the laser-matter interaction $H_{\mathrm{int}}(t)$ in the wave-function formalism.[7,11] Time-dependent perturbation theory may alternatively be formulated in the density-matrix formalism.[10,90] The latter is more general in that it allows for the inclusion of finite temperature effects and a phenomenological description of relaxation phenomena. In this chapter, we are concerned with the description of the dynamics at conical intersections in a fully microscopic manner, and temperature effects play a minor role. The wave-function formalism is therefore appropriate for our purposes. Writing the time-dependent wave function as

$$|\Psi(t)\rangle = \sum_{N=0}^{\infty}|\Psi^{(N)}(t)\rangle, \tag{26}$$

$$|\Psi^{(N)}(t)\rangle = i\int_{-\infty}^{t} dt'\, e^{-iH_M(t-t')}\boldsymbol{\mu}\cdot\boldsymbol{E}(t')|\Psi^{(N-1)}(t')\rangle, \tag{27}$$

we obtain for the polarization

$$\mathbf{P}(t) = \sum_{N=0}^{\infty}\mathbf{P}^{(2N+1)}(t), \tag{28}$$

$$\mathbf{P}^{(2N+1)}(t) = 2\,\mathrm{Re}\sum_{i=0}^{N}\langle\Psi^{2(N-i)}(t)|\Phi_0^d\rangle\boldsymbol{\mu}_{\boldsymbol{02}}\langle\Phi_2^d|\Psi^{(2i+1)}(t)\rangle. \tag{29}$$

Owing to the initial condition (23), the linear ($\mathbf{P}^{(1)}$) and third-order ($\mathbf{P}^{(3)}$) polarizations are the first nonvanishing terms of the expansion.

The total number of nonzero terms occurring in (28) depends crucially on whether the following conditions are fulfilled:

(i) rotating-wave approximation (RWA): Within the RWA[58] only resonant optical transitions (e.g. $\propto e^{i(\omega-h_2)t}$) are considered, whereas nonresonant transitions (e.g. $\propto e^{i(\omega+h_2)t}$) are disregarded. This reduces the number of terms by a factor of two *in each order* of the expansion (26).

(ii) weak-field limit: In the case of small laser intensities, it is sufficient to consider the nonlinear response only to lowest (i.e. third) order.

(iii) nonoverlapping laser pulses: If the laser fields do not overlap in time, we need to consider only one electric field $\mathbf{E}_i(t)$ in each time integration (27) instead of two. When speaking of nonoverlapping pulses, we will always assume that the pump field $\mathbf{E}_1$ arrives before the probe field $\mathbf{E}_2$.

(iv) phase-averaged detection: If the spectral signals [e.g. Eqs. (7) and (9)] are averaged over many laser shots [as it is the case in common pump-probe (PP) experiments], only signals proportional to $\mathbf{E}_1^{2n}\mathbf{E}_2^{2m}$ survive the inherent averaging over the individual phases of the fields. Using phase-locked pulses,[55] however, it is also possible to monitor signals proportional to $\mathbf{E}_1^{2n+1}\mathbf{E}_2^{2m+1}$.

An important experimental criterion to discriminate the various spectroscopic processes arising in Eq. (28) is the emission direction $\mathbf{k}$ of the polarization. Because the incident electric fields $\mathbf{E}_1$, $\mathbf{E}_2$ radiate along their wave vectors $\mathbf{k}_1$, $\mathbf{k}_2$, the emission directions $\mathbf{k}$ of the thus induced polarization are given as linear combinations of $\mathbf{k}_1$ and $\mathbf{k}_2$. In the most general case (i.e. when none of the assumptions above hold) it is clear that we get an enormous number of contributions and corresponding emission directions $\mathbf{k}$ in the expansion (28). Employing the RWA, however, it has been shown in Ref. 25 that the polarization of $(2N+1)$th order only radiates into the directions

$$\mathbf{k} = j(\mathbf{k}_2 - \mathbf{k}_1) + \mathbf{k}_2 \tag{30}$$

where j runs from $-(N+1)$ to N. As a direct consequence of (30), we obtain in linear response only emission into $\mathbf{k}_1$ and $\mathbf{k}_2$ directions, while the third-order polarizations may radiate along the directions $\mathbf{k}_1$, $\mathbf{k}_2$, $2\mathbf{k}_2 - \mathbf{k}_1$, and $2\mathbf{k}_1 - \mathbf{k}_2$. Assuming furthermore nonoverlapping pulses, it is easy to show that, even *in arbitrary order of the radiation field*, there is only emission into the directions $\mathbf{k}_1$, $\mathbf{k}_2$, and $2\mathbf{k}_2 - \mathbf{k}_1$ (i.e. regardless of N, $j = -1, 0, 1$).[31]

In the following, we want to derive and discuss expressions for the polarizations of various important spectroscopic processes. To simplify the notation, we define

$$\widehat{\mu}_{kk'} = \left|\Phi_k^d\right\rangle \boldsymbol{\epsilon_i} \cdot \boldsymbol{\mu}_{kk'} \left\langle\Phi_{k'}^d\right|, \tag{31}$$

and consider henceforth the projection P of the electric polarization $\mathbf{P}$ onto the polarization vector $\boldsymbol{\epsilon_i}$ of the field E_i. Due to the initial condition (23), the third-order polarization $\mathrm{P}^{(3)}(t)$ represents the lowest-order nonlinear response of the medium to the electric field. The third-order polarization in $\mathbf{k}_2$ direction consists of resonance Raman and stimulated-emission contributions[10,23]

$$\mathrm{P}^{(3)}_{\mathbf{k_2}}(t) = 2\,\mathrm{Re}\{P_{\mathrm{RA}}(t) + P_{\mathrm{SE}}(t)\}. \tag{32}$$

Inserting the first-order and second-order wave functions (26) into (28) and arranging the electric fields according to the stimulated-emission process, we obtain for the stimulated-emission polarization

$$\begin{aligned} P_{\mathrm{SE}}(t) &= \langle\Psi^{(2)}_{\mathbf{k_1}-\mathbf{k_2}}(t)|\widehat{\mu}_{02}|\Psi^{(1)}_{\mathbf{k_1}}(t)\rangle \\ &= ie^{i\mathbf{k_2}\cdot\mathbf{x}}\int_{-\infty}^{t} dt' E_2(t')\langle\Psi^{(1)}_{\mathbf{k_1}}(t')|\widehat{\mu}_{20}e^{iH_M(t-t')}\widehat{\mu}_{02}e^{-iH_M(t-t')}|\Psi^{(1)}_{\mathbf{k_1}}(t')\rangle, \end{aligned} \tag{33}$$

where we have labeled the wave functions by the subscript $n\mathbf{k_1} - m\mathbf{k_2}$ to indicate the interactions with the electric fields $\boldsymbol{E}_1^n$, $\boldsymbol{E}_2^{*m}$. Note that Eq. (33) resembles the expression for the linear polarization, except that the initial ground-state wave function $|\Phi_0^d\rangle$ in the linear polarization has been replaced by the nonstationary excited-state wave function $|\Psi^{(1)}_{\mathbf{k_1}}(t)\rangle$ in (33). One may thus interpret the stimulated-emission polarization as the *linear* response of a *nonstationary* system.[91] The stimulated-emission polarization therefore reflects the time evolution of the excited-state wave function $|\Psi^{(1)}_{\mathbf{k_1}}(t)\rangle$.

Similarly, we obtain for the Raman contribution

$$
\begin{aligned}
P_{\mathrm{RA}}(t) &= \langle \Psi^{(0)}(t)|\widehat{\mu}_{02}|\Psi^{(3)}_{\mathbf{k_2}}(t)\rangle + \langle \Psi^{(2)}(t)|\widehat{\mu}_{02}|\Psi^{(1)}_{\mathbf{k_2}}(t)\rangle \\
&= ie^{i\mathbf{k_2}\cdot\mathbf{x}}\int_{-\infty}^{t} dt' E_2(t')\Big\{\langle \Psi^{(0)}(t')|e^{iH_M(t-t')}\widehat{\mu}_{02}e^{-iH_M(t-t')}\widehat{\mu}_{20}|\Psi^{(2)}(t')\rangle \\
&\quad + \langle \Psi^{(2)}(t')|e^{iH_M(t-t')}\widehat{\mu}_{02}e^{-iH_M(t-t')}\widehat{\mu}_{20}|\Psi^{(0)}(t')\rangle\Big\}. \qquad (34)
\end{aligned}
$$

Note that $|\Psi^{(2)}(t')\rangle$ represents the nonstationary ground-state wave function prepared by the pump pulse. The Raman polarization thus reflects the time evolution of the ground-state wave function $|\Psi^{(2)}(t')\rangle$.[91]

To make contact with a widely used alternative formulation of nonlinear spectroscopy, we rewrite, for example, the stimulated-emission polarization (33) as

$$
\begin{aligned}
P_{\mathrm{SE}}(t) = i^3 e^{i\mathbf{k_2}\cdot\mathbf{x}}\int_{-\infty}^{t} dt_3 \int_{-\infty}^{t_3} dt_2 \int_{-\infty}^{t_2} dt_1 E_2(t_3) \\
\times \{E_1^*(t_2)E_1(t_1)R_1(t-t_3, t_3-t_2, t_2-t_1) \\
+ E_1(t_2)E_1^*(t_1)R_2(t-t_3, t_3-t_2, t_2-t_1)\}. \qquad (35)
\end{aligned}
$$

Here

$$
\begin{aligned}
&R_1(t_3, t_2, t_1) \\
&\quad = \langle \Phi_0^d|e^{iH_M t_1}\widehat{\mu}_{02}e^{iH_M t_2}\widehat{\mu}_{20}e^{iH_M t_3}\widehat{\mu}_{02}e^{-iH_M(t_1+t_2+t_3)}\widehat{\mu}_{20}|\Phi_0^d\rangle, \qquad (36) \\
&R_2(t_3, t_2, t_1) \\
&\quad = \langle \Phi_0^d|\widehat{\mu}_{02}e^{iH_M(t_1+t_2)}\widehat{\mu}_{20}e^{iH_M t_3}\widehat{\mu}_{02}e^{-iH_M(t_2+t_3)}\widehat{\mu}_{20}e^{-iH_M t_1}|\Phi_0^d\rangle, \qquad (37)
\end{aligned}
$$

are nonlinear dipole response functions, which account for the molecular dynamics associated with excited-state emission processes.[10] In a similar way, it is possible to express any contribution to the polarization $P^{(N)}(t)$ in terms of the corresponding nonlinear response function $R_i(t_N, t_{N-1}, \ldots, t_2, t_1)$. Because the nonlinear response functions carry the complete dynamical information of a given spectroscopic process, the response-function formalism allows us to decompose the computation of the polarization into the calculation of purely molecular quantities (i.e. $R_i(t_3, t_2, t_1)$) and subsequent time integrations. The characterization of nonlinear optical processes in terms of nonlinear response functions has been extensively discussed by Mukamel and collaborators.[10,13,74]

The perturbative evaluation of the TFG spontaneous emission signal follows similar lines. Starting from Eq. (13), using the approximation (16), calculating $\mathbf{P}(t)$ to first order in the pump field, and retaining only sequential contributions in the RWA, one arrives at the result[10,72,73]

$$\begin{aligned} S_{st}(t_0,\omega_0) \propto \mathrm{Re} \int_{-\infty}^{\infty} dt \int_0^{\infty} dt_3 \int_0^{\infty} dt_2 \int_0^{\infty} dt_1 \\ \times E_t(t-t_0)E_t(t-t_3-t_0)E_L(t-t_3-t_2)E_L(t-t_3-t_2-t_1) \\ \times e^{-(\gamma-i\omega_0)t_3} \left\{ R_1(t_3,t_2,t_1)e^{i\omega_L t_1} + R_2(t_3,t_2,t_1)e^{-i\omega_L t_1} \right\}. \end{aligned} \tag{38}$$

Here the frequency ω_L and the envelope $E_L(t)$ characterize the excitation pulse, and R_1, R_2 are the third-order nonlinear response functions defined in Eqs. (36) and (37). Clearly, if there is no time gating ($\gamma = 0,\ E_t = 1$), then the TFG spectrum reduces to the frequency-domain fluorescence spectrum. On the other hand, by comparing Eq. (38) with Eqs. (8) and (35), one realizes that the TFG SE is equivalent to the excited-state (stimulated-emission) contribution to the integrated pump-probe spectrum for non-overlapping pulses. The filter thus defines an effective carrier frequency ω_0 of the probe, and the temporal gate function represents the probe envelope centered at t_0. The only difference stems from the imperfection of the frequency filter γ, which controls the spectral resolution of the TFG SE.

The close similarity between the TFG SE and pump-probe spectra has repeatedly been emphasized in the literature.[7,10,65,66] It should be noted, however, that the equivalence between the TFG SE signal and the stimulated-emission contribution to the sequential integral pump-probe signal holds only in the leading (second) order in the pump and probe pulses. In this case also the "bare" TFG SE spectrum coincides with the stimulated-emission contribution to the dispersed pump-probe spectrum.[92] It is of importance that both stimulated emission (from the electronically excited state) and stimulated Raman (from the ground state) processes contribute to the overall pump-probe signal, even in the case of sequential, nonoverlapping pump and probe pulses. On the other hand, if the excitation and gate pulses do not overlap, the spontaneous emission consists solely of the fluorescence (excited state) component. Experimentally, one cannot easily separate the ground and excited state contribution to the pump-probe signal. The TFG fluorescence signal from the excited state is, on the other hand, free from contributions of the ground state dynamics.

Finally, it is instructive to discuss the relation of the integral pump-probe signals derived above from the electronic polarization to the corresponding expressions obtained from the calculation of electronic population probabilities. To this end, we consider the stimulated-emission polarization (33) and rewrite the the integral signal (8) in the suggestive form

$$I_{\mathrm{In}}(\omega_2, \Delta t) \propto \langle \Psi^{(2)} | \Phi_0^d \rangle \langle \Phi_0^d | \Psi^{(2)} \rangle, \tag{39}$$

where $|\Psi^{(2)}\rangle$ denotes the second-order wave function (26) accounting for the interaction of the system with the pump and probe pulses, respectively, and the operator $|\Phi_0^d\rangle\langle\Phi_0^d|$ affects the projection on the electronic ground state. We thus obtain the simple and physically appealing result that the integral stimulated-emission signal is directly proportional to the field-induced population in the electronic ground state. In complete analogy, the excited-state absorption spectrum and the ionization spectrum may be written as the field-induced population in the higher-lying and ionic electronic states, respectively.

3.2. *Photoelectron Spectra*

To describe ionization processes, the molecular Hamiltonian, given in Eq. (21), has to be extended to include ionization continua. As a specific example, we shall consider a molecular system that comprises the (uncoupled) electronic ground state $|\Phi_0^d\rangle$, the diabatic excited electronic states $|\Phi_1^d\rangle$, $|\Phi_2^d\rangle$, which are vibronically coupled by the matrix element $h_{12} = W_{12}$, and two ionization continua $|\Phi_1^{(k)}\rangle$, $|\Phi_2^{(k)}\rangle$, which are vibronically coupled by the matrix element $\tilde{h}_{12} = \tilde{W}_{12}$:

$$H_M = \sum_{n,m=0}^{2} |\Phi_n^d\rangle h_{nm} \langle \Phi_m^d| + \sum_{n,m=1}^{2} \int_0^\infty dE_k |\Phi_n^{(k)}\rangle (\tilde{h}_{nm} + E_k \delta_{nm}) \langle \Phi_m^{(k)}|. \tag{40}$$

Here $\tilde{h}_{nn}$ represents the vibrational Hamiltonian of the ionic state $|\Phi_n^{(k)}\rangle$, and the index k labels the energy E_k of the continuum electrons. In addition, we generalize the molecule-field interaction to allow for radiative couplings between $|\Phi_0^d\rangle$ and $|\Phi_2^d\rangle$ (for simplicity, it is assumed that $|\Phi_1^d\rangle$ is dark in absorption) and for radiative couplings between the excited states $|\Phi_1^d\rangle$,

$|\Phi_2^d\rangle$ and the respective continua $|\Phi_1^{(k)}\rangle$, $|\Phi_2^{(k)}\rangle$

$$H(t) = H_M + H_{\text{int}}(t), \tag{41}$$

$$H_{\text{int}}(t) = -|\Phi_2^d\rangle \boldsymbol{\mu_{20}} \cdot \mathbf{E}(t)\langle\Phi_0^d| + \text{h.c.} - \sum_{l=1}^{2} \int dE_k |\Phi_l^{(k)}\rangle \boldsymbol{\mu_l}(E_k) \cdot \mathbf{E}(t)\langle\Phi_l^d| + \text{h.c.} \tag{42}$$

In Eq. (42) it has been assumed that the excited state $|\Phi_1^d\rangle$ can ionize, because of symmetry or electronic-structure selection rules, only into the continuum $|\Phi_1^{(k)}\rangle$. Correspondingly, $|\Phi_2^d\rangle$ can only ionize into the continuum $|\Phi_2^{(k)}\rangle$. It is straightforward to extend the formulation to account for more general situations.

In atoms and molecules, the photoionization cross section near the ionization threshold is finite and often depends only weakly on the energy E_k of the continuum electron. It is therefore reasonable to approximate the ionization cross section near threshold by the Heaviside step function

$$\sigma_l(E_k) \propto \Theta(E_k). \tag{43}$$

The total (electronic plus nuclear) wave function $\Psi(t)$ is determined by the time-dependent Schrödinger equation (24) with the initial condition (23). In direct analogy to the case of photon absorption and emission [cf. Eq. (39)], the ionization signals defined in Eqs. (18) and (19) are obtained from the second-order wave function.

Calculations of the ion yield in dependence on the pulse delay time Δt and on the parameters of the laser pulses have been performed in Refs. 86 and 93 for simple one-dimensional models of excited-state vibrational motion and vibronic coupling. It has been found that for the vibronic-coupling examples considered and for suitably chosen pulse parameters, the ion signal as a function of Δt maps very well the adiabatic electronic population probability.[93] As an example of a molecular system comprising conical intersections, Sec. 5.1 presents a calculation of the time-resolved photoelectron spectrum of pyrazine.

3.3. *Computational Aspects*

To discuss the computational aspects of the perturbative approach, we focus on multidimensional systems, where the direct diagonalization of the molecular Hamiltonian H_M is in general not feasible. Hence, we need to adopt

an eigenstate-free representation and compute the three-time correlation functions $R_j(t_3, t_2, t_1)$ by numerical time-dependent propagation methods. Although straightforward in principle, this procedure is clearly too time-consuming in practice. To obtain a computationally more manageable formulation, we restrict ourselves to the case of nonoverlapping laser pulses. The stimulated-emission polarization can then be expressed in terms of a two-time (instead of a three-time) correlation function. Dropping unimportant prefactors, the polarization may be written in the instructive form

$$P_{\mathrm{SE}}(t, \Delta t) = \int_{-\infty}^{t} dt' E_2(t') P^{\delta}(t, \Delta t), \tag{44}$$

$$P^{\delta}(t, t') = \left\langle \Psi_{\mathrm{P}} | e^{iH_M t'} \widehat{\mu}_{20} e^{iH_M (t-t')} \widehat{\mu}_{02} e^{-iH_M t} | \Psi_{\mathrm{P}} \right\rangle, \tag{45}$$

$$|\Psi_{\mathrm{P}}\rangle = i \int_{-\infty}^{\infty} dt E_1(t) e^{iH_M t} \widehat{\mu}_{20} e^{-H_M t} |\Phi_0^d\rangle. \tag{46}$$

Here $|\Psi_{\mathrm{P}}\rangle$ represents the nonstationary excited-state wave function prepared by the pump pulse and we have introduced the "impulsive polarization" $P^{\delta}(t, \Delta t)$, that is, the polarization for an an idealized δ-function probe pulse.

Equation (44) suggests a convenient perturbative evaluation scheme for transient spectra: One first calculates the impulsive polarization $P^{\delta}(t, t')$, and subsequently obtains via Eq. (44) the polarization for probe pulses of arbitrary frequency and duration. Particularly in the case of long probe pulses or pulses with several carrier frequencies, it is clear that this scheme provides a substantial saving of computational effort. As shown below, it also provides a very efficient way to calculate ionization spectra. Since it is often advantageous to calculate the impulsive polarization $P^{\delta}(t, t')$ in a nonperturbative manner, the method has also been referred to as "mixed nonperturbative/perturbative scheme".[94]

Note that the application of the convolution scheme in the simple form (44) requires that the nonlinear polarization contains only a single interaction with the probe laser field. Apart from the transient transmittance spectrum considered above, this condition is also fulfilled for related detection schemes such as time-resolved fluorescence, ionization, and excited-state absorption. Coherent spectroscopic signals such as the photon-echo, on the other hand, contain two interactions with the probe laser field, thus requiring the calculation of the full three-time response function, followed by a double convolution.

In practice, it turns out to be advantageous to calculate the *spectrum* $P^{\delta}(\omega, \Delta t)$ of the impulsive polarization, that is, the Fourier transform of $P^{\delta}(t, \Delta t)$ with respect to t. The physically appealing feature of $P^{\delta}(\omega, \Delta t)$ is that this quantity can be viewed as the generalization of the linear absorption spectrum of a stationary state to the transient absorption spectrum of a nonstationary state.[11] Inserting (44) into Eq. (9), the dispersed transmittance spectrum for finite probe pulses can be written as[60]

$$I_{\mathrm{D}}(\omega, \Delta t) = 2\omega \,\mathrm{Im}\, E_2(\omega) \int_{-\infty}^{\infty} \mathrm{d}t E_2(t) P^{\delta}(\omega, t). \tag{47}$$

The integral pump-probe signal is then given as integral over all emission frequencies ω

$$I_{\mathrm{In}}(\omega_2, \Delta t) = 2\omega \,\mathrm{Im} \int_0^{\infty} d\omega E_2^*(\omega - \omega_2) \int_{-\infty}^{\infty} dt E_2(t) P^{\delta}(\omega, t). \tag{48}$$

It is noted that in order to perform a spectral analysis of $P^{\delta}(t, \Delta t)$ with a standard fast Fourier transform routine, one needs to assure that the polarization has decayed completely. In practice, this requirement results either in invoking a phenomenological damping $\propto e^{-\gamma t}$ of the polarization (which artificially broadens the spectrum) or in a large propagation time of the polarization (which is computationally expensive). To avoid this problem, it has been suggested to employ a filter-diagonalization method[95–97] for the spectral analysis of $P^{\delta}(t, \Delta t)$.[94]

It should be stressed that the convolution scheme is particularly advantageous for the calculation of photoelectron spectra. Recalling that both the photoelectron spectrum [Eq. (19)] and the stimulated emission spectrum [Eq. (39)] can be written in terms of the second-order wave function projected on a detector state, it is clear that the convolution scheme (48) may also be applied to the calculation of ionic detector states. Hence, we obtain for the photoelectron spectrum[98]

$$\begin{aligned} I_{\mathrm{Ion}}(E_k, \Delta t) = 2 \,\mathrm{Im} \int_0^{\infty} d\omega E_2^*[\omega - (\omega_2 - E_k)] \\ \times \int_{-\infty}^{\infty} dt' E_2(t') e^{-\mathrm{i}(\omega_2 - E_k)t'} P^{\delta}(\omega, t'). \end{aligned} \tag{49}$$

Denoting the probe frequency used for the excited-state absorption by ω_A and the probe frequency used for photoionization by ω_I, a comparison of

the signals (48) and (49) directly recovers the relation $\omega_A = \omega_I + E_k$. It is therefore possible to obtain the continuous photoelectron spectrum from a single transient-absorption calculation, thus circumventing the cumbersome discretization of the electron continuum.

The perturbative evaluation of pump-probe spectra simplifies further, if we assume that only the excited electronic states $|\Phi_1^d\rangle$ and $|\Phi_2^d\rangle$ are coupled through a nonadiabatic coupling W_{12} in Eq. (21), whereas the coupling to the energetically well-separated electronic ground state $|\Phi_0^d\rangle$ may be neglected to a first approximation. This means that only the dynamics in the *excited* electronic states needs to be treated in terms of a eigenstate-free wave-packet propagation. The nuclear dynamics in the electronic *ground* state, on the other hand, may be described in terms of unperturbed basis functions (e.g. harmonic-oscillator functions), the eigenstates $|\mathbf{v}\rangle$ and eigenvalues $\epsilon_{\mathbf{v}}$ of which are known analytically. Inserting the sum over vibrational eigenstates of the electronic ground state $\sum_{\mathbf{v}} |\mathbf{v}\rangle\langle\mathbf{v}|$ into (45), we thus obtain[99]

$$P^{\delta}(t,t') = \sum_{\mathbf{v}} D_{\mathbf{v}}(t) D_{\mathbf{v}}^{*}(t'), \tag{50}$$

$$D_{\mathbf{v}}(t) = e^{i\epsilon_{\mathbf{v}} t} \langle \mathbf{v}|\langle \Phi_0^d|\hat{\mu}_{02} e^{-iH_M t}|\Phi_{\mathrm{P}}^d\rangle. \tag{51}$$

Owing to the fact that the model Hamiltonian (21) is diagonal as far as the electronic ground state is concerned, the evaluation of the two-time correlation function $C_{\mathrm{SE}}(t,t')$ has been reduced to a *single* propagation of the excited-state wave function.

While the computational strategies outlined above represent numerically exact methods, several workers have suggested an approximate calculation of time-resolved pump-probe spectra.[10,66,100–104] With this end in mind, we rewrite the integral stimulated-emission signal (39) as

$$I_{\mathrm{In}}(\omega_2, \Delta t) \propto \langle \Psi_P | P^{\dagger} P | \Psi_P \rangle, \tag{52}$$

$$P = \int_{-\infty}^{\infty} dt' E_2(t') e^{-iH_M(\Delta t - t')} \hat{\mu_{02}} e^{iH_M(\Delta t - t')}, \tag{53}$$

where we have introduced the operator P, which accounts for the field-matter interaction in a perturbative manner, while the intramolecular interaction is treated to all orders.

Equations (52) and (53) facilitate an highly efficient evaluation of transient absorption/emission spectra in the spirit of the semiclassical

Franck–Condon approximation.[10,66,100–105] The short-time approximation $e^{-ih_2t}e^{ih_1t} \approx e^{-i(h_2-h_1)t}$ inherent to this ansatz can be extended to the case of nonadiabatically coupled electronic states through the following approximations[106]

$$[h_n, h_m] = 0, \tag{54}$$

$$[h_n, W_{nm}] = 0, \tag{55}$$

i.e. in addition to Eq. (54) we moreover need to assume that the vibronic coupling operators W_{nm} commute with the vibrational Hamiltonians h_n. Since these commutators generally depend on vibrational momenta, this approximation amounts to neglecting the motion of the vibrational wave packet during the probe pulse.[100] Clearly, this assumption can only be valid for sufficiently short probe pulses.

Considering various representative model systems of vibronic coupling, a number of approximative expressions for the operator P have been derived by Dilthey *et al.*[106] An important example is the so-called "internal case", in which the radiation field induces transitions between two vibronically coupled states $|\Phi_1^d\rangle$ and $|\Phi_2^d\rangle$. Since both emission and absorption processes may occur in this case, the measured spectroscopic signal is given as the difference between absorption and emission signals

$$I_{\mathrm{In}}(\omega_2, \Delta t) = \langle \Psi_P | (E^\dagger E - A^\dagger A) | \Psi_P \rangle, \tag{56}$$

where E and A are the operators corresponding to the emission and absorption process, respectively. It turns out that these operators are most conveniently expressed in the adiabatic electronic representation. Introducing adiabatic electronic basis states $|\psi_n^{ad}\rangle = \sum_m S_{nm}|\Phi_m^d\rangle$ via the unitary transformation $S = \{S_{nm}\}$, the adiabatic operator is given by $P^{ad} = S^\dagger P S$. Neglecting, furthermore, off-resonant terms, we obtain the simple result

$$E_{ad}^\dagger E_{ad} - A_{ad}^\dagger A_{ad} = \frac{1}{4}|\mu_{12}|^2 \frac{\Delta^2}{W^2} e^{-2\alpha\tau^2(\omega_2-2W)^2} \left(|\psi_2^{ad}\rangle\langle\psi_2^{ad}| - |\psi_1^{ad}\rangle\langle\psi_1^{ad}| \right), \tag{57}$$

where $\Delta = \frac{1}{2}(W_2 - W_1)$ and $W = \sqrt{\Delta^2 + W_{12}^2}$ represent the energy difference between the diabatic and adiabatic electronic states, respectively. As previously discussed by Meyer and Köppel,[107] in the case of internal radiative coupling, the light field induces transitions between *adiabatic* electronic states. The intensity of these transitions are weighted by a Gaussian function reflecting the resonance condition $\omega_2 = 2W = V_2 - V_1$, where τ is the

duration of the probe pulse and $1/\alpha = 16 \ln 2$. The prefactor $\Delta/W = \cos 2\varphi$ involves the diabatic/adiabatic mixing angle φ, thus relating the diabatic transition dipole matrix element μ_{12} to its adiabatic counterpart.

In the "external case", one considers radiative transitions from the coupled states $|\Phi_1^d\rangle$, $|\Phi_2^d\rangle$ to one (or several) additional "detector state(s)" $|\psi_d\rangle$. Radiative $|\Phi_1^d\rangle \leftrightarrow |\Phi_2^d\rangle$ transitions between the coupled states $|\Phi_1^d\rangle$, $|\Phi_2^d\rangle$ are assumed to be dipole forbidden. Adopting again the adiabatic representation, a similar analysis yields $I_{\mathrm{In}}(\omega_2, \Delta t) = \langle \Psi_P | P^\dagger P | \Psi_P \rangle$ with

$$P_{ad}^\dagger P_{ad} = \frac{1}{4}\mu^2 \sum_{n=1,2} e^{-2\alpha\tau^2[\omega_2 - (V_n - W_d)]^2} S_{2n}^2 |\psi_n^{ad}\rangle\langle\psi_n^{ad}|. \tag{58}$$

In the limiting case of an impulsive probe pulse ($\tau_2 = 0$), the Gaussian resonance factors vanish and we obtain the simple result

$$P^\dagger P = \frac{1}{4}\mu^2 |\Phi_2^d\rangle\langle\Phi_2^d|, \tag{59}$$

i.e. in the impulsive limit the *diabatic* electronic population probability $\langle\Psi(t)|\Phi_2^d\rangle\langle\Phi_2^d|\Psi(t)\rangle$ is measured.[7,99,107]

Let us finally consider the case of ionization detection. In this case, the approximate description is particularly advantageous.[100,101,106] Since ionization formally corresponds to an external absorption process into an ionic state $|\psi^{(k)}\rangle$, we may directly employ the nonadiabatic Franck–Condon formalism developed above to calculate the time-resolved photoelectron spectrum (19). Hence, the electron continuum needs not to be discretized, but solely appears in the Gaussian resonance factors, which now read

$$\exp\{-2\alpha\tau^2[\omega_2 - (E_k + \tilde{V}_I - V_n)]^2\}, \tag{60}$$

i.e. to be resonant, a photon with frequency ω_2 must provide the energy between the adiabatic state $|\psi_n^{ad}\rangle$ and the ionic state $|\psi_I^{(k)}\rangle$ as well as the electron energy E_k.

It is noted that the approximations given above virtually reduce the costs of explicit pump-probe simulations to the costs of a standard time-dependent wave-packet propagation. Apart from interpretative purposes, the Franck–Condon formulation therefore cuts the computational effort considerably. Since the theory requires no explicit discretization of a continuum of electronic states, this is particularly true for the description of femtosecond time-resolved photoelectron spectroscopy.

4. Calculation of Spectra: Nonperturbative Approach

4.1. *Absorption and Emission of Photons*

Besides the commonly applied perturbative evaluation of spectroscopic signals, recently also nonperturbative descriptions have been considered.[25,26,108–110] Assuming, as usual, an optically thin sample, the only formal difference between the two formulations is whether the electric polarization $\mathbf{P}(t)$ is evaluated in a perturbative or nonperturbative manner. As a consequence, the definitions of time- and frequency-resolved PP signals are completely equivalent in both formulations. Besides the obvious point that one needs to propagate the wave function with a time-dependent Hamiltonian instead of an time-independent one, the calculation of PP signals appears to be rather similar in both formulations.

The nonperturbative calculation of PP or four-wave mixing spectra involves, however, an additional problem. As explained above, the overall polarization consists of several contributions

$$\mathbf{P}(t) = 2\,\mathrm{Re}\sum_{n,m} \boldsymbol{P}_{nm}(t)\exp(i(n\mathbf{k}_1 + m\mathbf{k}_2)\mathbf{x}), \tag{61}$$

which, experimentally as well as in a perturbative calculation, are easily distinguished via the direction of the wave vector $\mathbf{k} = n\mathbf{k}_1 + m\mathbf{k}_2$ of the emitted radiation. For example, the coherent emission due to the photon-echo effect is observed in the directions $2\mathbf{k}_2 - \mathbf{k}_1$ and $2\mathbf{k}_1 - \mathbf{k}_2$, while the transmission of the pump and probe pulse due to stimulated emission and resonance Raman processes is observed in the $\mathbf{k}_1$ and $\mathbf{k}_2$ direction, respectively.

In a nonperturbative calculation, however, we obtain, by evaluating Eq. (25), the *overall* polarization of the system, which is given as sum of all these processes. Furthermore, for the sake of simplicity, one usually assumes a *coherent* electric field in the theoretical description. The pump and probe pulses are thus phase-locked, giving rise to a number of contributions to the polarization, which are not observed in standard PP experiments, where the signal is incoherently averaged over many laser shots. Thus, although we know that in the weak-field limit the overall polarization reduces to the results from lowest-order perturbation theory, we still have to distinguish the different contributions to $\mathbf{P}(t)$ in order to calculate a specific experimental PP signal. In most nonperturbative PP calculations this problem has been circumvented by considering the time evolution of the system (following pulsed excitation) instead of PP signals,[108,109] or by assuming a

strongly repulsive excited potential-energy surface, and restricting oneself to the time-dependent dynamics in the electronic ground state.[111]

In the following, we briefly discuss a general approach to extract the individual contributions and spectroscopic signals from the overall polarization,[25,110] and discuss the simplifications that arise when the usual assumptions (i.e. nonoverlapping and weak laser fields, slowly-varying envelope assumption, and RWA) are invoked.

The basic idea how to determine the directional dependence of the nonlinear polarization in a nonperturbative calculation is rather simple and is most easily demonstrated by an example. Let us first consider nonoverlapping laser fields within the RWA, and let us suppose that we only want to discriminate the (phase-insensitive) $\mathbf{k}_2$ emission from the (phase-sensitive) $\mathbf{k}_1$ and $2\mathbf{k}_2 - \mathbf{k}_1$ contributions. Rewriting the overall polarization as

$$\boldsymbol{P}(\phi) = \sum_n \boldsymbol{P}_n \exp(in\phi), \tag{62}$$

where $n\phi = n\mathbf{k}_1\mathbf{x}$ denotes the phase which the polarization acquires through the interaction with the pump field, it is clear that the terms $\boldsymbol{P}_{-1}, \boldsymbol{P}_0$, and $\boldsymbol{P}_1$ represent the polarization in the $2\mathbf{k}_2 - \mathbf{k}_1$, $\mathbf{k}_2$, and $\mathbf{k}_1$ directions, respectively. Performing two separate calculations of the overall polarization $\mathbf{P}(\phi)$ employing the phases $\phi_1 = 0, \phi_2 = \pi$, it is easy to see that the polarizations in $\mathbf{k}_2$ and $\mathbf{k}_1$, $2\mathbf{k}_2 - \mathbf{k}_1$ are given by the linear combinations

$$\mathbf{P}_{\mathbf{k_2}} = \mathrm{Re}\{\boldsymbol{P}(0) + \boldsymbol{P}(\pi)\}, \tag{63}$$

$$\mathbf{P}_{\mathbf{k}_1, 2\mathbf{k}_2 - \mathbf{k}_1} = \mathrm{Re}\{\boldsymbol{P}(0) - \boldsymbol{P}(\pi)\}. \tag{64}$$

As a second example, allow for overlapping laser fields within the RWA and ask for the polarizations up to third order into all possible directions, i.e. into $\mathbf{k}_2$, $\mathbf{k}_1$, $2\mathbf{k}_2 - \mathbf{k}_1$, and $2\mathbf{k}_1 - \mathbf{k}_2$. The calculation of the overall polarization $\boldsymbol{P}(\phi)$ for the phases $\phi_k = k\pi/2$ $(k = 0, 1, 2, 3)$ yields a linear system of four equations for the $\boldsymbol{P}_n$ in (62), the solution of which yields the desired polarizations

$$\mathbf{P}_{\mathbf{k_2}} = \tfrac{1}{2}\mathrm{Re}\{\boldsymbol{P}(0) + \boldsymbol{P}(\pi/2) + \boldsymbol{P}(\pi) + \boldsymbol{P}(3\pi/2)\}, \tag{65}$$

$$\mathbf{P}_{\mathbf{k_1}} = \tfrac{1}{2}\mathrm{Re}\{\boldsymbol{P}(0) - \boldsymbol{P}(\pi)\} + \tfrac{1}{2}\mathrm{Im}\{\boldsymbol{P}(\pi/2) - \boldsymbol{P}(3\pi/2)\}, \tag{66}$$

$$\mathbf{P}_{2\mathbf{k}_2 - \mathbf{k}_1} = \tfrac{1}{2}\mathrm{Re}\{\boldsymbol{P}(0) - \boldsymbol{P}(\pi)\} + \tfrac{1}{2}\mathrm{Im}\{\boldsymbol{P}(3\pi/2) - \boldsymbol{P}(\pi/2)\}, \tag{67}$$

$$\mathbf{P}_{2\mathbf{k}_1 - \mathbf{k}_2} = \tfrac{1}{2}\mathrm{Re}\{\boldsymbol{P}(0) - \boldsymbol{P}(\pi/2) + \boldsymbol{P}(\pi) - \boldsymbol{P}(3\pi/2)\}. \tag{68}$$

From the above examples, the generalization of the procedure to cases including arbitrary nonlinear processes of any order is straightforward. In Ref. 110 the case of four-wave mixing experiments with three incident laser fields has been discussed. To calculate the contributions of the polarization in N directions, one has to perform N calculations of the overall polarization $\boldsymbol{P}(\phi)$ with different phases ϕ, and solve the resulting linear system of equations for the $\boldsymbol{P}_n$ in (62). Beyond the RWA, however, one needs to generalize the ansatz (62) and "tag" both the interactions with the pump and the probe fields with phases $\phi^{(1)} = \mathbf{k}_1\mathbf{x}$ and $\phi^{(2)} = \mathbf{k}_2\mathbf{x}$, respectively, thus performing a two-dimensional Fourier analysis of the overall polarization.

Analogously to experiment, we thus obtain the nonlinear response of the molecular system resolved in the directions of emission, but summed up over all contributions in each direction. Assuming nonoverlapping laser fields within the RWA, it is moreover possible to separate the PP signals arising from the stimulated Raman and the stimulated emission contribution, respectively.[25] This important feature, which is rather helpful in the interpretation of complex PP spectra (see below), stems from the fact that after the interaction with the pump pulse we may separately consider the electronic ground-state component $\langle\Phi_0^d|\Psi(t)\rangle$ or excited-state component $\langle\Phi_1^d|\Psi(t)\rangle$ of the total wave function.

4.2. *Photoelectron Spectra*

In the nonperturbative approach, we transform, as usual, the time-dependent Schrödinger equation into the interaction picture. The Hamiltonians (41) and (42) are separated into an electronically diagonal and time-independent part H_d and a non-diagonal part W^0 according to

$$H_d = \sum_{l=0}^{2} |\Phi_l^d\rangle h_l \langle\Phi_l^d| + \sum_{l=1,2} \int_0^\infty dE_k |\Phi_l^{(k)}\rangle(\tilde{h}_l + E_k)\langle\Phi_l^{(k)}|, \quad (69)$$

$$W^0(t) = \{|\Phi_1^d\rangle W_{12}\langle\Phi_2^d| - |\Phi_2^d\rangle\boldsymbol{\mu}_{20}\cdot\mathbf{E}(t)\langle\Phi_0^d| - \sum_{l=1,2}\int_0^\infty dE_k|\Phi_l^{(k)}\rangle\boldsymbol{\mu}_l\mathbf{E}(t)\langle\Phi_l^d|\} + \text{h.c.} \quad (70)$$

With the unitary time-evolution operator of the unperturbed system, $U_d(t) = e^{-iH_d t}$, we obtain the Schrödinger equation in the interaction

picture

$$i\frac{\partial}{\partial t}|\Phi_I^d(t)\rangle = W_I^0(t)|\Phi_I^d(t)\rangle, \tag{71}$$

$$W_I^0(t) = U_d^\dagger(t)W^0(t)U_d(t), \tag{72}$$

$$|\Phi_I^d(0)\rangle = |\Phi_0^d\rangle|\mathbf{0}\rangle. \tag{73}$$

To solve Eq. (71), $|\Psi_I(t)\rangle$ is expanded in a direct-product basis of electronic and vibrational basis states as

$$|\Psi_I(t)\rangle = \sum_{\boldsymbol{\nu}}\sum_{l=0}^{2} C_{\boldsymbol{\nu},l}(t)|\Phi_l^d\rangle|\boldsymbol{\nu}\rangle + \sum_{l=1,2}\int_0^\infty dE_k C_{\boldsymbol{\nu},l}(E_k,t)|\Phi_l^{(k)}\rangle|\boldsymbol{\nu}\rangle. \tag{74}$$

Insertion of the expansion (74) into Eq. (71) yields a set of coupled first-order differential equations.

A specific aspect of the ionization problem are the expansion coefficients $C_{\boldsymbol{\nu},l}(E_k,t)$ related to the electronic continua. Their dependence on the continuous variable E_k leads to a noncountably infinite set of differential equations. To arrive at a computationally manageable scheme, the continua have to be discretized. An ingenious discretization scheme, which proves particularly efficient in the present context, has been proposed by Burkey and Cantrell.[112] The energy-dependent coefficients are expanded in terms of polynomials which are orthogonal with respect to the ionization cross section as weight function (see Ref. 24 for details). It has been shown that for pulses of short duration only a small number of expansion terms has to be considered, which renders this scheme very efficient for femtosecond PP applications.[24]

With the expansion

$$C_{\boldsymbol{\nu},l}(E_k,t) = \sum_{n=0}^{N} C_{\boldsymbol{\nu},ln}(t)U_n(E_k), \tag{75}$$

where the $U_n(E_k)$ are related in a simple manner to Legendre polynomials,[24] we finally arrive at a simple, although possibly very large, system of ordinary first-order differential equations

$$i\dot{\mathbf{C}}(t) = \mathbf{W}(t)\mathbf{C}(t). \tag{76}$$

Due to the sparsity and transparent structure of the matrix $\mathbf{W}(t)$, very efficient strategies can be implemented for the solution of Eq. (76). Since the elements of $\mathbf{W}(t)$ are time-dependent, it is advantageous to employ

a numerical propagator with automatic step-size control. In Refs. 24 and 113 it has been shown that the Bulirsch–Stoer algorithm[114] is particularly useful for these purposes. Obviously, it is possible to investigate strong-field effects in pump-probe ionization with this formalism.

In terms of the expansion coefficients $C_{\boldsymbol{\nu},ln}(t)$, the time and energy resolved photoelectron signal (19) is given by[24]

$$I_{ion}(E_k, \Delta t) = \sum_{l=1,2} \sum_{\boldsymbol{\nu}} \sum_{n} |C_{\boldsymbol{\nu},ln}(t) U_n(E_k)|^2. \tag{77}$$

The ion yield signal (18) is given by

$$I_{ion}\Delta t) = \int_0^\infty dE_k I_{ion}(E_k, \Delta t) = \sum_{l=1,2} \sum_{\boldsymbol{\nu}} \sum_{n} |C_{\boldsymbol{\nu},ln}(t)|^2. \tag{78}$$

Simulations of femtosecond time-resolved photoelectron spectra have first been performed with this formalism for a three-mode model of the S_1-S_2 conical intersection in pyrazine[24] (see below). With the same technique, Schön and Köppel have explored the real-time detection of pseudorotational motion due to Jahn–Teller and pseudo-Jahn–Teller couplings in Na_3.[113] The same problem has been addressed within the perturbational formalism by Dobbyn and Hutson.[115] Charron and Suzor–Weiner have treated the femtosecond photoionization dynamics of NaI within the nonperturbative approach, considering also passive control scenarios to influence the fragmentation pattern of NaI.[116]

When considering the femtosecond photoionization dynamics of complex systems, a completely exact evaluation of the time and energy resolved photoelectron spectrum is often not really necessary. Approximative schemes which require significantly lower computational effort are valuable in such cases. Within the nonperturbative formalism, Meier *et al.* have proposed an efficient computational scheme which incorporates the multi-configuration time-dependent Hartree method.[117] An approximate method which is based on a classical-trajectory description of the nuclear dynamics has been elaborated by Hartmann, Heidenreich, Bonacic–Koutecky and coworkers[118] and applied, among other systems,[119] to the time-resolved photoionization spectroscopy of conical intersections in sodium fluoride clusters.[120]

For a discussion of the calculation of time and angle resolved photoelectron spectra, we refer to the recent papers of Seideman and collaborators[27,89,121,122] and Takatsuka, McKoy and collaborators.[88,123] As

shown for an interesting example (photophysics of octatetraene) in Ref. 122, the photoelectron angular distribution can, in suitable cases, provide a clear signature of the electronic character of the transient intermediate state. The change of the electronic wave function during the internal-conversion process can thus be followed in real time. Very recently, the first calculation of the time-resolved photoelectron angular distribution of an internally converting molecule ($S_2 \rightarrow S_1$ decay in pyrazine) has been reported by Suzuki *et al.*[124]

5. Representative Applications

The conical intersection between the $S_1(n\pi^*)$ and $S_2(\pi\pi^*)$ excited states of pyrazine probably represents the most extensively and carefully investigated example of dynamical effects associated with a conical intersection in a polyatomic molecule,[7,24,99,125–137] see also Chapters 7, 9, 14 and 15. This system therefore is well suited as a testbed for the development of the theory and of computational techniques for the calculation of time-resolved spectra associated with conical intersections. The pioneering calculations on the real-time detection of ultrafast nonadiabatic dynamics via transient transmittance, time and frequency gated fluorescence and time-resolved photoelectron spectroscopy have been performed for this example.[7,24,99]

Other applications, where femtosecond time-resolved spectra have been calculated for systems with conical intersections, include time- and frequency-resolved spontaneous emission spectra for NO_2,[71] transient transmittance spectra for models of polyene photochemistry,[7,25,92] femtosecond ion yield and photoelectron spectra of Jahn–Teller and pseudo-Jahn–Teller coupled states of Na_3[113,115] and femtosecond ion yield signals for conical intersections in sodium fluoride clusters.[120] Furthermore, Chapter 18 of this book considers the theoretical description of laser control of photochemical reactions mediated by a conical intersection.[138,139] In the following, we give a brief review of selected calculations of transmittance and photoelectron spectra to illustrate the practical applications of the theoretical formalism described in Secs. 3 and 4 above.

5.1. *The S_1–S_2 Conical Intersection in Pyrazine*

Due to the prominent vibronic coupling between the $S_1(n\pi^*)$ and $S_2(\pi\pi^*)$ excited states as well as $I_0(n^{-1})$ and $I_1(\pi^{-1})$ cation states, respectively,

pyrazine has served as a prototype example to study ultrafast internal-conversion processes in polyatomic molecules.[7,24,99,125–137] In a series of high-level *ab initio* investigations, Domcke and coworkers have characterized low-lying conical intersections of the adiabatic potential-energy surfaces of these states.[7,125–129] Adopting a diabatic electronic representation, they furthermore have constructed a model Hamiltonian using the vibrational normal coordinates pertaining to the electronic ground state. Most dynamical studies have focused on the $S_2 \rightarrow S_1$ internal conversion process and the associated nonadiabatic wave-packet motion on a femtosecond time scale.[130–134] Simulations of time- and frequency resolved pump-probe experiments have suggested that it should be possible to observe this ultrafast electronic and vibrational relaxation dynamics in real time.[7,24,59,135] As representative examples, we present in the following calculations of the time-resolved transmittance and the photoelectron spectrum of pyrazine.

5.1.1. *Transmittance Spectra*

The calculated integral transient transmittance spectrum in the energy range of the $S_2(\pi\pi^*)$ state of pyrazine, plotted as a function of the delay time Δt and the carrier frequency ω_2 of the probe pulse, is shown in Fig. 1. Gaussian laser pulses of low intensity and 20 fs duration have been assumed.[7] The S_0–S_1 transition dipole moment has been set to zero for simplicity (the oscillator strength of the S_0–$S_1(n\pi^*)$ transition is at least a factor of ten smaller than the S_0–$S_2(\pi\pi^*)$ oscillator strength). Possible absorption into higher excited states has been neglected. The pump-probe signal has been calculated numerically exactly through nonperturbative evaluation of the electronic polarization, thus taking explicitly into account overlapping laser fields, non-rotating-wave contributions and higher-order corrections. Within the limits of the three-mode model of pyrazine,[130] the pump-probe signal shown in Fig. 1 may therefore be regarded as direct simulation of a possible experiment.

After an initial peak at delay times where the pump and the probe fields overlap, the pump-probe signal is seen to split up into two components; a dominant, slightly oscillating feature centered at the electronic gap Δ of the S_0–S_2 transition ($\omega_2 \approx 4.8\,\mathrm{eV}$), and a weaker red-shifted contribution, centered at $\omega_2 \approx 3.4\,\mathrm{eV}$. As is shown below, the first component at $\omega_2 \approx \Delta$ is mostly due to stimulated resonance Raman scattering, thus reflecting

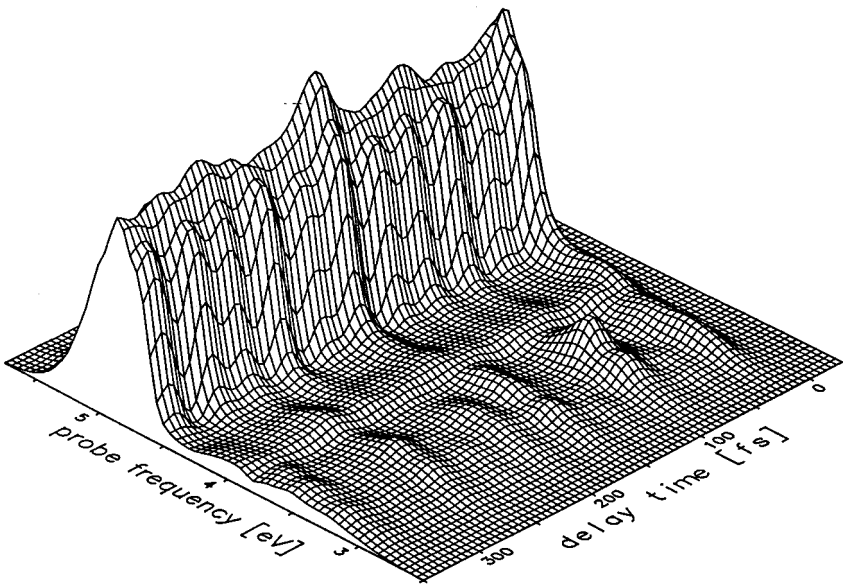

Fig. 1. The integral transient transmittance spectrum of pyrazine, calculated for a three-mode model of the S_1–S_2 conical intersection.[7] Gaussian laser pulses of 20 fs duration have been assumed.

coherent harmonic motion in the electronic ground state. The red-shifted component, on the other hand, represents the stimulated-emission contribution to the signal. It exhibits complex oscillatory structures and reflects the nonadiabatic wave-packet dynamics in the coupled excited electronic states.

To distinguish ground-state and excited-state dynamics, one would like to separately consider the Raman and the stimulated-emission contribution. Experimentally, this can be done by either considering the time-resolved fluorescence spectrum, or by using a polarization-sensitive detection scheme, that suppresses the ground-state contribution to the transmittance spectrum.[140] To calculate individual contributions to the total pump-probe signal, the perturbative evaluation of the electronic polarization often is advantageous. Figure 2 shows (a) the Raman and (b) the stimulated-emission contribution to the transient transmittance spectrum. The stimulated Raman contribution is seen to manifest itself as broad, only slightly oscillating background emission located at the CW absorption bands of

pyrazine. It is interesting to note that, although we have exclusively considered the S_0–S_2 transition dipole moment in the calculation, there is a weak Raman emission centered at the S_1 absorption band ($\omega_2 \approx 4\,\mathrm{eV}$) due to intensity borrowing induced by vibronic coupling. In contrast to the quasistationary appearance of the Raman contribution, the stimulated-emission spectrum (b) exhibits an irreversible initial decay on a time scale of about 20 fs, accompanied by a significant red-shift of the emission. As discussed below, the dynamical red-shift and the coherent oscillations of the stimulated emission reflect the ultrafast $S_2 \rightarrow S_1$ internal-conversion process in pyrazine.

Being mainly interested in the dynamics associated with the conical intersection of the S_1 and S_2 excited electronic states, we focus in the following on the excited-state contribution to the pump-probe spectrum. Figures 2 and 3 compare three different excited-state pump-probe signals, namely the integral stimulated-emission spectrum (2b), the time-resolved fluorescence spectrum (3a), and the dispersed stimulated-emission spectrum (3b). As has been discussed above, the integral stimulated-emission spectrum and the time-resolved fluorescence spectrum are rather similar. Because of the ω^3 prefactor, though, the spontaneous emission for low frequencies is somewhat weaker than the stimulated emission. It should be noted that the time-resolved fluorescence spectrum requires only probe pulses of a single color (to clock the upconversion process), while the frequency resolution of the integral transmittance spectrum is given by using probe pulses with different carrier frequencies ω_2. The dispersed transmittance spectrum Fig. 3(b) has been evaluated for two probe carrier frequencies, $\omega_2 = 4.8\,\mathrm{eV}$ and $\omega_2 = 3.4\,\mathrm{eV}$. For emission frequencies $\omega \approx \omega_2$, the dispersed spectrum closely resembles the integral and the fluorescence spectra. Owing to the limited spectral width of 20 fs laser pulses, however, the dispersed transmittance spectrum for a single probe frequency ω_2 reveals only a small fraction of the total emission spectrum. In other words, even when dispersing the transient transmittance spectrum, one still needs probe pulses of several colors to probe the complete emission spectrum. From Figs. 2 and 3 one can conclude that, for the model under consideration, the three different excited-state pump-probe spectra yield essentially equivalent information on the molecular dynamics.

In what follows, we wish to investigate in some more detail the monitoring of the ultrafast excited-state relaxation dynamics, which is exhibited, for

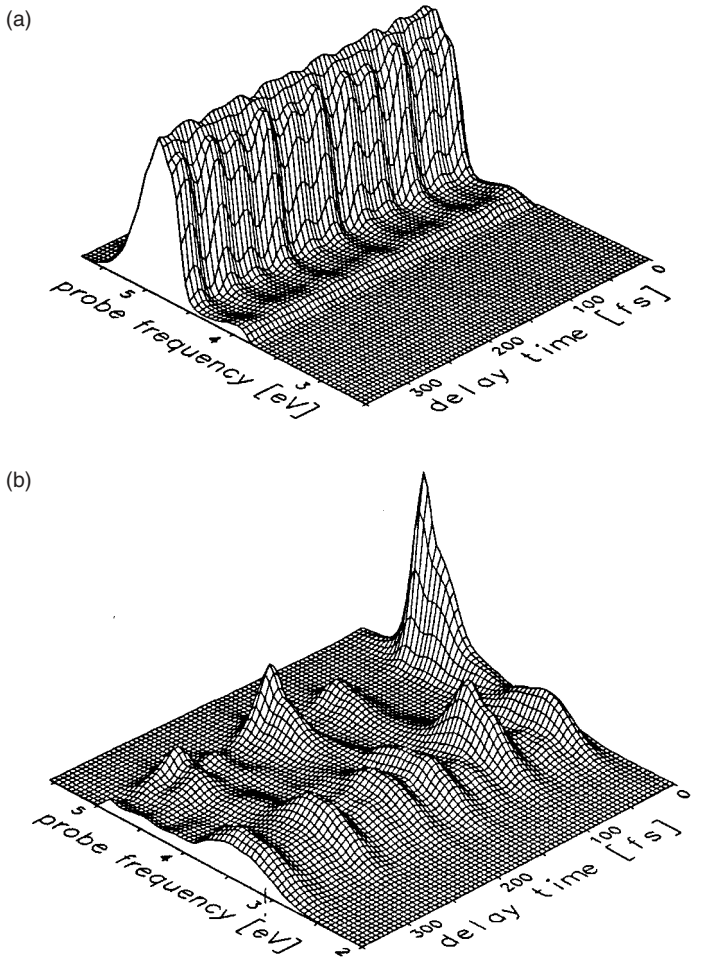

Fig. 2. Decomposition of the integral transient transmittance spectrum into the stimulated-Raman (a) and stimulated-emission (b) contributions.

example, in the stimulated-emission spectrum [Fig. 2b]. After a rapid initial decay within $\approx$ 20fs, the pump-probe spectrum splits up into a dominant red-shifted component and a weaker blue part of the emission. The red-shift of the emission signal reflects the transition from the initially prepared S_2 levels to high vibrational levels of the S_1 surface, from which, according to the Condon principle, emission can be stimulated only to correspondingly

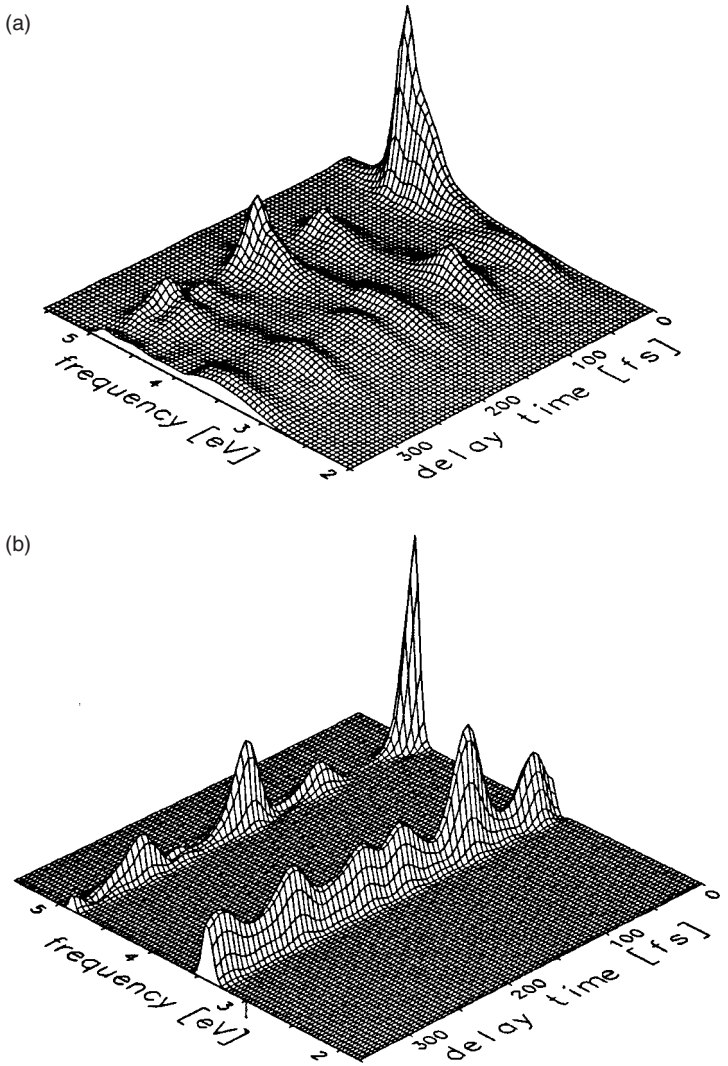

Fig. 3. Time and frequency resolved fluorescence signal (a) and dispersed stimulated-emission spectra (for two probe carrier frequencies, $\omega_2 = 4.8\,\mathrm{eV}$ and $\omega_2 = 3.4\,\mathrm{eV}$) (b). Gaussian laser pulses of 20 fs duration have been assumed.[7]

high levels of S_0.[99] The blue part of the spectrum, on the other hand, reflects the recurrences of the excited-state wave packet to its initial position. This is most easily seen from Eq. (33), which shows that blue probe wavelengths favor stimulated emission into the initial vibrational state $|\mathbf{0}\rangle$. For a blue-shifted probe laser, the autocorrelation function thus gives the main contribution to the stimulated-emission signal.

It has been shown that in the limit of ultrashort laser pulses the stimulated-emission pump-probe signal is proportional to the population probability of the initially excited diabatic state $|\Phi_2^d\rangle$, see Eq. (59) and Refs. 7, 99 and 141. As has been emphasized in Chapter 9, the electronic population probability $P_2(t)$ represents a key quantity in the discussion of internal-conversion processes, as it directly reflects the non-Born–Oppenheimer dynamics (in the absence of vibronic coupling, $P_2(t) = const.$). It is therefore interesting to investigate to what extent this intramolecular quantity can be measured in a realistic pump-probe experiment with finite laser pulses. It is clear from Eq. (33) that the detection of $P_2(t)$ is facilitated if a probe pulse is employed that stimulates a major part of the excited-state vibrational levels into the electronic ground state, that is, the probe laser should be tuned to the maximum of the emission band. Figure 4(a) compares the diabatic population probability $P_2(t)$ with a cut of the stimulated-emission spectrum for $\omega_2 \approx 3.4\,\text{eV}$, i.e. at the center of the red-shifted emission band. Apart from the first 20 fs, where the probe laser is not resonant with the emission [cf. Fig. 2(b)], the pump-probe signal is seen to capture the overall time evolution of electronic population probability. Pump-probe experiments thus have the potential to directly monitor electronic populations and thus non-Born–Oppenheimer dynamics in real time.[7,99]

Figure 4(a) also demonstrates that laser pulses of finite duration tend to smooth out the details of molecular time-dependent observables. To give a representative example of the dependence of the pump-probe signals on the pulse duration, Fig. 4 compares pump-probe signals obtained for pulse durations (a) $\tau_1 = \tau_2 = 20\,\text{fs}$, (b) $\tau_1 = 0,\ \tau_2 = 20\,\text{fs}$, and (c) $\tau_1 = \tau_2 = 40\,\text{fs}$. It is interesting to note that impulsive preparation of the molecular system with a δ-function pulse (b) results only in minor changes of the pump-probe signal. This indicates that in the present case the impulsive limit is virtually achieved by resonant 20 fs pulses, as the pulse duration is shorter than the characteristic (e.g. vibrational) time scales of the molecular system. The

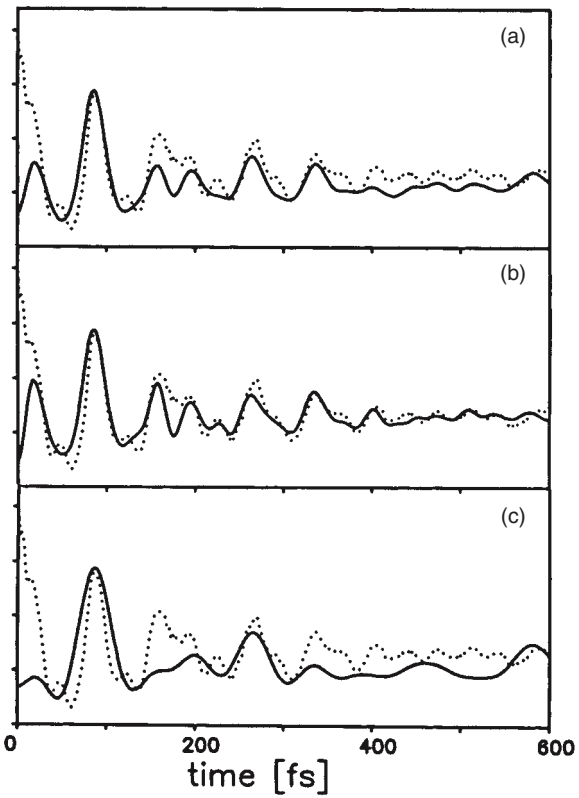

Fig. 4. Integral stimulated-emission signals for the three-mode model of pyrazine (full lines), obtained for pulse durations (a) $\tau_1 = \tau_2 = 20\,\text{fs}$, (b) $\tau_1 = 0, \tau_2 = 20\,\text{fs}$, and (c) $\tau_1 = \tau_2 = 40\,\text{fs}$. It is seen that laser pulses of 20 fs duration are sufficiently short to monitor the time evolution of the diabatic electronic population probability (dotted lines).

time resolution achieved with pulses of 40 fs duration (c) starts to become inadequate to monitor the quantum beats of the electronic population in real time. Nevertheless, the very existence of partial recurrences of the electronic population can still be observed.

5.1.2. *Photoelectron Spectra*

The first numerically exact simulation of a time-resolved photoelectron spectrum for a multidimensional vibronic-coupling system was reported

more than ten years ago by Seel and Domcke.[24] Employing the nonperturbative methodology outlined in Sec. 4.2, these authors performed a nonseparable three-mode model calculation of pyrazine, including the S_2–S_1 vibronic interaction, the I_0, I_1 ionization continua, and the field-matter interaction. Furthermore, they discussed in some detail which electronic and vibrational observables of the molecular system may be monitored by the time-resolved photoelectron spectrum, depending on the selection rules of the model, the energy of the photoelectrons, and the properties of the laser fields. As a representative example from this study, Fig. 5 shows the total ionization yield calculated for a pump-probe experiment employing an ultrashort pump pulse that is resonant to the S_0–S_2 transition and time-delayed probe pulses which are resonant to the S_1–I_0 transition. In this case, the ionization signal reflects the time-dependent population probability of the diabatic S_1 state (see Fig. 4), thus monitoring directly the $S_2 \rightarrow S_1$ internal-conversion process.

Also shown in Fig. 5 are results for the total ionization yield obtained by the semiclassical Franck–Condon approximation[106] introduced in Eqs. (60) and (58). As discussed above, this theory is only valid for sufficiently short probe pulses. While this condition is well satisfied for probe pulse up to ≈20 fs duration [panels (a) and (b)], the approximation is seen to introduce spurious structures in the case of 32 fs pulses [panel (c)]. Since the Franck–Condon approximation reduces the cost of explicit pump-probe simulations to the cost of a standard time-dependent wave-packet propagation, one obtains an overall computational speed-up of about two orders of magnitude compared to the full nonperturbative calculation.

Recent experimental studies on pyrazine by Radloff and coworkers[142] have renewed the interest in a theoretical description of the photoelectron spectroscopy of this system. In the following, we present representative results from an exact quantum-mechanical study[92] that extends the work of Seel and Domcke in several points: (i) New high-level *ab initio* data[127,129] are employed to parameterize the model Hamiltonian. (ii) An additional vibrational mode (ν_{9a}) is included which is known to be important for the $S_2 \rightarrow S_1$ internal conversion process. (iii) The vibronic coupling between the I_0 and I_1 cation states is explicitly taken into account. (iv) To account for the relatively long probe laser pulses used in the experiment, the convolution scheme presented in Eq. (49) is employed.

Figure 6 shows the energy diagram of the electronic states of pyrazine and the laser excitation scheme. In the experiment of Radloff and

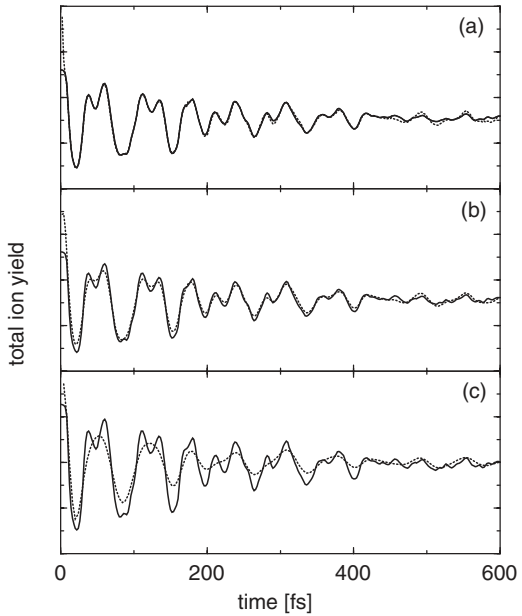

Fig. 5. Total ionization yield as obtained for a three-mode model of pyrazine. Compared are exact results (dotted lines), obtained from a nonperturbative calculation,[24] and approximate results (solid lines), obtained by the classical Franck–Condon approximation.[106] The duration of the probe pulses is (a) $\tau = 4\,\mathrm{fs}$, (b) $\tau = 16\,\mathrm{fs}$, and (c) $\tau = 32\,\mathrm{fs}$.

coworkers,[142] the pump pulse resonantly ($\omega_1 = 4.66\,\mathrm{eV}$) excites the S_2 state of pyrazine, while the probe pulse with frequency $\omega_2 = 6.2\,\mathrm{eV}$ ionizes the molecule. Since the probe laser is not resonant with any electronic transition of ground-state pyrazine, photoinduced ionization is only achieved if the probe follows the pump. Within the approximation of independent electrons, photoionization of the $S_1[^1B_{3u}(n\pi^*)]$ state leads to the ion ground state $I_0[^2A_g(n^{-1})]$, while the first excited ion state $I_1[^2B_{1g}(\pi^{-1})]$ results from ionization of the $S_2[^1B_{2u}(\pi\pi^*)]$ state.

Applying Eq. (39) to this case, the time-resolved photoelectron spectrum can be written as[92]

$$I_{\mathrm{Ion}}(E_k, \Delta t) = I_{11} + I_{22} + I_{12} + I_{21}, \tag{79}$$

$$I_{nm} = \langle \Psi_n^{(2)} | \Psi_m^{(2)} \rangle, \tag{80}$$

$$|\Psi_n^{(2)}\rangle = i \int_{-\infty}^{t} dt' E_2(t') e^{-iH_M(t-t')} \widehat{\mu}_n e^{iH_M(t-t')} |\Psi_P\rangle, \tag{81}$$

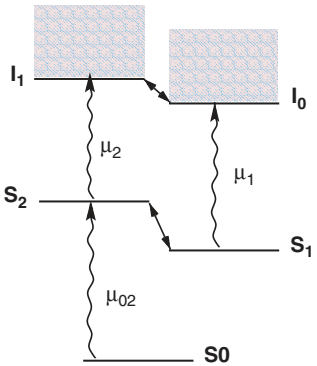

Fig. 6. Energy diagram of the electronic states of pyrazine and laser excitation scheme of the pump-probe experiment considered.

where $|\Psi_n^{(2)}\rangle$ denotes the second-order wave function describing the ionization of the electronic state $|\Phi_n^d\rangle$ $(n = 1, 2)$, and $\widehat{\mu}_n = |\psi_n^{(k)}\rangle\widehat{\mu}\langle\Phi_n^d|$ denotes the corresponding transition dipole operator. The photoelectron spectrum consists of four contributions: The terms I_{11} and I_{22} describe the ionization of the S_1 or the S_2 state of pyrazine, respectively. Furthermore, there are cross terms I_{12} and I_{21} involving both dipole transitions $\widehat{\mu}_1$ and $\widehat{\mu}_2$. These contributions appear as a consequence of the vibronic coupling of the ionic states I_0 and I_1.

Assuming Gaussian laser pulses of 40 fs duration, Fig. 7 displays the time-resolved photoelectron spectrum as obtained for the four-mode model of pyrazine. Shown are the contributions (a) $I_{22}(E_k, \Delta t)$ and (b) $I_{11}(E_k, \Delta t)$ stemming from the ionization of the S_2 and S_1 states of pyrazine, respectively, as well as (c) the total spectrum defined in Eq. (79). The S_2 signal exhibits a pulse-limited onset at $\Delta t = 0$, which is followed by a rapid initial decay on a 20 fs time scale. Within the same time, the S_1 signal is seen to rise. The time-resolved ionization signals therefore clearly monitor the ultrafast $S_2 \rightarrow S_1$ internal-conversion due to the low-lying conical intersection of these states. The total spectrum, on the other hand, is quite complex and requires a careful analysis. This is because the spectra of all contributions overlap and due to the occurrence of the cross-term signals I_{12} and I_{21}. Furthermore, the time-resolved photoelectron spectrum exhibits various frequency-dependent recurrences of the signal,

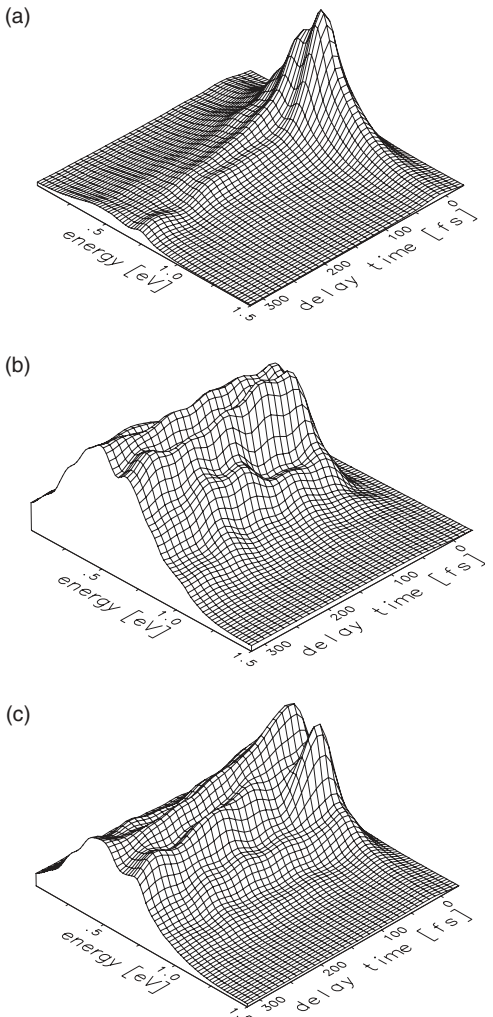

Fig. 7. Time-resolved photoelectron spectrum as obtained for the four-mode model of pyrazine, assuming 40 fs pump and probe pulses. Shown are the contributions (a) $I_{22}(E_k, \Delta t)$ and (b) $I_{11}(E_k, \Delta t)$, stemming from the ionization of the S_2 and S_1 states of pyrazine, respectively, as well as (c) the total spectrum, defined in Eq. (79).

reflecting multidimensional coherent wave-packet motion on the coupled S_1–S_2 potential-energy surfaces.[7,24,130,131]

In order to compare to the experimental data reported by Radloff and coworkers,[142] a duration of 100 fs has been chosen for the probe pulse. At this time resolution, the coherent features of the ionization signal are averaged out. Therefore it is more instructive to consider cuts of the spectrum as shown in Fig. 8 for the delay times (a) 0 fs, (b) 50 fs, and (c) 300 fs. Shown are the contributions pertaining to the S_1 (long dashed lines), the S_2 (short dashed lines), and the cross terms (thin full lines), respectively, as well as the total spectrum (thick full lines). Again, the decay of the S_2 signal and the increase of the S_1 signal can be seen clearly. Moreover, the S_1 signal is seen to undergo a significant red-shift, thus reflecting the vibrational relaxation of the highly excited states in the S_1-state. Interestingly, the cross terms are seen to considerably contribute to the spectral features of the total spectrum, thereby complicating the interpretation of the photoelectron spectrum.

The location of the central peaks of the spectrum as well as the sharp decrease at larger energies is found to be in qualitative agreement with experimental data[142] shown in Fig. 8(d). Furthermore, the 20 fs time scale of the initial $S_2 \rightarrow S_1$ decay found in the simulation can also be deduced from the experimental data. However, the experimental spectrum shows a considerable contribution of photoelectrons with low energy, which is absent in the calculation. Since the inclusion of additional vibrational modes in the calculation is expected to lead to only a slight increase of low-energy electrons, the calculation seems to miss a reaction channel that is present in experiment. A possible explanation for the discrepancy between experiment and theory is the occurrence of auto-ionizing Rydberg states. Multi-photon ionization experiments performed by Ito and coworkers indeed indicate that highly excited Rydberg states and their autoionization may significantly contribute to the ionization spectrum of pyrazine.[143]

Although in the case of pyrazine the interpretation is complicated by cross-term signals and auto-ionizing Rydberg states, the experimental and theoretical investigations nevertheless demonstrate the considerable potential of femtosecond time-resolved photoelectron spectroscopy. As a beautiful example of a more favorable case, Stolow and coworkers have recently presented time-resolved ionization studies on decatetraene.[144] In direct analogy to the discussion presented above, they managed to monitor the $S_2 \rightarrow S_1$ internal conversion associated with a conical intersection in real time.

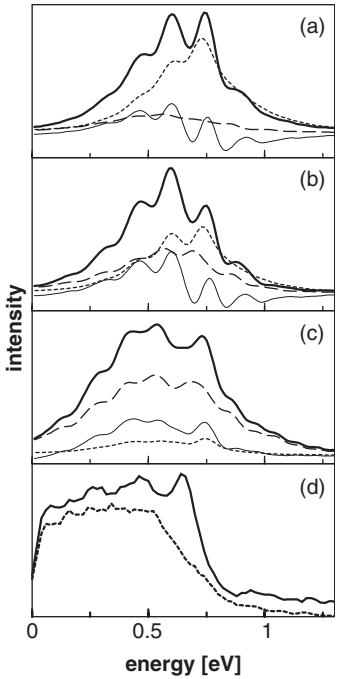

Fig. 8. Cuts of the calculated photoelectron spectrum at delay times (a) 0 fs, (b) 50 fs, and (c) 300 fs, assuming probe pulses of 100 fs duration. Shown are the contributions pertaining to the S_1 (long dashed lines), the S_2 (short dashed lines), and the cross terms (thin full lines), respectively, as well as the total spectrum (thick full lines). (d) The experimental photoelectron spectra at delay times 0 fs (full line) and 300 fs (short dashed line).[142]

5.2. *Time-Resolved Fluorescence for the $\tilde{X}$–$\tilde{A}$ Conical Intersection in NO_2*

In a series of papers, Hirsch, Buenker, Petrongolo and collaborators have determined accurate three-dimensional diabatic potential-energy functions for the conically intersecting $\tilde{X}^2A_1$ and $\tilde{A}^2B_2$ states of NO_2, see Refs. 145 and 146 and references therein. Santoro and Petrongolo have elaborated a detailed picture of the time-dependent wave-packet dynamics of this system initiated by ultrafast excitation of the $\tilde{A}^2B_2$ state.[147] The stationary absorption and emission spectra of NO_2 are discussed in Chapter 16 (see also Chapter 7 and Refs. 7 and 99 for a brief discussion of the

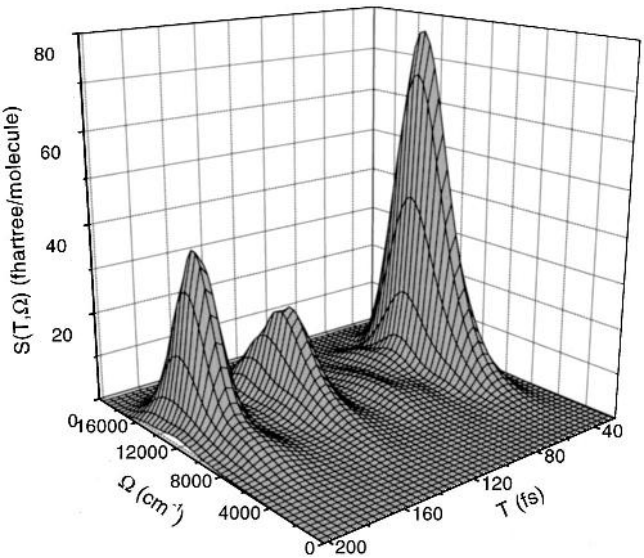

Fig. 9. Time and frequency resolved spontaneous emission spectrum for the $\tilde{X}^2A_1$–$\tilde{A}^2B_2$ conical intersection in NO_2.[71] A duration of 14 fs has been assumed for the pump and gate pulses.

photodetachment spectrum of NO_2^-). The time- and frequency-resolved spontaneous emission of NO_2 has recently been analyzed by Santoro *et al.*[71] within the theoretical framework obtained in Secs. 2.2 and 3.1 above.

A representative result of this work is shown in Fig. 9. A duration of 14 fs has been assumed for both pump pulse and time gate, which is appropriate to resolve the time evolution of the electronic and vibrational dynamics (primary the NO_2 bending mode). The emission is seen to be red-shifted by about 2000 cm^{-1} compared to the absorption maximum (at $\simeq$16 000 cm^{-1}). Figure 10 shows, for comparison, the diabatic (dotted line) and adiabatic (dashed line) populations of the $\tilde{A}^2B_2$ state. It is seen that the time dependence of the TFG SE spectrum correlates very well with the adiabatic population $P_A(t)$ in this example.

For the example of the S_1–S_2 conical intersection in pyrazine it has been found (see above) that the spontaneous and stimulated emission spectra reflect the population probability of the *diabatic* $S_2(\pi\pi^*)$ state to a good approximation. In NO_2, on the other hand, the population probability of

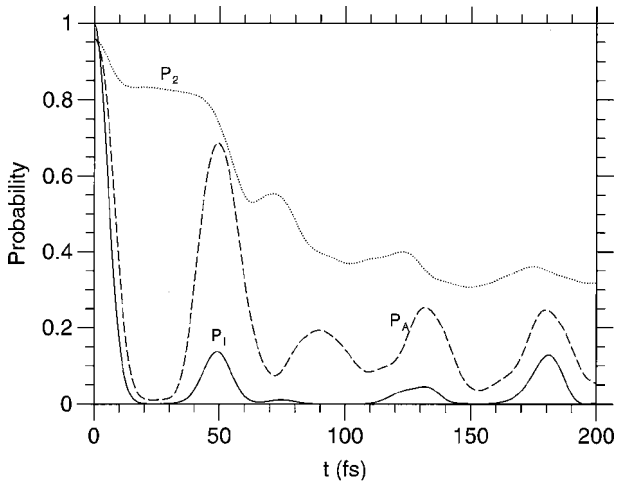

Fig. 10. Diabatic (P_2, dotted line) and adiabatic (P_A, dashed line) electronic population probabilities of the $\tilde{A}$ state for the $\tilde{X}^2A_1$–$\tilde{A}^2B_2$ conical intersection in NO_2.[71] P_I (full line) represents the population probability of the initially-prepared Franck–Condon state.

the *adiabatic* $\tilde{A}^2B_2$ state is detected. The difference arises from the fact that in pyrazine both nonadiabatically coupled excited states can radiate to the ground state, whereas in NO_2 the lower of the nonadiabatically coupled states is the electronic ground state, which cannot emit fluorescence. These findings are in agreement with an earlier analysis by Meyer and Köppel[107] and our results (57) and (59), which show that the frequency-integrated time-resolved fluorescence should reflect the diabatic excited-state population in the so-called external case (both of the coupled states can fluoresce to the ground state), while it should reflect the adiabatic excited-state population probability in the so-called internal case (the fluorescence occurs within nonadiabatically coupled states).

5.3. *A Simple Model of the Photoisomerization of Retinal in Rhodopsin*

As emphasized throughout this book, an important aspect of the ultrafast photodynamics via conical intersections is the fact that only a few degrees of freedom are involved in the process. This finding suggests that, on a subpicosecond time scale, even complex molecular systems may be described in

terms of a highly reduced model system. As an example of this idea, Seidner *et al.* have proposed a simple model of nonadiabatic *cis-trans* photoisomerization which includes the vibronic coupling of the lowest singlet states (S_0, S_1), a large-amplitude torsional mode, as well as one or two accepting modes for the radiationless transition. [25,148] Exact time-dependent wavepacket calculations have been reported, including up to four nuclear degrees of freedom, showing that these models are suitable to reveal basic features of photoisomerization and internal-conversion dynamics.

As an application of this approach, it has recently been suggested to use a vibronically coupled two-mode two-state system to model the photoisomerization of retinal in rhodopsin.[98] Due to its importance for the first step in vision, there has been considerable effort to understand this photoreaction.[149,150] The matrix elements of the molecular Hamiltonian (21) of the model read[98]

$$T = -\frac{1}{2m}\frac{\partial^2}{\partial\varphi^2} - \frac{\omega}{2}\frac{\partial^2}{\partial q^2}, \tag{82}$$

$$W_{nn} = W_n^R(\varphi) + \tfrac{1}{2}\omega q^2 + \delta_{1n}\kappa q, \tag{83}$$

$$W_{01} = W_{10} = \lambda q, \tag{84}$$

where m is the effective mass of the reaction coordinate, while ω and λ denote the frequency and the interstate-coupling of the coupling mode, respectively. According to quantum-chemical calculations[151,152] and resonance Raman experiments,[153,154] it can be assumed that the coupling coordinate mainly reflects the ethylenic stretch mode of the polyene chain. Due to the low symmetry of retinal, this coordinate also exhibits a nonvanishing excited-state gradient κ. The chemical aspects of the model are reflected by the reaction-mode potentials[148]

$$\begin{aligned} W_0^R(\varphi) &= \tfrac{1}{2}V_0(1-\cos\varphi), \\ W_1^R(\varphi) &= E_1 - \tfrac{1}{2}V_1(1-\cos\varphi), \end{aligned} \tag{85}$$

which are drawn in Fig. 11(a) (see also the cover illustration of this book). Note that the excited-state potential $W_1^R(\varphi)$ is inverted, i.e. the upper diabatic electronic state for $\varphi = 0$ (*cis* configuration) becomes the lower one for $\varphi = \pi$ (*trans* configuration). The isomerization potentials (85) are parameterized such that the experimentally measured energy relations of the photoreaction are reproduced, that is, the energy storage of the photoreaction ($\Delta E = 32\,\mathrm{kcal/mol}$) and the center wavelengths of the *cis* and

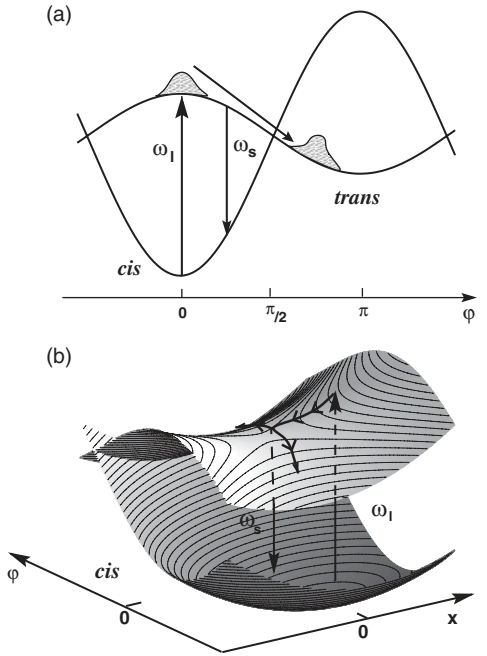

Fig. 11. Adiabatic potential-energy surfaces (PESs) of the two-state model of the *cis–trans* isomerization in rhodopsin. (a) Cut of the PESs along the reaction coordinate φ. Upon vertical excitation by a laser of frequency ω_l, a vibrational wave packet is prepared which gives rise to transient emission of frequency ω_s. (b) Schematic representation of the multidimensional PESs as a function of the reaction coordinate φ and a collective Condon-active coordinate x.

trans absorption bands $\lambda_{cis} = 500\,\text{nm}$ and $\lambda_{trans} = 570\,\text{nm}$.[155] The effective mass m pertaining to the motion along φ can be obtained by requiring that isomerization takes place within 200 fs as observed in time-resolved experiments. It should be stressed that the thus defined reaction coordinate does not necessarily correspond to a specific internal coordinate of retinal (e.g. the C_{11}=C_{12} torsional mode) but collectively accounts for the energy relations of the reaction. The effect of the protein environment is thereby included in the parameters m, E_1, V_0, V_1 of the model.

5.3.1. *Transmittance Spectra*

Employing the nonperturbative methodology outlined in Sec. 4.1, numerically exact simulations of the photoinduced dynamics and various optical

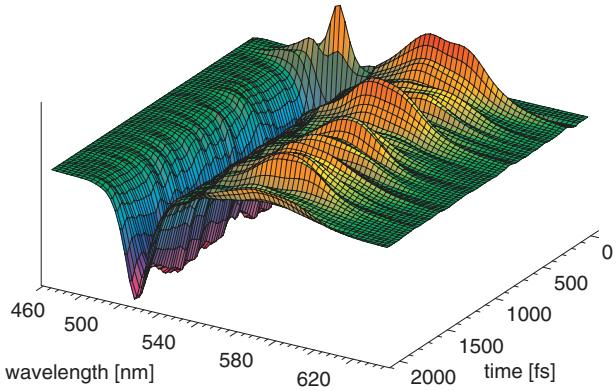

Fig. 12. Simulated transient absorption spectrum as obtained for the two-mode model of the *cis-trans* isomerization in rhodopsin. The spectral band at 500 nm reflects the dynamics of the reactants, while the 570 nm band reflects the absorbance of the photoproducts.

spectra have been reported for this two-state two-mode model.[98] The most challenging application of the model is the explanation of the transient absorption experiments on rhodopsin.[156,157] In the experiment of Wang *et al.*,[157] rhodopsin was excited by a 35 fs pump pulse at 500 nm and transient changes in absorption were measured from 450–640 nm by employing 10 fs probe pulses. Figure 12 shows the theoretical simulation of this experiment, as obtained for the proposed model of the *cis-trans* isomerization in rhodopsin. In agreement with the experiment, the time- and frequency-resolved spectrum consists of two spectral bands centered at 500 and 570 nm. For early times ($t \approx 0$), the signal at 500 nm is dominated by a strong (positive-going) excited-state absorption feature at 500 nm which changes into a (negative-going) bleach signal after $t \gtrsim 50$ fs. For larger times, ground-state bleach, stimulated emission, as well as excited-state absorption contribute to the 500 nm band, which therefore mainly reflects the dynamics of the *cis* reactant. The signal at 570 nm, on the other hand, reaches its first maximum at ≈200 fs, thus reflecting the onset of the *trans* photoproduct absorbance. Both parts of the spectrum are seen to exhibit a pronounced beating with a period of ≈ 500 fs, corresponding to a frequency of $\approx 60\,\mathrm{cm}^{-1}$.

As a comparison of experiment and theory, Fig. 13 shows cuts of the transient absorption spectrum at (a) 500 nm and (b) 570 nm. The

simulations clearly reproduce the $60\,\mathrm{cm}^{-1}$ oscillations, which are seen to be shifted in phase by 180° for the two signals. This beating is superimposed by high-frequency oscillations which are qualitatively matched by the calculation, e.g. the simulation for 570 nm reproduces the two intermediate maxima at $t \approx 400$ and 1000 fs. The deviations between experiment and theory observed for $t \gtrsim 1500$ fs indicate that at these times additional degrees of freedom not considered in the model need to be included. To explain the femtosecond spectra in terms of the isomerization dynamics of the molecular model employed, Fig. 13(c) shows the time-dependent probability of the system to be in the *cis* configuration of the upper adiabatic electronic state $[P_1^{cis}(t)]$ and in the *trans* configuration of the lower adiabatic state $[P_0^{trans}(t)]$, respectively. The similarity between the intramolecular quantities and the simulated spectra clearly suggests that the 500 and 570 nm signals monitor the dynamics of the reactants and photoproducts, respectively. In particular, the analysis shows that the $60\,\mathrm{cm}^{-1}$ oscillations of the transient absorption signal can be attributed to quasiperiodic motion along the *diabatic* reaction potential curve W_1^R. Hereby the traveling wave packet causes photoproduct-absorbance in the S_0 *trans* configuration and an excited-state absorption from the S_1 *cis* configuration that is shifted in phase by 180°. Furthermore, the theory reproduces the high-frequency (170 and $240\,\mathrm{cm}^{-1}$) components of the transient signals, which are a consequence of the bifurcations of the wave packet. It should be stressed that the vibrational frequencies thus established have not been assumed beforehand, but are merely a consequence of the (independently determined) parameters of the reaction potentials. In conclusion, it has been shown that — even for a complex biophysical system such as rhodopsin — the subpicosecond dynamics associated with a conical intersection can be modeled in terms of a simple low-dimensional system.

5.3.2. *Fluorescence Spectra*

Although the model described above has been found to qualitatively reproduce femtosecond transient transmittance experiments on rhodopsin,[157] it cannot reproduce the experimental fluorescence and resonance Raman spectra of rhodopsin.[153,154,158] This is because the Raman spectra exhibit a number of vibrational modes that are not included in the model. While these modes may not directly be involved in the photochemical reaction

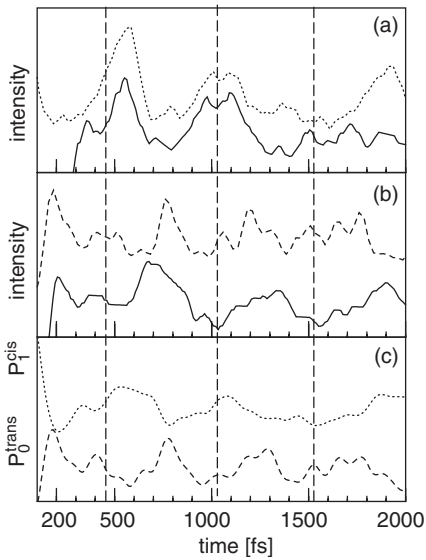

Fig. 13. Comparison of calculated and experimental (full lines, adopted from Ref. 157) transient absorbance of rhodopsin at (a) 500 nm and (b) 570 nm. An exponential component has been subtracted from the 500 nm signals in order to facilitate the representation of the oscillations. (c) Time-dependent probability of the system to be in the *cis* configuration of the upper adiabatic electronic state (dotted line) and in the *trans* configuration of the lower adiabatic state (dashed line), respectively. The vertical dashed lines mark the prominent beating with a period of $\approx$ 500 fs.

monitored in the time-resolved experiments, they obviously contribute to the Raman spectra and therefore also to the fluorescence emission. In order to account for these effects, the Condon-active vibrational modes need to be included in an appropriate theory of secondary emission. To this end, we adopt the harmonic ansatz

$$H_B = \sum_{n=0,1} |\Phi_n^d\rangle\langle\Phi_n^d| \sum_j \tfrac{1}{2}\omega_j(p_j^2 + x_j^2) + \delta_{n1} c_j x_j, \qquad (86)$$

whereby the frequencies ω_j and excited-state gradients c_j are chosen to reproduce the 23 additional resonance Raman excitations observed in experiment. Since about twenty Raman-active modes of retinal should be considered and because of the nonseparability of the vibronic-coupling Hamiltonian H_M, it is clear that the resulting total problem $H = H_M + H_B$ cannot be treated quantum-mechanically exactly. Therefore, we pursue the

following strategy. The isomerization Hamiltonian H_M is meant to account for the strongest interactions in the system which predominantly determine the initial nonadiabatic photochemical reaction. The dynamics of these degrees of freedom is therefore treated exactly, while the effects due to weakly coupled vibrational modes of the Hamiltonian H_B may be taken into account in an approximate manner via a time-dependent Hartree (or time-dependent self-consistent-field) ansatz.[159–161] Although it is clear that this quite simple approximation breaks down for large coupling and propagation times, it may be expected to provide a qualitative description of the short-time dynamics of the system.[162] Alternatively, it has been suggested to account for the additional degrees of freedom within a Redfield-type theory[133,134,163] and by various mixed quantum-classical methods.[164,165]

Employing this extended model, the experimental CW absorption and resonance Raman spectra of rhodopsin have qualitatively been reproduced.[162] Being interested in the time evolution of the excited-state dynamics, however, it is of particular interest to consider the time- and frequency-resolved fluorescence spectrum of the system. In the following we restrict ourselves to the discussion of the impulsive emission spectrum $\propto P^{\delta}(\omega, \Delta t)$, defined in Eq. (45). Neglecting the specific effects of the detector, this idealized time- and frequency-resolved spectrum is independent of laser-field properties and therefore reflects directly the excited-state dynamics of the system. Figure 14 shows the impulsive emission spectrum as obtained for (a) the two-mode and (b) the 25-mode model of rhodopsin. Both signals exhibit an ultrafast initial decay within 200 fs which is followed by prominent recurrences of the emission with a period of ≈500 fs. As discussed above, these recurrences reflect coherent wave-packet motion along the reaction-mode potential $W_1^R(\varphi)$. Compared to the two-mode model, the recurrences of the 25-mode model are somewhat shifted in time and decay on a picosecond time scale. In particular, the emission of spectrum (b) is red-shifted to spectrum (a) by $\approx 1000\,\mathrm{cm}^{-1}$, which reflects the reorganization energy $E_R = \sum_j c_j^2/2\omega_j = 1200\,\mathrm{cm}^{-1}$ of the additional Condon-active modes.

It is noted, however, that the experimental CW fluorescence spectrum exhibits a still larger Stokes shift of $\approx 4500\,\mathrm{cm}^{-1}$.[166] This finding indicates that an appropriate theoretical description of the femtosecond isomerization in rhodopsin needs to account for the interaction of retinal

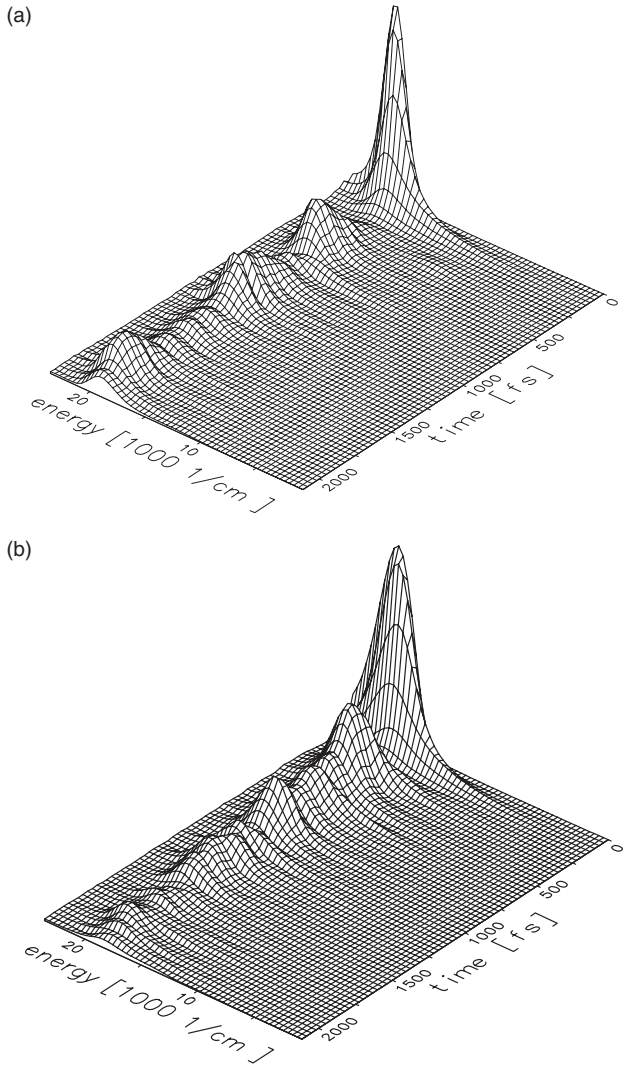

Fig. 14. Impulsive time- and frequency resolved fluorescence spectra as obtained for (a) the two-mode model and (b) the 25-mode model of rhodopsin. The prominent recurrences of the emission reflect quasiperiodic wave-packet motion on coupled adiabatic potential-energy surfaces.

with the protein environment in a microscopic manner. *Ab initio* molecular-dynamics simulations of organic chromophores in polar solvents have shown that excited-state energies of the solvated chromophore can be significantly shifted compared to isolated-molecule conditions.[167,168] Hence the averaging over solvent conformations does not only lead to a significant inhomogeneous broadening of the spectra, but may also result in a large solvent-induced Stokes shift. To account for these effects, we assume that the low-frequency protein motion can also be modeled by the harmonic ansatz (86). Frequencies ω_j and coupling constants c_j are chosen according to the distribution for an Ohmic bath with a overall chromophore-bath coupling $\alpha = 16.3$ and a cut-off frequency $\omega_C = 400\,\mathrm{cm}^{-1}$. Employing this "spectroscopic model" of the photoisomerization of retinal in rhodopsin, we have calculated various absorption and emission spectra.[162] As a representative example, Fig. 15 shows the impulsive time- and frequency-resolved fluorescence spectrum. Again, the signal exhibits a rapid initial decay within $\approx$100 fs which is followed by recurrences of the emission. Compared to the case of the two- and 25-mode models shown in Fig. 14, however, the emission exhibits a much larger Stokes shift of about $4000\,\mathrm{cm}^{-1}$. Furthermore, the overall emission decays faster due to the larger level density of the spectroscopic model.

To illustrate the initial time evolution exhibited by the multidimensional model of rhodopsin, Fig. 11(b) shows a two-dimensional representation of the potential-energy surfaces consisting of the reaction coordinate φ and the coordinate $x = \{x_j\}$ which collectively represents all Condon-active modes. The coupling coordinate q is set to zero, i.e. the two-dimensional adiabatic potential-energy surfaces of the ground and excited electronic state intersect via an one-dimensional crossing seam. Apart from the optical transitions indicated by bold arrows, the figure also displays the minimum-energy path of the photoisomerization reaction. Starting out in the Franck–Condon region, the minimum-energy path follows the slope on the upper adiabatic potential-energy surface. Since the descent is flat along φ and steep along x, the minimum-energy path first follows the direction of the Condon-active modes, before it continues along the isomerization coordinate. This indicates that the red-shifted maximum of the fluorescence spectrum is caused by the energy lowering of $\sum_j c_j^2/2\omega_j$ due to the Condon-active modes.

It is interesting to compare this "static" picture of over-damped nuclear motion along the minimum-energy path with the true *dynamical* time

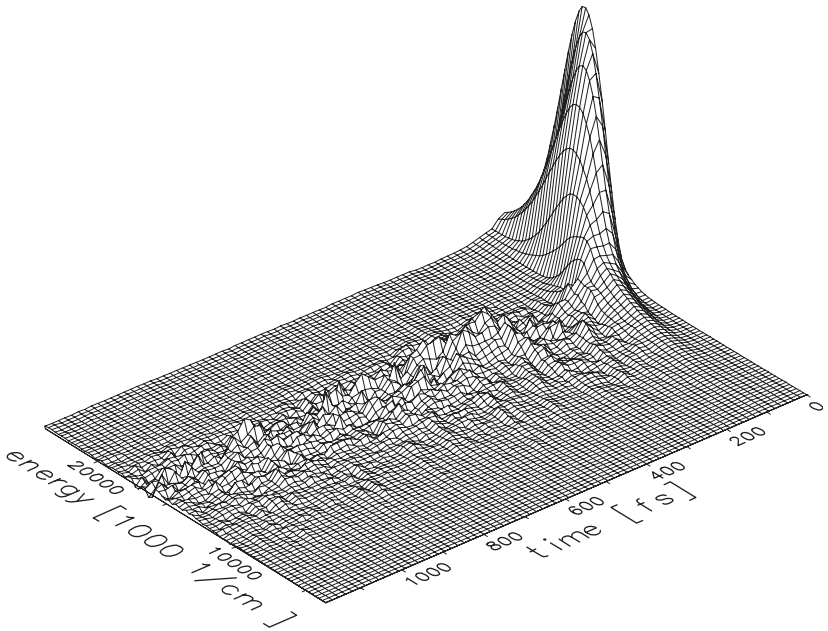

Fig. 15. Impulsive time- and frequency resolved fluorescence spectra as obtained for the 25-mode model of rhodopsin coupled to a harmonic bath.

evolution of the molecular system. Explicit calculations of the time-dependent excited-state wave function (data not shown) reveal that the wave packet is hardly ever found on the minimum-energy path.[169] Following excitation to the Franck–Condon region, it rather performs several pronounced oscillations along the x coordinate on the upper adiabatic potential-energy surface, before it disappears in the photochemical funnel of the intersecting potential-energy surfaces. Similar results have also been obtained in *ab initio* molecular-dynamics simulations of stilbene.[170] Due to the highly idealized topology of the potential-energy surfaces in our model, nevertheless, the wave packet follows the minimum-energy path at least on the average.

6. Conclusions

We have outlined the theoretical description of femtosecond time-resolved spectroscopy of the photophysical and photochemical dynamics at conical

intersections. Because of their potential to directly observe the ultrafast excited-state processes, we have focused on transient transmittance, time-resolved fluorescence, and time-resolved ionization spectroscopy.

A molecular system with a conical intersection represents a multidimensional nonseparable problem, which hampers the calculation of nonlinear spectra when using the established formalism of multi-time correlation functions. To calculate femtosecond time-resolved spectra for these systems, we have discussed several strategies, employing both the perturbative as well as the nonperturbative approach. In the general case of complicated spectroscopic processes with several, possibly overlapping, laser fields, it has proven advantageous to employ the nonperturbative formalism for the calculation of femtosecond time-resolved spectra. The nonperturbative approach allows us to directly simulate a given spectroscopic experiment. Considering simple spectroscopic processes, such as transient absorption, emission, or ionization with nonoverlapping and low-intensity laser pulses, a perturbative calculation is often advantageous. The perturbative formulation allows us to first calculate the impulsive response of the system, and subsequently evaluate spectroscopic signals for various probe pulse properties via convolution techniques. In particular, it has been shown that the convolution scheme also allows us to circumvent the cumbersome discretization of the electron continuum, thus providing an efficient way to calculate photoelectron spectra. Furthermore, an approximate evaluation of the perturbative formulation using the semiclassical Franck–Condon formulation has been shown to afford a computationally inexpensive and often accurate calculation of femtosecond pump-probe spectra.

To illustrate the practical application of the theoretical formalism, we have discussed several representative examples that demonstrate the potential of femtosecond time-resolved spectroscopy. Since typically only a few degrees of freedom (say, 2–4) are involved in the ultrafast photodynamics via a conical intersection, explicit simulations of spectroscopic experiments for polyatomic molecules are nowadays possible on a routine basis. As an example of a state-of-the-art simulation of a femtosecond experiment on a polyatomic system, we have presented "first-principles" calculations of the time-resolved photoelectron spectra of pyrazine. Although in this case the interpretation was found to be quite complicated, the investigations nevertheless demonstrated the considerable potential of a joint experimental/theoretical study of the dynamics at conical intersections. Employing

collective coordinates, moreover, it has been shown that — even for a complex biophysical system such as rhodopsin — the femtosecond dynamics and spectra associated with a conical intersection can be modeled in terms of a simple low-dimensional system.

Acknowledgments

We are grateful to our students that have been involved in these studies, in particular, Stefan Dilthey, Susanne Hahn, Matthias Seel, and Luis Seidner. This work has been supported by the Deutsche Forschungsgemeinschaft and the Fonds der Chemischen Industrie.

References

1. J. Michl and V. Bonačić-Koutecký, *Electronic Aspects of Organic Photochemistry* (Wiley, New York, 1990).
2. M. Klessinger and J. Michl, *Excited States and Photochemistry of Organic Molecules* (VCH, New York, 1995).
3. S. Xantheas, S. T. Elbert and K. Ruedenberg, *Theor. Chim. Acta* **78**, 365 (1991).
4. F. Bernardi, M. Olivucci and M. A. Robb, *Chem. Soc. Rev.* **25**, 321 (1996).
5. R. Schinke, *Photodissociation Dynamics* (University Press, Cambridge, 1993).
6. D. Yarkony, *J. Phys. Chem.* **100**, 18612 (1996).
7. W. Domcke and G. Stock, *Adv. Chem. Phys.* **100**, 1 (1997).
8. P. F. Barbar, W. H. Knox, G. A. Mourou and A. H. Zewail, Eds., *Ultrafast Phenomena IX* (Springer, Heidelberg, 1994).
9. T. Elsaesser, J. G. Fujimoto, D. A. Wirsma and W. Zinth, Eds., *Ultrafast Phenomena XI* (Springer, Heidelberg, 1998).
10. S. Mukamel, *Principles of Nonlinear Optical Spectroscopy* (University Press, Oxford, 1995).
11. W. Pollard and R. A. Mathies, *Ann. Rev. Phys* **43**, 497 (1992).
12. S. H. Lin, B. Fain and N. Hamer, *Adv. Chem. Phys.* **79**, 133 (1990).
13. S. Mukamel, *Ann. Rev. Phys. Chem.* **41**, 647 (1990).
14. B. Grimberg, V. Lozovoy, M. Dantus and S. Mukamel, *J. Phys. Chem.* **A106**, 697 (2002).
15. M. Mitsunaga and C. L. Tang, *Phys. Rev.* **A35**, 1720 (1987).
16. Y. J. Yan, L. E. Fried and S. Mukamel, *J. Phys. Chem.* **93**, 8149 (1989).
17. W. B. Bosma, Y. J. Yan and S. Mukamel, *J. Chem. Phys.* **93**, 3863 (1990).
18. B. Fain, S. H. Lin and V. Khidekel, *Phys. Rev.* **A47**, 3222 (1993).
19. J. M. Jean, *J. Chem. Phys.* **101**, 10464 (1994).
20. Y. Yan, W. Zhang and J. Che, *J. Chem. Phys.* **106**, 2212 (1997).

21. G. Stock and W. Domcke, *J. Opt. Soc. Am.* **B7**, 1970 (1990).
22. G. Stock and W. Domcke, *J. Chem. Phys.* **B7**, 1970 (1990).
23. Y. Shen, *The Principles of Nonlinear Optics* (Wiley, New York, 1984).
24. M. Seel and W. Domcke, *J. Chem. Phys.* **95**, 7806 (1991).
25. L. Seidner, G. Stock and W. Domcke, *J. Chem. Phys.* **103**, 3998 (1995).
26. B. Wolfseder, L. Seidner, G. Stock and W. Domcke, *Chem. Phys.* **217**, 275 (1997).
27. T. Seideman, *J. Chem. Phys.* **107**, 7859 (1997).
28. S. Williams and D. Imre, *J. Chem. Phys.* **92**, 6636 (1988).
29. H. Metiu and V. Engel, *J. Opt. Soc. Am.* **B7**, 1709 (1990).
30. H. Mahr and M. D. Hirsch, *Opt. Commun.* **13**, 96 (1975).
31. A. Mokhtari, A. Chebira and J. Chesnoy, *J. Opt. Soc. Am.* **B7**, 1551 (1990).
32. T. Dunn, I. Walmsley and S. Mukamel, *Phys. Rev. Lett.* **74**, 884 (1995).
33. I. V. Rubtsov, H. Shirota and K. Yoshihara, *J. Phys. Chem.* **A103**, 1801 (1999).
34. L. R. Khundkar and A. H. Zewail, *Ann. Rev. Phys. Chem.* **41**, 15 (1990).
35. T. Baumert, B. Bühler, R. Thalweiser and G. Gerber, *Phys Rev. Lett.* **64**, 733 (1990).
36. S. Rutz, K. Kobe, H. Kühling, E. Schreiber and L. Wöste, *Z Physik* **D26**, 276 (1993).
37. J. M. Smith, C. Lakshminarayan and J. L. Knee, *J. Chem. Phys.* **93**, 4475 (1990).
38. J. Purnell, S. Wei, S. A. Buzza and A. W. Castleman, *J. Phys. Chem.* **97**, 12530 (1993).
39. A. P. Baronavski and J. C. Owrutsky, *Chem. Phys. Lett.* **221**, 419 (1994).
40. A. P. Baronavski and J. C. Owrutsky, *J. Phys. Chem.* **99**, 10077 (1995).
41. W. Radloff, T. Freudenberg, H.-H. Ritze, V. Stert, K. Weyers and F. Noak, *Chem. Phys. Lett.* **245**, 400 (1995).
42. C. C. Hayden and D. W. Chandler, *J. Phys. Chem.* **99**, 7897 (1995).
43. C. Hayden and A. Stolow, in *Photoionization and Photodetachment*, Ed. C.-Y. Ng (World Scientific, Singapore, 1999), p. 91.
44. C. Schick and P. Weber, *J. Phys. Chem.* **A105**, 3735 (2001).
45. J. Song, M. Tsubouchi and T. Suzuki, *J. Chem. Phys.* **115**, 8810 (2001).
46. D. Neumark, *Ann. Rev. Phys. Chem.* **52**, 255 (2001).
47. H. Okamoto, *J. Phys. Chem.* **A104**, 4182 (2000).
48. W. Kwok, C. Ma, D. Phillips, P. Matousek, A. Parker and M. Towrie, *J. Phys. Chem.* **A104**, 4188 (2000).
49. D. A. Wiersma, Ed., *Femtosecond Reaction Dynamics* (North Holland, Amsterdam, 1994).
50. C. De Schreyver *et al.*, Eds., *Femtochemistry* (Wiley-VCH, Weinheim, 2001).
51. C. V. Shank and E. P. Ippen, *Appl. Phys. Lett.* **26**, 62 (1975).
52. J. Chesnoy and A. Mokhtari, *Phys. Rev.* **A38**, 3566 (1988).
53. M. J. Rosker, F. W. Wise and C. L. Tang, *Phys. Rev. Lett.* **57**, 321 (1986).

54. H. L. Fragnito, J. Y. Bigot, P. C. Becker and C. V. Shank, *Chem. Phys. Lett.* **160**, 101 (1989).
55. N. F. Scherer, A. Mantro, L. D. Ziegler, M. Du, R. J. Carlson, J. A. Cina and G. R. Fleming, *J. Chem. Phys.* **96**, 4180 (1992).
56. W. P. de Boeij, M. S. Pshenichnikov and D. A. Wiersma, *Chem. Phys. Lett.* **238**, 1 (1995).
57. A. Icsevgi and W. E. Lamb, *Phys. Rev.* **185**, 517 (1969).
58. F. Bloch and A. Siegert, *Phys. Rev.* **57**, 522 (1940).
59. G. Stock and W. Domcke, *Chem. Phys.* **124**, 227 (1988).
60. G. Stock and W. Domcke, *Phys. Rev.* **A45**, 227 (1992).
61. R. Heather and H. Metiu, *J. Chem. Phys.* **90**, 6903 (1989).
62. S. H. Lin, B. Fain and C. Y. Yeh, *Phys. Rev.* **A41**, 2718 (1990).
63. M. Hayashi *et al.*, *J. Phys. Chem.* **A102**, 4256 (1998).
64. J. Lu, F. Shao, K. Fan and S. Du, *J. Chem. Phys.* **114**, 3373 (2001).
65. F. Shuang, C. Yang and Y. Yan, *J. Chem. Phys.* **114**, 3868 (2001).
66. L. W. Ungar and J. A. Cina, *Adv. Chem. Phys.* **100**, 171 (1997).
67. J. H. Eberly and K. Wódkiewicz, *J. Opt. Soc. Am.* **67**, 1252 (1977).
68. V. Wong and I. Walmsley, *J. Opt. Soc. Am.* **B12**, 1491 (1995).
69. P. Kowalczyk, C. Radzewicz, J. Mostowski and I. A. Walmsley, *Phys. Rev.* **A42**, 5622 (1990).
70. A. Zucchetti, W. Vogel, D.-G. Welsch and I. Walmsley, *Phys. Rev.* **A60**, 2716 (1999).
71. F. Santoro, C. Petrongolo and A. Lami, *J. Chem. Phys.* **113**, 4073 (2000).
72. M. Gelin, A. Pisliakov and W. Domcke, *Phys. Rev.* **A65**, 062507 (2002).
73. S. Mukamel, C. Ciordas-Ciurdariu and V. Khidekel, *IEEE J. Quantum. Electron.* **32**, 1278 (1996).
74. S. Mukamel, C. Ciordas-Ciurdariu and V. Khidekel, *Adv. Chem. Phys.* **101**, 345 (1997).
75. G. S. Agrawal, in *Springer Tracts in Modern Physics* (Springer-Verlag, Berlin, 1984), Vol. 70.
76. T. Rose, M. J. Rosker and A. H. Zewail, *J. Chem. Phys.* **88**, 6672 (1988).
77. T. Rose, M. J. Rosker and A. H. Zewail, *J. Chem. Phys.* **91**, 7415 (1989).
78. M. Schmitt, G. Knopp, A. Materny and W. Kiefer, *Chem. Phys. Lett.* **280**, 339 (1997).
79. K. Fuke and R. Takasu, *Bull. Chem. Soc. Jpn.* **68**, 3309 (1995).
80. S. Trushin, W. Fuß, T. Schikarski, W. Schmid and K. Kompa, *J. Chem. Phys.* **106**, 9386 (1997).
81. C. Meier and V. Engel, *Chem. Phys. Lett.* **212**, 691 (1993).
82. A. Assion, M. Geisler, J. Helbing, V. Seyfried and T. Baumert, *Phys. Rev.* **A54**, 4605 (1996).
83. V. Stert, W. Radloff, C. Schulz and I. Hertel, *Eur. Phys. J.* **D5**, 97 (1999).
84. V. Engel and H. Metiu, *J. Chem. Phys.* **90**, 6116 (1989).
85. V. Engel and H. Metiu, *J. Chem. Phys.* **91**, 1596 (1989).

86. V. Engel, *Chem. Phys. Lett.* **178**, 130 (1991).
87. K. Müller-Dethlefs and E. W. Schlag, *Ann. Rev. Phys. Chem.* **42**, 109 (1991).
88. Y. Arasaki, K. Takatsuka, K. Wang and V. McKoy, *J. Chem. Phys.* **112**, 8871 (2000).
89. T. Seideman, *Ann. Rev. Phys. Chem.* **53**, 41 (2002).
90. W. H. Louisell, *Quantum Statistical Properties of Radiation* (Wiley, New York, 1973).
91. W. Pollard, S.-Y. Lee and R. A. Mathies, *J. Chem. Phys.* **92**, 4012 (1990).
92. S. Hahn and G. Stock, *J. Phys. Chem.* **105**, 2626 (2001).
93. M. Seel and W. Domcke, *Chem. Phys.* **151**, 59 (1991).
94. S. Hahn and G. Stock, *Chem. Phys. Lett.* **296**, 137 (1998).
95. M. R. Wall and D. Neuhauser, *J. Chem. Phys.* **102**, 8011 (1995).
96. V. A. Mandelshtam and H. S. Taylor, *Phys. Rev. Lett.* **78**, 3274 (1997).
97. V. A. Mandelshtam and H. S. Taylor, *J. Chem. Phys.* **107**, 6756 (1997).
98. S. Hahn and G. Stock, *Phys. Chem. Chem. Phys.* **3**, 2331 (2001).
99. G. Stock, R. Schneider and W. Domcke, *J. Chem. Phys.* **90**, 7184 (1989).
100. M. Braun, C. Meier and V. Engel, *J. Chem. Phys.* **103**, 7907 (1995).
101. M. Braun, C. Meier and V. Engel, *J. Chem. Phys.* **105**, 530 (1996).
102. R. Zadoyan, Z. Li, C. C. Martens and V. A. Apkarian, *J. Chem. Phys.* **101**, 6648 (1994).
103. M. Sterling, R. Zadoyan and V. A. Apkarian, *J. Chem. Phys.* **104**, 6497 (1996).
104. Y.-C. Shen and J. A. Cina, *J. Chem. Phys.* **110** 9793 (1999).
105. M. Lax, *J. Chem. Phys.* **20**, 1752 (1952).
106. S. Dilthey, S. Hahn and G. Stock, *J. Chem. Phys.* **112**, 4910 (2000)
107. H.-D. Meyer and H. Köppel, *J. Chem. Phys.* **81**, 2605 (1984).
108. A. Hammerich, R. Kosloff and M. Ratner, *J. Chem. Phys.* **97**, 6410 (1992).
109. G. Ebel and R. Schinke, *J. Phys. Chem.* **101**, 1865 (1994).
110. S. Meyer and V. Engel, *Appl. Phys.* **B71**, 293 (2000).
111. U. Banin, A. Bartana, S. Ruhman and R. Kosloff, *J. Chem. Phys.* **101**, 8461 (1994).
112. R. Burkey and C. Cantrell, *J. Opt. Soc. Am.* **B2**, 451 (1985).
113. J. Sochön and H. Köppel, *J. Phys. Chem.* **A103**, 8579 (1999).
114. J. Stoer and R. Bulirsch, *Einführung in die Numerische Mathematik II* (Springer, Berlin, 1978), second edn.
115. A. Dobbyn and J. Hutson, *J. Phys. Chem.* **98**, 11428 (1994).
116. E. Charron and A. Suzor-Weiner, *J. Chem. Phys.* **108**, 3922 (1998).
117. C. Meier, V. Engel and U. Manthe, *J. Chem. Phys.* **109**, 36 (1998).
118. M. Hartmann, J. Pittner, V. Bonacic-Kouteckey, A. Heidenreich and J. Jortner, *J. Chem. Phys.* **108**, 3096 (1998).
119. R. Mitrik, M. Hartmann, B. Stranca, V. Bonacic-Koutecky and P. Fantucci, *J. Phys. Chem.* **A105**, 8892 (2001).

120. M. Hartmann, J. Pittner and V. Bonacic-Koutecky, *J. Chem. Phys.* **114**, 2106 (2001).
121. S. Althorpe and T. Seideman, *J. Chem. Phys.* **110**, 147 (1999).
122. T. Seideman, *J. Chem. Phys.* **113**, 1677 (2000).
123. Y. Arasaki, K. Takatsuka, K. Wang and V. McKoy, *J. Chem. Phys.* **114**, 7941 (2001).
124. Y. Suzuki, M. Stener and T. Seideman, *J. Chem. Phys.* **118**, 4432 (2003).
125. R. Schneider and W. Domcke, *Chem. Phys. Lett.* **150**, 235 (1988).
126. L. Seidner, G. Stock, A. L. Sobolewski and W. Domcke, *J. Chem. Phys.* **96**, 5298 (1992).
127. C. Woywod, W. Domcke, A. L. Sobolewski and H.-J. Werner, *J. Chem. Phys.* **100**, 1400 (1994).
128. G. Stock, C. Woywod, W. Domcke, T. Swinney and B. S. Hudson, *J. Chem. Phys.* **103**, 6851 (1995).
129. L. Seidner, W. Domcke and W. von Niessen, *Chem. Phys. Lett.* **205**, 117 (1993).
130. R. Schneider, W. Domcke and H. Köppel, *J. Chem. Phys.* **92**, 1045 (1990).
131. U. Manthe and H. Köppel, *J. Chem. Phys.* **93**, 345, 1658 (1990).
132. G. A. Worth, H.-D. Meyer and L. S. Cederbaum, *J. Chem. Phys.* **109**, 3518 (1998).
133. T. Gerdts and U. Manthe, *Chem. Phys. Lett.* **295**, 167 (1998).
134. A. Kühl and W. Domcke, *Chem. Phys.* **259**, 227 (2000).
135. G. Stock and W. Domcke, *J. Phys. Chem.* **97**, 12466 (1993).
136. G. Stock, *J. Chem. Phys.* **103**, 2888 (1995).
137. A. Raab, G. Worth, H.-D. Meyer and L. Cederbaum, *J. Chem. Phys.* **110**, 936 (1999).
138. L. Kurtz, A. Hofmann and R. de Vivie-Riedle, *J. Chem. Phys.* **114**, 6151 (2001).
139. C. M. Tesch, L. Kurtz and R. de Vivie-Riedle, *Chem. Phys. Lett.* **343**, 633 (2001).
140. M. Morgen, W. Price, P. Ludowise and Y. Chen. *J. Chem. Phys.* **102**, 8780 (1995).
141. W. Domcke and H. Köppel, *Chem. Phys. Lett.* **140**, 133 (1987).
142. V. Stert, P. Farmanara and W. Radloff, *J. Chem. Phys.* **112**, 4460 (2000).
143. A. Goto, M. Fujii and M. Ito, *J. Chem. Phys.* **91**, 2268 (1986).
144. V. Blanchet, M. Z. Zgierski, T. Seideman and A. Stolow, *Nature (London)* **401**, 52 (1999).
145. G. Hirsch, R. Buenker and C. Petrongolo, *Mol. Phys.* **73**, 1085 (1991).
146. E. Leonardi, C. Petrongolo, G. Hirsch and R. Buenker, *J. Chem. Phys.* **105**, 9051 (1996).
147. F. Santoro and C. Petrongolo, *J. Chem. Phys.* **110**, 4419 (1999).
148. L. Seidner and W. Domcke, *Chem. Phys.* **186**, 27 (1994).
149. R. R. Birge, *Biochim. Biophys.* **1016**, 293 (1990).

150. M. Ottolenghi and M. Sheves, *Isr. J. Chem.* **35**, 1 (1995).
151. A. Bifone, H. J. M. de Groot and F. Buda, *J. Phys. Chem.* **B101**, 2954 (1997).
152. M. Garavelli, P. Celani, F. Bernardi, M. A. Robb and M. Olivucci, *J. Am. Chem. Soc.* **119**, 6891 (1997).
153. G. L. Loppnow and R. A. Mathies, *Biophys. J.* **54**, 35 (1988).
154. S. W. Lin, M. Groesbeek, I. van der Hoef, P. Verdegen, J. Lugtenburg and R. A. Mathies, *J. Phys. Chem.* **B102**, 2787 (1998).
155. S. Hahn and G. Stock, *J. Phys. Chem.* **B104**, 1146 (2000).
156. R. W. Schoenlein, L. A. Peteanu, Q. Wang, R. A. Mathies and C. V. Shank, *Science* **254**, 412 (1991).
157. Q. Wang, R. W. Schoenlein, L. A. Peteanu, R. A. Mathies and C. V. Shank, *Science* **266**, 422 (1994).
158. A. P. Shreve and R. A. Mathies, *J. Phys. Chem.* **99**, 7285 (1995).
159. R. B. Gerber, V. Buch and M. A. Ratner, *J. Chem. Phys.* **77**, 3022 (1982).
160. Z. Kotler and E. Neria, *Comput. Phys. Commun.* **63**, 234 (1991).
161. M. H. Beck, A. Jäckle, G. A. Worth and H.-D. Meyer, *Phys. Rep.* **324**, 1 (2000).
162. S. Hahn and G. Stock, *Chem. Phys.* **259**, 297 (2000).
163. S. Hahn and G. Stock, *J. Chem. Phys.* **116**, 1085 (2002).
164. G. Stock, *J. Chem. Phys.* **103**, 10015 (1995).
165. H. Wang, M. Thoss and W. H. Miller, *J. Chem. Phys.* **115**, 2979 (2001).
166. G. G. Koechendoerfer and R. A. Mathies, *J. Phys. Chem.* **100**, 14526 (1996).
167. I. P. Mercer, I. R. Gould and D. R. Klug, *J. Phys. Chem.* **B103**, 7720 (1999).
168. A. E. Cárdenas, R. Krems and R. D. Coalson, *J. Phys. Chem.* **A103**, 9469 (1999).
169. B. Balter, S. Dilthey, S. Hahn, M. Thoss and G. Stock, *J. Chem. Phys.* **119**, 4204 (2003).
170. C. D. Berweger, F. Müller-Plathe and W. F. van Gunsteren, *J. Chem. Phys.* **108**, 8773 (1998).

This page intentionally left blank

CHAPTER 18

NONADIABATIC QUANTUM DYNAMICS AND CONTROL STRATEGIES

Regina de Vivie-Riedle and Angelika Hofmann
Max-Planck-Institut für Quantenoptik
Hans-Kopfermann-Str.1, D-85748 Garching, Germany

Contents

1. Introduction

Observation of molecular processes in real time[1] and coherent control of the underlying quantum phenomena by means of external laser fields constitute the modern field of femtoscience[2]. The dynamics of chemical and physical processes can be monitored using ultrashort laser pulses and a variety of

molecular systems ranging from dimers to large biomolecules are studied in gas as well as in condensed phase.[3–9] In combination with quantum dynamical calculations, a detailed microscopic understanding of the reaction mechanisms can be achieved. Based on this knowledge, it is promising to design concepts for the control of molecular processes.

Theoretical control schemes were first proposed in the 1980s, working either in the frequency[10] or in the time domain.[11,12] Soon after, they could be realized experimentally by the groups of Gerber[13] and Zewail.[14] The applied pump-dump approach influences the system by varying the pump pulse parameters or the delay time between the pump and the probe pulse. An extension and combination of both concepts is the so called self-learning control, relying on closed-loop learning algorithms to optimize the laser fields. This leads to the concepts of optimal control theory (OCT) proposed and developed by the groups of Rabitz[15,16] and Tannor, Rice and Kosloff.[17,18] In contrast to the above mentioned schemes, the whole shape of the laser field is now optimized to guide the chemical reaction from the initial to the final state. First experimental implementations were realized using ultrafast pulse shaping techniques in combination with genetic algorithms,[19–21] followed by many experiments controlling more complex chemical reactions[22,23] and even biomolecules.[24]

In general, the optimal control strategies are designed to allow the control of a molecular system without previous knowledge of its properties. However, we prefer to base our control attempts on a previously obtained microscopic understanding of the underlying molecular mechanisms. This allows us to choose more subtle control targets and increase the efficiency of the overall process.

The capability to understand chemical reactions on the atomic scale and subsequently to design control strategies will be illustrated for photoinduced reactions via conical intersections. The ultrafast photochemical ring opening of cyclohexadiene,[25–28] which occurs within 200 fs in gas as well as in condensed phase, is taken as an example. This reaction has been studied quantum chemically,[29,34] by resonance-Raman spectroscopy[35,36] and by femtosecond spectroscopy[25–28] offering already a wealth of information. After photoexcitation to the S_2 state, the molecule decays within a few femtoseconds to the S_1 state, from where the relaxation to the ground state is mediated by at least two conical intersections.

To handle the complex reactive process, we first focus on the dynamics on the S_1 surface to study how the system evolves towards the conical intersections. Therefore we introduce a reduced set of reactive coordinates, develop the corresponding Hamiltonian and study the time evolution of the system by means of wavepacket propagations on the calculated *ab initio* potential reaction surface. In the following steps, we include the nonadiabatic coupling elements as well as the laser-molecule interaction to describe the complete relaxation process. The final aim is to drive the reaction systematically through either one or the other of the two conical intersections and thus to influence the resulting product distribution.

2. Laser-Molecule Interaction and Optimal Control Theory

To deal with photoinduced chemical processes involving several potential surfaces, we need to incorporate the interaction between the molecule and the incident light pulses into the quantum mechanical description. In the semiclassical dipole approximation, the time-dependent Schrödinger equation for two potential energy surfaces V_1 and V_2 coupled by the laser field reads as:

$$i\hbar\frac{\partial}{\partial t}\Psi(t) = \left\{\begin{pmatrix} T+V_1 & V_{12} \\ V_{21} & T+V_2 \end{pmatrix} - \varepsilon(t)\begin{pmatrix} 0 & \mu_{12} \\ \mu_{21} & 0 \end{pmatrix}\right\}\Psi(t) \qquad (1)$$

where T is the kinetic energy operator of the nuclei, V_{12} a possible time-independent coupling, and μ_{12} the transition dipole moment. In principle, the laser field $\varepsilon(t)$ can be varied in frequency, phase, and amplitude. In bound state problems, the prepared wavepacket consists of a coherent superposition of vibrational eigenstates:

$$\begin{aligned} |\Psi(t)\rangle &= c_1|\chi_1\rangle e^{i\omega_1 t} + c_2|\chi_2\rangle e^{i\omega_2 t} + \cdots \\ |\Psi(t)|^2 &= |c_1\chi_1|^2 + |c_2\chi_2|^2 + c_1^* c_2 \cos[(\omega_1-\omega_2)t]\chi_1^*\chi_2 + \cdots . \end{aligned} \qquad (2)$$

The coherence is reflected in the third term of the density function which is therefore called interference term. In our context we use the term "passive" control, if particular wavepackets are prepared in the Franck–Condon (FC) region by specific pump laser pulses which are then turned off. In this case, the weight of the partial waves does no longer change after the excitation, the further change is only due to the time-dependent phases, while the wavepackets evolve under the influence of the potential surfaces. The term "active" control is used, if the laser field remains turned on during the

intended reaction. In this case, the laser field guides the system from the initial state out of the FC region to the final outcome, which means that the coefficients c_i remain time-dependent during the whole reaction, allowing for a more direct control. Reactive systems complicate the situation, as they involve reactive coordinates without any periodicity. From experiment alone, it can often not be decided with certainty whether the observed signal coincides with the reaction path or just represents a movement orthogonal to it. Therefore theoretical investigations are extremely important to clarify the mechanisms.

Shapeable ultrashort laser pulses simultaneously provide many parameters to communicate with the internal motion and to achieve different objectives. Their optimal shape can be found by applying optimal control algorithms. Possible control objectives are complete population transfer between stable initial and final states, as well as maximization of expectation values, i.e. the preparation of a specially shaped wavepacket at a preselected area on the reaction surface.

The optimization of a laser field $\varepsilon(t)$ driving the system from an initial state $\Psi_i(0)$ at time $t = 0$ to the selected target area (defined by the projection operator X) at time $t = T$ can be reduced to maximizing the functional L given by:[16,37,38]

$$\begin{aligned} &L[\Psi_i(t), \Psi_f(t), \varepsilon(t)] \\ &= |\langle \Psi_i(T)|X|\Psi_i(T)\rangle|^2 - \alpha_0 \int_0^T \frac{|\varepsilon(t)|^2}{s(t)} dt \\ &- 4\,\mathrm{Re}\left\{ \langle \Psi_i(T)|X|\Psi_i(T)\rangle \cdot \int_0^T \langle \Psi_f(t)|\frac{i}{\mathrm{h}}[H - \mu\varepsilon(t)] + \frac{\partial}{\partial t}|\Psi_i(t)\rangle dt \right\} \end{aligned} \quad (3)$$

with the auxiliary wavefunction Ψ_f being a Lagrange multiplier. Variation of this functional leads to the following set of coupled differential equations:

$$\begin{aligned} \varepsilon(t) &= -\frac{s(t)}{\mathrm{h}\alpha_0} \cdot \mathrm{Im}\{\langle \Psi_i(T)|X|\Psi_i(T)\rangle \langle \Psi_f(t)|\mu|\Psi_i(t)\rangle\}, \\ i\mathrm{h}\frac{\partial}{\partial t}\Psi_i(t) &= [H - \mu\varepsilon(t)]\Psi_i(t) \quad \text{with} \quad \Psi_i(0) = \Phi_i, \\ i\mathrm{h}\frac{\partial}{\partial t}\Psi_f(t) &= [H - \mu\varepsilon(t)]\Psi_f(t) \quad \text{with} \quad \Psi_f(T) = X\Phi_i(T). \end{aligned} \quad (4)$$

The first one determines the optimal electric field in terms of the evolving wavepackets Ψ_i and Ψ_f, while the next two equations guarantee their compliance with the Schrödinger equation under the influence of the laser field $\varepsilon(t)$. To satisfy the demand of a smooth switch on and off behavior of the laserfield, the shape function $s(t)$ is introduced. The penalty factor α_0 limits the time-averaged laser intensity and T denotes the overall pulse duration. Solving this set of nonlinear differential equations iteratively, leads to a laser field which is optimized for the given task.

3. Choice of Dynamical Coordinates and Reduced Hamiltonian

In order to treat high-dimensional problems like the ring opening reaction of cyclohexadiene (CHD) quantum mechanically, the system under consideration has to be reduced. Instead of using a reaction path formalism,[39,40] we want to construct reaction surfaces for a reduced number of degrees of freedom. Therefore, we first need to select process-adapted coordinates which should describe the relevant structural changes and contain all modes active on the intrinsic timescale of the reaction, namely the femtosecond time regime.

The first step of our investigation mostly concentrates on the S_1 dynamics. As the molecular geometry continuously changes during the reaction, a large number of normal modes is involved, thus making the often used normal mode expansion unattractive. Instead we reduce the present system to reactive coordinates, each of which includes projections on several normal modes.

The selection procedure is based on a thorough analysis of the geometrical structures which are known to be important in the relevant region of the full coordinate space (e.g. the ground state geometry, the geometry of the conical intersections and intermediate structures involved).[29,31,32] We found the modes depicted in Fig. 1(a) to fulfill our requirements most appropriately.

Three C_2-symmetric modes are involved: The torsions β and γ as well as R, which denotes the length of the σ-bond where the ring opening occurs. The remaining asymmetric motion is represented by the angle α. These coordinates are suitable to describe the molecular geometries. However, for the dynamical description of the system, we transfer them into a set of only

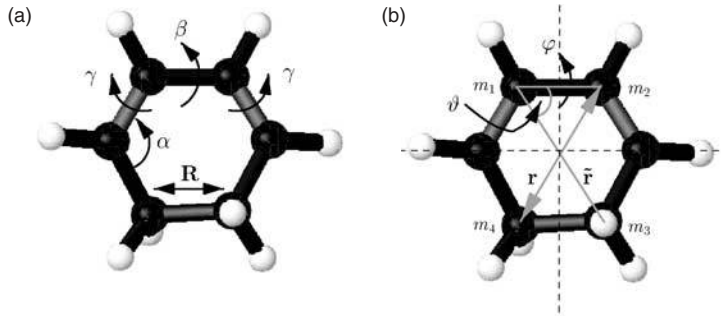

Fig. 1. Reduced set of coordinates for the ring opening of CHD.

three coordinates [see Fig. 1(b)], eliminating at the same time some of the derivative couplings in the kinetic part of the Hamiltonian.

The asymmetric coordinate is then represented by the length of the diagonal r, using a linear approximation for the angle α, whereas the second diagonal $\tilde{r}$ is kept constant. The C_2-symmetric angle ϑ describes a scissors-like motion leading to a stretching of the σ-bond. Finally, the remaining symmetric coordinate φ distorts the molecule further away from planarity, comprising both the torsions β and γ.

Starting with the full nuclear kinetic energy operator, a reduced Hamiltonian suitable for our reactive coordinates shall be derived. For this purpose, all H-atoms are assigned to the corresponding C-atoms. Then the masses of the remaining six atoms are contracted to four points of mass according to the broken lines in Fig. 1(b).

The mass of the C-atom located between m_1 and m_4 in the ring structure is split between these two (accordingly for m_2 and m_3). By eliminating the center of mass motion and transforming to mass-weighted Cartesian Jacobi coordinates, one is left with nine degrees of freedom, which are then transformed to the previously selected reactive coordinates. Considering the aforementioned assumptions, we finally arrive at a reduced Hamiltonian in three dimensions[a]:

$$T = -\frac{1}{2}\left\{\frac{B}{r}\partial_{rr}^2 + \left(\frac{B}{r^2} + \frac{\tilde{B}}{\tilde{r}}\right)\left(\frac{1}{\sin^2\vartheta}\partial_{\varphi}^2 + \partial_{\vartheta}^2 + \cot\vartheta\partial_{\vartheta}\right)\right\} \qquad (5)$$

[a] $\left(\partial_x = \dfrac{\partial}{\partial x}\right)$

where the inverse reduced masses B and $\tilde{B}$ are given by

$$B = \frac{1}{m_2} + \frac{1}{m_4},\ \tilde{B} = \frac{1}{m_1} + \frac{1}{m_3}. \tag{6}$$

4. Reaction Surfaces

As we describe the dynamics of a reactive chemical process, we do not use a harmonic expansion approach for the potential energy surface (PES), but instead we rely on *ab initio* calculations. The PES are determined for the relevant region of the coordinate space spanned by our selected coordinates, fully optimized with respect to the remaining internal coordinates. Subsequently, the data points are projected onto the reduced set of reactive coordinates, which can for the dynamical calculations be further restricted to (r, φ).

In the case of the CHD ring opening, we could benefit from previous calculations of ground and excited states[29,31,32,41,42] which were performed with GAUSSIAN94[43] on the CASSCF level. Stationary points like minima and transition states as well as the minimum energy path were evaluated in the complete coordinate space. For some single points, electron correlation corrections were performed on the CASPT2 level. According to Refs. 30 and 31, the influence of the electron correlation results in an overall decrease in energy and does not change the topology of the interacting surfaces.

All available *ab initio* data points are incorporated in our studies and additional calculations were performed to complete the reactive surfaces. After the projection onto the (r, φ)-coordinate space, the Thin-Plate-Spline method[44] is used to interpolate the 2D-surfaces. This allows their representation on arbitrary grids, which is necessary for the wavepacket propagations.

The resulting PES for ground and first excited state are shown in Fig. 2. The depicted area includes the equilibrium geometries of educt (cyclohexadiene) and product (cZc-hexatriene) states on the ground state, the Franck–Condon (FC) region, the transition region from the S_2 to the S_1 surface, and two conical intersections (CoIns) with the ground state, marked by circles. The intersection $\mathrm{CoIn}_{\mathrm{min}}$ is located at the energetically lowest point in the intersection space, slightly above the pericyclic minimum of the S_1 state, whereas the C_2-symmetric intersection C_2-CoIn lies energetically higher. The third circle marks the position where the transition from the S_2 to the

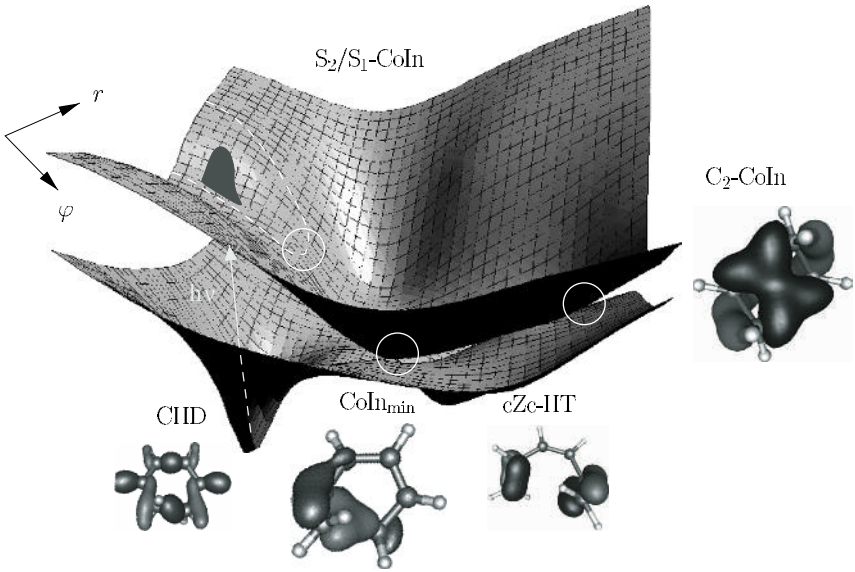

Fig. 2. Interpolated PES for the ground and excited state. The S_2 surface in the FC region is merged with the S_1 surface for the subsequent dynamics to form the shown excited state (see Sec. 3).

S_1 surface takes place and where our investigations of the S_1 dynamics start. Molecular orbitals mirroring the change in electron density are presented for the equilibrium geometries and the two S_1/S_0 CoIns. The molecular orbital, which mainly constitutes the σ-bond in CHD, contributes to the π-system in hexatriene and changes in between to form a three-center bond at $\mathrm{CoIn_{min}}$, involving three C-atoms, respectively a four-center bond at C_2-CoIn formed by four C-atoms (Fig. 2).

The two conical intersections are the final points of a recently found crossing seam[34] which is expected to lie in the energetically accessible region. As this crossing seam is not yet included in our calculations, its possible effects will be discussed in the context of the dynamics.

5. Quantum Dynamics on the S_1 Surface

The propagations start in the region of the S_2/S_1 crossing with several initial wavepackets of different widths. All of them are chosen to be of the

order of magnitude of the width of a ground state wavepacket of CHD for the following reasons:

Photoexcitation of cyclohexadiene by ultrashort laser pulses transfers the ground state wavepacket to the ^1B state. Starting from the FC region, the system is initially accelerated towards a conical intersection where it changes rapidly to the ^2A state. This S_2/S_1-CoIn is reached after a barrierless evolution within in a very short time. Therefore one may expect that the wavepacket is not altered too much up to this point and the widths for an initial Gaussian wavepacket (located at S_2/S_1-CoIn) can be assumed to be comparable to the width of the ground state wavepacket. (For the same reason, it seems to be appropriate to merge the S_2 and S_1 PES in this region.) A possible influence of the S_2/S_1-CoIn is taken into account by exploring a large range of widths with different ratios $\Delta r/\Delta\varphi$, representing different initial shapes. At the same time, this gives us a first estimate to what extent the dynamics can be influenced by initial state preparation.

The wavepacket is prepared far away from the S_1 equilibrium and instantaneously starts to oscillate with a period of about 15 fs along the coordinate φ. This oscillation period is in good agreement with the predicted S_1 frequency given in Ref. 39. Simultaneously, a kind of breathing mode starts to evolve in r-direction (with a "period" of about 10 fs) which first results in an additional broadening of the wavepacket along this direction. Due to the interference of both motions the wavepacket bifurcates (Fig. 3), with the result that both conical intersections with the ground state are reached. Although the high-energy parts of the wavepacket always have enough energy to reach C_2-CoIn, we note the different evolution depending on the initial preparation.

In a next step we now want to simulate the complete transfer to the ground state, for which both S_1 and S_0 potential surfaces together with their nonadiabatic coupling elements are needed.

6. Nonadiabatic Coupling Elements

The complete Hamiltonian including the nonadiabatic coupling between the two degenerate states reads:

$$H = \begin{pmatrix} T_n & K_{12} \\ -K_{12} & T_n \end{pmatrix} + \begin{pmatrix} V_1 & 0 \\ 0 & V_2 \end{pmatrix}, \tag{7}$$

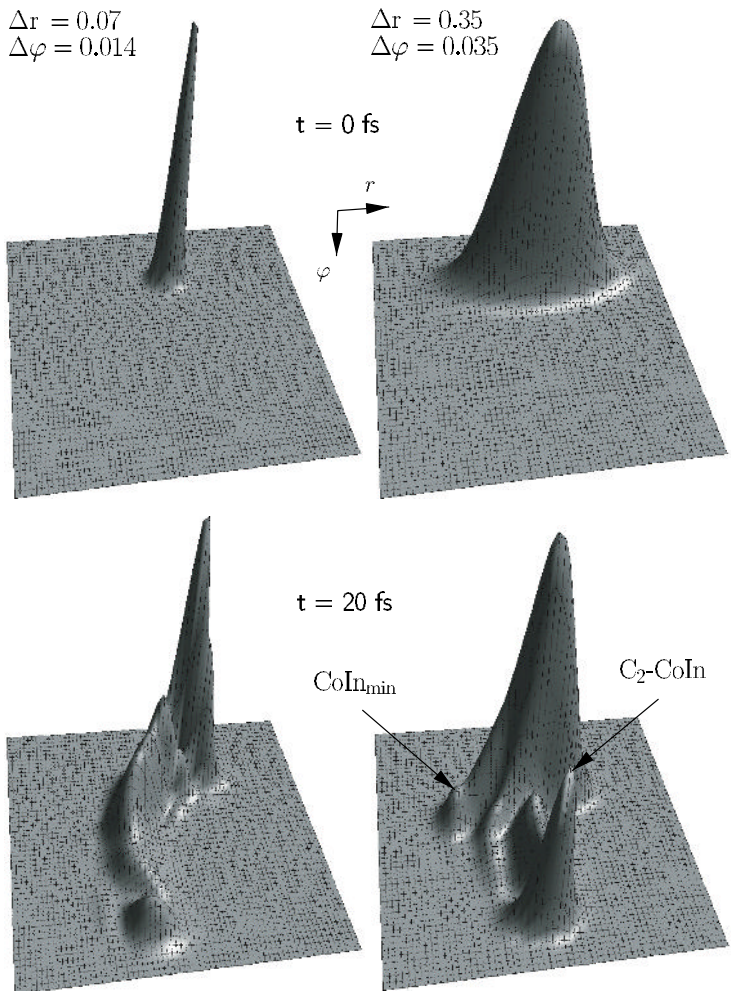

Fig. 3. Evolution of the wavepacket on the S_1 surface for two sets of initial widths. After 20 fs both conical intersections are reached and the wavepacket has started to bifurcate. The arrows denote the locations of the two conical intersections (left: $\mathrm{CoIn_{min}}$, right: C_2-CoIn).

where T_n denotes the kinetic energy of the nuclei and $V_{1,2}$ the adiabatic potentials. K_{12} is the nonadiabatic coupling term

$$K_{12} = -\sum_j \frac{1}{m_j} \left(f_{12}^{(j)} \partial_{x_j} + \frac{1}{2} g_{12}^{(j)} \right) \tag{8}$$

with m_j the mass of the jth atom and x_j Cartesian nuclear coordinates. This coupling would be neglected in Born–Oppenheimer approximation, but plays a crucial role in the vicinity of conical intersections.[45] The first- and second-order derivative (nonadiabatic) coupling elements for the electronic wavefunctions $\Phi_{1,2}$ are given by

$$f_{12}^{(j)} = \langle \Phi_1 | \partial_{x_j} \Phi_2 \rangle \quad \text{and} \quad g_{12}^{(j)} = \langle \Phi_1 | \partial_{x_j}^2 \Phi_2 \rangle. \tag{9}$$

Quantum mechanical calculations in the vicinity of conical intersections usually adopt the diabatic picture, where the derivative couplings need not be included directly (see, e.g. Ref. 46 and references therein). However, in our case this approach is not well suited. First of all, we need to consider large parts of both reaction surfaces, excited and ground state, to monitor the complete relaxation process. The coordinates adequate to describe the whole dynamics are most certainly not identical with those suitable for a diabatization around a single CoIn. Even worse, at least two separate conical intersections must be included.[47] In general, different CoIns in many dimensions (in our case 36) cannot be expected to join the same diabatic representation. Even if it were possible to construct a common diabatic description (which need not necessarily exist), we believe attempts in this direction are not promising. Besides ignoring the dynamical needs far away from the CoIns, they would most certainly be too cumbersome for dynamical calculations, whereby the difficulties increase with the number of dimensions and accessible intersections.

Thus, we are forced to stick to the adiabatic representation, which raises other problems. As the complete nuclear Schrödinger equation is solved for both coupled states, all quantum effects like interferences or phase effects are included (see Sec. 7), but one needs to keep track of the phases of the electronic wavefunctions while computing the nonadiabatic coupling elements (NAC). Additionally, we are faced with the strong localization of the NACs, which requires many grid points for the wavepacket propagation and makes the calculations quite time consuming.

The NACs were calculated at the CASSCF-level using MOLPRO[48] and then transformed to the reactive coordinates. As the coupling is large in some degrees of freedom not explicitly included in our wavepacket propagation, we project them onto our subspace spanned by r and φ. This is done for 9 additional coordinates which exhibit large coupling elements but are — apart from the coupling — not crucial for the dynamics. The

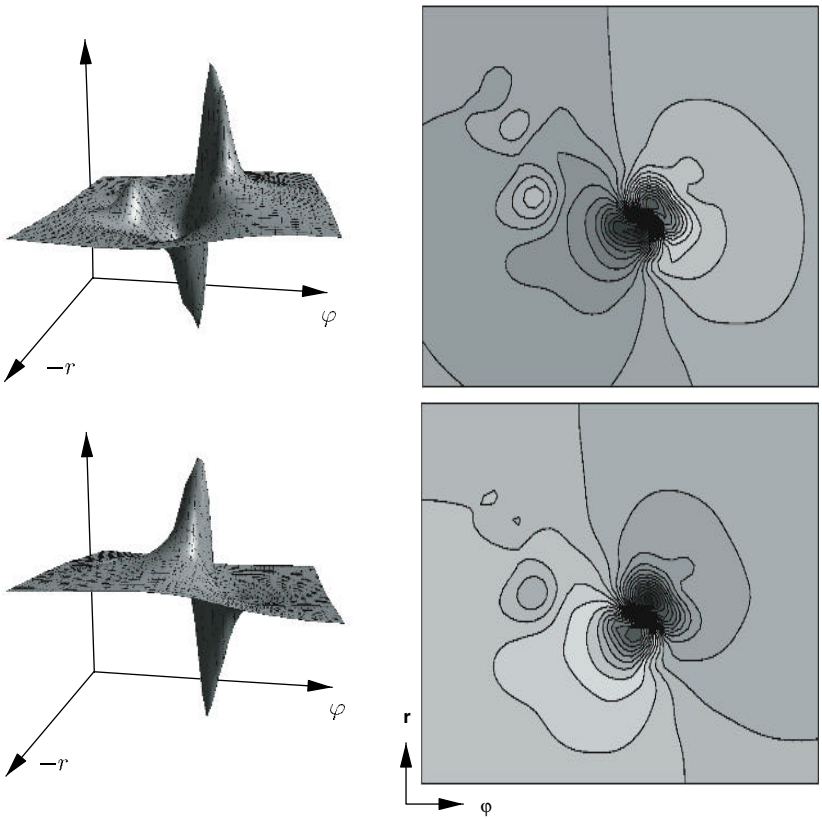

Fig. 4. Nonadiabatic coupling elements $\tilde{f}^{r}_{12}$(top) and $\tilde{f}^{\varphi}_{12}$(bottom) in the vicinity of $CoIn_{min}$. The plots extend over $\Delta r = 0.02$ Å, $\Delta\varphi = 0.42°$.

projection method is roughly similar to the procedure which was already employed for the PES;[47] it leads to a consistent description of the PES and NACs, which includes the "static" aspects and neglects only the "dynamic" contributions of the coordinates outside our subspace. The resulting NACs $\tilde{f}^{r}_{12}$ and $\tilde{f}^{\varphi}_{12}$ (already including the masses) in the vicinity of both CoIns are shown in Figs. 4 and 5. They exhibit the typical spiky behaviour; the coupling is even more localized around $CoIn_{min}$ (Fig. 4) in comparison with the symmetric intersection (Fig. 5). The smaller peaks present in $\tilde{f}^{r}_{12}$ ($CoIn_{min}$) originate from the projection and constitute contributions of the additional dimensions.

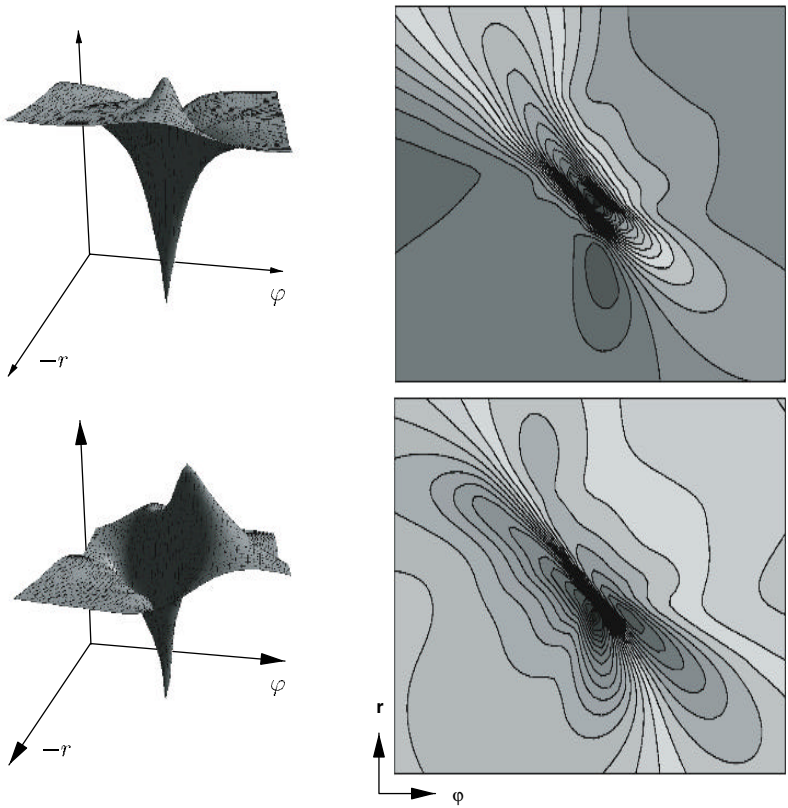

Fig. 5. Nonadiabatic coupling elements $\tilde{f}_{12}^{r}$(top) and $\tilde{f}_{12}^{\varphi}$ (bottom) around C_2-CoIn spanning a region of $\Delta r = 0.06\,\text{Å}$, $\Delta\varphi = 1°$.

The second derivative terms g_{12}^{j} of the nonadiabatic coupling are mostly much smaller than the first derivative terms and hence are usually believed to be negligible. However, their omission will lead to a non-hermitian Hamiltonian due to a non-hermitian coupling

$$K^{(j)} = \tilde{f}_{12}^{(j)} \partial_{q_j} \begin{pmatrix} 0 & 1 \\ -1 & 0 \end{pmatrix} \tag{10}$$

in the adiabatic description. This can be easily seen noting that the hermiticity of $K^{(j)}$ requires

$$K_{12}^{(j)} = \tilde{f}_{12}^{(j)} \partial_{q_j} \stackrel{!}{=} -(K_{12}^{j})^{\dagger} \tag{11}$$

and taking

$$\begin{aligned}(\tilde{f}_{12}^{(j)})^\dagger &= \tilde{f}_{12}^{(j)},\\ (\partial_{q_j})^\dagger &= -\partial_{q_j}\end{aligned} \tag{12}$$

into account.

As for an operator $A = BC$ with $B^\dagger = B$ and $C^\dagger = -C$

$$A^\dagger = -BC + [B, C] \tag{13}$$

holds, requiring A to be anti-hermitian ($A = -A^\dagger$) is equivalent to

$$[B, C] = 0. \tag{14}$$

In the actual case $B = \tilde{f}_{12}^{(j)}$ and $C = \partial_{q_j}$ do not commute, thus $K_{12}^{(j)}$ is not anti-hermitian and therefore the total Hamiltonian is not hermitian. To avoid this artifact, the non-hermitian part must be compensated which can be achieved by anti-symmetrizing $A = \tilde{f}_{12}^{(j)}\partial_{q_j}$:

$$\begin{aligned}\tilde{A} &= \frac{A - A^\dagger}{2} = A - \frac{1}{2}[B, C]\\ &\Rightarrow \tilde{A} = -\tilde{A}\end{aligned} \tag{15}$$

In the present case

$$\begin{aligned}[f, \partial_q]\Psi &= f\partial_q\Psi - (\partial_q f)\Psi - f\partial_q\Psi\\ &= -(\partial_q f)\Psi\end{aligned} \tag{16}$$

holds and we arrive at the following extension

$$\tilde{f}_{12}^{(j)}\partial_{q_j} \rightarrow \tilde{f}_{12}^{(j)}\partial_{q_j} + \tfrac{1}{2}\partial_{q_j}\tilde{f}_{12}^{(j)} \tag{17}$$

leading to

$$\tilde{K}_{12}^{(j)} \approx \sum_j \left(\tilde{f}_{12}^{(j)}\partial_{q_j} + \frac{1}{2}\partial_{q_j}\tilde{f}_{12}^{(j)}\right). \tag{18}$$

Identifying (6.11) to be the first part of the decomposition

$$g_{12}^{(j)} = \partial_{x_j} f_{12}^{(j)} + h_{12}^{(j)}; \tag{19}$$

we now only neglect the hermitian part $h_{12}^{(j)} = \langle\partial_{x_j}\Phi_1|\partial_{x_j}\Phi_2\rangle$ of $g_{12}^{(j)}$.

A detailed analysis reveals that boundary effects of the finite grid also play an important role. The derivative operator ∂_{q_j} on a finite grid is not

anti-hermitian and therefore the arising boundary effects have to be compensated to guarantee the hermiticity of the Hamiltonian.[49] Taking into account all these points, one can finally perform wavepacket propagations in the adiabatic representation. As the adiabatic description is sometimes questioned referring to the issue of geometrical phases and the need for *ad hoc* vector potentials, we will allow for a short excursion to clarify these questions.

7. Conical Intersections and Geometric Phases

In the context of conical intersections, the concept of the geometrical or Berry phase is often discussed with the claim that an adiabatic wavefunction would change its sign circulating around a conical intersection. However, the generality of this phase change is not given; it is a possible, but not a mandatory feature.

Following the line of arguments in Ref. 50, we will therefore illustrate the conditions for the occurrence of such a phase jump, going back to the transformation between diabatic and adiabatic wavefunctions:

$$\begin{pmatrix} \Phi_1^{\text{adiab}} \\ \Phi_2^{\text{adiab}} \end{pmatrix} = \begin{pmatrix} \cos\theta & \sin\theta \\ -\sin\theta & \cos\theta \end{pmatrix} \begin{pmatrix} \Phi_1^{\text{diab}} \\ \Phi_2^{\text{diab}} \end{pmatrix}. \tag{20}$$

The angle θ is given by

$$\begin{aligned} \cos 2\theta &= \frac{\Delta H^{\text{diab}}}{D} \\ \sin 2\theta &= \frac{H_{12}^{\text{diab}}}{D} \end{aligned} \tag{21}$$

with

$$\Delta H^{\text{diab}} = \frac{H_{11}^{\text{diab}} - H_{22}^{\text{diab}}}{2},\ D = \sqrt{(\Delta H^{\text{diab}})^2 + (H_{12}^{\text{diab}})^2}. \tag{22}$$

If the electronic wavefunction is chosen to be real, the two conditions for degeneracy, $\Delta H^{\text{diab}} = 0$ and $H_{12}^{\text{diab}} = 0$, define two F-1-dimensional hypersurfaces whose F-2-dimensional intersection surface represents the space of degeneracy.

Equations (20) and (22) lead to two statements:

- The adiabatic wavefunction is dominated by different diabatic states in the two subspaces separated by the hypersurface $\Delta H^{\text{diab}} = 0$.

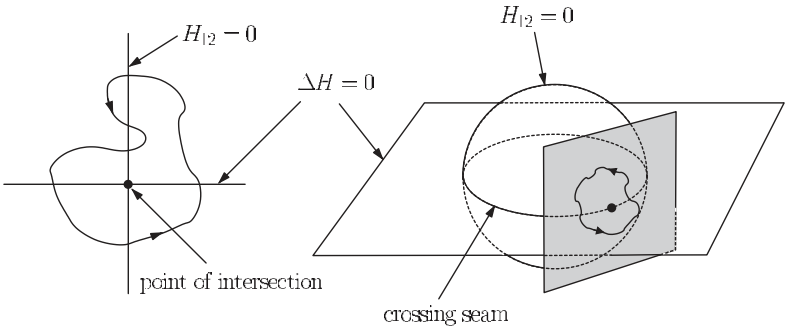

Fig. 6. Example of closed pathways around a conical intersection. In two dimensions (left), the space of degeneracy reduces to a single point and a phase jump is observed for the corresponding adiabatic wavefunction. In the three-dimensional example (right) the space of degeneracy of the two hypersurfaces $H_{12}^{\mathrm{diab}} = 0$ (sphere) and $\Delta H^{\mathrm{diab}} = 0$ (plane) is a line; a tangential plane (gray) will touch the sphere and therefore the crossing seam in only one single point. In this plane a closed path around the conical intersection will pass the surface $\Delta H^{\mathrm{diab}} = 0$ twice, but the $H_{12}^{\mathrm{diab}} = 0$ sphere not at all, and therefore no phase jump will take place.

- The smaller of the two diabatic coefficients changes sign at $H_{12}^{\mathrm{diab}} = 0$.

In summary, the following phase theorem holds:[50]

Along an arbitrarily shaped closed path around a conical intersection, the adiabatic wavefunction only changes sign if the hypersurface $H_{12}^{\mathrm{diab}} = 0$ is passed an odd number of times on each side of $\Delta H^{\mathrm{diab}} = 0$.

In the easiest case of a zero-dimensional space of degeneracy in a two-dimensional coordinate space — often referred to in the literature — this condition is always fulfilled (see Fig. 6). On the contrary, it is not possible for higher dimensional problems to make a prediction concerning the resulting phase without detailed knowledge of the two hypersurfaces $H_{12}^{\mathrm{diab}} = 0$ and $\Delta H^{\mathrm{diab}} = 0$. To illustrate this statement, a three-dimensional example without phase jump is shown in Fig. 6.

We want to point out that the CHD model outlined in Sec. 3 is not a truly two-dimensional case. Instead, it is a 36 dimensional problem projected onto two dimensions which do not coincide with the diabatic branching space of the conical intersections. For this reason, it remains unclear whether to expect a phase jump or not.

Controversial opinions can be found whether or not an *ad hoc* vector potential has to be introduced into the Schrödinger equation to account

for the geometric phase. Therefore we will shortly present the essentials according to Ref. 51.

First of all, the nonadiabatic coupling terms themselves can be regarded as such a vector potential. With the decomposition of Eq. (18), the coupled Born–Oppenheimer equations become[b]:

$$-\frac{1}{2m}\nabla^2\Psi + \left(V - \frac{1}{2m}f^2 - E\right)\Psi - \frac{1}{2m}(2f\cdot\nabla + \nabla f)\Psi = 0 \tag{23}$$

which can also be written as

$$\frac{1}{2m}(\boldsymbol{p} - \mathrm{i}f)^2\Psi + (V - E)\Psi = 0. \tag{24}$$

From Eq. (24) it becomes immediately clear that $\mathrm{i}f$ can be regarded as a SU(2)-vector potential.

Another source of confusion is based on the fact that often only one Born–Oppenheimer surface is used for the adiabatic approach. This ansatz is justified either in the absence of conical intersections or if the degeneracy occurs at inaccessibly high energies and one is only interested in low-energy dynamics encircling but not crossing it (e.g. pseudorotation). Following this adiabatic approach, the off-diagonal nonadiabatic coupling elements shall be transformed into diagonal elements. For this purpose, the unitary transformation matrix G must diagonalize the matrix f; in this case the coupled equations for the resulting wavefunction $\chi = G^{-1}\Psi$ (see Ref. 50) read as

$$\left(-\frac{1}{2m}\nabla^2 + \tilde{V}_1 - E \pm \frac{i}{2m}(2f_{12}\cdot\nabla + \nabla f_{12})\right)\chi_1 - \frac{1}{2}(\tilde{V}_2 - \tilde{V}_1)(\chi_1 - \chi_2) = 0 \tag{25}$$

where $\tilde{V}_k = V_k - \frac{1}{2m}f_{12}^2$. If the energy of the system is low enough, such that the excited state is nearly unpopulated, then $|\chi_1 - \chi_2| = |\Psi_2|$ can be neglected and Eq. (25) becomes nearly decoupled:

$$\left(\frac{1}{2m}(\boldsymbol{p} \pm f_{12})^2 + (V_1 - E)\right)\chi_j = 0, \quad j = 1, 2. \tag{26}$$

Now it is easy to show that both equations give the same solution and it is thus sufficient to consider only one of them. In this single surface approximation, f_{12} represents the vector potential which is necessary to include

[b]For the sake of simplicity, all masses are taken to be equal, f is the matrix of the coupling vectors f_{kl}, and $h_{kl} = \langle\nabla\Phi_k|\nabla\Phi_l\rangle = \sum_m\langle\nabla\Phi_k|\Phi_m\rangle\langle\Phi_m|\nabla\Phi_k\rangle = \sum_m f^*_{mk}f_{ml} = (f^2)_{kl}$.

phase effects due to the actually coupled higher-lying potential surface. In contrast, we treat the complete coupled nuclear Schrödinger equations and thus possible phase effects are included naturally without additional approximations (see also Ref. 52).

8. Wavepacket Dynamics on the Coupled S_1/S_0 Potential Surfaces

The propagation on the non-adiabatically coupled PES starts at the S_2/S_1 CoIn with a Gaussian wavepacket roughly simulating the situation after instantaneous excitation (widths: $\Delta r = 0.07$ au, $\Delta\varphi = 0.014$ au, for the choice of initial conditions, see Ref. 47). By the time the system enters the S_1 surface, it has already gained momentum along φ, according to the energy gap between the FC point and the S_2/S_1 CoIn. Therefore, our initial wavepacket is provided with the corresponding amount of momentum.

Figure 7 shows several snapshots of the excited and ground state wavefunction. For the chosen initial conditions, the crossover to the ground state already starts after approx. 10 fs. While the wavepacket is oscillating back and forth in the excited state, it drips through both CoIns to the S_0 state (the snapshots at 14 and 20 fs show for both CoIns the largest peak appearing on the ground state surface).

The resulting depopulation of the excited state is depicted in Fig. 8 (bottom, full line). To study the effect of each CoIn separately, the same initial wavepacket is propagated again, but this time with only one or the other CoIn active (the NAC in the vicinity of the other CoIn is set to zero). As can be seen in Fig. 8, the return to the ground state proceeds predominantly via the C_2-CoIn with the width of the steps corresponding to the oscillation in the excited state. This dominance is also reflected in the "peak size" of the wavepacket appearing in the ground state after passing the CoIns, see Fig. 7.

Closing artificially the symmetric intersection reveals that the crossover to the ground state at the $\mathrm{CoIn}_{\mathrm{min}}$ also takes place in a stepwise manner, but with a much smaller coupling efficiency (Fig. 8 top). Consequently, the return to the ground state is very slow. This behavior is due to the fact that the nonadiabatic coupling region around the $\mathrm{CoIn}_{\mathrm{min}}$ is roughly ten times smaller compared to the vicinity of the C_2-CoIn. The integral $\int r^2 dr d\varphi \tilde{f}_{12}^{r,\varphi}$ is 20–30 times larger for the symmetric intersection, although

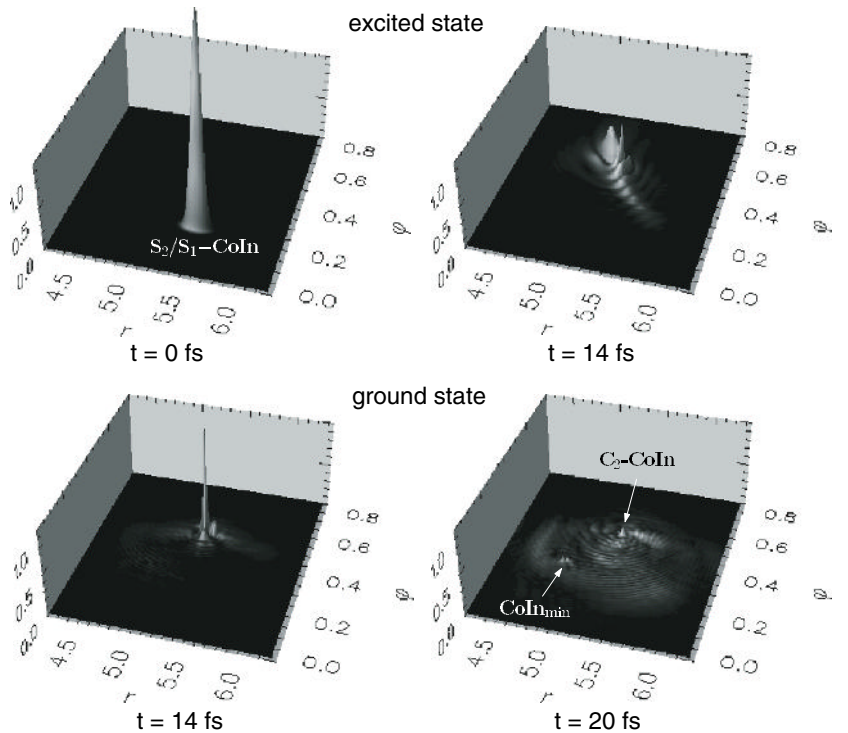

Fig. 7. Snapshots of the wavepacket dynamics passing the CoIns. The upper row shows the probability density in the excited state, the lower one in the ground state (z-scale constant in each row).

the absolute value of the NAC is larger in the vicinity of the asymmetric CoIn. In consequence, most of the transfer to the ground state proceeds via the C_2-CoIn, whereas $CoIn_{min}$ plays only a minor role.

The wavepacket propagation on the coupled surfaces was performed for 80 fs. During that time, more than 20% of the excited-state wavepacket have returned to the electronic ground state. Thus the timescale lies in the same order of magnitude as several experiments which reported relaxation times around 250 fs.[25,28]

After returning to the ground state, the wavepacket bifurcates again. From both conical intersections, pathways lead to CHD as well as to

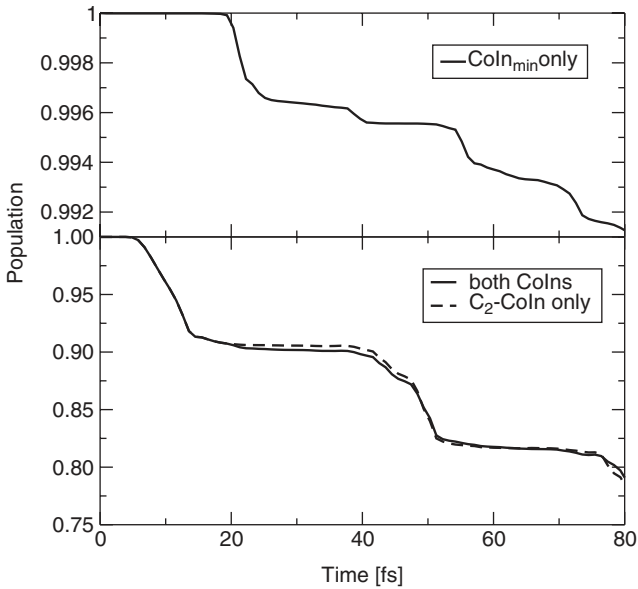

Fig. 8. Norm of the excited state. The full line in the lower panel shows the full calculation; for the dashed line the $CoIn_{min}$ channel has artificially been closed. The upper plot stems from a run where the transition was only allowed at the asymmetric intersection. The steps are due to the oscillation of the excited state wavepacket.

hexatriene, however the product ratio differs. The resulting product yield is estimated by gathering all the parts of the hot ground state wavepacket which reach one or the other equilibrium geometry. For the chosen initial conditions, we find a ratio of 60 : 40 (CHD : HT) after 80 fs. Artificially closing $CoIn_{min}$ has no effect, whereas closing the dominant C_2-CoIn slows down the reaction velocity and changes the ratio to 70 : 30. The calculated rate as well as the ratio 60 : 40 agree very well with the experimental findings of 40% hexatriene (see Refs. 27, 28 and 35 and references therein).

Recent quantum chemical calculations proved the existence of a whole crossing seam between $CoIn_{min}$ and C_2-CoIn.[41] However, as the characteristic features of the excited state surface are not altered, the branching of the excited wavepacket will probably remain the dominant feature and the main effect of the crossing seam will be an enhancement of the transfer rate and therefore an acceleration of the relaxation process.

9. Inclusion of the Laser Pulse and Control Strategies

After understanding the S_1/S_0 dynamics, we extend our investigations towards the FC-region to directly study the effect of the laser excitation.

Two pulses with a FWHM of 11 and 180 fs were selected for excitation. As expected from the previous S_1/S_0 studies, the prepared excited wavepackets show different subsequent time evolutions. The longer pulse results in a broader wavepacket distribution on the S_1 surface, spreading over large areas of the reaction surface, whereas the short fs-pulse excitation results in a more localized wavepacket, dominantly accelerated and focused into the C_2-CoIn. Following the relaxation transfer of this localized wavepacket reveals that nearly the complete transfer occurs through the symmetric conical intersection. Thus the influence of changing only one parameter, the pump-pulse duration, points to the possibility to control the molecular dynamics and thereby enhance the transfer through one of the conical intersections.

To gain more — in our sense "active" — control over molecular systems, we can employ OCT for the control of expectation values [Eq. (3)]. As a performance test we arbitrarily selected three different positions on a bound 2D potential surface (Fig. 9) with a projection operator X defining ellipsoidal areas (broken line). The objective is to localize a wavepacket at these selected positions. The resulting final wavepackets and corresponding optimized pulse shapes show that it is possible to localize wavepackets at nearly any desired position using specific optimal pulses. This concept was already applied to the NaH_2 collision complex to focus an excited state wavepacket to a conical intersection and to control the transfer through it.[53] In the future we intend to apply the same concept of active control to drive the cyclohexadiene-hexatriene system selectively through either one of its conical intersections and to control thereby the distribution of product states and the velocity of the relaxation process.

10. Conclusion

The photoinduced electrocyclic ring opening reaction of cyclohexadiene provides an interesting example of a complex ultrafast reaction mediated by multiple conical intersections. For the short time domain, we derived a realistic dynamical model and performed quantum dynamical calculations.

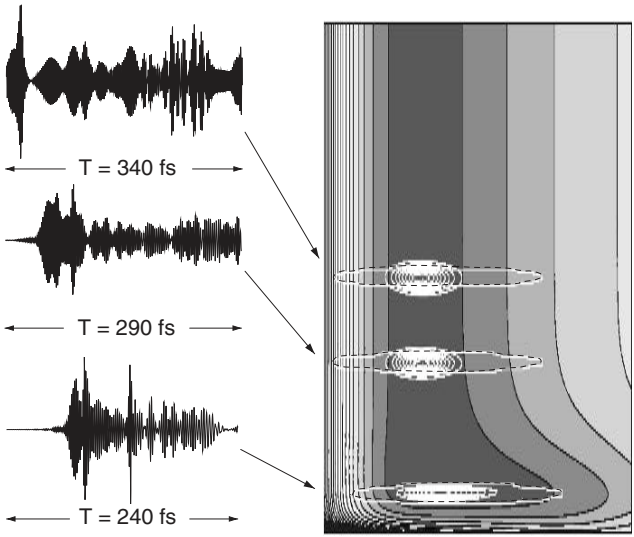

Fig. 9. Demonstration of the capability of the OCT to create wavepackets localized in nearly arbitrary regions.

Thereby it became evident that the description of such a reactive system absolutely needs *ab initio* ingredients such as reaction surfaces and nonadiabatic coupling elements to set a realistic stage for the subsequent wavepacket propagation. Furthermore, it was necessary to adapt the adiabatic approach for the coupled dynamics in order to describe simultaneously the transfer through multiple conical intersections. On this basis it was possible to obtain a microscopic understanding of the relaxation process.

The return to the ground state takes place dominantly through the symmetric conical intersection, contrarily to the predictions solely based on potential energy arguments which would prefer the energetically more favourable $\mathrm{CoIn}_{\mathrm{min}}$. Artificially closing either one of them allowed a detailed analysis of the final product yield. As expected from the topology of the ground state potential surface, the product distribution as well as the reaction velocity are sensitive to the conical intersection passed.

These findings open the possibility to control the final product yield and the reaction rate by guiding the wavepacket selectively through one of the conical intersections. Thus the analysis of the reaction mechanism allows us to define intermediate control objectives in contrast to taking a

final product as the target. The possibility to define intermediate control objectives may reduce the complexity of the optimal control field.

Including the laser pulse excitation and varying its pulse duration, we could underline our first assumption that coherent control should be possible. A short femtosecond pulse nearly drives the whole wavepacket through the symmetric C_2-CoIn. Though multiple reactive coordinates are included, the coherence of the initially prepared wavepacket survives to refocus again and again at the C_2-CoIn. For a model system we could show that it is possible to localize an arbitrarily shaped wavepacket at nearly any desired position of a potential hypersurface and that control of the product yield through a conical intersection can be achieved. In a future step we will transfer this OCT concept to the ring opening of CHD and its derivatives to actively control the product yield and the reaction velocity.

Acknowledgments

We want to thank Dorothee Geppert who has performed part of the dynamic and control calculations. Most of the work has been carried out on the CRAY T3E and the SP-Cluster of the RZG in Garching with financial support by the MPG and the DFG.

References

1. A. H. Zewail, *J. Phys. Chem.* **A104**, 5660 (2000).
2. H. Rabitz, R. de Vivie-Riedle, M. Motzkus and K. Kompa, *Science* **288**, 824 (2000).
3. J. Manz and L. Wöste, *Femtosecond Chemistry*, Vols. I and II (Verlag Chemie Weinheim, 1995).
4. M. Chergui, *Femtosecond Chemistry and Physics of Ultrafast Processes* (World Scientific, Singapore, 1996).
5. T. Baumert, M. Grosser, R. Thalweiser and G. Gerber, *Phys. Rev. Lett.* **67**, 3753 (1991).
6. R. S. Berry, V. Bonacic-Koutecký, Th. Leisner, J. Manz, B. Reischl-Lenz, H. Ruppe, S. Rutz, E. Schreiber, St. Vajda, R. de Vivie-Riedle, S. Wolf and L. Wöste, *Adv. Chem. Phys.* **101**, 101 (1997).
7. S. Wolf, G. Sommerer, S. Rutz, E. Schreiber, T. Leisner and L. Wöste, *Phys. Rev. Lett.* **74**, 4177 (1995).
8. S. Lochbrunner, A. J. Wurzer and E. Riedle, *J. Chem. Phys.* **112**, 10699 (2000).
9. M. L. Groot, M. H. Vos, I. Schlichting, F. van Mourik, M. Joffre, J. C. Lambry and J. L. Martin, *PNAS* **99**, 1323 (2002).

10. P. Brumer and M. Shapiro, *Chem. Phys. Lett.* **126**, 541 (1986).
11. D. J. Tannor and S. A. Rice, *J. Chem. Phys.* **83**, 5013 (1985).
12. D. J. Tannor, R. Kosloff and S. A. Rice, *J. Chem. Phys.* **85**, 5805 (1986).
13. T. Baumert and G. Gerber, *Isr. J. Chem.* **34**, 103 (1985).
14. A. H. Zewail, *Adv. Chem. Phys.* **101**, 3 (1997).
15. W. Zhu, J. Botina and H. Rabitz, *J. Chem. Phys.* **108**, 1953 (1998).
16. W. Zhu and H. Rabitz, *J. Chem. Phys.* **109**, 385 (1998).
17. I. R. Sola, J. Santamaria and D. J. Tannor, *J. Phys. Chem.* **102**, 4301 (1998).
18. R. Kosloff, S. A. Rice, P. Gaspard, S. Tersigni and D. J. Tannor, *Chem. Phys.* **139**, 201 (1989).
19. C. J. Bardeen, V. V. Yakolev, K. R. Wilson, C. D. Carpenter, P. M. Weber and W. S Warren, *Chem. Phys. Lett.* **280**, 151 (1997).
20. A. Assion, T. Baumert, T. Brixner, B. Kiefer, V. Seyfried, M. Strehle and G. Gerber, *Science*, **282**, 919 (1998).
21. Š. Vajda, A. Bartelt, E. C. Kaposta, T. Leisner, C. Lupulescu, S. Minetmoto, P. Rosendo-Francisco and L. Wöste, *Chem. Phys.* **267**, 231 (2001).
22. R. J. Levis, G. M. Menkir and H. Rabitz, *Science* **292**, 709 (2001).
23. T. Brixner, N. H. Damrauer, P. Niklaus and G. Gerber, *Nature* **414**, 57 (2001).
24. Jennifer L. Herek, Wendel Wohlleben, Richard J. Cogdell, Dirk Zeidler and M. Motzkus, *Nature* **417**, 533 (2002).
25. S. A. Trushin, W. Fuß, T. Schikarski, W. E. Schmid and K. L. Kompa, *J. Chem. Phys.* **106**, 9386 (1997).
26. S. Lochbrunner, W. Fuß, W. E. Schmid and K. L. Kompa, *J. Chem. Phys.* **A102**, 9334 (1998).
27. S. H. Pullen, N. A. Anderson, L. A. Walker II and R. J. Sension, *J. Chem. Phys.* **107**, 4985 (1997).
28. S. H. Pullen, N. A. Anderson, L. A. Walker II and R. J. Sension, *J. Chem. Phys.* **108**, 556 (1998).
29. P. Celani, F. Bernardi, M. A. Robb and M. Olivucci, *J. Phys. Chem.* **100**, 19364 (1996).
30. P. Celani, S. Ottani, M. Olivucci, F. Bernardi and M. A. Robb, *J. Am. Chem. Soc.* **116**, 10141 (1994).
31. M. Garavelli, F. Bernardi, P. Celani, M. A. Robb and M. Olivucci, *J. Photochem. Photobiol.* **A114**, 109 (1998).
32. M. Garavelli, F. Bernardi, M. Olivucci, T. Vreven, S. Klein, P. Celani and M. A. Robb, *Faraday Discuss.* **110**, 51 (1998).
33. M. Garavelli, P. Celani, M. Fato, M. J. Bearpark, B. R. Smith, M. Olivucci and M. A. Robb, *J. Phys. Chem.* **A101**, 2023 (1997).
34. M. Garavelli, C. S. Page, P. Celani, M. Olivucci, W. E. Schmid, S. A. Trushin and W. Fuß, *J. Phys. Chem.* **A105**, 4458 (2001).
35. M. O. Trulson, G. D. Dollinger and R. A. Mathies, *J. Chem. Phys.* **90**, 4274 (1989).

36. P. J. Reid, S. J. Doig, S. D. Wickham and R. A. Mathies, *J. Am. Chem. Soc.* **115**, 4754 (1993).
37. R. de Vivie-Riedle, K. Sundermann and Marcus Motzkus, *Faraday Discuss.* **113**, 303 (1999).
38. R. de Vivie-Riedle and K. Sundermann, *Appl. Phys.* **B71**, 285 (2000).
39. W. H. Miller, N. C. Handy and J. E. Adams, *J. Chem. Phys.* **72**, 99 (1980).
40. B. A. Ruf and W. H. Miller, *J. Chem. Soc.* **84**, 1523 (1988).
41. M. Olivucci, private communication.
42. M. Garavelli, private communication.
43. M. J. Frisch, G. W. Trucks, H. B. Schlegel, P. M. W. Gill, B. G. Johnson, M. A. Robb, J. R. Cheeseman, T. Keith, G. A. Petersson, J. A. Montgomery, K. Raghavachari, M. A. Al-Laham, V. G. Zakrzewski, J. V. Ortiz, J. B. F. and J. Cioslowski, B. B. Stefanov, A. Nanayakkara, M. Challacombe, C. Y. Peng, P. Y. Ayala, W. Chen, M. W. Wong, J. L. Andres, E. S. Replogle, R. Gomperts, R. L. Martin, D. J. Fox, J. S. Binkley, D. J. Defrees, J. Baker, J. P. Stewart, M. Head-Gordon, C. Gonzalez and J. A. Pople, *GAUSSIAN94, Revision E.2* (Gaussian, Inc., Pittsburgh, PA, 1995).
44. R. Franke, *Comput. Math. Appl.* **8**, 273 (1982).
45. D. R. Yarkony, *J. Chem. Phys.* **114**, 2601 (2001).
46. W. Domcke and G. Stock, *Adv. Chem. Phys.* **100**, 1 (1997).
47. A. Hofmann and R. de Vivie-Riedle, *J. Chem. Phys.* **112**, 5054 (2000).
48. H.-J. Werner and P. Knowles, *MOLPRO, Version 2000.1* (1999).
49. A. Hofmann and R. de Vivie-Riedle, *Chem. Phys. Lett* **34**, 299 (2001).
50. G. J. Atchity and K. Ruedenberg, *J. Chem. Phys.* **110**, 4208 (1999).
51. M. Baer, *Chem. Phys.* **259**, 123 (2000).
52. T. J. Martinez, *Chem. Phys. Lett.* **272**, 139 (1997).
53. D. Geppert, *Diploma Thesis* (LMU Muenchen, 2001).

This page intentionally left blank

INDEX